BIODEGRADABLE MATRICES AND COMPOSITES

EDITED BY: Alessandro Pegoretti, Yu Dong and Miroslav Slouf

frontiers Research Topics

About Frontiers

Frontiers is more than just an open-access publisher of scholarly articles: it is a pioneering approach to the world of academia, radically improving the way scholarly research is managed. The grand vision of Frontiers is a world where all people have an equal opportunity to seek, share and generate knowledge. Frontiers provides immediate and permanent online open access to all its publications, but this alone is not enough to realize our grand goals.

Frontiers Journal Series

The Frontiers Journal Series is a multi-tier and interdisciplinary set of open-access, online journals, promising a paradigm shift from the current review, selection and dissemination processes in academic publishing. All Frontiers journals are driven by researchers for researchers; therefore, they constitute a service to the scholarly community. At the same time, the Frontiers Journal Series operates on a revolutionary invention, the tiered publishing system, initially addressing specific communities of scholars, and gradually climbing up to broader public understanding, thus serving the interests of the lay society, too.

Dedication to Quality

Each Frontiers article is a landmark of the highest quality, thanks to genuinely collaborative interactions between authors and review editors, who include some of the world's best academicians. Research must be certified by peers before entering a stream of knowledge that may eventually reach the public - and shape society; therefore, Frontiers only applies the most rigorous and unbiased reviews.
Frontiers revolutionizes research publishing by freely delivering the most outstanding research, evaluated with no bias from both the academic and social point of view. By applying the most advanced information technologies, Frontiers is catapulting scholarly publishing into a new generation.

What are Frontiers Research Topics?

Frontiers Research Topics are very popular trademarks of the Frontiers Journals Series: they are collections of at least ten articles, all centered on a particular subject. With their unique mix of varied contributions from Original Research to Review Articles, Frontiers Research Topics unify the most influential researchers, the latest key findings and historical advances in a hot research area! Find out more on how to host your own Frontiers Research Topic or contribute to one as an author by contacting the Frontiers Editorial Office: researchtopics@frontiersin.org

BIODEGRADABLE MATRICES AND COMPOSITES

Topic Editors:
Alessandro Pegoretti, University of Trento, Italy
Yu Dong, Curtin University, Australia
Miroslav Slouf, Institute of Macromolecular Chemistry (ASCR), Czechia

EDITORS BIOGRAPHY

Prof. Alessandro Pegoretti

Full Professor, Head of Polymers and Composites Laboratory

Department of Industrial Engineering, University of Trento,
via Sommarive 9, 38123 Trento, Italy

Webpage: http://www.ing.unitn.it/~pegorett/

Email: alessandro.pegoretti@unitn.it

Phone: +39 0461 282452

Biography

Prof. Alessandro Pegoretti is currently full Professor at the Department of Industrial Engineering, University of Trento. The main aim of his research activity is to investigate the structure-properties relationships in polymer, polymer blends, composites and nanocomposites, with particular attention to their mechanical behavior. Main fields of interests are deformation, yield and fracture mechanics of polymers and composites, processing and characterization of multiphase polymeric materials (micro- and nanocomposites, and blends), durability of polymeric and composite materials, environmentally sustainable polymers and composites (biodegradable, from renewable resources, fully recyclable), polymers and composites with functional properties (electrical conductivity, shape memory, strain and damage monitoring, self-healing, etc.). He is an author or co-author of more than 240 peer-reviewed journal articles, 12 book chapters and 3 patents. He serves as Specialty Chief Editor of Frontiers in Materials - Polymeric and Composite Materials section, associate editor of the Journal of Reinforced Polymers and Composites. He is member of the editorial board member of various Journals such as Express Polymer Letters, Composite Interfaces, Materials, Journal of Composite Science, Applied Sciences, International Journal of Polymer Science, Journal of Applied Biomaterials and Functional Materials, as well as Journal of Nanomaterials.

Dr. Yu Dong

Senior Lecturer in Mechanical Engineering

School of Civil and Mechanical Engineering, GPO Box U 1987, Curtin University, WA 6845, Australia

Webpage: https://staffportal.curtin.edu.au/staff/profile/view/Y.Dong/

Email: y.dong@curtin.edu.au
Phone: +61 8 92669055

Fax: +61 8 92662681

Biography

Dr. Yu Dong is currently a Senior Lecturer within the School of Civil and Mechanical Engineering at Curtin University, Perth, Australia. His main research interests are polymer nanocomposites, electrospun nanofibers/nanocomposites, green composites, nanomaterial processing and characterization, micromechanical modeling, finite element analysis, statistical design of experiments and engineering education. He has published over 70 peer-reviewed journal articles and 30 fully referred conference papers, written 10 book chapters and edited 3 technical books. He serves as an associate editor of Frontiers in Materials (Polymeric and Composite Materials section) and Applied Nanoscience, Springer Nature with the specialty recognition of nanomaterials and nanocomposites.

Dr. Miroslav Slouf

Senior Research Fellow, Head of Department of Polymer Morphology

Institute of Macromolecular Chemistry, Czech Academy of Sciences, Heyrovskeho nam. 2, 16206 Prague 6, Czech Republic

Webpage: https://www.imc.cas.cz/en/research/research-departments/polymer-materials-and-technologies/polymer-morphology/staff

Email: slouf@imc.cas.cz

Phone: +420 296 809 291

Biography

Dr. Miroslav Slouf is currently a Senior Research Fellow and Head of Department of Polymer Morphology at the Institute of Macromolecular Chemistry, the Czech Academy of Sciences, in Prague, Czech Republic, as well as Associate Professor at the Faculty of Chemistry at the Brno University of Technology, Brno, Czech Republic. He works in the field of morphology, electron microscopy and micromechanical properties of polymer materials. His main research interests comprise biodegradable polymer blends for local release of antibiotics, ultrahigh molecular weight polyethylene for total joint replacements, and relations between structure, macro- and micromechanical properties of polymers. He is an author or co-author of more than 250 peer-reviewed journal articles, 4 book chapters and 5 patents. He serves as an associate editor of Frontiers in Materials (Polymeric and Composite Materials section), a member of advisory editorial board in Open Materials Science, and a member of the board of the Czechoslovak Microscopy Society.

Table of Contents

PART B: BIOCOMPOSITE MATERIALS

Editorial: Biodegradable Matrices and Composites

Alessandro Pegoretti [1]*, Yu Dong [2] and Miroslav Slouf [3]

[1] Department of Industrial Engineering, University of Trento, Trento, Italy, [2] School of Civil and Mechanical Engineering, Curtin University, Perth, WA, Australia, [3] Institute of Macromolecular Chemistry, Czech Academy of Sciences, Prague, Czechia

Editorial on the Research Topic

Biodegradable Matrices and Composites

Biodegradable and ecofriendly materials attract an increasingly high attention from polymer and composite researchers and manufactures as they can contribute to a more sustainable global development policy, to significantly reduce non-recyclable plastic wastes and limit the impact on the environment. A thorough understanding of both advantages and limitations of biodegradable matrices and composite materials is the key to their reasonable, precisely targeted and effective applications in order to benefit wide communities. The attention in the field of real applications is focused mostly on packaging materials, but automotive, construction, and agriculture are also important fields. As for medical applications, biodegradable matrices and composites are used mostly due to their tunable biodegradability, which is often combined with controlled and localized drug release. The term of *biodegradable composites* comprises a wide range of at least two-phase hybrid materials in which either fillers or matrix or both must be chosen from biodegradable sources. Hence, those matrices based on biodegradable polymers are also well-recognized as *biodegradable matrices*. On the other hand, fillers being the minority phase act as a reinforcement in most biodegradable composites. However, with respect to polymer blends, the minority phase often plays a different role as an impact modifier, a plasticizer or a compatibilizer, as opposed to its drug carrier status in medical applications. Particular cautions should always be taken in the case of composites containing synthetic polymers as matrices, whose biodegradability, biocompatibility, and/or environmental impact may be rather questionable. On the other hand, composites containing bio-based biodegradable polymers as matrices can be fine-tuned to exhibit good tensile, impact and creep properties in spite of lower resistance to moisture, leading to poor mechanical performance at high humidity or aqueous conditions.

The Research Topic on *Biodegradable Matrices and Composites* is focused on recent advances in preparation and characterization of biodegradable polymeric matrices and their composites with the main objective to understand their processing-structure-property relationship at nano-, micro-, and macroscale. Both conventional biodegradable polymers and related biodegradable composites and more recent biodegradable nanocomposites reinforced with nanoparticles and nanofillers are covered to address various aspects, including but not limited to their mechanical, thermal and barrier properties, biodegradability, environmental sustainability, renewability and recyclability, limitations and applications in building constructions, automobiles, medical devices, and material packaging.

The edited book for this Research Topic comprises a special issue collection of 24 contributions represented by 1 mini review, 3 full review, 1 perspective, and 19 original research articles, which are classified into *Part A: Biodegradable Polymers, Blends, and Matrices* and *Part B: Biodegradable Composite Materials*. In Part A, Mistretta et al. investigated mechanical, structural and optical properties of polylactic acid (PLA), polybutylene adipate terephthalate (PBAT), and

PBAT/PLA blends, as well as their surface properties and water vapor permeability before and after the exposure to UV irradiation in order to evaluate their durability and suitability for the conservation of culture heritage. Apicella et al. developed a sustainable food-packaging solution with antimicrobial effectiveness and high functional performance by spreading PLA/ Ethyl-Nα-dodecanoyl-L-arginate (LAE) coating solution on a recyclable polyethylene-terephthalate (PET) substrate. *E. coli* CECT 434 strain as a pathogenic agent was employed to test antimicrobial activity of such multilayer films in liquid culture media. Ten percentage of LAE was found to be the minimum concentration to warrant total inhibition without significantly altering the functionalities of the developed systems. Iozzino et al. prepared biphasic samples (half amorphous and the other half crystalline) of PLA using micro-injection molding. Hydrolysis tests were carried out to monitor their degradability, which indicated that crystalline regions exhibited slightly better resistance to the hydrolysis as opposed to amorphous phase. Fortelny et al. reported a comprehensive review on morphology, compatibility, and mechanical properties of PLA/poly(ε-caprolactone) (PCL) blends in order to control blend toughness and crystallinity so that the blending of PLA and PCL can result in desirable materials with well-tailored mechanical properties. Among other things, the review showed how to prepare *super-tough* PLA/PCL blends without compatibilization. Nevoralová et al. evaluated the effect of blending PCL with thermoplastic starch (TPS) on the final biodegradation rate of such blends in both compost and soil environments. Very fast biodegradation with the initial similar rate to that of pure TPS in both environments was clearly identified for the blends containing 70% TPS with a co-continuous morphology. Whereas, 30% TPS blends demonstrated the particle morphology of starch phase in PCL matrix, indicating a dominant effect of the matrix on the biodegradation course. Delamarche et al. investigated the relationships between physical properties and tailored biodegradability for poly(butylene succinate) (PBS)/PLA blends using a deep eutectic solvent (DES). It was shown that molar masses, crystallinity, yield, morphologies, and surface properties were crucial to control the biodegradability of blend materials. Aliotta et al. studied a multiphase ternary system comprising two different elastomers of PBAT and polyolefin elastomer grafted with glycidyl methacrylate (POE-g-GMA) being added into PLA matrix, as compared with PLA and PLA/PBAT binary blends with maximum 10 wt% PBAT. It was found that the best compromise between impact, tensile properties and biodegradability content could be achieved by using a reactive plasticizer EJ-400. Rigotti et al. evaluated the effect of blending poly(3-hydroxybutyrate) [P(3HB)] to linear low density polyethylene (LLDPE) at the P(3HB) concentrations in the range of 10–50 wt% on hydrolytic degradation, water absorption, thermal and mechanical properties as a function of hydrolysis time. It was demonstrated that the use of biodegradable plastic P(3HB) at a relative amount of 20 wt% to substitute for LLDPE could successfully develop a desirable material in order to meet processability requirements with better tailored mechanical properties even after prolonged hydrolytic degradation treatment. Neisiany, Enayati, Kazemi-Beydokhti et al. provided a mini review on current state-of-art development

of multilayered biodegradable electrospun membranes along with new insights into the future of tailored membranes toward practical applications. Mohammadzadehmoghadam and Dong investigated the impact of gelatin content on material properties and structures of silk fibroin (SF) nanofibers crosslinked with glutaraldehyde vapor (GTA) to understand the potential application of such biodegradable material matrices in tissue scaffolding. The detailed characterization was performed by scanning electron microscopy (SEM), Fourier transform infrared spectroscopy (FTIR), mechanical testing, degree of crosslinking test, water uptake test, water contact angle measurements, X-ray diffraction (XRD) analysis, as well as biocompatibility assessment using fibroblast cells. Adverse effect of GTA crosslinking was detected to reduce the capacity of supporting the cell activity despite improved mechanical properties of nanofiber mats. GTA optimization became essential to further modulate physico-chemical properties of SF/gelatin nanofiber mats in order to achieve stable materials with favorable bioactive properties and more active cellular response in tissue engineering. Zaidi et al. reported the incorporation of epoxidized natural rubber (ENR) as a biodegradable toughening agent, which could enhance toughness properties of polyhydroxybutyrate-co-valerate (PHBV) biodegradable composites and also improve their biodegradability in a more substantial manner, when compared with the addition of commonly used toughening agent PBAT.

In Part B, Aini et al. presented the detailed review with respect to the performance of lignin-filled rubber composites using different approaches including mixing methods, surface modification hybrid fillers and so on in order to gain the insights to the advances in the development of green rubber products. Girijappa et al. thoroughly reviewed different sources of natural fibers, their properties as well as the effect of modification and treatments on natural fibers, etc. with major applications targeting the reinforcements for polymer composites. Salim et al. investigated the effect of fiber surface treatments (i.e., alkali treatment, alkali treatment at elevated temperature, and hear treatment) on the durability of kenaf fiber reinforced acrylic based polyester composites under accelerated weathering exposure for potential applications in automotive industry. Moreover, the excellent fiber-matrix adhesion associated with these treatments may also decrease the water absorption rate by such composite materials. Aouat et al. assessed the influence of combined humid atmosphere and temperature on the morphology, chemical structures, and physical properties of neat PLA, PLA/PLA-grafted-maleic anhydride (PLA-*g*-MA)/microcrystalline cellulose (MCC) and PLA/PLA-*g*-MA/cellulose nanowhisker (CNW) biodegradable composite fibers. It has been found that the durability of PLA fibers to hygrothermal degradation can be established in the following order: PLA > PLA/PLA-*g*-MA/MCC > PLA/PLA-*g*-MA/CNW where the MCC and CNW concentrations are 1 wt% and PLA-*g*-MA content is 7 wt%. Slouf et al. successfully prepared biodegradable microfibrillar PCL/PLA/organophilic montmorillonite composites. It was reported that the macro- and micromechanical properties of all intermediate products and final microfibrillar composites were related not only to the composition and morphology, but also to the crystallinity of

both components. In particular, the modulus of such composites reached almost twice higher value in comparison with the original PCL matrix. Li et al. provided a physical and chemical analysis of chicken feather (ChF) biocarbon generated at different pyrolysis temperatures, which were further combined with PLA matrix to generate 100% sustainable composites. The authors analyzed their thermal properties, mechanical properties, and composition. The valorized ChF as sustainable natural fillers can be a safe and suitable alternative used for composite applications in order to reduce their waste disposal. Ujcic, Krejcikova et al. demonstrated a two-step preparation of TPS using both solution casting and melt mixing to prepare TPS/TiO$_2$ composites with homogeneous filler dispersion even at high filler concentrations up to 20 wt%. The same approach was also employed to uniformly disperse antibiotic (ATB) vancomycin at 10 wt% in TPS systems. The interactions among TPS, TiO$_2$ particles, and ATB molecules gave rise to the shift of glass transition temperatures to higher values along with stiffening effect on corresponding composites. It has been proven through standard antimicrobial susceptibility tests that neither thermal processing nor the addition of TiO$_2$ influence the ATB, which remains active in both TBS/ATB and TPS/TiO$_2$/ATB composites. Fully biodegradable TPS composites are believed to be very promising materials for biomedical applications with respect to local release of antibiotics. Ferrari et al. developed new green composite material with the incorporation of natural additives such as shredded walnut shells and organic fraction of municipal solid waste (MW) into poly(vinyl) alcohol (PVA) for the improvement of mechanical properties of composites. The addition of walnut shells indicated the increases in glass transition temperature and flexural modulus reached about 50% along with the reduction in flexural strength by ∼30%. Furthermore, when added with a low amount of water, the inclusion of MW resulted in increasing strain at break by 100%. Bugatti et al. evaluated the recovery and upgrade of tomato processing residues to be used for the manufacture of innovative green composites based on tomato peels (TPs) and natural halloysite nanotubes (HNTs) loaded with carvacrol as a natural antibacterial agent. Thermal properties of such biodegradable composites were improved with increasing the filler loading as opposed to worse mechanical properties, which especially took place at higher loading levels associated with the poor interaction between HNTs and matrix. No dramatic increase was detected in the degree of hydrophilicity of biodegradable composites. This phenomenon might be attributed to the role of hydrophobic carvacrol acting as hydrophobic coating for HNTs. Finally prepared biodegradable composites exhibited a long-term release of antimicrobial agents, greatly benefiting their wide applications in food packaging. Abdullah and Dong mentioned the comprehensive material development of PVA/starch (ST)/HNT biodegradable composite films for sustainable packaging. Such films possessed high water resistance, good biodegradability, acceptable transparency, as well as overall migration rates to target sustainable food packaging particularly for lipophilic and acidic foodstuffs. Ujcic, Nevoralova et al. compared wheat and tapioca TPS and their composites with TiO$_2$-based nanoparticles (i.e., isometric TiO$_2$ nanoparticles and high-aspect-ratio titanate nanotubes) where

TPS composites were prepared by a combined technique using solution casting and melt mixing. Such a combined technique was proven to be effective to the manufacture of TPS composites with homogeneous filler dispersion regardless of starch sources and types. The type of TPS matrix (i.e., wheat or tapioca) was shown to have significant impact on the properties of resulting composites in which isometric TiO$_2$ nanoparticles yielded very good filler dispersion while TiNT nanotubes tended to form microsized aggregates within both TPS matrices. Liu et al. successfully developed CNW/graphene nanoplatelet (GN) composite films with respect to the GN role as rigid fillers, and further evaluated filler-matrix interactions to concurrently improve their thermal, electrical, and mechanical properties, which were difficult to achieve in conventional nanocomposite materials. Such CNW/GN composite films are anticipated to be potentially effective multifunctional materials in the field of electronic packaging. Finally, Neisiany, Enayati, Sajkiewicz et al. briefly reviewed recently reported work on nanocomposite hydrogels based on chiral functionalized nanomaterials. This work can pave the way for the development of biodegradable hydrogels toward real practical applications.

In summary, this edited book offers a diverse range of biodegradable polymers, their blends and biodegradable composite materials, focusing on their fabrication, characterization and widespread applications. It can be deemed as a good overview for materials engineers and scientists, experienced researchers and postgraduate students, as well as industrial staff working in research & development sectors to rapidly move forward to innovative and ecofriendly materials for significantly reducing conventional petroleum-based plastic wastes at disposal.

AUTHOR CONTRIBUTIONS

YD prepared the initial editorial draft while AP and MS provided further comments and feedback. YD, AP, and MS jointly finalized the editorial work. All authors contributed to the article and approved the submitted version.

ACKNOWLEDGMENTS

Check for
updates

Durability of Biodegradable Polymers for the Conservation of Cultural Heritage

Maria C. Mistretta[1], Francesco P. La Mantia[1]*, Vincenzo Titone[1], Bartolomeo Megna[1], Luigi Botta[1] and Marco Morreale[2]

[1] Department of Engineering, University of Palermo, Palermo, Italy, [2] Faculty of Engineering and Architecture, Kore University of Enna, Enna, Italy

The use of polymers for conservation of cultural heritage is related to the possibility to slow down or stop natural deterioration which, in many cases, corresponds to stopping the entrance of liquid water and to favor spontaneous water vapor removal. Unfortunately, hydrophobicity is generally favored by surface roughness and thus competitive with transparency. It is therefore important to find an optimal balance hydrophobicity, transparency and durability (especially to photooxidation). However, polymers typically used for applications in this field come from non-renewable resources and are not biodegradable. In this work, the mechanical, structural, and optical properties of PLA, PBAT, and a PBAT/PLA blends, as well as surface properties and water vapor permeability, were investigated before and after exposure to UV irradiation, in order to evaluate their durability and suitability for conservation of cultural heritage.

Keywords: biodegradable polymers, durability, cultural heritage, conservation, mechanical properties, permeability

INTRODUCTION

The most important characteristics of polymers for conservation of cultural heritage are related to the capability to slow down, or possibly stopping, the ongoing deterioration; however, since one mostly causes of deterioration are related to the presence of water, the most important goal is to stop the entrance of liquid water and to facilitate spontaneous water vapor removal. Therefore, hydrophobicity is particularly important. However, one of the surface properties most affecting the actual hydrophobicity is the roughness: typically, hydrophobicity increases on increasing the surface roughness. Since the latter is competitive with transparency (which typically decreases on increasing the roughness), a further challenge is to tailor the polymer coating thickness in order to find the best compromise in terms of hydrophobicity, transparency, and durability. Furthermore, a good durability requires a suitable resistance to photooxidation and a good water vapor permeability after treatment.

The first category of polymeric materials to be actually investigated for application in this field was represented by acrylic polymers (Feller, 1978, 1994; Favaro et al., 2006). Their actual resistance to water and photooxidation was evaluated (Melo et al., 1999; Borgia et al., 2001; Chiantore and Lazzari, 2001) finding an unsatisfactory stability under UV irradiation, as well as inadequate water barrier properties over time. Thus, fluorinated polymers were taken into account as possible alternatives, showing some encouraging results, but also questionable surface adhesion properties (Frediani et al., 1982; Torrisi, 2008; Licchelli et al., 2013). Therefore, further efforts were focused

on copolymers or blends from both acrylic and fluorinated polymers (Mazzola et al., 2003; Malshe and Sangaj, 2009). Furthermore, silanes and siloxanes (Tsakalof et al., 2007; Vacchiano et al., 2008; Ershad-Langroudi et al., 2017) also showed interesting properties in terms of impermeability and protection against color loss, although these were strongly dependent on the specific substrate. Polymers from cellulose have been extensively used and studied for application on cultural heritage, finding that both cellulose ethers (Feller and Wilt, 1990) and nitrate (Selwitz, 1988) have some stability issues. Finally, PEG was recently proposed in order to consolidate collapsible soil, highlighting interesting properties (Zimbardo et al., 2019).

However, all of the above discussed solutions are based on traditional polymers, coming from non-renewable resources and not biodegradable, with the well-known related issues of environmental impacts: the increasing demand for better use of natural resources and reduction of the environmental impacts related to the use of plastics currently require the search for alternative and more environment-friendly solutions (Bastioli, 2005; Song et al., 2009; Lo Re et al., 2013; Morreale et al., 2015). Furthermore, one of the main problems related to the use for conservation of cultural heritage (especially, for stone conservation) is related to reversibility (Andreotti et al., 2018). In fact, any protective coating should be removable in the future if needed, or at least retreatable. Unfortunately, traditional organic coatings have been found to be hardly removable (even using solvents) after some years of exposure to outdoor conditions, and go on aging and progressively losing their properties. This suggests, therefore, the use of biodegradable materials in replacement for non-biodegradable one; in particular, biodegradable polymers should spontaneously disappear from the underlying stone, after their properties (namely, water barrier and repellence properties) are lost (Andreotti et al., 2018).

With regard to the actual suitability of biodegradable polymers for cultural heritage conservation, the Literature does not report a high amount of data in this context.

Ocak et al. (2009) studied the behavior of some biodegradable polymers such as zein, chitosan, polyhydroxybutyrate (PHB), and poly-lactic acid (PLA) in terms of protection capability of marble surfaces under SO_2. They found that the latter two were less suitable to protect against sulphatation.

Giuntoli et al. (2012) prepared some PLA samples, functionalized through fluorinated alcohols as co-initiators of polymerization, finding that the polymers coming from the L-lactide showed higher water protection in comparison to those coming from a racemic mixture of L- and D-lactide.

Ocak et al. (2015) investigated the behavior of a PLA-montmorillonite nanocomposite in terms of protection of marble surfaces against air pollution. The presence of the nanofiller evidenced an increased hydrophobicity, and therefore higher impermeability to environment waters and, at the same time, reduced water vapor permeability.

Sacchi et al. (2012) performed several investigations on different systems such as a lactic acid omopolymer and two lactic acid copolymers (copolymerized with a commercial low molecular weight perfluoropolyether). Their suitability to protect marble against aging (simulated by thermohygrometric cycles and UV irradiation) was studied, finding an enhancement of the water-repellent behavior in comparison to non-fluorinated PLA; this was kept even after thermohygrometric aging, while UV aging led, in some cases, to a detachment between the polymer layer and the marble substrate, depending on the kind of marble examined.

Andreotti et al. (2018) studied the behavior of PHA for stone protection, finding interesting results in terms of effectiveness and compatibility, while further improvements of durability and applicability still seem necessary.
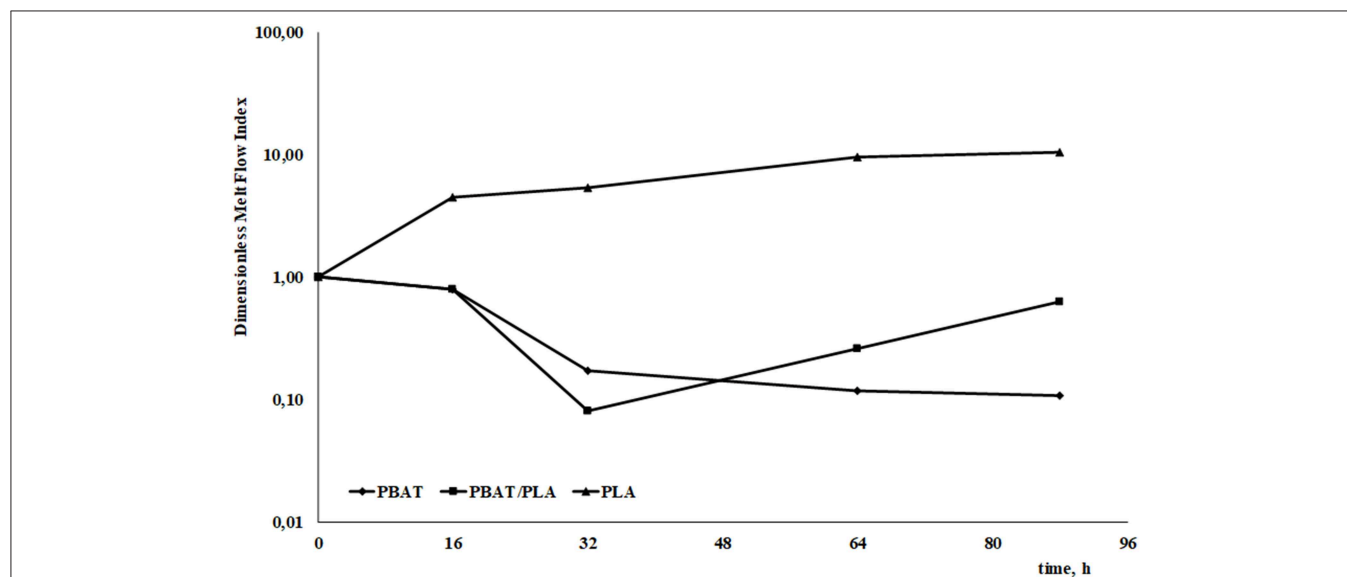
FIGURE 1 | Dimensionless MFI of the three system (pristine and photooxidized for 128 h).

Xing et al. (2017) prepared PBAT/lignin UV-blocking films. More in details, they grafted bio-based 10-undecenoic and oleic acids on soda lignin via solvent methods and then blended the lignin, as well as the lignin ester derivatives, with PBAT. They found good lignin dispersion, thermal stability and retaining of tensile properties up to 10–20 wt% filler loading, and very good UV-barrier properties even after 50 h of irradiation.

It can be deduced from this brief literature report, that the suitability of a polymer system as protective layer on stone is dependent on its durability, which in its turn is related to the loss of hydrophobicity. The latter can depend on photooxidation (photooxidation, in fact, leads to the increase of polar groups on the surface, and therefore to an increase of hydrophilicity). Furthermore, most of the available information regards PLA, while less information is available about other polymers, such as for instance PBAT.

The photooxidation behaviors of PLA and PBAT have been reported in the literature (Ikada, 1997; Tsuji et al., 2006; Janorkar et al., 2007; Nakayama and Hayashi, 2007; Kijchavengkul et al., 2010; Zaidi et al., 2010; Gardette et al., 2011; Stloukal et al., 2012). With regard to PLA, the mechanisms involved are a photolytic mechanism leading to the breaking of the C-O bond in the macromolecular chain and a photooxidative mechanism leading to the formation of hydroperoxides and, in turn, of carboxylic acids and ketones (Janorkar et al., 2007); moreover, also the Norrish II mechanism can be involved (Tsuji et al., 2006; Nakayama and Hayashi, 2007), although under UV irradiation at wavelengths higher than 300 nm, different chain scission mechanisms were found (Gardette et al., 2011). With concern to the PBAT, degradation can occur via Norrish I and II chain scission, and can also lead to significant crosslinking phenomena due to the free radicals generated during the Norrish I path (Kijchavengkul et al., 2010; Stloukal et al., 2012).

In this work, therefore, we focused on the investigation on the mechanical and optical properties of PLA, PBAT, and a PBAT/PLA blend, with particular concern on the behavior after exposure to UV irradiation. The main objective was to evaluate the suitability and durability of these materials for conservation of cultural heritage.

EXPERIMENTAL

The materials used in this work were: a PLA sample, commercially known as Ingeo 4032D (NatureWorks, USA), having a MFI equal to 7 g/10 min (at 210°C and 2.16 kg), a density of 1.24 g/cm^3 and a melting point between 155 and 170°C; a PBAT sample, commercially known as Ecoflex (BASF, Germany) with a MFI between 2.7 and 4.9 g/10 min; a sample of PBAT/PLA blend, commercially known as Ecovio (BASF, Germany) with a MFI between 5 and 11 g/10 min. The neat, non-aged systems were compared also to a reference commercial fluoropolymer sample, Fluoline HY (CTS, Italy), that is a high molecular weight fluorinated elastomer, typically used as protective layer for porous stone substrates.

Sheets of all the samples (previously conditioned in a vacuum oven at 70°C for 4 h) were prepared by compression molding at $T = 170°C$ (except for the PLA which was molded at 190°C) in a Carver (USA) laboratory press.

The obtained specimens (thickness of about 300 μm) were exposed to accelerated weathering in a "Q-UV" chamber (Q-Labs Corp., USA) containing eight "UVB-313" lamps up to about 128 h, according to the procedures described elsewhere (Morreale et al., 2013) at 70°C.

Mechanical (tensile) tests were carried out according to ASTM D638 both on weathered and unweathered specimens (90 × 10 × 0.3–0.5 mm) using an Instron (USA) mod. 3365 universal testing machine. The elastic modulus was measured at 1 mm/min deformation speed. When the deformation reached 10%, the crosshead speed was increased to 100 mm/min until final breaking. The values of the elastic modulus, E, tensile strength, TS, and elongation at break, EB, were calculated as average of 10 tests, with an adequate reproducibility (±7%).

FTIR spectra in ATR mode were obtained by using a Perkin-Elmer (USA) Spectrum One spectrometer, using the embedded SpectrumOne software. The spectra were obtained through 16 scans with a 4 cm^{-1} resolution. Measurements were obtained from the average of triplicate samples. Particular attention was focused on the carbonyl peak centered at 1,720 cm^{-1}, which was used to measure the dimensionless carbonyl index (ratio between the carbonyl peak area of the sample at a given photooxidation time and carbonyl peak area of the unirradiated sample) in order monitoring the photooxidation.

UV-Vis spectra were obtained on triplicates using a Specord 252 (Analytik Jena, Germany) spectrometer in the 190–1,100 nm range.

Melt Flow index (MFI) values were measured using a CEAST (Italy) equipment at 170°C under a 2.16 kg load, as the average of four measurements (data reproducibility: ±5%).

The cross-linked fraction was evaluated by measuring the residual gel fraction obtained after Soxhlet extraction using boiling tetrahydrofuran (THF) on triplicates.

Enthalpy of fusion of the samples was measured by differential scanning calorimetry (DSC), using a Shimadzu (Japan) DSC-60 apparatus, with 5°C/min heating rate from 40 to 200°C, as the average of four measurements (data reproducibility: ±6%).

TABLE 1 | Enthalpy of fusion of pristine (unirradiated) and photooxidized (128 h) samples.

	Exposure time, h	ΔH(PLA), J/g	ΔH(PBAT), J/g
PLA	0	1.59 ± 0.06	–
PLA	128	48.41 ± 1.9	–
PBAT	0	–	5.45 ± 0.27
PBAT	128	–	5.57 ± 0.28
PLA/PBAT	0	1.22 ± 0.07	4.28 ± 0.26
PLA/PBAT	128	1.62 ± 0.1	0.56 ± 0.03

For the blend sample, the enthalpies of fusion of the two phases are reported.

Contact angle measurements (in order evaluating wettability of the investigated materials) were performed using a First Ten Angstrom (USA) FTA1000C system, with demineralized water (on four samples, data reproducibility: ±4%).

Water vapor permeability measurements were performed on samples (diameter 4.5 cm) coming from the above mentioned compression-molded sheets, at 25°C and 50% relative humidity, using a BYK-Gardner (Germany) permeability cup. Permeability constant was calculated as the average of four measurements by normalizing the measured weight loss of each sample against the sample thickness (data reproducibility: ±7%), according to the procedures described elsewhere (Iizuka et al., 2016; Hendrickx et al., 2017).
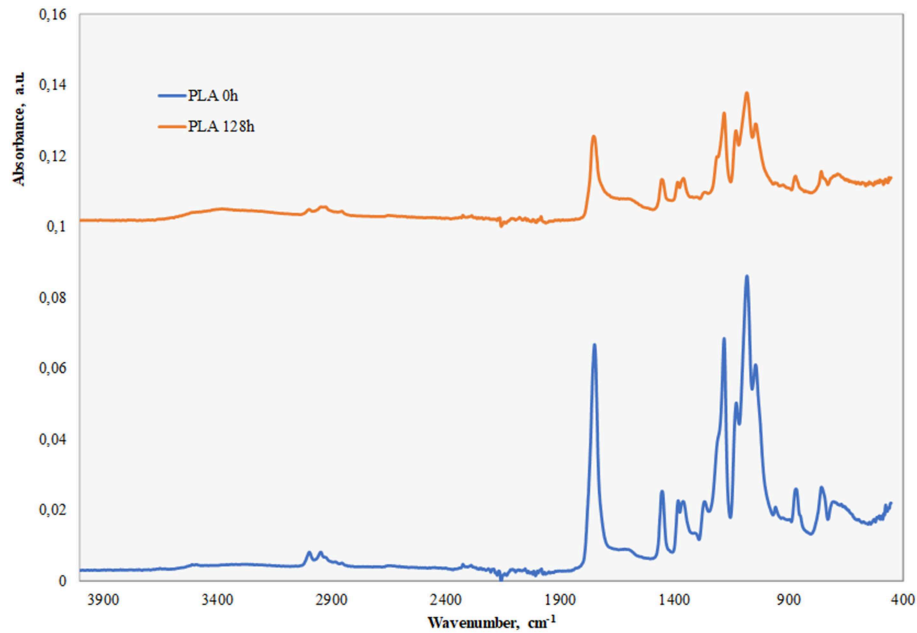
FIGURE 2 | ATR spectra of pristine and photooxidized PLA.
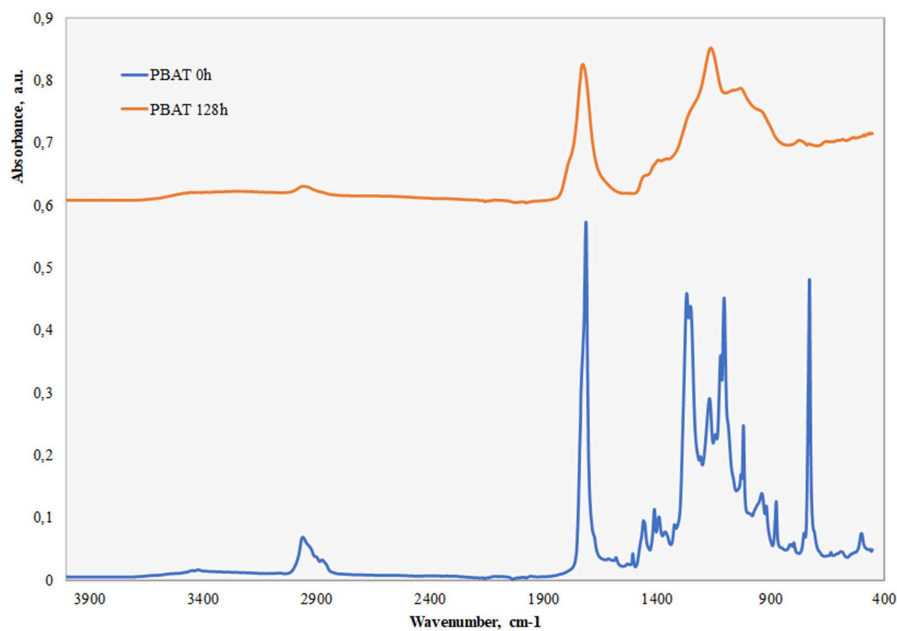
FIGURE 3 | ATR spectra of pristine and photooxidized PBAT.

RESULTS AND DISCUSSION

In **Figure 1**, the dimensionless MFI values are reported, as a function of the irradiation time.

The gel fraction values of the three pristine (unirradiated) samples were obviously zero; after 128 h irradiation they were found to be still zero in the PLA sample, while they increased to 6.8 in the PBAT, and 22.6 in the PLA/PBAT.

The photooxidation of PLA, therefore, gives rise to a decrease of the molecular weight—increase of the MFI value—and no presence of cross-linking was detected. These results indicate that the photooxidation proceeds to breakage of the macromolecules
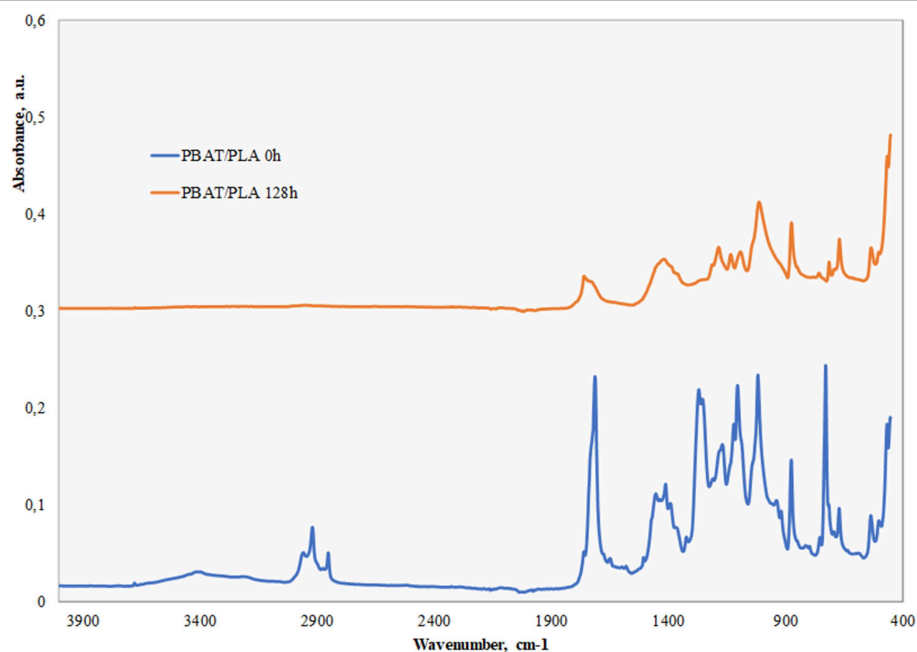
FIGURE 4 | ATR spectra of pristine and photooxidized blend.
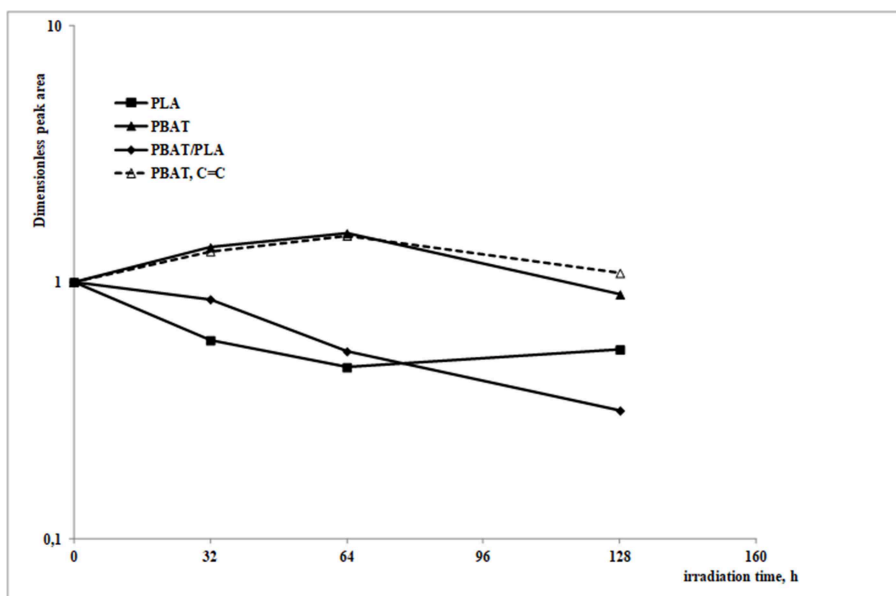
FIGURE 5 | Dimensionless peak area of the three investigated systems in the 1,860–1,600 cm^{-1} region (continuous lines) and peak area of PBAT in the 900–1,100 cm^{-1} region (dotted line), as a function of the irradiation time.

and oxidation of the carbon atoms. PBAT and the PBAT/PLA blend show similar behaviors, with a decrease of molecular weight but, on the contrary, a formation of cross-linking structures is observed in both of the systems. According to the reported results, it is evident that the cross-linking occurs only in the PBAT phase and that the increase of the crosslinking

in the blend, in comparison to neat PBAT, suggests that PLA degradation (which follows a chain scission path) and the related degradation products promote PBAT degradation (which, on the other hand, mainly follows a crosslinking path). The observation of **Figure 1** further indicates that the PBAT undergoes significant crosslinking phenomena (in particular, after 32 h) resulting in a
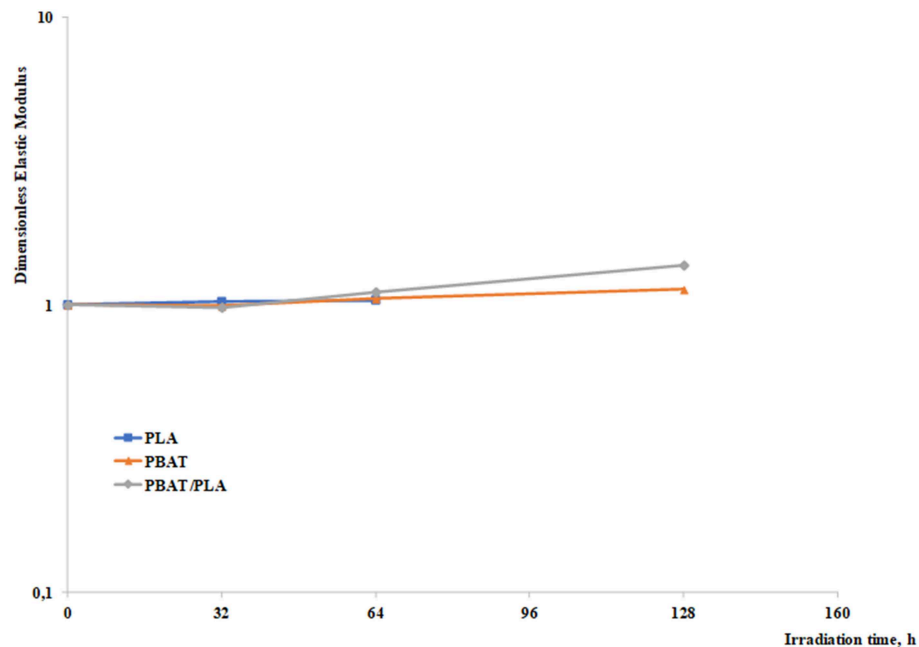
FIGURE 6 | Dimensionless elastic modulus as a function of the irradiation time.
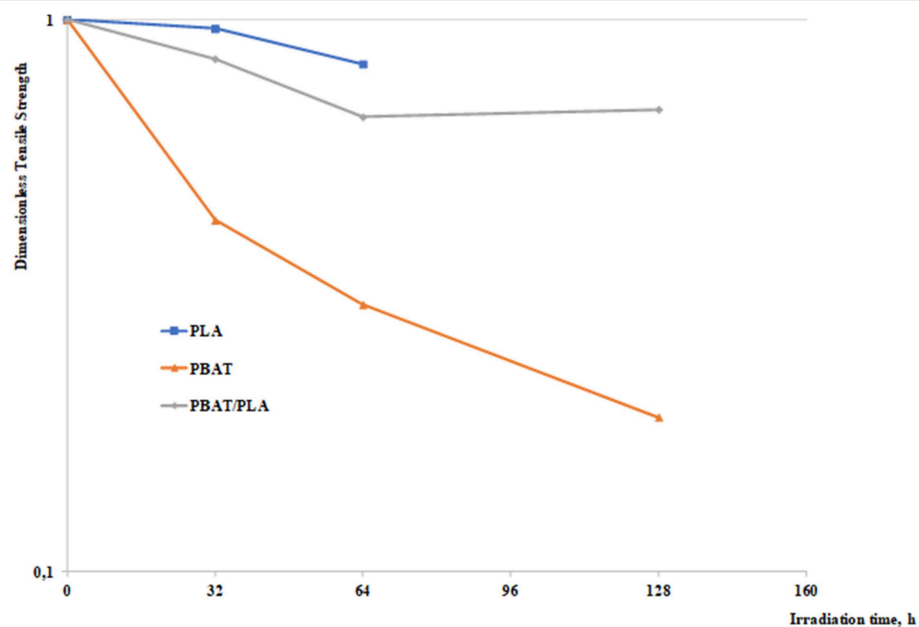
FIGURE 7 | Dimensionless tensile strength as a function of the irradiation time.

decrease of the MFI, and this is even more important in the blend, where the crosslinking of the PBAT fraction is able to lead to a decrease of the MFI even though the greater part of the blend is composed by PLA. On the other hand, the role of the chain-scission degradation of PLA gains importance on increasing the photooxidation time, leading to a gradual reversal of the trend.

The enthalpies of fusion of the three samples, virgin and photooxidized, are reported in **Table 1**.

It can be observed that, in substantial agreement with the crosslinking (gel fraction) data, the crystallinity generally decreases on increasing the crosslinking rate.

Figures 2–4 report the ATR spectra of virgin and photooxidized PLA, PBAT, and PLA/PBAT blend, respectively.

As regards the PLA, the main peaks to be observed are: 871 cm^{-1} (-CH- bending), 1,453 (-CH3 bending), 1,745 cm^{-1} (C=O axial deformation vibration), 1,087, 1,129, and 1,184 cm^{-1} (stretching of the –CO- bond).

In the case of PBAT, the main peaks are: 729 cm^{-1} (-CH2-stretching), 1,104, 1,120, and 1,165 cm^{-1} (-CO- stretching), and 1,730 cm^{-1} (C=O axial deformation vibration). The blend shows the typical peaks from both of the two components, in particular at 1,745, 1,730, 1,453, 1,087–1,104–1,165, 871, and 729 cm^{-1}. The reported peaks are in agreement with literature data (Dias Fernandes et al., 2017).

The ATR spectra of the PLA show a decrease of the peak located at 1,745 cm^{-1}, thus indicating a reduction of the esters, but at the same time the overall carbonyl peak area does not change significantly, thus suggesting chain scission degradation, in agreement with the hypotheses derived from the previously discussed data. With regard to PBAT, a somewhat similar decrease and a widening of the carbonyl peak was observed, but in this case also two shoulders at 1,790 and 1,750 cm^{-1} appear, related to the formation of free carbonyls and low molecular weight esters, respectively. These two findings suggest that Norrish-I type chain scission reactions occurred (Gardette et al., 2011).

Furthermore, a broadened peak around 1,000 cm^{-1} was observed, indicating the formation of C=C bonds, thus suggesting that also Norrish-II type chain scission reactions occurred (Gardette et al., 2011).

With regard to the blend, the peak modifications substantially mirror those of the individual components. However, such peak modifications are significantly sharper.

In order to deepen the analysis, the dimensionless carbonyl peak area (calculated as the ratio between the peak from 1,600 to 1,860 cm^{-1} at a given photooxidation time and the same before photooxidation) as a function of irradiation time is reported in **Figure 5**.

As previously discussed, a reduction of the carbonyl peak upon increasing the UV exposure time should happen, mainly attributable to chain scission reactions (especially Norrish I type). However, as the oxidation goes on, it gives rise to different oxidation species such as free carbonyls and low molecular

TABLE 2 | Elastic modulus, tensile strength and elongation at break of the three unirradiated samples.

	E, MPa	TS, MPa	EB, %
PLA	1585 ± 63	42 ± 1.7	4 ± 0.2
PBAT	48 ± 3.4	20 ± 1.4	820 ± 41
PLA/PBAT	111 ± 7.8	9.3 ± 0.5	327 ± 20
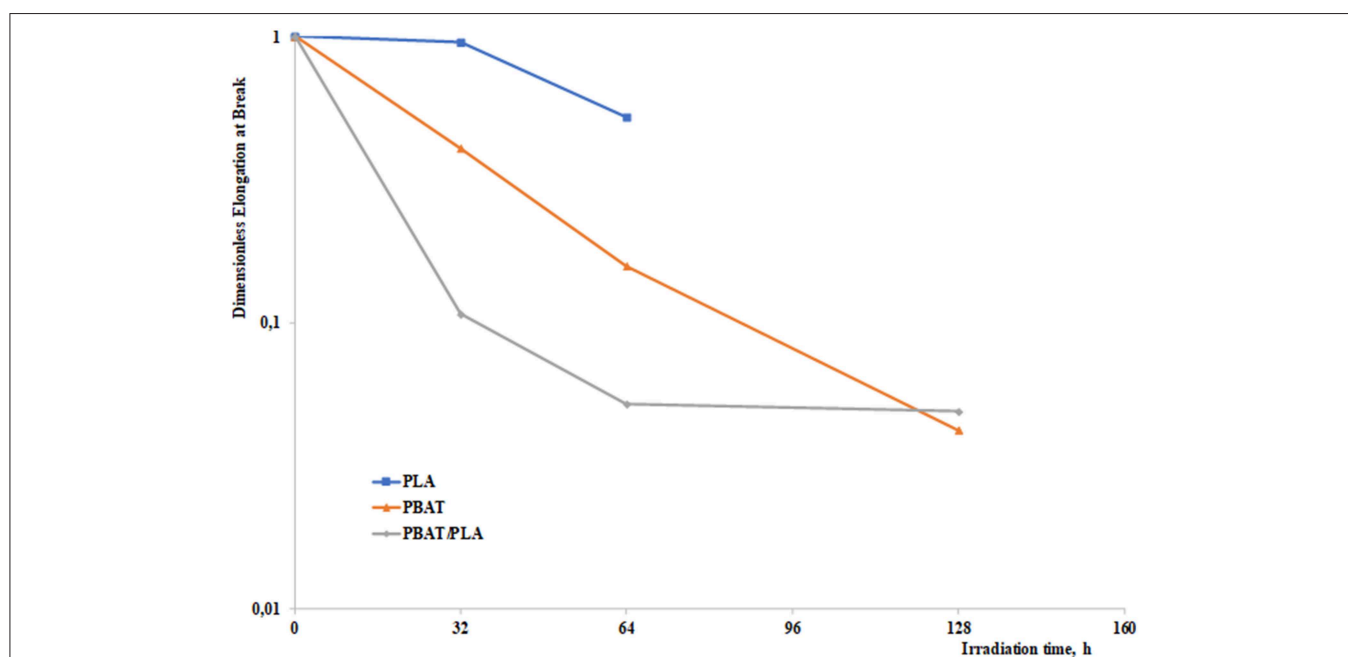
FIGURE 8 | Dimensionless elongation at break as a function of the irradiation time.

weight esters, which allow the overall carbonyl peak area to not decrease much, or to keep practically constant; in the case of PBAT, C=C bonds are formed, reasonably due to Norrish II type chain scission reactions, which slightly increase the related peak area (between 900 and 1,100 cm^{-1}, see dotted line in the same **Figure 5**).

The degradation has a deep effect on the mechanical properties that can strongly change during the photooxidation. In **Figures 6–8**, the dimensionless values of the elastic modulus, E, tensile strength, TS, and elongation at break, EB, are drawn as a function of the irradiation time for the three materials (PLA values reported only up to 64 h, since
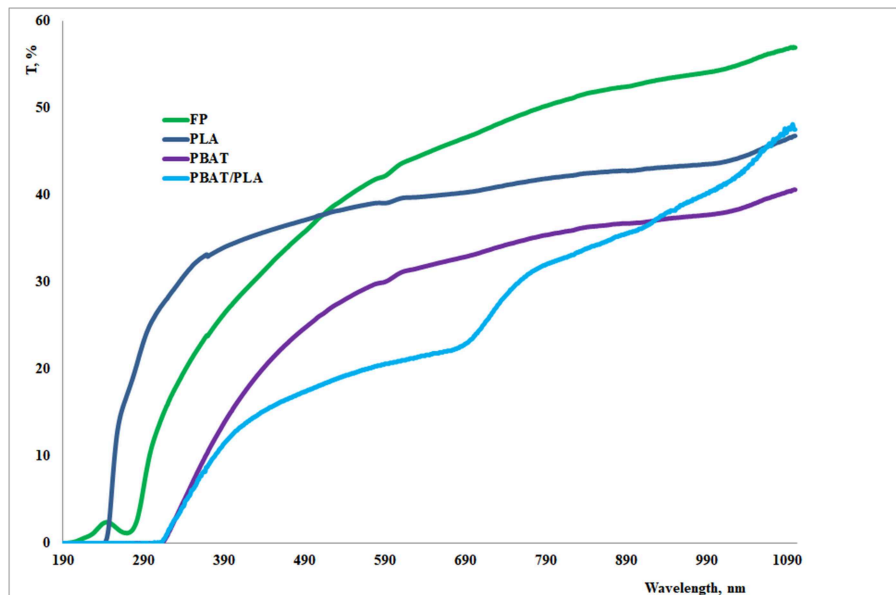
FIGURE 9 | UV spectra of the pristine samples.
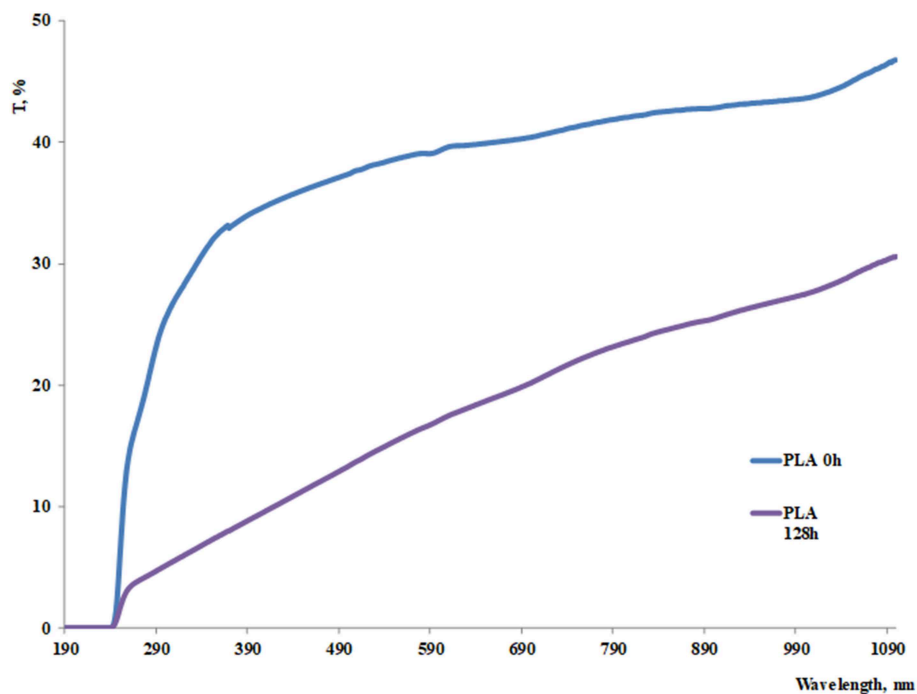
FIGURE 10 | UV spectra of pristine and 128 h-irradiated PLA.

the samples became excessively brittle after that exposure time). The dimensionless values have been calculated by dividing the values at each irradiation time by those of the same virgin (unirradiated) polymer, which are reported in **Table 2**.

As expected, the blend has intermediate properties in terms of rigidity and deformability, while the tensile strength experiences antagonistic effects.

It can be observed that the photooxidation had significantly detrimental effects on the ductility (EB) of the materials, in
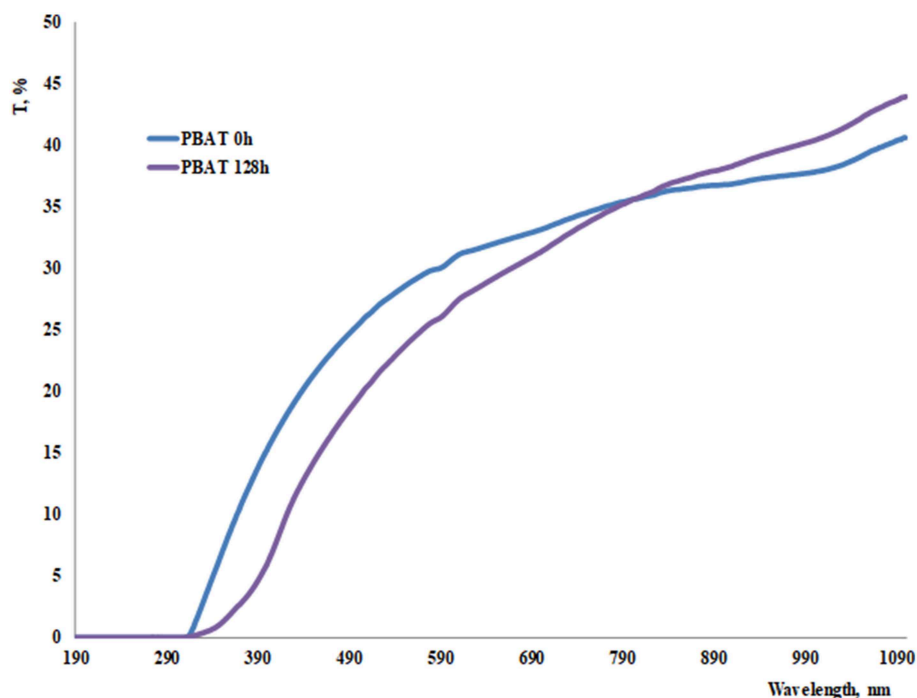
FIGURE 11 | UV spectra of pristine and 128 h-irradiated PBAT.
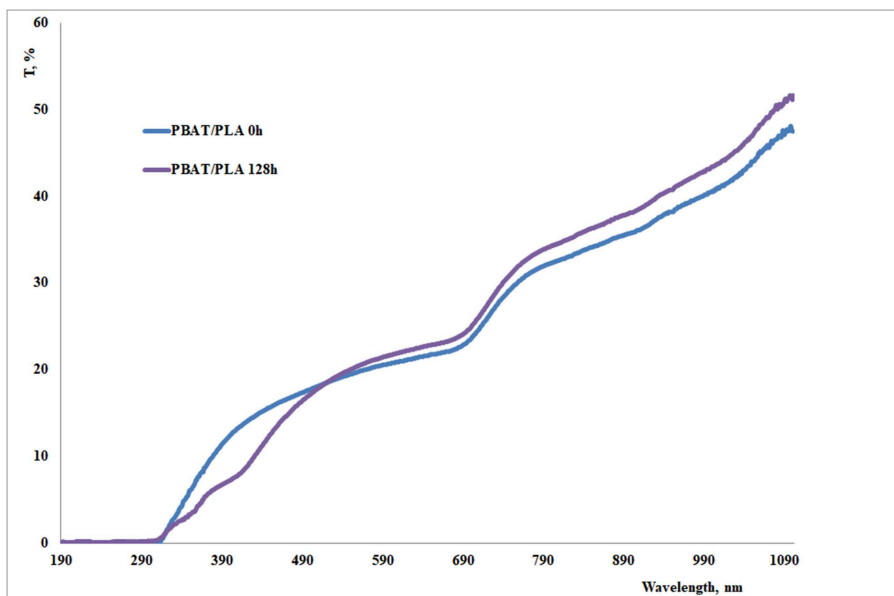
FIGURE 12 | UV spectra of pristine and 128h-irradiated PBAT/PLA blend.
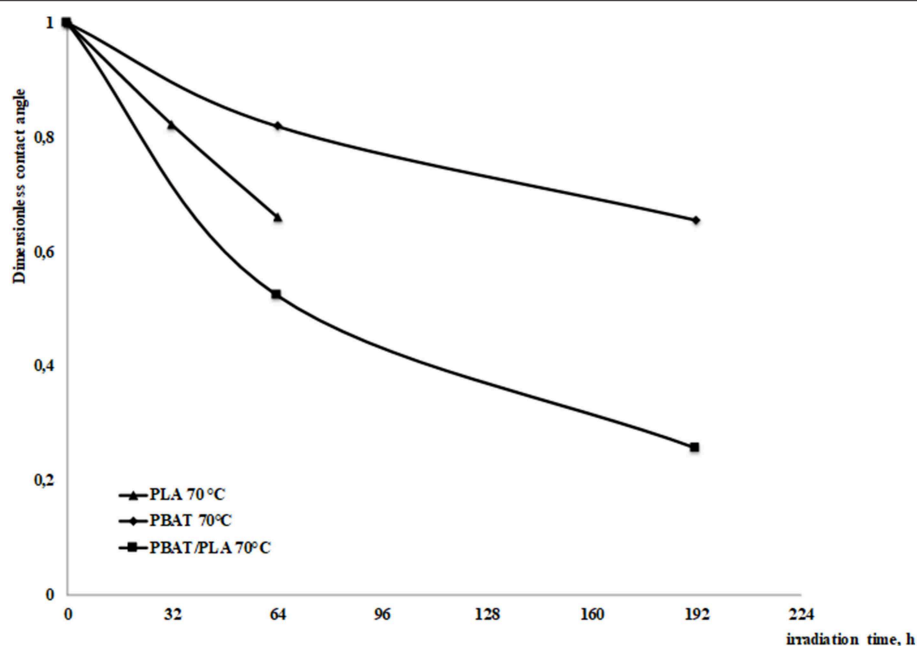
FIGURE 13 | Dimensionless contact angles measured for the investigated systems.

agreement with the previous discussions on the reduction of molecular weight and crosslinking phenomena. With regard to the tensile resistance (TS), all of the three materials undergo (as expectable on the basis of the above consideration) a reduction, but with remarkable differences: while the PLA undergoes limited worsening of the TS, the PBAT undergoes a drop. This may be due to the different embrittlement kinetics of the two materials (see **Figure 8**), which lead to premature breaking of PBAT. On the other hand, the blend shows a different behavior, with significantly lower reduction of the TS in comparison to the PBAT, in apparent contrast with the deductions that could be drawn on the basis of the embrittlement. This is explainable, however, considering that the blend experienced increased crosslinking phenomena, which mitigate the loss of tensile resistance. At the same time, there is some increase or no change of the modulus, due to the above discussed phenomena of crosslinking and chain scission.

Due to its use for covering cultural heritage, the optical properties play a very important role.

Figure 9 shows the UV spectra of virgin fluoropolymer, PLA, PBAT, and PBAT/PLA blend, while **Figures 10–12** report the comparison to the spectra obtained after 128 h photooxidation of the same samples. The transmittance (and thus transparency) in the visible range (380–740 nm) of the reference fluoropolymer is, on average, slightly higher, however the values of the biodegradable polymers appear to be comparable. On increasing the photooxidation time, it slightly decreases in the PBAT, while the reduction is higher in the PLA; however, in the case of the blend, in the 490–780 nm range, the values are almost unchanged. This suggests that the investigated polymer

blend should be suitable for cultural heritage applications, in terms of maintaining the main optical properties over time, although the use of suitable antioxidants would obviously improve the behavior.

Contact angle measurements at different photooxidation times were measured, and are shown in **Figure 13**.

It was not possible to measure the values of the PLA samples irradiated more than 64 h since the specimens were significantly damaged due to the photooxidation. It is observed that the contact angle decreases on increasing the photooxidation time, due to the increasing amount of polar groups formed during the degradation (as discussed previously) and the increasing rugosity of the surfaces. This is a further confirmation of the interpretations provide with regard to the results coming from spectral analysis.

Finally, the measured values of specific water vapor permeability were found to be 1.35 ± 0.07 g/mm in the reference fluorinated elastomer; with regard to the biodegradable systems, it was found to change from 5.41 ± 0.32 to 2.95 ± 0.37 g/mm in the case of PBAT, and from 6.79 ± 0.47 to 2.88 ± 0.2 g/mm in the case of the PBAT/PLA blend. Therefore, the biodegradable systems are in the same order of magnitude and thus comparable to the reference fluoropolymer. Also in this case, it was not possible to measure the values of the PLA samples irradiated more than 64 h since the specimens were significantly damaged due to the photooxidation It is thus observed that, after the UV aging treatment, the specific permeability significantly decreases in comparison to the neat unirradiated systems. This is in agreement with the previously discussed results, since it can be explained on the basis of the increased crosslinked fraction and the variations of crystallinity degree.

CONCLUSIONS

In this work, the mechanical, structural and optical properties of PLA, PBAT, and a PBAT/PLA blends, as well as surface properties and water vapor permeability, were investigated before and after exposure to UV irradiation. The main objective was to evaluate the suitability and durability of these materials for conservation of cultural heritage.

Photooxidation followed a complex path, involving mainly chain scission in the PLA and crosslinking in the PBAT, while synergistic effects were found in the blend.

The mechanical properties of the blend were intermediate between those of the neat PLA and PBAT; however, the UV exposure led to different worsening of the three systems, pointing out that the blend undergoes more limited decay of the main mechanical properties, in comparison to the neat PBAT.

Water vapor permeability was found to decrease on increasing the exposure time; the UV transmittance in the visible range slightly decreased in the PBAT, while the reduction was higher in the PLA; in the case of the blend, the values in the 490–780 nm range were almost unchanged, although the overall transmittance was lower.

The obtained results suggest that the PBAT/PLA blend investigated in this work could be suitable for cultural heritage applications, and that the next advisable steps should consist in experimenting the addition of suitable antioxidants in order to improve the overall performance.

DATA AVAILABILITY

The datasets generated for this study are available on request to the corresponding author.

AUTHOR CONTRIBUTIONS

FL and MCM designed the experiments. VT, MCM, and LB performed the experiments. All of the authors analyzed the data. FL supervised the work. FL, MM, and BM wrote the paper (original draft, reviewing, and editing).

FUNDING

REFERENCES

Andreotti, S., Franzoni, E., Degli Esposti, M., and Fabbri, P. (2018). Poly(hydroxyalkanoate)s-based hydrophobic coatings for the protection of stone in cultural heritage. *Materials* 11, 1–26. doi: 10.3390/ma11010165

Bastioli, C. (ed). (2005). *Handbook of Biodegradable Polymers*. Akron, OH: iSmithers Rapra Publishing.

Borgia, G. C., Bortolotti, V., Camaiti, M., Cerri, F., Fantazzini, P., and Piacenti, F. (2001). Performance evolution of hydrophobic treatments for stone conservation investigated by MRI. *Magn. Reson. Imaging* 19, 513–516. doi: 10.1016/S0730-725X(01)00281-8

Chiantore, O., and Lazzari, M. (2001). Photo-oxidative stability of paraloid acrylic protective polymers. *Polymer* 42, 17–27. doi: 10.1016/S0032-3861(00)00327-X

Dias Fernandes, T. M., Amorim Moreira Leite, M. C., Furtado de Sousa, A. M., Russi Guimaraes Furtado, C., Alves Escocio, V., and Nazareth de Silva, A. L. (2017). Improvement in toughness of polylacide/Poly(butylene adipate-co-terephthalate) blend by adding nitrile rubber. *Polym. Bull.* 74, 1713–1726. doi: 10.1007/s00289-016-1798-9

Ershad-Langroudi, A., Fadaii, H., and Ahmadi, K. (2017). Silane/siloxane surface treatment for cohesion ability and strengthening agent of historical stone. *Conserv. Sci. J.* 1, 23–31. doi: 10.30699/ics.journal.01.23

Favaro, M., Mendichi, R., Ossola, F., Russo, U., Simon, S., Tomasin, P., et al. (2006). Evaluation of polymers for conservation treatments of outdoor exposed stone monuments, Part I: photo-oxidative weathering. *Polym. Degrad. Stab.* 91, 3083–3096. doi: 10.1016/j.polymdegradstab.2006.08.012

Feller, R. L. (1978). "Standards in the evaluation of thermoplastic resins," in *Proceedings ICOM Committee for Conservation, 5th Triennial Meeting* (Zagreb).

Feller, R. L. (1994). *Accelerated Aging - Photochemical and Thermal Aspects*. Ann Arbor, MI: The J. Paul Getty Trust.

Feller, R. L., and Wilt, M. (1990). *Evaluation of Cellulose Ethers for Conservation*. Getty Conservation Institute. ISBN 0-89236-099-2.

Frediani, P., Manganelli Del Fa', C., Matteoli, U., and Tiano, P. (1982). Use of perfluoropolyethers as water repellents: study of their behaviour on pietra serena a Florentine building stone. *Stud. Conserv.* 27, 31–37. doi: 10.1179/sic.1982.27.1.31

Gardette, M., Therias, S., Gardette, J. L., Murariu, M., and Dubois, P. (2011). Photooxidation of polylactide/calcium sulphate composites. *Polym. Degrad. Stab.* 96, 616–623. doi: 10.1016/j.polymdegradstab.2010.12.023

Giuntoli, G., Rosi, L., Frediani, M., Sacchi, B., and Frediani, P. (2012). FluoroFunctionalized PLA polymers as potential water-repellent coating materials for protection of stone. *J. Appl. Polym. Sci.* 125, 3125–3133. doi: 10.1002/app.36469

Hendrickx, R., Ferreira, E. S., Boon, J. J., Desmarais, G., Derome, D., Angelova, L., et al. (2017). Distribution of moisture in reconstructed oil paintings on canvas during absorption and drying: a neutron radiography and NMR study. *Stud. Conserv.* 62, 393–409. doi: 10.1080/00393630.2016.1181899

Iizuka, S., Murata, K., Sekine, M., and Sato, C. (2016). A novel cup with a pressure-adjusting mechanism for high-temperature water vapor transmission rate measurements. *Polym. Test.* 50, 73–78. doi: 10.1016/j.polymertesting.2015.11.018

Ikada, E. (1997). Photo and biodegradable polyesters. photodegradation behaviors of aliphatic polyesters. *J. Photopolym. Sci. Technol.* 10, 265–270. doi: 10.2494/photopolymer.10.265

Janorkar, A. V., Metters, A. T., and Hirt, D. E. (2007). Degradation of Poly(L-Lactide) films under ultraviolet-induced photografting and sterilization conditions. *J. Appl. Polym. Sci.* 106:1042. doi: 10.1002/app.24692

Kijchavengkul, T., Auras, R., Rubino, M., Alvarado, E., Montero, J. R. C., and Rosales, J. M. (2010). Atmospheric and soil degradation of aliphatic aromatic polyester films. *Polym. Degrad. Stab.* 95, 99–107. doi: 10.1016/j.polymdegradstab.2009.11.048

Licchelli, M., Malagodia, M., Weththimunia, L. M. L., and Zanchia, C. (2013). Waterrepellent properties of fluoroelastomers on a very porous stone: effect of the application procedure. *Prog. Org. Coat.* 76, 495–503. doi: 10.1016/j.porgcoat.2012.11.005

Lo Re, G., Morreale, M., Scaffaro, R., and La Mantia, F. P. (2013). Biodegradation paths of Mater-Bi®/kenaf biodegradable composites. *J. Appl. Polym. Sci.* 129, 3198–3208. doi: 10.1002/app.39027

Malshe, V. C., and Sangaj, N. S. (2009). Fluorinated acrylic copolymers Part I: study of clear coatings. *Prog. Org. Coat.* 53, 207–211. doi: 10.1016/j.porgcoat.2005.03.003

Mazzola, M., Frediani, P., Bracci, S., and Salvini, A. (2003). New strategies for the synthesis of partially fluorinated acrylic polymers as possible materials for the protection of stone monuments. *Eur. Polym. J.* 39, 1995–2003. doi: 10.1016/S0014-3057(03)00110-1

Melo, M. J., Bracci, S., Camaiti, M., Chiantore, O., and Piacenti, F. (1999). Photodegradation of acrylic resins used in the conservation of stone. *Polym. Degrad. Stab.* 66, 23–30. doi: 10.1016/S0141-3910(99)00048-8

Morreale, M., Dintcheva, N. T., and La Mantia, F. P. (2013). Accelerated weathering of PP based nanocomposites: Effect of the presence of maleic anhydryde grafted polypropylene. *eXPRESS Polym. Lett.* 7, 703–715. doi: 10.3144/expresspolymlett.2013.67

Morreale, M., Liga, A., Mistretta, M. C., Ascione, L., and Mantia, F. P. (2015). Mechanical, thermomechanical and reprocessing behavior of green composites from biodegradable polymer and wood flour. *Materials* 8, 7536–7548. doi: 10.3390/ma8115406

Nakayama, N., and Hayashi, T. (2007). Preparation and characterization of poly(L-lactic acid)/TiO2 nanoparticle nanocomposite films with high transparency and efficient photodegradability. *Polym. Degrad. Stab.* 92, 1255–1264. doi: 10.1016/j.polymdegradstab.2007.03.026

Ocak, Y., Sofuoglu, A., Tihminlioglu, F., and Böke, H. (2009). Protection of marble surfaces by using biodegradable polymers as coating agent. *Prog. Org. Coat.* 66, 213–220. doi: 10.1016/j.porgcoat.2009.07.007

Ocak, Y., Sofuoglu, A., Tihminlioglu, F., and Böke, H. (2015). Sustainable bio-nano composite coatings for the protection of marble surfaces. *J. Cult. Herit.* 16, 299–306. doi: 10.1016/j.culher.2014.07.004

Sacchi, B., Cantisani, E., Giuntoli, G., Salvini, S., Scopetani, C., Rosi, L., et al. (2012). "Bio-polymers as stone protective," in *12th International Congress on Deterioration and Conservation on Stone* (New York, NY), 22–26.

Selwitz, C. (1988). *Cellulose Nitrate in Conservation.* Marina del Key, CA: Getty Conservation Institute.

Song, J. H., Murphy, R. J., Narayan, R., and Davies, G. B. (2009). Biodegradable and compostable alternatives to conventional plastics. *Philos. Trans. R. Soc. Lond. B Biol. Sci.* 364, 2127–2139. doi: 10.1098/rstb.2008.0289

Stloukal, P., Verney, V., Commereuc, S., Rychly, J., Matisova-Rychlá, L., Pis, V., et al. (2012). Assessment of the interrelation between photooxidation and biodegradation of selected polyesters after artificial weathering. *Chemosphere* 88, 1214–1219. doi: 10.1016/j.chemosphere.2012.03.072

Torrisi, A. (2008). Evaluation of five fluorinated compounds as calcarenite protective. *J. Cult. Herit.* 9, 135–145. doi: 10.1016/j.culher.2007.07.006

Tsakalof, A., Manoudis, P., Karapanagiotis, I., Chryssoulakis, I., and Panayiotou, C. (2007). Assessment of synthetic polymeric coatings for the protection and preservation of stone monuments. *J. Cult. Herit.* 8, 69–72. doi: 10.1016/j.culher.2006.06.007

Tsuji, H., Echizen, Y., and Nishimura, Y. (2006). Photodegradation of biodegradable polyesters: a comprehensive study on poly(L-lactide) and poly(3-caprolactone). *Polym. Degrad. Stab.* 91, 1128–1137. doi: 10.1016/j.polymdegradstab.2005.07.007

Vacchiano, C. D., Incarnato, L., Scarfato, P., and Acierno, D. (2008). Conservation of tuff-stone with polymeric resins. *Constr. Build. Mater.* 22, 855–865. doi: 10.1016/j.conbuildmat.2006.12.012

Xing, Q., Ruch, D., Dubois, P., Wu, L., and Wang, W. J. (2017). Biodegradable and high-performance poly(butylene adipate-co-terephthalate)–lignin UV-blocking films. *ACS Sustain. Chem. Eng.* 5, 10342–11035. doi: 10.1021/acssuschemeng.7b02370

Zaidi, L., Kaci, M., Bruzaud, S., Bourmaud, A., and Grohens, Y. (2010). Effect of natural weather on the structure and properties of polylactide/Cloisite 30B nanocomposites. *Polym. Degrad. Stab.* 95, 1751–1758. doi: 10.1016/j.polymdegradstab.2010.05.014

Zimbardo, M., Ercoli, L., Megna, B., and Scaffaro, R. (2019). Collapsibility of metastable sand by non-conventional oedometer tests. *Granul. Matter* 21:1. doi: 10.1007/s10035-018-0854-6

Sustainable Active PET Films by Functionalization With Antimicrobial Bio-Coatings

Annalisa Apicella, Paola Scarfato, Luciano Di Maio and Loredana Incarnato *

Department of Industrial Engineering, University of Salerno, Fisciano, Italy

The realization of antimicrobial films through the incorporation of active agents into a polymer matrix is a promising alternative to the direct addition of antimicrobials into the food matrix. To this aim, the goal of this work was to develop a sustainable, food packaging solution with antimicrobial effectiveness and high functional performance, based on Ethyl-Nα-dodecanoyl-L-arginate (LAE). Active biodegradable coatings, easy soluble to be removed, were realized by spreading a Polylactic acid/LAE coating solution, at different antimicrobial concentration (from 0 to 20%), on a recyclable Polyethylene-terephthalate substrate. The antimicrobial activity of the multilayer films was tested *in vitro* against *E.Coli* CECT 434 strain as pathogenic agent in liquid culture media. Moreover, the LAE chemical interaction with the PLA matrix was investigated, as well as its effect on the adhesion, wetting, optical and barrier properties of the films. The results pointed out that that the minimum LAE concentration incorporated already guarantees an antimicrobial activity comparable to commercial antimicrobial packaging solutions, and that, among the systems investigated, 10% LAE is the minimum concentration guaranteeing total inhibition without significantly altering the functionalities of the developed systems.

Keywords: antimicrobial packaging, ethyl-Nα-dodecanoyl-L-arginate (LAE), polylactic acid (PLA), PET, coating, biodegradable film

INTRODUCTION

Active packaging solutions have gained increasing attention in the last years from the food industry, since microbial contamination after processing is one of the major causes of foodborne diseases, representing both a public concern and an economic issue (Higueras et al., 2013; Coronel-León et al., 2016). At the same time, consumers demand is increasingly addressed toward the consumption of fresh-like, safe food products, with high organoleptic quality, prolonged shelf-life, and with fewer chemicals addition (Apicella et al., 2019).

The realization of antimicrobial packaging films, through the incorporation of active molecules into the bulk matrix, represents an innovative approach capable to avoid the direct addition, by dipping or spraying, of large antimicrobial amounts onto the food surface, where a large portion of spoilage and contamination occurs. As a matter of fact, the rapid diffusion of the antimicrobial into the food matrix results in an immediate reduction of bacterial populations, but does not allow controlling the metabolism growth of surviving biomass after depletion of antimicrobial residues (Chi-Zhang et al., 2004; Landi et al., 2014). The use of polymers as carriers, instead, allows the gradual delivery of the active agent during the storage and distribution of food packaging, with less antimicrobial concentration, tunable release and tailor-made applications (Lagaron, 2011).

The main challenges in this field are related to the production of effective packaging systems, with good functional properties, realized through easy-scalable, conventional technologies in use in food packaging industry and, last but not least, with high eco-sustainability (Scarfato et al., 2015a; Apicella et al., 2018a). In fact, the recent concerns toward waste-management issues and shortage of resources, have increasingly shifted the research focus to the development of eco-compatible and sustainable packaging solutions, by means of biomass-derived biodegradable or completely recyclable polymers, or a combination of both (Scarfato et al., 2015b; Zainab and Dong, 2019).

At the same time, the selection of the proper antimicrobial, as well as the choice of its optimal loading, is an important and not an easy task in the design and application of antimicrobial packaging (Becerril et al., 2013; Wicochea-Rodríguez et al., 2019). Some of these substances can modify the organoleptic profile of the packaged foodstuff, or can be used only for a small variety of foods, or can affect the functional properties (i.e., gas permeability, tensile strength, transparency, thermal stability, etc.) of the packaging material, or can have migration limits (European Commission, 2009; Aznar et al., 2013; Muriel-Galet et al., 2014; Paciello et al., 2015; Bugatti et al., 2019).

One of the most innovative and powerful antimicrobial compounds, not showing much of these drawbacks, is Ethyl-Nα-dodecanoyl-L-arginate (LAE). LAE is a derivative of lauric acid, L-arginine and ethanol, which showed an extensive spectrum of antimicrobial activity against Gram positive and Gram-negative bacteria, as well as yeasts and molds (Infante et al., 1997; Bakal and Diaz, 2005; Pezo et al., 2012). It interacts, as a cationic surfactant, on the cytoplasmic membrane of microorganisms increasing the cell permeability without causing lysis (Nerin et al., 2016). Among the major positive features, LAE has been classified as Generally Recognized as Safe (GRAS) and food preservative by the Food and Drug Administration (FDA), is chemically stable, has low cost, and does not provide any taste or odor, in compliance with European Regulation on active food packaging materials (Otero et al., 2014).

Previous published researches already addressed the realization of packaging films incorporated with LAE, realized by solvent casting technique (Muriel-Galet et al., 2012; Rubilar et al., 2016; Moreno et al., 2017; Haghighi et al., 2019). However, to the best of our knowledge, limited information is available concerning the development of sustainable packaging solutions based on PET films, functionalized with LAE-activated bio-coatings, and produced with conventional techniques easy-scalable at industrial level.

On the basis of the aforementioned considerations, the goal of this study was to develop antimicrobial, multifunctional, and sustainable food packaging films, based on LAE, by means of coating technology. The multilayer films were realized by spreading an amorphous PLA coating layer (C), incorporated at different concentrations of LAE, on a Bi-oriented PET substrate (S). PET was selected as web layer thanks to its excellent functional properties, as oxygen and water vapor barrier, high tensile strength, and thanks to its complete recyclability (Di Maio et al., 2017). Amorphous PLA coating already demonstrated to provide sealant layer to polyester films (Barbaro et al., 2015), in addition to its good optical properties, good processability, and environmental benefits (Scarfato et al., 2017). In addition, the biodegradable layer is easy to be removed by non-toxic solvents, ensuring the complete recovery of the recyclable substrate (Bugnicourt et al., 2013), and the coating technology ensures to avoid thermal stresses to heat sensitive active compounds.

The antimicrobial effectiveness of the active films was assessed by means of microbiological tests, using *E. Coli* CECT 434 strain as pathogenic agent. Moreover, the produced systems were characterized in order to ascertain the effect of the active phase on the chemical, morphological, and functional properties of the polymeric films.

MATERIALS AND METHODS

Materials

Commercial biaxially oriented poly(ethylene terephthalate) (BOPET) film (Nuroll S.p.a, Italy), with 23 μm thickness and corona treated surface, was used as substrate (S). PLA4060 (Natureworks, Minnetonka, USA), characterized by a D-lactide content of 12 wt%, was used for the coating layer (C). Ethyl-Nα-dodecanoyl-L-arginate (LAE) was provided by Vedeqsa Grupo LAMIRSA (Terrassa, Barcelona, Spain). All the solvents used were analytical grade.

Preparation of the Active Systems

Antimicrobial coated films were realized according to the method explained by Barbaro et al. (2015), with some modifications. The PLA coating solution was prepared by dissolving the polymer in acetone (mass ratio 20:80) and subsequently adding LAE at different percentages (0, 5, 10, and 20% w/wt). The casting mixture was spread on the BOPET substrate by means of a K Hand Coater (RK, Printocoat Instruments Ltd., Litlington, UK), equipped with stainless steel closed wound rod, with wire diameter equal to 0.64 mm, yielding final coatings with an average thickness of the coating layer comprised between 7 and 10 microns.

Table 1 resumes the list of the prepared films (named SC, SC5, SC10, and SC20). The PET substrate (S) was also used as comparison.

Characterization Methods
ATR-FTIR Analyses
Fourier Transform Infrared spectra of the films were collected by a Thermo Scientific Nicolet 600 FT-IR, equipped with a

TABLE 1 | List of the prepared systems, at different percentages of active phase.

Sample film	LAE concentration (wt %)	Thickness of the coating layer (μm)	Total thickness (μm)
S	0	0	23
SC	0	7 ± 0.5	30 ± 0.5
SC5	5	7 ± 0.9	30 ± 0.9
SC10	10	8 ± 1.0	31 ± 1.0
SC20	20	10 ± 1.2	34 ± 1.2

Smart Performer accessory for attenuated total-reflection (ATR) measurement using a ZnSe crystal. The operating spectral range was set at 650–4,000 cm^{-1}, with a resolution of 4 cm^{-1} and 64 scans per sample. Normalization and peak integration was performed using Omnic software.

Field Emission Scanning Electron Microscopy (FESEM) Analyses

Field Emission Scanning Electron Microscopy (SEM) analyses were conducted on the film sections, which were cut cryofracturing them in liquid nitrogen normally to the extrusion direction, sputter coated with gold (Agar Auto Sputter Coater mod. 108A, Stansted, UK) at 30 mA for 160 s, and analyzed using a field emission scanning electron microscope (mod. LEO 1525, Carl Zeiss SMT AG, Oberkochen, Germany).

Delamination Tests

In order to evaluate the adhesion strength of the PLA coatings, delamination tests were carried out by SANS dynamometer (mod. CMT 4000 by MTS, China), equipped with a 10 N load cell, according with the standards ASTM F88-00 and ASTM 2029. In particular, the coated films were cut in strips of 200 × 25 mm^2 area, sealed with a Brugger HSG-C (Germany) heat sealing machine at 120°C for 1s, by applying a force of 690 N, and stored for 48 h in environmental condition prior to analysis. Then, the bonding strength was evaluated in tensile mode at 250 mm/min until delamination failure of the seal. The maximum load reported is considered as the maximum bond strength of the coating on a specific substrate (expressed as N/25 mm). For each sample type, at least 10 measurements were performed to assess the reproducibility of the results.

Static Water Contact Angle and Surface Tension Characterization

Static contact angle measurements were performed with a First Ten Angstrom Analyzer System 32.0 mod. FTA 1000 (First Ten Angstroms, Inc., Portsmouth, VA, USA), according to the standard test method ASTM D5946. The drop volume was taken within the range where the contact angle did not change with the variation of the volume (2 ± 0.5 μL). Each reported value of the θ angle is the average of at least 10 replicate measurements. The dispersion (γ_s^d) and polar (γ_s^p) components of the surface energy (SE) for all the samples were calculated according to the Owens-Wendt geometric mean equation (Owens and Wendt, 1969), using distilled water and ethylene glycol as testing liquids. The SE components (mN/m) for water are: $\gamma = 72.1$, $\gamma^d = 19.9$, $\gamma^p = 52.2$, and for ethylene glycol are: $\gamma = 48$, $\gamma^d = 29$, $\gamma^p = 19$ (here γ is the total SE, and γ^d and γ^p are the dispersion and polar components, respectively) (Zonder et al., 2014).

Antimicrobial Activity Assays

The antimicrobial effectiveness of the films was tested against the Gram-negative bacteria *E. Coli* CECT 434 (ATCC 25922), selected because of its relevance in food industry. Stock culture was stored at −18°C in Nutrient Broth (Sigma-Aldrich, Missouri, USA) with 40% Glycerol. Subcultures were grown overnight in

Tryptic Soy Broth (TSB, Sigma-Aldrich) plus 0.6% Yeast Extract (YE, Sigma-Aldrich) at 37°C prior to each experiment.

The minimum inhibitory concentration (MIC) and the minimum bactericidal concentration (MBC) of LAE against the selected strain was determined in TSBYE. 1.2 g of LAE was diluted in 100 mL of Milli-Q water to obtain a concentration of 12,000 ppm, and then serial dilutions between 80 and 4 μg/mL were made up in sterile TSBYE to study MIC and MBC. Hundred microliter of ∼10^4 CFU/mL of microorganism in exponential phase was inoculated in each test tube. The tubes were incubated at 37°C overnight, then, 100 μL from each tube was plated and incubated at 37°C overnight (M100-S18, 2008). MIC was reported as the lowest antimicrobial concentration that inhibited the growth of the pathogen microorganism, while the MBC was defined as the lowest concentration at which no colonies growth was observed in the medium (TSBYE), and they were not culturable after plating onto Tryptic Soy Agar (TSA, Sigma-Aldrich) (Muriel-Galet et al., 2012; Higueras et al., 2013).

In vitro microbial tests on the films were performed by cutting 2.5 × 2.5 cm^2 of multilayer film samples at different LAE concentration (0, 5, 10, and 20%), sterilizing them by UV lamp on both sides, and placing them in a sterile tube containing 5 ml of TSBYE medium. Aliquots containing 100 μL of ∼10^4 CFU/mL of microorganism in exponential phase were inoculated in each test tube, and incubated at 37°C and 300 rpm overnight. Depending on the turbidity of the tubes, serial dilutions with physiological saline were made and plated in Petri dishes with 20 mL TSA culture medium. Colonies visible to naked eye were counted after incubation at 37°C overnight (Paciello et al., 2013). The negative controls (i.e., films in liquid medium without *E. Coli*) were also prepared. Counts were performed in triplicate.

Water Vapor Permeability Tests

Water vapor permeability was measured by M7002 Water Vapor Permeation Analyzer (Systech Instruments Ltd, Oxfordshire, UK) according to the standard ASTM F 1249. Films were tested at 23°C and 50% R.H., and the results, performed in triplicate, were expressed as PWV (g m/(m^2 Pa s)), calculated as the following equation (Li et al., 2015):

$$P_{WV} = \frac{WVTR \times L}{\Delta P} \qquad (1)$$

where WVTR is the water vapor transmission rate (g/m^{2}s) measured through the film, L is the average film thickness (m), and ΔP is the partial water vapor pressure difference (Pa) across the two sides of the film.

Optical Analyses

The optical properties of the films were evaluated by measuring the UV-Visible transmittance of the films from 200 to 800 nm with Perkin Elmer UV-Visible Spectrophotometer Lambda 800. The transparency of the films was evaluated by measuring the Transmittance % of visible light at 550 nm, according to the ASTM D1746-03.

RESULTS AND DISCUSSION

ATR-FTIR Analyses

Possible changes in intra- and intermolecular interactions due LAE addition into the PLA matrix were explored by Fourier transform infrared spectroscopy (FT-IR), which is sensitive to the structural conformation and local molecular motions. Due to the limited penetration depth of infrared radiation into the sample in the ATR-FT-IR measurement geometry, the spectra were collected on the thin PLA coating layers (namely C, C5, C10, and C20), at different percentages of antimicrobial, and compared to the spectrum of LAE, which is shown in **Figure 1A**. The absorption band at 3,320 cm^{-1} corresponds mainly to the ν(N-H) stretching vibration of hydrogen bonded N-H functionalities. The double peaks at 2,927 and 2,850 cm^{-1} can be assigned to antisymmetric and symmetric stretching vibrations of CH$_3$ and CH$_2$ functionalities, ν_{as}(CH$_3$/CH$_2$) and ν_s(CH$_3$/CH$_2$), respectively. The small peak around 1,740 cm^{-1} suggest the presence of carbonyl groups, the one at 1,560 cm^{-1} corresponds to the δ(N-H) bending vibrations (amide-II) combined with ν(C–N) stretching, the peak at 1,655 cm^{-1} is due to the ν(C=O) stretching vibration (amide-I), while the band situated around 1,027 cm^{-1} can be assigned to a ν(C–O) stretching vibration. Similar outcomes shown by other authors (Haghighi et al., 2019).

As it is possible to observe from **Figures 1B–D**, the PLA characteristic absorption peaks remains essentially unaltered, and the LAE characteristic absorption peaks are observable only by increasing the antimicrobial content in the coating layers. In particular, for the samples at 10 and 20% LAE (C10 and C20, respectively), the absorption bands at 2,927, 2,850, 1,655, and 1,027 cm^{-1} are detectable. The absence of changes in the intensities and positions of the major PLA and LAE bands suggests the realization of a physical mixture, with no chemical interaction between the two phases. Similar results were also reported by other authors (Rubilar et al., 2016; Gaikwad et al., 2017).

FESEM Analyses

As it is known, the microstructural properties of composite films depend on the compatibility between all the film components, affecting the final physical, mechanical, barrier, and optical properties (Attaran et al., 2015). To this aim, the distribution of the active phase inside the PLA matrix and the quality of the interlayer adhesion were investigated through SEM analyses. **Figures 2A,B** show the cross-section micrographs of SC and SC10 films, respectively, taken as an example. Images analyses display the PLA coating layer, in which few small voids are recognizable due to solvent evaporation, over the BOPET substrate, characterized by an oriented morphology. The absence of visible LAE powder domains inside the coating layer highlights the good dispersion and homogeneous distribution of the antimicrobial into the polymer matrix. Moreover, the absence of voids in the cross sectional area of the investigated films pointed out the good adhesion of the coating layers on the substrate.

Evaluation of Adhesion Strength and Surface Wettability

To determine the adhesion strength, delamination tests were performed as described in the methods section. The delamination occurred by separating the coating, thermally sealed at the defined temperature, by means of a dynamometer. The bonding strength, reported in **Table 2**, represents the force required to delaminate the PLA coating from the web.

The results show that the adhesion strength of the PLA coating layers was not significantly affected by the antimicrobial addition up to LAE concentrations equal to 10% (SC10 sample), whereas a decrease in the bonding strength for the SC20 film, equal to 2.56 ± 0.35 N/25 mm, was observed.

The adhesion strength strictly depends on the amount of polar and dispersion bonds between the substrate film and the coating (Lindner et al., 2017).

To this aim, the polar (γ_s^p) and dispersion (γ_s^d) components of the surface energy were calculated from water and ethylene glycol static contact angle measurements, as described in Par. 2.3.4, and displayed in **Table 2**.

The reported surface energy values show that the adhesion force is optimal when the γ_s^p and γ_s^d values are of the same order of magnitude, and maximum when their ratio is close to unity. On the other hand, when the difference between the γ_s^p and γ_s^d values is more pronounced, as in the case of SC20 sample, where it is of one order of magnitude, a significant drop in bonding strength is observable, which however remains acceptable for the film application in food packaging.

Antimicrobial Activity of the Active Bio-Coated Films With LAE

The antimicrobial activity of the multilayer films against *E. Coli* growth was then determined by the liquid medium method described in the experimental section.

A preliminary study, previously carried out on only the PLA coating layers, showed the antimicrobial effectiveness of the coatings in releasing the active agent and inhibiting the proliferation of microorganisms, with a total inhibition at the LAE concentration of 20% (Apicella et al., 2018b).

However, in the real packaging applications, the release does not occur symmetrically on both sides of the coating, and the different layout of systems can determine differences in the mass transport of the active agent. Therefore, it is necessary to study in depth the antimicrobial efficacy of the active multilayer films in real geometry and application conditions.

In first analysis, the MIC and the MBC for LAE were evaluated in the test conditions described in the methods section. The corresponding values are reported in **Table 3**, and are equal to 51 and 63 ppm, respectively. These values, different from previous results reported in the literature, highlight the influence of medium composition, of the method used (in terms of incubation time, inoculum concentration, and temperature), as well as of the strain used, in the quantification of the activity of the antimicrobial agent (Muriel-Galet et al., 2012).

Afterwards, the microbiological tests were conducted on the SC samples, at different LAE concentrations (0, 5, 10, and 20%)
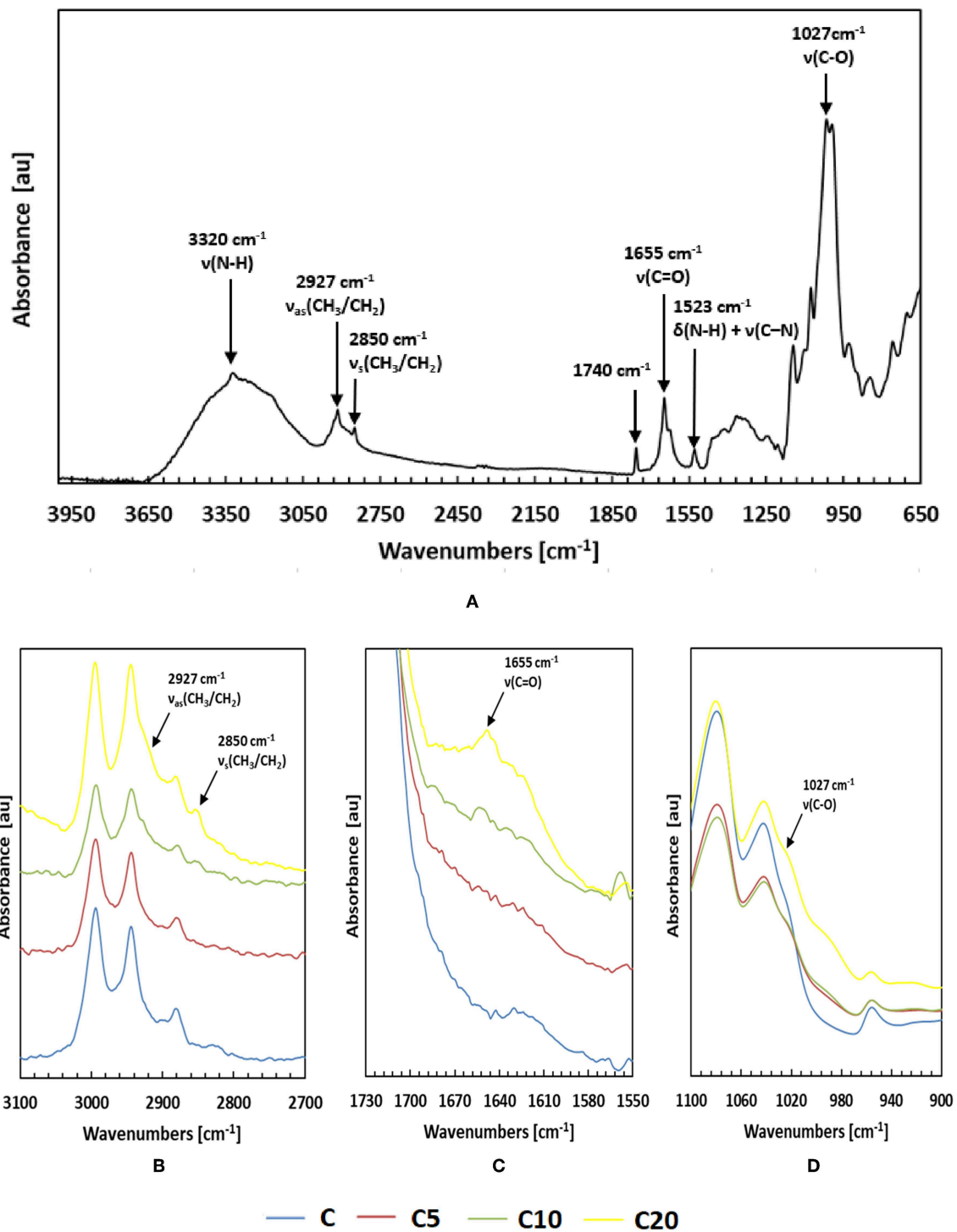
FIGURE 1 | ATR-FTIR spectra of LAE **(A)** and of the thin PLA coating layers C, C5, C10, and C20, loaded at 0, 5, 10, and 20% LAE, respectively **(B–D)**.

and with exposed surface area equal to 6.25 cm^2, according to the conditions described in the experimental section.

The results are reported in **Table 3**, and are expressed as logarithm of colony forming units (Log(CFU)) and log reduction value (LRV). Data regarding the control sample are also reported as reference. For further comprehension, **Figure 3** shows the pictures of the tested tubes after incubation at 37°C overnight, in comparison with the control sample.
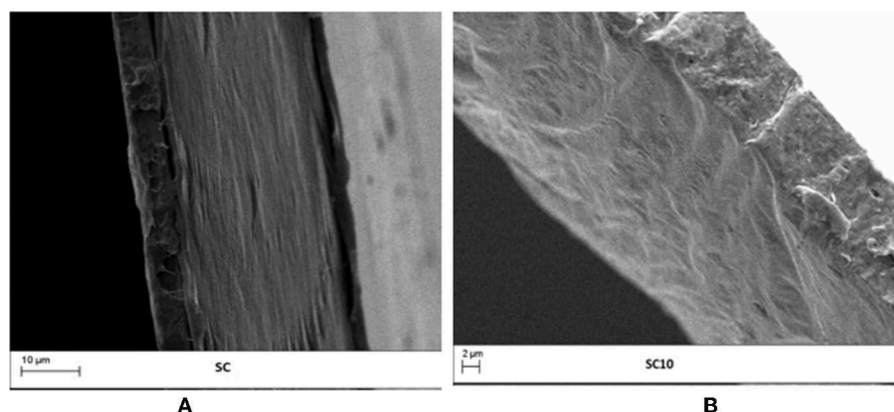
FIGURE 2 | Cross-sectional SEM micrographs of: **(A)** SC and **(B)** SC10 films.

TABLE 2 | Bonding strenght (N/25 mm), static water (CAw), and ethylene glycol (CA$_{EG}$) contact angles, and dispersion (γ_s^d) and polar (γ_s^p) components of the surface energy for the neat PET substrate film (S) and for the SC coated films at 0, 5, 10, and 20% LAE concentration.

Sample film	Bonding strenght (N/25 mm)	CAw (°)	CA$_{EG}$ (°)	γ_s^d	γ_s^p
S	Not sealable	65.3 ± 2.8	39.5 ± 0.9	18.8	19.3
SC	3.20 ± 0.4	65.8 ± 1.0	54.3 ± 1.3	7.4	28.6
SC5	3.12 ± 0.3	55.9 ± 1.1	43.1 ± 1.2	7.9	36.5
SC10	3.10 ± 0.8	54.2 ± 1.3	41.3 ± 1.1	7.9	38.1
SC20	2.56 ± 0.3	46.4 ± 2.2	40.5 ± 1.3	4.2	51.4

TABLE 3 | Minimum inhibitory concentration (MIC) and minimum bactericidal concentration (MBC) of LAE against *E. Coli*, and antimicrobial activity for the SC coated films at 0, 5, 10, and 20% LAE concentration., expressed as logarithm of colony forming units (Log(CFU)) and log reduction value (LRV).

Sample	*Escherichia Coli* CECT 434			
	MIC (ppm)	MBC (ppm)	Log(CFU)	LRV
LAE	51	63	–	–
Control	–	–	10.96 ± 0.69	–
SC	–	–	10.88 ± 1.22	0
SC5	–	–	5.79 ± 0.60	5.17
SC10	–	–	Total inhibition	
SC20	–	–	Total inhibition	

As expected, the unloaded SC sample was not effective in inhibiting the microbial growth, with an LRV value equal to 0 and a consistent turbidity in all the tubes containing the film samples (**Figure 3A**). On the other hand, the LAE addition caused a consistent (>5 log) reduction of the microorganism viable counts even at the lowest percentage analyzed. In fact, the multilayer film loaded at 5% LAE (SC5) caused a growth reduction of 5.17 log against *E. Coli*, while LAE concentration equal to 10%, or higher, produced total inhibition against the microorganism tested. What is more, the pictures comparison in **Figures 3B–D** showed a progressive increase in the optical clarity when compared to the control sample, and the disappearance of the bottom cellular deposit at LAE 10 and 20% (SC10 and SC20, respectively). It is worth to point out that the LRV value obtained even at the lowest concentration of LAE, indicates at least a partial deliver of the agent sufficient to achieve an antimicrobial effect comparable with or higher than currently commercially available antimicrobial films and coatings for foods and pharmaceuticals (Molling et al., 2014), while the 10% LAE concentration is the minimum guaranteeing total inhibition of microbial growth among the investigated systems.

These promising results highlight that the developed packaging solutions are efficient even at the minimum concentration of active agent investigated, and pave the way to more in depth studies on the release kinetics, aimed at optimizing the films in terms of antimicrobial concentration and coating thickness.

Water Vapor Permeability (WVP) Measurements

In order to better investigate the effects of the systems composition on the barrier performance of the samples, water vapor permeability tests were carried out, and outcomes are reported in **Table 4**. All the coated films (SC), with respect to the PET substrate (S), show an increase in the water vapor permeability values. However, this is mainly due to the normalization over the total thickness of the films, in which the amorphous PLA layer does not offer any resistance to the transport of water molecules (Robertson, 2013; Halász et al., 2015). A slight further increase in the water vapor permeability is observable at the highest LAE content, i.e., in the SC20 sample.

Optical Analyses

In packaging applications, the transmission of visible and ultraviolet light are important parameters to preserve and protect
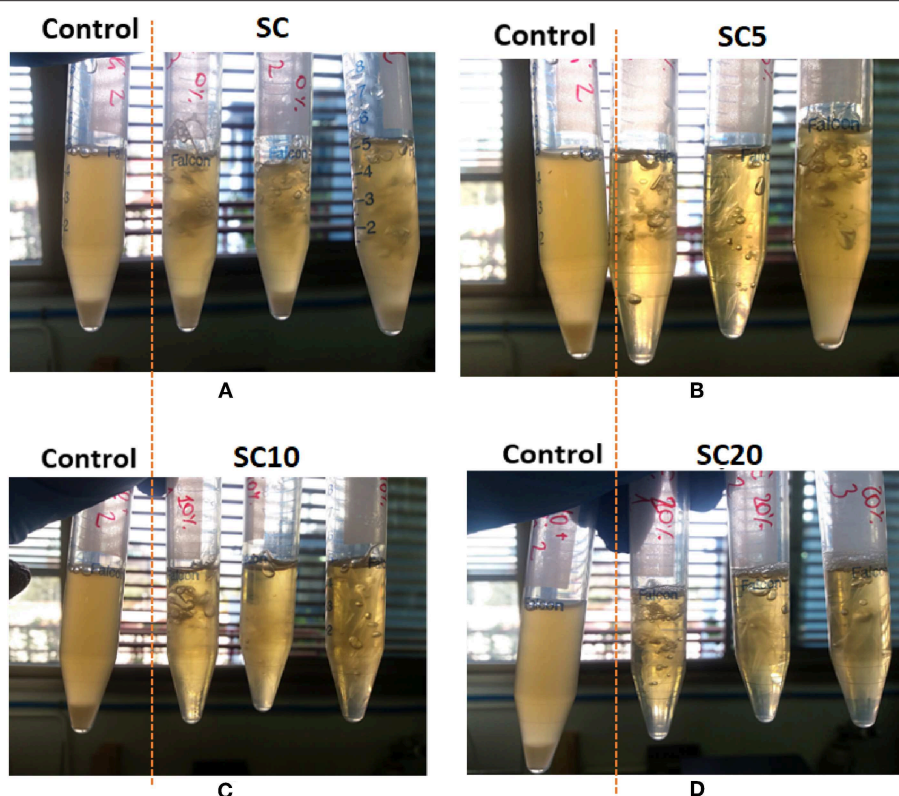
FIGURE 3 | Images of the tested safe-lock tubes inoculated with E. Coli and containing the SC coated films produced at different concentration of active agent: 0% LAE **(A)**, 5% LAE **(B)**, 10% LAE **(C)**, and 20% LAE **(D)**, after incubation at 37°C overnight, in comparison with the control sample.

TABLE 4 | Water vapor permeability (P_{WV}) and UV-Vis transmittance at 550 nm (T_{550}%) for the neat PET substrate film (S) and for the SC coated films at 0, 5, 10, and 20% LAE concentration.

Sample film	$P_{WV} * 10^{12}$ (g m/(m^2 Pa s)	T_{550} (%)
S	0.74 ± 0.01	84.3
SC	1.11 ± 0.04	84.3
SC5	1.12 ± 0.02	73.2
SC10	1.14 ± 0.02	69.1
SC20	1.25 ± 0.12	60.1

FIGURE 4 | UV-Vis transmission spectra of the neat PET substrate film (S) and for the SC coated films at 0, 5, 10 and 20% LAE concentration.

food products until they reach the consumer, as well as to get an attractive transparent package. To evaluate the transparency of samples, UV-Vis measurements were carried out. PET and PLA are known to have excellent optical properties, in this sense the LAE effect on transparency was investigated. In UV-Vis spectra reported in **Figure 4**, the transmittance percentage T% is reported as a function of wavelength for the neat substrate (S) the coated SC films at different content of the active phase. The transparency of the multilayer films, defined as the transparency of visible light in short range of 540–560 nm, was therefore evaluated measuring the transmission at 550 nm (T_{550}%), and the values for the investigated samples are reported in **Table 4**.

As observable from the comparison among the S and SC samples, the PLA coating did not affect the transparency of the

PET substrate, which remains the highest, with a T_{550}% value equal to 84.3% in both films. The further LAE addition to the polymer matrix determines a slight decrease in the transmittance at 550 nm, which becomes more significant at LAE concentration equal to 20% (T_{550}% of SC20 equal to 60.1%). In this latter case,
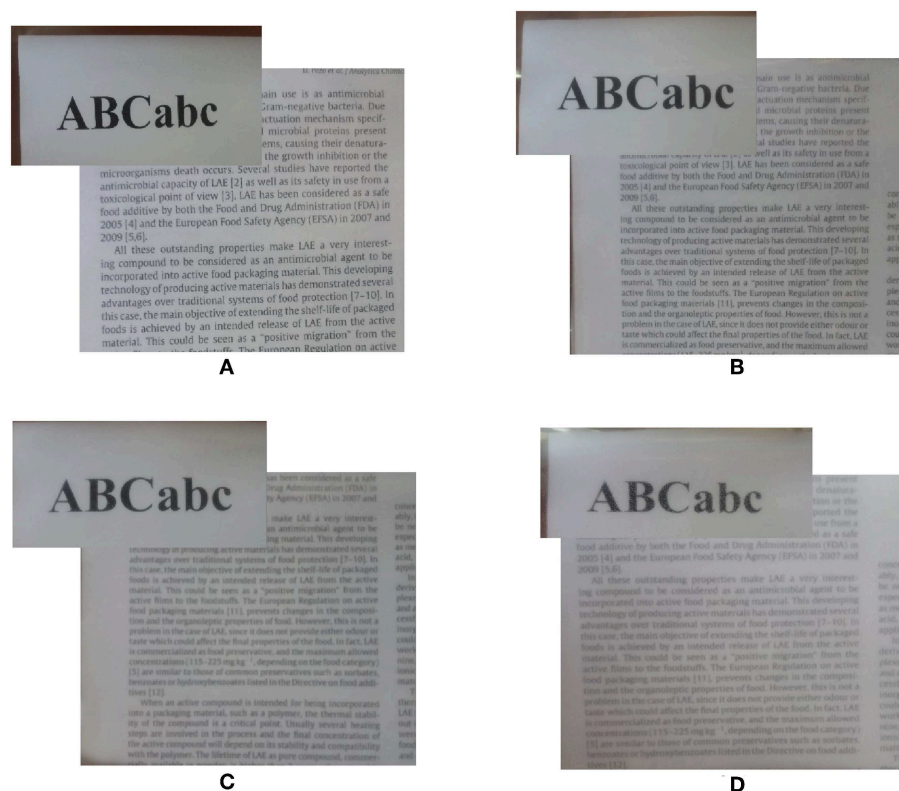
FIGURE 5 | Pictures of the SC coated films at different concentration of active agent: 0% LAE **(A)**, 5% LAE **(B)**, 10% LAE **(C)**, and 20% LAE **(D)**.

the increase in film cloudiness, with respect to the SC, SC5 and SC10 samples, is also visible in **Figure 5**.

CONCLUSIONS

In this work, innovative multifunctional and eco-sustainable antimicrobial packaging solutions have been successfully developed, through a conventional technique commonly applied in packaging industry. The produced films combine the structural and barrier performance of PET with the PLA sealing capacity and the LAE antimicrobial activity.

The chemical, physical and functional analyses carried out on the active multilayer films showed the good dispersion and homogeneous distribution of LAE into the polymer matrix, as well as the good adhesion of the coating layer on the substrate. Moreover, LAE addition did not modify the macromolecular structure of PLA.

Microbiological tests pointed out the effectiveness of the produced systems in releasing the antimicrobial agent and inhibiting microbial growth. In particular, the inhibition of microbial strain was found proportional to the LAE concentration into the PLA matrix, with 5.17 log decrease of viable counts at 5% LAE and total inhibition measured for coating formulations at higher LAE content.

In particular, it was pointed out that, by increasing the LAE concentration up to 10%, the functional performance of the films,

in terms of adhesion, water vapor barrier and optical properties, were not significantly affected. On the other hand, increasing LAE content at 20%, a worsening of the PET film functionalities was observed. On the basis of these results, it comes out that the 10% LAE configuration allowed to obtain the best performance in terms of total microbial inhibition and functional properties.

DATA AVAILABILITY STATEMENT

All datasets generated for this study are included in the manuscript/supplementary files.

AUTHOR CONTRIBUTIONS

AA and LI: conceived and designed the experiments. AA: performed the experiments and the original draft preparation. AA, LD, and PS: conceptualization. LD, PS, and LI: review and editing of the manuscript. All authors discussed and revised the manuscript.

ACKNOWLEDGMENTS

REFERENCES

Apicella, A., Adiletta, G., Di Matteo, M., and Incarnato, L. (2019). Valorization of olive industry waste products for development of new eco-sustainable, multilayer antioxidant packaging for food preservation. *Chem. Eng. Trans.* 75, 85–90. doi: 10.3303/CET1975015

Apicella, A., Scarfato, P., D'Arienzo, L., Garofalo, E., Di Maio, L., and Incarnato, L. (2018b). Antimicrobial biodegradable coatings based on LAE for food packaging applications. *AIP Confer. Proc.* 1981:020010. doi: 10.1063/1.5045872

Apicella, A., Scarfato, P., Di Maio, L., Garofalo, E., and Incarnato, L. (2018a). Evaluation of performance of PET packaging films based on different copolyester O₂-scavengers. *AIP Confer. Proc.* 1981:020130. doi: 10.1063/1.5045992

Attaran, S. A., Hassan, A., and Wahit, M. U. (2015). Materials for food packaging applications based on bio-based polymer nanocomposites. *J. Thermoplast. Compos. Mater.* 30, 143–173. doi: 10.1177/0892705715588801

Aznar, M., Gómez-Estaca, J., Vélez, D., Devesa, V., and Nerín, C. (2013). Migrants determination and bioaccessibility study of ethyl lauroyl arginate (LAE) from a LAE based antimicrobial food packaging material. *Food Chem. Toxicol.* 56, 363–370. doi: 10.1016/j.fct.2013.02.018

Bakal, G., and Diaz, A. (2005). The lowdown on lauric arginate: food antimicrobial hammers away at plasma membrane, disrupting a pathogen's metabolic process. *Food Qual.* 12, 54–61. Available online at: https://www.foodqualityandsafety.com/article/the-lowdown-on-lauric-arginate/

Barbaro, G., Galdi, M. R., Di Maio, L., and Incarnato, L. (2015). Effect of BOPET film surface treatments on adhesion performance of biodegradable coatings for packaging applications. *Eur. Polym. J.* 68, 80–89. doi: 10.1016/j.eurpolymj.2015.04.027

Becerril, R., Manso, S., Nerin, C., and Gómez-Lus, R. (2013). Antimicrobial activity of Lauroyl Arginate Ethyl (LAE), against selected food-borne bacteria. *Food Control* 32, 404–408. doi: 10.1016/j.foodcont.2013.01.003

Bugatti, V., Brachi, P., Viscusi, G., and Gorrasi, G. (2019). Valorization of tomato processing residues through the production of active bio-composites for packaging applications. *Front. Mater.* 6:34. doi: 10.3389/fmats.2019.00034

Bugnicourt, E., Schmid, M., Nerney, O. M., Wildner, J., Smykala, L., Lazzeri, A., et al. (2013). Processing and validation of whey-protein-coated films and laminates at semi-industrial scale as novel recyclable food packaging materials with excellent barrier properties. *Adv. Mater. Sci. Eng.* 2013, 1–10. doi: 10.1155/2013/496207

Chi-Zhang, Y., Yam, K., and Chikindas, M. L. (2004). Effective control of Listeria monocytogenes by combination of nisin formulated and slowly released into a broth system. *Int. J. Food Microbiol.* 90, 15–22. doi: 10.1016/S0168-1605(03)00168-5

Coronel-León, J., López, A., Espuny, M. J., Beltran, M. T., Molinos-Gómez, A., Rocabayera, X., et al. (2016). Assessment of antimicrobial activity of Nᵅ -lauroyl arginate ethylester (LAE®) against *Yersinia enterocolitica* and *Lactobacillus plantarum* by flow cytometry and transmission electron microscopy. *Food Control* 63, 1–10. doi: 10.1016/j.foodcont.2015.10.050

Di Maio, L., Marra, F., Apicella, A., and Incarnato, L. (2017). Evaluation and modeling of scavenging performances of active multilayer PET based films for food preservation. *Chem. Eng. Trans.* 57, 1879–1884. doi: 10.3303/CET1757314

European Commission (2009). Commission regulation (EC) No 450/2009 of 29 May 2009 on active and intelligent materials and articles intended to come into contact with food. *Off. J. Eur. Union* L135, 3–11. Available online at: http://data.europa.eu/eli/reg/2009/450/oj

Gaikwad, K. K., Lee, S. M., Lee, J. S., and Lee, Y. S. (2017). Development of antimicrobial polyolefin films containing lauroyl arginate and their use in the packaging of strawberries. *J. Food Meas. Charact.* 11, 1706–1716. doi: 10.1007/s11694-017-9551-0

Haghighi, H., De Leo, R., Bedin, E., Pfeifer, F., Siesler, H. W., and Pulvirenti, A. (2019). Comparative analysis of blend and bilayer films based on chitosan and gelatin enriched with LAE (lauroyl arginate ethyl) with antimicrobial activity for food packaging applications. *Food Pack. Shelf Life* 19, 31–39. doi: 10.1016/j.fpsl.2018.11.015

Halász, K., Hosakun, Y., and Csóka, L. (2015). Reducing water vapor permeability of poly(lactic acid) film and bottle through layer-by-layer deposition of green-processed cellulose nanocrystals and chitosan. *Int. J. Polym. Sci.* 2015:954290. doi: 10.1155/2015/954290

Higueras, L., Lopez-Carballo, G., Hernandez-Munoz, P., Gavara, R., and Rollini, M. (2013). Development of a novel antimicrobial film based on chitosan with LAE (Ethyl-Nα-dodecanoyl-l-arginate) and its application to fresh chicken. *Int. J. Food Microbiol.* 165, 339–345. doi: 10.1016/j.ijfoodmicro.2013.06.003

Infante, M., Pinazo, A., and Seguer, J. (1997). Non-conventional surfactants from amino acids and glycolipids: structure, preparation and properties. *Colloids Surf. A* 123–124, 49–70. doi: 10.1016/S0927-7757(96)03793-4

Lagaron, J. M. (2011). *Multifunctional and Nanoreinforced Polymers for Food Packaging*. Cambridge: Woodhead Publishing.

Landi, C., Paciello, L., De Alteriis, E., Brambilla, L., and Parascandola, P. (2014). High cell density culture with S. cerevisiae CEN.PK113-5D for IL-1β production: optimization, modeling, and physiological aspects. *Bioproc. Biosyst. Eng.* 38, 251–261. doi: 10.1007/s00449-014-1264-8

Li, G., Shankar, S., Rhim, J.-W., and Oh, B.-Y. (2015). Effects of preparation method on properties of poly(butylene adipate-co-terephthalate) films. *Food Sci. Biotechnol.* 24, 1679–1685. doi: 10.1007/s10068-015-0218-5

Lindner, M., Rodler, N., Jesdinszki, M., Schmid, M., and Sängerlaub, S. (2017). Surface energy of corona treated PP, PE and PET films, its alteration as function of storage time and the effect of various corona dosages on their bond strength after lamination. *J. Appl. Polym. Sci.* 135:45842. doi: 10.1002/app.45842

Molling, J., Seezink, J., Teunissen, B., Muijrers-Chen, I., and Borm, P. (2014). Comparative performance of a panel of commercially available antimicrobial nanocoatings in Europe. *Nanotechnol. Sci. Appl.* 7, 97–104. doi: 10.2147/NSA.S70782

Moreno, O., Gil, À., Atarés, L., and Chiralt, A. (2017). Active starch-gelatin films for shelf life extension of marinated salmon. *LWT Food Sci. Technol.* 84, 189–195. doi: 10.1016/j.lwt.2017.05.005

Muriel-Galet, V., López-Carballo, G., Gavara, R., and Hernández-Muñoz, P. (2012). Antimicrobial food packaging film based on the release of LAE from EVOH. *Int. J. Food Microbiol.* 157, 239–244. doi: 10.1016/j.ijfoodmicro.2012.05.009

Muriel-Galet, V., López-Carballo, G., Hernández-Muñoz, P., and Gavara, R. (2014). Characterization of ethylene-vinyl alcohol copolymer containing lauril arginate (LAE) as material for active antimicrobial food packaging. *Food Pack. Shelf Life* 1, 10–18. doi: 10.1016/j.fpsl.2013.09.002

Nerin, C., Becerril, R., Manso, S., and Silva, F. (2016). "Ethyl Lauroyl Arginate (LAE): antimicrobial activity and applications in food systems," in *Antimicrobial Food Packaging,* ed J. Barros-Velázquez (London: Elsevier Science), 305–312.

Otero, V., Becerril, R., Santos, J. A., Rodríguez-Calleja, J. M., and Cristina Nerín, García-López, M. L. (2014). Evaluation of two antimicrobial packaging films against Escherichia coli O157:H7 strains *in vitro* and during storage of a Spanish ripened sheep cheese (Zamorano). *Food Control* 42, 296–302. doi: 10.1016/j.foodcont.2014.02.022

Owens, D. K., and Wendt, R. C. (1969). Estimation of the surface free energy of polymers. *J. Appl. Polym. Sci.* 13, 1741–1747. doi: 10.1002/app.1969.070130815

Paciello, L., Falco, F. C., Landi, C., and Parascandola, P. (2013). Strengths and weaknesses in the determination of yeast cell viability by ATP-based bioluminescence assay. *Enzyme Microb. Technol.* 52, 157–116. doi: 10.1016/j.enzmictec.2012.12.011

Paciello, L., Landi, C., Orilio, P., Di Matteo, M., Zueco, J., and Parascandola, P. (2015). Bread making with Saccharomyces cerevisiae CEN.PK113-5D expressing lipase A from bacillus subtilis: leavening characterisation and aroma enhancement. *J. Food Sci. Technol.* 50, 2120–2128. doi: 10.1111/ijfs.12876

Pezo, D., Navascués, B., Salafranca, J., and Nerín, C. (2012). Analytical procedure for the determination of Ethyl Lauroyl Arginate (LAE) to assess the kinetics and specific migration from a new antimicrobial active food packaging. *Anal. Chim. Acta.* 745, 92–98. doi: 10.1016/j.aca.2012.07.038

Robertson, G. L. (2013). *Food Packaging Principles and Practice, 3rd Edn.* Boca Raton, FL: CRC Press.

Rubilar, J. F., Candia, D., Cobos, A., Díaz, O., and Pedreschi, F. (2016). Effect of nanoclay and Ethyl-Nα-dodecanoyl-L-arginate hydrochloride (LAE) on physico-mechanical properties of chitosan films. *LWT Food Sci. Technol.* 72, 206–214. doi: 10.1016/j.lwt.2016.04.057

Scarfato, P., Avallone, E., Galdi, M. R., Di Maio, L., and Incarnato, L. (2015a). Preparation, characterization, and oxygen scavenging capacity of biodegradable α-tocopherol/PLA microparticles for active food packaging applications. *Polym. Compos.* 38, 981–986. doi: 10.1002/pc.23661

Scarfato, P., Di Maio, L., and Incarnato, L. (2015b). Recent advances and migration issues in biodegradable polymers from renewable sources for food packaging. *J. Appl. Polym. Sci.* 132:42597. doi: 10.1002/app.42597

Scarfato, P., Di Maio, L., Milana, M. R., Giamberardini, S., Denaro, M., and Incarnato, L. (2017). Performance properties, lactic acid specific migration and swelling by simulant of biodegradable poly(lactic acid)/nanoclay multilayer films for food packaging. *Food Addit. Contam. Part A* 34, 1730–1742. doi: 10.1080/19440049.2017.1321786

Wicochea-Rodríguez, J. D., Chalier, P., Ruiz, T., and Gastaldi, E. (2019). Active food packaging based on biopolymers and aroma compounds: how to design and control the release. *Front. Chem.* 7:398. doi: 10.3389/fchem.2019.00398

Zainab, W. A., and Dong, Y. (2019). Biodegradable and water resistant poly(vinyl) alcohol (PVA)/starch (ST)/glycerol (GL)/halloysite nanotube (HNT) nanocomposite films for sustainable food packaging. *Front. Mat.* 6:58. doi: 10.3389/fmats.2019.00058

Zonder, L., Mccarthy, S., Rios, F., Ophir, A., and Kenig, S. (2014). Viscosity ratio and interfacial tension as carbon nanotubes distributing factors in melt-mixed blends of polyamide 12 and high-density polyethylene. *Adv. Polym. Technol.* 33:21427. doi: 10.1002/adv.21427

Micromolded Polylactid Acid With Selective Degradation Rate

Valentina Iozzino, Annarita De Meo* and Roberto Pantani

Department of Industrial Engineering, University of Salerno, Fisciano, Italy

Poly(Lactic Acid), PLA represents a very interesting polymer for industrial applications because of its good processability, the possibility of being obtained from renewable sources, good physical properties, biocompatibility, and biodegradability. The major depolymerization mechanism and the step that controls the rate of PLA biodegradation in compost is represented by the hydrolysis. The characteristic of being degradable is not per se an advantage: the inclination to degrade in the presence of water represents a limit for specific industrial applications, especially for durable components that are designed for long-period utilization such as in the automotive, electronic, and agricultural sectors, as well as in medical applications. Being able to control the degradation rate would be a real advantage: a product should preserve its characteristics during processing and for a time comparable to its application but should be nevertheless fully biodegradable at longer times. Furthermore, a gradient of properties could allow producing samples in which some portions degrade at a faster rate and some others at a slower one. Different methods can be used to influence the degradation rate of PLA, some examples are blending, copolymerization and surface modification. However, these change the physical properties of the material. Any factor influencing the rate of hydrolysis can affect the biodegradation process. The objective of this work is verifying the possibility to modulate the rate of degradation in the same part, in time and at different rates. The method is represented by a technique that influences locally the morphology of the samples. Biphasic samples (half amorphous and the other half crystalline) were obtained by micro-injection molding and the degradation process was monitored by means of hydrolysis tests. The analysis confirmed the crystalline regions show a slightly better resistance to the hydrolysis compared to the amorphous.

Keywords: PLA, micromolding, crystallinity, hydrolysis, mechanical properties

INTRODUCTION

In the last decades, environmental and economic challenges led scientists and producers to replace, in part, oil-based polymers with biodegradable. Poly(l,l-lactide) acid, hereafter called PLA, represents a good candidate. PLA is a thermoplastic characterized by a high value of strength and a high modulus. The resources that are used to produce PLA, like rice, corn or wheat, are annually renewable. Moreover, it is compostable and can be recycled (Drumright et al., 2000; Sawyer, 2003), producing this polymer consumes carbon dioxide (Dorgan et al., 2001). Another advantage of the PLA is its biocompatibility, especially for biomedical applications, in fact, it is not toxic for local tissues (Farah et al., 2016). Furthermore, the degradation products do not affect tissue healing. The

use of PLA, that was limited for medical and dental applications in the past, is turning into common applications like packaging and single-use products.

Being interested in the use of PLA in engineering areas and in applications for higher added value, currently, many scientists focused their attention in the production of new biodegradable polymers that have better processability, mechanical properties, and thermal resistance, as well as long durability and stability (Murariu and Dubois, 2016). In the last years, the market is turning to more "durable" biomaterials like engineering parts for electronics and automotive industry (Drumright et al., 2000; Auras et al., 2004; Guptaa et al., 2007; Jamshidian et al., 2010; Nampoothiri et al., 2010; Babu et al., 2013; Raquez et al., 2013; Murariu et al., 2014; Wertz et al., 2014). The concern for the use of this polymer to satisfy the market needs of bioplastics with a long duration, in sectors such as electronics and automotive components and obtain a processability similar to that of the existing polymers, is causing a rapid growth in PLA production.

The PLA products can be obtained by using the common processing techniques like extrusion, injection molding and compression molding (Garlotta, 2001; McKeen, 2014). Ghosh et al. (2008) verified that the technique for shear controlled orientation in injection molding, called SCORIM, can have an effect on the final energy at break as well as the maximum stress. However, due to its high viscosity, and a relatively narrower processing windows with respect to other resins, only under particular conditions, PLA can be processed by microinjection molding and most of the literature research focused on the microinjection molding of PLA composites or blends (Zhao et al., 2018; Zhou et al., 2018).

To enhance PLA properties, many efforts are undertaken via different techniques and modifications, adding additives (Iozzino et al., 2018) or by realizing physical treatments (Harris and Lee, 2008; De Santis et al., 2017). Some workers proved that by increasing the crystallinity of PLA products the chemical and thermal resistances improve (Gamez-Perez et al., 2011). For this reason, the study of the crystallization kinetics of PLA was of relevant importance (Pantani et al., 2010).

The degradation of biopolymers is the result of two mechanisms: the chemical hydrolysis and the water and oligomer diffusion. In order to estimate the effects of one of the two mechanisms, the hydrolytic degradation kinetics in the chemical regime, the study can be performed in solution (Zhang et al., 1994; De Jong et al., 2001). Different authors suggest an Arrhenius-dependent kinetics (Tsuji, 2003; Weir et al., 2004; Speranza et al., 2014). Many papers concerned the hydrolysis of PLA, studying the elements that can affect the mechanism of chain scission like the molecular weight, the temperature and the chain stereo-configuration (Lostocco and Huang, 1998; Drumright et al., 2000; Gorrasi and Pantani, 2017). Some workers verified that the carboxyl end groups accelerate the hydrolysis of PLA (Li et al., 1990; Hocking et al., 1995), and the kinetics solution is determined by the pH of the degrading medium (De Jong et al., 2001). The mechanism of hydrolysis is still under investigation, in fact, some authors verified that the scission of the chains occurs randomly also in acid (Shih, 1995) or in basic conditions (Belbella et al., 1996). The process of chain scission

compared to the end scission determines a substantial reduction of the physical properties (Gleadall et al., 2014). Although, the influence of the stereochemical composition is still not clear (Gorrasi and Pantani, 2013).

The control of the biodegradation rate is interesting for the application in many sectors (Ha and Xanthos, 2010). There are several techniques that can be used to modify the rate of biodegradation. Examples are developments of blends, copolymers and use of particular fillers (Arias et al., 2014; Stloukal et al., 2015; Iozzino et al., 2018).

Literature research reveals that the morphology itself of the PLA can affect its degradation. Since the possibility for the water molecules to enter inside the rigid crystalline regions is extremely limited, the crystalline portion of PLA parts show higher resistance to the hydrolysis respect to amorphous regions. When different crystallinity levels are present in the part, the hydrolysis proceeds breaking the chains in the amorphous regions, therefore, removing the oligomers and monomers that are soluble in water, only intact crystalline regions remain (Tsuji, 2010). Others (Pantani and Sorrentino, 2013) demonstrated, also, that the initial morphology of PLA parts has a high influence on the degradation, in particular on the swelling and flake off processes. Completely amorphous PLA showed a higher degradation than semicrystalline PLA in presence of the same conditions of hydrolytic process (Fukushima et al., 2013). The amount of hydrolysis found for amorphous PLA parts was considerably high. In crystalline polymers the hydrolytic attack of ester bonds can be favorite.

The aim of this work is the production of parts with different morphologies, investigate the effect of the hydrolysis on the degradation of the poly-lactid acid parts and therefore observe the establishment of a profile of the properties inside each sample. In particular, thin PLA bars characterized by different crystallinity along the length were produced by microinjection molding adopting a novel technique that permits the local control of the temperature during and after the process thus affecting the crystallization in a selected region of the sample (De Santis and Pantani, 2016). The crystallinity, the evolution of the molecular weight and the mechanical properties of biphasic samples with different times of hydrolysis were investigated.

MATERIALS AND METHODS

Material

The material used in this work is a commercial PLA, the 4032D, supplied by Natureworks. Its D-enantiomer content is approximately equal to 2%. The molecular weight distribution detected by chromatography: Mn 119,000 g/mol and Mw 207,000 g/mol. In order to prevent viscosity degradation, each test was preceded by a drying procedure for the material that was kept for 8 h at 60°C under vacuum.

Samples Preparation

PLA bars were produced by injection molding with a Haake MiniJet Machine and a mold with a cavity geometry of 10 × 4 mm with a thickness of 0.25 mm. Micromolding was carried out at a melt temperature of 220°C, injection pressure of 150 bar,

FIGURE 1 | Schematic of the steps for the parts production.

FIGURE 2 | Assembly for penetration test and scheme of the test.

FIGURE 3 | Temperature measurements during the process.
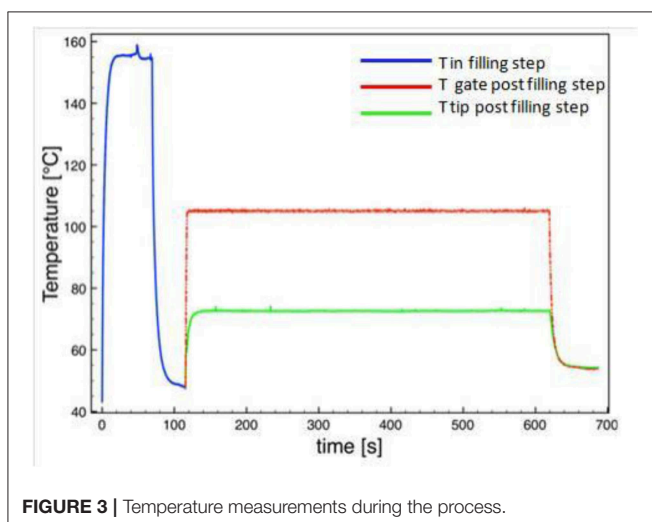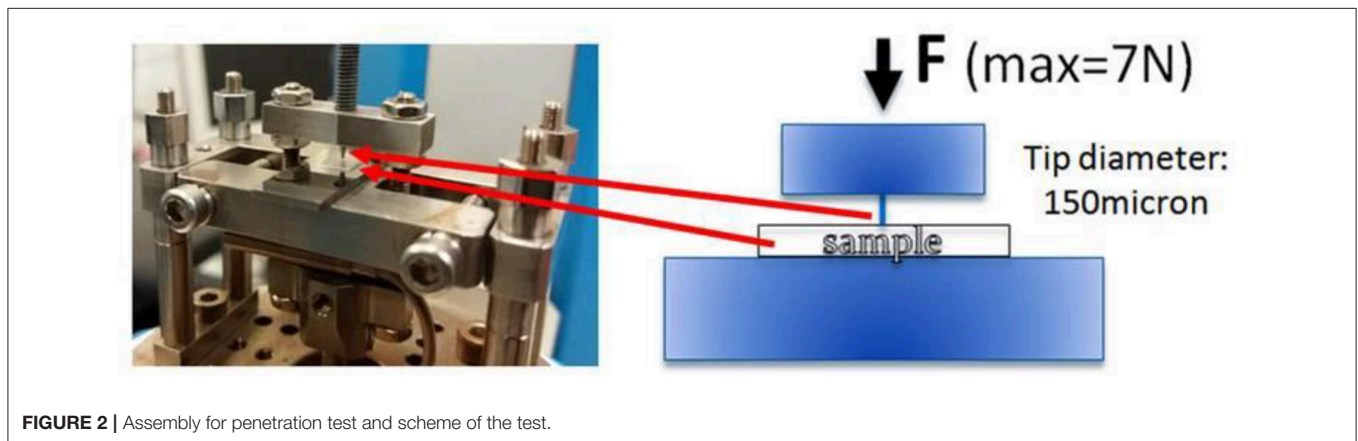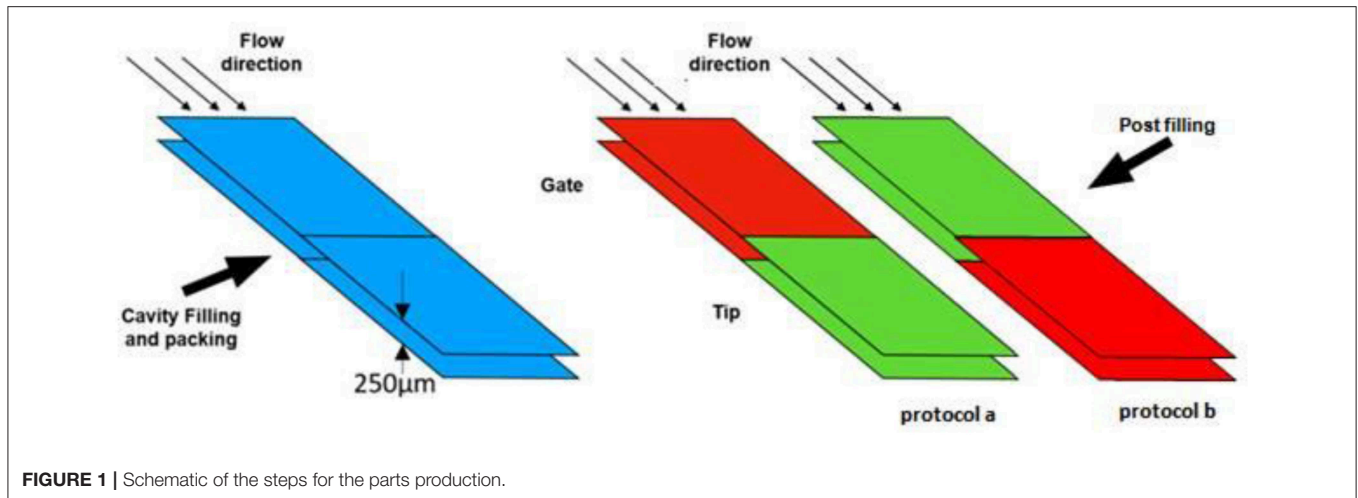
post injection pressure of 140 bar. The whole process was carried out under a nitrogen atmosphere. The cavity was inserted in a special mold equipped with a control system for the temperature of the cavity surfaces. This system adopted resistances to heat the surfaces of the cavity by Joule effect and thermocouples that allowed controlling the temperature by switching the current to the heaters. As showed in **Figure 1**, the process involved different steps: after the cavity surfaces were heated up to 160°C the molten PLA was injected into the thin the cavity (injection step), the material was cooled by switching off the resistances from about 160°C to about 50°C in 15 s (cooling step). Then only one zone of the solid injected sample was kept at 105°C for 500 s (annealing step). Since the PLA has very slow crystallization kinetics, the region of the injection-molded parts that did not experience the annealing step resulted to be fully amorphous. The region that was kept at 105°C (De Meo et al., 2018) resulted crystalline. Two protocols were used to produce the samples for the degradation study. In protocol "a," after the filling and cooling steps, the region under annealing is the one after the gate. In the protocol "b," the region under annealing is the tip of the sample (**Figure 1**).

Hydrolysis

The degradation of the PLA parts was investigated by means of hydrolysis tests. Each sample was immersed into distilled water. In line with the ASTM and ISO standards, the biodegradation experiments were carried out at 58°C. The samples have been

put individually in containers with distillated water where the quantity of water [ml] was 800 times the quantity of the dried sample [g]. A thermostatic bath equipped with a lid was adopted to mantain the temperature constant and equal to 58°C during the hydrolysis experiments. After every 24 h of hydrolysis, the water of each sample was analyzed by using a Crison pH-meter at 25°C. The water used in this work has a pH value of about 6.5. The water of each sample was replaced by the same amount of fresh distilled water to assure that the pH value of the hydrolysis medium remains constant. This operation was carried out by using a syringe which needle diameter is 0.2 mm. In order to carry out the necessary analysis, the samples were collected and dried in vacuum conditions at

60°C for about 3 h and then weighed. The samples, for the whole hydrolysis test, remain in their vessels, to avoid losses of the hydrolyzed material. All tests were carried out on at least three samples. The results reported refer to the average upon all the tests. The hydrolysis of all samples was carried out for about 60 days. After 60 days, since the samples became fragments with a very small mass an accurate analysis was not possible anymore.

Calorimetry

Calorimetric analysis were carried out to monitor the crystallinity with the time of hydrolysis. A Mettler DSC822 in flowing nitrogen atmosphere was used for this purpose. To obtain reliable measurements, the indium, which is a standard material, was used to calibrate the heat flow and the temperature Thermograms were obtained by considering a mass of about 5 mg for each sample and the following thermal program:

- Heating at 10°C/min from −10°C to 200°C (first heating);
- Isothermal step for 5 min at 200°C;
- Cooling step at 10°C/min from 200°C to−10°C (cooling);
- Heating at 10°C/min from −10°C to 200°C (second heating).

Gel Permeation Chromatography (GPC)

As hydrolysis proceeds, the evolution of molecular weight of the microparts was monitored by performing GPC analyses. A HPLC Waters (Milford, MA, USA) fitted out with an auto-sampler. After dissolving the parts in thetrahydrofuran (THF), considering a ratio between the sample mass and the quantity of solvent at 50°C equal to 1 [g/mol], a 0.45 μm filter Chromafil PTFE was used for the investigation.

Mechanical Tests

The breaking force was evaluated by means of penetration mechanical tests. The dynamic mechanical measurements were
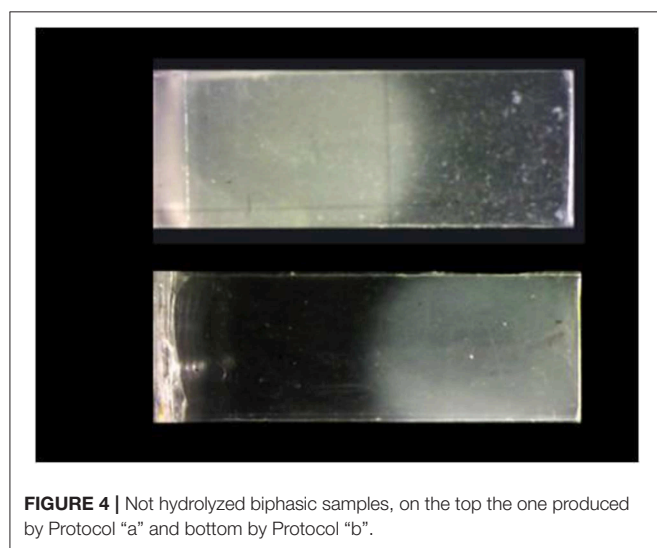
FIGURE 4 | Not hydrolyzed biphasic samples, on the top the one produced by Protocol "a" and bottom by Protocol "b".
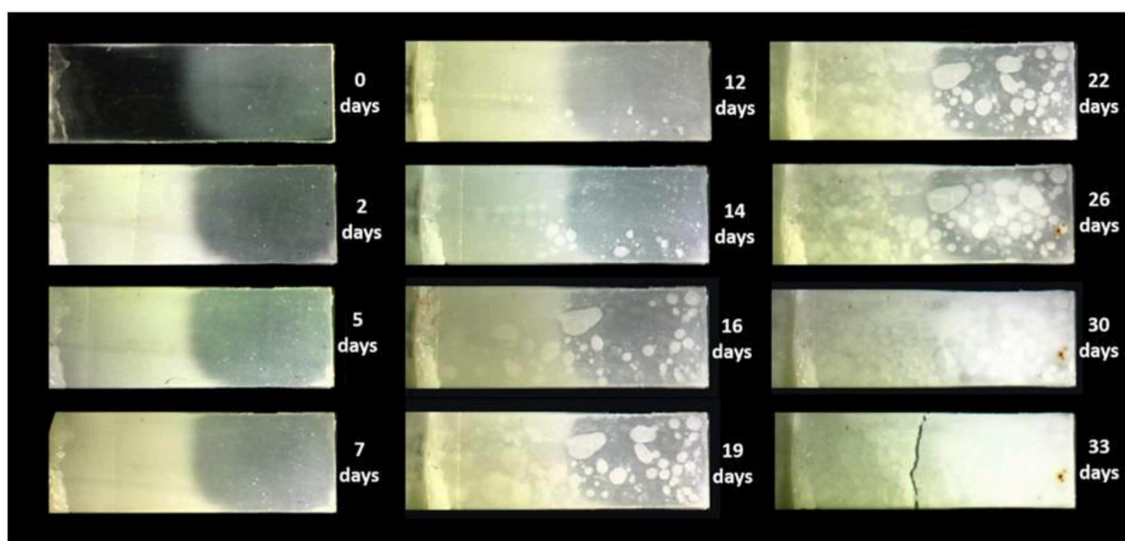
FIGURE 5 | Images of hydrolyzed samples of micro-injected biphasic PLA sample (amorphous gate, crystalline tip).

performed by using the Perkin Elmer DMA 8000 (Waltham, MA, USA). The machine is equipped with a tip that has a diameter of 150 μm. For each experiments, the maximum value of force was equal to 7 N and the load rate was 0.2 N/min. A schematic of the device used is shown in **Figure 2**. The sample was placed under the tip with an increasing force up to the maximum allowed value of 7 N (the instrumental limit). DMA returned the values of the force and the displacement of the tip.

RESULTS AND DISCUSSION

Micromolding

PLA bars were obtained by microinjection molding. To permit the filling in the microcavity and prevent a premature solidification, a value of temperature between the glass transition

FIGURE 6 | DSC analysis of micro-injected biphasic PLA sample (amorphous tip, crystalline gate), first scan.

FIGURE 7 | DSC analysis of micro-injected biphasic PLA sample (amorphous gate, crystalline tip), first scan.

temperature and the melting temperature was applied at the surface of the cavity without changing the temperature of the rest of mold. The special system, as showed in **Figure 3**, is able to increase the temperature of the cavity surfaces from 60°C, temperature of the mold, to 150°C. That value was set just before the filling, manually activated at the machine, and was kept until the injection step ended. After that, by switching off the heaters the rapid cooling led the surfaces in less than 10 s to 60°C. Without extracting the sample from the mold the preparation of each sample included a second step in which an isothermal step (crystallization step) involved only an area of the injected samples. A temperature of 105°C was applied for 500 s. In these conditions, a low crystallization time is expected (De Meo et al., 2018).

Hydrolysis

The hydrolysis mechanism represents the main cause is the main of depolymerization in fact, it controls the biodegradation in compost. The hydrolysis rate, therefore, indicates the rate of degradation during composting. The samples were put in distilled water and at the set time were taken out and dried for the needed investigations: optical, calorimetric, GPC and mechanical analysis.

Optical Observations

All the samples were observed and photographed under polarized light. As showed in the **Figure 4** there was a clear difference between the two regions of the sample: the amorphous region was transparent whereas the crystalline one appeared opaque. Analyzing the images of the samples under hydrolysis it is evident that the crystalline zone of the sample remained unchanged for a time of 12 days (**Figure 5**). The appearance of the amorphous zone changed after the second day turning from transparent to opaque. The same phenomenon was already observed in the PLA (Pantani and Sorrentino, 2013). This could be due to the micro-fractures due to the water moving away from the sample during the drying phase. Obviously, the crystalline zone had a lower water permeability at least for the first 25 days of hydrolysis. From 30 days there were no differences between the two different morphologies. The degradation tests confirmed that crystalline regions had a slightly better resistance to hydrolysis.

Calorimetric Analysis

From the results of the DSC analysis, before the hydrolysis (samples 0 days) reported in **Figures 6**, **7**, it is evident that there was a difference between the phases: there were crystallization
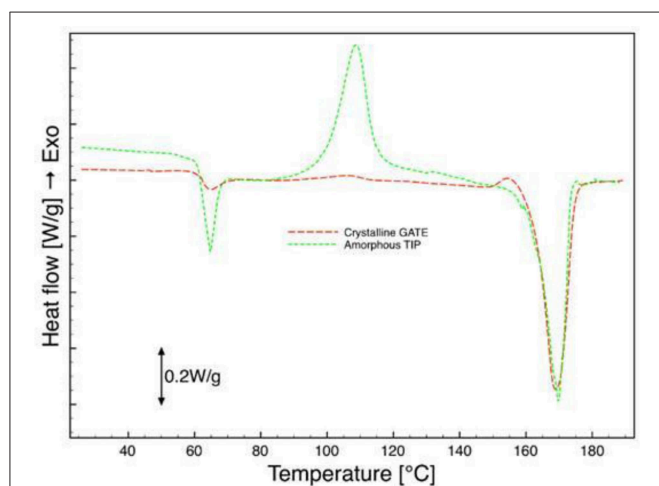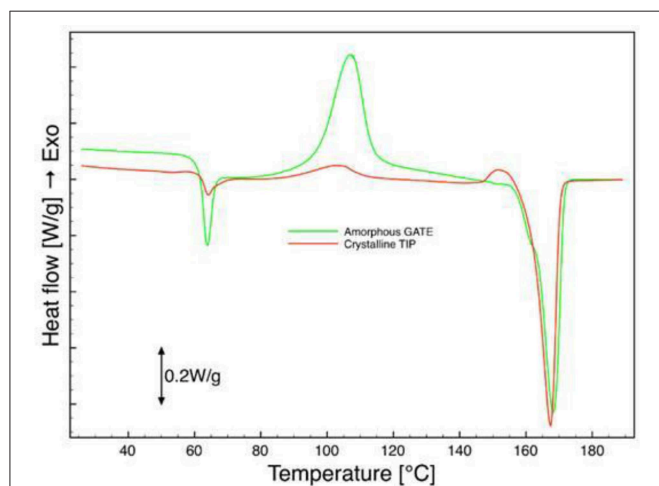
TABLE 1 | Crystalline degree of the biphasic samples before the hydrolysis.

Protocol	Region detected	Xc [%]
a	Gate	30
a	Tip	Negligible
b	Gate	Negligible
b	Tip	35

and melting peaks for the amorphous phase and there was only a melting peak for the crystalline phase. The Glass Transition Temperature and the Melting Temperature exhibited the same values for both phases. T_g and T_m, also, are very similar to those observed in the pellet indicating no degradation had occurred in the manufacturing process, neither in the crystallization step. The degree of crystallization calculated from the analysis of the thermograms is negligible for the amorphous region in all the samples, whereas for the crystalline phase, in the case of both protocols adopted, "a" and "b," the values were between 30 and 35% (**Table 1**). In all the biphasic samples, the crystallization degree reached in the annealing step was then close to the maximum achievable for this grade of PLA when crystallized from the molten state.

During hydrolysis a small piece from each region of the sample was analyzed by calorimetry with the same protocol used for the sample 0 days. **Figures 8**, **9** show the DSC curves obtained from the amorphous zone and the crystalline one respectively. In both cases, the Tg is clear only in the case of the sample 0 days whereas it is not detectable from hydrolyzed samples. Before the hydrolysis, the melting temperature is 169.3°C for the crystalline zone and 167.3°C for the amorphous zone. After 40 days of hydrolysis in both regions it is 156.8°C.

The evolution of the crystallinity degree with the time of hydrolysis is reported in **Figure 10**. As expected, an increase in the crystallinity degree was observed. This result could be due to the erosion of the amorphous regions and the crystallization of the amorphous ones. As the hydrolysis proceeds the crystallization is more fast in the amorphous region than in the crystalline one. The difference in crystallization rate probably indicates a slower degradation of the crystalline zone with respect
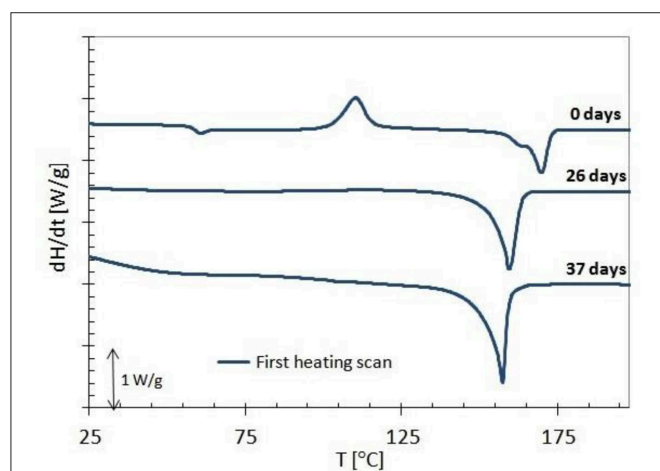
FIGURE 8 | DSC curves of amorphous zone of biphasic samples at different time of degradation.
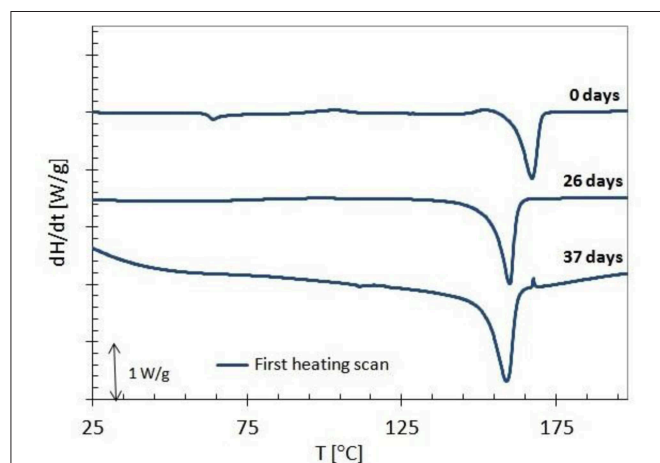
FIGURE 9 | DSC curves of crystalline zone of biphasic samples at different time of degradation.
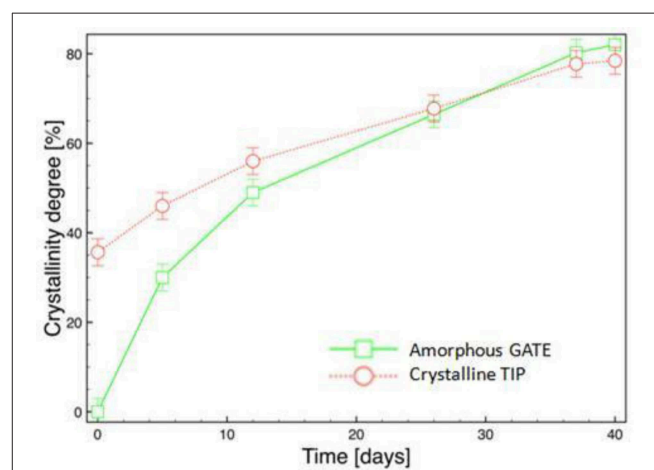
FIGURE 10 | Evolution of degree of crystallinity during hydrolysis of micro-injected biphasic PLA sample (amorphous gate, crystalline tip).
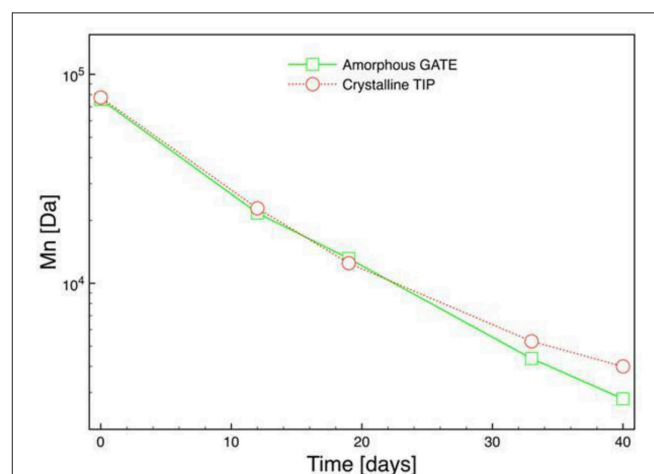
FIGURE 11 | Evolution of number average molecular weight (M_n) during hydrolysis of micro-injected biphasic PLA sample (amorphous gate, crystalline tip).
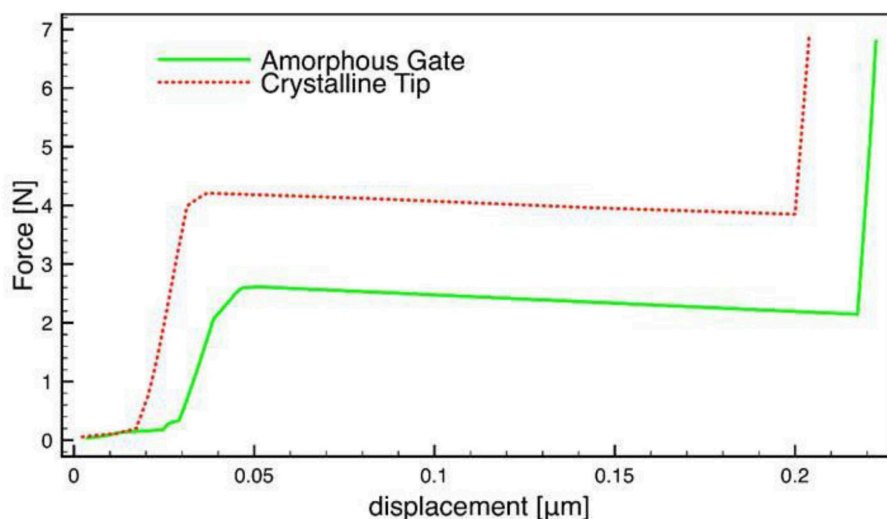
FIGURE 12 | Example of evolution of the force vs. displacement in the two zones (amorphous and crystalline) of the same hydrolyzed sample for which the break is observed.

to the amorphous one. After 25 days of hydrolysis, however, no significant difference can be observed between the values of the X_c of the two morphologies.

Molecular Weight

Figure 11 shows the evolution of the number average molecular weight (M_n) as the hydrolysis of micro-injected biphasic PLA samples proceeds. No differences in the evolution of M_n as the hydrolysis proceeds: after 35 days we can see that M_n for the crystalline zone is a slightly higher than for the amorphous zone. The analysis of the evolution in time of M_n, and the molecular weight of the repeating unit permitted evaluating the kinetic constant of the hydrolysis process, $k' = k \times \rho/M$, where ρ is the density of the polymeric part (about 1.21 Kg/m^3), M is the molecular weight of the repeating unit (72 g/mol for the PLA 4032D) (Gorrasi and Pantani, 2013). The value k' represents the kinetic constant of the process of hydrolysis:

$$k' = - \frac{d \ln (M_n - M)}{dt}$$

The kinetic constants calculated by the evolution of the average molecular weight in each region gave a value of 0.086 days^{-1} for the amorphous and a value of 0.081 days^{-1} for the crystalline zone showing a small difference between the two regions. This could be ascribed to the process used to produce the samples: the high shear imposed by the micro-injection molding could have generated precursors of crystallites that easily grew once the hydrolysis began. Dimensions and arrangement of the crystalline structure as well as a different orientation from the gate to the tip of the sample probably have an effect on the process highlighting the need for future investigations on the phenomenon.
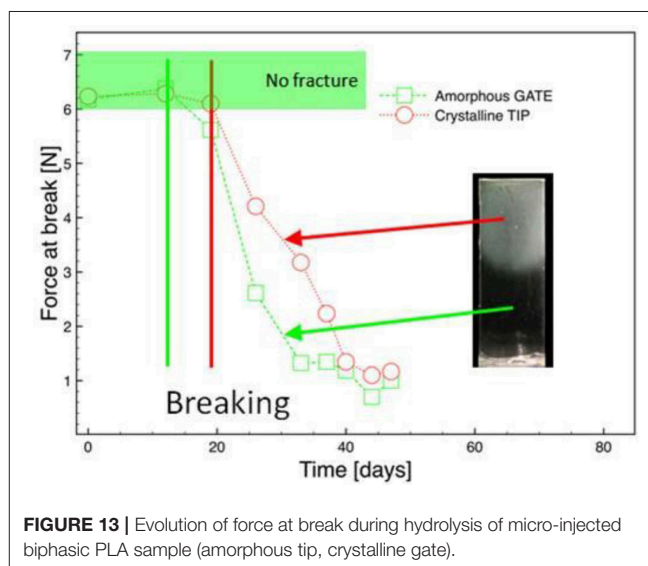
FIGURE 13 | Evolution of force at break during hydrolysis of micro-injected biphasic PLA sample (amorphous tip, crystalline gate).

Mechanical Tests

The resistance to the penetration was evaluated with the time of the hydrolysis. In each region of the sample, the mechanical test gave the force applied and the corresponding displacements (**Figure 12**). The maximum force applied was 7 N. Observing the **Figure 13**, it is evident that up to 12 days, no fracture was detected in either phase. After 19 days, the sample did not withstand the force applied and broke. As the hydrolysis proceeds a decreasing mechanical stresses was needed to break the sample. For the crystalline phase the force at break is slightly higher than the one noticed in the amorphous phase.

CONCLUSIONS

In this work, biphasic samples of PLA were obtained by micro-injection molding. For this purpose a new dynamic mold temperature control system for rapid heating and cooling of the mold was used. The system allowed filling a microcavity and produce bars with a thickness of 0.25 mm. Half bar, after the injection, was kept at 105°C for 500 s to permit a rapid crystallization. The biphasic samples were then hydrolyzed. The hydrolysis process was monitored by considering: the evolution of the degree of crystallinity of the samples by means of the differential scanning calorimetry technique (DSC), the evolution of the molecular weights by means of gel permeation chromatography (GPC), changes in mechanical behavior. For all the sample, in both morphologies, X_c increases as the hydrolysis proceeds. The value of X_c of the crystalline phase, increases more slowly than the X_c of the amorphous phase as the hydrolysis proceeds: this probably indicates a slower degradation of the crystalline zone than of the amorphous zone. The molecular weights decrease for both zones of the two samples. We could observe a slightly slower reduction of M_n with time for the crystalline regions with respect to the amorphous ones as the hydrolysis proceeds. On analyzing the mechanical tests the amorphous zone showed higher frangibility than the crystalline revealing that the crystalline regions present a slightly better resistance to the hydrolysis.

DATA AVAILABILITY STATEMENT

All datasets generated for this study are included in the article/supplementary material.

AUTHOR CONTRIBUTIONS

RP designed theexperiments and supervised the work. AD was responsible for the preparation of the samples and wrote the draft of the paper. VI performed the tests of hydrolysis and the characterization of the samples. All the authors reviewed and accepted.

REFERENCES

Arias, V., Höglund, A., Odelius, K., and Albertsson, A.-C. (2014). Tuning the degradation profiles of poly(l-lactide)-based materials through miscibility. *Biomacromolecules* 151, 391–402. doi: 10.1021/bm401667b

Auras, R., Harte, B., and Selke, S. (2004). An overview of polylactides as packaging materials. *Macromol. Biosci.* 4, 835–864. doi: 10.1002/mabi.200400043

Babu, R., O'Connor, K., and Seeram, R. (2013). Current progress on bio-based polymers and their future trends. *Prog. Biomater* 2:8. doi: 10.1186/2194-0517-2-8

Belbella, A., Vauthier, C., Fessi, H., Devissaguet, J. P., and Puisieux, F. (1996). *In vitro* degradation of nanospheres from poly(D,L-lactides) of different molecular weights and polydispersities. *Int. J. Pharmaceut.* 129, 95–102. doi: 10.1016/0378-5173(95)04258-X

De Jong, S. J., Arias, E. R., Rijkers, D. T. S., van Nostrum, C. F., Kettenes-van den Bosch, J. J., and Hennink, W. E. (2001). New insights into the hydrolytic degradation of poly(lactic acid): participation of the alcohol terminus. *Polymer* 42, 2795–2802. doi: 10.1016/S0032-3861(00)00646-7

De Meo, A., De Santis, F., and Pantani, R. (2018), Dynamic local temperature control in micro-injection molding: effects on poly(lactic acid) morphology. *Polym Eng Sci.* 58, 586–591. doi: 10.1002/pen.24784

De Santis, F., and Pantani, R. (2016). Development of a rapid surface temperature variation system and application to micro-injection molding. *J. Mater. Process. Technol.* 237, 1–11. doi: 10.1016/j.jmatprotec.2016.05.023

De Santis, F., Volpe, V., and Pantani, R. (2017). Effect of molding conditions on crystallization kinetics and mechanical properties of poly(lactic acid). *Polym. Eng. Sci.* 57, 306–311. doi: 10.1002/pen.24414

Dorgan, J. R., Lehermeier, H. J., Palade, L. I., and Cicero, J. (2001). Polylactides: properties and prospects of an environmentally benign plastic from renewable resources. *Macromol. Symp.* 175, 55–66. doi: 10.1002/1521-3900(200110)175:1<55::AID-MASY55>3.0.CO;2-K

Drumright, R. E., Gruber, P. R., and Henton, D. E. (2000). Polylactic acid technology. *Adv. Mater.* 12, 1841–1846. doi: 10.1002/1521-4095(200012)12:23<1841::AID-ADMA1841>3.0.CO;2-E

Farah, S., Anderson, D. G., and Langer, R. (2016). Physical and mechanical properties of PLA, and their functions in widespread applications — a comprehensive review. *Adv. Drug Deliv. Rev.* 107, 367–392. doi: 10.1016/j.addr.2016.06.012

Fukushima, K., Feijoo, J. L., and Yang, M. C. (2013). Comparison of abiotic and biotic degradation of PDLLA, PCL and partially miscible PDLLA/PCL blend. *Eur. Polym. J.* 49, 706–717. doi: 10.1016/j.eurpolymj.2012.12.011

Gamez-Perez, J., Nascimento, L., Bou, J., Franco-Urquiza, E., Santana, O., Carrasco, F., et al. (2011). Influence of crystallinity on the fracture toughness of poly(lactic acid)/montmorillonite nanocomposites prepared by twin-screw extrusion. *J. Appl. Polym. Sci.* 120, 896–905. doi: 10.1002/app.33191

Garlotta, D. (2001). A literature review of poly(lactic acid). *J. Poly. Environ.* 9, 63–84. doi: 10.1023/A:1020200822435

Ghosh, S., Vianac, J. C., Reisab, R. L., and Manoa, J. F. (2008). Oriented morphology and enhanced mechanical properties of poly(l-lactic acid) from shear controlled orientation in injection molding. *Mater. Sci. Eng.* A. 490, 81–89. doi: 10.1016/j.msea.2008.01.003

Gleadall, A., Pan, J., Kruft, M. A., and Kellomäki, M. (2014). Degradation mechanisms of bioresorbable polyesters. Part 1. effects of random scission, end scission and autocatalysis. *Acta Biomater.* 10, 2223–2232. doi: 10.1016/j.actbio.2013.12.039

Gorrasi, G., and Pantani, R. (2013). Effect of PLA grades and morphologies on hydrolytic degradation at composting temperature: assessment of structural modification and kinetic parameters. *Polym. Degrad. Stab.* 98, 1006–1014. doi: 10.1016/j.polymdegradstab.2013.02.005

Gorrasi, G., and Pantani, R. (2017). "Hydrolysis and biodegradation of poly(lactic acid)," in *Synthesis, Structure and Properties of Poly(lactic acid). Advances in Polymer Science*, Vol. 279, eds M. Di Lorenzo and R. Androsch (Cham: Springer), 119–152. doi: 10.1007/12_2016_12

Guptaa, B., Revagadea, N., and Hilbornb, J. (2007). Poly(lactic acid) fiber: an overview. *Prog. Poly. Sci.* 32, 455–482. doi: 10.1016/j.progpolymsci.2007.01.005

Ha, J. U., and Xanthos, M. (2010). Novel modifiers for layered double hydroxides and their effects on the properties of polylactic acid composites. *Appl. Clay Sci.* 47, 303–310. doi: 10.1016/j.clay.2009.11.033

Harris, A. M., and Lee, E. C. (2008). Improving mechanical performance of injection molded PLA by controlling crystallinity. *J. Appl. Polym. Sci.* 107, 2246–2255. doi: 10.1002/app.27261

Hocking, P. J., Timmins, M. R., Scherer, T. M., Fuller, R. C., Lenz, R. W., and Marchessault, R. H. (1995). Enzymatic degradability of poly(beta-hydroxybutyrate) as a function of tacticity. *J. Macromol. Sci. Pure Appl. Chem. A* 32, 889–894. doi: 10.1080/10601329508010302

Iozzino, V., Askanian, H., Leroux, F., Verney, V., and Pantani, R. (2018). Poly(lactic acid)-based nanobiocomposites with modulated degradation rates. *Materials* 11:E1943. doi: 10.3390/ma11101943

Jamshidian, M., Tehrany, E. A., Imran, M., Jacquot, M., and Desobry, S. (2010). Poly-lactic acid: production, applications, nanocomposites, and release studies. *Compr. Rev. Food Sci. Food Saf.* 9, 552–571. doi: 10.1111/j.1541-4337.2010.00126.x

Li, S. M., Garreau, H., and Vert, M. (1990). Structure property relationships in the case of the degradation of massive aliphatic poly-(α-hydroxy acids) in aqueous-media. 1. poly(DL-lactic acid). *J. Mater. Sci. Mater. Med.* 1, 123–130. doi: 10.1007/BF00700871

Lostocco, M. R., and Huang, S. J. (1998). The hydrolysis of poly(lactic acid) poly(hexamethylene succinate) blends. *Polym. Degrad. Stab.* 61, 225–230. doi: 10.1016/S0141-3910(97)00138-9

McKeen, L. W. (2014). "Plastics used in medical devices," in *Handbook of Polymer Applications in Medicine and Medical Devices* (William Andrew Publishing), 21–53.

Murariu, M., and Dubois, P. (2016). PLA composites: from production to properties. *Adv. Drug Deli. Rev.* 107, 17–46. doi: 10.1016/j.addr.2016.04.003

Murariu, M., Laoutid, F., Dubois, P., Fontaine, G., Bourbigot, S., Devaux, E., et al. (2014). "Pathways to biodegradable flame retardant polymer (nano) composites," in *Polymer Green Flame Retardants*, eds C. D. Papaspyrides and P. Kiliaris (Amsterdam; Oxford, UK; Waltham, MA: Elsevier), 709–773.

Nampoothiri, K. M., Nair, R. N., and John, R. P. (2010). An overview of the recent developments in polylactide (PLA) research. *Bioresour. Technol.* 101, 8493–8501. doi: 10.1016/j.biortech.2010.05.092

Pantani, R., De Santis, F., Sorrentino, A., De Maio, F., and Titomanlio, G. (2010). Crystallization kinetics of virgin and processed poly(lacticacid). *Poly. Degrad. Stabil.* 95:1148. doi: 10.1016/j.polymdegradstab.2010.04.018

Pantani, R., and Sorrentino, A. (2013). Influence of crystallinity on the biodegradation rate of injection-moulded poly(lactic acid) samples in controlled composting conditions. *Poly. Degrad. Stabil.* 98, 1089–1096. doi: 10.1016/j.polymdegradstab.2013.01.005

Raquez, J.-M., Habibi, Y., Murariu, M., and Dubois, P. (2013). Polylactide (PLA)-based nanocomposites. *Prog. Pol. Sci.* 38, 1504–1542. doi: 10.1016/j.progpolymsci.2013.05.014

Sawyer, D. J. (2003). Bioprocessing – no longer a field of dreams. *Macromol. Symp.* 201, 271–281. doi: 10.1002/masy.200351130

Shih, C. (1995). A graphical method for the determination of the mode of hydrolysis of biodegradable polymers. *Pharm. Res.* 12, 2036–2060. doi: 10.1023/A:1016276830464

Speranza, V., De Meo, A., and Pantani, R. (2014). Thermal and hydrolytic degradation kinetics of PLA in the molten state. *Poly. Degrad. Stabil.* 100, 37–41. doi: 10.1016/j.polymdegradstab.2013.12.031

Stloukal, P., Kalendova, A., Mattausch, H., Laske, S., Holzer, C., and Koutny, M. (2015). The influence of a hydrolysis-inhibiting additive on the degradation

and biodegradation of PLA and its nanocomposites. *Poly. Test.* 41, 124–132. doi: 10.1016/j.polymertesting.2014.10.015

Tsuji, H. (2003). *In vitro* hydrolysis of blends from enantiomeric poly(lactide)s. Part 4: well-homo-crystallized blend and nonblended films. *Biomaterials* 24, 537–547. doi: 10.1016/S0142-9612(02)00365-4

Tsuji, H. (2010). "Hydrolytic degradation," in *Poly (Lactic Acid) Synthesis, Structures, Properties, Processing, and Applications*, eds R. F. Grossman, D. Nwabunma, R. Auras, L. Lim, S. E. Selke, and H. Tsuji (Wiley), 343–381.

Weir, N. A., Buchanan, F. J., Orr, J. F., Farrar, D. F., and Dickson, G. R. (2004). Degradation of poly-L-lactide. Part 2: increased temperature accelerated degradation. *Proc. Inst. Mech. Eng. Part H-J. Eng. Med.* 218, 321–330. doi: 10.1243/0954411041932809

Wertz, J. T., Mauldin, T. C., and Boday, D. J. (2014). Polylactic acid with improved heat deflection temperatures and self-healing properties for durable goods applications. *ACS Appl. Mater. Interfaces* 6, 18511–18516. doi: 10.1021/am5058713

Zhang, X. C., Wyss, U. P., Pichora, D., and Goosen, M. F. A. (1994). An investigation of poly(lactic acid) degradation. *J. Bioact. Compat. Poly.* 9, 80–100. doi: 10.1177/088391159400900105

Zhao, Z.-G., Yang, Q., Coates, P., Whiteside, B., Kelly, A., Huang, Y.-J., et al. (2018). Structure and property of microinjection molded poly(lactic acid) with high degree of long chain branching. *Ind. Eng. Chem. Res.* 57, 11312–11322. doi: 10.1021/acs.iecr.8b01597

Zhou, S., Hrymak, A. N., and Kamal, M. R. (2018). Properties of microinjection-molded multi-walled carbon nanotubes-filled poly(lactic acid)/poly[(butylene succinate)-co-adipate] blend nanocomposites. *J. Mater. Sci.* 53, 9013–9025. doi: 10.1007/s10853-018-2193-8

frontiers
in Materials

Phase Structure, Compatibility, and Toughness of PLA/PCL Blends: A Review

Ivan Fortelny[1], Aleksandra Ujcic[1], Luca Fambri[2] and Miroslav Slouf[1]*

[1] Institute of Macromolecular Chemistry, Czech Academy of Sciences, Prague, Czechia, [2] Department of Industrial Engineering, University of Trento, Trento, Italy

Results of the studies dealing with the toughness of polylactic acid/polycaprolactone (PLA/PCL) blends are analyzed with respect to the PCL particle size, PLA matrix crystallinity, and presence of a compatibilizer. It is shown that a high toughness or even "super-toughness" of PLA/PCL blends without a compatibilizer can be achieved for blends with the proper size of PCL particles. Nevertheless, the window for obtaining the super-tough PLA/PCL blends is quite narrow, as the final impact strength is very sensitive to multiple parameters: namely the blend composition, PLA matrix crystallinity, and PCL particle size. Available literature data suggest that the optimal composition for PLA/PCL blends is around 80/20 (w/w). The PLA/PCL(80/20) blends keep high stiffness of PLA matrix and the concentration of PCL particles is sufficient to achieve high toughness. The PLA/PCL(80/20) blends with low-crystallinity PLA matrix (below ca 10%) exhibit the highest toughness for bigger PCL particles (weight average diameter above 1 μm), while the blends with high-crystallinity PLA matrix (above ca 30%) exhibit the highest toughness for smaller PCL particles (weight average diameter below 0.5 μm). The addition of a compatibilizer may improve the toughness only on condition that it helps to achieve a suitable particle size. The toughness of both non-compatibilized and compatibilized PLA/PCL blends with optimized morphology can be more than 15 times higher in comparison with neat PLA.

Keywords: biopolymer blends, poly(lactic acid), polycaprolactone, impact strength, crystallinity, particle size distribution

INTRODUCTION

Poly(lactic acid) (PLA) is frequently reported as one of the most promising biodegradable polymers synthesized from natural resources as it can be used in many technical applications, especially in packaging (Lunt, 1998; Garlotta, 2002; Auras et al., 2004; Averous and Pollet, 2012). At the same time medical grade PLA continues to be a favorable material for many medical applications such as the tissue engineering (Patrício et al., 2013) and bone fixation devices (Todo et al., 2007) due to its well documented biocompatibility, full biodegradability, and high stiffness resulting from the relatively high glass transition temperature (T_g) (Fambri and Migliaresi, 2010). Preparation from natural resources and biodegradability suggest PLA as substitution of some plastics made from fossil fuels in a broad range of applications. However, brittleness is a strong drawback for practical applications of neat PLA. Various methods of PLA toughening were summarized by Krishnan et al. (2016). Generally, most efficient method for an improvement of toughness of a brittle polymer is

its blending with soft, ductile polymers (Bucknall, 2000; Horak et al., 2005). Poly(ε-caprolactone) (PCL) is soft, biocompatible and biodegradable semicrystalline polyester (Pitt, 1990; Krishnan et al., 2016) with a rubbery amorphous phase at room temperature as its T_g is around $-60°C$ and its melting temperature is in the range of 55–70°C. Therefore, PLA/PCL blends should keep favorable biocompatibility and biodegradability and should show enhanced impact strength with respect to neat PLA. The main objective of the preparation of PLA/PCL blends, where PLA is a major component, is the substantial enhancement of PLA toughness with minimum reduction of its stiffness.

Further problem for many technical applications of PLA and PLA/PCL blends is their mechanical performance at elevated temperature. Commercial grades of PLA are mixtures of L-isomer and a small amount of D-isomer (Standau et al., 2019). Therefore, commercial PLA's are semicrystalline with melting temperature, T_m, between 140 and 180°C in dependence on the enantiomeric purity (Fambri and Migliaresi, 2010) and glass transition temperature, T_g, which usually ranges from 55 to 65°C (Auras et al., 2004; Krishnan et al., 2016). However, the rate of the PLA crystallization is slow (Auras et al., 2004; Liu et al., 2014; Murariu et al., 2015; Zhang et al., 2018), frequently slower than the cooling rate used in common polymer processing devices (Zhang et al., 2018). Consequently, the crystallinity of PLA in its blends processed by common procedures tends to be very low, typically lower than 10% (Bai et al., 2012, 2013; Ostafinska et al., 2015, 2017). Therefore, the softening temperature of products prepared from neat PLA and PLA/PCL blends at common processing conditions is controlled by the T_g of PLA. At room temperature, the differences between the moduli of PLA with a low (below 10%) and high crystallinity (above 30%) are not critical. The same is true for PLA/PCL blends. It follows from the literature data (Perego et al., 1996; Kelnar et al., 2016) that the ratio of moduli of materials containing PLA with a high and with a low crystallinity does not exceed 1.25. At elevated temperatures, however, the moduli of low- and high-crystallinity PLA may differ significantly: Bai et al. (2013) found that the modulus of PLA/PCL (80/20) blends with a high-crystallinity PLA matrix was 20 times higher than the modulus of an analogous blend with a low-crystallinity of PLA matrix at the temperature of 80°C. Our measurements at the same temperature led to even higher moduli ratio of 100 for neat PLA and the ratio of 75 for PLA/PCL (80/20) blend. These results discriminate PLA and PLA/PCL blends with a low crystallinity of PLA for many technical applications where good mechanical properties of the material at elevated temperatures are required. Crystallinity of PLA can be enhanced by the annealing during processing and/or by the addition of a convenient nucleation agent.

This review is focused mostly on the toughening of the most common, commercially available PLA polymers, which consist of L-isomer with a small amount of D-isomer, as described above. Other PLA polymers include poly(L-lactic acid) with 100% enantiomeric purity (PLLA), which is polymerized from the pure L-isomer, poly(D-lactic acid) (PDLA), prepared from pure D-isomer, and poly(D,L-lactide) (PDLLA), which derives from a mixture of the L- and D-isomers. Pure PLLA and PDLA can achieve a higher crystallinity than common commercial PLA (Nakajima et al., 2017) but their rate of crystallization is still quite low. PDLLA cannot crystalize. PLLA and PDLLA are commonly used in biomedical applications. We use the above abbreviations in the relation to samples described in the literature. However, it should be mentioned that some authors describe PLA containing small fracture of D-isomer as PLLA.

The impact strength of polymer blends depends on the size distribution of the dispersed particles of the soft polymer in the matrix of the brittle one (Bucknall and Paul, 2009, 2013). Generally, super-tough polymer blends can be obtained only for a certain range, often quite narrow, of sizes of soft polymer particles. The theory of impact behavior of polymer blends is quite complex (Bucknall and Paul, 2013). The lower bound of the suitable particle sizes is given by the minimal size of soft particles needed for their efficient cavitation. The upper bound for a certain blend composition is given by inter-droplet distance which should be shorter than a critical distance for development of cracks or shear bands in the polymer matrix. The optimum particle size depends on dominating mechanism of energy dissipation in the matrix (multiple crazing or shear yielding). Small elastomer particles (weight-average diameter, d_w, in the range 0.2–0.4 μm) are efficient when shear yielding dominates the toughening mechanism, e.g., for ductile matrices of polypropylene or polyamide, whereas larger particles (d_w between 2 and 3 μm) are more effective when multiple crazing dominates, e.g., for brittle matrices of polystyrene or poly(methyl methacrylate) (Bucknall and Paul, 2009). Thus, the optimum particle size distribution depends on the structure of the matrix, especially on its crystallinity.

In order to achieve optimal particle size distribution for toughening, it is necessary to understand the relation among the processing conditions of PLA/PCL blends, the rheological properties of the components and the resulting morphology of the blends. Polymer blends are mostly prepared by melt mixing in extruders or batch mixers. They are further processed by injection molding, extrusion, blow molding or compression molding. The phase structure of polymer blends is formed and developed during their compounding and processing. Evolution of the phase structure in flowing molten polymer blends has been studied intensively experimentally (mostly for blends of synthetic polymers) and theoretically during last 40 years (Horak et al., 2005; Huang, 2011; Fortelny and Juza, 2019). Evolution of the droplets-in-matrix morphology (which is typical of PLA/PCL blends discussed in this contribution) during simple shear or elongational flow is *qualitatively* well understood. However, *quantitative* prediction of particle size distribution in real systems is extremely challenging due to complexity of the flow fields in mixing and processing devices and complex rheological behavior of molten polymers. The results of previous studies can be briefly summarized as follows: (i) The particle sizes in the blends containing the same components and prepared at the same conditions increase with the concentration of the minor component. (ii) The smallest particle size is usually obtained when viscosities of the dispersed phase and matrix are comparable. (iii) The particle size increases with interfacial

tension between the blend components. (iv) The particle size in molten blends increases in quiescent state and in slow flow, which means that an increase in the particle size appears during compression molding. (v) Addition of a compatibilizer decreases the size of the dispersed particles during mixing and stabilizes the blend morphology at processing; this effect is stronger for blends with a higher content of the dispersed phase.

This review aims at the evaluation of the results of studies of the morphology, compatibility and mechanical properties of PLA/PCL blends with respect to the control of the blend toughness and crystallinity. The conclusions of this contribution should answer the question if and how the blending of PLA with PCL can lead to the material with required mechanical properties.

TOUGHNESS OF PLA/PCL BLENDS WITHOUT COMPATIBILIZERS

Many papers have been focused on the morphology and mechanical properties of PLA/PCL blends. As for the stiffness, all studies are in agreement that the modulus and yield strength of PLA/PCL blends decreases with the PCL content. This behavior is typical of the blends combining stiff and soft polymers (Horak et al., 2005) and thus the stiffness is not discussed in the following text. However, the results related to the toughening of PLA by means of blending with PCL seem to be contradictory at first sight. These results are discussed below. The ratios of toughness, a_{Bl}/a_{PLA}, and elongation at break, $\varepsilon_{Bl}/\varepsilon_{PLA}$, of PLA/PCL blends to neat PLA together with crystallinity of PLA, w_c^{PLA}, and average diameter of PCL particles, d, are summarized in **Table 1**.

Studies Reporting Low Toughness of PLA/PCL Blends

None or weak enhancement in the toughness of PLA by its blending with PCL has been found in a major part of previous studies. López-Rodríguez et al. (2006) found very small increase in strain at break (to 1.3%) together with strong decrease in strength at yield and strength at break for PLLA/PCL (80/20) blends in comparison with neat PLLA. Carmona et al. (2015) found only a small increase in elongation at break for an extrusion prepared PLA/PCL (50/50) blend with respect to PLA but strong decrease with respect to PCL. Gardella et al. (2014) and Monticelli et al. (2014) obtained the same elongation at break for PLA/PCL (70/30) blend prepared in a batch mixer as for neat PLA. The blend contained remarkable amount of large PCL particles.

Tsuji and Ikada (1996) studied the morphology and the properties of the blends of poly(D,L-lactide) containing 50% of D-isomer (PDLLA) with PCL, which were prepared by solution casting. They found that the dependence of the elongation at break on the PDLLA/PCL composition is non-monotonic with a minimum around 50/50 composition. Similar dependence of the elongation at break on the composition of the blends prepared from 100% L-isomer of PLA (PLLA) with PCL was obtained by Tsuji et al. (2003). Simoes et al. (2009) found negligible increase in elongation at break and about twice

TABLE 1 | Ratio of toughness, a_{Bl}/a_{PLA}, and ratio of elongation at break, $\varepsilon_{Bl}/\varepsilon_{PLA}$, of PLA/PCL blends and neat PLA as a function of diameter of PCL particles, d, and crystallinity of PLA matrix, w_c^{PLA}.

PLA/PCL	w_c^{PLA} [%]	d [μm]	a_{Bl}/a_{PLA}	$\varepsilon_{Bl}/\varepsilon_{PLA}$	References
80/20[a]	–	–	–	2.6	López-Rodríguez et al., 2006
70/30	low	2.0[b]	–	~1	Gardella et al., 2014; Monticelli et al., 2014
75/25	<5	2–5[c]	~2[d]	1.5	Simoes et al., 2009
80/20[a]	66	>1[c]		1.5[e]	Vilay et al., 2009
80/20	–	0.8[f]	–	5	Finotti et al., 2016
85/15[a]	~25	2[c]	1.5[g]	–	Todo et al., 2007
80/20	17	–	–	~20	Yeh et al., 2009
77.5/22.5	17	1–3[c]	<1[d]	3.5	Ferri et al., 2016
80/20	<10	~0.8[h]	7[i]	–	Bai et al., 2012, 2013
80/20	~50	~0.4[h]	11[i]	–	Bai et al., 2012, 2013
80/20	~5	<0.5[c]	2.5[i]	~60	Urquijo et al., 2015
80/20	~10	0.6[f]; 1.3[j]	16[k]	–	Ostafinska et al., 2015
80/20	9	0.6[f]; 2.2[j]	16.6[k]; 21.0[g]	–	Ostafinska et al., 2017
80/20	12	0.8[f]; 2.4[j]	16.1[k]; 7.1[g]	–	Ostafinska et al., 2017
80/20	16	0.9[f]; 3.6[j]	2.8[k]; 3.2[g]	–	Ostafinska et al., 2017
80/20[l]	36	≥0.6[f]; ≥2.2[j]	~10[k]	–	–

[a] PLLA matrix; [b] Maximum of graphical diameter distribution; [c] Estimated from the figure; [d] Unnotched Charpy impact strength; [e] Fracture energy from tensile testing; [f] Number average of d; [g] Instrumented impact testing; [h] Weight average of d; [i] Notch Izod impact strength; [j] Volume average of d; [k] Notched Charpy impact strength; [l] Our unpublished result, blend containing 1% of talc.

larger Charpy impact strength for PLA/PCL (75/25) blends in comparison with neat PLA. Mittal et al. (2015) found only a small increase in the value of elongation at break of the PLA/PCL (50/50) blends with respect to neat PLA, deeply below the additive value.

Vilay et al. (2009) studied the morphology, thermal behavior, and mechanical properties of PLLA/PCL blends. They found only weak increase in the elongation at break with the increasing content of PCL in the PLLA/PCL blends. Similar result for elongation at break was obtained also by Finotti et al. (2016) for PLA/PCL blends with commercial PLA. Only very small increase in the impact strength was found for PLLA/PCL (85/15) blends having crystallinity of PLLA matrix about 25% by Todo et al. (2007). Authors of the above studies and authors of a review considering these results (Imre and Pukánszky, 2013) concluded that PLA and PCL are incompatible polymers, i.e., that their large interfacial tension results in coarse morphologies and inferior mechanical performance. Therefore, the compatibilization was

regarded as necessary for the preparation of PLA/PCL blends with high toughness.

Recently, Kassos et al. (2019) studied the effect of concentration of PCL on mechanical properties of samples of PLA/PCL blends prepared by the mixing in a twin screw extruder, followed by an injection molding. They found that the notched Izod impact strength increased with increasing content of PCL. However, this increase was quite weak: The impact strength of PLA/PCL (70/30) was about twice of that for neat PLA. Moreover, they observed strange dependence of elongation at break on PCL concentration: After strong increase for PLA/PCL (95/5) blend, the elongation at break decreased for higher amounts of PCL (compositions 80/20 and 70/30) to the values comparable with neat PLA.

Studies Reporting High Toughness of PLA/PCL Blends

Surprisingly enough, the results of a few other studies are in a partial or full contradiction with the conclusions in the previous section. Takayama et al. (2011) studied the character of the fracture in PLA/PCL blends without and with a compatibilizer. They found ductile character of the fracture in the quenched PLA/PCL blends. On the other hand, brittle fracture was detected for PLA/PCL blends annealed with the aim to enhance crystallinity of PLA. Yeh et al. (2009) found a steep increase in the strain at break with the content of PCL above 10% for PLA/PCL blends. Similar dependence of the strain at break on the content of PCL in PLA/PCL blends was found also Zhao and Zhao (2016) for injection molded samples.

Ferri et al. (2016) studied elongation at break and unnotched Charpy impact strength of PLA/PCL blends containing up to 30% of PCL. The blends were prepared by extrusion followed by injection molding. The authors found substantial increase in the elongation at break but no enhancement of the impact strength of the blends with respect to neat PLA. Quiles-Carrillo et al. (2018) studied the toughness of PLA blends containing 40% of a mixture of PCL with thermoplastic starch (TPS). They found substantial increase in the elongation at break for the blends having content of TPS up to 20%. On the other hand, the notched Charpy impact strength of PLA/PCL (60/40) blend was only about 3 times higher than that of the neat PLA.

Bai et al. (2012) studied the effect of the crystallinity of the PLA matrix on the impact strength of PLA/PCL blends. The samples of these blends were prepared by the extrusion followed by the injection molding using a HAAKE MiniJet. The crystallinity of PLA was controlled by the concentration of a nucleation agent [N,N',N" tricyclohexyl-1,3,5-benzene-tricarboxylamide (TMC)] and by the temperature of the mold. It was found that the notched Izod impact strength of neat PLA was almost independent of its crystallinity. On the other hand, the impact strength of PLA/PCL blends grew with the crystallinity of PLA. The rate of this growth increased with the increasing content of PCL in the blends. The PLA/PCL (80/20) blend with the PLA crystallinity about 50% showed the impact strength more than 13 times higher in comparison with neat PLA.

In their further paper, Bai et al. (2013) studied the dependence of the impact strength on the size of PCL particles in PLA/PCL (80/20) blends with a low and high crystallinity of the PLA matrix. The blends were prepared by the same technology as in the preceding paper (Bai et al., 2012). The PCL particle size distribution and the PLA crystallization were controlled by the addition of TMC and the variation of the extruder screw rotation speed, by the mold temperature and by the annealing time in the mold. The dependence of the notched Izod impact strength on the weight average of the PCL droplet diameter, d_w, differed for the blends with low- and high-crystallinity PLA matrix. For the blends with the low PLA crystallinity (6.5–9.5%), the maximum impact strength was achieved for d_w between 0.7 and 1.1 μm. For the blends with the high PLA crystallinity (46–48%), the maximum of the impact strength was found for d_w between 0.3 and 0.5 μm. This was is in quite good agreement with the value of d_w between 0.2 and 0.4 μm referred for blends with semicrystalline matrixes elsewhere (Bucknall and Paul, 2009). These dependences are reproduced in **Figure 1**. It should be mentioned that the maximum value of the impact strength achieved for the blends with the high PLA crystallinity was almost two times higher than that of the blends with a low PLA crystallinity.

Urquijo et al. (2015) studied the dependence of morphology and mechanical properties on the PCL content in PLA/PCL blends prepared by extrusion followed by injection molding. They detected a fine morphology of the PLA/PCL blends and a good adhesion between the PLA and PCL phases. The elongation at break was strongly enhanced by the addition of 10% of PCL and did not change with further increase in the PCL amount till 40%. The notched Izod impact strength increased monotonically with the increasing content of PCL in the blends. The values of the ratios a_{Bl}/a_{PLA} and $\varepsilon_{Bl}/\varepsilon_{PLA}$ for PLA/PCL (80/20) blends can be found in **Table 1**. However, the ratio of the impact strength of the PLA/PCL (80/20) blend to that of neat PLA was substantially

FIGURE 1 | Comparison of dependences of the impact strength on the size of PCL particles in PLA/PCL(80/20) blends with almost amorphous and with highly crystalline PLA matrices. Reprinted with permission from Bai et al. (2013). Copyright 2013, Elsevier.
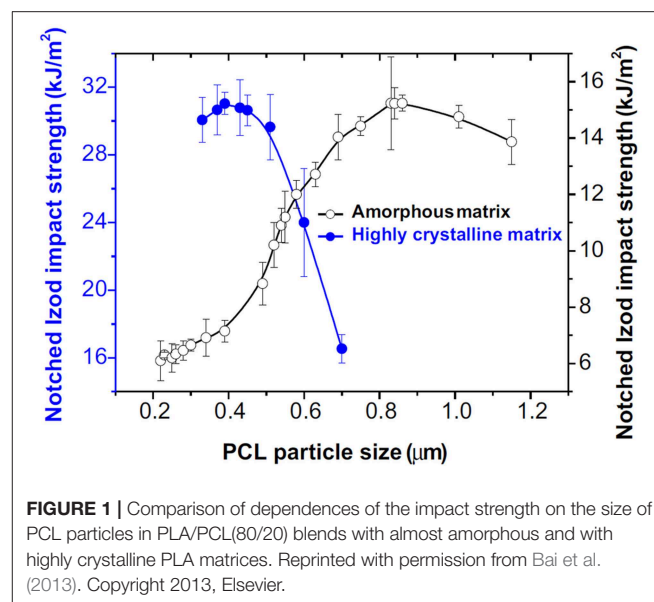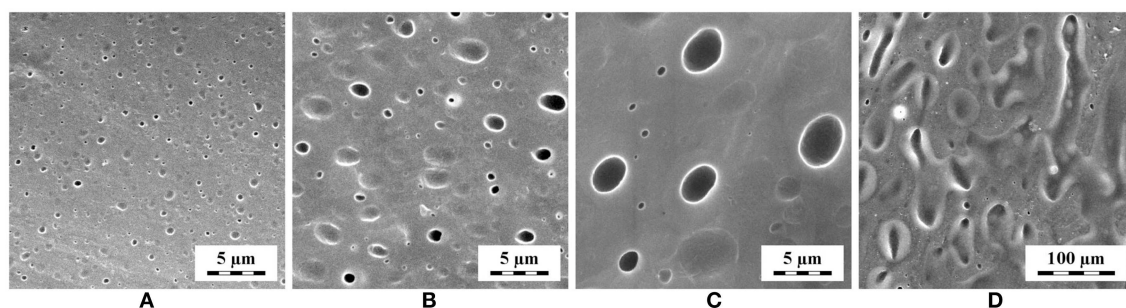
FIGURE 2 | SEM micrographs showing morphology of compression molded PLA/PCL blends with composition (wt.%/wt%): **(A)** 90/10, **(B)** 80/20, **(C)** 70/30, and **(D)** 60/40. The samples were smoothed and PCL was etched off as described in Ostafinska et al. (2015). Note the scale change in the last micrograph with coarse continuous morphology of PCL phase.

lower (almost 3 times) than the maximum ratio observed by Bai et al. (2013) for PLA/PCL blends with a low-crystallinity PLA matrix. This could be attributed to the fact that the PCL particle size in the study of Urquijo et al. (2015) was below the optimum size reported by Bai et al. (2013) for the blends with the similar PLA crystallinity.

Ostafinska et al. (2015) studied the dependence of the morphology and mechanical properties of the PLA/PCL blends (with almost the same viscosities of the PLA and PCL components) on the content of PCL for the blends prepared by the melt-mixing in a batch mixer followed by the compression molding. The crystallinity of PLA in these blends was between 6.4 and 9.7%. It was found that PLA/PCL blends with PCL content till 30% formed typical droplets-in-matrix morphology, where the size of PCL particles increased with the PCL concentration, while the PCL content above 40% resulted in coarse co-continuous morphology, as evidenced **Figure 2**. Charpy notched impact strength of PLA/PCL blends steeply increased with the content of PCL up to 20%. Further increase in the amount of PCL led to a decrease in the impact strength of the PLA/PCL blends. The impact strength of PLA/PCL (80/20) blend was more than 16 times higher in comparison with neat PLA (**Figure 3**). This was even higher than the maximum ratio achieved by Bai et al. (2013) for the blends with the high crystallinity of PLA (**Table 1**). The decrease in the impact strength with the increasing content of PCL for the blends with the PCL content above 20% appeared simultaneously with the steep increase in the average particle size, which was accompanied by the increasing width of the particle size distribution.

Further paper of Ostafinska et al. (2017) was focused on the effect of melt viscosity of the PLA matrix on the morphology and toughness of PLA/PCL (80/20) blends, prepared by same procedure as in their preceding paper (Ostafinska et al., 2015). It was found that the number and volume averages of diameters of the PCL droplets increased with the decreasing viscosity, i.e., molecular weight, of the PLA matrix (**Figure 4**). Neat samples of PLA had similar impact strength and their viscosity decreased in in the following order: PLA1 > PLA2 > PLA3, where PLA1 was identical with PLA used in the preceding study (Ostafinska et al., 2015) and had almost the same viscosity as PCL. The
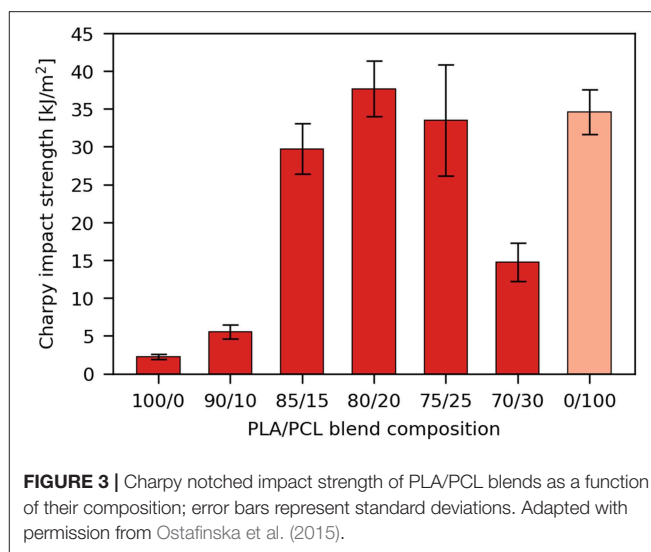
FIGURE 3 | Charpy notched impact strength of PLA/PCL blends as a function of their composition; error bars represent standard deviations. Adapted with permission from Ostafinska et al. (2015).

toughness of the blends was characterized not only by the Charpy notched impact strength, but also by the instrumented impact testing. Both Charpy notched impact strength (determined from non-instrumented impact testing) and total fracture energy (determined from instrumented impact testing) decreased with the increasing size of PCL particles (**Figure 5**). PLA1/PCL blend showed super-tough behavior (i.e., the blend toughness was higher than the toughness of either of its two components) but PLA3/PCL blend showed toughness only slightly enhanced in comparison with neat PLA3. The toughness of PLA2/PCL blend was in between the values found for the PLA1/PCL and PLA/PCL blends. Detailed analysis of load-deflection diagrams from instrumented impact testing (**Figure 6**) revealed that the particle morphology influenced not only final total values of fracture energy, but also the entire character of fracture. The fracture mechanism changed from *elastic-plastic with stable crack propagation* (**Figure 6A**; blend PLA1/PCL), to *elastic-plastic stable followed by unstable crack propagation* (**Figure 6B**; blend PLA2/PCL), and finally to *linear elastic* or *brittle* (**Figure 6C**; blend PLA3/PCL).
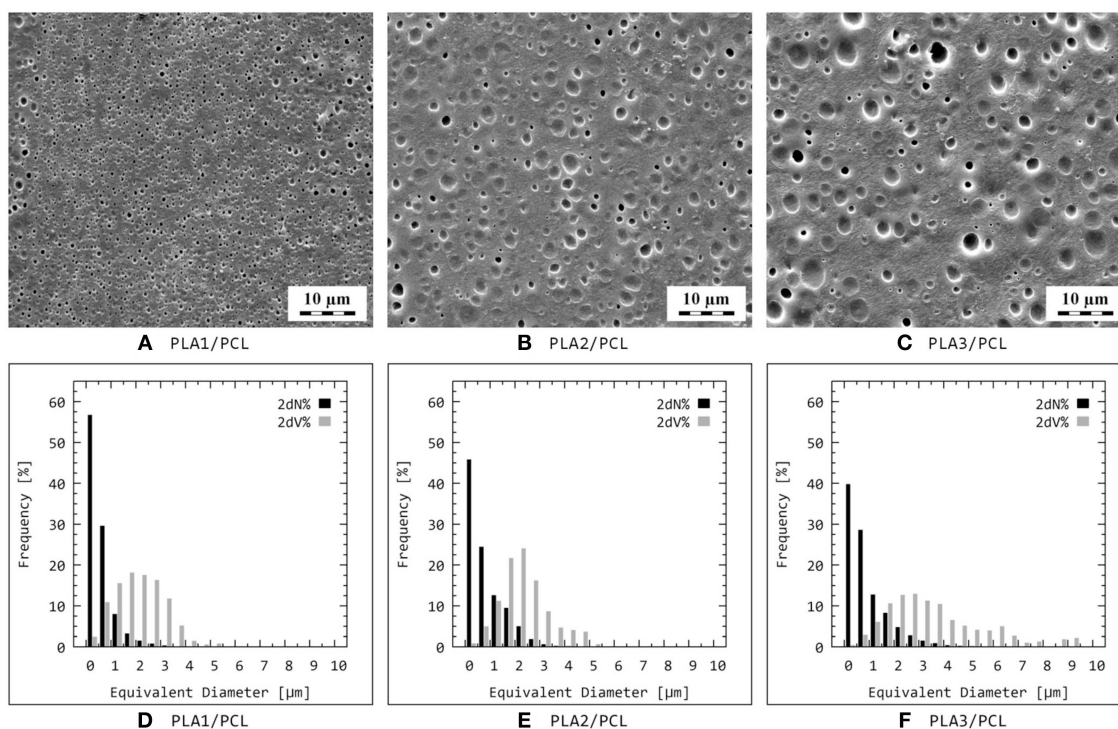
FIGURE 4 | SEM micrographs **(A–C)** and corresponding particle size distributions **(D–F)** of PLA/PCL (80/20) blends prepared from three different PLAs with decreasing viscosity [η(PLA1) > η(PLA2) > η(PLA3)]. The abbreviations 2dN% and 2dV% denote number and volume distributions, respectively. Reprinted with permission from Ostafinska et al. (2017). Copyright 2017, Elsevier.
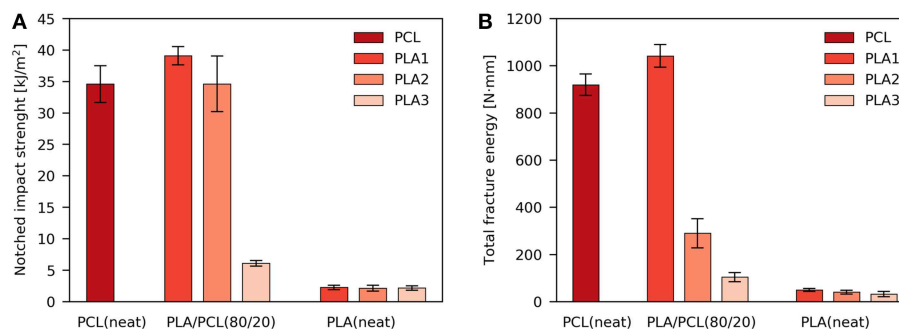
FIGURE 5 | The values of **(A)** non-instrumented and **(B)** instrumented Charpy notched impact strength for PLA/PCL(80/20) blends with decreasing viscosity of the matrix, whose morphology is shown in **Figure 4**. Adapted with permission from Ostafinska et al. (2017).

Recently, we tried to obtain PLA/PCL (80/20) blends with a sufficient toughness and an enhanced crystallinity by the addition of talc as a nucleation agent and/or by the modification of thermal treatment during the compression molding, using sample preparation procedure analogous to that described in Ostafinska et al. (2015) and Ostafinska et al. (2017). We found that the annealing time necessary for enhancement of PLA crystallinity above 40% in blends without talc is detrimental for the impact strength of PLA/PCL (80/20) blends. On the other hand, after addition of 1% of talc, the crystallinity of about 36% and Charpy notched impact strength almost 10 times higher

in comparison with neat PLA were obtained (**Table 1**, the last row). This impact strength was substantially lower than that for PLA/PCL (80/20) blends having PLA crystallinity below 10% (compare **Table 1** and **Figure 3**) but it could be sufficient for a number of applications.

The Reasons of Variable Results in the Literature

The explanation of different results of previous studies is somewhat complicated by the fact that the authors used various

FIGURE 6 | Load-deflection curves (*F-f* diagrams) of PLA/PCL(80/20) blends from the instrumented Charpy notched-impact test. The blends were prepared from the three different types of PLA with decreasing viscosity as described in Ostafinska et al. (2017): **(A)** the highest viscosity of PLA, **(B)** a medium viscosity of PLA, and **(C)** the lowest viscosity of PLA. Morphology of the blends and their integral impact strength are shown in **Figures 4**, **5**, respectively. A_{el}, A_{pl}, and A_R represent elastic, plastic and residual part of total fracture energy, respectively. F_g and f_g are the characteristic load and deflection values at yield, corresponding to the transition from elastic to elastic-plastic behavior, respectively; F_m and f_m are the characteristic load and deflection values corresponding to the onset of crack propagation, respectively. Adapted with permission from Ostafinska et al. (2017).

grades of PLA and various methods of the PLA/PCL blends preparation, such as direct continuous or discontinuous melt blending, or solution mixing. On the other hand, neither the small differences in the content of D-isomer in PLA, nor differences in molecular weights of PLA and/or PCL should have a decisive effect to the interfacial tension and adhesion between PLA and PCL. Therefore, the PLA/PCL blends cannot be considered as incompatible in the sense that they cannot exhibit good mechanical performance. However, differences in the molecular weights have strong impact to the rheological properties of polymers, which together with compounding and processing conditions control the size of PCL particles. As mentioned in the introduction, it is well known that the toughness of polymer blends depends critically on the size of the dispersed particles of a blend soft component (Bucknall, 2000; Horak et al., 2005; Bucknall and Paul, 2009, 2013). The optimum particle size for the maximization of the impact strength at a certain volume fraction of the dispersed phase is a function of the dominating toughening mechanism which depends on the

crystallinity of the matrix. An analysis of the above results lead us to the conclusion that different toughening mechanisms are dominating in PLA/PCL blends with a low crystallinity PLA (till about 10%) and with a high crystallinity PLA (above 30%). Therefore, the optimum size of PCL particles is substantially different for the blends with a low and with a high crystallinity of PLA.

For example, we believe that the discrepancy between the strong enhancement of elongation at break and rather small enhancement of impact strength, observed by Urquijo et al. (2015) for PLA/PCL blends with a low crystallinity of PLA, results from unfavorable size of PCL particles and not from the incompatibility of PLA and PCL grades used in given study. According to results of Bai et al. (2013), the PCL particles in the study of Urquijo et al. (2015) seem to be too small for efficient improvement of the impact strength. However, their concentration and fine dispersion are sufficient to improve maximum elongation of the blend. We conclude that a too rough phase structure of PLA/PCL blends leads to insufficient improvement both impact strength and elongation at break. On the other hand, a very fine phase structure (such as that observed by Urquijo et al., 2015) can lead to the insufficient impact strength (especially for the blends with a low crystallinity of PLA), but the extensibility can be quite large.

The dependence of the impact strength of PLA/PCL (80/20) blends on the size of PCL particles was well documented by Bai et al. (2013). Moreover, the results of Bai et al. (2013) were confirmed by later studies of Ostafinska et al. (2015, 2017): The average size of the PCL droplets in super-tough PLA/PCL (80/20) blends with low crystallinity PLA matrix detected in Ostafinska et al. (2015, 2017) was in a good agreement with results in Bai et al. (2013). The weight average of the particle diameter, $d_w = 0.8\,\mu m$ obtained for the maximum impact strength in Bai et al. (2013) corresponded quite well to the diameter number average, $d_n = 0.6\,\mu m$, and diameter volume average, $d_V = 1.3\,\mu m$, determined in Ostafinska et al. (2015). It should be mentioned that zones with different particle size appear in PLA/PCL blends prepared by the methods, which are supposed to yield the samples with uniform phase structure (Fortelny et al., 2015; Ostafinska et al., 2015, 2017). Therefore, the droplet size distribution in references (Ostafinska et al., 2015, 2017) was evaluated by MDISTR program package (Slouf et al., 2015), which takes this nonuniformity into account. The non-uniformity of the phase structure negatively affects the reliability of conventional methods of determination of the average droplet size based on evaluation of several hundreds of particles (Fortelny et al., 2008). Further complication for determination of optimum size of PCL particles is obvious non-uniformity in the morphology of samples prepared by injection molding. Morphology of these samples changes from shell to core and depends on the sample shape and dimensions. Therefore, it can be only estimated that d_w somewhat below $0.5\,\mu m$ is optimal for PCL particles in PLA/PCL (80/20) blends with a high crystallinity of PLA. PCL particles with d_w somewhat above $1\,\mu m$ seems to be most efficient for toughening of PLA/PCL (80/20) blends with a low crystallinity of PLA.

Nevertheless, it is apparent that the relatively low impact strength of the PLA/PCL blends in Urquijo et al. (2015) could be explained as a consequence of smaller size of PCL droplets than was optimal for the blends with a low PLA crystallinity. On the other hand, the brittle behavior of the PLA/PCL (70/30) blends obtained in Gardella et al. (2014) and Monticelli et al. (2014) and the decrease of toughness in the blends with content of PCL above 20% detected in Ostafinska et al. (2015) were apparently caused by too large size of the PCL droplets and by their broad size distribution.

Summary: Compatibility of PLA and PCL Polymers

It can be concluded that PLA and PCL are not incompatible because their blends can exhibit good mechanical properties. It means that the value of the interfacial tension between PLA and PCL does not prevent the preparation of PLA/PCL blends with a fine phase structure and a sufficient adhesion at the interface. On the other hand, the toughness of the PLA/PCL blends is extremely sensitive to the size of PCL particles. This was confirmed by the fact that an increase of number average diameter, d_n, from 0.6 to 0.9 μm and of volume average diameter, d_V, from 2.2 to 3.6 μm for PLA/PCL (80/20) blends led to the decrease in the Charpy notch impact strength from 38 to 6 kJ/m^2 and to the change in the character of the blend fracture from ductile to brittle (Ostafinska et al., 2017). Therefore, the size of PCL particles must be carefully controlled during the processing of PLA/PCL blends that should exhibit high toughness. It is not an easy task, especially for the blends where enhanced crystallinity of PLA is required. These blends should contain small PCL particles (with d_w below about 0.5 μm) and simultaneously their preparation requires elevated temperature and longer time in a hot press or a mold even if a nucleation agent is added (Bai et al., 2013). Unfortunately, an increase in the PCL particle size during melt annealing is quite rapid; d_V increased about twice during compression molding of PLA/PCL (80/20) blend and even stronger increase in the size of PCL particles was detected for blends with a higher content of PCL (Fortelny et al., 2015).

TOUGHNESS OF PLA/PCL BLENDS CONTAINING A COMPATIBILIZER

Most of the studies dealing with the effect of a compatibilizer on the structure and properties of PCL/PLA blends have been inspired by the assumption that the addition of a compatibilizer is necessary for the preparation of the blends with high toughness. Nevertheless, as explained and evidenced in the previous section, a compatibilization is not necessary for the tough PLA/PCL blends. On the other hand, compatibilizers can help with a preparation of the polymer blends with a fine phase structure for broader range of rheological properties of the components and for broader range of mixing conditions. It is also very important that compatibilizer can efficiently suppress changes in the phase structure during polymer blends processing (Macosko et al., 1996; Marić and Macosko, 2002; Horak et al., 2005).

There are three methods of compatibilization of immiscible polymer blends (Huang, 2011). At physical (or additive) compatibilization (Horak et al., 2005; Huang, 2011), block or graft copolymers with blocks identical, miscible or similar with the blend components are added to the blend during a compounding. At reactive compatibilization (Horak et al., 2005; Huang, 2011), copolymers (mostly grafted) are formed during the blend melt-mixing due to chemical reactions between functional groups on the blend components; the newly-formed copolymers act as compatibilizers. Addition of an admixture of functionalized components and/or initiation by reactive low-molecular-weight agents is frequently applied at reactive compatibilization. More recently it was found that also some nanofillers can serve as efficient compatibilizers for polymer blends besides of block and graft copolymers (Ray et al., 2004; Huang, 2011; de Luna and Filippone, 2016). The effects of various types of compatibilizers are discussed below. The ratios of values of the impact strength (a) and of the elongation at break (ε) for both compatibilized and non-compatibilized (neat) blends, a_{comp}/a_{neat}, and, $\varepsilon_{comp}/\varepsilon_{neat}$, respectively, are summarized in **Table 2**.

Additive Compatibilization of PLA/PCL Blends

Several papers were focused on compatibilization of PLA/PCL blends with various premade PLA-PCL block copolymers, and those detailing the effects on mechanical properties are summarized in **Table 2**. Dell'Erba et al. (2001) showed that the addition of PLLA-b-PCL-b-PLLA triblock copolymer to PLLA/PCL blends substantially reduced the size of PCL particles. Mechanical properties of PLLA/PCL/PLLA-b-PCL-b-PLLA blends were not studied in this paper. Wu et al. (2010) studied the effect of diblock PCL-b-PLA and triblock PLA-b-PCL-b-PLA copolymers on the morphology and the viscoelastic properties of PLA/PCL (30/70) blends. They found that the both copolymers improved the interfacial properties and substantially reduced the size of PCL particles. The compatibilization of PLA/PCL blends by PCL-b-PLA block copolymer was studied also by Kim et al. (2000). However, the study was focused on the crystallinity of the blend components and did not provide the mechanical properties of the compatibilized blends. Recently, Xiang et al. (2019) studied compatibilization efficiency of PLLA-b-PCL block copolymers having various compositions and molecular weights for PLLA/PCL (80/20) blends prepared in a batch mixer. Addition of 5% of these copolymers caused reduction of the PCL particle size and substantially enhanced elongation at break. PLLA-b-PCL copolymers with similar contents of PLLA and PCL and with large molecular weights showed the largest effects. Impact strength of the blends was not determined in this study.

Further studies dealt with compatibilization of PLA/PCL by premade block copolymers having blocks miscible with the blend components. Maglio et al. (2004) studied the effect of PLLA-b-PCL-b-PLLA and diblock copolymer of PLLA with poly(ethylene oxide) (PEO) on the size of PCL droplets in PLLA/PCL (70/30) blends. They found that the addition of 2% of PLLA-b-PCL-b-PLLA or PLLA-b-PEO substantially reduced

TABLE 2 | Ratios of toughness, a_{comp}/a_{neat}, and elongation at break, $\varepsilon_{comp}/\varepsilon_{neat}$, of compatibilized and neat blends for various compatibilizers.

PLA/PCL	Compatibilizer	a_{comp}/a_{neat}	$\varepsilon_{comp}/\varepsilon_{neat}$	References
70/30[a]	2wt. % of PEO-PPO-PEO[b]	~3.5[c]	–	Vilay et al., 2010
80/20	5 phr of PEG-PPG-PEG[d]	–	~18	Wachirahuttapong et al., 2016
80/20[e]	10 wt. % PCL-PEG[f]	–	~9	Na et al., 2002
95/5	5 wt. % of PCL-PBD[g] or PCL-PC[h]	–	~18	Finotti et al., 2016
80/20	5 wt. % of PCL-PBD[g]	–	1.8	Finotti et al., 2016
80/20	5 wt. % of PCL-PC[h]	–	1.2	Finotti et al., 2016
70/30	10% of PLA substituted with PLA-g-MA[i]	–	7.5	Gardella et al., 2014
85/15[j]	1 wt. % of LTI[k]	1.8[l]	–	Takayama et al., 2011
85/15[m]	1 wt. % of LTI[k]	16[l]	–	Takayama et al., 2011
80/20	0.5 phr of LTI[k]	8.6[n]	12	Harada et al., 2008
85/15	3 wt. % of GMA[o]	1.9[p]	16	Chee et al., 2013
70/30	0.3 phr of DCP[q]	2.5–3.8[r,s]	5–7[p]	Semba et al., 2007
70/30	2 wt. % of POSS-PCL-PLA[t]	–	2.5	Monticelli et al., 2014
70/30	1 wt. % of HSAG[u]	–	3.7	Forouharshad et al., 2015

[a]PLLA matrix; [b]Polyethylene oxide-b-polypropylene oxide-b-polyethylene oxide; [c]Fracture energy from tensile testing; [d]Poly(ethylene glycol)-b-poly(propylene glycol)-b-poly(ethylene glycol); [e]PDLLA matrix; [f]Polycaprolactone-b-poly(ethylene glycol); [g]Polycaprolactone–b-polybutanediol; [h]Polycaprolactone-b-polycarbonate; [i]Polylactic acid grafted with maleic anhydride; [j]Quenched sample; [k]Lysine triisocyanate; [l]Fracture energy; [m]Annealed sample; [n]Notched Charpy impact strength; [o]Glycidyl methacrylate; [p]Unnotched Izod impact strength; [q]Dicumyl peroxide; [r]Depend on mixing conditions; [s]Notched Izod impact strength; [t]Polyhedral oligomeric silsesquioxane grafted with polylactic acid-b-polycaprolactone block copolymer; [u]High surface area graphite.

the size of PCL particles; PLLA-*b*-PEO was more efficient than PLLA-*b*-PCL-*b*-PLLA copolymer. Mechanical properties of the compatibilized blends were not characterized. Vilay et al. (2010) studied the compatibilization efficiency of a copolymer of PEO and poly(propylene oxide) (PPO) (triblock copolymer PEO-*b*-PPO-*b*-PEO) for PLLA/PCL (70/30) blends. They found that the addition of the copolymer reduced the size of PCL particles and enhanced interfacial adhesion. Fracture energy of PLLA/PCL/PEO-*b*-PPO-*b*-PEO blends steeply increased with the content of PEO-*b*-PPO-*b*-PEO. Wachirahuttapong et al. (2016) studied the effect of triblock copolymer poly(ethylene glycol)-poly(propylene glycol)-poly(ethylene glycol) (PEG-*b*-PPG-*b*-PEG) on the morphology and mechanical properties of PLA/PCL blends. They assumed that PEG-*b*-PPG-*b*-PEG copolymer behaved as plasticizer in PLA/PCL blends and, therefore, reduced size of PCL particles in blends with low PCL contents. The elongation at break increased with the amount of added PEG-*b*-PPG-*b*-PEG. Na et al. (2002) studied the structure,

the thermodynamic properties, and the mechanical properties of PLLA/PCL and PDLLA/PCL blends compatibilized with PCL-*b*-PEG. They showed that PCL-*b*-PEG copolymers can be an efficient compatibilizer for PLA/PCL but detected only a moderate improvement in the elongation at break. The largest $\varepsilon_{comp}/\varepsilon_{neat}$ was achieved for PDLLA/PCL (80/20) compatibilized with 10% of PCL-*b*-PEG.

Finotti et al. (2016) studied the compatibilization of PLA/PCL blends by low-molecular-weight block copolymers of ε-caprolactone with tetra-methylene ether glycol or aliphatic polycarbonate. The addition of 5% of the copolymers substantially reduced the size of PCL droplets in the PLA/PCL (80/20) blends. The elongation at break of PLA/PCL was relatively low but it increased with the PCL content. Surprisingly, the compatibilized PLA/PCL (95/5) blends showed a high elongation at break, which was much larger than that for the compatibilized PLA/PCL (80/20) blends. Dias and Chinelatto (2019) compatibilized PLA/PCL (75/25) with low-molecular-weight triblock copolymer ε-caprolactone-tetrahydrofuran-ε-caprolactone. Addition of the copolymer did not lead to the reduction of the size of PCL particles and had negligible effect on the Izod impact strength of the blend. On the other hand, strain at break increased substantially with copolymer content in the blend. Song et al. (2018) found a decrease in the size of PCL particles and substantial increase in elongation at break for PLA/PCL (80/20) and (70/30) blends after addition of a small amount of polyoxymethylene (POM). They explained compatibilization effect of POM as a consequence of hydrogen bonds formation between POM and PLA and PCL chains. The authors did not study the effect of POM on the impact strength of PLA/PCL blends.

Reactive Compatibilization of PLA/PCL Blends

The reactive compatibilization of PLA/PCL blends was studied quite intensively by various authors for composition with PCL in the range 15–30% by wt., as summarized in **Table 2**. Gardella et al. (2014) studied the effect of the substitution of a part of PLA by maleic-anhydride-grafted polylactide (PLA-g-MA) on the morphology and toughness of PLA/PCL (70/30) blends. It was found that the average size and the width of the size distribution of PCL particles decreased with the amount of PLA substituted with PLA-g-MA. Also the melting enthalpy of PLA increased with the amount of PLA-g-MA. However, the highest increase in the elongation at break with respect to the neat PLA/PCL (70/30) was observed when just 10% of PLA was substituted with PLA-g-MA, whereas higher contents of PLA-g-MA led to surprising decrease in the elongation at break.

Takayama et al. (2011) added 1% of lysine triisocyanate (LTI) to PLA/PCL (85/15) blends. They found that PLA/PCL/LTI contained smaller PCL particles and had a higher fracture energy than the original PLA/PCL blend. Annealing of the *compatibilized* PLA/PCL/LTI blend lead to an increase in the PLA crystallinity and caused an increase in the fracture energy. On the other hand, annealing of the *non-compatibilized* PLA/PCL blend was followed by a pronounced decrease in its fracture

energy. Harada et al. (2008) compared efficiency of 4 isocyanates at reactive compatibilization of PLA/PCL blends. They found that LTI is the most efficient compatibilizer. Addition of LTI during compounding led to a remarkable reduction of the size of PCL particles and to a strong increase in the notched and unnotched Charpy impact strengths and in the elongation at break.

Chee et al. (2013) studied the reactive compatibilization of a PLA/PCL blend by the addition of glycidyl methacrylate (GMA) at blending. They found that the elongation at break and the unnotched Izod impact strength of PLA/PCL (85/15) blend increased with the amount of added GMA until 3%. For more than 3% of GMA, the blend impact strength and the elongation at break decreased with the amount of GMA. Shin and Han (2013) studied the effects of the addition of GMA and of the following irradiation of PLA/PCL/GMA blends. They found that the addition of GMA without the following irradiation led to a decrease in the size of the PCL droplets and to an increase in the elongation at break of the PLA/PCL blends. The ratio $\varepsilon_{comp}/\varepsilon_{neat} \approx 6$ was achieved for PLA/PCL/GMA blends without irradiation. The stiffness of PLA/PCL/GMA blends increased and their elongation at break decreased with the applied irradiation dose due to induced crosslinking.

Semba et al. (2007) studied the effect of dicumyl peroxide (DCP) and the split of feeding on the mechanical properties of PLA/PCL (70/30) blends prepared by a compounding in a twin screw extruder followed by an injection molding. They found that the elongation at break of the PLA/PCL blend was substantially large than that of the neat PLA. It was further enhanced by the addition of DCP. Only slight dependence of the elongation at break on the feeding procedure was detected. Notched Izod impact strength of PLA/PCL blend was less than twice of that for neat PLA. Addition of DCP enhanced notch Izod impact strength to the value about three times larger than that for neat PLA. The differences among the final properties for the samples prepared by various feeding procedures were lower than those caused by the DCP addition.

Compatibilization of PLA/PCL Blends by Means of Nanofillers

Various nanofillers were added to PLA/PCL blends with the aim to improve their toughness. Monticelli et al. (2014) compatibilized PLA/PCL (70/30) blends with functionalized polyhedral oligomeric silsequioxane (POSS) molecules. POSS's having different functional groups and POSS's grafted with PCL-*b*-PLA block copolymers were employed. It was found that the POSS's containing a hydroxyl group and especially the POSS's grafted with PCL-*b*-PLA reduced the size of the PCL particles and improved the adhesion between PLA and PCL. Only the addition of POSS-g-PCL-*b*-PLA led to remarkable improvement in the elongation at break but still to insufficient value (only to 2.5 times of neat PLA as shown in **Table 2**). Impact strength of these blends was not measured.

Urquijo et al. (2016) studied the effect of organically modified montmorillonite (OMMT) on the structure and the mechanical properties of PLA/PCL (80/20) blends. They found that the stiffness of PLA/PCL/OMMT nanocomposites increased, while the elongation at break and notched Izod impact strength decreased with the increasing content of OMMT. The decrease in the elongation at break was from 140% for PLA/PCL (80/20) to 15% for PLA/PCL/OMMT (80/20/6). The notched Izod impact strength decreased from about 30 J/m for neat blend to about 15 J/m for composite containing almost 6% of OMMT. Sabet and Katbab (2009) showed that addition of modified montmorillonite reduced size of the PCL particles in PLA/PCL (80/20) blends. The effect was strengthened by further addition of maleic anhydride grafted polypropylene. The toughness of PLA/PCL blends was not determined in this paper.

Forouharshad et al. (2015) studied the effect of the addition of high surface area graphite (HSAG) on the morphology and the properties of PLA/PCL. They found a decrease in the PCL particle size and a rather small increase in elongation at break of the blends as a consequence of the addition of HSAG. This increase was insufficient for practical applications because the achieved elongation at break for PLA/PCL (70/30) blend was equal to neat PLA only.

Summary: Compatibilization and Toughness of PLA/PCL Blends

Analysis of the above-mentioned results leads us to the conclusion that the improvement of the toughness of PLA/PCL blends by the addition of a compatibilizer is caused mostly by the fact that the compatibilizer influences the average size of the PCL particles. In numerous compatibilized PLA/PCL blends studied previously, the toughness had not been improved significantly after the addition of a compatibilizer (**Table 2**). It seems that the optimum size of the PCL droplets with respect to the crystallinity of PLA (for pure PLLA and PLA with a low content of D-isomer) is decisive also for toughness of PLA/PCL blends regardless of the compatibilization. However, the compatibilization can help to obtain tough PLA/PCL blends with inconvenient rheological properties of their molten components, when the PCL particles are too big to achieve the high toughness. This is especially important for the blends with a high crystallinity of PLA matrix, where small PCL particles are needed for achievement of high impact strength of PLA/PCL blends. Moreover, a proper compatibilizer can stabilize the size of the PCL particles in the PLA/PCL blends during their further processing.

OUTLOOK TO PREPARATION OF TOUGH PLA/PCL BLENDS

The analysis of literature suggests that the size distribution of PCL particles is decisive for the toughness of PLA/PCL blends independently of the presence of a compatibilizer. The optimum size of the PCL particles depends on the degree of crystallinity of PLA. The impact strength of the PLA/PCL blends with a certain composition is extremely sensitive to the size of PCL particles (Ostafinska et al., 2017). Therefore, the optimum PCL particle size for the blends with a certain composition and given crystallinity of the PLA matrix should be known in order to prepare the PLA/PCL blend with the maximum impact

strength. This requirement is of unusually high importance for PLA/PCL blends in comparison with common blends of synthetic polymers, such as polypropylene/ethylenepropylene rubber blends (Pitt, 1990), due to a quite narrow window of the size of PCL particles for which sufficiently high impact strength of PLA/PCL blends can be achieved. The determination of the optimum size of the PCL particles is not a trivial task. The droplet size in samples prepared by some processing methods, e.g., by injection molding, obviously varies and depends on specific locations of the specimen. Moreover, the PLA/PCL blends showed non-uniform phase structure (with different zones containing smaller or bigger particles) even in samples prepared by compression molding, which was expected to show a weak dependence of droplet size on the specific location within the final specimen (Ostafinska et al., 2015, 2017).

Our analysis of the results for PLA/PCL blends with a low crystallinity of PLA matrix (up to ∼10%) confirmed that previous authors prepared blends containing PCL droplets with various sizes, which ranged from quite small (diameters below $0.5\,\mu m$) to fairly large (diameters above $3\,\mu m$). The size of the PCL particles depended on the choice of the rheological properties of the blend components (through their molecular weights) and on the methods of the blend mixing and processing. The application of an efficient compatibilization method could reduce the size of PCL particles and stabilize the morphology of PLA/PCL blends during further processing.

The preparation of the PLA/PCL blends with a high crystallinity of PLA matrix (for high stiffness at elevated temperatures) and the optimum size of PCL particles (for high toughness) seems to be even more difficult task. The optimum size of the PCL particles in the PLA/PCL blends with high-crystallinity matrix is lower in comparison to the blends with a low-crystallinity matrix. For the blends without a compatibilizer, the small PCL particles can be obtained only by intensive mixing followed by fast injection molding. It should be mentioned that not all commercial grades of PLA are designed for injection molding. There is a certain necessary time of annealing in the temperature range above T_g of PLA needed for its crystallization even for the blends containing efficient nucleation agents (Bai et al., 2012, 2013). Moreover, even short annealing of the PLA/PCL blends usually leads to an increase in the size of PCL particles because PLA matrix at higher temperatures above its T_g softens and PCL minority phase above its T_m melts, which results in the reorganization of PCL particles. Therefore, choice of efficient method of preparation of PLA/PCL blends with enhanced crystallinity of PLA and optimum size of PCL particles is very challenging. Detailed

information about the crystallization of PLA during various temperature regimes is necessary for the optimization of the blend preparation method. The compatibilization of PLA/PCL blends with a high crystallinity of PLA seems to be more important than in the case of the blends with a low crystallinity of PLA.

The structure and the properties of the matrix are decisive for the optimal size distribution of soft (elastomer) dispersed particles serving for the improvement of the matrix toughness (Bucknall, 2000; Horak et al., 2005). Therefore, the dependences of the toughness of blends of PLA with other elastomeric biopolymers on the size of elastomeric droplets are expected to be similar to those for PLA/PCL blends.

CONCLUSIONS

PLA and PCL are immiscible polymers but their interfacial tension is quite low. Therefore, PLA/PCL blends having good mechanical properties, namely the high impact strength, can be prepared without the addition of a compatibilizer.

The toughness of the PLA/PCL blends is highly sensitive to the size of PCL particles. The optimum size of PCL particles decreases with the crystallinity of PLA matrix.

The compatibilization of the PLA/PCL blends can stabilize their phase structure during the processing and help with the optimization of the PCL particle size. This holds especially in the case of the unfavorable rheological properties of the PLA and PCL components and/or the unfavorable methods of the PLA/PCL preparation.

The determination of the optimum size of PCL particles as a function of PLA crystallinity and establishing the efficient methods for reproducible preparation of the stable PLA/PCL blends with the required size of PCL particles are challenges for future research.

AUTHOR CONTRIBUTIONS

IF summarized literature and wrote a major part of the manuscript with contributions of AU, LF, and MS. MS initiated the project focused on biodegradable PLA/PCL blends, prepared images for the manuscript, and finalized the manuscript.

FUNDING

REFERENCES

Auras, R., Harte, B., and Selke, S. (2004). An overview of polylactides as packaging materials. *Macromol. Biosci* 4, 835–864. doi: 10.1002/mabi.200400043

Averous, L., and Pollet, E. (2012). *Environmental Silicate Nano-Biocomposites.* London: Springer, 13–39.

Bai, H., Huang, C., Xiu, H., Gao, Y., Zhang, Q., and Fu, Q. (2013). Toughening of poly(L-lactide) with poly(epsilon-caprolactone): combined effects of matrix

crystallization and impact modifier particle size. *Polymer* 54, 5257–5266. doi: 10.1016/j.polymer.2013.07.051

Bai, H., Xiu, H., Gao, J., Deng, H., Zhang, Q., Yang, M., et al. (2012). Tailoring impact toughness of poly(L-lactide)/poly(epsilon-caprolactone) (PLLA/PCL) blends by controlling crystallizatior of PLLA matrix. *ACS Appl. Mater. Interfaces* 4, 897–905. doi: 10.1021/am201564f

Bucknall, C. B. (2000). "Deformation mechanisms in rubber-toughened polymers," in *The Polymer Blends, V. 2: Performance*, eds. C.

B. Bucknall, and D. R. Paul (New York: John Wiley & Sons), 83–136.

Bucknall, C. B., and Paul, D. R. (2009). Notched impact behavior of polymer blends: part 1: new model for particle size dependence. *Polymer* 50, 5539–5548. doi: 10.1016/j.polymer.2009.09.059

Bucknall, C. B., and Paul, D. R. (2013). Notched impact behaviour of polymer blends: part 2: dependence of critical particle size on rubber particle volume fraction. *Polymer* 54, 320–329. doi: 10.1016/j.polymer.2012.11.019

Carmona, V. B., Correa, A. C., Marconcini, J. M., and Mattoso, L. H. C. (2015). Properties of a biodegradable ternary blend of thermoplastic starch (TPS), poly(epsilon-caprolactone) (PCL) and poly(lactic acid) (PLA). *J. Polym. Environ.* 23, 83–89. doi: 10.1007/s10924-014-0666-7

Chee, W. K., Ibrahim, N. A., Zainuddin, N., Rahman, M. F. A., and Chieng, B. W. (2013). Impact toughness and ductility enhancement of biodegradable poly(lactic acid)/poly(ε-caprolactone) blends via addition of glycidyl methacrylate. *Adv. Mater. Sci. Eng.* 2013:976373. doi: 10.1155/2013/976373

de Luna, M. S., and Filippone, G. (2016). Effects of nanoparticles on the morphology of immiscible polymer blends - challenges and opportunities. *Europ. Polym. J.* 79, 198–218. doi: 10.1016/j.eurpolymj.2016.02.023

Dell'Erba, R., Groenickx, G., Maglio, G., Malinconico, M., and Migliozzi, A. (2001). Immiscible polymer blends of semicrystalline biocompatible components: thermal properties and phase morphology analysis of PLLA/PCL blends. *Polymer* 42, 7831–7840. doi: 10.1016/S0032-3861(01)00269-5

Dias, P., and Chinelatto, M. A. (2019). Effect of poly(ε-caprolactone-b-tetrahydrofuran) triblock copolymer concentration on morphological, thermal and mechanical properties of immiscible PLA/PCL blends. *J. Renew. Mater.* 7, 129–138. doi: 10.32604/jrm.2019.00037

Fambri, L., and Migliaresi, C. (2010). "Crystallization and thermal properties," in *Poly(lactic acid): Synthesis, Structures, Properties, Processing, and Applications*, eds R. Auras, L. T. Lim, S. E. M. Selke, and H. Tsuji (Hoboken, NJ: John Wiley & Sons), 113–124. doi: 10.1002/9780470649848.ch9

Ferri, J. M., Fenollar, O., Jorda-Vilaplana, A., Garcia-Sanoguera, D., and Balart, R. (2016). Effect of miscibility on mechanical and thermal properties of poly(lactic acid)/polycaprolactone blends. *Polym. Int.* 65, 453–463. doi: 10.1002/pi.5079

Finotti, P. F. M., Costa, L. C., and Chinelatto, M. A. (2016). Effect of chemical structure of compatibilizers on the thermal, mechanical and morphological properties of immiscible PLA/PCL blends. *Macromol. Symp.* 368, 24–29. doi: 10.1002/masy.201600056

Forouharshad, M., Gardella, L., Furfaro, D., Galimberti, M., and Monticelli, O. (2015). A low-environmental-impact approach for novel bio-composites on PLLA/PCL blends and high surface area graphite. *Eur. Polym. J.* 70, 28–36. doi: 10.1016/j.eurpolymj.2015.06.016

Fortelny, I., and Juza, J. (2019). Description of the droplet size evolution in flowing immiscible polymer blends. *Polymers* 11, 1–31. doi: 10.3390/polym11050761

Fortelny, I., Lapcikova, M., Lednicky, F., Stary, Z., and Krulis, Z. (2008). Nonuniformity of phase structure in immiscible polymer blends. *Polym. Eng. Sci.* 48, 564–571. doi: 10.1002/pen.20985

Fortelny, I., Ostafinska, A., Michalkova, D., Juza, J., Mikesova, J., and Slouf, M. (2015). Phase structure evolution during mixing and processing of poly(lactic acid)/polycaprolactone (PLA/PCL) blends. *Polym. Bull.* 72, 2931–2947. doi: 10.1007/s00289-015-1445-x

Gardella, L., Calabrese, M., and Monticelli, O. (2014). PLA maleation: an easy and effective method to modify the properties of PLA/PCL immiscible blends. *Colloid Polym. Sci.* 292, 2391–2398. doi: 10.1007/s00396-014-3328-3

Garlotta, D. (2002). A literature rewiew of poly(lactic acid). *J. Polym. Environ.* 9, 63–81 doi: 10.1023/A:1020200822435

Harada, M., Iida, K., Okamoto, K., Hayashi, H., and Hirano, K. (2008). Reactive compatibilization of biodegradable poly(lactic acid)/poly(ε-caprolactone) blends with reactive processing agents. *Polym. Eng. Sci.* 48, 1359–1368. doi: 10.1002/pen.21088

Horak, Z., Fortelny, I., Kolarik, J., Hlavata, D., and Sikora, A. (2005). "Polymer blends," in *The Encyclopedia of Polymer Science and Technology*, ed. J. Kroschwitz (New York, NY: John Wiley & Sons), 1–59. doi: 10.1002/0471440264.pst276

Huang, H.-X. (2011). "Macro, micro and nanostructured morphologies of multiphase polymer systems", in *The Handbook of Multiphase Polymer Systems*, eds. A. Boudenne, L. Ibos, Y. Candau, and S. Thomas (Chichester, UK: John Wiley & Sons), 161–249. doi: 10.1002/9781119972020.ch6

Imre, B., and Pukánszky, B. (2013). Compatibilization in bio-based and biodegradable polymer blends. *Europ. Polym. J.* 49, 1215–1233. doi: 10.1016/j.eurpolymj.2013.01.019

Kassos, N., Kelly, A. L., Gough, T., and Gill, A. A. (2019). Synergistic toughening and compatibisation effect of poly(butylene succinate) in PLA/poly-caprolactone blends. *Mater. Res. Express* 6:035313. doi: 10.1088/2053-1591/aaf7c1

Kelnar, I., Fortelny, I., Kapralkova, L., Kratochvil, J., Angelov, B., and Nevoralova, M. (2016). Effect of layered silicates on fibril formation and properties of PCL/PLA microfibrillar composites. *J. Appl. Pol. Sci.* 133, 1–9. doi: 10.1002/app.43061

Kim, C.-H., Cho, K. Y., Choi, E.-J., and Park, J.-K. (2000). Effect of P(/LA-co-εCL) on the compatibility and crystallization behavior of PCL/PLLA blends. *J. Appl. Polym. Sci.* 77, 226–231. doi: 10.1002/(SICI)1097-4628(20000705)77:1<226::AID-APP29>3.0.CO;2-8

Krishnan, S., Pandey, P., Mohanty, S., and Nayak, S. K. (2016). Toughening of polylactic acid: an overview of research progress. *Polym.-Plast. Technol. Eng.* 55, 1623–1652. doi: 10.1080/03602559.2015.1098698

Liu, G., Zhang, X., and Wang, D. (2014). Tailoring crystallization: towards high-performance poly(lactic acid). *Adv. Mater.* 26, 6905–6911. doi: 10.1002/adma.201305413

López-Rodríguez, N., López-Arraiza, A., Meaurio, E., and Sarasua, J. R. (2006). Crystallization, morphology, and mechanical behavior of poly(lactide)/poly(ε-caprolactone) blends. *Polym. Eng. Sci.* 46, 1299–1308. doi: 10.1002/pen.20609

Lunt, J. (1998). Large-scale production, properties and commercial applications of polylactic acid polymers. *Polym. Degrad. Stab.* 59,145–152. doi: 10.1016/S0141-3910(97)00148-1

Macosko, C. W., Guegan, P., Khandpur, A. K., Nakayama, A., Marechal, P., and Inoue, T. (1996). Compatibilizers for melt blending: premade block copolymers. *Macromolecules* 29, 5590–5598. doi: 10.1021/ma9602482

Maglio, G., Malinconico, M., Migliozzi, A., and Groeninckx, G. (2004). Immiscible poly(L-lactide)/poly(ε-caprolactone) blends: influence of the addition of a poly(L-lactide)-b-poly(oxyethylene) block copolymer on thermal behavior and morphology. *Macromol. Chem. Phys.* 205, 946–950. doi: 10.1002/macp.200300150

Marić, M., and Macosko, C. W. (2002). Block copolymer compatibilizers for polystyrene/poly(dimethylsiloxane) blends. *J. Polym. Sci. [B]*. 40, 346–357. doi: 10.1002/polb.10098

Mittal, V., Akhtar, T., and Matsko, N. (2015). Mechanical, thermal, rheological and morphological properties of binary and ternary blends of PLA, TPS and PCL. *Macromol. Mater. Eng.* 300, 423–435. doi: 10.1002/mame.201400332

Monticelli, O., Calabrese, M., Gardella, L., Fina, A., and Gioffredi, E. (2014). Silsesquioxanes: novel compatibilizing agents for tuning the microstructure and properties of PLA/PCL immiscible blends. *Eur. Polym. J.* 58, 69–78. doi: 10.1016/j.eurpolymj.2014.06.021

Murariu, M., Dechief, A.-L., Ramy-Ratiarison, R., Paint, Y., Raques, J.-M., and Dubois, P. (2015). Recent advances in production of poly(lactic acid) (PLA) nanocomposites: a versatile method to tune crystallization properties of PLA. *Nanocomposites* 1, 71–82. doi: 10.1179/2055033214Y.0000000008

Na, Y., He, Y., Shuai, X., Kikkawa, Y., Doi, Y., and Inoue, Y. (2002). Compatibilization effect of poly(ε-caprolactone)-b-poly(ethylene glycol) block copolymers and phase morphology analysis in immiscible poly(lactide)/poly(ε-caprolactone) blends. *Biomacromolecules* 3, 1179–1186. doi: 10.1021/bm020050r

Nakajima, H., Dijkstra, P., and Loos, K. (2017). The recent development in biobased polymers toward general and engineering applications; polymers that are upgraded from biodegradable polymers, analogous to petroleum-derived polymers, and newly developed. *Polymers* 9:523. doi: 10.3390/polym9100523

Ostafinska, A., Fortelny, I., Hodan, J., Krejcikova, S., Nevoralova, M., Kredatusova, J., et al. (2017). Strong synergistic effects in PLA/PCL blends: impact of PLA matrix viscosity. *J. Mech. Behavior Biomed. Mater.* 69, 229–241. doi: 10.1016/j.jmbbm.2017.01.015

Ostafinska, A., Fortelny, I., Nevoralova, M., Hodan, J., Kredatusova, J., and Slouf, M. (2015). Synergistic effects in mechanical properties of PLA/PCL blends with optimized composition, processing, and morphology. *RSC Adv.* 5, 98971–98982. doi: 10.1039/C5RA21178F

Patrício, T., Glória, A., and Bártolo, P. (2013). Mechanical and biological behaviour of PCL and PCL/PLA scaffolds for tissue engineering applications. *Chem. Eng. Trans.* 32, 1645–1650. doi: 10.3303/CET1332275

Perego, G., Cella, G. D., and Bastioli, C. (1996). Effect of molecular weight and crystallinity on poly(lactic acid) mechanical properties. *J. Appl. Pol. Sci.* 59, 37–43. doi: 10.1002/(SICI)1097-4628(19960103)59:1<37::AID-APP6>3.0.CO;2-N

Pitt, C. G. (1990). "Poly-ε-caprolactone and its copolymers," in *The Biodegradable Polymers as Drug Delivery Systems*, eds. R. Langer, and M. Chasin (New York, NY: Marcel Dekker), 71–120.

Quiles-Carrillo, L., Montanes, N., Pineiro, F., Jorda-Vilaplana, A., and Torres-Giner, S. (2018). Ductility and toughness improvement of injection-molded compostable pieces of polylactide by melt blending with poly(ε-caprolactone) and thermoplastic starch. *Materials* 11:2138. doi: 10.3390/ma11112138

Ray, S. S., Pouliot, S., Bousmina, M., and Utracki, L. A. (2004). Role of organically modified layered silicate as an active interfacial modifier in immiscible polystyrene/polypropylene blends. *Polymer* 45, 8403–8413. doi: 10.1016/j.polymer.2004.10.009

Sabet, S. S., and Katbab, A. A. (2009). Interfacially compatibilized poly(lactic acid)/polycaprolactone/organoclay nanocomposites with improved biodegradability and barrier properties: effect of the compatibilizer structural parameters and feeding route. *J. Appl. Polym. Sci.* 111, 1954–1963. doi: 10.1002/app.29210

Semba, T., Kitagawa, K., Ishiaku, U. S., Kotaki, M., and Hamada, H. (2007). Effect of compounding procedure on mechanical properties and dispersed phase morphology of poly(lactic acid)/polycaprolactone blends containing peroxide. *J. Appl. Polym. Sci.* 103, 1066–1074. doi: 10.1002/app.25311

Shin, Y. B., and Han, D. H. (2013). Compatibilization of immiscible poly(lactic acid)/poly(e-caprolactone) blend through electron-beam irradiation with the addition of a compatibilizing agent. *Radiat. Phys. Chem.* 83, 98–104. doi: 10.1016/j.radphyschem.2012.10.001

Simoes, C. L., Viana, J. C., and Cunha, A. M. (2009). Mechanical properties of poly(ε-caprolactone) and poly(lactic acid) blends. *J. Appl. Polym. Sci.* 112, 345–352. doi: 10.1002/app.29425

Slouf, M., Ostafinska, A., Nevoralova, M., and Fortelny, I. (2015). Morphological analysis of polymer systems with broad particle size distribution. *Polym. Test.* 42, 8–16. doi: 10.1016/j.polymertesting.2014.12.012

Song, Z., Huang, X., Lu, X., Lv, Q., Xu, N., Pang, S., et al. (2018). Improvement of microstructures and properties of poly(lactic acid)/poly(e-caprolactone) blends compatibilized with polyoxymethylene. *J. Appl. Pol. Sci.* 135, 1–13. doi: 10.1002/app.46536

Standau, T., Zhao, C., Castellon, S. M., Bonten, C., and Altstadt, V. (2019). Chemical modification and foam processing of polylactide (PLA). *Polymers*. 11, 1–38. doi: 10.3390/polym11020306

Takayama, T., Todo, M., and Tsuji, H. (2011). Effect of annealing on the mechanical properties of PLA/PCL and PLA/PCL/LTI polymer blends. *J. Mech. Behav. Biomed. Mater.* 4, 255–260. doi: 10.1016/j.jmbbm.2010.10.003

Todo, M., Park, S.-D., Takayama, T., and Arakawa, K. (2007). Fracture micromechanisms of bioabsorbable PLLA/PCL polymer blends. *Eng. Frac. Mech.* 74, 1872–1883. doi: 10.1016/j.engfracmech.2006.05.021

Tsuji, H., and Ikada, Y. (1996). Blends of aliphatic polyesters. I. Physical properties and morphologies of solution-cast blends from poly(DL-lactide) and poly(ε-caprolactone). *J. Appl. Polym. Sci.* 60, 2367–2375. doi: 10.1002/(SICI)1097-4628(19960627)60:13<2367::AID-APP8>3.0.CO;2-C

Tsuji, H., Yamada, T., Suzuki, M., and Itsuo, S. (2003). Blends of aliphatic polyesters. Part 7. Effect of poly(L-lactide-co-ε-caprolactone) on morphology, structure, crystallization, and physical properties of blends of poly(L-lactide) and poly(ε-caprolactone). *Polym. Int.* 52, 269–275. doi: 10.1002/pi.1093

Urquijo, J., Dagreou, S., Guerrica-Echevarria, G., and Eguiazabal, J. I. (2016). Structure and properties of poly(lactic acid)/poly(ε-caprolactone) nanocomposites with kinetically induced nanoclay location. *J. Appl. Polym. Sci.* 133:43815. doi: 10.1002/app.43815

Urquijo, J., Guerrica-Echavarria, G., and Eguiazabal, J. I. (2015). Melt processed PLA/PCL blends: effect of processing method on phase structure, morphology, and mechanical properties. *J. Appl. Polym. Sci.* 132:42641. doi: 10.1002/app.42641

Vilay, V., Mariatti, M., Ahmad, Z., Pasomsouk, K., and Todo, M. (2009). Characterization of the mechanical and thermal properties and morphological behavior of biodegradable poly(L-lactide)/poly(epsilon-caprolactone) and poly(L-lactide)/poly(butylene succinate-co-L-lactate) polymeric blends. *J. Appl. Polym. Sci.* 114, 1784–1792. doi: 10.1002/app.30683

Vilay, V., Mariatti, M., Ahmad, Z., Pasomsouk, K., and Todo, M. (2010). Improvement of microstructures and properties of biodegradable PLLA and PCL blends compatibilized with a triblock copolymer. *Mater. Eng. Sci. A* 527, 6930–6937. doi: 10.1016/j.msea.2010.07.079

Wachirahuttapong, S., Thongpin, C., and Sambatsompop, N. (2016). Effect of PCL and compatibility contents on the morphology, crystallization and mechanical properties of PLA/PCL blends. *Energy Procedia* 89, 198–206. doi: 10.1016/j.egypro.2016.05.026

Wu, D., Zhang, Y., Yuan, L., Zhang, M., and Zhou, W. (2010). Viscoelastic interfacial properties of compatibilized poly(epsilon-caprolactone)/polylactide blend. *J. Polym. Sci. [B].* 48, 756–765. doi: 10.1002/polb.21952

Xiang, W., Feng, L., Bian, X., Zhang, B., Sun, B., Liu, Y., et al. (2019). Toughening modification of PLLA with PCL in the presence of PCL-b-PLLA diblock copolymers as compatibilizer. *Polym. Adv. Technol.* 30, 963–972. doi: 10.1002/pat.4530

Yeh, J.-T., Wu, C.-J., Tsou, C.-H., Chai, W.-L., Chow, J.-D., Huang, C.-Y., et al. (2009). Study on the crystallization, miscibility, morphology, properties of poly(lactic acid)/poly(ε-caprolactone) blends. *Polym.-Plast. Technol. Eng.* 48, 571–578. doi: 10.1080/03602550902824390

Zhang, M., Shi, X., Dia, X., Huo, C., Xie, J., Li, X., et al. (2018). Improving the crystallization and fire resistance of poly(lactic acid) with nano-ZIF-8@GO. *J. Mater. Sci.* 53, 7083–7093. doi: 10.1007/s10853-018-2049-2

Zhao, H., and Zhao, G. (2016). Mechanical and thermal properties of conventional and microcellular injection molded poly(lactic acid)/poly(ε-caprolactone) blends. *J. Mech. Behavior Biomed. Mater.* 53, 59–67. doi: 10.1016/j.jmbbm.2015.08.002

Structure Characterization and Biodegradation Rate of Poly(ε-caprolactone)/Starch Blends

Martina Nevoralová[1], Marek Koutný[2], Aleksandra Ujčić[1], Zdeněk Starý[1], Jana Šerá[2], Helena Vlková[1], Miroslav Šlouf[1], Ivan Fortelný[1] and Zdeněk Kruliš[1]*

[1] Institute of Macromolecular Chemistry, Czech Academy of Sciences, Prague, Czechia, [2] Faculty of Technology, Tomas Bata University in Zlín, Zlín, Czechia

The present paper focuses on the effects of blending poly (ε-caprolactone) (PCL) with thermoplastic starch (TPS) on the final biodegradation rate of PCL/TPS blends, emphasizing the type of environment in which biodegradation takes place. The blends were prepared by melt-mixing the components before a two-step processing procedure, which strongly affects the degree of plasticization and therefore the final material morphology, as was detailed in the previous work, was used for the thermoplastic starch. The concentration row of pure PCL over PCL/TPS blends to pure TPS was analyzed for biodegradation in two different environments (compost and soil), as well as from a morphological, thermomechanical, rheological, and mechanical point of view. The morphology of all the samples was studied before and after biodegradation. The biodegradation rate of the materials was expressed as the percentage of carbon mineralization, and significant changes, especially after exposure in soil, were recorded. The crystallinity of the measured samples indicated that the addition of thermoplastic starch has a negligible effect on PCL-crystallization. The blend with 70% of TPS and a co-continuous morphology demonstrated very fast biodegradation, with the initial rate almost identical to pure TPS in both environments while the 30% TPS blend exhibited particle morphology of the starch phase in the PCL matrix, which probably resulted in a dominant effect of the matrix on the biodegradation course. Moreover, some molecular interaction between PCL and TPS, as well as differences in flow and mechanical behavior of the blends, was determined.

Keywords: poly (ε-caprolactone), thermoplastic starch, biodegradation rate, soil, morphology

INTRODUCTION

The biodegradation rate of polymeric materials is a crucial issue becoming more important due to increasing environmental concerns (Swain et al., 2004; Jayasekara et al., 2005; Rochman et al., 2013; Narancic et al., 2018). One of the solutions to the problem is the development and usage of materials made of biodegradable polymers like poly (ε-caprolactone) (PCL) (Funabashi et al., 2009), starch, and others. PCL is a hydrophobic and partially crystalline aliphatic polyester with excellent deformability (Singh et al., 2003; Imre and Pukánszky, 2013; Rudnik, 2013), but some of its characteristics, e.g., low melting temperature ($T_m \sim 60°C$) (Funabashi et al., 2009; Düskünkorur, 2012) or relatively low strength, prevent a broader application of this polymer, which is at present

very popular, e.g., for biomedical or tissue applications (Singh et al., 2003; Leja and Lewandowicz, 2010; Chang et al., 2017). The use of PCL materials in the food-packaging industry and agriculture is very advantageous due to their resistance to water and oil, non-toxicity, and biodegradability (Funabashi et al., 2009; Rudnik, 2013). Therefore, many attempts have been made to combine PCL with other polymers to modify its properties and degradation in the environment (Bastioli, 1998; Averous et al., 2000; Wang et al., 2003; Campos et al., 2012; Mittal et al., 2015; Ostafinska et al., 2015).

A parallel interest in the field of developing new and especially inexpensive and biodegradable materials has led to a substantive amount of research in polymer blends containing starch (Wang et al., 1995; Averous et al., 2000; Avérous, 2004). Starch is a mixture of amylose and amylopectin (Sessini et al., 2018). In order to obtain a homogeneous thermoplastic material, native starch must be plasticized to disrupt the starch grains and reduce the amount of intramolecular and intermolecular hydrogen bonds. Thermoplastic starch (TPS) is generally prepared by gelatinization of native starch (Avérous, 2004) in the presence of an appropriate plasticizer under the influence of heat and shear (Wang et al., 2003; Parulekar and Mohanty, 2007). Thermoplastic materials based on starches can be prepared by solution casting, melt mixing, or the combination of both methods, which was described in detail in our previous work (Ostafińská et al., 2017a). Unfortunately, the application of materials based on thermoplastic starches is still limited because of their poor water resistance and low mechanical strength (Wang et al., 2003).

For the reasons mentioned above, PCL/TPS blends seem to be interesting and promising low-cost biodegradable materials with tailored properties, and have thus recently been extensively investigated (Avérous, 2004; Rudnik, 2013; Villar et al., 2017). The final properties of immiscible polymer blends depend directly on their morphology, which is affected particularly by blend composition and interfacial tension, but also by rheological properties of blend components and processing conditions (Horák et al., 2005; Imre and Pukánszky, 2013). Depending on the origin of native starch, and thus on the amylose and amylopectin content, the viscosity and elasticity of the plasticized materials can vary substantially (Huneault and Li, 2012; Nevoralová et al., 2019). Due to immiscibility of PCL and starch (Shaw, 1985), PCL/TPS blends exhibit heterogeneous phase structure (Imre and Pukánszky, 2013). Therefore, it is obvious that the optimization of the rheological properties of any immiscible polymer blend including PCL/TPS and the resulting morphologies is essential to obtain materials with balanced end-use properties tailored to specific application (Fortelný et al., 2008). Nevertheless, to the best of our knowledge, both the rheological behavior and the morphology of starch-based biodegradable polymer blends have not been discussed in detail.

Depending on the morphology and surrounding conditions, each polymer degrades at least to some extent. Generally, polymers can be described as degradable when degradation leads to a reduction in molecular weight by chain scission of the main chain on a certain time scale depending on environmental conditions and on whether the final products

are of low molecular weight. In biodegradable polymers, the cleavage of the chain is often caused by enzymatic processes that are usually accompanied and supported by physicochemical phenomena leading to a complete degradation of the polymer (Imre and Pukánszky, 2013). According to several authors (Wang et al., 2003; Khatiwala et al., 2008; Mudhoo et al., 2011), PCL, as a member of the aliphatic polyesters group, is a material susceptible to microbial degradation. According to Bastioli, a product can be claimed as biodegradable even though the PCL homopolymer biodegradation rate is very low (Bastioli, 1998). The biodegradation of PCL involves a simple hydrolysis of ester bonds and/or an enzymatic attack (Albertsson and Varma, 2002; Rutkowska et al., 2002; Düskünkorur, 2012). The biodegradability of PCL was observed in the presence of microorganisms in diverse environments, including river and lake waters, sewage sludge, farm soil, paddy soil, creek sediment, roadside sediment, pond sediment, and compost (Rutkowska et al., 2002; Khatiwala et al., 2008; Leja and Lewandowicz, 2010). During the degradation process in a biotic environment, the amorphous fraction of PCL degrades before the crystalline fraction (Leja and Lewandowicz, 2010).

According to literature, PCL can be biodegraded within a period ranging from a few months to several years depending on its molecular weight, degree of crystallinity, morphology, porosity, sample thickness, and the surrounding environment (Labet and Thielemans, 2009; Leja and Lewandowicz, 2010). It is assumed that the low melting point of PCL should be favorable for composting as a means of disposal, because the temperature obtained during composting is usually around or above PCL melting temperature (60°C). Sánchez et al. mentioned that thermophilic composting is one of the promising technologies for transforming biodegradable plastics into fertilizers (Sanchez et al., 2000). Jayasekara and co-workers reported that molar mass and crystallinity are the main factors affecting biodegradability (Jayasekara et al., 2005). Furthermore, it has been reported that the presence of polysaccharides in the case of mixtures enhances the biodegradation rate of PCL (Vroman et al., 2009; Düskünkorur, 2012). Many authors have also pointed out that the degradation of the more readily biodegradable component controls the rate of degradation of polymer blends (Jayasekara et al., 2005; Leja and Lewandowicz, 2010).

From the biodegradation environment point of view there are a lot of studies with inconsistent conclusions. On the one hand, PCL appears to be readily biodegradable under industrial composting conditions defined by ISO 14855. On the other hand, reports on PCL biodegradability in soil reveal a surprising variability of results from fast degradation characterized by a PCL mass loss of 95% in 1 year (Potts et al., 1973) or even about 90% in 5 months (Narancic et al., 2018) to very slow biodegradation of the same material expressed by a mass loss of only 32% after 2 years (Innocenti, 2005). Such an extreme inconsistency is hard to explain, especially since some important details of the material parameters or the soil environment used were not always comprehensively stated in all the studies (Innocenti, 2005). Generally, the molecular weight (M_w) of the polymer appears to play an important role in the PCL biodegradation (Cesur, 2018).

Blends of PCL and starch are assumed to be completely biodegradable because each component of the blends is readily biodegradable (Iwamoto and Tokiwa, 1994; Vikman et al., 1999; Wang et al., 2003; Jayasekara et al., 2005). The rate of degradation of polymer blends is initially controlled by the degradation of the more readily biodegradable component. The initial degradation process interferes with the structural integrity of the polymer and considerably increases the surface area for enzyme attack. The exposure of the remaining polymer to microbes and secreted degradative enzymes is then enhanced (Jayasekara et al., 2005). Increasing the hydrophilicity of the polymers should increase their susceptibility to enzymatic attack, so this should also be seen on the rate of biodegradation of PCL/TPS mixtures depending on the ratio of these components (Jayasekara et al., 2005). Vikman et al. analyzed PCL/TPS samples prepared in the piece form and in the milled form (Vikman et al., 1999). The authors reported that the surface area of the samples was a very important parameter for biodegradation and that the PCL layer on the surface of the blend slowed the biodegradation process. In addition, the degradation of this blend was more rapid at higher blending temperatures, a fact that the authors associated with a coarser phase structure of the blend. Generally, it is often very difficult to compare published results because of different starch types used, as this significantly affects the course of biodegradation experiments, too. Although the topic of PCL blends with TPS has been the center of attention for several years, the effect of their morphology on the rate of biodegradation has not been systematically studied enough.

The aim of this paper is to contribute to a better understanding of the relationships between the composition and the PCL/TPS blend's morphology and following from that their biodegradation rate in two different environments—compost and soil.

EXPERIMENTAL

Materials

The polymers used in this study were commercial polyester— poly(ε-caprolactone) Capa 6800 (PCL) supplied by Perstorp Group (Sweden) in granular form with an average molecular weight of M_w 80,000 g·mol^{-1} and the melting point of 58°C, and wheat starch A "Soltex NP1," provided by Amylon a.s. (Czech Republic). Anhydrous glycerol from Lachner (Czech Republic) with purity > 99% was used as a plasticizer. Hydrochloric acid (HCl) was purchased from Lachner (Czech Republic). Aqueous solutions were prepared using distilled water.

Preparation of Blend Samples

The PCL/TPS-blends and their neat polymer samples were prepared by melt-mixing procedure in micro-extruder DSM (Netherlands).

Thermoplastic starch component of blends was prepared by a two-step process, which was described in detail in our previous work (Ostafińska et al., 2017a). During this procedure, the starch, glycerol (30 wt. %) and distilled water (water/starch = 6/1) were premixed with a magnetic stirrer for 30 min at laboratory temperature and then the mixture was kept in conditions of continuous agitation for another 15 min at elevated temperature

(above 65°C) until the viscosity increased significantly. Then the mixture was cast in a Petri dish into a form of about 2-mm-thick film and dried at laboratory temperature (at relative humidity RH = 50–55%) for 2–3 days, followed by 4 days in a desiccator with saturated solution of sodium bromide (RH = 57%) (Ostafinska et al., 2018). In the following step, the thermoplastic starch film was cut into small pieces and after that homogenized by melt-mixing at screw speed of 160 rpm and temperature of 130°C for 8 min. Finally, the TPS-material was compression-molded in a Fontijne Grotnes (Netherlands) hydraulic press at 130°C (2 min at 50 kN and then 1 min at 100 kN) into rectangular specimens with a thickness of 2 mm and 4 mm, which were subsequently cooled down to laboratory temperature for 15 min.

The blends were prepared by the melt-mixing of PCL (dried in vacuum oven at 40°C for 12 h) together with homogenized TPS at the same conditions as those of homogenization TPS-procedure in the respective weight ratio of the individual blend's components (PCL/TPS 70/30, 50/50, and 30/70). Due to a relative low melting point of PCL, the blending temperature of neat PCL was set to 120°C.

Methods of Characterization
Differential Scanning Calorimetry

Differential scanning calorimetry (DSC) analysis was carried out in a TA Instruments Q2000 calorimeter with nitrogen as purge gas (50 cm^3 min^{-1}). The instrument was calibrated using indium as a standard. Samples of ~10 mg were encapsulated into aluminum hermetic pans. The analysis was performed in a heating–cooling–heating from −90 to 150°C cycle at a constant heating rate of 10°C·min^{-1}. The crystallinity degree (X_c) of samples was calculated by the following equation (1):

$$ X_c = \frac{H_m}{W \times H_m^0} \times 100 \tag{1} $$

where H_m is the experimental fusion enthalpy [Jg^{-1}], H_m^0 is the fusion enthalpy of 100% crystalline PCL, which is, according to Nagata and Yamamoto (2009), equal to 135 Jg^{-1}, and W is the weight fraction of PCL in the sample. The values presented in the paper are average values from two independent measurements. Therefore, no standard deviations were evaluated. Generally, the reproducibility of these measurements was very good, and the values did not differ by more than 5%.

Scanning Electron Microscopy

The phase structure morphology of the PCL/TPS blends and homogeneity of their pure components were observed with a scanning electron microscope (SEM) Quanta 200 FEG (FEI, Czech Republic) using secondary electron imaging at 10 kV. Before the observation in the SEM, the samples were fractured in liquid nitrogen, then the fractured surface was smoothed, and the TPS-phase of cryo-fractured surface of all blends was etched out in 6 N HCl solution for 10 min. The prepared samples were fixed on a metallic support with a conductive silver paste (Leitsilber G302; Christine Groepl, Austria) and finally sputtered with ~4-nm-thin platinum layer by means of a vacuum sputter coater

SCD 050 (Balzers, Liechtenstein) in order to prevent charging and minimize sample damage due to the electron beam.

Rheological Characterization

Rheological behavior of the investigated materials was studied using a rotational rheometer Physica MCR 501 (Anton Paar GmbH, Austria) equipped with a convection temperature device (CTD 450) in dynamic mode. To minimize the water evaporation effect before the measurement, all the samples were stored in a desiccator. The basic rheological characteristics of PCL/TPS blends and their neat components were examined in oscillatory shear flow using parallel-plate geometry with a plate diameter of 25 mm. Frequency sweep experiments were performed in the frequency range from 10^{-1} to 10^2 rad/s at strain amplitude of 0.05% and constant temperature of 120°C. Linear viscoelasticity region was determined by dependence of the storage modulus on strain amplitude of deformation at constant frequency of 1 Hz. The thermal stability of the materials during rheological measurements was confirmed by time sweeps experiments at 120°C. To ensure uniform temperature field all samples were equilibrated for 2 min prior to the measurements start.

Thermo-Mechanical Characterization

The thermo-mechanical characterization of investigated PCL/TPS blends and neat components was tested by dynamic mechanical thermal analysis (DMTA) in rectangular torsion geometry using the same rheometer used for their basic rheological characterization. Temperature sweeps were carried out in the temperature range from −80 to 150°C with the heating rate of 3°C min^{-1} at constant frequency of 1 Hz and strain of 0.05% set on the base of an amplitude sweep. The results of the three specimens of each material were averaged.

Micro-Indentation Hardness Testing

Micromechanical properties of the samples were characterized by means of instrumented micro-indentation hardness testing (Micro-Combi Tester, CSM Instruments, Switzerland). Smooth surfaces for micro-indentation testing were prepared from compression molded plates (thickness 2 mm), which were also used for the above-described rheological and DMA measurements. The plates were cut perpendicularly with a rotary microtome (RM 2255; Leica, Austria) using a freshly broken glass knife (Glass Knife Maker EM KMR3; Leica, Austria). For each sample, at least two independent cut surfaces were prepared and at least 15 indentations were performed on each surface. Therefore, each micromechanical property represents an average of at least 30 independent measurements. The indentations were performed with a diamond square pyramid with geometry according to Vickers (angle between two non-adjacent phases 136°). The indenter was forced against the polymer surface with the following parameters: maximum load $F = 50$ gf (490.5 mN), dwell time (time of maximal load) $t = 60$ s, and fast linear loading and unloading rate 24,000 mN/min (400 mN/s). For given experimental conditions, the average size of the imprints was $>100\,\mu$m, which was higher than the average size phase domains in all studied systems. Consequently, the micro-indentation results represented the whole system and could be compared

with macroscopic properties. Final F-h curves (where F is the loading force and h is the penetration depth) were employed in the calculation of four micromechanical properties: indentation hardness (H_{IT}), indentation modulus (E_{IT}), indentation creep (C_{IT}), and the elastic part of the indentation work (η_{IT}). All calculations were performed within the original software coming with the indenter (Indentation 5.18, CSM Instruments, Switzerland), according to the theory of Oliver and Pharr (1992); the details about the calculation of C_{IT} and η_{IT} were described elsewhere (Herrman, 2011; Slouf et al., 2018).

Biodegradation Tests

Biodegradation Under Composting Conditions

The method utilized was based on a previously published protocol by Dřímal et al. (2007) with some modifications. Biodegradation tests were performed in 500 ml biometric flasks equipped with septa mounted on stoppers. Three components were weighed into the flasks: polymer film samples cut into 2 mm pieces (100 mg), mature compost (2.5 g of dry weight) and perlite (5 g). Sample flasks were incubated at 58°C. Head space gas was sampled at appropriate intervals through the septum with a gas-tight needle and conducted through a capillary into the gas analyzer (UAG, Stanford Instruments, USA) to determine the concentration of CO_2. From the CO_2 concentration found, the percentage of mineralization relative to the carbon content of the sample was calculated. The endogenous production of the CO_2 by compost in blank incubations was always subtracted to obtain values representing net sample mineralization.

Biodegradation in Soil Condition

The laboratory procedure used was based on ISO 17556 but was miniaturized and adapted for small laboratory samples of materials. Biodegradation tests (Stloukal et al., 2016) were realized in 500 mL flasks with septa mounted on the stoppers. The flasks contained polymer samples (50 mg), topsoil [15 g, perlite (5.0 g) and mineral medium (10.8 mL)]. The flasks were incubated at 25°C. Head space gas was sampled at appropriate intervals through the septum with a gas-tight needle and conducted through a capillary into the gas analyzer (UAG, Stanford Instruments, USA) to determine the concentration of CO_2. The percentage of net mineralization with respect to the carbon content of the initial samples was calculated. Three parallel flasks were run for each sample, along with four blanks.

RESULTS AND DISCUSSION

Characterization of the Prepared Materials
Differential Scanning Calorimetry

Differential scanning calorimetry measurements of all samples reveal structure changes of PCL/TPS blends induced by blending with different TPS amounts (**Table 1**). The crystallinity (X_c) of the samples was calculated from the DSC curves recorded at the second heating ensuring the same thermal history of the samples. The DSC curves can be found in a **Supplementary File**.

With increasing amount of starch in the PCL/TPS blends T_m of PCL slightly decreased, which is in agreement with measurements of Averous et al. (2000). Rather negligible changes

Physical quantities	PCL	PCL/TPS 70/30	PCL/TPS 50/50	PCL/TPS 30/70
T_m [°C]	57.3	56.7	56.7	55.8
T_c [°C]	30.8	30.2	28.2	26.7
ΔH_m [J·g^{-1}]	66.9	73.5	67.3	59.5
X_c [%]	49.6	54.5	49.9	44.1

in T_m partially within the experimental error of the measurement do not allow any conclusions regarding the PCL melting behavior changes induced by blending with TPS. No effect of the TPS on the PCL melting indicates immiscibility of PCL and thermoplastic starch. Contrary to this finding, Mittal et al. (2015) observed a significant decrease in T_m with increasing the TPS amount in the PCL/TPS blends, from which a partial miscibility or strong interactions between the components was deduced. A possible explanation of these contradictory findings in the literature can be seen in properties of thermoplastic starches used, which can differ significantly in composition (amylose/amylopectin ratio) and/or plasticizing system (type and amount of plasticizer). The proportion of PCL crystalline phase X_c increased after addition of 30% of TPS. This increase in matrix crystallinity in the presence of particles of minority phase is attributed to an enhanced nucleation at the interface (Sakai et al., 2009; Zhang et al., 2011). The enhanced nucleation by the interface can be further inferred from a decrease of T_c of PCL in PCL/TPS 50/50 and 30/70 blends. Although the crystallinity of the blend with 30 weight percent of TPS in comparison with the pure PCL slightly increased, the further increase in TPS content in the blends already led to the crystallinity decrease (PCL/TPS 50/50 and 30/70). In contrast to PCL/TPS (70/30) in the blend with 70% of TPS, the crystallinity is lower in comparison with the neat PCL. This blend has a co-continuous structure as it is shown in the following chapter with partially fine PCL domains. In such case geometrical constraints can suppress mobility of polymer chains and their crystallization. Since the DSC method is not sensitive enough for determination of glass transition in the case of semicrystalline polymers [often used for glass transition and crystallization temperature detection (Qiu et al., 2003)], the influence of adding different amount of TPS on changes of the glass transition of the final materials was not convincing. Therefore, these transitions were also analyzed by more sensitive DMTA method (see below **Figure 3** and **Table 2**).

Morphology Before Biodegradation

The micrographs in **Figure 1** display a representative morphology of the investigated samples before their composting or soil exposure. **Figures 1A,E** show a typical pure component morphology of the blend, i.e., PCL and wheat thermoplastic starch, respectively. Due to the plasticization procedure used, the TPS structure was almost homogeneous, in agreement with our previous work (Ostafinska et al., 2018). The other three micrographs, **Figures 1B–D**, demonstrate appropriate

heterogeneous structure of the PCL/TPS blends. Polymer blend structure depends on many factors (processing conditions, ratio of blend components, etc.) and, thus, resulting morphology can vary. PCL/TPS 70/30 blend exhibits particle morphology of starch phase in PCL matrix (see **Figure 1B**). The size of TPS particles is typically in the range of few microns. Such a rather fine structure is in agreement with other studies on PCL/TPS blends found in the literature (Li and Favis, 2010; Huneault and Li, 2012) and suggests good compatibility between PCL and TPS. As pointed out by Huneault and Li (2012) and Koh et al. (2018), the compatibility in the TPS blends is influenced by the type and amount of plasticizing system, which affects both the viscosity of the TPS and the interactions between the blend components. A blend with 50 and 75% of TPS (see **Figures 1C,D**) shows morphology with irregular TPS domains. However, these starch domains are pronouncedly finer in a 50/50 blend (**Figure 1C**) than in the case of the PCL/TPS 30/70 blend (see **Figure 1D**). Although exact analysis of phase continuity was not performed, the structures observed are considered co-continuous, because by selective etching of both components, i.e., TPS by HCl and PCL by tetrahydrofuran (not shown) the specimens did not lose mechanical integrity. Formation of co-continuous structure in this blend is supported by distinctly lower viscosity of PCL in comparison with starch phase (see **Figure 2B**). Therefore, PCL, albeit a minority component, tends to form a continuous phase. Furthermore, Li and Favis (2010) proposed that a broad range of co-continuity in TPS blends can be explained by the high elasticity of the TPS component displaying gel-like behavior in the molten state (cf. **Figure 2A** and the discussion in the following section). On the one hand, a high elasticity prevents the deformation of molten particles in the flow; but on the other hand, once the particles are deformed, the elasticity hinders coalescence and/or retraction of irregular domains in the spherical shape and thus stabilizes the phase structure.

Rheological Characterization

The obtained rheological results clearly show relationship between specific concentration ratio of the blend components and the resulting rheological properties. Frequency sweeps of all analyzed samples at the temperature of 120°C are shown in **Figure 2**.

The frequency dependence of the storage modulus (**Figure 2A**) of the blends and the neat PCL and TPS plasticized by a two-step process exhibited a relatively large increase in the modulus of elasticity of more than 4 orders of magnitude with increasing TPS ratio in blend at an angular frequency of 0.1 rad/s. The blends containing 50% of TPS and more, which exhibit co-continuous phase structure (cf. **Figures 1C,D**), demonstrated gel-like behavior with nearly the same slope of the storage modulus curves. Since both the storage and loss modules ran in parallel, the corresponding damping factors (tan δ = G''/G') were almost constant in the whole frequency range measured, except for the first point at the lowest angular frequency. Moreover, the damping factor of these blends is smaller than one, i.e., solid-like behavior dominates. On the contrary, the PCL/TPS 70/30 sample, i.e., the system with the smallest amount of starch
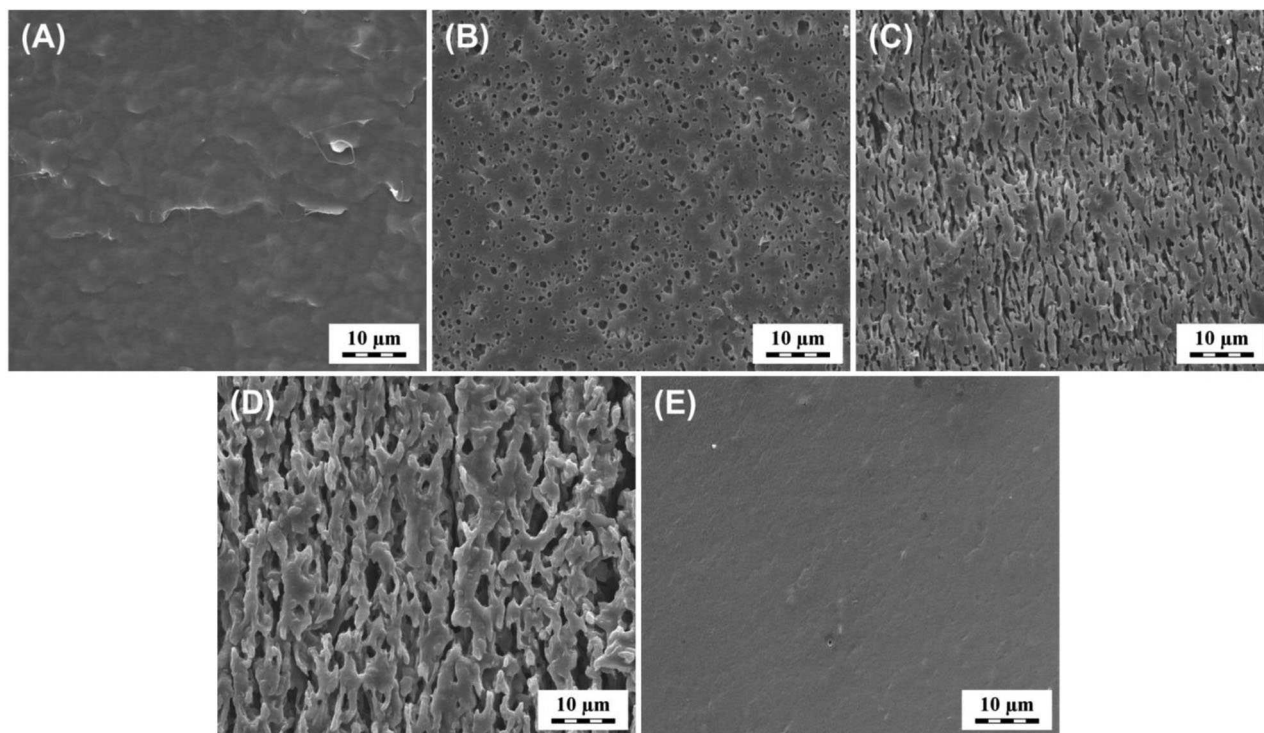
FIGURE 1 | SEM micrographs of smoothed pure components **(A)** PCL, **(E)** TPS and of smoothed etched surfaces of polymer blends, **(B)** PCL/TPS (70/30), **(C)** PCL/TPS (50/50), and **(D)** PCL/TPS (30/70) before biodegradation. Holes in the images correspond to TPS component of the blends etched off with 6 N HCl solution.

phase, showed a higher loss modulus than storage modulus values, meaning that the blend displayed behavior closer to pure PCL. PCL also demonstrated the lowest viscosity as expected (**Figure 2B**). Based on the recorded frequency dependencies of the complex viscosities of all melts (**Figure 2B**), the values have been increasing with increasing amount of TPS.

Dynamic Thermo-Mechanical Characterization

The thermo-mechanical behavior of the PCL/TPS blends, which was analyzed by dynamic mechanical thermal analysis, is shown in **Figure 3**. The thermodynamic results have provided information about the differences in flow behavior of the studied materials considering the weight ratio of blend components from the region below glass transition temperatures to their processing temperature. Thermal transitions, i.e., glass transitions of PCL- and TPS-phase of prepared materials, were determined from the maxima of the damping factor dependence on temperature.

The TPS displayed two glass transition temperatures corresponding to the glycerol-rich and starch-rich phases at -63 and $6.6°C$, which is a typical feature of plasticized starch materials (Averous et al., 2000; Taguet et al., 2009; Li and Favis, 2010). The discussion of the thermal behavior of the PCL/TPS blends is complicated by the fact that the peaks of the glass transitions of the PCL and glycerol-rich TPS phases are overlapping (T_g of PCL was $-58.1°C$ and T_g of glycerol-rich phase of TPS was $-63°C$). The PCL/TPS blends in this region 1 glass transition

T_{g1} gradually decreasing with TPS content (**Table 2**). Therefore, it is hard to draw any strict conclusion about the miscibility of PCL and TPS from this shift. The glass transition temperature of the starch-rich phase T_{g2} in all the blends has been shifted from $6.6°C$ for neat TPS toward lower temperatures with increasing PCL content to $-6.0°C$ for the PCL/TPS 70/30 blend (**Table 2**). In accordance with literature (Zhang et al., 2011), from this finding, strong molecular interactions based on hydrogen bonds between the carbonyl groups of PCL and hydroxyl groups of thermoplastic starch could be inferred (Matzinos et al., 2002; Rodriguez-Gonzalez et al., 2004). In the specific case of PCL and TPS, the situation is even more complicated, because PCL is soluble in glycerol, used as a plasticizer for TPS, at the processing temperature of $120°C$. Moreover, phase separation in the TPS phase after blending leading to formation of a glycerol-rich layer at the interface is reported in the literature (Taguet et al., 2009; Koh et al., 2018). Thus, redistribution of glycerol between the PCL and TPS phases during melt mixing and subsequent cooling cannot be excluded.

All the blends demonstrated viscoelastic solid behavior in the whole temperature range, except for the blend with 30 wt. % of TPS, which changed to viscoelastic liquid at about $80°C$. This change is characterized by the intersection of the G′ and G″ curves (tan $\delta = 1$). Based on this result and in agreement with the frequency sweeps data (**Figure 2**), it could be concluded that in the PCL/TPS 70/30 blend, the PCL-phase has a dominant effect on the final rheological properties. Among all sample types, this

FIGURE 2 | Dependence of **(A)** storage modulus G' and damping factor tan δ, and **(B)** complex viscosity $|\eta^*|$ on the angular frequency ω of PCL/TPS-blends and their neat components ($T = 120°$C and strain amplitude of 0.05%) (the dashed line shows tan $\delta = 1$).

FIGURE 3 | Temperature dependence of damping factor tan δ of PCL/TPS blends and their pure components (the dashed line shows tan $\delta = 1$).

TABLE 2 | Glass transition temperatures (T_{g1} and T_{g2}) of the samples.

Temperature [°C]	PCL	PCL/TPS 70/30	PCL/TPS 50/50	PCL/TPS 30/70	TPS
T_{g1}	−58.1	−58.2	−59.6	−62.2	−63.0
T_{g2}		−6.0	−2.9	0.4	6.6

FIGURE 4 | Dependence and linear fit (red line) of the complex modulus absolute value $|G^*|$ of PCL/TPS blends and their neat components on blend composition at frequency of 1 Hz, strain of 0.05% and temperature of 25°C.

blend and neat PCL showed behavior advantageous for example from the processing point of view.

For an evaluation of the compatibility of polymer blend components from rheological data logarithmic additivity rule is commonly used. This approach was adopted for complex modulus values at 25°C extracted from dynamic thermo-mechanical measurements. Fully immiscible blends usually show negative deviations from the additivity rule. As can be seen from **Figure 4**, the complex modulus follows the logarithmic additivity rule with a high accuracy. This agreement implies that the interfacial adhesion is high enough to ensure the stress transfer between phases and that PCL and TPS can be considered compatible.

Micro-Indentation Hardness Testing

Another tool for characterizing blend compatibility is the micro-indentation technique. The complete results of micro-indentation hardness testing measurements are summarized in **Table 3**.

The comparison of the micro-indentation results with predictive models is given in **Figure 5**.

To the first approximation, all the properties can be compared with the linear model (additivity law; dotted lines in **Figure 5**). The additivity law predicts that any final property of the system (P) is a linear combination of the properties of individual components:

$$P = \sum_i v_i P_i \qquad (2)$$

where v_i and P_i are volume fractions and given properties of the individual components, respectively. The additivity law holds very well for polymer composites with infinitely long oriented fibers or for semicrystalline polymers (containing amorphous and crystalline phases). For most other polymer systems, however, the additivity law represents the upper achievable limit unless synergistic effects are observed (Ostafińska et al., 2017a; Ostafinska et al., 2018). In most cases, real mechanical properties are below the additivity law predictions due to the interface, which usually represents the weakest point. This was observed for all micromechanical properties in this work (E_{IT}, H_{IT}, C_{IT}, and η_{IT}–**Figures 5A–D**), but the negative deviations from additivity law were rather small, which indicated sufficient interfacial adhesion between the components (Šlouf et al., 2007). The strong interfacial adhesion, suggested by the behavior of E_{IT}, H_{IT}, C_{IT}, and η_{IT}, was consistent with other results in this study: (i) the non-etched fracture surfaces displayed no clear interface between the two phases, **Figure 1**, and (ii) dynamic thermo-mechanical measurements (**Figure 4**).

Moreover, the strong interfacial adhesion and good compatibility between TPS and PCL could be confirmed by the application of the equivalent box model (EBM; described in Kolařík, 1995, 1996), which could be applied to E_{IT} and H_{IT} (but not for C_{IT} and η_{IT}, which are beyond the EBM scope). Consequently, we could compare E_{IT} and H_{IT} experimental data with the theoretical EBM predictions:

$$E_b = E_1 v_{1p} + E_2 v_{2p} + \frac{v_s^2}{\left[\left(\frac{v_{1s}}{E_1}\right) + \left(\frac{v_{2s}}{E_2}\right)\right]} \tag{3}$$

$$H_b = H_1 v_{1p} + H_2 v_{2p} + AH_1 v_s \tag{4}$$

The details of the EBM model and the meaning of all its parameters were described elsewhere (Kolařík, 1996; Ostafińska et al., 2017a,b). Briefly, E_b and H_b represent the indentation modulus and hardness of the blend, E_i and H_i stand for the elastic modulus and the hardness of the individual components, and v_{ij} represents volume fractions of the components (the first subscript identifies the components and the second subscript

TABLE 3 | Results of micro-indentation hardness testing (the values present arithmetic mean and standard deviation from 30 independent measurements).

Code of sample	H_{IT} [MPa]	E_{IT} [GPa]	C_{IT} [%]	η_{IT} [%]
PCL	51.6 ± 1.6	0.68 ± 0.02	10.6 ± 0.3	43.4 ± 0.3
PCL/TPS 70/30	31.3 ± 1.2	0.50 ± 0.02	16.6 ± 0.5	33.8 ± 0.9
PCL/TPS 50/50	20.2 ± 0.9	0.42 ± 0.03	25.4 ± 0.9	25.3 ± 1.0
PCL/TPS 30/70	11.3 ± 0.6	0.37 ± 0.03	40.2 ± 1.1	14.7 ± 0.8
TPS	5.9 ± 0.5	0.24 ± 0.05	65.6 ± 3.2	10.1 ± 1.1
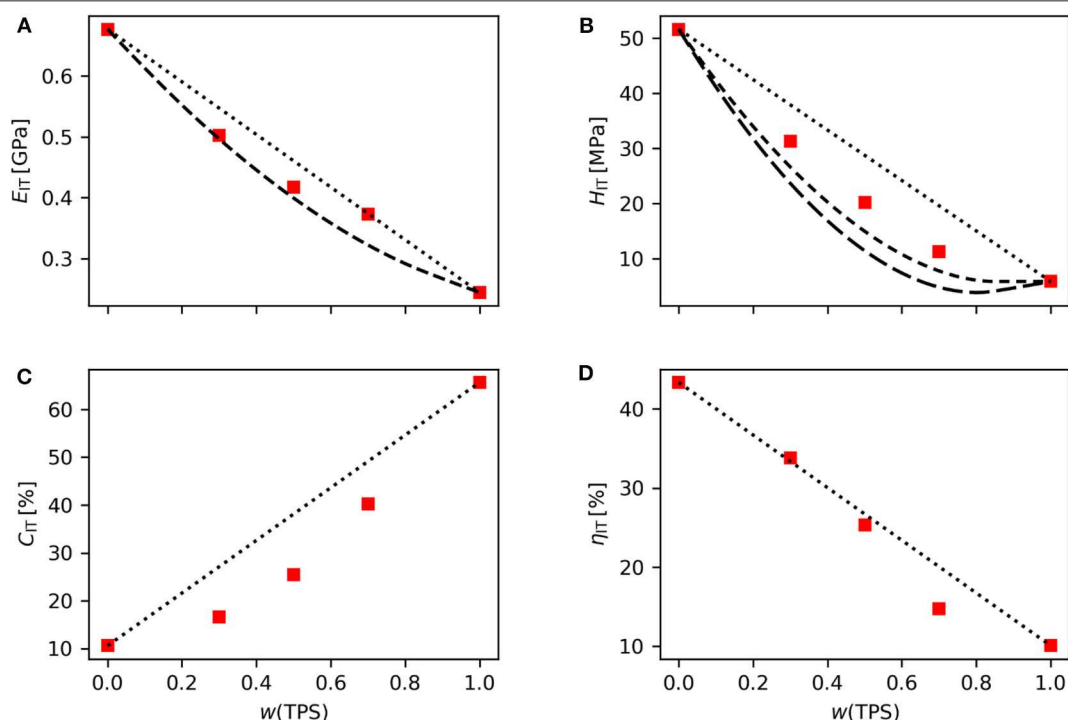
FIGURE 5 | Comparison of experimentally determined micromechanical properties (E_{IT}, H_{IT}, C_{IT}, and η_{IT}) with predictive models (dotted line = linear model/additive law, and dashed lines = EBM model). The linear model is applicable to all properties **(A–D)**; EBM theory has been developed and verified only for E_{IT} **(A)** and H_{IT} **(B)**. In case of H_{IT}, **(B)** the EBM prediction was calculated for both perfect interfacial adhesion (Equation 4 with A = 1; short dashed line) and for zero interfacial adhesion (according to Equation 4 with A = 0; long dashed line).

determines the volume of the component in parallel and serial branch of the EBM model, which correspond to the volume fractions with continuous and particulate morphology, respectively). The continuity of the components (i.e., the volume fractions v_{ij}) can be determined experimentally or estimated from percolation theory that predicts that continuity of the minority component starts at critical volume fraction $v_{cr} = 0.156$. Although the default, percolation theory-based value of the critical volume fraction ($v_{cr} = 0.156$) may seem rather low, many previous studies documented that EBM predictions calculated with this default value were in very good agreement with experimental results (Kolařík, 1996; Vacková et al., 2012; Ostafinska et al., 2015; Ostafińska et al., 2017a,b). In order to understand v_{cr} parameter properly, it is also important to realize that it represents the composition at which a small fraction of minority phase may start to be continuous according to percolation theory, while most of this phase still exhibits particulate structure. This is more evident if we calculate all volume fractions v_{ij} (i.e., v_{1p}, v_{2p}, v_{1s}, and v_{2s} in Equations 3 and 4) as described elsewhere (Kolařík, 1996; Ostafinska et al., 2018). Therefore, default value of critical volume fraction may be regarded as a parameter, which (i) represents the theoretically predicted composition at which the first signs of co-continuity may appear and which (ii) corresponds reasonably well with experimental results if more detailed analysis of morphology for given system is not available (Kolařík, 1995, 1996, 2000). The last parameter A describes interfacial adhesion (the values $A = 0$ and 1 mean negligible and perfect adhesion, respectively). We performed the EBM calculations (based on default $v_{cr} = 0.156$) for both E_{IT} and H_{IT} (**Figure 5**, dashed lines). Moreover, for H_{IT}, the calculation was made for both minimal interfacial adhesion ($A = 0$; short dashed line) and maximal interfacial adhesion ($A = 1$; long dashed line). The fact that the experimental values of E_{IT} were higher than the EBM predictions (**Figure 5A**) indicated good compatibility and strong interface between PCL and TPS (Kolařík, 2000; Vacková et al., 2012; Ostafinska et al., 2018). The good PCL/TPS compatibility was confirmed also by the experimental values of H_{IT} (**Figure 5B**) which corresponded better to the EBM prediction based on maximal interfacial adhesion (**Figure 5B**, short dashed line corresponding to Equation 4 with $A = 1$) than to the EBM prediction based on minimal interfacial adhesion (**Figure 5B**, long dashed line corresponding to Equation 4 with $A = 0$). If the blends had been incompatible (i.e., if the interfacial adhesion was negligible and $A = 0$), the experimental values of $H_{IT} \approx Y$ would have shown a local minimum as documented elsewhere (Kolařík, 1995; Šlouf et al., 2007). Furthermore, the good interfacial adhesion in our PCL/TPS systems was indicated not only by the micro-indentation experiments described in this section, but also by rheological measurements described in the previous section (see **Figure 4** and its discussion above).

The applicability of the EBM model to micromechanical properties has been justified theoretically and verified experimentally in our previous studies (Ostafinska et al., 2015; Ostafińska et al., 2017a,b; Ostafinska et al., 2018). We conclude that all micromechanical properties (E_{IT}, H_{IT}, C_{IT}
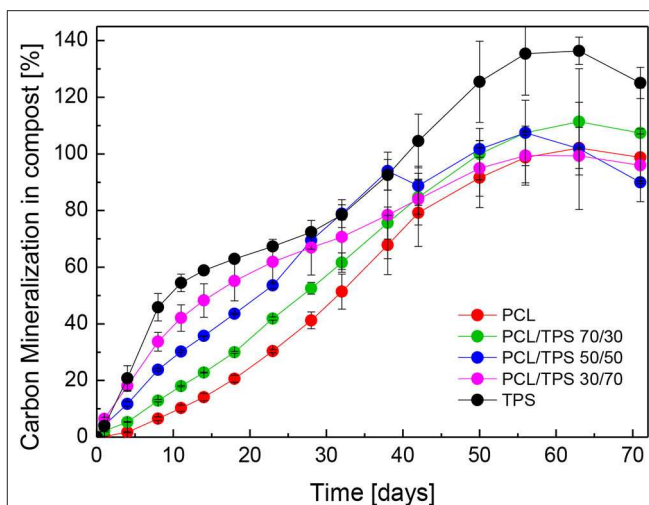
FIGURE 6 | Biodegradation rate of PCL/TPS blends and their pure components under the composting conditions.
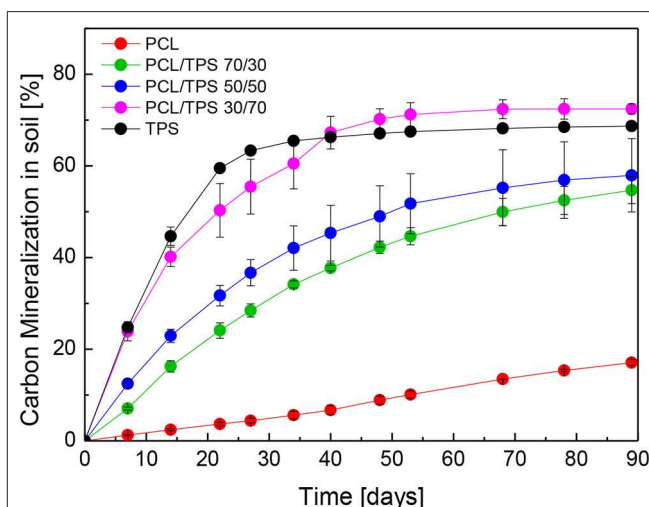
FIGURE 7 | Biodegradation rate of PCL/TPS blends and their pure components in soil conditions ($T = 25°C$).

and η_{IT}) were close to the linear model predictions and two micromechanical properties (E_{IT} and H_{IT}) were higher than the EBM model predictions, which could be attributed to the very good compatibility and strong interfacial adhesion between the blend components.

Biodegradation
Biodegradation Under Composting Conditions

The conditions of industrial composting are characterized by the temperature of $58°C$, which is already in the melting temperature region of PCL. Consequently, the crystalline parts of PCL do not represent an obstacle for enzymes and the biodegradation of all the materials was relatively rapid (see **Figure 6**). However, still the initial rate of biodegradation reflected the content of the easily biodegradable starch. In PCL/TPS 30/70, the curve even followed

the initial fast phase, which probably witnesses the build-up of the microbial biomass. In the later phase of the biodegradation the materials with higher PCL contents, even pure PCL, aligned with the other materials and reached the total biodegradation almost simultaneously. Thus, all the PCL based blend materials were well compatible with the composting as an eventual projected end-of-life solution. The biodegradation of several samples over 100% is not unusual especially in compost environment, which contains a large amount of organic carbon. The part of this carbon can be mobilized by the microorganisms induced with the sample addition.

Biodegradation in Soil Conditions

Very fast biodegradation of the neat TPS reached about 70% mineralization at the end of the experiment (see **Figure 7**). It is not unusual that a fast degrading material does not reach a higher level of mineralization because an important part of the carbon is bound in the biomass and subsequently released on a much slower rate. ISO 17556 (2012) expects validity of the test at a minimal 60% mineralization of an easily degradable reference material. Biodegradation in soil was governed by the PCL content in the materials. As mentioned in the introduction, soil biodegradation of the different PCL grades can differ

FIGURE 8 | SEM micrographs of sample surface: **(A)** PCL, **(B)** PCL/TPS 70/30, **(C)** PCL/TPS 50/50, **(D)** PCL/TPS 30/70 before biodegradation and **(E)** PCL, **(F)** PCL/TPS 70/30, **(G)** PCL/TPS 50/50, **(H)** PCL/TPS 30/70 after 20 days of biodegradation in soil.

FIGURE 9 | SEM micrographs of fracture surfaces: **(A)** PCL, **(B)** PCL/TPS 70/30, **(C)** PCL/TPS 50/50, **(D)** PCL/TPS 30/70 before biodegradation and **(E)** PCL, **(F)** PCL/TPS 70/30, **(G)** PCL/TPS 50/50, **(H)** PCL/TPS 30/70 after 20 days of biodegradation in soil.

considerably, depending mainly on the molecular weight of the polymer and the crystallinity of the resulting material. Here, relatively high molecular weight PCL was used, so it could be expected that the biodegradation of PCL and the PCL phase in the blends could be retarded. The initial rate of the biodegradation clearly reflected the morphology of the materials. The PCL/TPS 30/70, in which the starch forms a continuous phase, decomposed at the initial rate almost identical to the neat TPS. In contrast, the PCL/TPS 50/50 and the PCL/TPS 70/30 were initially mineralized at much slower rate, probably because the continuous PCL phase restricted to some extent the availability of TPS to the enzymes. It was not clearly evident whether the TPS content was able to accelerate the biodegradation of the PCL phase, on the other hand, the PCL content was successfully used to retard the biodegradation of the TPS phase, which could be useful in certain applications where the material comes into contact with microorganisms and must retain its properties for a given time.

Morphology Characterization After Biodegradation

Morphological changes in the materials during the biodegradation process in soil and the microbial colonization of samples were observed by SEM. SEM micrographs of the samples surfaces before and after 20 days of incubation in soil

at 25°C are shown in **Figure 8**. The initial samples showed a smooth surface in the case of the neat PCL (**Figure 8A**) and morphological structures of the PCL/TPS samples reflecting the pattern of domains of PCL and TPS (**Figures 8B–D**). The surface of the PCL/TPS 50/50 sample (**Figure 8C**) seems to be smoother than the surfaces of blends with majority phases of PCL and TPS, respectively (**Figures 8B,D**). After the indicated period of biodegradation, neat PCL exhibited surface cracks but only scarcely present microorganisms (**Figure 8E**). On the contrary TPS containing samples are covered with biofilm consisting mainly of fungal hyphae and fungal spores (**Figures 8F–H**). It could be estimated that the density of the biofilm is increasing with the TPS content in samples.

The similar situation could be seen on the pictures showing the fracture surfaces of the samples (**Figure 9**). From the micrographs of blends before biodegradation (**Figures 9A–D**) it is hard to distinguish individual phases, probably because the fracture path does not follow the interface preferentially. This can be taken as another hint of good interfacial adhesion between PCL and TPS together with findings from rheological and mechanical measurements discussed before. Initial sample morphologies again reflected the blending of the components whereas this time the PCL/TPS 30/70, the PCL/TPS 70/30, and the PCL/TPS 30/70 (**Figures 9B,D**) were different with much higher apparent inhomogeneity in the PCL/TPS 30/70 sample (**Figure 9D**). After the biodegradation, the structural degradation
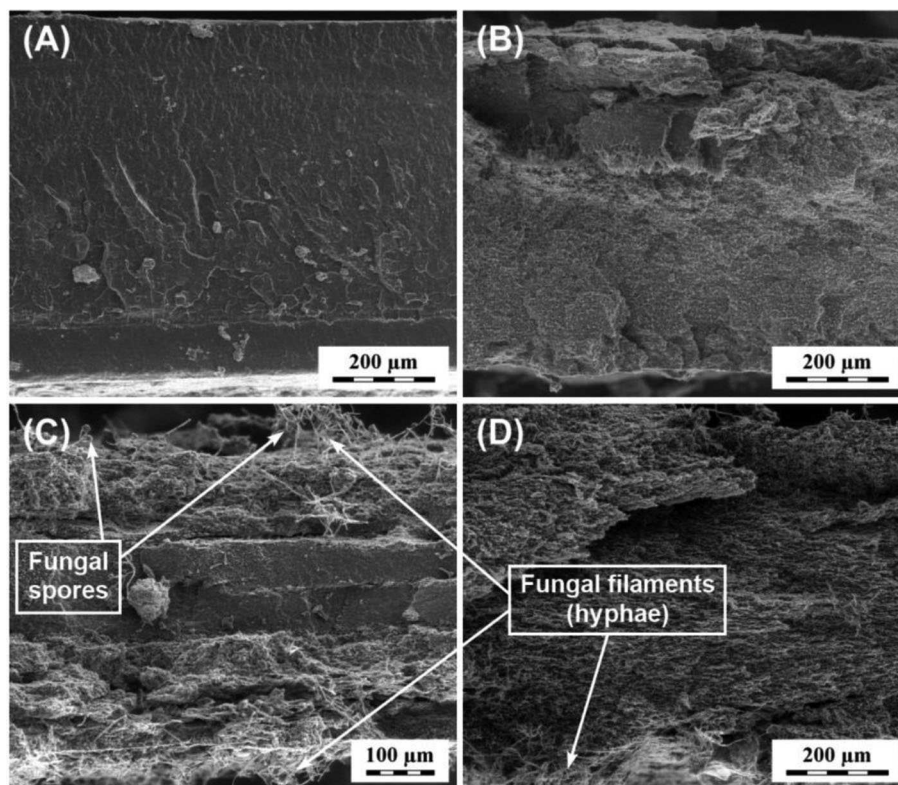
FIGURE 10 | SEM micrographs of fracture surfaces with lower magnification showing the whole profile of the sample films: **(A)** PCL, **(B)** PCL/TPS 70/30, **(C)** PCL/TPS 50/50, **(D)** PCL/TPS 30/70 after 20 days of biodegradation in soil.

of the sample was clearly a function of the TPS content, where the voids in the structure most probably were a consequence of the starch degradation and disappearance. These voids were colonized with microorganisms. These were not apparent in the PCL and PCL/TPS 70/30 samples (**Figure 9F**) but could be seen as thin bacterial filaments, probably actinomycetes, in the PCL/TPS 50/50 sample (**Figure 9G**), and also as much thicker fungal filaments and conidia in the PCL/TPS 30/70 sample (**Figure 9H**).

The pictures of the fractured specimens made at a lower magnification (**Figure 10**) showing the whole thickness of the samples clearly illustrate the biodegradation progress from the specimen surface to its center. The PCL and PCL/TPS 70/30 samples are eroded in the thin surface layer only, while the PCL/TPS 50/50 sample (**Figure 10C**) exhibited deep erosion and penetration of the fungal hyphae and only a central layer comprising about one third of the material thickness stayed relatively unaffected. The PCL/TPS 30/70 sample (**Figure 10D**) was then completely eroded in the whole its thickness.

The pattern of morphological changes during biodegradation suggests the importance of organization of the blend phases. Whereas, the easily biodegradable TPS phase inclusions are surrounded and isolated by the continuous PCL phase in the PCL/TPS 70/30 material (**Figure 1**) in the PCL/TPS 50/50 and PCL/TPS 30/70 materials, TPS creates a continuous phase of interconnected domains, which greatly facilitate the penetration of enzymes and microorganisms and as a consequence the erosion and biodegradation of the material.

CONCLUSION

The present article has demonstrated that the morphology of the PCL/TPS blends and their resulting properties, particularly their biodegradability, can be controlled by the composition of their components.

The PCL/TPS blends investigated were characterized in detail by rheological, thermomechanical, and micromechanical measurements. The results of these examinations showed that there are interactions between PCL and TPS and that these polymers form compatible polymer blends with good interfacial adhesion.

The measurements showed that the addition of thermoplastic starch has a negligible effect on the final crystallization of PCL in the blends. Thus, our results indicate that the PCL crystallinity is not a dominant parameter determining the biodegradation rate, as has often been declared in the literature.

From our findings, a correlation between the biodegradation course of the samples and the size of the interfacial area can be inferred. It significantly changes due to the ratio of PCL/TPS blend components. Nevertheless, according to our results and in agreement with the literature, the interactions and the structure formation are rather complex in these blends, because the TPS plasticizer is miscible with PCL at processing temperatures and, thus, the interpretation of the findings and predictions regarding the final properties are difficult.

The composting conditions were characterized by the temperature, which is already in the melting temperature region

of PCL. Thus, the crystalline parts of PCL did not represent an obstacle for enzymes and the biodegradation of all the materials was relatively rapid. Biodegradation in soil brought out more remarkable differences between blends with different TPS content. Biodegradation evaluation of the PCL/TPS samples in the soil environment revealed that firstly, voids in the samples appeared due to faster TPS biodegradation and were then colonized by microorganisms. These were not apparent in the neat PCL and PCL/TPS 70/30 blend but could be clearly distinguished in the PCL/TPS 50/50 as thin bacterial filaments and as much thicker fungal filaments and conidia in the case of PCL blended with 70 wt. % of plasticized starch. The initial rate of biodegradation increased with the content of easily biodegradable starch in the sample. The materials with higher PCL contents were initially mineralized at much slower rate because the continuous PCL phase successfully restricted the availability of TPS for enzymes. The key role of the phase structure for the biodegradation course was further confirmed by morphological analysis of the samples after biodegradation.

The findings obtained from the study presented in this paper show that controlling phase structure by blends composition enables one to tailor the biodegradation rate of the PCL/TPS blends. Following from that, the results are applicable in production of environmental-friendly materials.

DATA AVAILABILITY STATEMENT

All datasets generated for this study are included in the article/**Supplementary Material**.

AUTHOR CONTRIBUTIONS

MN and MK designed the study. AU prepared the samples. SEM sample visualization was done by MN and AU. MN performed the DSC, rheology, and DMTA measurements and together with ZS, ZK, and IF evaluated and made the final interpretation of the results. HV carried out the micro-indentation hardness testing and MŠ processed and evaluated these data. JŠ performed all the biodegradation measurement and MK explicated the collected biodegradation data. MN, MK, and ZS prepared the draft of the manuscript, which was finalized in cooperation with all co-authors.

ACKNOWLEDGMENTS

SUPPLEMENTARY MATERIAL

The Supplementary Material for this article can be found online at: https://www.frontiersin.org/articles/10.3389/fmats.2020.00141/full#supplementary-material

REFERENCES

Albertsson, A.-C., and Varma, I. K. (2002). "Aliphatic polyesters: synthesis, properties and applications," in *Degradable Aliphatic Polyesters I*, eds. G. Scott and D. Gileat (London: Springer), 1–40. doi: 10.1007/3-540-45734-8_1

Avérous, L. (2004). Biodegradable multiphase systems based on plasticized starch: a review. *J. Macromol. Sci. Polym. Rev.* 44, 231–274. doi: 10.1081/MC-200029326

Averous, L., Moro, L., Dole, P., and Fringant (2000). Properties of thermoplastic blends: starch-polycaprolactone. *Polymer*. 41, 4157–4167. doi: 10.1016/S0032-3861(99)00636-9

Bastioli, C. (1998). Biodegradable materials–present situation and future perspectives. *Macromol. Symp.* 135, 193–204. doi: 10.1002/masy.19981350122

Campos, A., de Marconato, J. C., and Martins-Franchetti, S. M. (2012). The influence of soil and landfill leachate microorganisms in the degradation of PVC/PCL films cast from DMF. *Polímeros* 22, 220–227. doi: 10.1590/S0104-14282012005000029

Cesur, S. (2018). The effects of additives on the biodegradation of polycaprolactone composites. *J. Polym. Environ.* 26, 1425–1444. doi: 10.1007/s10924-017-1029-y

Chang, H.-M. M., Huang, C.-C. C., Parasuraman, V. R., Jhu, J.-J. J., Tsai, C.-Y. Y., Chao, H.-Y. Y., et al. (2017). *In vivo* degradation of poly (ε-caprolactone) films in gastro intestinal (GI) tract. *Mater. Today Commun.* 11, 18–25. doi: 10.1016/j.mtcomm.2017.01.006

Dřímal, P., Hoffmann, J., and Družbík, M. (2007). Evaluating the aerobic biodegradability of plastics in soil environments through GC and IR analysis of gaseous phase. *Polym. Test.* 26, 729–741. doi: 10.1016/j.polymertesting.2007.03.008

Düskünkorur, H. (2012). *Biopolyester Synthesis by Enzymatic Catalysis and Development of Nanohybrid Systems*. Available online at: https://tel.archives-ouvertes.fr/tel-00864276

Fortelný, I., Lapčíková, M., Lednický, F., Starý, Z., and Kruliš, Z. (2008). Nonuniformity of phase structure in immiscible polymer blends. *Polym. Eng. Sci.* 48, 564–571. doi: 10.1002/pen.20985

Funabashi, M., Ninomiya, F., and Kunioka, M. (2009). Biodegradability Evaluation of Polymers by ISO 14855-2. *Int. J. Mol. Sci.* 10, 3635–3654. doi: 10.3390/ijms10083635

Herrman, K. (Ed.) (2011). *Hardness Testing: Principles and Applications*. Novelty, OH: ASM International.

Horák, Z., Fortelný, I., Kolařík, J., Hlavatá, D., and Sikora, A. (2005). "Polymer blends," in *Encyclopedia of Polymer Science and Technology* (John Wiley & Sons), 1–59. doi: 10.1002/0471440264.pst276

Huneault, M. A., and Li, H. (2012). Preparation and properties of extruded thermoplastic starch/polymer blends. *J. Appl. Polym. Sci.* 126, E96–E108. doi: 10.1002/app.36724

Imre, B., and Pukánszky, B. (2013). Compatibilization in bio-based and biodegradable polymer blends. *Eur. Polym. J.* 49, 1215–1233. doi: 10.1016/j.eurpolymj.2013.01.019

Innocenti, F. D. (2005). "Biodegradation behaviour of polymers in the soil," in *Handbook of Biodegradable Polymers*, ed C. Bastioli (Shrewsbury: Rapra Technology Limited), 57–102.

Iwamoto, A., and Tokiwa, Y. (1994). Effect of the phase structure on biodegradability of polypropylene/poly(ε-caprolactone) blends. *J. Appl. Polym. Sci.* 52, 1357–1360. doi: 10.1002/app.1994.070520920

Jayasekara, R., Harding, I., Bowater, I., and Lonergan, G. (2005). Biodegradability of a selected range of polymers and polymer blends and standard methods for assessment of biodegradation. *J. Polym. Environ.* 13, 231–251. doi: 10.1007/s10924-005-4758-2

Khatiwala, V. K., Shekhar, N., Aggarwal, S., and Mandal, U. K. (2008). Biodegradation of poly(ε-caprolactone) (pcl) film by alcaligenes faecalis. *J. Polym. Environ.* 16, 61–67. doi: 10.1007/s10924-008-0104-9

Koh, J. J., Zhang, X., and He, C. (2018). Fully biodegradable poly(lactic acid)/starch blends: a review of toughening strategies. *Int. J. Biol. Macromol.* 109, 99–113. doi: 10.1016/j.ijbiomac.2017.12.048

Kolařík, J. (1995). Prediction of the yield strength of polymer blends. *Polym. Netw. Blends* 5, 87–93.

Kolařík, J. (1996). Simultaneous prediction of the modulus and yield strength of binary polymer blends. *Polym. Eng. Sci.* 36, 2518–2524. doi: 10.1002/pen.10650

Kolařík, J. (2000). Positive deviations of the modulus and yield strength of blends consisting of partially miscible polymers. *J. Macromol. Sci. B* 39, 53–66. doi: 10.1081/MB-100100371

Labet, M., and Thielemans, W. (2009). Synthesis of polycaprolactone: a review. *Chem. Soc. Rev.* 38, 3484. doi: 10.1039/b820162p

Leja, K., and Lewandowicz, G. (2010). Polymer biodegradation and biodegradable polymers. *Polish J. Environ. Stud.* 19, 255–266.

Li, G., and Favis, B. D. (2010). Morphology development and interfacial interactions in polycaprolactone/thermoplastic-starch blends. *Macromol. Chem. Phys.* 211, 321–333. doi: 10.1002/macp.200900348

Matzinos, P., Tserki, V., Kontoyiannis, A., and Panayiotou, C. (2002). Processing and characterization of starch/polycaprolactone products. *Polym. Degrad. Stab.* 77, 17–24. doi: 10.1016/S0141-3910(02)00072-1

Mittal, V., Akhtar, T., and Matsko, N. (2015). Mechanical, thermal, rheological and morphological properties of binary and ternary blends of PLA, TPS and PCL. *Macromol. Mater. Eng.* 300, 423–435. doi: 10.1002/mame.201400332

Mudhoo, A., Mohee, R., Unmar, G. D., and Sharma, S. K. (2011). "Degradation of biodegradable and green polymers in the composting environment," in *A Handbook of Applied Biopolymer Technology: Synthesis, Degradation and Applications*, eds S. K. Sharma and A. Mudhoo (Cambridge: RSC), 332–364.

Nagata, M., and Yamamoto, Y. (2009). Synthesis and characterization of photocrosslinked poly(ε-caprolactone)s showing shape-memory properties. *J. Polym. Sci. Part A Polym. Chem.* 47, 2422–2433. doi: 10.1002/pola.23333

Narancic, T., Verstichel, S., Chaganti, S. R., Morales-Gamez, L., Kenny, S. T., Wilde, B., et al. (2018). Biodegradable plastic blends create new possibilities for end-of-life management of plastics but they are not a panacea for plastic pollution. *Environ. Sci. Technol.* 52, 10441–10452. doi: 10.1021/acs.est.8b02963

Nevoralová, M., Ujčić, A., Kodakkadan, Y. N. V., and Starý, Z. (2019). Rheological characterization of starch-based biodegradable polymer blends. *AIP Conf. Proc.* 2017:050005. doi: 10.1063/1.5109511

Oliver, W. C., and Pharr, G. M. (1992). An improved technique for determining hardness and elastic modulus using load and displacement sensing indentation experiments. *J. Mater. Res.* 7, 1564–1583. doi: 10.1557/JMR.1992.1564

Ostafińska, A., Fortelný, I., Hodan, J., Krejčíková, S., Nevoralová, M., Kredatusová, J., et al. (2017a). Strong synergistic effects in PLA/PCL blends: impact of PLA matrix viscosity. *J. Mech. Behav. Biomed. Mater.* 69, 229–241. doi: 10.1016/j.jmbbm.2017.01.015

Ostafinska, A., Fortelny, I., Nevoralova, M., Hodan, J., Kredatusova, J., and Slouf, M. (2015). Synergistic effects in mechanical properties of PLA/PCL blends with optimized composition, processing, and morphology. *RSC Adv.* 5, 98971–98982. doi: 10.1039/C5RA21178F

Ostafińska, A., Mikešová, J., Krejčíková, S., Nevoralová, M., Šturcová, A., Zhigunov, A., et al. (2017b). Thermoplastic starch composites with TiO₂ particles: preparation, morphology, rheology and mechanical properties. *Int. J. Biol. Macromol.* 101, 273–282. doi: 10.1016/j.ijbiomac.2017.03.104

Ostafinska, A., Vackova, T., and Slouf, M. (2018). Strong synergistic improvement of mechanical properties in HDPE/COC blends with fibrillar morphology. *Polym. Eng. Sci.* 58, 1955–1964. doi: 10.1002/pen.24805

Parulekar, Y., and Mohanty, A. K. (2007). Extruded biodegradable cast films from polyhydroxyalkanoate and thermoplastic starch blends: fabrication and characterization. *Macromol. Mater. Eng.* 292, 1218–1228. doi: 10.1002/mame.200700125

Potts, J. E. E., Clendinning, R. A. A., Ackart, W. B. B., and Niegisch, W. D. D. (1973). "The biodegradability of synthetic polymers," in *Polymer Science and Technologyolymers and Ecological Problems*, ed J. Guillet (New York, NY: Plenum Press), 61–79. doi: 10.1007/978-1-4684-0871-3_4

Qiu, Z., Ikehara, T., and Nishi, T. (2003). Poly(hydroxybutyrate)/poly(butylene succinate) blends: miscibility andnonisothermal crystallization. *Polymers* 44, 2503–2508. doi: 10.1016/S0032-3861(03)00150-2

Rochman, C. M., Browne, M. A., Halpern, B. S., Hentschel, B. T., Hoh, E., Karapanagioti, H. K., et al. (2013). Classify plastic waste as hazardous. *Nature* 494, 169–171. doi: 10.1038/494169a

Rodriguez-Gonzalez, F. J., Ramsay, B. A., and Favis, B. D. (2004). Rheological and thermal properties of thermoplastic starch with high glycerol content. *Carbohydr. Polym.* 58, 139–147. doi: 10.1016/j.carbpol.2004.06.002

Rudnik, E. (2013). "Compostable polymer properties and packaging applications," in *Plastic Films in Food Packaging*, ed S. Ebnesajjad (Waltham, MA: Elsevier), 217–248. doi: 10.1016/B978-1-4557-3112-1.00013-2

Rutkowska, M., Krasowska, K., Heimowska, A., Steinka, I., Janik, H., Haponiuk, J., et al. (2002). Biodegradation of modified poly(e-caprolactone) in different environments. *Polish J. Environ. Stud.* 11, 413–420.

Sakai, F., Nishikawa, K., Inoue, Y., and Yazawa, K. (2009). Nucleation enhancement effect in poly(L-lactide) (PLLA)/poly(ε-caprolactone) (PCL) blend induced by locally activated chain mobility resulting from limited miscibility. *Macromolecules* 42, 8335–8342. doi: 10.1021/ma901547a

Sanchez, J. G., Tsuchii, A., and Tokiwa, Y. (2000). Degradation of polycaprolactone at 50°C by a thermotolerant aspergillus sp. *Biotechnol. Lett.* 22, 849–853. doi: 10.1023/A:1005603112688

Sessini, V., Arrieta, M. P., Fernández-Torres, A., and Peponi, L. (2018). Humidity-activated shape memory effect on plasticized starch-based biomaterials. *Carbohydr. Polym.* 179, 93–99. doi: 10.1016/j.carbpol.2017.09.070

Shaw, M. T. (1985). "Microscopy and other methods of studying blends," in *Polymer Blends and Mixtures*, eds D. J. Walsh, J. S. Higgins, and A. Maconnachie (Dordrecht: Springer), 480. doi: 10.1007/978-94-009-5101-3_3

Singh, R., P., Pandey, J. K., Rutot, D., Degée, P., and Dubois, P. (2003). Biodegradation of poly(ε-caprolactone)/starch blends and composites in composting and culture environments: The effect of compatibilization on the inherent biodegradability of the host polymer. *Carbohydr. Res.* 338, 1759–1769. doi: 10.1016/S0008-6215(03)00236-2

Šlouf, M., Kolařík, J., and Kotek, J. (2007). Rubber-toughened polypropylene/acrylonitrile-co-butadiene-co-styrene blends: Morphology and mechanical properties. *Polym. Eng. Sci.* 47, 582–592. doi: 10.1002/pen.20727

Slouf, M., Pavlova, E., Krejcikova, S., Ostafinska, A., Zhigunov, A., Krzyzanek, V., et al. (2018). Relations between morphology and micromechanical properties of alpha, beta and gamma phases of iPP. *Polym. Test.* 67, 522–532. doi: 10.1016/j.polymertesting.2018.03.039

Stloukal, P., Jandikova, G., Koutny, M., and Sedlarík, V. (2016). Carbodiimide additive to control hydrolytic stability and biodegradability of PLA. *Polym. Test.* 54, 19–28. doi: 10.1016/j.polymertesting.2016.06.007

Swain, S. N., Biswal, S. M., Nanda, P. K., and Nayak, P. L. (2004). Biodegradable soy-based plastics: opportunities andchallenges. *J. Polym. Environ*. 12, 35–42. doi: 10.1023/B:JOOE.0000003126.14448.04

Taguet, A., Huneault, M. A., and Favis, B. D. (2009). Interface/morphology relationships in polymer blends with thermoplastic starch. *Polymers* 50, 5733–5743. doi: 10.1016/j.polymer.2009.09.055

Vacková, T., Slouf, M., Nevoralová, M., and Kaprálková, L. (2012). HDPE/COC blends with fibrous morphology and their properties. *Eur. Polym. J.* 48, 2031–2039. doi: 10.1016/j.eurpolymj.2012.09.005

Vikman, M., Hulleman, S. H. D., Van Der Zee, M., Myllarinen, P., and Feil, H. (1999). Morphology and enzymatic degradation of thermoplastic starch-polycaprolactone blends. *J. Appl. Polym. Sci.* 74, 2594–2604. doi: 10.1002/(SICI)1097-4628(19991209)74:11<2594::AID-APP5>3.0.CO;2-R

Villar, M. A., Barbosa, S. E., García, M. A., Castillo, L. A., and López, O. V. (2017). "Starch-based materials in food packaging," in *Processing, Characterization and Aplications*, eds A. M. Villar, S. E. Barbosa, and O. V. López (Cambridge: Elsevier; Academic Press), 336.

Vroman, I., Tighzert, L., Vroman, I., and Tighzert, L. (2009). Biodegradable polymers. *Materials* 2, 307–344. doi: 10.3390/ma2020307

Wang, X.-L., Yang, K.-K., and Wang, Y.-Z. (2003). Properties of starch blends with biodegradable polymers. *J. Macromol. Sci. Part C Polym.* 43, 385–409. doi: 10.1081/MC-120023911

Wang, X. J., Gross, R. A., and McCarthy, S. P. (1995). Rheological study of biodegradable blends of starch and polyvinyl alcohol. *J. Environ. Polym. Degrad.* 3, 161–167. doi: 10.1007/BF02068467

Zhang, K., Ran, X., Wang, X., Han, C., Han, L., Al., et al. (2011). Improvement in toughness and crystallization of poly(l-lactic acid) by melt blending with poly(epichlorohydrin-co-ethylene oxide). *Polym. Eng. Sci.* 51, 2370–2380. doi: 10.1002/pen.22009

Tailoring Biodegradability of Poly(Butylene Succinate)/Poly(Lactic Acid) Blends With a Deep Eutectic Solvent

Emma Delamarche[1,2], Agnès Mattlet[1], Sébastien Livi[1], Jean-François Gérard[1], Rémy Bayard[2] and Valérie Massardier[1]*

[1] Université de Lyon INSA Lyon, CNRS UMR 5223, Ingénierie des Matériaux Polymères, Villeurbanne, France, [2] Université de Lyon INSA Lyon, DEEP Déchets Eaux Environnement Pollutions, EA 7429, Villeurbanne, France

Biodegradable polymers concern an important topic for innovation in materials, as they are supposed to contribute to the reduction in the amount of waste materials, which lead to microplastics with similar properties as conventional polymer materials. Poly(butylene succinate) and poly(lactic acid) blends are polymers with interesting properties offering possible alternatives to some conventional petrochemical-sourced polymers. Some of the physical properties of such blends can be tailored from the addition of small amounts of deep eutectic solvents (DESs) that can act as compatibilizers, i.e., interfacial agents between poly(butylene succinate) (PBS) and poly(lactic acid) (PLA). In our study, materials formulated with a DES having a coarse morphology according to the dispersed particle sizes display thermal and mechanical properties rather close to the non-compatibilized PBS/PLA blends but a higher ability to biodegrade. In comparison with PBS/PLA blend, biodegradation experiments show that PBS/PLA/DES blend exhibits higher weight losses and faster fragmentation under conventional conditions. A significant decrease in PLA melting temperature under composting conditions, i.e., at 58°C, is observed indicating that PLA phase is the component mainly concerned. As a conclusion, this work demonstrates that morphologies as well as the biodegradability process can be tailored by adding a small amount of a DES in such biosourced polymer blends. Indeed, designing polymer materials, for which degradation processes are targeted in the dispersed phase, i.e., in multiple locations of the material, can be an efficient route to "predegrade" phases in a polymer matrix to accelerate macroscopic biodegradation.

Keywords: polymer, polyester, deep eutectic solvent, biodegradation, composting

INTRODUCTION

Plastics are everywhere in our everyday life and, unfortunately, in our natural environment, where their chemical stability can be considered as a main drawback. As a consequence, combination of life properties, i.e., properties required for their use and controlled end-of-life, is a major scientific challenge offered to polymer scientists. In this perspective, bio-based polymers such as poly(butylene succinate) (PBS) and PLA can offer a good balance between mechanical and thermal properties and ability to biodegrade as they are dispersed in air, soil, or water media.

PBS, produced by polycondensation of fossil or bio-based succinic acid and 1,4 butanediol, can substitute low-density polyethylene or even poly(butylene-adipate-co-terephtalate) (PBAT) in many applications. PBS and its copolymers are also of interest as they are able to biodegrade in various environments (Xu and Guo, 2010; Zeng et al., 2016). Their biodegradation rate can be tuned via synthesis conditions, i.e., copolymerization or from their formulation. For mechanical reinforcement, PBS can be blended with PLA, with which it is partially miscible, to associate the properties of both polymers (Shibata et al., 2006; Bhatia et al., 2007; Deng and Thomas, 2015). PBS/PLA material that are at least partially bio-sourced and biodegradable can be used as agricultural mulching films, stretch films, bags, and kitchenware, for example (Livi et al., 2018).

Morphologies, thermal, and mechanical properties can be tuned from a relevant choice of the formulation compositions (Livi et al., 2015). The capacity for hydrolysis is often correlated with material properties as well as natural conditions.

Biodegradation corresponds to the degradation of organic matter into water, CO_2 and/or CH_4, and biomass, by the action of microorganisms. At first, fragmentation increases the surface area, enabling microorganisms to attach. Physical means such as grinding and/or chemical degradation (such as hydrolysis), leading to lower molecular weight polymer, which are more easily assimilated by microorganisms (Witt et al., 1996), are responsible for fragmentation. Then, microorganisms mineralize fragments and oligomers into simple molecules and biomass (Witt et al., 1996; Castelan, 2010). Concerning the environment, higher temperatures, if they do not kill microorganisms, often lead to faster degradation, and a degradation temperature close or higher than the glass transition temperature (T_g) favors the biodegradation process. Indeed, at temperatures above the T_g of a polymer, increased chain mobility facilitates access to enzymes (Weinberger et al., 2017), as well as water absorption (Siparsky et al., 1997). This explains that, at temperatures under their T_g, polyesters such as PLA are not likely to degrade, whereas they significantly age at temperatures close to their T_g (Agarwal et al., 1998; Itävaara et al., 2002; Yagi et al., 2009; Karamanlioglu and Robson, 2013). Humidity fosters the degradation by increasing the hydrolysis rate and by favoring microorganisms activity and transport (Gu et al., 1994). pH influences the degradation, and PLA chains degrade more rapidly in alkaline conditions than in neutral or acidic conditions (Makino et al., 1986; Schliecker et al., 2003).

Material properties are also key parameters influencing biodegradation. Synthetic polymers can be manufactured with different properties such as crystallinity, glass transition, and melting temperatures, and their ability for versatility can be considered as an advantage over natural polymers like chitosan, gelatin, starch, etc. (Vieira et al., 2013; Díaz et al., 2014; Pellis et al., 2016).

Polymers, with hydrolysable bonds, such as polyesters, are likely to degrade in presence of enzymes naturally present in the environment. In addition to lower volumes of discarded plastic materials, degradation in natural environment can contribute to soil fertility.

Parameters such as morphology, crystallinity, hydrophilicity, and molar masses can significantly influence biodegradation in natural media. Husarova et al. observed that, under composting conditions, PLA having a high specific surface area degrade faster in biotic media. Rudnik observed the same tendency under soil burial conditions with PLA (Rudnik and Briassoulis, 2011; Husárová et al., 2014). Moreover, degradability decreases when increasing hydrophobicity (Höglund et al., 2010). Morphologies with multiphase materials can also favor bacteria and enzyme activities from the creation of pathways made after the disappearance of the easiest phase to be biodegraded (Delamarche et al., 2020).

The degradation rate is smaller for polymers with high degrees of crystallinity, as crystallites are less accessible to enzymes and to water. Thus, amorphous PLA degrades faster than semi-crystalline PLA both in abiotic medium and in aerobic condition under composting conditions (Zhou and Xanthos, 2008; Pantani and Sorrentino, 2013).
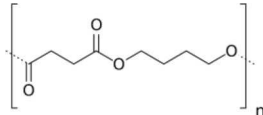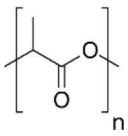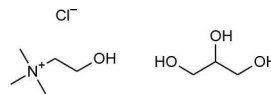
Hydrophilic character is preferred for improving affinity with bacteria and enzymes that can catalyze hydrolysis of the polyester chains. Lower molecular weight are in favor of faster degradation and Husarova et al. showed that, under composting conditions and in abiotic aqueous conditions, low molecular weight PLA degrades faster than high molecular weight PLA (Husárová et al., 2014).

The first part of this work considers the design and characterization of PBS/PLA blends with and without a small amount of a deep eutectic solvent (DES). DESs prepared by mixing two components display a melting temperature lower than the ones of the individual components. DESs exhibit similar properties to few ionic liquids and are widely studied, as they are considered to contribute to environment-friendly solutions. For such a route, choline chloride/glycerol DES exhibits a low toxicity and can be considered relevant for "green" applications (Radošević et al., 2015). In the present work, this DES is expected to act as an interfacial agent in PBS/PLA blends. Considering a similar way, PBAT/PLA or PP/PA blends were studied with considering phosphonium-based ionic liquids (Yousfi et al., 2014; Lins et al., 2015). For thermoplasticization of starch, Decaen et al. showed that choline chloride permits a good compromise between limited chain scission and thermomechanical properties (Decaen et al., 2017).

The present study aims to investigate the relationships between physical properties and biodegradation for these polymer blends and to investigate the role of the addition of a DES. Material data such as molar masses, crystallinity yield, morphologies, and surface properties are reported, as these ones are known to control biodegradability (Delamarche et al., 2020).

To assess biodegradability, 3-month degradation essays were conducted, i.e., under composting conditions at 58°C (higher than PBS glass transition temperature, T_g, and close to the one of PLA) in deionized water and NaOH solution, under soil burial conditions, as well as in humid atmosphere at room temperature. Weight loss data, ^{1}H NMR, and differential scanning calorimetry (DSC) measurements were considered to follow the biodegradation of PLA.

Abbreviation	Full name	M_n (g mol^{-1})	Melting temperature T_m (°C)	Structural formula
PBS	Poly(butylene succinate)	50 kDa	113	
PLA	Poly(lactic acid)	34 kDa	170	
DES	Choline chloride/glycerol	231.72	–	

MATERIALS AND METHODS

Materials

The various polymers used in this study are listed in **Table 1**. PBS and PLA were supplied as pellets by Natureplast (denoted PBE 003 and PLA 005 grades, respectively). L-Lactic acid/D-lactic acid contents for the considered PLA is 94:6 mol-% (Dorigato et al., 2012). Choline chloride/glycerol (1:2 mole ratio), a hydrophilic DES, was supplied by Scionix Co.

Processing of PBS/PLA Blends

Polymer pellets were dried in an oven at 70°C for 12 h. Pellets and additives were extruded using a 15-g capacity DSM microextruder (Midi 2000 Heerlen, NL) with corotating screws (*L/D* ratio equal to 18) at 190°C with a 100-rpm speed for 3 min. PBS/PLA (60:40 wt ratio) and PBS/PLA/DES (60:40:1 wt ratio) were extruded. Extruded coupons were injected in a 10-cm^3 mold at 30°C to obtain 2-mm thick and 4-mm wide dumbbell-shaped specimens. Thin films (0.2 mm) were processed under compression at 210°C and considered for aging experiments.

Characterization Experimental Techniques

Molar Masses

Molar masses were determined using a size exclusion chromatography (SEC) equipment, comprising Agilent Technologies columns, a light scattering detector, and a Shimadzu RID-10A detector. Three milligram samples were cut and dissolved in chloroform (1 mg/ml). Analysis took place at 30°C under a 1-ml/min flow. $\frac{dn}{dc}$ used was 0.06 ml/g for PBS and 0.0237 for PLA (Malmgren et al., 2006).

^{1}H NMR

One-dimensional ^{1}H NMR spectroscopy was used to determine the PBS and PLA contents of the blends (see formula, **Figure 1**). Samples, cut from films, were dissolved in CDCl$_3$ and analyzed at 25°C using a Bruker Advance III spectrometer (400 MHz), equipped with a 5-mm multinuclear broadband probe (BBFO+). To evaluate the weight percentage of PBS and PLA in the blends, peak resonance (a) of PLA (CH) at 5.1 ppm and resonance peak

FIGURE 1 | Poly(butylene succinate) (PBS) and poly(lactic acid) (PLA) and associated ^{1}H NMR spectra, showing end groups peaks.
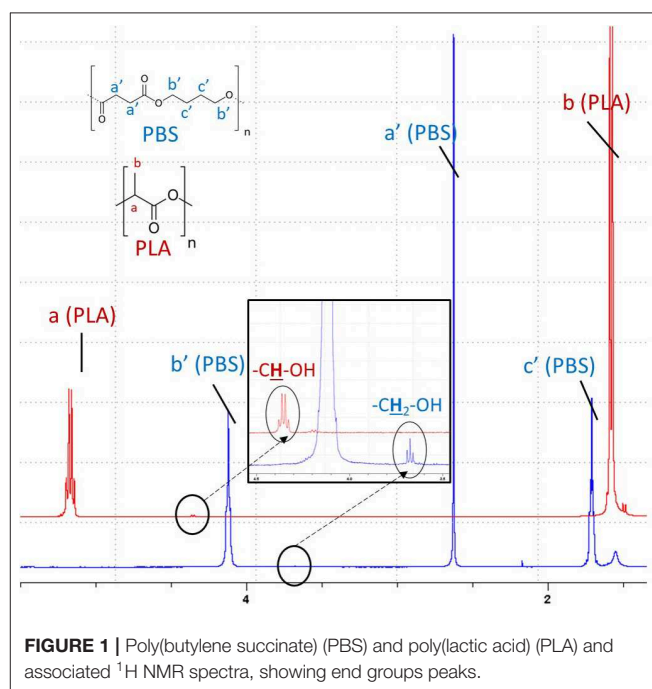
(a) of PBS (CH$_2$) at 2.6 ppm were considered to calculate the weight content of PBS:

$$f_{(PBS)} = \frac{\frac{I_{a(PBS)}}{4}}{\frac{I_{a(PBS)}}{4} + I_{a(PLA)}}$$

$$wt\%_{(PBS)} = \frac{f_{(PBS)} \times M_{PBS}}{f_{(PBS)} \times M_{PBS} + \left[1 - f_{(PBS)}\right] \times M_{PLA}} \times 100$$

with $f_{(PBS)}$ the molar fraction of PBS and $wt\%_{(PBS)}$ the weight content of PBS.

End group analysis was carried out to calculate mean molar masses of PBS. It was assumed that each polyester chain exhibits one hydroxyl and one carboxylic end groups. Resonance peak

of hydroxyl end group (CH_2-OH) of PBS, appearing at 3.7 ppm (Labruyère et al., 2014), was integrated as well as CH_2 (a) one in the monomer repeating unit at 2.6 ppm. $\overline{M_n}$ was determined as follows:

$$\overline{M_n} = \frac{I_a}{4} \times \frac{2}{I_{CH_2-OH}} \times M_{PBS}$$

with M_{PBS} = 172.2 g/mol, I_a the integral of resonance peak CH_2 in the polymer repeating unit, and I_{CH_2-OH} the integral of resonance peak of hydroxyl end group (CH_2-OH).

To evaluate the molar mass of PLA phase after processing, the hydroxyl end group of PLA (CH–OH) signed at 4.34 ppm and CH (a) of the monomer at 5.1 ppm were analyzed to calculate the molar mass. However, this peak is close to peak (b) of PBS. Hence, PLA end-chain titration was carried out after extracting PLA from the PBS/PLA blend with the following protocol. First, samples were dissolved in $CHCl_3$. Then, tetrahydrofuran was added to induce precipitation of PBS. After filtration and solvent evaporation, the remaining PLA and PBS oligomers (soluble in THF) were analyzed by NMR in $CDCl_3$. $\overline{M_n}$ was determined as follows:

$$\overline{M_n} = \frac{I_a}{1} \times \frac{1}{I_{CH-OH}} \times M_{PLA}$$

with M_{PLA} = 72.1 g/mol, I_a the CH peak integral in the polymer repeat unit, I_{CH-OH} the integral of peak of hydroxyl end group (CH–OH). Spectra of pristine PBS and PLA are displayed in **Figure 1**.

Thermal Properties

DSC analyses were carried out using a TA Instruments equipment. Samples were subjected twice to a thermal cycle considering heating and cooling ramps of 10 K min^{-1}, from −70 to 200°C and from 200 to −70°C.

Crystallinity yields were calculated according to the following equation:

$$\chi_{c,p} = \frac{\Delta H_m}{wt_p \times \Delta H_{0,p}} \times 100$$

where wt_p is the weight fraction of the polymer (PBS or PLA), and $H_{0,p}$ is the enthlapy of 100% crystalline polymer (Marten et al., 2003; Shi et al., 2012).

$$\Delta H_{0,PBS} = 110.3 \, J/g$$
$$\Delta H_{0,PLA} = 93 \, J/g$$

Thermogravimetric analyses were carried out using a TA Instrument equipment. Samples were subjected to a heating rate of 20 K min^{-1} under nitrogen atmosphere from 25 to 600°C. Temperatures at which 1% of the initial weight was lost $T_{1\%deg}$ (°C) and degradation temperatures T_{degPLA} and T_{degPBS} (obtained from the maxima of the derivative curves of the weight loss as a function of temperature) were determined.

Morphologies

Transmission electron microscopy was carried out at the Technical Center of Microstructures of Lyon using a Philips CM 120 microscope with an accelerating voltage of 80 kV. Samples (80–100 nm thick) were cut using an ultramicrotome equipped with a diamond knife and set on copper grids.

Dynamic Mechanical Spectroscopy

Dynamic mechanical measurements were carried out using an ARES G2 rheometer. The heating rate was 3 K min^{-1} from −60 to 90°C at a frequency of 1 Hz. The change in shear storage modulus, G', and shear loss modulus, G'', were determined. $\tan(\delta)$ was considered to determine the alpha-relaxation temperatures, T_α, related to T_g of PBS and PLA. T_α was considered as the difference between $T_{\alpha(PBS)}$ and $T_{\alpha(PLA)}$.

Mechanical Properties

Uniaxial tensile tests were conducted using an INSTRON 33R4469 tensile machine at 25°C. Dumbbell specimens were tested for a 50-mm/min elongation speed. Young's modulus and maximum and average strain at break were determined.

Degradation Experiments

Degradation experiments for 3 months were performed considering films exposed to various environments. Every month, two samples of each formulation were recovered, washed with deionized water, and gently dried on absorbent paper. Then, they were dried in a vacuum oven at 30°C for 12 h and kept in a closed desiccator. Weight losses were calculated as follows (W_0 being the weight before degradation experiment and W_t the weight after degradation experiment):

$$Weight \ loss \ (\%) = \frac{W_0 - W_t}{W_0} \times 100$$

Abiotic Hydrolysis

Abiotic hydrolysis was conducted at 58°C in deionized water and in alkaline solution (NaOH 0.01 M). Films (1.25 × 1.5 × 0.02 cm^3) were disposed in 10 ml of aqueous solution in individual closed flasks.

Composting

Composting was conducted at 58°C in open containers. Compost was from composting facility of Racine—Ecopole la Rize (Décines-Charpieu, France). Organic matter percentage was obtained by calcination of dry samples and was found to be 58.2 ± 0.3 wt-%. The water content and ability to retain water were analyzed. Polymer samples (2.5 × 1.5 × 0.02 cm^3) were buried 15 cm beneath the surface. Moisture content was regularly adjusted to be 90% of the maximum capacity of water retention.

Soil Burial

Soil burial experiment was conducted at room temperature in open containers. Soil was from LyonTech Campus La Doua, Villeurbanne, France. Organic matter percentage was obtained by calcination of dry samples and was found to be 21 ± 3 wt-%. Water composition and ability to retain water of the soil were analyzed as well. Polymer samples (2.5 × 1.5 × 0.02 cm^3) were

FIGURE 2 | TEM images of **(a)** poly(butylene succinate) (PBS)/poly(lactic acid) (PLA) (60:40) wt phr, **(b,c)** PBS/PLA/deep eutectic solvent (DES) (60:40:1) wt phr.

buried 10 cm beneath the surface. Moisture content was regularly adjusted to 90% of the maximum capacity of water retention.

Humid Atmosphere

Polymer samples (2.5 × 1.5 × 0.02 cm) were disposed in a closed transparent chamber with humidity-saturated air at room temperature.

RESULTS AND DISCUSSION

DES as Interfacial Agents in PBS/PLA Blends

TEM images (**Figure 2**) confirm that PBS matrix and PLA (appearing as white domains of the dispersed phase) are not miscible (Bhatia et al., 2007). PLA in PBS/PLA blends are irregularly dispersed (**Figure 2a**). Adding DES (**Figure 2b**) leads to the formation of a PBS-rich continuous phase and the presence of larger PLA domains (up to 45 μm^2). In addition, inclusions of PBS are observed in PLA-dispersed domains, indicating the start of phase inversion (**Figure 2c**). In fact, Wu et al. reported that, as the weight fraction of PBS is up to 60 wt-%, PBS becomes the continuous phase and the inversion content is close to 50 wt-% (Wu et al., 2012). At molecular scale, eutectic solvent is observed at the interface.

The fact that the addition of DES, which is made of an ionic liquid and a solvent, induces larger PLA domains was not expected regarding our earlier studies. Indeed, Lins et al. added 1% of phosphonium-based ionic liquids in PBAT/PLA blends and observed smaller PLA droplets as well as a rather homogeneous size distribution. This phenomenon suggests that IL locates in the interfacial zones due to strong interactions with the ester groups leading to a decrease in the interfacial tension (Lins et al., 2015). Furthermore, Leroy et al. studied the addition of choline chloride/glycerol in PBS–zein blends and showed that DES behaves as a compatibilizing agent leading to a finer dispersion of zein in the PBS matrix (Leroy et al., 2012).

Tensile properties analyses of PBS/PLA blends reported in **Table 2A** show that the PLA phase, having a higher modulus compared to PBS, acts as a reinforcing component leading to higher Young's modulus (Qiu et al., 2016). The strain at break is slightly improved with the addition of DES, which can be explained by better adhesion between PBS and PLA, provided by DES acting as an interfacial agent.

TABLE 2 | (A) Mechanical properties of neat poly(butylene succinate) (PBS) and poly(lactic acid) (PLA) and PBS/PLA blends (uniaxial tension; 50 mm min^{-1}) and **(B)** dynamic mechanical analysis of PBS/PLA blends without and with deep eutectic solvent (DES) (1 wt phr) at 1 Hz, 3 K/min.

(A)			
Material	**Young's modulus (MPa)**	**Strain at break (%)**	**Maximum strain at break (%)**
PBS	320 ± 27	310 ± 90	385
PLA	3,500*	5*	–
PBS/PLA	603 ± 57	391 ± 84	418
PBS/PLA/DES	619 ± 17	424 ± 66	490
(B)			
Material	$T_{\alpha,\mathrm{PBS}}$ (°C)	$T_{\alpha,\mathrm{PLA}}$ (°C)	ΔT_α (°C)
PBS/PLA	−25.6	61.1	86.7
PBS/PLA/DES	−24.3	59.7	84.0

*Data provided in product datasheet.

Data from dynamic mechanical analyses are summarized in **Table 2B**. The observation of two distinct α-relaxation temperatures related to PBS and PLA phases confirm that PBS and PLA are not fully miscible (Deng and Thomas, 2015).

Number average molar mass, $\overline{M_n}$, weight average molar weight, $\overline{M_w}$, and dispersity, $\overline{M_w}/\overline{M_n}$, determined with SEC, are reported in **Figures 3a–c**. As PLA and PBS are not distinguishable on SEC chromatograms, $\overline{M_n}$ of distinct PBS and PLA phases are determined by end group titration using ^{1}H NMR spectroscopy as well (**Figure 3d**). Average molar masses calculated using ^{1}H NMR titration (**Figure 3d**) are significantly lower than molar masses measured using SEC (**Figure 3a**). Since it is assumed that polymers are not branched, end-group titration may underestimate real values. Hence, instead of discussing absolute average molar masses, only trends are studied in this work.

PBS/PLA blends with DES exhibit significantly lower molar masses of involved polymer components. This suggests that the DES leads to chain scissions, as observed by Park and Xanthos for neat PLA (Park and Xanthos, 2009). This could be due to transesterification reactions leading to random chain scissions first (Lins et al., 2015). It was observed by Freyermouth that no or few transesterification reactions can take place
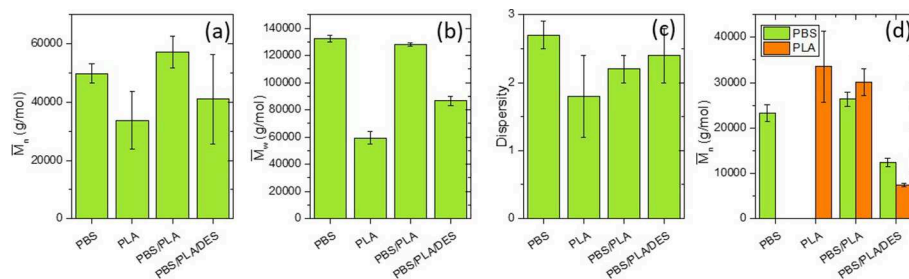
FIGURE 3 | $\overline{M_n}$, $\overline{M_w}$, and dispersity of poly(butylene succinate) (PBS), poly(lactic acid) (PLA), and PBS/PLA (60:40) wt phr blends determined by size exclusion chromatography (SEC) in CHCl₃ **(a–c)**, and calculated using ¹H NMR **(d)**.
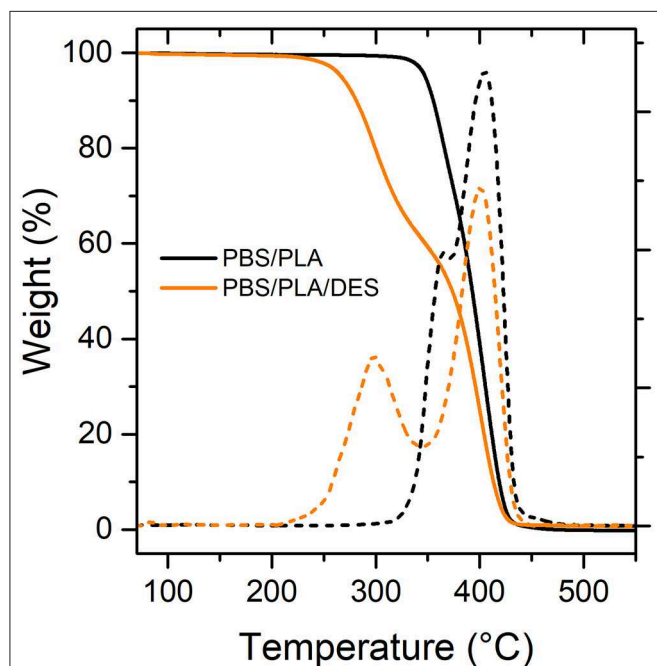
FIGURE 4 | Thermogravimetric analyses (TGA) traces of poly(butylene succinate) (PBS)/poly(lactic acid) (PLA) blends (60:40) wt phr. Dashed curves are derivative curves.

TABLE 3 | Degradation temperatures of poly(butylene succinate) (PBS) and poly(lactic acid) (PLA) phases and degradation temperature for 1% wt loss from thermogravimetric analyses (TGA) (heating rate: 20 K min⁻¹; nitrogen atmosphere).

Material	$T_{1\% \text{ deg.}}$ (°C)	$T_{\text{deg PLA}}$ (°C)	$T_{\text{deg,PBS}}$ (°C)
PBS	304	–	409
PLA	319	379	–
PBS/PLA	324	365	405
PBS/PLA/DES	228	298	401

Degradation temperatures T_{degPLA} and T_{degPBS} were obtained from the maxima of the derivative curves of the weight loss as a function of temperature.

between PBS and PLA in PBS/PLA blends after 105 min at 180°C (Freyermouth, 2014); however, the addition of DES could lead to different results, given the important degradation phenomenon taking place during processing. Nevertheless, no additional resonance peak, which is a signature of a possible transesterification phenomenon, could be evidenced using ¹H NMR spectroscopy.

Hence, although transesterification is not observable, it is clear that DES causes thermal degradation during material processing, leading to lower molar masses. This seems to favor miscibility between PBS and PLA, as evidenced by the merging of alpha relaxation peaks in DMA spectra (**Table 2B**). These conclusions are in agreement with the ones issued from thermogravimetric analyses (**Figure 4**, **Table 3**), which show that PBS/PLA/DES blends degrade at lower temperature than PLA/PBS blend. They

are also in agreement with DSC results (**Table 4**), which show a lower crystallization temperature (T_c) when DES is present in the blends.

Degradation Mechanisms Observed at Microscale

Fragmentation process to small fragments of samples is reported in **Figure 5**.

PBS/PLA/DES blends exhibit fringes after degradation in alkaline environment (**Figure 5B**). TEM images showed that PLA domains are elongated in PBS/PLA/DES materials (**Figure 2b**). Assuming that the microstructure is similar whatever the processing conditions, this phenomenon can be explained by a faster degradation of PLA phase compared to the PBS one. Weight loss data (**Figure 6**) also supports the proposed mechanism. In fact, in alkaline medium at 58°C, PBS/PLA/DES blend exhibits a higher weight loss during the first month of exposure, i.e., up to 20 wt-% loss compared to non-modified PBS/PLA blend. After 3 months exposure, data cannot be provided for PBS/PLA/DES blends as not all fragments could be recovered (which means leading to very efficient biodegradation). In deionized water, PBS/PLA blend containing DES shows a higher weight loss compared to neat PBS/PLA blend. In a similar way, under composting conditions at 58°C, PBS/PLA/DES blend undergoes a rather high weight loss, i.e., 18% after 2 months exposure.

As a conclusion, PBS/PLA blends modified with a DES degrade faster than neat PBS/PLA blends, but it is expected that $T_{1\%\text{deg.}}$ at 228°C does not significantly disturb extrusion
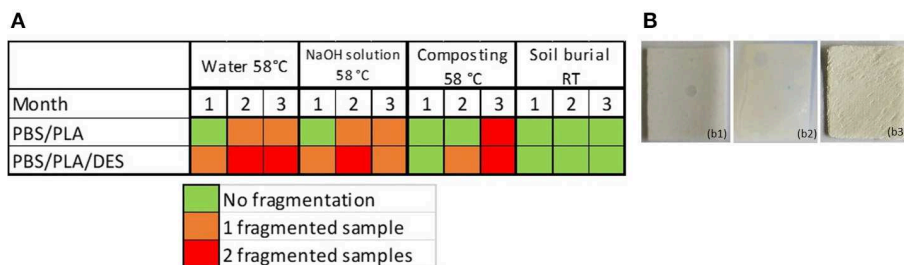
FIGURE 5 | (A) Fragmentation observed during aging experiments after various exposure times: 1, 2, and 3 months. **(B)** Photographies of poly(butylene succinate) (PBS)/poly(lactic acid) (PLA) blend (60:40) wt phr after 1 **(b1)** and 3 **(b2)** months of exposure and PBS/PLA/deep eutectic solvents (DES) (60:40:1) wt phr **(b3)** after 3 months of exposure in NaOH solution at 58°C.

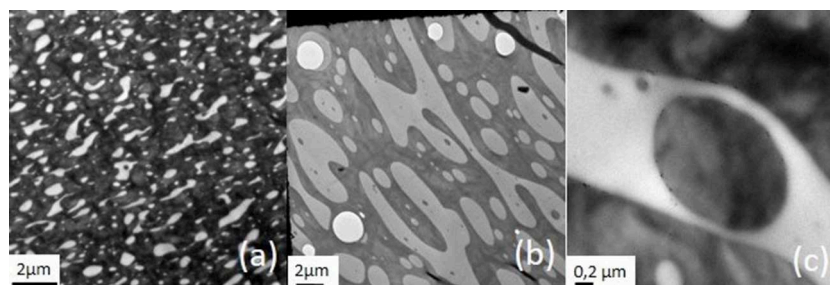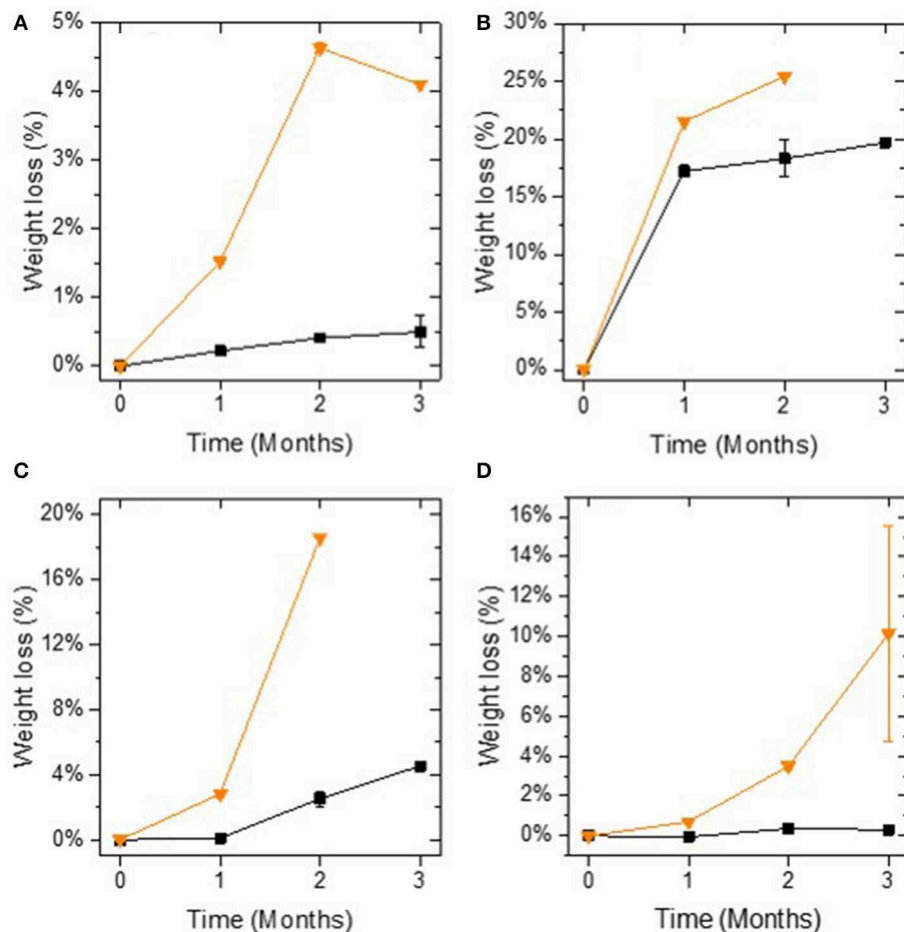**FIGURE 6 |** Weight loss (%) of poly(butylene succinate) (PBS)/poly(lactic acid) (PLA) (60:40) wt phr (black) and PBS/PLA/deep eutectic solvents (DES) (60:40:1) wt phr (orange) in deionized water at 58°C **(A)**, in 0.01 M NaOH solution at 58°C **(B)**, under composting conditions at 58°C **(C)**, and under soil burial conditions at room temperature **(D)**. Results are given with standard deviation. If not shown, only one sample could be recovered and weighted.

(at 190°C) and compression molding (at 210°C) with short residence times. Moreover, the lower thermal stability in the presence of DES should not reduce the applications profile. Considering the fact that the molar masses of the polyesters in the presence of DES are lower than for unmodified PBS/PLA blends, PBS/PLA/DES blends are susceptible to lose integrity faster. Furthermore, it is known that PLA degrades well at 58°C (Agarwal et al., 1998; Itävaara et al., 2002; Yagi et al., 2009). It can
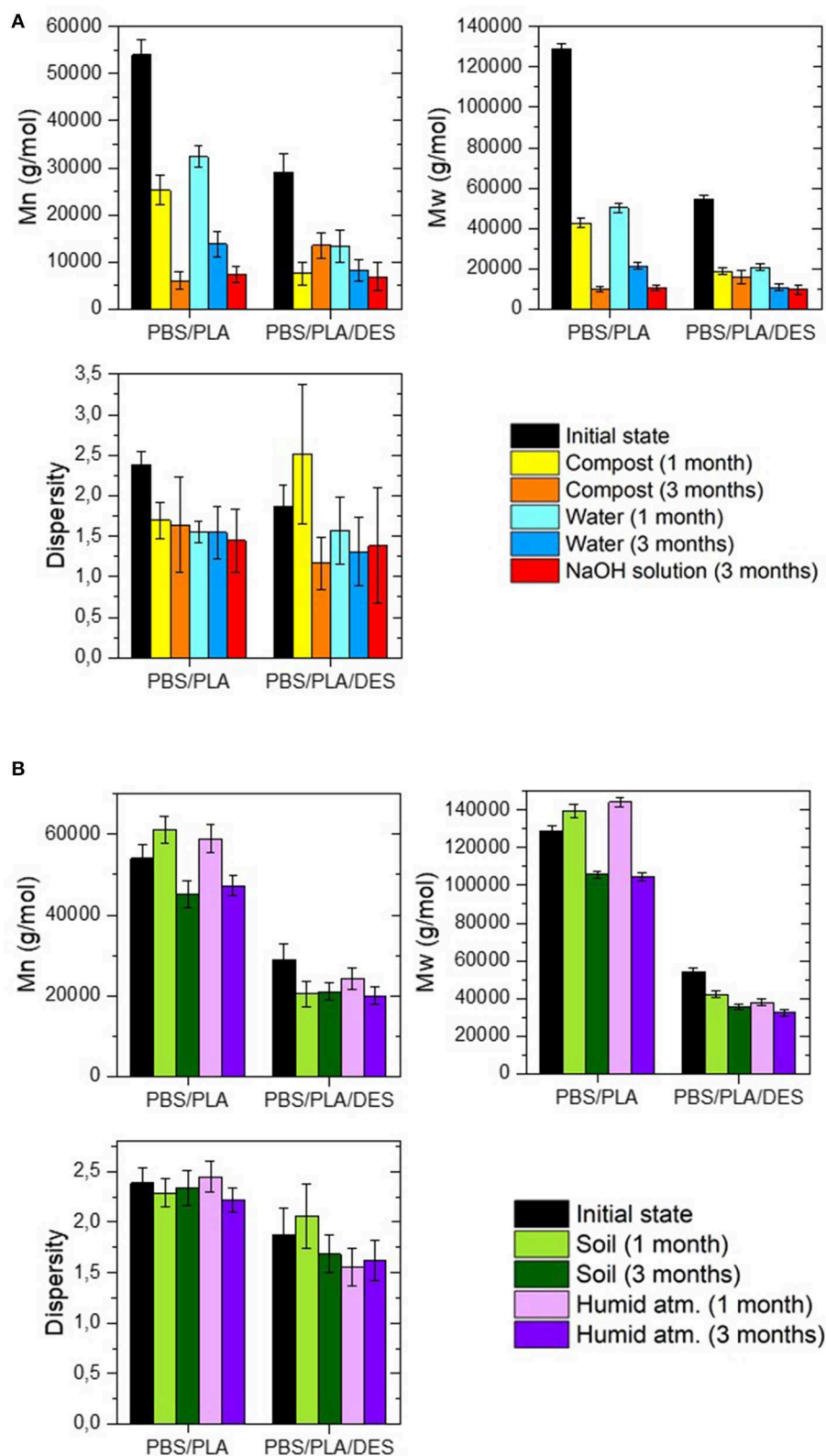
FIGURE 7 | $\overline{M_n}$, $\overline{M_w}$, and dispersity of poly(butylene succinate) (PBS)/poly(lactic acid) (PLA) blends measured with $CHCl_3$-deep eutectic solvents (DES), after degradation under composting conditions, in water, and in NaOH solution at 58°C **(A)**, and under soil burial conditions and in humid atmosphere at room temperature **(B)**.

be supposed that PLA chains are the weakest component in the materials at such temperature.

At room temperature under soil burial conditions, PBS/PLA/DES blends show a larger weight loss, but this phenomenon cannot be reproduced after 3 months exposure. For choline chloride/glycerol, having a low toxicity (Radošević et al., 2015) and being hydrophilic, it might improve surface affinity with microorganisms, whereas it might not be the case for PBS/PLA blend. Nevertheless, heterogeneities of composition could occur in the biodegradation medium regarding the populations of microorganisms, i.e., depending on the location in the container. Specimens left under humid atmosphere did not exhibit any weight loss after 3 months exposure.

Molar Masses Changes During Biodegradation

Molar masses determined using SEC are reported in **Figure 7**. As PLA and PBS are not distinguishable on SEC chromatograms, the variation of refractive index vs. concentration, dn/dc, of neat PBS (0.06) was used to calculate the average molar masses polymer in blends. Hence, the resulting $\overline{M_n}$ were used to evidence the trends, as these ones are semiquantitative values.

$\overline{M_n}$ of PBS phases only was determined by chain end titration using ^{1}H NMR spectroscopy (**Table 5**). As said earlier, molar masses determined using ^{1}H NMR titration might underestimate real values since it was assumed that polymer chains are not branched.

Under composting conditions and in deionized water at 58°C (**Figure 7A**), molar masses decrease is significant above 1 month of exposure and does not change afterwards for PBS/PLA blends including DES, suggesting that $\overline{M_n}$ reaches a limit of ~10,000 g mol^{-1}. From this limit, polymer chains might diffuse into the biodegradation medium. Dispersity decreases with degradation

time. The molar mass loss under composting conditions is similar to its loss after exposure in deionized water, suggesting that the main degradation mechanism under composting conditions is abiotic hydrolysis. If biotic degradation occurs, it does not induce a significant loss of molecular weight at the core of the samples, but may be responsible for surface etching.

At room temperature, under humid atmosphere and soil burial conditions (**Figure 7B**), PBS/PLA blends modified with DES exhibit a molar mass loss after the first month of exposure. After 3 months of exposure, all the blends exhibit a loss of molar mass. The molecular weight loss after exposure under soil burial conditions is similar to that after exposure under humid atmosphere conditions, suggesting again that the main degradation mechanism, causing a loss of molar mass under soil burial conditions, is abiotic hydrolysis.

Molecular Scale Analysis of the Degradation Mechanisms

After 3 months of exposure, materials were analyzed in CDCl$_3$ using ^{1}H NMR spectroscopy, to observe the changes in PBS and PLA contents (**Figure 8**). PLA and PBS weight contents in PBS/PLA/DES blends were found to be 68:32 after 3 months of exposure under alkaline conditions, 72:28 after exposure under composting conditions, and remained unchanged otherwise. This result is in agreement with the fact that PLA phase degrades faster than PBS and then diffuses out of the material at 58°C.

Melting and crystallization of PBS and PLA in the blends were studied using DSC (**Figures 9**, **10**). Owing to the occurrence of the cold crystallization exothermal peak of PLA overlapping the

TABLE 4 | Glass transition, melting, and crystallization temperatures of poly(butylene succinate) (PBS), poly(lactic acid) (PLA), PBS/PLA (60:40 wt phr), PBS/PLA/deep eutectic solvents (DES) (60:40:1 wt phr) films determined using differential scanning calorimetry (DSC) (heating/cooling rate of 10 K min^{-1} under nitrogen atmosphere) before exposure.

Material	$T_{g,PBS}$ (°C)	$T_{g,PLA}$ (°C)	$T_{m,PBS}$ (°C)	$T_{m,PLA}$ (°C)	T_c (°C)
PBS	−29	–	116	–	92
PLA	–	60	–	177	95
PBS/PLA	−29	62	115	176	91
PBS/PLA/DES	−28	63	114	171	88–104
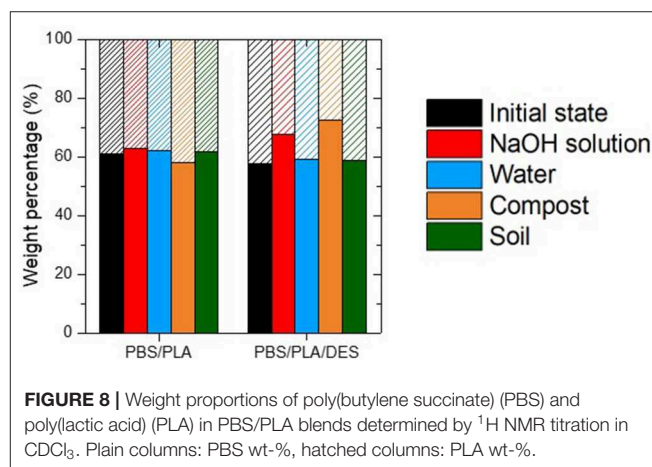
FIGURE 8 | Weight proportions of poly(butylene succinate) (PBS) and poly(lactic acid) (PLA) in PBS/PLA blends determined by ^{1}H NMR titration in CDCl$_3$. Plain columns: PBS wt-%, hatched columns: PLA wt-%.

TABLE 5 | $\overline{M_n}$ of poly(butylene succinate) (PBS)/poly(lactic acid) (PLA) and PBS/PLA/deep eutectic solvents (DES) blends determined using size exclusion chromatography (SEC) and ^{1}H NMR (PBS end group titration) after 3 months degradation.

$\overline{M_n} \cdot (kgmol^{-1})$	Initial state		Compost		Water		NaOH		Soil	
	SEC	^{1}H NMR	SEC	^{1}H NMR	SEC	^{1}H NMR	SEC	^{1}H NMR	SEC	^{1}H NMR
PBS/PLA	54.0 ± 3.4	27.9 ± 1.6	6.1 ± 2.0	3.5 ± 0.2	13.9 ± 2.8	6.6 ± 0.4	7.4 ± 1.8	6.0 ± 0.3	45.2 ± 3.3	24.9 ± 1.7
PBS/PLA/DES	29.0 ± 4.0	12.4 ± 1.0	13.6 ± 2.7	5.8 ± 0.3**	8.2 ± 2.3	5.7 ± 0.3	6.9 ± 3.1	3.4 ± 0.2	21.0 ± 2.2	14.5 ± 1.0

*__Determined at the second month._
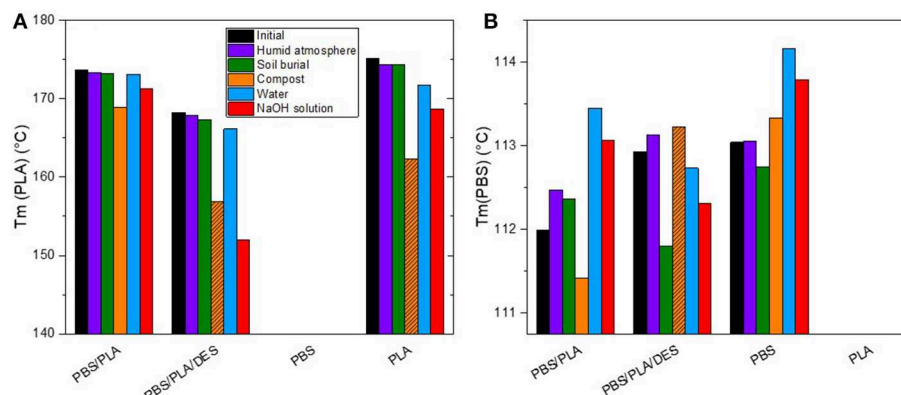
FIGURE 9 | Melting temperatures of polybutylene succinate (PBS) **(B)** and polylactic acid (PLA) **(A)** in PBS/PLA blends after 3 months degradation determined using differential scanning calorimetry (DSC) (first heating ramp). Hatched columns represent values determined at month 2.

endothermal melting peak of PBS, the changes in enthalpy were difficult to assess. Hence, the data are not reported in this article.

For PBS/PLA/DES blends, the melting temperature of PLA (**Figure 9A**) slightly decreases after exposure in deionized water, but significantly lower values were measured after degradation in NaOH solution and compost. This decrease in melting temperature of PLA during degradation has been observed by Pantani and Sorrentino and was attributed to the presence of low molar mass chains (Pantani and Sorrentino, 2013). The melting temperature attributed to PBS phases does not change significantly after degradation experiments (**Figure 9B**). These observations are in agreement with the fact, as said earlier, that PLA domains are significantly degraded in PBS/PLA blends containing DES during exposure at 58°C.

The crystallization phenomena in the PBS/PLA blends was studied with considering a $10\,\text{K}\,\text{min}^{-1}$ cooling ramp from molten state (**Figures 10C,D**). PBS/PLA blends without DES show no change in their crystallization behavior after degradation at room temperature (under soil burial conditions and humid atmosphere). The crystallization temperature remains unchanged, i.e., ∼94°C. However, after degradation at 58°C, a separation of the two peaks can be observed. A first peak, close to 103°C could be attributed to the PLA crystallization and a second one at lower temperatures to PBS crystallization. This second peak reaches its maximum at ∼71°C after degradation in NaOH solution and under composting conditions, while it was at ∼84°C after degradation in deionized water.

PBS/PLA/DES exhibits two distinct crystallization peaks before degradation experiments. No significant change is observed after degradation at room temperature. However, after exposure at 58°C, the small peak, attributed to PLA crystallization, broadens and its intensity diminishes, which is in agreement with the fact that PLA chains degraded and the shorter ones diffused out of the matrix during degradation. The crystallization peak of PBS is slightly shifted to lower temperatures after degradation exposure. PLA melting peak (**Figures 10A,B**) appears to be broad. After degradation at 58°C, this melting phenomenon is hardly observable. As seen earlier, this observation could be associated with the PLA

degradation with diffusion out of the PBS continuous phase. Furthermore, enthalpy of crystallization increases significantly after degradation in NaOH solution.

CONCLUSION

In this study, PBS/PLA blends were processed with addition of a DES, i.e., choline chloride/glycerol, which could act as a compatibilizer (interfacial agent). It was observed that the PLA dispersed phase in the PBS matrix exists as larger domains when DES is added to the PBS/PLA blends compared to the neat PBS/PLA blend. DES addition leads PBS/PLA/DES blend to display some decrease in molar mass values, similar mechanical properties, and decrease in thermal stability. Degradation tests under different conditions show improved degradation of PBS/PLA blends in the presence of DES, which enhances chain scissions (Decaen et al., 2017). Nevertheless, from molar masses measurements, it can be concluded that DES induces a significant decrease in PLA molar masses and consequently a lower thermal stability.

It is assumed that the good stability of PBS and degradation of mainly PLA during processing is associated with maintenance of mechanical properties and higher ability to biodegrade.

Biodegradation experiments performed at 58°C show that the PBS/PLA blends degrade faster. It is also observed that PLA phase undergoes the most important degradation phenomenon during exposure In fact, this phenomenon is evidenced by the slight decrease in PLA melting temperature as well as of the PLA weight content. Therefore, at macroscale, a significant weight loss and fragmentation process are demonstrated. Thus, it can easily be assumed that the PLA phase is the weakest component in such blends, leading to a fast loss of integrity. This shows that designing polymer materials, for which degradation processes are targeted in the dispersed phase, i.e., in multiple locations of the material, can be an efficient route to accelerate macroscopic biodegradation.

However, PLA dispersed phase is not affected to the same extent after exposure at room temperature. In fact, it is well-known that PLA does not easily degrade under mesophilic
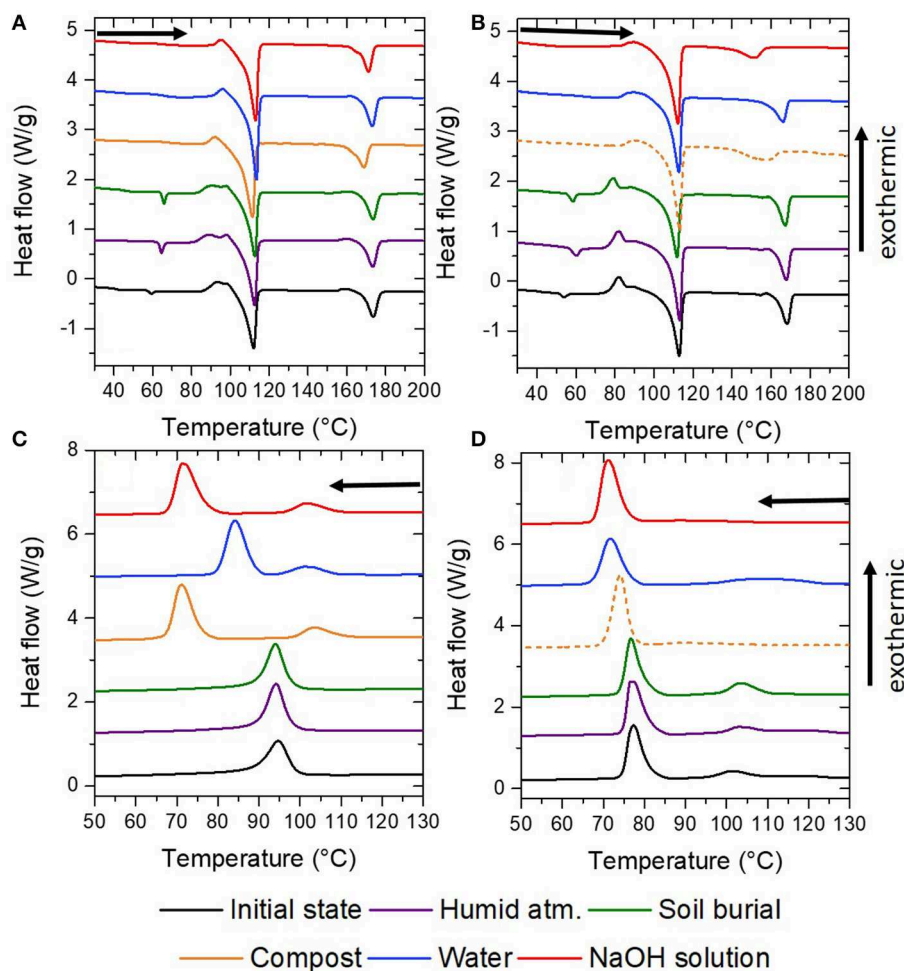
FIGURE 10 | Crystallization and melting curves of poly(butylene succinate) (PBS)/poly(lactic acid) (PLA) blends during cooling and heating ramps at 10°C/min, before and after degradation. **(A,C)** PBS/PLA, **(B,D)** PBS/PLA/deep eutectic solvents (DES). Dashed curves were acquired after 2 months because samples could not be studied in third month.

conditions (Agarwal et al., 1998; Itävaara et al., 2002; Yagi et al., 2009). At room temperature, it is difficult to identify which polymer, if any, constitutes a weak component as no significant change is observed using DSC. ^{1}H NMR does not evidence large changes in PBS/PLA contents, even though PBS/PLA/DES blend exhibits an important weight loss under soil burial conditions. Nevertheless, under soil burial conditions, blend containing DES shows a larger weight loss than the neat PBS/PLA blend.

Regarding molar masses analyses, it is observed that the molar mass decrease remains very similar under abiotic and biotic conditions at a same temperature. This suggests that hydrolysis remains the main degradation mechanism for polyester-based blends. However, blends including DES exhibit surprisingly higher weight loss than without additive under soil burial conditions at room temperature, showing that biotic degradation probably occurs at the surface of the exposed coupons. This phenomenon can be due to the choline chloride/glycerol nature, which has a hydrophilic character and displays a low toxicity.

This study shows that eutectic solvents can be used to tune mechanical properties of polymer blends as well as their biodegradability in the environment. Furthermore, degradation products must be identified and their eco-toxicity should be studied. Affinity with microorganisms of the DES is being studied and will be reported later.

DATA AVAILABILITY STATEMENT

The datasets generated for this study are available on request to the corresponding author.

AUTHOR CONTRIBUTIONS

SL, VM, and J-FG: conceptualization. SL, AM, ED, VM, and RB: methodology. AM, ED, VM, and SL: formal analysis and investigation. ED, AM, and VM: visualization. ED, VM, and SL: writing—original draft preparation. SL, J-FG, RB, and VM:

REFERENCES

Agarwal, M., Koelling, K. W., and Chalmers, J. J. (1998). Characterization of the degradation of polylactic acid polymer in a solid substrate environment. *Biotechnol. Prog.* 14, 517–526. doi: 10.1021/bp980015p

Bhatia, A., Gupta, R. K., Bhattacharya, S. N., and Choi, H. J. (2007). Compatibility of biodegradable poly (lactic acid) (PLA) and poly (butylene succinate) (PBS) blends for packaging application. *Korea Austr. Rheol. J.* 19, 125–131.

Castelan, G. (2010). Polymères biodégradables. *Tech. l'Ingénieur* 33.

Decaen, P., Rolland-Sabaté, A., Guilois, S., Jury, V., Allanic, N., Colomines, G., et al. (2017). Choline chloride vs choline ionic liquids for starch thermoplasticization. *Carbohydr. Polym.* 177, 424–432. doi: 10.1016/j.carbpol.2017.09.012

Delamarche, E., Massardier, V., Bayard, R., and Dos Santos, E. (2020). "A review to guide eco-design of polymer materials," in *Reactive and Functional Polymers*, Vol. 2, ed. T. J. Gutierrez (Springer).

Deng, Y., and Thomas, N. L. (2015). Blending poly(butylene succinate) with poly(lactic acid): ductility and phase inversion effects. *Eur. Polym. J.* 71, 534–546. doi: 10.1016/j.eurpolymj.2015.08.029

Díaz, A., Katsarava, R., and Puiggalí, J. (2014). Synthesis, properties and applications of biodegradable polymers derived from diols and dicarboxylic acids : from polyesters to poly (ester amide)s. *Int. J. Mol. Sci.* 15, 7064–7123. doi: 10.3390/ijms15057064

Dorigato, A., Sebastiani, M., Pegoretti, A., and Fambri, L. (2012). Effect of silica nanoparticles on the mechanical performances of poly(Lactic Acid). *J. Polym. Environ.* 20, 713–725. doi: 10.1007/s10924-012-0425-6

Freyermouth, F. (2014). *Etude et Modification des Propriétés du Poly (Butylène Succinate), un Polyester Biosourcé et Biodégradable*. Villeurbanne: INSA de Lyon.

Gu, J. D., Yang, S., Welton, R., Eberiel, D., McCarthy, S. P., and Gross, R. A. (1994). Effect of environmental parameters on the degradability of polymer films in laboratory-scale composting reactors. *J. Environ. Polym. Degrad.* 2, 129–135. doi: 10.1007/BF02074781

Höglund, A., Hakkarainen, M., and Albertsson, A. C. (2010). Migration and hydrolysis of hydrophobic polylactide plasticizer. *Biomacromolecules* 11, 277–283. doi: 10.1021/bm901157h

Husárová, L., Pekarová, S., Stloukal, P., Kucharczyk, P., Verney, V., Commereuc, S., et al. (2014). Identification of important abiotic and biotic factors in the biodegradation of poly(l-lactic acid). *Int. J. Biol. Macromol.* 71, 155–162. doi: 10.1016/j.ijbiomac.2014.04.050

Itävaara, M., Karjomaa, S., and Selin, J. F. (2002). Biodegradation of polylactide in aerobic and anaerobic thermophilic conditions. *Chemosphere* 46, 879–885. doi: 10.1016/s0045-6535(01)00163-1

Karamanlioglu, M., and Robson, G. D. (2013). The influence of biotic and abiotic factors on the rate of degradation of poly(lactic) acid (PLA) coupons buried in compost and soil. *Polym. Degrad. Stabil.* 98, 2063–2071. doi: 10.1016/j.polymdegradstab.2013.07.004

Labruyère, C., Talon, O., Berezina, N., Khousakoun, E., and Jérôme, C. (2014). Synthesis of poly(butylene succinate) through oligomerization - cyclization - ROP route. *RSc Adv.* 4, 38643–38648. doi: 10.1039/C4RA03373F

Leroy, E., Decaen, P., Jacquet, P., Coativy, G., Pontoire, B., Reguerre, A. L., et al. (2012). Deep eutectic solvents as functional additives for starch based plastics. *Green Chem.* 14, 3063–3066. doi: 10.1039/c2gc36107h

Lins, L. C., Livi, S., Duchet-Rumeau, J., and Gérard, J.-F. (2015). Phosphonium ionic liquids as new compatibilizing agents of biopolymer blends composed of poly(butylene-adipate-co-terephtalate)/poly(lactic acid) (PBAT/PLA). *RSC Adv.* 5, 59082–59092. doi: 10.1039/C5RA10241C

Livi, S., Duchet-Rumeau, J., and Gerard, J.-F. (2018). *Biodegradable and Biosourced Polymeric Material*. Patent no. WO2018108881 (A1). Villeurbanne.

Livi, S., Duchet-Rumeau, J., Gérard, J. F., and Pham, T. N. (2015). Polymers and ionic liquids: a successful wedding. *Macromol. Chem. Phys.* 216, 359–368. doi: 10.1002/macp.201400425

Makino, K., Ohshima, H., and Kondo, T. (1986). Mechanism of hydrolytic degradation of poly(l-lactide) microcapsules: effects of ph, ionic strength and buffer concentration. *J. Microencapsul.* 3, 203–212. doi: 10.3109/02652048609031574

Malmgren, T., Mays, J., and Pyda, M. (2006). Characterization of poly(lactic acid) by size exclusion chromatography, differential refractometry, light scattering and thermal analysis. *J. Therm. Anal. Calorim.* 83, 35–40. doi: 10.1007/s10973-005-7066-0

Marten, E., Müller, R. J., and Deckwer, W. D. (2003). Studies on the enzymatic hydrolysis of polyesters - I. Low molecular mass model esters and aliphatic polyesters. *Polym. Degrad. Stabil.* 80, 485–501. doi: 10.1016/S0141-3910(03)00032-6

Pantani, R., and Sorrentino, A. (2013). Influence of crystallinity on the biodegradation rate of injection-moulded poly(lactic acid) samples in controlled composting conditions. *Polym. Degrad. Stabil.* 98, 1089–1096. doi: 10.1016/j.polymdegradstab.2013.01.005

Park, K. I., and Xanthos, M. (2009). A study on the degradation of polylactic acid in the presence of phosphonium ionic liquids. *Polym. Degrad. Stabil.* 94, 834–844. doi: 10.1016/j.polymdegradstab.2009.01.030

Pellis, A., Haernvall, K., Pichler, C. M., Ghazaryan, G., Breinbauer, R., and Guebitz, G. M. (2016). Enzymatic hydrolysis of poly (ethylene furanoate). *J. Biotechnol.* 235, 47–53. doi: 10.1016/j.jbiotec.2016.02.006

Qiu, T. Y., Song, M., and Zhao, L. G. (2016). Testing, characterization and modelling of mechanical behaviour of poly (lactic-acid) and poly (butylene succinate) blends. *Mech. Adv. Mater. Modern Process.* 2:7. doi: 10.1186/s40759-016-0014-9

Radošević, K., Bubalo, M. C., Srček, V. G., Grgas, D., Dragicević, T. L., and Redovniković, I. R. (2015). Evaluation of toxicity and biodegradability of choline chloride based deep eutectic solvents. *Ecotoxicol. Environ. Safety* 112, 46–53. doi: 10.1016/j.ecoenv.2014.09.034

Rudnik, E., and Briassoulis, D. (2011). Degradation behaviour of poly(lactic acid) films and fibres in soil under Mediterranean field conditions and laboratory simulations testing. *Ind. Crops Prod.* 33, 648–658. doi: 10.1016/j.indcrop.2010.12.031

Schliecker, G., Schmidt, C., Fuchs, S., and Kissel, T. (2003). Characterization of a homologous series of D,L-lactic acid oligomers; a mechanistic study on the degradation kinetics *in vitro*. *Biomaterials* 24, 3835–3844. doi: 10.1016/s0142-9612(03)00243-6

Shi, Q., Zhou, C., Yue, Y., Guo, W., Wu, Y., and Wu, Q. (2012). Mechanical properties and *in vitro* degradation of electrospun bio-nanocomposite mats from PLA and cellulose nanocrystals. *Carbohydr. Polym.* 90, 301–308. doi: 10.1016/j.carbpol.2012.05.042

Shibata, M., Inoue, Y., and Miyoshi, M. (2006). Mechanical properties, morphology, and crystallization behavior of blends of poly(l-lactide) with poly(butylene succinate-co-l-lactate) and poly(butylene succinate). *Polymer* 47, 3557–3564. doi: 10.1016/j.polymer.2006.03.065

Siparsky, G. L., Voorhees, K. J., Dorgan, J. R., and Schilling, K. (1997). Water transport in polylactic acid (PLA), PLA/polycaprolactone copolymers, and PLA/polyethylene glycol blends. *J. Environ. Polym. Degrad.* 5, 125–136.

Vieira, A. C., Guedes, R. M., and Tita, V. (2013). Considerations for the design of polymeric biodegradable products. *J. Polym. Eng.* 33, 293–302. doi: 10.1515/polyeng-2012-0150

Weinberger, S., Canadell, J., Quartinello, F., Yeniad, B., Arias, A., Pellis, A., et al. (2017). Enzymatic degradation of poly(ethylene 2,5-furanoate) powders and amorphous films. *Catalysts* 7:318. doi: 10.3390/catal7110318

Witt, U., Müller, R.-J., and Deckwer, W.-D. (1996). Evaluation of the biodegradability of copolyesters containing aromatic compounds by investigations of model oligomers. *J. Environ. Polym. Degrad.* 4, 9–20. doi: 10.1007/BF02083878

Wu, D., Yuan, L., Laredo, E., Zhang, M., and Zhou, W. (2012). Interfacial properties, viscoelasticity, and thermal behaviors of poly(butylene succinate)/polylactide blend. *Ind. Eng. Chem. Res.* 51, 2290–2298. doi: 10.1021/ie2022288

Xu, J., and Guo, B.-H. (2010). "Microbial succinid acid, its polymer poly(butylene succinate), and applications," in *Plastics from Bacteria: Natural Functions and Applications,* Vol. 14 (Berlin; Heidelberg: Springer-Verlag), 85–119.

Yagi, H., Ninomiya, F., Funabashi, M., and Kunioka, M. (2009). Anaerobic biodegradation tests of poly(lactic acid) under mesophilic and thermophilic conditions using a new evaluation system for methane fermentation in anaerobic sludge. *Int. J. Mol. Sci.* 10, 3824–3835. doi: 10.3390/ijms10093824

Yousfi, M., Livi, S., and Duchet-Rumeau, J. (2014). Ionic liquids: a new way for the compatibilization of thermoplastic blends. *Chem. Eng. J.* 255, 513–524. doi: 10.1016/j.cej.2014.06.080

Zeng, R. T., Hu, W., Wang, M., Zhang, S. D., and Zeng, J. B. (2016). Morphology, rheological and crystallization behavior in non-covalently functionalized carbon nanotube reinforced poly(butylene succinate) nanocomposites with low percolation threshold. *Polym. Test.* 50, 182–190. doi: 10.1016/j.polymertesting.2016.01.003

Zhou, Q., and Xanthos, M. (2008). Nanoclay and crystallinity effects on the hydrolytic degradation of polylactides. *Polym. Degrad. Stabil.* 93, 1450–1459. doi: 10.1016/j.polymdegradstab.2008.05.014

Check for updates

Thermal, Mechanical and Micromechanical Analysis of PLA/PBAT/POE-g-GMA Extruded Ternary Blends

Laura Aliotta[1], Vito Gigante[1], Oriana Acucella[1], Francesca Signori[1,2] and Andrea Lazzeri[1,2]*

[1] DICI-Department of Civil and Industrial Engineering, University of Pisa, Pisa, Italy, [2] IPCF-CNR, Area della Ricerca di Pisa, Pisa, Italy

In order to toughen Poly(lactic) acid and binary blends with low PBAT content while maintaining a high biodegradability of the final material, poly(lactic) acid (PLA)/poly(butylene-adipate-co-terephthalate) (PBAT)/ polyolefin elastomer grafted with glycidyl methacrylate (POE-g-GMA) extruded ternary blends have been investigated in this work from a thermal, mechanical, and rheological point of view. The two elastomers have been added in different amounts as dispersed phases into the PLA matrix, paying attention to the final objective: the design of a 90% biodegradable formulation according to EN 13432. These ternary blends exhibited improved impact properties but still low elongation at break. Consequently, to the ternary composition with the best compromise of PLA quantity, biodegradability and thermo-mechanical properties (81 wt.% PLA, 9 wt.% PBAT, and 10 wt.% POE-g-GMA) a small quantity (10 wt.%) of a biobased plasticizer was added in order to further increase the impact properties in parallel with the tensile flexibility. Two types of plasticizers were investigated, one not reactive [Acetyl Tributyl Citrate (ATBC)], and one reactive [Glycidyl ether (EJ-400)]. A micromechanical study, in order to investigate the toughening mechanism of these systems, was carried out on the final formulations. They were also examined by dilatometric tests and elasto-plastic fracture mechanics correlating the data obtained to the morphology and to the rheological properties. In conclusion, the best compromise between impact, tensile properties and biodegradability content was achieved using the reactive plasticizer (EJ-400) whose interaction with the matrix is confirmed by the FT-IR analysis.

Keywords: rubber toughening, poly(lactic) acid, biodegradable polymers, ternary blends, mechanical properties

INTRODUCTION

Several and important qualities for everyday life, associated to low processing costs, make plastics fundamental in different sectors. About 150 million tons of plastics are used everywhere and its consumption is expected to grow up in the next years (La Mantia et al., 2017; Cinelli et al., 2019). Nevertheless, the society is acquiring a new awareness to adapt the third millennium consumerist and technological needs to the respect of the environment and of the human health. At this purpose, investigation on biodegradable polymers is of fundamental importance. The resistance of polymeric materials to chemical, physical and biological degradation has become a crucial problem and wastes are not acceptable. A possible alternative to classical polymers can be biodegradable polymers

(biobased and not) that fulfill the conditions of biodegradability, biocompatibility and release of low or null toxicity. Nowadays, these biodegradable polymers can be the solution to overcome the effect of plastic wastes on the environment caused by the limited disposal methods. Differently to bio-based polymers, derived partially or completely from renewable resources, biodegradable polymers are not determined by the origin of the raw material. According to the biodegradability definition: "a given substance can be completely converted into water, CO_2, and biomass through the action of microorganisms such as fungi and bacteria" (Platt, 2006). This property does not depend on the origin of the raw materials, but it depends just from the chemical composition. Biodegradability is a certified characteristic (European Committee for Standardisation, 1999). In according to EN 13432 norm: "the polymer must be converted to CO_2 (by over 90%) within 180 days under specific conditions of temperature, humidity, and oxygen level." (Künkel et al., 2016). In many fields, biodegradability gives to a product an additional value.

Among of all biodegradable polymers, poly(lactic acid) (PLA), that is fully biobased, shows very good mechanical properties, complete renewability and low production cost if compared to other biodegradable polymers (Gross and Kalra, 2002). Nevertheless, processing drawbacks, brittleness, slow crystallization rate, poor toughness and limited thermal resistance (due to its glass transition temperature around 60°C) limit the use of PLA in several markets (Barletta and Puopolo, 2019). Physical performance of PLA can be improved through numerous methods including copolymerization (Anderson et al., 2008; Phuong et al., 2014), plasticization (Baiardo et al., 2003; Coltelli et al., 2008), rubber toughening (Su et al., 2009; Gigante et al., 2019), rigid filler toughening (Murariu and Dubois, 2016; Aliotta et al., 2019), and physical blending (Zhang et al., 2014; Sedničková et al., 2018).

However, PLA brittleness is the main drawback, in order to improve PLA toughness and flexibility, binary blends of PLA with other ductile polymers have been widely reported; remarkably, less literature is present about multiphase blends, in particular ternary plasticized blends. Some interesting results have been reported for PLA-based multicomponent blends having significant improvement in mechanical properties (Anderson and Hillmyer, 2004; Grande and Carvalho, 2011; Kunthadong et al., 2015; Nagarajan et al., 2018). Sarazin et al. (2008) evaluated ternary blends with PLA, polycaprolactone (PCL), and termoplastic starch (TPS) (Sarazin et al., 2008). They showed that adding PCL to PLA/TPS binary blends, the tensile ductility increases; consequently to reach brilliant combined performances, blending PLA/TPS with another flexible polymer could be an useful method. Ren et al. (2009) instead, stated that biodegradable ternary blends of TPS, PLA and Poly(butylene adipate-co-terephthalate) (PBAT) give good impact resistance when a low content of compatibilizer (an anhydride functionalized polyester) is added.

On the basis of these evidences, in this work, the impact resistance of PLA was improved using a ternary blend approach without compromising the end of life biodegradability (following the EN 13432 standard). Small amounts of PBAT and a polyolefin

elastomer grafted with Glycidyl Methacrylate (POE-g-GMA) were added as dispersed phase into PLA matrix.

The idea adopted in this work was to use PBAT, coupled with POE-g-GMA, to reach a good compromise between an acceptable increment of impact resistance (thanks to POE-g-GMA) and, at the same time, a noteworthy improvement in tensile flexibility (thanks to PBAT).

It is known that PLA/PBAT binary blends (from until 20 wt.% of PBAT content), processed via melt blending in a twin screw extruder, lead to a well dispersed systems of PBAT particles into the PLA matrix (Jiang et al., 2006; Hamad et al., 2018). This morphology is attributable to the high immiscibility between the two polymers, that depends to their different solubility parameters [PLA $\sim$ 10.1 $(cal/cm^3)^{1/2}$ and PBAT $\sim$ 22.95 $(cal/cm^3)^{1/2}$] and it causes a weak interfacial adhesion between the two phases (Kumar et al., 2010). Furthermore, the addition of PBAT changes the melt rheology increasing the melt processability window (Gu et al., 2008). From a mechanical point of view, PBAT improves the ductility of PLA without compromising, in an evident way, its strength. Until the 2.5 wt.% PBAT content, the ductile fracture of PLA/PBAT binary blends form a compatible system (Yeh et al., 2009).

Glycidyl methacrylate (GMA) grafted polyolefin elastomers (POE) are often used in polyester blends (Hu et al., 1996; Forghani et al., 2018). Consequently, as PLA shows a good chemical functionality (Sun et al., 2011) it can be combined with POE-g-GMA. It has been stated that epoxy groups react with carboxyl or hydroxyl groups of polyesters, the end hydroxyl and/or carboxyl groups of PLA react with epoxy groups of POE-g-GMA via nucleophilic substitution under appropriate extrusion conditions. For this reason, with PLA/POE-g-GMA blends, a large toughening effect can be expected if a *in-situ* copolymer at the interfaces could form during extrusion enabling a good particle matrix adhesion, a good dispersion and a small particles size of the rubbery phase (Su et al., 2009). Therefore, it will be expected that POE-g-GMA could have a significant toughening effect on PLA thanks to the possible reaction that can occur between the epoxy groups of POE-g-GMA and carboxyl end-groups of PLA.

To use the potentiality of these two already elastomers described (PBAT and POE-g-GMA), a compromise has to be found as far as concern concentration, morphology and resulting properties. First of all, it is necessary to conduct a first screening step to set the suitable composition; then an optimization of the best formulation can be made adding a plasticizer that improves the processability, the elongation at break and impact properties at room temperature (Plackett et al., 2003; Quero et al., 2012; Mallegni et al., 2018).

In this work, a detailed study has been conducted, in fact a rheological, thermal, mechanichal and morphological characterization has been carried out on semi-industrial extruded ternary blends of PLA/PBAT/POE-g-GMA. At the best composition, small amounts of two different biodegradable plasticizers [Acetyl Tributyl Citrate (ATBC) (not reactive) and Glycidyl ether (EJ-400, reactive)] were added. A study of the micromechanical deformation processes was carried out on the best ternary blends where the parallel growth

of the impact strength and of the tensile ductility could be observed. In particular, the effect of the plasticizer addition was deeply investigated also through the FT-IR analysis of the chemical bonds formed as a result of mutual interaction. Thanks to the use of a videoextensometer capable to register both axial and trasversal elongation it was possible to register the volume variation and correlate the volume increment to the micormechanichal deformation processes (debonding, cavitation, voids growth...). Also the capability of the plasticized ternary blends to absorb energy at slow rate was investigated by the elasto-plastic fracture mechanics approach based on the ESIS load separation criterion.

MATERIALS AND METHODS

Materials (Chemicals)

The materials used for this work (data taken from technical datasheets) were:

- PLA2003D purchased from NatureWorks (thermoforming and extrusion grade), [melt flow index (MFI): 6 g/10 min (210°C, 2.16 kg), nominal average molar mass: 200,000 g/mol, density: 1.24 g/cm^3]. It contains about 4% of D-lactic acid units to lower the melting point and the crystallization tendency improving the processability during the melting extrusion.
- PBAT: Ecoflex C1200 purchased from BASF. It is a biodegradable, random aliphatic-aromatic copolyester based on the monomers 1.4-butanediol, adipic acid and terephthalic acid, [MFI: 2.7–5 g/10 min (190°C, 2.16 kg), nominal average molar mass: 126,000 g/mol, density 1.26 g/cm^3].
- POE-g-GMA: trade name SOG2, purchased from Fine-blend Compatibilizer Jiangsu Co., Ltd. [MFI: 2–5 g/10 min (190°C, 2.16 kg), nominal average molar mass: 220,000 g/mol, density of 0.88 g/cm^3, and grafted ratio of 0.8–1.2 wt%].
- ATBC from Tecnosintesi S.p.A. was used as not reactive plasticizer. ATBC is prepared by the acetylation of tributylcitrate and it appears as a colorless liquid largely used with PLA (Maiza et al., 2016) [density: 1.05 g/cm^3, molecular weight: 402.5 g/mol].
- Glyether Resin (EJ-400) from Jsi Co., Ltd., was used as reactive plasticizer that it would act both as plasticizer and compatibilizer [density 1.21 g/cm^3, molecular weight: 305 g/eq].

Blends and Specimens' Preparation

Binary and ternary blends with different compositions (**Table 1**), containing as dispersed phases in PLA matrix different amounts of PBAT alone or PBAT and POE-g-GMA, were extruded with a semi-industrial COMAC EBC 25HT twin screw extruder (L/D = 44) to achieve granules of about 2 mm diameter. After the evaluation of the ternary blends containing the best compromise between PLA quantity, biodegradability and mechanical properties, comparing them with pure PLA and

binary blends PLA/PBAT, the effect of the addition of two different plasticizers (ATBC and EJ-400) was evaluated. Before the extrusion, all solid materials were dried in a ventilated oven for at least 24 h. PLA and PBAT were introduced into the main extruder feeder. POE-g-GMA, was fed, separately, from a specific feeder which allows, fixed the weight percentage to be added, a constant concentration in the melt during the extrusion. The plasticizers were introduced by the use of a peristaltic pump (Verderflex–Vantage 3000) suitably calibrated to guarantee a constant flow rate maintaining the fixed plasticizing concentration. During the extrusion, the temperature profile in the zones from 1 to 11 was: 150/180/180/180/185/185/185/185/170/165/150°C, with the die zone at 150°C. The screw rate was 260 rpm. The extruded filaments were cooled in a water bath at room temperature and reduced in pellets by an automatic cutter. All pellets were finally dried in a Piovan DP 604-615 dryer at 60°C.

After the extrusion, pelletized binary and ternary blends were molded using a Megatech H10/18 injection molding machine to obtain dog-bone (Haake Type 3) and parallelepiped Charpy specimens (ISO179). The operative conditions of injection molding process are reported in **Table 2**.

Torque Characterization

An indirect measurement of the viscosity during the extrusion can be obtained through torque measurements. These measures were performed on 6 g of melt pellets by using a MiniLab II

TABLE 1 | Blends name and compositions.

Blend name	Mass composition (%)				
	PLA	PBAT	POE-g-GMA	ATBC	EJ
PLA	100	0	0	0	0
95-5	95	5	0	0	0
90-10	90	10	0	0	0
(95-5)+10POE	85.5	4.5	10	0	0
(95-5)+15POE	80.75	4.25	15	0	0
(95-5)+20POE	76	4	20	0	0
(90-10)+10POE	81	9	10	0	0
(90-10)+15POE	76.5	8.5	15	0	0
(90-10)+20POE	72	8	20	0	0
(90-10-10)+10ATBC	72.9	8.1	9	10	10
(90-10-10)+10EJ	72.9	8.1	9	10	10

TABLE 2 | Injection molding conditions.

	Binary and ternary blends	Plasticized ternary blends
Temperature profile from feeder to the injection zone (°C)	175 / 180 / 185	170 / 165 / 160
Mold Temperature (°C)	50	40
Injection Holding Time (s)	10	15
Cooling Time (s)	10–15	15
Injection Pressure (bar)	100	90

Haake[TM] twin-screw microcompounder, equipped with conical screws, at 180°C and 100 rpm. The extrusion was monitored for 1 min and every 10 s an assessment of the torque value was recorded. The measurements were carried out three times and the average value was reported.

Mechanical Characterization

For tensile and dilatometry tests Haake Type 3 dog-bone tensile bars (width: 5 mm, length: 25 mm, thickness 1.5 mm) were used. Tensile tests were carried out, at room temperature, at a crosshead speed of 10 mm/min on an MTS Criterion model 43 universal tensile testing machine equipped with a 10 kN load cell and interfaced with a computer running MTS Elite Software. Tests were conducted not before 24 h from specimen injection molding. At least ten specimens were tested for each blend and the average values were reported.

Tensile dilatometry tests were also carried out with MTS universal tensile testing machine at a crosshead speed of 10 mm/min. Given the large quantity of blends prepared, dilatometry tests were carried out only for the best compositions. At least five samples for each selected material were tested at room temperature. Transversal and axial specimen elongations were recorded, during tensile test, using a video extensometer (GenieHM1024 Teledyne DALSA camera) interfaced with a computer running ProVis software (Fundamental Video Extensometer); the data in real-time were then transferred to MTS Elite software in order to measure not only the axial and transversal strains but also the load value. The two lateral strain components were assumed to be equal and the volume strain was calculated using the following equation (Lazzeri et al., 2004; Aliotta et al., 2019):

$$\frac{\Delta V}{V_0} = (1 + \varepsilon_1)(1 + \varepsilon_2)^2 - 1 \tag{1}$$

where ΔV is the change in volume, V_0 the original volume, ε_1 the longitudinal (or axial) strain, and ε_2 the lateral strain.

Impact tests were performed on V-notched specimens (width:10 mm, length:80 mm, thickness: 4 mm, V-notch 2 mm at 45°) using a 15 J Charpy pendulum of an Instron CEAST 9050. The standard method ISO179:2000 was followed. For each blend, at least ten specimens, at room temperature, were tested.

Three-point bending tests were carried out, on the best blends, to evaluate the energy accumulated by the sample before the fracture with the already cited MTS universal testing machine. The methodology used to calculate fracture energy at the starting point of crack propagation (J_{Ilim}) follows the ESIS TC4 load separation protocol (Bernal et al., 1996; Baldi et al., 2013). According to this protocol, the tests must to be carried out at 1 mm/min crosshead speed on $80 \times 10 \times 4$ mm SENB specimens cut in two different ways: "*sharp*" (half notched samples) and "*blunt*" (drilled in the center with a 2 mm diameter hole and then cut for half width). The sharp notch (5 mm) was achieved using compressed air during the cutting process to limit the "*notch closing*" material phenomenon due to overheating caused by the cutter. A manual cutter, used as a broaching machine through the rapid entry and exit of the blade from the specimen, was manipulated obtaining a notch without plastic deformation or

heating due to the passage of the blade. A "*sacrificial specimen*" placed under the "*good one*" was used to guarantee a correct notch of the sample without closure (qualitatively evaluated with a "passing" paper) and avoiding plastic deformation around to it. At least five specimens were tested for each selected blends.

The J_{lim} value has been calculated following the Load Separation Criterion (Sharobeam and Landes, 1991). This procedure (Baldi et al., 2010, 2013; Agnelli et al., 2012; Blackman et al., 2015) is based on the construction of the load separation parameter curve, obtained from the load P vs. displacement u in the three-point bending tests. The curves were recorded for the two types of specimens (*sharp* and *blunt*). In the sharp specimens the fracture propagation occurs, whereas in the blunt the crack growth does not occur (only plastic deformation occurs).

The S_{sb} curve (Equation 2) represents the variation of load separation parameter and it is defined as:

$$S_{sb} = \frac{P_s}{P_b}|u_{pl} \tag{2}$$

where s and b indicate the sharp and the blunt notched specimens, respectively. The plastic displacement u_{pl}, instead, is expressed as:

$$u_{pl} = u - P \cdot C_0 \tag{3}$$

where u is the total displacement and C_0 is the initial elastic specimen compliance. Baldi et al. (Baldi et al., 2013; Agnelli et al., 2018) noticed that fracture initiation can be a complex progressive process for ductile polymers, characterized by the slow development of the crack front across the thickness of fracture transition. This limit point represents a pseudo-initiation of fracture. Defined the limit point, the corresponding J_{lim} can be evaluated by Equation 4:

$$J_{lim} = \frac{2 \cdot U_{lim}}{b \cdot (w - a_0)} \tag{4}$$

where U_{lim} is the elastic behavior limit point, b is the sample thickness, w is the sample width and a_0 is the initial crack length.

FT-IR Characterization

ATR spectra were recorded on rectangular Charpy specimens, at room temperature in the 400–4000 cm^{-1} range, by means of a Nicolet 380 FT-IR spectrometer equipped with a smart iTX ATR accessory. The 1700–1800 cm^{-1} range was investigated in details, to evaluate whether a shift of the ester carbonyl stretching absorption peak occurred as a consequence of the addition of POE-g-GMA on 90/10 PLA/PBAT blends and as a consequence of the addition of ATBC and EJ-400 on ternary blends. This behavior would indicate the presence of physical interactions among PLA matrix and the additives.

Thermal Characterization

Thermal properties were investigated by calorimetric analysis using a Q200 TA-Instrument differential scanning calorimeter (DSC) equipped with a RSC cooling system. Nitrogen, set at 50 mL/min, was used as purge gas for all measurements. Indium was adopted as a standard for temperature and enthalpy

calibration of DSC. The materials used for DSC analysis were cut from the dog-bone injection molding specimens. The sampling was carried out exactly in the same region of the injection molded specimens to avoid differences ascribable to different cooling rates in the specimen thickness. Aluminum pans with samples were sealed before measurement and the mass of the samples used varied between 10 and 15 mg. The samples were heated from room temperature at 10°C/min to 200°C under a nitrogen atmosphere and held for 5 min to remove the previous thermal history. Then, the samples were cooled at 10°C/min to −50°C and held for 5 min then they were heated again at 10°C/min to 200°C to record the crystallization and melting behaviors.

Melting temperature (T_m) and the cold crystallization temperature (T_{cc}) of the blends were recorded at the maximum of the melting peak and at the minimum of the cold crystallization peak, respectively. The enthalpies of melting (ΔH_m) and cold crystallization (ΔH_{cc}) were determined from the corresponding peak areas in the second heating thermograms. The crystallinity percentage (X_{cc}) of PLA and its blends was calculated as follows:

$$X_{cc(PLA)} = \frac{\Delta H_{m(PLA)} - \Delta H_{cc(PLA)}}{\Delta H^{\circ}_{m(PLA)} wt._{PLA}} \cdot 100 \qquad (5)$$

where $\Delta H_{m(PLA)}$ is the melting enthalpy of PLA, $\Delta H_{cc(PLA)}$ is the cold crystallization enthalpy of PLA, and $\Delta H^{\circ}_{m(PLA)}$ is the melting enthalpy of 100% crystalline PLA that is 93 J/g (Wang et al., 2018), $wt._{(PLA)}$ is the weight fraction of PLA in the blends.

Morphological Characterization

In order to investigate the morphology of the best ternary systems, the cryogenic fractured cross-sections of the Charpy samples were analyzed, after gold sputtering, by a FEI Quanta 450 FEG scanning electron microscope (SEM) (magnifications 4000x for **Figure 3** and 500x for **Figure 9**) equipped with a Large Field Detector for low kV imaging simultaneous secondary electron (SE).

The fracture surface of specimens broken during tensile test offers the best reliable information about the deformation mechanism. Consequently, to study and to better clarify the micromechanics deformation, after the tensile test some specimens have been cold fractured along the tensile direction. The specimens were coated, by using a sputter coater Edward S150B, with a thin layer of gold prior to microscopy to avoid charge build up.

RESULTS AND DISCUSSION

First Screening on Binary and Ternary Blends

The first methods used to evaluate the feasibility of ternary blends composition were the uniaxial static tensile test and the Charpy impact test. A comparison between ternary PLA/PBAT/POE-g-GMA ternary blends and pure PLA and PLA/PBAT binary blends was carried out. The basis from which this work started (a binary blend with 5 and 10% of PBAT dispersed into the PLA matrix) was substantiated by a double reason: not increase the

petro-quantity, although biodegradable, of the entire formulation and to evaluate the processes of toughening and increase of ductility with the addition of the two elastomers but always within a continuous PLA matrix. The addition of POE-g-GMA was of 10, 15, and 20 wt.% on the two starting binary blends (readjusting the formulations in such a way that the mass composition can be 100%).

For the ternary blends, the results of tensile tests (**Table 3** and **Figure 1**) showed a decrement of Young's modulus increasing the rubber content. Despite of the elastomer addition, the elongation at break increases only slightly, and the ternary blends did not show a yielding point (as the pure PLA and the binary blends did). It is clear that 10 wt.%. of PBAT guarantees a substantial improvement in the elongation at break, which is lost with the addition of the third phase. However, the effect of POE-g-GMA is evident analyzing the **Figure 1D** in which 10 wt.% of polyolefin elastomer addition guarantees a Charpy impact strength value almost tripled compared to pure PLA and binary blends. This improvement in the Charpy Impact Resistance is remarkable if compared also to other binary PLA-PBAT systems reported in literature (Zhang et al., 2009).

The mechanical results indicate that these ternary blends show dissimilar deformation mechanisms when the loading conditions change (for example in tensile and impact tests). Tensile tests, indeed, are carried at slow rate while impact tests at higher rate (Zhang et al., 2014).

The torque trends of the pure materials (PLA, PBAT, and POE-g-GMA) and of the ternary blends are showed in **Figure 2**, in order to assess and study the melt strength during the extrusion. It can be observed that PLA showed a melt strength double respect to that of the materials used as dispersed phase. PBAT and POE-g-GMA were characterized by comparable torques, and consequently their processability was similar. For the (95-5) based ternary blends not significant torque changes were encountered increasing the POE-g-GMA content. On the other hand, for the (90-10) based ternary blends, viscosity decreases increasing the POE-g-GMA content, as previously reported for similar cases (Signori et al., 2009).

Figure 3A reports a SEM image of the (90-10)+10POE blend in which irregular platelets of POE-g-GMA and spherical particles of PBAT are dispersed separately into the PLA matrix. For ternary systems, in which there are two dispersed phases in a continuous matrix, like the systems studied in this work, two distinct types of phase morphology can be encountered. Dekkers et al. (1991) stated that one situation can be characterized by two dispersed phases in which one is encapsulated in the other (core–shell morphology). Alternatively, the two phases are dispersed separately into the matrix (Dekkers et al., 1991). The mechanical properties and the rheology of ternary blends are significantly affected by their morphology (Luzinov et al., 1999; Xue et al., 2018). Furthermore, it is important to underline which factors affect the phase structure of multicomponent blends. Viscosity of components [in linear proportionality with the torque (Gupta and Srinivasan, 1993)], composition and interfacial interaction between phases are the main factors that influence the morphology of ternary polymer blends (Utracki and Shi, 1992).

TABLE 3 | Mechanical results of tensile tests with experimental deviation.

Blend name	Elastic modulus (GPa)	Stress at break (MPa)	Elongation at break (%)	Yield stress (MPa)	Elongation at yield (%)	Charpy impact resistance (kJ/m²)
PLA	3.2 ± 0.09	55.0 ± 1.00	2.5 ± 0.30	/	/	3.0 ± 0.31
95-5	3.1 ± 0.22	20.1 ± 1.22	6.4 ± 0.71	58.6 ± 2.10	4.6 ± 0.25	3.3 ± 0.23
90-10	2.7 ± 0.05	24.5 ± 0.75	12.4 ± 2.60	54.1 ± 1.80	4.8 ± 0.18	3.4 ± 0.10
(95-5)+10POE	2.8 ± 0.07	37.4 ± 2.09	4.4 ± 0.21	/	/	6.7 ± 1.01
(95-5)+15POE	2.5 ± 0.05	32.4 ± 0.87	3.9 ± 0.08	/	/	6.8 ± 0.61
(95-5)+20POE	2.1 ± 0.23	27.7 ± 0.19	4.5 ± 0.19	/	/	6.9 ± 0.92
(90-10)+10POE	2.1 ± 0.17	34.6 ± 1.03	4.4 ± 0.11	/	/	7.2 ± 0.93
(90-10)+15POE	2.1 ± 0.03	31.2 ± 1.69	4.4 ± 0.19	/	/	7.2 ± 0.94
(90-10)+20POE	1.6 ± 0.14	27.0 ± 0.13	4.4 ± 0.13	/	/	7.3 ± 0.44
(90-10-10)+10ATBC	1.2 ± 0.10	15.5 ± 0.70	13.8 ± 0.70	21.7 ± 0.91	4.5 ± 0.21	7.5 ± 0.15
(90-10-10)+10EJ	1.5 ± 0.22	18.9 ± 1.85	8.0 ± 0.90	22.8 ± 0.79	4.3 ± 0.79	9.1 ± 0.81

FIGURE 1 | Mechanical properties for PLA, binary blends and ternary blends: **(A)** Elastic Modulus; **(B)** Stress at break; **(C)** Elongation at break (%); **(D)** Charpy Impact Resistance.
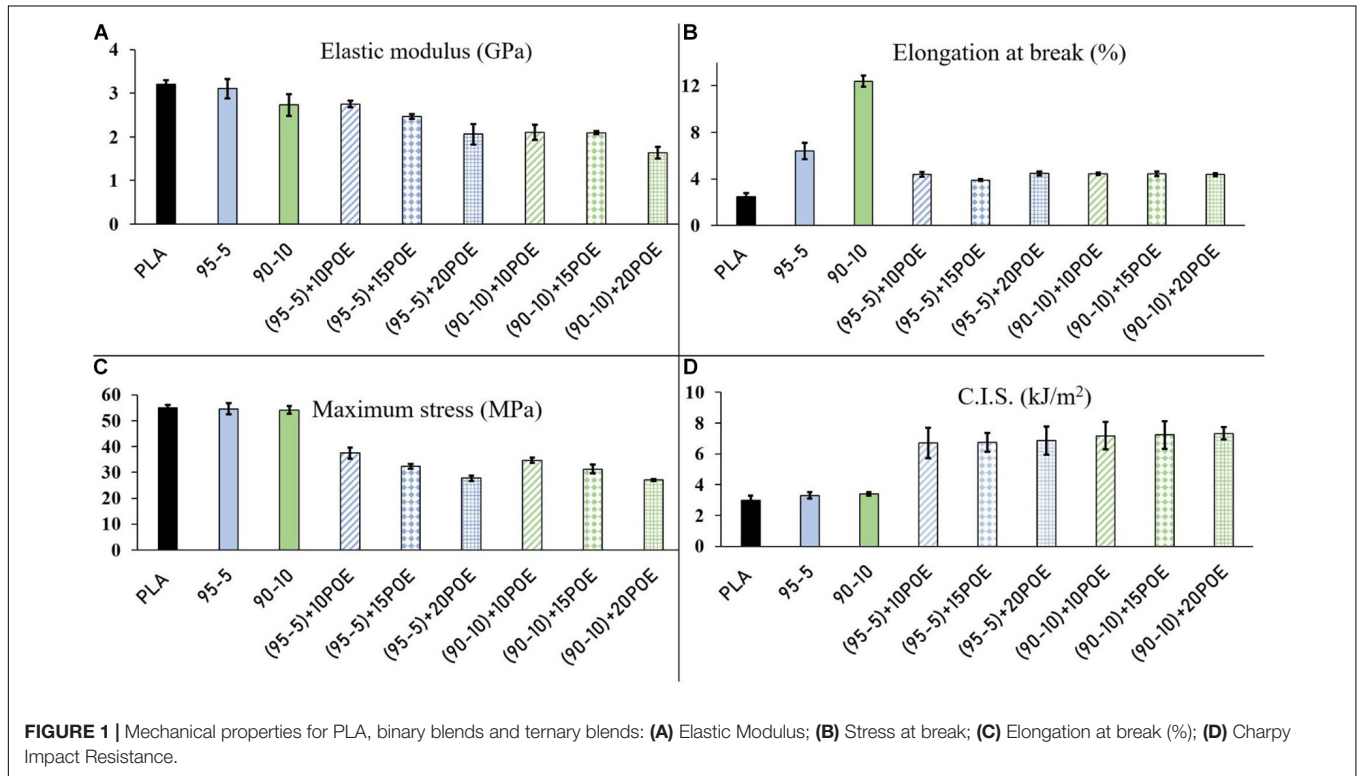
The effect of interfacial tension between phases on the morphology for a ternary system (in which A is the continuous phase and B and C are the dispersed phases) can be evaluated by the spreading coefficient (λ_{BC} of the B-phase on the C-phase) defined as (Hemmati et al., 2001):

$$\lambda_{BC} = \gamma_{AC} - \gamma_{AB} - \gamma_{BC} \qquad (6)$$

where γ_x are the interfacial tension for each component pair. If λ_{BC} is positive, the B-phase will encapsulate the C-phase. Similarly, for λ_{CB} the equation will be:

$$\lambda_{CB} = \gamma_{AB} - \gamma_{AC} - \gamma_{BC} \qquad (7)$$

A core–shell morphology is characterized by a positive value of λ_{CB}; the C-phase will encapsulate the B-phase. On the other hand, both negative lambda values will return a dispersed system where the B and C phases are separated in the matrix. **Table 4** reports the lambda results for the ternary systems analyzed. The values of interfacial tensions were taken from literature (Wu, 1985; Nofar et al., 2015). It can be observed that both λ_{BC} and λ_{CB} are negative. This result means that PBAT and POE-g-GMA form two distinct dispersed phases in the PLA matrix. This morphology was indeed verified by SEM analysis (**Figure 3**).

Differential scanning calorimeter heating curves of PLA, PBAT, POE-g-GMA and ternary blends after crystallizing from melt are shown in **Figure 4**. The thermal properties of PLA and PBAT correspond to what is reported in literature (Cao et al., 2003; Al-Itry et al., 2012). PLA shows a glass transition temperature around 60°C, a cold crystallization temperature

FIGURE 2 | Torque trends for pure polymers and differences with ternary blends.

FIGURE 3 | SEM micrographs of plasticized ternary blends in comparison with (90-10)+10POE: **(A)** (90-10)+10POE; **(B)** (90-10-10)+10ATBC; **(C)** (90-10-10)+10EJ.
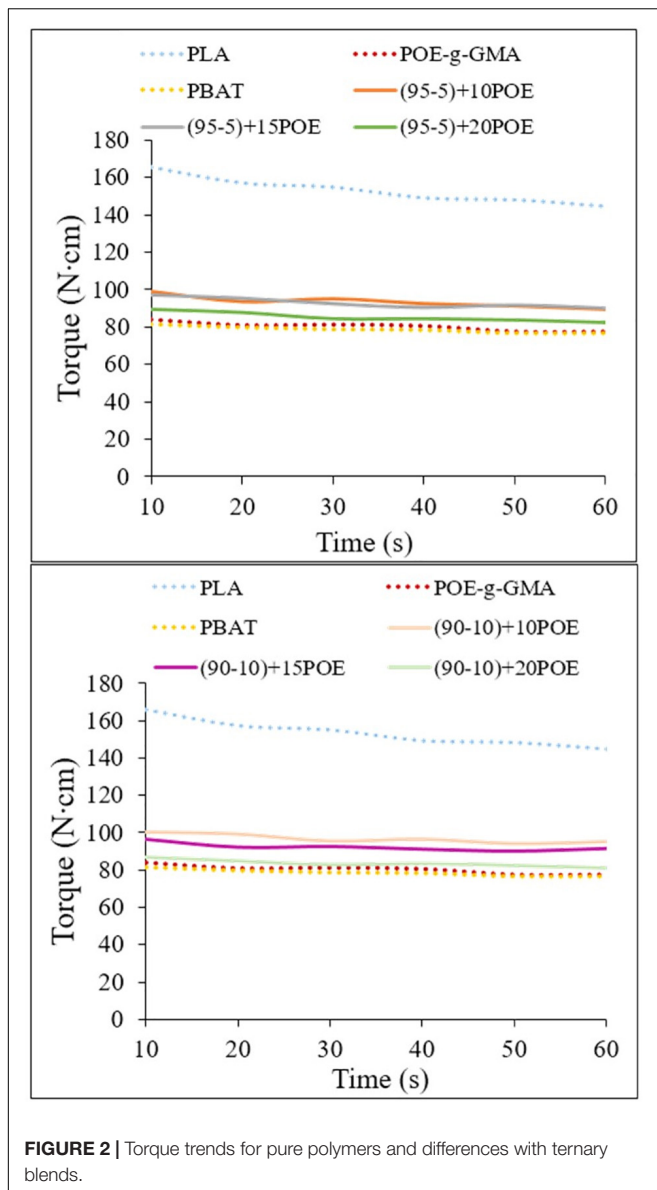
around 110°C and melting temperature around 150°C. The crystallization rate of PLA due to the presence of D-units is very low and, consequently, also the crystallinity content that it is around 3%. Concerning neat PBAT, its second heating scan showed a glass transition centered at around −35°C and a broad melting peak around 120°C consistent to what can be found in literature (Kumar et al., 2010).

In the thermogram of POE-g-GMA the glass transition temperature is not visible, according to datasheet and literature (Su et al., 2009) it must occur around −40°C. Two melting peaks are present in the POE-g-GMA thermogram. One melting peak at around 60°C degree that it is related to grafted polyethylene octane and another melting peak in correspondence of 160°C that it is typical of polypropylene. This melting behavior is typical of polyethylene octane rubber in which also traces of polypropylene are present (Svoboda et al., 2010).
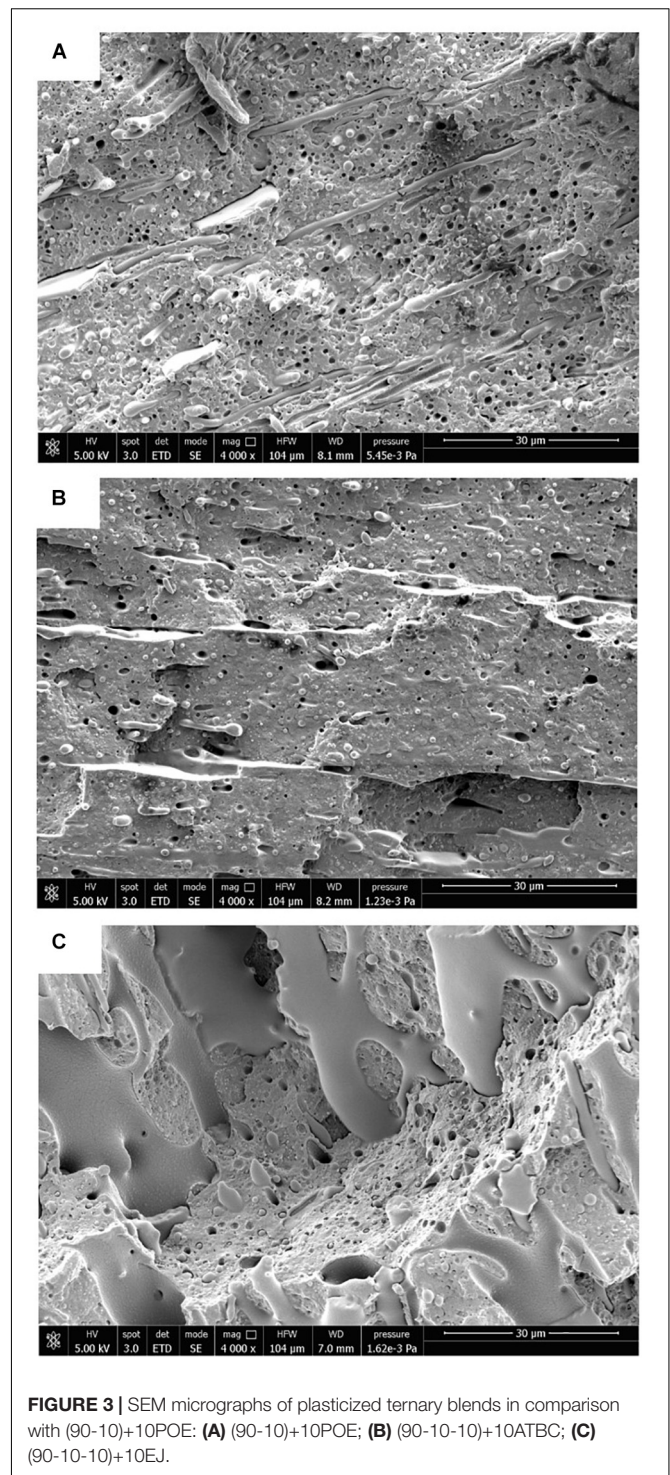
Analyzing the ternary blends, it can be observed that increasing the content of POE-g-GMA, it does not affect either the glass transition or the melting peak. The cold crystallization temperature and the melting temperature of PLA decrease with the addition of PBAT and POE-g-GMA. It can be observed that in all ternary blends there is a large cold crystallization exothermal peak, the area of which is similar to that of the

TABLE 4 | Spreading coefficient and interfacial interaction for the PLA / PBAT/ POE-g-GMA system.

Material name	γ (180°C)	γ_p (180°C) (mN/m)	γ_d (180°C) (mN/m)	γ_{AB} (180°C) (mN/m)	γ_{AC} (180°C) (mN/m)	γ_{BC} (180°C) (mN/m)	λ_{CB} (mN/m)	λ_{BC} (mN/m)
A (PLA)	43	11.5	31.5	0.4	6.9	8.7	−15.26	−2.16
B (PBAT)	46	10	36					
C (POE-g-GMA)	30.7	8.6	22.1					
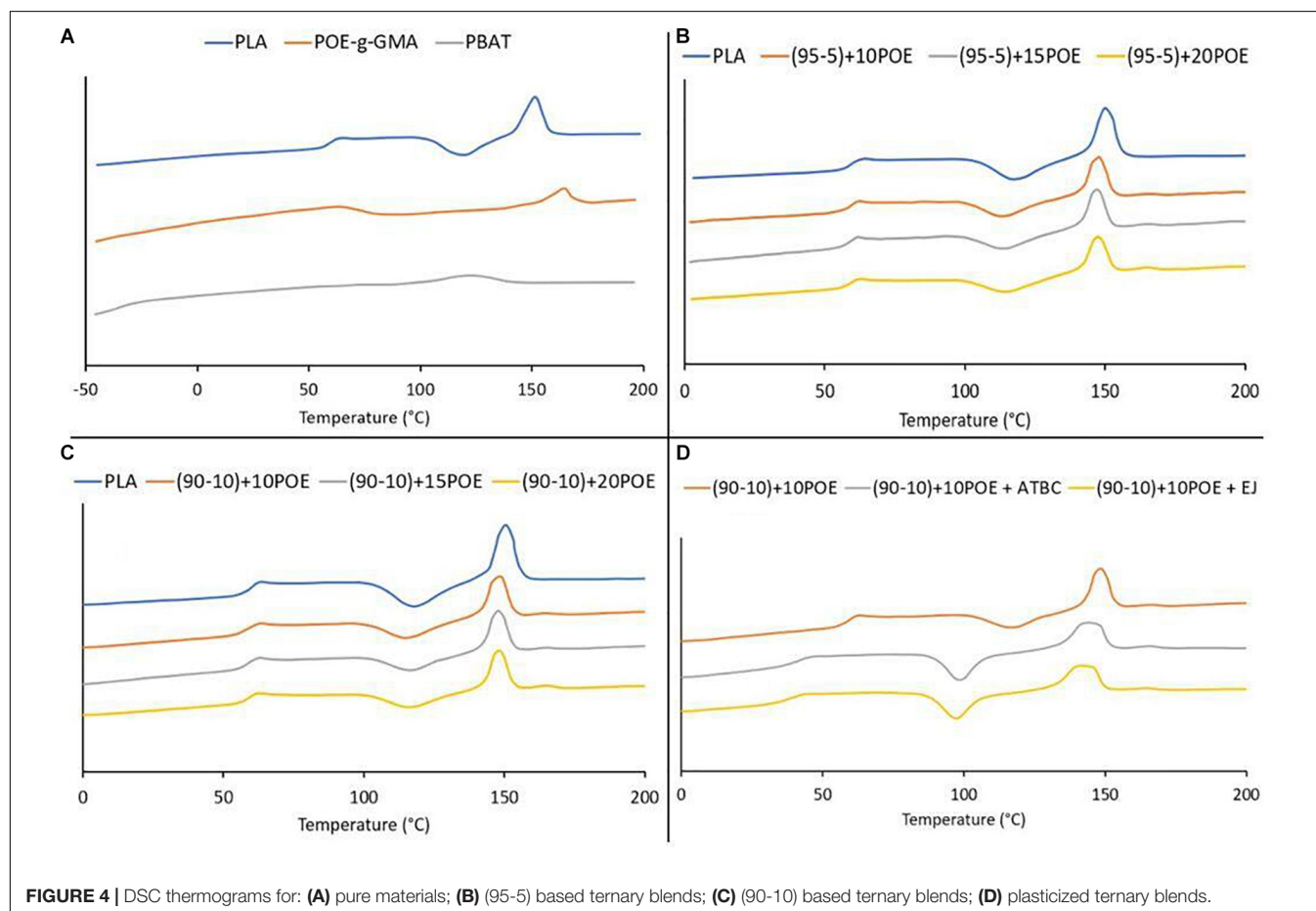
FIGURE 4 | DSC thermograms for: **(A)** pure materials; **(B)** (95-5) based ternary blends; **(C)** (90-10) based ternary blends; **(D)** plasticized ternary blends.

melting endotherm peak; this suggests that the PLA is almost in the amorphous state (Ishida et al., 2009) as confirmed by the PLA crystallinity content percentage reported in **Table 5**. However, the addition of PBAT and POE-g-GMA enables the crystallization ability of PLA encouraging the mobility of PLA molecular chains; as a consequence a slightly increase in the PLA crystallinity content is registered (Jiang et al., 2006; Arruda et al., 2015; Wang et al., 2018).

A second melting peak due to the presence of the polypropylene in POE-g-GMA is observed for all ternary blends; increasing the POE-g-GMA content this secondary peak is more pronounced.

Effect of Plasticizers on Ternary Blends

On the basis of the mechanical and thermal results showed in the previous section, it emerged that the ternary blend (90-10)+10POE can be chosen as starting point for the final

formulation. The choice is justified because it has a high impact resistance value (around 7.2 kJ/m^2), not losing significantly in stiffness and strength at break. In addition, the starting composition (81% wt. PLA, 9% wt. PBAT, 10% wt. POE-g-GMA) allows to remain within the definition of biodegradable material, an important feature for the possible exploitation of this formulation in different sectors. More specifically, this formulation contains a not so high quantity of not biodegradable POE-g-GMA, and the EN 13432 standard is respected.

Nevertheless, in order to further increase the polymers mobility, connected to the improvement of elongation at break without losing the achieved impact resistance, two different types of plasticizers were added (at 10 wt.%) to the (90-10)+10POE formulation. The chosen quantity (10 wt.%) of plasticizer would provide a good balance of the final mechanical properties (good elongation at break and at the same time would likely improve Charpy impact resistance) (Baiardo et al., 2003).

TABLE 5 | Main thermal properties taken from DSC second run for samples heated at 10°C/min.

Blend Name	T_g (°C)	T_{cc} (°C)	$T_{m,peak1}$ (°C)	$T_{m,peak2}$ (°C)	$\Delta H_{m,peak1}$ (J/g)	ΔH_{cc} (J/g)	X_{cc} (%)
PLA	62	118	151	/	23.1	19.9	3.4
PBAT	−36	/	124	/	12.9	/	/
POE-g-GMA	/	/	61	164	27.1	/	/
(95-5)+10POE	61	113	147	/	18.2	12.5	7.2
(95-5)+15POE	61	114	147	164	16.7	10.6	8.2
(95-5)+20POE	61	114	147	165	16.7	10.6	8.6
(90-10)+10POE	61	116	148	166	17.0	13.2	5.1
(90-10)+15POE	61	117	148	166	15.5	10.8	6.7
(90-10)+20POE	61	117	148	166	15.5	9.9	8.4
(90-10-10)+10ATBC	43	98	142	165	17.7	14.7	4.6
(90-10-10)+10EJ	45	99	142	167	17.0	13.7	5.1

When a liquid plasticizer is added, a torque decrement is recorded due to the decrease of melt viscosity (Coltelli et al., 2008). This behavior was confirmed for the plasticized ternary blends for which a torque decrement (below the torque value of the pure rubbers) was registered (**Figure 5**). These results are related to the lubricating effect and enhanced chain mobility that the addition of plasticizers does (Alias and Ismail, 2019). This viscosity decrement was also reflected in the processing conditions: the extrusion temperature profile was decreased of 5°C and also the injection temperature profile was decreased (**Table 2**).

The mechanical tests of the plasticized ternary blend showed very interesting results (**Figure 6** and **Table 3**). In addition to the expected increase in elongation at break, a further increment of Charpy Impact Strength was achieved with the addition of plasticizers. Furthermore, in the tensile tests, a more ductile stress-strain curve was recorded and the materials showed a yielding behavior that was not present in the previous ternary blends. On the other hand, as it can be expected, the plasticizer addition reduces the Elastic Modulus of the final material.

The mechanical results showed that EJ-400 reached the best compromise in terms of mechanical properties providing the highest value of Charpy impact resistance (9.1 kJ/m^2), a good value of elongation at break (around 8%) and an acceptable decrement of the Elastic Modulus, thus making this formulation functional for injection molded objects having a good stiffness without losing the flexibility.

To evaluate and deeply understand the effective toughness enhancement of the plasticized ternary blends, the elasto-plastic fracture mechanics approach has been applied to evaluate the J_{Ilim} value (energy absorbed at the moment of the crack

FIGURE 5 | Torque trend for plasticized ternary blends.
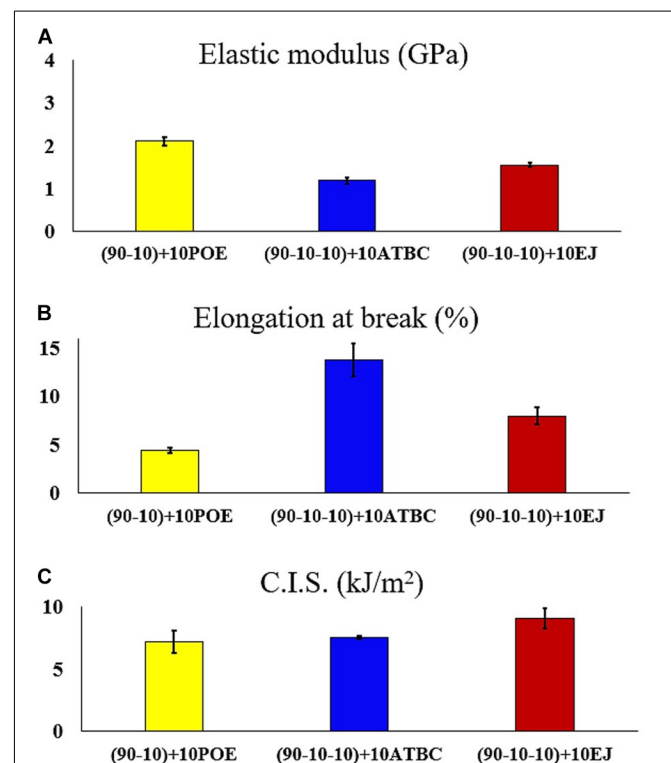
FIGURE 6 | Mechanical properties for plasticized ternary blends: **(A)** Elastic Modulus; **(B)** Elongation at break; **(C)** Charpy Impact Resistance.

propagation during a slow-rate test) and the results are reported in **Figure 7**. For all ternary systems a good J_{Ilim} value was obtained. This value, is very high if compared to the "brittle" G value of PLA found in literature [2.97 kJ/m^2 (Nascimento et al., 2010; Todo and Takayam, 2012)] and also if compared to PLA/PBAT binary blends with 10 wt.% of PBAT (6.5 kJ/m^2 Gigante et al., 2019). The fracture energy released at the beginning of the crack propagation is very impressive both for the plasticized blends and the (90-10)+10POE blend. However, the best J_{Ilim} value (13.6 kJ/m^2) was registered for the blend containing EJ-400 in accordance with the results obtained from quasi-static tensile tests. The improvement in toughness seems to be correlated to the presence of the reactive plasticized system (EJ-400) that would compatibilise the rubber domains within the PLA matrix. This behavior can be explained stating that the epoxy groups of this reactive plasticizer, going to bind with the hydroxyl groups of the PLA, developing a structure that allows the improvement of the ductility of the final blend. The decreasing of energy absorbed from slow rate three-point bending test (1 mm/min) to impact test (4.08 m/s) even if not

so evident, is well known in literature (Bucknall et al., 2000; Inberg et al., 2002).

In order to correlate the toughening mechanism to morphology, mechanical results and micromechanical deformation mechanism, dilatometric tests were carried out on these blends. Data of volume change (calculated according
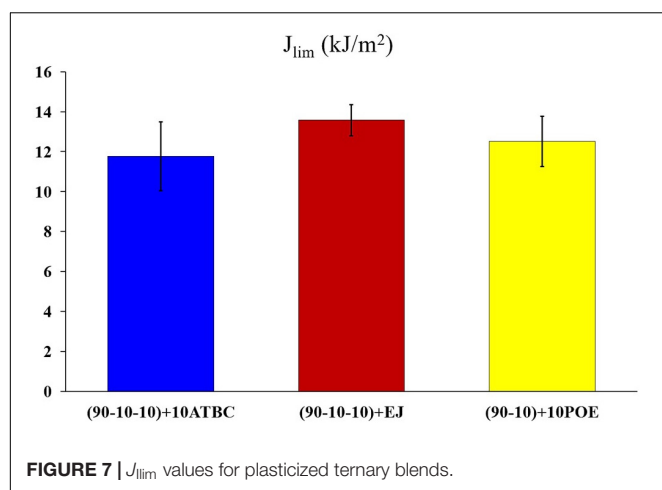
FIGURE 7 | J_{Ilim} values for plasticized ternary blends.
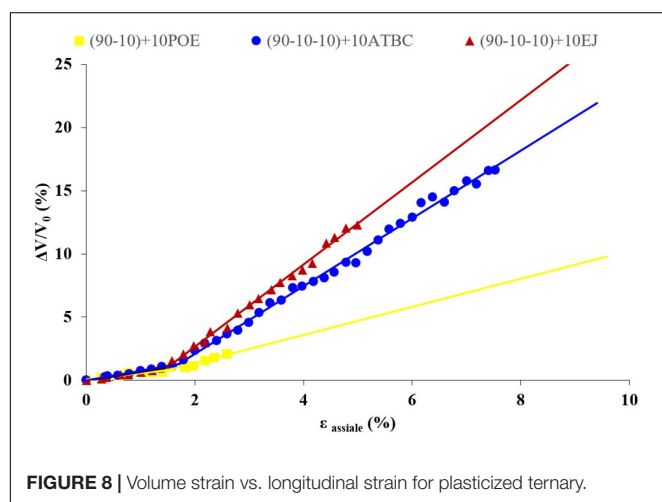
FIGURE 8 | Volume strain vs. longitudinal strain for plasticized ternary.
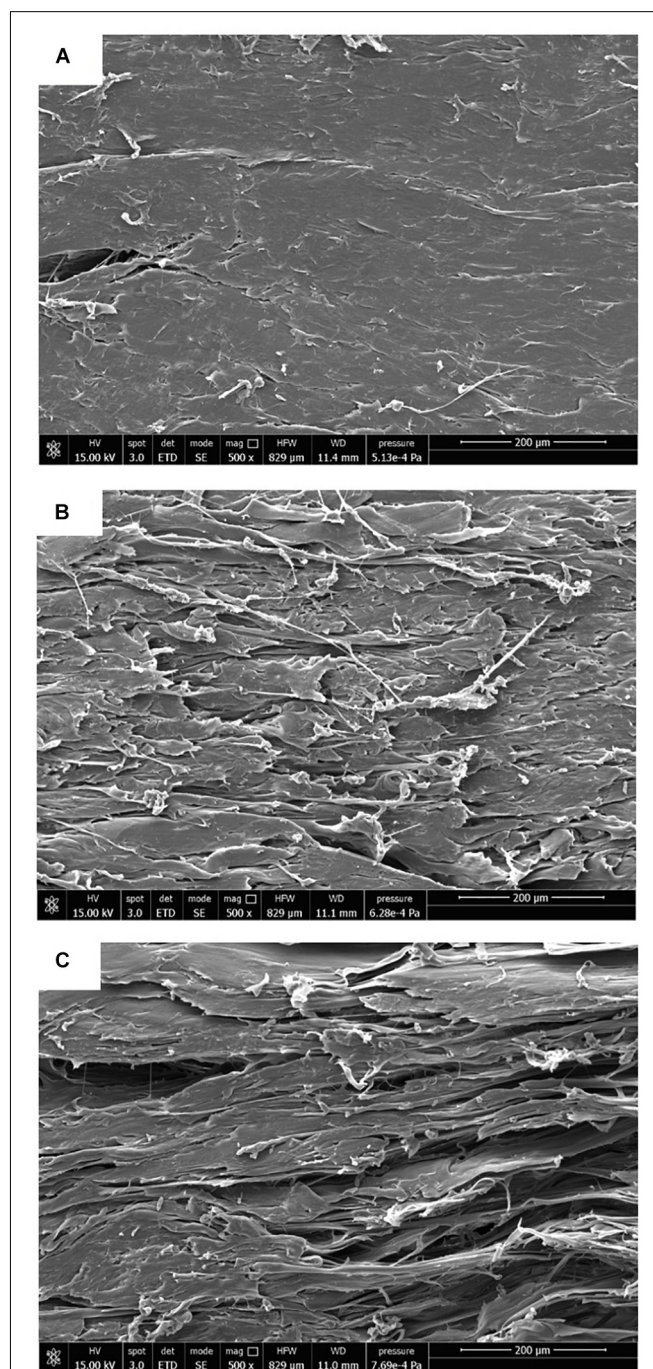
FIGURE 9 | SEM micrographs at the surface of the tensile specimen cryo-fractured along the draw direction for: **(A)** (90-10)+10POE; **(B)** (90-10-10)+10ATBC; **(C)** (90-10-10)+10EJ.

to Equation 1) during tensile tests are shown in **Figure 8** as a function of axial elongation percentage. For the unplasticized (90-10)+10POE ternary system it was not possible to collect data for axial elongation higher than 3% due to the breakage of the specimens.

For the three systems analyzed, different extents of volume increase with increasing of the specimen elongation can be observed. The blend containing EJ-400 exhibits the highest volume increase that it is maintained over the whole range of elongation explored. The blend with ATBC show a similar trend but with a minor volume increment with the axial elongation. These results indicate that the presence of plasticizers in the blend favored dilatation processes that can be related to different micromechanical mechanisms (matrix crazing, debonding of secondary phase particles and cavitation of rubber particles) (Yokoyama and Ricco, 1998). Three different steps are involved during the deformation of rubber-toughened polymers: elastic deformation, plastic strain softening, and strain hardening in yielding zone. Due to stress concentrations around rubber particles, they started to deform and induce cavitation (Alias and Ismail, 2019). The dominant mechanism of micromechanical deformation varies and it is influenced by the chemical structure deformation, the composition of the matrix material, and also by the test temperature, the strain rate and the morphology (shape and size of the rubber particles) (Michler and Bucknall, 2001; Li and Shimizu, 2009).

The point in which the slope change occurs in the volume strain curves (**Figure 8**), detects the longitudinal elongation value for which the cavitation takes place. It can be deduced that the cavitation mechanism starts before the yield point (that for both plasticized ternary blend it is registered around 4% of axial elongation), this behavior was found in literature for other rubber toughened systems (Borggreve and Gaymans, 1988; Lazzeri and Bucknall, 1993, 1995; Yokoyama and Ricco, 1998). At low rates, the volume strain-behavior of the ternary systems analyzed appears to be not so different. The greater difference between the ternary system can be observed at higher rates for which the accelerated voiding process is evident for the plasticized ternary systems. In particular, the ternary blend containing EJ-400 seems

to have a more accelerated voiding process. To better understand the data obtained, SEM micrographs at the surface of the specimens, after the uniaxial tensile test, cryo-fractured along the tensile direction were carried out (**Figure 9**). First of all, it can be observed that, differently from the unplasticized ternary blends, many big voids, elongated along the tensile direction, are present. A greater and more extensive voids quantity can be seen for the ternary blend containing EJ-400. This result is in accordance with the dilatometric results for which is higher the slope of the volume strain curve. Also the mechanical results are in accordance. In fact, the Charpy impact resistance is higher for the EJ-400 blend but the elongation at break is lower than the ATBC blend. This is due to the fact that an excessive quantity of void reduces the load bearing section of the sample during the tensile test, triggering a premature specimen breakage.

It has been demonstrated in literature, that EJ-400 is an efficient plasticizer for PLA/rubber systems able to improve the blend compatibility (Mallegni et al., 2018). From the SEM micrographs of (90-10)+10POE ternary blends (**Figure 3**), it can be observed that a more homogeneous dispersed distribution of rubber domains inside the PLA matrix occurred. On the other hand, weak adhesion between the rubber domains and the PLA matrix can be observed for the unplasticized ternary blend.

The thermograms of plasticized ternary blends (shown in **Figure 4D**) exhibits also in this case three main transitions: glass transition, cold crystallization exotherm and melting endotherm. The measured value with relative enthalpies are summarized in **Table 5**. The effect of the plasticizer addition seems not depend from the type of plasticizer used. It is well-known that the plasticizers lower the glass transition temperature (Baiardo et al., 2003). A marked decrement of T_g can be observed for the plasticized ternary blends. This phenomenon influenced the injection molding conditions in fact the mold temperature, set in proximity of T_g, passed from 50°C to 40°C. The incorporation of plasticizers also decreased the cold crystallization temperature by approximately 20°C. However, the addition of POE-g-GMA and also of plasticizers restricts the crystalline ability of PLA as it can be observed from the crystallinity percentage value
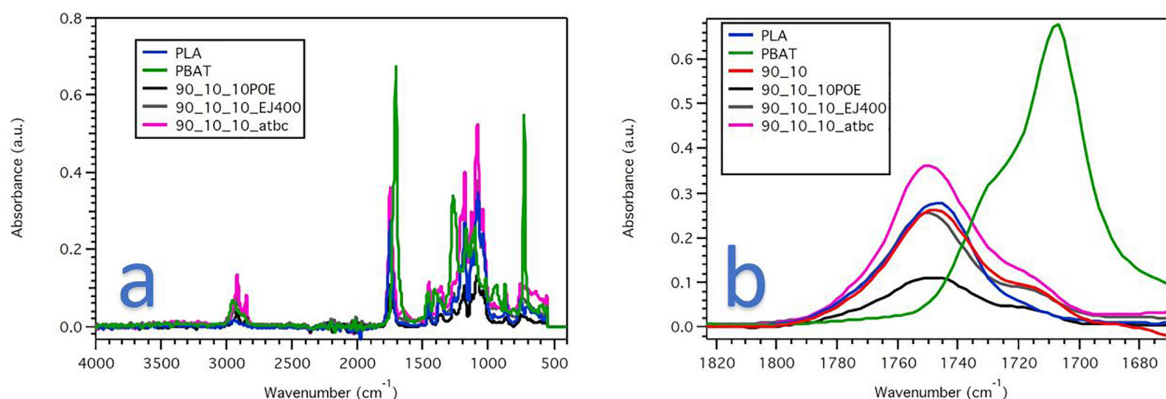
FIGURE 10 | (A) ATR spectra of binary and ternary blends and **(B)** detail of the 1700–1800 cm^{-1} range.

of plasticized ternary compared to the unplasticized one. This behavior was found in literature for a similar system (Zhao et al., 2015). A multiple melting behavior, typical of PLA (Di Lorenzo, 2006; AAliotta et al., 2017) appears for the plasticized blends. This behavior was induced by the presence of plasticizer during the melting process when the unperfected crystals had sufficient time to melt and reorganize into perfect crystals and re-melt at higher temperature (Zhao et al., 2015).

FT-IR spectra of PLA and PBAT were compared to those of the 90/10 blends, containing POE and ATBC or EJ400 (**Figure 10A**). Among other, a strong absorbance peak was detected in the 1700–1800 wavenumber range, attributable to the carbonyl ester C = O stretching of polyesters, both in main chain (PLA and PBAT) as well as in side chains (POE). Noteworthy, the detail of the 1700–1800 wavenumber range (**Figure 10B**) showed a slight shift toward higher wavenumber (1747 cm^{-1}) as a consequence of introduction of POE with respect to pure PLA (1743 cm^{-1}) in 90/10 blends. Remarkably, the introduction of ATBC or EJ400 in 90/10/10 blends further shifted the carbonyl stretching shift to 1751 cm^{-1} (**Figure 10B**). These behaviors suggest that slightly different average dipole distribution around the carbonyl ester groups in PLA occurred as a consequences of the introduction of POE and ATBC or POE and EJ400, confirming the interaction of the PLA matrix with the additives.

CONCLUSIONS

In this study a multiphase ternary system, with two different types of elastomers (PBAT and POE-g-GMA) added in different amounts into a PLA matrix, was investigated and compared with PLA and PLA/PBAT binary blends with maximum 10% wt. of PBAT. The purpose of the present work was to find a compromise in the use of both elastomers (PBAT and POE-g-GMA) as dispersed phases into a PLA matrix to improve impact resistance of PLA using a ternary blend approach without compromising the end of life biodegradability (following the EN 13432 standard). This idea was developed studying many papers in which PBAT caused an improvement in tensile flexibility via direct melt blending with PLA, while POE-g-GMA can increase impact properties.

The work was characterized by a first step in which PLA/PBAT and POE-g-GMA ternary blends were extruded and compared, from the mechanical and thermal point of view, with PLA and binary blends PLA-PBAT. Thanks to an analytical study based on interfacial tensions and morphological considerations, in this screening phase it was found that the two rubber phases stay separated and dispersed in the PLA matrix, evidence confirmed

also by SEM analysis. Very good impact properties were achieved for these ternary systems, however, the elongation at break under uniaxial tensile test was not adequate. As a consequence, to the best ternary blend (81 wt.% PLA, 9 wt.% PBAT, and 10 wt.% POE-g-GMA) the effect of plasticizer addition in small amount (10 wt.%) was investigated. Two types of plasticizers were selected: one reactive (EJ-400) and one not reactive (ATBC). Dilatometric tests and the elasto-plastic fracture mechanics were analyzed to clarify the toughening mechanism and also to correlate it with the blends morphology.

It has been demonstrated that the reactive plasticizer EJ-400, improving the compatibility of the rubber domains into the PLA matrix, is a more effective plasticizer. A good balance of tensile results and impact resistance was achieved and confirmed by the J_{Ilim} value and volume strain curves. The best formulation, with the addition of EJ-400, guarantees a useful compromise in terms of mechanical properties providing the highest value of Charpy impact resistance (9.1 kJ/m^2), a good value of elongation at break (around 8%) and an acceptable decrement of the Elastic Modulus with respect to pure PLA and binary blends, making this formulation functional for injection molded PLA based objects and issues that need biodegradability approval, acceptable thermal properties, wide processability window, a good stiffness and, above all, high impact properties (given by a small amount of POE-g-GMA) without losing in terms of elongational flexibility, typical of PBAT.

DATA AVAILABILITY STATEMENT

The original contributions presented in the study are included in the article/supplementary material, further inquiries can be directed to the corresponding author.

AUTHOR CONTRIBUTIONS

LA and VG performed the experimental work and wrote the original draft of the manuscript. AL supervised the study results, the discussion and revised the manuscript. OA contributed to the experimental results. FS performed FT-IR analysis and contributed to the discussion.

ACKNOWLEDGMENTS

REFERENCES

Agnelli, S., Baldi, F., Castellani, L., Pisoni, K., Vighi, M., and Laiarinandrasana, L. (2018). Study of the plastic deformation behaviour of ductile polymers: use of the material key curves. *Mech. Mater.* 117, 105–115. doi: 10.1016/j.mechmat. 2017.11.002

Agnelli, S., Baldi, F., and Riccò, T. (2012). A tentative application of the energy separation principle to the determination of the fracture resistance (JIc) of rubbers. *Eng. Fract. Mech.* 90, 76–88. doi: 10.1016/j.engfracmech.2012.04.020

Alias, N. F., and Ismail, H. (2019). An overview of toughening polylactic acid by an elastomer. *Polym. Technol. Mater.* 58, 1399–1422. doi: 10.1080/25740881.2018. 1563118

Aliotta, L., Cinelli, P., Coltelli, M. B., and Lazzeri, A. (2019). Rigid filler toughening in PLA-Calcium Carbonate composites: effect of particle surface treatment and matrix plasticization. *Eur. Polym. J.* 113, 78–88. doi: 10.1016/j.eurpolymj.2018.12.042

Aliotta, L., Cinelli, P., Coltelli, M. B., Righetti, M. C., Gazzano, M., and Lazzeri, A. (2017). Effect of nucleating agents on crystallinity and properties of poly (lactic acid) (PLA). *Eur. Polym. J.* 93, 822–832. doi: 10.1016/j.eurpolymj.2017.04.041

Al-Itry, R., Lamnawar, K., and Maazouz, A. (2012). Improvement of thermal stability, rheological and mechanical properties of PLA. PBAT and their blends by reactive extrusion with functionalized epoxy. *Polym. Degrad. Stab.* 97, 1898–1914. doi: 10.1016/j.polymdegradstab.2012.06.028

Anderson, K. S., and Hillmyer, M. A. (2004). The influence of block copolymer microstructure on the toughness of compatibilized polylactide/polyethylene blends. *Polymer* 45, 8809–8823. doi: 10.1016/j.polymer.2004.10.047

Anderson, K. S., Schreck, K. M., and Hillmyer, M. A. (2008). Toughening Polylactide. *Polym. Rev.* 48, 85–108. doi: 10.1080/15583720701834216

Arruda, L. C., Magaton, M., Bretas, R. E. S., and Ueki, M. M. (2015). Influence of chain extender on mechanical, thermal and morphological properties of blown films of PLA/PBAT blends. *Polym. Test.* 43, 27–37. doi: 10.1016/j.polymertesting.2015.02.005

Baiardo, M., Frisoni, G., Scandola, M., Rimelen, M., Lips, D., Ruffieux, K., et al. (2003). Thermal and mechanical properties of plasticized Poly(L-lactic acid). *J. Appl. Polym. Sci.* 90, 1731–1738. doi: 10.1002/app.12549

Baldi, F., Agnelli, S., and Riccò, T. (2010). On the applicability of the load separation criterion in determining the fracture resistance (JIC) of ductile polymers at low and high loading rates. *Int. J. Fract.* 165, 105–119. doi: 10.1007/s10704-010-9510-9

Baldi, F., Agnelli, S., and Riccò, T. (2013). On the determination of the point of fracture initiation by the load separation criterion in J-testing of ductile polymers. *Polym. Test.* 32, 1326–1333. doi: 10.1016/j.polymertesting.2013.08.007

Barletta, M., and Puopolo, M. (2019). Thermo-mechanical properties of injection molded components manufactured by engineered biodegradable blends. *J. Polym. Environ.* 27, 2105–2118. doi: 10.1007/s10924-019-01500-4

Bernal, C. R., Montemartini, P. E., and Frontini, P. M. (1996). The use of load separation criterion and normalization method in ductile fracture characterization of thermoplastic polymers. *J. Polym. Sci. Part B Polym. Phys.* 34, 1869–1880.

Blackman, B., Baldi, F., Castellani, L., Frontini, P., Laiarinandrasana, L., Pegoretti, A., et al. (2015). Application of the load separation criterion in J-testing of ductile polymers: a round-robin testing exercise. *Polym. Test.* 44, 72–81. doi: 10.1016/j.polymertesting.2015.03.019

Borggreve, R. J. M., and Gaymans, R. J. (1988). Impact modification of poly(caprolactam) by copolymerization with a low molecular weight polybutadiene. *Polymer* 29, 1441–1446. doi: 10.1016/0032-3861(88)90308-4

Bucknall, C. B., Heather, P. S., and Lazzeri, A. (2000). Rubber toughening of plastics. *J. Mater. Sci.* 24, 2255–2261. doi: 10.1007/BF02385450

Cao, X., Mohamed, A., Gordon, S. H., Willett, J. L., and Sessa, D. J. (2003). DSC study of biodegradable poly(lactic acid) and poly(hydroxy ester ether) blends. *Thermochim. Acta* 406, 115–127. doi: 10.1016/S0040-6031(03)00252-1

Cinelli, P., Seggiani, M., Mallegni, N., Gigante, V., and Lazzeri, A. (2019). Processability and degradation of PHA-based composites in terrestrial environments. *Int. J. Mol. Sci.* 20:284. doi: 10.3390/ijms20020284

Coltelli, M. B., Della Maggiore, I., Bertoldo, M., Signori, F., Bronco, S., and Ciardelli, F. (2008). Poly(lactic acid) properties as a consequence of poly(butylene adipate-co-terephthalate) blending and acetyl tributyl citrate plasticization. *J. Appl. Polym. Sci.* 110, 1250–1262. doi: 10.1002/app.28512

Dekkers, M. E. J., Hobbs, S. Y., and Watkins, V. H. (1991). Morphology and deformation behaviour of toughened blends of poly(butylene terephthalate), polycarbonate and poly(phenylene ether). *Polymer* 32, 2150–2154. doi: 10.1016/0032-3861(91)90039-L

Di Lorenzo, M. L. (2006). Calorimetric analysis of the multiple melting behavior of poly(L-lactic acid). *J. Appl. Polym. Sci.* 100, 3145–3151. doi: 10.1002/app.23136

European Committee for Standardisation (1999). *EN 13432. Requirements for Packaging Recoverable through Composting and Biodegradation–Test Scheme and Evaluation Criteria for the Final Acceptance of Packaging.* Brussels: European Committee for Standardisation.

Forghani, E., Azizi, H., Karabi, M., and Ghasemi, I. (2018). Compatibility, morphology and mechanical properties of polylactic acid/polyolefin elastomer foams. *J. Cell. Plast.* 54, 235–255. doi: 10.1177/0021955X16681450

Gigante, V., Canesi, I., Cinelli, P., Coltelli, M., and Lazzeri, A. (2019). Rubber toughening of Polylactic acid (PLA) with Poly(butylene adipate-co-terephthalate) (PBAT): mechanical properties, fracture mechanics and analysis of brittle – ductile behavior while varying temperature and test speed. *Eur. Polym. J.* 115, 125–137. doi: 10.1016/j.eurpolymj.2019.03.015

Grande, R., and Carvalho, A. J. F. (2011). Compatible ternary blends of chitosan/poly(vinyl alcohol)/poly(lactic acid) produced by oil-in-water emulsion processing. *Biomacromolecules* 12, 907–914. doi: 10.1021/bm101227q

Gross, R. A., and Kalra, B. (2002). Biodegradable polymers for the environment. *Science* 297, 803–807. doi: 10.1126/science.297.5582.803

Gu, S. Y., Zhang, K., Ren, J., and Zhan, H. (2008). Melt rheology of polylactide/poly(butylene adipate-co-terephtahlate) blends. *Carbohydr. Polym.* 74, 79–85. doi: 10.1016/j.carbpol.2008.01.017

Gupta, A. K., and Srinivasan, K. R. (1993). Melt rheology and morphology of PP/SEBS/PC ternary blend. *J. Appl. Polym. Sci.* 47, 167–184.

Hamad, K., Kaseem, M., Ayyoob, M., Joo, J., and Deri, F. (2018). Polylactic acid blends: the future of green, light and tough. *Prog. Polym. Sci.* 85, 83–127. doi: 10.1016/j.progpolymsci.2018.07.001

Hemmati, M., Nazokdast, H., and Panahi, H. S. (2001). Study on morphology of ternary polymer blends. I. Effects of melt viscosity and interfacial interaction. *J. Appl. Polym. Sci.* 82, 1129–1137. doi: 10.1002/app.1947

Hu, G., Sun, Y., and Lambla, M. (1996). Effects of processing parameters on the in situ compatibilization of polypropylene and poly (butylene terephthalate) blends by one-step reactive extrusion. *J. Appl. Polym. Sci.* 61, 1039–1047.

Inberg, J. P. F., Takens, A., and Gaymans, R. J. (2002). Strain rate effects in polycarbonate and polycarbonate/ABS blends. *Polymer* 43, 2795–2802. doi: 10.1016/S0032-3861(02)00081-2

Ishida, S., Nagasaki, R., Chino, K., Dong, T., and Inoue, Y. (2009). Toughening of Poly(L-lactide) by Melt Blending with Rubbers. *J. Appl. Polym. Sci.* 559–566. doi: 10.1002/app.30134

Jiang, L., Wolcott, M. P., and Zhang, J. (2006). Study of biodegradable polylactide/poly(butylene adipate-co-terephthalate) blends. *Biomacromolecules* 7, 199–207. doi: 10.1021/bm050581q

Kumar, M., Mohanty, S., Nayak, S. K., and Rahail Parvaiz, M. (2010). Effect of glycidyl methacrylate (GMA) on the thermal, mechanical and morphological property of biodegradable PLA/PBAT blend and its nanocomposites. *Bioresour. Technol.* 101, 8406–8415. doi: 10.1016/j.biortech.2010.05.075

Künkel, A., Becker, J., Börger, L., Hamprecht, J., Koltzenburg, S., Loos, R., et al. (2016). "Polymers, Biodegradable," in *Ullmann's Encyclopedia of Industrial Chemistry Major Reference Works*, 1–29. doi: 10.1002/14356007.n21_n01.pub2

Kunthadong, P., Molloy, R., Worajittiphon, P., Leejarkpai, T., Kaabbuathong, N., and Punyodom, W. (2015). Biodegradable plasticized blends of Poly(L-lactide) and cellulose acetate butyrate: from blend preparation to biodegradability in real composting conditions. *J. Polym. Environ.* 23, 107–113. doi: 10.1007/s10924-014-0671-x

La Mantia, F. P., Morreale, M., Botta, L., Mistretta, M. C., Ceraulo, M., and Scaffaro, R. (2017). Degradation of polymer blends: a brief review. *Polym. Degrad. Stab.* 145, 79–92. doi: 10.1016/j.polymdegradstab.2017.07.011

Lazzeri, A., and Bucknall, C. B. (1993). Dilatational bands in rubber-toughened polymers. *J. Mater. Sci.* 28, 6799–6808. doi: 10.1007/BF00356433

Lazzeri, A., and Bucknall, C. B. (1995). Applications of a dilatational yielding model to rubber-toughened polymers. *Polymer* 36, 2895–2902. doi: 10.1016/0032-3861(95)94338-T

Lazzeri, A., Thio, Y. S., and Cohen, R. E. (2004). Volume strain measurements on CACO3/polypropylene particulate composites: the effect of particle size. *J. Appl. Polym. Sci.* 91, 925–935. doi: 10.1002/app.13268

Li, Y., and Shimizu, H. (2009). Improvement in toughness of poly (l-lactide)(PLLA) through reactive blending with acrylonitrile–butadiene–styrene copolymer (ABS): morphology and properties. *Eur. Polym. J.* 45, 738–746. doi: 10.1016/j.eurpolymj.2008.12.010

Luzinov, I., Xi, K., Pagnoulle, C., Huynh-Ba, G., and Jérôme, R. (1999). Composition effect on the core–shell morphology and mechanical properties of ternary polystyrene/styrene–butadiene rubber/polyethylene blends. *Polymer* 40, 2511–2520.

Maiza, M., Benaniba, M. T., and Massardier-Nageotte, V. (2016). Plasticizing effects of citrate esters on properties of poly(lactic acid). *J. Polym. Eng.* 36, 371–380. doi: 10.1515/polyeng-2015-0140

Mallegni, N., Phuong, T. V., Coltelli, M. B., Cinelli, P., and Lazzeri, A. (2018). Poly(lactic acid) (PLA) based tear resistant and biodegradable flexible films by blown film extrusion. *Materials* 11:148. doi: 10.3390/ma11010148

Michler, G. H., and Bucknall, C. B. (2001). New toughening mechanisms in rubber modified polymers. *Plast. Rubber Compos.* 30, 110–115. doi: 10.1179/146580101101541516

Murariu, M., and Dubois, P. (2016). PLA composites: from production to properties. *Adv. Drug Deliv. Rev.* 107, 17–46. doi: 10.1016/j.addr.2016.04.003

Nagarajan, V., Mohanty, A. K., and Misra, M. (2018). Blends of polylactic acid with thermoplastic copolyester elastomer: effect of functionalized terpolymer type on reactive toughening. *Polym. Eng. Sci.* 58, 280–290. doi: 10.1002/pen.24566

Nascimento, L., Gamez-Perez, J., Santana, O. O., Velasco, J. I., Maspoch, M. L., and Franco-Urquiza, E. (2010). Effect of the recycling and annealing on the mechanical and fracture properties of Poly(Lactic Acid). *J. Polym. Environ.* 18, 654–660. doi: 10.1007/s10924-010-02295

Nofar, M., Maani, A., Sojoudi, H., Heuzey, M. C., and Carreau, P. J. (2015). Interfacial and rheological properties of PLA/PBAT and PLA/PBSA blends and their morphological stability under shear flow. *J. Rheol.* 59, 317–333. doi: 10.1122/1.4905714

Phuong, V. T., Coltelli, M.-B., Cinelli, P., Cifelli, M., Verstichel, S., and Lazzeri, A. (2014). Compatibilization and property enhancement of poly(lactic acid)/polycarbonate blends through triacetin-mediated interchange reactions in the melt. *Polymer* 55, 4498–4513. doi: 10.1016/j.polymer.2014.06.070

Plackett, D., Andersen, T. L., Pedersen, W. B., and Nielsen, L. (2003). Biodegradable composites based on L-polylactide and jute fibres. *Compos. Sci. Technol.* 63, 1287–1296. doi: 10.1016/S0266-3538(03)00100-3

Platt, D. K. (2006). *Biodegradable Polymers: Market Report*. London: iSmithers Rapra Publishing.

Quero, E., Müller, A. J., Signori, F., Coltelli, M. B., and Bronco, S. (2012). Isothermal cold-crystallization of PLA/PBAT blends with and without the addition of acetyl tributyl citrate. *Macromol. Chem. Phys.* 213, 36–48. doi: 10.1002/macp.201100437

Ren, J., Fu, H., Ren, T., and Yuan, W. (2009). Preparation, characterization and properties of binary and ternary blends with thermoplastic starch, poly(lactic acid) and poly(butylene adipate-co-terephthalate). *Carbohydr. Polym.* 77, 576–582. doi: 10.1016/j.carbpol.2009.01.024

Sarazin, P., Li, G., Orts, W. J., and Favis, B. D. (2008). Binary and ternary blends of polylactide, polycaprolactone and thermoplastic starch. *Polymer* 49, 599–609. doi: 10.1016/j.polymer.2007.11.029

Sedničková, M., Pekaøová, S., Kucharczyk, P., Bočkaj, J., Janigová, I., Kleinová, A., et al. (2018). Changes of physical properties of PLA-based blends during early stage of biodegradation in compost. *Int. J. Biol. Macromol.* 113, 434–442. doi: 10.1016/j.ijbiomac.2018.02.078

Sharobeam, M. H., and Landes, J. D. (1991). The load separation criterion and methodology in ductile fracture mechanics. *Int. J. Fract.* 47, 81–104. doi: 10.1007/BF00032571

Signori, F., Coltelli, M. B., and Bronco, S. (2009). Thermal degradation of poly(lactic acid) (PLA) and poly(butylene adipate-co-terephthalate) (PBAT) and their blends upon melt processing. *Polym. Degrad. Stab.* 94, 74–82. doi: 10.1016/j.polymdegradstab.2008.10.004

Su, Z., Li, Q., Liu, Y., Hu, G. H., and Wu, C. (2009). Compatibility and phase structure of binary blends of poly(lactic acid) and glycidyl methacrylate grafted poly(ethylene octane). *Eur. Polym. J.* 45, 2428–2433. doi: 10.1016/j.eurpolymj.2009.04.028

Sun, S., Zhang, M., Zhang, H., and Zhang, X. (2011). Polylactide toughening with epoxy-functionalized grafted acrylonitrile–butadiene–styrene particles. *J. Appl. Polym. Sci.* 122, 2992–2999.

Svoboda, P., Theravalappil, R., Svoboda, D., Mokrejs, P., Kolomaznik, K., Mori, K., et al. (2010). Elastic properties of polypropylen/ethylene-octene copolymer blends. *Polym. Test.* 29, 742–748. doi: 10.1016/j.polymertesting.2010.05.014

Todo, M., and Takayam, T. (2012). "Fracture mechanisms of biodegradable PLA and PLA/PCL blends," in *Biomaterials-Physics and Chemistry*, ed. R. Pignatello (London: IntechOpen), doi: 10.5772/24199

Utracki, L. A., and Shi, Z. H. (1992). Development of polymer blend morphology during compounding in a twin-screw extruder. Part I: droplet dispersion and coalescence—a review. *Polym. Eng. Sci.* 32, 1824–1833. doi: 10.1002/pen.760322405

Wang, X., Mi, J., Wang, J., Zhou, H., and Wang, X. (2018). Multiple actions of poly(ethylene octene) grafted with glycidyl methacrylate on the performance of poly(lactic acid). *RSC Adv.* 8, 34418–34427. doi: 10.1039/C8RA07510G

Wu, S. (1985). Phase structure and adhesion in polymer blends: a criterion for rubber toughening. *Polymer* 26, 1855–1863. doi: 10.1016/0032-3861(85)90015-1

Xue, B., He, H., Zhu, Z., Li, J., Huang, Z., Wang, G., et al. (2018). A Facile fabrication of high toughness poly(lactic acid) via reactive extrusion with poly(butylene succinate) and ethylene-methyl acrylate-glycidyl methacrylate. *Polymers* 10, 1–15. doi: 10.3390/polym10121401

Yeh, J., Tsou, C., Huang, C., Chen, K., and Wu, C. (2009). Compatible and Crystallization Properties of Poly (lactic acid)/ Poly (butylene adipate- co -terephthalate) Blends. *J. Appl. Polym. Sci.* 116, 680–687. doi: 10.1002/app

Yokoyama, Y., and Ricco, T. (1998). Toughening of polypropylene by different elastomeric systems. *Polymer* 39, 3675–3681. doi: 10.1016/S0032-3861(97)10358-5

Zhang, K., Nagarajan, V., Misra, M., and Mohanty, A. K. (2014). Supertoughened renewable PLA reactive multiphase blends system: phase morphology and performance. *ACS Appl. Mater. Interfaces* 6, 12436–12448. doi: 10.1021/am502337u

Zhang, N., Wang, Q., Ren, J., and Wang, L. (2009). Preparation and properties of biodegradable poly(lactic acid)/poly(butylene adipate-co-terephthalate) blend with glycidyl methacrylate as reactive processing agent. *J. Mater. Sci.* 44, 250–256. doi: 10.1007/s10853-008-3049-4

Zhao, Y., Lang, X., Pan, H., Wang, Y., Yang, H., Zhang, H., et al. (2015). Effect of mixing poly(lactic acid) with glycidyl methacrylate grafted poly(ethylene octene) on optical and mechanical properties of the blown films. *Polym. Eng. Sci.* 55, 2801–2813. doi: 10.1002/pen.24171

Check for updates

Thermo-Mechanical Behavior and Hydrolytic Degradation of Linear Low Density Polyethylene/Poly(3-hydroxybutyrate) Blends

Daniele Rigotti*, Andrea Dorigato and Alessandro Pegoretti*

Department of Industrial Engineering and INSTM Research Unit, University of Trento, Trento, Italy

In this work, a commercial linear low density polyethylene (LLDPE) utilized for packaging applications was melt compounded with different amounts (from 10 up to 50 wt. %) of poly(3-hydroxybutyrate) [P(3HB)], with the aim to evaluate the possibility to partially replace LLDPE with a biodegradable matrix obtained from renewable resources. The processability, microstructural, and thermo-mechanical behavior of the resulting blends was investigated. Melt flow index (MFI) values of the LLDPE matrix were not much affected until a P(3HB) content of 20 wt.%, while for higher P(3HB) concentrations an evident decrease of the viscosity was detected. Scanning electron microscope (SEM) observations on the blends highlighted that at limited P(3HB) concentrations the secondary phase was homogeneously dispersed in form of isolated domains, while at a P(3HB) content of 50 wt.% a continuous layered morphology could be detected. Thermogravimetric analysis (TGA), differential scanning calorimetry (DSC) and Fourier transform infrared spectroscopy (FT-IR) did not evidence any chemical or physical interaction between the two polymer phases. Quasi-static tensile tests and dynamical mechanical analysis showed that the introduction of P(3HB) led to a pronounced stiffening effect, while the progressive drop of the yield and ultimate mechanical properties could be attributed to the weak interfacial adhesion and poor compatibility between the two matrices. The resistance to hydrolytic degradation of the LLDPE/P(3HB) blends was evaluated over a period of 100 days of immersion in water at 50°C. It was observed that the weight variation and the decrease of the tensile properties due to the hydrolytic process on the biodegradable phase were evident only for a P3HB content of 50 wt.%. In conclusion, this work showed that the partial replacement of LLDPE with a biobased P(3HB) could lead to the development of an innovative blend with good processability and mechanical properties, until a P(3HB) amount of 20 wt.%.

Keywords: polyethylene, polyhydroxyalkanoates, blends, mechanical properties, degradation

INTRODUCTION

In the last few decades global climate change and ecosystems deterioration have been the main driving forces for a progressive switch from a take-make-dispose economy based on continuous growth and increasing resource throughput to a circular economy in which resource input, waste, emission, and energy leakage are minimized by slowing, closing, and narrowing material and energy loops (Geissdoerfer et al., 2017). Circular Economy is receiving increasing attention as an effective way to prevent and/or reduce industrial waste and increase the efficiency of the production processes, reaching thus a better equilibrium and harmony between economy, environment, and society. This can be achieved through a better manufacturing strategy that focuses on long-lasting design, maintenance, repair, reuse, remanufacturing, refurbishing, and recycling (Ghisellini et al., 2016; Kalmykova et al., 2018). Accumulation of non-degradable plastics is one of the main problems for the environment and human health, because of the generation of secondary microplastics and nanoplastics, release of hazardous chemicals during manufacturing, use and the following landfilling, incineration, or improper disposal (Soroudi and Jakubowicz, 2013; Laycock et al., 2017). Thanks to their limited weight, flexibility and durability, plastics production has reached 380 million tons in 2015, and about 40% of this amount is applied in packaging field (Groh et al., 2019). For as concerns the management of the packaging waste, its reuse and recycling could reduce their environmental impact, delivering thus both economic and environmental benefits (Dilkes-Hoffman et al., 2018; Geueke et al., 2018). However, recycling would be neither practical nor economical for certain applications such as bags, agricultural mulch films, and food packaging (Pedroso and Rosa, 2005). Due to safety issues, it is particularly challenging to fully recycle food packaging waste to produce new food package, because of the presence of contaminants and/or chemicals that can directly migrate from the packaging into the food or beverage (Groh et al., 2019).

Considering the difficulties in recycling plastics for packaging applications, it is thus clear that biopolymers could represent a valuable solution to reduce the environmental burden associated to the life cycle of industrial packages. In fact, packaging is the largest market for biopolymers, accounting for about 58% of the total volume share. Despite this, biopolymers market represents today only a limited percentage of the total plastics production (Niaounakis, 2019). Processing biodegradable plastics under composting conditions at the end of their life could be preferred over recycling for these kinds of applications (Geueke et al., 2018). However, the end of life of biopolymers is a debatable issue. Even if recycling of biodegradable polymers does not exploit their biodegradability, the disposal of biopolymer articles through biodegradation has the disadvantage of discarding valuable raw materials and could lead to environmental problems such as the emission of methane. To reduce the consumption of renewable resources used for the synthesis of biopolymers is important to be able to recycle them. In this way, biopolymers waste may become a valuable alternative feedstock for monomers and intermediates (Hahladakis and Iacovidou, 2018).

Most of the traditional thermoplastic used as packaging materials are polyolefins, such as high-density polyethylene (HDPE), low-density polyethylene (LDPE), and polypropylene (PP). Polyethylene is a general-purpose thermoplastic polymer with good processing and mechanical properties as well as relative low price. In particular, linear low-density polyethylene (LLDPE), thanks to its elevated tear and impact strength, is generally applied in film production for the packaging. LLDPE is constituted by a linear hydrocarbon backbone with short chain branching, formed by a copolymer of ethylene and an α-olefin or diene (i.e., butene, hexane, or octene) (Dorigato et al., 2010a,b, 2011, 2013; Dorigato and Pegoretti, 2012, 2013). It finds large application in grocery bags, heavy duty shipping sacks, agricultural films, pipes, liners for consumers, landfills, and waste ponds (Hancox, 1992). An important issue for economic and environmental reasons is the problem of post-consumer recycling of this material, since the use of these plastics is continuously increasing (Hole and Hole, 2019).

Polyhydroxyalkanoates (PHAs) are generally considered a promising group of biopolymers from renewable resources and bacteria and they possess a high potential as bio-based and biodegradable plastic packaging materials in the transition toward a circular economy (Ragaert et al., 2019). Among all the PHAs, poly(3-hydroxybutyrate) [P(3HB)] is one of the most innovative thermoplastic. P(3HB) is synthesized by microorganism as an intracellular storage product under suitable growth conditions (abundant carbon source, limited sources of oxygen, phosphorous, or nitrogen). The carbon is assimilated and converted into hydroxyalkanoate monomers, polymerized, and stored in the cell cytoplasm. The resulting polymer is a biocompatible high molecular weight crystalline polyester that can be used to produce films and foils for the packaging industry and tissue engineering (Chen and Hajnal, 2015; Valentini et al., 2019). Moreover, P(3HB) can be degraded by microorganisms (i.e., bacteria, fungi, and algae) under different environmental conditions (Wang et al., 2014; Emadian et al., 2017; Pakalapati et al., 2018).

Nowadays, the major challenge in the biopolymers research is to partially/totally replace conventional petroleum-based polymers with the biodegradable ones, in view of a more sustainable development. Therefore, blending biodegradable polymers with traditional plastics, such as polyethylene, has recently received considerable attention, in order to simultaneously improve/tailor the physical properties of the resulting materials and lower their environmental burden. A key point to be investigated in these systems is whether the biodegradable component could be effectively biodegraded by the microorganisms under certain conditions, and whether the remaining polyolefinic phase could be even degraded (Chandra and Rustgi, 1998). Several research efforts were thus made in this direction, through the development of different LDPE/biopolymer blends, such as LDPE/wax (Krupa and Luyt, 2000, 2001), LDPE/starch (Nguyen et al., 2016; Datta and Halder, 2019) and LDPE/PLA (Bhasney et al., 2019) systems. It was demonstrated that the degradation of polyethylene can be accelerated by environmental factors such as temperature, UV irradiation or the action of microorganisms (Restrepo-Flórez

et al., 2014). For instance, Veethahavya et al. (2016) investigated the possibility to accelerate the biodegradation through microorganisms digestion of LDPE upon blending with natural polymers, finding that in liquid cultures the degradation rate of LDPE increased with the starch concentrations. Only a limited number of papers addressing the thermo-mechanical properties and the degradative behavior of LLDPE/P(3HB) blends are available in the open scientific literature. In these work, the attention was mainly focused on the morphology, highlighting that the blend components are thermodynamically incompatible and a clearly distinguishable interface is formed between the disperse phase (PHB) and the continuous matrix LDPE (Ol'khov et al., 2000; Pankova et al., 2010). With packaging application in mind, this immiscibility was exploited to regulate the resistance to hydrolysis and biodegradation through the control of water permeability studying the interaction between the two polymer phases against water according to Flory–Huggins theory (Pankova et al., 2010). Biodegradability of LDPE/PHB blends was extensively studied and also improved when natural additives such as castor oil or guar gum were inserted (Burlein and Rocha, 2014; Rocha and Moraes, 2015). Pro-oxidant additives, such as oxidized polyethylene wax, represent a promising solution to the problem of the environment contamination and could reduce the phase separation of LDPE with PHB and increased the biodegradation during aging in soil (Rosa et al., 2007).

Therefore, the present work aims to investigate the effect of blending P(3HB) to LLDPE at different concentrations (from 10 to 50 wt.%). A systematic investigation of the processability, of the microstructural and of the thermo-mechanical properties of the resulting blends was performed. Particular attention was devoted to the hydrolytic degradation of these systems, analyzing the water absorption, and the change of the thermal and mechanical performances of the samples as a function of the hydrolysis time.

EXPERIMENTAL PART

Materials
Poly(3-hydroxybutyrate) was provided by Biomer (Schwalbach, Germany) in form of white powder ($M_w = 3.7 \pm 0.2 \cdot 10^5$ Da, density = 1.18 g/cm^3). Preliminary NMR studies on the obtained powder (not reported for sake of brevity) showed the characteristic signals of poly-3-hydroxybutyrate [P(3HB)] (i.e., C=O, -OCH-, -CH$_2$-, and –CH$_3$), excluding thus the presence of poly-hydroxyvalerate (PHV) or of poly-4-hydroxybutyrate [P(4HB)] in the purchased material. Linear low-density polyethylene used in this work was Flexirene® CL10 (density of 0.918 g/cm^3, melting temperature of 120°C, melt flow index (MFI) at 190°C and 2.16 kg of 2.6 g/10 min), provided by Versalis Spa (San Donato Milanese, Italy) in form of granules.

Sample Preparation
Prior compounding, both LLDPE and P(3HB) were dried in an oven at 80°C for 24 h. The two polymers were mixed at different relative concentrations with a Thermo Haake Rheomix® 600 melt compounder at 190°C. After some preliminary trials, a rotor speed of 60 rpm and a compounding time of 10 min were

selected, in order to provide a good homogenization of the blends. The resulting materials were then hot pressed at 190°C for 10 min in a Carver hot plate press, applying a pressure of 2.5 MPa, to obtain square sheets with a length of 20 cm and a thickness of about 1 mm. In this way, neat LLDPE, neat P(3HB) and LLDPE/P(3HB) blends with different P(3HB) concentrations, ranging from 10 up to 50 wt.%, were prepared. Samples were designated indicating the relative content of LLDPE and P(3HB) phases, i.e., LLDPE_x_PHB_y, where x and y are the weight percentage of LLDPE and P(3HB), respectively.

Experimental Techniques
In order to evaluate the processability of the resulting blends, melt flow index (MFI) measurements were performed according to ASTM D1238–04 standard, by using a Kyeness 4003DE plastomer at a temperature of 180°C under a load of 2.16 kg investigating about 10 g of material for each sample. This testing parameters were selected in order to evaluate the MFI under the same conditions for all the samples.

Morphological properties of the cryo-fractured surface of the LLDPE/PHB blends were determined by using a Zeiss Supra 40 high resolution field emission scanning electron microscope (FESEM), operating at an acceleration voltage of 4 kV. Prior to be observed, samples were covered with a conductive platinum/palladium coating deposited through a sputter coater.

FT-IR spectroscopy was conducted with a Perkin Elmer Spectrum One machine, in order to analyze the vibrational transitions inside molecules of the different samples. This analysis was performed in a wavenumber range between 650 and 4,000 cm^{-1}.

DSC measurements were performed on one specimen for each sample in order to get information about the glass transition, crystallization, and melting temperature of the material. DSC tests were carried out with a Mettler DSC30 calorimeter under a nitrogen flow of 10 ml/min. A heating run from −100 to 200°C was followed by a cooling stage to −100°C and by a second heating run up to 200°C. All the scans were performed at a heating or cooling rate of 10°C/min. In this way, it was possible to determine the melting (T_m) and crystallization temperature (T_c) of LLDPE and P(3HB). The crystallinity degree (X_c) was computed as the ratio between the melting enthalpy of the samples and the reference value of the fully crystalline polymers, i.e., 293 J/g for LLDPE and 146 J/g for P(3HB) (Barham et al., 1984).

Knowing the critical issues of P(3HB) regarding its thermal degradation, it is extremely important to determine the thermal degradation of the blends. For this purpose, thermogravimetric analysis (TGA) was performed on one specimen for each sample through a TA Instruments TGAQ500 thermobalance, operating under a nitrogen flow of 10 ml/min in a temperature interval between 30 and 700°C, setting a heating rate of 10°C/min.

Viscoelastic behavior of the blends as a function of the temperature was investigated through dynamical mechanical analysis (DMA) with a TA Instrument DMA Q800. The tests were carried out in tensile mode on a rectangular specimen for each
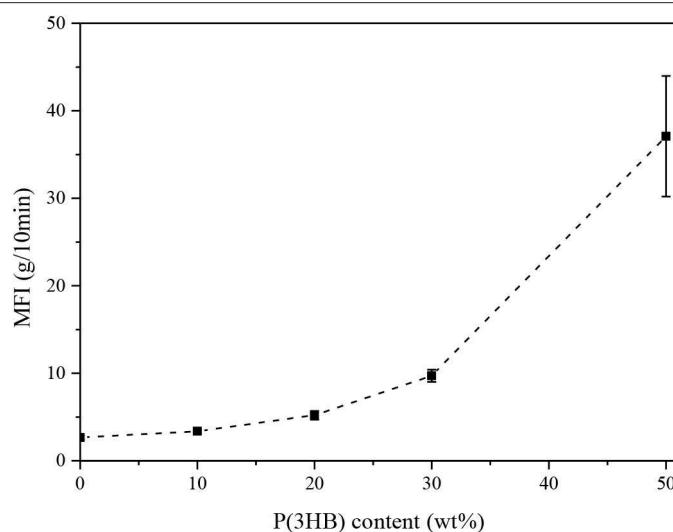
FIGURE 1 | MFI values of neat LLDPE and LLDPE/P3HB blends (T = 180°C, load = 2.16 kg). Error bars represent the standard deviation.

sample with dimension of $30 \times 5 \times 1 \, \text{mm}^3$ in a temperature range between −100 and 100°C, at a heating rate of 3°C/min and a testing frequency of 1 Hz.

Quasi-static tensile properties of the different polymer blends were evaluated at ambient temperature with an Instron 5969 electromechanical testing machine, testing ISO 527 1BA dogbone specimens, having a gage length of 30 mm. Elastic modulus (E) was evaluated at 0.25 mm/min with an extensometer with a gage length of 12.5 mm, setting a maximum deformation of 1%. E was computed as secant modulus between deformation levels of 0.05% and 0.25%. Tensile stress at yield (σ_y), stress at break (σ_b), and strain at break (ε_b) were determined without the use of an extensometer, setting a crosshead speed of 1 mm/min. At least five specimens were tested for each sample.

In order to evaluate the resistance to hydrolysis, the blends were subjected to hydrolytic degradation tests, simulating a low run-off condition. The analysis was conducted in a thermostatically controlled bath at a constant temperature of 50°C. ISO 527 1BA dumbbell specimens were immersed in 80 ml of distilled water and the run-off condition was simulated by performing a periodically change of water every week, for a total duration of the tests of 100 days. Some samples were periodically extracted and dried in a vacuum oven at a temperature of 60° C for 90 h, in order to eliminate the absorbed water. The evaluation of hydrolytic degradation on the dried samples was performed by calculating the relative variation in weight of the specimens. Moreover, DSC tests were carried out on the same samples to monitor the trend of the crystallinity degree of LLDPE with the hydrolysis time, and also quasi-static tensile tests were performed to evaluate their elastic modulus and yield strength. For these tests, the same testing conditions applied for non-hydrolyzed samples were adopted.

RESULTS AND DISCUSSIONS

One of the main issues in the production of polyethylene-based film for packaging applications is the processability of the resulting materials. Therefore, the evaluation of the viscosity of the produced blends in the molten state is of utmost importance. **Figure 1** summarizes the MFI values of neat LLDPE and relative blends at different P(3HB) concentrations.

It is interesting to observe how the MFI increases with the P(3HB) amount, thus indicating a progressive lowering of the viscosity of the blends in the molten state. For instance, at a P(3HB) loading of 50 wt.%, a MFI value of 37 g/10 min was reached. While the observed MFI increase is rather limited up to a biopolymer concentration of 20 wt.%, a more rapid increase can be detected at higher P(3HB) amounts. Considering that the selected LLDPE grade is generally used for the production of extruded film for food packaging, it is clear that the retention of the original MFI is a fundamental processability requirement for this process (Van Krevelen and Te Nijenhuis, 2009). MFI suggested for polyethylene in this manufacturing process is between 1 and 20 g/10 min (Patel, 2016) so it can be concluded that a P(3HB) content of 50 wt.% is probably not suitable for the production of extruded packaging films.

SEM analysis was then carried out, in order to appreciate the most important morphological features of the blends. In **Figures 2A–D** some representative micrographs of the cryofracture surfaces of LLDPE and of the relative blends are reported. As expected, the fracture profile of neat LLDPE is rather smooth (**Figure 2A**), while in the blends at low P(3HB) content the secondary phase is present in round domains homogenously distributed within the LLDPE matrix, with a mean size ranging from 2 to 4 μm (see **Figures 2B,C**). In these micrographs, the presence of the P(3HB) phase can be often detected by the holes produced during the cryofracturing operations. In any case,
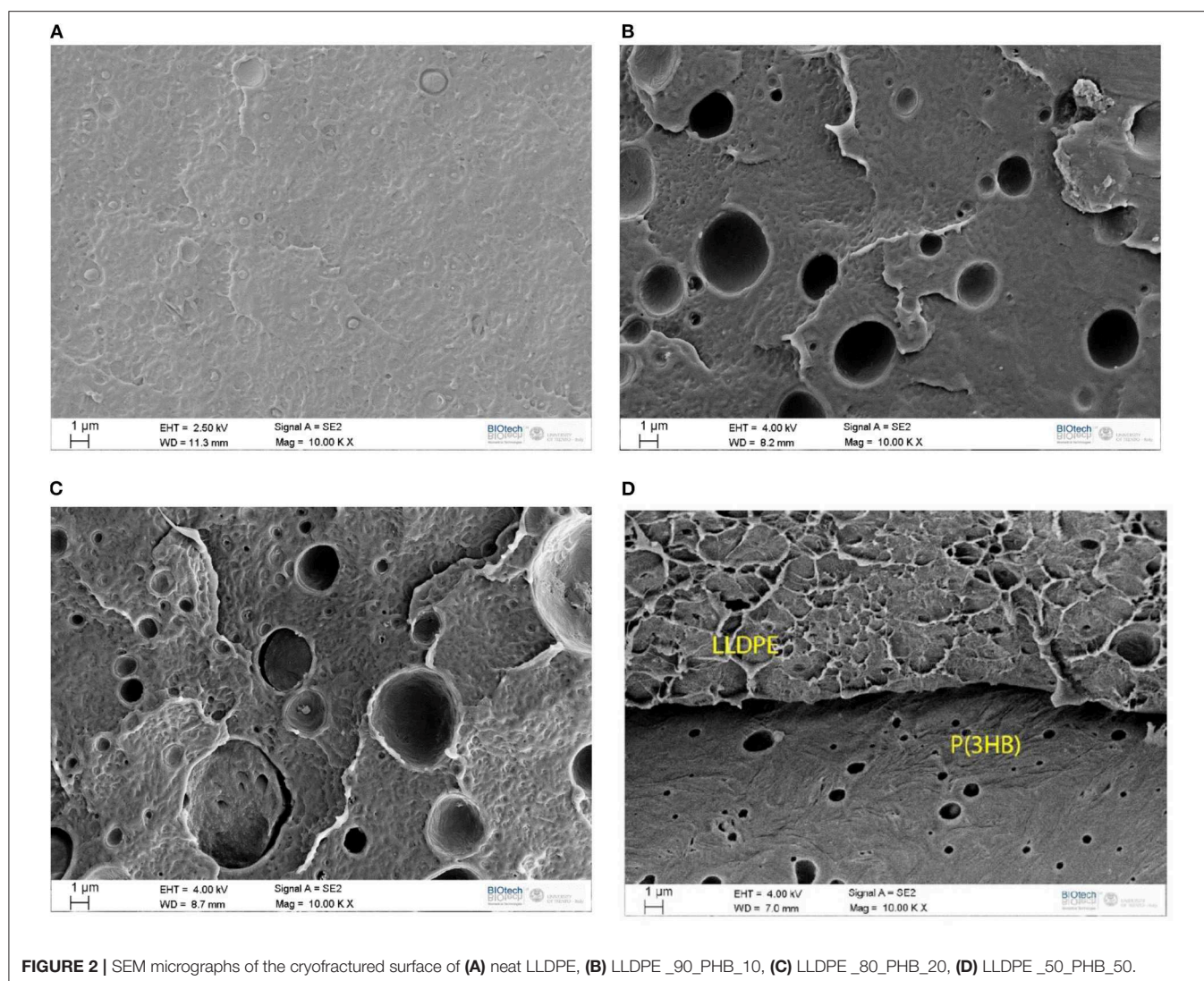
FIGURE 2 | SEM micrographs of the cryofractured surface of **(A)** neat LLDPE, **(B)** LLDPE _90_PHB_10, **(C)** LLDPE _80_PHB_20, **(D)** LLDPE _50_PHB_50.

a rather limited interfacial adhesion between the two polymer phases, with an evident debonding, can be clearly seen. This is a first indication of the limited miscibility between the two constituents. At a P(3HB) amount of 50 wt.% a co-continuous morphology with a clear separation of the two phases can be seen (**Figure 2D**). The obtained microstructure depends on polymer molecular structure, composition, the method of blend preparation and also by the surface free energy (Venugopal and Krause, 1992; Walheim et al., 1997). LLDPE could have an average molecular weight higher than that of P(3HB) according to MFI, it is reasonable to consider that higher molecular weight polymers experiences a larger entropy penalty at the surface in respect of the lower molecular weight ones so the blend surface is expected to be depleted in LLDPE and enriched in P(3HB) as results of reduced conformational entropy (Wattenbarger et al., 1990; Bower, 2002). Moreover, the amplitude of entropically driven surface segregation is found to be proportional to the backbone density of substitute and small differences in this value could lead to strong surface segregation (Wu and Fredrickson,

1996). Therefore, the linear polymer, i.e., LDPE, concentration is expected to increase moving from the surface to the bulk respect to the concentration of the thicker "microbranched" polymer, i.e., P(3HB).

FT-IR spectra of neat matrices [i.e., LLDPE and P(3HB)] and of their relative blends are reported in **Figure 3**. Neat LLDPE sample shows characteristic peaks related to the antisymmetric (2,916 cm^{-1}) and symmetric (2,848 cm^{-1}) stretching vibrations of CH of saturated hydrocarbons and to the bending of the CH at 1,463 cm^{-1} (Gulmine et al., 2002). Increasing the amount of P(3HB) it is possible to observe the characteristic peak of this polyester, i.e., the stretching vibration of the C=O at 1,720 cm^{-1} (Padermshoke et al., 2005). From the FT-IR spectra of the blended samples it is not possible to detect any reflection different from those typical of the neat constituents, meaning that the two polymers are not miscible and that no physical and/or chemical interaction is present between the two polymer phases. Quite interestingly, the spectra of the LLDPE_50_PHB_50 is very similar to that of the neat PHB. According to the SEM

FIGURE 3 | FT-IR spectra of neat LLDPE, neat P(3HB), and relative LLDPE/P(3HB) blends.
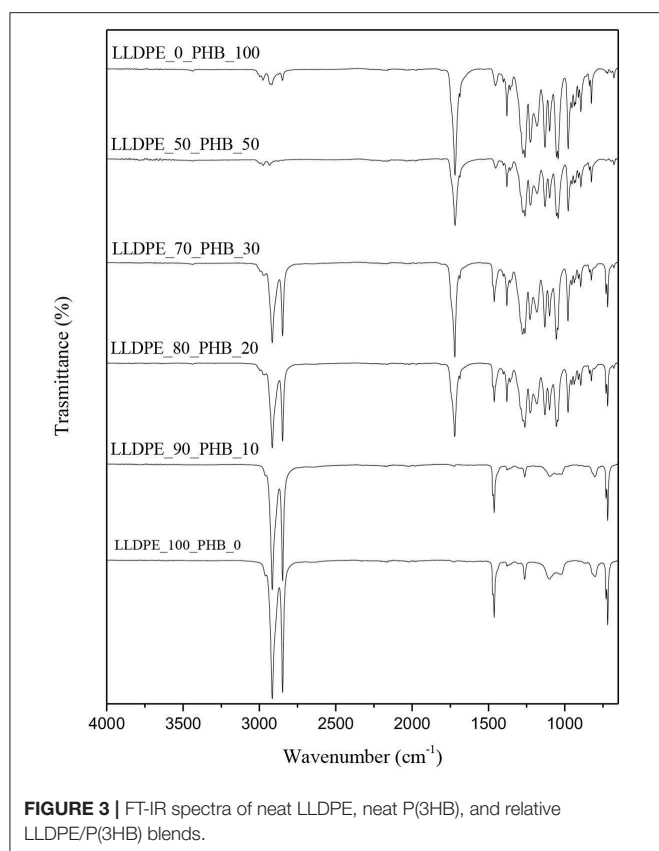
images (see **Figure 2D**) and the previous considerations, it can be assumed that at elevated P(3HB) concentrations a superficial film of P(3HB) is formed on the samples, thus hiding the IR signal of the polyolefin phase.

Thermal properties of the neat matrices and of the blended samples were investigated by using differential scanning calorimetry (DSC). In **Figures 4A,B**, representative DSC thermograms for the first heating and the cooling cycle are shown, while in **Table 1** the most important results in terms melting temperature (T_m), crystallization temperature (T_c), and the degree of crystallinity (X_c) are summarized.

Melting peaks of LLDPE and P(3HB) are clearly distinguishable in DSC thermograms collected during the first heating scan, and the intensity of these peaks is proportional to the relative amounts of the constituents within the blends. In the cooling scan, the crystallization peak of P(3HB) can be detected only for PHB contents higher than 50%, while for lower P(3HB) amounts it is hidden by the crystallization peak of the LLDPE constituent. From the results reported in **Table 1** it can be concluded that the melting and the crystallization temperature of both the LLDPE and the PHB phases seem to be substantially unaffected by the relative composition of the blends. The same can be said for the crystallinity content of the LLDPE. Quite interestingly, the presence of the LLDPE in the blends seems to hinder the crystallization process of the PHB phase, lowering thus the X_c values, especially at elevated

LLDPE contents. Further studies will be required to have a better comprehension of this aspect. However, also from DSC thermograms it can be concluded that the interaction between the two polymer constituents in the blends is rather limited, and immiscible blends are formed all the tested compositions.

Thermogravimetric analysis (TGA) was then performed, in order to evaluate the thermal stability of the LLDPE/P(3HB) blends. This is a very important point, due to the well-known processability limits of P(3HB) (Yeo et al., 2017). The curves of the weight loss as a function of the temperature and their corresponding derivative curves are presented in **Figures 5A,B**.

The curves show two distinct degradation steps, relative to P(3HB) and LLDPE phases, respectively. LLDPE starts to degrade at temperatures higher than 400°C, while P(3HB) starts to thermally decompose at temperatures higher than 240°C. Considering that the melting temperature of P(3HB) from DSC tests resulted to be at 176°C (see **Table 1**), it can be concluded that the processability window of these blends, even if rather restricted, is still suitable for the production of extruded films for packaging applications. The degradation temperature of the LLDPE and P(3HB) phases within the blends, associated to the maximum mass loss rate, is respectively located at around 440 and 270°C, and is not substantially influenced by the relative concentration of the constituents in the blends. This confirms again the limited interaction between the two polymer phases. It is also interesting to notice that the residual mass at 700°C is very near to zero for all the tested compositions, meaning that both the neat samples and the blended specimens are completely decomposed into gaseous products even under an inert atmosphere. Due to the narrow processability window of P(3HB), the compounding temperature was set at 190°C, in order to guarantee the complete melting of the P(3HB) and minimize the risk of its thermal degradation.

DMA tests were performed to evaluate the viscoelastic properties of the blends and their thermal transitions. DMA curves showing the trends of the storage modulus (E′) and of the loss tangent (tanδ) are shown in **Figures 6A,B**. At a general level, it can be seen that the progressive introduction of the P(3HB) within the blends leads to an important stiffening effect, with an increase of the storage modulus and a corresponding lowering of the tanδ values.

Differently from DSC thermograms, in DMA curves of the neat P(3HB) sample it is possible to detect the presence of the T_g, located at around 30°C (see tanδ peak in **Figure 6B**). This signal is still visible in the LLDPE_50_PHB_50 blends, while for lower PHB contents it practically disappears. Therefore, the introduction of a relatively stiff polymer like P(3HB) can increase the dimensional stability of the blends at ambient temperature, but for temperatures above 30°C (i.e., higher than the T_g of PHB) a strong decrease of the dimensional stability of the material can occur in the blends at elevated PHB amounts. This issue must be taken in serious consideration for the intended application of the blends as food packaging films.

Representative stress-strain curves of neat LLDPE and of the relative blends at different PHB amounts are reported in **Figure 7**, while in **Table 2** the results of the most important tensile properties are summarized.
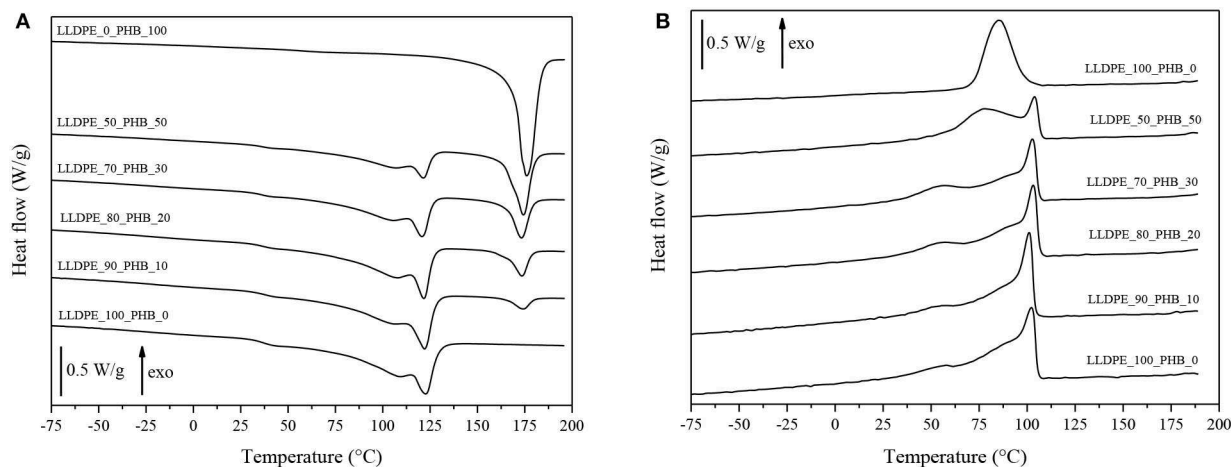
FIGURE 4 | DSC thermograms of neat LLDPE, neat P(3HB), and relative LLDPE/P(3HB) blends. **(A)** First heating and **(B)** cooling scan.

TABLE 1 | Results of DSC tests neat LLDPE and relative LLDPE/P(3HB) blends (first heating scan).

Sample	T_m LLDPE (°C)	T_m P(3HB) (°C)	X_c LLDPE (%)	X_c P(3HB) (%)	T_c LLDPE (°C)	T_c P(3HB) (°C)
LLDPE_100_PHB_0	122.7	–	43.9	–	102.3	–
LLDPE _90_PHB_10	122.0	174.0	44.0	53.1	101.0	–
LLDPE _80_PHB_20	121.8	173.5	43.3	56.9	103.1	–
LLDPE _70_PHB_30	120.7	173.4	41.5	60.2	102.7	–
LLDPE _50_PHB_50	121.3	174.4	40.5	60.4	103.9	77.1
LLDPE _0_PHB_100	–	176.0	–	67.1	–	85.2

T_m, melting temperature (first heating scan); X_c, crystallinity degree (first heating scan); T_c, crystallization temperature (cooling scan).
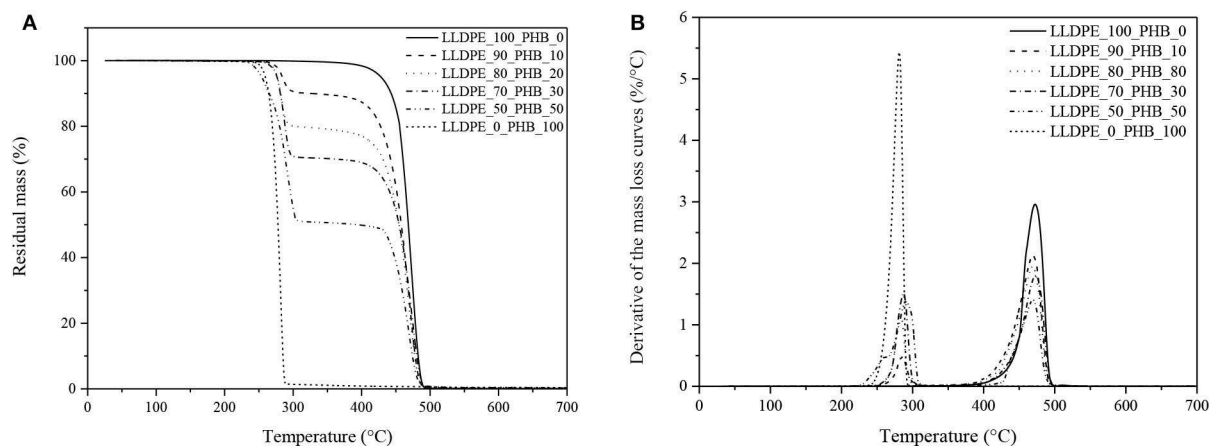
FIGURE 5 | Thermogravimetric analysis on neat LLDPE, neat P(3HB) and relative LLDPE/P(3HB) blends. **(A)** Residual mass and **(B)** derivative of the mass loss curves.

In these tests, it was not possible to obtain the values of the tensile properties of neat P(3HB), because it was too brittle. According to DMA analysis, the progressive introduction of a stiff polymer like P(3HB) leads to a remarkable increase of the elastic modulus (E). For instance, with a P(3HB) amount of 30 wt.% it is possible to double the original stiffness of the LLDPE matrix, and raising the P(3HB) concentration to 50 wt.% the elastic modulus is even four times higher. As a drawback, ultimate elongation values (ε_b) are strongly reduced. Even if until a P(3HB) concentration of 20 wt.% the observed ε_b drop is not dramatic, a harsher decrease can be seen at elevated P(3HB) loadings. Similar results regarding the elastic modulus

FIGURE 6 | Dynamical mechanical analysis of neat LLDPE, neat P(3HB) and relative LLDPE/P(3HB) blends (frequency = 1 Hz). **(A)** Storage modulus and **(B)** loss tangent curves.

FIGURE 7 | Representative stress-strain curves from quasi-static tensile tests of neat LLDPE and relative LLDPE/P(3HB) blends.
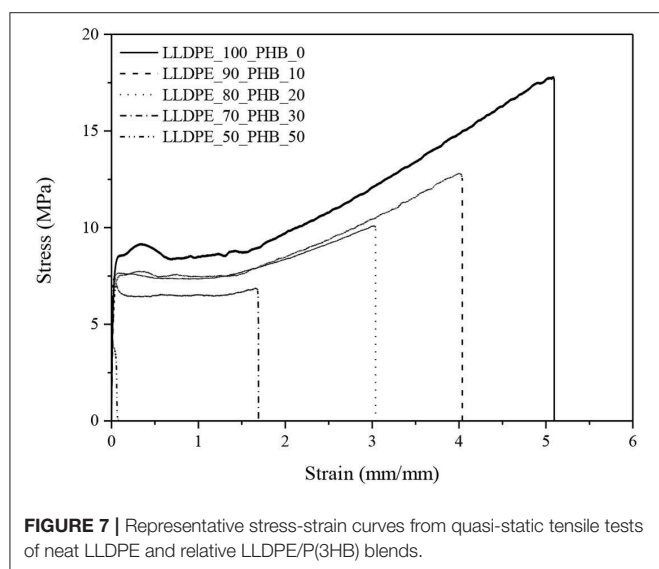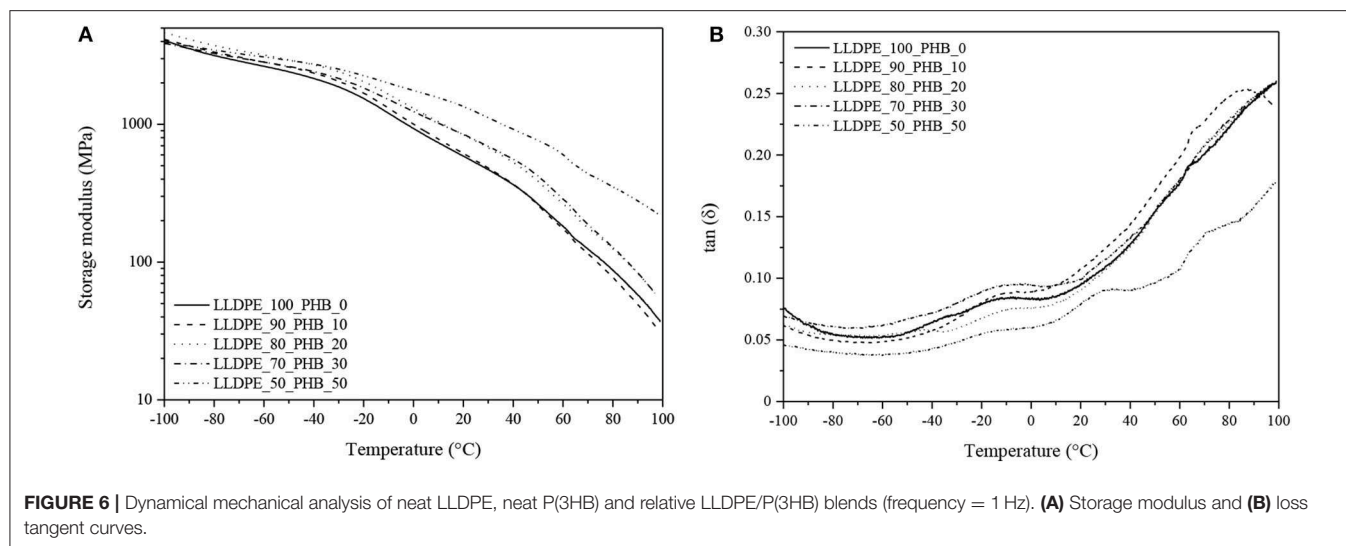
TABLE 2 | Results of quasi-static tensile tests on neat LLDPE and relative LLDPE/P(3HB) blends.

Sample	Elastic modulus (MPa)	Yield strength (MPa)	Tensile strength (MPa)	Strain at break (mm/mm)
LLDPE_100_PHB_0	195 ± 18	9.1 ± 0.1	16.6 ± 2.1	4.8 ± 0.8
LLDPE_90_PHB_10	208 ± 21	8.0 ± 0.2	13.4 ± 0.8	4.1 ± 0.2
LLDPE_80_PHB_20	311 ± 43	7.6 ± 0.1	10.0 ± 0.8	3.0 ± 0.4
LLDPE_70_PHB_30	377 ± 27	7.4 ± 0.1	6.9 ± 0.4	1.6 ± 0.4
LLDPE_50_PHB_50	794 ± 133	6.6 ± 0.8	3.8 ± 0.9	0.1 ± 0.1

and the elongation at break were found by Burlein and Rocha, the stiffness of LDPE has been doubled with an addition of 30% of P(3HB) and a drop in the elongation at break from 100 to 16%

have been reported increasing the concentration from 20 to 30% (Burlein and Rocha, 2014). The same considerations are valid also for the tensile strength (σ_b). It is also interesting to notice that also the yield strength values (σ_y) are progressively reduced upon the PHB addition. According to the indication reported in our previous works of polyolefin based nanocomposites (Dorigato et al., 2012), an enhancement of the yield strength is generally related to a rather strong filler-matrix interaction, otherwise σ_y would decrease. In fact, in polyolefins filled with traditional microfillers (talk, mica, calcium carbonate) the increase in the stiffness of the material is generally accompanied to an heavy drop of the yield stress, because these fillers do not bear the load in the direction of deformation (Ahmed and Jones, 1990; Nielsen and Landel, 1994; Galeski, 2003). Thus, the low degree of miscibility and the rather limited interfacial interaction between the two polymeric constituents of these blends detected in microstructural and thermal analysis seems to be supported by the observed drop of the yield (and also of the failure) tensile properties.

Hydrolytic degradation tests were finally performed, in order to evaluate the influence of the PHB introduction on the thermo-mechanical behavior of the blends at different hydrolysis treatment times. In these tests, the characterization activity was focused on the evaluation of the variation of the weight, of the crystallinity degree and of the quasi-static tensile performances (normalized with respect to the mechanical properties before the treatment). The trends of these properties for the different blends formulations as a function of the treatment time is graphically represented in **Figures 8A–D**. From weight variation curves (see **Figure 8A**) it is possible to notice that the weight gain is more intense in the first 10 days of hydrolytic treatment, while a stabilization occurs for longer times. It can be generally concluded that the weight gain is rather limited for all the tested compositions, and only with a P(3HB) content of 50 wt.% a maximum weight variation of 0.25% can be registered. For as concerns the thermal properties, it can be seen from **Figure 8B** that the variation of the LLDPE crystallinity degree
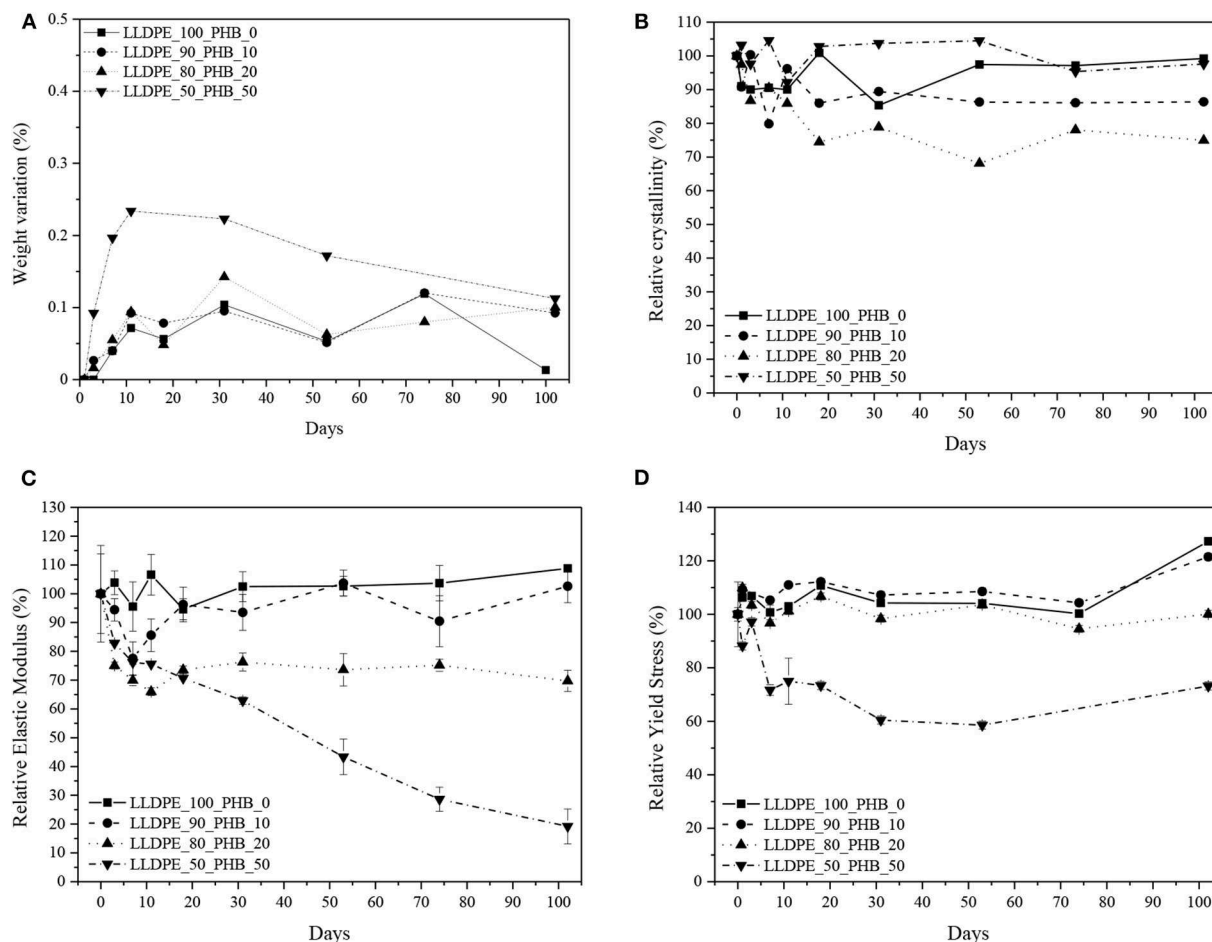
FIGURE 8 | Results of hydrolytic degradation tests on neat LLDPE and relative LLDPE/P(3HB) blends. **(A)** Weight variation, **(B)** relative crystallinity degree of LLDPE, **(C)** relative elastic modulus, **(D)** relative yield stress. Error bars represent the standard deviation.

is completely absent or rather limited at all the PHB contents, without any clear correlation with the treatment duration and/or the P(3HB) concentration.

More interesting information can be obtained from the analysis of the mechanical properties. From the trends of the relative elastic modulus reported in **Figure 8C**, it can be seen that the introduction of P(3HB) determines a fast lowering of the stiffness of the material in the first 10 days of hydrolysis, while for longer times the observed decrease is less intense. The drop of the stiffness of the material seems to be proportional to the P(3HB) amount. For instance, the relative variation of the elastic modulus after 100 days with a P(3HB) content of 20 wt.% is about 30%, while increasing the P(3HB) concentration up to 50 wt.% the relative drop is as high as 80%. This means that after 100 days of hydrolytic treatment the pristine dimensional stability of this blend is completely compromised. A similar trend can be detected considering the stress at yield values (see **Figure 8D**), even if in this case the observed drop is more limited.

The relative variation of the σ_y values is practically negligible until a P(3HB) concentration of 20 wt.%, while increasing the P(3HB) amount up to 50 wt.% a σ_y drop of about 30% can be

seen after 100 days. The observed decrease of the mechanical properties at a P(3HB) content of 50 wt.% could be directly correlated to the morphological features of this blend. In fact, SEM micrographs highlighted that at this blend composition a change in the morphology can be observed, with a formation of a continuous P(3HB) phase with layered structure (see **Figure 2D**). In these conditions, it can be hypothesized that the hydrolytic degradation process can freely take place in the P(3HB) phase, that is not entrapped anymore in the LLDPE matrix. It can be therefore concluded that the prepared blends demonstrate a good hydrolytic degradation resistance until a P(3HB) concentration of 20 wt.%, with a good retention of the original thermo-mechanical properties even after a prolonged treatment.

CONCLUSIONS

Different amounts of Poly(3-hydroxybutyrate) P(3HB) were melt compounded with a Linear Low Density Polyethylene (LLDPE) matrix, and the resulting materials were characterized from a microstructural and thermo-mechanical point of view, with the

aim to evaluate the possibility to partially replace LLDPE with a novel biobased plastic.

MFI measurements evidenced that the pristine processability of the LLDPE matrix was not substantially affected until a P(3HB) content of 20 wt.%, while for higher P(3HB) amounts an evident drop of the viscosity was observed. SEM micrographs highlighted that the two polymer constituents have a limited miscibility and a scarce interfacial interaction degree, while at a P(3HB) content of 50 wt.% a co-continuous phase can be detected. Also DSC, TGA, and FT-IR measurements did not highlight any chemical or physical interaction between the two polymer phases. A pronounced increase of the stiffness of the blends with the P(3HB) amount was detected through DMA and quasi-static tensile tests, while the low compatibility between the constituents determined a heavy drop of both the yield and the failure tensile properties. Hydrolytic degradation tests, performed over a timeframe of 100 days, showed that the decrease of the mechanical properties in the treated blends was evident only for P(3HB) contents higher than 20 wt.%. It was therefore demonstrated that the substitution of LLDPE with a biobased plastic like P(3HB) at a relative amount of 20 wt.% leads to the development of a material with suitable processability requirements and good mechanical properties, even after a prolonged hydrolytic degradation treatment.

DATA AVAILABILITY STATEMENT

The datasets generated for this study are available on request to the corresponding author.

AUTHOR CONTRIBUTIONS

DR performed most of the experimental activities. AD analyzed the data and wrote the manuscript. AP conceived the project and corrected the manuscript.

ACKNOWLEDGMENTS

REFERENCES

Ahmed, S., and Jones, F. R. (1990). A review of particulate reinforcement theories for polymer composites. *J. Mater. Sci.* 25, 4933–4942. doi: 10.1007/BF00580110

Barham, P. J., Keller, A., Otun, E. L., and Holmes, P. A. (1984). Crystallization and morphology of a bacterial thermoplastic: poly-3-hydroxybutyrate. *J. Mater. Sci.* 19, 2781–2794. doi: 10.1007/BF01026954

Bhasney, S. M., Bhagabati, P., Kumar, A., and Katiyar, V. (2019). Morphology and crystalline characteristics of polylactic acid [PLA]/linear low density polyethylene [LLDPE]/microcrystalline cellulose [MCC] fiber composite. *Compos. Sci. Technol.* 171, 54–61. doi: 10.1016/j.compscitech.2018.11.028

Bower, D. (2002). *An Introduction to Polymer Physics.* Cambridge: Cambridge University Press. doi: 10.1017/CBO9780511801280

Burlein, G. A. D., and Rocha, M. C. G. (2014). Mechanical and morphological properties of LDPE/PHB blends filled with castor oil pressed cake. *Mater. Res.* 17, 97–105. doi: 10.1590/S1516-14392013005000196

Chandra, R., and Rustgi, R. (1998). Biodegradable polymers. *Prog. Polym. Sci.* 23, 1273–1335. doi: 10.1016/S0079-6700(97)00039-7

Chen, G. Q., and Hajnal, I. (2015). The 'PHAome'. *Trends Biotechnol.* 33, 559–564. doi: 10.1016/j.tibtech.2015.07.006

Datta, D., and Halder, G. (2019). Effect of media on degradability, physico-mechanical and optical properties of synthesized polyolefinic and PLA film in comparison with casted potato/corn starch biofilm. *Process Safety Environ. Protect.* 124, 39–62. doi: 10.1016/j.psep.2019.02.002

Dilkes-Hoffman, L. S., Lane, J. L., Grant, T., Pratt, S., Lant, P. A., and Laycock, B. (2018). Environmental impact of biodegradable food packaging when considering food waste. *J. Clean. Prod.* 180, 325–334. doi: 10.1016/j.jclepro.2018.01.169

Dorigato, A., D'amato, M., and Pegoretti, A. (2012). Thermo-mechanical properties of high density polyethylene - fumed silica nanocomposites: effect of filler surface area and treatment. *J. Polymer Res.* 19, 9889–9899. doi: 10.1007/s10965-012-9889-2

Dorigato, A., Dzenis, Y., and Pegoretti, A. (2013). Filler aggregation as a reinforcement mechanism in polymer nanocomposites. *Mech. Mater.* 61, 79–90. doi: 10.1016/j.mechmat.2013.02.004

Dorigato, A., and Pegoretti, A. (2012). Fracture behaviour of linear low density polyethylene - fumed silica composites. *Eng. Fract. Mech.* 79, 213–224. doi: 10.1016/j.engfracmech.2011.10.014

Dorigato, A., and Pegoretti, A. (2013). (Re)processing effects on linear low-density polyethylene/silica nanocomposites. *J. Polymer Res.* 20, 92–101. doi: 10.1007/s10965-013-0092-x

Dorigato, A., Pegoretti, A., Fambri, L., Lonardi, C., Slouf, M., and Kolarik, J. (2011). Linear low density polyethylene - cycloolefin copolymer blends. *Express Polymer Lett.* 5, 23–37. doi: 10.3144/expresspolymlett.2011.4

Dorigato, A., Pegoretti, A., and Kolarik, J. (2010a). Nonlinear tensile creep of linear low density polyethylene/fumed silica nanocomposites: time-strain superposition and creep prediction. *Polymer Compos.* 31, 1947–1955. doi: 10.1002/pc.20993

Dorigato, A., Pegoretti, A., and Penati, A. (2010b). Linear low-density polyethylene/silica micro- and nanocomposites: dynamic rheological measurements and modelling. *Express Polymer Lett.* 4, 115–129. doi: 10.3144/expresspolymlett.2010.16

Emadian, S. M., Onay, T. T., and Demirel, B. (2017). Biodegradation of bioplastics in natural environments. *Waste Manag.* 59, 526–536. doi: 10.1016/j.wasman.2016.10.006

Galeski, A. (2003). Strength and toughness of crystalline polymer systems. *Prog. Polym. Sci.* 28, 1643–1699. doi: 10.1016/j.progpolymsci.2003.09.003

Geissdoerfer, M., Savaget, P., Bocken, N. M. P., and Hultink, E. J. (2017). The Circular Economy – A new sustainability paradigm? *J. Clean. Prod.* 143, 757–768. doi: 10.1016/j.jclepro.2016.12.048

Geueke, B., Groh, K., and Muncke, J. (2018). Food packaging in the circular economy: overview of chemical safety aspects for commonly used materials. *J. Clean. Prod.* 193, 491–505. doi: 10.1016/j.jclepro.2018.05.005

Ghisellini, P., Cialani, C., and Ulgiati, S. (2016). A review on circular economy: the expected transition to a balanced interplay of environmental and economic systems. *J. Clean. Prod.* 114, 11–32. doi: 10.1016/j.jclepro.2015.09.007

Groh, K. J., Backhaus, T., Carney-Almroth, B., Geueke, B., Inostroza, P. A., Lennquist, A., et al. (2019). Overview of known plastic packaging-associated chemicals and their hazards. *Sci. Total Environ.* 651, 3253–3268. doi: 10.1016/j.scitotenv.2018.10.015

Gulmine, J. V., Janissek, P. R., Heise, H. M., and Akcelrud, L. (2002). Polyethylene characterization by FTIR. *Polym. Test.* 21, 557–563. doi: 10.1016/S0142-9418(01)00124-6

Hahladakis, J. N., and Iacovidou, E. (2018). Closing the loop on plastic packaging materials: what is quality and how does it affect their circularity? *Sci. Total Environ.* 630, 1394–1400. doi: 10.1016/j.scitotenv.2018.02.330

Hancox, N. J. (1992). *Introduction to Industrial Polymers, 2nd Edn.* Munich: Hanser. doi: 10.1016/0261-3069(93)90097-F

Hole, G., and Hole, A. S. (2019). Recycling as the way to greener production: a mini review. *J. Clean. Prod.* 212, 910–915. doi: 10.1016/j.jclepro.2018.12.080

Kalmykova, Y., Sadagopan, M., and Rosado, L. (2018). Circular economy – from review of theories and practices to development of implementation tools. *Resour. Conserv. Recyc.* 135, 190–201. doi: 10.1016/j.resconrec.2017.10.034

Krupa, I., and Luyt, A. S. (2000). Thermal properties of uncross-linked and cross-linked LLDPE/wax blends. *Polym. Degrad. Stab.* 70, 111–117. doi: 10.1016/S0141-3910(00)00097-5

Krupa, I., and Luyt, A. S. (2001). Thermal and mechanical properties of extruded LLDPE/wax blends. *Polym. Degrad. Stab.* 73, 157–161. doi: 10.1016/S0141-3910(01)00082-9

Laycock, B., Nikolić, M., Colwell, J. M., Gauthier, E., Halley, P., Bottle, S., et al. (2017). Lifetime prediction of biodegradable polymers. *Prog. Polym. Sci.* 71, 144–189. doi: 10.1016/j.progpolymsci.2017.02.004

Nguyen, D. M., Do, T. V. V., Grillet, A. C., Ha Thuc, H., and Ha Thuc, C. N. (2016). Biodegradability of polymer film based on low density polyethylene and cassava starch. *Int. Biodeterior. Biodegrad.* 115, 257–265. doi: 10.1016/j.ibiod.2016.09.004

Niaounakis, M. (2019). Recycling of biopolymers – the patent perspective. *Eur. Polym. J.* 114, 464–475. doi: 10.1016/j.eurpolymj.2019.02.027

Nielsen, L. E., and Landel, R. F. (1994). *Mechanical Properties of Polymers and Composites.* New York, NY: Dekker.

Ol'khov, A. A., Iordanskii, A. L., Zaikov, G. E., Shibryaeva, L. S., Litvinov, I. A., and Vlasov, S. V. (2000). Morphologically special features of poly(3-hydroxybutyrate)/low-density polyethylene blends. *Polym. Plast. Technol. Eng.* 39, 783–792. doi: 10.1081/PPT-100101403

Padermshoke, A., Katsumoto, Y., Sato, H., Ekgasit, S., Noda, I., and Ozaki, Y. (2005). Melting behavior of poly(3-hydroxybutyrate) investigated by two-dimensional infrared correlation spectroscopy. *Spectrochim. Acta Part A* 61, 541–550. doi: 10.1016/j.saa.2004.05.004

Pakalapati, H., Chang, C. K., Show, P. L., Arumugasamy, S. K., and Lan, J. C. W. (2018). Development of polyhydroxyalkanoates production from waste feedstocks and applications. *J. Biosci. Bioeng.* 126, 282–292. doi: 10.1016/j.jbiosc.2018.03.016

Pankova, Y. N., Shchegolikhin, A. N., Iordanskii, A. L., Zhulkina, A. L., Ol'khov, A. A., and Zaikov, G. E. (2010). The characterization of novel biodegradable blends based on polyhydroxybutyrate: the role of water transport. *J. Mol. Liq.* 156, 65–69. doi: 10.1016/j.molliq.2010.04.018

Patel, R. M. (2016). "2 - Polyethylene," in *Multilayer Flexible Packaging, 2nd Edn,* ed J. R. Wagner (William Andrew Publishing), 17–34. doi: 10.1016/B978-0-323-37100-1.00002-8

Pedroso, A. G., and Rosa, D. S. (2005). Mechanical, thermal and morphological characterization of recycled LDPE/corn starch blends. *Carbohydr. Polym.* 59, 1–9. doi: 10.1016/j.carbpol.2004.08.018

Ragaert, P., Buntinx, M., Maes, C., Vanheusden, C., Peeters, R., Wang, S., et al. (2019). "Polyhydroxyalkanoates for food packaging applications," in *Reference Module in Food Science* (Elsevier). doi: 10.1016/B978-0-08-100596-5.22502-X

Restrepo-Flórez, J. M., Bassi, A., and Thompson, M. R. (2014). Microbial degradation and deterioration of polyethylene – A review. *Int. Biodeterior. Biodegrad.* 88, 83–90. doi: 10.1016/j.ibiod.2013.12.014

Rocha, M. C. G., and Moraes, L. R. D. C. (2015). Low density polyethylene (LDPE) blends based on Poly(3-Hydroxi-Butyrate) (PHB) and Guar Gum (GG) biodegradable polymers. *Polímeros* 25, 42–48. doi: 10.1590/0104-1428.1495

Rosa, D. D. S., Gaboardi, F., Guedes, C. D. G. F., and Calil, M. R. (2007). Influence of oxidized polyethylene wax (OPW) on the mechanical, thermal, morphological and biodegradation properties of PHB/LDPE blends. *J. Mater. Sci.* 42, 8093–8100. doi: 10.1007/s10853-007-1701-z

Soroudi, A., and Jakubowicz, I. (2013). Recycling of bioplastics, their blends and biocomposites: a review. *Eur. Polym. J.* 49, 2839–2858. doi: 10.1016/j.eurpolymj.2013.07.025

Valentini, F., Dorigato, A., Rigotti, D., and Pegoretti, A. (2019). Polyhydroxyalkanoates/fibrillated nanocellulose composites for additive manufacturing. *J. Polym. Environ.* 27, 1333–1341. doi: 10.1007/s10924-019-01429-8

Van Krevelen, D. W., and Te Nijenhuis, K. (eds.). (2009). "Chapter 24 - processing properties," in *Properties of Polymers, 4th Edn* (Amsterdam: Elsevier), 799–818. doi: 10.1016/B978-0-08-054819-7.00024-8

Veethahavya, K. S., Rajath, B. S., Noobia, S., and Kumar, B. M. (2016). Biodegradation of low density polyethylene in aqueous media. *Proc. Environ. Sci.* 35, 709–713. doi: 10.1016/j.proenv.2016.07.072

Venugopal, G., and Krause, S. (1992). Development of phase morphologies of poly(methyl methacrylate)-polystyrene-toluene mixtures in electric fields. *Macromolecules* 25, 4626–4634. doi: 10.1021/ma00044a025

Walheim, S., Böltau, M., Mlynek, J., Krausch, G., and Steiner, U. (1997). Structure formation via polymer demixing in spin-cast films. *Macromolecules* 30, 4995–5003. doi: 10.1021/ma9619288

Wang, Y., Yin, J., and Chen, G. Q. (2014). Polyhydroxyalkanoates, challenges and opportunities. *Curr. Opin. Biotechnol.* 30, 59–65. doi: 10.1016/j.copbio.2014.06.001

Wattenbarger, M. R., Chan, H. S., Evans, D. F., and Dill, K. A. (1990). Surface-induced enhancement of internal structure in polymers and proteins. *J. Chem. Phys.* 93, 8343–8351. doi: 10.1063/1.459317

Wu, D. T., and Fredrickson, G. H. (1996). Effect of architecture in the surface segregation of polymer blends. *Macromolecules* 29, 7919–7930. doi: 10.1021/ma9602278

Yeo, J. C. C., Muiruri, J. K., Thitsartarn, W., Li, Z., and He, C. (2017). Recent advances in the development of biodegradable PHB-based toughening materials: approaches, advantages and applications. *Mater. Sci. Eng.* 92, 1092–1116. doi: 10.1016/j.msec.2017.11.006

frontiers
in Materials

Check for
updates

Multilayered Bio-Based Electrospun Membranes: A Potential Porous Media for Filtration Applications

Rasoul Esmaeely Neisiany[1]*, Mohammad Saeid Enayati[2], Amin Kazemi-Beydokhti[3], Oisik Das[4] and Seeram Ramakrishna[5]

[1] Department of Materials and Polymer Engineering, Faculty of Engineering, Hakim Sabzevari University, Sabzevar, Iran, [2] Institute of Fundamental Technological Research, Polish Academy of Sciences, Warsaw, Poland, [3] Chemical Engineering Department, Faculty of Petroleum and Petrochemical Engineering, Hakim Sabzevari University, Sabzevar, Iran, [4] Material Science Division, Department of Engineering Sciences and Mathematics, Luleå University of Technology, Luleå, Sweden, [5] Centre for Nanofibers and Nanotechnology, Department of Mechanical Engineering, National University of Singapore, Singapore, Singapore

Among the different polymeric membranes, electrospun membranes have shown promising performance for filtration applications through the facile and controlled preparation method leading to tailored material structure. Furthermore, multilayered bio-based electrospun membranes exhibited superior filtration performance, considering they are eco-friendly with superior mechanical properties and better adsorption efficiency compared to the single-layered electrospun membranes. The aim of this mini-review is to reveal the current state-of-art development of multilayered bio-based electrospun membranes and to provide new insights into the future of tailored membranes toward practical applications.

Keywords: electrospinning, nanofibers, tailored membrane, bio-based multilayered membranes, filtration

INTRODUCTION

The rapid development of industries has led to particulate matter pollution that poses serious threats to the global environment, resources, and public health. Polymeric membranes are attracting attention for their efficient filtration of pollutants and microorganisms from many resources such as water, air, food, and microbiological fluids because of their high mechanical strength, their chemical, thermal, and corrosion resistance, and their minimal production of harmful by-products (Gandavadi et al., 2019; Lv et al., 2019; Ma et al., 2019a). Among the different polymeric membranes, bio-based polymers, i.e., cellulose nanofibers (CNFs), cellulose nanocrystals (CNCs), chitosan, and protein-based nanofibers, all gleaned from renewable resources, have shown superior performance during the filtration of water and microbiological fluids (Charcosset, 2012; Lv et al., 2018). Bio-based membranes have been developed and adopted to overcome the drawbacks of conventional polymeric materials. Additionally, they offer better production rates, more efficient adsorption, and greater potential in filtration performance. Several bio-based polymers have been employed and investigated for filtration purposes in pristine nature or after some modification, such as grafting, blending, and using custom-tailored copolymers in order to enhance the membrane performance. Bio-based polymers, such as poly(vinyl alcohol) (PVA), cellulose acetate (CA), polylactic acid (PLA), poly(glycolic acid), and chitosan, have been studied, since these polymers are eco-friendly, biocompatible and biodegradable, and have higher hydrophilicity and consequently

lower membrane fouling features (Ma et al., 2011a; Sencadas et al., 2012; Mi et al., 2014; Wei et al., 2014).

Various methods such as casting technologies, interfacial polymerization, phase inversion, controlled stretching of thin polymeric films, and electrospinning are used to produce both dense and porous membranes. The porous membranes are normally categorized based on their average pore size. The pore size ranges from 0.1 to 5 μm in microfiltration (MF) for the removal of particles such as bacteria and protozoa, and between 0.01 and 0.1 μm in ultrafiltration (UF) membranes for the eradication of proteins, viruses, colloids, and emulsified oils. Furthermore, nanofiltration (NF) and reverse osmosis (RO) membranes are used for the removal of particles in the range of 1–10 nm and 0.1–1 nm, respectively (Suja et al., 2017). **Figure 1A** schematically shows the pore size ranges of MF, UF, NF, and RO processes. Among the methods for fabrication of porous polymeric membranes, electrospinning is one of the easiest and most cost-efficient techniques to produce fibrous membranes with a wide range of fiber diameter and porosity for the filtration of polluted water, air, considering the ability for bactericidal activity and dye scavenging (Lv et al., 2018; Ma et al., 2019b). Although the electrospun fibrous membranes offer a highly porous non-woven structure, making them suitable for MF, UF, and even NF, they usually exhibit poor mechanical strength due to weak fiber–fiber connections via physical entanglements. Furthermore, the biofouling issues are another drawback of electrospun membranes. Several approaches such as nanomaterial incorporation (Vijay Kumar et al., 2019), as well as surface chemistry manipulation or using bio-based polymers (Liu Z. et al., 2019; Lv et al., 2019; Zhu et al., 2019), have been investigated to address the aforementioned shortcomings. Multilayered electrospun membranes have been proposed to facilitate the combination of electrospun nanofibers with bio-based nanoparticles and nanowhiskers to overcome such obstacles (Qin and Wang, 2008).

Multilayered fibrous membranes are usually composed of various layers, where each layer is separately fabricated to designed pore size and desired surface characteristics. The first layer is usually prepared in a way to perform pre-filtration and provide high mechanical strength during the high flux filtration. On the other hand, the pore size and adsorption selectivity of the next layers are designed based on the application (Liu X. et al., 2019). Furthermore, deposition of the functionalized nanomaterials, on the mid or top layer, provides efficient adsorption performance to eliminate contaminants such as bacteria, viruses, heavy metal ions, dyes, and toxins (Karim et al., 2017; Araga and Sharma, 2019). The past few decades attempted to industrialize the electrospinning technique as the most versatile method for the production of nanofibrous networks. However, the goal still remains to be achieved. Taking into account the practical applications, weak mechanical performance is a serious obstacle that is yet to be overcome. In general, as a result of the incomplete orientation of polymeric chains along the fiber axis, tensile strength and Young's modulus of non-woven electrospun mats do not exceed 300 MPa and 3 GPa, respectively (Yao et al., 2014). Due to insufficient strength, there is a high

risk for the users in the case of filter splitting. Filter split would also lead to the shortening of the functionality of the membrane, which would be economically detrimental (Zhu et al., 2017).

An ISI Web of Science literature search revealed that several review articles have been published on the development of single-layered electrospun membranes for filtration applications (Suja et al., 2017; Zhu et al., 2017; Nabeela Nasreen et al., 2019). However, these studies neither focus on state-of-art multilayered membranes nor on bio-based electrospun membranes. Therefore, the current mini-review is directed toward tailored pore size and size distribution in the electrospun membranes and the recent developments in the two- and three-layer bio-based nanofibrous membranes.

TAILORED MEMBRANE STRUCTURE FOR FILTRATION APPLICATION

Electrospun nanofibers have attracted substantial attention in numerous applications such as filtration (Bassyouni et al., 2019), tissue engineering (Kouhi et al., 2019), wound dressing (Rezvani Ghomi et al., 2019), encapsulation for drug delivery operation (Ranjbar-Mohammadi et al., 2016), and self-healing (Neisiany et al., 2017), because of their facile and cost-efficient fabrication method and special features (Mohammadzadehmoghadam and Dong, 2019). Electrospinning offers versatile production of fibers with diameters in the order of 10 nanometers to several micrometers from a variety of raw materials (Kumar et al., 2019). Moreover, electrospun membranes have several advantages for filtration application due to their high amount of porosity (approximately 80%), including both open and interconnected pore structures and high specific surface area. The classic electrospinning setup involves a high voltage power source, a syringe pump to precisely feed the polymer solution, a grounded collector, an electrically conductive spinneret, and a polymer solution to be electrospun. While the process looks simple, the electro-hydrodynamic and rheological interactions make it complicated (Lee et al., 2018). The processing parameters (such as the applied voltage, feed rate, and air gap) as well as polymer solution parameters (such as concentration, conductivity, and viscosity of solution, molecular weight of the polymer, and solvent evaporation characteristics), and environmental parameters (temperature and humidity) deterministically dictate the spinnability and the prepared fiber characteristics (Huang et al., 2003).

In the case of MF, UF, and NF, the pore size of the membrane controls the filtration performance. Ma et al. (2011a) showed that for a randomly oriented electrospun nanofiber mat, when the membrane porosity was constantly kept at ca. 80 vol%, the pore size of the nanofibrous membrane had a precise correlation with the diameter of the electrospun fibers. The authors reported the average pore size of the nanofibrous membranes to be ca. 3 ± 1 times the nanofiber average diameter. Furthermore, the maximum pore size of the nanofibrous membrane was ca. 10 ± 2 times the nanofiber average diameter (Ma et al., 2011a). Therefore, with simple alteration of the electrospinning effective parameters (e.g., solution and operation parameters), a wide
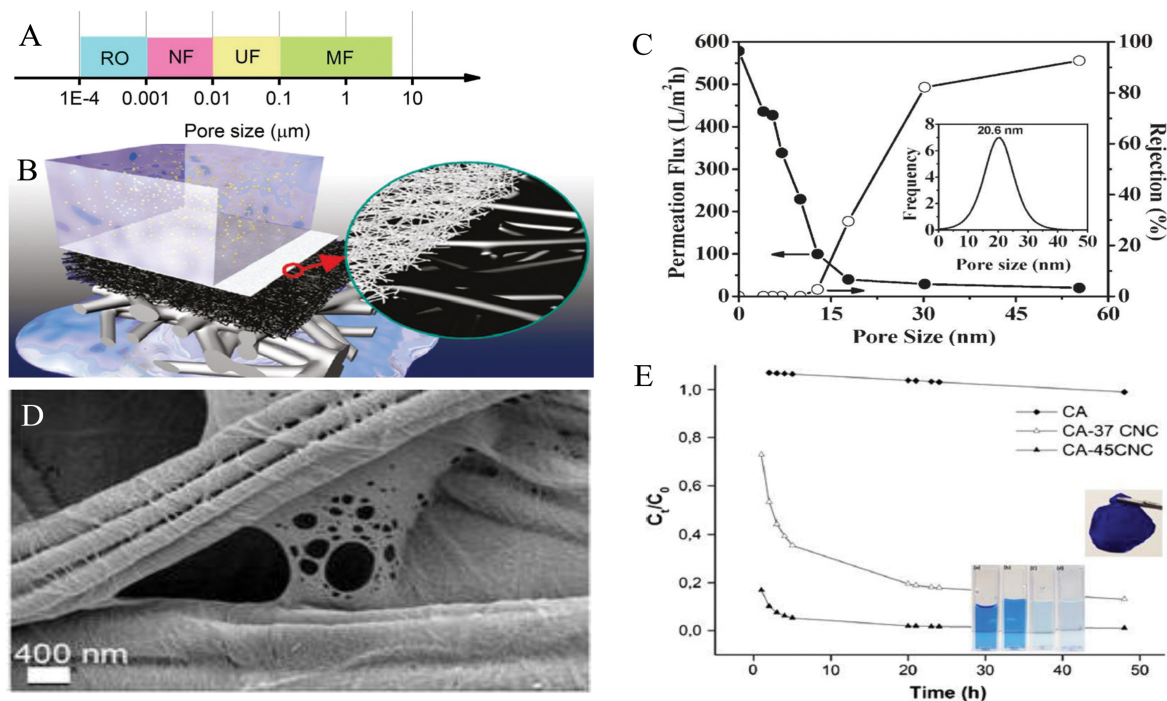
FIGURE 1 | (A) The pore sizes of MF, UF, NF, and RO processes. **(B)** Schematic illustration of the three-layered fibrous membrane, and **(C)** its filtration performance (Ma et al., 2011b), reproduced with permission from the American Chemical Society. **(D)** The SEM image of the electrospun CA nanofibers coated by CNCs, and **(E)** its filtration performance as a function of CNC content during the time (Goetz et al., 2018), reproduced under the terms of the Creative Commons Attribution (CC BY 3.0) license.

range of average nanofiber diameter and consequently pore size can be designed and obtained.

Additionally, specific molecule or ligand immobilization onto the membrane surfaces leads to affinity membranes with selectively captured targeted molecules for use in technologically advanced processes such as membrane filtration and fixed-bed liquid chromatography (Park et al., 2007; Esmaeely Neisiany et al., 2020). This immobilization allows for the purification of molecules according to the differences in biological functions or physical/chemical properties rather than molecular size (Ma et al., 2006). Several ligands, proteins, and enzymes were immobilized on a broad range of biodegradable electrospun polymers (such as PVA, PGA, and PLA) depending on the requirement. An affinity membrane that simultaneously combines size-based filtration and high selectivity is now an attractive approach for purifying and filtering biological fluids (Fu et al., 2018; Ng et al., 2019).

LAYERED ELECTROSPUN NANOFIBROUS MEMBRANES

As discussed in the section "Tailored Membrane Structure for Filtration Application," electrospun membranes have some limitations, including low mechanical properties and thermal and chemical stability (Barhate and Ramakrishna, 2007). To overcome these drawbacks, the addition of different

nanomaterials into the spinning solution has been widely tested (Enayati et al., 2019). However, the addition of a high volume of reinforcing fibers creates difficulties in the electrospinning process and significantly decreases the properties of the prepared nanofibers (Naseri et al., 2015). Therefore, multilayered electrospun membranes were proposed as a potential alternative for the easier combination of electrospun nanofibers with bio-based nanoparticles and nanowhiskers to address the above-mentioned shortcomings, i.e., low mechanical strength and fouling. **Figure 1B** schematically presents a three-layered fibrous membrane (including a supporting layer), which usually consists of conventional microfibers, an electrospun mid-layer, and a top barrier layer. **Figure 1C** presents the filtration performance of this membrane, which is composed of microfibers, electrospun nanofibers, and CNFs as a top barrier layer (Ma et al., 2011b). Comprehensive research on the development of multilayered electrospun membranes has been carried out by Hadi et al. (2019) at Stony Brook University in the United States. Most of the researches have employed non-biodegradable polymers such as polyacrylonitrile (PAN), polyvinylidene fluoride (PVDF), and polysulfone (PSU) (Díez et al., 2018). Goetz et al. (2018) at Luleå University of Technology in Sweden, and Zhao et al. (2019) in China investigated the development of fully bio-based multilayered electrospun membranes, which were subsequently reviewed. However, most of the research on multilayered electrospun membranes has been based on the combination of synthesized and bio-based polymers. These types of membranes

for air filtration were comprehensively reviewed by the Huang group (Zhu et al., 2017; Lv et al., 2018). **Table 1** summarizes the details of the reported multilayered membranes composed of synthesized, poly (ethylene terephthalate) (PET) and PAN, and bio-based polymers.

Goetz et al. (2018) infused chitin nanocrystals onto the electrospun CA mesofibers. The prepared hierarchical structure showed a wide range of pore sizes due to the combination of electrospun CA mesofibers (fiber diameter of 0.5–3.3 μm) and chitin nanocrystals (diameter of 10–30 nm). This led to the development of multilayered biodegradable membranes with 10 nm pore sizes. The incorporation of the chitin nanocrystals at the junction points of the electrospun CA mesofibers increased the mechanical strength and modulus of the two-layered membranes by 131 and 340%, respectively, compared to single-layered CA electrospun mesofibers. Furthermore, the hydrophobic nature of the CA mats changed to super hydrophilic upon incorporation of the chitin nanocrystals. This consequently decreased biofilm formation and abiotic fouling significantly. The prepared multilayered biodegradable membrane showed potential in MF of biological and organic contaminants from the water.

Recently, Nair and Mathew (2017) reported a combination of electrospinning and electrospraying techniques to fabricate a bilayer composite membrane based on the electrospun CA membrane coated by CNCs for cationic dye adsorption. The authors showed that the combination of electrospinning and electrospraying improved the availability of the CNCs on the surfaces of the electrospun CA nanofibers compared to the embedding of CNCs into the electrospun solution. This consequently enabled efficient dye adsorption due to higher surface area. Elsewhere, Goetz et al. (2018) developed a layered membrane structure wherein electrospun CA nanofibers were impregnated with several concentrations of CNCs. **Figure 1D** displays the SEM micrograph of the CA nanofibers coated by CNCs. It can be observed that a wide range of porosities was induced after the coating of the electrospun CA nanofibrous membrane by a very fine CNC layer (diameter of 5–10 nm). The hierarchical structure considerably enhanced the mechanical properties, surface area, hydrophilicity, and filtration performance of the membrane, compared to the neat CA electrospun nanofibrous membrane. The filtration performance of the membrane substantially increased by the incorporation of CNC and increasing the CNC content, as well (**Figure 1E**).

Zhao et al. (2019) created a fully bio-based three-layered electrospun membrane via electrospinning of poly(3-hydroxybutyrate-co-3-hydroxyvalerate) (PHBV) and CA, followed by the casting of chitosan. PHBV was selected as a fibrous substrate due to its good biodegradability and spinnability. Since PHBV fibers were not fine enough to provide the filtration demand, they were covered by electrospun CA nanofibers as a mid-fibrous supporting layer. The prepared two-layered electrospun membranes, with different fiber diameters, introduced a high porosity and interconnected pores, while the chitosan top barrier layer, prepared via the phase inversion technique, and improved the rejection ratio of

TABLE 1 | Multilayered membranes composed of synthesis and bio-based polymers.

First layer	Second layer	Third layer	Pore size (nm)	Porosity (%)	Application	References
Non-woven PET microfibers	PVA	N/A	200	71	Oil in water UF	Tang et al., 2009
Non-woven PET microfibers	PVA	N/A	210–300	N/A	MF for water purification	Liu et al., 2013
CA	CNC	N/A	6.6–10.6	N/A	Dye adsorption	Nair and Mathew, 2017
CA	CNC	N/A	N/A	69–83	Water purification	Goetz et al., 2018
PVA	PAN	N/A	172–1,027	85	Heavy metal adsorption	Liu X. et al., 2019
Non-woven PET microfibers	PAN	Cellulose and chitin nanofibers	20	N/A	Water purification and virus adsorption	Ma et al., 2011b
Non-woven PET microfibers	PAN	Cellulose nanofibers	20–650	N/A	NF of heavy metal ions	Wang et al., 2014
Non-woven PET microfibers	PAN	Grafted cellulose nanofibers by cysteine	450–600	78–83	MF and adsorption of chromium (VI) and lead (II)	Yang et al., 2014
Non-woven PET microfibers	PAN	Infectious polymerized cellulose nanofibers	N/A	N/A	RO for the desalination	Wang et al., 2017
Non-woven PET microfibers	PAN	Cellulose nanofibers	30–40	80	UF of proteins	Hadi et al., 2019
PHBV	CA	Chitosan	N/A	N/A	Metal ions adsorption from water	Zhao et al., 2019

the membrane. Furthermore, the chitosan functional groups improved the membrane efficiency by adsorbing metal ions or other contaminants from water.

CONCLUSION AND FUTURE INSIGHTS

The development of multilayered electrospun membranes offers an opportunity for filtration applications, including MF, UF, NF, RO, and FO, as well as adsorption of heavy metal ions. The high porosity of the electrospun layer (approximately 80%) offers higher flux, reducing the energy consumption, in comparison with conventional membranes. On the other hand, incorporation of nanosized biomaterials such as cellulose, with an average diameter of 5–10 nm, yields a wide pore size distribution for capturing very fine particles, even with 30 nm diameters. In addition, the hydrophilic nature of cellulose considerably decreases the fouling of the membrane and makes it more biocompatible and biodegradable. However, more research is required to develop a fully biodegradable multilayer electrospun membrane with a wide range of pore

sizes. Besides the PVA, CA, and chitosan, other bio-based polymers can be investigated for the fabrication of the electrospun nanofibrous layers with specific applications. From the economic point of view, it is required to exploit other cost-efficient nanofiber fabrication approaches, particularly in preparing tailored nanofibers, such as solution blowing, co-axial electrospinning, and centrifugal spinning. This will consequently address the concerns of the various industries regarding the development of low-cost, non-toxic, and environmentally friendly nanofibrous membranes. Finally, it would be necessary to comprehensively explore the filtration performance of such electrospun membranes and address the global concerns on widespread air polluting sources.

AUTHOR CONTRIBUTIONS

RN, ME, AK-B, and OD summarized the literature and wrote a major part of the manuscript. OD and SR conducted the deep review, editing, guidance, and supervision. All authors have read and approved the article for publication.

REFERENCES

Araga, R., and Sharma, C. S. (2019). Amine functionalized electrospun cellulose nanofibers for fluoride adsorption from drinking water. *J. Polym. Environ.* 27, 816–826. doi: 10.1007/s10924-019-01394-2

Barhate, R. S., and Ramakrishna, S. (2007). Nanofibrous filtering media: filtration problems and solutions from tiny materials. *J. Membr. Sci.* 296, 1–8. doi: 10.1016/j.memsci.2007.03.038

Bassyouni, M., Abdel-Aziz, M. H., Zoromba, M. S., Abdel-Hamid, S. M. S., and Drioli, E. (2019). A review of polymeric nanocomposite membranes for water purification. *J. Ind. Eng. Chem.* 73, 19–46. doi: 10.1016/j.jiec.2019.01.045

Charcosset, C. (2012). "1 - Principles on membrane and membrane processes," in *Membrane Processes in Biotechnology and Pharmaceutics*, ed. C. Charcosset (Amsterdam: Elsevier), 1–41. doi: 10.1016/b978-0-444-56334-7.00001-0

Díez, B., Amariei, G., and Rosal, R. (2018). Electrospun composite membranes for fouling and biofouling control. *Ind. Eng. Chem. Res.* 57, 14561–14570. doi: 10.1021/acs.iecr.8b04011

Enayati, M. S., Neisiany, R. E., Sajkiewicz, P., Behzad, T., Denis, P., and Pierini, F. (2019). Effect of nanofiller incorporation on thermomechanical and toughness of poly (vinyl alcohol)-based electrospun nanofibrous bionanocomposites. *Theor. Appl. Fract. Mech.* 99, 44–50. doi: 10.1016/j.tafmec.2018.11.006

Esmaeely Neisiany, R., Enayati, M. S., Sajkiewicz, P., Pahlevanneshan, Z., and Ramakrishna, S. (2020). Insight into the current directions in functionalized nanocomposite hydrogels. *Front. Mater.* 7:25. doi: 10.3389/fmats.2020.00025

Fu, Q., Duan, C., Yan, Z., Si, Y., Liu, L., Yu, J., et al. (2018). Electrospun nanofibrous composite materials: a versatile platform for high efficiency protein adsorption and separation. *Compos. Commun.* 8, 92–100. doi: 10.1016/j.coco.2017.11.007

Gandavadi, D., Sundarrajan, S., and Ramakrishna, S. (2019). Bio-based nanofibers involved in wastewater treatment. *Macromol. Mater. Eng.* 304:1900345. doi: 10.1002/mame.201900345

Goetz, L. A., Naseri, N., Nair, S. S., Karim, Z., and Mathew, A. P. (2018). All cellulose electrospun water purification membranes nanotextured using cellulose nanocrystals. *Cellulose* 25, 3011–3023. doi: 10.1007/s10570-018-1751-1

Hadi, P., Yang, M., Ma, H., Huang, X., Walker, H., and Hsiao, B. S. (2019). Biofouling-resistant nanocellulose layer in hierarchical polymeric membranes: synthesis, characterization and performance. *J. Membr. Sci.* 579, 162–171. doi: 10.1016/j.memsci.2019.02.059

Huang, Z.-M., Zhang, Y. Z., Kotaki, M., and Ramakrishna, S. (2003). A review on polymer nanofibers by electrospinning and their applications in

nanocomposites. *Compos. Sci. Technol.* 63, 2223–2253. doi: 10.1016/s0266-3538(03)00178-7

Karim, Z., Hakalahti, M., Tammelin, T., and Mathew, A. P. (2017). In situ TEMPO surface functionalization of nanocellulose membranes for enhanced adsorption of metal ions from aqueous medium. *RSC Adv.* 7, 5232–5241. doi: 10.1039/c6ra25707k

Kouhi, M., Jayarama Reddy, V., Fathi, M., Shamanian, M., Valipouri, A., and Ramakrishna, S. (2019). Poly (3-hydroxybutyrate-co-3-hydroxyvalerate)/fibrinogen/bredigite nanofibrous membranes and their integration with osteoblasts for guided bone regeneration. *J. Biomed. Mater. Res. A* 107, 1154–1165. doi: 10.1002/jbm.a.36607

Kumar, M., Hietala, M., and Oksman, K. (2019). Lignin-based electrospun carbon nanofibers. *Front. Mater.* 6:62. doi: 10.3389/fmats.2019.00062

Lee, J. K. Y., Chen, N., Peng, S., Li, L., Tian, L., Thakor, N., et al. (2018). Polymer-based composites by electrospinning: preparation & functionalization with nanocarbons. *Prog. Polym. Sci.* 86, 40–84. doi: 10.1016/j.progpolymsci.2018.07.002

Liu, X., Ma, H., and Hsiao, B. S. (2019). Interpenetrating nanofibrous composite membranes for water purification. *ACS Appl. Nano Mater.* 2, 3606–3614. doi: 10.1021/acsanm.9b00565

Liu, Y., Wang, R., Ma, H., Hsiao, B. S., and Chu, B. (2013). High-flux microfiltration filters based on electrospun polyvinylalcohol nanofibrous membranes. *Polymer* 54, 548–556. doi: 10.1016/j.polymer.2012.11.064

Liu, Z., Ma, W., Zhang, M., Zhang, Q., Xiong, R., and Huang, C. (2019). Fabrication of superhydrophobic electrospun polyimide nanofibers modified with polydopamine and polytetrafluoroethylene nanoparticles for oil–water separation. *J. Appl. Polym. Sci.* 136:47638. doi: 10.1002/app.47638

Lv, D., Wang, R., Tang, G., Mou, Z., Lei, J., Han, J., et al. (2019). Ecofriendly electrospun membranes loaded with visible-light-responding nanoparticles for multifunctional usages: highly efficient air filtration, dye scavenging, and bactericidal activity. *ACS Appl. Mater. Interfaces* 11, 12880–12889. doi: 10.1021/acsami.9b01508

Lv, D., Zhu, M., Jiang, Z., Jiang, S., Zhang, Q., Xiong, R., et al. (2018). Green electrospun nanofibers and their application in air filtration. *Macromol. Mater. Eng.* 303:1800336.

Ma, H., Burger, C., Hsiao, B. S., and Chu, B. (2011a). Ultra-fine cellulose nanofibers: new nano-scale materials for water purification. *J. Mater. Chem.* 21, 7507–7510.

Ma, H., Burger, C., Hsiao, B. S., and Chu, B. (2011b). Ultrafine polysaccharide nanofibrous membranes for water purification. *Biomacromolecules* 12, 970–976. doi: 10.1021/bm1013316

Ma, W., Ding, Y., Zhang, M., Gao, S., Li, Y., Huang, C., et al. (2019a). Nature-inspired chemistry toward hierarchical superhydrophobic, antibacterial and biocompatible nanofibrous membranes for effective UV-shielding, self-cleaning and oil-water separation. *J. Hazardous Mater.* 384:121476. doi: 10.1016/j.jhazmat.2019.121476

Ma, W., Zhang, M., Liu, Z., Kang, M., Huang, C., and Fu, G. (2019b). Fabrication of highly durable and robust superhydrophobic-superoleophilic nanofibrous membranes based on a fluorine-free system for efficient oil/water separation. *J. Membr. Sci.* 570-571, 303–313. doi: 10.1016/j.memsci.2018.10.035

Ma, Z., Masaya, K., and Ramakrishna, S. (2006). Immobilization of Cibacron blue F3GA on electrospun polysulphone ultra-fine fiber surfaces towards developing an affinity membrane for albumin adsorption. *J. Membr. Sci.* 282, 237–244. doi: 10.1016/j.memsci.2006.05.027

Mi, X., Vijayaragavan, K. S., and Heldt, C. L. (2014). Virus adsorption of water-stable quaternized chitosan nanofibers. *Carbohyd. Res.* 387, 24–29. doi: 10.1016/j.carres.2014.01.017

Mohammadzadehmoghadam, S., and Dong, Y. (2019). Fabrication and characterization of electrospun silk fibroin/gelatin scaffolds crosslinked with glutaraldehyde vapor. *Front. Mater.* 6:91. doi: 10.3389/fmats.2019.00091

Nabeela Nasreen, A. S., Sundarrajan, S., Syed Nizar, A. S., and Ramakrishna, S. (2019). Nanomaterials: solutions to water-concomitant challenges. *Membranes* 9:40. doi: 10.3390/membranes9030040

Nair, S. S., and Mathew, A. P. (2017). Porous composite membranes based on cellulose acetate and cellulose nanocrystals via electrospinning and electrospraying. *Carbohyd. Polym.* 175, 149–157. doi: 10.1016/j.carbpol.2017.07.048

Naseri, N., Mathew, A. P., Girandon, L., Fröhlich, M., and Oksman, K. (2015). Porous electrospun nanocomposite mats based on chitosan–cellulose nanocrystals for wound dressing: effect of surface characteristics of nanocrystals. *Cellulose* 22, 521–534.

Neisiany, R. E., Lee, J. K. Y., Khorasani, S. N., and Ramakrishna, S. (2017). Towards the development of self-healing carbon/epoxy composites with improved potential provided by efficient encapsulation of healing agents in core-shell nanofibers. *Polym. Test.* 62, 79–87.

Ng, I. S., Song, C. P., Ooi, C. W., Tey, B. T., Lee, Y.-H., and Chang, Y.-K. (2019). Purification of lysozyme from chicken egg white using nanofiber membrane immobilized with Reactive Orange 4 dye. *Int. J. Biol. Macromol.* 134, 458–468. doi: 10.1016/j.ijbiomac.2019.05.054

Park, K., Ju, Y. M., Son, J. S., Ahn, K.-D., and Han, D. K. (2007). Surface modification of biodegradable electrospun nanofiber scaffolds and their interaction with fibroblasts. *J. Biomater. Sci. Polym. Ed.* 18, 369–382.

Qin, X.-H., and Wang, S.-Y. (2008). Electrospun nanofibers from crosslinked poly(vinyl alcohol) and its filtration efficiency. *J. Appl. Polym. Sci.* 109, 951–956.

Ranjbar-Mohammadi, M., Zamani, M., Prabhakaran, M. P., Bahrami, S. H., and Ramakrishna, S. (2016). Electrospinning of PLGA/gum tragacanth nanofibers containing tetracycline hydrochloride for periodontal regeneration. *Mater. Sci. Eng. C* 58, 521–531. doi: 10.1016/j.msec.2015.08.066

Rezvani Ghomi, E., Khalili, S., Nouri Khorasani, S., Esmaeely Neisiany, R., and Ramakrishna, S. (2019). Wound dressings: current advances and future directions. *J. Appl. Polym. Sci.* 136:47738.

Sencadas, V., Correia, D. M., Ribeiro, C., Moreira, S., Botelho, G., Gómez Ribelles, J. L., et al. (2012). Physical-chemical properties of cross-linked chitosan electrospun fiber mats. *Polym. Test.* 31, 1062–1069.

Suja, P. S., Reshmi, C. R., Sagitha, P., and Sujith, A. (2017). Electrospun nanofibrous membranes for water purification. *Polym. Rev.* 57, 467–504.

Tang, Z., Wei, J., Yung, L., Ji, B., Ma, H., Qiu, C., et al. (2009). UV-cured poly(vinyl alcohol) ultrafiltration nanofibrous membrane based on electrospun nanofiber scaffolds. *J. Membr. Sci.* 328, 1–5.

Vijay Kumar, V., Ramakrishna, S., Kong Yoong, J. L., Esmaeely Neisiany, R., Surendran, S., and Balaganesan, G. (2019). Electrospun nanofiber interleaving in fiber reinforced composites—Recent trends. *Mater. Des. Process. Commun.* 1:e24.

Wang, X., Yeh, T.-M., Wang, Z., Yang, R., Wang, R., Ma, H., et al. (2014). Nanofiltration membranes prepared by interfacial polymerization on thin-film nanofibrous composite scaffold. *Polymer* 55, 1358–1366.

Wang, Z., Ma, H., Chu, B., and Hsiao, B. S. (2017). Fabrication of cellulose nanofiber-based ultrafiltration membranes by spray coating approach. *J. Appl. Polym. Sci.* 134:44583.

Wei, Z., Zhao, H., Zhang, J., Deng, L., Wu, S., He, J., et al. (2014). Poly(vinyl alcohol) electrospun nanofibrous membrane modified with spirolactam–rhodamine derivatives for visible detection and removal of metal ions. *RSC Adv.* 4, 51381–51388.

Yang, R., Aubrecht, K. B., Ma, H., Wang, R., Grubbs, R. B., Hsiao, B. S., et al. (2014). Thiol-modified cellulose nanofibrous composite membranes for chromium (VI) and lead (II) adsorption. *Polymer* 55, 1167–1176.

Yao, J., Bastiaansen, W. M. C., and Peijs, T. (2014). High strength and high modulus electrospun nanofibers. *Fibers* 2, 158–186.

Zhao, X., Liu, Y., Shuai, Z., and Wang, C. (2019). Preparation and performance of three-layered structure composite membrane for heavy metal ions and hazardous dyes rejection. *Polym. Eng. Sci.* 59, E322–E329.

Zhu, M., Han, J., Wang, F., Shao, W., Xiong, R., Zhang, Q., et al. (2017). Electrospun nanofibers membranes for effective air filtration. *Macromol. Mater. Eng.* 302:1600353.

Zhu, M., Xiong, R., and Huang, C. (2019). Bio-based and photocrosslinked electrospun antibacterial nanofibrous membranes for air filtration. *Carbohyd. Polym.* 205, 55–62. doi: 10.1016/j.carbpol.2018.09.075

Fabrication and Characterization of Electrospun Silk Fibroin/Gelatin Scaffolds Crosslinked With Glutaraldehyde Vapor

Soheila Mohammadzadehmoghadam and Yu Dong*

School of Civil and Mechanical Engineering, Curtin University, Perth, WA, Australia

Bombyx mori silk fibroin (SF) /gelatin nanofiber mats with different blend ratios of 100/0, 90/10, and 70/30 were prepared by electrospinning and crosslinked with glutaraldehyde (GTA) vapor at room temperature. GTA was shown to induce the conformational transition of SFs from random coils to β sheets along with increasing nanofiber diameters with the addition of gelatin into SFs. It was found that by increasing the gelatin content, crosslinking degree was enhanced from 34% for pure SF nanofiber mats to 43% for SF/gelatin counterparts at the blend ratio of 70/30, which directly affected mechanical properties, porosity, and water uptake capacity (WUC) of prepared nanofiber mats. The addition of 10 and 30 wt% gelatin into SFs improved tensile strengths of SF/gelatin nanofiber mats by 10 and 27% along with moderate increases in Young's modulus by 12 and 27%, respectively, as opposed to plain SF counterparts. However, both porosity and WUC were found to decrease from 62 to 405% for pristine SF nanofiber mats to 47 and 232% for SF/gelatin counterparts at the blend ratio of 70/30 accordingly. To further evaluate the combined effect of GTA crosslinking and gelatin content on biological response of SF/gelatin scaffolds, the proliferation assay using 3T3 mouse fibroblast was conducted. In comparison with pure SFs, cell proliferation rate was lower for SF/gelatin constructs, which declined when the gelatin content increased. These results indicated that the adverse effect of GTA crosslinking on cell response may be ascribed to imposed changes in morphology and physiochemical properties of SF/gelatin nanofiber mats. Although crosslinking could be used to improve mechanical properties of nanofiber mats, it reduced their capacity to support the cell activity. GTA optimization is required to further modulate the physico-chemical properties of SF/gelatin nanofiber mats in order to obtain stable materials with favorable bioactive properties and promote cellular responses for tissue engineering applications.

Keywords: silk fibroin (SF), gelatin, glutaraldehyde, nanofibers, electrospinning, tissue engineering

INTRODUCTION

Tissue engineering is a cutting-edge technology for the reconstruction of damaged or lost tissues and organs with the aid of engineered tissue scaffolds in order to produce an active microenvironment to restore functions in the regeneration process, which is generally followed by the integration with host tissues. Extracellular matrix (ECM) plays a pivotal role in cell survival, migration and differentiation in addition to the presentation and storage of growth factors and signal detection (Thein-Han et al., 2009; Kim et al., 2012; Lai et al., 2014). Hence, one of main targets is to design tissue scaffolds with the recapitulation of ECM architectures by using various approaches such as phase separation (Akbarzadeh and Yousefi, 2014), self-assembly (Hartgerink et al., 2001), electrospinning (Ibrahim et al., 2017), solvent casting and particulate leaching (Sin et al., 2010). In between, electrospun nanofibers have gained enormous attention due to their intriguing characteristics including large surface area, high porosity with interconnected pores. In this process, a high electrical voltage is often applied to a polymer solution in a finite distance between a capillary and a collecting substrate. As a result, a polymer jet is ejected from the charged capillary along with the solvent evaporation to allow for the production of continuous polymeric microfibers or nanofibers received on the collecting substrate (Agarwal et al., 2008; Bhardwaj and Kundu, 2010; Ingavle and Leach, 2014).

Native ECM is a complex of polyprotein and polysaccharide with nanofibrous structures. Accordingly, it has been well-documented that using protein and polysaccharides for biomaterials not only mimics ECM structures but also remarkably improves cell attachment, proliferation, and differentiation for tissue regeneration (Li et al., 2005; Allori et al., 2008; Khadka and Haynie, 2012; Wang et al., 2016). In this context, SFs extracted from Bombyx mori are considered as a promising fibrous biomaterial consisting of heavy chains (350 kDa) and light chains (25 kDa) linked together by a disulfide bond. The high molar-mass chains primarily contain Gly-Ala-Gly-Ala-Gly-Ser, which can form stable anti-parallel β-sheet crystallites and contribute greatly to the rigidity and tensile strength of SFs. The β-sheet crystalline structures of fibroins (silk-II conformation) can take up to 70% entire protein structures. Crystalline domains are surrounded by hydrophilic and non-repetitive amorphous regions (silk I conformation) with typical silk resilience (Zafar et al., 2015; Qi et al., 2017). SFs offer distinctive features including good biocompatibility, oxygen and water vapor permeability, biodegradability, low inflammatory responses, non-blood clotting effects, and good mechanical properties (Kundu et al., 2013; Li et al., 2013; Bhattacharjee et al., 2017). Hence it has attracted significant attention in the development of new advanced materials for tissue engineering applications. Furthermore, the properties of SFs may not completely meet the requirements for tissue engineering applications since it is very difficult to regulate cell proliferation and differentiation when SF nanofibers are used alone. For instance, due to the lack of bioactive peptides, SFs do not support cell biological activities as satisfactorily as other proteins like collagen and gelatin (Buitrago et al., 2018).

As a result, it appears to be more efficient to produce SFs with optimum properties when blended with other proteins (Morgan et al., 2008; Yin et al., 2009).

Gelatin is an inexpensive natural polymer derived from a partial hydrolysis of collagen, which is considered to be non-immunogenic, biodegradable, easy to process and biocompatible for clinic use (Aldana and Abraham, 2017; Babitha et al., 2017). Such a protein also has the natural cell binding motifs like arginine-glycine-aspartic acid (RGD) that is favorable for cell activities. However, gelatin is rarely used alone owing to its high brittleness, and thus needs to be modified with several methods including crosslinking, grafting and blending (Hersel et al., 2003; Zhang et al., 2006; Wongputtaraksa et al., 2012; Taddei et al., 2013; Poursamar et al., 2016).

Notwithstanding above-mentioned properties possessed by SFs and gelatin, their applications in tissue engineering alone are quite limited arising from poor mechanical properties and unstable structures under physiological conditions (Taddei et al., 2013; Yao et al., 2016). To overcome this demerit, crosslinking methods based on natural or synthetic reagents are employed, among which glutaraldehyde (GTA) is the most common crosslinker due to its high efficiency in stabilizing collagenous materials. Despite the lower cytotoxicity of other crosslinkers, they still cannot match GTA in collagen stabilization and its risk of cytotoxicity can be reduced by the treatment prior to the usage or decreasing the GTA concentration (Cheung and Nimni, 1982; Bigi et al., 2001). Zhang et al. (2006) found that GTA vapor promoted the content of α-helix structures for electrospun gelatin fibers, further leading to the improvements of both their thermal stability and mechanical properties. Wang et al. (2014) reported that GTA induced the conformational transition of SF films from random coils to β sheets, and had the effect on the interaction between peptide chains of SFs, resulting in great changes in mechanical and dissolution properties.

Electrospun SF/gelatin nanofiber mats have already been developed and evaluated, as evidenced by Yin et al. (2009) to treat such mats with methanol and confirm their conformational changes from random coils to β-sheet structures. Besides, it was noted that the β-sheet structures increased with addition of gelatin, resulting in the improvement of their mechanical properties. Okhawilai et al. (2010) employed carbodiimide hydrochloride (EDC) and N-hydroxysuccinimide (NHS) solutions to crosslink electrospun Thai SF/gelatin fiber mats, which resulted in their controllable biodegradation. Shan et al. (2015) reported that wound dressings were prepared based on electrospun SF/gelatin fiber mats loaded with astragaloside IV without using any crosslinking agents despite a time-consuming electrospinning process for 30 h. Such prepared dressings were found to enhance the cell adhesion and proliferation with good in vitro biocompatibility. The recent study carried out by Dadras Chomachayi et al. (2018) revealed that SF/gelatin fiber mats containing antibacterial agents could be crosslinked by GTA, subsequently subjected to methanol treatment. It was demonstrated that bulk hydrophilicity and mass loss of SF mats were enhanced with the addition of gelatin.

Nonetheless, to our best knowledge, crosslinking electrospun SF/gelatin nanofibers with GTA has been rarely addressed

particularly with very limited biological applications. The aim of this study lies in the evaluation for the effect of gelatin content on material properties and structures of SF nanofibers crosslinked with GTA in order to understand the potential use of such biomaterial matrices as scaffolds for tissue engineering by means of scanning electron microscopy (SEM), Fourier transform infrared spectroscopy (FTIR), mechanical testing, degree of crosslinking tests, water uptake tests, water contact angle measurements, X-ray diffraction (XRD) analysis and biocompatibility assessment based on fibroblast cells.

MATERIALS AND METHODS

Materials

Cocoons of Bombyx mori silkworms were supplied by The Yarn Tree Co. (A quality, Greenville, SC, USA). Gelatin from porcine skin (type A, 300 bloom), glutaraldehyde (GTA) (grade I, 25% in H_2O), hydrochloric acid (HCl), sodium carbonate (Na_2CO_3), lithium bromide (LiBr), sodium bicarbonate ($NaHCO_3$), 2,4,6-trinitro-benzene-sulfonic acid (TNBS), methanol and formic acid were purchased from Sigma Aldrich Pty Ltd (NSW, Australia). All chemicals were used without modification as material-processing grades.

SF Preparation

Bombyx mori cocoons were boiled in an aqueous solution of 0.02M Na_2CO_3 for 30 min, and then were rinsed thoroughly with distilled water. Degummed SFs were then dissolved in 9.3 M LiBr solutions at 60°C for 4 h and dialyzed in deionized water for 48 h using a dialysis membrane (12,400 MWCO, Sigma Aldrich). The dialysate was passed through a filter with the pore size of 0.22 μm to remove insoluble debris and freeze-dried in order to obtain finally prepared SFs.

Electrospinning

To prepare electrospinning solutions, SFs were dissolved in 99% formic acid and stirred for 2 h with a KA®-RCT basic magnetic stirrer. Afterwards, a desired amount of gelatin was added and the mixture was further stirred for 1 h to prepare a homogeneous solution. SF/gelatin solutions with different weight ratios (i.e., 100/0, 90/10, 70/30) were prepared at the final solution concentration of 13 wt%/v. Gelatin solution with 13 wt% concentration in formic acid was also prepared as a control sample. For electrospinning setup, SF/gelatin solution was loaded in a 10 ml syringe with a blunt needle (inner diameter: 0.6 mm). Solution flow rate was fixed at 0.3 ml/h and a high voltage of 16 kV was applied to the droplets of injected solutions. Resulting nanofibers were collected on a plate collector with a distance of 13 cm from syringe tip. The collected nanofiber mats were dried overnight in a fume hood at room temperature. The electrospinning process was conducted on a NaBond NEU commercial nanofiber electrospinning unit (NaBond Technologies Co., Ltd., Shenzhen, China) at the ambient condition.

To enhance the structural stability of SF/gelatin fibrous scaffolds, the crosslinking process was carried out by exposing nanofibers to the vapor of 20% (v/v) GTA at room temperature for 6 h. After crosslinking, samples were immersed in 0.1 M glycine aqueous solution for 30 min to block the residues of aldehyde groups.

EXPERIMENTAL CHARACTERIZATION

Viscosity Measurement

Prepared solution viscosities used for electrospinning were measured via a Modular Advanced Rheometer System (Haake MARS, Thermo Electron Corp., Germany) and data were extracted via HAAKE RheoWin Data Manager Software. The shear rate was linearly increased from 10 to 100 s^{-1} with the temperature being maintained at 25°C.

Scanning Electron Microscopy (SEM)

Fiber morphology was observed by Zeiss EVO 40XVP SEM at an accelerating voltage of 15 kV. Samples were fixed on SEM stubs and sputter coated with platinum prior to the SEM observation. The average fiber diameter was determined by randomly measuring 100 fibers (fiber number $N = 100$) from each SEM image using ImageJ® software and expressed as "mean ± standard deviation".

Fourier Transform Infrared (FTIR) Spectroscopy

The conformational characterization of fibrous scaffolds was carried out by 100FT-IR Spectrometer-Perkin (Japan) with the resolution of 4 cm^{-1} at the spectral range of 4,000–400 cm^{-1} using an attenuated total reflectance (ATR) method.

X-Ray Diffraction (XRD) Analysis

The crystalline structures of SF/gelatin nanofiber mats were determined by X-ray diffractometer D8 Advance (Bruker AXS, Germany), with a Cu Kα radiation source (wavelength λ = 0.1541 nm) at 40 kV and 40 mA using a LynxEye detector. All XRD samples were scanned from diffraction angles 2θ = 5–30° at a scan rate of 0.015°/s.

Degree of Crosslinking

The degree of crosslinking of samples were determined using TNBS assay, as described by Bubnis and Ofner (1992). Briefly, 1–3 mg scaffolds were immersed in 1 ml solution with 4% (w/v) $NaHCO_3$ and 1 ml freshly prepared solution containing 0.5% (w/v) TNBS. After 2 h incubation at 40°C, 3 mL solution with 6 M HCl was added and further heated at 60°C for 90 min. After cooling down to room temperature, the resulting solution was diluted with 5 ml deionized water, and the absorbance was measured at 345 nm with a UV/vis spectrometer (BioPhotometer plus, Eppendorf, Hamburg, Germany). The degree of crosslinking was calculated as follows:

$$\text{Degree of crosslinking } (\%) = \left(\frac{A_0 - A_C}{A_0} \right) \times 100\% \quad (1)$$

Where A_0 and A_C are the absorbances of SF/gelatin nanofiber mats before and after crosslinking, respectively. The relevant tests were performed three times under the same condition to report average data and standard deviations.

Contact Angle and Water Uptake Measurements

To evaluate the hydrophilicity of SF/gelatin nanofiber mats, water contact angles were measured using a CAM101 goniometer (KSV Instruments Ltd, Finland). A droplet of water (volume: 5 μl) was deposited onto the scaffold surface and droplet images were automatically captured as a function of time. The droplet volume was controlled using a threaded plunger syringe (81341 Lauer tip syringe, Hamilton). The contact angle was calculated by CAST™2.0 software based on these captured images. The average data were obtained from the measurements of 5 samples in each batch for test reproducibility.

In order to measure water uptake capacity (WUC) of SF and SF/gelatin nanofiber mats, corresponding samples in size of 1 × 1 cm with three replicates from each mat were dried in vacuum to obtain the initial sample mass (w_0). Subsequently, they were soaked in distilled water at room temperature for 24 h. The excess water on the surface was removed with filter paper, which was followed by measuring the mass of wet sample w. The WUC was then calculated as follows:

$$Water\ uptake\ (\%) = \left(\frac{W - W_0}{W_0} \right) \times 100\% \quad (2)$$

Porosity

The porosity of SF/gelatin nanofiber mats were determined using their apparent density ($\rho_{apparent}$) and bulk density (ρ_{bulk}) as shown in Equation (3). In between, $\rho_{apparent}$ in the unit of g/cm^3 was estimated on the basis of scaffold mass $m_{scaffold}$ (g), scaffold thickness t (cm), and scaffold area A (cm^2) according to Equation (4). The samples were cut into $A = 2$ cm^2 and the thickness of scaffolds was measured by using a micrometer at four different positions of nanofiber mats in order to obtain the average measurements.

As for the parameter of ρ_{bulk}, bulk densities of SFs and gelatin (i.e., ρ_{SF} and $\rho_{gelatin}$) were referred to as 1.25 and 1.35 g/cm^3, respectively (Andiappan et al., 2013; Zhan et al., 2016b). Corresponding bulk density of SF/gelatin nanofiber mats ρ_{bulk} was calculated in Equation (5) in which $w_{gelatin}$ and w_{SF} denoted the mass fractions of gelatin and SFs, respectively. Five samples for each material batch were used with finally reported average data and standard deviations.

$$Porosity = \left(1 - \left[\frac{\rho_{apparent}}{\rho_{bulk}} \right] \right) \times 100\% \quad (3)$$

$$\rho_{apparent} = \frac{m_{scaffold}}{t \times A} \quad (4)$$

$$\frac{1}{\rho_{bulk}} = \frac{w_{gelatin}}{\rho_{gelatin}} + \frac{w_{SF}}{\rho_{SF}} \quad (5)$$

Tensile Testing

Strip-like tensile testing samples were cut from SF/gelatin nanofiber mats in dimensions of 10 × 30 mm and glued onto a cardboard frame according to an explicit sample preparation procedure mentioned by Huang et al. (2004). Afterwards, the frame edges of cardboard were cut and mechanical testing was conducted on a Lloyds EZ50 universal testing machine at the

crosshead speed of 10 mm/min with ambient temperature of 25°C and humidity of 65% (gauge length: 30 mm). Sample thickness was measured using a micrometer at five different positions on nanofiber mats to record the average data in range from 200 to 530 μm.

Cell Culture

Mouse fibroblast cells line 3T3 (European Collection of Cell Cultures, Porton Down, UK) were cultured in RPMI-1640 (Gibco, Thermo Fisher Scientific) supplemented with 10% fetal bovine serum (FBS, Serana Europe GmBH), 10 mM HEPES, 1 mM sodium pyruvate, and 2 mM glutamine (all from Gibco) in a humidified 37°C incubator, which was maintained at 5% CO_2. Cells were subcultured before reaching 70% confluence (i.e., every 2 days).

Proliferation Assay

To study the cell viability on scaffolds, fibrous scaffolds were cut into disc-like samples (diameter: 12 mm) and placed into petri dishes for 40-min UV sterilization. Thereafter, SF/gelatin nanofiber mats were soaked in Dulbecco modified eagle medium (DMEM, Gibco) for 1 h prior to cell seeding in order to facilitate the cell attachment onto nanofiber surfaces. The 3T3 cells were detached by 0.05% trypsin-EDTA (Life Technologies) from the culture flask and seeded on scaffolds in 12-well plates with a cell density of 2 × 10^3 per scaffold, and were further allowed to adhere at 37°C for 30 min. After the seeding duration for 30 min, each culture well was topped up with 2 ml culture media. Cell growth was analyzed by transferring scaffolds into the 96-well plate and adding 20 μl CellTiter-Blue reagent (Promega) at different time periods, namely day 1 and day 3 for measurements. The plates were incubated in a humidified incubator at 37°C subjected to the equilibration with 5% CO_2 for 4 h, and the fluorescence intensity was measured on an EnSpire Multimode plate reader (Perkin Elmer, Waltham, MA).

RESULTS AND DISCUSSION

Solution Viscosity

One of key factors in determining the fiber morphology is solution viscosity, which is directly correlated with solution concentration and molecular weight of polymers (Amariei et al., 2017). Since the concentration of SF/gelatin solution is maintained at 13 wt%, the blend ratio of SF/gelatin can be the only parameter to affect the solution viscosity. The shear viscosity at a fixed shear rate of 100 s^{-1} was measured and is presented in **Figure 1**. It was found that solution viscosity was gradually enhanced with increasing the gelatin content, which could affect their electrospinnability and fiber morphology. A similar trend was reported by Bao et al. (2008) in which blending gelatin with SFs improved both the viscosity and spinnability of prepared solutions.

Fiber Morphology

Figures 2A–C show SEM images of GTA crosslinked SF/gelatin nanofiber mats at different blend ratios. Evidently, all scaffolds demonstrated homogeneous, bead-free nanofibrous

FIGURE 1 | Viscosity measurement of SF/gelatin solution at a constant shear rate of 100 s^{-1}.

FIGURE 2 | SEM micrographs of GTA crosslinked nanofiber mats: (A) SF, (B) SF/gelatin at the blend ratio of 90/10, and (C) SF/gelatin at the blend ratio of 70/30.
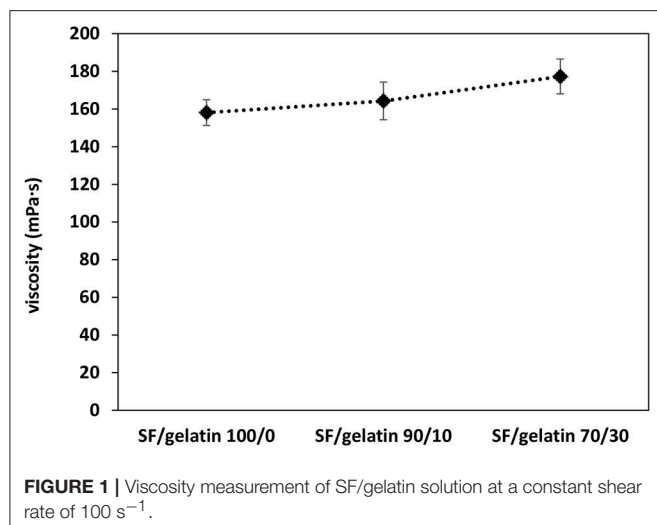
structures. Besides, nanofibers appeared to be rubbery with fusion at fiber junctions (cross-links), which was ascribed to partial dissolution of fiber segments as a result of the exposure to moisture-rich glutaraldehyde vapor. Furthermore, the slight shrinkage of nanofiber mats was manifested relative to their original sizes, which was associated with the decreasing size of inter-fibrous pores (Jeong and Park, 2014).

As seen from **Figures 3A–C**, average fiber diameters for SFs and SF/gelatin nanofiber mats at blend ratios of 90/10 and 70/30 were determined to be 403.5, 422.7, and 426.4 nm, respectively. With increasing the gelatin content, it was evident that larger nanofibers with a narrow diameter distribution took place, which was in good agreement with those obtained by Dadras Chomachayi et al. (2018) for similar fiber materials. Large fiber diameters could be associated with an increase in solution viscosity with the addition of gelatin, as confirmed from our aforementioned viscosity data to induce higher jet resistance for the generation of thicker fibers. Additionally, more uniform fiber distribution implied the improvement of electrospinnability of SF/gelatin solution when the gelatin content increased (Okhawilai et al., 2010).

FTIR Analysis

The FTIR spectra of GTA modified nanofiber mats are depicted in **Figure 4**. The spectrum of gelatin sample shows characteristic peaks at around 3,304 cm^{-1} for amide A (N–H stretching vibration), 1,640 cm^{-1} for amide I (C = O stretch), 1,539 cm^{-1} for amide II (C–N stretching and N–H bending), and 1,240 cm^{-1} for amide III (N–H in phase bending and C–N stretching vibration) (Ki et al., 2005; Gomes et al., 2013; Amadori et al., 2015; Lee et al., 2017).

With respect to plain SF nanofiber mats, FTIR peaks centered at 1,627 and 1,522 cm^{-1} in **Figure 4A** are assigned to amide I and amide II, respectively, which are a typical characteristic for β-sheet structures. FTIR spectra of SF/gelatin nanofiber mats at the blend ratios of 90/10 and 70/30 depict characteristic peaks similar to SFs, implying that the presence of gelatin does not hinder the GTA induced transformation of SF from random-coil to β-sheet conformation (Gil et al., 2006; Silva et al., 2008; Zhou et al., 2010).
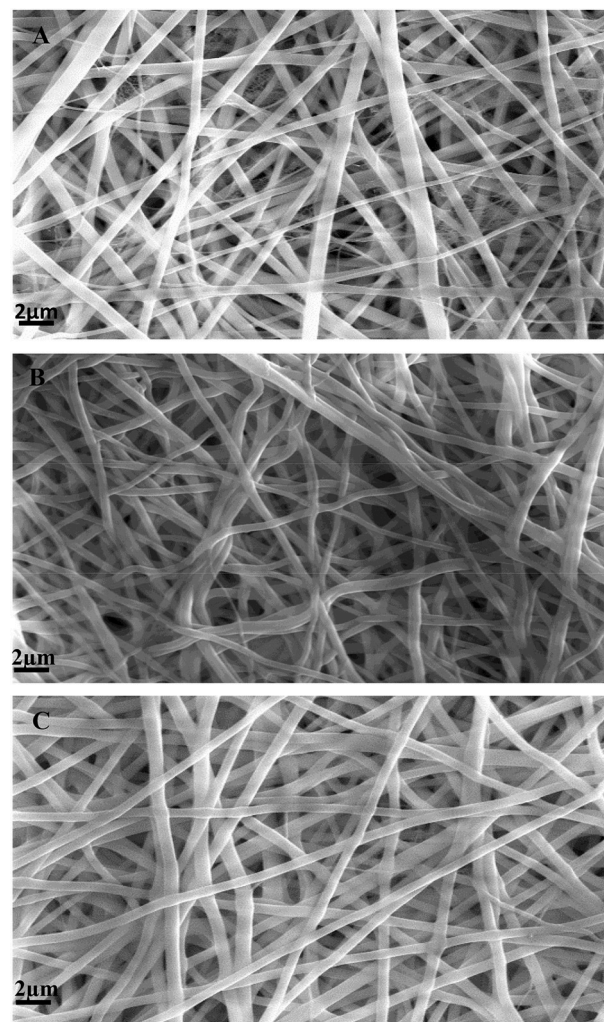
XRD Analysis

Figure 5 shows the X-ray diffraction patterns of crosslinked SF, gelatin and SF/gelatin nanofiber mats. Gelatin shows a reflection at 2θ angle of 18.2° corresponding to α-helical structures (Zhan et al., 2016a). The XRD pattern of SF demonstrates diffraction peaks at 14.51 and 17.29°, as well as a less intense peak at 20.74° to confirm the existence of β-sheet structures (Tao et al., 2007; Malay et al., 2008; De Moraes et al., 2010). In SF/gelatin nanofiber mats, diffraction patterns are almost the same as those of SF counterparts, suggesting that β-sheet conformation remains in SF within SF/gelatin nanofiber mats in good accordance with our obtained FTIR data.
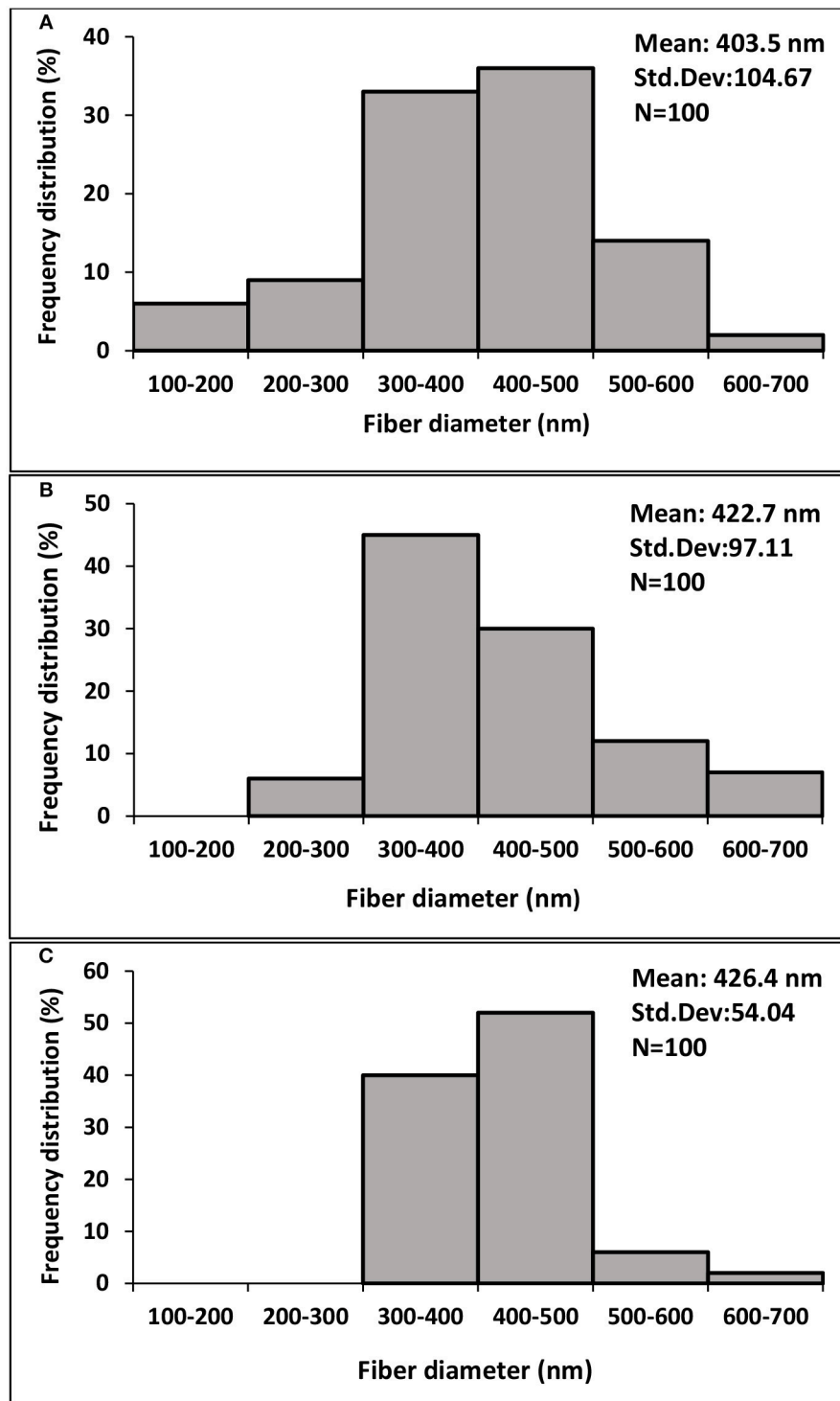
FIGURE 3 | Fiber diameter distribution diagrams of GTA crosslinked nanofiber mats based on **(A)** SF, **(B)** SF/gelatin 90/10, **(C)** SF/gelatin 70/30. "Std. Dev" represents the standard deviation of data.

Degree of Crosslinking

GTA crosslinked proteins through their aldehyde groups' reaction with free amino groups of lysine and hydroxylysine amino acid residues of polypeptide chains, form the bonds similar to those of Schiff bases (Cheung and Nimni, 1982; Olde Damink et al., 1995). Since gelatin had more free $-NH_2$ groups

FIGURE 4 | FTIR spectra of GTA crosslinked nanofiber mats: **(A)** SF, **(B)** SF/gelatin at the blend ratio of 90/10, **(C)** SF/gelatin at the blend ratio of 70/30, and **(D)** gelatin. "SF/G" represents silk fibroin/gelatin.

FIGURE 5 | XRD patterns of GTA crosslinked nanofiber mats: **(A)** SF, **(B)** SF/gelatin at the blend ratio of 90/10 **(C)** SF/gelatin at the blend ratio of 70/30, and **(D)** gelatin. "SF/G" represents silk fibroin/gelatin.

FIGURE 6 | (A) Degree of crosslinking and **(B)** porosity of GTA crosslinked SF nanofiber mats and SF/gelatin nanofiber mats.

available for the crosslinking effect, the degree of crosslinking appeared to be relatively low for pure SFs. Whereas, the addition of gelatin enhanced the degree of crosslinking (Ratanavaraporn et al., 2014). Therefore, as shown in **Figure 6A**, SF/gelatin
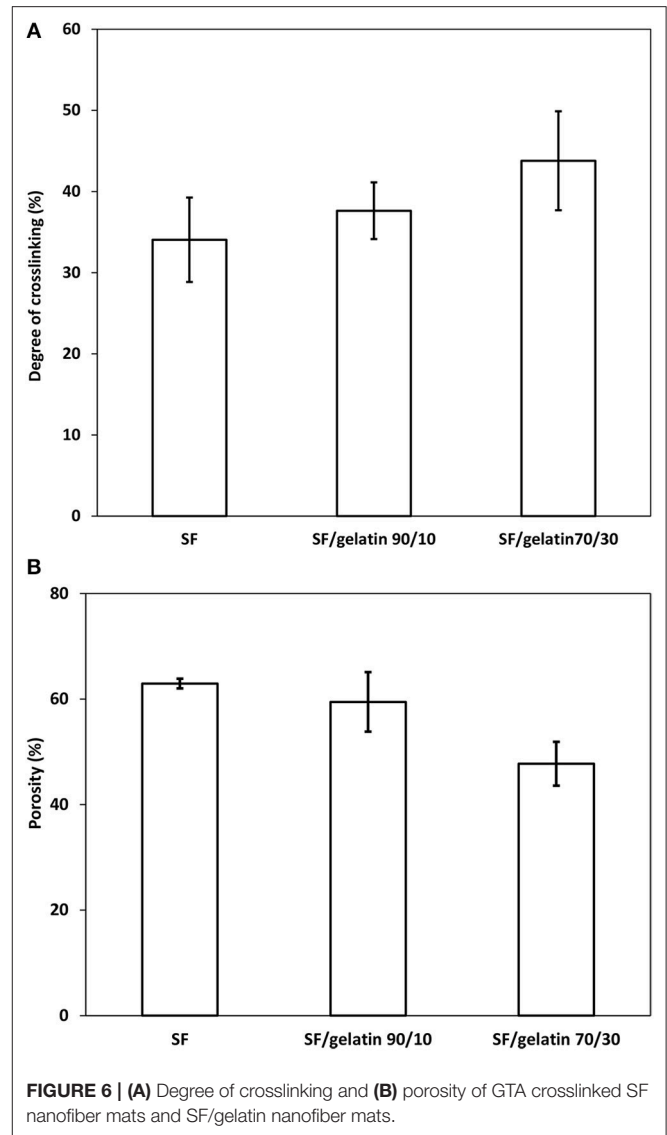
nanofiber mats prepared at the blend ratio of 70/30 had the highest crosslinking degree up to 43% as opposed to the lowest value of 34% for SFs.

Porosity Measurement

It is essential to have tissue scaffolds possess a certain level of porosity in order to achieve homogeneous cell distribution and interconnection for engineered tissues. In particular, higher porosity can regulate the nutrient uptake and facilitate the oxygen diffusion (Annabi et al., 2010). As observed in **Figure 6B**, with respect to GTA modified nanofiber mats, increasing the gelatin content appeared to decrease the porosity of SF/gelatin nanofiber mats. The porosities of SF/gelatin nanofiber mats at the blend ratios of 90/10 and 70/30 were determined to be 59 and 47%, respectively as opposed to 62% for neat SF counterparts. According to our degree of crosslinking data, the addition of gelatin to SFs gave rise to a higher degree of crosslinking, which in turn yielded more fiber twining and adhesive features

FIGURE 7 | Water uptake capacity for GTA crosslinked SF nanofiber mats and SF/gelatin nanofiber mats after 24 h and corresponding contact angles.
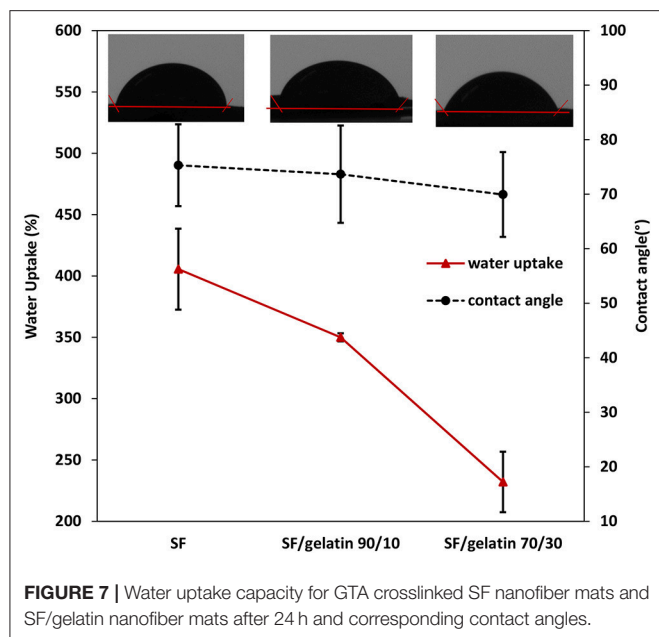
with the reduction of mat porosity. The SEM images exhibit in **Figures 2A–C** validated these results, indicating compressed and contracted structures for crosslinked scaffolds with higher gelatin contents.

Contact Angle and Water Uptake Capacity

To investigate the effect of gelatin on hydrophilic properties of SF/gelatin nanofiber mats, water contact angles and water uptake capacity of crosslinked mats were measured with associated results being presented in **Figure 7**. The contact angles of all nanofiber mats were <90°, which was indicative of a typical hydrophilic feature. The addition of gelatin was shown to cause a slight decrease in contact angle of nanofiber mats from 75.31 ± 7.5° for SF nanofiber mats to 69.94 ± 7.68° for SF/gelatin counterparts at the blend ratio of 70/30, which was expected to be associated with the hydrophilic nature of gelatin (Kim et al., 2009). On the other hand, the WUC of SFs was much higher with the value of 405% as opposed to 350 and 232% for SF/gelatin nanofiber mats at the blend ratios of 90/10 and 70/30, respectively, as illustrated in **Figure 7**. Such a finding was ascribed to the incorporation of gelatin into SF matrices with GTA crosslinking effect, resulting in denser structures and increasing the compaction degree among molecules so that it was difficult for the entry of water molecules (Zhou et al., 2013). Besides, higher gelatin contents led to lower fiber porosity, thereby limiting the water diffusion into fiber mats. Xiao et al. (2012) reported a similar behavior for SF/gelatin hydrogels crosslinked with genipin, which suggested that the wettability of fiber mats could be modulated by adjusting SF/gelatin blend ratios.

Mechanical Properties

Figures 8A,B show tensile tested samples before and after failure along with typical stress–strain curves of nanofiber

mats, respectively. It is quite evident that there are different mechanical performances between SF/gelatin nanofiber mats at various SF/gelatin blend ratios. Both tensile strength and Young's modulus increased monotonically with increasing the gelatin content in SF/gelatin nanofiber mats when compared with those of SF nanofiber mats **Figures 9A,B**. The incorporation of 10 and 30 wt % gelatin into SFs led to 10 and 27% increases in tensile strength, as well as the moderate improvements by 12 and 27% in Young's modulus, respectively when compared with those of neat SF nanofiber mats. In contrast, elongation at break decreased from 20 for SFs to 16% for SF/gelatin nanofiber mats at the blend ratio of 70/30, which signified that increasing the gelatin content tended to cause more brittle material nature with less flexibility shown in **Figure 9C**. Based on crosslinking degree data in **Figure 6A**, the crosslinking density became higher with increasing the gelatin content, thereby molecular chains of proteins were restrained by crosslinking points, and thus led to stiffer and more robust nanofiber mats. Besides, it should be noted that the formation of intermolecular interaction between SFs and gelatin rendered the structural integrity of nanofiber mats and yielded the increase in mechanical properties (Zhu et al., 2015; Du et al., 2016; Selvaraj and Fathima, 2017). Moreover, according to morphological changes, higher gelatin content appeared to give rise to higher crosslinking density with resulting fiber fusion, thereby decreasing the porosity and increasing fiber entanglement leading to the strength enhancement (Simonet et al., 2014; Yin et al., 2017).

Proliferation Assay

The cell viability and proliferation as a function of time on scaffolds is indicative of cellular compatibility and appropriateness for tissue engineering applications. To acquire an insight into cytocompatibility of SF/gelatin nanofiber mats, 3T3 cells were seeded onto GTA modified SF/gelatin scaffolds. Their growth was quantified using the proliferation assay with associated results being displayed in **Figure 10**. After 1 day, no significant difference in proliferation took place between SF nanofiber mats and SF/gelatin nanofiber mats with different SF/gelatin blend ratios. However, after 3 days, cell proliferation was significantly increased in all samples. The analysis of cell proliferation profiles suggested that the rate of proliferation was higher in SFs as compared to the proliferation in SF/gelatin nanofiber mats at blend ratios of both 90/10 and 70/30. It was generally expected that biological responses would be improved with increasing the gelatin content, which was interpreted by the presence of more available integrin binding sites (Telemeco et al., 2005; Ghasemi-Mobarakeh et al., 2008; Wu et al., 2011). Surprisingly, an opposite trend occurred, in which higher SF/gelatin blend ratio decreased the cell proliferation. One plausible reason was that crosslinking consumed the glutamate and aspartate residues in Arg-Gly-Asp (RGD) in gelatin, and thereby reduced the cell reactivity of scaffolds (Grover et al., 2012). Moreover, the alteration in morphology, porosity and WUC of scaffolds with the addition of gelatin, as mentioned earlier, could be likely responsible for this behavior. For example, the previous study by Yeo et al. (2008)

FIGURE 8 | (A) A representative testing sample before and after tensile failure, **(B)** Typical stress-strain curves of GTA crosslinked SF nanofiber mats and SF/gelatin nanofiber mats.

FIGURE 9 | Mechanical properties of GTA crosslinked SF nanofiber mats and SF/gelatin nanofiber mats: **(A)** Young's modulus, **(B)** tensile strength, and **(C)** elongation at break.
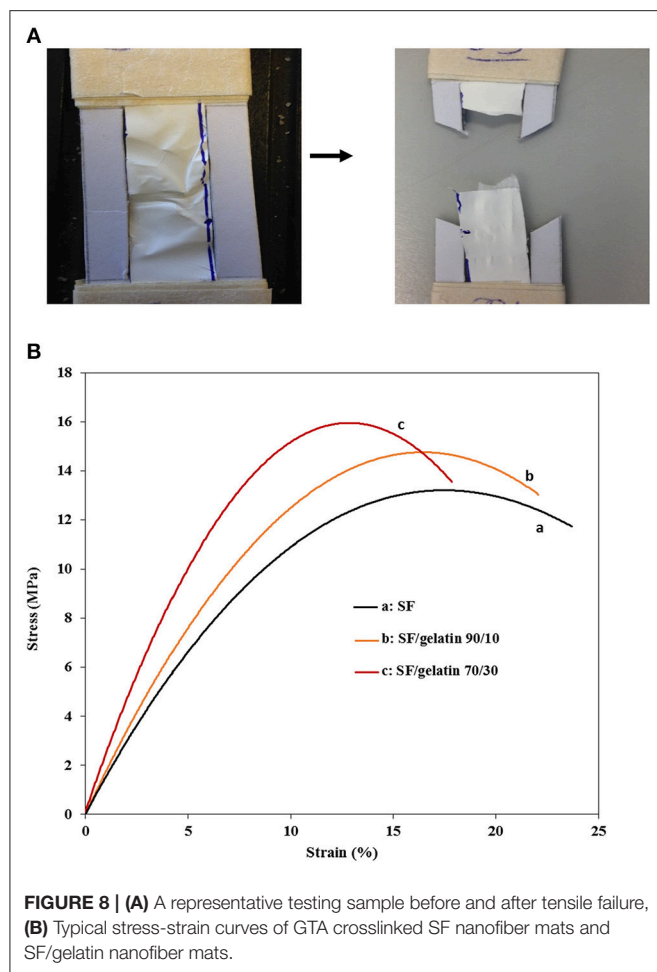
showed the reduction in cellular responses of keratinocytes for GTA crosslinked SF/collagen nanofiber mats as compared to neat SF counterparts, which was ascribed to the different conformation formation of blended SF/collagen nanofiber mats due to the interaction between collagen and SFs. Yao et al. (2016) reported that higher gelatin content in PCL/gelatin fiber mats did not necessarily result in better cell response and underlined the role of physical microenvironment such as mechanical properties in the dictation of cellular responses. In addition, Grover et al. (2012) demonstrated the detrimental effect of gelatin crosslinking on cell response as a consequence of changes in physical properties such as roughness and stiffness of gelatin films as well as a reduction in the number of available cell binding sites. However, in our system, the reduction in both porosity and WUC with increasing the gelatin content could be responsible for lower cell proliferation. It was well-documented that highly porous structures with interconnected pores facilitated the cell migration and provided the nutrients and gas exchange for cell proliferation (Soliman et al., 2011; Stachewicz et al., 2017). Besides, higher WUC assisted the biofluid transport, cell migration, which also assisted in the growth of new cells. Moreover, the water storage helped to store growth factors and offered compressive characteristics of
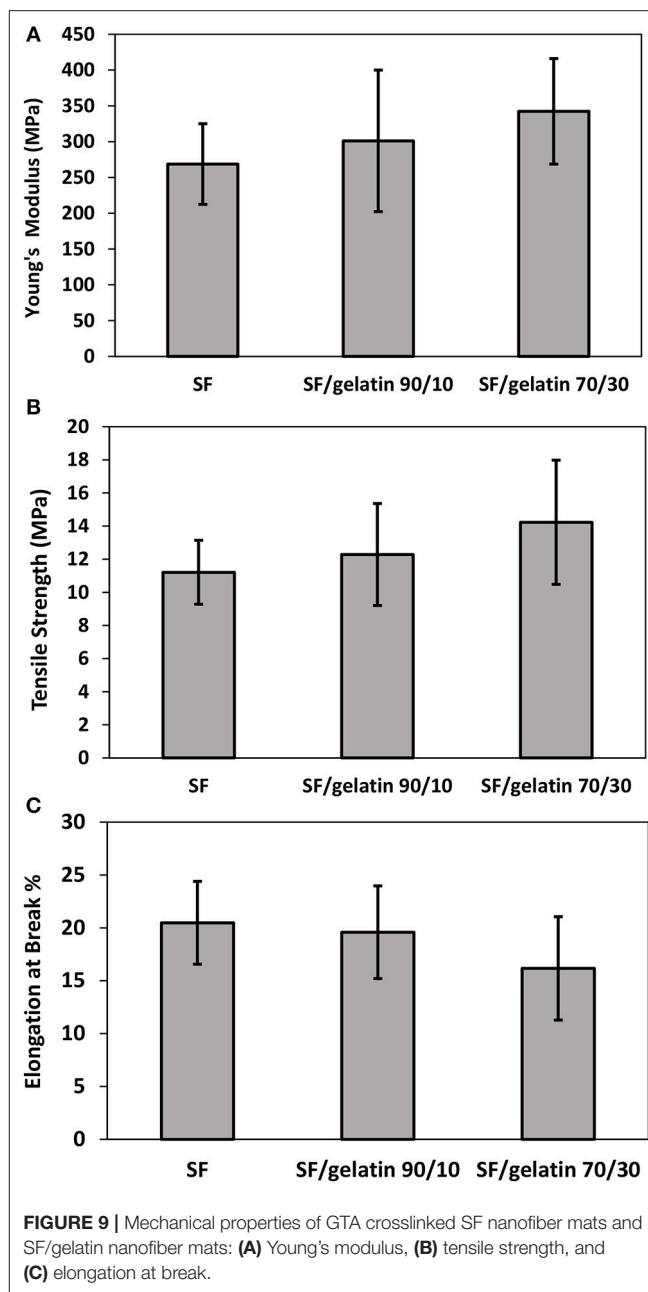
regrown tissues (Singh et al., 2016). Therefore, superior porosity and WUC of pristine SFs facilitated the nutrient transport and diffusion of signaling molecules when compared with SF/gelatin nanofiber scaffolds. Accordingly, more spaces could be provided for cell proliferation and migration, thereby yielding higher proliferation rates. Overall, it was suggested that GTA vapor could successfully stabilize SF/gelatin nanofiber mats, change their morphology and improve their mechanical properties as well. However, further studies for GTA optimization is required to modulate the physico-chemical properties of SF/gelatin nanofiber mats in order to obtain stable materials with favorable bioactive properties and promote cellular responses for tissue engineering applications.

FIGURE 10 | Proliferation of 3T3 fibroblasts seeded on GTA crosslinked SF nanofiber mats and SF/gelatin nanofiber mats after the first and third days of cell culture.
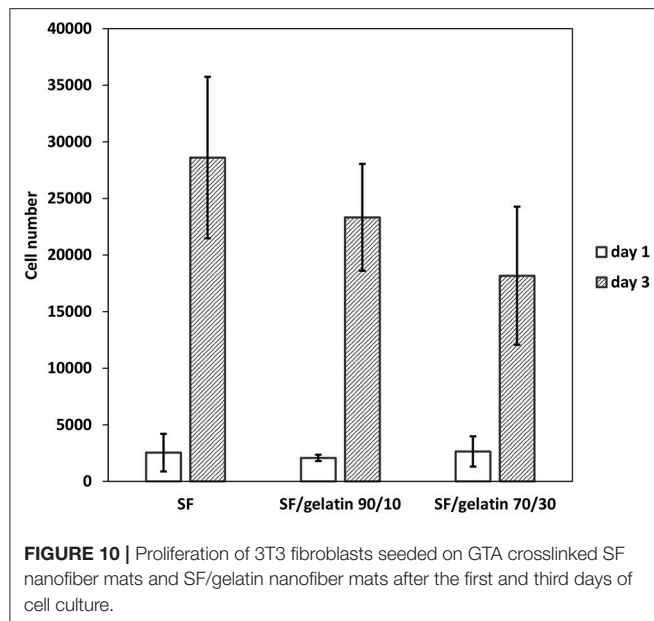
CONCLUSIONS

SF/gelatin nanofiber mats with different SF/gelatin blend ratios were successfully prepared by electrospinning and stabilized with GTA. The prepared mats possessed different porosities, WUC and tensile properties depending on the gelatin content. The incorporation of 10 and 30 wt% gelatin into SFs resulted in 10 and 27% increases in tensile strength and moderate improvements of Young's modulus for SF/gelatin nanofiber mats by 12 and 27%, respectively, as opposed to those of SF counterparts. However, increasing the gelatin content decreased the porosity and WUC of SF/gelatin nanofiber mats accordingly. In particular, it was surprising that SF/gelatin

nanofiber mats at the blend ratio of 70/30 demonstrated the lowest 3T3 fibroblast cell responses for proliferation rates. Such a finding might be partly associated with the fact that GTA crosslinking tended to induce changes in physical characteristics of microenvironments by ways of WUC and porosity at higher gelatin content levels, which clearly played an important role in the regulation of cellular functions. Overall, our initial results suggested the superiority of SF nanofiber mats to those SF/gelatin counterparts. Nonetheless, further studies are required to be conducted for the optimization of GTA crosslinking for SF/gelatin scaffolds, in which favorable bioactive properties of gelatin may be achieved when blended with SFs for tissue scaffolding applications.

DATA AVAILABILITY

The datasets for this article are not publicly available because SM has not finally submitted her PhD thesis that this article is based upon for data confidentiality. Requests to access the datasets should be directed to Y.Dong@curtin.edu.au.

AUTHOR CONTRIBUTIONS

SM did the experimental work in relation to preparation, characterization, and property measurements of material samples. SM and YD analyzed the data and jointly prepared the research manuscript.

ACKNOWLEDGMENTS

REFERENCES

Agarwal, S., Wendorff, J. H., and Greiner, A. (2008). Use of electrospinning technique for biomedical applications. *Polymer* 49, 5603–5621. doi: 10.1016/j.polymer.2008.09.014

Akbarzadeh, R., and Yousefi, A. M. (2014). Effects of processing parameters in thermally induced phase separation technique on porous architecture of scaffolds for bone tissue engineering. *J. Biomed. Mater. Res.* 102, 1304–1315. doi: 10.1002/jbm.b.33101

Aldana, A. A., and Abraham, G. A. (2017). Current advances in electrospun gelatin-based scaffolds for tissue engineering applications. *Int. J. Pharm.* 523, 441–453. doi: 10.1016/j.ijpharm.2016.09.044

Allori, A. C., Sailon, A. M., and Warren, S. M. (2008). Biological basis of bone formation, remodeling, and repair—Part II: extracellular matrix. *Tissue Eng.* 14, 275–283. doi: 10.1089/ten.teb.2008.0083

Amadori, S., Torricelli, P., Rubini, K., Fini, M., Panzavolta, S., and Bigi, A. (2015). Effect of sterilization and crosslinking on gelatin films. *J. Mater. Sci.* 26:69. doi: 10.1007/s10856-015-5396-4

Amariei, N., Manea, L. R., Bertea, A. P., Bertea, A., and Popa, A. (2017). The influence of polymer solution on the properties of electrospun 3D nanostructures. *IOP Conf. Ser.: Mater. Sci. Eng.* 209:012092. doi: 10.1088/1757-899X/209/1/012092

Andiappan, M., Sundaramoorthy, S., Panda, N., Meiyazhaban, G., Winfred, S. B., Venkataraman, G., et al. (2013). Electrospun eri silk fibroin scaffold coated with hydroxyapatite for bone tissue engineering applications. *Prog. Biomater.* 2:6. doi: 10.1186/2194-0517-2-6

Annabi, N., Nichol, J. W., Zhong, X., Ji, C., Koshy, S., Khademhosseini, A., et al. (2010). Controlling the porosity and microarchitecture of hydrogels for tissue engineering. *Tissue Eng. Part B Rev.* 16, 371–383. doi: 10.1089/ten.teb.2009.0639

Babitha, S., Rachita, L., Karthikeyan, K., Shoba, E., Janani, I., Poornima, B., et al. (2017). Electrospun protein nanofibers in healthcare: a review. *Int. J. Pharm.* 523, 52–90. doi: 10.1016/j.ijpharm.2017.03.013

Bao, W., Zhang, Y., Yin, G., and Wu, J. (2008). The structure and property of the electrospinning silk fibroin/gelatin blend nanofibers. *e-Polymers* 8:098. doi: 10.1515/epoly.2008.8.1.1131

Bhardwaj, N., and Kundu, S. C. (2010). Electrospinning: a fascinating fiber fabrication technique. *Biotechnol. Adv.* 28, 325–347. doi: 10.1016/j.biotechadv.2010.01.004

Bhattacharjee, P., Kundu, B., Naskar, D., Kim, H. W., Maiti, T. K., Bhattacharya, D., et al. (2017). Silk scaffolds in bone tissue engineering: an overview. *Acta Biomater.* 63, 1–17. doi: 10.1016/j.actbio.2017.09.027

Bigi, A., Cojazzi, G., Panzavolta, S., Rubini, K., and Roveri, N. (2001). Mechanical and thermal properties of gelatin films at different degrees of glutaraldehyde

crosslinking. *Biomaterials* 22, 763–768. doi: 10.1016/S0142-9612(00)00236-2

Bubnis, W. A., and Ofner, C. M. (1992). The determination of ε-amino groups in soluble and poorly soluble proteinaceous materials by a spectrophotometric method using trinitrobenzenesulfonic acid. *Anal. Biochem.* 207, 129–133. doi: 10.1016/0003-2697(92)90513-7

Buitrago, J. O., Patel, K. D., El-Fiqi, A., Lee, J.-H., Kundu, B., Lee, H.-H., et al. (2018). Silk fibroin/collagen protein hybrid cell-encapsulating hydrogels with tunable gelation and improved physical and biological properties. *Acta Biomater.* 69, 218–233. doi: 10.1016/j.actbio.2017.12.026

Cheung, D. T., and Nimni, M. E. (1982). Mechanism of crosslinking of proteins by glutaraldehyde II. Reaction with monomeric and polymeric collagen. *Connect. Tissue Res.* 10, 201–216. doi: 10.3109/03008208209034419

Dadras Chomachayi, M., Solouk, A., Akbari, S., Sadeghi, D., Mirahmadi, F., and Mirzadeh, H. (2018). Electrospun nanofibers comprising of silk fibroin/gelatin for drug delivery applications: thyme essential oil and doxycycline monohydrate release study. *J. Biomed. Mater. Res. Part A* 106, 1092–1103. doi: 10.1002/jbm.a.36303

De Moraes, M. A., Nogueira, G. M., Weska, R. F., and Beppu, M. M. (2010). Preparation and characterization of insoluble silk fibroin/chitosan blend films. *Polymers* 2, 719–727. doi: 10.3390/polym2040719

Du, Y., Gao, X. Q., Wang, Z. Y., Jin, D., Tong, S., and Wang, X. K. (2016). Construction and characterization of three-dimensional silk fibroin-gelatin scaffolds. *J. Hard Tissue Biol.* 25, 269–276. doi: 10.2485/jhtb.25.269

Ghasemi-Mobarakeh, L., Prabhakaran, M. P., Morshed, M., Nasr-Esfahani, M.-H., and Ramakrishna, S. (2008). Electrospun poly(ε-caprolactone)/gelatin nanofibrous scaffolds for nerve tissue engineering. *Biomaterials* 29, 4532–4539. doi: 10.1016/j.biomaterials.2008.08.007

Gil, E. S., Frankowski, D. J., Bowman, M. K., Gozen, A. O., Hudson, S. M., and Spontak, R. J. (2006). Mixed protein blends composed of gelatin and Bombyx mori silk fibroin: effects of solvent-induced crystallization and composition. *Biomacromolecules* 7, 728–735. doi: 10.1021/bm050622i

Gomes, S. R., Rodrigues, G., Martins, G. G., Henriques, C. M. R., and Silva, J. C. (2013). *In vitro* evaluation of crosslinked electrospun fish gelatin scaffolds. *Mater. Sci. Eng. C* 33, 1219–1227. doi: 10.1016/j.msec.2012.12.014

Grover, C. N., Gwynne, J. H., Pugh, N., Hamaia, S., Farndale, R. W., Best, S. M., et al. (2012). Crosslinking and composition influence the surface properties, mechanical stiffness and cell reactivity of collagen-based films. *Acta Biomater.* 8, 3080–3090. doi: 10.1016/j.actbio.2012.05.006

Hartgerink, J. D., Beniash, E., and Stupp, S. I. (2001). Self-assembly and mineralization of peptide-amphiphile nanofibers. *Science* 294, 1684–1688. doi: 10.1126/science.1063187

Hersel, U., Dahmen, C., and Kessler, H. (2003). RGD modified polymers: biomaterials for stimulated cell adhesion and beyond. *Biomaterials* 24, 4385–4415. doi: 10.1016/S0142-9612(03)00343-0

Huang, Z.-M., Zhang, Y. Z., Ramakrishna, S., and Lim, C. T. (2004). Electrospinning and mechanical characterization of gelatin nanofibers. *Polymer* 45, 5361–5368. doi: 10.1016/j.polymer.2004.04.005

Ibrahim, D. M., Kakarougkas, A., and Allam, N. K. (2017). Recent advances on electrospun scaffolds as matrices for tissue-engineered heart valves. *Mater. Today Chem.* 5, 11–23. doi: 10.1016/j.mtchem.2017.05.001

Ingavle, G. C., and Leach, J. K. (2014). Advancements in electrospinning of polymeric nanofibrous scaffolds for tissue engineering. *Tissue Eng. Part B Rev.* 20, 277–293. doi: 10.1089/ten.teb.2013.0276

Jeong, L., and Park, W. H. (2014). Preparation and characterization of gelatin nanofibers containing silver nanoparticles. *Int. J. Mol. Sci.* 15, 6857–6879. doi: 10.3390/ijms15046857

Khadka, D. B., and Haynie, D. T. (2012). Protein—and peptide-based electrospun nanofibers in medical biomaterials. *Nanomed. Nanotechnol. Biol. Med.* 8, 1242–1262. doi: 10.1016/j.nano.2012.02.013

Ki, C. S., Baek, D. H., Gang, K. D., Lee, K. H., Um, I. C., and Park, Y. H. (2005). Characterization of gelatin nanofiber prepared from gelatin–formic acid solution. *Polymer* 46, 5094–5102. doi: 10.1016/j.polymer.2005.04.040

Kim, S. E., Heo, D. N., Lee, J. B., Kim, J. R., Park, S. H., Jeon, S. H., et al. (2009). Electrospun gelatin/polyurethane blended nanofibers for wound healing. *Biomed. Mater.* 4:044106. doi: 10.1088/1748-6041/4/4/044106

Kim, T. G., Shin, H., and Lim, D. W. (2012). Biomimetic scaffolds for tissue engineering. *Adv. Funct. Mater.* 22, 2446–2468. doi: 10.1002/adfm.201103083

Kundu, B., Rajkhowa, R., Kundu, S. C., and Wang, X. (2013). Silk fibroin biomaterials for tissue regenerations. *Adv. Drug Deliv. Rev.* 65, 457–470. doi: 10.1016/j.addr.2012.09.043

Lai, G.-J., Shalumon, K. T., Chen, S.-H., and Chen, J.-P. (2014). Composite chitosan/silk fibroin nanofibers for modulation of osteogenic differentiation and proliferation of human mesenchymal stem cells. *Carbohydr. Polym.* 111, 288–297. doi: 10.1016/j.carbpol.2014.04.094

Lee, J. B., Ko, Y. G., Cho, D., Park, W. H., and Kwon, O. H. (2017). Modification and optimization of electrospun gelatin sheets by electronbeam irradiation for soft tissue engineering. *Biomater. Res.* 21:14. doi: 10.1186/s40824-017-0100-z

Li, M., Mondrinos, M. J., Gandhi, M. R., Ko, F. K., Weiss, A. S., and Lelkes, P. I. (2005). Electrospun protein fibers as matrices for tissue engineering. *Biomaterials* 26, 5999–6008. doi: 10.1016/j.biomaterials.2005.03.030

Li, Z. H., Ji, S. C., Wang, Y. Z., Shen, X. C., and Liang, H. (2013). Silk fibroin-based scaffolds for tissue engineering. *Front. Mater. Sci.* 7, 237–247. doi: 10.1007/s11706-013-0214-8

Malay, Ö., Yalçin, D., Batigün, A., and Bayraktar, O. (2008). SF.258 Characterization of silk fibroin/hyaluronic acid polyelectrolyte complex (PEC) films. *J. Therm. Anal. Calorim.* 94, 749–755. doi: 10.1007/s10973-008-9368-5

Morgan, A. W., Roskov, K. E., Lin-Gibson, S., Kaplan, D. L., Becker, M. L., and Simon, C. G. (2008). Characterization and optimization of RGD-containing silk blends to support osteoblastic differentiation. *Biomaterials* 29, 2556–2563. doi: 10.1016/j.biomaterials.2008.02.007

Okhawilai, M., Rangkupan, R., Kanokpanont, S., and Damrongsakkul, S. (2010). Preparation of Thai silk fibroin/gelatin electrospun fiber mats for controlled release applications. *Int. J. Biol. Macromol.* 46, 544–550. doi: 10.1016/j.ijbiomac.2010.02.008

Olde Damink, L. H. H., Dijkstra, P. J., Van Luyn, M. J. A., Van Wachem, P. B., Nieuwenhuis, P., and Feijen, J. (1995). Glutaraldehyde as a crosslinking agent for collagen-based biomaterials. *J. Mater. Sci. Mater. Med.* 6, 460–472. doi: 10.1007/BF00123371

Poursamar, S. A., Lehner, A. N., Azami, M., Ebrahimi-Barough, S., Samadikuchaksaraei, A., and Antunes, A. P. M. (2016). The effects of crosslinkers on physical, mechanical, and cytotoxic properties of gelatin sponge prepared via *in-situ* gas foaming method as a tissue engineering scaffold. *Mater. Sci. Eng. C* 63, 1–9. doi: 10.1016/j.msec.2016.02.034

Qi, Y., Wang, H., Wei, K., Yang, Y., Zheng, R.-Y., Kim, I. S., et al. (2017). A review of structure construction of silk fibroin biomaterials from single structures to multi-level structures. *Int. J. Mol. Sci.* 18:237. doi: 10.3390/ijms18030237

Ratanavaraporn, J., Kanokpanont, S., and Damrongsakkul, S. (2014). The development of injectable gelatin/silk fibroin microspheres for the dual delivery of curcumin and piperine. *J. Mater. Sci. Mater. Med.* 25, 401–410. doi: 10.1007/s10856-013-5082-3

Selvaraj, S., and Fathima, N. N. (2017). Fenugreek incorporated silk fibroin nanofibers—a potential antioxidant scaffold for enhanced wound healing. *ACS Appl. Mater. Interfaces* 9, 5916–5926. doi: 10.1021/acsami.6b16306

Shan, Y.-H., Peng, L.-H., Liu, X., Chen, X., Xiong, J., and Gao, J.-Q. (2015). Silk fibroin/gelatin electrospun nanofibrous dressing functionalized with astragaloside IV induces healing and anti-scar effects on burn wound. *Int. J. Pharm.* 479, 291–301. doi: 10.1016/j.ijpharm.2014.12.067

Silva, S. S., Maniglio, D., Motta, A., Mano, J. F., Reis, R. L., and Migliaresi, C. (2008). Genipin-modified silk-fibroin nanometric nets. *Macromol. Biosci.* 8, 766–774. doi: 10.1002/mabi.200700300

Simonet, M., Stingelin, N., Wismans, J. G. F., Oomens, C. W. J., Driessen-Mol, A., and Baaijens, F. P. T. (2014). Tailoring the void space and mechanical properties in electrospun scaffolds towards physiological ranges. *J. Mater. Chem. B* 2, 305–313. doi: 10.1039/C3TB20995D

Sin, D., Miao, X., Liu, G., Wei, F., Chadwick, G., Yan, C., et al. (2010). Polyurethane (PU) scaffolds prepared by solvent casting/particulate leaching (SCPL) combined with centrifugation. *Mater. Sci. Eng. C* 30, 78–85. doi: 10.1016/j.msec.2009.09.002

Singh, B. N., Panda, N. N., Mund, R., and Pramanik, K. (2016). Carboxymethyl cellulose enables silk fibroin nanofibrous scaffold with enhanced biomimetic potential for bone tissue engineering application. *Carbohydr. Polym.* 151, 335–347. doi: 10.1016/j.carbpol.2016.05.088

Soliman, S., Sant, S., Nichol, J. W., Khabiry, M., Traversa, E., and Khademhosseini, A. (2011). Controlling the porosity of fibrous scaffolds by modulating the fiber diameter and packing density. *J. Biomed. Mater. Res. Part A* 96, 566–574. doi: 10.1002/jbm.a.33010

Stachewicz, U., Szewczyk, P. K., Kruk, A., Barber, A. H., and Czyrska-Filemonowicz, A. (2017). Pore shape and size dependence on cell growth into electrospun fiber scaffolds for tissue engineering: 2D and 3D analyses using SEM and FIB-SEM tomography. *Mater. Sci. Eng. C.* 95, 397–408. doi: 10.1016/j.msec.2017.08.076

Taddei, P., Chiono, V., Anghileri, A., Vozzi, G., Freddi, G., and Ciardelli, G. (2013). Silk fibroin/gelatin blend films crosslinked with enzymes for biomedical applications. *Macromol. Biosci.* 13, 1492–1510. doi: 10.1002/mabi.201300156

Tao, W., Li, M., and Zhao, C. (2007). Structure and properties of regenerated Antheraea pernyi silk fibroin in aqueous solution. *Int. J. Biol. Macromol.* 40, 472–478. doi: 10.1016/j.ijbiomac.2006.11.006

Telemeco, T. A., Ayres, C., Bowlin, G. L., Wnek, G. E., Boland, E. D., Cohen, N., et al. (2005). Regulation of cellular infiltration into tissue engineering scaffolds composed of submicron diameter fibrils produced by electrospinning. *Acta Biomater.* 1, 377–385. doi: 10.1016/j.actbio.2005.04.006

Thein-Han, W. W., Saikhun, J., Pholpramoo, C., Misra, R. D., and Kitiyanant, Y. (2009). Chitosan–gelatin scaffolds for tissue engineering: physico-chemical properties and biological response of buffalo embryonic stem cells and transfectant of GFP–buffalo embryonic stem cells. *Acta Biomater.* 5, 3453–3466. doi: 10.1016/j.actbio.2009.05.012

Wang, Y., Wang, X., Shi, J., Zhu, R., Zhang, J., Zhang, Z., et al. (2016). A biomimetic silk fibroin/sodium alginate composite scaffold for soft tissue engineering. *Sci. Rep.* 6:39477. doi: 10.1038/srep39477

Wang, Y. X., Qin, Y. P., Kong, Z. J., Wang, Y. J., and Ma, L. (2014). Glutaraldehyde cross-linked silk fibroin films for controlled release. *Adv. Mater. Res.* 887–888, 541–546. doi: 10.4028/www.scientific.net/AMR.887-888.541

Wongputtaraksa, T., Ratanavaraporn, J., Pichyangkura, R., and Damrongsakkul, S. (2012). Surface modification of Thai silk fibroin scaffolds with gelatin and chitooligosaccharide for enhanced osteogenic differentiation of bone marrow-derived mesenchymal stem cells. *J. Biomed. Mater. Res. Part B Appl. Biomater.* 100, 2307–2315. doi: 10.1002/jbm.b.32802

Wu, S. C., Chang, W. H., Dong, G. C., Chen, K. Y., Chen, Y. S., and Yao, C. H. (2011). Cell adhesion and proliferation enhancement by gelatin nanofiber scaffolds. *J. Bioact. Compat. Polym.* 26, 565–577. doi: 10.1177/0883911511423563

Xiao, W., Liu, W., Sun, J., Dan, X., Wei, D., and Fan, H. (2012). Ultrasonication and genipin cross-linking to prepare novel silk fibroin-gelatin composite hydrogel. *J. Bioact. Compat. Polym.* 27, 327–341. doi: 10.1177/0883911512448692

Yao, R., He, J., Meng, G., Jiang, B., and Wu, F. (2016). Electrospun PCL/Gelatin composite fibrous scaffolds: mechanical properties and cellular responses. *J. Biomater. Sci. Polym. Ed.* 27, 824–838. doi: 10.1080/09205063.2016.1160560

Yeo, I. S., Oh, J. E., Jeong, L., Lee, T. S., Lee, S. J., Park, W. H., et al. (2008). Collagen-based biomimetic nanofibrous scaffolds: preparation and characterization of collagen/silk fibroin bicomponent nanofibrous structures. *Biomacromolecules* 9, 1106–1116. doi: 10.1021/bm700875a

Yin, G., Zhang, Y., Bao, W., Wu, J., Shi, D., Dong, Z., et al. (2009). Study on the properties of the electrospun silk fibroin/gelatin blend nanofibers for scaffolds. *J. Appl. Polym. Sci.* 111, 1471–1477. doi: 10.1002/app.28963

Yin, Y., Pu, D., and Xiong, J. (2017). Analysis of the comprehensive tensile relationship in electrospun silk fibroin/polycaprolactone nanofiber membranes. *Membranes* 7:E67. doi: 10.3390/membranes7040067

Zafar, M. S., Belton, D. J., Hanby, B., Kaplan, D. L., and Perry, C. C. (2015). Functional material features of Bombyx mori silk light versus heavy chain proteins. *Biomacromolecules* 16, 606–614. doi: 10.1021/bm501667j

Zhan, J., Morsi, Y., Ei-Hamshary, H., Al-Deyab, S. S., and Mo, X. (2016a). *In vitro* evaluation of electrospun gelatin–glutaraldehyde nanofibers. *Front. Mater. Sci.* 10, 90–100. doi: 10.1007/s11706-016-0329-9

Zhan, J., Morsi, Y., Ei-Hamshary, H., Al-Deyab, S. S., and Mo, X. (2016b). Preparation and characterization of electrospun *in-situ* cross-linked gelatin-graphite oxide nanofibers. *J. Biomater. Sci. Polym. Ed.* 27, 385–402. doi: 10.1080/09205063.2015.1133156

Zhang, Y. Z., Venugopal, J., Huang, Z. M., Lim, C. T., and Ramakrishna, S. (2006). Crosslinking of the electrospun gelatin nanofibers. *Polymer* 47, 2911–2917. doi: 10.1016/j.polymer.2006.02.046

Zhou, J., Cao, C., Ma, X., and Lin, J. (2010). Electrospinning of silk fibroin and collagen for vascular tissue engineering. *Int. J. Biol. Macromol.* 47, 514–519. doi: 10.1016/j.ijbiomac.2010.07.010

Zhou, Z., Yang, Z., Huang, T., Liu, L., Liu, Q., Zhao, Y., et al. (2013). Effect of chemical cross-linking on properties of gelatin/hyaluronic acid composite hydrogels. *Polym. Plastics Technol. Eng.* 52, 45–50. doi: 10.1080/03602559.2012.718400

Zhu, J., Yang, F., He, F., Tian, X., Tang, S., and Chen, X. (2015). A tubular gelatin scaffold capable of the time-dependent controlled release of epidermal growth factor and mitomycin C. *Colloids Surf. B Biointerf.* 135, 416–424. doi: 10.1016/j.colsurfb.2015.06.049

Soil Biodegradation of Unidirectional Polyhydroxybutyrate-Co-Valerate (PHBV) Biocomposites Toughened With Polybutylene-Adipate-Co-Terephthalate (PBAT) and Epoxidized Natural Rubber (ENR)

Zain Zaidi*, Damia Mawad and Alan Crosky

School of Materials Science and Engineering, University of New South Wales, Sydney, NSW, Australia

The detrimental impact of discarded plastics on the environment has become of increasing concern and this has led to the development of environmentally friendly "green" polymers. PHBV is one such green polymer that offers biodegradability and renewability, however its mechanical performance is quite limited. This can be improved by reinforcement with natural fibers to form green composites, which offer better mechanical properties while retaining biodegradability. There are, however, few studies examining the biodegradation of toughened PHBV composites. In this work, the biodegradation properties of PHBV/30 vol.% unidirectional flax composites both untoughened and toughened with PBAT and ENR, were studied. Composites were prepared by compression molding PHBV powder interleaved with unidirectional flax fabric. The toughening agents were cryoground and mixed with the PHBV powder prior to molding. Biodegradation was conducted in a natural outdoor soil environment and biodegradability was evaluated through weight loss analysis, optical microscopy and electron microscopy. The biodegradability of neat PHBV was minimal but was increased markedly by addition of flax fibers. The toughened composites showed a faster degradation rate than untoughened PHBV/flax, with PHBV/ENR/flax composites having the highest rate likely due to a specific strain of bacteria found worldwide in soil that attacks natural rubber. The biodegradation properties of the composites were superior to those of conventional plastics used in applications such as computer and mobile phone casings, which indicates potential suitability of this class of materials for these applications.

Keywords: biodegradation, PHBV, unidirectional, ENR, PBAT, soil

INTRODUCTION

Disposed plastics have increasingly gained attention of the globe in the past 5 years due to their harmful effects on the environment and this has driven the development of environmentally benign "green" polymers (La Mantia and Morreale, 2011). These polymers biodegrade rather than persist in the environment. Although biodegradability can provide a commercial advantage,

mechanical performance is still paramount for fulfilling the load carrying requirements in engineering applications and biopolymers are yet to compete with synthetic polymers in this area. The mechanical performance of "green" plastics can, however, be improved through fiber reinforcement. Natural plant fibers are attractive as the reinforcement since they are renewable and biodegradable. Incorporation of these fibers into biopolymers provides a fully "green composite." One application which has become of particular concern in recent years is electronic waste, often referred to as e-waste (Ball, 2003). In the e-waste stream, the casings of items such as mobile phones, computers, and printers are of particular interest since these items have only short lives but are made from materials which degrade only slowly. This is an area that could benefit considerably from the use of green materials.

The naturally occurring bacterial polyester, poly(hydroxybutyrate-co-valerate) (PHBV), is a green polymer with a hydrolysable carbon backbone, which allows it to be degraded by bacteria and enzymes and thus limit landfill saturation (Modi et al., 2016). PHBV has been reinforced by a variety of types of natural fibers previously—abaca (Shibata et al., 2002; Bledzki and Jaszkiewicz, 2010; Adam et al., 2013), hemp (Keller, 2003; Hermida and Mega, 2007; Michel and Billington, 2014), kenaf (Avella et al., 2007; Buzarovska et al., 2007; Persico et al., 2011; Russo et al., 2013), jute (Bledzki and Jaszkiewicz, 2010; Adam et al., 2013), coir (Javadi et al., 2010c), and flax (Bledzki and Jaszkiewicz, 2010; Adam et al., 2013). The majority of the work to date has involved short fibers, particulates and nanofibers, with very little work having been conducted on continuous long natural fibers.

Two major studies have investigated continuous fiber reinforcement of PHBV previously. Luo and Netravali (1999) prepared PHBV [3 mol.% hydroxyvalerate (HV)]/unidirectional (UD) pineapple leaf fiber composites, containing 0–28 vol.% fiber, using the film stacking/hot pressing route and reported at least 3-fold increases in tensile modulus and strength at 28 vol.%. Bourban et al. (1997) prepared PHBV (3 mol.% HV)/regenerated cellulose fiber composites with 9.9 and 26.5 vol.% fiber by filament winding and hot pressing. The authors reported at least 10-fold increases in tensile modulus and strength at 26.5 vol.%. In comparison, most short-fiber additions to PHBV have resulted in increases in mechanical properties of a maximum of 2-fold, at volume fractions of 30%. Unfortunately, the large increases due to continuous fibers were accompanied by up to 85% reductions in elongation to break, indicating a heavily embrittling effect of the fibers.

Composites are normally toughened by a variety of agents to counter the embrittling effect of fiber addition. Polybutylene adipate-co-terephthalate (PBAT) and epoxidized natural rubber (ENR) have been added as toughening agents to PHBV/natural fiber composites in many studies but these have all been short-fiber reinforced composites (Javadi et al., 2010a,b,c; Nagarajan et al., 2013a,b; Zhang et al., 2014a,b). There are no studies where unidirectional fibers and toughening agents have been added simultaneously to PHBV to produce a well-rounded high performing green composite.

Although the mechanical properties can be improved through fiber reinforcement and toughening, it is pertinent that the final product be biodegradable. Biodegradation studies have been conducted on untoughened PHBV/natural fiber composites but there is little to no literature on the biodegradation properties of toughened PHBV composites. The biodegradability of PHBV has been shown by numerous studies to become enhanced after fiber addition. Batista et al. (2010) examined the biodegradation of their PHBV (9.8 mol.% HV)/peach palm particle (PPp) composites, in a soil mix containing equal parts of fertile soil (with low clay content), horse manure, and beach sand. The authors reported, from SEM observations, that their neat PHBV showed cavities after 2 months, which became more pronounced after 5 months. They found that addition of PPp increased the biodegradation rate progressively with increased PPp content, which they attributed to the presence of a gap between the particles and matrix which increased (from $\sim$2.5 to $\sim$10 μm) with particle content. The gap allowed moisture and microorganisms progressively better access to internal PHBV surfaces. After 5 months, the particles showed significant detachment from the matrix and began showing degradation themselves, as evidenced by the presence of cavities within the particles. Similar observations of fibers enhancing the biodegradation of PHBV have been reported for PHBV/lyocell (Shibata et al., 2004), PHBV/flax (Barkoula et al., 2010), and PHBV/abaca (Shibata et al., 2002).

In this work, PHBV was simultaneously reinforced with unidirectional flax and toughened with PBAT or ENR50. The mechanical, thermal, and morphological properties of the resulting composites have been reported previously in Zaidi and Crosky (2019). This study focuses on the biodegradation properties of those composites and elucidates the effect of PBAT and ENR on the biodegradation of PHBV/flax composites.

EXPERIMENTAL

Materials

PHBV (ENMAT® Y1000) was obtained from Tianan Biologic Material Co., China. This commercial grade of PHBV contains 3 mol.% HV (Srithep et al., 2013) and has a melt flow index (MFI) of 2.5 g/10 min at 170°C (Michel and Billington, 2014) and a density of 1.25 g/cm^2 (Srubar et al., 2012). PBAT (Ecoflex® C1200 F) was obtained from BASF, Germany. This commercial grade of PBAT has an MFI of 3.5 g/10 min and a density of 1.26 g/cm^3 (Savadekar et al., 2015). Epoxidized natural rubber with 50% epoxidation (ENR50) was used here and was obtained under the trade name Epoxyrene-50® from Industrial Organics, Australia. It has a density of 1.02 g/cm^2 (Mohamad et al., 2006). Quasi-unidirectional flax (trade name FlaxPly® UD 180) was obtained from LINEO, Belgium. The fabric was supplied with an epoxy-based sizing that constituted 16 wt.% of the fabric to improve resin impregnation properties. The fabric consisted of thick longitudinal warp yarns interconnected with thin twisted weft yarns at a spacing of 3 mm using a 4 over/4 under repeating interlacing pattern. The fabric had an areal weight of 180 grams per square meter. The density of flax is 1.4 g/cm^3 (Vanleeuw et al., 2015).

Composite Preparation

Unidirectional composite laminates were fabricated in 200 × 200 mm steel picture frame molds with fitting lids using a 50-ton water cooled hot press built by DSTO Australia. 4 ply laminates ~1.5 mm thick were fabricated by placing pre-cut plies of unidirectional flax cloth having dimensions of 200 × 200 mm in the picture frame mold. The composites were fabricated from matrix material in the powder form, with the powder being carefully spread using a flat 50 mm wide soft brush to obtain a uniform distribution.

For the toughened composites, the PBAT and ENR50 were first cryoground into powder using a Spex® Freezer Mill and then mixed with the PHBV matrix powder. The precool time was 10 min, with the grinding then being conducted at 10 Hz for 3 cycles, each consisting of 2 min grinding followed by 2 min cool down. Due to the self-healing nature of ENR50 (Rahman et al., 2013), 0.1 g PHBV powder per gram of ENR50 was added for cryogrinding of ENR50 as the PHBV powder prevented ENR50 powder from coalescing back into a solid mass.

Prior to hot pressing the laminates, the layup was dried (in the mold) in a vacuum oven for 24 h at 80°C to remove moisture. Drying at temperatures of ~80°C for at least 24 h, with or without vacuum, is common practice for PHBV and natural fibers (Rossa et al., 2013; Russo et al., 2013; Srithep et al., 2013; Zhang et al., 2014b; Berthet et al., 2015). The mold was then immediately transferred to the preheated hot press and the laminates compression molded at 180°C and 3.5 MPa for 12 min. A target fiber volume fraction of 0.30 was selected for the study since similar volume fractions have been used widely in the literature. The volume fraction of ENR or PBAT in the toughened composites was 30 vol.%.

Biodegradability Test Setup

Sample Preparation

Neat PHBV samples were cut from the molded plates. The PHBV/flax, PHBV/PBAT/flax, and PHBV/ENR/flax composite samples were cut from the 4 ply laminates.

High-impact polystyrene (HIPS) was used as a control material. Specimens 1 mm thick were cut from the outer plastic casing of a commercial printer that had reached its end of life.

Square specimens measuring 10 × 10 mm were guillotine-cut from the plates and a 1-mm hole was drilled through the center.

Soil Burial

Based on preliminary trials, a location within Centennial Parklands, Sydney was selected for burial of samples for the test. The underlying soil at Centennial Parklands is known as Botany Sand, which is a well-sorted medium sand containing <1% clay. It is subrounded and has high sphericity, a density of 2.65 g/cm^3 and its composition has been reported via x-ray diffraction (XRD) to be quartz dominant, with the clay fraction containing kaolinite and illite (Kelly, 1994).

For each material, a 0.8-mm aluminum wire was threaded through each of the three replicates and arranged in a radial pattern as shown in **Figure 1**. A 300-mm white plastic cable tie was then attached to the center. Colored cable ties of different colors were then attached to the top of the white cable tie to
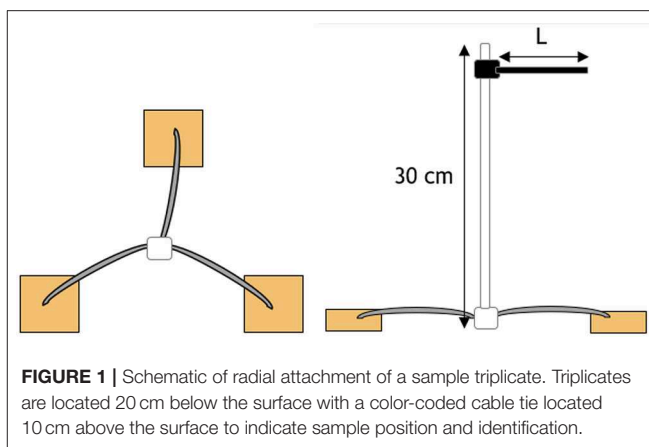
FIGURE 1 | Schematic of radial attachment of a sample triplicate. Triplicates are located 20 cm below the surface with a color-coded cable tie located 10 cm above the surface to indicate sample position and identification.
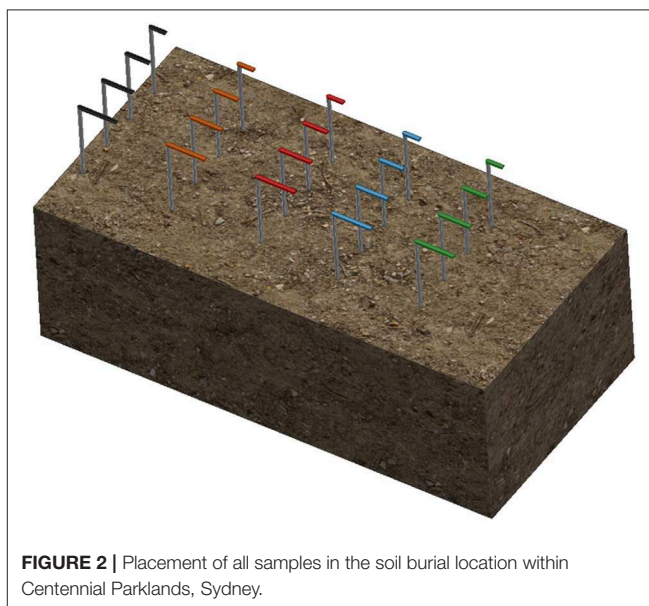
FIGURE 2 | Placement of all samples in the soil burial location within Centennial Parklands, Sydney.

identify the different materials. The colored cable ties were cut to different lengths (L) such that the length corresponded to the duration of the burial period.

A trench measuring 600 × 300 × 200 mm was dug at the selected location and the samples were laid laterally across the trench with a spacing of 50 mm. The soil taken from the trench was used to backfill the trench to the surface. The layout of the samples is shown in **Figure 2**. The moisture content was governed by natural rainfall.

The soil biodegradation test was conducted on the samples for a maximum burial duration of 112 days, with samples removed for measurement at 28, 56, 84, and 112 days from burial. The samples were buried from the 28th April 2017 for up to 4 months. Three replicate samples were used for each time period for each of the five materials.

Measurements

Biodegradation was evaluated through mass loss and surface characterization.

Daily rainfall data was obtained for the May to August period from the Bureau of Meteorology website, weather station 066062 – Sydney (Observatory Hill). The rainfall data was then superimposed with the mass loss data to examine possible correlations between the rainfall pattern and mass loss.

Mass Loss

Before burial, samples were dried in an oven at 80°C for 24 h and the initial mass W_I was recorded. After retrieval from the burial site, the samples were washed with distilled water, dried at 80°C for 24 h, and the final mass W_f was recorded. The mass loss, ΔW was determined according to:

$$\Delta W \ (\%) = \left(\frac{W_I - W_f}{W_I} \right) \times 100 \qquad (1)$$

Surface Characterization

After weighing the retrieved samples, their surface features were examined using an ECLIPSE low power optical microscope fitted with a Nikon 600 camera at 5X magnification.

After examination by optical microscopy, the samples were sputter coated with gold using an EMITECH K550x gold coating unit and examined using a HITACHI S-3400N scanning electron microscope (SEM) operating at 10 kV.

RESULTS

Mass Loss

The mass loss obtained after each period of time for the neat PHBV, PHBV/flax, PHBV/PBAT/flax, PHBV/ENR/flax, and the HIPS control samples is shown graphically in **Figure 3** along with rainfall data.

The HIPS control and neat PHBV samples showed negligible mass losses of 0.4 and 0.5%, respectively, with no appreciable change during the test period.

In contrast the three composites all showed substantial mass losses which increased progressively with time, but at different rates. The highest mass loss was recorded for PHBV/ENR/flax with the lowest being recorded for PHBV/flax. The mass losses after 112 days were 6% for PHBV flax, 9% for PHBV/PBAT/flax and 17% for PHBV/ENR flax.

The rainfall was quite intermittent over the course of the testing. There were several periods of rainfall of 10 mm or more with a fall of 60 mm being received over just a few days in one case, **Figure 3**. However, there appeared to be no distinct correlation between the biodegradation results and the rainfall pattern for the time intervals used in the study.

Surface Characterization
Optical Microscopy

Micrographs of the surface of the HIPS control sample before testing and after the different time intervals are shown in **Figure 4**. The surface of the sample before testing had a textured appearance associated with its former use as a printer casing. No change in the surface was observed throughout the test period, consistent with the absence of any appreciable mass change.

The surface of neat PHBV samples is shown for the various time intervals in **Figure 5**. For these samples, color fading was observed with time, as well as coverage of the surface by light colored regions which increased progressively with time and covered most of the surface by 112 days.

Micrographs of the surface of the PHBV/flax samples are shown in **Figure 6**. Color fading was again observed with time and was more pronounced than in the neat PHBV. With the color fading, the flax fibers became more visible under the surface after 28 days (red arrows), and microcracks began to appear after 56 days (red arrows). Small purple areas of discoloration were also observed at the longest time (red arrows).

Figure 7 shows micrographs of the surface of the PHBV/PBAT/flax samples for the various time intervals.
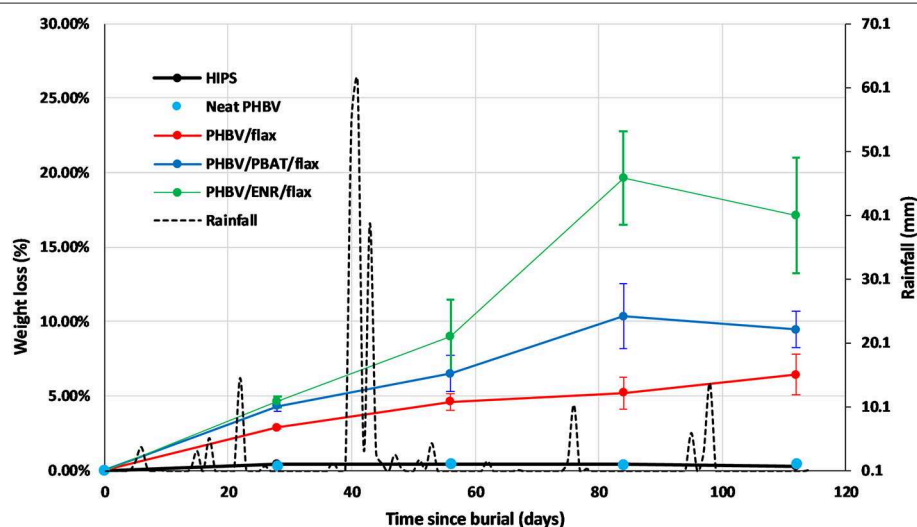
FIGURE 3 | Mass loss curves of HIPS control, neat PHBV, PHBV/flax, PHBV/PBAT/flax, PHBV/ENR/flax, and rainfall data for May to August 2017 period. Error bars represent standard deviation for $n = 3$ samples.

FIGURE 4 | Optical micrographs of HIPS at 0, 28, 84, and 112 days.

FIGURE 5 | Optical micrographs of neat PHBV at 0, 28, 84, and 112 days.
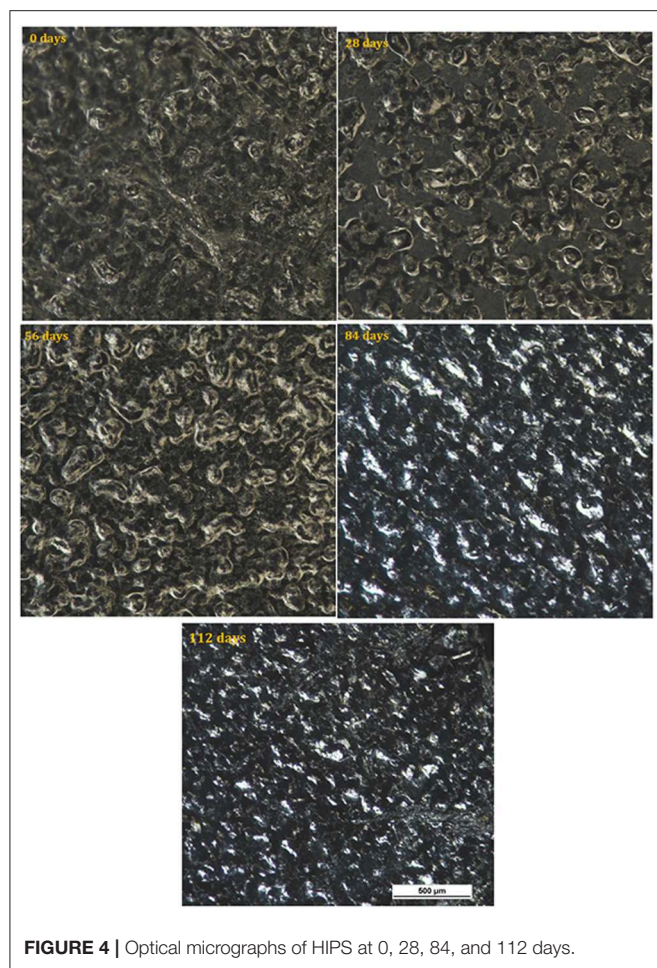
Progressive fading and discoloration occurred with increasing burial time. Microcracks and purplish regions were again observed.

Micrographs of the PHBV/ENR/flax samples for the various time intervals are shown in **Figure 8**. Progressive fading and discoloration were again observed, but this was less pronounced than for PHBV/flax and PHBV/PBAT/flax samples. Microcracks were again observed and purplish and yellow regions were observed at the longer times.

SEM

Initial surfaces

The initial surfaces are shown for all samples in **Figure 9**. All samples showed smooth, featureless surfaces before soil burial, except for the HIPS sample which, as mentioned earlier, showed a degree of roughness.

After 28 days

The five different materials are shown after 28 days burial in **Figure 10**. The HIPS sample showed no detectable change as a result of burial. The neat PHBV sample showed faint craze-like markings and some coarse pits. The PHBV/flax, PHBV/PBAT/flax, and PHBV/ENR/flax composite samples all began to exhibit microcracks ∼50 μm wide, together with some
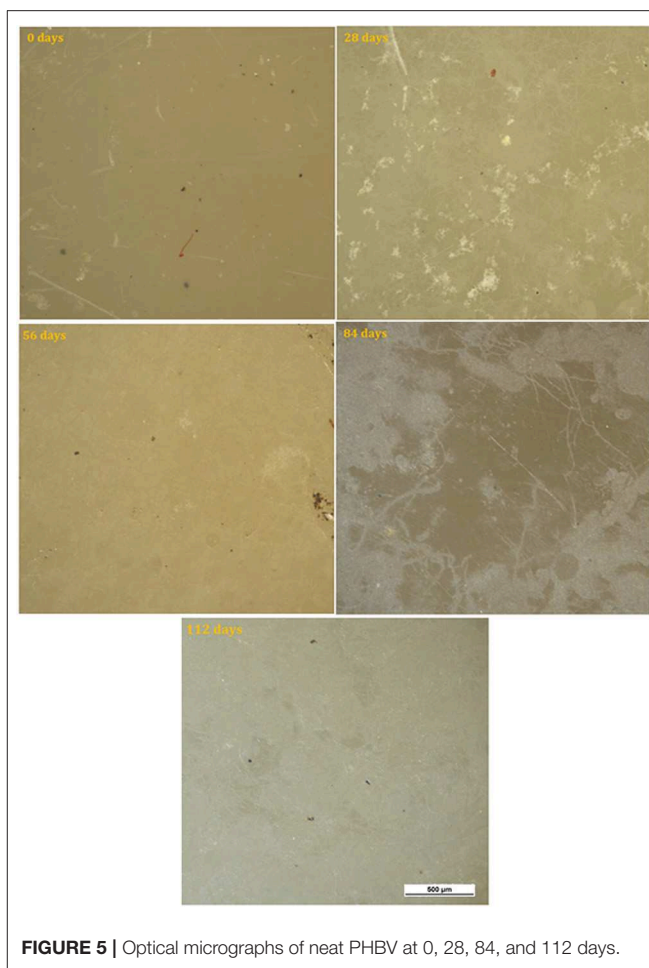
coarse pits. Light colored patches were also evident across the surface but were more prevalent in the PHBV/PBAT/flax and PHBV/ENR/flax samples than in the PHBV/flax composite.

A region in one of the composites where fibers have become exposed at the surface is shown in **Figure 11**. The elementary fibers have begun to separate from the fiber bundles while filaments <1 μm in diameter have developed from the fibers.

After 56 days

The five different materials are shown after 56 days burial in **Figure 12**. No change was again observed for the HIPS samples. For the neat PHBV samples, the craze markings seen after 28 days burial had become wider and more pronounced, while the surface had begun to become patchy and rougher. The PHBV/flax, PHBV/PBAT/flax, and PHBV/ENR/flax composite samples all showed an increasing level of cracking with the cracks being wider, frequently revealing the flax fibers beneath the surface. The filamentous structures on the flax fibers seen after 28 days in the PHBV/flax, PHBV/PBAT/flax, and PHBV/ENR/flax samples had also become larger and elementary fiber separation was more pronounced. Filamentous structures had begun to develop on
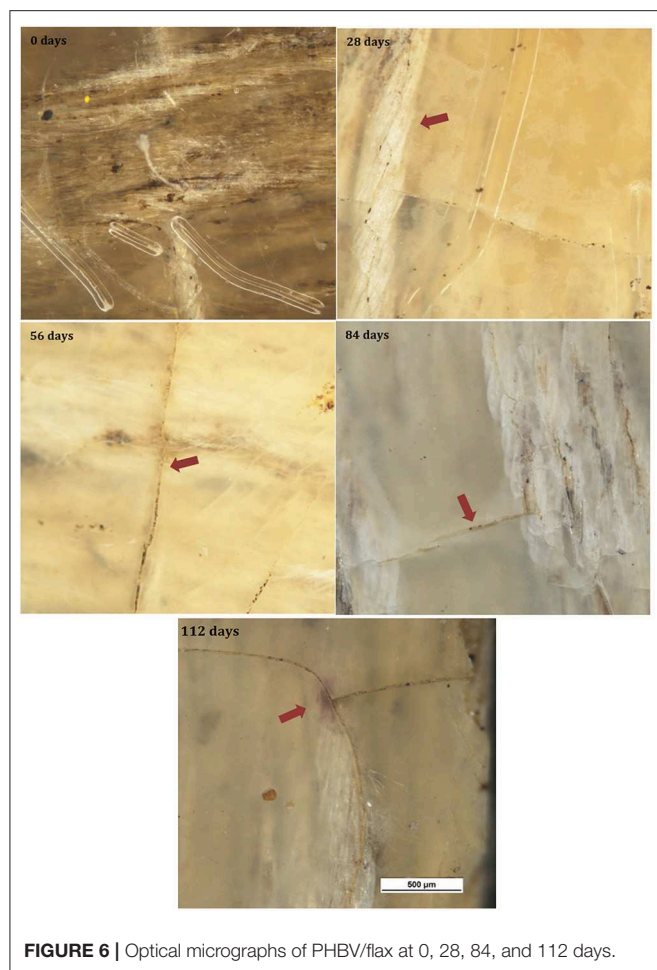
FIGURE 6 | Optical micrographs of PHBV/flax at 0, 28, 84, and 112 days.

FIGURE 7 | Optical micrographs of PHBV/PBAT/flax at 0, 28, 84, and 112 days.

the surface of the PHBV/ENR/flax composite and these appeared to be associated with ENR particles. Peanut shaped features ~5 μm long had also begun to appear on the PHBV/ENR/flax sample.

After 84 days

The five different materials are shown after 84 days burial in **Figure 13**. The HIPS sample remained unchanged. Neat PHBV became more pitted with pits being much deeper. Cracking in composite samples continued to grow and reveal fibers underneath the surface. The filamentous structures became more extensive on PHBV/PBAT/flax and PHBV/ENR/flax. Some filaments began growing out of the surface, having a hollow and cylindrical appearance.

After 112 days

Changes in the samples after 112 days burial are shown in **Figure 14**. The HIPS control sample remained essentially unchanged. For all other samples, the pitting had become essentially continuous across the surface but otherwise there was minimal further change.

DISCUSSION

Mass Loss

The control HIPS sample underwent negligible loss in mass during burial, as is expected for a non-biodegradable polymer (Ebadi-Dehaghani et al., 2016). A negligible degradation rate (0.47% in 112 days) was also observed for neat PHBV. This is contrary to the reported degradation rates for PHBV, given in **Table 1**, which are more substantial. However, the data given in **Table 1** is for PHBV grades with higher HV contents (5–13%) than the grade used in the present study (3% HV) and this may be responsible for the difference. Differences in soil may also have had an effect.

It is noted that the PHBV samples were buried in close proximity to the composite samples raising the possibility of interference from the latter. However, similarly low rates of degradation were obtained for the neat PHBV samples in preliminary trials in which the PHBV samples were tested separately from the composites. It is concluded therefore that any interference from the composites on the degradation rate of neat PHBV would have been minimal.

FIGURE 8 | Optical micrographs of PHBV/ENR/flax at 0, 28, 84, and 112 days.
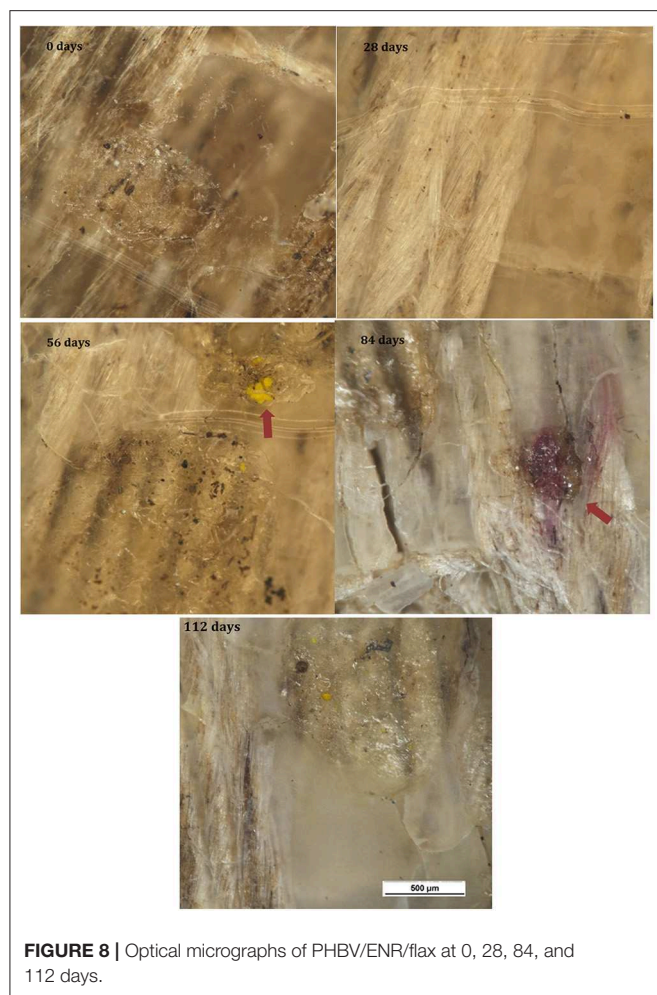
While the mass loss was negligible for the PHBV samples, the SEM micrographs did show evidence of some biodegradation at the exposed surface.

Unlike the neat PHBV, the composites showed substantial degradation rates, with the mass losses after 112 days being 7–17%. The increased mass loss due to natural fiber addition is a common observation in the literature, as flax fibers are highly biodegradable. Alimuzzaman et al. (2014) reported a mass loss of 90% for flax after 60 days of burial in compost, attributed to all the components of flax—cellulose, lignin, and pectin—being biodegradable. The authors had also reinforced polylactic acid (PLA) with flax and reported that flax addition increased the biodegradability of PLA, as the water-absorbent nature of flax allowed water and microorganisms to be absorbed into the interior of the sample through the cut edges of the composite. Batista et al. (2010) have also reported higher rates of biodegradation in PHBV/peach palm particle composites than in neat PHBV. Their findings were based on visual and SEM examination since excessive disintegration of the composite samples precluded accurate mass loss measurement. They attributed the higher rate of degradation in the composites to gaps between the fiber particles and the matrix providing

channels for microorganisms to reach the inner bulk of the composite, thus allowing degradation from the interior as well as from the surface.

The composites examined by Batista et al. (2010) would be expected to have fibers exposed at the surface but fibers were generally not exposed on the molded surfaces of the composites examined in the present study. However, fibers would be exposed at the cut edges of the samples and ingress of microorganisms might have been possible along the fiber matrix interfaces and through the lumens. The microcracks which developed in the composites during soil burial would also have facilitated microorganism ingress.

The degradation rate was faster in both the toughened composites than in the untoughened composite, with the mass loss after 112 days being ~50% higher for PHBV/PBAT/flax and more than double for the PHBV/ENR/flax. Kumagai and Doi (1992) observed that blends of PHB degraded faster than the pure polymer, which was attributed to phase separation during the blending process. This suggests that the interfaces between the toughening agents and the PHBV matrix may have provided paths for microorganism ingress.

The higher rate of degradation observed for the ENR toughened composite than its PBAT toughened counterpart is attributed to natural rubber being a common target of a bacterial order commonly found in soil known as the actinomycetes (Ali Shah et al., 2013). In contrast, biodegradation of PBAT has been reported to be minimal (Tsutsumi et al., 2003; Trinh Tan et al., 2008; Ali Shah et al., 2013). It is noted, however, that the ENR particles were much coarser than the PBAT particles (Zaidi and Crosky, 2019) and this may also have affected the degradation rate.

Pantani and Sorrentino (2013) conducted biodegradation studies on PLA and reported that crystallinity is a factor that affects the biodegradation rate of PLA, with the rate being faster for amorphous samples compared to crystalline samples. The authors attributed this to crystallinity affecting the diffusion of water into the sample and presenting difficulty in access to the polymer chains for enzymatic attack by the microorganisms. Differences in time of saturation for PHBV/flax and the toughened composites might therefore be due to differences in crystallinity between the two types of samples, as the toughened composites would have had a much lesser crystallinity as a result of addition of amorphous PBAT and ENR, as discussed in Zaidi and Crosky (2019).

Surface Degradation

One feature observed for the neat PHBV samples as well as the composites was color fading. Color fading has also been observed for PHBV/abaca (Teramoto et al., 2004), PHBV/peach palm particles (PPp) (Batista et al., 2010), and PHBV/lyocell (Shibata et al., 2004) composites. This is attributed to micro-pitting of the surface, as was observed in the SEM images shown earlier. This increases the surface roughness of the samples, and the rougher surface would subsequently scatter light to a greater extent.

With increased burial time, the level of pitting increased, initially being localized but eventually becoming more uniformly spread. The pitted regions are considered to most likely be areas
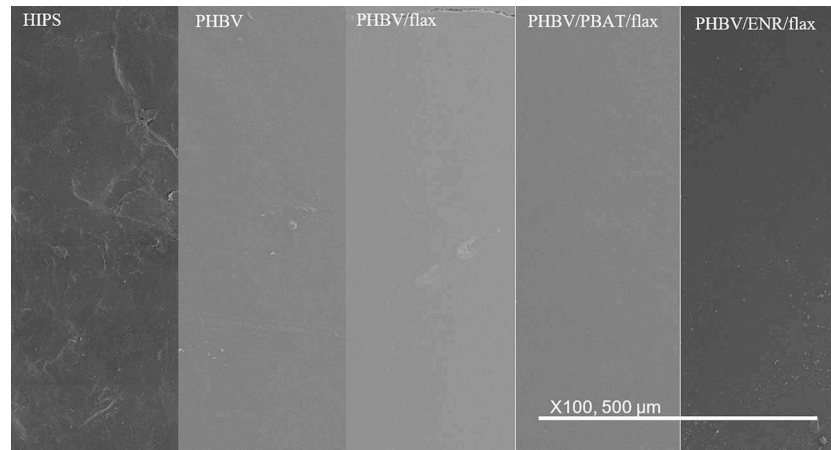
FIGURE 9 | SEM images of initial surfaces of all materials.
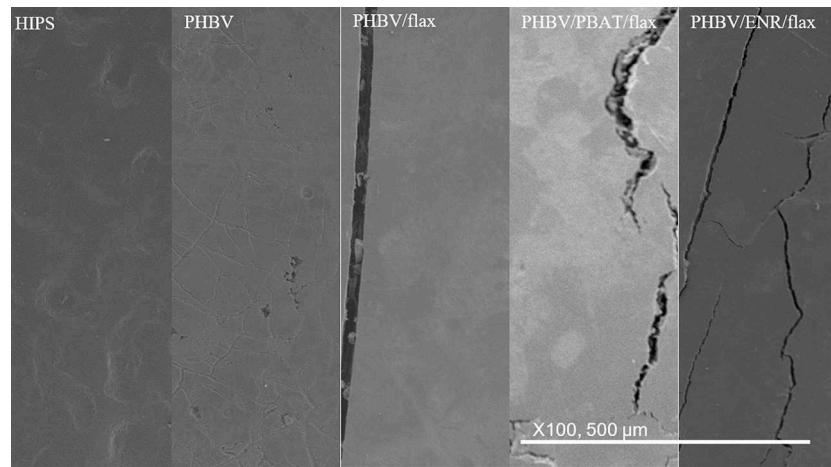
FIGURE 10 | SEM images of surfaces of all materials after 28 days.
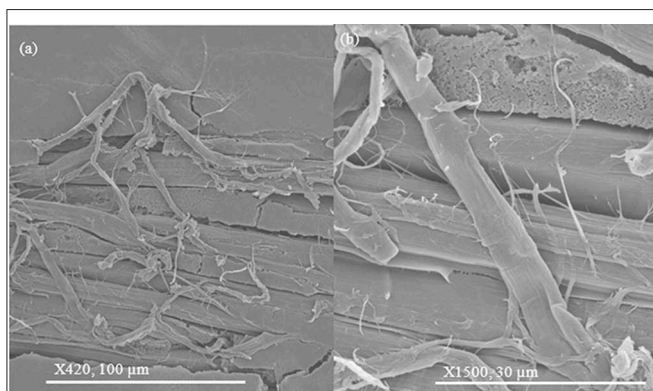
FIGURE 11 | SEM images of fine filaments developing from the flax fibers after 28 days at **(a)** 420X; **(b)** 1500X magnification.

of reduced molecular weight resulting from hydrolysis of the polymer chains, which is reported to be one of the causes of the onset of degradation.

The localized pitted regions, which were seen as light-colored regions when viewed using SEM, were more pronounced on the PHBV/ENR/flax and PHBV/PBAT/flax samples than on the PHBV/flax composite. This is attributed to lower crystallinity caused by the addition of the toughening agents (Zaidi and Crosky, 2019), since amorphous regions are known to degrade preferentially to crystalline regions (Abe and Doi, 1999; Woolnough et al., 2010).

Some workers have reported fragmentation (Teramoto et al., 2004; Batista et al., 2010) during biodegradation but this was only observed in the present study where the fibers were close to the surface, **Figure 11**. In these cases, it appeared that the microorganisms had exploited the fiber matrix interfaces, as proposed by Batista et al. (2010).
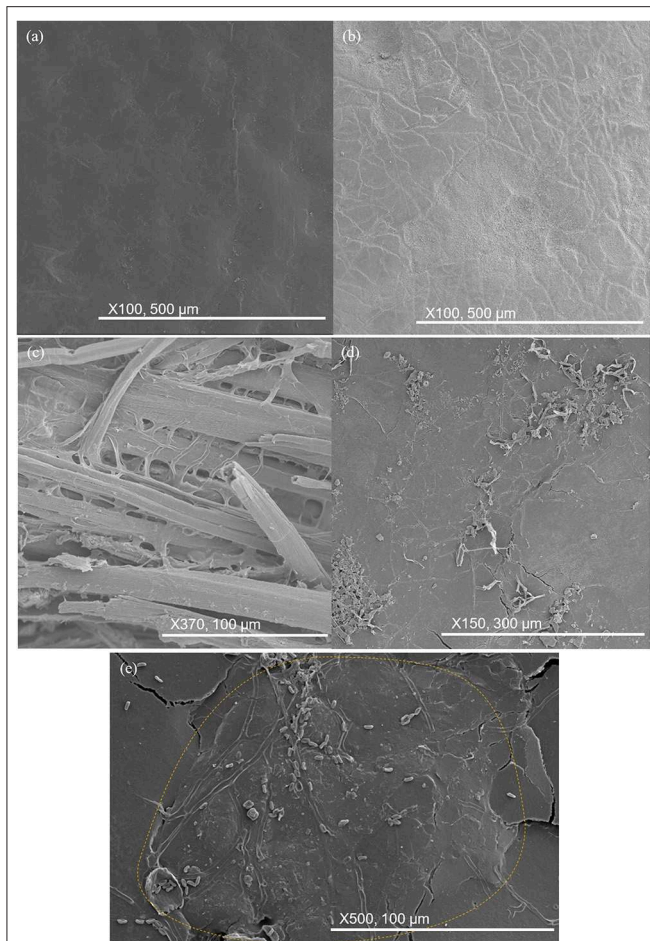
FIGURE 12 | SEM images of key changes in samples after 56 days. **(a)** HIPS remains unchanged; **(b)** craze markings on neat PHBV; **(c)** elementary fiber separation in composite samples; **(d)** filamentous structures growing on ENR particles; **(e)** peanut-shaped objects observed on ENR particles.
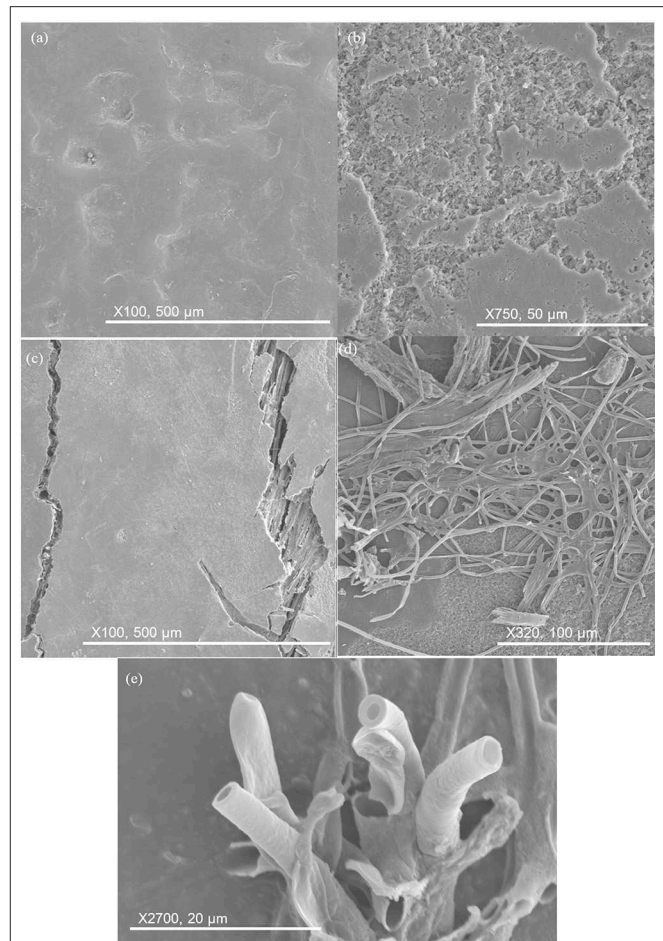
FIGURE 13 | SEM images of key changes after 84 days. **(a)** HIPS remains unchanged; **(b)** pits deepening in neat PHBV; **(c**) surface cracking in composite samples, revealing fiber underneath; **(d)** filament proliferation on PHBV/PBAT/flax and PHBV/ENR/flax; **(e)** filaments maturing and growing out of surface, having hollow and cylindrical appearance.

As noted above the composites developed surface cracking during soil burial but this was not observed for the neat PHBV. This difference is attributed to the higher level of PHBV crystallinity in the composites induced by nucleation at the fibers, as discussed in earlier work by Zaidi and Crosky (2019).The increased level of crystallinity would result in increased brittleness.

Submicron-sized filamentous structures were observed on flax fibers which had been exposed at the surface, **Figure 11**. These are likely to be fungi, which have been reported to be the primary cause of lignin-degradation (Kirk and Farrell, 1987; Avella et al., 2000). This is consistent with the observation of elementary fiber separation since lignin binds the elementary fibers together (Yan et al., 2014) and the observed separation into elementaries indicates that the lignin has been degraded.

Filamentous structures, together with peanut shaped features, were observed on the surfaces of the toughened composites. These are considered likely to be fungal hyphae, which are cylindrical cells that grow from one end and start branching
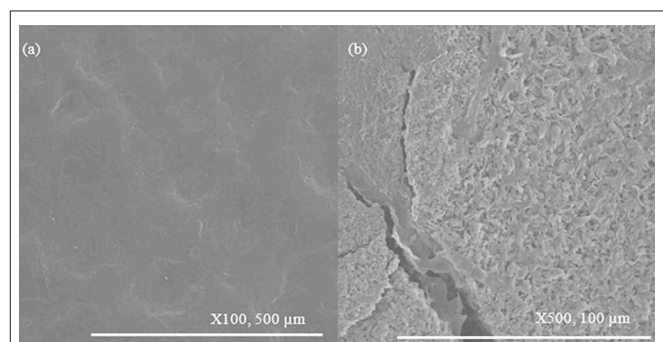
FIGURE 14 | SEM images of key changes in samples after 112 days. **(a)** HIPS remains unchanged; **(b)** pitting becomes continuous for all other samples.

to form a system of hyphae known as mycelium. The peanut shaped features are likely to be spores that initiate the hyphae structure. This is consistent with the reduction in the number of

TABLE 1 | Mass loss data for neat PHBV reported in various studies.

Mass loss %	At # of days from burial	Medium	Grade	Reference
10–11	84	Garden soil	Zeneca PHBV 5 mol.% HV	Avella et al., 2000
20–23	168	"	Zeneca PHBV 5 mol.% HV	"
20	224	Soil	Biopol unspecified HV	Barkoula et al., 2010
32	150	Soil	Biofan A-1000 11 mol.% HV	Teramoto et al., 2004
40	90	Soil	Biophane A-1000 (from same supplier as Teramoto *et al.* so presumably also 11 mol.%HV)	Shibata et al., 2004

peanut shaped features observed with increased development of the filamentous structures. The spores lie dormant, get dispersed through the air and, after landing on a suitable substrate, germinate under favorable conditions (Carlile, 1995). It would be expected that the spores would infiltrate into the soil, especially during periods of rain, thus allowing them to contact the buried samples.

Passos et al. (2015) observed spores and fungal hyphae on PHBV film after 1 month of degradation by a fungal solution containing the fungus *Paecilomyces variotii* which is an ascomycete commonly found in soil. The peanut-shaped objects in the present study resemble the spores observed by these authors. Similar structures were observed by Stieven Montagna et al. (2017) when PHBV/graphite nanosheet (GNS) nanocomposites were subject to biodegradation by the fungus *Penicillium funiculosum* commonly found in soil.

While filamentous structures were observed on both toughened composites, they were more prevalent and more complex on the ENR toughened samples than on the PBAT toughened samples. It is probable that some of the filamentous structures seen on the ENR toughened samples were due to an order of actinobacteria known as the actinomycetes, which are known to be primary attackers of natural rubber (Ali Shah et al., 2013). This order contains one of the largest bacterial genera, *Streptomyces*, which is found worldwide in soil (Faghri Zonooz and Salouti, 2011). The Streptomyces genera forms a filamentous structure which is similar to fungal mycelium. The actinomycete order are the only bacteria which form a filamentous structure (Castillo et al., 2005).

In view of the above it is considered that actinomycete bacteria and fungal mycelium were both active in the biodegradation of the ENR toughened composite samples, but only the latter were active in the PBAT toughened samples. This is considered to be the principal cause of the higher degradation rate seen for the PHBV/ENR/flax composites.

CONCLUSIONS

Negligible biodegradation occurred in the PHBV which showed a maximum mass loss of 0.5% over the 112 days exposure period. The rate of degradation was, however, substantial for all the composites and was higher in the two toughened composites than in the untoughened PHBV/flax composite. Of the toughened composites PHBV/ENR flax showed the highest degradation rate with a mass loss of 17% being recorded after 112 days, compared with 9% PHBV/PBAT/flax and 6% for PHBV/flax. Filamentous structures were seen on flax fibers which had been exposed at the surface. These are considered to have been fungi which have been reported to be the primary cause of lignin-degradation, consistent with the observation of elementary fiber separation.

Other filamentous structures, together with peanut shaped features, were observed on the surfaces of the toughened composites. Filamentous structures were more prevalent and more complex on the ENR toughened samples than on the PBAT toughened samples. It is probable that some of the filamentous structures seen on the ENR toughened samples were due to an order of actinobacteria known as the actinomycetes, which are known to be primary attackers of natural rubber. The presence of these microorganisms is considered to be the primary reason for the faster degradation of the PHBV/ENR/flax composites.

These results indicate that the incorporation of ENR as a bio-based toughening agent for PHBV/natural fiber composites not only enhances the toughness properties of the biocomposites but enhances their biodegradability substantially more than is achieved by addition of the commonly used toughening agent PBAT. These properties can broaden the scope of application for PHBV-based toughened and untoughened biocomposites.

DATA AVAILABILITY STATEMENT

The datasets generated for this study are available on request to the corresponding author.

AUTHOR CONTRIBUTIONS

ACKNOWLEDGMENTS

conducting soil burial was provided by Associate Professor Bryce Kelly from the School of Biological, Earth and Environmental Sciences (BEES), UNSW. Technical support with electron microscopy was provided by Dr. Simon Hager and Dr. Katie Levick from the Electron Microscopy Unit (EMU), UNSW.

REFERENCES

Abe, H., and Doi, Y. (1999). Structural effects on enzymatic degradabilities for poly[(R)-3-hydroxybutyric acid] and its copolymers. Int. J. Biol. Macromol. 25, 185–192. doi: 10.1016/S0141-8130(99)00033-1

Adam, J., Korneliusz, B. A., and Agnieszka, M. (2013). Dynamic mechanical thermal analysis of biocomposites based on PLA and PHBV - A comparative study to PP counterparts. J. Appl. Polym. Sci. 130, 3175–3183. doi: 10.1002/app.39562

Ali Shah, A., Hasan, F., Shah, Z., Kanwal, N., and Zeb, S. (2013). Biodegradation of natural and synthetic rubbers: a review. Int. Biodeterior. Biodegrad. 83, 145–157. doi: 10.1016/j.ibiod.2013.05.004

Alimuzzaman, S., Gong, R. H., and Akonda, M. (2014). Biodegradability of nonwoven flax fiber reinforced polylactic acid biocomposites. Polym. Compos. 35, 2094–2102. doi: 10.1002/pc.22871

Avella, M., Bogoeva-Gaceva, G., Buzarovska, A., Errico, M. E., Gentile, G., and Grozdanov, A. (2007). Poly(3-hydroxybutyrate-co-3-hydroxyvalerate)-based biocomposites reinforced with kenaf fibers. J. Appl. Polym. Sci. 104, 3192–3200. doi: 10.1002/app.26057

Avella, M., La Rota, G., Martuscelli, E., Raimo, M., Sadocco, P., Elegir, G., et al. (2000). Poly(3-hydroxybutyrate-co-3-hydroxyvalerate) and wheat straw fibre composites: thermal, mechanical properties and biodegradation behaviour. J. Mater. Sci. 35, 829–836. doi: 10.1023/A:1004773603516

Ball, P. (2003). Material witness: e-waste not. Nat. Mater. 2:76. doi: 10.1038/nmat823

Barkoula, N. M., Garkhail, S. K., Peijs, T., Barkoula, N. M., Garkhail, S. K., and Peijs, T. (2010). Biodegradable composites based on flax/polyhydroxybutyrate and its copolymer with hydroxyvalerate. Ind. Crop. Prod. 31, 34–42. doi: 10.1016/j.indcrop.2009.08.005

Batista, K. C., Silva, D. A. K., Coelho, L. A. F., Pezzin, S. H., Pezzin, A. P. T., Batista, K. C., et al. (2010). Soil biodegradation of PHBV/peach palm particles biocomposites. J. Polym. Environ. 18, 346–354. doi: 10.1007/s10924-010-0238-4

Berthet, M. A., Angellier-Coussy, H., Chea, V., Guillard, V., Gastaldi, E., and Gontard, N. (2015). Sustainable food packaging: valorising wheat straw fibres for tuning PHBV-based composites properties. Compos. Part A Appl. Sci. Manuf. 72, 139–147. doi: 10.1016/j.compositesa.2015.02.006

Bledzki, A. K., and Jaszkiewicz, A. (2010). Mechanical performance of biocomposites based on PLA and PHBV reinforced with natural fibres - A comparative study to PP. Compos. Sci. Technol. 70, 1687–1696. doi: 10.1016/j.compscitech.2010.06.005

Bourban, C., Karamuk, E., de Fondaumiere, M. J., Ruffieux, K., Mayer, J., and Wintermantel, E. (1997). Processing and characterization of a new biodegradable composite made of a PHB/V matrix and regenerated cellulosic fibers. J. Envir. Polym. Degrad. 5, 159–166.

Buzarovska, A., Bogoeva-Gaceva, G., Grozdanov, A., Avella, M., Gentile, G., and Errico, M. (2007). Crystallization behavior of poly(hydroxybytyrate-co-valerate) in model and bulk PHBV/kenaf fiber composites. J. Mater. Sci. 42, 6501–6509. doi: 10.1007/s10853-007-1527-8

Carlile, M. J. (1995). "The success of the hypha and mycelium," in The Growing Fungus, eds G. M. Gadd and N. A. R. Gow (New York, NY: Springer), 3. doi: 10.1007/978-0-585-27576-5_1

Castillo, U., Myers, S., Browne, L., Strobel, G., Hess, W. M., Hanks, J., et al. (2005). Scanning electron microscopy of some endophytic streptomycetes in snakevine - Kennedia nigricans. Scanning 27, 305–311. doi: 10.1002/sca.4950270606

Ebadi-Dehaghani, H., Barikani, M., Borhani, S., Bolvardi, B., Khonakdar, H. A., Jafari, S. H., et al. (2016). Biodegradation and hydrolysis studies on polypropylene/polylactide/organo-clay nanocomposites. Polym. Bull. 73, 3287–3304. doi: 10.1007/s00289-016-1655-x

Faghri Zonooz, N., and Salouti, M. (2011). Extracellular biosynthesis of silver nanoparticles using cell filtrate of Streptomyces sp. ERI-3. Sci. Iranica 18, 1631–1635. doi: 10.1016/j.scient.2011.11.029

Hermida, E. B., and Mega, V. I. (2007). Transcrystallization kinetics at the poly(3-hydroxybutyrate-co-3-hydroxyvalerate)/hemp fibre interface. Compos. Part A Appl. Sci. Manuf. 38, 1387–1394. doi: 10.1016/j.compositesa.2006.10.006

Javadi, A., Kramschuster, A. J., Pilla, S., Lee, J., Gong, S., and Turng, L.-S. (2010a). Processing and characterization of microcellular PHBV/PBAT blends. Polym. Eng. Sci. 50, 1440–1448. doi: 10.1002/pen.21661

Javadi, A., Srithep, Y., Lee, J., Pilla, S., Clemons, C., Gong, S., et al. (2010b). Processing and characterization of solid and microcellular PHBV/PBAT blend and its RWF/nanoclay composites. Compos. Part A Appl. Sci. Manuf. 41, 982–990. doi: 10.1016/j.compositesa.2010.04.002

Javadi, A., Srithep, Y., Pilla, S., Lee, J., Gong, S., and Turng, L.-S. (2010c). Processing and characterization of solid and microcellular PHBV/coir fiber composites. Mater. Sci. Eng. C 30, 749–757. doi: 10.1016/j.msec.2010.03.008

Keller, A. (2003). Compounding and mechanical properties of biodegradable hemp fibre composites. Compos. Sci. Technol. 63, 1307–1316. doi: 10.1016/S0266-3538(03)00102-7

Kelly, B. F. J. (1994). Electrical properties of sediments and the geophysical detection of ground water contamination (Ph.D). University of New South Wales, Australia.

Kirk, T. K., and Farrell, R. L. (1987). Enzymatic "combustion": the microbial degradation of lignin. Annu. Rev. Microbiol. 41, 465–501. doi: 10.1146/annurev.mi.41.100187.002341

Kumagai, Y., and Doi, Y. (1992). Enzymatic degradation of binary blends of microbial poly (3-hydroxybutyrate) with enzymatically active polymers. Polym. Degrad. Stab. 37, 253–256. doi: 10.1016/0141-3910(92)90167-4

La Mantia, F. P., and Morreale, M. (2011). Green composites: a brief review. Compos. Part A Appl. Sci. Manuf. 42, 579–588. doi: 10.1016/j.compositesa.2011.01.017

Luo, S., and Netravali, A. N. (1999). Interfacial and mechanical properties of environment-friendly 'green' composites made from pineapple fibers and poly(hydroxybutyrate-co-valerate) resin. J. Mat. Sci. 34, 3709–3719. doi: 10.1023/A:1004659507231

Michel, A., and Billington, S. (2014). Nonlinear constitutive model for anisotropic biobased composite materials. J. Eng. Mech. 140:04014083. doi: 10.1061/(ASCE)EM.1943-7889.0000773

Modi, S. J., Cornish, K., Koelling, K., and Vodovotz, Y. (2016). Fabrication and improved performance of poly(3-hydroxybutyrate-co-3-hydroxyvalerate) for packaging by addition of high molecular weight natural rubber. J. Appl. Polym. Sci. 133:43937. doi: 10.1002/app.43937

Mohamad, Z., Ismail, H., and Chantara Thevy, R. (2006). Characterization of epoxidized natural rubber/ethylene vinyl acetate (ENR-50/EVA) blend: effect of blend ratio. J. Appl. Polym. Sci. 99, 1504–1515. doi: 10.1002/app.22154

Nagarajan, V., Misra, M., and Mohanty, A. K. (2013a). New engineered biocomposites from poly(3-hydroxybutyrate-co-3-hydroxyvalerate) (PHBV)/poly(butylene adipate-co-terephthalate) (PBAT) blends and switchgrass: fabrication and performance evaluation. Ind. Crops Prod. 42, 461–468. doi: 10.1016/j.indcrop.2012.05.042

Nagarajan, V., Mohanty, A. K., and Misra, M. (2013b). Sustainable green composites: value addition to agricultural residues and perennial grasses. ACS Sustainable Chem. Eng. 1, 325–333. doi: 10.1021/sc300084z

Pantani, R., and Sorrentino, A. (2013). Influence of crystallinity on the biodegradation rate of injection-moulded poly(lactic acid) samples in controlled composting conditions. Polym. Degrad. Stab. 98, 1089–1096. doi: 10.1016/j.polymdegradstab.2013.01.005

Passos, T. M., Marconato, J. C., and Franchetti, S. M. M. (2015). Biodegradation of films of low density polyethylene (LDPE), poly(hydroxibutyrate-co-valerate) (PHBV), and LDPE/PHBV (70/30) blend with Paecilomyces variotii. Polimeros 25, 29–34. doi: 10.1590/0104-1428.1432

Persico, P., Acierno, D., Carfagna, C., and Cimino, F. (2011). Mechanical and thermal behaviour of ecofriendly composites reinforced by Kenaf and Caroà fibers. Int. J. Polym. Sci. 2011, 1–7. doi: 10.1155/2011/841812

Rahman, M. A., Sartore, L., Bignotti, F., and Di Landro, L. (2013). Autonomic self-healing in epoxidized natural rubber. *ACS Appl. Mater. Interfaces* 5, 1494–1502. doi: 10.1021/am303015e

Rossa, L. V., Scienza, L. C., and Zattera, A. J. (2013). Effect of curaua fiber content on the properties of poly(hydroxybutyrate-co-valerate) composites. *Polym. Compos.* 34, 450–456. doi: 10.1002/pc.22432

Russo, P., Carfagna, C., Cimino, F., Acierno, D., and Persico, P. (2013). Biodegradable composites reinforced with Kenaf fibers: thermal, mechanical, and morphological issues. *Adv. Polym. Technol.* 32, E313–E322. doi: 10.1002/adv.21282

Savadekar, N. R., Kadam, P. G., and Mhaske, S. T. (2015). Studies on the effect of nano-alumina on the performance properties of poly(butylene adipate-co-terephthalate) composite films. *J. Thermoplast. Compos. Mater.* 28, 1522–1536. doi: 10.1177/0892705713513292

Shibata, M., Oyamada, S., Kobayashi, S., Yaginuma, D., Shibata, M., Oyamada, S., et al. (2004). Mechanical composites and biodegragability of green composites based on biodegradable polyesters and lyocell fabric. *J. Appl. Polym. Sci.* 92, 3857–3863. doi: 10.1002/app.20405

Shibata, M., Takachiyo, K.-I., Ozawa, K., Yosomiya, R., and Takeishi, H. (2002). Biodegradable polyester composites reinforced with short abaca fiber. *J. Appl. Polym. Sci.* 85, 129–138. doi: 10.1002/app.10665

Srithep, Y., Ellingham, T., Peng, J., Sabo, R., Clemons, C., Turng, L.-S., et al. (2013). Melt compounding of poly (3-hydroxybutyrate-co-3-hydroxyvalerate)/nanofibrillated cellulose nanocomposites. *Polym. Deg. Stabil.* 98, 1439–1449. doi: 10.1016/j.polymdegradstab.2013.05.006

Srubar, W. V., Pilla, S., Wright, Z. C., Ryan, C. A., Greene, J. P., Frank, C. W., et al. (2012). Mechanisms and impact of fiber-matrix compatibilization techniques on the material characterization of PHBV/oak wood flour engineered biobased composites. *Compos. Sci. Technol.* 72, 708–715. doi: 10.1016/j.compscitech.2012.01.021

Stieven Montagna, L., Amaral Montanheiro, T. L. d., Chiodi Borges, A., Yumi Koga-Ito, C., Paula Lemes, A., Cerqueira Rezende, M. (2017). Biodegradation of PHB/GNS nanocomposites by *Penicillium funiculosum*. *J. Appl. Polym. Sci.* 13(4), n/a-n/a. doi: 10.1002/app.44234

Teramoto, N., Urata, K., Ozawa, K., and Shibata, M. (2004). Biodegradation of aliphatic polyester composites reinforced by abaca fiber. *Polym. Degrad. Stab.* 86, 401–409. doi: 10.1016/j.polymdegradstab.2004.04.026

Trinh Tan, F., Cooper, D. G., Maric, M., and Nicell, J. A. (2008). Biodegradation of a synthetic co-polyester by aerobic mesophilic microorganisms. *Polym. Degrad. Stab.* 93, 1479–1485. doi: 10.1016/j.polymdegradstab.2008.05.005

Tsutsumi, C., Hayase, N., Nakagawa, K., Tanaka, S., and Miyahara, Y. (2003). The enzymatic degradation of commercial biodegradable polymers by some lipases and chemical degradation of them. *Macromol. Symp.* 197, 431–442. doi: 10.1002/masy.200350737

Vanleeuw, B., Carvelli, V., Barburski, M., Lomov, S. V., and van Vuure, A. W. (2015). Quasi-unidirectional flax composite reinforcement: deformability and complex shape forming. *Compos. Sci. Technol.* 110, 76–86. doi: 10.1016/j.compscitech.2015.01.024

Woolnough, C. A., Yee, L. H., Charlton, T., and Foster, L. J. R. (2010). Environmental degradation and biofouling of 'green' plastics including short and medium chain length polyhydroxyalkanoates. *Polym. Int.* 59, 658–667. doi: 10.1002/pi.2746

Yan, L., Chouw, N., and Jayaraman, K. (2014). Flax fibre and its composites – A review. *Compos. Part B Eng.* 56, 296–317. doi: 10.1016/j.compositesb.2013.08.014

Zaidi, Z., and Crosky, A. (2019). Unidirectional rubber-toughened green composites based on PHBV. *Sustainability* 11:2411. doi: 10.3390/su11082411

Zhang, K., Misra, M., and Mohanty, A. K. (2014a). Toughened sustainable green composites from poly(3-hydroxybutyrate-co-3-hydroxyvalerate) based ternary blends and *Miscanthus* biofiber. *ACS Sustainable Chem. Eng.* 2, 2345–2354. doi: 10.1021/sc500353v

Zhang, K., Nagarajan, V., Zarrinbakhsh, N., Mohanty, A. K., and Misra, M. (2014b). Co-injection molded new green composites from biodegradable polyesters and miscanthus fibers. *Macromol. Mater. Eng.* 299, 436–446. doi: 10.1002/mame.201300189

frontiers
in Materials

Check for
updates

Lignin as Alternative Reinforcing Filler in the Rubber Industry: A Review

Nor Anizah Mohamad Aini[1], Nadras Othman[1]*, M. Hazwan Hussin[2], Kannika Sahakaro[3] and Nabil Hayeemasae[3]

[1] School of Material and Mineral Resources Engineering Campus, Universiti Sains Malaysia, Nibong Tebal, Malaysia, [2] School of Chemical Science, Universiti Sains Malaysia, Minden Heights, Malaysia, [3] Department of Rubber Technology and Polymer Science, Faculty of Science and Technology, Prince of Songkla University, Songkhla, Thailand

Lignin has potential as a reinforcing filler and to become an alternative to carbon black in the rubber industry. This is because it is formed from cheaper materials with abundant annually renewable sources and has low weight, high biological efficiency, and wide ecological adaptability. The utilization of bio-filler in the rubber industry has garnered increasing attention from researchers due to increasing environmental concerns over the toxic effects of carbon black on health and the environment. This article is intended to summarize current efforts in the development of a green and sustainable rubber product. Instead of focusing on silica and alternative rubber matrix-like guayule and Russian dandelion, it looks at lignin, which also has potential as a reinforcing filler and can enable the development of competitive green rubber composites. Lignin has several special characteristics such as good mechanical, physico-chemical, biodegradability, and antioxidant properties and excellent thermal stability. However, the incorporation of lignin in a rubber matrix is not straightforward, and this needs to be overcome with certain suitable solutions because of the polarity of lignin molecules, which contributes to strong self-interactions. Consequently, chemical modification of lignin is often used to improve the dispersion of lignin in elastomers, or a compatibilizer is added to enhance interfacial adhesion between lignin and the rubber matrix. This review attempts to compile relevant knowledge about the performance of lignin-filled rubber composite using different approaches such as mixing method, surface modification, hybrid fillers, etc. This study is expected to gain significant interest from researchers globally on the subject of lignin-based rubber composites and the advancement of development in green rubber products.

Keywords: lignin, alternative carbon black, chemical modification, mixing technique, rubber-lignin properties

INTRODUCTION

Given the many applications of rubber in industrial parts such as hoses, tires, seals, cushions, etc., it should be acknowledged that many aspects need to be considered and understood. To obtain excellent performance from rubber compounds, a reinforcing filler is needed to provide reinforcement. Specifically, in the tire technology area, reinforcement is known as the incorporation of finely divided (mineral) particles into vulcanized compounds that improve abrasion, tearing,

cutting, and rupture resistance due to their stiffness and hardness (Medalia and Kraus, 1994). Tires are the most prominent rubber items, both in terms of importance and in terms of the volume of production. Most of the natural rubber, synthetic rubber, and 90% of the worldwide production of carbon black are used in the tire industry. This is due to the ability of rubber to enhance the strength of the tire. In spite of the functionalities of carbon black as the reinforcing filler, it is petrochemical and non-degradable material, and a large amount of energy is consumed in its production. Moreover, the hazardous effect of the utilization of carbon black has polluted the environment, starting from the production process, which emits carbon dioxide into the atmosphere (Attharangsan et al., 2012). It further contributes to the critical environmental situation when tires run on roads. The high rolling resistance of tires adds friction and causes engines to burn extra fuel, which leads in turn to more greenhouse gas emissions.

Indeed, the stock reduction of oil-based material and environmental issues so as the global warming phenomenon have inspired researchers to focus on the development of a green tire formulated from renewable resources (Thakur and Singha, 2010; Langan et al., 2011; Thakur et al., 2011). Recent trends in technology innovation for green tires incorporate a bio-filler to substitute carbon black. Several potential green fillers from new resources have attracted a great amount of attention from researchers, such as lignins, which are renewable, bio-degradable, inexpensive, light-weight, and abundant (Setua et al., 2000; Košíková and Gregorová, 2005; Bogoeva-Gaceva et al., 2007; Eichhorn et al., 2010; Mishra et al., 2012; Bajpai et al., 2013; Hussin et al., 2014).

Lignin is the second most abundant natural resource (Gosselink et al., 2004; Faruk et al., 2012; Kakroodi et al., 2013; Kazemi et al., 2013). It is an aromatic polymer (Lora and Glasser, 2002; Fitigau et al., 2013) that acts as a glue to hold cellulose and hemicellulose together in plants, to strengthen cell walls, and to protect plants against parasites and disease (Erdocia et al., 2014; Kakroodi et al., 2014; Lang et al., 2018). The complex structure of amorphous lignin is interestingly formed by the attachment of different functional groups such as methoxyl, phenolic, hydroxyl, and carbonyl groups. A huge amount of lignin by-product is produced by the paper and pulp industries, and about ∼98% of that is usually burned to generate energy or just disposed of in landfill, hence posing a major disposal problem (Mohan and Karthikeyan, 1997; Zhang and Chuang, 2001; Kumar et al., 2009; Doherty et al., 2011; Saake and Lehnen, 2012; Laurichesse and Avérous, 2014; Lang et al., 2018). Therefore, the development of new technologies is crucial to explore the functionality of this precious by-product further, not only for use in low- and medium-value applications but in high-value applications as well (Hämäläinen et al., 2018). Many applications that have been explored by researchers, for example, as adhesive (Gosselink et al., 2004), stabilizing agents (De Paoli and Furlan, 1985), reinforcing agents (Kumaran and De, 1978; Setua et al., 2000; Benko et al., 2014), superabsorbent hydrogels, and phenolic resin (Suhas et al., 2007; Kumar et al., 2009; Hu et al., 2011).

The main goal of this review is to focus on lignin-derived compounds as bio-renewable filler as well as the performance and properties of lignin-reinforced rubber composites. The overall characteristics of lignin-filled rubber composites with different methods of modification and mixing techniques of the lignin into rubber compound, which influences the properties of the lignin-filled rubber compound, are also discussed. Lastly, upcoming trends in lignin-reinforced rubber composites will be presented as the review's conclusion.

CONVENTIONAL CARBON BLACK IN RUBBER COMPOSITE

Rubber Composite
A wide variety of rubber compositions are used in the tire industry. The base elastomers that are commonly used consist of blends of natural rubber (NR), butadiene rubber (BR), styrene-butadiene rubber (SBR), ethylene-propylene-diene rubber (EPDM), and epoxidized natural rubber (ENR). Apparently, the utilization of rubber without filler does not provide good properties for any application. Therefore, filler is used to impart better properties to rubber products, with carbon black or silica used commercially. Other ingredients with different functionalities are also incorporated into rubber compounds depending on the application, i.e., softeners, vulcanizing agents, accelerators, activators, retarders, and anti-degradants. As is widely known, accelerators are used to increase the rate and density of cross-linking and are activated by an activator, while retarders are used to prevent rubber scorching and to delay the vulcanization process. Furthermore, anti-degradants are important for applications like tire production to prevent degradation by oxygen, ozone, heat, or other factors (Ignatz-Hoover et al., 2003; Datta et al., 2007).

Rubber Matrix
NR is the most common raw material used as the main component in tire manufacturing and possesses impressive characteristics such as green strength and tensile strength due to its spontaneous crystallization when exposed to strain. It is a unique biopolymer and is the best raw material for manufacturing tires for cars, trucks, and aircraft. Besides, NR is a unique material that has valuable properties that synthetic rubber lacks. Due to the rapid development of economies such as in those of China and India, the demand for NR is continuing to increase, and prices have become increasingly volatile (Beilen and Poirier, 2007; Soratana et al., 2017). Furthermore, with the spread of fungal disease harming rubber trees and the tendency of farmers to plant more profitable palm oil rather than rubber (Jawjit et al., 2010), the chances of natural rubber prices shooting up are high.

BR is the second-largest volume of synthetic rubber produced after SBR. This is commonly blended with NR in the sidewall and treads of tires. It has been found that its low glass transition temperature, Tg, results in exceptional abrasion resistance and low rolling resistance. Thus, a blend of NR/BR is the focus for tire applications incorporating ingredients such as carbon black, curatives, and a high concentration of anti-degradants

to provide weather resistance (Waddell, 1998; Hamed, 2012). The addition of SBR lowers the price and imparts good wear and bonding properties, as well as good heat aging properties and abrasion resistance. It also possesses a non-crystalline and non-polar character with a low gum tensile strength of about ~2 MPa (Chakraborty et al., 2009). Atashi and Shiva (2010) focused on optimizing the failure properties of passenger car tire tread compounds with combinations of NR, SBR, and BR. They modified the curing conditions and the behavior of the rubber matrixes. Hao et al. (2001) also found that the Mooney viscosity and scorch time of hybrid rubber SBR/NR composites showed improvement when they modified the curing conditions.

Besides, the dynamic conditions of a tire, especially the sidewall, which is easily attacked by ozone, give rise to a demand for life-extension by improving ozone and thermo-oxidative resistance. Blending EPDM with NR and BR has shown good potential for ozone resistance (Sahakaro et al., 2007). This is because the EPDM phase dispersed in rubber blends provides an internal anti-ozonant to highly unsaturated rubbers since it is an ozone-resistant polymer. The modification of NR with a random distribution of epoxy groups together with a polymer backbone forms ENR (Pire et al., 2011). The existence of these epoxy groups imparts ENR with miscibility with other polymers (Narathichat et al., 2012) or active fillers (Sengloyluan et al., 2014) through reactive compatibilization as they are reacted with nucleophilic reagents (Chang et al., 2007; Nguyen et al., 2012; Zhang et al., 2012).

Carbon Black as a Common Reinforcing Filler

Carbon black is ultrafine powder manufactured by the burning of hydrocarbons in a limited supply of air (Drogin, 1968; Huang, 2002). Aggregate size and shape and the number of particles per aggregate play important roles in the determination of the structure of carbon black. Carbon black with high branching contains many prime particles that are referred to as high-structure black, with stronger attractive forces between aggregates. This means that more energy is required in the process of dispersion to break the chain. High-structure black has the tendency to produce larger aggregate grains in contact, with smaller distances between aggregate grains. This attribute is important in achieving high electrical conductivity (Huang, 2002).

For tire manufacturing, carbon black is used extensively as the reinforcing filler. Several mechanical properties of tires are reinforced such as its modulus, tear strength, and wear characteristics (Khalil et al., 2007; Yu et al., 2016a). The usage of carbon black as a reinforcing filler, which started in the twentieth century, has produced a ten-fold increase in the service life of tires. This phenomenon is due to the strong interaction formed between the surface of carbon black and the rubber matrix (Brennan et al., 1964; Leblanc, 2002; Fukahori, 2003; Hoshikawa et al., 2016). The incorporation of carbon black has an important effect not only on the mechanical properties but also on the dynamic properties of the tires (Schaefer et al., 2000; ten Brinke, 2002; Hilonga et al., 2012). Aside from solely focusing on the strength of a tire, improvements of the tire's dimensional stability, conductive filler, ultraviolet light stabilizer, colorant, and antioxidant to extend the service lifetime of rubber are also

important (Huang, 2002). Since then, carbon black has continued to be used significantly in tires and also other rubber products as a reinforcing material, and up to 30% of rubber compounds involve the incorporation of carbon black (Sudin and Swamy, 2006; Siti Suhaily et al., 2013).

Eco-Toxicological Effect

Carbon black is an oil-based rubber reinforcing filler. Several types of carbon blacks are available with different characteristic properties. Incomplete combustion or thermal degradation through pyrolysis produce furnace and thermal blacks (Huang, 2002), which are mainly used in sectors such as rubber and polymer composites. The production process by the pyrolysis method using liquid or gas hydrocarbons emits carbon dioxide gas. Moreover, carbon black is harmful not only to the environment but also to humans, as it is proven to cause pulmonary inflammation through repeated inhalation in animal models (Morfeld et al., 2006). Furthermore, the millimeter size of carbon black in pellet form in industry is transformed into powder form once it is introduced into the mixer (Huang, 2002; Wang et al., 2003). The pellet form is only used for ease of transportation and handling of carbon black in the rubber industry. But then, reversion into the aggregated state may occur due to the shear forces that are applied during the mixing process, which breaks apart the agglomerates and produces particles ranging from 70 to 500 nm, potentially increasing the risk of exposure for workers (Basfar et al., 2002).

Currently, there are major issues associated with fossil fuel, such as global warming, increases in price, depletion, and the large dependence of carbon blacks on oil supplies, so that the world faces critical issues to ensure that it has enough energy and natural resources. With increasing prices and the demand to ensure a safe environment and healthy population, the carbon black utilized in tire manufacturing must be substituted with other eco-friendly and naturally based fillers (Ehrburger-Dolle et al., 1994; Snowdon et al., 2014). Therefore, the research community is continuing in its efforts to find the best solution to give better properties for a "green" composite. Many researchers are making efforts to develop an alternative material to substitute carbon black (Zafarmehrabian et al., 2012; Jiang et al., 2013).

GREEN TIRE TECHNOLOGY

The term "green tire" refers to entirely new types of tire that are built completely from sustainable material. It is also known as an "eco-friendly" tire, which does not pose a threat to the environment. As people are giving their attention and focus toward environmental protection, the utilization of various natural biomasses is being examined to replace carbon black as a filler in NR polymer matrix to produce greener tires. Three features are considered: fuel efficiency, wet grip, and noise. These green tires employ a special type of tightly bonded rubber in the tread blocks that enhances the physical and mechanical properties in terms of abrasion resistance and more energy being retained during driving. This means that a lower rolling resistance is established, and thus less engine power is needed for rotating the tires, which results in fuel efficiency in the automobile industry. Many researchers have explored

a sustainable material substitute for oil-based carbon black as the reinforcing filler to produce green tire composites (Guy et al., 2009; Hilonga et al., 2012; Hirayama and Saron, 2012; Zafarmehrabian et al., 2012; Siti Suhaily et al., 2013; Sarkawi et al., 2015).

In the early 1990s, Michelin introduced the "Green Tire" technology in the tire industry, which involved a full substitute of carbon black by silica as the reinforcing filler in passenger tire treads (Zafarmehrabian et al., 2012). However, the manufacturer faced major difficulties in the construction of the green tire due to the polar nature of silica, which is incompatible with the non-polar rubber matrix. Some researchers then discovered that organosilanes acted as an outstanding bonding material between silica and the rubber matrix (Park and Cho, 2003; Atashi and Shiva, 2010; Kaewsakul et al., 2014). Thus, silica/organosilane technology was developed to ensure that excellent performance was obtained from the green tire. This technology contributed to savings in automotive fuel, since it reduced rolling resistance by approximately 20% compared to a tire reinforced by carbon black (Hall and Moreland, 2001; Niedermeier et al., 2002; Hilonga et al., 2012; Sarkawi et al., 2015).

Other than Michelin, Goodyear and Bridgestone play a major role in tire manufacturing, as they are also investing in green technologies, specifically tire technology, and are expanding their market share in the tire industry. Based on a report published by Mathews (2018) from Tech Sci Research recently, they anticipated that domestic production of tires in the United States will be boosted by fuel-efficient tire technology, thus inducing a need to find alternative raw materials for use in tire manufacturing. Other than silica filler, another option has also been studied for replacing traditional rubber and chemical usage in the tire industry. In 2015, the company Evonik reported the development of a liquid polybutadiene that makes the silica/silane system more compatible with the rubber matrix of tires (Braum and Jacobi, 2017).

Alternative Renewable Rubber Matrix

Rubber trees (*Hevea brasiliensis*) are largely composed of poly (*cis*-1,4–isoprene) and mainly grow in vulnerable areas such as South East Asia and a small part of Africa. The demand for tires and the consumption of natural rubber are expected to increase in line with the increase in the global population and the expansion of the automobile industry. Hence, the carbon footprint is expected to become greater, contributing to global warming. Resource depletion is also a major issue. Even though the source for the synthesis of natural rubber is more than 2,000 plant species, only *H. brasiliensis* is used for commercial production (Mooibroek and Cornish, 2000; Cornish, 2017). Thus, alternative crops for natural rubber are important to sustain the natural rubber supply, its long-term productivity improvement, and best-in-class technology availability for natural rubber production (Cornish, 2017). A few species such as dandelions (e.g., *Taraxacum brevicorniculatum*) and guayule (*Parthenium argentatum*) are possible alternative rubber sources (Mooibroek and Cornish, 2000; Beilen and Poirier, 2007; Schmidt et al., 2010; Venkatachalam et al., 2013).

Russian Dandelion

The prospects of plants such as dandelion as an alternative natural rubber source look brighter because of its inherent natural rubber potential and its metabolic processes, which affect the rubber synthesis and became the focus of study with the aim of enhancing its annual productivity (Laibach et al., 2015). In the 1930s−1950s, Russian dandelion was cultivated as a domestic source of rubber in the Soviet Union. After World War II, it was cultivated to overcome a shortage of rubber in Europe. It is scientifically known as *T. brevicorniculatum* and is a member of the Asteraceae family. The plant has bright yellow flowers made of many tiny florets. Its roots contain 15 percent latex of a quality similar to that of the rubber tree, making it a viable alternative (Cheng, 1963). The latex containing the rubber and producing proteins contributes to the formation of long polyisoprene chains, which generates high elasticity, high tensile strength, and low-temperature flexibility, making it an ideal raw material for tire manufacturing (Venkatachalam et al., 2013). Dandelion also has the advantage of growing annually, unlike Hevea, which usually takes from seven to 10 years to produce latex, and this certainly helps to reduce the dependence on Hevea for rubber and makes dandelion cost-competitive as a natural rubber source. Continental have produced the first tires where the tread uses 100 percent dandelion natural rubber as a polymer. The biggest plans to manufacture consumer road tires made from dandelion-derived rubber will be realized in 5–10 years. It has been proven that durable tires produced from dandelion rubber can replace tires produced from Hevea, as its quality is comparable to that of traditional natural rubber. In some applications, dandelion rubber performs even better than traditional natural rubber; specifically, it provides good grip on wet surfaces.

Guayule

Guayule is an evergreen plant that can be found in the dry area of the south-west USA to the north of Mexico and, therefore, can be grown in environments different from natural rubber (*H. brasiliensis*) trees. Moreover, the rubber constituent it contains is very similar to that in natural rubber (*H. brasiliensis*) trees and it is able to produce a sufficient quantity of natural rubber for commercial rubber application (Benedict et al., 2008; Laibach et al., 2015). This is thus expected to become a valuable new source for tire-grade rubber in commercial applications. The cultivation of the guayule takes a shorter time than that of natural rubber trees; it takes about 3 years before the trees are ready for harvesting and processing to obtain natural rubber (Ray et al., 2005; Beilen and Poirier, 2007).

A part of Bridgestone's plan in its research is to optimize the natural rubber content in the guayule plant and evaluate its application in a broader range of tire types and rubber compounds (Ray et al., 2005; Soratana et al., 2017). In 2015, the Bridgestone group took an impressive step toward the expansion and diversification of renewable resources by producing the first tire made 100% from guayule-derived natural rubber. In order to reduce its environmental footprint, the company built similar passenger tires that use guayule natural rubber instead of natural rubber from Hevea in all of the tire's major natural
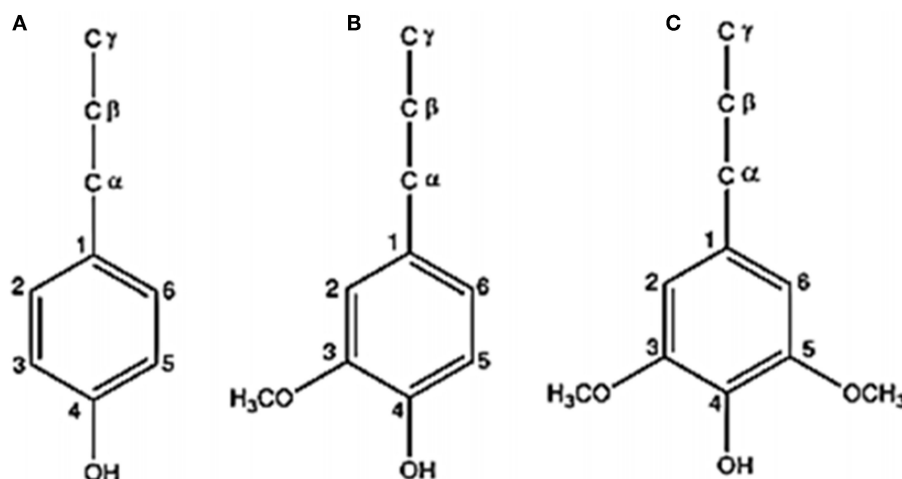
FIGURE 1 | Major phenylpropanoid units of lignin **(A)** *p*-caumaryl alcohol (*p*-hydroxylphenyl), **(B)** coniferyl alcohol (guaiacyl), and **(C)** sinapyl alcohol (syringyl) (this is reproduced with permission from Budapest University of Technology and Economics, Faculty of Mechanical Engineering, Department of Polymer Engineering; Jiang et al., 2013).

rubber components, including the tread, sidewall, and bead filler (Rasutis et al., 2015; Cornish, 2017).

LIGNIN AS AN ALTERNATIVE FILLER FOR RUBBER COMPOUNDS

Chemistry and Properties of Lignin

Lignin is the second most abundant renewable natural resource next to cellulose. It consists of three-dimensionally amorphous polymer chains, which play an important mechanical support role in the plant. This structure acts as a glue that holds the fibers together and a stiffening agent within the fibers (Thakur and Thakur, 2015). It imparts rigidity and impact strength to the cell walls in plants (Feldman, 2016) and protects them from harsh environmental conditions such as water, etc. (Teaca et al., 2013; Thakur and Thakur, 2015). Even though lignin is thermally stable as compared to cellulose and hemicellulose, by contrast, it is responsible for the ultraviolet (UV) biodegradation of the materials (Singha et al., 2009). The bonds between lignin and carbohydrate are covalent in nature and are composed of benzyl esters and phenyl glycol-sides (Doherty et al., 2011).

Lignin possesses a phenylpropanoid backbone along with phenolic and benzylic hydroxyl, methoxyl, and carbonyl substitutions (Gosselink et al., 2004; Jiang et al., 2013; Bahl et al., 2014a). The basic structural units of lignin are *p*-coumaryl alcohol (*p*-hydroxyphenyl, H), coniferyl alcohol (guaiacyl, G), and sinapyl alcohol (syringyl, S) (**Figure 1**). Lignin is generally available as a major byproduct from a number of industries such as in papermaking, ethanol production from biomass, etc., and is generally burned to recover energy-pulping chemicals or used in enzymatic or acid hydrolysis processes (Setua et al., 2000). Considerable efforts are now being made to effectively utilize waste lignin as one of the components of polymer matrices for high-performance composite applications (Watkins et al., 2014).

Furthermore, the abundant functional groups on its surface is one of the reasons why it is widely studied as a reinforcing filler of plastics and rubber. In this context, the functional groups provide the possibility for chemical modification to ensure compatibility with an appropriate matrix polymer (Frigerio, 2014). The common linkage to form a three-dimensional network structure is β-O-4, α-O-4, β-5, 5-5, 4-O-5, β-1, and β-β bonds, which link the basic structural units of lignin (Vainio et al., 2004). Typical softwood lignin is based generally on coniferyl alcohol units and is also called G lignin (Capanema et al., 2005; Dashtban et al., 2010). It is isolated through different types of delignification processes with different sources, but their structure is very similar and highly polydisperse. Moreover, another class is hardwood lignin, which contains a mixture of G and S units. The third type of monomeric unit, based on G, S, and H units, is found in other plants such as cereals, greases, and other non-woods (Suhas et al., 2007). The *p*-hydroxylphenyl type aromatic rings increase the reactivity due to the free positions at three and five, and thus, a large fraction of these groups is essential for the use of lignin in foam applications. Generally, lignin isolated from different resources has been reported to have molecular masses in the range of 1,000–20,000 g/mol (Doherty et al., 2011; Thakur et al., 2014).

The chemical structure and properties of lignin vary with the plant from which it is derived, either extracted as a byproduct or extracted directly from lignocellulosic materials (Thakur et al., 2014), as well as extraction method used (Watkins et al., 2014). Lignin offers great advantages such as high abundance, light weight, cost-competitiveness, biodegradability, and environmental friendliness. In view of it being insoluble in water (hydrophobic) and stable in nature, achieving efficient transportation of water and nutrition in the cells of plant (Nordstrom et al., 2013), and having an antioxidant, antimicrobial, and biodegradable nature, along with its CO_2 neutrality and reinforcing capability (Pouteau et al., 2003; Boeriu

et al., 2004; Doherty et al., 2011; Bertini et al., 2012) it is an excellent alternative for the development of innovative polymer composite materials (Frigerio, 2014; Watkins et al., 2014).

Lignin as a Natural Alternative Source

Due to their contribution to addressing economic and environmental challenges, there has been a noticeable increasing trend in the rigorous study of bio-based composites by researchers from industry and also academia. The study includes the production of rubber composites containing lignin. Lignin is included in rubber products to enhance their properties and also lower their prices (Kumaran and De, 1978; Botros et al., 2006; Feldman, 2016). However, previous studies of lignin-filled rubbers revealed the incompatibility of polar lignin and non-polar rubber (Setua et al., 2000; Kosikova et al., 2007; Barana et al., 2016). This has generated further study of the incorporation of lignin into the rubber matrix by using various mixing methods and modifications to achieve better performance.

The published literature on lignin in the rubber industry is highlighted in **Table 1**. The hydrophilicity behavior of lignin causes difficulties in terms of the dispersion of lignin in the rubber matrix as well as in the properties of the end rubber product. A lot of approaches have been taken by researchers to improve the process of rubber compound preparation and enhance the flexibility of the final composites (Vieira et al., 2011). One approach to utilize lignin for rubber application is by using simple blending with a rubber matrix (Shukla et al., 1998; Setua et al., 2000; Botros et al., 2006; Barana et al., 2016). However, such rubber compounds suffered from low compatibility and poor disperse-ability. Therefore, further research applied high-temperature dynamic heat treatment (HTDHT) to improve the dispersion of lignin and enhance the properties of the composite (Jiang et al., 2015). Based on various reports, the latex co-precipitation method has achieved excellent outcomes (Ouyang et al., 2009; Asrul et al., 2013; John et al., 2014; Yu et al., 2015, 2016a,b). The process is quite complicated but is a positive approach to enhance the distribution of lignin in the rubber matrix, which results in rubber composites with better mechanical properties. In addition, surface modification using a coupling agent and compatibilizer also has a large impact on the properties of the lignin-filled rubber composite.

Mixing Technique of Lignin Into Rubber Composites

The mixing method is one of the factors that determine the properties of a rubber compound. It may produce poor quality if an unsuitable method is chosen, as this may affect not only the rheological characteristics but also the mechanical and physical properties. This is because, with an unsuitable method, the rubber material does not blend evenly or the reinforcing process may not even be initiated. The main reasons for the incorporation of lignin into rubber compounds as a substitute for an oil-based filler are economical and environmental concerns. In addition, the improvement of properties including compatibility, stabilization, reinforcement, and cost-effectiveness (Botros et al., 2006; Feldman, 2016) is also important. Several mixing methods have been explored to develop the best product properties in

terms of mechanical and rheological characteristics. However, the addition of the dry powder form of lignin usually leads to severe coalescence of lignin particles and poor properties in the blends.

Conventional Milling

The used of a conventional two roll mill machine has been common in the rubber industry, especially for tire compounds, and is frequently adopted because of its availability. The properties of the compound depend highly on the skill of the operator and also the ingredients involved. Unfortunately, direct mixing of dry powder lignin into the rubber matrix shows little or almost no reinforcing effect, and the filler is considered to behave as inert (Barana et al., 2016). The reinforcing ability of lignin for rubber depends on two factors: the particle size of the lignin and the interfacial interactions between the lignin and the rubber matrix (Shukla et al., 1998; Botros et al., 2006; Jiang et al., 2015) due to the high content of hydroxyl groups in the lignin surface. The incompatibility obtained was due to a cavity forming around lignin agglomerates, resulting in poor interfacial adhesion and poor compatibility between lignin and rubber.

As an alternative, Jiang et al. (2015) prepared a rubber compound using a laboratory two roll mill in which the lignin was incorporated into ENR. Then, before the mixing process was initiated with other ingredients on the two roll mill, the rubber compounds went through a high-temperature dynamic heat treatment (HTDHT) procedure (180°C) using an internal mixer. The impact of using this method was that lignin was well-dispersed and exhibited great compatibility with ENR, forming a reactive compound. Thus, it is possible to maximize the reinforcing efficiency of lignin by this *in situ* dispersion and compatibilization strategy when a conventional sulfur-vulcanized system is applied. The success of this method was proven by FESEM photos, as shown in **Figure 2**, which clarifies the perfect lignin distribution.

Latex Co-precipitation

Forming a lignin-rubber compound via latex co-precipitation is a common method used besides other conventional mixing methods to incorporate lignin into rubber latex and form a rubber masterbatch. This method enhanced reinforcement ability and improved the properties of the compound (Košíková and Gregorová, 2005; Asrul et al., 2013; Yu et al., 2015). Previous studies have illustrated that lignin can reach the reinforcement level of carbon black or silica by the co-precipitation of rubber latex and alkaline solutions of lignin (Jiang et al., 2013, 2015). Košíková and Gregorová (2005) reported that the lignin samples act as an active filler in rubber compounds. This is because a positive value of the coefficient of activity, α_F, of 0.6631 was obtained and increased the reinforcing characteristic. Furthermore, latex co-precipitation method exhibited a good result, with homogenous distribution in the rubber compound and a finer particle size of lignin formed (Košíková and Gregorová, 2005; Jiang et al., 2013). This was proven by SEM photos, as shown in **Figure 3**. Furthermore, the flocculation and

TABLE 1 | Applications of lignin in the rubber industry.

	Type of lignin	Rubber type	Mixing method	Application	Finding	References
1	Lignin	NBR	Conventional mixing	Reinforcing filler; modified with hexamine	Better thermal stability of NBR compound than phenolic resin or carbon black	Shukla et al., 1998
2	Lignin	NBR	Conventional mixing	Reinforcing filler; addition of benzoyl peroxide	Other mechanical properties better than phenolic resin but inferior to carbon black. In contrast, showed better thermal stability than carbon black	Setua et al., 2000
3	Sulfur-free lignin	NR (SMR20)	Internal mixer at 70°C	Antioxidant filler	Possibility to replace commercial antioxidant at concentrations of 4–8 phr based on antioxidant activity. Hybrid of lignin/IPPD exhibited highest antioxidant efficiency	Gregorová et al., 2006
4	Thiolignin and soda lignin	NR	Conventional mixing	Filler—impact on thermal stability toward NR compound	Improved thermal stability; optimum thiolignin loading was 15–20 phr	Botros et al., 2006
5	Sulfur-free lignin	NR	Internal mixer at 70°C	Reinforcing filler	Lignin used as filler increased the resistance of NR vulcanizates to thermooxidative degradation in air	Kosikova et al., 2007
6	Alkali lignin	NR latex	Latex co-coagulating	Reinforcing filler	Improved oil resistance of rubber latex film and enhanced strength at loading between 10 and 12 wt.%	Asrul et al., 2013
7	Sulfate lignin	NR latex	Latex co-coagulating	Reinforcing filler—fabricate colloidal lignin-poly (diallyldimethylammonium chloride) (PDADMAC) complexes (LPCs) to form NR/lignin nanocomposites	LPCs homogenously distributed in NR matrix and improved mechanical properties, thermal, and thermo-oxidative stability of NR compound	Jiang et al., 2013
8	Sulfate lignin	SBR	Latex co-coagulating	Cationic lignin montmorillonite (CLM) as nanofiller	Higher co-coagulating rate of CLM as compared to unmodified lignin. Improved performance of composite with 10 phr of CLM	Yu et al., 2015
9	Lignin from Caryota fiber	NR latex	Latex co-coagulating	Reinforcing filler—extract with simple method and cheaper source	Improved main mechanical properties and abrasion resistance, with optimum loading 20–25 phr	John et al., 2014
10	Sulfate lignin	ENR	Conventional mixing and high-temperature dynamic heat treatment (HTDHT)	Reinforcing filler—using in-situ mixing method in rubber matrix	Lignin aggregated and immiscible with ENR matrix and improved performance of composite	Jiang et al., 2015
11	Sulfate lignin	SBR Latex	Co-coagulating latex	Reinforcing filler—form lignin-novalac epoxy resin	Good reinforcement properties and improved initial thermal stability of rubber composite	Yu et al., 2015
12	Alkali lignin [from bagasse resource]	NR	Latex co-coagulating—prepare lignin/NR compound; two roll mill—added lignin/NR compound with other ingredient	Reinforcing filler—hybrid filler of silica/lignin	Weaken the Payne effect and improve process-ability, anti-aging resistance, and anti-flex cracking. Exhibited optimal overall mechanical properties at 20 phr of lignin and 30 phr of silica	Yu et al., 2016a
13	Industrial sulfate lignin	NBR	Latex coagulating compounding (NBR/lignin) and other ingredients mixed by two roll mill method	Reinforce the rubber by lignin-epoxy resin networks	Lignin-epoxy resin improved oil resistance ability and mechanical performance, crosslinking density, and thermal stability of rubber composites	Yu et al., 2016b
14	Kraft pipe lignin	NR	Convective mixing; open two roll mill	Reinforcing filler with addition of glycerolysate as plasticizer	Superior tensile properties; highest hardness and abrasiveness for NR compound with 5 phr of lignin. SEM images proved a positive interaction between rubber chain and lignin particle	Datta et al., 2017

(Continued)

TABLE 1 | Continued

	Type of lignin	Rubber type	Mixing method	Application	Finding	References
15	Sulfur-free lignin [steam explosion process]	NR [STR 20] and SBR 1500	Mixed using Haake mixer	Reinforcing filler as partial replacements for carbon black	Low performance due to high amount of impurities [ash and polysaccharide] and polarized hydroxyl groups, which interfered with lignin–rubber interactions Modification of lignin by hexamethylenetetramine treatment slightly improved the properties	Frigerio et al., 2014
16	Kraft lignin and calcium lignosulphonate	SBR	Two-step mixing using brabender (1st step) and two roll mill (2nd step)	Hybrid reinforcing filler: carbon black/lignin	Both lignins capable of forming coating layers on CB particles that maintain the fractal nature of CB particles This made hybrid filler particles stiffer and contributed to a reduction of loss tangent values by 10%	Bahl et al., 2014a
17	Kraft lignin	SBR	Two-step mixing using brabender (91st step) and two roll mill (2nd step)	Hybrid filler/coupling agent (polybutadiene-g-pentafluorostyrene: Pb-g-PPFS) to replace KL/CB hybrid fillers	Presence of KL/Pb-g-PPFS increased the stiffness, reduced energy dissipation, and improved failure properties due to enhanced coupling between rubber and filler Tensile strength improved 10% as compared to KL/CB hybrid filler, but stiffness not much different	Bahl et al., 2014b
18	Soda grass lignin; softwood Kraft lignin; purified lignin; bio-ethanol wheat straw lignin; rice husk lignin by NaOH extraction	NR latex	Two approaches; co-precipitation and dry mixing by internal mixer	As antioxidant in rubber composite	Co-precipitation approaches gave effective homogenous distribution compared to dry mixing and improved the mechanical properties of NR compounds before aging Difference in phenolic content for 5 types of lignin observed: soda lignin showed higher OIT and good correlation between phenolics concentration, antioxidant activity, and molecular weight	Barana et al., 2016
19	Sodium sulfate	Nitrile rubber	Conventional two roll mill	As a plasticizer—replacing DOP partially and completely by lignin	Increased the viscosity with good tackiness and improved the curing characteristics and physical properties before and after aging at 10 phr of lignin	Jagadale et al., 2016
20	Alkali lignin	EPDM	Conventional two roll mill	Coupling agent	Presence of lignin in EPDM rubber improved adhesion—improved the mechanical properties and thermal stability	Xu et al., 2015
21	Kraft lignin	NBR	Conventional mixing using open two roll mill	Reinforcing agent—compared with CB and phenolic resin	NBR composites with three types of fillers showed good biodegradability Lignin filler gave better thermal stability in NBR composites, superior oil and fuel resistance of nitrile rubber, and higher modulus at 100% elongation, elongation at break, and tear strength than with neat NBR	Agarwal et al., 2014
22	Alkali lignin	NBR	Banbury mixer	As reinforcing filler substitute CB	Lignin/CB/NBR composites showed better performance than CB-filled rubber composite—presence of lignin resulted in high strength and modulus but maintained elasticity Thermal stability and high-temperature oil resistance of rubber composites also improved	Wang et al., 2018

filtration of lignin/rubber co-precipitates were extremely slow. This also seriously limits the development of lignin-based rubber composites.

Modification and Lignin-Based Application

The modification method is known as a method to increase the interfacial bonding strength between lignin and the rubber
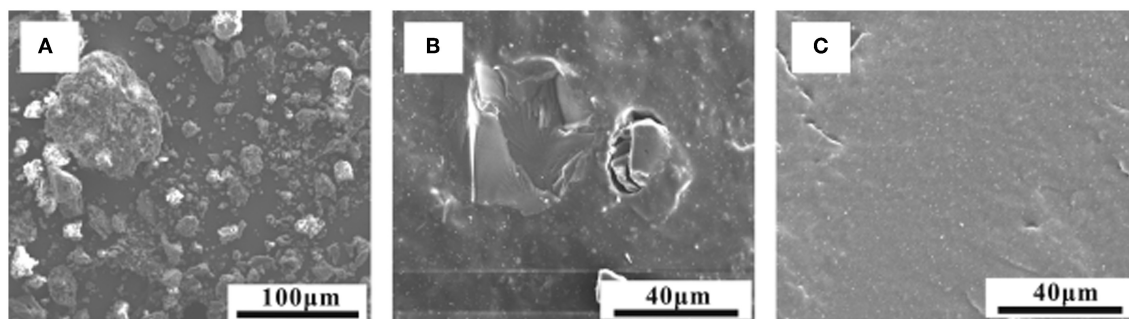
FIGURE 2 | FESEM photos of **(A)** lignin powder, **(B)** directly mixed, and **(C)** heat-treated lignin/ENR composites (this is reproduced with permission from John Wiley and Sons; Jiang et al., 2015).
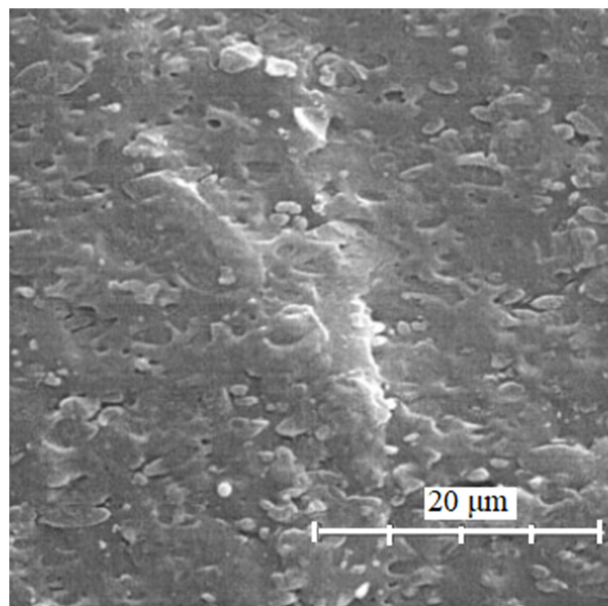
FIGURE 3 | SEM photo of SBR compound containing 50 phr of lignin as a reinforcing filler at a magnification of x5,000 (this is reproduced with permission from John Wiley and Sons; Košíková and Gregorová, 2005).

matrix. This is because the reinforcement effect of lignin is not as good as that of carbon black due to the poor dispersion ability of lignin in rubber and the poor interfacial adhesion between lignin and the rubber matrix. Chemical modification in rubber-based applications is generally carried out either through (1) chemical modification of the lignin surface, (2) the use of substitute chemicals or additives during mixing that contain functional groups that are capable of forming a bridge between lignin and rubber matrix, or (3) the rubber matrix being modified to achieve better compatibility and end-product properties. Researchers have tried many approaches to improve the reinforcement effect of lignin and rubber (Bahl et al., 2014a,b; Bova et al., 2016; Tran et al., 2016; Ikeda et al., 2017; Miao and Hamad, 2017) and have achieved various levels of success in enhancing the adhesion and dispersion of lignin in the rubber matrix, as has been reported in previous studies (Laurichesse and Avérous, 2014; Thakur et al., 2014).

Techniques using coupling agents and adhesion agents for improving interfacial bonding have also been reported (Bahl et al., 2014b; Wang et al., 2018). These approaches produced covalent bonds between the lignin and the rubber matrix, thus enhancing the interfacial bonding. Furthermore, the chemical modification aims to improve the compatibility between lignin filler and non-polar rubber matrices by surface modification of lignins such as with hexamethylenetetramine (Setua et al., 2000; Frigerio et al., 2014; Thakur et al., 2014; Jiang et al., 2015) and cyclohexylamine (Bahl and Jana, 2014). This treatment basically involves the reaction of lignin and formaldehyde and is reported to provide excellent abrasion resistance and enhancement of tire properties.

A recent new approach to enhancing the dispersion and compatibility of lignin in the rubber matrix was to introduce the construction of a dual crosslinking network. A dual crosslinking network consists of the covalent bonds formed between sulfur and carbon atoms in rubber and sacrificial non-covalent bonds formed among lignins and Zn^{2+} ions. The development of high-performance lignin-filled rubber was explored by adding Zn-based coordination bonds (Wang et al., 2018) and forming networks consisting of sulfur covalent bonds and the dynamic coordination of sacrificial bonds, as shown in **Figure 4**. The mechanism of sacrificial bonding provided the outstanding properties of a strong and tough rubber compound (Sun et al., 2012; Schmitt et al., 2015; Zhang et al., 2016; Wang et al., 2018).

In addition, fabricating nano-lignin and performing nano-scale distribution using colloidal lignin-Poly(diallyldimethylammonium chloride) (PDADMAC) complexes (LPCs) showed an enhancement of the reinforcement ability (Jiang et al., 2013) in NR/lignin nanocomposites, as shown in **Figure 5**. Lignin was viewed as an anionic polyelectrolyte (colloidal) when phenolic hydroxyl and carboxylic groups were ionized. As a result, LPCs were homogeneously distributed in the NR matrix, which resulted in improved mechanical properties and thermal and thermo-oxidative stability for the NR/LPC composites. Pillai and Renneckar (2009) and Yang et al. (2005) showed, through FTIR spectra, there was interaction between lignin units and PDADMAC chains.

FIGURE 4 | Schematic representation of a dual crosslinking network for lignin/carbon black/NBR composites [this is reproduced with permission from MDPI (Basels); Wang et al., 2018].
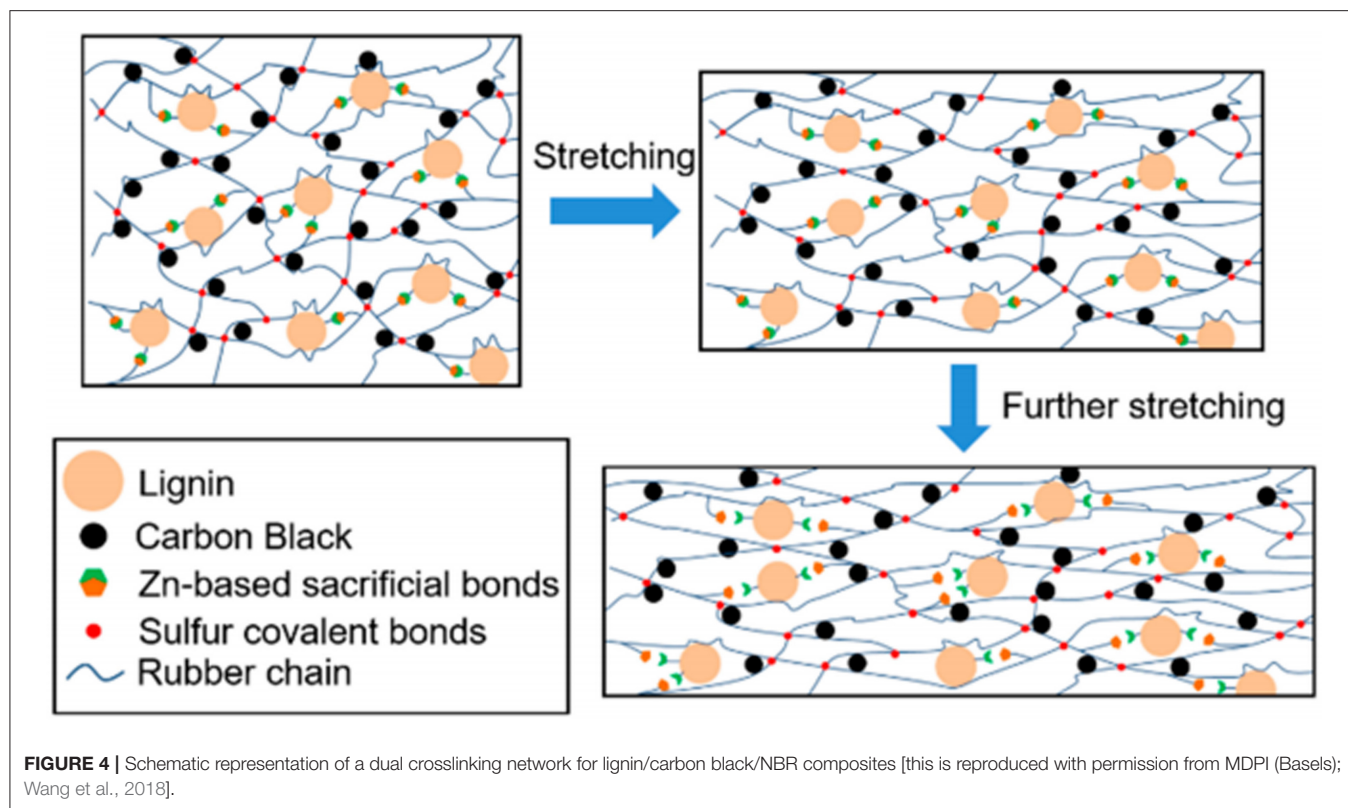
Another method suggested is to graft polymers onto lignin using controlled radical polymerization, and this method has shown advantages (Wang et al., 2011) over modified lignin. This approach improved the surface reactivity by converting phenolic or aliphatic hydroxyl group into new functionalized groups like ketone or aldehyde, hence enhancing the reinforcement characteristic compared to the crude version (Shukla et al., 1998). However, the grafting method also has high potential for modification, since it achieves comparable results to the co-precipitation mixing method but has a shorter process time.

Furthermore, chemical modification such as acetylation of hydroxyl groups has also been reported to achieve the same improvement in terms of compatibility and dispersion in the rubber matrix (Bertini et al., 2012; Barana et al., 2016). However, the reliability of phenolic hydroxyl groups must be safeguarded, as their modification results in the inhibition of antioxidant properties (Sadeghifar and Argyropoulos, 2015). Surface modifications have provided the external surface of lignin agglomerates with a better affinity toward the rubber matrix. In addition, the interaction of sodium lignosulfonates (SLS) with carbon nanotubes was studied by Liu et al. (2007). A similar study looked at the surface functionalization of MWNTs using Kraft lignin and its use in energy storage applications (Milczarek and Nowicki, 2013).

Moreover, researchers are also paying a lot of attention to hybrid technologies with carbon black (Bahl et al., 2014a), silica (Strzemiecka et al., 2016; Yu et al., 2016a), montmorillonite (Cao et al., 2013; Jiang et al., 2014), and layered double hydroxides

(LDHs) (Xiao et al., 2013). This technique mostly provides good reinforcing ability to the rubber compound. According to Bahl et al. (2014a), a hybrid filler between lignin and carbon black could lower the viscoelastic loss. Meanwhile, a lignin-montmorillonite hybrid filler was prepared by direct dehydration of the mixture of black liquor and montmorillonite and was used to reinforce acrylonitrile butadiene rubber (NBR) (Cao et al., 2013). However, this method is time-consuming and is not suitable for large-scale manufacturing. Furthermore, the modification of lignin in a rubber compound by using a hybrid method is unsatisfactory in terms of lignin dispersion and lignin–rubber interaction.

Reinforcement Studies of Lignin-Rubber Composites

The addition of reinforcing agents often changes the properties of a rubber composite. It not only improves the mechanical properties, such as toughness, but also influences the thermal properties. Many researchers have focused on different approaches, and some of them have used different accelerator systems (Kumaran and De, 1978) and different types of crosslink agents (Nando and De, 1980) to study the network structure involved in lignin-filled rubber composites in detail, hence evaluating the properties obtained.

Cure Properties
The effect of the substitution of carbon black with natural lignin has been studied in great depth by researchers. Gradual

FIGURE 5 | Schematic representation of the fabrication of nanolignin for the preparation of natural rubber (NR)/lignin nanocomposite (this is reproduced with permission from Budapest University of Technology and Economics, Faculty of Mechanical Engineering, Department of Polymer Engineering; Jiang et al., 2013).
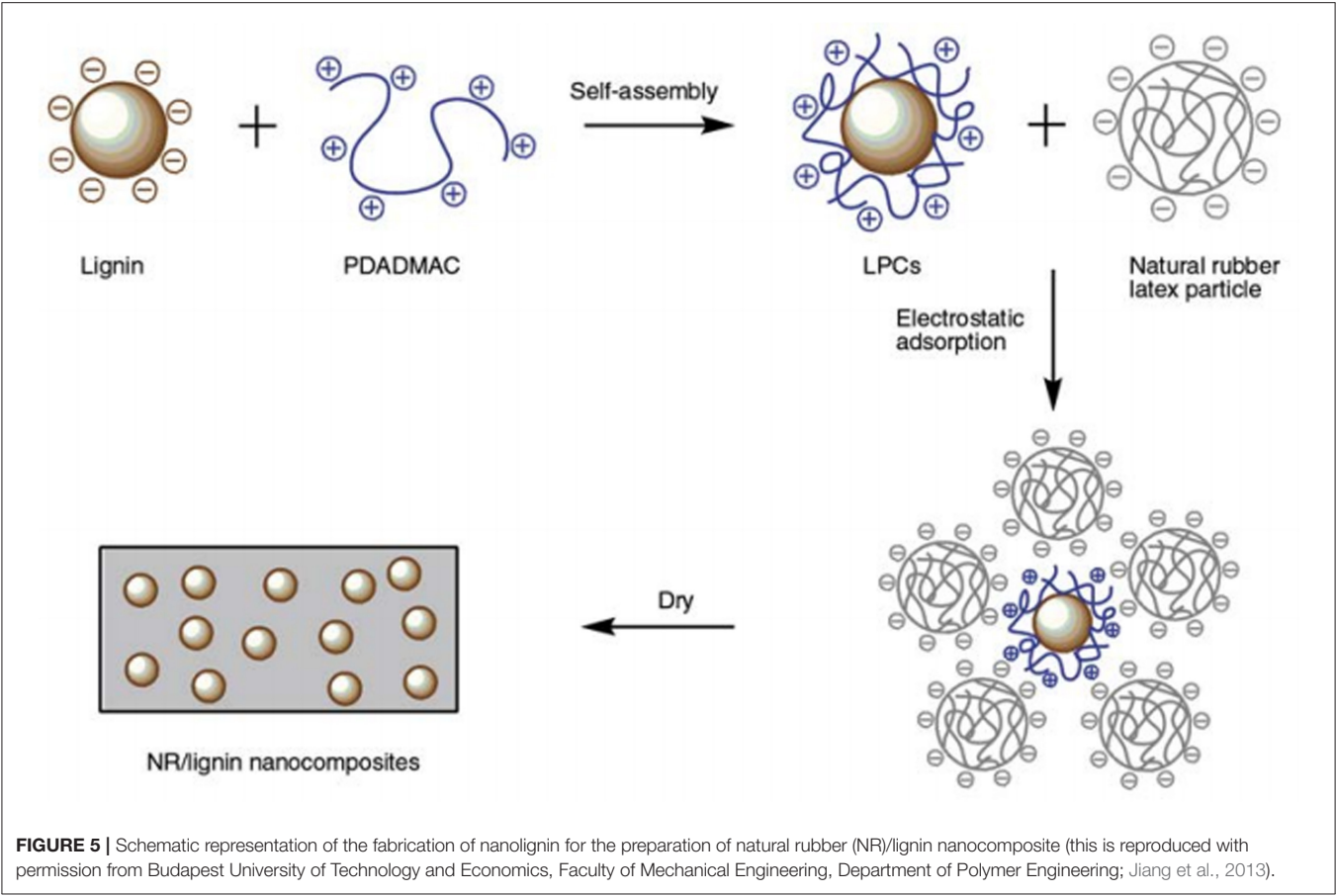
TABLE 2 | Comparison of mechanical properties with different formulations.

No.	Preparation method	Formulation	Tensile strength [MPa]	Elongation at break [%]	M300 [MPa]	Hardness [Shore A]	References
1	Nano-lignin and NR prepared by latex co-precipitation	L-0	25.24	654	2.00	38	Jiang et al., 2013
	Lignin-Poly(diallyldimethylammonium chloride) complexes (LPCs) fabricated via self-assembly technology	L-3	23.91	701	1.96	37	
		LPCs-3	27.51	715	2.25	40	
2	Softwood Kraft Lignin (SWK) mixed into NR by two different methods, namely co-precipitation, and dry mixing	NR (neat)	15.02	586	3.25	–	Barana et al., 2016
		NR/SWK	23.76	578	4.55	–	
		NR/SWK (dry mixing)	14.39	521	3.23	–	
3	Lignin/novolac epoxy resin (F51) incorporated in SBR by a combination of latex compounding and melt mixing	SBR/L-0/F51-0	2.2	339.7	1.9	40	Yu et al., 2015
		SBR/L-0/F51-10	3.0	382.3	2.7	37.9	
		SBR/L-50/F51-0	16.4	787.4	3.6	64	
		SBR/L-50/F51-10	23.2	681.6	6.7	70	

replacement of carbon black with lignin has increased the scorch and optimum cure time, t_{S2} and t_{90}, respectively, and reduced the curing rate index (CRI) and the crosslink density of the lignin-filled rubber composite. The inclusion of lignin into the rubber matrix delayed the vulcanization of rubber due to the effect of

radical scavenging by hindered phenol groups in lignin (Liu et al., 2013; Wang et al., 2018). Torque values were decreased by the presence of lignin, indicating worse interfacial adhesion between unmodified lignin and rubber matrix segments compared to solely carbon black (Wang et al., 2018). However, researchers
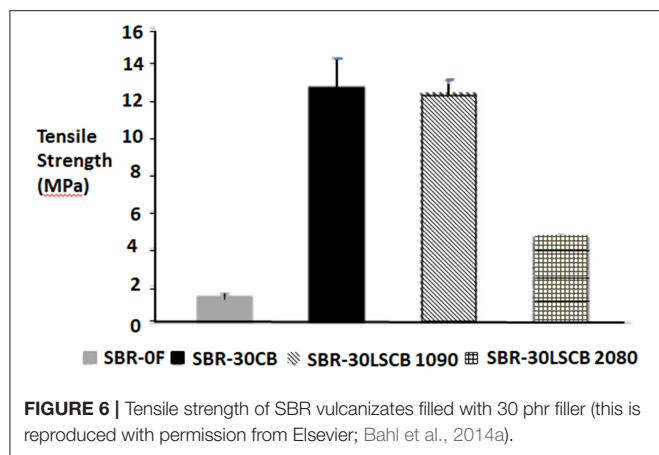
FIGURE 6 | Tensile strength of SBR vulcanizates filled with 30 phr filler (this is reproduced with permission from Elsevier; Bahl et al., 2014a).

TABLE 3 | Comparison of the thermal and thermo-oxidative decomposition for NR without lignin, NR/lignin, and NR/LPCs composites (this is reproduced with permission from Budapest University of Technology and Economics, Faculty of Mechanical Engineering, Department of Polymer Engineering; Jiang et al., 2013).

Sample Code	Thermal decomposition			Thermo-oxidative decomposition		
	$T_{5\%}$ [°C]	$T_{50\%}$ [°C]	T_{max} [°C]	$T_{5\%}$ [°C]	$T_{50\%}$ [°C]	T_{max} [°C]
Lignin-0 phr	283.5	375.1	370.0	289.2	372.8	358.8
Lignin-3 phr	310.7	385.4	381.0	294.3	379.6	368.6
LPCs-3 phr	312.0	390.7	386.5	288.6	373.9	372.5

reported that lignin was dispersed well in natural rubber and made the compound more scorch-resistant and improved the optimum cure time (Nando and De, 1980).

Curing behavior is also dependent on the curing system used. The distribution of different types of crosslinks is affected by the reversion time, and the inclusion of lignin showed that it actually takes part during the vulcanization process and that the mechanism is due to the thermal stability itself. Besides, the conventional vulcanization (CV) system delayed the optimum cure time, but the semi-efficient (semi-EV) and efficient vulcanization (EV) systems increased the cure rate (Nando and De, 1980; Shukla et al., 1998; Kakroodi and Sain, 2016). Nevertheless, some studies reported that the presence of lignin decreased the crosslink density and the number of polysulphidic crosslinks while maintaining the number of disulfidic and monosulfidic crosslinks (Kumaran and De, 1978; Kakroodi and Sain, 2016). They suggested that the incorporation of lignin in the rubber matrix masked some of the cross-linking sites on the rubber molecules. Normally, acidic functional groups in lignin particles should interrelate with the basic rubber components.

Mechanical Properties

In practice, the interaction of filler particles with one another does not constantly yield the expected and desired effects. Theoretically, the mechanical properties shown differently depend on the modification and formulation used, as summarized in **Table 2**. The properties show significant improvement compared to control samples. Hybrid fillers were reported by Wang et al. (2002) as the best way to gain the optimum balance of tire properties, particularly rolling resistance, wet traction, and wear resistance. The combination of lignin with montmorillonite (Cao et al., 2013; Jiang et al., 2014), layered double hydroxides (Xiao et al., 2013), and carbon black (Košíková and Gregorová, 2005; Xiao et al., 2013; Bahl et al., 2014a) as hybrid fillers in rubber composites resulted in higher tensile strength, thermal stability, and low rolling resistance. This was because the components of the hybrid filler worked together, with the lignin suppressing the formation of a filler network and, in return, the other fillers assisting in the dispersion of lignin in the rubber matrix. Despite this, time consumption is an issue in

the preparation of these lignin-based hybrid fillers. Moreover, the organic solvent used in this process is unfavorable for industrial production (Jiang et al., 2015).

The incorporation of lignin into the rubber matrix can prevent the loss of mechanical properties that arises due to oxidative degradation. Setua et al. (2000) reported that unmodified lignin showed poor tensile strength compared to DCP-modified lignin. The tensile strength at failure of vulcanized rubber reflected the true reinforcement behavior of the hybrid filler, as the tensile strength and elongation at break were the failure properties. The result obtained by Bahl et al. (2014a) for the tensile strength of the SBR-30/LS/CB compound with an LS:CB ratio by weight of 10:90 (30 phr) was closed to that of the compound of SBR-30/CB (30 phr). However, the tensile strength dropped dramatically for the hybrid filler compound with a 20:80 LS:CB weight ratio, as shown in **Figure 6**. This was due to strong interaction between lignin and carbon black, which resisted the breakage of the networks and prevented dispersion by shear forces during compounding. Furthermore, the incorporation of lignin improved the Young's modulus of the rubber compounds in the whole range of deformations without compromising elongation at break (Barana et al., 2016). This was due to the protection given by lignin against degradation processes in the rubber matrix during mixing with high mechanical and thermo-oxidative stresses. However, flex crack resistance could sometimes be improved even at lower cross-link density of the rubber, and there was also an increase in crack growth resistance due to the higher percentage of disulfidic crosslinks (Kakroodi and Sain, 2016).

Thermal Properties

The thermal stability of rubber composites was investigated through thermal decomposition, as displayed in **Table 3** (Jiang et al., 2013). Environmental stresses such as oxygen and heat led to undesirable chemical changes in polymers, such as loss of ductility, loss of surface quality, and changes in their molecular weights and structures (Kakroodi and Rodrigue, 2013; Kakroodi and Sain, 2016). The changes to rubber molecular weights were due to chain scission followed by cross-linking of the produced macro-radicals with unsaturated C=C double bonds. Furthermore, the formation and accumulation of small molecules such as H_2, carbon monoxide, carbon dioxide, and monomers can cause cracks and crazes in the rubber. Nevertheless, the inclusion of lignin into the natural rubber compound enhanced the thermal stability. The strong interaction among lignin and
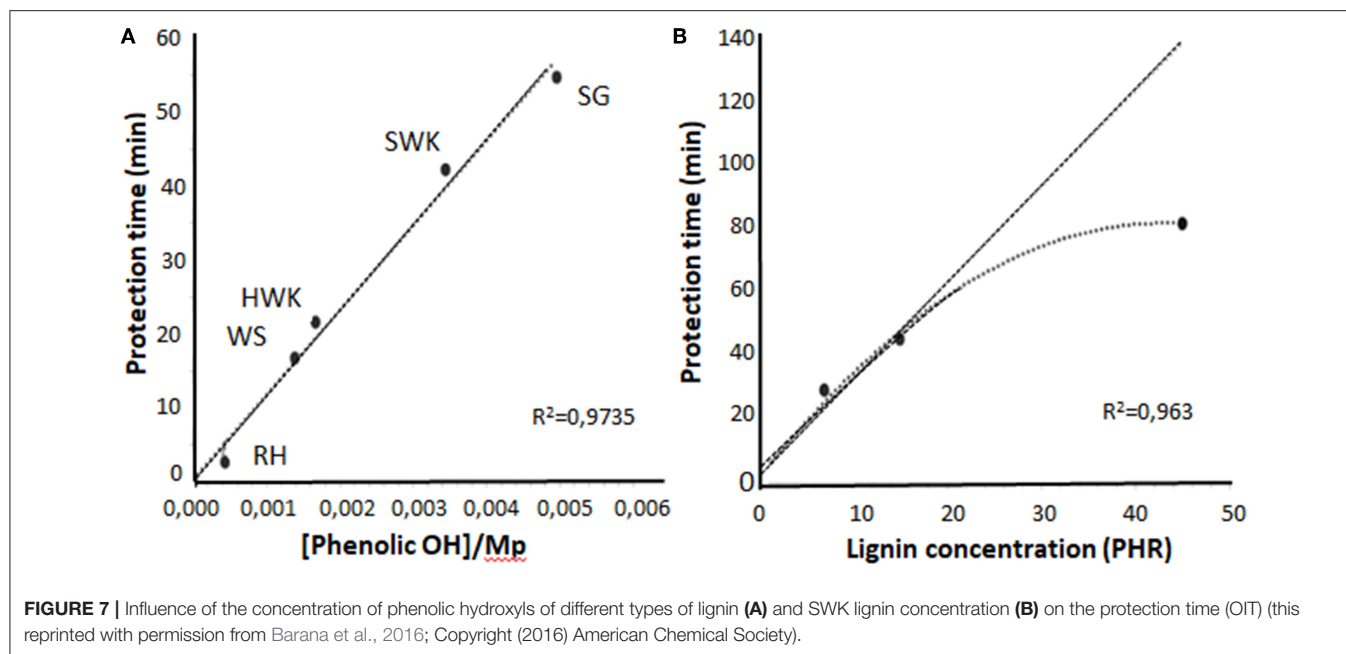
FIGURE 7 | Influence of the concentration of phenolic hydroxyls of different types of lignin **(A)** and SWK lignin concentration **(B)** on the protection time (OIT) (this reprinted with permission from Barana et al., 2016; Copyright (2016) American Chemical Society).

NR molecular chains provided various effects like branching, surface, and size effects (Peng et al., 2007; Jiang et al., 2013).

Furthermore, the hindered complex phenolic hydroxyls of lignin acted to improve and stabilize the reaction during thermal testing, which was initiated by oxygen and its radical types (Pouteau et al., 2003; Barana et al., 2016) as shown in **Figure 7**. Different types of lignin have different concentrations of phenolic hydroxyls that contribute to the stability of the polymer. Sometimes, the modification of lignin showed lower thermal stability as compared to unmodified lignin (Jiang et al., 2013). This might be due to the interaction within phenolic radical cations, as this would weaken the ability of phenolic hydroxyls to scavenge free radicals in lignin. Besides, lignin has been used to improve thermal properties, since it acts as a flame retardant and has good thermal insulating properties (Xing et al., 2013). In addition, the lignin gives protection to the rubber matrix against degradation processes during mixing at high mechanical and thermo-oxidative stresses.

Dynamic Mechanical Properties (DMA)

The dynamic mechanical behavior of a rubber compound is generally characterized using DMA testing and analysis. The storage modulus (E') and loss tangent (tan δ) against temperature have been analyzed to observe the influence of Kraft lignin on the thermomechanical properties of natural rubber composites. The storage modulus showed a positive correlation with the elastic modulus of rubber composites and was proportionate to the crosslink density (Geethamma et al., 2005; Cao et al., 2013; Yu et al., 2015). Meanwhile, the loss tangent is related to the energy dissipation as heat (Jiang et al., 2015). According to Datta and Parcheta (2017), the incorporation of Kraft lignin in natural rubber composites leads to a decrease in the stiffness and an increase in the damping capacity of the natural rubber matrix. The value of the storage modulus strongly decreased in the temperature range between −60 and −20°C, which is

related to the glass transition temperature, T_g, of the natural rubber matrix; this can be observed from the midpoint of the decreasing part of the curve approaching T_g. This is closely associated with the relaxation of the natural rubber chains. The cooperative motion of macromolecules induces the dissipation of energy at a temperature of the maximum tan δ. After −25°C, the curve characteristics are related to the remaining crystalline regions melting in the macromolecule chains from the natural rubber matrix.

However, Robertson and Rackaitis (2011) mentioned that the increment in storage modulus implied the characteristic of materials with higher stiffness, which should be associated with the addition of rigid lignin particles, enhancement of filler–rubber interactions, and the reinforcing nature of lignin on rubber materials. Increasing the lignin content in rubber composites shifted its tan δ peaks to higher temperatures and continually increased the T_g taken at the maximum value of tan δ peaks. This phenomenon can be clearly seen in case of the utilization of lignin in ENR rubber, in which the molecules of ENR are covalently bonded to lignin particles during the mixing process in the presence of high temperature. The bonds strongly restrict the mobility of the chain segments of ENR. Besides, the tan δ peak height significantly decreases with increasing lignin content. As reported earlier, the increase in the T_g of nanoparticle-filled polymer composite was generally <10°C, which indicates the uniform dispersion of lignin and changes in the network structure of lignin/ENR composites (Jiang et al., 2015).

Oil/Solvent Resistance Properties

Less attention has been given to the topic of oil resistance characteristics. However, the hydrophilic properties of lignin will give advantages to the rubber compound, improving its oil resistance characteristics (Asrul et al., 2013), and will have a good influence on the natural rubber compound, as it has
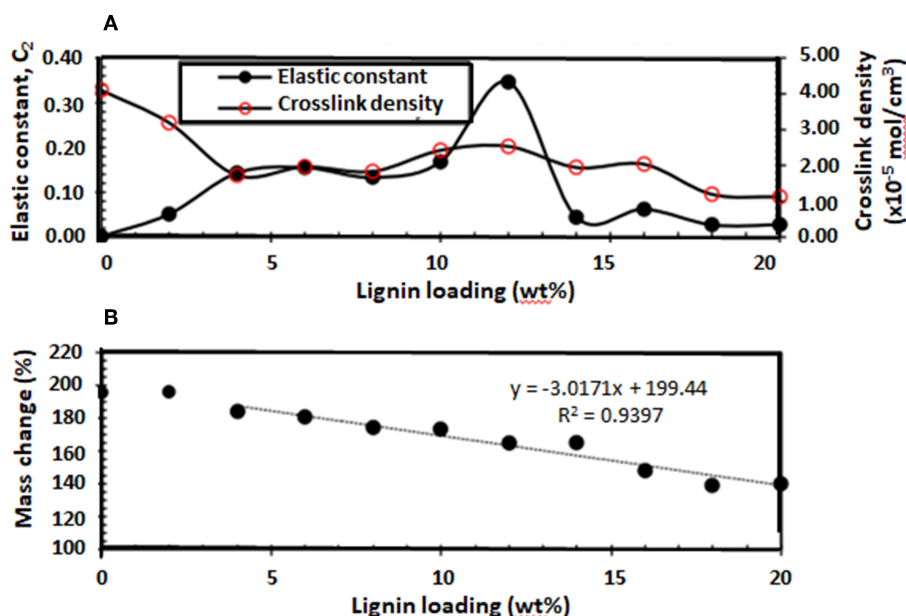
FIGURE 8 | Effect of lignin loadings on the **(A)** crosslink density and elastic constant, C_2, and **(B)** percentage mass change (this is reproduced with permission from Asrul et al., 2013).

low oil and solvent resistance. The degree of absorption also depends on the type of oil used. The presence of lignin, even in a small amount, in the rubber significantly reduced the adsorption level of a rubber compound, as reported by Asrul et al. (2013). This indicated the formation of chain entanglement from secondary bonding between lignin and rubber molecules (**Figure 8**), affecting the mass changes of the lignin-filled rubber sample. These characteristics impacted the properties of the rubber compound, which reduced the stiffness and strength of the compound as well as giving it poor chemical resistance and low dimensional stability. However, the opposite effect has been seen with a modified lignin-filled rubber compound, which had better swelling resistance, even higher than carbon black-filled rubber. This was highlighted by Setua et al. (2000), who showed that surface treatment increased the polarity of the lignin.

FUTURE PERSPECTIVES

Lignin has unique properties and has attracted many researchers to explore and determine its potential applications in a variety of industries. The delignification processes of lignin are well-documented, and many of its main properties have been reported. However, more studies are required on product commercialization and manufacturing processes for composites based on lignin. The main reason for this paper is to cause scientists and researchers to look at the potential of lignin as a reinforcing filler in the rubber industry as a substitute for carbon black due to the depletion of oil stock and the harm the latter brings to the environment. Many studies in recent years have focused on the utilization of lignin in synthetic rubber and less so in natural rubber. Incorporating a lignin particle into an unsaturated chain rubber matrix may have a toughening effect. Numerous experiments have been performed since the 1940s

to determine which mixing methods contribute good composite properties. Until now, simple and efficient ways to formulate lignin/rubber composites with excellent interfacial interaction and dispersion quality are yet to be found. However, we have here compiled and compared the best modification and mixing methods for lignin as a reinforcing filler or an additive to rubber compounds; this can now be used for future studies. The appropriate method will play an important role in providing optimized properties, especially for green tire applications.

AUTHOR CONTRIBUTIONS

NO, MH, KS, and NH contributed to the conception and revision of the manuscript. The manuscript was mainly written by NM and was edited by NO.

FUNDING

ACKNOWLEDGMENTS

REFERENCES

Agarwal, K., Prasad, M., Sharma, R. B., and Setua, D. K. (2014). Novel bio-degradable lignin reinforced NBR composites. *Int. J. Energy Eng.* 4, 47–62.

Asrul, M., Othman, M., Zakaria, M., and Fauzi, M. S. (2013). Lignin filled unvulcanisednatural rubber latex: effectsof lignin on oil resistance, tensile strength and morphology of rubber films. *Int. J. Eng. Sci. Invent.* 2, 38–43.

Atashi, H., and Shiva, M. (2010). Formulation for passenger tread tire compound based on styrene butadiene rubber/cis-butadiene rubber/natural rubber blend and semi-dispersible silica/carbon black filler system. *Asian J. Chem.* 22, 7519–7530.

Attharangsan, S., Ismail, H., Bakar, M. A., and Ismail, J. (2012). Carbon black (CB)/rice husk powder (RHP) hybrid filler-filled natural rubber composites: Effect of CB/RHP ratio on property of the composites. *Polym. Plast. Technol. Eng.* 51, 655–662. doi: 10.1080/03602559.2012.662256

Bahl, K., and Jana, S. C. (2014). Surface modification of lignosulfonates for reinforcement of styrene-butadiene rubber compounds. *J. Appl. Polym. Sci.* 131, 1–9. doi: 10.1002/app.40123

Bahl, K., Miyoshi, T., and Jana, S. C. (2014a). Hybrid fillers of lignin and carbon black for lowering of viscoelastic loss in rubber compounds. *Polymer* 55, 3825–3835. doi: 10.1016/j.polymer.2014.06.061

Bahl, K., Swanson, N., Pugh, C., and Jana, S. C. (2014b). Polybutadiene-g-polypentafluorostyrene as a coupling agent for lignin-filled rubber compounds. *Polymer* 55, 6754–6763. doi: 10.1016/j.polymer.2014.11.008

Bajpai, P. K., Meena, D., Vatsa, S., and Singh, I. (2013). Tensile behavior of nettle fiber composites exposed to various environments. *J. Nat. Fibers* 10, 244–256. doi: 10.1080/15440478.2013.791912

Barana, D., Ali, S. D., Salanti, A., Orlandi, M., Castellani, L., Hanel, T., et al. (2016). Influence of lignin features on thermal stability and mechanical properties of natural rubber compounds. *ACS Sustain. Chem. Eng.* 4, 5258–5267. doi: 10.1021/acssuschemeng.6b00774

Basfar, A. A., Abdel-Aziz, M. M., and Mofti, S. (2002). Influence of different curing systems on the physico-mechanical properties and stability of SBR and NR rubbers. *Radiat. Phys. Chem.* 63, 81–87. doi: 10.1016/S0969-806X(01)00486-8

Beilen, J. B., Van, and Poirier, Y. (2007). Guayule and russian dandelion as alternative sources of natural rubber. *Crit. Rev. Biotechnol.* 27, 217–231. doi: 10.1080/07388550701775927

Benedict, C. R., Greer, P. J., and Foster, M. A. (2008). The physiological and biochemical responses of guayule to the low temperature of the Chihuahuan Desert in the biosynthesis of rubber. *Ind. Crops Prod.* 27, 225–235. doi: 10.1016/j.indcrop.2007.09.003

Benko, D. A., Hahn, B. R., Cohen, M. P., Dirk, S. M., and Cicotte, K. N. (2014). *Functionalized lignin, Rubber Containing Functionalized Lignin and Products Containing Such Rubber Composition.* United States Patent No. 8664305B2, 6–12.

Bertini, F., Canetti, M., Cacciamani, A., Elegir, G., Orlandi, M., and Zoia, L. (2012). Effect of ligno-derivatives on thermal properties and degradation behavior of poly(3-hydroxybutyrate)-based biocomposites. *Polym. Degrad. Stab.* 97, 1979–1987. doi: 10.1016/j.polymdegradstab.2012.03.009

Boeriu, C. G., Bravo, D., Gosselink, R. J. A., and Van Dam, J. E. G. (2004). Characterisation of structure-dependent functional properties of lignin with infrared spectroscopy. *Industr. Crops Products* 20, 205–218. doi: 10.1016/j.indcrop.2004.04.022

Bogoeva-Gaceva, G., Avella, M., Malinconico, M., Buzarovska, A., Grozdanov, A., Gentile, G., et al. (2007). Natural fiber eco-composites. *Polym. Compos.* 28, 98–107. doi: 10.1002/pc.20270

Botros, S. H., Eid, M. A. M., and Nageeb, Z. A. (2006). Thermal stability and dielectric relaxation of natural rubber/soda lignin and natural rubber/thiolignin composites. *J. Appl. Polym. Sci.* 99, 2504–2511. doi: 10.1002/app.22865

Bova, T., Tran, C. D., Balakshin, M. Y., Chen, J., Capanema, E. A., and Naskar, A. K. (2016). An approach towards tailoring interfacial structures and properties of multiphase renewable thermoplastics from lignin–nitrile rubber. *Electron. Suppl. Mater. Green Chem.* 18, 5423–5437. doi: 10.1039/C6GC01067A

Braum, M. V., and Jacobi, M. A. M. (2017). Silica grafted with epoxidized liquid polybutadienes: its behavior as filler for tire tread compounds. *Rubber Chem. Technol.* 90, 173–194. doi: 10.5254/rct.16.83760

Brennan, J. J., Jermyn, T. E., and Boonstra, B. B. (1964). Carbon black–polymer interaction: a measure of reinforcement. *J. Appl. Polym. Sci.* 8, 2687–2706. doi: 10.1002/app.1964.070080615

Cao, Z., Liao, Z., Wang, X., Su, S., Feng, J., and Zhu, J. (2013). Preparation and properties of NBR composites filled with a novel black liquor – montmorillonite complex. *J. Appl. Polym. Sci.* 127, 3725–3730. doi: 10.1002/app.37984

Capanema, E. A., Balakshin, M. Y., and Kadla, J. F. (2005). Quantitative characterization of a hardwood milled wood lignin by nuclear magnetic resonance spectroscopy. *J. Agric. Food Chem.* 53, 9639–9649. doi: 10.1021/jf0515330

Chakraborty, S., Sengupta, R., Dasgupta, S., Mukhopadhyay, R., Bandyopadhyay, S., Joshi, M., et al. (2009). Synthesis and characterization of styrene butadiene rubber-bentonite clay nanocomposites. *Polym. Eng. Sci.* 49, 1279–1290. doi: 10.1002/pen.21367

Chang, Y.-W., Mishra, J. K., Cheong, J.-H., and Kim, D.-K. (2007). Thermomechanical properties and shape memory effect of epoxidized natural rubber crosslinked by 3-amino-1,2,4-triazole. *Polym. Int.* 56, 694–698. doi: 10.1002/pi.2203

Cheng, T.-H. (1963). Utilization of wild plants in communist China. *Econ. Bot.* 19, 3–15. doi: 10.1007/BF02971180

Cornish, K. (2017). Alternative natural rubber crops: why should we care? *Technol. Innov.* 18, 245–256. doi: 10.21300/18.4.2017.245

Dashtban, M., Schraft, H., Syed, T. A., and Qin, W. (2010). Fungal biodegradation and enzymatic modification of lignin. *Int. J. Biochem. Mol. Biol.* 1, 36–50.

Datta, J., and Parcheta, P. (2017). A comparative study on selective properties of Kraft lignin–natural rubber composites containing different plasticizers. *Iran. Polym. J.* 26, 453–466. doi: 10.1007/s13726-017-0534-0

Datta, J., Parcheta, P., and Surówka, J. (2017). Softwood-lignin/natural rubber composites containing novel plasticizing agent: preparation and characterization. *Ind. Crops Prod.* 95, 675–685. doi: 10.1016/j.indcrop.2016.11.036

Datta, R. N., Huntink, N. M., Datta, S., and Talma, A. G. (2007). Rubber vulcanizates degradation and stabilization. *Rubber Chem. Technol.* 80, 436–480. doi: 10.5254/1.3548174

De Paoli, M.-A., and Furlan, L. T. (1985). Sugar cane bagasse-lignin as photo-stabilizer for butadiene rubber. *Polym. Degrad. Stab.* 11, 327–337. doi: 10.1016/0141-3910(85)90036-9

Doherty, W. O. S., Mousavioun, P., and Fellows, C. M. (2011). Value-adding to cellulosic ethanol: lignin polymers. *Ind. Crops Prod.* 33, 259–276. doi: 10.1016/j.indcrop.2010.10.022

Drogin, I. (1968). Carbon black. *J. Air Pollut. Control Assoc.* 18, 216–228. doi: 10.1080/00022470.1968.10469118

Ehrburger-Dolle, F., Lahaye, J., and Misono, S. (1994). Percolation in carbon black powders. *Carbon N. Y.* 32, 1363–1368. doi: 10.1016/0008-6223(94)90123-6

Eichhorn, S. J., Dufresne, A., Aranguren, M., Marcovich, N. E., Capadona, J. R., Rowan, S. J., et al. (2010). Review: current international research into cellulose nanofibres and nanocomposites. *J. Mater. Sci.* 45, 1–33. doi: 10.1007/s10853-009-3874-0

Erdocia, X., Prado, R., Corcuera, M. Á., and Labidi, J. (2014). Influence of reaction conditions on lignin hydrothermal treatment. *Front. Energy Res.* 2:13. doi: 10.3389/fenrg.2014.00013

Faruk, O., Bledzki, A. K., Fink, H. P., and Sain, M. (2012). Biocomposites reinforced with natural fibers: 2000-2010. *Prog. Polym. Sci.* 37, 1552–1596. doi: 10.1016/j.progpolymsci.2012.04.003

Feldman, D. (2016). Lignin nanocomposites. *J. Macromol. Sci. Part A Pure Appl. Chem.* 53, 382–387. doi: 10.1080/10601325.2016.1166006

Fitigau, I. F., Peter, F., and Boeriu, C. G. (2013). Oxidative polymerization of lignins by laccase in water-acetone mixture. *Acta Biochim. Pol.* 60, 817–822. doi: 10.18388/abp.2013_2065

Frigerio, P. (2014). *Biopolymers in Elastomers: Lignins as Biofiller for Tyre Compound.* Ph.D. thesis, University of Milano Bicacco, Italy.

Frigerio, P., Zoia, L., Orlandi, M., Hanel, T., and Castellani, L. (2014). Application of sulphur-free lignins as a filler for elastomers: effect of hexamethylenetetramine treatment. *BioResources* 9, 1387–1400. doi: 10.15376/biores.9.1.1387-1400

Fukahori, Y. (2003). The mechanics and mechanism of the carbon black reinforcement of elastomers. *Rubber Chem. Technol.* 76, 548–566. doi: 10.5254/1.3547760

Geethamma, V. G., Kalaprasad, G., Groeninckx, G., and Thomas, S. (2005). Dynamic mechanical behavior of short coir fiber reinforced natural rubber composites. *Compos. Part A Appl. Sci. Manuf.* 36, 1499–1506. doi: 10.1016/j.compositesa.2005.03.004

Gosselink, R. J. A., Abächerli, A., Semke, H., Malherbe, R., Käuper, P., Nadif, A., et al. (2004). Analytical protocols for characterisation of sulphur-free lignin. *Ind. Crops Prod.* 19, 271–281. doi: 10.1016/j.indcrop.2003.10.008

Gregorová, A., Košíková, B., and Moravčík, R. (2006). Stabilization effect of lignin in natural rubber. *Polym. Degrad. Stab.* 91, 229–233. doi: 10.1016/j.polymdegradstab.2005.05.009

Guy, L., Daudey, S., Cochet, P., and Bomal, Y. (2009). New insights in the dynamic properties of precipitated silica filled rubber using a new high surface silica. *Raw Mater. Appl.* 62, 383–391.

Hall, D. E., and Moreland, J. C. (2001). Fundamentals of rolling resistance. *Rubber Chem. Technol.* 74, 525–539. doi: 10.5254/1.3547650

Hämäläinen, V., Grönroos, T., Suonp,ää, A., Heikkil,ä, M. W., Romein, B., Ihalainen, P., et al. (2018). Enzymatic processes to unlock the lignin value. *Front. Bioeng. Biotechnol.* 6:20. doi: 10.3389/fbioe.2018.00020

Hamed, G. R. (2012). "Materials and compounds," in *Engineering with Rubber*, 11–36. doi: 10.3139/9783446428713.002

Hao, P. T., Ismail, H., and Hashim, A. S. (2001). Study of two types of styrene butadiene rubber in tire tread compounds. *Polymer Test.* 20, 539–544. doi: 10.1016/S0142-9418(00)00073-8

Hilonga, A., Kim, J., Sarawade, P. B., Quang, D. V., Shao, G. N., Elineema, G., et al. (2012). Synthesis of mesoporous silica with superior properties suitable for green tire. *J. Ind. Eng. Chem.* 18, 1841–1844. doi: 10.1016/j.jiec.2012.04.015

Hirayama, D., and Saron, C. (2012). Chemical modifications in styrene-butadiene rubber after microwave devulcanization. *Ind. Eng. Chem. Res.* 51, 3975–3980. doi: 10.1021/ie202077g

Hoshikawa, Y., An, B., Kashihara, S., Ishii, T., Ando, M., Fujisawa, S., et al. (2016). Analysis of the interaction between rubber polymer and carbon black surfaces by efficient removal of physisorbed polymer from carbon-rubber composites. *Carbon N. Y.* 99, 148–156. doi: 10.1016/j.carbon.2015.12.003

Hu, L., Pan, H., Zhou, Y., and Zhang, M. (2011). Methods to improve lignin's reactivity as a phenol substitute and as replacement for other phenolic. *Bioresources* 6, 3515–3525. doi: 10.15376/biores.6.3.3515-3525

Huang, J. C. (2002). Carbon black filled conducting polymers and polymer blends. *Adv. Polym. Technol.* 21, 299–313. doi: 10.1002/adv.10025

Hussin, M. H., Rahim, A. A., Mohamad Ibrahim, M., Perrin, D., Yemloul, M., and Brosse, N. (2014). Impact of catalytic oil palm fronds (OPF) pulping on organosolv lignin properties. *Polym. Degrad. Stab.* 109, 33–39. doi: 10.1016/j.polymdegradstab.2014.06.016

Ignatz-Hoover, F., To, B. H., Datta, R. N., De Hoog, A. J., Huntink, N. M., and Talma, A. G. (2003). Chemical additives migration in rubber. *Rubber Chem. Technol.* 76, 747–768. doi: 10.5254/1.3547765

Ikeda, Y., Junkong, P., Yokohama, H., Kitano, R., Phakkeeree, T., Kato, A., et al. (2017). Reinforcing biofiller "Lignin" for high performance green natural rubber nanocomposites. *RSC Adv.* 7, 5222–5231. doi: 10.1039/C6RA26359C

Jagadale, S. C., Chavan, R. P., Rajkumar, K., Shinde, D. N., and Patil, C. L. (2016). Lignin as a plasticizer in nitrile rubber, it's effect on properties. *Int. J. Res. Eng. Appl. Sci.* 6, 78–84.

Jawjit, W., Kroeze, C., and Rattanapan, S. (2010). Greenhouse gas emissions from rubber industry in Thailand. *J. Clean. Prod.* 18, 403–411. doi: 10.1016/j.jclepro.2009.12.003

Jiang, C., He, H., Jiang, H., Ma, L., and Jia, D. M. (2013). Nano-lignin filled natural rubber composites: preparation and characterization. *Express Polym. Lett.* 7, 480–493. doi: 10.3144/expresspolymlett.2013.44

Jiang, C., He, H., Yao, X., Yu, P., Zhou, L., and Jia, D. (2015). *In situ* dispersion and compatibilization of lignin/epoxidized natural rubber composites: Reactivity, morphology and property. *J. Appl. Polym. Sci.* 132, 1–10. doi: 10.1002/app.42044

Jiang, C., He, H., Yu, P., Wang, D. K., Zhou, L., and Jia, D. M. (2014). Plane-interface-induced lignin-based nanosheets and its reinforcing

effect on styrene-butadiene rubber. *Express Polym. Lett.* 8, 619–634. doi: 10.3144/expresspolymlett.2014.66

John, S., Issac, J. M., and Alex, R. (2014). Mechanical properties of natural rubber composites reinforced with lignin from Caryota fibre. *Int. J. Emerg. Technol. Adv. Eng.* 4, 567–570.

Kaewsakul, B. W., Sahakaro, K., and Dierkes, W. K. (2014). "Flocculation kinetics and filler-rubber interaction *in silica*-reinforced natural rubber compounds," in *Presented at the Fall 186th Technical Meeting* of Rubber Division (Nashville, TN: ACS), 1–20.

Kakroodi, A. R., Cheng, S., Sain, M., and Asiri, A. (2014). Mechanical, thermal, and morphological properties of nanocomposites based on polyvinyl alcohol and cellulose nanofiber from *Aloe vera* rind. *J. Nanomater.* 2014:903498. doi: 10.1155/2014/903498

Kakroodi, A. R., Kazemi, Y., and Rodrigue, D. (2013). Mechanical, rheological, morphological and water absorption properties of maleated polyethylene/hemp composites: effect of ground tire rubber addition. *Compos. Part B Eng.* 51, 337–344. doi: 10.1016/j.compositesb.2013.03.032

Kakroodi, A. R., and Rodrigue, D. (2013). Degradation behavior of maleated polyethylene/ground tire rubber thermoplastic elastomers with and without stabilizers. *Polym. Degrad. Stab.* 98, 2184–2192. doi: 10.1016/j.polymdegradstab.2013.08.017

Kakroodi, A. R., and Sain, M. (2016). "Lignin-reinforced rubber composites," in *Lignin in Polymer Composites*, eds O. Faruk and M. Sain (Waltham, MA: Mathew Deans), 195–206. doi: 10.1002/marc.201900059

Kazemi, Y., Cloutier, A., and Rodrigue, D. (2013). Mechanical and morphological properties of wood plastic composites based on municipal plastic waste. *Polym. Compos.* 34, 487–493. doi: 10.1002/pc.22442

Khalil, H. P. S. A., Noriman, N. Z., Ahmad, M. N., Ratnam, M. M., and Fuaad, N. A. N. (2007). Polyester composites filled carbon black and activated carbon from bamboo (gigantochloa scortechinii): physical and mechanical properties. *J. Reinf. Plast. Compos.* 26, 305–320. doi: 10.1177/0731684407065066

Košíková, B., and Gregorová, A. (2005). Sulfur-free lignin as reinforcing component of styrene-butadiene rubber. *J. Appl. Polym. Sci.* 97, 924–929. doi: 10.1002/app.21448

Kosikova, B., Gregorova, A., Osvald, A., and Krajcovicova, J. (2007). Role of lignin filler in stabilization of natural rubber-based composites. *J. Appl. Polym. Sci.* 103, 1226–1231. doi: 10.1002/app.24530

Kumar, M. N. S., Mohanty, A. K., Erickson, L., and Misra, M. (2009). Lignin and its applications with polymers. *J. Biobased Mater. Bioenergy* 3, 1–24. doi: 10.1166/jbmb.2009.1001

Kumaran, M. G., and De, S. K. (1978). Utilization of lignins in rubber compounding. *J. Appl. Polym. Sci.* 22, 1885–1893. doi: 10.1002/app.1978.070220711

Laibach, N., Hillebrand, A., Twyman, R. M., Prufer, D., and Gronover, C. S. (2015). Identification of a *Taraxacum brevicorniculatum* rubber elongation factor protein that is localized on rubber particles and promotes rubber biosynthesis. *Plant J.* 82, 609–620. doi: 10.1111/tpj.12836

Lang, J. M., Shrestha, U. M., and Dadmun, M. (2018). The effect of plant source on the properties of lignin-based polyurethanes. *Front. Energy Res.* 6:4. doi: 10.3389/fenrg.2018.00004

Langan, P., Gnanakaran, S., Rector, K. D., Pawley, N., Fox, D. T., Cho, D. W., et al. (2011). Exploring new strategies for cellulosic biofuels production. *Energy Environ. Sci.* 4, 3820–3833. doi: 10.1039/c1ee01268a

Laurichesse, S., and Avérous, L. (2014). Chemical modification of lignins: towards biobased polymers. *Prog. Polym. Sci.* 39, 1266–1290. doi: 10.1016/j.progpolymsci.2013.11.004

Leblanc, J. L. (2002). Rubber-filler interactions and rheological properties in filled compounds. *Prog. Polym. Sci.* 27, 627–687. doi: 10.1016/S0079-6700(01)00040-5

Liu, J., Liu, H., Deng, L., Liao, B., and Guo, Q. (2013). Improving aging resistance and mechanical properties of waterborne polyurethanes modified by lignin amines. *J. Appl. Polym. Sci.* 130, 1736–1742. doi: 10.1002/app.39267

Liu, Y., Gao, L., and Sun, J. (2007). Noncovalent functionalization of carbon nanotubes with sodium lignosulfonate and subsequent quantum dot decoration. *J. Phys. Chem. C* 111, 1223–1229. doi: 10.1021/jp066018z

Lora, J. H., and Glasser, W. G. (2002). Recent industrial applications of lignin: a sustainable alternative to nonrenewable materials. *J. Polym. Environ.* 10, 39–48. doi: 10.1023/A:1021070006895

Mathews, K. (2018). *Fuel Efficient Green Tyre Technology to Roll the Tyre Industry in United States*. Press Release, Tech Sci Research, New York, NY.

Medalia, A. I., and Kraus, G. (1994). "Reinforcement of elastomers by particulate fillers," in *Science and Technology of Rubber* (Newton, MA: Academic Press), 387–418. doi: 10.1016/B978-0-08-051667-7.50013-5

Miao, C., and Hamad, W. Y. (2017). Controlling lignin particle size for polymer blend applications. *J. Appl. Polym. Sci.* 134, 1–10. doi: 10.1002/app.44669

Milczarek, G., and Nowicki, M. (2013). Carbon nanotubes/kraft lignin composite: characterization and charge storage properties. *Mater. Res. Bull.* 48, 4032–4038. doi: 10.1016/j.materresbull.2013.06.022

Mishra, S., Usha Rani, G., and Sen, G. (2012). Microwave initiated synthesis and application of polyacrylic acid grafted carboxymethyl cellulose. *Carbohydr. Polym.* 87, 2255–2262. doi: 10.1016/j.carbpol.2011.10.057

Mohan, S. V., and Karthikeyan, J. (1997). Removal of lignin and tannin colour from aqueous solution by adsorption onto activated charcoal. *J. Environ. Pollut.* 97, 183–187. doi: 10.1016/s0269-7491(97)00025-0

Mooibroek, H., and Cornish, K. (2000). Alternative sources of natural rubber. *Appl. Microbiol. Biotechnol.* 53, 355–65. doi: 10.1007/s002530051627

Morfeld, P., Büchte, S. F., Wellmann, J., McCunney, R. J., and Piekarski, C. (2006). Lung cancer mortality and carbon black exposure: Cox regression analysis of a cohort from a German carbon black production plant. *J. Occup. Environ. Med.* 48, 1230–1241. doi: 10.1097/01.jom.0000215282.23531.b9

Nando, G. B., and De, S. K. (1980). Effect of lignin on the network structure and properties of natural rubber mixes vulcanized by conventional, semiefficient and efficient vulcanization systems. *J. Appl. Polym. Sci.* 25, 1249–1252. doi: 10.1002/app.1980.070250625

Narathichat, M., Kummerlowe, C., Vennemann, N., Sahakaro, K., and Nakason, C. (2012). Influence of epoxide level and reactive blending on properties of epoxidized natural rubber and nylon-12 blends. *Adv. Polym. Technol.* 31, 118–129. doi: 10.1002/adv.20243

Nguyen, T. H., Tangboriboonrat, P., Rattanasom, N., Petchsuk, A., Opaprakasit, M., Thammawong, C., et al. (2012). Polylactic acid/ethylene glycol triblock copolymer as novel crosslinker for epoxidized natural rubber. *J. Appl. Polym. Sci.* 124, 164–174. doi: 10.1002/app.35088

Niedermeier, W., Frohlich, J., and Lugisland, H. D. (2002). Reinforcement mechanism in the rubber matrix by active fillers. *Raw Mater. Appl.* 55, 356–366.

Nordstrom, Y., Norberg, I., Sjoholm, E., and Drougge, R. (2013). A new softening agent for melt spinning of softwood kraft lignin. *J. Appl. Polym. Sci.* 129, 1274–1279. doi: 10.1002/app.38795

Ouyang, X., Ke, L., Qiu, X., Guo, Y., and Pang, Y. (2009). Sulfonation of alkali lignin and its potential use in dispersant for cement. *J. Dispers. Sci. Technol.* 30, 1–6. doi: 10.1080/01932690802473560

Park, S., and Cho, K. (2003). Filler – elastomer interactions : influence of silane coupling agent on crosslink density and thermal stability of silica / rubber composites. *J. Colloid Interface Sci.* 267, 86–91. doi: 10.1016/s0021-9797(03)00132-2

Peng, Z., Kong, L. X., Li, S. D., Chen, Y., and Huang, M. F. (2007). Self-assembled natural rubber/silica nanocomposites: its preparation and characterization. *Compos. Sci. Technol.* 67, 3130–3139. doi: 10.1016/j.compscitech.2007.04.016

Pillai, K. V., and Renneckar, S. (2009). Cation-π interactions as a mechanism in technical lignin adsorption to cationic surfaces. *Biomacromolecules* 10, 798–804. doi: 10.1021/bm801284y

Pire, M., Norvez, S., Iliopoulos, I., Le Rossignol, B., and Leibler, L. (2011). Imidazole-promoted acceleration of crosslinking in epoxidized natural rubber/dicarboxylic acid blends. *Polymer* 52, 5243–5249. doi: 10.1016/j.polymer.2011.09.032

Pouteau, C., Dole, P., Cathala, B., Averous, L., and Boquillon, N. (2003). Antioxidant properties of lignin in polypropylene. *Polym. Degrad. Stab.* 81, 9–18. doi: 10.1016/S0141-3910(03)00057-0

Rasutis, D., Soratana, K., McMahan, C., and Landis, A. E. (2015). A sustainability review of domestic rubber from the guayule plant. *Ind. Crops Prod.* 70, 383–394. doi: 10.1016/j.indcrop.2015.03.042

Ray, D. T., Coffelt, T. A., and Dierig, D. A. (2005). Breeding guayule for commercial production. *Ind. Crops Prod.* 22, 15–25. doi: 10.1016/j.indcrop.2004.06.005

Robertson, C. G., and Rackaitis, M. (2011). Further consideration of viscoelastic two glass transition behavior of nanoparticle-filled polymers. *Macromolecules* 44, 1177–1181. doi: 10.1021/ma102631h

Saake, B., and Lehnen, R. (2012). Lignin. *Ullmann's Encycl. Ind. Chem.* 21, 21–36. doi: 10.1002/14356007.a15_305.pub3

Sadeghifar, H., and Argyropoulos, D. S. (2015). Correlations of the antioxidant properties of softwood kraft lignin fractions with the thermal stability of its blends with polyethylene. *ACS Sustain. Chem. Eng.* 3, 349–356. doi: 10.1021/sc500756n

Sahakaro, K., Naskar, N., Datta, R. N., and Noordermeer, J. W. M. (2007). Blending of NR/BR/EPDM by reactive processing for tire sidewall applications. 1. preparation, cure characteristics and mechanical properties. *J. Appl. Polym. Sci.* 103, 2538–2546. doi: 10.1002/app.25088

Sarkawi, S. S., Dierkes, W. K., and Noordermeer, J. W. M. (2015). Morphology of silica-reinforced natural rubber: the effect of silane coupling agent. *Rubber Chem. Technol.* 88, 359–372. doi: 10.5254/rct.15.86936

Schaefer, D. W., Rieker, T., Agamalian, M., Lin, J. S., Fischer, D., Sukumaran, S., et al. (2000). Multilevel multilevel structure structure of of reinforcing reinforcing silica and carbon silica and carbon. *J. Appl. Crystallogr.* 33, 587–591. doi: 10.1107/S0021889800001199

Schmidt, T., Lenders, M., Hillebrand, A., Van Deenen, N., Munt, O., Reichelt, R., et al. (2010). Characterization of rubber particles and rubber chain elongation in *Taraxacum koksaghyz*. *BMC Biochem.* 11:11. doi: 10.1186/1471-2091-11-11

Schmitt, C. N. Z., Politi, Y., Reinecke, A., and Harrington, M. J. (2015). Role of sacrificial protein-metal bond exchange in mussel byssal thread self-healing. *Biomacromolecules* 16, 2852–2861. doi: 10.1021/acs.biomac.5b00803

Sengloyluan, K., Sahakaro, K., Dierkes, W. K., and Noordermeer, J. W. M. (2014). Silica-reinforced tire tread compounds compatibilized by using epoxidized natural rubber. *Eur. Polym. J.* 51, 69–79. doi: 10.1016/j.eurpolymj.2013.12.010

Setua, D. K., Shukla, M. K., Nigam, V., Singh, H., and Mathur, G. N. (2000). Lignin-reinforced rubber composites. *Polym. Compos.* 21, 988–995. doi: 10.1002/pc.10252

Shukla, M. K., Nigam, V., Singh, H., Setua, D. K., and Mathur, G. N. (1998). "Lignin reinforced rubber composites," in *Proceedings of Composite Materials* (Jamshedpur), 233–245.

Singha, A. S., Thakur, V. K., Mehta, I. K., Shama, A., Khanna, A. J., Rana, R. K., et al. (2009). Surface-modified hibiscus sabdariffa fibers : physicochemical, thermal, and morphological properties evaluation. *Int. J. Polym. Anal. Charact.* 14, 695–711. doi: 10.1080/10236660903325518

Siti Suhaily, S., Abdul Khalil, H. P. S., Wan Nadirah, W. O., and Jawaid, M. (2013). "Bamboo based biocomposites material, design and applications," in *Materials Science - Advanced Topics*, 489–517. doi: 10.5772/56057

Snowdon, M. R., Mohanty, A. K., and Misra, M. (2014). A study of carbonized lignin as an alternative to carbon black. *ACS Sustain. Chem. Eng.* 2, 1257–1263. doi: 10.1021/sc500086v

Soratana, K., Rasutis, D., Azarabadi, H., Eranki, P. L., and Landis, A. E. (2017). Guayule as an alternative source of natural rubber: a comparative life cycle assessment with Hevea and synthetic rubber. *J. Clean. Prod.* 159, 271–280. doi: 10.1016/j.jclepro.2017.05.070

Strzemiecka, B., Klapiszewski, L., Jamrozik, A., Szalaty, T. J., Matykiewicz, D., Sterzynski, T., et al. (2016). Physicochemical characterization of functional lignin-silica hybrid fillers for potential application in abrasive tools. *Materials.* 9:E517. doi: 10.3390/ma9070517

Sudin, R., and Swamy, N. (2006). Bamboo and wood fibre cement composites for sustainable infrastructure regeneration. *J. Mater. Sci.* 41, 6917–6924. doi: 10.1007/s10853-006-0224-3

Suhas, Carrott, P. J. M., and Ribeiro Carrott, M. M. (2007). Lignin – from natural adsorbent to activated carbon : a review. *Bioresour. Technol.* 98, 2301–2312. doi: 10.1016/j.biortech.2006.08.008

Sun, J.-Y., Zhao, X., Illeperuma, W. R. K., Chaudhuri, O., Oh, K. H., Mooney, D. J., et al. (2012). Highly stretchable and tough hydrogels. *Nature* 489, 133–136. doi: 10.1038/nature11409

Teaca, C.-A., Rosu, D., Bodirlau, R., and Rosu, L. (2013). Structural changes in wood under artificial UV light irradiation determined by FTIR spectroscopy and color measurements – a brief review. *Bioresources* 8, 1478–1507. doi: 10.15376/biores.8.1.1478-1507

ten Brinke, A. (2002). *Silica Reinforced Tyre Rubbers*. Ph.D. thesis, University of Twente, Netherlands.

Thakur, V. K., and Singha, A. S. (2010). KPS-initiated graft copolymerization onto modified cellulosic biofibers. *Int. J. Polym. Anal. Charact.* 15, 471–485. doi: 10.1080/1023666X.2010.510294

Thakur, V. K., Singha, A. S., and Misra, B. N. (2011). Graft copolymerization of methyl methacrylate onto cellulosic biofibers. *J. Appl. Polym. Sci.* 122, 532–544. doi: 10.1002/app.34094

Thakur, V. K., and Thakur, M. K. (2015). Recent advances in green hydrogels from lignin: a review. *Int. J. Biol. Macromol.* 72, 834–847. doi: 10.1016/j.ijbiomac.2014.09.044

Thakur, V. K., Thakur, M. K., Raghavan, P., and Kessler, M. R. (2014). Progress in green polymer composites from lignin for multifunctional applications: a review. *ACS Sustainable Chem. Eng.* 2:5. doi: 10.1021/sc500087z

Tran, C. D., Chen, J., Keum, J. K., and Naskar, A. K. (2016). A new class of renewable thermoplastics with extraordinary performance from nanostructured lignin-elastomers. *Adv. Funct. Mater.* 26, 2677–2685. doi: 10.1002/adfm.201504990

Vainio, U., Maximova, N., Hortling, B., Laine, J., Stenius, P., Simola, L. K., et al. (2004). Morphology of dry lignins and size and shape of dissolved kraft lignin particles by X-ray scattering. *Langmuir* 20, 9736–9744. doi: 10.1021/la048407v

Venkatachalam, P., Geetha, N., Sangeetha, P., and Thulaseedharan, A. (2013). Natural rubber producing plants: an overview. *Afr J. Biotechnol.* 12, 1297–1310. doi: 10.5897/AJBX12.016

Vieira, M. G. A., Da Silva, M. A., Dos Santos, L. O., and Beppu, M. M. (2011). Natural-based plasticizers and biopolymer films: a review. *Eur. Polym. J.* 47, 254–263. doi: 10.1016/j.eurpolymj.2010.12.011

Waddell, W. H. (1998). Tire black sidewall surface discoloration and non-staining technology: a review. *Rubber Chem. Technol.* 71, 590–618. doi: 10.5254/1.3538493

Wang, H., Liu, W., Huang, J., Yang, D., and Qiu, X. (2018). Bioinspired engineering towards tailoring advanced lignin/rubber elastomers. *Polymers* 10:1033. doi: 10.3390/polym10091033

Wang, J., Yao, K., Korich, A. L., Li, S., Ma, S., Ploehn, H. J., et al. (2011). Combining renewable gum rosin and lignin: towards hydrophobic polymer composites by controlled polymerization. *J. Polym. Sci. Part A Polym. Chem.* 49, 3728–3738. doi: 10.1002/pola.24809

Wang, M.-J., Grey, C. A., Reznek, S. A., Mahmud, K., and Kutsovsky, Y. (2003). Carbon black. *Kirk-Othmer Encycl. Chem. Technol.* 4, 761–803. doi: 10.1002/0471238961.0301180204011414.a01.pub2

Wang, M.-J., Kutsovsky, Y., Zhang, P., Murphy, L. J., Laube, S., and Mahmud, K. (2002). New generation carbon-silica dual phase filler part I. Characterization and application to passenger tire. *Rubber Chem. Technol.* 75, 247–263. doi: 10.5254/1.3544975

Watkins, D., Nuruddin, M., Hosur, M., Tcherbi-Narteh, A., and Jeelani, S. (2014). Extraction and characterization of lignin from different biomass resources. *J. Mater. Res. Technol.* 4, 26–32. doi: 10.1016/j.jmrt.2014.10.009

Xiao, S., Feng, J., Zhu, J., Wang, X., Yi, C., and Su, S. (2013). Preparation and characterization of lignin-layered double hydroxide/styrene-butadiene rubber composites. *J. Appl. Polym. Sci.* 130, 1308–1312. doi: 10.1002/app.39311

Xing, W., Yuan, H., Zhang, P., Yang, H., Song, L., and Hu, Y. (2013). Functionalized lignin for halogen-free flame retardant rigid polyurethane foam: preparation, thermal stability, fire performance and mechanical properties. *J. Polym. Res.* 20:234. doi: 10.1007/s10965-013-0234-1

Xu, G., Yan, G., and Zhang, J. (2015). Lignin as coupling agent in EPDM rubber: thermal and mechanical properties. *Polym. Bull.* 72, 2389–2398. doi: 10.1007/s00289-015-1411-7

Yang, D. Q., Rochelte, J. F., and Sacher, E. (2005). Spectroscopic evidence for π-π interaction between poly(diallyl dimethylammonium) chloride and multiwalled carbon nanotubes. *J. Phys. Chem. B* 109, 4481–4484. doi: 10.1021/jp044511+

Yu, P., He, H., Jia, Y., Tian, S., Chen, J., Jia, D., et al. (2016a). A comprehensive study on lignin as a green alternative of silica in natural rubber composites. *Polym. Test.* 54, 176–185. doi: 10.1016/j.polymertesting.2016.07.014

Yu, P., He, H., Jiang, C., Jia, Y., Wang, D., Yao, X., et al. (2016b). Enhanced oil resistance and mechanical properties of nitrile butadiene rubber/lignin composites modified by epoxy resin. *J. Appl. Polym. Sci.* 133, 1–10. doi: 10.1002/app.42922

Yu, P., He, H., Jiang, C., Wang, D., Jia, Y., Zhou, L., et al. (2015). Reinforcing styrene butadiene rubber with lignin-novolac epoxy resin networks. *Express Polym. Lett.* 9, 36–48. doi: 10.3144/expresspolymlett.2015.5

Zafarmehrabian, R., Gangali, S. T., Ghoreishy, M. H. R., and Davallu, M. (2012). The effects of silica/carbon black ratio on the dynamic properties of the tread compounds in truck tires. *J. Chem.* 9, 1102–1112. doi: 10.1155/2012/571957

Zhang, H. J., Sun, T. L., Zhang, A. K., Ikura, Y., Nakajima, T., Nonoyama, T., et al. (2016). Tough physical double-network hydrogels based on amphiphilic triblock copolymers. *Adv. Mater.* 28, 4884–4890. doi: 10.1002/adma.201600466

Zhang, P., Huang, G., Qu, L., Nie, Y., and Weng, G. (2012). Study on the self-crosslinking behavior based on polychloroprene rubber and epoxidized natural rubber. *J. Appl. Polym. Sci.* 125, 1084–1090. doi: 10.1002/app.34508

Zhang, Q., and Chuang, K. T. (2001). Adsorption of organic pollutants from effluents of a Kraft pulp mill on activated carbon and polymer resin. *Adv. Environ. Res.* 5, 251–258. doi: 10.1016/S1093-0191(00)00059-9

Check for
updates

Natural Fibers as Sustainable and Renewable Resource for Development of Eco-Friendly Composites: A Comprehensive Review

Yashas Gowda Thyavihalli Girijappa, Sanjay Mavinkere Rangappa, Jyotishkumar Parameswaranpillai and Suchart Siengchin*

Department of Mechanical and Process Engineering, The Sirindhorn International Thai–German Graduate School of Engineering, King Mongkut's University of Technology North Bangkok, Bangkok, Thailand

The increase in awareness of the damage caused by synthetic materials on the environment has led to the development of eco-friendly materials. The researchers have shown a lot of interest in developing such materials which can replace the synthetic materials. As a result, there is an increase in demand for commercial use of the natural fiber-based composites in recent years for various industrial sectors. Natural fibers are sustainable materials which are easily available in nature and have advantages like low-cost, lightweight, renewability, biodegradability, and high specific properties. The sustainability of the natural fiber-based composite materials has led to upsurge its applications in various manufacturing sectors. In this paper, we have reviewed the different sources of natural fibers, their properties, modification of natural fibers, the effect of treatments on natural fibers, etc. We also summarize the major applications of natural fibers and their effective use as reinforcement for polymer composite materials.

Keywords: natural fiber, sustainable and renewable resource, eco-friendly composites, applications of natural fibers, reinforcement for composites materials, treatments on natural fibers

INTRODUCTION

Material selection in design and manufacturing of a sustainable product plays a vital role in the field of engineering design. The materials are used to explore their physical properties along with their mechanical properties to make the product better one and reach its customer satisfaction levels. The polymer composite materials are one of such materials which provide the ease of processing, productivity, and cost reduction (Faruk et al., 2012; Al-Oqla and Sapuan, 2014; Sanjay and Suchart, 2019). The composites are tailor-made materials which have a unique quality where the properties can be altered by varying the different reinforcement and matrix phase (Bledzki and Gassan, 1999; Yogesha, 2017). Compared with the synthetic fibers, the natural fibers have many advantages due to their abundance, availability, and low cost (Arpitha et al., 2017; Madhu et al., 2019b). The natural fibers are introduced instead of synthetic fibers to make the composites lighter. The density of natural fibers (1.2–1.6 g/cm^3) is lower than glass fiber (2.4 g/cm^3), which leads to the making of the light-weight composites. As a result, there is an increase in the demand for the commercial use of natural fiber-based composites in various industrial sectors. Therefore, natural fibers such as hemp, jute, sisal, banana, coir, and kenaf are extensively used in the production of the lightweight

FIGURE 1 | Constituents of plant fibers (Faruk et al., 2014).
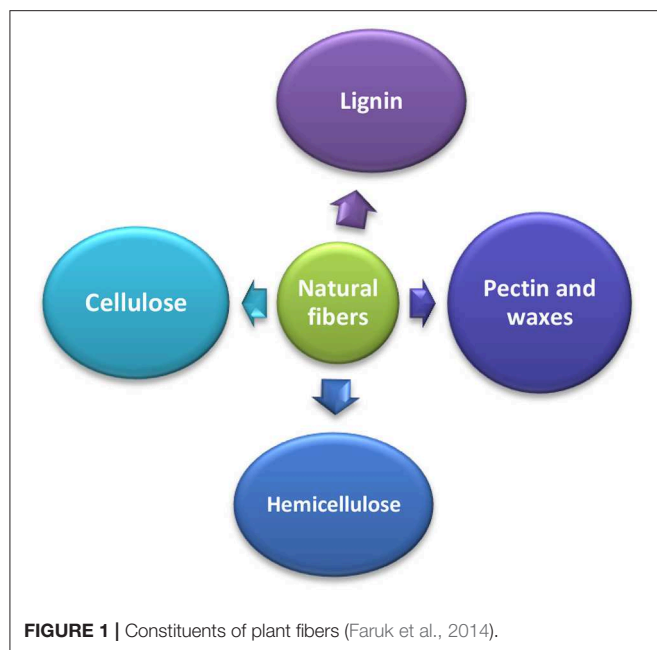
composites (Sreekala and Thomas, 2003; Thakur et al., 2014; Oksman et al., 2016). The natural fiber-based composites have been used in automotive interior linings (roof, rear wall, side panel lining), furniture, construction, packaging, and shipping pallets, etc. (Oksman, 2001; Lau et al., 2018; Sood and Dwivedi, 2018; Santhosh Kumar and Hiremath, 2019). Natural fibers are extracted from different plants and animals (chicken feather, hair, etc.) (Aziz and Ansell, 2004; Huda et al., 2006; Kicinska-Jakubowska et al., 2012). The plant fibers are made up of constituents like cellulose, lignin, hemicellulose, pectin, waxes, and water-soluble substances, which is represented in **Figure 1**. The presence of cellulose which is hydrophilic in nature affects the interfacial bonding between the polymer matrix and the fibers because the matrix is hydrophobic. Chemical treatment of the natural fibers is one of the ways to optimize the interaction between the fibers and polymer matrix. As it reduces the OH functional groups present on the fiber surface and also it increases the surface roughness and hence enhances the interfacial interaction between the matrix and the fibers (Liu et al., 2005; Mahjoub et al., 2014; Manimaran et al., 2017; Athith et al., 2018; Sanjay et al., 2019a). The study of natural fibers is very essential to develop eco-friendly composites.

SOURCE, PROPERTIES, AND APPLICATIONS OF NATURAL FIBERS

Kenaf (*Hibiscus cannabinus*)

The kenaf fibers are one of the important fibers belongs to bast fibers and it is mainly used for paper and rope production (Hamidon et al., 2019; Omar et al., 2019). Kenaf is a fibrous plant. They are stiff, strong, and tough and have high resistance to insecticides. These plants are cultivated 4,000 years ago in Africa, Asia, America, and some parts of Europe (Saba et al., 2015; Zamri

et al., 2016; Shahinur and Hasan, 2019b). The fibers are extracted from flowers, outer fiber, and inner core. The outer fiber is known as bast which makes 40% of the stalks dry weight and the inner core comprises of 60% of stalks dry weight. The kenaf plants upon harvesting are processed by using a mechanical fiber separator and the whole stalk is used in pulping. The extracted fibers must be treated chemically or bacterially to separate it from the non-fibrous substances like wax, pectin, and other substances (Suharty et al., 2016; Arjmandi et al., 2017). These fibers can be converted into fine woven fabrics. Kenaf fibers are environmentally friendly as they are completely biodegradable. In the olden days, these fibers were used for textiles, cords, ropes, storage bags, and Egyptians used it for making boats. Nowadays these fibers are made as composites along with other materials and are used in automotive, construction, packaging, furniture, textiles, mats, paper pulp, etc. (Nishino et al., 2003; Anuar and Zuraida, 2011; Atiqah et al., 2014; Kipriotis et al., 2015).

Hemp (*Cannabis sativa*)

The Hemp is one of the kinds of plants species grown mainly in Europe and Asia. It grows up to 1.2–4.5 m and 2 cm in diameter (Bhoopathi et al., 2014; Réquilé et al., 2018). The inner girth is surrounded by core, and the outer layer is the bast fiber and it is attached to the inner layer by glue-like substance or pectin. These fibers are used in rope, textiles, garden mulch, the assortment of building material and animal beddings. In recent developments, it is used to fabricate different composites (Li et al., 2006; Martin et al., 2013; Väisänen et al., 2018). The hemp plants are harvested, and the woody core from bast fibers is separated by a sequence of mechanical process. The woody core is cleaned to obtain the required core content and sometimes they are cut to the desired size. While the separated bast fibers are further processed to form yarn or bundles (Clarke, 2010; Duval et al., 2011; Fang et al., 2013; Raman Bharath et al., 2015; Sam-Brew and Smith, 2015).

Jute (*Corchorus capsularis*)

The jute an important natural fiber grown in parts of Asia including India, Bangladesh, China, and Myanmar (Khan and Khan, 2014; Das, 2017; Shahinur and Hasan, 2019a). The jute plant grows up to 15–20 cm in 4 months, and the fibers are extracted after harvesting which is about 4 months from cultivation. The retting process is done either with the help of chemicals ($N_2H_8C_2O_4$, Na_2SO_3, etc.) or biologically (Rahman, 2010). In biological retting, the stalks which are harvested are arranged in bundles and allowed to soak in water for about 20 days (Banik et al., 2003; Behera et al., 2012). This removes the pectin between the bast and the wood core which helps in the separation of the fibers. Then these fibers are allowed to dry.

Flax (*Linum usitatissimum*)

The flax fibers are produced from the prehistoric period. These fibers are separated from the stems of the plant *Linum usitatissimum* is mainly used to produce linen (Ruan et al., 2015; De Prez et al., 2018; Bourmaud et al., 2019). These are cellulosic plants but they are more in crystalline form. These fibers measure up to 90 cm length and diameter of 12–16 μm. Netherlands, Belgium, and France are the leading manufacturers

of these fibers. These fibers are used in furniture materials, textiles bed sheets, linen, interior decoration accessories, etc. (Van de Weyenberg et al., 2003; Charlet et al., 2010; Angelini and Tavarini, 2013; Ramesh, 2019). The fiber extraction involves the retting, and scorching both this process will make some alterations in the properties of the fibers. The retting involves the enzymes which degrade the pectin around the flax fibers which results in separation of fibers. Canada is the largest flax producer and exporter in the world, produced about 872,000 tons (Bos et al., 2006; Zafeiropoulos and Baillie, 2007; Martin et al., 2013; Zhu et al., 2013).

Ramie (*Boehmeria nivea*)

Ramie is one of the herbaceous perennial plants cultivated extensively in the region native to China, Japan, and Malaysia where it has been used for over a century as one of the textile fabrics (Nam and Netravali, 2006; Rehman et al., 2019; Yang et al., 2019). Ramie is a non-branching, fast-growing plant which grows up to 1–2 m height. The fibers extracted from the stem are the strongest and longest of the natural bast fibers. They are used to make sweaters in combination with cotton, also it is used in upholstery, gas mantle, fishing nets, and marine packings, etc. (Cengiz and Babalik, 2009; Marsyahyo et al., 2009; Sen and Jagannatha Reddy, 2011b). In addition to this attempt has been made for developing bio-based products by utilizing them in the field of automotive, furniture, construction, etc. The ramie fibers are extensively used for the production of a wide range of textiles, pulp, and paper, agrochemicals, composites, etc. The processing of the ramie fibers is similar to linen from flax (Angelini and Tavarini, 2013; Bunsell, 2018).

Nettle (*Urtica dioica*)

Nettle is the commonly grown herbaceous plant consists of 35–40 different species generally grown in Europe, Asia, Northern Africa, and North America (Bacci et al., 2009; Akgül, 2013; Lanzilao et al., 2016). The plant usually grows up to 2 m in length, the leaves are soft and green which are 3–15 cm long. The leaves and stems are generally hairy and have stinging hairs on them (Cummings and Olsen, 2011; Fang et al., 2013; Bourgeois et al., 2016). The fiber extraction is done by harvesting the plants during the flowering period. The fiber is extracted either by retting the stalks or by decorticating. The typical applications of nettle fibers are in the textile industry, bioenergy, animal housing, etc. Nowadays attempts have been made to use the nettle fibers on an industrial scale (Bacci et al., 2009; Mortazavi and Moghaddam, 2010).

Pineapple Leaf (*Ananas comosus*)

The pineapple plant is one of the abundantly cultivated plants which is easily available. The pineapple leaf fiber is crop waste after pineapple cultivation. It is a short tropical plant grows up to 1–2 m and the leaves are in cluster form consists of 20–30 leaves of about 6 cm wide. Approximately, 90–100 tons of pineapple leaves are grown per hectare. Among the different natural fibers, pineapple leaf fibers show good mechanical properties. Pineapple leaf fibers are multicellular and lingo-cellulosic. The fibers were extracted by hand using

the scrapers (Kengkhetkit and Amornsakchai, 2012; Laftah and Abdul Rahaman, 2015; Todkar and Patil, 2019). The various applications are in automobiles, textile, mats, construction, etc. The treated and surface-modified fibers are used for making conveyor belt cord, air-bag, advanced composites, etc. (Paridah et al., 2004; Jawaid and Abdul Khalil, 2011; Reddy and Yang, 2015; Al-Maharma and Al-Huniti, 2019).

Sisal (*Agave sisalana*)

The sisal is one of the most used natural fibers and Brazil is one of the largest producers of this fiber. It is a species native to south Mexico consists of the rosette of leaves grows up to 1.5–2 m tall (Naveen et al., 2018; Sanjay et al., 2018; Senthilkumar et al., 2018; Devaraju and Harikumar, 2019). The sisal produces about 200–250 commercially usable leaves in the life span of 6–7 years. The sisal fibers are having good range of mechanical properties and are used in the automotive industry, shipping industry (for mooring small craft and handling cargo), civil constructions, used as fiber core of the steel wire cables of elevators, agricultural twine or baler twine, etc. (Mihai, 2013; Ramesh et al., 2013; Nirmal et al., 2015; Aslan et al., 2018).

Date Palm (*Phoenix dactylifera*)

The date palm is known as palm extensively grown for its fruit. The biodiversity of the date palm is all over the world comprising around 19 species with more than 5,000 cultivators all around the world (Wales and Blackman, 2017; Alotaibi et al., 2019; Rivera et al., 2019). The date palm trees (*Phoenix dactylifera* L.) are the tallest among the Phoenix species and can grow up to 23 m height (Al-Oqla and Sapuan, 2014; Gheith et al., 2018; Masri et al., 2018). The date palm rachis and leaves are accumulated in large quantity after the harvesting of the date farm fruits every year in the farming lands of different countries. These fibers can be used as the potential cellulosic fiber sources. These fibers from leaves and rachis can be used as the reinforcement for thermoplastic and thermosetting polymers. Some researchers have found ways to use the date palm fibers in the automotive application (Alawar et al., 2009; Arunachalam, 2012; Liu et al., 2018).

Cotton (*Gossypium*)

Cotton belongs to the sub-tribe Hibisceae and family of Malvaceae is an important agricultural crop (Elmogahzy and Farag, 2018). It is the commonly used natural fiber for the production of cloths. The cotton is grown in tropical and subtropical regions, and China is the largest producer of cotton followed by India and the United States (Mwaikambo et al., 2000; Colomban and Jauzein, 2018). Among the various species of cotton, upland cotton (*Gossypium hirsutum*) and pima cotton (*Gossypium barbadense*) are the most popular (Zou et al., 2011; Al-Oqla et al., 2015; Sharma et al., 2017). The leaves of the cotton are removed and are collected and compressed into truckload-sized "modules." Later the modules are transported to processing plant known as the cotton gin. The gin separates the seeds, sticks, burrs, etc. from the cotton fibers. The cotton fiber is used extensively in textile industries, and recently attempts have been made to develop the composites for industrial applications

(Cheung et al., 2009; Gupta and Srivastava, 2016; Balaji and Senthil Vadivu, 2017).

Coconut Fiber (*Cocos nucifera*)

The coconut fiber is obtained from the husk of the coconut fruit. Among the different natural fibers, coconut fiber is the thickest. Coconut trees are mainly grown in tropical regions (Nair, 2010; Arulandoo et al., 2016; Danso, 2017). The major share of the commercially produced coconut fiber comes from India, Sri Lanka, Indonesia, Philippines, and Malaysia (Pham, 2016). Coir fiber, in particular, is a light and strong fiber that has been attracted scientific and commercial importance due to their specific characteristics and availability (Sen and Jagannatha Reddy, 2011a). Compared to other typical natural fibers, coconut fiber has higher lignin and lower cellulose and hemicellulose, together with its high microfibrillar angle, offers various valuable properties, such as resilience, strength, and damping, wear, resistance to weathering, and high elongation at break. The coir fiber is used for making ropes, mats, mattresses, brushes, in the upholstery industry, agriculture, construction, etc. (Al-Oqla and Sapuan, 2014; Verma and Gope, 2014; Sengupta and Basu, 2016; dos Santos et al., 2018).

Kapok (*Ceiba pentandra*)

Kapok belongs to the Bombacaceae family. It grows in tropical regions (Arumugam, 2014; Zheng et al., 2015). Kapok fiber is silk cotton and the color of the fiber is yellowish or light brown. The fibers enclose the kapok seeds. Kapok fibers are cellulosic fibers, light-weight, and hydrophobic (Prachayawarakorn et al., 2013; Wang et al., 2019). Conventionally, kapok fiber is used as buoyancy material, oil-absorbing material, reinforcement material, adsorption material, biofuel, etc. (Tye et al., 2012; Dong et al., 2015; Zheng et al., 2015).

Bamboo (Bambusoideae)

Bamboo fiber is also known as natural glass fiber due to the alignment of fibers in the longitudinal directions (Zakikhani et al., 2014; Wang and Chen, 2016). It is one of the extensively available trees in the dense forests especially in China, about 40 families, and 400 species are found (Fan and Weclawski, 2016; Van Dam et al., 2018). Bamboo fiber is used as reinforcement in polymeric materials due to its light-weight, low cost, high strength, and stiffness. Bamboo has been traditionally used for making houses, bridges, traditional boats, etc. The fibers extracted from bamboo are used as reinforcement for making advanced composites in various industries (Deshpande et al., 2000; Osorio et al., 2011; Zakikhani et al., 2014).

Silk (*Bombyx mori*)

Silk fibers are extracted from silkworms for the clothing purpose since ancient times. Silk is produced largely in China, South Asia, and Europe (Das and Natarajan, 2019; Shera et al., 2019). Fibers are extracted from the Cocoons which are the larvae of the insects undergoing complete metamorphosis. Silk fibers possess good mechanical properties such as high strength, extensibility, and compressibility (Yuan et al., 2010; Murugesh Babu, 2016; Castrillón Martínez et al., 2017; McGregor, 2018).

POSSIBILITIES TO ENHANCE THE PROPERTIES OF NATURAL FIBERS

The disadvantage of natural fiber composites includes poor fiber-matrix interfacial bonding, poor wettability, water absorption, and moisture absorption. The hydrophilic nature of the natural fibers caused poor interfacial interaction between the polymer matrix and the fiber. Hence, it is required to optimize the fibers by chemical treatments and surface treatments (Gassan and Bledzki, 1999; George et al., 2001; Li et al., 2007; Manimaran et al., 2018; Rangappa and Siengchin, 2018; Sanjay et al., 2018; Yashas Gowda et al., 2018).

Chemical Treatments

The recent trends in the development of the newer materials have led in replacing materials like glass and carbon reinforced composites with the natural fibers reinforced composites, for example in automobile interior, pedestrian bridge, shipping pallets, composite roof tiles, furniture, toys, etc. (Senthamaraikannan et al., 2016; Senthamaraikannan and Kathiresan, 2018; Madhu et al., 2019a; Sanjay et al., 2019b). However, the main drawback of natural fibers as reinforcement is that they are incompatible with thermoplastics due to their hydrophilic nature which results in the poor interfacial interaction between the fibers and matrix. This result in the poor mechanical properties of the composites. Therefore, the modification of natural fibers is required to make them less hydrophilic. Here an attempt is made to brief about various chemical treatments on natural fibers (Sepe et al., 2018).

Alkaline Treatment

The natural fiber consists of lignin, pectin, waxy materials, and natural oils which covers the outside layer of the fiber cell wall (Liu et al., 2004; Edeerozey et al., 2007; Hamidon et al., 2019). The chemical treatment alters the structure of the natural fibers, and sodium hydroxide (NaOH) is one of the chemical reagent used for this process (Rong et al., 2001; Baiardo et al., 2002; Sgriccia et al., 2008). The alkaline reagent is used to alter the structure of the cellulose in the plant fibers by cleaning the surface and the process called alkalization. Mwaikambo and Ansell treated hemp, jute, sisal, and kapok fibers with the NaOH at 20°C for about 48 h and washed using distilled water and acetic acid to neutralize the excess of NaOH. The thermal properties, surface morphology, and crystallinity index of the treated and untreated fibers were studied. The studies revealed that the chemically treated fibers showed the better fiber-resin adhesion lead to an increase in interfacial energy and thus enhancing the thermal and mechanical properties of the composites (Mwaikambo and Ansell, 2002). Kenaf fiber mats were treated with the NaOH solution for 24 h at a temperature of 45°C. The mats were washed with tap water after the chemical treatment and were immersed in the distilled water containing 1% acetic acid to neutralize the excess of NaOH and the mats were dried for 12 h at 45°C in an oven. The mats were then treated with 5% aminopropyl triethoxysilane diluted with an aqueous solution of methanol. The authors observed a significant increase in mechanical properties for the treated kenaf fiber modified PP

composites (Asumani et al., 2012). In an interesting work, the retting process was used to extract the fibers from Napier grass and the aqueous sodium hydroxide solution, about 2–5% is used to treat the Napier grass fibers at room temperature for about 30 min to remove the hemicelluloses and to clean the fibers. The fibers then washed with distilled water repeatedly and dried at 100°C. The alkalization has reduced the amount of hemicellulose in fiber, thus resulting in better mechanical property than that of untreated fiber (Reddy et al., 2012). The Carica papaya fibers were treated with the 5% concentration of NaOH by varying the soaking time from 15 to 90 min at the room temperature. The excess of NaOH from the surface was washed repeatedly using distilled water and was dried for about 56 h. The fibers treated at 60 min with 5% alkaline solution showed the optimum results which showed that complete elimination of hemicelluloses and lignin (Saravanakumaar et al., 2018).

Silane Treatment
The sugar palm fibers are treated with 2% saline and 6% NaOH for 3 h. The authors observed an improved interfacial interaction between the fiber and thermoplastic polyurethane after the treatment (Atiqah et al., 2018). Kabir et al. reviewed the treatment of silane on the surface of natural fibers. They stated that the silane groups act as a coupling agent between the fiber and the matrix and hence improvement's in mechanical properties are observed (Kabir et al., 2012). In an interesting work, Bodur et al. studied the changes in tensile strength and Young's modulus of composites treated with silane for different soaking times. The results were compared with untreated fiber composites. The authors observed significant improvement in strength when compared with untreated fibers. The improvement in strength is due to the formation of silanol (Si-OH) groups that form strong bonds with the –OH groups of the fibers. The remaining Si-OH undergo condensation with adjacent Si-OH groups. The hydrophobic polymerized silane thus formed can attach to the polymer matrix via van der Waals forces. As a result, silane groups form an interface between the fiber and polymer and provides a good interfacial interaction. The high tensile strength of the low-density polyethylene composites is due to good interfacial interaction between the fiber and polymer matrix (Bodur et al., 2016).

Acetylation Treatment
Acetylation of the natural fibers is the process of introducing an acetyl group on the surface of the fibers. This process was used to reduce the hydrophilic nature of fibers providing stability to the composites. The acetylation increases the fiber-matrix adhesion properties, hence the strong bond provides good properties to the natural fiber-based composites (Hill et al., 1998; Rong et al., 2001; Sreekala and Thomas, 2003). The OH groups of the fibers react with the acetyl groups thus making the fibers more hydrophobic. Generally, lignin and hemicellulose which contain the hydroxyl group react with acetyl groups to become hydrophobic. Normally, before treatment with glacial acetic acid, the natural fiber is alkali-treated. The alkali-treated fibers were soaked in glacial acetic acid for 1 h and later soaked for 2–5 min in acetic anhydride containing two drops of concentrated H_2SO_4.

The fibers were then washed and dried at 80°C using an oven for 6 h (Paul et al., 1997; Manikandan Nair et al., 2001; Mishra et al., 2003).

Peroxide Treatment
The impact of peroxide treatment on the mechanical properties of the cellulose fibers reinforced polymer composites has been studied by various researchers. The peroxides decomposed to form free radicals. The generated free radicals react with the hydrogen group of the cellulose fibers and polymer matrix. The peroxide treatment of natural fibers is carried out after alkalization. The alkaline treated fibers were immersed in ca. 6% concentration of benzoyl peroxide or dicumyl peroxide in acetone for about 30 min (Sreekala et al., 2000, 2002; Li et al., 2007).

Benzoylation Treatment
Benzoylation is used to decrease the hydrophilic nature of the fibers (Ali et al., 2016). The fiber-matrix bonding is improved by this treatment which increases the strength of the composites. For benzoylation, the fibers are first treated with NaOH followed by benzoyl chloride (C_6H_5COCl) treatment for 15 min. Later the fibers were isolated and treated with ethanol for 1 min and finally washed with distilled water and dried in an oven at 80°C for 24 h (Manikandan Nair et al., 2001; Zhang et al., 2005). The thermal stability of the treated fibers was higher than that of the untreated fibers.

Potassium Permanganate (KMnO$_4$) Treatment
The potassium permanganate is used as the chemical reagent to modify the interfacial interaction between the fiber and matrix. Different treatment methodologies are introduced. In one of the studies, the alkaline treated fibers were treated with potassium permanganate for different concentration (0.005–0.205 %) for 1 min and dried using the oven (Khan et al., 2006). Zaman et al. treated the jute fabrics with $KMnO_4$ along with acetone for different concentration (0.02, 0.03, 0.05, and 0.5%) and soaking times (1, 2, 3, and 5 min) and was dried in the oven (Zaman et al., 2010).

Stearic Acid Treatment
The non-woven jute fibers were immersed in different concentration of stearic acid in anhydrous ethanol from 1 min to up to 4 h and dried at 100°C for 1 h (Dolez et al., 2017). The 1% stearic acid mixed in ethyl alcohol and poured to a steel vessel containing alkali-treated short Sansevieria fibers along with stirring. Then the fibers were dried in woven at 80°C for 45 min (Sreenivasan et al., 2012). **Table 1** summarizes the different chemical treatments used for natural fibers.

EFFECT OF TREATMENTS ON NATURAL FIBERS

The chemical treatments of the natural fibers mainly enhance the properties of the fiber by modifying their microstructure along with improvement in wettability, surface morphology, chemical groups and tensile strength of the fibers (Saba et al., 2014; Dolez

TABLE 1 | Chemical treatments for different natural fibers.

Name of the fiber	Chemical reagents used	References
Pineapple leaf	c-aminopropyl trimethoxy silane (Z-6011) and c-methacrylate propyl trimethoxy silane (Z-6030)	Threepopnatkul et al., 2009
Green coconut	NaOCl, NaOCl/NaOH, or H_2O_2	Threepopnatkul et al., 2009
Alfa	NaOH	Rokbi et al., 2011, p. 2092–2097
Carica Papaya	NaOH	Saravanakumaar et al., 2018
Kenaf	NaOH	Asumani et al., 2012
Hemp	(3-glycidyloxypropyl)trimethoxysilane	Sepe et al., 2018
Ramie	NaOH, NaOH-Saline, Silane	Debeli et al., 2018
Pineapple leaf	NaOH and KOH	Senthilkumar et al., 2019
Prosopis juliflora	Potassium permanganate ($KMnO_4$)	Saravanakumar et al., 2014
Sisal	Stearic acid	Paul et al., 1997
Okra bast	$NaClO_2$	Arifuzzaman Khan et al., 2009
Flax	Methyl methacrylate (MMA)	Kaith and Kalia, 2007

et al., 2017; Preet Singh et al., 2017; Halip et al., 2018; Yu et al., 2019). The chemical treatment of the fiber improved the interfacial adhesion between the fiber surface and polymer matrix thereby the thermomechanical properties of the composites. The chemical treatment on ramie fibers has shown that the treatment of fibers with alkaline or saline or the combined treatment results in the improvement of the tensile strength (Gassan and Bledzki, 1997; Thakur and Thakur, 2014; Varghese and Mittal, 2017; Debeli et al., 2018; Sanjay et al., 2019a). The chemical treatment is one of the important techniques used to reduce the hydrophilic nature of the natural fibers also it improves the adhesion with the matrix. The structural and morphological changes can be observed with the treatment of the fibers, and this is mainly due to the removal of non-cellulosic substances from the natural fibers. The significant improvements of the properties of the composites are reported after different chemical treatments along with the increase in the thermal stability of the composites reinforced with natural fibers (Singh et al., 1996; Xie et al., 2010; Xu et al., 2013; Chen et al., 2018).

NATURAL FIBERS AS REINFORCEMENT FOR COMPOSITES MATERIALS

Over the past few decades, attempts have been made in developing the materials which replace the existing materials to have better mechanical and tribological properties for various applications (Arpitha and Yogesha, 2017; Abdellaoui et al., 2019). In view of this the monolithic materials are replaced by the fibers and materials such as carbon, glass, aramid fibers which

are extensively used in aerospace, automotive, construction, and sporting industries, etc. (Balakrishnan et al., 2016; Pickering et al., 2016; Asim et al., 2018). However, these materials have some disadvantages like non-biodegradability, non-renewability, high-energy requirement for production, and also harmful to the environment as the production of these materials releases enormous amounts of carbon dioxide into the atmosphere. Therefore, to overcome all these drawbacks researchers has made an attempt to study on the different natural fiber-reinforced composites which have better properties so that they can replace synthetic fibers in various applications (Wambua et al., 2003; Li et al., 2007; Sanjay et al., 2015; Mochane et al., 2019). As the demand for the newer materials which have better properties than the existing ones upsurges, the researchers have tried different types of natural materials with different natural fibers obtained from fruits, seeds, leaves, stem, animals, etc. (Sanjay et al., 2019a). The properties of a few important natural fibers are presented in **Table 2**. As discussed above, the natural fibers are modified by using different chemical treatments thus modifying the properties and increasing the properties of natural fiber composites. Also, the polymers and other synthetic materials have been used along with the natural fibers to enhance the properties of the natural fibers and these ideas have led to the development of several hybrid composites reinforced with natural fibers, and filler materials (Sawpan et al., 2011; Boopalan et al., 2013; Pickering et al., 2016; Sanjay et al., 2016; Madhu et al., 2018).

PROPERTIES OF NATURAL FIBER COMPOSITES

Environmental awareness has attracted researchers to make new composites with more than one reinforcement of natural resources by hybridization. Hybridization involves a combination of fillers and natural fiber that results in increased mechanical properties of the composites (Khan et al., 2005; Borba et al., 2013). Many numbers of literature are available which shows the mechanical properties of the natural fiber composites. The mechanical performance of fiber-reinforced composites can be affected by many factors including the volume or weight fraction of the reinforcement, the orientation of the fibers, the fiber aspect ratio, fiber-matrix adhesion, fiber alignment, distribution, use of additives, and chemical treatment of fibers. It is important to add that the moisture absorption of the composites also affects the mechanical behavior of the composites which leads to the poor interfacial bonding between fiber and hydrophobic matrix polymer (Zakikhani et al., 2014; Biswas et al., 2015; Kinloch et al., 2015; Pickering et al., 2016; Dixit et al., 2017).

In the automotive industry, asbestos-based brake pads and lining couplings, etc., are not preferred due to its carcinogenic nature. The replacements to asbestos fiber include ceramic fiber, steel fiber, alumina fiber, glass fiber, carbon fiber, aramid fiber, and their combinations. However, the production cost of these fibers is very high and are not environmentally friendly. Xin et al. studied the friction and wear properties of treated sisal

TABLE 2 | Properties of natural fibers (Pandey et al., 2010; Ku et al., 2011; Komuraiah et al., 2014; Gurunathan et al., 2015).

Fiber	Density (g/cm^3)	Tensile strength (MPa)	Young's modulus (GPa)	Elongation at break (%)
Jute	1.23	325–770	37.5–55	2.5
Flax	1.38	700–1,000	60–70	2.3
Hemp	1.35	530–1,110	45	3
Ramie	1.44	915	23	3.7
Banana	1.35	721.5–910	29	2
Bagasse	1.2	290	17	1.1
Henequen	1.4	500	13.2	4.8
Pineapple	1.5	1,020–1,600	71	0.8
Kenaf	1.2	745–930	41	1.6
Coir	1.2	140.5–175	6	27.5
Sisal	1.2	460–855	15.5	8
Abaca	1.5	410–810	41	3.4
Cotton	1.21	250–500	6–10	7
Nettle	1.51	650	38	1.7

fiber reinforced composites as a substitute for asbestos-based brake pads. The treated sisal fiber reinforced composite exhibits properties equivalent to the commercial friction composite. The authors recommend treated sisal is an ideal substitute of asbestos for brake pads (Xin et al., 2007).

The thermal stability is vital and at present is recognized to be one of the most important elements in the use of fibers as reinforcement for the composite. The chemical treatment of the natural fibers will improve the interfacial bonding between the matrix and fibers leads to improvement in thermal property of the composites (Panaitescu et al., 2016; Balan et al., 2017; Zegaoui et al., 2018).

Joseph et al. studied the thermal stability and crystallization behavior of sisal/polypropylene composites. The sisal fibers were treated with a urethane derivative of polypropylene glycol (PPG/TDI), maleic anhydride-modified polypropylene (MAPP) and KMnO. The thermal properties of the composites were measured using thermogravimetric analysis and differential scanning calorimetry. The authors observed superior thermal properties for the treated fiber reinforced composites (Joseph et al., 2003). The crystallinity also influences the thermal stability of the natural fiber composites. As the crystallinity of the material increased the thermal degradation temperature also increased (Nasser et al., 2016). The thermogravimetry analysis of date palm trunk (DPTRF), leaf stalk (DPLST), sheath or leaf sheath (DPLSH), and fruit bunch stalk (DPFBS) fibers was carried out and analysis revealed that DPFBS and DPLST fibers have good thermal stability and might be applied in industrial manufacture of composites, which require high thermal resistance (Alotaibi et al., 2019).

The pineapple reinforced polyethylene composites were studied for the electrical properties and found that due to the increased interfacial polarization and orientation with an increase in the number of fibers in composites the dielectric property increases (Jayamol et al., 1997). Similarly, the composites prepared with using the sisal fiber showed electric anisotropic behavior (Chand and Jain, 2005). It is observed

that the chemical treatments like alkali, stearic acid, peroxide, acetylation, and permanganate decrease the dielectric property of composites due to the decrease in hydrophilicity of the composite (Li et al., 2000). The electrical properties of phenol formaldehyde composites modified with banana fiber have been studied. The dielectric constant decreased with fiber loading and fiber treatment. For hybrid composites with glass fiber, the dielectric constant decreased with increasing glass fiber concentration (Joseph and Thomas, 2008).

APPLICATIONS

Automotive and aircraft industries have been actively manufacturing different kinds of natural fibers parts for their interior components (Sanjay et al., 2016; Puttegowda et al., 2018). Insulation materials are also made from natural fibers for different application areas, such as blowing insulation, pouring insulation, impact sound insulation materials and ceiling panels for thermal insulation, and acoustic soundproofing (Akin, 2010). Natural fibers show a sustainable future in architecture, with a vast variety of building materials, shapes, and even improving current commonly used materials. The use of synthetic fibers in the field of architecture could be substituted with natural fibers. It is used as material for sunscreens, cladding, walling, and flooring (Steffens et al., 2017). The natural fibers such as flax, hemp, sisal, and wool are now used in Mercedes-Benz components (Holbery and Houston, 2006). The coir/polyester-reinforced composites were used in the mirror casing, paperweights, voltage stabilizer cover, projector cover, helmet, and roof (Khondker et al., 2005). The flax fibers were used in GreenBente24 boat (Ticoalu et al., 2010). Rice husk fiber, cotton, ramie, jute fiber, kenaf are used in various applications like building materials, furniture industry, clothing, ropes, sewing thread, fishing nets, packing materials, and paper manufacture (Sen and Jagannatha Reddy, 2011b). Lots of efforts have been made to increase the use of natural fiber composites in the automotive industry,

particularly in car interiors. Besides the use for car interior parts, it also used for manufacturing exterior auto body components (Shuit et al., 2009; Monteiro et al., 2010; Shinoj et al., 2011; Mohammed et al., 2015).

DEGRADATION OF THE NATURAL FIBERS REINFORCED POLYMERS

In the present scenario, there is an increase in awareness regarding the environmental pollutions due to industrial waste which has led to replacing the harmful synthetic materials with more eco-friendly materials. The use of plastics is increased especially for household and commercial use. The use of plastic products leads to the accumulation of non-biodegradable wastes and are a threat to the ecological system. Therefore, extensive research has been carried out over the last decade on the biodegradation of plastics. Natural fibers along with the synthetic biodegradable materials can be used to develop biocomposites which have benefits toward the environment like biodegradability, renewability of base material, and reduction in emission of greenhouse gasses. Degradation offers a lot of advantages such as the reduction of plastic waste and reduction in the cost of waste management (Fakhrul and Islam, 2013; Gunti et al., 2018).

Degradation of the composite occurs with the breakdown of the composite materials, as well as with the loss of mechanical properties. In the outdoor environment, the degradation of natural fiber reinforced composites is influenced by atmospheric moisture, temperature, ultraviolet light and activities of microscopic organisms. The degradation occurs by the breakdown of hemicelluloses, lignin, and cellulose of the fiber. This can cause damage to the bonding between fibers and polymer matrix. Thus, leads to the lowering of the mechanical properties of the composites (de Melo et al., 2017). The kenaf/POM composites were subjected to weathering by exposing to moisture, water spray, and UV light in an accelerated weathering chamber and the materials showed lower tensile strength and this result was attributed to the degradation of the cellulose, hemicelluloses, and lignin of kenaf fibers (Abdullah et al., 2013). The effect of weathering on the degradation of jute/phenolic composites was investigated by Azwa et al. (2013). It shows that 2 years of UV exposure on jute/phenolic composites has decreased the tensile strength by about 50%. The authors observed resin cracking, bulging, fibrillation, and black spots after exposure to weathering.

It is necessary to promote the use of natural fibers as reinforcement in the polymer so that the materials become biodegradable to some extent. Proper degradation of the plastics must be a better way to avoid the harmful effects on the environment. Therefore, one must always look for the plastics

which are compostable or degradable. However, this cannot be implemented for every material but can be reduced with the use of biopolymers to some extent (Chauhan and Chauhan, 2015; Thiagamani et al., 2019).

FUTURE MARKET TRENDS

In current market trends, natural fibers reinforced polymers are experiencing comprehensive growth with good prospects in automotive and construction industries. Bast fiber such as hemp, kenaf, flax, etc., are preferred for automotive applications. On the other hand, wood plastic composite is the material of choice for construction industries. Looking at the developments of the current trends Europe is predicted to remain as the largest market for natural fiber-reinforced composites due to the high acceptance level of environmentally friendly composite materials by automotive industries, government agencies, and growth in small scale environmentally friendly industries. The improvement in materials performance will drive the growth of natural fiber reinforced polymer composites in new potential areas. Natural fiber composites are new in electrical, electronics and sporting segments, however, it has the potential to capture a good market share in the future.

CONCLUSIONS

Increased environmental awareness has resulted in the utilization of natural fiber as an effective reinforcement material in polymer matrix composites. Natural fibers are proficient materials which can replace the existing synthetic fibers. The fibers are usually extracted from plants and animals often offer poor resistance to moisture and incompatible nature of fibers become the main disadvantage. Therefore, modification of material properties has done through chemical treatments of natural fibers which improve the adhesion between the fibers and matrix and enhance the mechanical properties of the composites. In the near future, the natural fiber will become one of the sustainable and renewable resources in the composite field which can replace synthetic fibers in many applications.

AUTHOR CONTRIBUTIONS

All authors listed have made a substantial, direct and intellectual contribution to the work, and approved it for publication.

REFERENCES

Abdellaoui, H., Raji, M., Essabir, H., Bouhfid, R., and el kacem Qaiss, A. (2019). "Mechanical behavior of carbon/natural fiber-based hybrid composites," in *Mechanical and Physical Testing of Biocomposites, Fibre-Reinforced Composites*

and Hybrid Composites, eds M. Jawaid, M. Thariq, and N. Saba (Woodhead Publishing), 103-122. doi: 10.1016/B978-0-08-102292-4.00006-0

Abdullah, M. Z., Dan-mallam, Y., Sri, P., and Megat, M. (2013). Effect of environmental degradation on mechanical properties of kenaf/polyethylene terephthalate fiber reinforced polyoxymethylene

hybrid composite. *Adv. Mater. Sci. Eng.* 2013:671481. doi: 10.1155/2013/671481

Akgül, M. (2013). Suitability of stinging nettle (*Urtica dioica* L.) stalks for medium density fiberboards production. *Compos. Part B Eng.* 45, 925–929. doi: 10.1016/j.compositesb.2012.09.048

Akin, D. E. (2010). "Chemistry of plant fibres," in *Industrial Applications of Natural Fibres: Structure, Properties and Technical Applications,* ed J. Müssing (West Sussex: John Wiley & Sons Ltd.), 13–22.

Alawar, A., Hamed, A. M., and Al-Kaabi, K. (2009). Characterization of treated date palm tree fiber as composite reinforcement. *Compos. Part B Eng.* 40, 601–606. doi: 10.1016/j.compositesb.2009.04.018

Ali, A., Shaker, K., Nawab, Y., Jabbar, M., Hussain, T., Militky, J., et al. (2016). Hydrophobic treatment of natural fibers and their composites — a review. *J. Ind. Text.* 47, 1–31. doi: 10.1177/1528083716654468

Al-Maharma, A., and Al-Huniti, N. (2019). Critical review of the parameters affecting the effectiveness of moisture absorption treatments used for natural composites. *J. Compos. Sci.* 3:27. doi: 10.3390/jcs3010027

Al-Oqla, F. M., and Sapuan, S. M. (2014). Natural fiber reinforced polymer composites in industrial applications: feasibility of date palm fibers for sustainable automotive industry. *J. Clean. Prod.* 66, 347–354. doi: 10.1016/j.jclepro.2013.10.050

Al-Oqla, F. M., Sapuan, S. M., Anwer, T., Jawaid, M., and Hoque, M. E. (2015). Natural fiber reinforced conductive polymer composites as functional materials: a review. *Synth. Met.* 206, 42–54. doi: 10.1016/j.synthmet.2015.04.014

Alotaibi, M. D., Alshammari, B. A., Saba, N., Alothman, O. Y., Sanjay, M. R., Almutairi, Z., et al. (2019). Characterization of natural fiber obtained from different parts of date palm tree (*Phoenix dactylifera* L.). *Int. J. Biol. Macromol.* 135, 69–76. doi: 10.1016/j.ijbiomac.2019.05.102

Angelini, L. G., and Tavarini, S. (2013). Ramie [*Boehmeria nivea* (L.) Gaud.] as a potential new fibre crop for the Mediterranean region: growth, crop yield and fibre quality in a long-term field experiment in Central Italy. *Ind. Crops Prod.* 51, 138–144. doi: 10.1016/j.indcrop.2013.09.009

Anuar, H., and Zuraida, A. (2011). Improvement in mechanical properties of reinforced thermoplastic elastomer composite with kenaf bast fibre. *Compos. Part B Eng.* 42, 462–465. doi: 10.1016/j.compositesb.2010.12.013

Arifuzzaman Khan, G. M., Shaheruzzaman, M., Rahman, M. H., Abdur Razzaque, S. M., Islam, M. S., and Alam, M. S. (2009). Surface modification of okra bast fiber and its physico-chemical characteristics. *Fibers Polym.* 10, 65–70. doi: 10.1007/s12221-009-0065-1

Arjmandi, R., Hassan, A., and Zakaria, Z. (2017). "Rice husk and kenaf fiber reinforced polypropylene biocomposites," in *Lignocellulosic Fibre and Biomass-Based Composite Materials*, eds M. Jawaid, M. T. Paridah, and N. Saba (Woodhead Publishing), 77–94. doi: 10.1016/B978-0-08-100959-8.00005-6

Arpitha, G. R., Sanjay, M. R., Senthamaraikannan, P., Barile, C., and Yogesha, B. (2017). Hybridization effect of sisal/glass/epoxy/filler based woven fabric reinforced composites. *Exp. Tech.* 41, 577–584. doi: 10.1007/s40799-017-0203-4

Arpitha, G. R., and Yogesha, B. (2017). Science direct an overview on mechanical property evaluation of natural fiber reinforced polymers. *Mater. Today Proc.* 4, 2755–2760. doi: 10.1016/j.matpr.2017.02.153

Arulandoo, X., Sritharan, K., and Subramaniam, M. (2016). *The Coconut Palm*, 2nd Edn. Elsevier. doi: 10.1016/B978-0-12-394807-6.00237-9

Arumugam, V. (2014). A preliminary investigation on Kapok/polypropylene nonwoven composites for sound absorption. *Ind. J. Fibre Text. Res.* 37, 385–388.

Arunachalam, V. (2012). Date palm. *Genomics Cultiv. Palms*, 49–59. doi: 10.1016/B978-0-12-387736-9.00004-2

Asim, M., Saba, N., Jawaid, M., and Nasir, M. (2018). "Potential of natural fiber/biomass filler-reinforced polymer composites in aerospace applications," in *Sustainable Composites for Aerospace Applications*, eds M. Jawaid and M. Thariq (Elsevier Ltd.), 253–268. doi: 10.1016/B978-0-08-102131-6.00012-8

Aslan, M., Tufan, M., and Küçükömeroglu, T. (2018). Tribological and mechanical performance of sisal-filled waste carbon and glass fibre hybrid composites. *Compos. Part B Eng.* 140, 241–249. doi: 10.1016/j.compositesb.2017.12.039

Asumani, O. M. L., Reid, R. G., and Paskaramoorthy, R. (2012). The effects of alkali–silane treatment on the tensile and flexural properties of short fibre non-woven kenaf reinforced polypropylene composites. *Compos Part A Appl. Sci. Manufact.* 43, 1431–1440. doi: 10.1016/j.compositesa.2012.04.007

Athith, D., Sanjay, M. R., Yashas Gowda, T. G., Madhu, P., Arpitha, G. R., Yogesha, B., et al. (2018). Effect of tungsten carbide on mechanical and tribological properties of jute/sisal/E-glass fabrics reinforced natural rubber/epoxy composites. *J. Ind. Text.* 48, 713–737. doi: 10.1177/1528083717740765

Atiqah, A., Jawaid, M., Ishak, M. R., and Sapuan, S. M. (2018). Effect of alkali and silane treatments on mechanical and interfacial bonding strength of sugar palm fibers with thermoplastic polyurethane. *J. Nat. Fibers* 15, 251–261. doi: 10.1080/15440478.2017.1325427

Atiqah, A., Maleque, M. A., Jawaid, M., and Iqbal, M. (2014). Development of kenaf-glass reinforced unsaturated polyester hybrid composite for structural applications. *Compos. Part B* 56, 68–73. doi: 10.1016/j.compositesb.2013.08.019

Aziz, S. H., and Ansell, M. P. (2004). The effect of alkalization and fibre alignment on the mechanical and thermal properties of kenaf and hemp bast fibre composites: part 1 - polyester resin matrix. *Compos. Sci. Technol.* 64, 1219–1230. doi: 10.1016/j.compscitech.2003.10.001

Azwa, Z. N., Yousif, B. F., Manalo, A. C., and Karunasena, W. (2013). A review on the degradability of polymeric composites based on natural fibres. *Mater. Des.* 47, 424–442. doi: 10.1016/j.matdes.2012.11.025

Bacci, L., Baronti, S., Predieri, S., and di Virgilio, N. (2009). Fiber yield and quality of fiber nettle (*Urtica dioica* L.) cultivated in Italy. *Ind. Crops Prod.* 29, 480–484. doi: 10.1016/j.indcrop.2008.09.005

Baiardo, M., Frisoni, G., Scandola, M., and Licciardello, A. (2002). Surface chemical modification of natural cellulose fibers. *J. Appl. Polym. Sci.* 83, 38–45. doi: 10.1002/app.2229

Balaji, V., and Senthil Vadivu, K. (2017). Mechanical characterization of coir fiber and cotton fiber reinforced unsaturated polyester composites for packaging applications mechanical characterization of coir fiber and cotton fiber reinforced. *J. Appl. Packag. Res.* 9, 12–19.

Balakrishnan, P., John, M. J., Pothen, L., Sreekala, M. S., and Thomas, S. (2016). "Natural fibre and polymer matrix composites and their applications in aerospace engineering," in *Advanced Composite Materials for Aerospace Engineering*, eds S. Rana and R. Fangueiro (Elsevier Ltd.), 365–383. doi: 10.1016/B978-0-08-100037-3.00012-2

Balan, A. K., Mottakkunnu Parambil, S., Vakyath, S., Thulissery Velayudhan, J., Naduparambath, S., and Etathil, P. (2017). Coconut shell powder reinforced thermoplastic polyurethane/natural rubber blend-composites: effect of silane coupling agents on the mechanical and thermal properties of the composites. *J. Mater. Sci.* 52, 6712–6725. doi: 10.1007/s10853-017-0907-y

Banik, S., Basak, M. K., Paul, D., Nayak, P., Sardar, D., Sil, S. C., et al. (2003). Ribbon retting of jute - a prospective and eco-friendly method for improvement of fibre quality. *Ind. Crops Prod.* 17, 183–190. doi: 10.1016/S0926-6690(02)00097-3

Behera, A. K., Avancha, S., Basak, R. K., Sen, R., and Adhikari, B. (2012). Fabrication and characterizations of biodegradable jute reinforced soy based green composites. *Carbohydr. Polym.* 88, 329–335. doi: 10.1016/j.carbpol.2011.12.023

Bhoopathi, R., Ramesh, M., and Deepa, C. (2014). Fabrication and property evaluation of banana-hemp-glass fiber reinforced composites. *Proc. Eng.* 97, 2032–2041. doi: 10.1016/j.proeng.2014.12.446

Biswas, S., Shahinur, S., Hasan, M., and Ahsan, Q. (2015). Physical, mechanical and thermal properties of jute and bamboo fiber reinforced unidirectional epoxy composites. *Proc. Eng.* 105, 933–939. doi: 10.1016/j.proeng.2015.05.118

Bledzki, A. K., and Gassan, J. (1999). Composites reinforced with cellulose based fibres. *Prog. Polym. Sci.* 24, 221–274. doi: 10.1016/S0079-6700(98)00018-5

Bodur, M. S., Bakkal, M., and Sonmez, H. E. (2016). The different chemical treatment methods. *J. Compos. Mater.* 50, 3817–3830. doi: 10.1177/0021998315626256

Boopalan, M., Niranjanaa, M., and Umapathy, M. J. (2013). Study on the mechanical properties and thermal properties of jute and banana fiber reinforced epoxy hybrid composites. *Compos. Part B Eng.* 51, 54–57. doi: 10.1016/j.compositesb.2013.02.033

Borba, P. M., Tedesco, A., and Lenz, D. M. (2013). Effect of reinforcement nanoparticles addition on mechanical properties of SBS/curauá fiber composites. *Mater. Res.* 17, 412–419. doi: 10.1590/S1516-14392013005000203

Bos, H. L., Müssig, J., and van den Oever, M. J. A. (2006). Mechanical properties of short-flax-fibre reinforced compounds. *Compos. Part A Appl. Sci. Manuf.* 37, 1591–1604. doi: 10.1016/j.compositesa.2005.10.011

Bourgeois, C., Leclerc, É. A., Corbin, C., Doussot, J., Serrano, V., Vanier, J. R., et al. (2016). L'ortie (*Urtica dioica* L.), une source de produits antioxidants et phytochimiques anti-âge pour des applications en cosmétique. *Comptes Rendus Chim.* 19, 1090–1100. doi: 10.1016/j.crci.2016. 03.019

Bourmaud, A., Siniscalco, D., Foucat, L., Goudenhooft, C., Falourd, X., Pontoire, B., et al. (2019). Evolution of flax cell wall ultrastructure and mechanical properties during the retting step. *Carbohydr. Polym.* 206, 48–56. doi: 10.1016/j.carbpol.2018.10.065

Bunsell, A. R. (ed.) (2018). "Introduction to the science of fibers," in *Handbook of Properties of Textile and Technical Fibres* (Woodhead Publishing), 1–20. doi: 10.1016/B978-0-08-101272-7.00001-8

Castrillón Martínez, D. C., Zuluaga, C. L., Restrepo-Osorio, A., and Álvarez-López, C. (2017). Characterization of sericin obtained from cocoons and silk yarns. *Proc. Eng.* 200, 377–383. doi: 10.1016/j.proeng.2017.07.053

Cengiz, T. G., and Babalik, F. C. (2009). The effects of ramie blended car seat covers on thermal comfort during road trials. *Int. J. Ind. Ergon.* 39, 287–294. doi: 10.1016/j.ergon.2008.12.002

Chand, N., and Jain, D. (2005). Effect of sisal fibre orientation on electrical properties of sisal fibre reinforced epoxy composites. *Compos. Part A Appl. Sci. Manuf.* 36, 594–602. doi: 10.1016/j.compositesa.2004.08.002

Charlet, K., Jernot, J. P., Breard, J., and Gomina, M. (2010). Scattering of morphological and mechanical properties of flax fibres. *Ind. Crops Prod.* 32, 220–224. doi: 10.1016/j.indcrop.2010.04.015

Chauhan, A., and Chauhan, P. (2015). Natural fibers and biopolymer. *J. Chem. Eng. Process Technol.* 6, 1–4. doi: 10.4172/2157-7048.S6-001

Chen, Y., Su, N., Zhang, K., Zhu, S., Zhu, Z., Qin, W., et al. (2018). Effect of fiber surface treatment on structure, moisture absorption and mechanical properties of luffa sponge fiber bundles. *Ind. Crops Prod.* 123, 341–352. doi: 10.1016/j.indcrop.2018.06.079

Cheung, H., Ho, M., Lau, K., Cardona, F., and Hui, D. (2009). Natural fibre-reinforced composites for bioengineering and environmental engineering applications. *Compos. Part B Eng.* 40, 655–663. doi: 10.1016/j.compositesb.2009.04.014

Clarke, R. C. (2010). Traditional fiber hemp (Cannabis) production, processing, yarn making, and weaving strategies-functional constraints and regional responses. Part 2. *J. Nat. Fibers* 7, 229–250. doi: 10.1080/15440478.2010.504043

Colomban, P., and Jauzein, V. (2018). "Silk: fibers, films, and composites-types, processing, structure, and mechanics," in *Handbook of Properties of Textile and Technical Fibres,* ed A. R. Bunsell (Woodhead Publishing), 137-183. doi: 10.1016/B978-0-08-101272-7.00005-5

Cummings, A. J., and Olsen, M. (2011). Mechanism of action of stinging nettles. *Wilderness Environ. Med.* 22, 136–139. doi: 10.1016/j.wem.2011. 01.001

Danso, H. (2017). Properties of coconut, oil palm and bagasse fibres: as potential building materials. *Proc. Eng.* 200, 1–9. doi: 10.1016/j.proeng.2017.07.002

Das, S. (2017). Mechanical properties of waste paper/jute fabric reinforced polyester resin matrix hybrid composites. *Carbohydr. Polym.* 172, 60–67. doi: 10.1016/j.carbpol.2017.05.036

Das, S., and Natarajan, G. (2019). "Silk fiber composites in biomedical applications," in *Materials for Biomedical Engineering*, eds V. Grumezescu and A. Mihai Grumezescu (Elsevier), 309-338. doi: 10.1016/B978-0-12-816872-1.00011-X

de Melo, R. P., Marques, M. F. V., Navard, P., and Duque, N. P. (2017). Degradation studies and mechanical properties of treated curauá fibers and microcrystalline cellulose in composites with polyamide 6. *J. Compos. Mater.* 51, 3481–3489. doi: 10.1177/0021998317690446

De Prez, J., Van Vuure, A. W., Ivens, J., Aerts, G., and Van de Voorde, I. (2018). Enzymatic treatment of flax for use in composites. *Biotechnol. Rep.* 20:e00294. doi: 10.1016/j.btre.2018.e00294

Debeli, D. K., Qin, Z., and Guo, J. (2018). Study on the pre-treatment, physical and chemical properties of ramie fibers reinforced poly (Lactic Acid) (PLA) biocomposite. *J. Nat. Fibers* 15, 596–610. doi: 10.1080/15440478.2017. 1349711

Deshpande, A. P., Bhaskar Rao, M., and Lakshmana Rao, C. (2000). Extraction of bamboo fibers and their use as reinforcement in polymeric composites. *J. Appl. Polym. Sci.* 76, 83–92 doi: 10.1002/(SICI) 1097-4628(20000404)76:1<83::AID-APP11>3.0.CO;2-L

Devaraju, A., and Harikumar, R. (2019). "Life cycle assessment of sisal fiber," in *Reference Module in Materials Science and Materials Engineering* (Elsevier Ltd.). doi: 10.1016/B978-0-12-803581-8.10552-1

Dixit, S., Goel, R., Dubey, A., Shivhare, P. R., and Bhalavi, T. (2017). Natural fibre reinforced polymer composite materials - A review. *Polym. Renew. Resour.* 8, 71–78. doi: 10.1177/204124791700800203

Dolez, P. I., Arfaoui, M. A., Dub,é, M., and David, É. (2017). Hydrophobic treatments for natural fibers based on metal oxide nanoparticles and fatty acids. *Proc. Eng.* 200, 81–88. doi: 10.1016/j.proeng.2017. 07.013

Dong, T., Xu, G., and Wang, F. (2015). Adsorption and adhesiveness of kapok fiber to different oils. *J. Hazard. Mater.* 296, 101–111. doi: 10.1016/j.jhazmat.2015.03.040

dos Santos, J. C., Siqueira, R. L., Vieira, L. M. G., Freire, R. T. S., Mano, V., and Panzera, T. H. (2018). Effects of sodium carbonate on the performance of epoxy and polyester coir-reinforced composites. *Polym. Test.* 67, 533–544. doi: 10.1016/j.polymertesting.2018.03.043

Duval, A., Bourmaud, A., Augier, L., and Baley, C. (2011). Influence of the sampling area of the stem on the mechanical properties of hemp fibers. *Mater. Lett.* 65, 797–800. doi: 10.1016/j.matlet.2010.11.053

Edeerozey, A. M. M., Akil, H. M., Azhar, A. B., and Ariffin, M. I. Z. (2007). Chemical modification of kenaf fibers. *Mater. Lett.* 61, 2023–2025. doi: 10.1016/j.matlet.2006.08.006

Elmogahzy, Y., and Farag, R. (2018). "Tensile properties of cotton fibers: importance, research, and limitations", in *Handbook of Properties of Textile and Technical Fibres*, ed A. R. Bunsell (Woodhead Publishing), 223-273. doi: 10.1016/B978-0-08-101272-7.00007-9

Fakhrul, T., and Islam, M. A. (2013). Degradation behavior of natural fiber reinforced polymer matrix composites. *Proc. Eng.* 56, 795–800. doi: 10.1016/j.proeng.2013.03.198

Fan, M., and Weclawski, B. (2016). "Long natural fibre composites," in *Advanced High Strength Natural Fibre Composites in Construction*, eds M. Fan and F. Fu (Woodhead Publishing), 141-177. doi: 10.1016/B978-0-08-100411-1.00006-6

Fang, H., Zhang, Y., Deng, J., and Rodrigue, D. (2013). Effect of fiber treatment on the water absorption and mechanical properties of hemp fiber/polyethylene composites. *J. Appl. Polym. Sci.* 127, 942–949. doi: 10.1002/app.37871

Faruk, O., Bledzki, A. K., Fink, H. P., and Sain, M. (2012). Biocomposites reinforced with natural fibers: 2000-2010. *Prog. Polym. Sci.* 37, 1552–1596. doi: 10.1016/j.progpolymsci.2012.04.003

Faruk, O., Bledzki, A. K., Fink, H. P., and Sain, M. (2014). Progress report on natural fiber reinforced composites. *Macromol. Mater. Eng.* 299, 9-26. doi: 10.1002/mame.201300008

Gassan, J., and Bledzki, A. K. (1997). The influence of fiber-surface treatment on the mechanical properties of jute-polypropylene composites. *Compos. Part A Appl. Sci. Manuf.* 28, 1001–1005. doi: 10.1016/S1359-835X(97)00042-0

Gassan, J., and Bledzki, A. K. (1999). Possibilities for improving the mechanical properties of jute/epoxy composites by alkali treatment of fibres. *Compos. Sci. Technol.* 59, 1303–1309. doi: 10.1016/S0266-3538(98)00169-9

George, J., Sreekala, M. S., and Thomas, S. (2001). A review on interface modification and characterization of natural fiber reinforced plastic composites. *Polym. Eng. Sci.* 41, 1471–1485. doi: 10.1002/pen.10846

Gheith, M. H., Aziz, M. A., Ghori, W., Saba, N., Asim, M., Jawaid, M., et al. (2018). Flexural, thermal and dynamic mechanical properties of date palm fibres reinforced epoxy composites. *J. Mater. Res. Technol.* 8, 853–860. doi: 10.1016/j.jmrt.2018.06.013

Gunti, R., Ratna Prasad, A. V., and Gupta, A. V. S. S. K. S. (2018). Mechanical and degradation properties of natural fiber-reinforced PLA composites: jute, sisal, and elephant grass. *Polym. Compos.* 39, 1125–1136. doi: 10.1002/pc.24041

Gupta, M. K., and Srivastava, R. K. (2016). Mechanical properties of hybrid fibers-reinforced polymer composite: a review. *Polym. Plast. Technol. Eng.* 55, 626–642. doi: 10.1080/03602559.2015.1098694

Gurunathan, T., Mohanty, S., and Nayak, S. K. (2015). A review of the recent developments in biocomposites based on natural fibres and their application perspectives. *Compos Part Appl. Sci. Manuf.* 77, 1–25. doi: 10.1016/j.compositesa.2015.06.007

Halip, J. A., Hua, L. S., Ashaari, Z., Tahir, P. M., Chen, L. W., and Uyup, M. K. A. (2018). "Effect of treatment on water absorption behavior of natural," in *Mechanical and Physical Testing of Biocomposites, Fibre-Reinforced Composites*

and Hybrid Composites, eds M. Jawaid, M. Thariq, and N. Saba (Woodhead Publishing), 141-156. doi: 10.1016/B978-0-08-102292-4.00008-4

Hamidon, M. H., Sultan, M. T. H., Ariffin, A. H., and Shah, A. U. M. (2019). Effects of fibre treatment on mechanical properties of kenaf fibre reinforced composites: a review. *J. Mater. Res. Technol.* 8, 3327–3337. doi: 10.1016/j.jmrt.2019.04.012

Hill, C. A. S., Khalil, H. P. S. A., and Hale, M. D. (1998). A study of the potential of acetylation to improve the properties of plant fibres. *Ind. Crops Prod.* 8, 53–63. doi: 10.1016/S0926-6690(97)10012-7

Holbery, J., and Houston, D. (2006). Natural-fiber-reinforced polymer composites in automotive applications. *JOM* 58, 80–86. doi: 10.1007/s11837-006-0234-2

Huda, M. S., Drzal, L. T., Mohanty, A. K., and Misra, M. (2006). Chopped glass and recycled newspaper as reinforcement fibers in injection molded poly(lactic acid) (PLA) composites: a comparative study. *Compos. Sci. Technol.* 66, 1813–1824. doi: 10.1016/j.compscitech.2005.10.015

Jawaid, M., and Abdul Khalil, H. P. S. (2011). Cellulosic/synthetic fibre reinforced polymer hybrid composites: a review. *Carbohydr. Polym.* 86, 1–18. doi: 10.1016/j.carbpol.2011.04.043

Jayamol, G., Bhagawan, S. S., and Thomas, S. (1997). Electrical properties of pineapple fibre reinforced polyethylene composites. *J. Polym. Eng.* 17, 383–404. doi: 10.1515/POLYENG.1997.17.5.383

Joseph, P. V., Joseph, K., Thomas, S., Pillai, C. K. S., Prasad, V. S., Groeninckx, G., et al. (2003). The thermal and crystallization studies of polypropylene composites. *Compos. Part A Appl. Sci. Manufact.* 34, 253–266. doi: 10.1016/S1359-835X(02)00185-9

Joseph, S., and Thomas, S. (2008). Electrical properties of banana fiber reinforced phenol formaldehyde composites. *J. Appl. Polym. Sci.* 109, 256–263. doi: 10.1002/app.27452

Kabir, M. M., Wang, H., Lau, K. T., and Cardona, F. (2012). Chemical treatments on plant-based natural fibre reinforced polymer composites: an overview. *Compos. Part B Eng.* 43, 2883–2892. doi: 10.1016/j.compositesb.2012.04.053

Kaith, B. S., and Kalia, S. (2007). Grafting of flax fiber (*Linum usitatissimum*) with vinyl monomers for enhancement of properties of flax-phenolic composites. *Polym. J.* 39, 1319–1327. doi: 10.1295/polymj.PJ2007073

Kengkhetkit, N., and Amornsakchai, T. (2012). Utilisation of pineapple leaf waste for plastic reinforcement: 1. A novel extraction method for short pineapple leaf fiber. *Ind. Crops Prod.* 40, 55–61. doi: 10.1016/j.indcrop.2012.02.037

Khan, J. A., and Khan, M. A. (2014). "The use of jute fibers as reinforcements in composites", in *Biofiber Reinforcements in Composite Materials*, eds O. Faruk and M. Sain (Woodhead Publishing), 3-34. doi: 10.1533/9781782421276.1.3

Khan, M. A., Hassan, M. M., and Drzal, L. T. (2005). Effect of 2-hydroxyethyl methacrylate (HEMA) on the mechanical and thermal properties of jute-polycarbonate composite. *Compos. Part A Appl. Sci. Manufact.* 36, 71–81. doi: 10.1016/S1359-835X(04)00178-2

Khan, M. A., Hassan, M. M., Taslima, R., and Mustafa, A. I. (2006). Role of pretreatment with potassium permanganate and urea on mechanical and degradable properties of photocured coir (cocos nucifera) fiber with 1,6-hexanediol diacrylate. *J. Appl. Polym. Sci.* 100, 4361–4368. doi: 10.1002/app.23863

Khondker, O. A., Ishiaku, U. S., Nakai, A., and Hamada, H. (2005). Fabrication and mechanical properties of unidirectional jute/PP composites using jute yarns by film stacking method. *J. Polym. Environ.* 13, 115–126. doi: 10.1007/s10924-005-2943-y

Kicinska-Jakubowska, A., Bogacz, E., and Zimniewska, M. (2012). Review of natural fibers. Part I—vegetable fibers. *J. Nat. Fibers* 9, 150–167. doi: 10.1080/15440478.2012.703370

Kinloch, A. J., Taylor, A. C., Techapaitoon, M., Teo, W. S., and Sprenger, S. (2015). Tough, natural-fibre composites based upon epoxy matrices. *J. Mater. Sci.* 50, 6947–6960. doi: 10.1007/s10853-015-9246-z

Kipriotis, E., Heping, X., Vafeiadakis, T., Kiprioti, M., and Alexopoulou, E. (2015). Ramie and kenaf as feed crops. *Ind. Crops Prod.* 68, 126–130. doi: 10.1016/j.indcrop.2014.10.002

Komuraiah, A., Kumar, N. S., and Prasad, B. D. (2014). Chemical composition of natural fibers and its influence on their mechanical properties. *Mech. Compos. Mat.* 50, 359–376. doi: 10.1007/s11029-014-9422-2

Ku, H., Wang, H., Pattarachaiyakoop, N., and Trada, M. (2011). A review on the tensile properties of natural fiber reinforced polymer composites. *Compos. Part B Eng.* 42, 856–873. doi: 10.1016/j.compositesb.2011.01.010

Laftah, W. A., and Abdul Rahaman, W. A. W. (2015). Chemical pulping of waste pineapple leaves fiber for kraft paper production. *J. Mater. Res. Technol.* 4, 254–261. doi: 10.1016/j.jmrt.2014.12.006

Lanzilao, G., Goswami, P., and Blackburn, R. S. (2016). Study of the morphological characteristics and physical properties of Himalayan giant nettle (*Girardinia diversifolia* L.) fibre in comparison with European nettle (*Urtica dioica* L.) fibre. *Mater. Lett.* 181, 200–203. doi: 10.1016/j.matlet.2016.06.044

Lau, K., Hung, P., Zhu, M. H., and Hui, D. (2018). Properties of natural fibre composites for structural engineering applications. *Compos. Part B Eng.* 136, 222–233. doi: 10.1016/j.compositesb.2017.10.038

Li, X., Tabil, L. G., and Panigrahi, S. (2007). Chemical treatments of natural fiber for use in natural fiber-reinforced composites: a review. *J. Polym. Environ.* 15, 25–33. doi: 10.1007/s10924-006-0042-3

Li, Y., Mai, Y., and Ye, L. (2000). Sisal® bre and its composites : a review of recent developments IM PA US AS DO ME US EX ON AS. *Compos. Sci. Technol.* 60, 2037–2055. doi: 10.1016/S0266-3538(00)00101-9

Li, Z., Wang, X., and Wang, L. (2006). Properties of hemp fibre reinforced concrete composites. *Compos. Part A Appl. Sci. Manuf.* 37, 497–505. doi: 10.1016/j.compositesa.2005.01.032

Liu, R., Lv, W., Wang, X., Zhai, M., Dong, P., and Wang, Z. (2018). Carbonization and combustion characteristics of palm fiber. *Fuel* 227, 21–26. doi: 10.1016/j.fuel.2018.02.088

Liu, W., Mohanty, A. K., Drzal, L. T., Askeland, P., and Misra, M. (2004). Effects of alkali treatment on the structure, morphology and thermal properties of native grass fibers as reinforcements for polymer matrix composites. *J. Mater. Sci.* 39:1051. doi: 10.1023/B:JMSC.0000012942.83614.75

Liu, W., Mohanty, A. K., Drzal, L. T., and Misra, M. (2005). Novel biocomposites from native grass and soy based bioplastic: processing and properties evaluation. *Ind. Eng. Chem. Res.* 44, 7105–7112. doi: 10.1021/ie050257b

Madhu, P., Sanjay, M. R., Pradeep, S., Subrahmanya Bhat, K., Yogesha, B., and Siengchin, S. (2019a). Characterization of cellulosic fibre from Phoenix pusilla leaves as potential reinforcement for polymeric composites. *J. Mater. Res. Technol.* 8, 2597–2604. doi: 10.1016/j.jmrt.2019.03.006

Madhu, P., Sanjay, M. R., Senthamaraikannan, P., Pradeep, S., Saravanakumar, S. S., and Yogesha, B. (2019b). A review on synthesis and characterization of commercially available natural fibers: Part II. *J. Nat. Fibers* 16, 25–36. doi: 10.1080/15440478.2017.1379045

Madhu, P., Sanjay, M. R., Senthamaraikannan, P., Pradeep, S., Siengchin, S., Jawaid, M., et al. (2018). Effect of various chemical treatments of prosopis juliflora fibers as composite reinforcement: physicochemical, thermal, mechanical, and morphological properties. *J. Nat. Fibers* 00, 1–12. doi: 10.1080/15440478.2018.1534191

Mahjoub, R., Yatim, J. M., Mohd Sam, A. R., and Hashemi, S. H. (2014). Tensile properties of kenaf fiber due to various conditions of chemical fiber surface modifications. *Constr. Build. Mater.* 55, 103–113. doi: 10.1016/j.conbuildmat.2014.01.036

Manikandan Nair, K. C., Thomas, S., and Groeninckx, G. (2001). Thermal and dynamic mechanical analysis of polystyrene composites reinforced with short sisal fibres. *Compos. Sci. Technol.* 61, 2519–2529. doi: 10.1016/S0266-3538(01)00170-1

Manimaran, P., Senthamaraikannan, P., Murugananthan, K., and Sanjay, M. R. (2018). Physicochemical properties of new cellulosic fibers from *Azadirachta indica* Plant. *J. Nat. Fibers* 15, 29–38. doi: 10.1080/15440478.2017.1302388

Manimaran, P., Senthamaraikannan, P., Sanjay, M. R., Marichelvam, M. K., and Jawaid, M. (2017). Study on characterization of furcraea foetida new natural fiber as composite reinforcement for lightweight applications. *Carbohydr. Polym.* 181, 650–658. doi: 10.1016/j.carbpol.2017.11.099

Marsyahyo, E., Jamasri, H. S. B., and Soekrisno (2009). Preliminary investigation on bulletproof panels made from ramie fiber reinforced composites for NIJ Level II, IIA, and IV. *J. Ind. Text.* 39, 13–26. doi: 10.1177/1528083708098913

Martin, N., Mouret, N., Davies, P., and Baley, C. (2013). Influence of the degree of retting of flax fibers on the tensile properties of single fibers and short fiber/polypropylene composites. *Ind. Crops Prod.* 49, 755–767. doi: 10.1016/j.indcrop.2013.06.012

Masri, T., Ounis, H., Sedira, L., Kaci, A., and Benchabane, A. (2018). Characterization of new composite material based on date palm leaflets and expanded polystyrene wastes. *Constr. Build. Mater.* 164, 410–418. doi: 10.1016/j.conbuildmat.2017.12.197

McGregor, B. A. (2018). "Physical, chemical, and tensile properties of cashmere, mohair, alpaca, and other rare animal fibers" in *Handbook of Properties of Textile and Technical Fibres*, ed A. R. Bunsell (Woodhead Publishing), 105-136. doi: 10.1016/B978-0-08-101272-7.00004-3

Mihai, M. (2013). Novel polylactide/triticale straw biocomposites : processing, formulation, and properties. *Polym. Eng. Sci.* 54. doi: 10.1002/pen.23575

Mishra, S., Mohanty, A. K., Drzal, L. T., Misra, M., Parija, S., Nayak, S. K., et al. (2003). Studies on mechanical performance of biofibre/glass reinforced polyester hybrid composites. *Compos. Sci. Technol.* 63, 1377-1385. doi: 10.1016/S0266-3538(03)00084-8

Mochane, M. J., Mokhena, T. C., Mokhothu, T. H., Mtibe, A., Sadiku, E. R., Ray, S. S., et al. (2019). Recent progress on natural fiber hybrid composites for advanced applications: a review. *Express Polym. Lett.* 13, 159–198. doi: 10.3144/expresspolymlett.2019.15

Mohammed, L., Ansari, M. N. M., Pua, G., Jawaid, M., and Islam, M. S. (2015). A review on natural fiber reinforced polymer composite and its applications. *Int. J. Polym. Sci.* 2015, 1–15. doi: 10.1155/2015/243947

Monteiro, S. N., Satyanarayana, K. G., Ferreira, A. S., Nascimento, D. C. O., Lopes, F. P. D., Silva, I. L. A., et al. (2010). Selection of high strength natural fibers. *Rev. Mater.* 15, 488–505. doi: 10.1590/S1517-70762010000400002

Mortazavi, S. M., and Moghaddam, M. K. (2010). An analysis of structure and properties of a natural cellulosic fiber (Leafiran). *Fibers Polym.* 11, 877–882. doi: 10.1007/s12221-010-0877-z

Murugesh Babu, K. (2016). "Silk from silkworms and spiders as high- performance fibers," in *Structure and Properties of High-Performance Fibers*, ed G. Bhat (Woodhead Publishing), 27-366. doi: 10.1016/B978-0-08-100550-7.00013-9

Mwaikambo, L. Y., and Ansell, M. P. (2002). Chemical modification of hemp, sisal, jute, and kapok fibers by alkalization. *J. Appl. Polym. Sci.* 84, 2222–2234. doi: 10.1002/app.10460

Mwaikambo, L. Y., Martuscelli, E., and Avella, M. (2000). Kapok/cotton fabric-polypropylene composites. *Polym. Test.* 19, 905–918. doi: 10.1016/S0142-9418(99)00061-6

Nair, K. P. P. (ed.) (2010). "The coconut palm (Cocos nucifera L.)," in *The Agronomy and Economy of Important Tree Crops of the Developing World* (Elsevier Ltd.), 67–109. doi: 10.1016/B978-0-12-384677-8.00003-5

Nam, S., and Netravali, A. N. (2006). Green composites. I. Physical properties of ramie fibers for environment-friendly green composites. *Fibers Polym.* 7, 372–379. doi: 10.1007/BF02875769

Nasser, R. A., Salem, M. Z. M., Hiziroglu, S., Al-Mefarrej, H. A., Mohareb, A. S., Alam, M., et al. (2016). Chemical analysis of different parts of date palm (*Phoenix dactylifera* L.) using ultimate, proximate and thermo-gravimetric techniques for energy production. *Energies* 9:374. doi: 10.3390/en9050374

Naveen, J., Jawaid, M., Amuthakkannan, P., and Chandrasekar, M. (2018). "Mechanical and physical properties of sisal and hybrid sisal fiber-reinforced polymer composites," in *Mechanical and Physical Testing of Biocomposites, Fibre-Reinforced Composites and Hybrid Composites*, eds M. Jawaid, M. Thariq, and N. Saba (Woodhead Publishing), 427-440. doi: 10.1016/B978-0-08-102292-4.00021-7

Nirmal, U., Hashim, J., and Megat Ahmad, M. M. H. (2015). A review on tribological performance of natural fibre polymeric composites. *Tribol. Int.* 83, 77–104. doi: 10.1016/j.triboint.2014.11.003

Nishino, T., Hirao, K., Kotera, M., Nakamae, K., and Inagaki, H. (2003). Kenaf reinforced biodegradable composite. *Compos. Sci. Technol.* 63, 1281–1286. doi: 10.1016/S0266-3538(03)00099-X

Oksman, K. (2001). High quality flax fibre composites manufactured by the resin transfer moulding process. *J. Reinf. Plast. Compos.* 20, 621–627. doi: 10.1177/073168401772678634

Oksman, K., Aitomäki, Y., Mathew, A. P., Siqueira, G., Zhou, Q., Butylina, S., et al. (2016). Review of the recent developments in cellulose nanocomposite processing. *Compos. Part A Appl. Sci. Manuf.* 83, 2–18. doi: 10.1016/j.compositesa.2015.10.041

Omar, M. F., Jaya, H., and Zulkepli, N. N. (2019). "Kenaf fiber reinforced composite in the automotive industry," in *Module in Materials Science and Materials Engineering* (Elsevier Ltd.). doi: 10.1016/B978-0-12-803581-8.11429-8

Osorio, L., Trujillo, E., Van Vuure, A. W., and Verpoest, I. (2011). Morphological aspects and mechanical properties of single bamboo fibers and flexural characterization of bamboo/ epoxy composites. *J. Reinf. Plast. Compos.* 30, 396–408. doi:,: 10.1177/0731684410397683

Panaitescu, D. M., Nicolae, C. A., Vuluga, Z., Vitelaru, C., Sanporean, C. G., Zaharia, C., et al. (2016). Influence of hemp fibers with modified surface on polypropylene composites. *J. Ind. Eng. Chem.* 37, 137–146. doi: 10.1016/j.jiec.2016.03.018

Pandey, J. K., Ahn, S. H., Lee, C. S., Mohanty, A. K., and Misra, M. (2010). Recent advances in the application of natural fiber based composites. *Macro Mater. Eng.* 295, 975–989. doi: 10.1002/mame.201000095

Paridah, M. T., Arib, R. M. N., Sapuan, S. M., Zaman, H. M. D. K., and Ahmad, M. M. H. M. (2004). Mechanical properties of pineapple leaf fibre reinforced polypropylene composites. *Mater. Des.* 27, 391–396. doi: 10.1016/j.matdes.2004.11.009

Paul, A., Joseph, K., and Thomas, S. (1997). Effect of surface treatments on the electrical properties of low-density polyethylene composites reinforced with short sisal fibers. *Compos. Sci. Technol.* 57, 67–79. doi: 10.1016/S0266-3538(96)00109-1

Pham, L. J. (2016). *Coconut (Cocos nucifera).* AOCS Press. doi: 10.1016/B978-1-893997-98-1.00009-9

Pickering, K. L., Efendy, M. G. A., and Le, T. M. (2016). A review of recent developments in natural fibre composites and their mechanical performance. *Compos. Part A Appl. Sci. Manuf.* 83, 98–112. doi: 10.1016/j.compositesa.2015.08.038

Prachayawarakorn, J., Chaiwatyothin, S., Mueangta, S., and Hanchana, A. (2013). Effect of jute and kapok fibers on properties of thermoplastic cassava starch composites. *Mater. Des.* 47, 309–315. doi: 10.1016/j.matdes.2012.12.012

Preet Singh, J. I., Dhawan, V., Singh, S., and Jangid, K. (2017). Study of effect of surface treatment on mechanical properties of natural fiber reinforced composites. *Mater. Today Proc.* 4, 2793–2799. doi: 10.1016/j.matpr.2017.02.158

Puttegowda, M., Rangappa, S. M., Jawaid, M., Shivanna, P., Basavegowda, Y., and Saba,N. (2018). "Potential of natural/synthetic hybrid composites for aerospace applications," in *Sustainable Composites for Aerospace Applications*, eds M. Jawaid and M. Thariq (Woodhead Publishing), 315-351. doi: 10.1016/B978-0-08-102131-6.00021-9

Rahman, M. S. (2010). "Jute-a versatile natural fibre. Cultivation, extraction and processing," in *Industrial Applications of Natural Fibres Industrial Applications of Natural Fibres: Structure, Properties and Technical Applications,* ed J. Müssig (Wiley), 135–161. doi: 10.1002/9780470660324.ch6

Raman Bharath, V. R., Vijaya Ramnath, B., and Manoharan, N. (2015). Kenaf fibre reinforced composites: a review. *ARPN J. Eng. Appl. Sci.* 10, 5483–5485.

Ramesh, M. (2019). Flax (*Linum usitatissimum* L.) fibre reinforced polymer composite materials: a review on preparation, properties and prospects. *Prog. Mater. Sci.* 102, 109–166. doi: 10.1016/j.pmatsci.2018.12.004

Ramesh, M., Palanikumar, K., and Reddy, K. H. (2013). Mechanical property evaluation of sisal-jute-glass fiber reinforced polyester composites. *Compos. Part B Eng.* 48, 1-9. doi: 10.1016/j.compositesb.2012.12.004

Rangappa, S. M., and Siengchin, S. (2018). Natural fibers as perspective materials. *KMUTNB Int. J. Appl. Sci. Technol.* 11:2018. doi: 10.14416/j.ijast.2018.09.001

Reddy, K. O., Maheswari, C. U., Shukla, M., and Rajulu, A. V. (2012). Chemical composition and structural characterization of Napier grass fibers. *Mater. Lett.* 67, 35–38. doi: 10.1016/j.matlet.2011.09.027

Reddy, N., and Yang, Y. (2015) "Bacterial cellulose fibers," in *Innovative Biofibers from Renewable Resources* (Berlin; Heidelberg: Springer), 307-329. doi: 10.1007/978-3-662-45136-6_61

Rehman, M., Gang, D., Liu, Q., Chen, Y., Wang, B., Peng, D., et al. (2019). Ramie, a multipurpose crop: potential applications, constraints and improvement strategies. *Ind. Crops Prod.* 137, 300–307. doi: 10.1016/j.indcrop.2019.05.029

Réquilé, S., Le Duigou, A., Bourmaud, A., and Baley, C. (2018). Peeling experiments for hemp retting characterization targeting biocomposites. *Ind. Crops Prod.* 123, 573–580. doi: 10.1016/j.indcrop.2018.07.012

Rivera, D., Obón, C., Alcaraz, F., Laguna, E., and Johnson, D. (2019). Date-palm (Phoenix, Arecaceae) iconography in coins from the Mediterranean and West Asia (485 BC−1189 AD). *J. Cult. Herit.* 37, 199–214. doi: 10.1016/j.culher.2018.10.010

Rokbi, M., Osmani, H., Imad, A., and Bensediq, N. (2011). Effect of chemical treatment on flexure properties of natural fiber-reinforced polyester composite. *Proc. Eng.* 10, 2092–2097. doi: 10.1016/j.proeng.2011.04.346

Rong, M. Z., Zhang, M. Q., Liu, Y., Yang, G. C., and Zeng, H. M. (2001). The effect of fiber treatment on the mechanical properties of unidirectional sisal-reinforced epoxy composites. *Compos. Sci. Technol.* 61, 1437–1447. doi: 10.1016/S0266-3538(01)00046-X

Ruan, P., Du, J., Gariepy, Y., and Raghavan, V. (2015). Characterization of radio frequency assisted water retting and flax fibers obtained. *Ind. Crops Prod.* 69, 228–237. doi: 10.1016/j.indcrop.2015.02.009

Saba, N., Paridah, M. T., and Jawaid, M. (2015). Mechanical properties of kenaf fibre reinforced polymer composite: a review. *Constr. Build. Mater.* 76, 87–96. doi: 10.1016/j.conbuildmat.2014.11.043

Saba, N., Tahir, P. M., and Jawaid, M. (2014). A review on potentiality of nano filler/natural fiber filled polymer hybrid composites. *Polymers (Basel).* 6, 2247–2273. doi: 10.3390/polym6082247

Sam-Brew, S., and Smith, G. D. (2015). Flax and Hemp fiber-reinforced particleboard. *Ind. Crops Prod.* 77, 940–948. doi: 10.1016/j.indcrop.2015.09.079

Sanjay, M. R., Arpitha, G. R., Naik, L. L., Gopalakrishna, K., and Yogesha, B. (2016). Applications of natural fibers and its composites: an overview. *Nat. Resour.* 7, 108–114. doi: 10.4236/nr.2016.73011

Sanjay, M. R., Arpitha, G. R., Senthamaraikannan, P., Kathiresan, M., Saibalaji, M. A., and Yogesha, B. (2019a). The hybrid effect of jute/kenaf/e-glass woven fabric epoxy composites for medium load applications: impact, inter-laminar strength, and failure surface characterization. *J. Nat. Fibers* 16, 600–612. doi: 10.1080/15440478.2018.1431828

Sanjay, M. R., Arpitha, G. R., and Yogesha, B. (2015). Study on mechanical properties of natural - glass fibre reinforced polymer hybrid composites : a review. *Mater. Today Proc.* 2, 2959–2967. doi: 10.1016/j.matpr.2015.07.264

Sanjay, M. R., Madhu, P., Jawaid, M., Senthamaraikannan, P., Senthil, S., and Pradeep, S. (2018). Characterization and properties of natural fiber polymer composites: a comprehensive review. *J. Clean. Prod.* 172, 566-581. doi: 10.1016/j.jclepro.2017.10.101

Sanjay, M. R., Siengchin, S., Parameswaranpillai, J., Jawaid, M., Pruncu, C. I., and Khan, A. (2019b). A comprehensive review of techniques for natural fibers as reinforcement in composites: preparation, processing and characterization. *Carbohydr. Polym.* 207, 108–121. doi: 10.1016/j.carbpol.2018.11.083

Sanjay, M. R., and Suchart, S. (2019). Lightweight natural fiber composites. *J. Appl. Agric. Sci. Technol.* 3:178. doi: 10.32530/jaast.v3i2.108

Santhosh Kumar, S., and Hiremath, S. S. (2019). "Natural fiber reinforced composites in the context of biodegradability: a review," in *Reference Module in Materials Science and Materials Engineering* (Elsevier Ltd.). doi: 10.1016/B978-0-12-803581-8.11418-3

Saravanakumaar, A., Senthilkumar, A., Saravanakumar, S. S., and Sanjay, M. R. (2018). Impact of alkali treatment on physico-chemical, thermal, structural and tensile properties of Carica papaya bark fibers. *Int. J. Polym. Anal. Charact.* 23, 529–536. doi: 10.1080/1023666X.2018.1501931

Saravanakumar, S. S., Kumaravel, A., Nagarajan, T., and Moorthy, I. G. (2014). Effect of chemical treatments on physicochemical properties of *Prosopis juliflora* fibers. *Int. J. Polym. Anal. Charact.* 19, 383–390. doi: 10.1080/1023666X.2014.903585

Sawpan, M. A., Pickering, K. L., and Fernyhough, A. (2011). Improvement of mechanical performance of industrial hemp fibre reinforced polylactide biocomposites. *Compos. Part A Appl. Sci. Manuf.* 42, 310–319. doi: 10.1016/j.compositesa.2010.12.004

Sen, T., and Jagannatha Reddy, H. N. (2011a). Application of sisal, bamboo, coir and jute natural composites in structural upgradation. *Int. J. Innov. Manag. Technol.* 2:186.

Sen, T., and Jagannatha Reddy, H. N. (2011b). Various industrial applications of hemp, kinaf, flax and ramie natural fibres. *Int. J. Innov. Manag. Technol.* 2.

Sengupta, S., and Basu, G. (2016). Properties of coconut fiber. *Ref. Modul. Mater. Sci. Mater. Eng.* doi: 10.1016/B978-0-12-803581-8.04122-9

Senthamaraikannan, P., and Kathiresan, M. (2018). Characterization of raw and alkali treated new natural cellulosic fiber from *Coccinia grandis*.L. *Carbohydr. Polym.* 186, 332–343. doi: 10.1016/j.carbpol.2018.01.072

Senthamaraikannan, P., Saravanakumar, S. S., Arthanarieswaran, V. P., and Sugumaran, P. (2016). Physico-chemical properties of new cellulosic fibers from the bark of Acacia planifrons. *Int. J. Polym. Anal. Charact.* 21, 207–213. doi: 10.1080/1023666X.2016.1133138

Senthilkumar, K., Saba, N., Rajini, N., Chandrasekar, M., Jawaid, M., Siengchin, S., et al. (2018). Mechanical properties evaluation of sisal fibre reinforced polymer composites: a review. *Constr. Build. Mater.* 174, 713–729. doi: 10.1016/j.conbuildmat.2018.04.143

Senthilkumar, K., Saba, N. R. N., Jawaid, M. C. M., and Siengchin, S. (2019). Effect of alkali treatment on mechanical and morphological properties of pineapple leaf fibre/polyester composites. *J. Polym. Environ.* 27, 1191–1201. doi: 10.1007/s10924-019-01418-x

Sepe, R., Bollino, F., Boccarusso, L., and Caputo, F. (2018). Influence of chemical treatments on mechanical properties of hemp fiber reinforced composites. *Compos. Part B Eng.* 133, 210–217. doi: 10.1016/j.compositesb.2017.09.030

Sgriccia, N., Hawley, M. C., and Misra, M. (2008). Characterization of natural fiber surfaces and natural fiber composites. *Compos. Part A Appl. Sci. Manuf.* 39, 1632–1637. doi: 10.1016/j.compositesa.2008.07.007

Shahinur, S., and Hasan, M. (2019a). "Jute/coir/banana fiber reinforced biocomposites: critical review of design, fabrication, properties and applications," in *Reference Module in Materials Science and Materials Engineering* (Elsevier Ltd.). doi: 10.1016/B978-0-12-803581-8.10987-7

Shahinur, S., and Hasan, M. (2019b). Natural fiber and synthetic fiber composites: comparison of properties, performance, cost and environmental benefits," in *Reference Module in Materials Science and Materials Engineering* (Elsevier Ltd.). doi: 10.1016/B978-0-12-803581-8.10994-4

Sharma, P., Pandey, A. K., and Srivastava, A. (2017). "Tensile and impact strength analysis of cotton fiber reinforced polymer composites," in *Arimpie.* Available online at: https://www.elkjournals.com/microadmin/UploadFolder/3781paper%2042.pdf.

Shera, S. S., Kulhar, N., and Banik, R. M. (2019). "Silk and silk fibroin-based biopolymeric composites and their biomedical applications," in *Materials for Biomedical Engineering*, eds V. Grumezescu and A. Mihai Grumezescu (Elsevier), 339-374. doi: 10.1016/B978-0-12-816872-1.00012-1

Shinoj, S., Visvanathan, R., Panigrahi, S., and Kochubabu, M. (2011). Oil palm fiber (OPF) and its composites: a review. *Ind. Crops Prod.* 33, 7–22. doi: 10.1016/j.indcrop.2010.09.009

Shuit, S. H., Tan, K. T., Lee, K. T., and Kamaruddin, A. H. (2009). Oil palm biomass as a sustainable energy source: a Malaysian case study. *Energy* 34, 1225–1235. doi: 10.1016/j.energy.2009.05.008

Singh, B., Gupta, M., and Verma, A. (1996). Influence of fiber surface treatment on the properties of sisal-polyester composites. *Poly. Compos.* 17, 910–918. doi: 10.1002/pc.10684

Sood, M., and Dwivedi, G. (2018). Effect of fiber treatment on flexural properties of natural fiber reinforced composites: a review. *Egypt. J. Pet.* 27, 775–783. doi: 10.1016/j.ejpe.2017.11.005

Sreekala, M. S., Kumaran, M. G., Joseph, S., Jacob, M., and Thomas, S. (2000). Oil palm fibre reinforced phenol formaldehyde composites: influence of fibre surface modifications on the mechanical performance. *Appl. Compos. Mater.* 7, 295–329. doi: 10.1023/A:1026534006291

Sreekala, M. S., Kumaran, M. G., and Thomas, S. (2002). Water sorption in oil palm fiber reinforced phenol formaldehyde composites. *Compos. Part A Appl. Sci. Manuf.* 33, 763–777. doi: 10.1016/S1359-835X(02)00032-5

Sreekala, M. S., and Thomas, S. (2003). Effect of fibre surface modification on water-sorption characteristics of oil palm fibres. *Compos. Sci. Technol.* 63, 861–869. doi: 10.1016/S0266-3538(02)00270-1

Sreenivasan, V. S., Ravindran, D., Manikandan, V., and Narayanasamy, R. (2012). Influence of fibre treatments on mechanical properties of short Sansevieria cylindrica/polyester composites. *Mater. Des.* 37, 111–121. doi: 10.1016/j.matdes.2012.01.004

Steffens, F., Steffens, H., and Oliveira, F. R. (2017). Applications of natural fibers on architecture. *Proc. Eng.* 200, 317–324. doi: 10.1016/j.proeng.2017.07.045

Suharty, N. S., Ismail, H., Diharjo, K., Handayani, D. S., and Firdaus, M. (2016). Effect of kenaf fiber as a reinforcement on the tensile, flexural strength and impact toughness properties of recycled polypropylene/halloysite composites. *Proc. Chem.* 19, 253–258. doi: 10.1016/j.proche.2016.03.102

Thakur, V. K., and Thakur, M. K. (2014). Processing and characterization of natural cellulose fibers/thermoset polymer composites. *Carbohydr. Polym.* 109, 102–117. doi: 10.1016/j.carbpol.2014.03.039

Thakur, V. K., Thakur, M. K., and Gupta, R. K. (2014). Review: raw natural fiber-based polymer composites. *Int. J. Polym. Anal. Charact.* 19, 256–271. doi: 10.1080/1023666X.2014.880016

Thiagamani, S. M. K., Krishnasamy, S., and Siengchin, S. (2019). Challenges of biodegradable polymers: an environmental perspective. *Appl. Sci. Eng. Prog.* 12, 2019. doi: 10.14416/j.asep.2019.03.002

Threepopnatkul, P., Kaerkitcha, N., and Athipongarporn, N. (2009). Composites: Part B Effect of surface treatment on performance of pineapple leaf fiber – polycarbonate composites. *Compos. Part B* 40, 628–632. doi: 10.1016/j.compositesb.2009.04.008

Ticoalu, A., Aravinthan, T., and Cardona, F. (2010). "A review of current development in natural fiber composites for structural and infrastructure applications," in *Southern Region Engineering Conference 11–12 November 2010, Toowoomba, Australia*, 1–5.

Todkar, S. S., and Patil, S. A. (2019). Review on mechanical properties evaluation of pineapple leaf fibre (PALF) reinforced polymer composites. *Compos. Part B Eng.* 2019:106927. doi: 10.1016/j.compositesb.2019.106927

Tye, Y. Y., Lee, K. T., Wan Abdullah, W. N., and Leh, C. P. (2012). Potential of *Ceiba pentandra* (L.) Gaertn. (kapok fiber) as a resource for second generation bioethanol: effect of various simple pretreatment methods on sugar production. *Bioresour. Technol.* 116, 536–539. doi: 10.1016/j.biortech.2012.04.025

Väisänen, T., Batello, P., Lappalainen, R., and Tomppo, L. (2018). Modification of hemp fibers (*Cannabis sativa* L.) for composite applications. *Ind. Crops Prod.* 111, 422–429. doi: 10.1016/j.indcrop.2017.10.049

Van Dam, J. E. G., Elbersen, H. W., and Daza Montaño, C. M. (2018). "Bamboo production for industrial utilization," in *Perennial Grassesfor Bioenergy and Bioproducts*, ed E. Alexopoulou (Academic Press; Elsvier), 175-216. doi: 10.1016/B978-0-12-812900-5.00006-0

Van de Weyenberg, I., Ivens, J., De Coster, A., Kino, B., Baetens, E., and Verpoest, I. (2003). Influence of processing and chemical treatment of flax fibres on their composites. *Compos. Sci. Technol.* 63, 1241–1246. doi: 10.1016/S0266-3538(03)00093-9

Varghese, A. M., and Mittal, V. (2017). "Surface modification of natural fibers," in *Biodegradable and Biocompatible Polymer Composites*, ed N. Gopal Shimpi (Woodhead Publishing), 115–155. doi: 10.1016/B978-0-08-100970-3.00005-5

Verma, D., and Gope, P. C. (2014). "The use of coir/coconut fibers as reinforcements in composites," in *Biofiber Reinforcements in Composite Materials*, eds O. Faruk and M. Sain (Elsevier Ltd.), 285–319. doi: 10.1533/9781782421276.3.285

Wales, N., and Blackman, B. K. (2017). Plant domestication: wild date palms illuminate a crop's sticky origins. *Curr. Biol.* 27, R702–R704. doi: 10.1016/j.cub.2017.05.070

Wambua, P., Ivens, J., and Verpoest, I. (2003). Natural fibres: can they replace glass in fibre reinforced plastics? *Compos. Sci. Technol.* 63, 1259–1264. doi: 10.1016/S0266-3538(03)00096-4

Wang, G., and Chen, F. (2016). "Development of bamboo fiber-based composites," in *Advanced High Strength Natural Fibre Composites in Construction,* ed M. Fan and F. Fu (Elsevier Ltd.), 235–255. doi: 10.1016/B978-0-08-100411-1.00010-8

Wang, H., Memon, H., Hassan, E. A. M., Miah, S., and Ali, A. (2019). Effect of jute fiber modification on mechanical properties of jute fiber composite. *Materials (Basel)* 12:E1226. doi: 10.3390/ma12081226

Xie, Y., Hill, C. A. S., Xiao, Z., Militz, H., and Mai, C. (2010). Silane coupling agents used for natural fiber/polymer composites: a review. *Compos. Part A Appl. Sci. Manuf.* 41, 806–819. doi: 10.1016/j.compositesa.2010.03.005

Xin, X., Xu, C. G., and Qing, L. F. (2007). Friction properties of sisal fibre reinforced resin brake composites. *Wear* 262, 736–741. doi: 10.1016/j.wear.2006.08.010

Xu, Y., Salmi, J., Kloser, E., Perrin, F., Grosse, S., Denault, J., et al. (2013). Feasibility of nanocrystalline cellulose production by endoglucanase treatment of natural bast fibers. *Ind. Crops Prod.* 51, 381–384. doi: 10.1016/j.indcrop.2013.09.029

Yang, G., Park, M., and Park, S.-J. (2019). Recent progresses of fabrication and characterization of fibers-reinforced composites: a review. *Compos. Commun.* 14, 34–42. doi: 10.1016/j.coco.2019.05.004

Yashas Gowda, T. G., Sanjay, M. R., Subrahmanya Bhat, K., Madhu, P., Senthamaraikannan, P., and Yogesha, B. (2018). Polymer matrix-natural fiber composites: an overview. *Cogent Eng.* 5, 1–13. doi: 10.1080/23311916.2018.1446667

Yogesha, B. (2017). ScienceDirect studies on natural / glass fiber reinforced polymer hybrid composites : an evolution. *Mater. Today Proc.* 4, 2739–2747. doi: 10.1016/j.matpr.2017.02.151

Yu, H., Wang, X., and Petru, M. (2019). The effect of surface treatment on the creep behavior of flax fiber reinforced composites under hygrothermal aging conditions. *Constr. Build. Mater* 208, 220–227. doi: 10.1016/j.conbuildmat.2019.03.001

Yuan, Q., Yao, J., Chen, X., Huang, L., and Shao, Z. (2010). The preparation of high performance silk fiber/fibroin composite. *Polymer (Guildf).* 51, 4843–4849. doi: 10.1016/j.polymer.2010.08.042

Zafeiropoulos, N. E., and Baillie, C. A. (2007). A study of the effect of surface treatments on the tensile strength of flax fibres: Part II. Application of Weibull statistics. *Compos. Part A Appl. Sci. Manuf.* 38, 629–638. doi: 10.1016/j.compositesa.2006.02.005

Zakikhani, P., Zahari, R., Sultan, M. T. H., and Majid, D. L. (2014). Extraction and preparation of bamboo fibre-reinforced composites. *Mater. Des.* 63, 820–828. doi: 10.1016/j.matdes.2014.06.058

Zaman, H. U., Khan, M. A., Khan, R. A., Rahman, M. A., Das, L. R., and Al-Mamun, M. (2010). Role of potassium permanganate and urea on the improvement of the mechanical properties of jute polypropylene composites. *Fibers Polym.* 11, 455–463. doi: 10.1007/s12221-010-0455-4

Zamri, M. H., Akil, H. M., and MohdIshak, Z. A. (2016). Pultruded kenaf fibre reinforced composites: effect of different kenaf fibre yarn tex. *Proc. Chem.* 19, 577–585. doi: 10.1016/j.proche.2016.03.056

Zegaoui, A., Ma, R., Dayo, A. Q., Derradji, M., Wang, J., Liu, W., et al. (2018). Morphological, mechanical and thermal properties of cyanate ester/benzoxazine resin composites reinforced by silane treated natural hemp fibers. *Chinese J. Chem. Eng.* 26, 1219–1228. doi: 10.1016/j.cjche.2018.01.008

Zhang, M. Q., Rong, M. Z., and Lu, X. (2005). Fully biodegradable natural fiber composites from renewable resources: all-plant fiber composites. *Compos. Sci. Technol.* 65, 2514–2525. doi: 10.1016/j.compscitech.2005.06.018

Zheng, Y., Wang, J., Zhu, Y., and Wang, A. (2015). Research and application of kapok fiber as an absorbing material: a mini review. *J. Environ. Sci. (China)* 27, 21–32. doi: 10.1016/j.jes.2014.09.026

Zhu, J., Zhu, H., Njuguna, J., and Abhyankar, H. (2013). Recent development of flax fibres and their reinforced composites based on different polymeric matrices. *Materials* 6, 5171–5198. doi: 10.3390/ma6115171

Zou, Y., Reddy, N., and Yang, Y. (2011). Reusing polyester/cotton blend fabrics for composites. *Compos. Part B Eng.* 42, 763–770. doi: 10.1016/j.compositesb.2011.01.022

Check for
updates

Accelerated Weathering and Water Absorption Behavior of Kenaf Fiber Reinforced Acrylic Based Polyester Composites

Muhamad Saifuddin Salim[1], Dody Ariawan[2], Mohd Fadli Ahmad Rasyid[1], Razaina Mat Taib[1], Mohd Zharif Ahmad Thirmizir[3] and Zainal Arifin Mohd Ishak[1,3]*

[1] School of Materials and Mineral Resources Engineering, Universiti Sains Malaysia, Nibong Tebal, Malaysia, [2] Mechanical Engineering Department, Engineering Faculty, Universitas Sebelas Maret, Surakarta, Indonesia, [3] Cluster for Polymer Composites, Science and Engineering Research Center, Universiti Sains Malaysia, Nibong Tebal, Malaysia

Non-woven kenaf fiber (KF) mat reinforced acrylic-based polyester resin composites were prepared by an impregnation process followed by compression molding. They were exposed to durability test of accelerated weathering and water absorption. Accelerated weathering test through UV irradiation caused modification in chemical, mechanical, surface appearance, and color change of the composites. Two competing reactions occurred throughout the exposure period, i.e., post-crosslinking and photo-oxidation process. FTIR analysis revealed that the former occurred at the early stage of exposure while the latter toward the end of the exposure, exhibited by an accentuated increase in carbonyl and vinyl index. The post-crosslinking process contributes to the improvement in flexural properties and thermal stability of the composites, whereas the oxidation process does not. SEM observation showed that the degradation by photo-oxidation resulted in the formation of voids and blisters on composite's sample. Water uptake of all composites was found to follow Fickian behavior. Good recoveries (exceeding 79%) of flexural properties were obtained upon re-drying. However, a significant reduction in flexural strength and modulus was obtained in the wet state condition. SEM observation revealed that full recovery was not possible because of the impairment of the—matrix interfacial region. Relatively higher flexural properties were exhibited by alkali-treated KF composites even after the durability test due to the improved strength and—matrix adhesion following the treatment.

Keywords: natural fiber reinforced composites, accelerated weathering degradation, water absorption, kenaf fiber mat, Acrodur resins

INTRODUCTION

The increase in environmental awareness is the vital factor that motivates many researchers to explore and develop new alternatives capable of replacing traditional polymer composite materials. The new alternatives (called "green composites") should have a lower negative environmental impact than the traditional polymer composite materials. Green composites can be defined as materials composed of, in part or wholly, constituents which come ultimately from a renewable resource (Baillie and Jayasinghe, 2004). This definition applies to the matrix and reinforcement

phase. Thus, by definition, natural fiber that reinforces polymer composites (NFPC) can be called green composites because the reinforcing fibers come from renewable sources. These fibers usually originated from some abundant plants, which make them inexpensive. Compared to inorganic-mineral like glass fiber, natural fibers are less abrasive toward processing machinery and tooling, less dangerous to the production employees in case of inhalation, and easy to be incinerated. They also lead to final composites with lower specific weight per strength, as well as, exhibiting thermal and acoustic insulation properties (Herrera-Franco and Valadez-González, 2004).

Current environmental concerns have stimulated interest in the recycling. Recyclability of NFPC is depending on the polymer matrices component either thermoplastic or thermosetting. Thermoplastics are easily recyclable as compared to thermosets because the polymer chain does not degrade when melted down, allowing this material to be reprocessed. On the other hand, thermoset matrix recycling is unfeasible because of the thoroughly cross-linked nature. Nevertheless, recent technologies are now being deployed in recycling thermoset composites. Recently, recycling thermoset composites could be carried out through mechanical recycling by grinding the thermoset composites into smaller particles/powder in order to be used as filler in other composites system or by thermal recycling for energy recovery (Pickering, 2006).

The industries are exploiting NFPC because of their lightweight characteristic and are cost-effective. These attributes make them as potential alternative materials to the expensive aramid, carbon, or glass fibers. Improved technology in manufacturing techniques in NFPC allows the automotive industry to use these composites for interior trimmings (Koronis et al., 2013). The first carmaker to use natural fibers as reinforcement in composites was Mercedes-Benz in the 90's, by manufacturing door panels from epoxy reinforced jute fibers composites (Rohit and Dixit, 2016). This trend was soon adopted by other major carmakers to fabricate various interior trimmings including roof upholstery, headrests, parcel shelves, and spare wheel cover using NFPC. Depending on the applications, it is sometimes necessary to improve the mechanical properties through the fiber pre-treatment, and the treated fibers are then used in several ways to obtain mats, non-woven structures, rowing etc. Among various types of natural fiber, kenaf fibers (KF; Hibiscus cannabinus) are largely grown in Malaysia because of climate suitability. The mechanical properties of KF are more or less identical to jute but are considered stronger, whiter and more lustrous (Umoru et al., 2014). The tensile strength and modulus are comparable to flax fiber, widely used in automotive parts of European cars (Karus and Kaup, 2002). Realizing the potential of KF for the manufacturing industry, the Malaysia government believe that this crop plant could be the third commodity plant of the nation after rubber and palm oil (Salim et al., 2019). The National Kenaf and Tobacco Board (NKTB) of Malaysia are playing a prominent role in promoting the usage of KF in various industries, including the automotive industry, in Malaysia.

Based on the polymer matrices point of view, the automotive industry demands a crucial characteristic and high selective polymer material in fulfilling the requirement of high

thermal stability and short processing time. Several works on conventional thermoset resins, such as polyester and vinyl ester, reported that these resins could reinforce natural fibers (Ariawan et al., 2017; Navaneethakrishnan and Athijayamani, 2017). However, the major drawback of these resins is the emission of styrene that occurs not only during processing, but also from the finished products. This limits the usage of these resins in the automotive industry, especially in the manufacturing interior trimmings for passenger cars (Islam and Miao, 2013). The introduction of environmentally friendly acrylic-based polyester resin by the trade name of Acrodur® resin by BASF has emerged as a new verdict in polymer binder technology. Dissimilar with traditional reactive resins, organic substances, for example, phenol or formaldehyde, are not released during the cross-linking process. Only water is the by-product during the cross-linking process (Karbstein et al., 2013). Below the crosslinking temperature, the resin exhibits thermoplastic properties allowing the resin to be processed using thermoplastic processing means. After the curing process, the material has thermoset properties with good chemical resistance, heat resistance and high structural integrity. The combination of ease processing, good mechanical properties, and environmentally friendly gives Acrodur® resin the enormous potential to be used as an alternative material in the automotive industry besides polyolefin thermoplastic. A prototype of natural fiber Acrodur® composites for the door trim of BMW 7 series has been developed recently by Dräxlmaier Group, Germany (Malnati, 2010).

In any application, the durability of materials is a serious concern. Environmental exposure, including sunlight exposure and moisture uptake during actual service, tends to degrade the natural fiber, especially at the exposed region. Besides, it degrades the polymer matrices that might deteriorate the mechanical properties of NFPC or even worse contribute to the parts failure during service. Durability in terms of environmental exposure is measured through the changes in mechanical performance, thermal, chemical, and the material appearances after experiencing a certain period of weathering test. Some commonest damaging effects in the composites are color fading, surface erosion, mechanical properties and weight losses which might shorten the service life of the product (Lopez et al., 2006). Water absorption property is another major factor that should be considered when dealing with NFPC. The characteristics of water absorption in NFPC are influenced by several factors: fiber content, fiber orientation, temperature, exposed surface area, fiber permeability, void content, and the hydrophilicity of individual components (Dhakal et al., 2007). The degradation of the fiber-matrix interface region due to the water absorption contributes to the reduction of stress transfer proficiencies; therefore, the mechanical properties of NFPC (Yang et al., 2011).

The properties of NFPC composites are determined by the constituent properties i.e., fiber and matrix as well as the properties of the fiber-matrix interface (Pothan et al., 2003). Excellent fiber-matrix interaction leads to an effective distribution of stress and load between fiber and matrix thus improving the mechanical strength of composites (Akil et al., 2011). The surface of the natural fibers can be modified physically

or chemically. However, the fundamental principle still remain the same i.e., removing the surface contamination and providing an intimate contact between the surfaces on a molecular scale (Mukhopadhyay and Fangueiro, 2009). The effective method is to roughen the surface of natural fiber to increase the contact area and facilitate mechanical interlocking (Edeerozey et al., 2007). Such surface modification would not only enhance the wettability of fibers toward polymer matrix that might improve the composite's strength, but would concurrently decrease the moisture absorption of the composites.

Alkali treatment or mercerization is one of the common chemical treatments that are proven to enhance the mechanical properties of the reinforced composites in several studies (Krishnan et al., 2018; Sepe et al., 2018). This treatment is by far the most efficient chemical treatment to improve the wettability of fibers toward resin and enhancing the fiber strength. It is interesting to discover that some studies reported a dramatically improve of natural fiber's tensile strength after elevated alkali treatment (Rong et al., 2001; Saha et al., 2010). Van de Weyenberg et al. (2006) pointed out that the enhancement of flexural and tensile properties of alkali treated flax fiber reinforced epoxy composites that they obtained were combination of better mechanical interlocking by the rougher topography, larger number of individual fibrils, and better chemical bonding owing to more hydroxyl groups on the fiber surface enable to form hydrogen bonds with the matrix resin. Besides improving the mechanical properties of NFPC, Sreekumar et al. (2009) also reported that alkali treated sisal fiber reinforced polyester composites absorbed less water at all water temperatures during hygrothermal test compared to the untreated one due to the removal of hydrophilic hemicellulose during alkalization. Heat treatment can be considered as an alternative ecological treatment as it does not required any usage of hazardous chemical. Several researchers found that this treatment has great influence in changing the mechanical properties, biological properties, color, hardness, and chemical properties of wood as lignocellulosic materials (Gündüz et al., 2008; Ates et al., 2009). In composite applications, previous research by Sreekumar et al. (2009) revealed that heat treatment of sisal fibers at 100°C for 4 h increased crystallinity and removed moisture in sisal fibers. This treatment resulted in the increase of tensile and flexural properties of sisal fiber composites, without significantly reducing the impact strength of composites like the alkali treatment, benzoylated, and permanganate treatment. In terms of durability toward natural weathering exposure, Ariawan et al. (2018) reported that alkali treated KF composite shows better durability compared to the heat treated KF composite particularly for the first 6 months exposure. However, they found that prolonged natural weathering exposure diminishes the effect of fiber treatment in enhancing mechanical properties.

To date, there have been several works done on the usage of Acrodur® resin in NFPC (Islam and Miao, 2013; Khalfallah et al., 2014; Salim et al., 2017). However, to the best of our knowledge, studies concerning weathering exposure to Acrodur® reinforced natural fiber composites have not been done. Previous study by the author has focused on the effect of fiber treatments toward the wettability and mechanical properties of Acrodur®

reinforced KF composites (Salim et al., 2019). Pursuant to that work, the current study aims to investigate the effect of fiber surface treatments i.e., alkali treatment, alkali treatment at elevated temperature and heat treatment toward the durability properties of the composites under an accelerated weathering exposure. This could be crucial in order to seek the viability of the composites to be used in automotive industry. Furthermore, excellent fiber to matrix adhesion following these treatments also might decrease the rate amount of water absorbed by the composites. Thus, the effect of surface treatment on water absorption properties of KF reinforced Acrodur® composites will also be reported in the current study.

MATERIALS AND METHODS

Materials
Untreated kenaf fiber (UTKF) was supplied by the National Kenaf and Tobacco Board (NKTB), Malaysia. These fibers then underwent a needle punching process to form a non-woven KF mat with an areal density of 1,350 g/m^2. The preparation of the mats was given elsewhere (Salim et al., 2011). Acrodur® resin 950 L used in this study was obtained from BASF. This resin is an aqueous acrylic resin based on modified polycarboxylic acid and a polyalcohol (crosslinking agent) that create a polyester thermoset material upon curing by crosslinking reaction at a temperature above 130°C (**Figure 1**).

Fiber Pre-treatment
Alkali treatment of KF in the form of non-woven mats was done by soaking the mats for 3 h in 6% NaOH solution. Post-treatment, the KF mats were rinsed with 1% acetic acid solution to neutralize the excess of NaOH followed by washing with distilled water before drying process in an oven for 24 h at 60°C. For elevated alkali treatment, similar procedure was applied except the treatment was executed in hot alkali solution at 60°C. The treatment was done in a water bath to ensure uniform heat application during the treatment. Heat treatment of NWKF was conducted by heating the non-woven KF mat at 140°C for 10 h inside air circulation oven based on optimum heat treatment of KF suggested by Ariawan et al. (2014).

Composite Preparation
Non-woven KF reinforced Acrodur® composites were prepared by resin impregnation process as reported elsewhere (Ahmad Rasyid et al., 2019). Post-impregnation, the semi-finished material (prepreg) was dried inside a vacuum oven at 60°C until the residual moisture was 15%. The prepregs were then compression molded using GOTECH model GT7014-H hydraulic hot press machine at 210°C with a pressure of 10 bar to produce the composite laminate. These parameters was selected based on the previous work by Salim et al. (2017). The composite samples were prepared with a fixed volume fraction of 45% V_f. Untreated KF composites, alkali- treated KF composites, alkali-treated KF composites at elevated temperature (60°C) and heat- treated KF composites are referred to as the UTKC, ATKC, AHTKC, and HTKC, respectively.
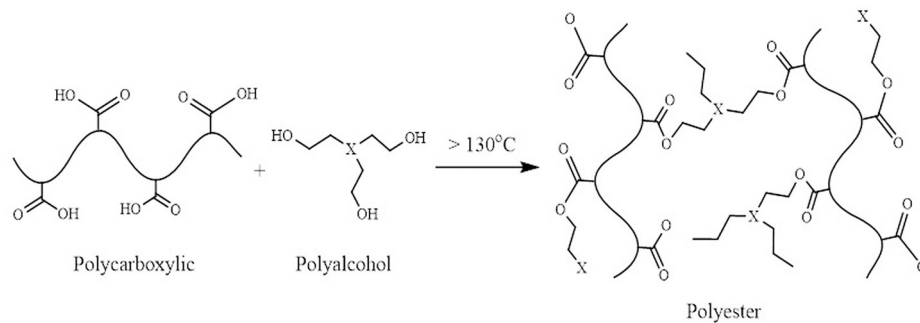
FIGURE 1 | Crosslinking reaction of Acrodur® resin (Islam and Miao, 2013).

TABLE 1 | Accelerated weathering parameters based on SAE J2412.

Parameter	Dark cycle	Light cycle
Black panel temperature	$38 \pm 3°C$	$70 \pm 3°C$
Relative Humidity (RH)	95%	50%
Cycle duration	$1\,h \pm 6\,min$	$3.8\,h \pm 6\,min$

Accelerated Weathering Test

The composite samples were subjected to accelerated weathering test using Q-SUN Xe-3 xenon arc chamber from Q-Lab (USA) according to SAE J2412 standard, i.e., accelerated exposure of automotive interior trim components using a controlled irradiance xenon-arc apparatus. The samples were fixed on the chamber tray and were subjected to accelerated weathering through dark and light cycle alternately with parameters as tabulated in **Table 1** until 1,500 h of total exposure time. Such exposure time was selected based on SEM analysis where significant changes appeared on the composites surfaces. The average UV irradiance was set to 0.55 W/m^2 at 340 nm wavelength and window filter was used to simulate the actual condition inside a passenger car. The samples were collected after 500 h interval of exposure time to determine the degree of degradation. Before the mechanical test, the samples were cleaned using a dry cloth and re-conditioned for 24 h at room temperature inside a desiccator.

Water Absorption

The water absorption study was conducted following ASTM D 570. Flexural samples were used to measure weight changes during the water absorption test. Initially, the samples were dried at 60°C for 24 h followed by their cooling to room temperature inside a desiccator. Then the samples were submerged into distilled water at room temperature. The weight changes overtime were taken periodically until equilibrium was achieved, meaning, no further increment to the sample's weight was observed. The water uptake percentage of the specimens was calculated at different time intervals by using Equation (1):

$$M\,(\%) = \left[\frac{M_t - M_o}{M_o} \right] \times 100 \tag{1}$$

where, M (%) is the water uptake, M_t is the weight of the wet sample at a given time, and Mo is the initial weight of the sample. Diffusion coefficient (D) was evaluated from the slope of moisture content vs. the square root of the time by Equation (2):

$$D = \left(\frac{h}{4M_m} \right)^2 \left(\frac{M_2 - M_1}{\sqrt{t_2} - \sqrt{t_1}} \right)^2 \tag{2}$$

where, M_1 and M_2 are the water content (percentage weight) at times t_1 and t_2, respectively, M_m is the maximum weight gain (%), and h is the thickness of composites (mm). Flexural test was then conducted on the wet and re-dried samples to evaluate the residual and recovery properties of the composites, respectively.

Physical Test

The color change of all samples was determined before and after UV irradiation at every 500 h intervals using a portable spectrophotometer Konica Minolta Chroma Meter model CR-400 (Japan) equipped with a CIELAB system. The CIELAB system measurement consists of three parameters, namely L*, a*, and b*, where L* represents lightness, which varies from 100 (white) to 0 (black), and a* and b* are the chromaticity indices, with +a* representing the red direction, –a* as green, +b* as yellow, and –b* as blue. The changes in a*, and b*, L* were calculated based on Equations (3)–(5), respectively.

$$\Delta a^* = a_2 - a_1 \tag{3}$$
$$\Delta b^* = b_2 - b_1 \tag{4}$$
$$\Delta L^* = L_2 - L_1 \tag{5}$$

where ΔL^*, Δa^*, and Δb^* are the differences in the initial and final values of a*, b*, and L*, respectively, a_1, b_1, and L_1 are the initial color parameters; and a_2, b_2, and L_2 are the color parameters after UV irradiation exposure. The total change in color (ΔE^*) was calculated based on ASTM D2244 using the Euclidean formula as shown in Equation (6). Lower ΔE^* value corresponds to a smaller color difference and indicates strong resistance to UV radiation. The measurement was done at five locations on each sample, and the average values were calculated.

$$\Delta E^* = \sqrt{(\Delta L^*)^2 + (\Delta a^*)^2 + (\Delta b^*)^2} \tag{6}$$

The chemical changes of the composites due to the accelerated weathering exposure were determined using a Fourier Transform Infrared Spectroscopy (FT-IR, Perkin-Elmer Spectrum One, USA), using potassium bromide (KBr) pellet method. Prior to the characterization, the discolored area of the exposed region (composite surface) was scraped off using scraping knife and thoroughly mixed with KBr. This mixture was compressed into pellets before FT-IR analysis. The transmittance spectra were recorded within the range of 400–4,000 cm^{-1} wavelength with a spectral resolution and number of scans of 1 cm^{-1} and 32 scans, respectively. The carbonyl and vinyl indexes were then calculated using the following Equations (7) and (8), respectively (Satoto et al., 1997).

$$\text{Carbonyl Index (\%)} = \frac{I_{1720}}{I_{2920}} \times 100 \qquad (7)$$

$$\text{Vinyl Index (\%)} = \frac{I_{914}}{I_{2920}} \times 100 \qquad (8)$$

where $I_{1,720}$ and I_{914} are the intensity peak of carbonyl and vinyl, respectively. These peaks were normalized to $I_{2,920}$ peak, attributed to the alkane stretching vibration of the methylene group (-C-H-) that was chosen as the reference peak.

Meanwhile surface appearance of composites after accelerated weathering and water absorption test were observed using FESEM model FEI Verios 460L. Fracture surface observation by FESEM also was conducted to investigate fiber-matrix adhesion and KF structure within the composites after water absorption test. All samples characterized by SEM were mounted on aluminum stubs and sputter-coated with gold before observation at a pressure of 2 mbar for 1 min.

Mechanical Testing

Flexural strength and modulus of the composites before and after the durability tests were determined using the three-point bending test method with sample geometry of 130 × 13 × 3 mm following the ASTM D790 standard and maintaining a span to depth ratio of 16:1. The test was conducted using Instron 5969 universal testing machine (USA) with a crosshead speed of 2 mm/min at room temperature and 50% relative humidity. The strength and modulus values given are the means from five individual samples.

Thermal Testing

The changes in thermal properties before and after the durability test were analyzed using Thermogravimetric analysis (TGA). The
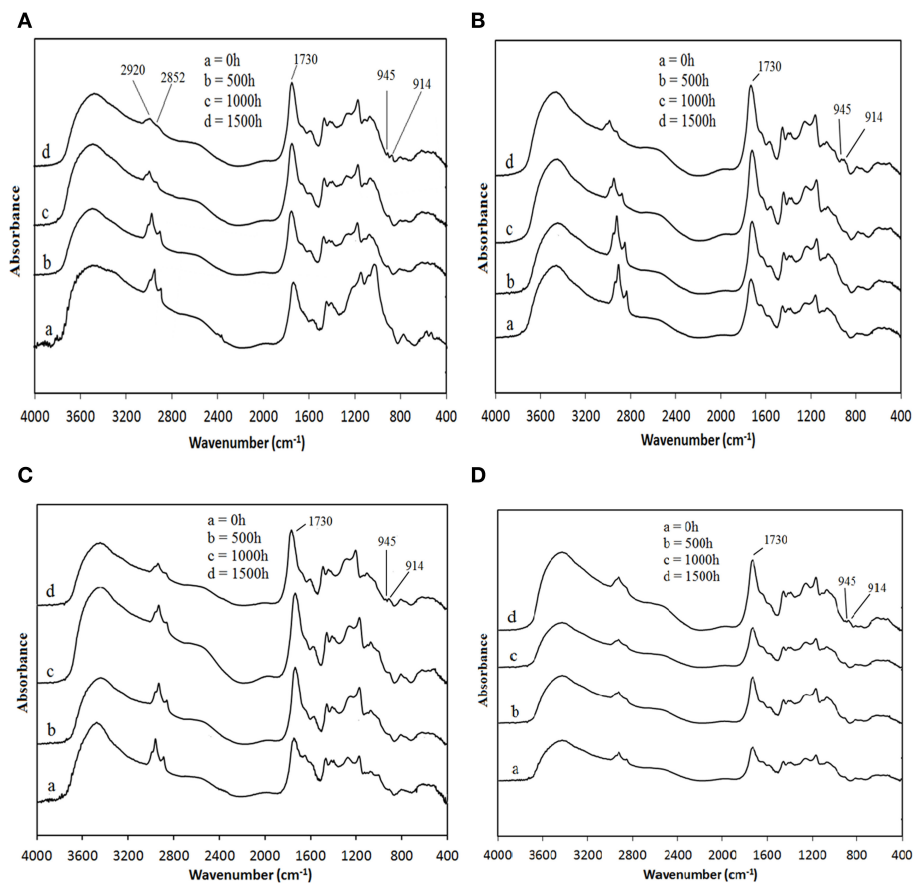

FIGURE 2 | FT-IR spectra of composites during weathering exposure (A) UTKC, (B) ATKC, (C) AHTKC, and (D) HTKC.

analysis was conducted using a Perkin Elmer Pyris Diamond TGA analyzer at a heating rate of 10°C/min at the room temperature range to 600°C. An average sample weight of 15 mg of each composite specimen was analyzed under an inert atmosphere of nitrogen gas.

RESULTS AND DISCUSSIONS

Accelerated Weathering Exposure

In this study, a Q-SUN Xe-3 weathering chamber using a xenon arc lamp was used to simulate sunlight irradiation. The xenon arc lamps produced the most realistic reproduction of full-spectrum sunlight, including ultraviolet (UV), visible light (VL), and infrared (IR) radiation. Regarding UV radiation, the spectrum can be subdivided into several ranges defined most broadly as a 10–400 nm wavelength. On the other hand, the bond dissociation energy of most polymeric matrices is within the range of 290–400 nm (Feldman, 2002; Gu, 2008). This wavelength lies in the same region of the UV-A and UV-B wavelengths, which is between 320 and 400 nm and between 280 and 320 nm, respectively. Therefore, several chemical reactions might occur, mainly on the exposed surface of composites as a result of these UV irradiations that might influence the mechanical properties of the composites.

FT-IR Analysis

Figures 2A–D exhibits the FT-IR spectra of composites before and after accelerated weathering exposure for 500, 1,000, and 1,500 h. Similar major absorbance peaks for the spectrums before and after exposure could be observed but with different intensities, indicating the same characteristic of chemical constituents within the composites. However, the presence of some additional peaks particularly after accelerating weathering test suggests some modifications did occur due to the exposure. **Table 2** summarizes the characteristics of the absorption peak of the spectrums.

The FT-IR spectra of the weathered samples of all composites revealed some changes, especially at the peak 1,720 cm^{-1} corresponding to the C=O stretching vibration of carbonyl groups. The carbonyl index (*CI*) was calculated based on Equation (7) to gain a better insight into these changes. According to **Table 3**, all composites did not exhibit an accentuated increase in the carbonyl index at the first 1,000 h exposure. This result could be related to the competition between the oxidation and crosslinking processes (Gulmine et al., 2003).

It seems to indicate that composite samples exposed to an accelerating weathering test below 1,000 h were favorable to undergo crosslinking process. The presence of chromophoric carbonyl groups within the polymer chain absorbs solar UV radiation and producing free radicals. These polymer radicals are then terminated via bimolecular recombination or crosslinking based on Norrish type I mechanism.

However, the *CI* of all composites was found to increase after 1,500 h exposure. This is due to the presence of oxidation products such as a mixture of carboxylic acid and ketone species as a result of photo-oxidative degradation of polyester (Ariawan et al., 2018). The FT-IR spectra of all composites exposed at a period of 1,500 h also showed the presence of the peaks at 945 and 914 cm^{-1}, which represent the vinyl groups. The formation of these groups can be verified by the increased vinyl index (VI) of the composites especially after 1,500 h exposure (see **Table 3**). This can be attributed to carbonyl degradation as consequences of polymer chain scission in both matrix and natural fiber via the Norrish type II mechanism (Azwa et al., 2013). The generation of carbonyl and vinyl groups through polymer chain scission resulted in the reduction in molecular weight and thereby might decrease the strength, toughness and fracture strain of polymers (Noriman and Ismail, 2011). The changes in mechanical properties of the composites after accelerated weathering exposure are reported in the following section Flexural Properties.

Changes in Surface Color

The UV radiation during the weathering test promotes photo-oxidative, thermo-oxidative, and photolytic reactions that impair the polymer properties (Pillay et al., 2009). The extent of degradation ranges from minor surface discoloration affecting the aesthetic appeal in indoor applications to extensive loss of mechanical properties (Müller et al., 2003). Even though there is no precise correlation between accelerated weathering and natural weathering test, Chang and Chang (2001) reported that discoloration in the accelerated light fastness test is 250 times more severe than that in the actual indoor exposure test. The characterization of the color changes concerning the exposure time of the indoor accelerated weathering test in this study was conducted based on CIELAB color.

Figure 3 exhibits the changes in the surface color index as exposure time increases. It can be seen that the accelerated

TABLE 2 | Characteristic FT-IR absorption peaks of composites.

Wavenumber (cm^{-1})	Corresponding functional group	References
2,920	CH$_2$ asymmetric C–H stretching vibration	Jia et al., 2010
2,852	CH$_2$ symmetric C–H stretching vibration	Lambert, 1987
1,720	Aromatic ester C=O stretching vibration	Jia et al., 2010
945	CH$_2$ out of plane wagging vibration	Thirmizir et al., 2011
914	CH$_2$ out of plane wagging vibration	Thirmizir et al., 2011

TABLE 3 | Carbonyl index and vinyl index of composites samples during accelerated weathering test.

Indexes	Carbonyl index, CI				Vinyl index, VI			
Exposure time (h)	0	500	1,000	1,500	0	500	1,000	1,500
UTKC	1.017	1.014	1.038	1.380	0.691	0.702	0.743	0.874
ATKC	1.033	1.033	1.068	1.379	0.669	0.650	0.714	0.756
AHTKC	1.045	1.051	1.068	1.483	0.661	0.737	0.714	0.774
HTKC	1.053	1.098	1.126	1.344	0.728	0.734	0.747	0.755
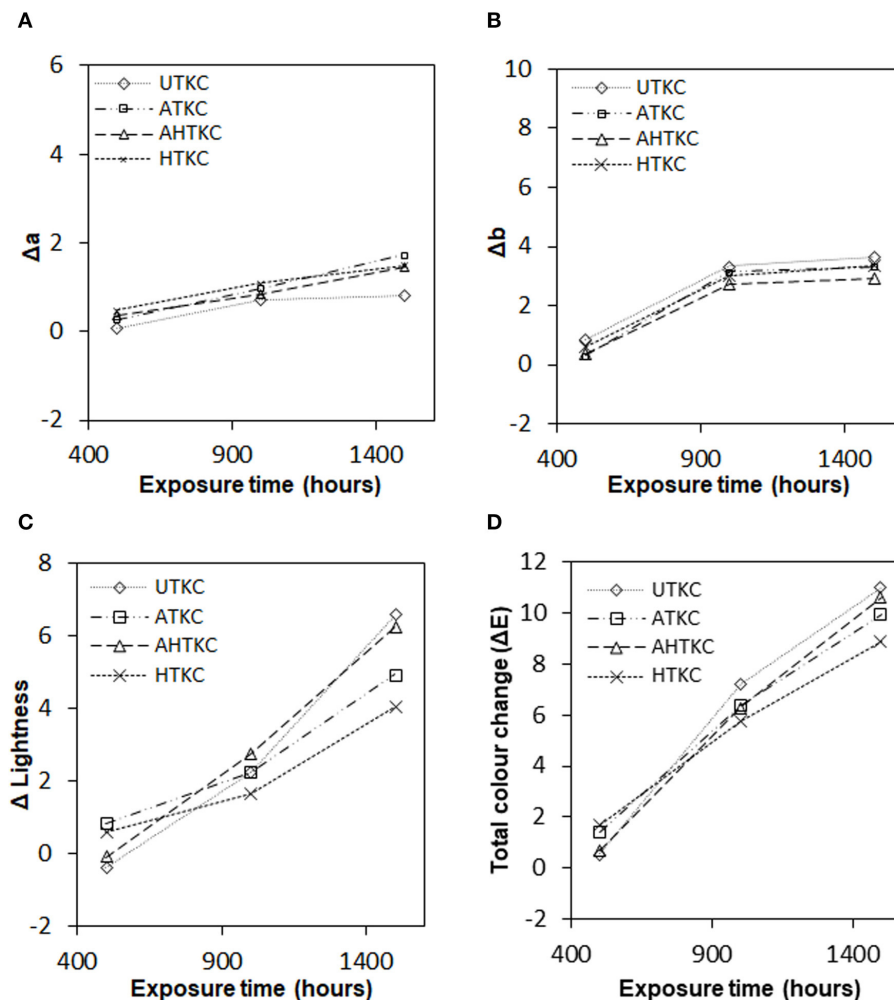
FIGURE 3 | Effect of accelerated weathering exposure on **(A)** the relationship between green and red color, **(B)** the relationship between blue and yellow color, **(C)** the brightness relationship between light and dark, and **(D)** total color change.

weathering exposure to the composites induced color alteration as shown by the changes in the color index components ΔL, Δa, Δb, and therefore resulting in the total color changes ΔE. As the exposure time increases, the composites only suffered minimal changes in Δa. On the contrary, all composites sustained a significant increment in ΔL and Δb which meant that the surface color became lighter and shifted toward yellow as the exposure time increases. This result is consistent with the work reported by Muasher and Sain (2006). They found that significant color fading (increased ΔL) and yellowing (increased Δb) of HDPE filled composites started to occur after exposure to a natural weathering test.

Lignin is the most sensitive constituent to light in lignocellulosic material, including natural fiber that is responsible for photochemical reactions. The oxidation of lignin initiated by the absorbed UV radiation leads to the formation of a paraquinone chromophoric structure, having α-carbonyl, biphenyl, and ring-conjugated double bond structures

(Butylina et al., 2012). These substances are the leading cause of discoloration, mainly giving the yellow characteristic of the exposed samples (Azwa et al., 2013). It is interesting to note that a more significant increase in ΔL for all composites occurred within the range of 1,000–1,500 h exposure time. This is attributed to the further degradation of chromophores that leads to color fading by a photobleaching process and generation of free radicals that may cause substantial degradation of lignin and photo-oxidation of cellulose and hemicellulose.

Regarding the polymeric matrix, the photochemical conversion is dependent on the spectral irradiance of the applied polychromatic light source, especially in the case of yellowing when it is the result of photodegradation and subsequent photobleaching of the chromophores causing yellowing. In general, the maximum sensitivity of polyesters (various formulations) to light spectrum is approximately at a 325 nm wavelength which lies in the region of UV-A (Rabek, 2012). Therefore, it can be

FIGURE 4 | Flexural properties of the composites with respect to the accelerated weathering exposure time **(A)** flexural strength and **(B)** flexural modulus.

FIGURE 5 | SEM images of surface appearance before and after weathering test for **(a)** UTKC, **(b)** ATKC, **(c)** AHTKC, and **(d)** HTKC.

presumed that the increase in the ΔL and Δb values was also contributed by the chromophores photodegradation within the polyester matrix.

Besides, high humidity applied during weathering exposure (90% RH during the light cycle) induces moisture absorption of hydrophilic cellulose and consequently promotes an oxidation reaction which facilitates the penetration of light, thereby, accelerating the photo-degradation effect in composites (Stark, 2006). The increase in total color change, ΔE of all the composites, as exposure time increases, was significantly contributed by the increase in the ΔL and Δb values.

Flexural Properties

Since the aging of polymers results from the competition between continuous crosslinking and chain scission, such competition could lead to the alteration of mechanical properties as the exposure time increases. **Figures 4A,B** depicts the changes in flexural strength and modulus of the composites concerning the accelerated weathering exposure. Prior to accelerated weathering test (0 h), flexural strength and modulus of AHTKC were the highest followed by ATKC, HTKC, and UTKC. This shows that fiber surface treatment could impart better flexural

properties to Acrodur[R] composites by improving fiber to matrix adhesion. Detailed explanations of the effect of surface treatment on wettability and mechanical properties of KF reinforced Acrodur[R] composites could be found in the author's previous work (Salim et al., 2019). In regard to accelerated weathering exposure, a general pattern was acquired where the flexural strength and modulus of all composites were found to increase slightly as the exposure time increases. Temperature and UV radiation can either impose scission of the chemical bonds of the matrix (i.e., main C–C chain scission), leading to photo/thermo-oxidation and crazing of the material (Segovia et al., 2000) or leading to polymer post-curing (Boinard et al., 2000).

As mentioned earlier, there were competing reactions between photo-oxidation and crosslinking process of the polymer matrices in which crosslinking was more dominant to occur during the initial stage of exposure. This occurrence might very well-describe the improvement in flexural properties and thermal stability of the composites exposed to weathering test up to 1,000 h. A similar observation was described by Woo et al. (2008). They found that the tensile strength of epoxy-organoclay nanocomposites increased after UV exposure for 1,000 h. According to them, the composites tensile strength increased because of the association to the favorable chain crosslinking process that is to occur.

Additionally, previous work by the authors found that the developed Acrodur® composites did not achieve a fully cured state, and the degree of crosslinking was reported to be around 84% (Salim et al., 2018). Combination of high temperature applied, and heat emitted by the UV light might also initiate further post-curing process of the pre-polymer to form rigid polyester. This condition might also contribute to the increment of the flexural properties.

On the contrary, the notable increase in the yellowing effect, and the significant increment in CI of the composite samples exposed for 1,500 h signify the onset of degradation by photo-oxidation occurring within the polymer matrices as well as KF. This was explained by the deterioration of thermal stability and a slight reduction of flexural properties of most composites after 1,500 h exposure. The decrease in these properties was due to the scissoring of polymer macromolecules (Bagherpour et al., 2009). The UV radiation that was absorbed by the polymer matrix resulted in the formation of free radicals. Once free radicals have been produced, reaction with oxygen generates hydroperoxides

that can dissociate further to produce a series of decompositions. Therefore, further degradation of the composites was expected to occur if the exposure period exceeded 1,500 h.

Figure 5 exhibits the SEM images of the composites before and after the accelerated weathering exposure for 1,500 h. The observation that was made, based on the color changes and SEM images, suggests that the composites endured yellowing but not cracking. However, the formation of blister and sink marks were observed on the composite's surface. According to Kaczmarek (1996), during UV irradiation of polymers, volatile degradation products are removed from the specimen surface, leaving behind pit or pore-type structures. In this current study, the formation of this structure could also be because of water evaporation during the post-curing process. Furthermore, during the light cycle, application of high temperature (70°C) and heat radiation from UV evaporated uncured substances leaving voids on the surface of the composite. The presence of blisters and sink marks could accelerate further degradation by providing pathways for oxygen diffusion into the specimen bulk for the photo-oxidation process to occur (Signor et al., 2003).

The flexural properties of the composites, however, were barely affected from 1,000 to 1,500 h of exposure time (see **Figures 4A,B**) even in the presence of blisters and voids. It should be noted that the defects mainly occur on the composite's surface. For that reason, the reinforcing ability of treated KF could still impart better flexural properties to the composites. As can be seen in **Figure 4**, AHTKC still exhibits the highest flexural strength and modulus followed by ATKC, HTKC, and UTKC throughout exposure time. The effectiveness of the surface treatment in improving the flexural properties of the composites was found to sustain after the weathering test.
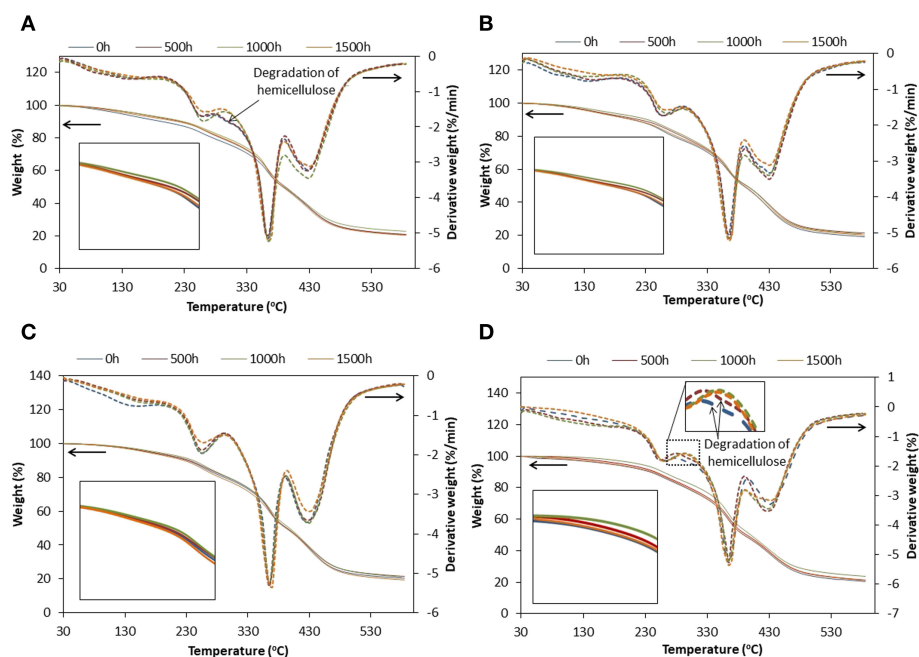

FIGURE 6 | TGA and DTG curves of composites after accelerated weathering exposure **(A)** UTKC, **(B)** ATKC, **(C)** AHTKC, and **(D)** HTKC.

Since the indoor condition of the accelerated weathering test was applied in the current study, no water spray cycle was conducted to simulate rain. This might result in a slower degradation rate. Zhao et al. (2010) reported a more severe degradation of polyester under accelerated weathering for an outdoor application using a similar xenon arc lamp that involved water spray for 12 min followed by 108 min dry condition with the RH value of 65%. The formation of crack was recorded as early as 400 h exposure. The presence of water might also accelerate the degradation mechanism (Bagherpour et al., 2009).

Thermal Properties

Thermogravimetric analysis (TGA) and the rate of derivative thermogravimetric analysis (DTG) curves for unexposed samples and weathered samples are shown in **Figures 6A–D**, while **Table 4** summarizes the thermal properties of the corresponding samples. Surprisingly, the accelerated weathering exposure was found to impart slight improvement in the thermal stability of the composite at least for the initial stage of exposure. This can be seen by the gradual increment of onset degradation temperature (T_{onset}) as well as the temperature at which 10% degradation occurs (T_{10}) of the composites for the first 1,000 h. This occurrence could be related to the polymer matrices post-curing as well as crosslinking process initiated by UV radiation that are more favored to occur over oxidation, especially during the first 1,000 h. The obtained result is in parallel with the previous FT-IR analysis that suggests the degradation by photo-oxidation was presumed to occur dominantly only after 1,000 h. This can be shown by the significantly increased *CI* of the composites samples that were exposed for 1,500 h as presented earlier in **Table 3**. In the literature, Ding and Liu (2006) also reported an increase in thermal stability of polyurethane sealant after exposure to UV-A radiation. They also found that the post-curing that occurred increased the tensile and hardness properties of the sealant.

The DTG curves of the unexposed and exposed composite samples generally exhibited similar decomposition stages with some noticeable changes after exposure. The first stage of weight losses for the composites occurs at 80°C and above due to the moisture evaporation from the composites constituent of KF and Acrodur® resin. Within the temperature 180–280°C, the weight losses of the composites were due to the decomposition of lower boiling point components of polyester as well as some portion

of hemicellulose, pectin and wax (Shebani et al., 2008). Since the degradation range of hemicellulose is between 220 and 320°C (Azwa et al., 2013), further decomposition of hemicellulose residual could also be detected by a small weight loss between 280 and 320°C for the unexposed sample of UTKC (see **Figure 6A**) and HTKC (see **Figure 6D**). This stage was not visible in alkali-treated KF composites of ATKC and AHTKC because of the absence of hemicellulose content in the KF and the elimination of this constituent during alkalization. It is interesting to note that this decomposition stage was also found to disappear for UTKC and HTKC samples that were exposed for 1,000 and 1,500 h. This indicates that the degradation of hemicellulose could occur during accelerated weathering by UV radiation via photo-oxidation.

The last stage of the decomposition of the composites is related to the degradation of the cross-linked acrylic polymer of the matrix resin that occurs at temperature between 280 and 525°C. The degradation stage at a temperature between 380 and 520°C was attributed to the decomposition of the cross-linked acrylic polymer (Akpan et al., 2017). The degradation rate at this stage could give a probable insight into the crosslinking formation that might occur by the post-curing and crosslinking process during weathering exposure. As it can be seen, the degradation peak of the composites exposed at 500 h and 1,000 exhibit higher intensity in the DTG curve compared to the unexposed samples and exposed samples at 1,500 h. This occurrence is generally applied to composites, which signifies that the post-curing and crosslinking process are most likely to occur at the initial stage of exposure while photo-oxidation that occurs at the final stage of exposure causes degradation of polyester.

WATER ABSORPTION PROPERTIES

Kinetic of Water Absorption

Figure 7 shows the water absorption curves for the composites. All samples exhibited a typical Fickian behavior, i.e., rapid water

TABLE 4 | Thermal properties of composites with respect to exposure time of accelerated weathering test.

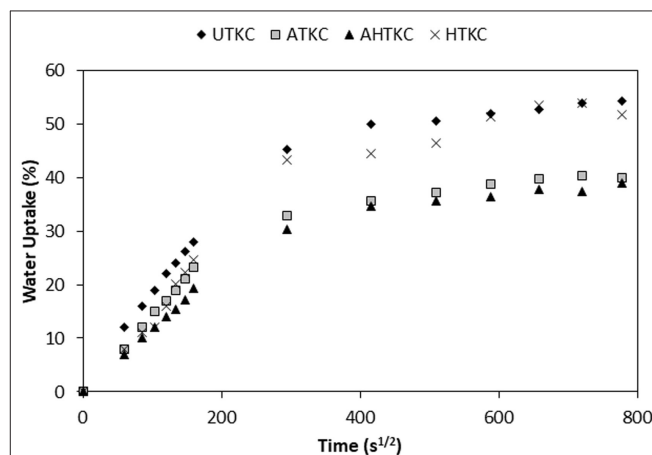| Weight loss (%)	Onset temperature, T_{onset} (°C)				Tempt. at 10% weight loss, (T_{10}) (°C)			
Exposure time (h)	0	500	1,000	1,500	0	500	1,000	1,500
UTKC	190	220	226	215	231	237	242	238
ATKC	208	222	228	218	234	240	243	235
AHTKC	231	234	242	232	237	240	246	237
HTKC	202	225	230	215	233	236	243	236

FIGURE 7 | Water absorption behavior of KF/Acrodur® composites.

uptake at the initial stage, and later a saturation level was attained without any further increase in water absorption. Generally, the maximum water uptake for KF reinforced composite (UTKC) in this current study was found to be significantly lower by almost 50% compared to KF/hemp reinforced Acrodur® composite reported by Medina and Schledjewski (2009).

However, the water uptake is higher, compared to other types of thermosetting resin and thermoplastic resin composites. Several studies have reported that the maximum water uptake of unsaturated polyester/KF composite of comparable fiber loading is in the range of 10–25% (Nosbi et al., 2010; Mazuki et al., 2011). Meanwhile, the water uptake for PP/kenaf fiber composites is within the range of 10–18% (Law and Ishak, 2011). This difference is because of the water-based property of Acrodur® resin. Before curing, the resin is hydrophilic and water-soluble. After thermally cured, besides providing rigidity and strength to the resin, the formation of crosslinking upon curing imparts hydrophobicity properties. During the composites' fabrication process, it is not applicable to obtain a complete curing reaction as it requires exposing the fiber at a high temperature (210°C) over a more extended period which might degrade the natural fiber. Indeed, Khalfallah et al. (2014) reported that the optimum degree of curing of Acrodur®/flax tape composite that is suitable in the automotive industry is 72%. Based on this, higher water uptake to Acrodur® KF composites can be expected as the uncured resin tends to be dissolved during water immersion, creating more voids to be filled up with water molecules.

Table 5 summarizes the maximum water uptake (M_m) and diffusion coefficient (D) of Acrodur® composites. It is interesting to note that fiber surface treatment could provide some

improvement in reducing the water absorption properties of the composites. ATKC and AHTKC exhibit a significant reduction in M_m by 25 and 30% and a slight decrease in D by 5 and 12% compared to UTKC, respectively. This may be attributed to the removal of hemicellulose and lignin during alkalization in which the removal was more effective by the application of heat as in the case of AHTKC composites. Hemicellulose is considered to be mainly responsible for water uptake, even though non-crystalline cellulose and lignin might also play an essential role in the water absorption process.

Furthermore, during alkalization, the amorphous waxy cuticle layer of the fibers, which holds the water molecules is removed, thereby limiting water containment in the composites (Sreekala et al., 2002). As a result, the maximum water uptake, M_m of the alkali treated KF composites was relatively lower compared to UTKC composite. Sreekala et al. (2002) explained that the water absorption is not only dependent on the fiber and matrix structures, but also the fiber–matrix interface. Alkali treatment to KF promotes the activation of hydroxyl groups of the cellulose unit by breaking the hydrogen bond, leading to good fiber/matrix interaction. Excellent interaction between the fibers and matrix might reduce the void along the interface, which consequently inhibits water penetration and reducing the D and M_m values of the alkali-treated KF composites. It is worth noting that HTKC exhibited a considerably lower D value with 1.34×10^{-11} m/s². This could be due to the swelling, and cell shrinking that contributed to less water absorption by cell walls (Ates et al., 2009). Despite that, the M_m value of HTKC was relatively higher than ATKC and AHTKC. Therefore, this signifies high total water uptake at the saturation level is contributed by water containment at the interfacial region because of poor fiber-matrix wettability.

Flexural Properties

Table 6 shows the flexural properties of the composites in wet and re-dried states. Water absorption causes a dramatic reduction in the flexural strength and flexural modulus of all composites. The significant reduction in flexural strength of composites could be associated with fiber swelling that compromises fiber-matrix interfacial bonding (Dhakal et al., 2007). Also, the

TABLE 5 | Water absorption properties of composites.

Composites	Maximum water uptake, M_m (%)	Diffusion coefficient, D ($\times 10^{-11}$ m/s²)
UTKC	54.27	1.42
ATKC	40.41	1.35
AHTKC	38.87	1.25
HTKC	49.80	1.34

TABLE 6 | Flexural properties of composites before and after subjected to water absorption.

Sample	Control		Wet		Re-dried	
	Strength (MPa)	Modulus (GPa)	Strength (MPa)	Modulus (GPa)	Strength (MPa)	Modulus (GPa)
UTKF	49.50 ± 2.56	4.32 ± 0.35	20.66 ± 1.53 (−58.26 ± 3.09)	1.90 ± 0.12 (−56.02 ± 2.78)	42.02 ± 2.31 [84.89 ± 4.67]	3.62 ± 0.11 [83.80 ± 2.55]
ATKC	56.40 ± 2.07	5.22 ± 0.16	27.76 ± 0.86 (−50.78 ± 1.52)	2.45 ± 0.10 (−53.07 ± 1.92)	45.73 ± 1.57 [81.08 ± 2.78]	4.18 ± 0.13 [80.00 ± 2.50]
AHTKC	58.35 ± 0.73	5.67 ± 0.09	32.95 ± 1.48 (−43.53 ± 2.54)	2.72 ± 0.05 (−52.03 ± 0.88)	48.01 ± 1.68 [82.27± 2.88]	4.60 ± 0.14 [81.13 ± 2.50]
HTKC	51.05 ± 0.64	5.24 ± 0.18	22.55 ± 0.96 (−55.82 ± 1.88)	2.20 ± 0.08 (−58.01 ± 1.52)	43.55 ± 2.05 [85.30 ± 4.01]	4.22 ± 0.14 [80.53 ± 2.67]

( )% change of wet sample toward control properties.
[ ]% recovery of re-dried sample toward control properties.
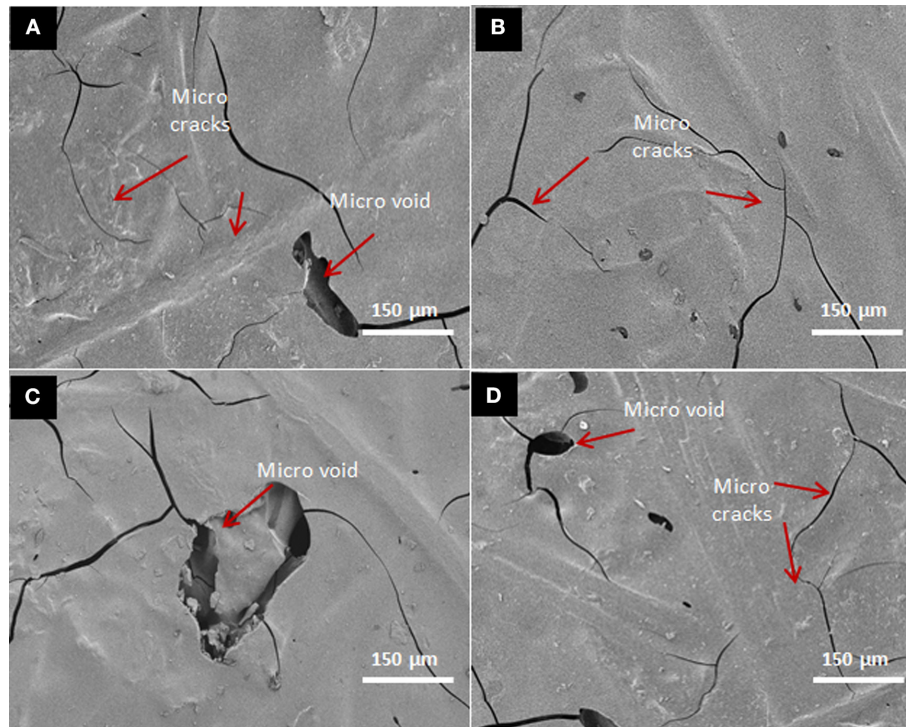
FIGURE 8 | SEM images of composites surfaces after water absorption test **(A)** UTKC, **(B)** ATKC, **(C)** AHTKC, and **(D)** HTKC.
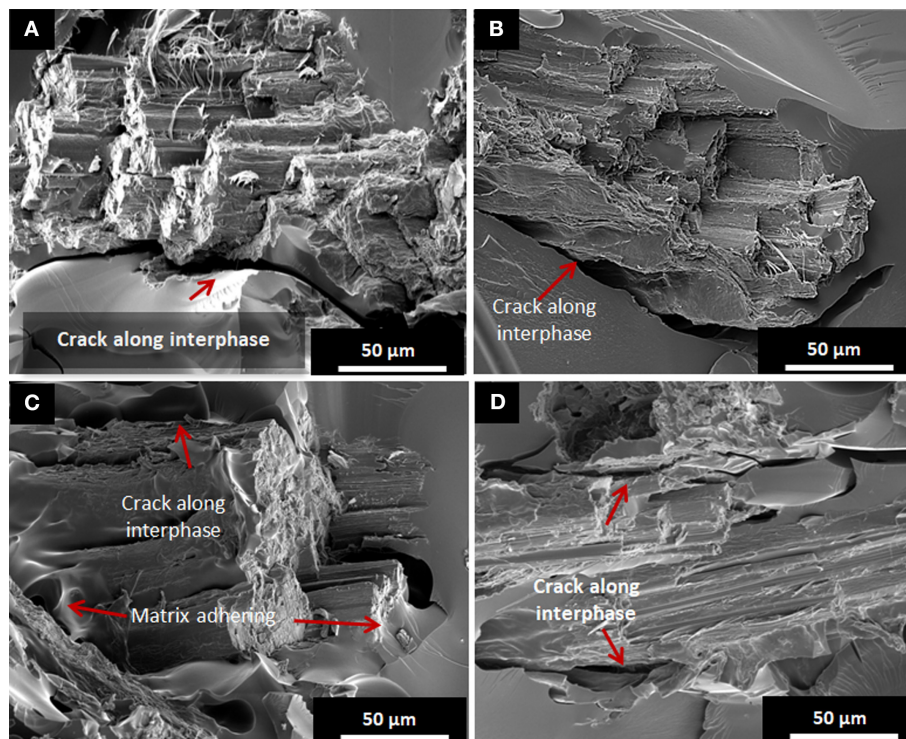

FIGURE 9 | SEM images of flexural fracture surfaces after water absorption test **(A)** UTKC, **(B)** ATKC, **(C)** AHTKC, and **(D)** HTKC.

water molecules act as plasticisers that reduce the rigidity of the cellulose structure and thus, the flexural modulus of the reinforced composites (Akil et al., 2009). Notwithstanding, slightly better retention strength in ATKC and AHTKC as compared to UTKC and HTKC were observed. This could be attributed to the improved fiber–matrix bonding which minimizes the adverse effect of the interfacial region by the water molecules penetration.

The flexural properties of all the composites exhibit good recovery (exceeding 79%) upon re-drying, suggesting that the role of water as plasticiser has been removed or has a reversible physical process. As stated by Bera et al. (2007) the re-drying process reduces the plasticization effect in composite constituents. However, full recovery of the flexural properties could not be achieved. This might be due to the defects or flaws imposed by water penetration and during the re-drying process.

Figures 8A–D exhibits the SEM images of composites surfaces while **Figures 9A–D** shows the fracture surfaces of the composites after being subjected to the water absorption test, followed by the re-drying step. The formation of micro-cracks and micro-voids observed on the surfaces of the composites might explain the reduction in flexural properties following the test. Notably, UTKC and HTKC exhibit a slightly better recovery percentage of flexural strength and flexural modulus upon re-drying compared to ATKC and AHTKC. The result suggests that water penetration, followed by re-dying, might reduce or diminish the treatment effect in enhancing fiber to matrix adhesion in ATKC and AHTKC. As stated by Dhakal et al. (2007) water absorption by hydrophilic KF could lead to interfacial de-bonding in the composites. This could be proven by the occurrence of a crack at an interfacial region that occurs in all composites regardless of the treatment applied, shown in **Figure 9**. However, AHTKC still exhibits the highest flexural strength and modulus compared to all composites. As observed in the SEM image of AHTKC fracture surfaces (see **Figure 9C**), there was still matrix resin that remained intact or adhered to KF. This could provide some reinforcing effect of the KF to the composites.

CONCLUSIONS

The current study analyses the effects of accelerated weathering and water absorption test of KF reinforced Acrylic-based polyester resin with the trade name of Acrodur®. The post-crosslinking process that occurs during the accelerated weathering test is found to improve the flexural and thermal properties of the composites at the early stage of exposure. Toward the final stage (total exposure of 1,500 h), slight decrease in flexural properties are recorded due to the photochemical degradation. This is confirmed by the FT-IR analysis, color change measurement, and reduction in thermal stability of the composites. All composites exhibit Fickian behavior in water absorption test conducted at room temperature. The flexural properties of various composites dramatically reduce after the test. However, upon re-drying, good recovery in flexural properties could be observed in all composites exceeding 80%. Full recovery is not possible because of the formation of crack at the fiber-matrix interfacial region. The efficiency of fiber surface treatment in improving flexural properties of composite could be seen at every condition even after the accelerated weathering and water absorption tests. KF reinforced Acrodur® composites exhibit excellent durability toward solar ray radiation, but the usage of these composites in the automotive industry is limited to the interior components, because of the permanent damage to the composite induced by water absorption.

AUTHOR CONTRIBUTIONS

MS, RM, MFA, and ZM designed the experiments. MS, DA, MFA, and MZA performed the experiments. ZM supervised the work. MS, RM, and ZM wrote the paper (original draft, reviewing, and editing). All of the authors analyzed the data.

REFERENCES

Ahmad Rasyid, M. F., Salim, M. S., Akil, H. M., Karger-Kocsis, J., and Mohd Ishak, Z. A. (2019). Non-woven flax fibre reinforced acrylic based polyester composites: the effect of sodium silicate on mechanical, flammability and acoustic properties. *Exp. Poly. Lett.* 13, 553–564. doi: 10.3144/expresspolymlett.2019.47

Akil, H. M., Cheng, L. W., Mohd Ishak, Z. A., Abu Bakar, A., and Abd Rahman, M. A., (2009). Water absorption study on pultruded jute fibre reinforced unsaturated polyester composites. *Comp. Sci. Technol.* 69, 1942–1948. doi: 10.1016/j.compscitech.2009.04.014

Akil, H. M., Omar, M. F., Mazuki, A. A. M., Safiee, S., Ishak, Z. A. M., and Abu Bakar, A. (2011). Kenaf fiber reinforced composites: a review. *Mater. Design* 32, 4107–4121. doi: 10.1016/j.matdes.2011.04.008

Akpan, E. I., Wetzel, B., and Friedrich, K. (2017). Processing and properties of short wood fiber/acrylate resin composites. *Poly. Comp.* 40, 91–98. doi: 10.1002/pc.24604

Ariawan, D., Mohd Ishak, Z. A., Mat Taib, R., Ahmad Thirmizir, M. Z., and Phua, Y. J. (2014). Effect of heat treatment on properties of kenaf fiber mat/unsaturated polyester composite produced by resin transfer molding. *Appl. Mech. Mater.* 699, 118–123. doi: 10.4028/www.scientific.net/AMM.699.118

Ariawan, D., Salim, M. S., Mat Taib, R., Ahmad Thirmizir, M. Z., and Mohammad Ishak, Z. A. (2018). Durability of alkali and heat-treated kenaf fiber/unsaturated polyester composite fabricated by resin transfer molding under natural weathering exposure. *Adv. Poly. Technol.* 37, 1420–1434. doi: 10.1002/adv.21801

Ariawan, D., Salim, M. S., Mat Taib, R., Ahmad Thirmizir, M. Z., and Mohd Ishak, Z. A. (2017). Interfacial characterisation and mechanical properties of heat treated non-woven kenaf fibre and its reinforced composites. *Comp. Interfaces* 6440, 1–17. doi: 10.1080/09276440.2017.1354562

Ates, S., Hakan Akyildiz, M., and Hasan Ozdemir, B. (2009). Effects of heat treatment on calabrian pine. *BioResources* 4, 1032–1043.

Azwa, Z. N., Yousif, B. F., Manalo, A. C., and Karunasena, W. (2013). A review on the degradability of polymeric composites based on natural fibres. *Mater. Design* 47, 424–442. doi: 10.1016/j.matdes.2012.11.025

Bagherpour, S., Bagheri, R., and Saatchi, A. (2009). Effects of concentrated HCl on the mechanical properties of storage aged fiber glass polyester composite. *Mater. Design* 30, 271–274. doi: 10.1016/j.matdes.2008.04.078

Baillie, C., and Jayasinghe, R. (2004). *Green Composites: Polymer Composites and the Environment. Woodhead Publishing Series in Composites Science and Engineering.* Cambridge, UK: Elsevier Science.

Bera, T., Mula, S., Ray, P. K., and Ray, B. C. (2007). Effects of thermal shocks and thermal spikes on hygrothermal behavior of glasspolyester composites. *J. Reinforced Plast. Comp.* 26, 725–738. doi: 10.1177/0731684409076732

Boinard, E., Pethrick, R. A., Dalzel-Job, J., and Macfarlane, C. J. (2000). Influence of resin chemistry on water uptake and environmental ageing in glass fibre reinforced composites-polyester and vinyl ester laminates. *J. Mater. Sci.* 35, 1931–1937. doi: 10.1023/A:1004766418966

Butylina, S., Hyvärinen, M., and Kärki, T. (2012). A study of surface changes of wood-polypropylene composites as the result of exterior weathering. *Poly. Degrad. Stabil.* 97, 337–45. doi: 10.1016/j.polymdegradstab.2011.12.014

Chang, H.-T., and Chang, S.-T. (2001). Correlation between softwood discoloration induced by accelerated lightfastness testing and by indoor exposure. *Poly. Degrad. Stabil.* 72, 361–365. doi: 10.1016/S0141-3910(01)00039-8

Dhakal, H. N., Zhang, Z. Y., and Richardson, M. O. W. (2007). Effect of water absorption on the mechanical properties of hemp fibre reinforced unsaturated polyester composites. *Comp. Sci. Technol.* 67, 1674–1683. doi: 10.1016/j.compscitech.2006.06.019

Ding, S. H., and Liu, D. Z. (2006). Durability evaluation of building sealants by accelerated weathering and thermal analysis. *Construct. Build. Mater.* 20, 878–881. doi: 10.1016/j.conbuildmat.2005.06.026

Edeerozey, A. M. M., Akil, H. M., Azhar, A. B., and ZainalAriffin, M. I. (2007). Chemical modification of kenaf fibers. *Mater. Lett.* 61, 2023–2025. doi: 10.1016/j.matlet.2006.08.006

Feldman, D. (2002). Polymer weathering: photo-oxidation. *J. Polym. Environ.* 10, 163–173. doi: 10.1023/A:1021148205366

Gu, H. (2008). Degradation of glass fibre/polyester composites after ultraviolet radiation. *Mater. Des.* 29, 1476–1479. doi: 10.1016/j.matdes.2007.07.010

Gulmine, J. V., Janissek, P. R., Heise, H. M., and Akcelrud, L. (2003). Degradation profile of polyethylene after artificial accelerated weathering. *Poly. Degrad. Stabil.* 79, 385–397. doi: 10.1016/S0141-3910(02)00338-5

Gündüz, G., Korkut, S., and Korkut, D. S. (2008). The effects of heat treatment on physical and technological properties and surface roughness of camiyani black pine (pinus nigra arn. subsp. pallasiana var. pallasiana) wood. *Biores. Technol.* 99, 2275–2280. doi: 10.1016/j.biortech.2007.05.015

Herrera-Franco, P. J., and Valadez-González, A. (2004). Mechanical properties of continuous natural fibre-reinforced polymer composites. *Comp. Appl. Sci. Manufact.* 35, 339–345. doi: 10.1016/j.compositesa.2003.09.012

Islam, M., and Miao, M. (2013). Optimising processing conditions of flax fabric reinforced acrodur biocomposites. *J. Comp. Mater.* 48, 3281–3292. doi: 10.1177/0021998313508995

Jia, Z., Li, X., and Zhao, Q. (2010). Effect of artificial weathering on surface properties of unsaturated polyester (UP) resin. *Mater. Chem. Phys.* 121, 193–197. doi: 10.1016/j.matchemphys.2010.01.021

Kaczmarek, H. (1996). Changes to polymer morphology caused by u.v. irradiation: 1. Surface damage. *Polym.* 37, 189–194. doi: 10.1016/0032-3861(96)81086-X

Karbstein, H., Funk, J., and Norton, J. (2013). "Lightweight bio-composites with Acrodur® resin technology," in *13th Annual Automotive Composites Conference and Exhibition* (Novi, MI: ACCE), 415–431.

Karus, M., and Kaup, M. (2002). Natural fibres in the European automotive industry. *J. Indust. Hemp* 7, 119–31. doi: 10.1300/J237v07n01_10

Khalfallah, M., Abbès, B., Abbès, F., Guo, Y. Q., Marcel, A., Duval, F., et al. (2014). Innovative flax tapes reinforced acrodur biocomposites: a new alternative for automotive applications. *Mater. Design* 64, 116–126. doi: 10.1016/j.matdes.2014.07.029

Koronis, G., Silva, A., and Fontul, M. (2013). Green composites: a review of adequate materials for automotive applications. *Comp. Eng.* 44, 120–127. doi: 10.1016/j.compositesb.2012.07.004

Krishnan, T., Jayabal, S., and Naveen Krishna, V. (2018). Tensile, flexural, impact, and hardness properties of alkaline-treated sunnhemp fiber reinforced polyester composites. *J. Nat. Fibers* 17, 326–336. doi: 10.1080/15440478.2018.1492488

Lambert, J. B. (1987). *Introduction to Organic Spectroscopy.* Lambertville, NJ: Macmillan.

Law, T. T., and Ishak, Z. A. M. (2011). Water absorption and dimensional stability of short kenaf fiber-filled polypropylene composites treated with maleated polypropylene. *J. Appl. Poly. Sci.* 120, 563–572. doi: 10.1002/app.33184

Lopez, J. L., Sain, M., and Cooper, P. (2006). Performance of natural-fiber-plastic composites under stress for outdoor applications: effect of moisture, temperature, and ultraviolet light exposure. *J. Appl. Poly. Sci.* 99, 2570–2577. doi: 10.1002/app.22884

Malnati, P. (2010). *Interior Innovation: The Value Proposition.* Computer Technology. Available online at: https://www.compositesworld.com/articles/interior-innovation-the-value-proposition (accessed October 10, 2019).

Mazuki, A. A. M., Akil, H. M., Safiee, S., Arifin, Z., Ishak, M., and AbuBakar, A. (2011). Degradation of dynamic mechanical properties of pultruded kenaf fiber reinforced composites after immersion in various solutions. *Comp. Eng.* 42, 71–76. doi: 10.1016/j.compositesb.2010.08.004

Medina, L. A., and Schledjewski, R. (2009). Water glass as hydrophobic additive for natural fiber reinforced composites. *J. Nanostruct. Poly. Nanocomp.* 5, 107–14. Available online at: http://www.escm.eu.org/docs/eccm13/0213.pdf

Muasher, M., and Sain, M. (2006). The efficacy of photostabilizers on the color change of wood filled plastic composites. *Polym. Degrad. Stab.* 91, 1156–1165. doi: 10.1016/j.polymdegradstab.2005.06.024

Mukhopadhyay, S., and Fangueiro, R. (2009). Physical modification of natural fibers and thermoplastic films for composites — a review. *J. Thermoplast. Comp. Mater.* 135, 134–162. doi: 10.1177/0892705708091860

Müller, U., Rätzsch, M., Schwanninger, M., Steiner, M., and Zöbl, H. (2003). Yellowing and IR-changes of spruce wood as result of UV-irradiation. *J. Photochem. Photobiol. Biol.* 69, 97–105. doi: 10.1016/S1011-1344(02)00412-8

Navaneethakrishnan, S., and Athijayamani, A. (2017). Taguchi method for optimization of fabrication parameters with mechanical properties in sisal fibre-vinyl ester composites. *Aust. J. Mech. Eng.* 15, 74–83. doi: 10.1080/14484846.2015.1093258

Noriman, N. Z., and Ismail, H. (2011). The effects of electron beam irradiation on the thermal properties, fatigue life and natural weathering of styrene butadiene rubber/recycled acrylonitrile-butadiene rubber blends. *Mater. Design* 32, 3336–3346. doi: 10.1016/j.matdes.2011.02.020

Nosbi, N., Akil, H. M., Mohd Ishak, Z. A., and Abu Bakar, A. (2010). Degradation of compressive properties of pultruded kenaf fiber reinforced composites after immersion in various solutions. *Mater. Design* 31, 4960–4964. doi: 10.1016/j.matdes.2010.04.037

Pickering, S. J. (2006). Recycling Technologies for thermoset composite materials-current status. *Comp. Appl. Sci. Manufact.* 37, 1206–1215. doi: 10.1016/j.compositesa.2005.05.030

Pillay, S., Vaidya, U. K., and Janowski, G. M. (2009). Effects of moisture and UV exposure on liquid molded carbon fabric reinforced nylon 6 composite laminates. *Comp. Sci. Technol.* 69, 839–846. doi: 10.1016/j.compscitech.2008.03.021

Pothan, L. A., Oommen, Z., and Thomas, Z. (2003). Dynamic mechanical analysis of banana fiber reinforced polyester composites. *Comp. Sci. Technol.* 63, 283–293. doi: 10.1016/S0266-3538(02)00254-3

Rabek, J. F. (2012). *Photostabilization of Polymers: Priciples and Application.* Dordrecht: Springer.

Rohit, K., and Dixit, S. (2016). A review - future aspect of natural fiber reinforced composite. *Poly. Renew. Res.* 7, 43–60. doi: 10.1177/204124791600700202

Rong, M. Z., Zhang, M. Q., Liu, Y., Yang, G. C., and Zeng, M. H. (2001). The effect of fiber treatment on the mechanical properties of unidirectional sisal-reinforced epoxy composites. *Comp. Sci. Technol.* 61, 1437–1447. doi: 10.1016/S0266-3538(01)00046-X

Saha, P., Manna, S., Chowdhury, S. R., Sen, R., Roy, D., and Adhikari, B. (2010). Enhancement of tensile strength of lignocellulosic jute fibers by alkali-steam treatment. *Biores. Technol.* 101, 3182–3187. doi: 10.1016/j.biortech.2009.12.010

Salim, M. S., Ahmad Rasyid, M. F., Abdullah, M. A., Mat Taib, R., and Mohd Ishak, Z. A. (2018). Mechanical, thermal and flammability properties of nonwoven kenaf reinforced acrylic based polyester composites: effect of water glass treatment. *IOP Confer Series Mater. Sci. Eng.* 368:012040. doi: 10.1088/1757-899X/368/1/012040

Salim, M. S., Ahmad Rasyid, M. F., Mat Taib, R., and Mohd Ishak, Z. A. (2017). Processing parameters optimisation of nonwoven kenaf reinforced acrylic based polyester composites. *AIP Confer. Proc.* 1901:110007. doi: 10.1063/1.5010548

Salim, M. S., Ariawan, D., Ahmad Rasyid, M. F., Ahmad Thirmizir, M. Z., Mat Taib, R., and Mohd, Ishak, Z. A. (2019). Effect of fibre surface treatment on interfacial and mechanical properties of non-woven kenaf fibre reinforced acrylic based polyester composites. *Poly. Comp.* 40, E214–E226. doi: 10.1002/pc.24605

Salim, M. S., Ishak, Z. A. M., and Abdul Hamid, S. (2011). Effect of stitching density of nonwoven fiber mat towards mechanical properties of kenaf reinforced epoxy composites produced by resin transfer moulding (RTM). *Key Eng. Mater.* 471–472, 987–992. doi: 10.4028/www.scientific.net/KEM.471-472.987

Satoto, R., Subowo, W. S., Yusiasih, R., Takane, Y., Watanabe, Y., and Hatakeyama, T. (1997). Weathering of high-density polyethylene in different latitudes. *Poly. Degrad. Stabil.* 56, 275–279. doi: 10.1016/S0141-3910(96)00213-3

Segovia, F., Ferrer, C., Salvador, M. D., and Amigó, V. (2000). Influence of processing variables on mechanical characteristics of sunlight aged polyester-glass fibre composites. *Poly. Degrad. Stabil.* 71, 179–184. doi: 10.1016/S0141-3910(00)00168-3

Sepe, R., Bollino, F., Boccarusso, L., and Caputo, F. (2018). Influence of chemical treatments on mechanical properties of hemp fiber reinforced composites. *Comp. Eng.* 133, 210–217. doi: 10.1016/j.compositesb.2017.09.030

Shebani, A. N., van Reenen, A. J., and Meincken, M. (2008). The effect of wood extractives on the thermal stability of different wood species. *Thermochim. Acta* 471, 43–50. doi: 10.1016/j.tca.2008.02.020

Signor, A. W., VanLandingham, M. R., and Chin, J. W. (2003). Effects of ultraviolet radiation exposure on vinyl ester resins: characterization of chemical, physical and mechanical damage. *Poly. Degrad. Stabil.* 79, 359–368. doi: 10.1016/S0141-3910(02)00300-2

Sreekala, M. S., Kumaran, M. G., and Thomas, S. (2002). Water sorption in oil palm Ⓡ ber reinforced phenol formaldehyde composites. *Comp. Appl. Sci. Manufact.* 33, 763–777. doi: 10.1016/S1359-835X(02)00032-5

Sreekumar, P. A., Thomas, S. P., Saiter, J. M., Joseph, K., Unnikrishnan, G., and Thomas, S. (2009). Effect of fiber surface modification on the mechanical and water absorption characteristics of sisal/polyester composites fabricated by resin transfer molding. *Comp. Appl. Sci. Manufact.* 40, 1777–1784. doi: 10.1016/j.compositesa.2009.08.013

Stark, N. M. (2006). Effect of weathering cycle and manufacturing method on performance of wood flour and high-density polyethylene composites. *J. Appl. Poly. Sci.* 100, 3131–3140. doi: 10.1002/app.23035

Thirmizir, A. M. Z., Mohd Ishak, Z. A., Rahim, M. T. R. S., and Mohamad Jani, S. (2011). Natural weathering of kenaf bast fibre-filled poly(butylene succinate) composites: effect of fibre loading and compatibiliser addition. *J. Poly. Environ.* 19, 263–273. doi: 10.1007/s10924-010-0272-2

Umoru, P. E., Boryo, Doris, E. A., Aliyu, A. O., and Adeyemi, O. O. (2014). Processing and evaluation of chemically treated kenaf bast (*Hibiscus cannabinus*). *Int. J. Scienti. Tech. Res.*3, 1–6. Available online at: http://www.ijstr.org/final-print/july2014/Processing-And-Evaluation-Of-Chemically-Treated-Kenaf-Bast-hibiscus-Cannabinus.pdf

Van de Weyenberg, I., Chi Truong, V. T., Vangrimde, B., and Verpoest, I. (2006). Improving the properties of UD flax fibre reinforced composites by applying an alkaline fibre treatment. *Comp. Appl. Sci. Manufact.* 37, 1368–1376. doi: 10.1016/j.compositesa.2005.08.016

Woo, R. S. C., Zhu, H., Leung, C. K. Y., and Kim, J.-K. (2008). Environmental degradation of epoxy-organoclay nanocomposites due to uv exposure : part II residual mechanical properties. *Comp. Sci. Technol.* 68, 2149–2155. doi: 10.1016/j.compscitech.2008.03.020

Yang, Y., Ota, T., Morii, T., and Hamada, H. (2011). Mechanical property and hydrothermal aging of injection molded jute/polypropylene composites. *J. Mater. Sci.* 46, 2678–2684. doi: 10.1007/s10853-010-5134-8

Zhao, Q., Jia, Z., Li, X., and Ye, Z. (2010). Surface degradation of unsaturated polyester resin in xe artificial weathering environment. *Mater. Design* 31, 4457–4460. doi: 10.1016/j.matdes.2010.04.004

Investigation on the Durability of PLA Bionanocomposite Fibers Under Hygrothermal Conditions

Tassadit Aouat[1,2], Mustapha Kaci[1]*, José-Marie Lopez-Cuesta[3] and Eric Devaux[4]

[1] Laboratoire des Matériaux Polymères Avancés, Faculté de Technologie, Université de Bejaia, Bejaia, Algeria, [2] Faculté des Sciences et de la Technologie, Université Yahia Farès, Médéa, Algeria, [3] Centre des Matériaux des Mines d'Alès, IMT Mines Alès, Alès, France, [4] École Nationale Supérieure des Arts et Industries Textiles, GEMTEX, Roubaix, France

Hygrothermal aging of neat poly(lactic acid) (PLA), PLA/microcrystalline cellulose (MCC), and PLA/cellulose nanowhiskers (CNW) fibers prepared by melt-spinning process was investigated at 95% relative humidity (RH) and two temperatures, i.e., 45 and 60°C. PLA bionanocomposite fibers were melt compounded at filler content of 1 wt% in the presence of PLA-grafted-maleic anhydride (PLA-g-MA) (7 wt%) used as compatibilizer. The influence of the type of cellulosic filler and the temperature on the hydrolytic degradation kinetics was evaluated through changes in molecular structure and physico-mechanical properties of the samples. The study showed, that all exposed fibers to hygrothermal aging, were subjected to chain scission mechanism responsible for the decrease in average molecular weight, thermal stability and tensile properties, however, more pronounced after 14 days at 60°C. Furthermore, an increase in crystallinity with a fast crystallization process was noticed for all exposed fibers. The study revealed that the hydrolysis rate increased by 5, 6, and 7 times after 14 days at 60°C compared to 25 days at 45°C for neat PLA, PLA/PLA-g-MA/MCC1, and PLA/PLA-g-MA/CNW1 fibers, respectively. This has been ascribed to the catalytic behavior of the cellulosic fillers which promotes water diffusion into the PLA matrix. Finally, the study concludes to the capacity of PLA fibers to better withdraw to hydrothermal aging in comparison to PLA/cellulose bionanocomposites. The durability of PLA fibers to hygrothermal degradation is established in the following order: PLA > PLA/PLA-g-MA/MCC1 > PLA/PLA-g-MA/CNW1.

Keywords: polylactide, cellulose, bionanocomposites, hygrothermal aging, hydrolysis

INTRODUCTION

The development of biodegradable and renewable polymeric materials as natural fiber composites is increasing significantly regarding their economic and ecological advantages (Vilaplana et al., 2010). The interest shown in biodegradable polymers meets the concerns of preserving the environment by minimizing the use of generally polluting petrochemical synthetic polymers and also by avoiding dependence on non-renewable resources. In this context, PLA, which belongs to the family of aliphatic polyesters, is one of the main representatives of the biodegradable polymers (Hajba et al., 2015). Moreover, PLA has good mechanical and optical properties, which are comparable to the conventional synthetic polymers, like polyolefin and PET. It is therefore widely used in many

applications involving food packaging, automotive parts, disposable tableware, sutures and drug delivery device (Chow et al., 2014). However, expanding the utilization of PLA to other industrial fields is rather limited due to its slow crystallization speed and brittleness to some extent (Sun et al., 2017). To overcome these issues, many studies have shown that adding natural fibers or cellulose nanomaterials is an effective, useful method to reinforce PLA (Mokhena et al., 2018). Cellulose due to its abundant availability, renewability, biodegradability, high strength and stiffness, could replace advantageously layered silicates, carbon nanomaterials and other metallic oxide fillers. According to the literature (Rahman et al., 2014), the theoretical modulus of the native cellulose is estimated at 167.5 GPa, which is one of the strongest and stiffest natural fibers available. Cellulose materials as cellulose nanofibers (CNF), cellulose nanowhiskers (CNW), and microcrystalline cellulose (MCC) have a high potential to act as reinforcing agents in biopolymers. However, the highly hydrophilic surface of cellulose makes it difficult to prevent fiber aggregation in hydrophobic polymers, such as PLA (Wang and Drzal, 2012). There are three main approaches available to improve the dispersion and the interface bonding of the cellulosic filler with the polymer matrix, through either polymer or filler modification, or the addition of a third component, i.e., a coupling agent, such as maleic anhydride grafted polymers (Hassaini et al., 2017; Hamad et al., 2018). In the current paper, which is a continuation of a previous work (Aouat et al., 2018), PLA-*g*-MA was used as the compatibilizer for the PLA/cellulose bionanocomposites to improve the matrix-filler affinity.

Furthermore, the sensitivity to moisture uptake is a well-known weakness, which limits the performance of biocomposite materials, due to the hydrophilic nature of the biopolymer matrix and/or the natural reinforcement (Vilaplana et al., 2010). Moisture uptake can induce swelling of the biocomposite which may impair interfacial strength and subsequently generate cracks in the matrix (Bayart et al., 2017). Swelling phenomenon is attributed to the interaction of the fiber cell-wall components (containing –OH, –COOH, and other polar groups) with water molecules via hydrogen bond formation (Islam et al., 2010). These are serious issues for long-term applications where the biocomposites may be exposed to the combined effect of high humidity and temperature conditions. Although, a recent publication (Mangin et al., 2018) has shown that incorporating miscible PMMA to flame-retarded PLA improves its resistance to hydrothermal aging, further studies are however necessary to better understanding the behavior of such materials in a high humid atmosphere or in water. This is a prerequisite for any outdoor application. Despite the technological importance of this research theme, few studies are unfortunately available in literature on degradation of PLA/cellulose biocomposite materials in hygrothermal conditions, and even less on melt-spun PLA fibers (Xian et al., 2018).

Therefore, the objective of this paper was to investigate the influence of combined humid atmosphere and temperature on the morphology, the chemical structure and the physical properties of neat PLA, PLA/PLA-*g*-MA/MCC1, and PLA/PLA-*g*-MA/CNW1 bionanocomposite fibers. The hygrothermal aging

was conducted in a climatic chamber at 95% RH and at two temperatures: 45 and 60°C. The filler size effect on the rate of hydrolysis of PLA fibers was also investigated. The choice of 45 and 60°C as the hygrothermal degradation temperatures was not arbitrary, it was justified by the fact that PLA fibers are in glassy state at 45°C and rubbery state at 60°C, considering that the transition temperature of PLA is around 60°C. Furthermore, 60°C is often the temperature which is used in clearing treatment of textile fibers in the industry.

EXPERIMENTAL

Materials Used

PLA was fiber-grade resin 6202D and supplied by Nature Works LLC. According to the manufacturer, the main physical characteristics of the polymer are as follows: density = 1.24 g/cm^3, glass transition temperature (T_g) = 60°C, and melting point (T_m) ∼160–170°C.

Microcrystalline cellulose (MCC) was supplied by Sigma-Aldrich under the trade name Avicel PH 101. MCC was also used as the raw material for extracting cellulose nanowhiskers (CNW) by using sulfuric acid hydrolysis in aqueous media (Aouat et al., 2018). Sulfuric acid 95–97% was purchased from Sigma-Aldrich. PLA-*g*-MA (∼3 wt.% of maleic anhydride) used as the compatibilizer for the cellulosic PLA fibers, was prepared in the laboratory Materia Nova (Mons, Belgium) by reactive extrusion using a Leistritz twin-screw extruder (L/D = 50).

Preparation of PLA/Cellulose Bionanocomposites

PLA and PLA bionanocomposite fibers were manufactured by two-step process. The first one consisted of preparing pellets by a Thermo-Haake co-rotating intermeshing twin-screw extruder (L/D = 25) according to the compositions reported in **Table 1**. In the second step, the pellets were used to obtain the multifilament fibers using a melt-spinning machine, Model Spinboy I, manufactured by Busschaert Engineering. Elaboration of PLA fibers has been detailed in a recent paper (Aouat et al., 2018).

TABLE 1 | Values of water uptake at saturation, water diffusion coefficient and activation energy of PLA, PLA/PLA-*g*-MA/MCC1, and PLA/PLA-*g*-MA/CNW1 fibers recorded at 45 and 60°C in hygrothermal conditions.

Fibers	Water uptake at saturation (%)		Water diffusion coefficient (m^2/s)		Activation energy (kcal/mol)
	45°C	60°C	45°C	60°C	
PLA (100 wt%)	0.51	1.17	2.36×10^{-16}	4.99×10^{-16}	10.5
PLA/PLA-*g*-MA/MCC1 (92/7/1 wt%)	1.7	1.94	4.13×10^{-16}	6.36×10^{-16}	6.08
PLA/PLA-*g*-MA/CNW1 (92/7/1 wt%)	1.3	1.55	3.38×10^{-16}	5.76×10^{-16}	7.48

Hygrothermal Aging

Both PLA and PLA bionanocomposite fibers in form of coils were subjected to hygrothermal aging in a climatic chamber of Model Excal 2221-HA at 95% RH and two temperatures, i.e., 45 and 60°C. The fibers were placed on metal grid in the center of the enclosure having the following dimensions: 50 × 50 × 75 cm. The climatic chamber used is equipped with the Spirale® software, which allows the aging parameters to be controlled. Fiber samples were removed periodically with time for characterization tests.

Technical Characterization

Water Uptake

The moisture uptake of PLA fibers was estimated by weighing. The samples removed from the climatic chamber, were immediately weighed (m_2) to avoid any moisture loss and weighed again after sampling before being replaced in the chamber. Percent moisture uptake (%H) is determined by Equation (1):

$$\%H = \%H_1 + \frac{m_2 - m_1}{m_2} \cdot 100 \qquad (1)$$

Where, %H is the percent moisture uptake, $\%H_1$ is the percent moisture uptake at previous removing; m_1 is the sample mass at previous removing, while m_2 is the sample mass currently noted.

In addition, the water uptake capacity of the exposed PLA and PLA bionanocomposite fibers in the climatic chamber was also expressed in terms of diffusion coefficient. Assuming that the PLA fibers have a cylindrical shape, the water diffusivity in the matrix is expressed by Equation (2) (Hossain et al., 2014):

$$D = \frac{\pi d^2}{16 W_s^2} \times \frac{(W_2 - W_1)^2}{\left(\sqrt{t_2} - \sqrt{t_1}\right)^2} \qquad (2)$$

Where, D is the water diffusion coefficient in $(m^2.s^{-1})$, d is the average diameter of the fiber in (m), Ws is the water uptake at saturation in (%) and $\frac{(W_2 - W_1)^2}{\left(\sqrt{t_2} - \sqrt{t_1}\right)^2}$ is the square slope of the linear portion of the curve of water uptake vs. root of time.

The activation energy of water diffusion (E_D) in (kcal/mol) was determined by linear regression through ($ln\,D$) vs. ($1/T$) according to Arrhenius equation, i.e., Equation (3) (Fayolle and Verdu, 2005):

$$lnD = a - \frac{E_D}{RT} \qquad (3)$$

Where, T is temperature in (K) and R, the ideal gas constant (8.32 kJ·mol^{-1}·K^{-1}).

Viscosimetric Measurements

Viscosimetric measurements were carried out in an Ubbelhode viscometer at 30°C with chloroform as solvent. Assuming the kinetic energy and shear corrections negligible, the Huggins equation was applied to estimate the intrinsic viscosity [η]. The latter is related to the viscosity average molecular weight ($\overline{M_v}$), by the Mark-Houwink-Sakurada equation: $[\eta] = K.\overline{M_v}^a$ (where, K and a, are empirical constants). For the PLA/chloroform system

at 30°C, K = 1.31×10^{-4} dl/g and a = 0.759 (Persson and Mikael, 2013). The extent of hydrolytic degradation of PLA fibers and its bionanocomposites is determined from the number of main-chain scission index (SI). SI is defined according to the following Equation (4) (Remili et al., 2009).

$$SI = [\overline{M_{v0}}/\overline{M_v}] - 1 \qquad (4)$$

Where $\overline{M_{v0}}$ and $\overline{M_v}$ are the viscosity-average molecular weight before and after hygrothermal exposure of the fibers. In addition, the hydrolysis rate was also followed by the hydrolysis rate constant (k) determined by the linear regression method.

Tensile Measurements

The tensile measurements were conducted on twisted fibers (80 monofilaments). A mechanical tester system MTS associated with a force sensor of 1 kN was used. In order to adjust the clamp load and to grip the sample with the least amount of stress, a special design for testing yarns was used (capstan grips). Capstan roller in addition to vise action allows the sample to be both clamped at the desired level and to be wound around the capstan to distribute the remaining stress via friction. The tensile properties were measured according to ISO 2062 standard test method. A loading speed of 200 mm/min and a distance of 200 mm between grips were applied. All mechanical tests were carried out by using specimens previously stored for at least 48 h at 20 ± 2°C at 50 ± 3% RH. The values were averaged out over five measurements for each sample.

Because of the variation in the fibers fineness, the tensile strength is expressed as tenacity (cN/tex), a specific value related to fineness (force per unit fineness). Fineness in tex (g/km), was determined by dividing the mass of fibers by their known length (Milanovic et al., 2012).

Differential Scanning Calorimetry (DSC)

DSC thermograms of PLA fibers were performed using a 2920 Modulated DSC (TA Instruments) before and after exposure to hygrothermal aging. The dried samples of an average weight of about 10 mg were placed in hermetically closed DSC capsules in nitrogen atmosphere at 50 ml/min. The heating and cooling steps were carried out at a rate of 10°C/min from 20 to 200°C and from 200 to 20°C, respectively. Glass transition temperature (T_g), cold crystallization temperature (T_{cc}) and melting temperature (T_m) were determined from the second heating cycle of the PLA fibers. The crystalline index (X_c) was calculated according to Equation (5) (Dadbin and Kheirkhah, 2014):

$$X_c(\%) = \frac{\Delta H_m - \Delta H_{cc}}{W \cdot \Delta H_{m0}} \cdot 100 \qquad (5)$$

Where, ΔH_m is the melting enthalpy of the sample, ΔH_{m0} is the melting enthalpy of 100% crystalline PLA, taken as 93 J/g (Fortunati et al., 2012). ΔH_{cc} is the crystallization enthalpy and W is the weight fraction of PLA in the bionanocomposite fibers.

Wide Angle X-Ray Scattering (WAXS)

WAXS measurements were carried out on a Philips PW1050 diffractometer. The X-ray patterns were recorded in a range of

2–40° with a step of 0.02° and step time of 2 s. The wavelength of the Cu/Kα rod surface was λ = 0,154 nm and the spectra were obtained at 20 mA with an accelerating voltage of 40 eV.

Thermogravimetric Analysis (TGA)

Thermogravimetric analysis (TGA) was performed on a Perkin Elmer Pyris-1 TGA thermo-balance (PerkinElmer, Waltham, MA, USA) operating under N_2 atmosphere in alumina crucibles containing around 10 mg of material and ranging from 30 to 900°C at a heating rate of 10°C/min.

Scanning Electron Microscopy (SEM)

SEM images of the fibers were recorded using a QUANTA 200 FEG (FEI Company) environmental scanning electron microscope at an acceleration voltage of 7–10 keV. Prior to any observation in scanning mode (SEM), the transversal surfaces of the fibers were sputter coated with carbon using a Carbon Evaporator Device CED030 (Balzers), to ensure good surface conductivity and to avoid any degradation.

Transmission Electron Microscopy (TEM)

TEM observations were carried out on a JEOL 1200EX TEM scanning electron microscope operating at an accelerating voltage of 100 kV. The samples were embedded in a LR white resin and ultrathin-sectioned at 70 nm using a Leica EM UC7 ultra-microtome with a diamond knife Ultra 45 (Nissei Sangyo). The sections were transferred to carbon-coated Cu grids of 300 meshes.

RESULTS AND DISCUSSION

Water Uptake (WU)

Belonging to the family of aliphatic polyesters, PLA and its bionanocomposites absorb moisture when they are immersed in water or exposed to a humid atmosphere. Moisture uptake phenomenon leads to property changes and degrades also the materials through hydrolysis (Elsawy et al., 2017). In this regard, water uptake (WU) kinetics of PLA, PLA/PLA-g-MA/MCC1, and PLA/PLA-g-MA/CNW1 fibers were determined at 45 and 60°C. The relative plots are shown in **Figures 1A–D**. Furthermore, the values of WU at saturation, diffusion coefficient, and activation energy are also provided in **Table 1**.

Figures 1A,B displays the curves of WU as a function of exposure time for PLA and PLA bionanocomposite fibers at 45 and 60°C, respectively. As expected, WU capacity of PLA matrix is lower compared to that of its bionanocomposites. Nevertheless,
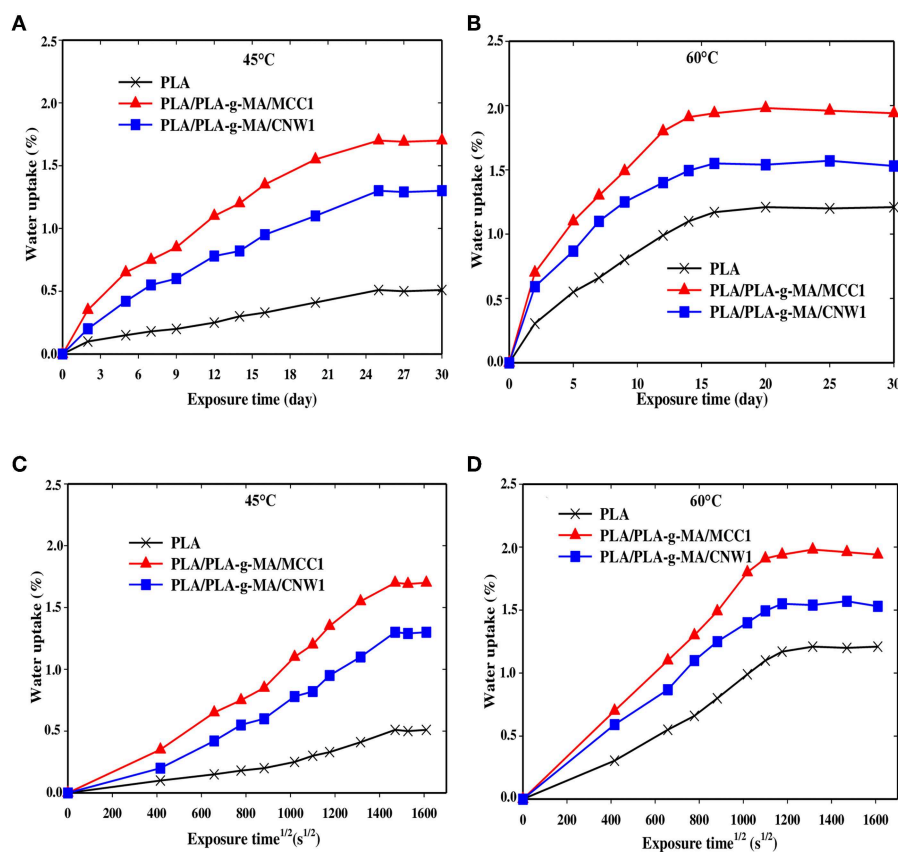

FIGURE 1 | Water uptake curves of PLA, PLA-g-MA/MCC1, and PLA-g-MA/CNW1 fibers vs. exposure time **(A)**: 45°C and **(B)**: 60°C and root of time **(C)** 45°C and **(D)**: 60°C, respectively in hygrothermal conditions.
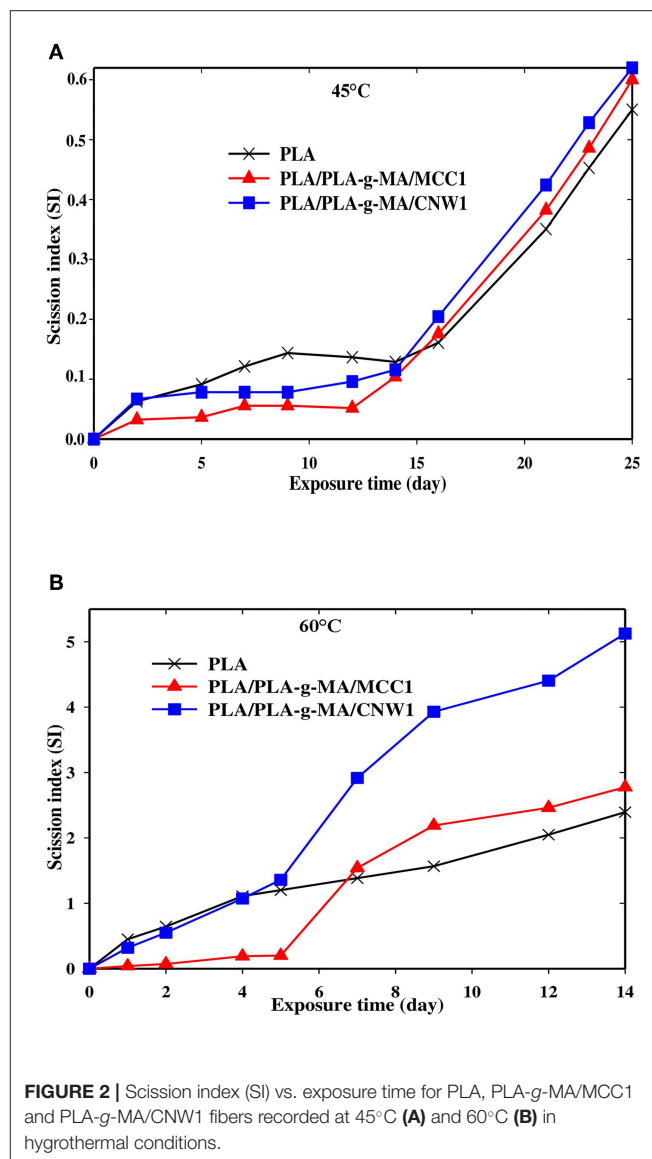
an increase in WU is observed for all fibers with increasing both exposure time and temperature, being less pronounced for PLA. It is also observed that for PLA bionanocomposite fibers filled with MCC1, WU % is much higher than those filled with CNW1, whatever the temperature. This may be due to higher level of crystallinity in PLA/PLA-g-MA/CNW1. Indeed, the downward trend in WU of highly crystalline polymers has already been reported by many authors (Zhou and Xanthos, 2008; Balakrishnan et al., 2011; Hossain et al., 2014; Mitchell and Hirt, 2015), which is attributed on one hand, to the barrier effect of impermeable crystallites, and on the other hand, to the tortuosity of water diffusion into the polymeric matrix. In addition, the filler specific surface is another parameter, which has to be considered, since the larger the filler specific surface, the higher the amount of water trapped.

Figures 1C,D show that WU of all fibers increases almost linearly with the root of time at 60°C compared to 45°C before reaching saturation. This suggests that water diffusion in PLA fibers is governed by Fick's law, which is in agreement with the data reported in the literature (Yew et al., 2005; Balakrishnan et al., 2011; Ndazi and Karlsson, 2011; Chow et al., 2014; Gil-Castell et al., 2014; Hossain et al., 2014; Yu et al., 2018). The increase of WU of PLA and its bionanocomposites with time may also result from the formation of strong polar groups during hydrolysis process, mainly hydrophilic acid functions and also from the increase of the free volume in PLA matrix (Mortaigne, 2005; Zhou and Xanthos, 2008). Indeed, Gupta et al. (2012) reported a decrease in contact angle of PLA with time and subsequently, an increase of its polarity in the course of the hydrolysis process.

Table 1 shows that the activation energy value of PLA fiber is much higher than that of PLA bionanocomposites with 38 and 72% increases compared to that of PLA/PLA-g-MA/CNW1, and PLA/PLA-g-MA/MCC1, respectively. The lower WU value of PLA results from its higher relative hydrophobic character compared to that of the bionanocomposites. This is consistent with the literature data (Yew et al., 2005; Zhou and Xanthos, 2008; Balakrishnan et al., 2011; Yu et al., 2018) reporting WU values of PLA ranging from 0.5 to 1.0%. In addition, the significant mass gain of PLA bionanocomposites over PLA mainly could be ascribed to the cellulosic fillers, which are highly hydrophilic materials. The presence of hydroxyl groups (OH) in MCC and CNW is favorable for the occurrence of hydrogen bonding with moisture (Elsawy et al., 2017). This is in a good agreement with many authors who reported that the incorporation of natural hydrophilic fillers to PLA increases its WU capacity. These include cellulose nanowhiskers (Hossain et al., 2012), sisal fibers (Gil-Castell et al., 2014, 2016), ramie fibers (Yu et al., 2018), coconut fibers (Wu, 2009), and wood pulp (Azwar et al., 2012).

Scission Index Evolution
The hydrolytic degradation kinetics of PLA fibers and its bionanocomposite were investigated by determining the scission index (SI) with exposure time. The plots are shown in **Figures 2A,B** for PLA and the bionanocomposite fibers at 45

FIGURE 2 | Scission index (SI) vs. exposure time for PLA, PLA-g-MA/MCC1 and PLA-g-MA/CNW1 fibers recorded at 45°C **(A)** and 60°C **(B)** in hygrothermal conditions.

and 60°C, respectively. Furthermore, **Table 2** summarizes the k values, which give the hydrolysis rate of the exposed fibers.

In **Figures 2A,B**, there is an increasing evolution of SI curves with time for all PLA fibers whatever the temperature meaning that the degradation mechanism predominantly occurring in the matrix is chain scission (Gajjar and King, 2014; Gil-Castell et al., 2014). Indeed, the literature (Elsawy et al., 2017) reported that under humid conditions, hydrolysis reactions occur between PLA ester groups and water molecules resulting in chain scission forming chain segments with low molecular weight (Girdthep et al., 2016; Lins et al., 2016; Lorenzo et al., 2016; Mohammad et al., 2016; Pinese et al., 2016; Stloukal et al., 2016; Yang et al., 2016). Moreover, the hydrolysis of PLA bionanocomposites is strongly dependent on the intrinsic characteristics of PLA matrix, the nature of fillers, their dispersion in the polymer and the environment conditions (humidity and temperature)

TABLE 2 | Hydrolysis parameters (hydrolysis rate constant k, coefficient of correlation R^2, timescale for diffusion and timescale of reaction) of PLA, PLA/PLA-g-MA/MCC1, and PLA/PLA-g-MA/CNW1 fibers at 45 and 60°C in hygrothermal conditions.

Fibers	k (J^{-1})		r^2/D_e (J)		1/k (J)	
	45°C	60°C (R^2)	45°C	60°C	45°C	60°C
PLA	0.0102 $R^2 = 0.85$	0.0568 $R^2 = 0.87$	37×10^5	17×10^5	98	18
PLA/PLA-g-MA/MCC1	0.0122 $R^2 = 0.82$	0.087 $R^2 = 0.95$	25×10^5	15×10^5	81	11
PLA/PLA-g-MA/CNW1	0.0125 $R^2 = 0.83$	0.1025 $R^2 = 0.90$	26×10^5	16×10^5	80	10

(Zhou and Xanthos, 2008; Maharana et al., 2009). In this regard, an increase in temperature from 45 to 60°C, results in a fast hydrolysis process of PLA. Thus, the k values given in **Table 3**, indicate that all PLA fibers are more sensitive to hydrolysis at 60°C than 45°C. Indeed, the k values of PLA, PLA/PLA-g-MA/MCC1 and PLA/PLA-g-MA/CNW1 fibers recorded after 14 days at 60°C are 5, 7, and 8 times higher than after 25 days at 45°C, respectively. At 60°C, which is the T_g of PLA, the chain mobility increases significantly, thus promoting water diffusion in the amorphous phase of PLA and subsequently a faster hydrolysis (Zhou and Xanthos, 2008; Balakrishnan et al., 2011; Castro-Aguirre et al., 2016). This is consistent with the data published by Copinet et al. (2004) and Zhou and Xanthos (2008) who reported a faster degradation of PLA at 60°C than at 45 and 50°C. From **Table 3**, the catalytic role of cellulosic fillers on PLA hydrolysis is highlighted, especially at 60°C. An increase in the k value by almost 53 and 80% is recorded for PLA/PLA-g-MA/MCC1 and PLA/PLA-g-MA/CNW1, respectively compared to that of neat PLA. This result is attributed to filler hydration, which is one of the key parameters responsible for accelerating the polymer hydrolytic degradation (Loo et al., 2005; Zhou and Xanthos, 2008). Accordingly, hydration phenomenon is explained by the easier accessibility to water of PLA in the presence of cellulosic fillers, which is in line with the water diffusion coefficient values shown in **Table 1**. Furthermore, the data provided in **Table 2** show clearly the effect of the specific surface of the cellulosic filler on the hydrolysis of PLA. Although, the accessibility to water of PLA/PLA-g-MA/MCC1 is easier than that filled with CNW1 as shown in **Table 1**, it is however observed that the latter is more vulnerable to hygrothermal degradation. Indeed, **Figure 2B** shows the presence of a short induction period of about 5 days for PLA/PLA-g-MA/MCC1 fibers at 60°C up to 14 days, whereas the chain scission mechanism starts up on exposure for both PLA and PLA/PLA-g-MA/CNW1 fibers. This behavior is explained as a result of the high capacity of MCC to store the absorbed water, therefore reducing the wettability of PLA matrix. Unlike, CNW leads to better and homogeneous hydration of PLA matrix, thus promoting hydrolysis. Similarly, Kummerer et al. (2011) reported that cellulose nanocrystals are more sensitive to degradation than MCC in an aqueous environment. **Table 2**

TABLE 3 | Values of Young's modulus, tenacity, and % elongation at maximum deformation of PLA, PLA/PLA-g-MA/MCC1, and PLA/PLA-g-MA/CNW1 fibers recorded at 45 and 60°C in hygrothermal conditions.

Fibers	Young's modulus (GPa)						Tenacity (CN/tex)						Elongation at maximum deformation (%)					
	PLA		PLA/PLA-g-MA/MCC1		PLA/PLA-g-MA/CNW1		PLA		PLA/PLA-g-MA/MCC1		PLA/PLA-g-MA/CNW1		PLA		PLA/PLA-g-MA/MCC1		PLA/PLA-g-MA/CNW1	
T (°C) Days	45	60	45	60	45	60	45	60	45	60	45	60	45	60	45	60	45	60
0	3.26	3.26	2.95	2.94	3.38	3.37	7.74	7.74	6.88	6.88	8.04	8.04	77.67	77.90	36.40	36.39	91.60	91.61
2	3.25	3.17	2.93	2.71	3.37	3.32	7.74	5.54	6.88	6.35	8.00	6.04	76.76	21.30	36.3	18.40	87.6	47.30
5	3.27	3.07	2.95	2.46	3.35	2.93	7.70	3.06	6.86	3.07	8.03	3.23	75.36	1.98	35.23	1.10	83.71	1.50
7	3.26	2.82	2.92	1.3	3.37	1.1	6.97	2.41	6.61	1.72	7.56	0.70	76.49	1.40	32.34	0.20	76.80	0.29
9	3.25	1.87	2.91	–	3.34	–	6.96	2.16	6.50	–	7.44	–	76.3	0.88	31.3	–	73.5	–
14	3.24	–	2.88	–	3.27	–	6.97	–	6.37	–	7.25	–	75.41	–	31.18	–	67.14	–
16	3.22	–	2.85	–	3.15	–	6.96	–	6.09	–	6.99	–	71.08	–	30.67	–	67.71	–
21	3.14	–	2.81	–	3.05	–	5.73	–	5.02	–	5.63	–	65.45	–	25.76	–	52.85	–
25	3.05	–	2.77	–	3.02	–	5.01	–	4.15	–	4.66	–	53.24	–	19.21	–	45.86	–

reports also the values of timescale for diffusion (r^2/De) for all fibers, which are much higher than those of timescale of reaction ($1/k$) at both 45 and 60°C. This indicates that the process of hydrolysis occurs mainly through a series of reactions rather than by a water diffusion process (Mitchell and Hirt, 2015).

Morphological Characterization

Figures 3–5 shows SEM images of both external and cross-sectional surfaces of PLA and PLA bionanocomposite fibers before exposure and after 25 days at 45°C and 14 days at 60°C. **Figure 3a** displays the external surface fiber of neat PLA before exposure. The surface is smooth and regular. After 25 days at 45°C, no noticeable change was observed on the surface of neat PLA as shown in **Figure 3b**. However, after 14 days at 60°C, some cracks were formed which were preferentially localized on the fiber sides (**Figure 3c**). Similar morphology has been observed by Yuan et al. (2002) on hygrothermal degradation of PLA fibers. In **Figure 3d**, the cross sectional surface fiber exhibits a homogeneous morphology, which seems intact without any damage. This result indicates that the hygrothermal aging of PLA occurs on the fiber surface rather than in the bulk. This is explained by the weak polarity of PLA which prevents the water diffusion from the surface to the bulk of material (Gupta et al.,

2012) in concordance with the WU data reported in **Table 1**. **Figure 4a** shows the SEM micrograph of the external surface of PLA/PLA-*g*-MA/MCC1 fiber before exposure. Although the surface appears smooth, its diameter is variable. Indeed, the diameter varies along the fiber passing from 65 to 100 μm, which is probably due to the presence of MCC aggregates of various sizes in PLA matrix. **Figure 4b** displays the external surface of PLA fiber filled with MCC1 after 25 days of exposure at 45°C. The surface seems also smooth, however a decohesion between MCC and PLA matrix was observed. This phenomenon became more pronounced after 14 days at 60°C as shown in **Figure 4c** since many cracks were formed randomly at the fiber surface, playing a role of degradation precursors. Conversely to PLA fiber, it can be seen in **Figure 4d** that the hydrolytic degradation of PLA/PLA-*g*-MA/MCC1 occurs not only on the fiber surface, but also in the bulk as clearly demonstrated by the formation of internal crack starting from the surface to the filler aggregate. **Figure 5a** shows regular PLA/PLA-*g*-MA/CNW1 fibers with a diameter very close to that of neat PLA. The surface morphology of the fibers remained almost unchanged after 25 days of exposure at 45°C (**Figure 5b**). However, after 14 days at 60°C, the bionanocomposite fiber was severely damaged with the appearance of a surface erosion phenomenon as shown

FIGURE 3 | SEM micrographs of external surface of a PLA fiber. **(a)** Before exposure, **(b)** after 25 days at 45°C, **(c)** after 14 days at 60°C, and **(d)** SEM micrograph of cross-sectional surface of a PLA fiber after 14 days at 60°C.
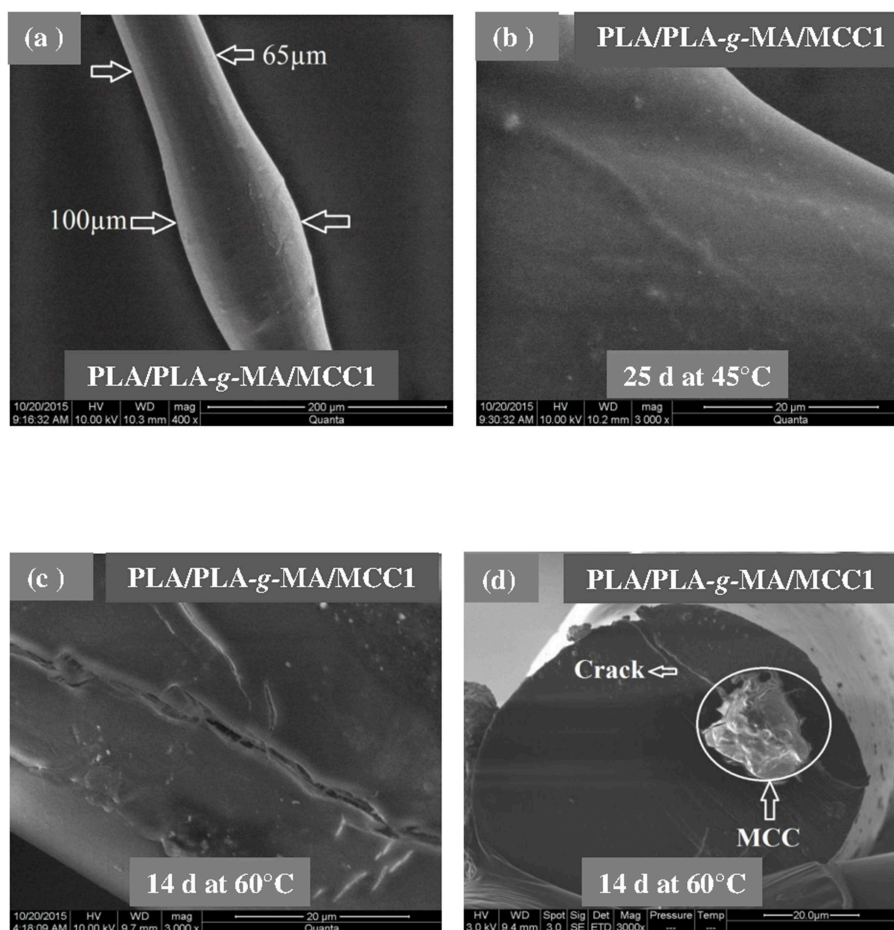
FIGURE 4 | SEM micrographs of external surface of a PLA/PLA-*g*-MA/MCC1 fiber. **(a)** Before exposure, **(b)** after 25 days at 45°C, **(c)** after 14 days at 60°C, and **(d)** SEM micrograph of cross-sectional surface of a PLA fiber after 14 days at 60°C.

in **Figure 5c**. Further, cracks of almost 10 μm long, regularly distributed on the surface and perpendicularly oriented to the fiber direction were observed. The cracks are probably formed due to the migration of various species including monomers and oligomers resulting from hydrolysis. In addition, the effect of hygrothermal aging on the morphological structure of neat PLA and PLA bionanocomposite fibers was also investigated by TEM. The corresponding TEM images are shown in **Figures 6** and **7**. **Figure 6a** shows the surface morphology of neat PLA before exposure. The sample exhibits a regular and homogenous morphology with no surface defects. After 25 days of exposure at 45°C, some microvoids were observed on the fiber surface (**Figure 6b**), whose number and size seemed to increase with increasing the temperature to 60°C as illustrated in **Figure 6c**. In **Figure 7a**, which corresponds to PLA/PLA-*g*-MA/CNW1 recorded before exposure, CNW particles are clearly distinguished from the PLA matrix by their whiteness and also by their typical rod shape. **Figure 7b** shows the presence of defects on the surface observed after 25 days at 45°C. The morphology of the bionanocomposite fiber exhibits

essentially microvoids similarly to neat PLA. However, after 14 days at 60°C, the CNW particles appeared as black spots of higher density as clearly shown in **Figure 7c**. This means that CNW were completely disintegrated during hydrolysis at 60°C. According to the literature (Pan et al., 2010; Ruiz et al., 2013), the aging of cellulosic fillers due to moisture uptake may lead to several structural and properties changes involving their depolymerization. At this stage, CNW showed a remarkable change in color from white to black (Dong et al., 1998; Jewena et al., 2016).

Tensile Measurements

Tensile properties, which are one of the main functional properties of polymers, are generally used as aging criteria to evaluate the durability of polymers in hygrothermal conditions (Chow et al., 2014). In this regard, tensile properties of PLA and PLA bionanocomposite fibers were investigated at 45 and 60°C and the data are summarized in **Table 3**. In addition, the kinetics curves of tenacity of PLA fibers plotted at 45 and 60°C are shown in **Figure 8**. According to **Table 3**, elongation
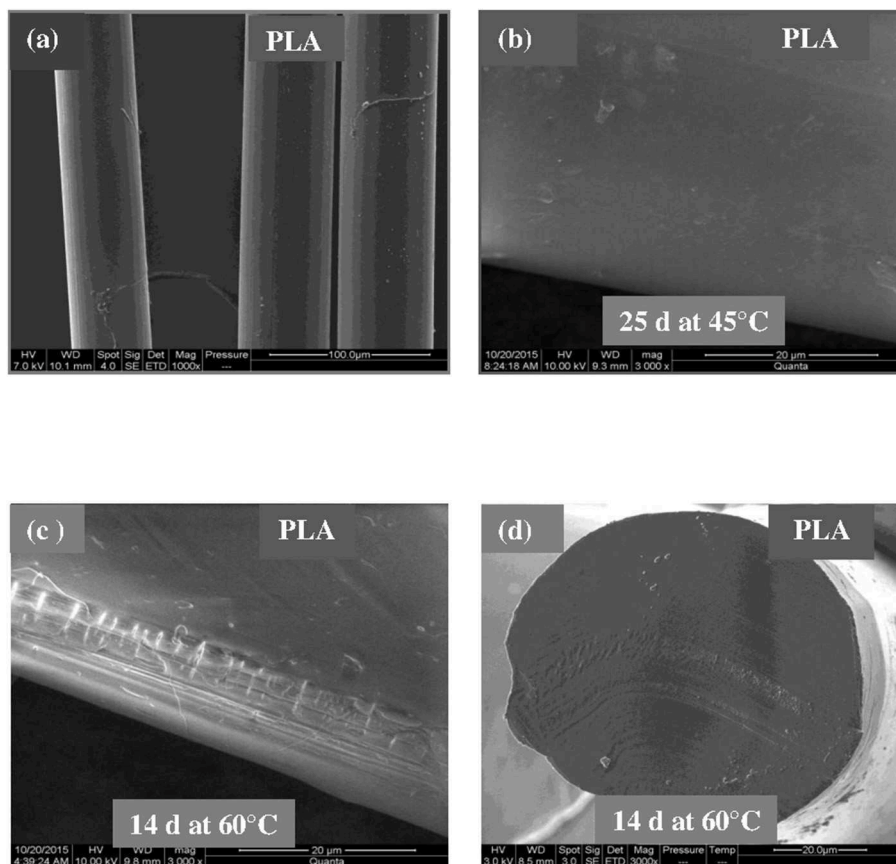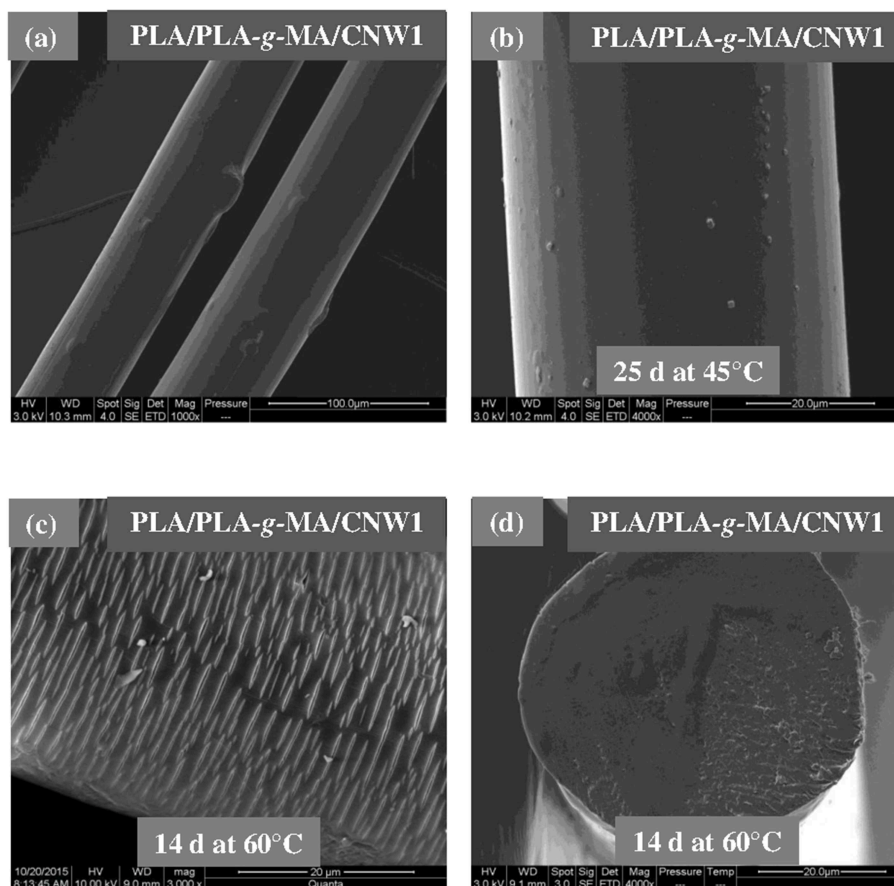
FIGURE 5 | SEM micrographs of external surface of a PLA/PLA-*g*-MA/CNW1 fiber. **(a)** Before exposure, **(b)** after 25 days at 45°C, **(c)** after 14 days at 60°C, and **(d)** SEM micrograph of cross-sectional surface of a PLA fiber after 14 days at 60°C.

at maximum deformation, Young's modulus and tenacity of the whole PLA fibers were reduced from hygrothermal exposure. Thus, at 45°C and after 25 days, the value of Young's modulus decreased by ∼8, 10, and 15% from the initial one for the neat PLA, PLA/PLA-*g*-MA/MCC1, and PLA/PLA-*g*-MA/CNW1, respectively. The decrease in Young's modulus may be attributed to the molecular weight decrease of PLA due to chain scission (Yu et al., 2018). Moreover, **Table 3** shows also that the loss in tensile properties of the exposed PLA fibers is logically more pronounced at 60°C than 45°C. Hence, after 7 days at 60°C, the PLA fibers were no longer stretchable, while at 45°C, the relative tenacity was almost stable up to 14 days. After this, a slight decrease in Young's modulus and elongation at maximum deformation was noted up to 25 days. It can be seen that the kinetics curves of relative tenacity and SI show similar trend. Whatever the filler specific surface, its incorporation in PLA matrix even at a very low content ratio, resulted in a decrease in the mechanical properties of the bionanocomposite fibers, especially at 60°C. As a matter of fact, more than 92% decrease in the initial relative toughness of PLA/PLA-*g*-MA/CNW1 fibers were observed after 7 days at 60°C, compared to 69% loss for

the neat PLA. Water diffusion at filler-matrix interface, could cause a differential swelling due to the difference in absorption capacity between the cellulosic filler and PLA resulting in the bionanocomposite degradation (Le Duigou et al., 2009; Yu et al., 2018). This corroborates the TEM analysis on the morphology of PLA/PLA-*g*-MA/CNW1 fibers, which clearly shows the complete disintegration of CNW particles causing structural defects, which are responsible for the deterioration of the tensile properties.

Thermal Properties

The effect of hygrothermal aging on thermal properties of neat PLA and PLA bionanocomposite fibers was investigated by DSC at 45 and 60°C. The detailed data recorded at the second heating cycle, are presented in **Table 4**. From the data in **Table 4**, T_g, T_{cc}, T_m, and X_c remained almost unchanged for all fibers at 45°C until 14 days of exposure. After this, T_g and T_{cc} slightly decreased by 1 and 2°C, respectively, while X_c of neat PLA, PLA/PLA-*g*-MA/MCC1, and PLA/PLA-*g*-MA/CNW1 increased by 2.2, 1.2, and 1.5 times, respectively compared to their initial values. However, at 60°C, the thermal characteristics of PLA
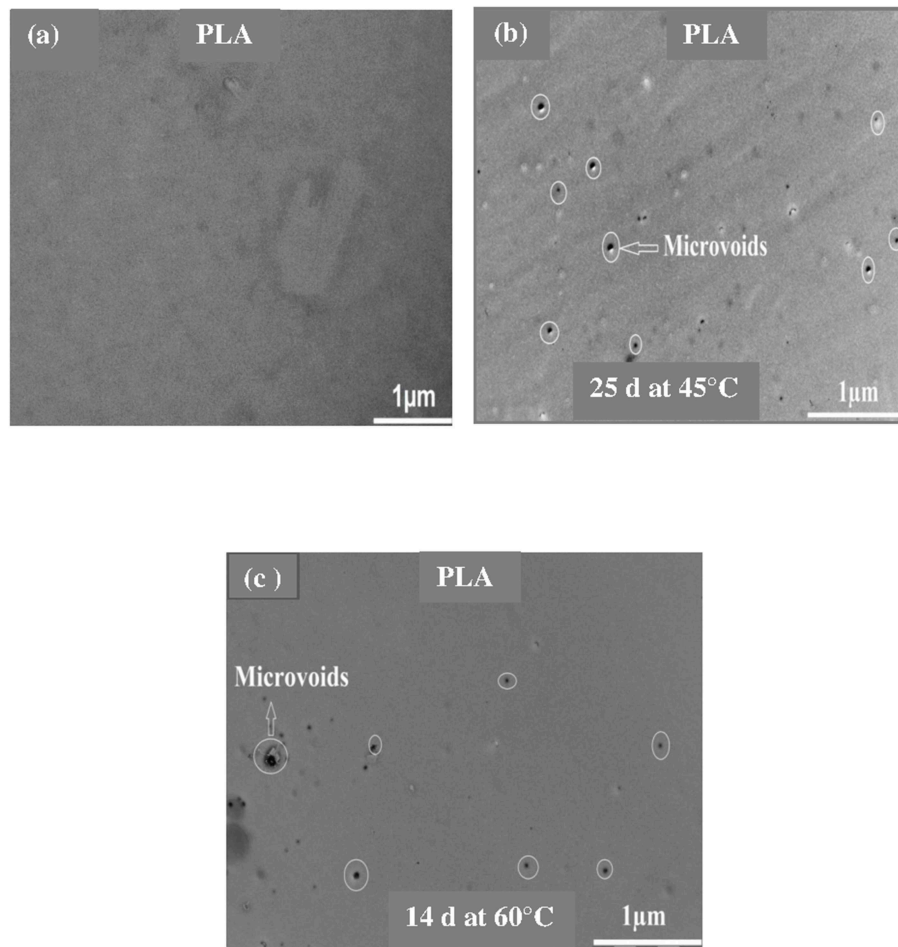
FIGURE 6 | TEM images of a PLA fiber. **(a)** Before exposure, **(b)** after 25 days at 45°C, and **(c)** 14 days at 60°C.

fibers, especially X_c, were significantly affected after 14 days of exposure. The hydrolytic splitting-chains of PLA, which proceeds preferentially in the amorphous regions, led to the formation of short chain segments (Yuan et al., 2002; Zhou and Xanthos, 2008) having enough energy to rearrange themselves and subsequently to crystallize (Loo et al., 2005; Zhang et al., 2008). This is in a good agreement with the data reported by Mitchell and Hirt (2015) who indicated an increase in X_c of PLA fibers from 11 to 41% after only 24 h at 60°C and 100%RH. Moreover, the cold crystallization temperature (T_{cc}) decreased considerably with exposure time at 60°C. This is consistent with the decrease in the activation energy, which promotes the chain mobility and subsequently, the crystallization process of PLA (Zhou and Xanthos, 2008; Chen et al., 2012; Santonja-Blasco et al., 2013). Furthermore, the incorporation of MCC and CNW into PLA matrix, even at a very low content, significantly reduced the thermal properties of the biocomposite material. **Table 4** indicates also a slight decrease in melting temperature (T_m) for the bionanocomposite fibers with exposure time. This is often attributed to the formation of less perfect crystallites or less

thermally stable ones which melt at low temperature (Zhang et al., 2008; Chen et al., 2012; Mitchell and Hirt, 2015). The presence of a double melting point in the DSC thermograms (not shown) for both PLA and PLA/PLA-*g*-MA/MCC1 fibers may result from complex phenomena involving polymorphism, melting-recrystallization-melting or short chains reorganization phenomena during heating (Ling and Spruiell, 2006; Shieh and Liu, 2007; Murariu et al., 2012; Santonja-Blasco et al., 2013). The lower melting peaks correspond to the imperfect crystallites, while the higher ones correspond to the perfect ones (Ma and Zhou, 2015).

Crystallinity Measurement by WAXS

The crystallinity structure of PLA and PLA bionanocomposite fibers was also investigated by WAXS at 45 and 60°C. The relative patterns are shown in **Figure 9**. It can be seen that all PLA fibers display a typical amorphous pattern before exposure. However, the semicristalline structure of PLA clearly appears on the WAXS spectra at 45°C, even more at 60°C. Thus, two peaks are observed; the most intense one is localized at $2\theta =$
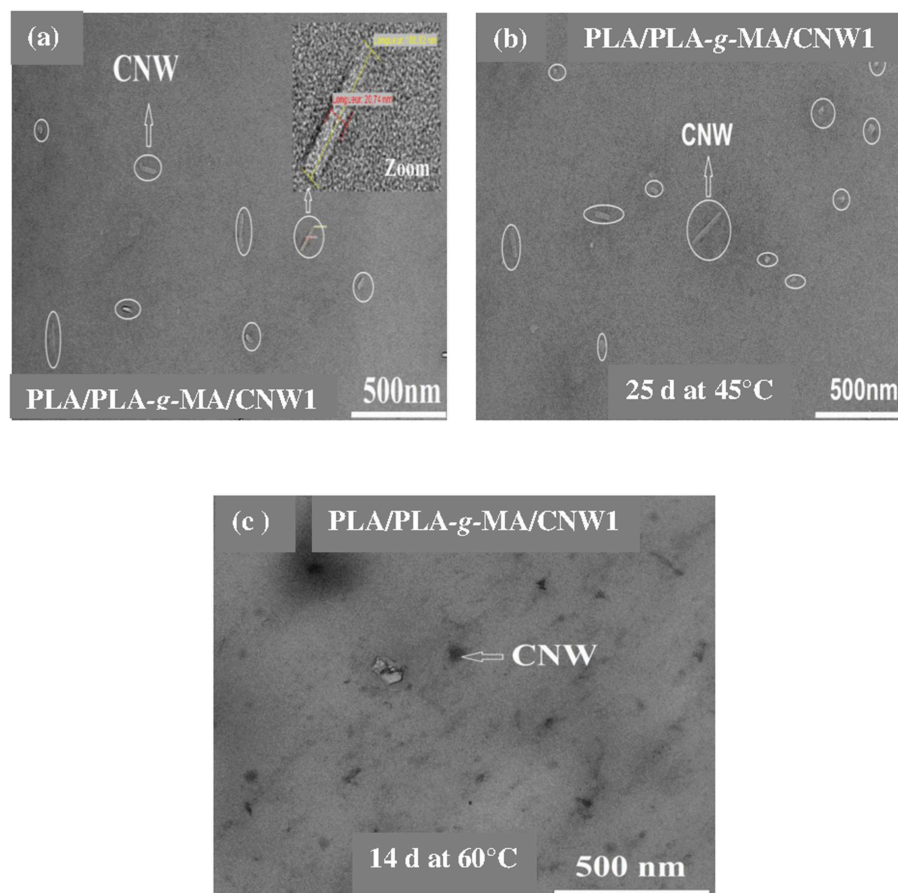
FIGURE 7 | TEM images of a PLA/PLA-*g*-MA/CNW1 fiber. **(a)** Before exposure, **(b)** after 25 days at 45°C, and **(c)** 14 days at 60°C.
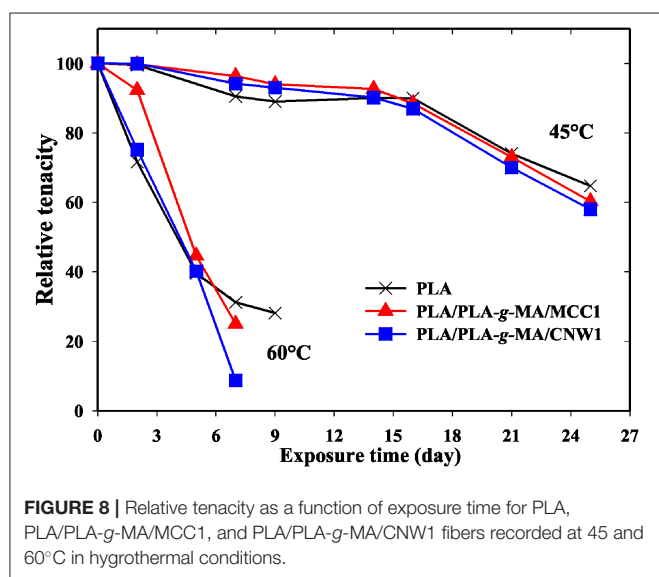
FIGURE 8 | Relative tenacity as a function of exposure time for PLA, PLA/PLA-*g*-MA/MCC1, and PLA/PLA-*g*-MA/CNW1 fibers recorded at 45 and 60°C in hygrothermal conditions.

16.7° corresponding to the crystallographic planes (110, 200) of PLA crystallites (Sullivan et al., 2015), while a second peak of less intensity is centered at 2θ = 18.9°, which is relative to the

(203) plane (Chen et al., 2012). The remarkable increase in peak intensity at 2θ = 16.7 and 18.9° in PLA fibers at 60°C up to 14 days is attributed to the increase in crystallinity of PLA and its bionanocomposites, however much higher for PLA/PLA-*g*-MA/CNW1. This result is consistent with the scission index (SI) and DSC data.

Thermal Stability

The effect of hygrothermal exposure on the thermal stability of PLA and its bionanocomposite fibers was investigated by TGA. **Table 5** summarizes the values of degradation temperature at 5 wt% loss ($T_{5\%}$) and 50 wt% loss ($T_{50\%}$) with exposure time. It is observed that $T_{5\%}$ of PLA fibers decreased significantly at 60°C, while $T_{50\%}$ was almost unchanged, particularly at 45°C. This is in a good agreement with the data published by Gil-Castell et al. (2016) who reported that the temperature at maximum degradation rate of PLA and PLA/sisal biocomposites remains constant after hydrolysis in water at 85°C, while the onset degradation temperature decreases significantly. **Table 5** shows also that after 14 days at 60°C, $T_{5\%}$ decreased considerably by 22, 52, and 56°C for neat PLA, PLA/PLA-*g*-MA/MCC1, and PLA/PLA-*g*-MA/CNW1, respectively. This is attributed to the catalytic role of cellulosic fillers in PLA, which accelerates

TABLE 4 | Thermal characteristics (T_g, T_{cc}, T_m, and X_c) of PLA, PLA/PLA-*g*-MA/MCC1, and PLA/PLA-*g*-MA/CNW1 fibers recorded at 45 and 60°C in hygrothermal conditions.

Fibers	Exposure time (days)	T_g (°C)		T_{cc} (°C)		T_m (°C)				X_c (%)	
		45°C	60°C	45°C	60°C	45°C	60°C	45°C	60°C	45°C	60°C
						T_{m1}	T_{m2}	T_{m1}	T_{m2}		
PLA	0	59.6	59.6	117.9	117.9	151.3	–	151.3	–	0.5	0.5
	2	59.2	59.6	117.2	116.6	151.1	–	151.3	156.2	0.6	0.7
	7	59.2	58.6	117.4	113.8	151.4	–	151.5	157.6	0.7	1.6
	9	59.4	57.9	117.1	108.7	151.1	–	151.5	158.4	0.7	3.2
	14	59.8	56.3	117.2	106.6	151.3	155.0	152.1	159.7	0.8	5.3
	16	58.9	–	116.9	–	151.3	155.3	–	–	0.8	–
	21	58.6	–	116.5	–	151.3	156.2	–	–	1.0	–
	25	58.1	–	115.2	–	151.4	156.3	–	–	1.1	–
PLA/PLA-*g*-MA/MCC1	0	58.8	58.8	128.2	128.2	154.8	–	154.8	–	1.8	1.8
	2	58.3	58.8	127.5	125.5	154.7	–	154.7	–	1.8	1.8
	7	58.9	58.0	127.9	123.3	155.8	–	154.0	158.9	1.8	2.2
	9	58.4	56.9	129.0	121.3	154.6	–	152.4	158.6	1.7	3.5
	14	58.6	54.1	128.5	111.3	155.6	–	151.4	158.1	1.8	7.5
	16	57.7	–	127.7	–	154.1	–	–	–	1.9	–
	21	57.6 53	–	127.0	–	154.0	–	–	–	2.1	–
	25	57.2	–	126.6	–	153.7	–	–	–	2.2	–
PLA/PLA-*g*-MA/CNW1	0	61.5	61.5	111.8	111.8	158.4	165.8	158.4	165.8	5.3	5.3
	2	61.3	60.4	111.3	109.0	158.8	165.8	158.3	165.6	5.4	7.5
	7	61.6	58.6	111.7	104.5	158.7	165.6	–	166.0	5.3	15.9
	9	61.0	58.5	111.0	101.7	158.2	165.8	–	164.5	5.8	17.3
	14	61.5	54.3	111.3	95.1	158.3	165.8	–	161.9	5.8	22.2
	16	60.7	–	110.9	–	157.8	165.0	–	–	6.1	–
	21	59.9	–	110,0	–	157.2	164.6	–	–	7.8	–
	25	59.7	–	108.9	–	157.1	164.1	–	–	8.1	–
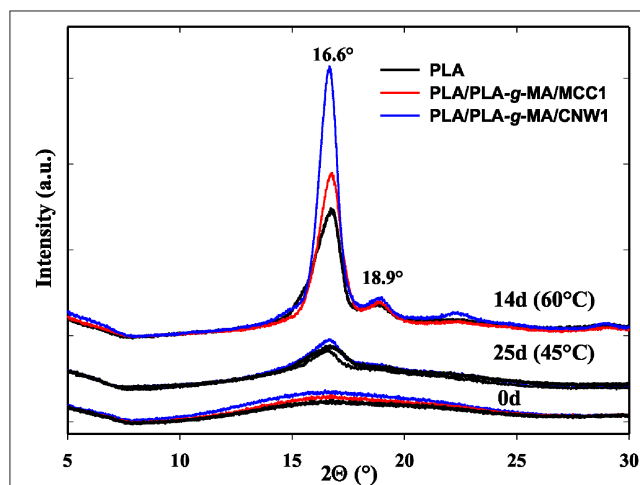
FIGURE 9 | WAXS patterns of PLA, PLA/PLA-*g*-MA/MCC1, and PLA/PLA-*g*-MA/CNW1 fibers recorded before exposure and after 25 days at 45 and 14 days at 60°C in hygrothermal conditions.

the hydrolysis process and consequently increases the fraction of short-length fragments, which can degrade at relatively low temperature (Gupta et al., 2012).

CONCLUSION

From this study, it can be concluded that under hygrothermal conditions (45/60°C and 95%RH), both PLA fibers and those based on PLA/PLA-*g*-MA/MCC1 and PLA/PLA-*g*-MA/CNW1 bionanocomposites undergo hydrolytic degradation, which proceeds mainly by chain scission mechanism. Consequently, an increase in SI and a decrease in $T_{5\%}$ and tensile properties (tenacity, modulus and elongation at maximum deformation) are observed for all samples, however more pronounced for the PLA bionanocomposite fibers. The decrease in properties depends on filler specific surface and temperature. After 14 days at 60°C, the hydrolysis rate constant is estimated to 5, 7, and 8 times faster for PLA, PLA/PLA-*g*-MA/MCC1, and PLAPLA-*g*-MA/CNW1, respectively compared to that recorded after 25 days at 45°C.

TABLE 5 | TGA data (T$_{5\%}$ and T$_{50\%}$) of PLA, PLA/PLA-g-MA/MCC1, and PLA/PLA-g-MA/CNW1 fibers recorded at 45 and 60°C in hygrothermal conditions.

Fibers		T$_{5\%}$ (°C)						T$_{50\%}$ (°C)					
		PLA		PLA/ PLA-g-MA/ MCC1		PLA/ PLA-g-MA/ CNW1		PLA		PLA/ PLA-g-MA/ MCC1		PLA/ PLA-g-MA/ CNW1	
Days	T (°C)	45	60	45	60	45	60	45	60	45	60	45	60
0		316	316	327	327	332	332	360	360	362	362	363	363
2		317	308	328	322	329	325	361	360	360	362	362	362
7		317	304	325	314	328	311	360	360	361	361	360	360
9		316	298	326	299	328	297	360	359	360	360	360	359
14		315	294	324	275	324	276	361	360	360	357	360	356
16		310	–	323	–	322	–	359	–	362	–	361	–
21		302	–	318	–	316	–	361	–	359	–	363	–
25		309	–	314	–	309	–	359	–	360	–	361	–

Moreover, crystallinity and crystallization rate of PLA fibers show a substantial increase during their exposure to hygrothermal aging. SEM observations show damaged topographies for all exposed fibers after 14 days at 60°C compared to those recorded after 25 days at 45°C due probably to the molecular mobility in the vicinity of the glass transition temperature of PLA (60°C). On the basis of all the results obtained, the durability of PLA fibers to hygrothermal degradation is established in the following order: PLA > PLA/PLA-g-MA/MCC1 > PLA/PLA-g-MA/CNW1.

DATA AVAILABILITY STATEMENT

The raw data supporting the conclusions of this article will be made available by the authors, without undue reservation, to any qualified researcher.

AUTHOR CONTRIBUTIONS

This manuscript has been written by MK. The manuscript is a part of the Ph.D. thesis of TA who has conducted the experimental work as well as the interpretation of the results. J-ML-C received TA in his laboratory for scientific internships several times, especially for the study of characterization of the morphology and properties of PLA fibers. ED received also TA in his laboratory for scientific internships several times for the preparation of the PLA, fibers by melt-spinning process.

REFERENCES

Aouat, T., Kaci, M., Devaux, E., Campagne, C., Cayla, A., Dumazert, L., et al. (2018). Morphological, mechanical and thermal characterization of poly(lactic acid)/cellulose multifilament fibers prepared by melt spinning. *Adv. Polym Technol.* 37:21779. doi: 10.1002/adv.21779

Azwar, E., Vuorinen, E., and Hakkarainen, M. (2012). Pyrolysis-GC-MS reveals important differences in hydrolytic degradation process of wood flour and rice bran filled polylactide composites. *Polym. Degrad. Stab.* 97, 281–287. doi: 10.1016/j.polymdegradstab.2011.12.017

Balakrishnan, H., Hassan, A., Imran, M., and Wahit, M. U. (2011). Aging of toughened poly(lactic acid) nanocomposites: water absorption, hygrothermal degradation and soil burial analysis. *J. Polym. Env.* 19, 863–875. doi: 10.1007/s10924-011-0338-9

Bayart, M., Gauvin, F., Foruzanmehr, R., Elkoun, S., and Robert, M. (2017). Mechanical and moisture absorption characterization of PLA composites reinforced with nano-coated flax fibers. *Fibers Polym.* 18, 1288–1295. doi: 10.1007/s12221-017-7123-x

Castro-Aguirre, E., Iniguez-Franco, F., Samsudin, H., Fang, X., and Auras, R. (2016). Poly(lactic acid)-mass production, processing, industrial applications, and end of life. *Adv. Drug Deliv. Rev.* 107, 333–336. doi: 10.1016/j.addr.2016.03.010

Chen, H., Chen, J., Chen, J., Yang, J., Huang, T., Zhang, N., et al. (2012). Effect of organic montmorillonite on cold crystallization and hydrolytic degradation of poly(L-lactide). *Polym. Degrad. Stab.* 97, 2273–2283. doi: 10.1016/j.polymdegradstab.2012.07.037

Chow, W. S., Leu, Y. Y., and Mohd Ishak, Z. A. (2014). Water absorption of poly(lactic acid) nanocomposites: effects of nanofillers and maleated rubbers. *Polym.-Plast. Technol. Eng.* 53, 858–863. doi: 10.1080/03602559.2014.886054

Copinet, A., Bertrand, C., Govindin, S., Coma, V., and Couturier, Y. (2004). Effects of ultraviolet light (315 nm), temperature and relative humidity on the degradation of polylactic acid plastic films. *Chemosphere* 55, 763–773. doi: 10.1016/j.chemosphere.2003.11.038

Dadbin, S., and Kheirkhah, Y. (2014). Gamma irradiation of melt processed biomedical PDLLA/HAP nanocomposites. *Radiat. Phys. Chem.* 97, 270–274. doi: 10.1016/j.radphyschem.2013.12.001

Dong, X.-M., Revol, J., and Gray, D. (1998). Effect of microcrystalline preparation conditions on the formation of colloid crystals of cellulose. *Cellulose* 5, 19–32. doi: 10.1023/A:1009260511939

Elsawy, M. A., Kim, K.-H., Park, J.-W., and Deep, A. (2017). Hydrolytic degradation of poly(lactic acid) (PLA) and its composites. *Renew. Sustain. Energy Rev.* 79, 1346–1352. doi: 10.1016/j.rser.2017.05.143

Fayolle, B., and Verdu, J. (2005). *Vieillissement Physique des Matériaux Polymères*. Techniques de l'Ingénieur. COR 108 V1.

Fortunati, E., Armentano, I., Zhou, Q., Puglia, D., Terenzi, A., Berglund, L. A., et al. (2012). Microstructure and nonisothermal cold crystallization of PLA composites based on silver nanoparticles and nanocrystalline cellulose. *Polym. Degrad. Stab.* 97, 2027–2036. doi: 10.1016/j.polymdegradstab.2012.03.027

Gajjar, C. R., and King, M. W. (2014). *Resorbable Fiber-Forming Polymers in Biotextile Applications.* (Raleigh, NC: Springer), 7–11.

Gil-Castell, G., Badia, J., Kittikorn, T., Strömberg, E., Ek, M., Karlsson, S., et al. (2016). Impact of hydrothermal ageing on the thermal stability, morphology and viscoelastic performance of PLA/sisal biocomposites. *Polym. Degrad. Stab.* 132, 87–96. doi: 10.1016/j.polymdegradstab.2016.03.038

Gil-Castell, O., Badia, J. D., Kittikorn, T., Stromberg, E., and Martinez-Felipe, A. (2014). Hydrothermal ageing of polylactide/sisal biocomposites. studies of water absorption behaviour and physico-chemical performance. *Polym. Degrad. Stab.* 108, 212–222. doi: 10.1016/j.polymdegradstab.2014.06.010

Girdthep, S., Worajittiphon, P., Leejarkpai, T., and Molloy, R. (2016). Effect of silver-loaded kaolinite on real ageing, hydrolytic degradation, and biodegradation of composite blown films based on poly(lactic acid) and poly(butylene adipate-co-terephthalate). *Eur. Polym. J.* 82, 244–259. doi: 10.1016/j.eurpolymj.2016.07.020

Gupta, B., Revagade, N., and Hilborn, J. (2012). *In vitro* degradation of dry-jet-wet spun poly(lactic acid) monofilament and knitted scaffold. *J. Appl. Polym. Sci.* 103, 2006–2012. doi: 10.1002/app.25241

Hajba, S., Czigany, T., and Tabi, T. (2015). Development of cellulose-reinforced poly(lactic acid) (PLA) for engineering applications. *Mater. Sci. Forum.* 812, 59–64. doi: 10.4028/www.scientific.net/MSF.812.59

Hamad, K., Kaseem, M., Ayyoob, M., Joo, J., and Deri, F. (2018). Poly(lactic acid) blends: the future of green, light and tough. *Prog. Polym. Sci.* 85, 83–122. doi: 10.1016/j.progpolymsci.2018.07.001

Hassaini, L., Kaci, M., Touati, N., Pillin, I., Kervoelin, A., and Bruzaud, S. (2017). Valorization of olive husk flour as filler for biocomposites based on poly(3-hydroxybutyrate-co-3-hydroxyvalerate):effects of silane treatment. *Polym. Test.* 59, 430–440. doi: 10.1016/j.polymertesting.2017.03.004

Hossain, K. M. Z., Ifty, H., Andrew, A., and Rudd, C. D. (2012). Physico-chemical and mechanical properties of nanocomposites prepared using cellulose nanowhiskers and poly(lactic acid). *J. Mater. Sci.* 47, 2675–2686. doi: 10.1007/s10853-011-6093-4

Hossain, K. M. Z., Parsons, A. J., Rudd, C. D., Ahmed, I., and Thielemans, W. (2014). Mechanical, crystallization and moisture absorption properties of melt drawn poly(lactic acid) fibers. *Eur. Polym. J.* 53, 270–281. doi: 10.1016/j.eurpolymj.2014.02.001

Islam, M. S., Pickering, K. L., and Foreman, N. J. (2010). Influence of hygrothermal ageing on the physico-mechanical properties of alkali-treated industrial hemp fiber reinforced poly(lactic acid) composites. *J. Polym. Env.* 18, 696–704. doi: 10.1007/s10924-010-0225-9

Jewena, N., Miyanomae, R., Sasaki, M., and Mashimo, T. (2016). Hydrothermal decomposition of cellulose using strong gravitational field. *J. Supercrit. Fluids* 120, 379–383. doi: 10.1016/j.supflu.2016.05.034

Kummerer, T. W., Menz, J., and Schubert, T. (2011). Biodegradability of organic nanoparticles in the aqueous environment. *Chemosphere* 82, 1387–1392. doi: 10.1016/j.chemosphere.2010.11.069

Le Duigou, A., Davies, P., and Baley, C. (2009). Seawater ageing of flax/poly(lactic acid) biocomposites. *Polym. Degrad. Stab.* 94, 1151–1162. doi: 10.1016/j.polymdegradstab.2009.03.025

Ling, X., and Spruiell, J. E. (2006). Analysis of the complex thermal behavior of poly(L-lactic acid) film. ii. samples crystallized from the melt. *J. Polym. Sci. B Polym. Phys.* 44, 3378–3391. doi: 10.1002/polb.20987

Lins, L. C., Wianny, F., Livi, S., Hidalgo, I. A., Dehay, C., Duchet-Rumeau, J., et al. (2016). Development of bioresorbable hydrophilic-hydrophobic electrospun scaffolds for neural tissue engineering. *Biomacromolecules* 17, 3172–3187. doi: 10.1021/acs.biomac.6b00820

Loo, S. C. J., Ooi, C. P., Wee, S. H. E., and Boey, Y. C. F. (2005). Effect of isothermal annealing on the hydrolytic degradation rate of poly(lactide-co-glycolide) (PLGA). *Biomaterials* 26, 2827–2833. doi: 10.1016/j.biomaterials.2004.08.031

Lorenzo, V., De Orden, M. U., and Martinez-Urreaga, J. (2016). Effect of different mechanical recycling processes on the hydrolytic degradation of poly(L-lactic acid). *Polym. Degrad. Stab.* 133, 339–348. doi: 10.1016/j.polymdegradstab.2016.09.018

Ma, M., and Zhou, W. (2015). Improving the hydrolysis resistance of poly(lactic acid) fiber by hydrophobic finishing. *Ind. Eng. Chem. Res.* 54, 2599–2605. doi: 10.1021/ie504814x

Maharana, T., Mohanty, B., and Negi, Y. S. (2009). Melt-solid polycondensation of lactic acid and its biodegradability. *Prog. Polym. Sci.* 34, 99–124. doi: 10.1016/j.progpolymsci.2008.10.001

Mangin, R., Vahabi, H., Sonnier, R., Chivas-Joly, C., Lopez-Cuesta, J.-M., and Cochez, M. (2018). Improving the resistance to hydrothermal ageing of flame-retarded PLA by incorporating miscible PMMA. *Polym. Degrad. Stab.* 155, 52–66. doi: 10.1016/j.polymdegradstab.2018.07.008

Milanovic, J., Kostic, M., Milanovic, P., and Skundric, P. (2012). Influence of TEMPO-Mediated oxidation on properties of hemp fibers. *Ind. Eng. Chem. Res.* 51, 9750–9759. doi: 10.1021/ie300713x

Mitchell, M. K., and Hirt, D. E. (2015). Degradation of PLA fibers at elevated temperature and humidity. *Polym. Eng. Sci.* 55, 1652–1660. doi: 10.1002/pen.24003

Mohammad, S., Kaffashi, B., Torabinejad, B., and Zamanian, A. (2016). *In-vitro* investigation and hydrolytic degradation of antibacterial nanocomposites based on PLLA/triclosan/nano-hydroxyapatite. *Polymer* 83, 101–110. doi: 10.1016/j.polymer.2015.12.015

Mokhena, T. C., Sefadi, J. S., Sadiku, E. R., John, M. J., Mochane, M. J., and Mtibe, A. (2018). Thermoplastic processing of PLA/cellulose nanomaterials composites. *Polymers* 10:1363. doi: 10.3390/polym10121363

Mortaigne, B. (2005). *Vieillissement des Composites-Mécanismes et- Méthodologie d'Etude.* Techniques de l'Ingénieur. AM 5320.

Murariu, M., Dechief, A.-L., Paint, Y., Peeterbroeck, S., Bonnaud, L., and Dubois, P. (2012). Polylactide (PLA)-halloysite nanocomposites : production, morphology and key-properties. *J. Polym. Env.* 20, 932–943. doi: 10.1007/s10924-012-0488-4

Ndazi, B. S., and Karlsson, S. (2011). Characterization of hydrolytic degradation of poly(lactic acid)/rice hulls composites in water at different temperatures. *Exp. Polym. Lett.* 5, 119–131. doi: 10.3144/expresspolymlett.2011.13

Pan, F. J. L., Shen, Z., Wu, L., Zhang, Y., and Zhou, X. (2010). Hydrothermal production of formic and acetic acids from syringol. *Appl. Phys. Eng.* 11, 613–618. doi: 10.1631/jzus.A1000043

Persson, M., and Mikael, S. C. (2013). The effect of process variables on the properties of melt-spun poly(lactic acid) fibres for potential use as scaffold matrix materials. *J. Mater. Sci.* 48, 3055–3066. doi: 10.1007/s10853-012-7022-x

Pinese, C., Gagnieu, C., Nottelet, B., Rondot-Couzin, C., Hunger, S., Coudane, J., et al. (2016). *In vivo* evaluation of hybrid patches composed of PLA based copolymers and collagen/chondroitin sulfate for ligament tissue regeneration. *J. Biomed. Mater. Res. Part B Appl. Biomater.* 3, 1–11. doi: 10.1002/jbm.b.33712

Rahman, M. M., Afrin, S., Haque, P., Islam, M., Islam, M. S., and Gafur, Md. A. (2014). Preparation and characterization of jute cellulose crystals-reinforced poly(lactic acid) biocomposite for biomedical applications. *Int. J. Chem. Eng.* 2014:842147. doi: 10.1155/2014/842147

Remili, C., Kaci, M., Kachbi, S., Bruzaud, S., and Grohens, Y. (2009). Photo-oxidation of polystyrene/clay nanocomposites under accelerated UV exposure : effect on the structure and molecular weight. *J. Appl. Polym. Sci.* 112, 2868–2875. doi: 10.1002/app.29806

Ruiz, A., Rodrı, R. M., Fernandes, B. D., Vicente, A., and Teixeira, A. (2013). Hydrothermal processing as an alternative for upgrading agriculture residues and marine biomass according to the biorefinery concept: A review. *Renew. Sustain. Energy Rev.* 21, 35–51. doi: 10.1016/j.rser.2012.11.069

Santonja-Blasco, L., Ribes-Greus, A., and Alamo, R. G. (2013). Comparative thermal, biological and photodegradation kinetics of polylactide and effect on crystallization rates. *Polym. Degrad. Stab.* 98, 771–784. doi: 10.1016/j.polymdegradstab.2012.12.012

Shieh, Y., and Liu, G. (2007). Temperature-modulated differential scanning calorimetry studies on the origin of double melting peaks in isothermally melt-crystallized poly(L-lactic acid). *J. Polym. Sci. Part B Polym. Phys.* 45, 466–474. doi: 10.1002/polb.21056

Stloukal, P., Jandikova, G., Koutny, M., and Sedla, V. (2016). Carbodiimide additive to control hydrolytic stability and biodegradability of PLA. *Polym. Test.* 54, 19–28. doi: 10.1016/j.polymertesting.2016.06.007

Sullivan, E. M., Moon, R. J., and Kalaitzidou, K. (2015). Processing and characterization of cellulose nanocrystals/poly(lactic acid) nanocomposite films. *Materials* 8, 8106–8116. doi: 10.3390/ma8125447

Sun, Z., Zhang, L., Liang, D., Xiao, W., and Lin, J. (2017). Mechanical and thermal properties of PLA biocompositesreinforced by coir fibers. *Int. J. Polym. Sci.* 2017:2178329. doi: 10.1155/2017/2178329

Vilaplana, F., Strömberg, E., and Karlsson, S. (2010). Environmental and resource aspects of sustainable biocomposites. *Polym. Degrad. Stab.* 95, 2147–2161. doi: 10.1016/j.polymdegradstab.2010.07.016

Wang, T., and Drzal, L. T. (2012). Cellulose nanofiber-reinforced poly(lactic acid) composites prepared by a water-based approach. *ACS Appl. Mater. Interfaces.* 4, 5079–5085. doi: 10.1021/am301438g

Wu, C.-S. (2009). Renewable resource-based composites of recycled natural fibers and maleated polylactide bioplastic: characterization and biodegradability. *Polym. Degrad. Stab.* 94, 1076–1084. doi: 10.1016/j.polymdegradstab.2009.04.002

Xian, X., Wang, X., Zhu, Y., Guo, Y., and Tian, Y. (2018). Effects of MCC content on the structure and performance of PLA/MCC biocomposites. *J. Polym. Env.* 26, 3484–3492. doi: 10.1007/s10924-018-1226-3

Yang, W., Fortunati, E., Dominici, F., Giovanale, G., Mazzaglia, A., Balestra, G. M., et al. (2016). Effect of cellulose and lignin on disintegration, antimicrobial and antioxidant properties of PLA active film. *Int. J. Biol. Macromol.* 89, 360–368. doi: 10.1016/j.ijbiomac.2016.04.068

Yew, G. H., Yusof, A. M. M., Mohd Ishak, Z. A., and Ishiaku, U. S. (2005). Water absorption and enzymatic degradation of poly(lactic acid)/rice starch composites. *Polym. Degrad. Stab.* 90, 488–500. doi: 10.1016/j.polymdegradstab.2005.04.006

Yu, T., Sun, F., Lu, M., and Li, Y. (2018). Water absorption and hygrothermal aging behavior of short ramie fiber reinforced poly(lactic acid) composites. *Polym. Compos.* 39, 1098–1104. doi: 10.1002/pc.24038

Yuan, X., Mak, F. T., and Yao, K. (2002). *In vitro* degradation of poly(L-lactic acid) fibers in phosphate buffered saline. *J. Appl. Polym. Sci.* 85, 936–943. doi: 10.1002/app.10490

Zhang, X., Espiritu, M., Bilyk, A., and Kurniawan, L. (2008). Morphological behaviour of poly(lactic acid) during hydrolytic degradation. *Polym. Degrad. Stab.* 93, 1964–1970. doi: 10.1016/j.polymdegradstab.2008.06.007

Zhou, Q., and Xanthos, M. (2008). Nanoclay and crystallinity effects on the hydrolytic degradation of polylactides. *Polym. Degrad. Stab.* 93, 1450–1459. doi: 10.1016/j.polymdegradstab.2008.05.014

Monitoring of Morphology and Properties During Preparation of PCL/PLA Microfibrillar Composites With Organophilic Montmorillonite

Miroslav Slouf[1]*, Aleksandra Ujcic[1], Martina Nevoralova[1], Tatana Vackova[1], Luca Fambri[2] and Ivan Kelnar[1]

[1] Institute of Macromolecular Chemistry, Academy of Sciences of the Czech Republic, Prague, Czechia, [2] Department of Industrial Engineering, University of Trento, Trento, Italy

Biodegradable microfibrillar composites PCL/PLA/C15, where PCL is poly(ε-caprolactone), PLA is poly(lactic acid), and C15 is organophilic montmorillonite, have been prepared. Microindentation hardness testing was employed in monitoring the gradual improvement of PCL stiffness due to PLA addition, C15 addition, flow-induced orientation, and changing crystallinity throughout the whole preparation process. Neat PCL after extrusion and injection molding was quite soft, but the stiffness of the material increased after melt-blending with 20 wt.% of PLA, after the addition of 2 wt.% of C15, and after the preparation of the final microfibrillar composite. The indentation modulus and indentation hardness of all intermediate products and the final PCL/PLA/C15 microfibrillar composite were associated not only with the composition and morphology but also with the crystallinity of both components. The modulus of the final PCL/PLA/C15 composite was almost two times higher in comparison with the original PCL matrix.

Keywords: biodegradable microfibrillar composites, polycaprolactone, poly(lactic acid), micromechanical properties, microindentation

INTRODUCTION

Poly(ε-caprolactone) (PCL) is a biodegradable semicrystalline polyester with the broad range of applications in medicine, packaging, microelectronics or adhesives (Labet and Thielemans, 2009). PCL exhibits low glass transition temperature and relatively soft crystalline phase, which results in its low stiffness and high ductility. The low stiffness of PCL is frequently enhanced by blending with stiffer polymers, such as biodegradable poly(lactic acid), PLA (Ostafinska et al., 2015, 2017; Navarro-Baena et al., 2016). An alternative way of increasing PCL stiffness is the preparation of composites with PLA-based fibers (Ju et al., 2013; Chen et al., 2014; Kelnar et al., 2016a), natural fibers (Chen et al., 2005; Cocca et al., 2015), and various nanofillers such as layered silicates (Chen and Evans, 2006; Chrissafis et al., 2007, Labidi et al., 2010; Neppalli et al., 2011), isometric silica nanoparticles (Chrissafis et al., 2007), TiO_2-based particles and nanotubes (Vackova et al., 2017), or carbon and halloysite nanotubes (Chrissafis et al., 2007; Lee and Chang, 2013).

As for polymer blending in general, PCL has the rare property of being miscible with numerous polymers such as poly(vinyl chloride) (PVC), acrylonitrile butadiene styrene (ABS), or polycarbonates (PC) (Labet and Thielemans, 2009). Some other polymers (such as functionalized polyolefins or natural rubber) exhibit reasonable mechanical compatibility with PCL, but the

blending with PLA was mostly reported to result in immiscible and non-compatible blends (Na et al., 2002; Tuba et al., 2011). Nevertheless, recently we have shown that under precisely optimized processing conditions, composition and viscosity ratios of the components, the compatible PLA/PCL systems with high stiffness (due to PLA matrix) and toughness (due to PCL particles acting as impact modifier) could be prepared (Ostafinska et al., 2015, 2017); similar results were achieved in parallel studies of Bai et al. (2012, 2013).

As for the reinforcing of PCL with PLA fibers, two great potential advantages emerge: (i) both polymers are biodegradable and the blend biodegradability can be controlled by composition, morphology and/or chemical modifications, and (ii) the blend properties can be optimized in a broad range starting from very stiff, brittle PLA to very tough, ductile PCL. As pointed out by Kelnar et al. (2016a), PCL/PLA blends (i.e., the blends with PCL matrix) have not been studied as broadly as PLA/PCL blends (i.e., the blends with PLA matrix, where PCL usually acts as impact modifier; Fortelny et al., 2019). Just a few papers have dealt with PCL/PLA blends or with PCL/PLA-based composites and most of them focused on different topics than reinforcing of PCL with PLA fibers: Jain et al. (2010) investigated PCL/PLA/talc composites from the point of view of morphology, crystallinity, and barrier properties, Wu et al. (2011) dealt with the selective localization of two different nanofillers (organoclay and carbon nanorubes) in PCL/PLA systems, Laredo et al. (2010) focused their attention on the conductivity of PCL/PLA blend filled with multiwall carbon nanotubes, Patricio and Bartolo (2013) described morphology and thermal stability of solvent casted PCL/PLA blends and their scaffolds, Haq et al. (2017) characterized mechanical properties of isotropic PCL/PLA blends, and Kelnar et al. (2017a) studied effect of blend ratio and graphite nanoplatelets localization on structure and properties of PCL/PLA systems. Navarro-Baena et al. (2016) prepared PCL/PLA blends with both PCL and PLA matrix and described their morphology, rheology, shape memory behavior and *in vitro* biodegradation rate. The few remaining studies dealing with PCL/PLA systems (Ju et al., 2013; Chen et al., 2014; Kelnar et al., 2016a,b,c, 2017b) were focused on the same subject like this contribution—on ehancing of PCL mechanical performance by means of PLA fibers, especially in combination with a suitable nanofiller. Kelnar et al. prepared melt-drawn microfibrillar composites (MFC) of PCL/PLA (80/20) containing organophilic montmorillonite (Kelnar et al., 2016a,b), halloysite (Kelnar et al., 2016c), or graphite nanoplatelets (Kelnar et al., 2017a) and achieved 2–3× higher tensile modulus of the final composites in comparison with pure PCL; the increase in modulus was accompanied by a moderate increase in the yield strength and a decrease in the toughness of the system. Analogous results were achieved by Ju et al. (2013), who melt-mixed PCL with commercial PLA fibers at 90°C (i.e., below the melting point of the polylactide fibers), although the overall increase in modulus was lower, ∼2× in comparison with the original PCL, depending on final PLA concentration which ranged from 5 to 40 wt.%. Chen et al. (2014) prepared multi-layered PCL

composites reinforced by electrospun PLA/PCL blend, reported that modulus increased almost twice in comparison to the neat PCL and concluded that PLA continuous fibers could act as the PCL reinforcement.

The comparison of the above-listed results suggests that one of the most promising methods of PCL reinforcing with PLA is the MFC concept, which maintains the biodegradability of the final product and which was used in the studies of Kelnar et al. (2016a,b,c); Kelnar et al. (2017a,b). The detailed description of the MFC method can be found, for example, in the recent work of Kakroodi et al. (2017). Briefly, the preparation of the MFC composite requires two polymers with different melting temperatures (T_m): melting temperature of dispersed/fibrillary phase (T_{m1}) needs to be at least 40°C higher than that of the matrix (T_{m2}). In the first step, the microfibers of the dispersed phase are formed during melt-blending in an extruder, followed by hot- or cold-stretching of the extrudate, which results in the thin bristle containing fibers of the dispersed phase, i.e., in the material with the MFC morphology. In the second step, the MFC bristle is processed to the final shape at a temperature *between T_{m1} and T_{m2}*, which keeps the microfibers from the first step. It is worth noting that MFC method was successfully employed in recent preparation of various other blends such as PP/PA6 (Huang et al., 2017), PLA/PA6 (Kakroodi et al., 2017), polyolefin elastomer/poly(trimethylene terephthalate) (Wei et al., 2016), PP/PC (Xia et al., 2016), HDPE/PA6 (Kelnar et al., 2015), or olefinic block compolymer/PP (Li et al., 2016). In some cases the authors added nanoparticles in order to improve rheological properties during MFC preparation and/or to improve mechanical properties of the final MFC composite (Kelnar et al., 2016a,b,c; Li et al., 2016). This has to be done also in our case of PCL/PLA composites, where organo-modified clay was added in order to improve the stability and reproducibility of the hot-stretching process, as discussed below.

In this work, we characterized the biodegradable PCL/PLA microfibrillar composite analogous to that previously studied (Ju et al., 2013; Chen et al., 2014; Kelnar et al., 2016a,b,c). We focused our attention on the detailed explanation, what was the real reason for the observed changes in PCL/PLA mechanical performance and why the improvement in mechanical performance could not be even higher. In order to achieve this objective, we tracked the changes of the PCL/PLA morphology, crystallinity, and local mechanical properties during the whole process of MFC preparation. The local properties of the small samples from the first step (thin extrudates and bristles) could not be assessed by traditional methods requiring large specimens. Instead, we have employed instrumented microindentation hardness testing (Balta-Calleja and Fakirov, 2000; Ostafinska et al., 2015, 2017), which could be performed on both intermediate products and final specimens for the tensile experiments. For the final products, the standard tensile properties and the microindentation properties of the composites were compared with predictive models and with each other to verify the reliability and reproducibility of the micromechanical characterization.

THEORETICAL BACKGROUND

This work is based on detailed evaluation of micromechanical properties of PCL/PLA/C15 systems and their comparison with morphology, crystallinity, macromechanical properties and several predictive models. The key relations employed throughout the rest of this work are summarized below.

Micromechanical Properties

It has been demonstrated (Balta-Calleja and Fakirov, 2000) that microhardness of numerous polymer systems obeys additive law (also known as rule of mixtures or linear model):

$$H = \sum_i v_i H_i \qquad (1)$$

where v_i and H_i are the volume fraction and microhardness of i-th component of the system. The additivity law can be applied also on semicrystalline polymers:

$$H = v_a H_a + v_c H_c = (1 - v_c) H_a + v_c H_c$$
$$= H_a + v_c(H_c - H_a) \qquad (2)$$

where the subscripts a and c denote amorphous and crystalline phase, respectively. Equation 2 shows that microhardness of semicrystalline polymers grows linearly with their crystallinity, v_c. The direct proportionality given by Equation 2 holds also for weight fraction of crystalline phase, w_c, due to the linear relation between the two quantities ($v_c = w_c \times \rho/\rho_c$; where ρ and ρ_c are density of the polymer and density of the crystalline phase, respectively). Tabor (1951) derived a formula relating microhardness (a micromechanical property) and yield stress (Y; a macromechanical property):

$$H \approx 3Y \qquad (3)$$

where the approximate sign indicates that the Tabor's relation was derived for ideally plastic solids, while for the elasto-visco-plastic materials, such as polymers systems, it is just a first approximation. Struik (1991) found another approximate formula, which was shown to hold for amorphous and semicrystalline polymers, relating their elastic modulus (E) with yield stress ($E \approx 30Y$). Combination of Struik's relation, Tabor's relation (Equation 3) and additivity law (Equation 2) gives us the final formula that connects microhardness, yield stress, elastic modulus, and crystallinity of semicrystalline polymers:

$$E \approx 30Y \approx 10H \propto v_c \qquad (4)$$

Due to the approximate nature of Tabor's and Struik's relations, the numerical constants in Equation 4 can vary in relatively broad range. However, the direct proportionality among the four quantities ($E \propto Y \propto H \propto v_c$) holds usually very well for given semicrystalline polymer as evidenced in numerous previous studies (Martinez-Salazar et al., 1988; Balta-Calleja and Fakirov, 2000; Flores et al., 2009, 2011; Slouf et al., 2015, 2018).

It is also worth mentioning that Equation 4 holds not only for macroscale tensile modulus (E), but also for microscale indentation modulus (E_{IT}), which is given by the fact that the two moduli are proportional ($E \approx E_{IT}$) as evidenced elsewhere (Hardiman et al., 2016, Lesan-Khosh et al., 2011).

Predictive Models for Polymer Blends and Composites

The simplest model for the prediction of properties of polymer blends and composites is linear model (LIN). It has no initial assumptions and can be applied to any property (P) of a system, for which we know the properties of individual components (P_i) and their volume fractions (v_i):

$$P = \sum_i v_i P_i \qquad (5)$$

Despite its simplicity, the LIN model holds very well for several combinations of polymer systems and properties. Firstly, the LIN model holds for some properties of systems with very strong interfacial adhesion. An example is the above-discussed microhardness of semicrystalline polymers [we note that Equation 1 is a special case of Equation 5 (Balta-Calleja and Fakirov, 2000)], where the interfacial adhesion between amorphous and crystalline phase is extremely strong as they are interconnected by polymer chains. Secondly, the LIN model holds for some properties of systems where the interfacial adhesion does not play an important role. A well-known example is the elastic modulus of composites with long oriented long fibers (Nielsen and Landel, 1994), where the interfacial adhesion between fibers and polymer matrix is unimportant. For most other systems and mechanical properties, LIN model represents the upper achievable theoretical limit, whereas the real mechanical performance is lower.

A more realistic model, applicable to isotropic binary polymer blends, was developed by Kolarik (1996) and called equivalent box model (EBM). The EBM model can predict elastic modulus and yield stress of polymer blends:

$$E = E_1 v_{1p} + E_2 v_{2p} + v_s^2 / [(v_{1s}/E_1) + (v_{2s}/E_2)] \qquad (6)$$
$$Y = Y_1 v_{1p} + Y_2 v_{2p} + A Y_1 v_s \qquad (7)$$

where E_i and Y_i represent the modulus and yield stress of the individual components, the volume fractions v_{ij} stand for the volume fractions [the first subscript i identifies the component (1 or 2) and the second subscript j determines the presence of the component in the parallel or serial branch of the EBM model (p or s) as explained elsewhere (Kolarik, 1996)], and coefficient A describes interfacial adhesion (A takes the values from 0 to 1, which correspond to zero and perfect adhesion, respectively). The volume fractions in parallel and serial branch of the model (v_{ij}) are connected with the particulate and continuous morphology of the components. The v_{ij} values can be either determined experimentally or estimated theoretically from percolation theory (Kolarik, 1996). In this work we used theoretical estimation, which had been demonstrated to be

quite good approximation for polymer blends (Kolarik, 1996; Ostafinska et al., 2015, Ostafinska et al., 2017). In conclusion, the EBM model takes into consideration basic morphology of the system (by means of volume fractions v_{ij} in Equation 6, 7) and interfacial adhesion (by means of parameter A in Equation 7).

In order to predict properties of final *anisotropic* microfibrillar composites (we note that the above described EBM model was developed for *isotropic* blends) and the influence of the platelets of organophilic montmorillonite, we employed also Halpin-Tsai equations (HT), which can predict elastic modulus of soft polymer matrices with hard fillers (Nielsen and Landel, 1994):

$$E = E_m \frac{1 + ABv_f}{1 - Bv_f} \qquad (8)$$

where E_m = modulus of the matrix, v_f = volume fraction of the filler and A, B are constants depending on filler geometry. It is worth mentioning that for very long fibers (AR $\rightarrow \infty$), the HT equation simplifies to the above discussed LIN model in the form: $E = v_m E_m + v_f E_f$. To predict the influence of *PLA fibers* (short oriented PLA fibers in PCL matrix) we used Equation 8 with constant $A = 2 \cdot$AR (AR = aspect ratio = fiber length/fiber diameter) and constant $B = [(E_f/E_m)-1]/[(E_f/E_m)-A]$. To predict the influence of *exfoliated montmorillonite* (unoriented organophilic montmorillonite in PCL/PLA matrix) we had to combine and average the calculations based on Equation 8 for parallel and perpendicular orientation of platelets as described elsewhere (Fornes and Paul, 2003). Finally, to predict the influence of *non-exfoliated montmorillonite* (isometric agglomerates of montmorillonite in PCL/PLA matrix) we employed simple Einstein equation (Maiti and Mahapatro, 1991):

$$E = E_m(1 + 2.5v_f) \qquad (9)$$

All predictive models (LIN model, EBM model, HT equations, and Einstein equation) were developed for macroscopic properties (elastic modulus and/or yield stress). Nevertheless, they could be applied also to corresponding micromechanical properties (indentation modulus and/or hardness). The applicability of the models to micromechanical properties has been justified theoretically by the approximate linear relationships between the macroscale and microscale properties (Equation 3 and 4) and verified experimentally in our previous studies (Ostafinska et al., 2015, 2017, 2018).

EXPERIMENTAL

Materials

Poly(lactic acid) (PLA) Ingeo 2002D (D-isomer content of 4.3 %; M_w = 2.53 × 10^5 g/mol; T_m = 150°C; melt flow index 6 g/10 min at 190°C and 2.16 kg; density 1.24 g.cm^{-3}) was a product of NatureWorks (www.natureworksllc.com). Poly(ε-caprolactone) (PCL) CAPA 6800 (M_w = 8×10^4 g/mol; T_m = 60°C; density 1.145 g.cm^{-3}) was a product of Perstorp (www.perstorp.com). The organo-modified clay Cloisite 15A (C15) was based on natural montmorillonite modified with

dialkyldimethylammonium chloride (95-meq/100-g), produced by Southern Clay Products, Inc. (TX, USA).

Preparation of Composites

Prior to melt-blending, PCL, PLA, and clay were dried at 45, 85, and 70°C, respectively, in a vacuum oven for 12 h. The mixing of all systems, with the exception of pure PLA, was carried out in a co-rotating segmented twin-screw extruder Brabender TSE 20, L/D 40, rotation speed 400 rpm, and temperatures of the respective zones (from feeding to die) of 170, 170, 170, 170, 175, and 180°C (for pure PLA the conditions were the same, but the temperature of all zones was set to 190°C due to the higher optimal processing temperature of PLA). The extruded bristle with the PCL/PLA 80/20 w/w composition was melt-drawn using an adjustable take-up device. The draw ratio (DR) was the ratio between the velocity of the take-up rolls and the initial velocity of the extruded bristle; DR = 5 was used in this study. Die diameter was 3 mm, the diameter of undrawn bristles was slightly above 3 mm (due to die-swell effect), and the diameter of drawn bristles was below 1 mm. Dog-bone specimens for tensile testing (gauge length 40 mm) were prepared in a laboratory micro-injection molding machine (DSM). The barrel and the mold temperatures were 137 and 30°C, respectively. The prepared samples are summarized in **Table 1**.

Characterization of Composites

Electron Microscopy

The phase morphology of all prepared samples (**Table 1**) was visualized using scanning electron microscopy (SEM; microscope Quanta 200 FEG; FEI, Czech Republic) and transmission electron microscopy (TEM; microscope Tecnai G2 Spirit Twin; FEI, Czech Republic).

SEM microscopy showed the overall morphology of the blends. All SEM micrographs were taken at accelerating voltage 10 kV using secondary electrons detector. The samples were broken under liquid nitrogen both parallel and perpendicular to the extrusion or injection molding direction. For selected specimens, the PLA phase was etched off using 20 % NaOH at room temperature for 30 min; this etching protocol was based on the faster hydrolysis of PLA in comparison with PCL. It is worth noting that the PLA fibrils could not be completely extracted from PCL matrix due to chemical similarity of both polyesters, which exhibit very similar solubility in most common solvents (Kelnar et al., 2016a, 2017b).

TEM microscopy was employed in visualization of the oMMT distribution in PCL/PLA blends. The ultrathin sections for TEM (thickness 60 nm) were prepared with an ultramicrotome (Ultracut UCT; Leica Austria) at cryo-conditions (sample and diamond knife temperature were −80 and −50°C, respectively). The ultrathin sections were transferred to a carbon-coated Cu grid and observed at 120 kV.

Differential Scanning Calorimetry

The differential scanning calorimetry (DSC) analysis was carried out using a Perkin-Elmer 8500 DSC apparatus. Samples of 5–10 mg were heated from 50 to 250°C at the heating rate of 10°C/min. Each specimen was measured two times and

TABLE 1 | List of investigated samples.

Sample	Composition	Preparation
PLA-EI	0/100	Injection molding from undrawn extrudate[a]
PCL-EI	100/0	Injection molding from undrawn extrudate[b]
PCL/PLA-E	80/20	Twin-screw extruder, undrawn extrudate
PCL/PLA-EI	80/20	Injection molding from undrawn extrudate
PCL/PLA/C15-E	80/20 + 2% of clay	Twin-screw extruder, undrawn extrudate
PCL/PLA/C15-EI	80/20 + 2% of clay	Injection molding from undrawn extrudate
PCL/PLA/C15-ED	80/20 + 2% of clay	Twin-screw extruder, melt-drawn bristle (DR = 5)[c]
PCL/PLA/C15-EDI	80/20 + 2% of clay	Inject. molding from melt-drawn bristle (DR = 5)[c]

[a]Extrusion of PLA at temperature of all zones set to 190°C; [b]Extrusion of PCL and all PCL/PLA systems at temperature of zones 170–180°C; [c]DR = draw ratio. The letters E, D, and I at the end of sample names mean that the samples were extruded, drawn and/or injection molded, respectively.

the results were averaged (standard deviations from just two measurements were not calculated, but experience shows that the standard deviations of final DSC crystallinities of semicrystalline polymers are usually around 2 %). The melting temperatures T_m of both polymers were identified as the maximum of their melting endotherms. The cold crystallization temperature T_{cc} of PLA was identified as the maximum of cold-crystallization exothermic peak. The crystallinity of PCL and PLA were calculated according to Equations 10, 11, respectively:

$$w_c^{PCL} = \frac{\Delta H_m(PCL)}{\Delta H_m^0(PCL) \cdot w(PCL)} \times 100\% \quad (10)$$

$$w_c^{PLA} = \frac{|\Delta H_m(PLA)| - |\Delta H_{cc}(PLA)|}{\Delta H_m^0(PLA) \cdot w(PLA)} \times 100\% \quad (11)$$

where ΔH_m and ΔH_{cc} are the enthalpy of melting and cold crystallization, respectively. In contrast to PCL crystallinity calculation (Equation 10), the PLA crystallinity calculation (Equation 11) has to take cold crystallization into account (Ostafinska et al., 2017). The crystalline fractions of PCL and PLA are related to pure polymers, i.e., the melting enthalpies were divided by weight fractions of PCL (w(PCL) in Equation 10) and PLA (w(PLA) in Equation 11), respectively. The same approach, which facilitates comparison of the crystallinities of the individual components in the systems with various compositions, was used in our previous studies (Ostafinska et al., 2015, 2017; Kelnar et al., 2016b). The values ΔH_m^0 denote the enthalpy of melting 100%-crystalline polymers (139.5 and 93.1 J/g for PCL and PLA, respectively). The enthalpy value for PLA ($\Delta H_m^0 = 93.1$ J/g), which was used also in our previous studies, was based on recent study of Lim et al. (2008), while some older studies reported slightly different value ($\Delta H_m^0 = 93.6$ J/g; Fischer et al., 1973).
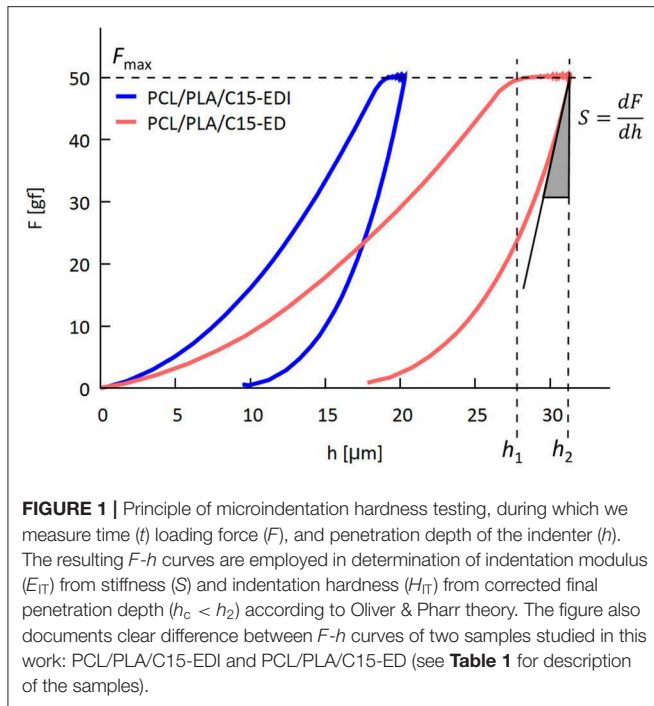
Macromechanical Properties: Tensile Testing

Tensile tests were carried out using an Instron 5800 apparatus at 22°C and crosshead speed of 20 mm/min. At least eight specimens were tested for each sample according to EN ISO 527. Young's modulus (E), yield stress (Y), and elongation at break (ε_b) were evaluated; the corresponding standard deviations did not exceed 10,

5, and 20%, respectively. For pure PLA polymer, which exhibited brittle behavior, the yield stress was approximated by the stress at break value ($Y \approx \sigma_b$). The tensile testing was carried out with injection molded specimens, which means that all properties were measured along the injection molding direction.

Micromechanical Properties: Microindentation Hardness Testing

Micromechanical properties were characterized by instrumented microindentation hardness tester (Micro-Combi Tester; CSM Instruments, Switzerland). Smooth cut surfaces for the microindentation experiments were prepared with a rotary microtome (RM 2155; Leica, Austria) using a freshly broken glass knife (Knifemaker 7800; LKB Bromma, Sweden). All microindentation results in this manuscript come from the cut surfaces perpendicular to extrusion, drawing and/or injection molding direction; this means that the loading force was parallel with the extrusion, drawing and/or injection molding direction. Therefore, the loading force in macro- and micromechanical measurements was applied along the same direction. For each specimen, at least three independent smooth surfaces were prepared, and at least 10 indentations were carried out per surface, i.e., each sample was measured >30× and the results were averaged. All indentations were performed with a Vickers indenter (diamond square pyramid, angle between two non-adjacent faces 136 deg). Details about experiment geometry have been described elsewhere (Balta-Calleja and Fakirov, 2000; Slouf et al., 2015, 2017). The indenter was forced against the polymer surface using loading force 50 gf (0.4905 N), loading time 6 s, and linear loading/unloading rate 25 N/min. For all prepared blends or composites and given experimental setup, the size of the indents on the polymer surface was >110 μm, i.e., well above the coarseness of the phase structure. Consequently, the microindentation experiments yielded averaged information about the properties of investigated systems, which could be compared with macroscopic measurements. The experimental F-h curves (**Figure 1**) were used to calculate indentation hardness (H_{IT}) and indentation modulus (E_{IT}) according to the theory of Oliver and

FIGURE 1 | Principle of microindentation hardness testing, during which we measure time (*t*) loading force (*F*), and penetration depth of the indenter (*h*). The resulting *F-h* curves are employed in determination of indentation modulus (E_{IT}) from stiffness (*S*) and indentation hardness (H_{IT}) from corrected final penetration depth ($h_c < h_2$) according to Oliver & Pharr theory. The figure also documents clear difference between *F-h* curves of two samples studied in this work: PCL/PLA/C15-EDI and PCL/PLA/C15-ED (see **Table 1** for description of the samples).

Pharr (1992):

$$H_{IT} = \frac{F_{max}}{A_p\left(h_c\right)} \tag{12}$$

$$E_{IT} \propto E_r = \frac{1}{2} * \frac{\sqrt{pi}}{\sqrt{A_p(h_c)}} * \frac{dF}{dh} \tag{13}$$

In Equations 12–13 above, F_{max} is maximum loading force, $A_p(h_c)$ is the projected area of the indentation (which is a function of the contact depth (h_c) as described elsewhere (Oliver and Pharr, 1992; Slouf et al., 2018), and $S = dF/dh$ denotes stiffness defined as the slope at the beginning of the unloading curve (see **Figure 1**). The indentation modulus (E_{IT}) was calculated from reduced modulus (E_r) using relation $1/E_r = (1-\nu_i^2)/E_i + (1-\nu_s^2)/E_{IT}$, where E_i is modulus of the indenter (for diamond: $E_i = 1,141$ GPa), ν_i is Poisson's ratio of the indenter (for diamond: $\nu_i = 0.07$), and ν_s is the Poisson's ration of the sample (in this work we calculated with approximate value $\nu_s = 0.4$).

Statistical Evaluation

Pre-processing of experimental data and basic statistical calculations were performed in a spreadsheet program (MS Excel). More advanced statistical processing and calculations was carried out by means of the freeware Python programming language and its modules for data analysis (McKinney, 2018). The data were transferred from MS Excel to Python using Pandas module, linear regressions, correlation coefficients and *p*-values were calculated by SciPy module, common figures were prepared by means of NumPy and Matplotlib modules, and the special statistical scatterplot matrix graphs were prepared by means of Seaborn module. Two statistical coefficients were

calculated in this work in order to quantify linear correlations: Pearson's correlation coefficients (*r*) and *p*-values (*p*). Detailed definitions of the coefficients can be found in statistical textbooks (Urdan, 2017). Briefly, Pearson's coefficients can take values from +1 (total positive linear correlation) through 0 (no linear correlation) to −1 (total negative linear correlation). The *p*-values, in our case, yield a probability that we would observe that strong (or stronger) linear correlation just by coincidence; the correlation is regarded as statistically significant if the calculated *p*-value is below the conventional value of 0.05 (i.e., if the probability is below 5 %).

RESULTS AND DISCUSSION

Processing-Induced Changes of Morphology

All prepared PCL/PLA/C15 systems are summarized in **Table 1** and their typical morphologies are shown in **Figures 2, 3**. All undrawn systems (PCL/PLA blends, and undrawn PCL/PLA/C15 composites) showed almost isotropic structure (**Figures 2A,B**). In the undrawn PCL/PLA blends, the PCL matrix contained nearly isometric PLA particles with diameter up to 1 μm (**Figure 2A**). Average particle size was ∼0.4 μm according to measurement of >100 particles in SEM micrographs. The particles were just slightly elongated in the extrusion direction (**Figure 2B**). In the undrawn PCL/PLA/C15 composites, the addition of C15 did not influence the PLA particle size significantly (micrographs not shown for the sake of brevity), but the main benefit of C15 was the improved stability of the extrusion process as discussed in the next paragraph. The undrawn systems after injection molding (samples PCL/PLA-EI and PCL/PLA/C15-EI) represent control samples with isometric PLA particles. Therefore, the comparison of these samples with the final drawn system (sample PCL/PLA-EDI, i.e., the final microfibrillar composite with PLA fibers, which is described in the next paragraph) can reveal the reinforcing effect of PLA fibers.

Melt-blending and extrusion of PCL/PLA blends without addition of C15 lead to a bristle with low melt strength: the extrusion was unstable, the extruded bristle exhibited variable thickness and its drawing was impossible. This was probably caused by an unfavorable combination of rheological parameters (Yi et al., 2010; Kelnar et al., 2016a). Addition of 2 wt.% of C15 resulted in much more stable bristle with uniform thickness, which lead to successful melt drawing up to draw ratio 5. In the drawn systems, the PLA particles formed short oriented fibers (**Figures 2C,D**). The fiber thickness decreased to ∼0.2 μm and their average aspect ratio (AR = L/d = fiber length / fiber thickness) increased to ∼4, as estimated from SEM micrographs. A comparison of volume of spherical particles in undrawn systems (**Figures 2A,B**; $d = 0.4$ μm $\Rightarrow V = 1/6 \cdot \pi \cdot d^3 = 0.034$ μm³) with the volume of elongated fibers in drawn systems (**Figures 2C,D**; $d = 0.2$ μm, AR = L/d = 4 $\Rightarrow V = 1/4 \cdot \pi \cdot d^2 \cdot L = \pi \cdot d^3 = 0.025$ μm³) suggested that some particle breakup had occurred
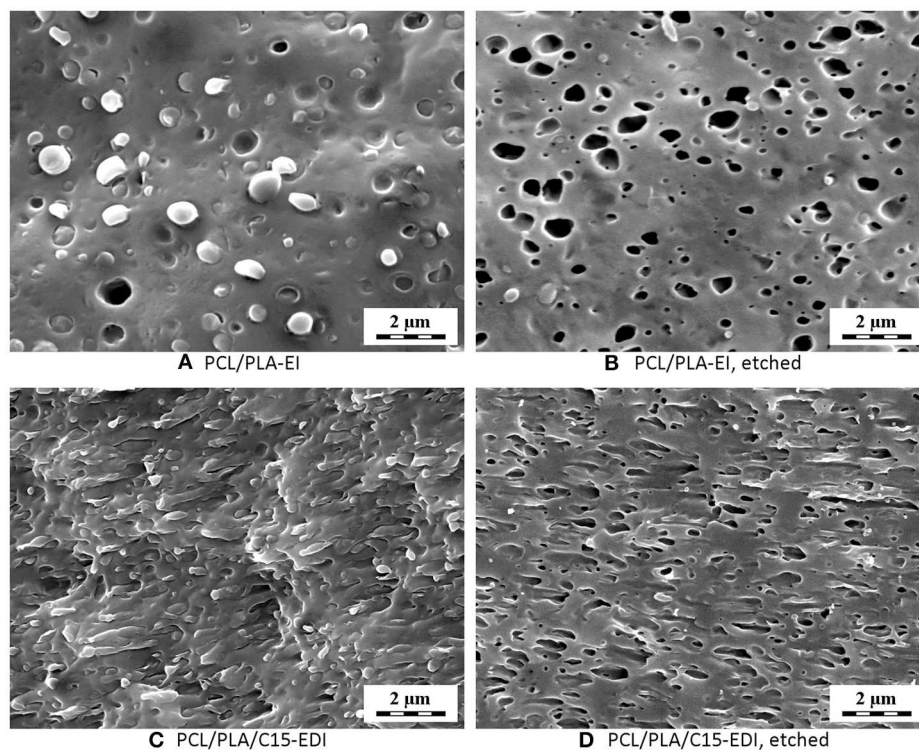
FIGURE 2 | SEM micrographs showing phase morphology of **(A,B)** PCL/PLA-EI blend from undrawn extrudate and **(C,D)** PCL/PLA/C15-EDI composite; the micrographs show fracture surfaces parallel with melt flow before **(A,C)** and after **(B,D)** etching; sample names are explained in **Table 1**.
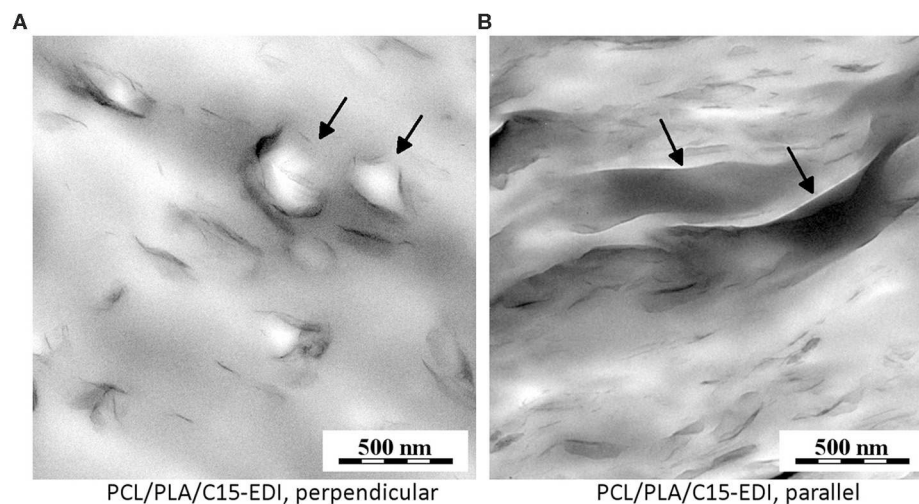
FIGURE 3 | TEM micrographs showing filler dispersion in PCL/PLA/C15-EDI composite: **(A)** perpendicular to the melt flow and **(B)** parallel with the melt flow. Black arrows show that the C15 agglomerates tended to envelope PLA particles, which were somewhat elongated in the direction of melt flow.

during the drawing process, but its extent had not been critical. It is worth noting that the value of AR ∼ 4 from the SEM micrographs of injection molded samples could be underestimated due to non-perfect fiber orientation and tangling. On the other hand, the experimentally determined average value was in good agreement with the predictive models, as discussed below.

The filler in PCL/PLA/C15 composites was just partially exfoliated, but both the agglomerates and single sheets were quite homogeneously distributed within the system as evidenced by

TABLE 2 | DSC results: melting points and crystallinities of PCL and PLA in all prepared samples.

Sample	T_m^{PCL} (°C)	ΔH_m^{PCL} (J/g)	w_c^{PCL} (%)	T_{cc}^{PLA} (°C)	ΔH_{cc}^{PLA} (J/g)	T_m^{PLA} (°C)	ΔH_m^{PLA} (J/g)	w_c^{PLA} (%)
PLA-EI	x	x	x	120.3	−0.8	151.1	9.0	8.8
PCL-EI	63.2	73.2	52.5	x	x	x	x	x
PCL/PLA-E	69.0	61.3	54.9	109.6	−3.7	149.5	4.8	6.1
PCL/PLA-EI	61.7	54.2	48.6	104.3	−2.3	151.5	5.5	17.3
PCL/PLA/C15-E	66.6	63.8	57.2	102.7	−3.4	150.6	4.2	4.1
PCL/PLA/C15-EI	62.7	59.9	53.7	96.6	−1.5	151.1	4.8	18.0
PCL/PLA/C15-ED	58.7	47.3	42.4	122.6	−2.2	150.1	2.4	1.3
PCL/PLA/C15-EDI	62.8	62.0	55.6	93.9	−1.0	152.1	5.0	21.7

T_m = melting peak or melting point, T_{cc} = cold crystallization peak, ΔH_m = melting enthalpy, ΔH_{cc} = cold crystallization enthalpy, and w_c = crystallinity calculated according to the description in Experimental section.

TEM micrographs (**Figure 3**). Although the insufficient contrast between the two polymer phases prevented us from precise localization of C15, the overall homogeneous dispersion of the filler (**Figure 3**) and theoretical considerations based on similar interfacial energies and wetting coefficients of the two polymers with respect to C15 (Kelnar et al., 2016a) indicated that the clay was present in both phases. Moreover, comparison of sections perpendicular (**Figure 3A**) and parallel (**Figure 3B**) to the melt flow showed some slight orientation of the clay agglomerates and nanoplatelets and suggested that they tended to partially envelop PLA fibers in the drawn sample PCL/PLA/C15-EDI—the diameter of numerous spherical structures in the perpendicular sections (**Figure 3A**; black arrows) and elongated structures in parallel sections (**Figure 3B**; black arrows) corresponded quite well to PLA fiber diameter as determined from SEM (**Figures 2C,D**; $d \sim 0.2\,\mu$m).

Processing-Induced Changes of Crystallinity and Micromechanical Properties

The two-step MFC preparation, i.e., the drawing at higher temperature followed by the injection molding at lower temperature, influenced the crystalline structure of both polymers (**Table 2**). Consequently, the crystallinity changes influenced the micromechanical properties (**Figure 4**). The correlation between crystallinity of the components and mechanical performance was linear (in agreement with theory, see Equation 4) and statistically significant (**Figure 5**).

The DSC experiments yielded two quantities: (i) overall crystallinities, w_c, and (ii) melting points, T_m. The values of T_m correlate with average lamellar thickness, l_c, according to Thompson-Gibbs equation (Gedde, 1995; Slouf et al., 2016). For PCL, both w_c and T_m were similar for all samples with the exception of drawn bristle before injection molding (sample PCL/PLA/C15-ED), where both parameters showed a notable decrease. For PLA, whose crystallinity is very sensitive to thermal history due to its cold crystallization (Ostafinska et al., 2015, 2017), the changes were more pronounced: the crystallinities of all injection molded specimens (PCL/PLA-EI, PCL/PLA/C15-EI, and PCL/PLA/C15-EDI) were systematically higher than

the crystallinities of extrudates before the injection molding step (PCL/PLA-E, PCL/PLA/C15-E, and PCL/PLA/C15-ED); the remarkable decrease in crystallinity was observed for drawn bristle (PCL/PLA/C15-ED). The PLA melting points followed similar trends like crystallinities, but their variations were not so strong.

Figure 4 documents the close relationship between micromechanical properties (H_{IT} and E_{IT}) and crystallinities of all studied systems (more precisely, the sum of crystallinities of both components, $w_c^{PCL} + w_c^{PLA}$). The strong correlations among the three parameters (H_{IT}, E_{IT} and the sum of crystallinities) could be confirmed statistically in the form of scatterplot matrix graph (**Figure 5**), which shows also Pearson's correlation coefficients (r) and p-values (p) for all pairs of correlated quantities. All correlations in **Figure 5** were strong, positive, and linear (r coefficients from 0.86 to 0.97, i.e., quite close to +1) and all were statistically significant (p-values from 0.003 to 0.014, i.e., well below 0.05). In conclusion, **Figures 4, 5** indicate that the decisive parameter for final mechanical performance is not only the morphology of the blends, but also crystallinity of both components, which changes during the two-step preparation process.

A general theoretical justification of the observed linear correlations between H_{IT}, E_{IT} and crystallinity of is based on Equation 4, which combines key results of several previous studies (Tabor, 1951; Struik, 1991; Balta-Calleja and Fakirov, 2000) as explained in section Theoretical Background. The specific justification why in our case the H_{IT} (and thus also E_{IT}) is proportional to the *sum of crystallinities* of both blend components is given below. We start with the general formula for additivity law (Equation 1). It is worth reminding that the additivity law works very well for specific cases, such as microhardness semicrystalline polymers (Balta-Calleja and Fakirov, 2000) and elastic modulus of composites with infinitely long oriented fibers (Nielsen and Landel, 1994), while for mechanical properties of polymer blends it is just the first approximation (Ostafinska et al., 2017, Ostafinska et al., 2018). In spite of its approximate nature, the additivity law has been employed successfully for prediction of microhardness of polymer blends and/or composites as proved by many classical studies of Balta-Calleja and co-workers (Balta-Calleja
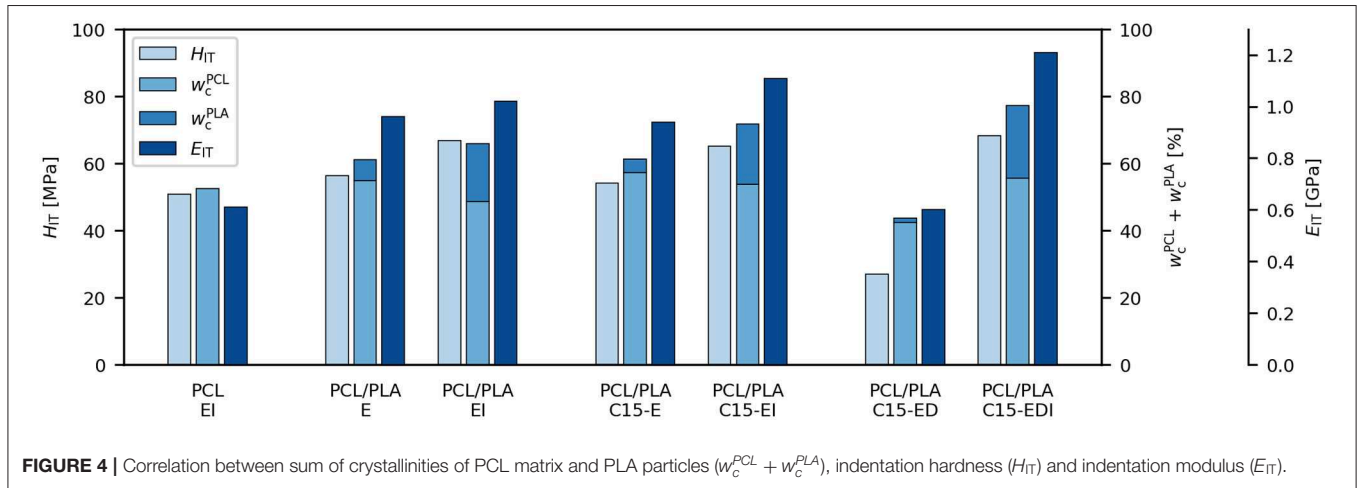
FIGURE 4 | Correlation between sum of crystallinities of PCL matrix and PLA particles ($w_c^{PCL} + w_c^{PLA}$), indentation hardness (H_{IT}) and indentation modulus (E_{IT}).

and Fakirov, 2000; Flores et al., 2009). In this work, we employ the additivity law to explain the basic observed trends, namely the fact that the elastic modulus, yield stress and hardness are roughly proportional to the sum of crystallinities of the components. The additivity law applied to microhardness of our PCL/PLA/C15 system reads:

$$H = \sum_i v_i H_i = v^{PCL} H^{PCL} + v^{PLA} H^{PLA} + v^{C15} H^{C15} \quad (14)$$

In Equation 14, we neglect the last member ($v^{C15} H^{C15}$) because it was demonstrated that isometric nanofillers at low concentrations (up to ca 6 %) do not influence microhardness (Flores et al., 2009; Vackova et al., 2017). Then we apply additivity law also to the blend components, which consist of amorphous (subscript a) and crystalline (subscript c) phase:

$$H = v^{PCL} \left(v_a^{PCL} H_a^{PCL} + v_c^{PCL} H_c^{PCL} \right)$$
$$+ v^{PLA} (v_a^{PLA} H_a^{PLA} + v_c^{PLA} H_c^{PLA}) \quad (15a)$$

$$H = v^{PCL} v_a^{PCL} H_a^{PCL} + v^{PCL} v_c^{PCL} H_c^{PCL}$$
$$+ v^{PLA} v_a^{PLA} H_a^{PLA} + v^{PLA} v_c^{PLA} H_c^{PLA} \quad (15b)$$

In Equation 15b, we neglect the first member ($v^{PCL} v_a^{PCL} H_a^{PCL}$) because the microhardness of the amorphous phase of semicrystalline polymers above their glass transition temperature is very low ($H_a^{PCL} \approx 0$) as shown by Balta-Calleja (Balta-Calleja and Fakirov, 2000). Then we slightly modify the equation (using a simple formula relating volume fractions of PLA; $v_a^{PLA} + v_c^{PLA} = 1$):

$$H = v^{PCL} v_c^{PCL} H_c^{PCL} + v^{PLA} v_a^{PLA} H_a^{PLA} + v^{PLA} v_c^{PLA} H_c^{PLA} \quad (16a)$$

$$H = v^{PCL} v_c^{PCL} H_c^{PCL} + v^{PLA} H_a^{PLA}$$
$$+ v^{PLA} v_c^{PLA} (H_c^{PLA} - H_a^{PLA}) \quad (16b)$$

Equation 16b can be re-arranged to separate the crystallinities (i.e., the volume fractions of the crystalline phases, v_c^{PCL} and v_c^{PLA},

which change during the preparation) from the other constant values (considering that all studied systems have constant ratio of PCL/PLA = 80/20 and that the hardness values of amorphous and crystalline phase for given polymer are constant):

$$H = v_c^{PCL} \left[v^{PCL} H_c^{PCL} \right] + v_c^{PLA} \left[v^{PLA} \left(H_c^{PLA} - H_a^{PLA} \right) \right]$$
$$+ [v^{PLA} H_a^{PLA}] \quad (17a)$$

$$H = v_c^{PCL} C_1 + v_c^{PLA} C_2 + C_3 \quad (17b)$$

where the constants C_1, C_2, and C_3 in Equation 17b substitute the corresponding constant expressions in square brackets in Equation 17a. In the final simplification of Equation 17b, we omit constant C_3 (as the constant does not influence the linear relationship we want to justify), we set $C_1 \approx C_2$ (this is very rough empirical simplification based on the fact that the influence of both components on the final hardness values is approximately the same—as confirmed by the results in **Figures 4**, **5**), and we exchange volume fractions of crystalline phases (v_c^{PCL} and v_c^{PLA}) for weight fractions (w_c^{PCL} and w_c^{PLA}), which is possible because the relation between volume and weight fractions is also linear ($v_c = w_c \times \rho/\rho_c$, where ρ is the density of the polymer and ρ_c is the density of its crystalline phase). Considering all simplifications above, we get the final approximate relation claiming that hardness in our specific case of PCL/PLA/C15 systems should be roughly proportional to the sum of crystallinities:

$$H \propto w_c^{PCL} + w_c^{PLA} \quad (18)$$

During the justification of Equation 18, we used numerous rough approximations such as (i) the assumption that the properties of PCL/PLA/C15 systems are described by simple additivity law (this is neither entirely precise nor completely wrong as shown in section: Influence of Composition, Morphology and Filler on Properties of Final MFC Composite), (ii) the neglection of the influence of the average lamellar thickness (this should not be critical as the contribution of lamellar thickness to final hardness value is relatively small (Flores
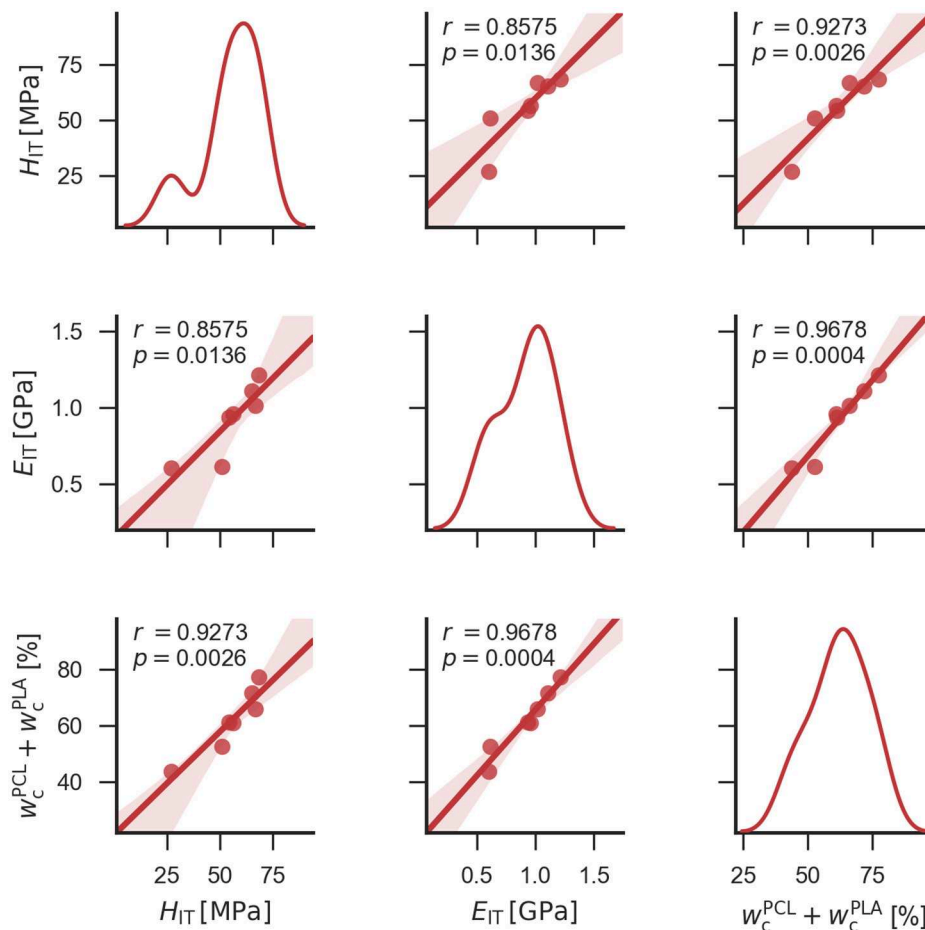
FIGURE 5 | Scatterplot matrix graph showing correlations among indentation hardness (H_{IT}), indentation modulus (E_{IT}) and sum of crystallinities of PCL and PLA ($w_c^{PCL} + w_c^{PLA}$). Diagonal elements of the graph display distribution of each quantity, while off-diagonal elements show correlations between each pair of quantities. Off-diagonal elements display also Pearson's correlation coefficients (r) and p-values (p). The scatterplot matrix graph, correlation coefficients and p-values were calculated with Python modules as described in Experimental section.

et al., 2009) and, moreover, in our case the values of lamellar thickness followed the same trends as crystallinities as discussed in section: Processing-Induced Changes of Crystallinity and Micromechanical Properties), and namely (iii) the assumption that the impact of both components on the microhardness value is approximately the same (this is not more than an intentional simplification based on the experimental results). Despite all approximations, the final relation represented by Equation 18 yields a theoretical explanation of the observed correlation and corresponds very well to the experimental results, as documented by the statistically significant linear correlations in **Figure 5**.

Comparison of Macro- and Micromechanical Properties for Injection Molded Specimens

Figures 6, **7** show the mechanical properties of injection molded samples. The advantage of the injection molded specimens consisted in the fact that their mechanical performance could be characterized both in macroscale (tensile testing)

and microscale (microindentation). This enabled us to verify the correlation between macro- and microscale properties, which was expected due to the theoretical considerations summarized in section Theoretical Background. Complete results of macro- and micromechanical measurements are summarized in **Table 3**.

Figure 6A documents that macroscale tensile modulus (E) and microscale indentation modulus (E_{IT}) followed the same trend. For injection molded samples, which had similar crystallinities of both components, the stiffness of PCL matrix gradually increased after blending with PLA, after the addition of C15, and, finally, after drawing. **Figure 6B** confirmed the linear correlation between E and E_{IT}, which was consistent with linear correlations given by Equation 4. The fact that the values of E_{IT} were slightly higher than the values of E is quite common (Trachida et al., 2007; Kranenburg et al., 2009; Lesan-Khosh et al., 2011) and could be attributed to specific features of micro- and nanoindentation experiments (Hardiman et al., 2016).

TABLE 3 | Macro- and micromechanical properties.

Sample	Tensile testing		Microindentation hardness testing			
	E (GPa)	Y (MPa)	E_{IT} (GPa)	e.s.d (E_{IT})	H_{IT} (MPa)	e.s.d (H_{IT})
PLA-EI	3.16	74.0	4.69	0.13	262.6	6.3
PCL-EI	0.34	17.0	0.61	0.02	50.9	2.1
PCL/PLA-E	x	x	0.96	0.05	56.3	6.1
PCL/PLA-EI	0.76	20.2	1.02	0.04	66.8	3.6
PCL/PLA/C15-E	x	x	0.94	0.01	54.2	1.6
PCL/PLA/C15-EI	0.79	20.1	1.11	0.03	65.2	1.9
PCL/PLA/C15-ED	x	x	0.60	0.03	26.9	1.2
PCL/PLA/C15-EDI	0.93	22.4	1.21	0.04	68.3	2.0

Relative standard deviations of E and Y were lower than 10 and 20%, respectively.

Figure 7A illustrates that also macroscale tensile yield stress (Y) and microscale indentation hardness (H_{IT}) showed good correlation and followed a similar trend as macro- and microscale elastic moduli (compare **Figures 6A**, **7A**). The linear relation between Y and H_{IT} (**Figure 7B**) was in agreement with Tabor's relation (Equation 3) and the value of the proportionality constant ($C = 3.15 \pm 0.07$) was in quite good agreement with theory ($C \approx 3$). In conclusion, the comparison of macro- and micromechanical properties, which were measured for bulk specimens, confirmed the validity of the theoretically predicted linear correlations among the measured quantities (E, E_{IT}, Y, and H_{IT}). Moreover, the good correlations between macro- and micromechanical properties evidenced the accuracy and precision of microindentation measurements, which were applied not only to bulk specimens (as shown in this section), but also to the thin extrudates and bristles (as discussed in the next section).
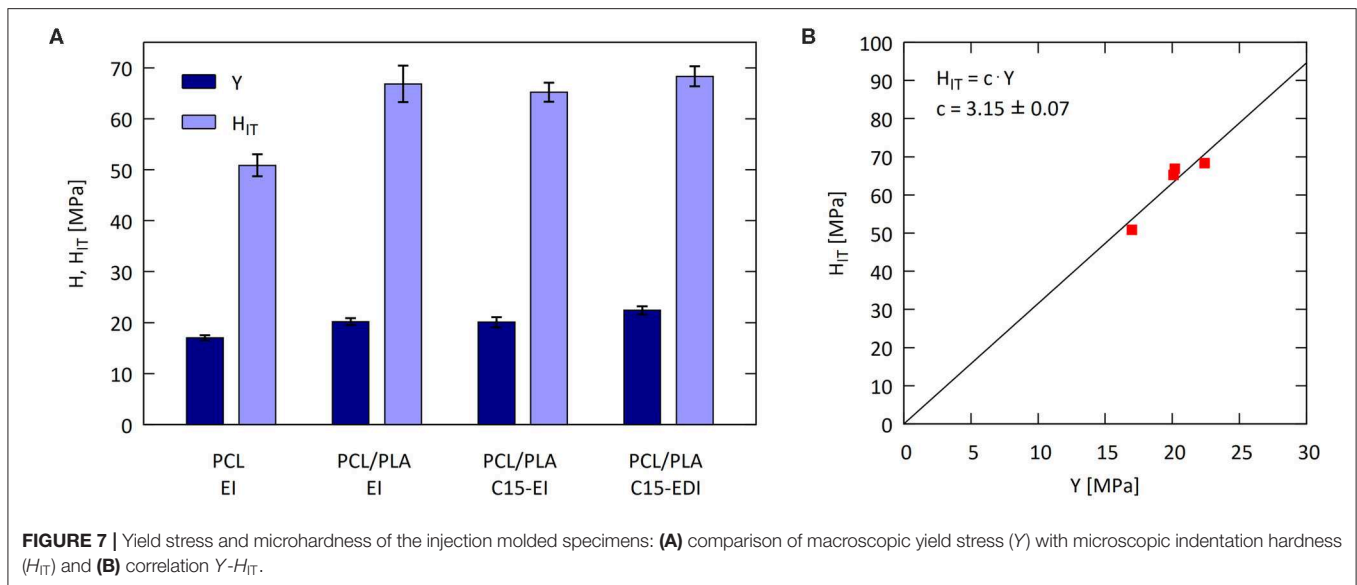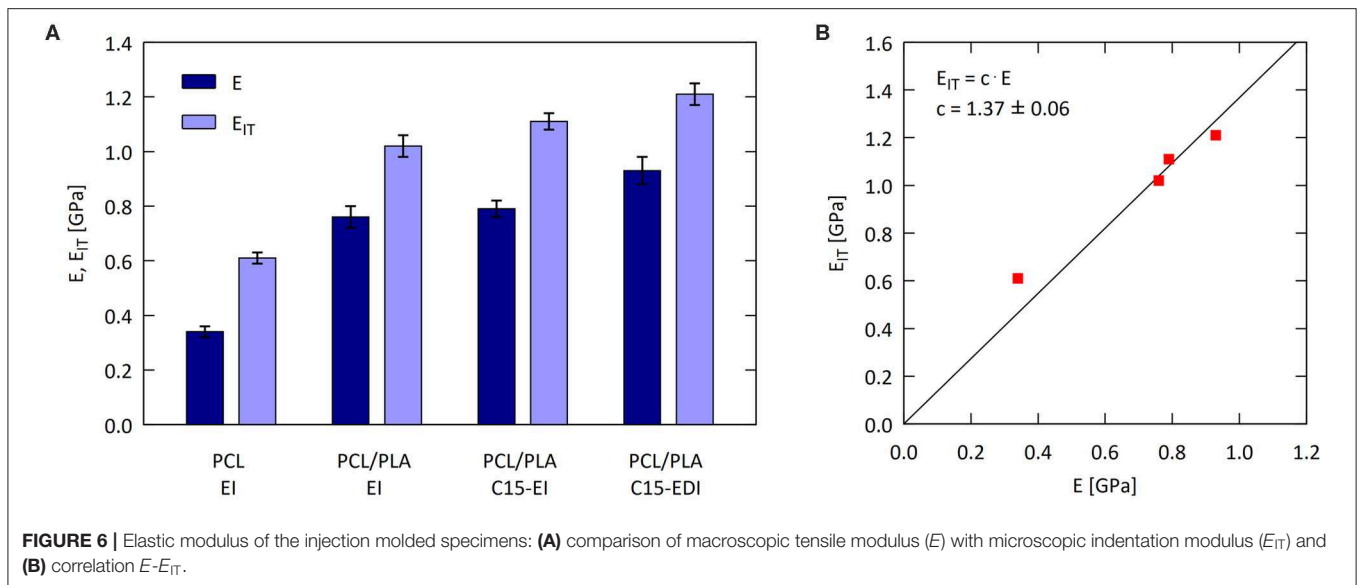
Figures 6, **7** indicate that the addition of PLA caused the main improvement of the stiffness of PCL/PLA systems (compare sample PCL with sample PCL/PLA-EI), while the effect of filler addition and drawing was minor (compare sample PCL/PLA-EI with samples PCL/PLA/C15-EI and PCL/PLA/C15-EDI). Despite the fact that the difference between isotropic blend (PCL/PLA-EI) and the final microfibrillar composite (PCL/PLA/C15-EDI) is relatively small, the positive effect of drawing is evident. The main reason why the effect of drawing was not higher in our specific case of PCL/PLA microfibrillar composites consisted in the relatively low aspect ratio of PLA fibers and other effects, which are discussed in the following section.

Influence of Composition, Morphology, and Filler on Properties of Final MFC Composite

Figure 8 shows the comparison of the experimentally determined mechanical properties (E_{IT} and H_{IT}) of all prepared PCL/PLA blends and composites with the predictive models. The models are described above in section Predictive Models for Polymer Blends and Composites; we just briefly summarize that the

LIN model is a simple rule of mixing, representing the upper achievable limit for mechanical properties of polymer blends, the EBM model is a more realistic prediction for isotropic polymer blends, and the HT model considers also possible anisotropy of the blend. The system with the lowest crystallinities of the components (PCL/PLA/C15-ED) showed the worst properties regardless of the fact that it was the semi-final product, in which the PCL matrix had already been reinforced by PLA fibers and by the addition of C15. This re-confirmed the key role of crystallinity for the improvement of final properties. In contrast, the final injection-molded microfibrillar composite (PCL/PLA/C15-EDI), which had all improvements like the above-discussed PCL/PLA/C15 *and* the highest crystallinities, showed the best properties. At first, the indentation modulus of PCL/PLA/C15-EDI exceeded the HT prediction calculated for short oriented fibers with aspect estimated from SEM (Equation 8, AR = 4). At second, the indentation hardness of PCL/PLA/C15-EDI surpassed the EBM prediction calculated for PCL/PLA blend with maximum interfacial adhesion (Equation 7; $A = 1$). This indicated good compatibility between the polymer components and some small additional positive effects of the crystallinity and filler on the final mechanical performance. Before we discuss these small improvements (subject of the next paragraph), we note that the rest of the samples always exhibited better mechanical performance after injection molding (samples PCL/PLA/C15-EI and PCL/PLA-EI) and worse mechanical performance without injection molding (samples PCL/PLA/C15-E and PCL/PLA-E). This was again connected with the increase in overall crystallinity, because the injection molding supported cold crystallization of PLA, while the PCL crystallinity in all samples with the exception of PCL/PLA-ED was similar, as evidenced by DSC (**Figure 4**).

Figure 9 focuses on the final microfibrillar composite PCL/PLA/C15-EDI and compares its experimentally determined indentation modulus (**Figure 9**, dotted line) with more detailed theoretical predictions. The final predictions were based on HT equations (Equation 8) because the SEM micrographs evidenced that the final composite PCL/PLA/C15-EDI was anisotropic, containing short oriented fibers (**Figures 2C,D**). As explained above in section Theoretical background, HT equations (Equation 8) were developed for such anisotropic

FIGURE 6 | Elastic modulus of the injection molded specimens: **(A)** comparison of macroscopic tensile modulus (E) with microscopic indentation modulus (E_{IT}) and **(B)** correlation E-E_{IT}.

FIGURE 7 | Yield stress and microhardness of the injection molded specimens: **(A)** comparison of macroscopic yield stress (Y) with microscopic indentation hardness (H_{IT}) and **(B)** correlation Y-H_{IT}.

systems, whereas LIN model (Equation 5) is just general rule of mixing, EBM model (Equations 6, 7) does not take anisotropy into account, and Einstein equation (Equation 9) assumes isotropic systems. Therefore, the calculations were performed for short oriented fibers according to HT equations (Equation 8) as a function of the aspect ratio of the PLA fibers. Additionally, we assumed that the orientation of crystalline lamellae within the PLA fibers was not changed significantly, because the cold crystallization was expected to change mostly the thickness, but not the orientation of the crystalline lamellae (which did not melt in the second processing step). This assumption is supported by our previous studies on analogous systems, which showed no signs of PLA isotropization at nanoscale level during preparation of microfibrillar composites (Kelnar et al., 2016a,b, 2017b). Finally, we assumed that the real AR was ~4

(**Figure 9**, dash-and-dot line), which was the value estimated from the analysis of SEM micrographs (**Figure 2**). The first model (**Figure 9**, Model 1) shows elastic modulus of the pure PCL/PLA microfibrillar composite (Equation 8, AR = 4, no filler). The second model (**Figure 9**, Model 2) shows the same system like Model 1 after addition of 2 wt. % of C15, supposing that the montmorillonite is not exfoliated and forms isometric agglomerates (the improvement of the PCL/PLA modulus due to isometric aggregates of C15 is calculated by means of Equation 9). The third model (**Figure 9**, Model 3) shows the same system like Model 2 after the increase of modulus of PLA fibers due to cold crystallization; we assumed increase of 10%, which is probably the maximum due to high T_g of PLA, resulting in high stiffness of the amorphous phase and *relatively* modest increase in stiffness due to higher crystallinity (Perego et al., 1996). The
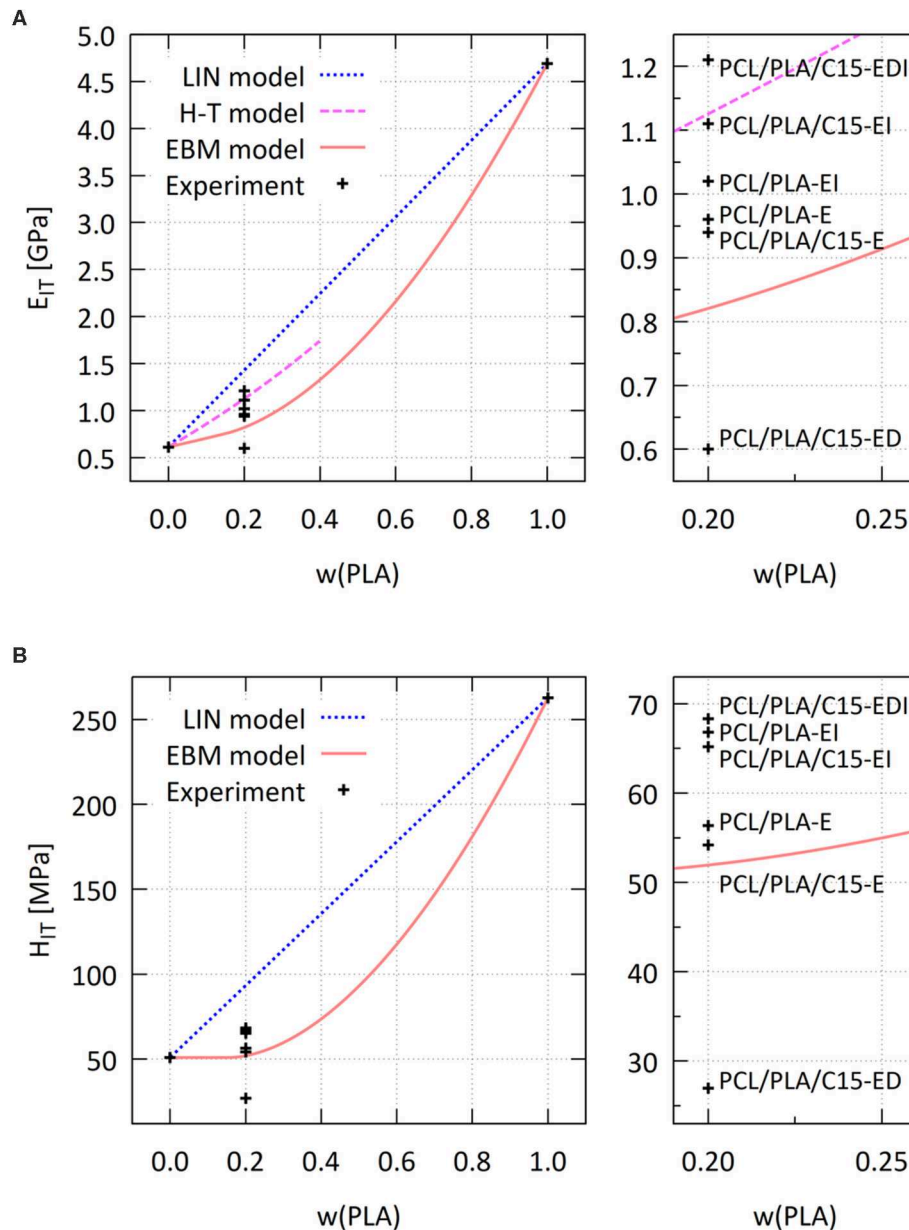
FIGURE 8 | Comparison of experimental values of **(A)** indentation modulus and **(B)** indentation hardness with theoretical predictions based on linear model (LIN; dotted line), Halpin-Tsai model for short oriented fibers with aspect ratio = 4 (HT; dashed line), and equivalent box model calculated with default parameters (EBM; full line); the smaller graphs on the right show enlarged areas with experimental points from all PCL/PLA/C15 systems (see **Table 1** for explanation of sample names).

increase in the PLA crystallinity might have been enhanced by orientation of PLA chains (Fambri et al., 2006). The increase in the PCL crystallinity was not included in Model 3 as it was not changed much with respect to the original PCL (as discussed above and documented in **Figure 4**). The fourth model (**Figure 9**, Model 4) is the same like Model 3, but it assumes that the montmorillonite consists of fully dispersed, randomly oriented platelets (calculation according to Equation 8) with AR ≈ 20 as estimated from TEM micrographs (**Figure 3**). The prediction of

E_{IT} based on Model 4 was clearly too high, which confirmed that most of the montmorillonite platelets was not exfoliated as observed in the TEM micrographs (**Figure 3**).

Comparison of all models with the experimental value of E_{IT} of PCL/PLA/C15-EDI in **Figure 9** showed that the best was the third model (i.e., **Figure 9**, Model 3: PCL/PLA-hCR/C15-n, PCL with oriented PLA fibers, increased crystallinity of PLA fibers and not-fully-exfoliated montmorillonite). According to this model, the properties of the final microfibrillar composite
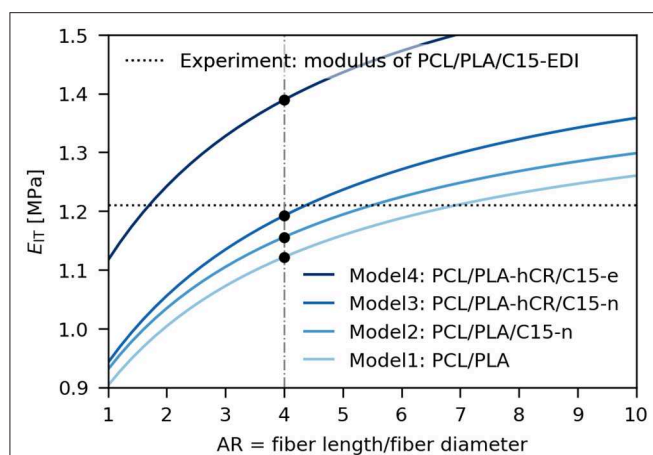
FIGURE 9 | Comparison of experimental elastic modulus of the final MFC composite, PCL/PLA/C15-EDI (dotted line), with theoretical predictions (full lines). Aspect ratio of PLA fibers (AR = 4) was estimated from SEM micrographs (dash-and-dot line). The first model (Model1: PCL/PLA) assumes just short oriented PLA fibers in PCL matrix. The second model (Model2: PCL/PLA/C15-n) adds correction for non-dispersed/isometric filler C15. The third model (Model3: PCL/PLA-hCR/C15-n) adds correction for increased modulus of PLA fibers due to their higher crystallinity. The fourth model (Model4: PCL/PLA-hCR/C15-e) is like Model3, but assumes fully dispersed C15 nanoplatelets with random orientation.

were improved not only due to the formation of the oriented PLA fibers in the PCL matrix, but also due to the increased crystallinity of the PLA fibers, and due to the presence of filler. The additional improvement in final stiffness due to the processing-induced increase in PLA crystallinity was in perfect agreement with all microindentation measurements. The final increase in modulus due to the presence of C15 filler (even if the montmorillonite was not fully exfoliated) was quite logical, being in agreement with theory, represented here by Equation 9. Last but not the least, the modeling in **Figure 9** suggests the possible ways and limitations of further improvement of modulus in PCL/PLA/C15 microfibrillar composites—it seems that the best performance would be achieved by better exfoliation of the montmorillonite filler.

CONCLUSIONS

Morphology and micromechanical properties of the PCL/PLA/C15 microfibrillar composites were monitored during the whole preparation process in order to elucidate the real reasons of the improvement of the mechanical properties. The microscopic and micromechanical measurements were compared with the final macroscopic properties. Both macro- and micromechanical properties were measured parallel with the direction of extrusion, drawing and/or injection molding. The main results could be summarized as follows:

At first, it has been confirmed that the two-step preparation of PCL/PLA microfibrillar composites is a complex process, during which both components change not only their

morphology, but also their crystallinity. This additional complexity was connected with the high sensitivity of PLA to thermal treatment, which was associated with the cold crystallization of the polymer. Moreover, the addition of the filler (organophilic montmorillonite, C15) was found necessary for given PCL/PLA system in order to stabilize the extrusion, to make the drawing of the bristles possible, and to obtain the reproducible final PCL/PLA/C15 microfibrillar composite.

At second, it has been demonstrated that the aspect ratio of PLA fibrils (estimated from SEM micrographs) was just one of the factors influencing the final stiffness (macroscopic tensile modulus and microindentation modulus) and yield (macroscopic yield stress and microindentation hardness). The second important factor was the overall crystallinity of both components (which changed significantly throughout the preparation process, as evidenced by DSC). The third factor was the addition of the filler, which might not be fully exfoliated (as documented by TEM analysis and confirmed by comparison of final properties with predictive models), but it improved both stability of the composites during drawing and the final mechanical performance. The combination of the above mentioned three factors resulted in the twofold increase of the elastic modulus of the final PCL/PLA/C15 composite in comparison with the original PCL polymer. Although the increase in elastic modulus after formation of PLA fibrils was relatively low in comparison with isotropic PCL/PLA systems (due to relatively low aspect ratio of PLA fibrils), the observed effects were in quite good agreement with theoretical predictive schemes (linear model, equivalent box model and Halpin-Tsai model), and even slightly exceeded the most relevant theoretical prediction based on the Halpin-Tsai model for systems with short oriented fibers.

Finally, it has been verified that the microindentation hardness testing is a suitable and reliable tool for the monitoring of the mechanical properties of polymer systems at various stages of their preparation, especially in the case of small specimens like in this study where we characterized the mechanical properties of thin extruded and drawn bristles. Moreover, the micromechanical measurements yielded very good and reproducible results also for the final dog-bone specimens, which could be subjected to standard macroscopic tensile testing. The correlation between the final macroscopic tensile testing and the microindentation measurements was very good. The reliability and reproducibility of our microindentation measurements were based on careful specimen preparation (perfectly smooth surfaces for indentation prepared by microtomy) and high number of experiments per sample (even for small specimens, we performed at least 30 indentations and averaged the results).

DATA AVAILABILITY STATEMENT

The datasets generated for this study are available on request to the corresponding author.

AUTHOR CONTRIBUTIONS

MS and IK designed the study, which was performed by AU and MN (electron microscopy), TV (micromechanical properties), LF (differential scanning calorimetry), and IK (preparation of MFC composites and macroscale tensile testing). AU searched the literature and prepared a draft of the introduction. MS evaluated the results and wrote the manuscript with the assistance of IK and LF. All authors contributed to the article and approved the submitted version.

REFERENCES

Bai, H., Huang, C., Xiu, H., Gao, Y., Zhang, Q., and Fu, Q. (2013). Toughening of poly(L-lactide) with poly(epsilon-caprolactone): combined effects of matrix crystallization and impact modifier particle size. *Polymer* 54, 5257–5266. doi: 10.1016/j.polymer.2013.07.051

Bai, H., Xiu, H., Gao, J., Deng, H., Zhang, Q., Yang, M., et al. (2012). Tailoring impact toughness of poly(L-lactide)/poly(epsilon-caprolactone) (PLLA/PCL) blends by controlling crystallization of PLLA matrix. *ACS Appl. Mater. Interfaces* 4, 897–905. doi: 10.1021/am201564f

Balta-Calleja, F. J., and Fakirov, S. (2000). *Microhardness of Polymers*, *1st Edn.*, Cambridge, UK: Cambridge University Press.

Chen, B., and Evans, J. R. G. (2006). Poly(ε-caprolactone)-Clay nanocomposites: structure and mechanical properties, *Macromolecules* 39, 747–754. doi: 10.1021/ma052154a

Chen, B., Sun, K., and Ren, T. (2005). Mechanical and viscoelastic properties of chitin fiber reinforced poly(e-caprolactone), *Eur. Polym. J.* 41, 453–457. doi: 10.1016/j.eurpolymj.2004.10.015

Chen, J., Lu, L., Wu, D., Yuan, L., Zhang, M., Hua, J., et al. (2014). Green Poly(ε-caprolactone) composites reinforced with electrospun polylactide/poly(ε-caprolactone) blend fiber mats, ACS Sustain. *Chem. Eng.* 2, 2102–2110. doi: 10.1021/sc500344n

Chrissafis, K., Antoniadis, G., Paraskevopoulos, K. M., Vassiliou, A., and Bikiaris, D. N. (2007). Comparative study of the effect of different nanoparticles on the mechanical properties and thermal degradation mechanism of *in situ* prepared poly(ε-caprolactone) nanocomposites, Compos. *Sci. Technol.* 67, 2165–2174. doi: 10.1016/j.compscitech.2006.10.027

Cocca, M., Avolio, R., Gentile, G., Di Pace, E., Errico, M. E., and Avella, M. (2015). Amorphized cellulose as filler in biocomposites based on poly(ε-caprolactone). *Carbohydr. Polym.* 118, 170–182. doi: 10.1016/j.carbpol.2014.11.024

Fambri, L., Bragagna, S., and Migliaresi, C. (2006). Biodegradable fibers of poly-L,DL-lactide 70/30 produced by melt spinning. *Macromol. Symp.* 234, 20–25. doi: 10.1002/masy.200650204

Fischer, E. W., Sterzel, H. J., and Wegner, G. (1973). Investigation of the structure of solution grown crystals of lactide copolymers by means of chemical reactions. *Kolloid Zu.Z.Polymere* 251, 980–990. doi: 10.1007/BF01498927

Flores, A., Ania, F., and Balta-Calleja, F. J. (2009). From the glassy state to ordered polymer structures: a microhardness study. *Polymer* 50, 729–746. doi: 10.1016/j.polymer.2008.11.037

Flores, A., Balta-Calleja, F. J., Di Marco, G., Sturniolo, S., and Pieruccini, M. (2011). Recrystallization processes in cold-crystallized poly(ethylene terephthalate): Interplay between structure evolution and conformational relaxation. *Polymer* 52, 3155–3162. doi: 10.1016/j.polymer.2011.05.013

Fornes, T. D., and Paul, D. R. (2003). Modeling properties of nylon 6/clay nanocomposites using composite theories. *Polymer* 44, 4993–5013. doi: 10.1016/S0032-3861(03)00471-3

Fortelny, I., Ujcic, A., Fambri, L., and Slouf, M. (2019). Phase structure, compatibility, and toughness of PLA/PCL blends: a review. *Front. Mater.* 6:206.doi: 10.3389/fmats.2019.00206

Gedde, U. W. (1995). "Crystalline polymers," in *Polymer Physics,* ed U. W. Gedde (London : Chapman & Hall), 131–168.

Haq, R. H. A., Rahman, M. N. A., Ariffin, A. M. T., Hassan, M. F., Yunos, M. Z., and Adzila, S. (2017). Characterization and mechanical analysis of

PCL/PLA composites for FDM feedstock filament, *IOP Conf. Ser. Mater. Sci. Eng.* 226:012038. doi: 10.1088/1757-899X/226/1/012038

Hardiman, M., Vaughan, T. J., and McCarthy, C. T. (2016). The effects of pile-up, viscoelasticity and hydrostatic stress on polymer matrix nanoindentation. *Polym. Test.* 52, 157–166. doi: 10.1016/j.polymertesting.2016.04.003

Huang, Y., He, Y., Ding, W., Yang, K., Yu, D., and Xin, C. (2017). Improved viscoelastic, thermal, and mechanical properties of *in situ* microfibrillar polypropylene/ polyamide 6,6 composites via direct extrusion using a triple-screw extruder, RSC *Adv.* 7, 5030–5038. doi: 10.1039/C6RA26734C

Jain, S., Reddy, M. M., Mohanty, A. K., Misra, M., and Ghosh, A. K. (2010). A new biodegradable flexible composite sheet from poly(lactic acid)/Poly(ε-caprolactone) blends and micro-talc, macromol. *Mater. Eng.* 295, 750–762. doi: 10.1002/mame.201000063

Ju, D., Han, L., Li, F., Chen, S., and Dong, L. (2013). Crystallization, mechanical properties, and enzymatic degradation of biodegradable poly(e-caprolactone) composites with poly(lactic acid) fibers, *Polym. Compos.* 34, 1745–1752. doi: 10.1002/pc.22578

Kakroodi, A. R., Kazemi, Y., Nofar, M., and Park, Ch.,B. (2017). Tailoring poly(lactic acid) for packaging applications via the production of fully bio-based *in situ* microfibrillar composite films, Chem. *Eng. J.* 308, 772–782. doi: 10.1016/j.cej.2016.09.130

Kelnar, I., Fortelny, I., Kapralkova, L., and Hromadkova, J. (2015). Effect of nanofiller on fibril formation in melt-drawn HDPE/PA6 microfibrillar composite, *Polym. Eng. Sci.* 55, 2133–2139. doi: 10.1002/pen.24055

Kelnar, I., Fortelny, I., Kapralkova, L., Kratochvil, J., Angelov, B., and Nevoralova, M. (2016a). Effect of layered silicates on fibril formation and properties of PCL/PLA microfibrillar composites, *J. Appl. Polym. Sci.* 133:43061. doi: 10.1002/app.43061

Kelnar, I., Kratochvil, J., Fortelny, I., Kapralkova, L., Zhigunov, A., Khunova, V., et al. (2016c). Effect of halloysite on structure and properties of melt-drawn PCL/PLA microfibrillar composites, *eXPRESS Polym. Lett.* 5, 381–393. doi: 10.3144/expresspolymlett.2016.36

Kelnar, I., Kratochvil, J., Fortelny, I., Kapralkova, L., Zhigunov, A., and Nevoralova, M. (2017b). Effect of graphite nanoplatelets on melt drawing and properites of PCL/PLA microfibrillar composites, *Polym. Compos.* 39, 3147–3156. doi: 10.1002/pc.24322

Kelnar, I., Kratochvil, J., and Kapralkova, L. (2016b). Crystallization and thermal properties of melt-drawn PCL/PLA microfibrillar composites, *J. Therm. Anal. Calorim.* 124, 799–805. doi: 10.1007/s10973-015-5142-7

Kelnar, I., Kratochvil, J., Kapralkova, L., Zhigunov, A., and Nevoralova, M. (2017a). Graphite nanoplatelets-modified PLA/PCL: effect of blend ratio and nanofiller localization on structure and properties, *J. Mech. Behav. Biomed. Mater.* 71, 271–278. doi: 10.1016/j.jmbbm.2017.03.028

Kolarik, J. (1996). Simultaneous prediction of the modulus and yield strength of binary polymer blends. *Polym. Eng. Sci.* 36, 2518–2524. doi: 10.1002/pen.10650

Kranenburg, J. M., Tweedie, C. A., van Vliet, K. J., and Schubert, U. S. (2009). Challenges and progress in high-throughput screening of polymer mechanical properties by indentation. *Adv. Mater.* 21, 3551–3561. doi: 10.1002/adma.200803538

Labet, M., and Thielemans, W. (2009). Synthesis of polycaprolactone: a review, Chem. *Soc. Rev.* 38, 3484–3504. doi: 10.1039/b820162p

Labidi, S., Azema, N., Perrin, D., and Lopez-Cuesta, J.-M. (2010). Organo-modified montmorillonite/poly(ε-caprolactone) nanocomposites prepared by melt intercalation in a twin-screw extruder, *Polym. Degrad. Stabil.* 85, 382–388. doi: 10.1016/j.polymdegradstab.2009.11.013

Laredo, E., Grimau, M., Bello, A., Wu, D. F., Zhang, Y. S., and Lin, D. P. (2010). AC conductivity of selectively located carbon nanotubes in poly(ε-caprolactone)/polylactide blend nanocomposites, *Biomacromolecules* 11, 1339–1347. doi: 10.1021/bm100135n

Lee, K. S., and Chang, Y.-W. (2013). Thermal, mechanical, and rheological properties of poly(ε-caprolactone)/halloysite nanotube nanocomposites. *J. Appl. Polym. Sci.* 128, 2807–2816. doi: 10.1002/app.38457

Lesan-Khosh, R., Bagheri, R., and Asgari, S. (2011). Nanoindentation of isotactic polypropylene: correlations between hardness, yield stress, and modulus on the local and global scales. *J. Appl. Polym. Sci.* 121, 930–938. doi: 10.1002/app.33635

Li, Z., Li, X., Sun, Ch., Shi, Y., Zhang, Q., and Fu, Q. (2016). Effect of nanoparticles on fibril formation and mechanical performance of olefinic block copolymer (OBC)/polypropylene (PP) microfibrillar composites. *RSC Adv.* 6, 86520–86530. doi: 10.1039/C6RA19026J

Lim, L.-T., Auras, R., and Rubino, M. (2008). Processing technologies for poly(lactic acid). *Prog. Polym. Sci.* 33, 820–852. doi: 10.1016/j.progpolymsci.2008.05.004

Maiti, S. N., and Mahapatro, P. K. (1991). Mechanical properties of i-PP/CaCO$_3$ composites. *J. Appl. Pol. Sci.* 42, 3101–3110. doi: 10.1002/app.1991.070421204

Martinez-Salazar, J., Garcia-Tijero, J. M., and Balta-Calleja, F. J. (1988). Microstructural changes in polyethylene-polypropylene blends as revealed by microhardness. *J. Mater. Sci.* 23, 862–866. doi: 10.1007/BF01153980

McKinney, W. (2018). *Python for Data Analysis. 2nd Edn.* O'Reilly, Boston.

Na, Y. H., He, Y., Shuai, X., Kikkawa, Y., Doi, Y., and Inoue, Y. (2002). Compatibilization effect of poly(ε -caprolactone)-b-poly(ethylene glycol) block copolymers and phase morphology analysis in immiscible poly(lactide)/poly(e-caprolactone) blends. *Biomacromolecules* 3, 1179–1186. doi: 10.1021/bm020050r

Navarro-Baena, I., Sessini, V., Dominici, F., Torre, L., and Kenny, J. M. (2016). Design of biodegradable blends based on PLA and PCL: From morphological, thermal and mechanical studies to shape memory behavior. *Polym. Degr. Stabil.* 132, 97–108. doi: 10.1016/j.polymdegradstab.2016.03.037

Neppalli, R., Causin, V., Marega, C., Saini, R., Mba, M., and Marigo, A. (2011). Structure, morphology, and biodegradability of poly(e-caprolactone)-based nanocomposites. *Polym. Eng. Sci.* 51, 1489–1496. doi: 10.1002/pen.21948

Nielsen, L. E., and Landel, R. F. (1994), *Mechanical properties of polymers and composites, 2nd Edn.* New York, NY: Marcel Dekker.

Oliver, W. C., and Pharr, G. M. (1992). An improved technique for determining hardness and elastic modulus using load and displacement sensing indentation experiments. *J. Mater. Res.* 7, 1564–1583. doi: 10.1557/JMR.1992.1564

Ostafinska, A., Fortelny, I., Hodan, J., Krejcikova, S., Nevoralova, M., Kredatusova, J., et al. (2017). Strong synergistic effects in PLA/PCL blends: Impact of PLA matrix viscosity, J. *Mech. Behav. Biomed. Mater.* 69, 229–241. doi: 10.1016/j.jmbbm.2017.01.015

Ostafinska, A., Fortelny, I., Nevoralova, M., Hodan, J., Kredatusova, J., and Slouf, M. (2015). Synergistic effects in mechanical properties of PLA/PCL blends with optimized composition, processing, and morphology. *RSC Adv.* 5, 98971–98982. doi: 10.1039/C5RA21178F

Ostafinska, A., Vackova, T., and Slouf, M. (2018). Strong synergistic improvement of mechanical properties in HDPE/COC blends with fibrillar morphology. *Polym. Eng. Sci.* 58, 1955–1964. doi: 10.1002/pen.24805

Patricio, T., and Bartolo, P. (2013). Thermal stability of PCL/PLA blends produced by physical blending process. *Procedia Eng.* 59, 292–297. doi: 10.1016/j.proeng.2013.05.124

Perego, G., Cella, G. D., and Bastioli, C. (1996). Effect of molecular weight and crystallinity on poly(lactic acid) mechanical properties. *J. Appl. Pol. Sci.* 59, 37–43. doi: 10.1002/(SICI)1097-4628(19960103)59:1<37::AID-APP6>3.0.CO;2-N

Slouf, M., Krejcikova, S., and Hromadkova, J. (2017). Relationship among molecular structure, supermolecular structure and micromechanical properties of semicrystalline polymers. *Chem. Listy* 111, 239–245.

Slouf, M., Pavlova, E., Krejcikova, S., Ostafinska, A., and Zhigunov, A., Krzyzanek, et al. (2018). Relationship between morphology and micromechanical properties of alpha, beta and gamma phases of iPP. *Polym. Test.* 67, 522–532. doi: 10.1016/j.polymertesting.2018.03.039

Slouf, M., Vackova, T., Nevoralova, M., and Pokorny, D. (2015). Micromechanical properties of one-step and sequentially crosslinked UHMWPEs for total joint replacements. *Polym. Test.* 41, 191–197. doi: 10.1016/j.polymertesting.2014.12.003

Slouf, M., Vackova, T., Zhigunov, A., Sikora, A., and Piorkowska, E. (2016). Nucleation of polypropylene crystallization with gold nanoparticles: relation between particle morphology and nucleation activity. *J. Macromol. Sci. B* 55, 393–410. doi: 10.1080/00222348.2016.1153402

Struik, L. C. E. (1991). Some problems in the non-linear viscoelasticity of amorphous glassy polymers. *J. Non Cryst. Solids* 131–133, 395–407. doi: 10.1016/0022-3093(91)90333-2

Tabor, D. (1951). *The Hardness of Metals*, New York, NY: Oxford University Press.

Trachida, D., Piccarolo, S., Loos, J., and Alexeev, A. (2007). Mechanical Characterization of Polymers on a Nanometer Scale through Nanoindentation. *A Study on Pile-up and Viscoelasticity. Macromolecules* 40, 1259–1267. doi: 10.1021/ma062140k

Tuba, F., Olah, L., and Nagy, P. (2011). Characterization of reactively compatibilized poly(D,L-lactide)/poly(ε-caprolactone) biodegradable blends by essential work of fracture method, *Eng. Fract. Mech.* 78, 3123–3133. doi: 10.1016/j.engfracmech.2011.09.010

Urdan, T. C. (2017). *Statistics in Plain English. 4th Edn.* New York, NY: Taylor & Francis.

Vackova, T., Kratochvil, J., Ostafinska, A., Krejcikova, S., Nevoralova, M., and Slouf, M. (2017). Impact of particle morphology on structure, crystallization kinetics and properties of PCL composites with TiO$_2$-based particles. *Polym. Bull.* 74, 445–464. doi: 10.1007/s00289-016-1723-2

Wei, L., Dong, J., Qi, Y., Sun, J., and Qin, S. (2016). *In situ* polyolefin elastomer/poly(trimethylene terephthalate) microfibrillar composites fabricated via multistage stretching extrusion, *Fiber. Polym.* 17, 1916–1924. doi: 10.1007/s12221-016-6309-y

Wu, D., Lin, D., Zhang, J., Zhou, W., Zhang, M., Zhang, Y., et al. (2011). Selective localization of nanofillers: effect on morphology and crystallization of PLA/PCL blends, macromol. *Chem. Phys.* 212, 613–626. doi: 10.1002/macp.201000579

Xia, X.-,Ch., Yang, W., He, S., Xie, D.-D., Zhang, R. Y., Tian, F., et al. (2016). Formation of various crystalline structures in a polypropylene/polycarbonate *in situ* microfibrillar blend during the melt second flow, *Phys. Chem. Chem. Phys.* 18, 14030–14039. doi: 10.1039/C6CP01426G

Yi, X., Xu, L., Wang, Y. L., Zhong, G. J., Ji, X., and Li, Z. M. (2010). Morphology and properties of isotactic polypropylene/poly(ethylene terephthalate) *in situ* microfibrillar reinforced blends: Influence of viscosity ratio. *Eur. Polym. J.* 46, 719–730. doi: 10.1016/j.eurpolymj.2009.12.027

Characterization of Chicken Feather Biocarbon for Use in Sustainable Biocomposites

Zonglin Li [1†], Christoff Reimer [1†], Maisyn Picard [1,2†], Amar K. Mohanty [1,2*†] and Manjusri Misra [1,2*†]

[1] Bioproducts Discovery and Development Centre, Department of Plant Agriculture, Crop Science Building, University of Guelph, Guelph, ON, Canada, [2] School of Engineering, University of Guelph, Guelph, ON, Canada

With over 1 billion tons of food waste generated annually, there is potential for the waste to be re-purposed. The generation of products from food-industry waste not only reduces the environmental burden of the materials but gives a new value to waste. A common waste material from the food industry is chicken feathers (ChF), a by-product of the chicken meat processing industry. In this work, ChF were subjected to slow pyrolysis at varying temperatures. A complete analysis was completed to determine the yield, ash, chemical composition and morphology of the samples. X-ray diffraction analysis indicated that lower temperature samples were more amorphous, whereas higher temperature samples exhibited more graphitic content. After characterization, the biocarbon was combined with poly(lactic acid) (PLA) to generate sustainable 100% biobased composites. Both composites had moduli that were more than 115% greater than that of the neat polymer. The success of the composites demonstrated that ChF biocarbon can be used as a sustainable and cost effective filler. The use of this material gives new purpose to a waste product and contributes to the goal of sustainable product development.

Keywords: biocarbon, biocomposite, sustainability, biodegradable, interface, chicken feathers

INTRODUCTION

According to the UN Food and Agriculture Organization has reported that nearly one third of food globally is lost or wasted, equating to nearly 1.3 billion tons of waste (Food Agriculture Organization of the United Nations, 2019). Food industry waste may be generated from food or beverage processing which may consist of such things as fruit/vegetable pomace, meat processing by-products or even nut shells. The majority of meats that are mass processed globally are pork, beef and chicken. Chicken alone is estimated to have 98.4 million tons processed in 2019 (United States Department of Agriculture, 2019). This is a large amount of waste which may carry an environmental burden. It is estimated that feathers constitute 5–7 wt.% of the chicken (Onifade et al., 1998), suggesting more than 4.7 million tons will be produced in 2019 alone.

Chicken feathers (ChFs) are an abundantly available food industry waste in need of valorization. With billions of kilograms generated from commercial meat processing of ChFs (Acda, 2010), there has been particular interest in the removal of these materials in an economical and environmentally considerate manner (Tesfaye et al., 2017). Although this waste can be incinerated, some of it may end up in landfill where it can produce methane gas. The production of methane gas possesses a

greater concern for global greenhouse gas production and atmospheric damage. As an alternative to landfill or incineration, some research has been conducted to look into the biodegradation of ChF through bacterial fermentation (Zaghloul et al., 2011). In some cases, the high protein content of feathers has suggested their use as animal feed stock, but some nutritional value is lost during processing and there could be concerns with digestibility (Papadopoulos, 1985).

An alternative to landfill, animal feed or incineration is to generate value added products from the waste. To do so, the complete composition is required to determine what can be extracted, whether the material is thermally stable and other key features. According to literature, ChFs contain about 82% crude protein, 2% crude fiber, 0.8% crude lipid, and 1.5% ash (Tesfaye et al., 2017). Of the protein content, 90% is made of keratin (Zaghloul et al., 2011) which has suggested it use in animal feed after proper treatment (Tesfaye et al., 2017). Based on the chemical composition and surplus of ChFs available, research has shifted its focus to the use of these materials in value-added applications.

The use of ChF to generate value-added composites has been studied by Cheng et al. In their work, ChF fibers were combine in a poly(lactic acid) (PLA) matrix to generate green composites. The ChF fibers were combined at weight concentrations of 2, 5, 8, and 10%. The authors determined that the addition of ChF fibers resulted in increasing the elastic modulus by 116%. Overall, the addition of ChF fibers to the PLA matrix resulted in successful development of composites that could be used in non-load bearing applications (Cheng et al., 2009). Other works also combined ChF with PLA and found similar results with increased stiffness (Özmen and Baba, 2017). To further improve the performance of ChF composites, Reddy et al. combined powdered ChFs and glycerol as a matrix with jute fiber reinforcement for compression molding applications (Reddy et al., 2014). From those works, ChF have proven to be a material capable of generating sustainable composites. However, there are other uses for waste ChF.

In addition to the use of ChF directly, there have been many efforts to carbonize the material through pyrolysis. Pyrolysis is a thermochemical conversion of biological waste. As a result of heating samples to high temperature in an inert atmosphere, the biomass is converted to syn-gas, bio-oil, and biocarbon (Mohanty et al., 2018). Currently, research has looked into the use of ChF biocarbon as a hydrogen storage material (Senoz and Wool, 2011), the development of microspheres (Gao et al., 2014), as well as supercapacitors (Zhao et al., 2015). There are many other potential uses for this ChF biocarbon in electronics and composites.

Composites containing biocarbon have been under substantial investigation. Biocarbon from other waste materials such as lignin (Demir et al., 2015) and miscanthus (Behazin et al., 2016) have been studied. The use of ChF biocarbon may have potential for unique composites. There are some limitations with biocarbon composites. The mechanical performance of the biocomposites is largely dependent on the size (Nagarajan et al., 2016), pyrolysis temperature and structure of the biocarbon. Like biocomposites made with other natural fibers, compatibilizers

can be used to improve performance (Codou et al., 2018). The combination of ideal biocarbon, matrix materials and compatibilizers can improve the biocomposites' performance and generate successful products for a number of applications.

The use of food processing industry waste to generate value-added products provides societal, economic and environmental benefits. The use of ChF diverts waste from landfill which may produce harmful gases such as methane and generates cost effective materials. This paper intends to provide a physical and chemical analysis of ChF biocarbon generated at two pyrolysis temperatures. The ChF biocarbon was combined with PLA matrix to generate sustainable composites. The thermal, mechanical properties and composition of the samples were analyzed. The valorization of ChF through the generation of sustainable natural filler for composites applications offers a safe and suitable alternative use for this material.

MATERIALS AND METHODS

Materials

Maple Leaf Foods Inc. (Canada) sterilized the chicken feathers (ChFs) in an autoclave steam sterilization system and then supplied the ChFs to the University of Guelph. For the preparation of polymer composites, Ingeo PLA 3251D (NatureWorks LLC, USA) was used as the polymer matrix.

Chicken Feather Preparation

The only pre-treatment to these materials were the sterilization upon receiving samples. ChFs were dried in an oven at 85°C in order to remove moisture. There were two samples of ChF analyzed in this work which included: (1) pulverized (powder) and (2) as received feathers. The pulverized samples were ground for 5–7 s in a cryogenic grinder (Lab made, modified by CCR Technologies, Canada) at 3,600 rpm. The ChF powder was dried in a vacuum oven at 85°C for 24 h before pyrolysis.

Pyrolysis

To produce biocarbon in greater quantities, ChFs and ChF powder were directly pyrolyzed in a large-scale tube furnace. A stainless steel reactor was manufactured *in situ* in substitution of the ceramic reactor. The pyrolyzer was supplied with a thermocouple to accurately measure the internal temperature, and an externally supped nitrogen source which was used during the process. The samples were then pyrolyzed at temperatures of 300 and 600°C with a residence time of 30 min. After pyrolysis, the furnace was cooled to room temperature. Samples collected after pyrolysis were ball milled for 1 h using a Retsch ball mill machine at 300 rpm. Ball milled samples were further characterized. The yield content was obtained by calculating the difference in mass of the original ChF in comparison resulting biocarbon left after pyrolysis.

Biocomposite Preparation

Biocomposites were made by combining PLA and ChF produced at two different biocarbon pyrolysis temperatures (300 and 600°C). Processing was conducted in a 15 mL micro-compounder, DSM Xplore, with a twin screw extruder

(Netherlands). The processing temperature was 190°C and the screw speed was 100 rpm. The retention time was 2 min before injection molding at 30°C in a DSM Xplore microinjection molding machine. ChF biocarbon content was set at 20 wt.% in this composite.

Maleic-anhydride grafted (MA-g) PLA composites were fabricated under the same conditions.

Characterization of Biocarbon
Ash content
Two methods were used to measure the ash content of ChF powder and ChF biocarbon: gravimetric and thermogravimetric. The gravimetric method was based on ASTM D1762-84 (reapproved 2013). Samples were loaded into a crucible, heated to 750°C for 6 h and then cooled. Final weights were obtained as per the ASTM standard. The thermogravimetric method, based on ASTM E1131-08, was completed by thermogravimetric analysis (TGA, Q500, TA Instruments, USA). ChF powder and ChF biocarbon were heated from room temperature to 110°C at a rate of 10°C/min and held for 5 min in a nitrogen atmosphere. Then, the samples were continued to be heated to 900°C at a rate of 10°C/min and kept for 15 min. After that, the atmosphere was switched to air and the samples kept at 900°C for another 10 min.

Fourier transform infrared spectroscopy (FTIR)
Spectra were obtained from a Thermo Scientific Nicolet 6700 FTIR spectrometer (Waltham, Massachusetts, USA). The attenuated total reflectance (ATR) mode was used and the spectra were obtained by 64 scans at a resolution of 4 cm^{-1}. The background samples of the surrounding atmosphere were taken prior to samples collection. The spectra were obtained between wave numbers of 500 and 4,000 cm^{-1} in transmittance mode.

TGA-FITR analysis
A TGA Q5500 (TA Instruments, USA) was used in combination with a FTIR machine of the same make as mentioned above. The experiment analyzed about 6 mg over a ramped heating (20°C/minute) of 25 to 650°C in an inert atmosphere. A total of 8 scans were taken per minute and combined. A Gram-Schmidt curve was made for further analysis to determine the relative absorbance of each volatile gas released during the pyrolysis study. A future study could be completed in further works as a comparison of this process to traditional petroleum-based fillers as well as the overall environmental impact.

Scanning electron microscopy/energy dispersive spectroscopy (SEM-EDS)
The elemental and morphology analyzes of ChF powder and ChF biocarbon were examined by a ProX scanning electron microscope (SEM) (Phenom-World BV, Eindhoven, The Netherlands) with energy-dispersive spectroscopy (EDS) integrated into the setup. SEM images were recorded at 10 kV accelerating voltage. The elemental determinations by EDS spectra were obtained at 10 kV under a 90 s collection time. In this process the samples were analyzed uncoated.

For PLA/ChF composite, the fractured surfaces of impact samples were sputtered with a thin layer of gold for 10 s. Then, SEM images of PLA/ChF composites were taken at 10 kV accelerating voltage.

X-ray diffraction spectroscopy
X-ray diffraction spectroscopy (XRD) of biocarbon was completed using a X-Ray Diffractometer (MultiFlex Rigaku, Rigaku, Japan) with a 2 kW CuKα source. A horizontal sample mount was also implemented in combination with a diffracted beam monochromator. Diffraction patterns were obtained between 5° and 50° with a scan speed of 1.2° per minute.

Raman spectroscopy
Raman spectroscopy was conducted on a DXR2 Raman Spectroscope (Thermo Scientific, USA). Raman analysis was used to determine the relative amounts of graphitic vs. disordered carbon in the samples. The machine was operated at 10 times zoom through a 50 μm slit.

Characterization of Composites
Thermal behavior
Thermogravimetric analysis (TGA) (TA instrument, Q500, USA) was used to characterize the thermal stability of the polymer composites. All samples experienced heating from room temperature to 600°C at a rate of 10°C/min in a nitrogen atmosphere. Differential scanning calorimetry (DSC) (TA instrument, Q200, USA) was used to study the melting temperature, glass transition temperature and crystallization temperature. Samples were placed in a nitrogen atmosphere and heated from 0 to 200°C at a rate of 10°C/min, held for 3 min and cooled to 0°C at a rate of 10°C/min.

Mechanical properties
An Instron 3382 Universal Testing Machine was used for the measurement of mechanical properties of PLA/ChF composites. ASTM D638 was used as a standard for the tensile test at room temperature with a rate of 5 mm/min. Flexural properties of PLA/ChF composites were characterized based on ASTM D790 with a testing rate of 1.4 mm/min and a span of 52 mm. Five test pieces of each sample were tested for tensile and flexural tests to take the average value, and all tensile and flexural properties were analyzed with Bluehill software.

RESULTS AND DISCUSSION
Chicken Feather Biocarbon
Yield
It is important to evaluate the pyrolysis yield to determine if the material is feasible for large scale applications, such as automotive parts. For this work, the yield of biocarbon for chicken feathers (ChFs) and powder at 300°C was 55% (**Table 1**). Comparatively, this is a high yield. However, at higher pyrolysis temperatures, the yield decreased to 25 and 16% for powder and feathers, respectively. The decrease in yield as the temperature increased has been reported by others (Budai et al., 2014; Arnold et al., 2016). There is often a decrease in yield at higher temperature because more constituents are decomposed, such as higher molecular weight molecules. This means that the oxygen and hydrogen groups in the material are removed at

Sample	Yield (wt.%)	Sample	Yield (wt.%)
ChF biocarbon 300°C (powder)	55.8	ChF biocarbon 600°C (powder)	25.3
ChF biocarbon 300°C (feather)	55.5	ChF biocarbon 600°C (feather)	16.1

TABLE 2 | Ash content of ChF and ChF biocarbon determined via gravimetric and TGA analyzes.

Sample	Ash content (%) Gravimeter	Ash content (%) TGA
ChF	1.5	1.5
ChF biocarbon 300°C powder	2.4	2.6
ChF biocarbon 300°C feather	2.4	2.7
ChF biocarbon 600°C powder	5.4	8.9
ChF biocarbon 600°C feather	8.0	7.6

FIGURE 1 | Ash content measured by TGA method.

higher temperatures. This was confirmed later through elemental analysis of the samples.

Ash Content

Ash content of biocarbon varies greatly depending on the feedstock material (Ronsse et al., 2013), and is mainly comprised of a combination of hydrogen, nitrogen, oxygen and sulfur (Tesfaye et al., 2017). The two methods to generate ash content are described above in the methods section. The ash content for the ChFs was found to be 1.5% regardless of the method (**Table 2**), which is consistent with literature (Wool, 2005). In fact, Wool (2005) suggested that the extremely low ash would make this waste material useful for fuel generation.

However, biocarbon samples experienced different values for the ash content dependent on the methods used. It is probable that the ChF samples did not experience the same trend as their maximal degradation temperature is substantially lower than that of the biocarbon and is not affected by the final operating temperature.

For the biocarbon samples, the maximal operating temperature for the gravimetric method, based on ASTM D1762-84 (reapproved 2013), was 750°C. By comparison, the TGA method, based on the ASTM E1131-08, reached a final operating temperature of 900°C. For example, the ash content of 600°C ChF biocarbon measured by the gravimetric method was 5.4%, but was 8.9% by the TGA method.

In addition to ash content, the TGA method also provided valuable information as to the content of highly volatile matter, volatile matter, and combustible material. An example of the analysis is displayed in **Figure 1**. A summary of all remaining materials can be found in **Table 3**. The volatile matter remaining in the 300°C sample was greater than that of the 600°C sample. This was a result of a lower pyrolysis temperature since less matter is removed during the process. Likewise, there is more combustible material for the higher temperature BC samples.
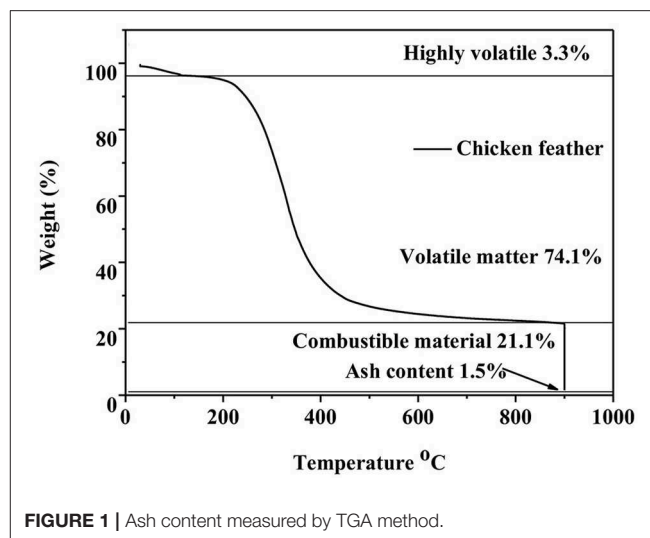
The combination of highly volatile and volatile material from chicken feathers was 77.4% which is very similar to other works with ChFs (Tesfaye et al., 2017; **Table 3**). The volatile materials are a combination of hydrocarbons, methane and carbon monoxide as well as some nitrogen gas and carbon dioxide (Tesfaye et al., 2017). When comparing the biocarbon sources, the lower pyrolysis temperature produced a larger percentage of volatile matter. This corresponds with literature where biomass sources with lower ignition temperatures often possess greater volatile matter content. This is a result of volatile content being directly correlated with heating rate and final temperature (Basu, 2010).

FTIR Analysis

FTIR spectra of the ChF powder and ChF biocarbon samples are shown in **Figure 2**. The ChFs show a distinctive peak at 3,279 cm^{-1} which can be attributed to the O-H stretching (Mothé et al., 2018). Another absorption band at 2,922 cm^{-1} corresponds to the aliphatic C-H stretching vibrations (Mothé et al., 2018). The peak at 1,482 cm^{-1} that is noted in ChFs and lower temperature biocarbon samples is associated with C-H stretching of alkanes (Azargohar et al., 2014). The peak at 1,660 cm^{-1} is assigned to C=O stretching vibrations, and the peaks at 1,513 and 1,445 cm^{-1} correspond to the amine groups N-H$_2$ and N-H, respectively (Mothé et al., 2018). In fact, Mothé et al. attributed these peaks to the keratin structures within the ChFs (Mothé et al., 2018). As determined in the elemental analysis below, there is approximately 3 wt.% of sulfur in the ChF samples, suggesting that the bands near 1,230 cm^{-1} may be related to the presence of thiol groups (Mothé et al., 2018). Lastly, the peak at 1,523 cm^{-1} is associated with the C=C bonds contained in the samples (Azargohar et al., 2014). The presence of this bond is later confirmed by Raman analysis.

The FTIR spectra for the biocarbon samples displayed a decrease in peak intensity from ChF where the 600°C samples show no peaks. The diminishing peaks are a result of removing

Sample	Type of sample	Pyrolysis temperature	Highly volatile matter (%)	Volatile matter (%)	Combustible materials (%)
ChF		–	3.3	74.1	21.1
ChF biocarbon	Powder	300°C	2.6	58.4	36.4
ChF biocarbon	Feather	300°C	1.9	60.6	34.8
ChF biocarbon	Powder	600°C	3.0	25.2	62.9
ChF biocarbon	Feather	600°C	6.0	15.4	71.0
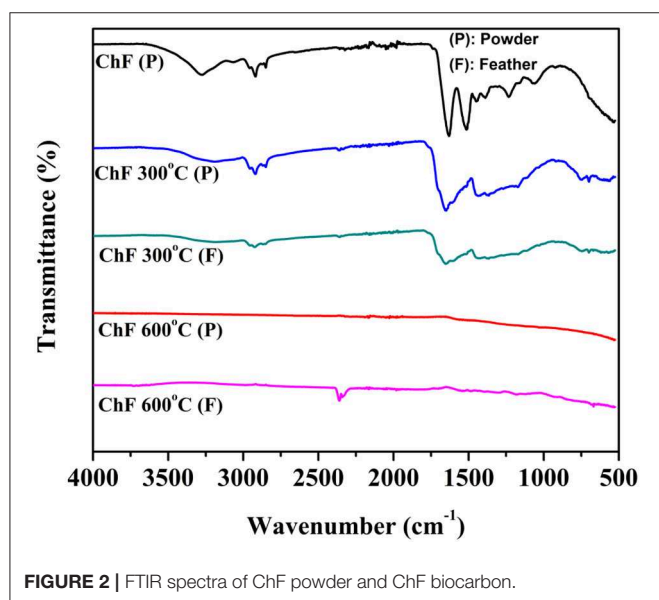
FIGURE 2 | FTIR spectra of ChF powder and ChF biocarbon.

the functional groups with higher pyrolysis temperatures having the greatest impact. This has also been found in works by Snowdon et al. with carbonized lignin (Snowdon et al., 2014). The largest peak in the 300°C biocarbon, around 1,640 cm^{-1}, is probably produced from C=O conjugated bonds (Snowdon et al., 2014).

TGA-FTIR Analysis

For most biomass sources, the commonly produced gases during pyrolysis include: carbon dioxide, methane, carbon monoxide and hydrogen gas (Domínguez et al., 2007). The volatile matter generated during the pyrolysis process is depicted in **Figure 3A**. This work obtained resulted similar to that of pyrolyzed turkey feathers. The gaseous products of turkey feather subject to pyrolysis in air were examined to determine the major gaseous materials. For the 600°C turkey feathers: hydrogen gas < methane < carbon dioxide < carbon monoxide (Domínguez et al., 2007). For this work, effluent containing carbonyl groups was in the greatest concentration followed by carbon dioxide. All volatile materials were identified from the Gram Schmidt curve in **Figure 3B**. Most of the volatiles were identified as similar to other FTIR-TGA analysis in literature (Singh et al., 2011; Ma et al., 2014). However, unique to ChFs, there is substantially more nitrogen content which is evolved as NH_4 from the samples. The production of NH_4

was much greater than the amount produced through pyrolysis of other types of biomasses (e.g., woody or grass-based). This was most likely attributed to the increased nitrogen content in the sample as confirmed in EDS and elemental analysis discussions below.

SEM-EDS

Morphological characteristics of ChF powder and ChF biocarbon samples at differing pyrolysis temperatures are shown in **Figure 4**. The ChF powder was cryogenically ground for only 5~7 s, resulting in variation of particle size and structure. The two most distinguishable structures in the ChF samples are fibrous tubes and large platelets (**Figure 4A**). The fibrous tubes may be from the barbs on the feathers whereas the platelets may be from the quill (calamus) and rachis (Belarmino et al., 2012). The ChF biocarbon samples pyrolyzed at 600°C displayed larger sizes than lower temperature samples. This was also found by Quosai et al. where the higher temperature samples had a greater surface area (Quosai et al., 2018). The larger surface area of the 600°C biocarbon may have fostered an increased opportunity for interactions with the polymer matrix and resulted in improved mechanical performance over 300°C samples, as noted below.

The elemental composition including carbon, nitrogen, oxygen, and sulfur was obtained via EDS for ChF and is displayed in **Table 4**. The ChF samples were found to have relatively similar amounts of C, N, and O around ∼30 wt.% and S content about 3.3 wt.%. Based on literature, there is a large variation of elemental composition of samples. The variation in experimental vs. literature is a result of different analysis methods as well as a difference in the quills vs. barbs content of the samples (Gao et al., 2014).

The elemental composition of ChF biocarbon was also obtained via EDS and is recorded in **Table 4**. It was found that the carbon content was similar for all samples, regardless of the pyrolysis temperature or original ChF structure (i.e. powder or feathers). Similar results were reported for nitrogen. The sulfur content of the BC samples decreased substantially as a result of disulfide bond cleavage at higher pyrolysis temperatures (Zhao et al., 2015). Essentially, the amounts of carbon, nitrogen and oxygen were similar as show via EDS. This was a unique finding for this work since other works have shown that increasing the pyrolysis temperature substantially increases carbon content. For example, green waste and wood biocarbon from 300 to 600°C pyrolysis temperature experienced more than 60% increase in carbon
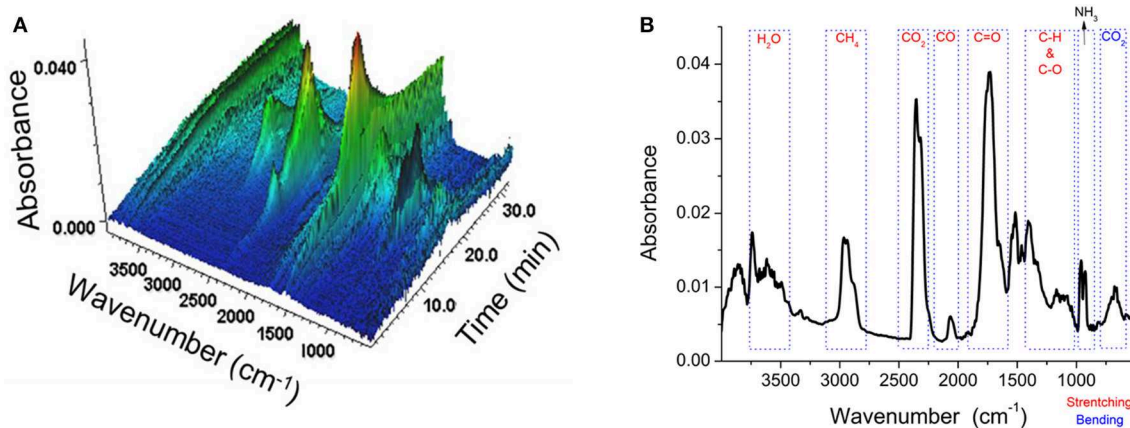
FIGURE 3 | TGA-FTIR analysis of chicken feathers with (A) maximal evolved volatiles and (B) Gram-Schmidt spectra.
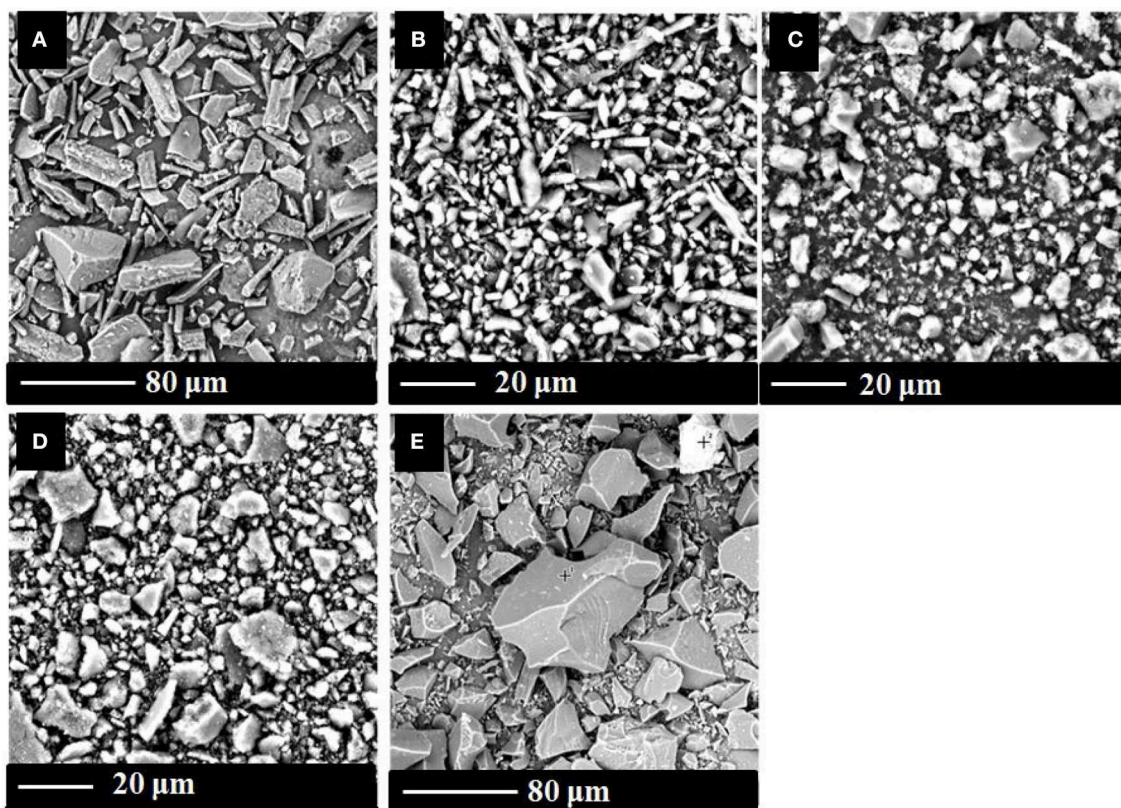

FIGURE 4 | SEM images of (A) ChF powder, (B) ChF biocarbon 300°C (powder), (C) ChF biocarbon 300°C (feathers), (D) ChF biocarbon 600°C (powder), and (E) ChF biocarbon 600°C (feathers).

content (Ronsse et al., 2013). This is most likely due to the higher nitrogen content in the samples as compared to other woody biomasses.

XRD Analysis

The XRD results of ChF powder and biocarbon samples pyrolyzed at different temperatures are shown in **Figure 5**. There were two distinguishable peaks at $2\theta = 9°$ and $19°$ for ChF. The peak at $9°$ is associated with the α-helix configuration of keratin, whereas the $19°$ is actually a combination of two indistinguishable peaks for the β-sheet structure of keratin for ChF samples (Ma et al., 2016). The structures for the 300°C biocarbon, regardless of whether the starting material was feathers or powder, resulted in a broad peak with its maximum

Sample	C	N	O	S	Other
As-received chicken feathers					
ChF	34.29 ± 4.21	32.73 ± 3.58	29.52 ± 1.74	3.36 ± 1.05	–
ChF (Gao et al., 2014)	47.40	15.12	7.16	–	30.32
ChF (Tesfaye et al., 2017)	59.14	14.21	24.34	2.17	–
Chicken feather biocarbon					
ChF 300°C powder	45.97 ± 5.48	34.41 ± 4.14	18.61 ± 0.22	1.03 ± 0.71	–
ChF 300°C feathers	42.98 ± 4.72	36.17 ± 4.43	23.60 ± 3.79	0.66 ± 0.59	–
ChF 600°C powder	46.64 ± 2.49	33.12 ± 6.08	20.14 ± 5.71	0.10 ± 0.05	–
ChF 600°C feathers	48.57 ± 4.09	35.76 ± 2.77	15.27 ± 1.85	0.19 ± 0.26	–
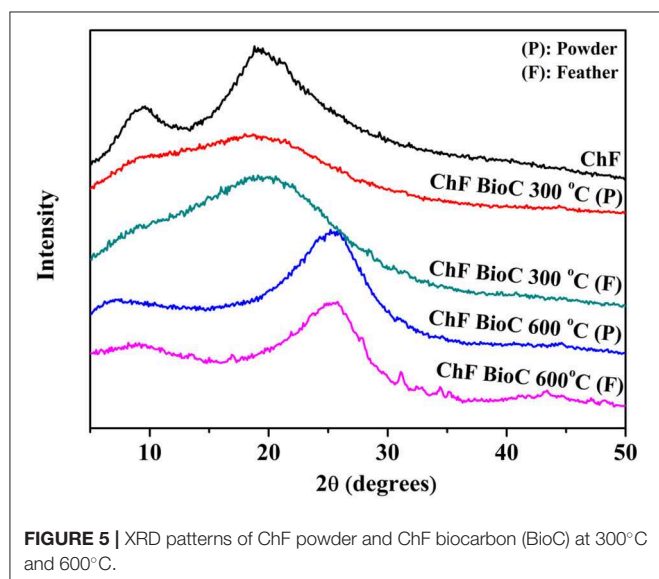
FIGURE 5 | XRD patterns of ChF powder and ChF biocarbon (BioC) at 300°C and 600°C.

the D and G bands, correspondingly and were found in both samples. This aligns with literature for other biocarbon samples (Anstey et al., 2016). In literature, the D band corresponds with the sp^2 orbital and represents the disordered content in the samples; whereas the G band is associated with the sp^2 orbitals of the graphitic content in the sample. The I_D/I_G ratios for the 300 and 600°C were 1.06 and 1.07, respectively, which describe the graphitization of the samples (Major et al., 2018). Biocarbon samples from other waste biomass that were pyrolyzed at 475°C (between the pyrolysis temperatures of this work) found similar ratios for I_D/I_G at 1.10 and 1.11 for wheat straw and poultry litter, respectfully (Azargohar et al., 2014). The Raman spectra are aligned with other results. The I_D band is associated with C-C bonds contained in aromatic rings (Li et al., 2006). The relative strength of this peak can be correlated with the large carbon content in the samples, as proven by elemental analysis. Furthermore, the I_G peak has been documented in literature to correspond to C=C, also found in aromatic structures (Li et al., 2006). The C=C bonds were confirmed in FTIR analysis.

at $2\theta = 20°$. In literature, this peak was associated with the amorphous carbon (Yu et al., 2018). However, the peak for the 600°C biocarbon reaches it maximal value at $2\theta = 26°$. This peak is more likely associated with graphitic carbon (Major et al., 2018), or more specifically the (002) plane (Yu et al., 2018). In literature, higher pyrolysis temperatures are associated with a reduction in interplanar d-spacing of the graphitic sheets such that the spacing between the planes decreases. This may explain the shift in peaks between the 300 and 600°C samples (Arnold et al., 2016).

Raman Spectroscopy

The Raman spectra for ChF biocarbon are displayed in **Figure 6**. The spectra were analyzed from 800 to 2,000 cm^{-1} to determine the graphitic content in the samples. A total of five peaks were used to fit the data, as used in literature (Anstey et al., 2016). The spectra for the feather and powder samples were similar, so only the powders are discussed in this section. The peak intensity is much greater for lower temperature ChF biocarbon. This was also found in samples which were derived from Miscanthus (Major et al., 2018). The peak maximums at 1,350 and 1,550 cm^{-1} for

Composites
Mechanical Performance

Biocomposites were made with combining 20 wt.% ChF (pulverized powder) biocarbon and 80 wt.% PLA. Tensile and flexural properties of neat PLA and ChF biocarbon composites are shown in **Figure 7**. The tensile strength, elongation at break and flexural strength decreased with increasing biocarbon content. The decrease in both tensile and flexural strength is common for samples with higher filler content. In fact, Chang et al. noted that biocarbon content >15 wt.% leads to agglomeration of the particles and reduced stress transfer (Chang et al., 2019). This was further confirmed by the reduction in impact strength compared to the neat polymer. However, the tensile and flexural moduli increased with the addition of filler. In fact, the highest composite values obtained were 16 and 26% greater than neat polymer for tensile and flexural modulus, respectfully. This finding is common for biocarbon composites since the biocarbon restricts the mobility of the matrix polymer chains, thereby increasing the stiffness of the samples (Ogunsona et al., 2018).
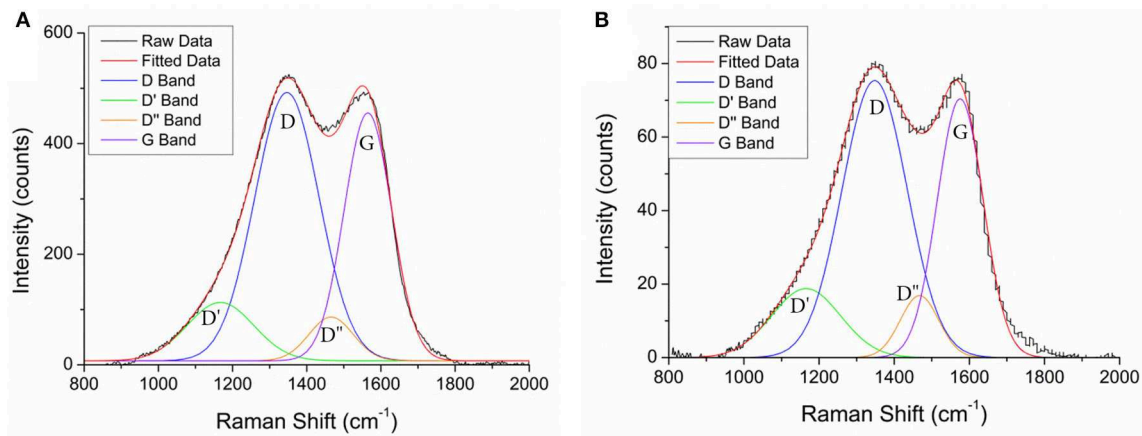
FIGURE 6 | Raman spectroscopy for ChF biocarbon at **(A)** 300°C and **(B)** 600°C.
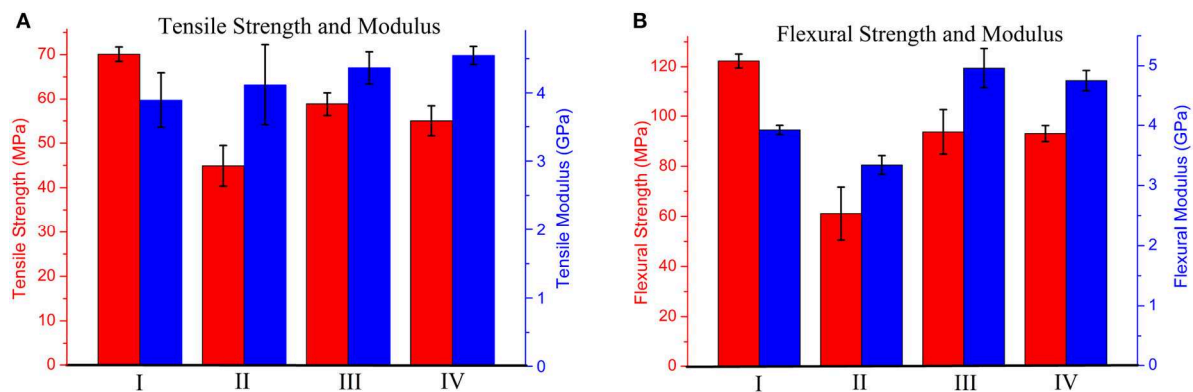

FIGURE 7 | ChF biocarbon composites **(A)** tensile strength and modulus, **(B)** flexural strength and modulus. Sample labels in the x axis are as follows: (I) Neat PLA, (II) 80/20 PLA/ biocarbon (300°C), (III) 80/20 PLA/biocarbon (600°C), (IV) 77/20/3 PLA/biocarbon/MA-g-PLA (600°C).

A compatibilizer, maleic-anhydride-grafted-PLA (MA-g-PLA), was combined at 3 wt.% with the 600°C biocarbon samples. The MA content of 3 wt.% was chosen based upon success in literature with natural fillers and PLA (Yu et al., 2014) as well as PBS (Gowman et al., 2018; Picard et al., 2019). To increase the adhesion between filler and matrix, compatibilizing agents have been studied with biocarbon (Codou et al., 2018). The 600°C biocarbon composite was chosen to be compatibilized based on its superior performance to the 300°C samples where the tensile strength and flexural strength increased by 31 and 53% from 300 to 600°C biocomposites, respectfully. The improvement in mechanical performance of samples containing MA-g-PLA was further confirmed via SEM (**Figure 8C**). The reduction of gaps between the biocarbon and matrix suggested improved interfacial adhesion between these constituents (Behazin et al., 2017a), resulting in improved stress transfer between the filler and compatibilized matrix (Picard et al., 2019).

The impact strength for the neat polymer was 22.9 J/m. However, the uncompatibilized sample experienced a reduction in impact strength as compared to the neat to 14.32 J/m for 300°C

ChF BC samples and 17.23 J/m for 600°C ChF BC samples. This was attributed to poor surface adhesion between the filler and matrix. Similar results have been reported in literature with other natural fillers as well (Picard et al., 2019). The addition of MA-g-PLA improved the impact strength to 19.53 J/m for the 77//20/3 (PLA/ChF biocarbon/Ma-g-PLA) samples. Similarly, increased impact strength from the addition of a compatibilizer has been found in literature with compatibilized biopolymer and miscanthus grass as the natural filler (Muthuraj et al., 2017). Further properties analysis showed that the addition of 20 wt.% ChF BC had no significant change on density with both samples exhibiting a density of 1.25 g/cm^{-3}.

The losses in mechanical performance of the ChF biocarbon at 20 wt.% in this work were comparable to that of ChF in PLA composites at weight percentages of 0–10. In fact, in this work the tensile modulus was 4 GPa or greater were as 5 wt.% ChF PLA composites experienced a max tensile modulus near 4 GPa but the other concentrations of ChFs resulted in inferior tensile moduli (Cheng et al., 2009). Although there were some challenges with mechanical performance it is important
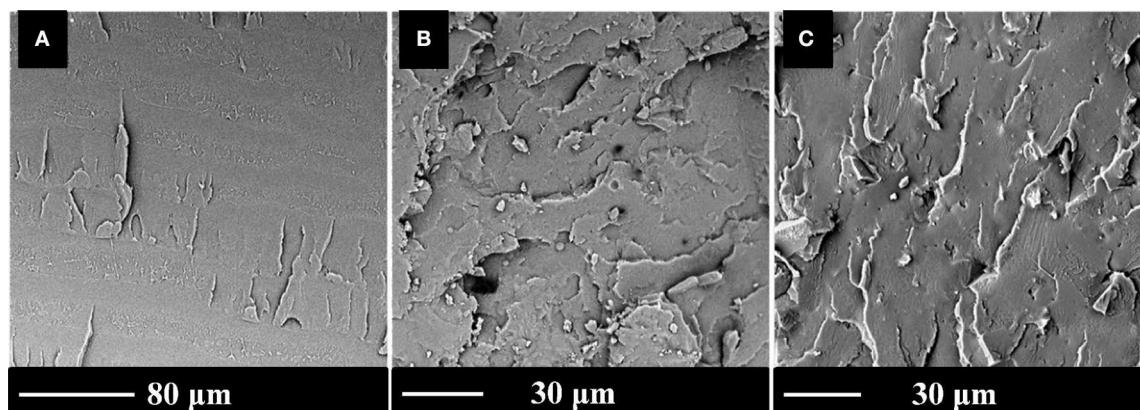
FIGURE 8 | SEM images of **(A)** neat PLA, **(B)** ChF biocarbon/PLA, and **(C)** compatibilized composites.

TABLE 5 | Thermal results obtained from digital scanning calorimetry for neat polymer and composites.

Sample	Pyrolysis temp.	T_g (°C)	T_m (°C)	T_c (°C)
PLA	N/A	60.9	167.9	94.8
80/20 PLA/BC	300°C	59.0	166.5	96.9
80/20 PLA/BC	600°C	58.9	167.9	96.5
77/20/3 PLA/BC/MA-g-PLA	600°C	57.8	167.2	95.7

TABLE 6 | TGA results for PLA and biocarbon composites in nitrogen environment.

PLA/ ChF biocarbon	Pyrolysis temperature	$T_{5\%}$ (°C)	T_{max} (°C)
100/0	N/A	307.5	359.0
80/20	300°C	284.5	333.2
80/20	600°C	272.3	318.6

to note that ChF biocarbon could also be combined with other higher strength materials such as engineering thermoplastics. In this case, the ChF biocarbon would offer superior thermal stability as well as little to no odor during the extrusion process as compared to ChFs. The volatile matter was already expelled from ChF biocarbon, as seen in the TGA-FTIR analysis and would not interfere with the extrusion process. Based on the TGA analyses, ChFs would degrade during the higher processing temperatures.

Differential Scanning Calorimetry

The glass transition temperature (T_g), melting temperature (T_m), and crystallization temperature (T_c) are displayed in **Table 5**. The T_g decreases with the addition of biocarbon. This is also noted in works with PLA and biocarbon (Salak et al., 2014). In this work, there was no notable change in the melt temperature that was taken from the second heating cycle. The melting temperature form the second heating had the thermal history removed and is, therefore, a more accurate measure. The T_c value slightly increased with the addition of biocarbon suggesting that the biocarbon may act as a nucleating agent for the PLA (Behazin et al., 2017b). Similar results were found with biocarbon and PP composites (Behazin et al., 2017b).

Thermogravimetric Analysis

The maximum degradation temperature and 5% weight loss are displayed in **Table 6**. The weight loss was around 5% at the end of the first heating plateau. The addition of biocarbon to the polymer increased the degradation rate, as noted from the lower temperature. This has often been found in literature with biocarbon in a polyamide matrix (Ogunsona et al., 2018). Overall, the polymer was found to be stable over the entire processing window. However, the addition of biocarbon slightly reduced the thermal stability of the samples. Other biocomposites also experience this decrease in thermal stability with addition of natural filler; for example natural filler composites made with apple pomace in BioPBS (Picard et al., 2019), biocarbon in polyamide (Ogunsona et al., 2018), and wood flour in PLA (Liu et al., 2010).

Surface Morphology

SEM images of the impact surfaces of neat polymer and composites are displayed in **Figure 8**. **Figure 8A** shows the typical fracture surface of PLA which is smooth as a result of the brittle, semi-crystalline nature of the polymer (Ferrarezi et al., 2013). The brittle nature of the polymer is confirmed by the relatively high tensile strength, as noted in **Figure 7A**. **Figure 8B** shows gaps between the ChF biocarbon and matrix material. As discussed earlier, this is noted as a decrease in interfacial adhesion and is the reason for reduced mechanical performance (Picard et al., 2019). From **Figure 8**, it was noted that the matrix remained relatively smooth with improved adhesion to the biocarbon. The SEM confirms that there was less de-cohesion between the filler and the biocarbon, resulting in less pull-out. Similar results were found in literature with compatibilized biocarbon composites (Codou et al., 2018) and confirmed by improved impact strength.

FEASIBILITY AND SUSTAINABILITY

The use biocarbon as a filler offers greater thermal stability over natural fillers from food/ beverage industry waste. For example apple pomace and grape pomace are wastes from the wine and cider or juice industries begin degradation at substantially lower temperatures. For example, 5% weight loss of the sample occurs at approximately 120°C (Picard et al., 2019) and 175°C (Gowman et al., 2018), respectfully. Neat chicken feather (ChF) fibers have been found to begin to lose 5 wt.% at just over 100°C (Özmen and Baba, 2017). Conversely, ChF biocarbon 300 and 600°C did not experience 5% weight loss until about 220 and 400°C, respectfully. This suggests that ChF biocarbon offers the added benefit of thermal stability and could function with high temperature engineering thermoplastics. Works comparing ChF to pyrolyzed ChF biocomposites have confirmed improved thermal stability (Senoz et al., 2013).

Moreover, ChF feather biocarbon is a food industry waste product and can be obtained at no cost. This is one advantage over petroleum produced carbon black. The production of biocarbon compared to petroleum products requires less energy during the heating process since carbon black requires conversion temperatures of 1,320–1,540°C (United States Environmental Protection Agency, 1983). In this work the maximal pyrolysis temperature was 600°C which is nearly half of carbon black. Also, ChF biocarbon is black in color and could replace carbon black where it is used as a coloring agent. Other works have investigate the viability of biocarbon and determined that it can be used as a feasible alternative as well as functional in non-electrical applications (Snowdon et al., 2014).

The use of ChF biocarbon as mentioned previous is also beneficial to that of plain ChF due to lesser concerns for odor. The evolved gases, displayed in TGA-FTIR analysis, would not be present during the extrusion process as compared to that of ChF alone. In addition to the previously discussed benefits of ChF biocarbon, the use of biocarbon materials has also been suggested to replace traditional in organic fillers such as mineral fillers (Myllytie et al., 2016). There is also a reduction in the density of biocarbon as compared to traditional inorganic fillers such as glass fiber and talc; to 1.3 g/cm^3 for biocarbon from 2.7 g/cm^3 for talc and glass fiber (Chang et al., 2019). This leads to light-weight composites and the corresponding benefits of reduced fuel consumption when implemented in the automotive industry. There are many benefits that have been discussed in relation to the implementation of ChF biocarbon in composite applications. The use of biologically based materials helps to improve the sustainability, cost, and adds value to newly made products.

CONCLUSIONS

Chicken feathers (ChF), a byproduct of the meat processing industry, are abundantly available and in need of new uses to avoid end of life in landfill or incineration. This work features the thermochemical conversion of ChFs to biocarbon

for value-added applications. ChFs were pyrolyzed at 300 and 600°C to generate sustainable natural filler for biocomposites. The biocarbon produced at 300°C resulted in a surprising yield of 55% and both biocarbon samples possessed exceptional thermal stability at much greater temperatures than that of many traditional natural fillers. With this in mind, ChF biocarbon was combined with PLA, a biodegradable and biobased plastic. The biocomposites were analyzed for their mechanical performance. Despite a decrease in tensile strength, the tensile modulus for each composite blend was greater than that of the neat polymer. SEM images determined the biocarbon was well-distributed throughout the matrix such that it could act as a reinforcing agent. The composites contained 20 wt.% of the 600°C ChF biocarbon, and a biobased biodegradable polymer also displayed improved flexural and tensile modulus over that of the neat polymer. ChF biocarbon has the added benefits of reduced odor during processing as compared to ChFs, as well the ChF biocarbon could function well as a replacement to traditional petroleum-based colorants like carbon black as well as mineral fillers like talc. The successful combination of natural filler and biobased, biodegradable polymer suggests the use of these biocomposites for sustainable packaging applications.

DATA AVAILABILITY STATEMENT

The raw data supporting the conclusions of this article will be made available by the authors, without undue reservation, to any qualified researcher.

AUTHOR CONTRIBUTIONS

FUNDING

ACKNOWLEDGMENTS

REFERENCES

Acda, M. N. (2010). "Sustainable use of waste chicken feather for durable and low cost building materials for tropical climates," in *Sustainable Agriculture: Technology, Planning and Management*, eds A. Salazar and I. Rios (Laguna Beach, CA: Nova Science Publishers, Inc.), 353–366.

Anstey, A., Vivekanandhan, S., Rodriguez-Uribe, A., Misra, M., and Mohanty, A. K. (2016). Oxidative acid treatment and characterization of new biocarbon from sustainable Miscanthus biomass. *Sci. Total Environ.* 550, 241–247. doi: 10.1016/j.scitotenv.2016.01.015

Arnold, S., Rodriguez-Uribe, A., Misra, M., and Mohanty, A. K. (2016). Slow pyrolysis of bio-oil and studies on chemical and physical properties of the resulting new bio-carbon. *J. Clean. Prod.* 172, 2748–2758. doi: 10.1016/j.jclepro.2017.11.137

Azargohar, R., Nanda, S., Kozinski, J. A., Dalai, A. K., and Sutarto, R. (2014). Effects of temperature on the physicochemical characteristics of fast pyrolysis bio-chars derived from Canadian waste biomass. *Fuel* 125, 90–100. doi: 10.1016/j.fuel.2014.01.083

Basu, P. (2010). "Biomass Characteristics," in *Biomass Gasification, Pyrolysis and Torrefaction*, eds R. Zanol and M. L. Kuhl (London: Elsevier Inc.), 27–63. doi: 10.1016/B978-0-12-374988-8.00002-7

Behazin, E., Misra, M., and Mohanty, A. K. (2017a). Compatibilization of toughened polypropylene/biocarbon biocomposites: a full factorial design optimization of mechanical properties. *Polym. Test.* 61, 364–372. doi: 10.1016/j.polymertesting.2017.05.031

Behazin, E., Misra, M., and Mohanty, A. K. (2017b). Sustainable biocarbon from pyrolyzed perennial grasses and their effects on impact modified polypropylene biocomposites. *Compos. Part B Eng.* 118, 116–124. doi: 10.1016/j.compositesb.2017.03.003

Behazin, E., Ogunsona, E., Rodriguez-Uribe, A., Mohanty, A. K., Misra, M., and Anyia, A. O. (2016). Mechanical, chemical, and physical properties of wood and perennial grass biochars for possible composite application. *BioResources* 11, 1334–1348. doi: 10.15376/biores.11.1.1334-1348

Belarmino, D. D., Ladchumananandasivam, R., Belarmino, L. D., Pimentel, J. R. D. M., da Rocha, B. G., Galvão, A. O., et al. (2012). Physical and morphological structure of chicken feathers (Keratin Biofiber) in natural, chemically and thermally modified forms. *Mater. Sci. Appl.* 03, 887–893. doi: 10.4236/msa.2012.312129

Budai, A., Wang, L., Gronli, M., Strand, L. T., Antal, M. J., Abiven, S., et al. (2014). Surface properties and chemical composition of corncob and miscanthus biochars: effects of production temperature and method. *J. Agric. Food Chem.* 62, 3791–3799. doi: 10.1021/jf501139f

Chang, B. P., Mohanty, A. K., and Misra, M. (2019). Sustainable biocarbon as an alternative of traditional fillers for poly(butylene terephthalate)-based composites: thermo-oxidative aging and durability. *J. Appl. Polym. Sci.* 136, 1–14. doi: 10.1002/app.47722

Cheng, S., Lau, K., Liu, T., Zhao, Y., Lam, P. M., and Yin, Y. (2009). Mechanical and thermal properties of chicken feather fiber/PLA green composites. *Compos. Part B Eng.* 40, 650–654. doi: 10.1016/j.compositesb.2009.04.011

Codou, A., Misra, M., and Mohanty, A. K. (2018). Sustainable biocarbon reinforced nylon 6/polypropylene compatibilized blends: effect of particle size and morphology on performance of the biocomposites. *Compos. Part A Appl. Sci. Manuf.* 112, 1–10. doi: 10.1016/j.compositesa.2018.05.018

Demir, M., Kahveci, Z., Aksoy, B., Palapati, N. K. R., Subramanian, A., Cullinan, H. T., et al. (2015). Graphitic biocarbon from metal-catalyzed hydrothermal carbonization of lignin. *Ind. Eng. Chem. Res.* 54, 10731–10739. doi: 10.1021/acs.iecr.5b02614

Domínguez, A., Menéndez, J. A., Fernández, Y., Pis, J. J., Nabais, J. M. V., Carrott, P. J. M., et al. (2007). Conventional and microwave induced pyrolysis of coffee hulls for the production of a hydrogen rich fuel gas. *J. Anal. Appl. Pyrolysis* 79, 128–135. doi: 10.1016/j.jaap.2006.08.003

Ferrarezi, M. M. F., de Oliveira Taipina, M., da Silva, L. C. E., and Gonçalves, M., Carmo Gonçalves, M. (2013). Poly(ethylene glycol) as a compatibilizer for poly(lactic acid)/thermoplastic starch blends. *J. Polym. Environ.* 21, 151–159. doi: 10.1007/s10924-012-0480-z

Food and Agriculture Organization of the United Nations (2019). *Global Initiative on Food Loss and Waste Reduction*. FAO. Available online at: http://www.fao.org/save-food/resources/keyfindings/en/ (accessed August 14, 2019).

Gao, L., Hu, H., Sui, X., Chen, C., and Chen, Q. (2014). One for two: conversion of waste chicken feathers to carbon microspheres and (NH4)HCO$_3$. *Environ. Sci. Technol.* 48, 6500–6507. doi: 10.1021/es5006708

Gowman, A., Wang, T., Rodriguez-Uribe, A., Mohanty, A. K., and Misra, M. (2018). Bio-poly(butylene succinate) and its composites with grape pomace: mechanical performance and thermal properties. *ACS Omega* 3, 15205–15216. doi: 10.1021/acsomega.8b01675

Li, X., Hayashi, J., and Li, C.-Z. (2006). FT-Raman spectroscopic study of the evolution of char structure during the pyrolysis of a Victorian brown coal. *Fuel* 85, 1700–1707. doi: 10.1016/j.fuel.2006.03.008

Liu, X., Khor, S., Petinakis, E., Yu, L., Simon, G., Dean, K., et al. (2010). Effects of hydrophilic fillers on the thermal degradation of poly(lactic acid). *Thermochim. Acta* 509, 147–151. doi: 10.1016/j.tca.2010.06.015

Ma, B., Qiao, X., Hou, X., and Yang, Y. (2016). Pure keratin membrane and fibers from chicken feather. *Int. J. Biol. Macromol.* 89, 614–621. doi: 10.1016/j.ijbiomac.2016.04.039

Ma, Z., Chen, D., Gu, J., Bao, B., and Zhang, Q. (2014). Determination of pyrolysis characteristics and kinetics of palm kernel shell using TGA-FTIR and model-free integral methods. *Energy Convers. Manag.* 89, 251–259. doi: 10.1016/j.enconman.2014.09.074

Major, I., Pin, J.-M., Behazin, E., Rodriguez-Uribe, A., Misra, M., and Mohanty, A. (2018). Graphitization of Miscanthus grass biocarbon enhanced by in situ generated FeCo nanoparticles. *Green Chem.* 20, 2269–2278. doi: 10.1039/C7GC03457A

Mohanty, A. K., Vivekanandhan, S., Pin, J.-M., and Misra, M. (2018). Composites from renewable and sustainable resources: challenges and innovations. *Science* 362, 536–542. doi: 10.1126/science.aat9072

Mothé, M. G., Viana, L. M., and Mothé, C. G. (2018). Thermal property study of keratin from industrial residue by extraction, processing and application. *J. Therm. Anal. Calorim.* 131, 417–426. doi: 10.1007/s10973-017-6845-8

Muthuraj, R., Misra, M., and Mohanty, A. K. (2017). Biodegradable biocomposites from poly(butylene adipate-co-terephthalate) and miscanthus: preparation, compatibilization, and performance evaluation. *J. Appl. Polym. Sci.* 134, 1–9. doi: 10.1002/app.45448

Myllytie, P., Misra, M., and Mohanty, A. K. (2016). Carbonized lignin as sustainable filler in biobased poly(trimethylene terephthalate) polymer for injection molding applications. *ACS Sustain. Chem. Eng.* 4, 102–110. doi: 10.1021/acssuschemeng.5b00796

Nagarajan, V., Mohanty, A. K., and Misra, M. (2016). Biocomposites with size-fractionated biocarbon: influence of the microstructure on macroscopic properties. *ACS Omega* 1, 636–647. doi: 10.1021/acsomega.6b00175

Ogunsona, E. O., Codou, A., Misra, M., and Mohanty, A. K. (2018). Thermally stable pyrolytic biocarbon as an effective and sustainable reinforcing filler for polyamide bio-composites fabrication. *J. Polym. Environ.* 26, 3574–3589. doi: 10.1007/s10924-018-1232-5

Onifade, A. A., Al-Sane, N. A., Al-Musallam, A. A., and Al-Zarban, S. (1998). A review: potentials for biotechnological applications of keratin-degrading microorganisms and their enzymes for nutritional improvement of feathers and other keratins as livestock feed resources. *Bioresour. Technol.* 66, 1–11. doi: 10.1016/S0960-8524(98)00033-9

Özmen, U., and Baba, B. O. (2017). Thermal characterization of chicken feather/PLA biocomposites. *J. Therm. Anal. Calorim.* 129, 347–355. doi: 10.1007/s10973-017-6188-5

Papadopoulos, M. C. (1985). Processed chicken feathers as feedstuff for poultry and swine. a review. *Agric. Wastes* 14, 275–290. doi: 10.1016/S0141-4607(85)80009-3

Picard, M. C., Rodriguez-Uribe, A., Thimmanagari, M., Misra, M., and Mohanty, A. K. (2019). Sustainable biocomposites from poly(butylene succinate) and apple pomace: a study on compatibilization performance. *Waste Biomass Valorization* 2019, 1–13. doi: 10.1007/s12649-019-00591-3

Quosai, P., Anstey, A., Mohanty, A. K., and Misra, M. (2018). Characterization of biocarbon generated by high- and low-temperature pyrolysis of soy hulls and coffee chaff: for polymer composite applications. *R. Soc. Open Sci.* 5, 1–16. doi: 10.1098/rsos.171970

Reddy, N., Jiang, J., and Yang, Y. (2014). Biodegradable composites containing chicken feathers as matrix and jute fibers as reinforcement. *J. Polym. Environ.* 22, 310–317. doi: 10.1007/s10924-014-0648-9

Ronsse, F., van Hecke, S., Dickinson, D., and Prins, W. (2013). Production and characterization of slow pyrolysis biochar: influence of feedstock type and pyrolysis conditions. *GCB Bioenergy* 5, 104–115. doi: 10.1111/gcbb.12018

Salak, F., Uemura, S., and Sugimoto, K. (2014). Thermal pretreatment of kudzu biomass (Pueraria lobata)as filler in cost-effective PLA biocomposite fabrication process. *Polym. Eng. Sci.* 55, 340–348. doi: 10.1002/pen.23909

Senoz, E., Stanzione, J. F., Reno, K. H., Wool, R. P., and Miller, M. E. N. (2013). Pyrolyzed chicken feather fibers for biobased composite reinforcement. *J. Appl. Polym. Sci.* 128, 983–989. doi: 10.1002/app.38163

Senoz, E., and Wool, R. P. (2011). Hydrogen storage on pyrolyzed chicken feather fibers. *Int. J. Hydrogen Energy* 36, 7122–7127. doi: 10.1016/j.ijhydene.2011.03.061

Singh, S., Wu, C., and Williams, P. T. (2011). Pyrolysis of waste materials using TGA-MS and TGA-FTIR as complementary characterisation techniques. *J. Anal. Appl. Pyrolysis* 94, 99–107. doi: 10.1016/j.jaap.2011.11.011

Snowdon, M. R., Mohanty, A. K., and Misra, M. (2014). A study of carbonized lignin as an alternative to carbon black. *ACS Sustain. Chem. Eng.* 2, 1257–1263. doi: 10.1021/sc500086v

Tesfaye, T., Sithole, B., Ramjugernath, D., and Chunilall, V. (2017). Valorisation of chicken feathers: characterisation of chemical properties. *Waste Manag.* 68, 626–635. doi: 10.1016/j.wasman.2017.06.050

United States Department of Agriculture (2019). *Livestock and Poultry: World Markets and Trade.* Available online at: https://apps.fas.usda.gov/psdonline/circulars/livestock_poultry.pdf (accessed August 13, 2019).

United States Environmental Protection Agency (1983). "6.1 Carbon Black," in *Compilation of Air Pollutant Emission Factors* (Washington, DC), 1–10. Available online at: https://www3.epa.gov/ttn/chief/ap42/ch06/final/c06s01.pdf (accessed November 12, 2019).

Wool, R. P. (2005). "Carbon Fibers from Chicken Feathers," in *Bio-Based Polymers and Composites*, eds R. P. Wool and X. S. Sun (New York, NY: Elsevier Inc.), 435–447. doi: 10.1016/B978-012763952-9/50005-8

Yu, M., Saunders, T., Su, T., Gucci, F., and Reece, M. (2018). Effect of heat treatment on the properties of wood-derived biocarbon structures. *Materials* 11:1588. doi: 10.3390/ma11091588

Yu, T., Jiang, N., and Li, Y. (2014). Study on short ramie fiber/poly(lactic acid) composites compatibilized by maleic anhydride. *Compos. Part A Appl. Sci. Manuf.* 64, 139–146. doi: 10.1016/j.compositesa.2014.05.008

Zaghloul, T. I., Embaby, A. M., and Elmahdy, A. R. (2011). Biodegradation of chicken feathers waste directed by Bacillus subtilis recombinant cells: scaling up in a laboratory scale fermentor. *Bioresour. Technol.* 102, 2387–2393. doi: 10.1016/j.biortech.2010.10.106

Zhao, Z., Wang, Y., Li, M., and Yang, R., (2015). High performance N-doped porous activated carbon based on chicken feather for supercapacitors and CO_2 capture. *RSC Adv.* 5, 34803–34811. doi: 10.1039/C5RA01569C

Thermoplastic Starch Composites With Titanium Dioxide and Vancomycin Antibiotic: Preparation, Morphology, Thermomechanical Properties, and Antimicrobial Susceptibility Testing

Aleksandra Ujcic[1], Sabina Krejcikova[1], Martina Nevoralova[1], Alexander Zhigunov[1], Jiri Dybal[1], Zdenek Krulis[1], Petr Fulin[2], Otakar Nyc[3] and Miroslav Slouf[1]*

[1] Institute of Macromolecular Chemistry, Czech Academy of Sciences, Prague, Czechia, [2] First Orthopedics Clinic of the First Faculty of Medicine of the Charles University, Motol University Hospital, Prague, Czechia, [3] Department of Medical Microbiology, Second Faculty of Medicine of the Charles University, Motol University Hospital, Prague, Czechia

Biodegradable composites of thermoplastic starch (TPS), titanium dioxide particles (TiO$_2$; average size 0.2 μm), and/or antibiotic (ATB; vancomycin) were prepared. Light and electron microscopy demonstrated that our recently developed, two-step preparation procedure yielded highly homogeneous TPS matrix with well-dispersed TiO$_2$ particles even for high filler concentrations (up to 20%). Oscillatory shear rheometry showed an increase in viscosity of TPS after addition of TiO$_2$ and ATB (from ca 2 × 10^5 Pa·s to ca 1 × 10^6 Pa·s at 1 rad/s and 120°C). However, the high viscosity of TPS/TiO$_2$/ATB composites did not prevent reproducible preparation of the composites by melt-mixing. Dynamic mechanical analysis proved a significant increase in shear moduli (storage, loss and complex modulus) of TPS after addition of TiO$_2$ and ATB (storage modulus increased from ca 25 MPa to more than 600 MPa at 1.33 rad/s at room temperature). Both rheological and mechanical properties indicated strong interactions among TPS matrix, filler, and antibiotics. The final TPS composites were soft enough to be cut with a sharp blade at room temperature, the TPS matrix was fully biodegradable, the TiO$_2$ filler was biocompatible, and the ATB could be released locally during the matrix degradation. Selected samples were tested for bacterial susceptibility using standard tube dilution test and disk diffusion test. The results proved that the ATB retained its bacteriostatic properties after the thermal processing of the composites. Therefore, the prepared TPS/TiO$_2$/ATB composites represent a promising material for biomedical applications related to the local release of antibiotics.

Keywords: thermoplastic starch, morphology, thermomechanical properties, local release of antibiotics, antibacterial activity

INTRODUCTION

Starch-based materials are attractive due to their biodegradability and wide range of applications, such as packaging, coating, agriculture, medicine, pharmacy, or even optoelectronics (Sarka et al., 2011, 2012; Saiah et al., 2012; Xie et al., 2013; Ghavimi et al., 2015; Oleyaei et al., 2016a; Campos-Requena et al., 2017; Dufresne and Castano, 2017; Javanbakht and Namazi, 2017; Kuswandi, 2017; Liu G. et al., 2017; Liu S. et al., 2017; Sarka and Dvoracek, 2017, Ilyas et al., 2018, Ilyas et al., 2019). However, the melting temperature of native starch is higher than its degradation temperature. Consequently, for most applications, it is necessary to transform the granular starch into an amorphous and homogenous thermoplastic matrix (Biliaderis, 2009; Bertolini, 2010; Visakh et al., 2012; Abral et al., 2019). Starch plasticization has been intensively investigated by many authors (Aichholzer and Fritz, 1998; Huang et al., 2005; Dai et al., 2008; Li et al., 2008; Pushpadass et al., 2008; Xie et al., 2012; Ostafinska et al., 2017). The results of these investigations showed that the preparation of thermoplastic starch (TPS) depended on many factors, such as the starch source (e.g., wheat, corn, and potato; Ao and Jane, 2007; Bertolini, 2010), plasticizer type (Dai et al., 2008; Pushpadass et al., 2008), and processing method (Altskar et al., 2008). The majority of starch-based composites have been prepared by single-step solution casting (SC; Campos et al., 2017; Dufresne and Castano, 2017; Guz et al., 2017; Javanbakht and Namazi, 2017; Liu S. et al., 2017; Pelissari et al., 2017; Ali et al., 2018; Abral et al., 2019) or single-step melt mixing (MM; Campos-Requena et al., 2017; Olivato et al., 2017). The TPS materials prepared by the above-mentioned single-step procedures were found to be homogeneous at the macroscopic level but showed various inhomogeneities, such as non-fully plasticized starch granules, at the microscopic level. Nevertheless, our recent work (Ostafinska et al., 2017) has demonstrated that a two-step procedure based on solution casting and subsequent melt mixing resulted in a highly homogeneous TPS matrix with very homogeneous dispersion of TiO_2 particles.

Significant attention has been devoted in the recent literature to the TPS-based composites with different kinds of fillers (Xie et al., 2013). This work is focused on TPS composites with titanium dioxide, with high content of filler (>10 wt.%), which have not been studied so far according to available literature, as summarized below. Common fillers employed in TPS composites comprise clays (Carvahlo et al., 2001; Dai et al., 2012; Kelnar et al., 2013; Oleyaei et al., 2016a; Campos-Requena et al., 2017; Olivato et al., 2017), graphene (Javanbakht and Namazi, 2017), carbon nanotubes (CNT) (Liu S. et al., 2017), natural fibers (Svagan et al., 2009; Campos et al., 2017; Kargarzadeh et al., 2017; Pelissari et al., 2017; Ilyas et al., 2018, 2019), polysaccharide-based crystals (Dufresne and Castano, 2017; Ali et al., 2018), and metal oxides and chalcogenides (Oleyaei et al., 2016b; Guz et al., 2017; Liu et al., 2018). Titanium dioxide (TiO_2) represents attractive filler in materials for biomedical applications due to its biocompatibility with bone cells and tissues (Webster et al., 1999, 2000; Sengottuvelan et al., 2017). This material has been widely studied in biodegradable composites, such as PLA/TiO_2 (Boccaccini et al., 2005), PLA/TiO_2-Bioglass (Boccaccini and

Blaker, 2006), PLA/PCL/TiO_2 (Mofokeng and Luyt, 2015a,b; Ostafinska et al., 2015), and PCL/TiO_2 (Tamjid et al., 2011; Gupta et al., 2012; Vackova et al., 2017). Nevertheless, just little information is currently available regarding the effects of TiO_2 on the properties of thermoplastic starch. Yun et al. (2012) investigated starch/polyvinyl alcohol/TiO_2 (5–15 wt.%) nanocomposites that show photocatalytic activity under UV and visible light irradiation. Fei et al. (2013) studied the influence of TiO_2 (0–8 wt.%) on the structure of TPS/polycaprolactone (PCL) blends. Razali et al. (2016) prepared TPS/TiO_2 (1 wt.%) composites reinforced with Donax grandis hypodermal fiber (DGHF) by solution casting followed by compression molding. These researchers reported that the addition of DGHF to TPS led to structural changes and increased the crystallinity of the composites. Furthermore, the addition of TiO_2 enhanced the crystallinity and resulted in a coarse fiber surface. Oleyaei et al. (2016a,b) studied TPS-based nanocomposites (prepared by solution casting) with the addition of TiO_2 (0.5–2 wt.%), and the same composites with the addition of both TiO_2 and sodium montmorillonite (MMT). They found that maximum improvement in mechanical properties for the TPS/TiO_2 composite was achieved for 1% of the filler, whereas for TPS/TiO_2/MMT the best results were obtained for 2 wt.% of TiO_2 and 3 wt.% of MMT. Furthermore, our recent study (Ostafinska et al., 2017) reported on the addition of low amounts of TiO_2 (0–3 wt.%) to TPS. It was demonstrated that the TiO_2 particles changed the crystallinity and rheological properties slightly due to the partial degradation of the TPS matrix during melt mixing.

In this work, we focused our attention on TPS/TiO_2 composites with higher filler content (up to 20%) that have not been reported in the literature to date. We wanted to verify that the previously described two-step preparation protocol of TPS composites, which yielded highly homogeneous TPS/TiO_2 systems for up to 3% of the filler (Ostafinska et al., 2017) will also be effective for the preparation of highly loaded TPS/TiO_2 composites. Moreover, we investigated whether the combination of a high-viscosity TPS matrix and a high filler concentration will result in a material with good thermomechanical properties that can be prepared using standard solution casting and melt mixing procedures. Finally, we prepared TPS/ATB and TPS/TiO_2/ATB composites in order to verify that thermally resistant antibiotics, such as vancomycin, can survive our two-step plasticization process and filler addition without losing their antibacterial activity.

EXPERIMENTAL

Materials

Wheat A-starch (S) was supplied by Amylon a.s., Czech Republic (type Soltex NP1; amylose content ∼25%; particle size 5–25 μm; total solids: 88.5%—CSN EN ISO 1666; SEM micrograph of the source starch shown in **Figure S1**). Anhydrous glycerol (G; min. 99%), hydrochloric acid (HCl; 35%) and sodium bromide (reagent grade; min. 99%) were obtained from Lach-Ner, Czech Republic. Commercial titanium dioxide (TiO_2; anatase, particles size 50–200 nm) was provided by Sigma-Aldrich, USA. The commercially available vancomycin antibiotic

Sample	S (wt.%)	G (wt.%)	TiX (wt.%)	ATB (wt.%)
TPS	70	30	–	–
TPS/TiO$_2$ (10%)	63.2	26.8	10	–
TPS/TiO$_2$ (20%)	56.2	23.8	20	–
TPS/ATB	63.2	26.8	–	10
TPS/TiO$_2$/ATB	56.2	23.8	10	10

All samples contain residual water after processing by solution casting and melt mixing (~5%).

(ATB; Vancomycin Mylan, obtained from Biologici Italia, Italy) was used in ATB-loaded composites.

Preparation of TPS/TiO$_2$/ATB Composites

All of the samples (**Table 1**) were prepared by the two-step method consisting of solution casting (SC) followed by melt mixing (MM) as described in more detail in our previous report (Ostafinska et al., 2017). All of the chemicals used for the sample preparation (see previous section) were stored in a refrigerator in order to minimize their possible degradation (which might be a problem especially for the biodegradable starch powder). Briefly, the samples were made by SC using a starch/glycerol ratio of 70/30 (wt.%) and starch/water ratio of 1/6. At first, starch powder, TiO$_2$ and/or ATB were dispersed in water using an ultrasonic bath for 1 min, and then the glycerol was added for 2 min. The prepared water suspension (starch with glycerol and all additives, which was premixed for 30 min at room temperature) was mixed at an elevated temperature until the viscosity increased significantly (at least 10 min at a temperature above 65°C), and the mixture became visually homogeneous. Then the solution was cast onto thin foils and dried at the ambient temperature for 2–3 days followed by storage for 4 days in a desiccator with a supersaturated NaBr solution (relative humidity = RH = 57%). The dried SC samples were melt mixed (5 min, 110°C, 100 rpm) in a microextruder (μ-processing DSM, Netherlands) and compression molded (SC + MM samples) at 110°C (4 min at 50 kN + 2 min at 150 kN) in a special frame by a hydraulic press (Fontijne Grotnes, Netherlands). Since the properties of the TPS samples are very sensitive to humidity, all of the samples were stored in a desiccator with a supersaturated NaBr solution immediately after the preparation and between all experiments. The aging of samples was performed at the same conditions, i.e., the samples were kept 6 months at ambient temperature, closed in a desiccator with supersaturated NaBr solution.

Characterization of TPS/TiO$_2$/ATB Composites

Light Microscopy

The overall homogeneity of the filler dispersion at lower magnifications was checked using a light microscope (Nikon Eclipse 80i; Nikon, Japan). Thin sections (~40 μm) were cut with a rotary microtome (RM 2155; Leica, Germany), placed in oil between the support and cover glasses and observed with transmitted light using bright field imaging.

Scanning Electron Microscopy

Morphology of the TPS matrix and composites at higher magnifications was visualized with a high resolution field-emission gun scanning electron microscope (SEM) (Quanta 200 FEG; FEI, Czech Republic) using secondary electron imaging (SEM/SE) and backscattered electron imaging (SEM/BSE) at 5–30 kV. The samples were broken in liquid nitrogen (below the glass transition temperature of TPS), fixed on a metallic support using silver paste (Leitsilber G302, Christine Groepl, Austria), and the fracture surfaces were covered with a thin Pt layer (~8 nm; vacuum sputter coater, SCD 050, Balzers, Liechtenstein). The SEM/SE and SEM/BSE micrographs showed mostly topographic and material contrast, respectively.

Attenuated Total Reflectance Infrared Spectroscopy

Infrared spectra of TiO$_2$, TPS, and composites (after preparation and after 6 months) were acquired with a Golden Gate single reflection attenuated total reflectance cell (ATR; Specac, Ltd., Orpington, Kent, UK) using a Fourier transform infrared spectrometer (FTIR; Thermo Nicolet Nexus 870; Thermo Fisher Scientific Inc., Waltham, Massachusetts, USA) purged with dry air. The spectrometer was equipped with a liquid nitrogen cooled mercury cadmium telluride (MCT) detector, and the ATR cell employed a diamond internal reflection element. The ATR FTIR spectra were recorded with a resolution of 4 cm^{-1}, and 256 scans were averaged per spectrum. After subtraction of the spectrum of the atmosphere, the baselines were corrected (linear baseline correction) and an advanced ATR correction was applied (the correction is defined and recommended within the control FTIR software OMNIC).

Wide-Angle X-Ray Scattering (WAXS)

Diffraction patterns were obtained using an Explorer high-resolution diffractometer (GNR Analytical Instruments, Italy). This instrument was equipped with a one-dimensional silicon strip detector Mythen 1K (Dectris, Switzerland). Samples were measured in a reflection mode. CuKα radiation (wavelength λ = 1.54 Å) monochromatized with a Ni foil (β filter) was used for diffraction experiments. The measurements were performed in the 2θ range of 3 to 50° with a step of 0.1°. The exposure time at each step was 10 s. The peak deconvolution procedure was carried out using the Fityk software (Wojdyr, 2010). The peak positions were employed to obtain the periodicities according to Bragg's law, $d = \lambda/2\sin\theta$, where λ was the X-ray wavelength and θ was the scattering angle. Crystallinities were estimated using the integral intensities of the diffraction signals of the crystalline (I_c) and amorphous (I_a) phases CR = $I_c/(I_c + I_a)$.

Rheometry

Rheological properties were studied in oscillatory shear flow using a Physica MCR 501 rheometer (Anton Paar GmbH, Austria). Special anti-slipping parallel-plate geometry of 25 mm diameter plates was used. The sample thickness was ~1 mm. The experiments were performed at 120°C

in the linear viscoelastic range (LVE range), confirmed by a strain sweep test at the frequency of 1 Hz. Dynamic frequency sweeps tests were carried out for the frequency range of 10^{-1}–10^2 rad/s at a strain of 0.05%. Each sample was measured at least three times and the results were averaged.

Dynamic Mechanical Analysis

Mechanical properties were evaluated by dynamic-mechanical analysis (DMA). The linear viscoelastic characteristics—the absolute value of complex modulus $|G^*|$, storage G', loss modulus G'' and loss factor $\tan(\delta)$—were measured in the rectangular torsion mode using a Physica MCR 501 rheometer (Anton Paar GmbH, Austria). First, the strain amplitude sweep tests were conducted at the frequency 1 Hz in order to determine the linear viscoelastic range of the TPS matrix and all of the TPS/TiO$_2$/ATB composites. Then, two types of experiments were performed: frequency sweeps and temperature sweeps. The frequency sweep measurements were carried out at room temperature (23°C) in the frequency range of 10^{-1} to 10^2 rad/s, the strain was set to 0.1%, and the results of at least two specimens with the dimensions of 20 × 10 × 1.5 mm were averaged. The temperature sweep measurements were carried out in the temperature range of −90 to 100°C (with a heating rate of 5°C/min), at a strain of 0.05%, and angular frequency of 6.28 rad/s. Each sample was measured at least three times and the results were averaged.

Antimicrobial Susceptibility Testing of TPS/TiO$_2$/ATB Composites

The classical microbiological tube dilution test and disk diffusion test were used to evaluate the antimicrobial susceptibility (activity) as described elsewhere (Jorgensen and Ferraro, 2009). Both TPS/ATB and TPS/TiO$_2$/ATB composites were used for these experiments. In the tube dilution test, the samples were dispersed into tubes containing 5 ml of Mueller Hinton broth (Oxoid; Czech Republic). The resulting concentration of vancomycin in the polymer was 32 mg/L. The injectable vancomycin was diluted in the same medium to achieve the concentration of 32 mg/L as well. All of the tested tubes including the control sample without the antibiotics were inoculated with a standardized bacterial suspension of the CCM 4223 *Staphylococcus aureus* reference strain (density according to McFarland = 1). In disk diffusion method, the samples were slightly pushed into Mueller Hinton (Oxoid; Czech Republic) agar surface inoculated with suspension of the reference strain CCM 4223 *Staphylococcus aureus* in saline (density according to McFarland = 0.5) and the inhibitory zone was observed. Each test was performed two times in order to verify the reproducibility.

RESULTS AND DISCUSSION

Morphology of TPS Composites

TPS/TiO$_2$ and TPS/TiO$_2$/ATB composites after solution casting (SC) and melt mixing (SC + MM) (**Table 1**) were observed by
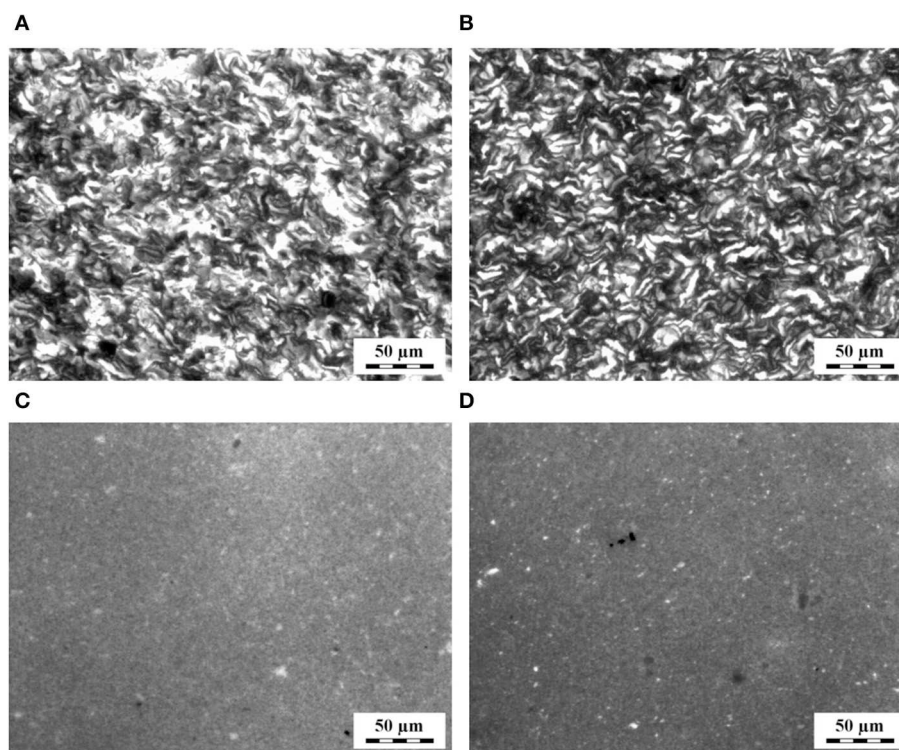

FIGURE 1 | LM micrographs showing the structure of the TPS/TiO$_2$ composites with **(A,C)** 10% and **(B,D)** 20% of the filler: **(A,B)** after solution casting and **(C,D)** after solution casting and melt mixing.

FIGURE 2 | SEM/SE micrographs showing TPS/TiO$_2$ composites with **(A,C)** 10% and **(B,D)** 20% of the filler: **(A,B)** after solution casting and **(C,D)** after solution casting and melt mixing.
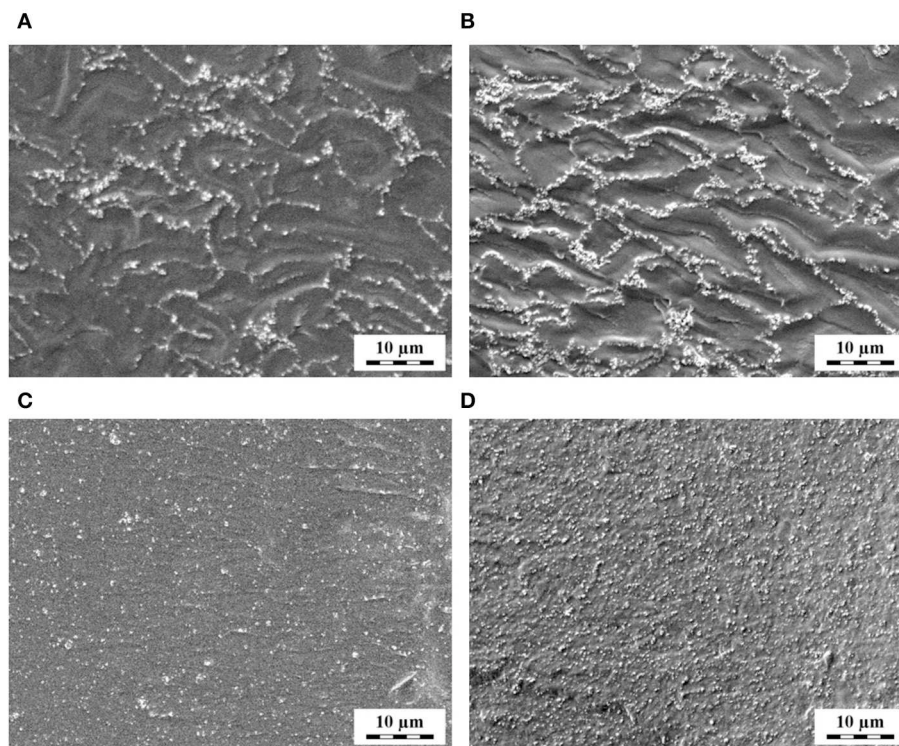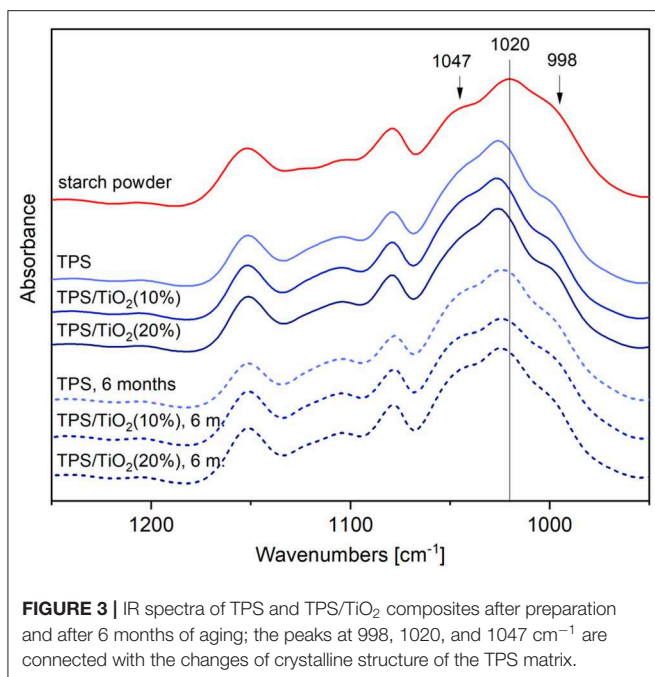
LM (**Figure 1**) and SEM (**Figure 2**). The lower magnification LM micrographs proved that the large agglomerates of TiO$_2$ particles, which were formed after SC (**Figures 1A,B**) were destroyed after SC + MM (**Figures 1C,D**). The higher magnification SEM micrographs showed that the TiO$_2$ particles tended to envelop the plasticized but not-fully merged starch granules after SC (**Figures 2A,B**), while the subsequent MM step resulted in the complete merging of starch granules and a highly homogeneous distribution of the TiO$_2$ nanoparticles (**Figures 2C,D**).

Both LM and SEM micrographs confirmed that the two-step preparation (SC + MM) was necessary to obtain fully plasticized starch with a homogeneously dispersed filler (up to 20 wt.%). SC led to non-fully merged starch granules, while MM alone resulted in non-plasticized granules and/or their agglomerates in the TPS matrix (**Figure S2**). This finding was in agreement with the results of our previous work (Ostafinska et al., 2017) on the TPS/TiO$_2$ composites with lower filler amounts (up to 3%). The morphological study also proved that the addition of ATB (up to 10 wt.%) had no effect on the morphology of the TPS matrix and on the dispersion of TiO$_2$ particles (**Figure S3**). Further morphological results suggested that even higher concentrations of TiO$_2$ (up to 25%) could be dispersed in the TPS matrix using our two-step SC + MM method (**Figure S4**) but the particles began to agglomerate and the viscosity of the composites increased too much, preventing their reproducible preparation and reliable rheological characterization.

IR and WAXS Characterization of TPS Composites

The changes in the structure between the native starch and the thermoplastic starch (after SC and after SC+MM) were studied in detail in our previous work (Ostafinska et al., 2017). In the present work, we characterized the structure of the TPS/TiO$_2$ composites prepared by SC+MM and their changes during aging. **Figure 3** shows ATR FTIR spectra of the composites together with the spectrum of the starch powder. The figure displays the bands in the 1,100–900 cm^{-1} region (C–O, C–C stretching, and C–O–H bending), which were shown to be sensitive to the changes in the crystalline structure of the starch (Capron et al., 2007): the intensity of the band at 1,022 cm^{-1} appeared to increase in more amorphous samples, while the bands at 1,000 and 1,047 cm^{-1} became more defined in more crystalline samples. In a recent study (Warren et al., 2016), it was shown that the relationship between the infrared spectra of the starches with different degrees of order is more complex than it had been previously appreciated; nevertheless, it was also confirmed that the main difference between the starches with high and low degrees of order is a shift of the band at 1,020 cm^{-1} to higher wavenumbers (Warren et al., 2016). As presented in **Figure 3**, our results showed that compared to the starch powder with the band at 1,020 cm^{-1}, the FTIR spectra of the composites exhibited a shift of that band to 1,027 cm^{-1}, while the relative intensities of the bands at 1,047 and 998 cm^{-1} decreased. This is explained

FIGURE 3 | IR spectra of TPS and TPS/TiO$_2$ composites after preparation and after 6 months of aging; the peaks at 998, 1020, and 1047 cm^{-1} are connected with the changes of crystalline structure of the TPS matrix.

FIGURE 4 | X-ray diffraction patterns of TPS and TPS/TiO$_2$ composites after preparation and after 6 months of aging. The diffraction pattern at the bottom is theoretically calculated diffractogram of anatase modification of titanium dioxide. The peaks of TPS are marked with their 2θ values.
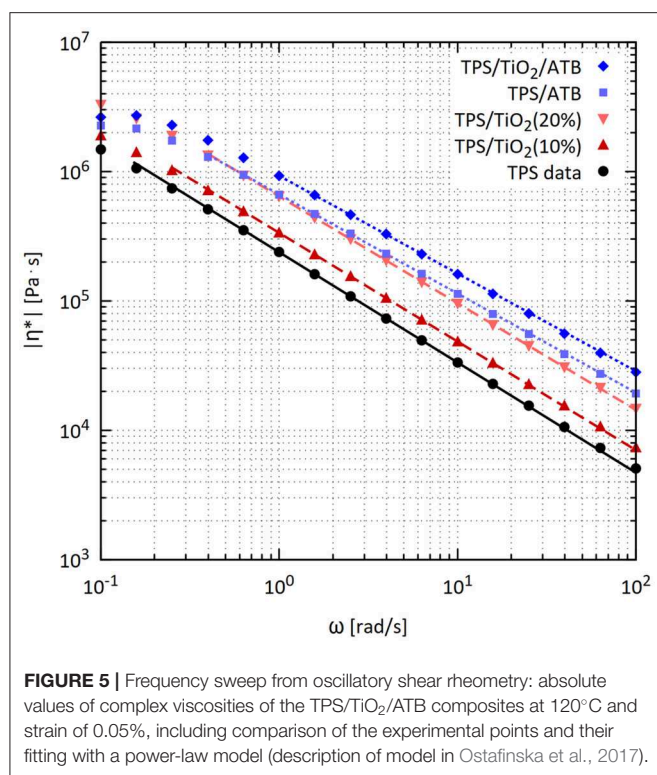
by the decrease in the crystallinity (short range ordering) of the starch in the composites, in agreement with our previous report (Ostafinska et al., 2017). Upon aging of the composites, small changes of the TPS crystalline structure could be observed: The central band in the FTIR spectra was shifted back in the direction of lower wavenumbers to 1,025 cm^{-1} and the intensities of the bands at 1,047 and 998 cm^{-1} increased, indicating an increase in ordering and recrystallization. Furthermore, the IR/ATR data suggested that the addition of TiO$_2$ and ATB did not influence the TPS matrix structure (**Figure S5**).

WAXS patterns are summarized in **Figure 4**. The diffractograms were normalized approximately to the same noise and then to the intensity of characteristic triplet of diffraction of TiO$_2$ anatase form (the three diffractions around $2\theta = 38°$). The diffraction peak positions of neat TPS were in reasonable agreement with the results of previous studies (Soest et al., 1996; Ostafinska et al., 2017). All TPS/TiO$_2$ composites showed sharp peaks corresponding TiO$_2$. The TPS crystalline structure did not change with time significantly as evidenced by the fact that most of the TPS diffraction peaks retained their positions and intensities. The moderate changes of crystalline structure were in agreement with FTIR results (**Figure 3**). One notable change was associated with the neat TPS sample, where the peak at $2\theta = 16.9°$ became much more pronounced after 6 months of aging. This corresponded to the starch crystallization into V$_H$ type crystals (retrogradation; Zobel et al., 1967; Rappenecker and Zugenmaier, 1981; Soest et al., 1996; Ilyas et al., 2018). Interestingly, this change was not observed in the TPS/TiO$_2$ composites, suggesting that the higher concentration of TiO$_2$ particles prevented standard TPS retrogradation and resulted in the formation of different crystalline structures that were not stable with time, as discussed below. A few lower-intensity TPS diffractions (mostly at $2\theta > 25°$) were observed
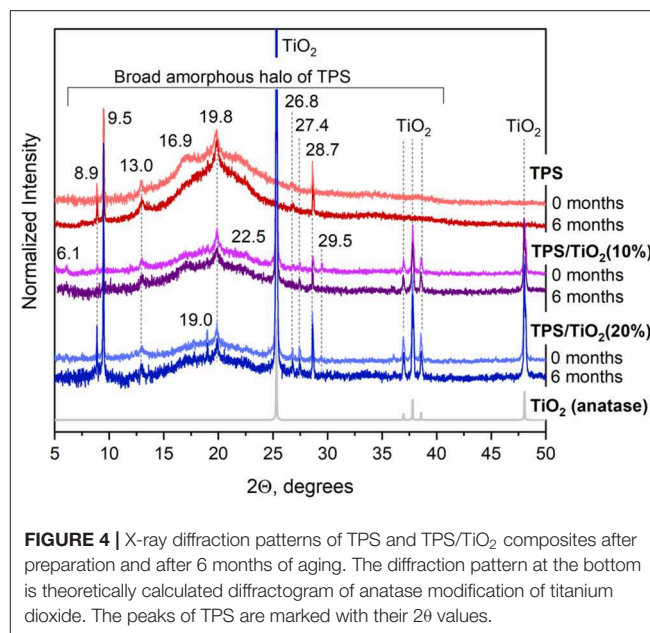
for TPS/TiO$_2$ composites in comparison with neat TPS, which confirmed that TiO$_2$ nanoparticles somewhat influenced the crystalline structure of TPS matrix. The overall TPS crystallinity *increased* with the addition of TiO$_2$ and then it *slightly decreased* after 6 months of aging. After the preparation, the neat TPS exhibited the crystallinity of 6.5%, whereas TPS/TiO$_2$ (10%) and TPS/TiO$_2$ (20%) showed the crystallinity of 9.8 and 24.8%, respectively. After 6 months of aging, the crystallinity of the neat TPS increased slightly (although the change from 6.5 to 6.8% was within experimental and/or fitting procedure error), while the crystallinities of the TPS/TiO$_2$ (10%) and TPS/TiO$_2$ (20%) composites somewhat decreased to 7.7 and 18.9%, respectively. Our tentative explanation consists in that TiO$_2$ particles promoted the ordering and crystallization of the starch during the *plasticization process*, but the TiO$_2$-induced crystalline structures were metastable and during the *aging process* were slowly destroyed by the plasticizer molecules. The concentration of plasticizer in TPS was almost constant as demonstrated by an independent TGA analysis (**Figure S6**). This explanation is supported by the fact that the observed changes (i.e., both TiO$_2$-induced increase in crystallization and the subsequent decrease in the crystallization during aging) were more intense for higher TiO$_2$ particle concentrations. In TPS composites with lower filler concentrations (and in the neat TPS observed in this work), the crystallinity tends to increase with time (Mina et al., 2012; Wang et al., 2015). However, in the TPS/TiO$_2$ composites with higher filler concentrations the crystallinity showed a reversed trend, as unambiguously proved by WAXS.

For neat TPS, both ATR FTIR and WAXS methods were in agreement that crystallinity slightly increased with aging due to retrogradation. For TPS/TiO$_2$ composites the situation was different: ATR FTIR results indicated a slight increase in the crystallinity and ordering with time, while WAXS results proved a measurable decrease in the TiO$_2$-induced crystallinity

FIGURE 5 | Frequency sweep from oscillatory shear rheometry: absolute values of complex viscosities of the TPS/TiO$_2$/ATB composites at 120°C and strain of 0.05%, including comparison of the experimental points and their fitting with a power-law model (description of model in Ostafinska et al., 2017).

with time. This could be explained by the core-shell structure of the prepared samples. ATR FTIR collects signal from the thin shell, i.e., from the very surface layer at the top of the sample, where the concentration of the plasticizers during aging decreases. Consequently, the above-proposed destruction of metastable crystalline structure due to plasticizers was limited and the dominating effect was a crystallinity increase due to retrogradation. WAXS collects signal from the bulk, because the X-rays penetrate inside the specimen, where concentration of the plasticizers is high. According our tentative explanation from the previous paragraph, the high concentration of plasticizers destroys the proposed metastable, TiO$_2$-induced TPS crystalline structures. Therefore, the dominating effect was the small crystallinity decrease. The formation of metastable crystalline structures due to high concentration of filler was rather surprising and not observed for lower concentration of fillers in previous studies, but we should note that TPS matrices with such high filler concentration have not been characterized by WAXS in the literature so far.

Rheological Properties

The rheological properties of TPS/TiO$_2$/ATB composites measured in the oscillatory shear at 120°C are shown in **Figures 5**, **6**. The logarithmic dependence of the TPS complex viscosity ($|\eta^*|$) on the angular frequency (ω) showed a linear decrease almost in the entire 0.1–100 rad/s range. A slight curvature down appeared only for the lowest frequencies. The storage modulus (G') was larger than the loss modulus (G'') in the entire range of ω. G' grew linearly with frequency for ω

above 0.4 rad/s in the logarithmic plot and curved down faintly with decreasing frequency for ω below 0.4 rad/s. This behavior corresponded to the slightly crosslinked polymers, physical gels or uncrosslinked polymers with high molecular weights, for which the Newtonian plateau in the viscosity and the crossing point of G' and G'' are shifted to a low ω (Mezger, 2014).

The complex viscosity ($|\eta^*|$) values of TPS/TiO$_2$ composites were very high in the entire range of frequencies (**Figure 5**), in agreement with previous studies (Della Valle et al., 1998; Deme et al., 2014; Ostafinska et al., 2017). The complex viscosities of TPS/TiO$_2$ exceeded the complex viscosity value for the pure TPS matrix. The storage and loss moduli of TPS/TiO$_2$ were higher than those of neat TPS in the entire frequency range. The enhancement of the rheological properties of TPS/TiO$_2$ with respect to neat TPS increased with the amount of TiO$_2$ in the composite. The shapes of the dependences of $|\eta^*|$, G' and G'' on ω for TPS/TiO$_2$ were essentially the same as those for neat TPS. There was no indication that TiO$_2$ formed a continuous physical network in TPS.

The previously studied composites with TiO$_2$ concentrations of up to 3% (Ostafinska et al., 2017) had the values of storage, loss, and complex modulus slightly lower than the corresponding values for pure TPS, which was attributed to the chain scissions of the TPS molecules at elevated temperatures. In this work, the moduli of the TPS/TiO$_2$ (10%) composites were already higher than those for TPS. This indicated that for a higher filler content, the reinforcing properties of the filler were already more dominant than the chain scissions of the TPS molecules at elevated temperature, resulting in the significantly higher moduli of the TPS/TiO$_2$ composites in comparison with the pure TPS matrix (**Figures 6A,B**).

The effect of the ATB addition on the rheological properties of TPS was more complex. Higher values of $|\eta^*|$, G' and G'' were found at ω above 1 rad/s for TPS/ATB (90/10) in comparison with TPS/TiO$_2$ (90/10); the same trend applied to TPS/TiO$_2$/ATB (80/10/10) in comparison with TPS/TiO$_2$ (80/20). In contrast to the TPS/TiO$_2$ composites, the shapes of the logarithmic plots of the rheological properties vs. ω for composites containing ATB differed remarkably from those for neat TPS. The decrease of $|\eta^*|$ with ω in the linear region of the logarithmic plot (above ω = 1 rad/s) was slower and the related increase in G' was steeper for the composites containing ATB than for neat TPS or for the TPS/TiO$_2$ composites. A decrease in the values of $|\eta^*|$ and G' for low frequencies with respect to the related values obtained by extrapolation from the linear regions of the logarithmic plots started at higher ω and was substantially higher for the composites with ATB than for neat TPS and TPS/TiO$_2$. This indicated that ATB enhanced the contribution of the elements with short relaxation times and suppressed the contribution of the elements with long relaxation times to the viscosity and elasticity of the composites. This was apparently a consequence of the complex, hydrogen-bond based interactions among starch, glycerol, and ATB.

Mechanical Properties

The dynamic moduli of TPS/TiO$_2$/ATB composites at room temperature (ω = 1.33 rad/s, deformation = 0.1%) are
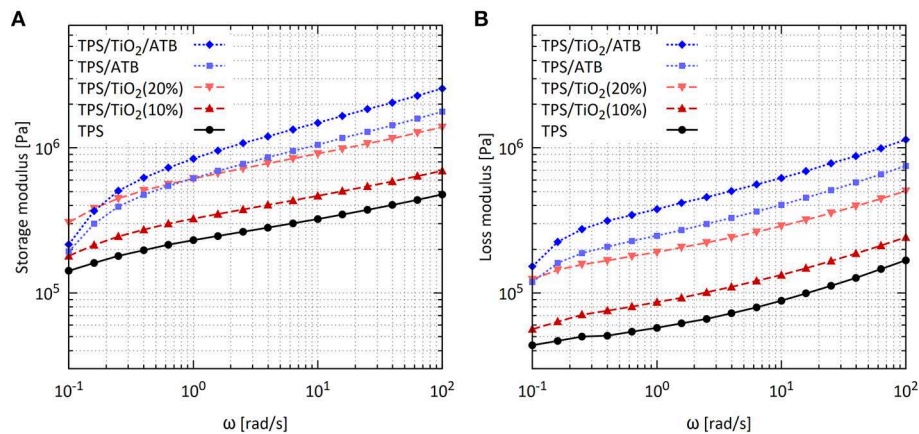
FIGURE 6 | Frequency sweeps from oscillatory shear rheometry: **(A)** Storage modulus G' and **(B)** loss modulus G'' **(B)** of the TPS/TiO$_2$/ATB composites at 120°C and strain of 0.05%.

summarized in **Figure 7**. The storage moduli (G') and complex moduli (|G*|) of all composites were higher than the corresponding moduli of the pure TPS matrix. With the addition of TiO$_2$ the storage moduli increased by 1.3 and 3 times for 10 and 20% of the filler, respectively. The modulus of the TPS/ATB samples was 20 times higher than that of TPS, confirming the strong interaction between ATB and TPS matrix. A further increase in the modulus of 1.4 times with respect to TPS/ATB (90/10) was obtained for the TPS/TiO$_2$/ATB (80/10/10) samples. This suggested that the influence of the filler content on the elastic modulus was approximately the same for both TPS (1.3× increase) and TPS/ATB (1.4× increase). Somewhat higher estimated standard deviations for the TPS/TiO$_2$ composites in comparison with the pure (and homogenous) matrix can be attributed to the fact that the mechanical properties are very sensitive to the homogeneity of material and also to the fact that TPS materials are sensitive to moisture content and aging (Della Valle et al., 1998).

Dynamic mechanical thermal analysis (DMTA) of the TPS/TiO$_2$/ATB composites was carried out in order to supplement room temperature measurements and to characterize the influence of TiO$_2$ and ATB on the phase changes in the TPS systems (**Figure 8**). Neat TPS systems after two-step preparation by SC + MM contained 30% of glycerol and 5% of residual water as evidenced by TGA (**Figure S6**). Their G'-curves (**Figure 8A**) showed behavior typical of gels with a low degree of crosslinking: above T_g, the elastic modulus curve clearly goes down, and G' is higher than G'' in the entire temperature range (**Figures 8A,B**) (Mezger, 2014, p. 195). These gel-like DMTA results can be attributed to the high-molecular weight branched amylopectin molecules. The loss modulus (G'') and the damping factor (tan(δ)) curves (**Figures 8B,C**) showed two local maxima corresponding to the two glass transition temperatures (T_g) typical of TPS with higher concentration of plasticizers (Mezger, 2014, p. 192). Generally, the addition of plasticizers to a polymer system decreases the T_g. A higher content of plasticizers may result in two glass transitions, indicating the presence of two separate phases with different plasticizer concentrations (Mezger, 2014, p. 196). In the specific case of TPS plasticized
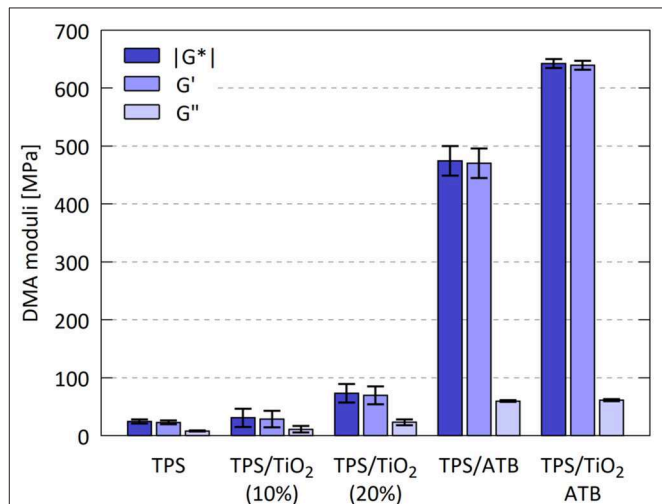

FIGURE 7 | Shear moduli (storage modulus G', loss modulus G'', and complex modulus |G*|) from DMTA analysis of the TPS/TiO$_2$/ATB composites, determined at room temperature, angular frequency 1.33 rad/s and strain of 0.1%; error bars represent standard deviations.

with glycerol in combination with water, the two observed maxima were assigned to the "glycerol-rich phase" (below 0°C) and the "starch-rich phase" (also "amylopectin-rich phase" or "glycerol-poor phase"; above 0°C); their exact location and intensity depends on the preparation protocol (Viguie et al., 2007; Bertolini, 2010; Saiah et al., 2012; Balakrishnan et al., 2017; Sessini et al., 2018). It is worth noting that DMTA analysis turned out to be a more sensitive tool for T_g detection than the DSC method, which was used in our previous work (Ostafinska et al., 2017) on analogous systems, where DSC was able to detect the "glycerol-rich phase" glass transition but not the "starch-rich phase" glass transition.

The influence of the additives on the DMTA properties of the TPS/TiO$_2$/ATB systems illustrated in **Figure 8** corresponded quite well to the expected trends. The addition of the filler
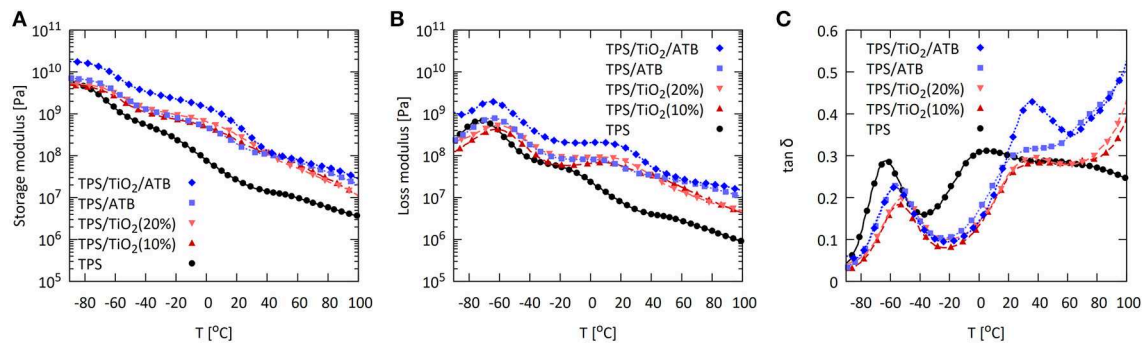
FIGURE 8 | Dynamic mechanical thermal analysis of the TPS/TiO$_2$/ATB composites at the angular frequency of 6.28 rad/s and strain of 0.05%: **(A)** Storage modulus G′, **(B)** loss modulus G″, and **(C)** damping factor tan(δ).

can strongly influence the overall stiffness of the composite (related to G') and the glass transition temperature of the matrix [related to the peaks of G'' and tan(δ)]. Typically, increasing filler concentration results in the shift of the G'-curve to higher values that is accompanied by the decreasing intensity and broadening of the G'' and tan(δ) peaks.

The stiffness of TPS (represented by absolute values of G' in the entire temperature range) increased both after the addition of the TiO$_2$ particles and ATB (**Figure 8A**). The only small exception were the lowest temperatures (at approximately $-90°C$), where the storage moduli of TPS and TPS/TiO$_2$ composites were approximately the same, while the ATB-containing systems exhibited higher G' at all temperatures. The increase in G' due to high-modulus inorganic TiO$_2$ particles was logical while the further G' increase after addition of organic ATB molecules appeared to arise from complex, and not-entirely understood interactions among the matrix, the TiO$_2$ particles and ATB, as discussed in the previous section dealing with rheology. Both the neat TPS matrix and all of the composites had storage moduli values higher than those of the loss moduli ($G' > G''$) in the entire temperature range (cf. **Figures 8A,B**), confirming the gel-like structure and physical stability of all systems (Ross-Murphy, 1995).

The two glass transition temperatures of the TPS composites (related to the G'' and tan(δ)curve peaks) showed similar changes (**Figures 8B,C**). The peaks corresponding to T_g of the "glycerol-rich phase" of all composites were slightly shifted toward higher temperatures (from $-63°C$ for TPS to $-55°C$ for the ATB composites and to $-52°C$ for the TiO$_2$ composites; **Figure 8C**). Additionally, the peaks corresponding to the T_g values of the "starch-rich phase" were shifted toward higher temperatures for all of the composites (from $5°C$ for TPS to $35°C$ for the ATB composites and to $39°C$ for the TiO$_2$ composites) and the filler effect was even stronger. Therefore, the addition of both TiO$_2$ and ATB slightly hindered the mobility of the glycerol-rich phase (TiO$_2$ more than ATB) and strongly decreased the mobility of the "starch-rich phase" (both additives showed approximately the same effect). This effect was described in similar systems (Viguie et al., 2007; Sessini et al., 2018) and it was attributed to attractive interactions, such as hydrogen bonding between the additives

and the TPS matrix, in the cases where all of the components (in our case: starch, glycerol, ATB vancomycin, and surfaces of the TiO$_2$ particles) contain –OH groups. Moreover, it was suggested that the T_g shift of the "starch-rich phase" was due to the lower molecular mobility of amylopectin chains in TPS (Viguie et al., 2007; Sessini et al., 2018).

Antibacterial Activity

TPS composites, such as TPS/ATB and TPS/TiO$_2$/ATB represent promising materials for the treatment of strong local infections. TPS is fully biocompatible and biodegradable and can be blended with other suitable biodegradable polymers (typically PCL) in order to adjust biodegradability rate and/or ATB release rate for given application. Inorganic particles, such as TiO$_2$ can be used to fine-tune the thermo-mechanical performance, as demonstrated in the previous sections above. However, it still must be determined whether the selected ATB (in our case: vancomycin) can survive the two-step sample preparation and retain its role as the active antimicrobial agent. In order to answer this question, two standard and well-established antimicrobial susceptibility tests were performed: tube dilution test and disk diffusion test (Jorgensen and Ferraro, 2009).

The tube test results are shown in **Figures 9A,B**. The test tubes were filled with water and loaded with a small piece of the TPS/ATB and TPS/TiO$_2$/ATB samples from which 32 mg/L of ATB was expected to be released within 24 h (Slouf et al., 2017). The concentration of 32 mg/L was selected as the maximal acceptable limit for most biomedical applications. The ATB-containing tubes were inoculated with a standardized bacterial suspension of *Staphylococcus aureus*. Following overnight incubation (ca. 18 h), the tubes were examined for visible bacterial growth as evidenced by turbidity. The bacterial broth culture remained clear in both tubes containing the systems with antibiotics (TPS/ATB and TPS/TiO$_2$/ATB; **Figure 9A**), proving that the released ATB could inhibit the bacterial growth. The control sample (pure TPS; **Figure 9B**) exhibited turbidity, evidencing the microbial growth.

The modified disk diffusion test (**Figures 9C–E**) confirmed the results obtained in the tube dilution test. The same fresh samples (similar to those used in the tube dilution tests)
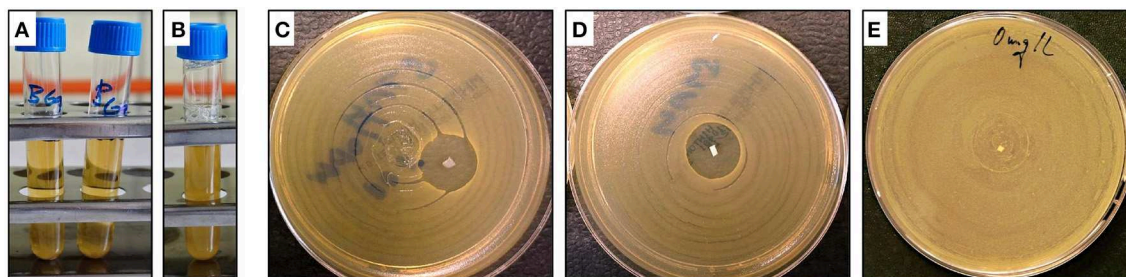
FIGURE 9 | Photographs showing the main results of antibacterial activity tests: **(A,B)** tube tests and **(C–E)** disk diffusion tests. Pictures of tubes **(A,B)** were made after 18 h of incubation: **(A)** shows translucent solutions of TPS/ATB (right) and TPS/TiO$_2$/ATB (left), while **(B)** shows turbid solution of control neat TPS sample. Pictures of disks **(C–E)** display clear inhibitory zones around small white rectangular samples of TPS/ATB **(C)** and TPS/ATB/TiO$_2$ **(D)**, while the control neat TPS sample exhibits no inhibitory zone **(E)**.

were pushed slightly into the agar plates inoculated with the *Staphylococcus aureus* reference strain (0.5 McFarland in saline). The plates were incubated for 18 h prior to the evaluation of the results. For TPS/ATB and TPS/TiO$_2$/ATB, typical inhibitory zones formed in the vicinity of the carrier indicated the release of the active ATB onto the agar medium (**Figures 9C,D**). This means that the antibiotics must have survived our SC + MM sample preparation and kept is antibacterial activity. Both inhibitory zones were similar, indicating that TiO$_2$ particles did not influence the ATB release. The control sample (pure TPS, **Figure 9E**) showed no inhibitory zone.

Both the tube test and the disk diffusion test demonstrated that a suitable ATB (such as vancomycin) that is resistant to elevated temperatures during solution casting (up to ca +80°C) and melt mixing (up to ca +120°C) can survive in the TPS in its active form. Moreover, the tests provided additional information regarding the different release rates of the TiO$_2$ particles and ATB molecules from TPS. The TiO$_2$ particles were not released from TPS to the solution and/or agar, as can be deduced from the fact that both solutions did not show visible white turbidity (**Figures 9A,B**). The particles must have been bonded well to the starch molecules by hydrogen bonds, because both components have an abundance of –OH groups. On the other hand, the ATB molecules can be released from the TPS structure even though ATB also contains –OH groups and interacts with TPS, as clearly evidenced by the rheological and thermomechanical measurements (**Figures 5–8**). However, for ATB, the osmotic pressure was evidently stronger than the effect of the hydrogen bonds that keep the ATB inside the thermoplastic starch.

Limitations of Current Study

TPS composites prepared in this work were characterized thoroughly regarding their morphology, rheology, and thermomechanical properties. The reproducibility of the preparation, the ideal homogeneity, and the full biodegradability make the prepared TPS composites suitable for biomedical applications for fast release of antibiotics during strong local infections. In potential applications, a temporary biodegradable TPS implant would release the ATB and then it would be safely degraded. However, the present work was focused on material

characterization, whereas the antimicrobial susceptibility testing was somewhat simplified. In future work, two issues should be taken into consideration: the real biocompatibility of TiO$_2$ particles and the *bactericidal effect* of ATB (not only the *bacteriostatic effect* like in this work).

For the biocompatibility of the TiO$_2$ particles, the situation is not entirely clear. Numerous authors have reported that TiO$_2$ micro- and/or nanoparticles are a fully biocompatible material (Webster et al., 1999, 2000; Sengottuvelan et al., 2017), which is also broadly used as a food additive (Dudefoi et al., 2017). However, quite recently other researchers started to raise concerns about the potential toxicity of TiO$_2$ micro- and/or nanoparticles, particularly at the higher particle concentrations. On the one hand, Dudefoi et al. concluded that food grade TiO$_2$ particles did not significantly alter the human gut microbiota (Dudefoi et al., 2017) and Cervantes et al. found that TiO$_2$ thin films did not affect the mitochondrial function and proliferation of CHO-K1 cells (Cervantes et al., 2016). On the other hand, Fu et al. (2014) studied the generation of the reactive oxygen species (ROS) by various nanomaterials, which is an important nanotoxicity mechanism. They pointed out that the toxicity of the nanomaterials (related to generation of ROS) depends on many factors, such as the size, shape, particle surface, surface positive charges, surface-containing groups, particle dissolution, metal ion release from nanometals and nanometal oxides, UV light activation, aggregation, mode of interaction with the cells, inflammation, and the pH of the medium (Fu et al., 2014). Furthermore, Yu et al. (2017) studied the toxicity of nano-TiO$_2$ (both anatase and rutile with similar particle sizes) for mammalian cells. They found that the anatase nano-TiO$_2$ had a high affinity to proteins, whereas the rutile nano-TiO$_2$ had a high affinity to phospholipids. They proved that crystal phase-related surface affinity plays an important role for the nanotoxicity of different biomolecules (Yu et al., 2017). Therefore, the TPS/ATB composites are expected to be fully biocompatible, while the TPS/TiO$_2$/ATB composites should be further tested for the potential toxicity of the contained particles that would be released into the organism during the biodegradation.

For the antimicrobial activity, the current study unambiguously proved the *bacteriostatic effect* of the TPS/ATB

and TPS/TiO$_2$/ATB composites, but we did not attempt to determine the *minimal inhibitory concentration* (MIC) and the final *bactericidal effect* of the released ATB. More detailed tests, such as those described elsewhere (Schwalbe et al., 2007; Sedlarik, 2013), were beyond the scope of the present work. These tests will be carried out in our future study, in which we will employ the experience from this contribution and prepare TPS samples with various ATB concentrations.

CONCLUSIONS

In this work, we have demonstrated that our two-step preparation of thermoplastic starch (TPS; Ostafinska et al., 2017), which consists of solution casting followed by melt mixing, is suitable for reproducible preparation of TPS/TiO$_2$ composites with homogeneous dispersion of the filler, even at high filler concentrations (up to 20 wt.%). Moreover, the preparation procedure is suitable also for the preparation of TPS systems containing homogeneously dispersed antibiotics (ATB; here: vancomycin at 10 wt.%). The addition of both TiO$_2$ and ATB increased the viscosity of the TPS matrix ∼5×, as evidenced by rheological measurements. The interactions among TPS, TiO$_2$ particles, and ATB molecules resulted in the shifts of the glass transition temperatures to higher values and in the overall stiffening of the material (ca 25× increase in storage modulus of TPS/TiO$_2$/ATB with respect to neat TPS). Finally, standard antimicrobial susceptibility tests proved that neither thermal processing nor addition of TiO$_2$ influence the ATB, which remains active in both TPS/ATB and TPS/TiO$_2$/ATB composites. Therefore, we conclude that the prepared fully biodegradable TPS composites are a very promising material for biomedical applications involving local release of antibiotics.

DATA AVAILABILITY STATEMENT

The datasets generated for this study are available on request to the corresponding author.

AUTHOR CONTRIBUTIONS

MS designed the study, which was performed by AU (the sample preparation and characterization by light microscopy, important contribution to interpretation of rheological data), SK (electron microscopy), MN (rheometry and dynamical mechanical analysis), AZ (wide-angle X-ray scattering), JD (infrared microscopy), PF and ON (antimicrobial susceptibility testing). ZK contributed to the sample preparation and data interpretation. AU with the help of MS interpreted the results prepared a draft of the manuscript. MS finalized and submitted the manuscript.

SUPPLEMENTARY MATERIAL

The Supplementary Material for this article can be found online at: https://www.frontiersin.org/articles/10.3389/fmats.2020.00009/full#supplementary-material

REFERENCES

Abral, H., Basri, A., Muhammad, F., Fernando, Y., Hafizulhaq, F., Mahardika, M., et al. (2019). A simple method for improving the properties of the sago starch films prepared by using ultrasonication treatment. *Food Hydrocolloid.* 93 276–283. doi: 10.1016/j.foodhyd.2019.02.012

Aichholzer, W., and Fritz, H.-G. (1998). Rheological characterization of thermoplastic starch materials. *Starch* 50, 77–83. doi: 10.1002/(SICI)1521-379X(199803)50:2/3<77::AID-STAR77>3.0.CO;2-P

Ali, A., Xie, F., Liu, H., Meng, L., Khalid, S., and Chen, L. (2018). Preparation and characterization of starch-based composite films reinforced by polysaccharide-based crystals. *Compos. Part B* 133, 122–128. doi: 10.1016/j.compositesb.2017.09.017

Altskar, A., Andersson, R., Boldizar, A., Koch, K., Stading, M., Rigdahl, M., et al. (2008). Some effects of processing on the molecular structure and morphology of thermoplastic starch. *Carbohydr. Polym.* 71, 591–597. doi: 10.1016/j.carbpol.2007.07.003

Ao, Z., and Jane, J. (2007). Characterization and modeling of the A- and B-granule starches of wheat, triticale, and barley. *Carbohydr. Polym.* 67, 46–55. doi: 10.1016/j.carbpol.2006.04.013

Balakrishnan, P., Sreekala, M. S., Kunaver, M., Huskic, M., and Thomas, S. (2017). Morphology, transport characteristics and viscoelastic polymer chain confinement in nanocomposites based on thermoplastic potato starch and cellulose nanofibers from pineapple leaf. *Carbohydr. Polym.* 169, 176–188. doi: 10.1016/j.carbpol.2017.04.017

Bertolini, A. (2010). *Starches: Characterization, Properties, and Applications*. Boca Raton, FL: Taylor & Francis Group, LLC.

Biliaderis, C. G. (2009). "Structural transitions and related physical properties of starch," in *Starch. Chemistry and Technology, A Volume in Food Science and Technology, 3rd Edn.*, eds J. BeMiller and R. Whistler (Cambridge, MA: Academic press), 293–372. doi: 10.1016/B978-0-12-746275-2.00008-2

Boccaccini, A. R., and Blaker, J. J. (2006). Poly(D,L-lactide) (PDLLA) foams with TiO$_2$ nanoparticles and PDLLA/TiO$_2$-Bioglass foam composites for tissue engineering scaffolds. *J. Mater. Sci.* 41, 3999–4008. doi: 10.1007/s10853-006-7575-7

Boccaccini, A. R., Gerhardt, L.-C., Rebeling, S., and Blaker, J. J. (2005). Fabrication, characterisation and assessment of bioactivity of poly(D,L lactid acid) (PDLLA)/TiO$_2$ nanocomposite films. *Compos. Part A* 36, 721–727. doi: 10.1016/j.compositesa.2004.11.002

Campos, A., Senta Neto, A. R., Rodrigues, V. B., Luchesi, B. R, Moreira, F. K. V., Correa, A. C., et al. (2017). Bionanocomposites produced from cassava starch and oil palm mesocarp cellulose nanowhiskers. *Carbohydr. Polym.* 175, 330–336. doi: 10.1016/j.carbpol.2017.07.080

Campos-Requena, V. H., Rivas, B. L., Perez, M. A, Figueroa, C. R., Figueroa, N. E., and Sanfuentes, E. A. (2017). Thermoplastic starch/clay nanocomposites loaded with essential oil consituents as packaging

for strawberries–*in vivo* entimicrobial synergy over *Botrytis cinerea*. *Postharvest Biol. Technol.* 129, 29–36. doi: 10.1016/j.postharvbio.2017.03.005

Capron, I., Robert, P., Colonna, P., Brogly, M., and Planchot, V. (2007). Starch in rubbery and glassy states by FTIR spectroscopy. *Carbohydr. Polym.* 68, 249–259. doi: 10.1016/j.carbpol.2006.12.015

Carvahlo, A. J. F., Curvelo, A. A. S., and Agnelli, J. A. M. (2001). A first insight of thermoplastic starch and kaolin. *Carbohydr. Polym.* 45, 189–194. doi: 10.1016/S0144-8617(00)00315-5

Cervantes, B., Lopez-Huerta, F., Vega, R., Hernandez-Torres, J., Garcia-Gonzalez, L., Salceda, E., et al. (2016). Cytotoxicity evaluation of anatase and rutile TiO_2 thin films on CHO-K1 cells *in vitro*. *Materials* 9:619. doi: 10.3390/ma9080619

Dai, H., Chang, P., Yu, J., and Ma, X. (2008). N,N-Bis(2-hydroxyethyl)formamide as a new plasticizer for thermoplastic starch. *Starch* 60, 676–684. doi: 10.1002/star.200800017

Dai, H., Sheng, X., An, L., Liu, N., Yu, J., and Ma, X. (2012). Preparation and properties of thermoplastic starch/montmorillonite nanocomposites using N,N-bis(2-hydroxyethyl)formamide as a new additive. *Polym. Compos.* 33, 225–231. doi: 10.1002/pc.22142

Della Valle, G., Buleon, A., Carreau, P. J., Lavoie, P. A., and Vergnes, B. (1998). Relationship between structure and viscoelastic behavior of plasticized starch. *J. Rheol.* 42, 507–525. doi: 10.1122/1.550900

Deme, F., Peuvrel-Disdier, E., and Vergnes, B. (2014). Rheology and morphology of polyester/thermoplastic flour blends. *J. Appl. Polym. Sci.* 131:40222. doi: 10.1002/app.40222

Dudefoi, W., Moniz, K., Allen-Vercoe, E., Ropers, M.-H., and Walker, V.K. (2017). Impact of food grade and nano-TiO_2 particles on a human intestinal community. *Food Chem. Toxicol.* 16, 242–249. doi: 10.1016/j.fct.2017.05.050

Dufresne, A., and Castano, J. (2017). Polysaccharide nanomaterial reinforced starch nanocomposites: a review. *Starch* 69:1500307. doi: 10.1002/star.201500307

Fei, P., Shi, Y., Zhou, M., Cai, J., Tang, S., and Xiong, H. (2013). Effects of nano-TiO_2 on the properties and stuctures of starch/poly(ε-caprolactone) composites. *J. Appl. Polym. Sci.* 130, 4129–4136. doi: 10.1002/app.39695

Fu, P. P, Xia, Q., Hwang, H.-M., Ray, P. C., and Yu, H. (2014). Mechanisms of nanotoxicity: generation of reactive oxygen species. *J. Food Drug Anal.* 22, 64–75. doi: 10.1016/j.jfda.2014.01.005

Ghavimi, S. A. A., Ebrahimzadeh, M. H., Shokrgozar, M. A., Solati-Hashjin, M., and Osman, N. A. A. (2015). Effect of starch content on the biodegradation of polycaprolactone/starch composite for fabricating *in situ* pore-forming scaffolds. *Polym. Test.* 43, 94–102. doi: 10.1016/j.polymertesting.2015.02.012

Gupta, K. K., Kundan, A., Mishra, P. K., Srivastava, P., Mohanty, S., Singh, N. K., et al. (2012). Polycaprolactone composites with TiO_2 for potential nanobiomaterials: tunable properties using different phases. *Phys. Chem. Chem. Phys.* 14, 12844–12853. doi: 10.1039/c2cp41789h

Guz, L., Candal, R., and Goyanes, S. (2017). Size effect of ZnO nanorods on physicochemical properties ofplasticized starch composites. *Carbohydr. Polym.* 157, 1611–1619. doi: 10.1016/j.carbpol.2016.11.041

Huang, M., Yu, J., and Ma, X. (2005). Ethanolamine as a novel plasticizer for thermoplastic starch. *Polym. Degrad. Stab.* 90, 501–507. doi: 10.1016/j.polymdegradstab.2005.04.005

Ilyas, R. A., Sapuan, S. M., Atiqah, A., Ibrahim, R., Abral, H., Ishak, M. R., et al. (2019). Sugar palm (*Arenga pinnata* [Wurmb.] Merr) starch films containing sugar palm nanofibrillated cellulose as reinforcement: water barrier properties. *Polym. Compos.* doi: 10.1002/pc.25379. [Epub ahead of print].

Ilyas, R. A., Sapuan, S. M., Ishak, M. R., and Zainudin, E. S. (2018). Development and characterization of sugar palm nanocrystalline cellulose reinforced sugar palm starch bionanocomposites. *Carbohydr. Polym.* 202, 186–202. doi: 10.1016/j.carbpol.2018.09.002

Javanbakht, S., and Namazi, H. (2017). Solid state photoluminescence thermoplastic starch film containing graphene quantum dots. *Carbohydr. Polym.* 176, 220–226. doi: 10.1016/j.carbpol.2017.08.080

Jorgensen, J. H., and Ferraro, M. J. (2009). Antimicrobial susceptibility testing: a review of general principles and contemporary practices. *Clin. Infect. Dis.* 49, 1749–1755. doi: 10.1086/647952

Kargarzadeh, H., Johar, N., and Ahmad, I. (2017). Starch biocomposite film reinforced by multiscale rice husk fiber. *Compos. Sci. Technol.* 151, 147–155. doi: 10.1016/j.compscitech.2017.08.018

Kelnar, I., Kapralkova, L., Brozova, L., Hromadkova, J., and Kotek, J. (2013). Effect of chitosan on the behaviour of the wheat B-starch nanocomposite. *Ind. Crops Prod.* 46, 186–190. doi: 10.1016/j.indcrop.2013.01.030

Kuswandi, B. (2017). Environmental friendly food nano-packaging. *Environ. Chem. Lett.* 15, 205–221. doi: 10.1007/s10311-017-0613-7

Li, G., Sarazin, P., and Favis, B. D. (2008). The relationship between starch gelatization and morphology control in melt-processed polymer blends with thermoplastic starch. *Macromol. Chem. Phys.* 209, 991–1002. doi: 10.1002/macp.200700637

Liu, G., Gu, Z., Hong, Y., Cheng, L., and Li, C. (2017). Electrospun starch nanofibres: recent advances, challenges, and strategies for potential pharmaceutical applications. *J. Controlled Release* 252, 95–107. doi: 10.1016/j.jconrel.2017.03.016

Liu, S., Li, X., Chen, L., Li, L., Li, B., and Zhu, J. (2017). Understanding physicochemical properties changes from multi-scale structures of starch/CNT nanocomposite films, *Int. J. Biol. Macromol.* 104, 1330–1337. doi: 10.1016/j.ijbiomac.2017.05.174

Liu, Y. X., Fan, L. L., Mo, X. Z., Yang, F., and Pang, J. Y. (2018). Effects of nanosilica on retrogradation properties and structures of thermoplastic cassava starch. *J. Appl. Polym. Sci.* 135:45687. doi: 10.1002/app.45687

Mezger, T. G. (2014). *The Rheology Handbook, 4th Edn.* Hannover: Vincentz Network GmbH.

Mina, J. H., Valadez, A., Herrera-Franco, P. J., and Toledano, T. (2012). Infuence of aging timeon the structural changes of cassava thermoplastic starch. *Mater. Res. Soc. Symp. Proc.* 1372, 21–27. doi: 10.1557/opl.2012.129

Mofokeng, J. P., and Luyt, A. S. (2015a). Morphology and thermal degradation studies of melt-mixed poly(lactic acid) (PLA)/poly(ε-caprolactone) (PCL) biodegradable polymer blend nanocomposites with TiO_2 as filler. *Polym. Test.* 45, 93–100. doi: 10.1016/j.polymertesting.2015.05.007

Mofokeng, J. P., and Luyt, A. S. (2015b). Dynamic mechanical properties of PLA/PHBV, PLA/PCL, PHBV/PCL blends and their nanocomposites with TiO_2 as nanofiller. *Thermochim. Acta* 613, 41–53. doi: 10.1016/j.tca.2015.05.019

Oleyaei, S. A., Almasi, H., Ghanbarzadeh, B., and Moayedi, A. A. (2016a). Synergistic reinforcing effect of TiO_2 and montmorillonite on potato starch nanocomposite films: thermal, mechanical and barrier properties. *Carbohydr. Polym.* 152, 253–262. doi: 10.1016/j.carbpol.2016.07.040

Oleyaei, S. A., Zahedi, Y., Ghanbarzadeh, B., and Moayedi, A. A. (2016b). Modification of physicochemical and thermal properties of starch films by incorporation of TiO_2 nanoparticles. *Int. J. Biol. Macromol.* 89, 256–264. doi: 10.1016/j.ijbiomac.2016.04.078

Olivato, J. B., Marini, J., Yamashita, F., Pollet, E., Grossmann, M. V. E., and Averous, L. (2017). sepiolite as a promising nanoclay for nano-biocomposites based on starch and biodegradable polyester. *Mater. Sci. Eng. C* 70:296302. doi: 10.1016/j.msec.2016.08.077

Ostafinska, A., Fortelny, I., Nevoralova, M., Hodan, J., Kredatusova, J., and Slouf, M. (2015). Synergistic effects in mechanical properties of PLA/PCL blends with optimized composition, processing, and morphology. *RSC Adv.* 5, 98971–98982. doi: 10.1039/C5RA21178F

Ostafinska, A., Mikesova, J., Krejcikova, S., Nevoralova, M., Sturcova, A., Zhigunov, A., et al. (2017). Thermoplastic starch composites with TiO_2 particles: preparation, morphology, rheology and mechanical properties. *Int. J. Biol. Macromol.* 101, 273–282. doi: 10.1016/j.ijbiomac.2017.03.104

Pelissari, F. M., Andrade-Mahecha, M. M., Amaral Sobral, P. J., and Menegalli, F. C. (2017). Nanocomposites based on banana starch reinforced with cellulose nanofibers isolated from banana peels. *J. Colloid Interface Sci.* 505, 154–167. doi: 10.1016/j.jcis.2017.05.106

Pushpadass, H., Marx, D. B., and Hanna, M. A. (2008). Effects of extrusion temperature and plasticizers on the physical and functional properties of starch films. *Starch* 60, 527–538. doi: 10.1002/star.200800713

Rappenecker, G., and Zugenmaier, P. (1981). Detailed refinement of the crystal structure of Vh-amylose. *Carbohydr. Res.* 89, 11–19. doi: 10.1016/S0008-6215(00)85225-8

Razali, S. M., Yusoff, M., Ramle, S. F. M., Bhat, I. U. H., Iman, A. H. M., and Razali, A. M. H. (2016). The potential of *Donax grandis* hypodermal fiber as a reinforcement in starch-based composite. *J. Polym. Mater.* 33, 677–684.

Ross-Murphy, S. B. (1995). Structure-property relationships in food biopolymer gels and solutions. *J. Rheol.* 39, 1451–1463. doi: 10.1122/1.550610

Saiah, R., Gatin, R., and Sreekumar, P. A. (2012). "Properties and biodegradation nature of thermoplastic starch," in *Thermoplastic Elastomers*, ed A. El-Sonbati (London: InTech), 57–78. doi: 10.5772/35348

Sarka, E., and Dvoracek, V. (2017). New processing and applications of waxy starch (a review). *J. Food Eng.* 206, 77–87. doi: 10.1016/j.jfoodeng.2017.03.006

Sarka, E., Krulis, Z., Kotek, J., Ruzek, K. A., Bubnik, Z., and Ruzkova, M. (2011). Application of wheat B-starch in biodegradable plastic materials. *Czech J. Food Sci.* 29, 232–242. doi: 10.17221/292/2010-CJFS

Sarka, E., Krulis, Z., Kotek, J., Ruzek, L., Vorisek, K., Kolacek, K., et al. (2012). Composites containing acetylated wheat B-starch for agriculture applications. *Plant Soil Environ.* 58, 354–359. doi: 10.17221/287/2012-PSE

Schwalbe, R., Steele-Moore, L., and Goodwin, A. C. (2007). *Antimicrobial Susceptibility Testing Protocols*. Boca Raton, FL: CRC Press, Taylor & Francis Group. doi: 10.1201/9781420014495

Sedlarik, V. (2013). *Antimicrobial Modifications of Polymers, Biodegradation*. Rolando Chamy and Francisca Rosenkranz, IntechOpen. Available online at: https://www.intechopen.com/books/biodegradation-life-of-science/antimicrobial-modifications-of-polymers

Sengottuvelan, A., Balasubramanian, P., Will, J., and Boccaccini, A. R. (2017). Bioactivation of titanium dioxide scaffolds by ALP-functionalization. *Bioact. Mater.* 2, 108–115. doi: 10.1016/j.bioactmat.2017.02.004

Sessini, V., Arriera, M. P., Fernandez-Torres, A., and Peponi, L. (2018). Humidity-activated shape memory effect on plasticized starch-based biomaterials. *Carbohydr. Polym.* 179, 93–99. doi: 10.1016/j.carbpol.2017.09.070

Slouf, M., Krulis, Z., Ostafinska, A., Nevoralova, M., Krejcikova, S., Horak, et al. (2017). *Polymerní Termoplastická Biodegradovatelná Kompozice pro Výrobu Vložek k Léčení a Prevenci Lokálních Infektu a Zpusob Její Prípravy*. Czech Patent CZ 307056. Prague: Czech Patent and Trademark Office.

Soest, J. J. G., Hulleman, S. H. D., de Wit, D., and Vliegenthart, J. (1996). Crystallinity in starchbioplastics. *Ind. Crops Prod.* 5, 11–22. doi: 10.1016/0926-6690(95)00048-8

Svagan, A. J., Hedenqvist, M. S., and Berglund, I. (2009). Reduced water vapour sorption in cellulose nanocomposites with starch matrix. *Compos. Sci. Technol.* 69, 500–506. doi: 10.1016/j.compscitech.2008.11.016

Tamjid, E., Bagheri, R., Vossoughi, M., and Simchi, A. (2011). Effect of TiO_2 morphology on *in vitro* bioactivity of polycaprolactone/TiO_2 nanocomposites. *Mater. Lett.* 65, 2530–2533. doi: 10.1016/j.matlet.2011.05.037

Vackova, T., Kratochvil, J., Ostafinska, A., Krejcikova, S., Nevoralova, M., and Slouf, M. (2017). Morphology, crystallization kinetics and rheology of PCL composites with TiO_2-based nanoparticles. *Polym. Bull.* 74, 445–464. doi: 10.1007/s00289-016-1723-2

Viguie, J., Molina-Boisseau, S., and Dufresne, A. (2007). Processing and characterization of waxy maize starch films plasticized by sorbitol and reinforced with starch nanocrystals. *Macromol. Biosci.* 7, 1206–1216. doi: 10.1002/mabi.200700136

Visakh, P. M., Mathew, P. A., Oksman, K., and Thomas, S. (2012). "Starch-basedbionanocomposites: processing and properties," in *Polysaccharide Building Blocks: A Sustainable Approach to the Developmentof Renowable Biomaterials*, eds Y. Habibi and L. A. Lucia (Hoboken, NJ: John Wiley & Sons, Inc.), 287–306. doi: 10.1002/9781118229484.ch11

Wang, S., Li, C., Copeland, L., Niu, Q., and Wang, S. (2015). Starch retrogradation: a comprehensive review. *Compr. Rev. Food. Sci. Food Saf.* 14, 568–585. doi: 10.1111/1541-4337.12143

Warren, F. J., Gidley, M. J., and Flanagan, B. M. (2016). Infrared spectroscopy as a tool to characterise starch ordered structure—a joint FTIR–ATR, NMR, XRD and DSC study. *Carbohydr. Polym.* 139, 35–42. doi: 10.1016/j.carbpol.2015.11.066

Webster, J., Ergun, C., Doremus, R. H., Siegel, R. W., and Bizios, R. (2000). Enhanced functions of osteoblasts on nanophase ceramics. *Biomaterials* 21, 1803–1810. doi: 10.1016/S0142-9612(00)00075-2

Webster, J., Siegel, W., and Bizios, R. (1999). Osteoblast adhesion on nanophase ceramics. *Biomaterials* 20, 1221–1227. doi: 10.1016/S0142-9612(99)00020-4

Wojdyr, M. (2010). Fityk: a general-purpose peak fitting program. *J. Appl. Cryst.* 43, 1126–1128. doi: 10.1107/S0021889810030499

Xie, F., Halley, P. J., and Averous, L. (2012). Rheology to understand and optimize processibility, structures and properties of starch polymeric materials. *Prog. Polym. Sci.* 37, 595–623. doi: 10.1016/j.progpolymsci.2011.07.002

Xie, F., Pollet, E., Halley, P. J., and Averous, L. (2013). Starch-based nano-biocomposites. *Prog. Polym. Sci.* 38, 1590–1628. doi: 10.1016/j.progpolymsci.2013.05.002

Yu, Q., Wang, H., Peng, Q., Li, Y., Liu, Z., and Li, M. (2017). Different toxicity of anatase and rutile TiO_2 nanoparticles on macrophages: Involvement of difference in affinity to proteins and phospholipids. *J. Hazard. Mater.* 335, 125–134. doi: 10.1016/j.jhazmat.2017.04.026

Yun, Y.-H., Youn, Y.-N., Yoon, S.-D., and Lee, J.-U. (2012). Preparation and physical properties of starch-based nanocomposite films with the addition of titanium oxide nanoparticles. *J. Ceram. Process. Res.* 13, 59–64.

Zobel, H. F., French, A. D., and Hinckle, M. E. (1967). X-Ray diffraction of oriented amylose fibers. II. Structure of V amylose. *Biopolymers* 5, 837–845. doi: 10.1002/bip.1967.360050906

Valorization of Food Industries Wastes for the Production of Poly(vinyl) Alcohol (PVA) Biodegradable Composites

Francesca Ferrari, Raffaella Striani, Carola Esposito Corcione* and Antonio Greco

Department of Engineering for Innovation, University of Salento, Lecce, Italy

This work is aimed to the development of new green composite materials by the incorporation of natural additives into poly(vinyl) alcohol (PVA). Two additives, shredded walnut shells and organic fraction of municipal solid waste (MW), were used to improve the mechanical properties of PVA. Both additives, derived from food industry wastes, were added in a PVA/water solution, which allowed to produce samples by the use of a pressure free process. Rheological analysis was performed in order to study the evolution of the material viscosity during thermal treatment, aimed at water removal. Samples obtained were characterized by means of differential scanning calorimetry (DSC), showing an improvement of the glass transition temperature brought by the addition of walnut shells. Finally, flexural tests were carried out on samples obtained after the incorporation of the different additives in PVA and compared with the mechanical properties of the neat matrix. Results obtained indicate the potential improvement brought by the addition of walnut shells, which allows increasing the flexural modulus of about 50%, at the expenses of a flexural strength reduction of about 30%. Also, at least for low amount of added water, the addition of MW was shown to provide an increase of the strain at break equal to 100%.

Keywords: poly(vinyl) alcohol, mechanical properties, water content, organic waste, rheological properties

INTRODUCTION

Poly(vinyl) alcohol (PVA) is a non-toxic, water soluble thermoplastic polymer obtained from the hydrolysis in ethanol of poly(vinyl) acetate. Unlike other polymers, which were produced starting by their monomer, PVA is obtained by the ester interchange with methanol of acetate groups in presence of anhydrous sodium methylate or aqueous sodium hydroxide (Saxena, 2004). Because of its non-toxic nature, PVA is employed since the first years of twentieth century for food packaging and medical disposals (DeMerlis and Schoneker, 2003). Also, due to its high biodegradability, PVA is often mixed with other biopolymers for the production of hydrophilic films, or in order to improve the mechanical response of the material (Limpan et al., 2012). As reported in PVA MSDS, the product is not classified as environmentally hazardous, and is characterized by very low eco toxicity toward different micro-organisms.

Because of its high solubility, PVA can be easily processed at low temperatures, through the addition of water, which brings a liquid solution, at relatively high concentrations of PVA, characterized by very low viscosity (Gaaz et al., 2015). In addition, PVA is characterized by very

low cost and low gas permeability toward oxygen and carbon anhydride. Moreover, PVA can be added to fiber reinforced composites in order to improve the fiber- matrix interfacial properties, through the development of strong bonds between its hydroxyl groups and the functionalized fillers (Mallakpour et al., 2014; Shang et al., 2015).

Despite its good behavior in terms of easy processing, low cost and high permeability, PVA lacks adequate mechanical properties in different lading conditions (Stammen et al., 2001): therefore, many studies were carried out on PVA in order to improve its mechanical properties, through the addition of different fillers. As an example, Abdullah and Dong (2019) showed that water absorption capacity and water solubility of nanocomposite films were decreased remarkably by 44.24 and 48.05%, respectively, with increasing the halloysite nanotube (HNT) content from 0 to 5 wt% when compared with those of biopolymer matrices. However, they did not performed mechanical charcaterizations of the PVA based composiets. On the other hand, Cadek et al. (2002) added multiwall carbon nanotubes in different amounts to PVA, increasing stiffness and hardness of the polymer. In details, it was found that, by adding various concentrations of nanotubes, both Young's modulus and hardness increased by factors of 1.8 and 1.6 at 1 wt% in PVA and 2.8 and 2.0 at 8 wt% in PVA (Cadek et al., 2002). Other studies were focused on the addition of fully exfoliated graphene oxide (GO) sheets and multi-walled carbon nanotubes (CNTs), thus obtaining a significant improvement in mechanical properties if compared to neat PVA films. In particular, it was shown that the yield strength and Young's modulus of GO–CNT/PVA composite films with 1 wt% GO and 0.5 wt% CNT have increased by 48 and 31%, respectively if compared to neat PVA (Li et al., 2011).

Alternatively, the production of bio-composites requires the addition of natural fillers or fibers, thus avoiding problems related to safety and toxicological impact, still preserving the excellent water solubility and biodegradability of PVA. Therefore, several studies were performed on the addition of naturally-derived reinforcements to PVA matrix.

Biodegradable cornstarch/PVA blends were prepared and characterized by many authors. The produced blends are characterized by a high hydrophilicity and poor mechanical properties, which, however, can be significantly improved by the methylation of cornstarch, as reported by Guohua et al. (2006).

Addition of methylcellulose (MC) was shown to improve the tensile strength of about 20% (Park et al., 2001). Furthermore, PVA nanocomposites were produced by adding Bamboo Charcoal (BC) nanoparticles via solution casting. Authors found an increase of lamellar size of PVA by the incorporation of BC, which in turns allowed for significant improvement in tensile strength and elastic modulus (Mohanad and Dong, 2018). In details, the incorporation of BC nanoparticles enhanced the elastic moduli of both crystalline and amorphous phases of PVA by ∼51 and ∼100%, respectively (Mohanad and Dong, 2018).

On the other hand, the possibility to reinforce PVA by means of food wastes was not yet fully investigated. The food waste recycling for this application assumes a primary importance, since it allows both the reinforcement of a matrix and the increase of the efficiency of waste management with the reduction of its negative effects on the environment and on population. This work was therefore aimed to the improvement of PVA mechanical properties by the addition
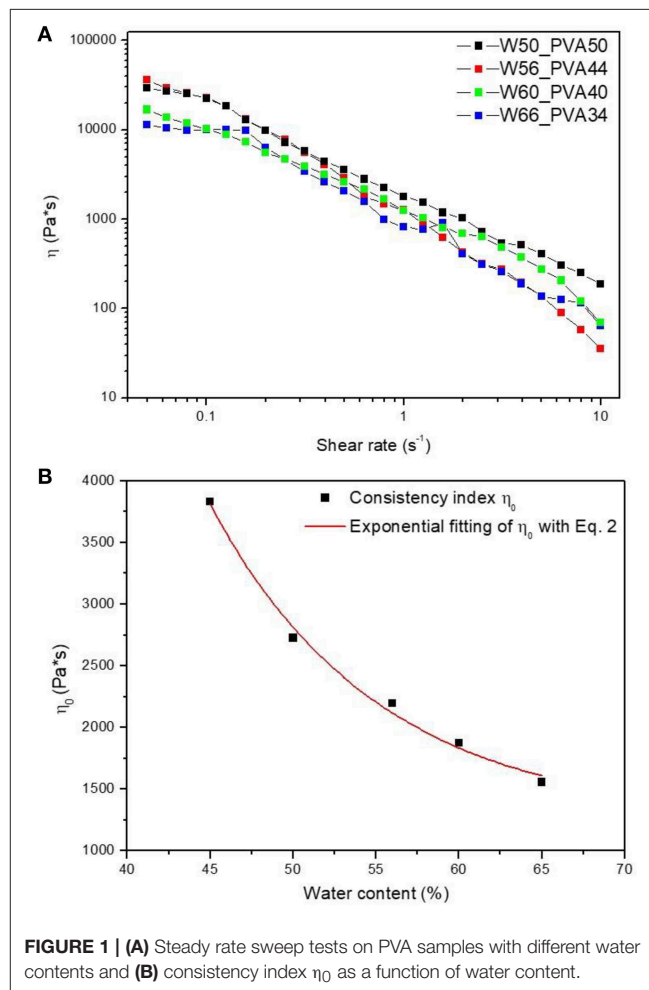
FIGURE 1 | (A) Steady rate sweep tests on PVA samples with different water contents and **(B)** consistency index η_0 as a function of water content.

TABLE 1 | Compositions of all the produced formulations.

Formulation	Water (%)	PVA (%)	Walnut shells (WS) (%)	Organic fraction of municipal solid waste (MW) (%)
W50_PVA50	50	50	0	0
W56_PVA44	56	44	0	0
W60_PVA40	60	40	0	0
W66_PVA34	66	34	0	0
W50_PVA25_WS25	50	25	25	0
W56_PVA22_WS22	56	22	22	0
W60_PVA20_WS20	60	20	20	0
W66_PVA17_WS17	66	17	17	0
W50_PVA25_MW25	50	25	0	25
W56_PVA22_MW22	56	22	0	22
W60_PVA20_MW20	60	20	0	20
W66_PVA17_MW17	66	17	0	17

of natural fillers derived from selected food waste of from the organic fraction of municipal solid waste (MW). The PVA blends obtained, characterized by a very high loading of natural fillers, where analyzed in terms of mechanical and thermal properties.

MATERIALS AND METHODS

The PVA used in this work is Kuraray Poval 3–85, a partially saponified grade of poly(vinyl) alcohol, supplied as fine powder/granules with a bulk density of 0.4–0.6 gcm^{-3}, a degree of hydrolysis of 84.2–86.2 mol% and a viscosity in a 4% aqueous solution of 3.4–4.0 mPa*s at 20°C. Walnut shells (WS) and organic fraction of municipal solid waste (MW) were obtained by the recycling of food industry. In order to accurately control the amount of water of the blends, all the fillers were completely dried before being mixed with water and PVA.

Afterwards, mixtures of PVA and different additives (**Table 1**) were produced by varying the water content between 50 and 65% in weight, keeping a constant ratio 1:1 (in weight) between PVA and the fillers (**Table 1**).

After mechanical mixing for 10 min at 60 rpm in a Haake Rheocord mixer at room temperature, all the mixtures were degassed and then poured *in silicon* molds and then kept in oven at 70°C. Samples were extracted from the oven after complete evaporation of the water, which was taken as the time necessary for two successive weighting in time intervals of 24 h differ

<0.1%. For comparison, mixtures with only PVA and water were also produced.

DSC analysis was performed on a Mettler Toledo 822 (Mettler Toledo, Greifensee, Switzerland) instrument under a nitrogen flux of 60 mL min^{-1}, applying an heating scan from 20 to 180°C, with a heating rate of 10°C/min. All the tested samples had a sample mass of 5 mg.

Rheological analyses were carried out on a Rheometrics Ares rheometer. Steady rate tests were carried out at 70°C varying the shear rate from 0.05 to 1 s^{-1} for viscosity measurement at different amounts of water. Also, dynamic temperature ramp tests were performed on PVA samples, in order to analyze the water evaporation during a heating scan from 25 to 70°C at 3°C/min on a parallel plate geometry, with a gap of 0.3 mm, constant oscillatory amplitude (1%) and frequency (1 Hz).

Flexural tests were performed on 100 × 10 × 3 mm samples, obtained after water evaporation, using a Lloyd LR5K and a crosshead speed of 1.5 mm/min, following the standard ASTM D790-00. Six samples for every composition were tested. Before

TABLE 2 | Fitting parameters of Equation (1) applied to the experimental curves of **Figure 1A** at different water content.

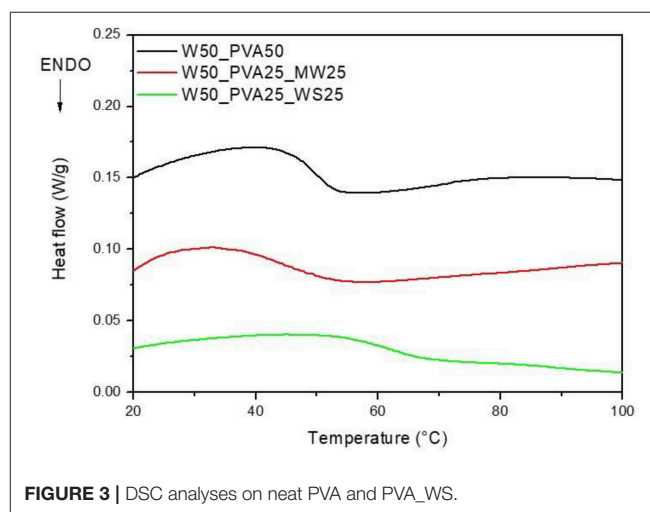| % of water	η_0 (Pa*s)	$n-1$	n
50	2725	−0.83	0.17
56	2196	−0.95	0.05
60	1873	−0.66	0.34
66	1554	−0.80	0.20

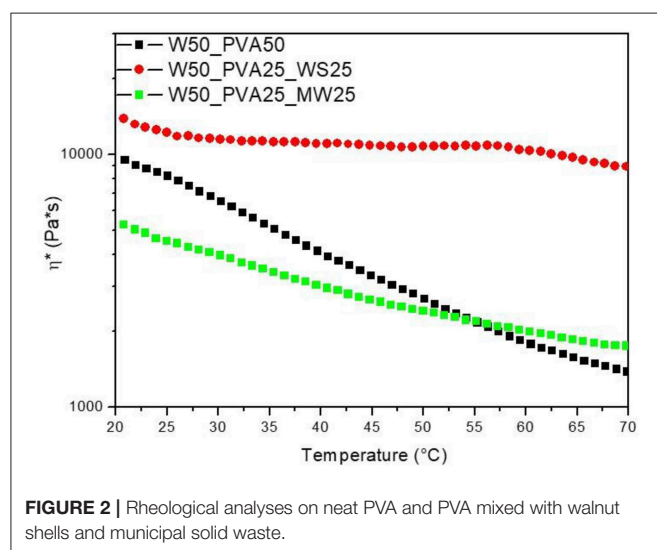**FIGURE 3** | DSC analyses on neat PVA and PVA_WS.

FIGURE 2 | Rheological analyses on neat PVA and PVA mixed with walnut shells and municipal solid waste.
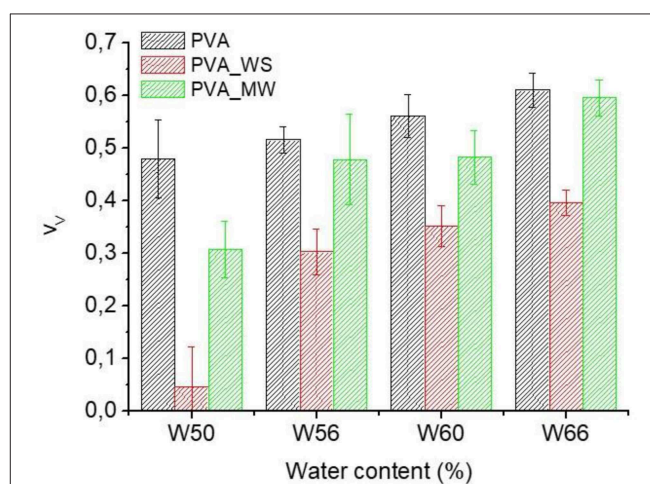

FIGURE 4 | Void fraction for PVA samples (v_V) with different amounts of water.

testing, samples were kept for 24 h at 70°C in order to allow complete water evaporation. Finally, an optical microscope Zeiss AXIO-LINKAM was used for the morphological characterization of the materials. The size of the pores was obtained as an average of 50 measurements.

EXPERIMENTAL RESULTS

Initially, rheological analyses were performed on neat PVA samples with different amount of water, ranging between 50 and 65°C, as reported in **Figure 1A**.

All the samples show a pseudo-plastic behavior, characterized by a viscosity decrease with increasing shear rate. Therefore, by considering a power law correlation between the viscosity and the shear rate:

$$\eta = \eta_0 \dot{\gamma}^{n-1} \tag{1}$$

the consistency index η_0 was calculated by fitting the curves in **Figure 1B**. L'origine riferimento non è stata trovata. (A). All the samples showed a similar qualitative behavior, with consistency index increasing by decreasing the water amount.
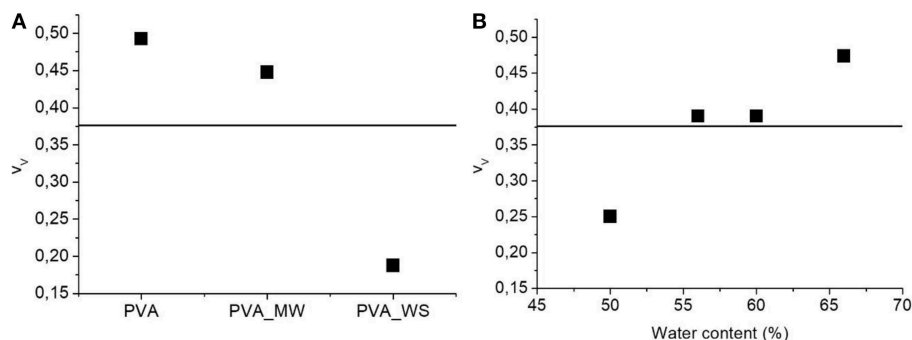
FIGURE 5 | ANOVA results for the void fraction as function of **(A)** type of additive and **(B)** water amount.
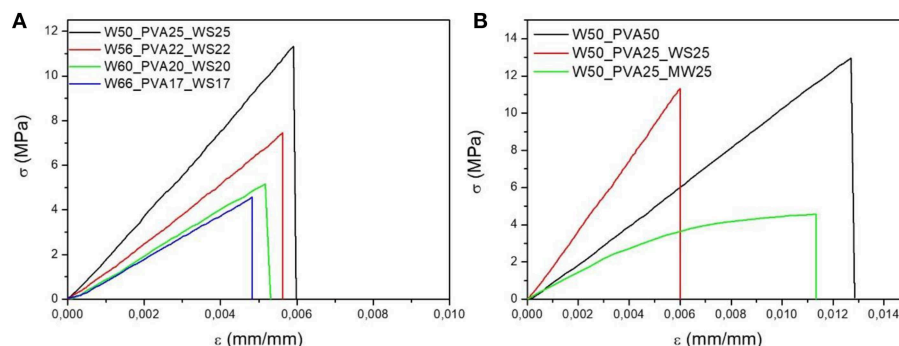
FIGURE 6 | Stress strain curves of PVA mixtures with **(A)** different water content, **(B)** different fillers. The characteristic values of the flexural modulus, strength and strain at break as a function of water content are reported in **Figures 8A–C,** respectively.

FIGURE 7 | ANOVA analysis results: average flexural modulus as a function of: **(A)** type of additive and **(B)** water amount.

Fitting parameters found for curves at different water content are shown in **Table 2**.

Results reported in Errore. L'origine riferimento non è stata trovata. (B) show an exponential decrease of η_0 by increasing water content according to Equation (2):

$$\eta = A_1 exp^{-\frac{wc}{t_1}} + \eta_0 \qquad (2)$$

where, η_0 is the offset (1252.53 Pa*s), A_1 indicates the amplitude (215684.81), wc is the water content and t_1 is the decay constant (10.14).

However, the viscosity evolution during heating was found to be significantly different for the different samples; results reported in **Figure 2** show that, at room temperature, the viscosity of PVA_WS is much higher than that of the two other systems, neat PVA and PVA_MW. This is attribute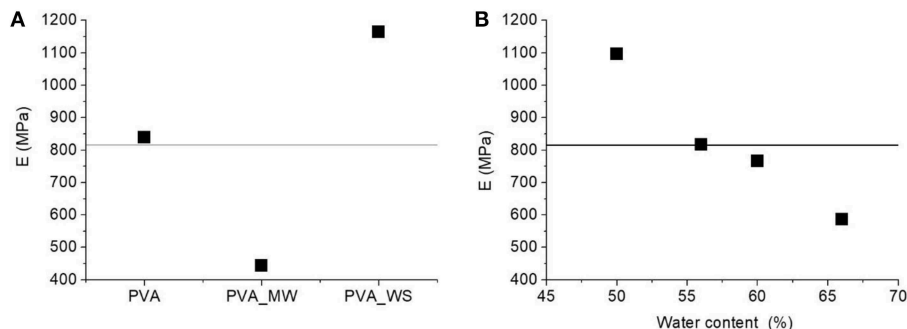d to the water absorption by neat PVA and PVA_MW, in contrast to PVA_WS, which absorbs much lower amounts of water. In turn, this latter result was attributed to the much higher water amounts absorbed by both PVA and MW, compared to WS.

Moreover, as reported in **Figure 2**, PVA shows a marked decrease of viscosity with increasing temperature; such decrease is mainly due to the viscosity decrease of water during heating. At higher temperatures (not shown in **Figure 2**) water evaporation causes a significant increase of the viscosity of PVA sample.

For PVA_MW, the slope of the viscosity curve is reduced, indicating that the effect of water viscosity decrease is counterbalanced by viscosity increase due to water evaporation. For PVA_WS, a further decrease of the slope of the curve indicates that in this sample water evaporation occurs at much lower temperatures compared to the other two samples.

The results of **Figure 2** can be correlated to the affinity between the material and water; for neat PVA, which is water soluble, a complete water adsorption causes a better retention of water during heating. Therefore, water evaporation occurs at much higher temperatures. Upon addition of MW, which is not completely water soluble, but absorbs some water, water release occurs, quite slowly, during heating. For WS, which does not absorb water, water release occurs much faster during the heating stage.

DSC analyses were carried out on neat PVA and PVA_WS samples, in order to evaluate the glass transition temperature (T$_g$) of the mixture. The DSC curves are reported in **Figure 3**.

As shown in **Figure 3**, an increase in Tg from about 49°C to about 61°C was obtained with the addition of walnut shells to PVA. In contrast, no significant change in the glass transition was observed upon addition of MW to PVA.

On the other hand, the development of a pressure-free process for the production of such components poses severe issues related to the void amount in the produced samples. To this purpose, density measurements were performed by using a pycnometer, in order to evaluate the density ρ of the component; afterwards, the

theoretical density ρ_T of each mixture was calculated by using the following equation:

$$\rho_{T=} \rho_{PVA} v_{PVA} + \rho_f v_f \qquad (3)$$

where:

- ρ_f and ρ_{PVA} are the density of the filler (measured to be 0.99 g/cm^3 for the solid waste and 1.50 g/cm^3 for the walnut shells) and PVA (1.19 g/cm^3 from the materials technical data sheet), respectively;
- v_{PVA} and v_f are the volume fraction of PVA and fillers, respectively.

Once the theoretical density was calculated, the adimensional void fraction v_v was estimated as:

$$v_v = 1 - \frac{\rho}{\rho_T} \qquad (4)$$

Where ρ is the measured density of the different samples, obtained as the average of 10 measurements. The void fraction for the produced PVA samples obtained by the use of Equation (4) is reported in **Figure 4**.
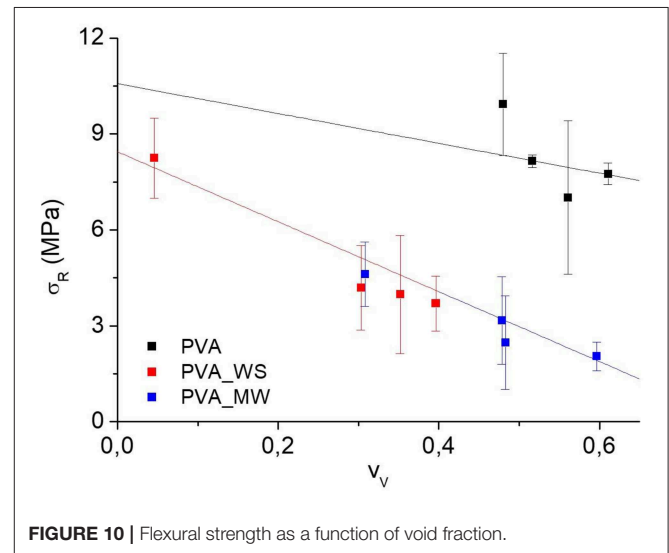
Also in view of the error bars reported in **Figure 4**, two-ways analysis of variance (ANOVA) was performed on the void fraction, considering both the type of additive and the amount of water as the sources of variation. ANOVA results are shown in **Figure 5**.

The p-value calculated for the type of additive is $1.56*10^{-25}$, much lower than the confidence value $p = 0.05$, indicating the relevant effect of the type of additive on the void fraction of the materials. In particular, referring to the average value estimated over the 4 levels of water amount, and reported in **Figure 5A**, the void fraction of PVA is reduced upon addition of MW, and more relevantly, upon addition of WS. Referring to the results of **Figure 2**, the void fraction is strictly correlated to the rate of water release during heating; in facts, for neat PVA, water release is very fast, and occurs during the isothermal step at 70°C; this results in the formation of a highly porous structure, as observed in **Figure 5A**. For PVA_MW, showing an intermediate evaporation rate, occurring at lower temperatures, the resulting void fraction is lower than that of neat PVA. Finally, for PVA_WS, showing a slow rate of evaporation at lower temperatures, the lowest void fraction is observed in **Figure 5**.

The average value of void fraction estimated over the 3 levels of type of additive at each level of water amount is reported in **Figure 5B**, showing a void fraction increase

TABLE 3 | ANOVA analysis results on experimental data of **Figures 8A–C**.

Source	DOF	SS	MS	F	p
Type of additive	2	$5.2*10^6$	$2.6*10^6$	$9.75*10^1$	$1.23*10^{-17}$
Water amount	3	$2.0*10^6$	$6.7*10^5$	$2.51*10^1$	$6.71*10^{-10}$
Error	48	$1.3*10^6$	$2.7*10^4$		
Total	59	$8.8*10^6$			

FIGURE 8 | Flexural modulus **(A)**, flexural strength **(B)**, and strain at break **(C)**, for PVA samples with different amounts of water and a constant 1:1 ratio between PVA and filler.

FIGURE 9 | Flexural modulus as a function of void fraction.

FIGURE 10 | Flexural strength as a function of void fraction.
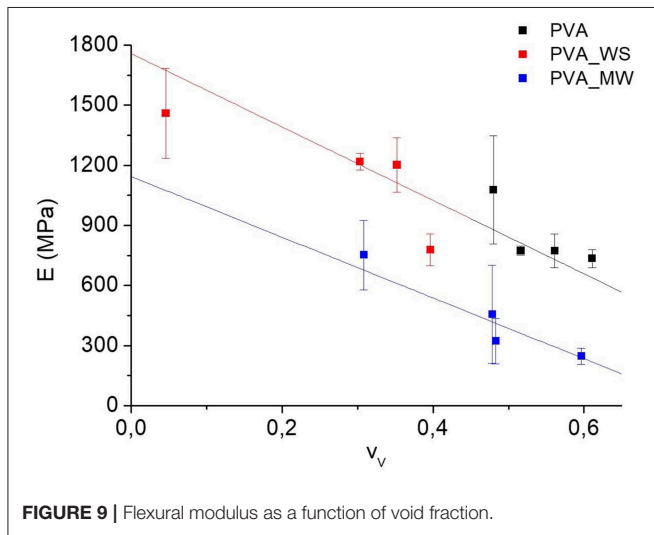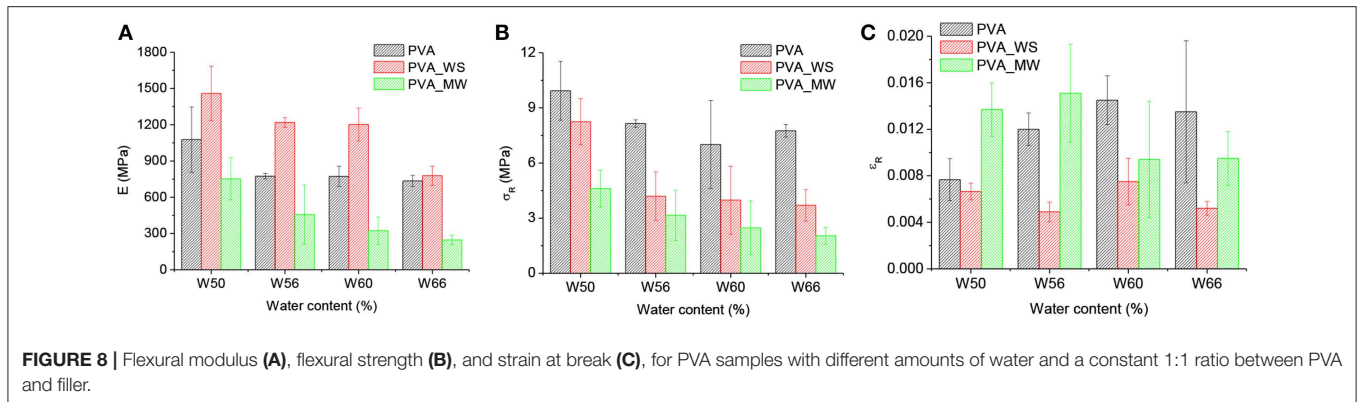
with increasing water amount; also in this case, the behavior can be explained by considering that, with increasing water amount, an higher rate of steam is released during heating, which, being partially entrapped in the sample, causes a higher void fraction.

Flexural tests were carried out on samples with different amounts of water, with and without filler addition, as reported in **Figures 6A,B**, respectively.

Initially, data obtained for the flexural modulus were analyzed by means of two-ways ANOVA, considering the type of additive and water amount as the sources of variation (factors).

The significance of each factor was tested by calculating the F value, as the ratio of the variance between the means to the variance of the experimental error. The F value was then used in order to calculate the corresponding p-value, which was then compared with the confidence level, $\alpha = 0.05$. According to ANOVA, $p > \alpha$, corresponds to the null hypothesis (equivalence of the means), whereas $p < \alpha$ indicates that the population means are significantly different (Montgomery, 2009).

Being A and B the number of levels of Factor 1 and Factor 2, respectively, the effect of each factor

was reported by estimating the Main Effects Averages (MEA) as:

$$\begin{cases} \overline{y_i} = \dfrac{\sum_{j=1}^{B} \sum_{n=1}^{N} y_{ijn}}{NB} & i = 1 \ldots . . A \\[3mm] \overline{y_j} = \dfrac{\sum_{i=1}^{A} \sum_{n=1}^{N} y_{ijn}}{NA} & j = 1 \ldots . . B \end{cases} \tag{5}$$

Being y_{ijn} the n-th replicate obtained at factor level i and j.

The results reported in **Table 3** for the p-values, in each case much lower than $\alpha = 0.05$, indicate the statistically relevant effect of both type of additive and water amount on the flexural modulus.

In particular, for each constant value of water amount, the addition of WS filler involves, an increase of the flexural modulus compared to neat PVA. In contrast, addition of MW results in a modulus decrease. This is highlighted in the ANOVA results reported in **Figure 7A**. Increasing the amount of water involves a decrease of the flexural modulus, as highlighted in **Figure 7B**. However, in this case, the water content has a different effect on the blends obtained with neat PVA, PVA_WS, and PVA_MW. In facts, for neat PVA, as reported in **Figure 7A**, the modulus decreases as the water amount is increased between 50 and 55%,

after which it reaches a plateau value, and a further increase of water amount has no significant influence on the modulus. For the PVA_WS and PVA_MW systems, a continuous decrease of the modulus is observed as the water amount is increased between 50 and 65%.

Also, the results for flexural strength were analyzed by means of ANOVA. In this case, the p-value estimated by considering the type of additive as the source of variation is $p = 1.7*10^{-14}$, which indicates the statistically relevant effect of the type of additive. Referring to the results of **Figure 8B** for each water amount, addition of WS or MW involves a decrease of flexural strength compared to net PVA. The p-value obtained by considering the water amount as the source of variation provides $p = 4.07*10^{-8}$, also indicating, according to the results of **Figure 8B**, a decrease of the strength as the water amount increases. However, the results for flexural strength, reported in **Figure 8B**, show that, as previously observed for the modulus, the strength of neat PVA decreases as the water amount is increased from 50 to 56%, but above this value further water amount increase does not involve any significant change in flexural strength. In contrast, for PVA_WS and PVA_MW, the strength continuously decreases as the water amount increases.

ANOVA performed on the strain at break, considering the type of additive as the source of variation, provides $p = 2.27*10^{-7}$, which confirms, according to the results of **Figure 8C**, that the strain at break of PVA_WS is statistically lower than that of PVA and PVA_MW. On the other hand, when considering the water amount of the source of variation, $p = 0.6$ indicates that the effect of the water amount is not statistically significant.

In view of the results reported in **Figures 4, 8**, the flexural modulus was plotted as a function of the void fraction, and the results are reported in **Figure 9**. Here, the strong correlation between modulus and void fraction can be observed.

Based on the correlation between flexural modulus and void fraction reported in **Figure 9**, the evolution of the flexural modulus or strength as a function of the void fraction can be expressed, by considering that the latter is a function of the type of additive and water amount:

$$P = P\left(v_V\left(AD, W\right)\right) \tag{6}$$

Therefore, a variation in the materials properties as a function of void fraction can be explained by considering the differential form of Equation (5):

$$\frac{dP}{dv_V} = \frac{\partial P}{\partial W}\frac{dW}{dv_V} + \frac{\partial P}{\partial AD}\frac{dAD}{dv_V} \tag{7}$$

According to Equation (6), the evolution of a property as a function of the void fraction can be explained by considering the dependence of the property on the amount of water ($\frac{\partial P}{\partial W}$) or on the type of additive ($\frac{\partial P}{\partial AD}$). This is because, in any case, as previously discussed in **Figure 4**, $\frac{dW}{dv_V}$ and $\frac{dAD}{dv_V}$ are both different from 0.

According to the results of **Figure 9**, linear fit shows that the data of PVA and PVA_WS fall on a single master curve. According to Equation (5), this indicates that the term $\frac{\partial P}{\partial AD}$ is null. Therefore, there is no direct dependence of the flexural modulus on the type of additive; instead the type of additive influences the void fraction, which in turn has a significant effect on the flexural modulus. This means, according to the results of **Figure 9**, that, for the same value of the void fraction, there is no significant difference between the samples PVA and PVA_WS. The situation when considering the PVA_MW is different; in this case, the data do not fall on a single master curve, and therefore the evolution of the flexural modulus can only be explained by considering also the term $\frac{\partial P}{\partial AD}$, indicating that, for the same void fraction, the modulus of PVA_MW is lower than that of PVA and PVA_WS.

The situation is quite different when considering the curves for flexural strength vs. void fraction, reported in **Figure 10**. In this case, the data for PVA_WS and PVA_MW fall on a single master curve. This indicates that the effect of adding WS of MW has no direct influence on the flexural strength; instead, different additives have a different effect on the void fraction, which in

TABLE 4 | Average pore diameter of PVA samples.

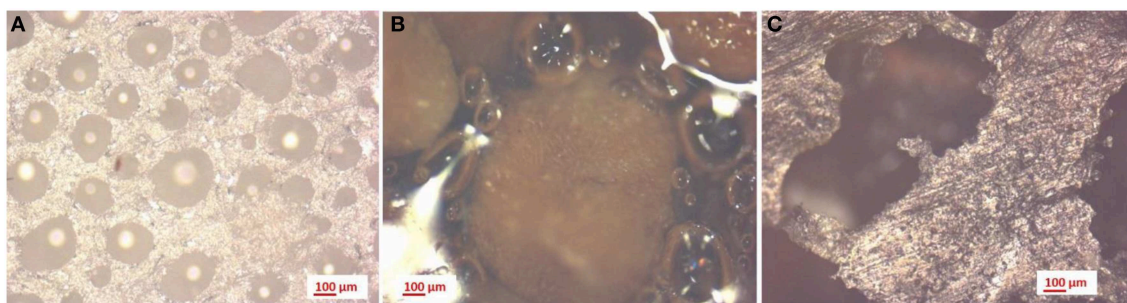|	Neat PVA	PVA_WS	PVA_MW
Average pore diameter (mm)	0.44 ± 0.08	0.20 ± 0.07	1.95 ± 0.7

FIGURE 11 | 50x magnification on PVA samples: **(A)** without additives, **(B)** with walnut shells, and **(C)** with mixed waste.

turn involves a change in the flexural strength. Therefore, for the same value of the void fraction, the flexural strength of samples PVA_WS and PVA_MW is not significantly different. In this case, the data of neat PVA do not fall on the same master curve, which again can be explained by considering the term $\frac{\partial P}{\partial AD}$ being different from zero. In this case, for the same void fraction, the flexural strength of PVA is higher than that of PVA_WS and PVA_MW.

Figure 11 shows the microscopic images of neat PVA samples (Figure 11A), PVA with walnut shells (Figure 11B) and organic fraction of municipal solid waste (Figure 11C), obtained with a 50X magnification. As reported in Table 4, the average dimension of the pores decreases with the addition of walnut shells on PVA. On the other hand, the addition of MW involved a strong increase in the pore dimension.

CONCLUSIONS

This work was focused on the reinforcement of PVA by the addition of natural fillers, derived from food industry wastes. In particular, the effect of a selected waste (walnut shells) and the organic fraction of municipal solid waste on PVA properties was explored. PVA samples, with and without filler addition, were produced by the use of a pressure free process, taking advantage of the water solubility of PVA.

The evolution of viscosity was then studied by rheological analysis. Although a decrease in viscosity with the increase in water content was found for all the samples, higher viscosities were achieved with PVA with walnut shells, due to its lower absorption of water. This in turn caused water release during the heating stage to occur at much lower temperatures. The release rate of water was found to deeply affect the porosity of the sample. In facts, a lower adsorption of water, causing water evaporation at lower temperatures, was found to have a beneficial effect on the reduction of porosity. Therefore, addition of food wastes caused a decrease of void fraction compared to neat PVA; however, the effect was more relevant for WS compared to MW.

The presence of voids significantly affected the mechanical response of the material. A decrease in modulus and flexural strength was detected by increasing water content, regardless of the additive addition. Furthermore, due to the lower amount of voids, PVA_WS showed an increase in stiffness compared to neat PVA. In contrast, addition of MW caused a stiffness decrease compared to neat PVA. However, this was balanced, at least for low amounts of water, by an increase of the ductility brought by the addition of MW. On the other hand, both additives caused a significant decrease of flexural strength compared to neat PVA. The experimental results obtained for PVA_WS show the potential of the developed approach for the production of PVA samples characterized by higher stiffness compared to neat PVA, as well a cost reduction and increase of the efficiency of waste management, with the reduction of its negative effects on the environment and on population.

DATA AVAILABILITY

The datasets generated for this study are available on request to the corresponding author.

AUTHOR CONTRIBUTIONS

FF and RS performed the experimental measurements. CE and AG supervised the activities.

REFERENCES

Abdullah, Z. W., and Dong, Y. (2019). Biodegradable and water resistant poly(vinyl) alcohol (PVA)/starch (ST)/halloysite nanotube (HNT) nanocomposite films for sustainable food packaging. *Front. Mater.* 6:58. doi: 10.3389/fmats.2019.00058

Cadek, M., Coleman, J. N., and Barron, V. (2002). Morphological and mechanical properties of carbon-nanotube-reinforced semicrystalline and amorphous polymer composites. *Appl. Phys. Lett.* 81:5123. doi: 10.1063/1.1533118

DeMerlis, C. C., and Schoneker, D. R. (2003). Review of the oral toxicity of polyvinyl alcohol (PVA). *Food Chem. Toxicol.* 41, 319–326. doi: 10.1016/S0278-6915(02)00258-2

Gaaz, T. S., Sulong, A. B., Akhtar, M. N., Kadhum, A. A., Mohamad, A. B., and Al-Amiery, A. A. (2015). Properties and applications of polyvinyl alcohol, halloysite nanotubes and their nanocomposites. *Molecules* 20, 22833–22847. doi: 10.3390/molecules201219884

Guohua, Z., Ya, L., Cuilan, F., Min, Z., Caiqiong, Z., and Zongdao, C. (2006). Water resistance, mechanical properties and biodegradability of methylated-cornstarch/poly(vinyl alcohol) blend film. *Polym. Degrad. Stab.* 91, 703–711. doi: 10.1016/j.polymdegradstab.2005.06.008

Li, Y., Yang, T., Yu, T., Zheng, L., and Liao, K. (2011). Synergistic effect of hybrid carbon nantube–graphene oxide as a nanofiller in enhancing the mechanical properties of PVA composites. *J. Mater. Chem.* 21, 10844–10851. doi: 10.1039/c1jm11359c

Limpan, N., Prodpran, T., Benjakul, S., and Prasarpran, S. (2012). Influences of degree of hydrolysis and molecular weight of poly (vinyl alcohol)(PVA) on properties of fish myofibrillar protein/PVA blend films. *Food Hydrocoll.* 29, 226–233. doi: 10.1016/j.foodhyd.2012.03.007

Mallakpour, S., Abdolmaleki, A., and Borandeh, S. (2014). l-Phenylalanine amino acid functionalized multi walled carbon nanotube (MWCNT) as a reinforced filler for improving mechanical and morphological properties of poly(vinyl alcohol)/MWCNT composite. *Prog. Org. Coat.* 77, 1966–1971. doi: 10.1016/j.porgcoat.2014.07.005

Mohanad, M., and Dong, Y. G. (2018). Elastic behavior of nanophases in polyvinyl alcohol (PVA)/bamboo charcoal (BC) nanocomposite films. *Front. Mater.* 5:44. doi: 10.3389/fmats.2018.00044

Montgomery, D. C. (2009). *Introduction to Statistical Quality Control*, 6th Edn. Hoboken, NJ: John Wiley and Sons.

Park, J.-S., Park, J.-W., and Ruckenstein, E. (2001). Thermal, and dynamic mechanical analysis of PVA/MC blend

hydrogels. *Polymer* 42, 4271–4280. doi: 10.1016/S0032-3861(00)00768-0

Saxena, S. K. (2004). *Polyvinyl Alcohol (PVA) Chemical and Technical Assessment (CTA)*. FAO.

Shang, S., Gan, L., Yuen, C. W. M., Jiang, S., and Luo, N. M. (2015). The synthesis of graphene nanoribbon and its reinforcing effect on poly(vinyl alcohol). *Compos. Part Appl. Sci. Manuf.* 68, 149–154. doi: 10.1016/j.compositesa.2014.10.011

Stammen, J. A., Williams, S., Ku, D. N., and Guldberg, R. E. (2001). Mechanical properties of a novel PVA hydrogel in shear and unconfined compression. *Biomaterials* 22, 799–806. doi: 10.1016/S0142-9612(00)00242-8

Valorization of Tomato Processing Residues Through the Production of Active Bio-Composites for Packaging Applications

Valeria Bugatti[1,2], Paola Brachi[3], Gianluca Viscusi[1] and Giuliana Gorrasi[1]*

[1] Department of Industrial Engineering, University of Salerno, Fisciano, Italy, [2] Nice Filler s.r.l., Naples, Italy, [3] National Research Council, Institute for Research on Combustion, Naples, Italy

The present work reports a study aimed at investigating the recovery and the upgrade of tomato processing residues through the preparation of innovative green composites based on tomato peels (TPs) and natural halloysite nanotubes (HNTs) loaded with carvacrol, as a natural antibacterial agent. The loading of carvacrol into HNTs was successfully achieved through a simple procedure that does not involve any chemical modifications of HNTs. Composite films with different amount of HNTs (i.e., 2.5, 5, 10, 20%wt) were prepared using mechanical milling in presence of water, followed by solvent casting method. The structural organization and the main physical properties of the obtained bio-based active composites have been deeply investigated. In particular, thermal and mechanical properties along with the films' interaction with water vapor were assessed and then correlated to the filler loading. Results show that the thermal behaviour of bio-composites improves with the filler loading. Conversely, the mechanical properties get worse, especially at higher loading, due to the poor interaction between HNTs and matrix. The presence of hydrophilic HNTs was found to not dramatically increase the degree of hydrophilicity of the of the materials, most likely due to the presence of hydrophobic carvacrol that acts as an hydrophobic coating for HNTs. The release of carvacrol was also analyzed. Results show that the obtained composites exhibit a long-term release of the antimicrobial agent, which suggests them to be promising candidate materials for food packaging application.

Keywords: tomato peels, halloysite, green composites, carvacrol, packaging

INTRODUCTION

The concern of the society about environmental issues and sustainability has increased greatly over the last decades. The replacement of fossil fuels with renewable biomass and bio-wastes as raw feedstocks, for the production of bio-chemicals and bio-materials, is an interesting option to respond to these concerns (Brachi et al., 2014).

Food packaging is currently one of the major source of plastic wastes (Kirwan and Strawbridge, 2003). The largest fraction of the materials used in the packaging industry comes from fossil fuels and is non-degradable, thus representing a serious environmental issue worldwide. The demand for the more eco-friendly and sustainable films and/or coatings for effective food packaging has, therefore, generated considerable interest in recent years. In particular, the development of new bio-materials from largely available and cheap residual biomass resources, such as agro-industrial residues, to produce green/edible packaging manufactures that meet aesthetic, mechanical and barrier requirements for food applications is one of the major challenges currently facing scientists

and technologists from different areas of expertise (Zhiguo et al., 2015; Eghbal and Choudhary, 2018; Kam et al., 2018). Edible packaging materials are, in fact, not just biodegradable in nature, thus avoiding the environmental damage and concerns about their disposal (Giosafatto et al., 2014a,b), but also have the characteristic of being eaten along with the food they contain, thereby offering greater opportunities for commercial application. For example, green films based on proteins and/or polysaccharides can be filled with a wide range of functional additives, thus acting as carriers for antioxidants, antimicrobials, flavoring agents, colorants and vitamins in more specific applications (Gorrasi et al., 2012; Gorrasi and Bugatti, 2016; Saha et al., 2016; Silva et al., 2016).

Tomato (*Lycopersicon esculentum*) represents the second most diffused vegetable crop worldwide, next to potato (Brachi et al., 2016a,b). Each year about 150 million tons are produced and consumed, and 40 million are processed products (i.e., peeled or unpeeled, tomato paste, whole or un-whole tomatoes) (Tomato News, 2014). The tomato processing typically generates two residual fractions, which compose 3–5 wt% of the whole tomato: (i) tomato peels, that is the byproduct of the peeling of tomatoes used for canning and (ii) tomato pomace that is a mixture crushed seeds, tomato peels and a small residue of pulp remaining after the processing for soup, juice or ketchup (Al Khraisat, 2015). Such wastes, due to the high organic content molecules (carbohydrates, proteins, fats, oils, etc.), if not opportunely managed, not only represent increasing disposal and potentially severe pollution problems, but they can also be a considerable loss of potentially valuable biomass and nutrients. In this context, the use of cheap and largely available wastes from tomato processing industry as a major component of edible films has been proposed in this work since it may offer a more sustainable and eco-friendly option to produce novel prototypes for food packaging application. In more detail, it may contribute to effectively reduce the environmental impact from both packaging and food industries simultaneously.

Despite aforementioned advantages, green/edible packaging manufactures have only experienced a limited development and use so far (Trends et al., 2013). Regarding bio-based food packaging, the main challenge is related to their inherent characteristics such as the poor barrier and mechanical properties. In addition, the difficulty in introducing and retaining for long periods any bacteriostatic or bacteriolitic substances able to preserve the food quality, because of the fast release from the material's bulk, has also hampered their diffusion (Gorrasi, 2015). In this regard, the possibility to encapsulate such substances within natural, biocompatible and non-toxic nano-containers, which allow for their sustained release, could offer a viable option to overcome the above drawback. Halloysite nanotubes (HNTs) are aluminumsilicate nanoparticles, having a hollow tubular shape, high aspect ratio and high strength, which make them suitable nanocarriers for biologically active molecules. Moreover, they can be effectively dispersed in polymeric matrices (biocompatible). Because of these properties, HNTs have proved to be very effective in the production of high-performance polymeric nanocomposites, specifically for the controlled release of active agents (Lvov et al., 2008; Cavallaro et al., 2011, 2013;

Gorrasi and Vertuccio, 2016; Scarfato et al., 2016; Bugatti et al., 2017; Gorrasi et al., 2017). In particular, their non-toxic nature (Vergaro et al., 2010; Fakhrullina et al., 2015), and effective encapsulation capacity make HNTs ideal nano-containers for antibacterial agents. In addition, Halloysites has been proven to be a biocompatible material in several recent reports on cell cultures (Lvov et al., 2016), and invertebrate models (Fakhrullina et al., 2015). In particular, studies by Lvov et al. (2016), where the toxicity of HNT was tested after 48 h of incubation with fibroblast and human breast cells, showed that it is much less harmful than ordinary sodium chloride salt (Massaro et al., 2017).

The preparation of bio-based nano-composites via the traditional melt mixing techniques is not a viable option since their melting temperatures are typically too close to the temperatures at which the thermal degradation of the natural matrices takes place. Mechanical milling (MM), as a solid state mixing, has turned out to be an economic and ecological alternative for achieving an efficient dispersion of nanofillers into bio-based and biodegradable matrices (Gorrasi and Sorrentino, 2015), as well as in oil derived polymers (Delogu et al., 2017). In addition to this, the advantage of working in dry conditions and with almost any type of polymer matrix at ambient temperature, opened new and unexpected routes for the preparation of advanced functional composites (Gorrasi et al., 2007). The use of mechanical energy contains several inherent advantages including the control of degradation processes associated with high temperatures, the strong reduction of environmental impact and the possibility of compatibilizing (recycle) immiscible blends derived from end used materials. The simultaneous dispersion of nanoparticles, the promotion of mechano-chemical reactions and the proper manipulation of thermo-sensitive active molecules (i.e., antimicrobials, oxygen scavengers and drugs, represent further fundamental advantages of this process in the framework of the formulation and preparation of novel polymer nanocomposites with functional properties.

In this context, mechanical milling was selected in this work for the preparation of novel green/edible composites consisting of tomato peels (TPs) as a bio-based matrix and carvacrol encapsulated into HNTs as a natural antibacterial agent. The structural organization and the main physical properties of the obtained active bio-based composites were investigated; in particular, thermal and mechanical properties along with the films' interaction with water vapor were assessed and then correlated to the filler loading. The sustained release of carvacrol was also analyzed. Finally, the study was complemented with in-depth characterization of tomato peels residues (i.e., ultimate and proximate analyses, calorific values measures, and cellulose, hemicellulose and lignin content determination), which may be useful to identify further suitable application routes.

EXPERIMENTAL SECTION

Raw Materials Sampling and Characterization

Tomato peels (TPs) used in this work were collected from a tomato processing industry located in Salerno (40°47′24.5″N,

14°46′15.8″E), Campania region (IT). Prior to use, the raw feedstock was subjected to some pretreatments. In particular, it was first placed in a ventilated fume hood for approximately 48 h of exposure to fresh air, which reduced its moisture content from about 80%wt to about 6%wt. Then, it was processed to reduce its particles size by using a batch knife mill (Grindomix GM 300 by Retsch) for 20 s at a speed as high as 3,200 rpm for three times. The milled sample was finally manually sieved and the size fraction smaller than 500 μm was kept for the following utilization. Halloysite nanoclay powders (CAS 1332-58-7) and carvacrol (CAS 499-75-2) were supplied from Sigma Aldrich (Italy) and were used as received.

The determination of volatile matter, moisture, ash content and fixed carbon in raw tomato peels was performed by using a TGA 701 LECO thermogravimetric analyzer by following the ASTM D5142. Elemental analysis was carried out according to ASTM D 5291-92 by using a CHN 2000 LECO analyzer for carbon, hydrogen and nitrogen. The oxygen content was finally calculated by subtracting the ash content and CHN from the total. All these analyses were performed in triplicate at least and the average values are reported in **Table 1**. The higher heating value (HHV, MJ/kg on a dry basis) of the dried samples was measured using an oxygen bomb calorimeter (Parr 6200 Calorimeter). The measurements were repeated twice and the average value was used for subsequent calculation of the low calorific value (LHV) according to the Equation (1):

$$LHVdry = HHVdry - 2.442 \cdot (8.936 \cdot Hdry/100) \qquad (1)$$

where H_{dry} represents the weight percent of hydrogen resulting from elemental analysis, and LHV and HHV are given in MJ/kg. The results are also presented in **Table 1**. The contents of extractives, hemicellulose, cellulose and lignin in raw tomato peels were also determined according to a previously reported procedure (Brachi et al., 2016a,b). Briefly, about 10 g of air-dried TPs passing through a 40 mesh screen were first submitted to Soxhlet extraction with an ethanol/toluene (1:2, v:v) solution in order to remove the extractives (i.e., fats, resin, wax, phenol, pigments, oils, and other organic compounds), which could affect the subsequent fiber analysis. In more details, the extraction was conducted for 24 h at the rate of about 8 siphon cycles per hour. Then, the resulting oven-dried, extractive-free solid sample (about 3 g) was submitted to a delignification process by treating it with sodium chlorite ($NaClO_2$, technical grade, 80%) and acetic acid (reagent grade) for about 6 h in a water bath at 70°C. The extractive- and lignin-free white holocellulose sample was subsequently treated with two sodium hydroxide solutions (17.5 and 8.3 wt%, respectively) and acetic acid (10 wt%) to isolate the α-cellulose fraction. The soluble fraction remaining after this treatment represents hemicellulose and pectins. Finally the lignin

TABLE 1 | Raw tomato peels properties.

	Present work	(Mangut et al., 2016)	(Toscano et al., 2015)	(Rossini et al., 2013)
Moisture (wt%, as received)	80.50	n.a.	n.a.	n.a.
PROXIMATE ANALYSIS (WT%, DRY BASIS)				
Volatile matter	86.52	84.51	n.a.	n.a
Fixed carbon	11.67	11.59	n.a	n.a
Ash	1.81	3.90	2.2	3.8
ULTIMATE ANALYSIS (WT%, DRY BASIS)				
C	58.38	55.81	60.08	56.8
H	7.72	7.88	8.51	8.1
N	1.49	1.51	1.76	2.4
O (by diff.)	30.60	30.88	26.34	28.8
CALORIFIC VALUE ANALYSIS (MJ/KG, DRY BASIS)				
HHV	25.82	22.06	n.a.	23.6
LHV	24.14	n.a.	26.02*	21.9
POLYMERIC COMPOSITION (WT%, DRY BASIS)				
Extractives	5.21	n.a.	n.a.	n.a.
Hemicellulose + pectins	52.40	n.a.	4.8	n.a.
α-cellulose	17.50	n.a.	22.5	n.a.
Lignin (by difference)	24.89	n.a.	46.9	n.a.

Dry ash free basis.

TABLE 2 | Content of chemical elements in raw tomato peels by ICP-MS analysis (left hand column), and EDX relative to SEM micrograph in **Figure 1C** (right hand column).

| Element	Concentration (g/kg, db)	Weight fraction (%)
Aluminum	9.36	
Arsenic	0.11	
Barium	3.14	
Beryllium	0.03	
Bismuth	0.07	
Cadmium	0.13	
Calcium	945.00	0.55
Chromium	0.26	
Copper	3.29	0.27
Gallium	0.18	
Iron	26.92	0.31
Magnesium	659.40	0.56
Manganese	10.98	
Mercury	0.02	
Molybdenum	0.75	
Nickel	1.02	0.18
Phosphorus	1111.00	
Potassium	8606.00	4.72
Silicon	63.97	0.33
Sodium	151.50	
Strontium	5.02	
Titanium	3.18	
Zinc	7.71	
Carbon		67.58
Oxygen		24.86
Chlorine		0.64
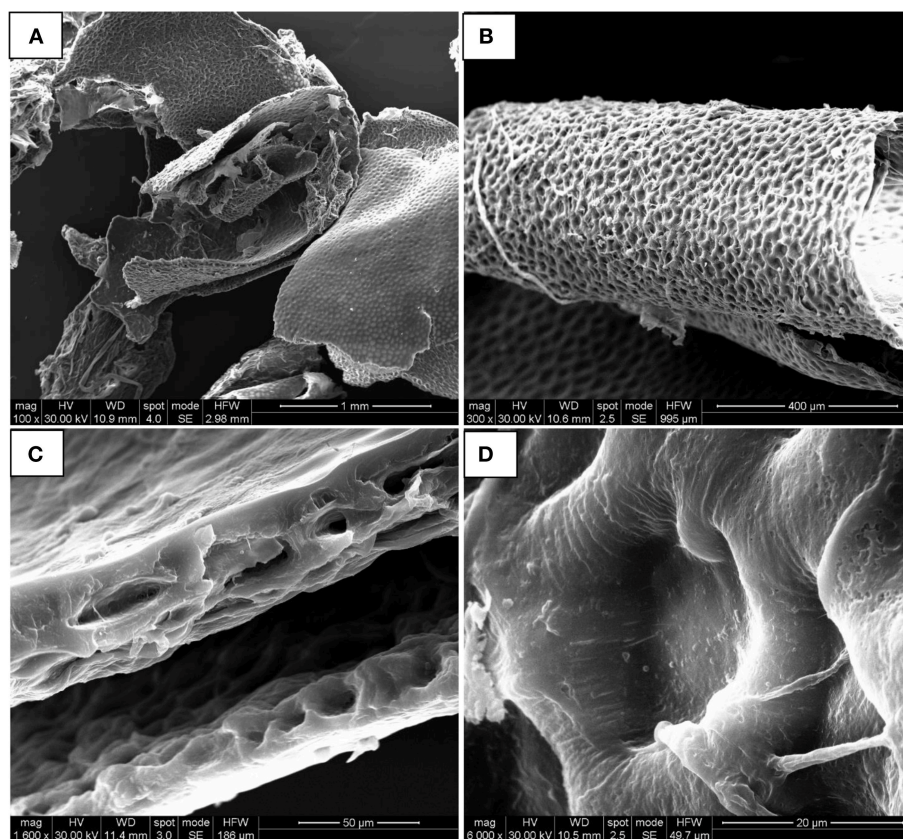
FIGURE 1 | Scanning electron microscopy (SEM) micrographs of tomato peels at 100× **(A)**, 300× **(B)**, 1,600× **(C)**, and 6,000× **(D)** magnification.

content was calculated by difference. The organic polymeric composition of TPs obtained through the above procedures, is shown in **Table 1**. The content of inorganic elements in raw tomato peels was determined by inductively coupled plasma-mass spectrometry (ICP-MS) by using an Agilent 7500 CE instrument. The results obtained from these analyses are shown in **Table 2**.

Preparation of HNTs-Carvacrol Nano-Hybrid

0.5 g of HNTs and 10 mL of carvacrol were firstly mixed and ultrasonicated by using an ultrasonicator UP200S for 30 min in an ice bath. The HNT-carvacrol mixture was then transferred into a vacuum jar connected to a vacuum pump; 1 mbar pressure was applied into the jar for 30 min to remove air inside HNTs, followed by the application of atmospheric pressure for 10 min to allow carvacrol molecules enter evacuated HNTs. The cycle was repeated three times to increase loading efficiency. The content of carvacrol (%wt) in the HNT-carvacrol hybrid was evaluated by the thermogravimetric analysis (**Figure 2A**) according to the following Equation (2):

$$X = \frac{R_{mix} - R_H}{R_s - R_H} \times 100 \qquad (2)$$

where X is the loaded carvacrol, R_{mix} is the weight loss percentage of the mixture, R_H and R_s are the weight loss percentages of halloysite and carvacrol, respectively. This equation assumes that the total weight loss of the single component is not affected by the other components present in mixture. The carvacrol amount detected with this method was $\cong 76\%$.

Preparation of Composites TPs/HNTs-Carvacrol

Composites TPs/HNTs-carvacrol were prepared by the following procedure. One gram of tomato peels was dissolved in 20 mL of distilled water and 2 mL of glycerol, as plasticizer. The obtained solution was stirred for 3 h at 70°C. The nano-hybrid was added to the tomato peels/glycerol/water solution in different amounts, in order to obtain nano-hybrid concentrations equal to 2.5, 5, 10, and 20 wt%. To allow the best intimate mixing between the different phases, after stirring the composite solution for 30 min, each composition was submitted to high energy ball milling at ambient temperature for 60 min. The apparatus used was a Retsh (Germany) planetary ball milling (PM 100), with a cylindrical steel jar of 50 cm^3 containing 5 tungsten carbide balls of 10 mm of diameter. The rotation speed was 640 rpm. The mixtures obtained were poured into Petri dishes and dried in an oven at 70°C for 7 days. Films of pure tomato peels were obtained using

the same experimental conditions. All films, having the thickness of about 600 μm, were then characterized. Composite samples will be coded as follows: TPs**x**HNTs-Carv**y** where **x** is the tomato peel amount and **y** is the HNTs-carvacrol load.

Methods of Investigation

SEM/EDX measurements were performed by a Fei Inspect Microscope. *X-ray diffraction* (XRD) patterns were taken, in reflection, with an automatic Bruker diffractometer (equipped with a continuous scan attachment and a proportional counter), using nickel-filtered Cu Kα radiation (Kα = 1.54050 Å) and operating at 40 kV and 40 mA, step scan 0.05° of 2Ï' and 3 s of counting time.

Thermogravimetric analyses (TGA) were carried out from 30 to 600°C (heating rate of 10°C/min) under air flow, using a Mettler TC-10 thermo-balance.

The mechanical properties of the samples were evaluated from stress-strain curves obtained using a dynamometric apparatus INSTRON 4301. The experiments were conducted at room temperature with the deformation rate of 5 mm/min. The initial
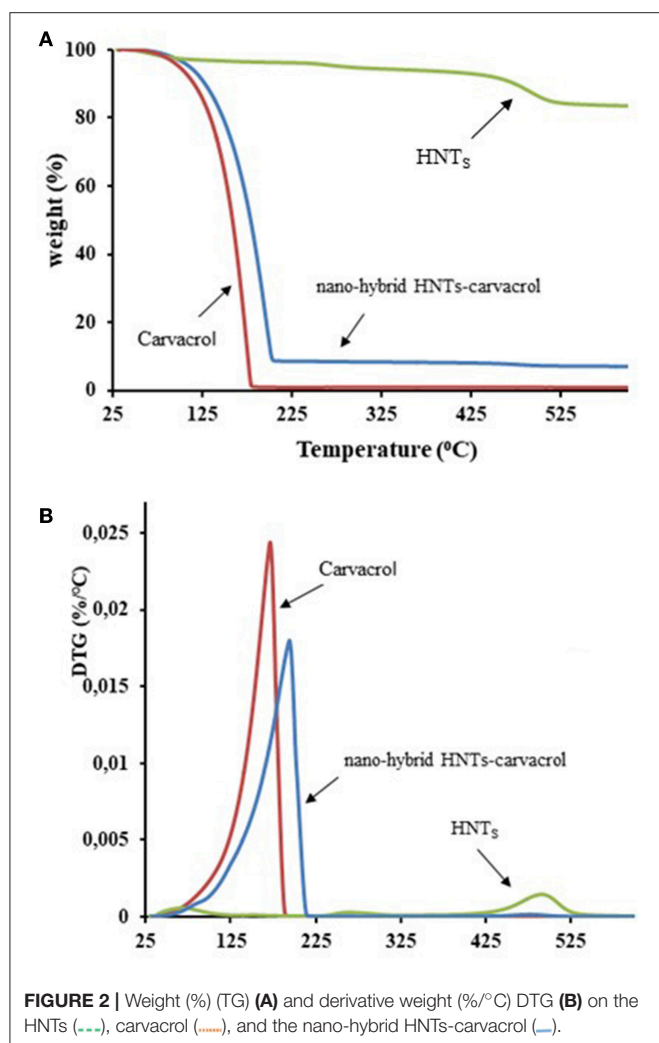
length of the samples was about 10 mm. Elastic moduli were derived from the linear part of the stress-strain curves, giving to the sample a deformation of 0.1%. Data were averaged on five samples.

Sorption of water, in controlled atmosphere and humidity on both TPs films and film composites (approximately 600 μm thickness), was investigated through the determination of moisture uptake of samples exposed at the same conditions of temperature and relative humidity (HR). The conventional static desiccator technique (Bellur et al., 2009; Vasquez and Coronella, 2009), which employs a glass desiccator containing a supersaturated salt water solution as a humidity control chamber, was employed. Specifically, three different salts, i.e., KBr, Mg(NO$_3$)$_2$, and CH$_3$COOK, were used in this work, which allow exposing samples to 80 ± 2, 53 ± 2 and 23 ± 2% of RH, respectively, at room temperature (i.e., 25 ± 2°C). In order to minimize temperature changes, the desiccator was partially submerged in a water bath. Approximately 100 mg of oven-dried samples were put into an open weighing bottle and then placed into the desiccator for testing. The humidity and temperature in the glass desiccator were checked using a digital thermo-hygrometer (30.5005 TFA Dostmann). Equilibrium moisture content (ECM) of each sample up to an exposure time of 60 days was measured by using a Kern DBS Halogen Moisture analyzer.

The release kinetics of carvacrol were performed by ultraviolet spectrometric measurement at ambient temperature, using a Spectrometer UV-2401 PC Shimadzu (Japan). The tests were performed using rectangular specimens of 4 cm^2 and same thickness (600 μm), placed into 25 mL of ethanol and stirred at 100 rpm in an orbital shaker (VDRL MOD. 711+, Asal S.r.l.). The medium release was withdrawn at fixed time intervals and replenished with fresh medium. The considered band was at 275 nm.

RESULTS AND DISCUSSION

Experimental results regarding composition (proximate analysis, fiber composition and ultimate) and calorific content of fresh TPs, as well as their comparison with the values found in the literature, are shown in **Table 1**. Comparing the obtained data with literature references (Rossini et al., 2013; Toscano et al., 2015; Mangut et al., 2016) some inconsistence emerge regarding the fiber composition of tomato peel, which conversely are not observed among the data from the proximate, the ultimate and the calorific-content analyses. In this regard, it is worth noting that a different analytical approach (van Soest method) has been used by Toscano et al. (2015), to quantify the individual components in tomato peels with respect that used in this research, following the Laboratory Analytical Procedures (LAP) established by National Renewable Energy Laboratory (NREL). It is well-known that methods that utilize different chemical means to separate and quantify the biomass components can give different compositional results for the same substrate (Templeton et al., 2014). Accordingly, the comparison of the analyzed values in this paper with the literature references confirms the consistency of the data shown here.
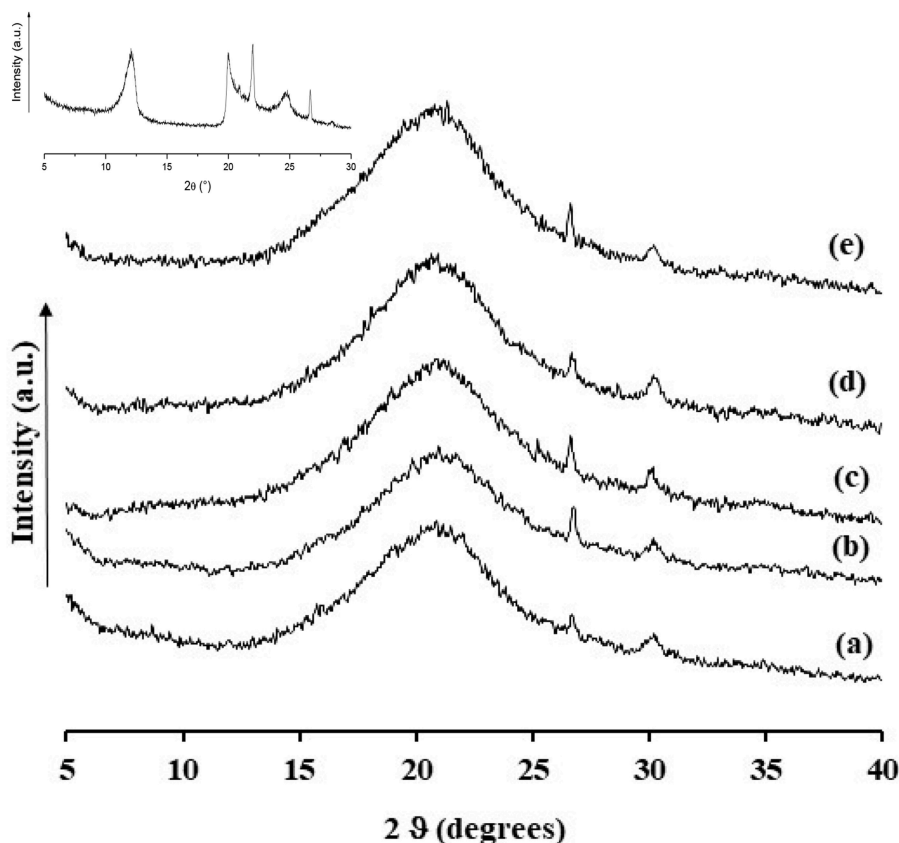

FIGURE 2 | Weight (%) (TG) **(A)** and derivative weight (%/°C) DTG **(B)** on the HNTs (╌╌), carvacrol (┈┈), and the nano-hybrid HNTs-carvacrol (━━).

FIGURE 3 | XRD analysis evaluated on films of TPs100HNTs-carv0 **(a)**, TPs97.5HNTs-carv2.5 **(b)**, TPs95HNTs-carv5 **(c)**, TPs90HNTs-carv10 **(d)**, TPs80HNTs-carv20 **(e)**; Inset: XRD of HNTs.
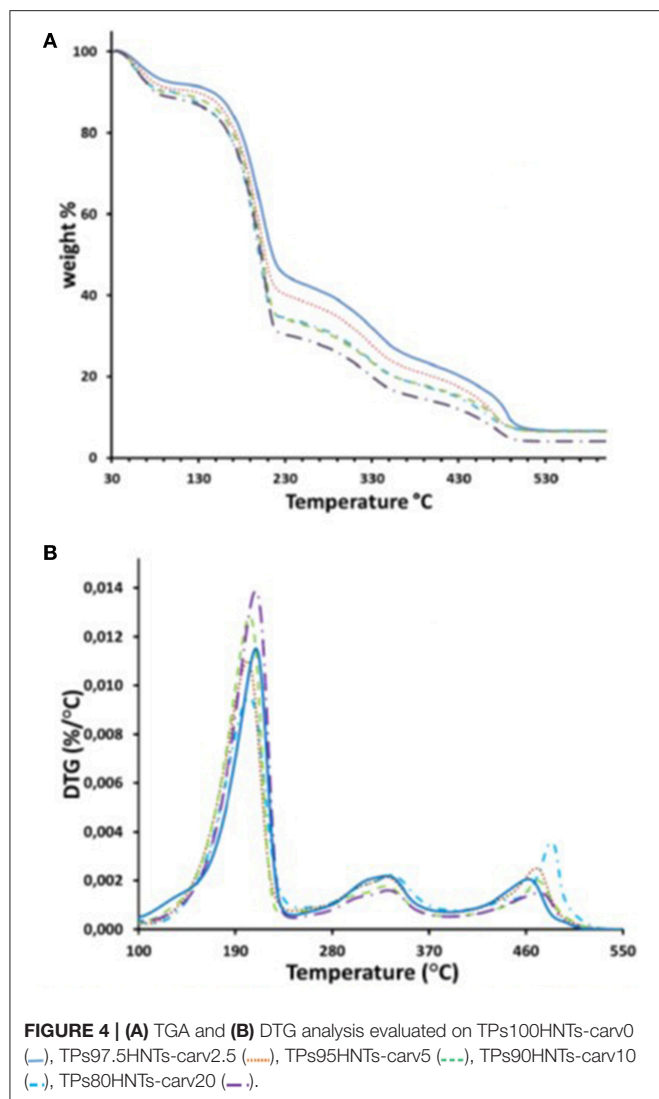
Figures 1A–D show the SEM micrographs of tomato peel samples obtained at different magnifications. It results that tomato peels are very thin, having a thickness of approximately 50 μm (**Figure 1C**) and exhibit a well-organized 3D honeycomb-like structure with large cavities, which provides a larger specific surface area (C-D). The Energy Dispersive X-ray (EDX) analysis of the tomato peel surface relative to the SEM micrograph in **Figure 1C** confirms that TPs contain a large amount of carbon (C), oxygen (O), and potassium (K) (**Table 2**), in agreement with data obtained by ultimate (**Table 1**) and ICP-MS analyses (**Table 2**). The presence of chlorine (Cl) in tomato peels is in accordance with the literature (Rossini et al., 2013), where it is reported that chlorine present in the tomato processing residues is mainly concentrated in the peel fraction.

Properties of Pure and Composite TP-Based Films

Carvacrol molecules inside and/or outside HNTs are very difficult to be accurately determined. The evaluation of the degradation temperatures of the HNTs, carvacrol and HNTs-carvacrol, through TGA analysis, can be used to give an indication about the molecules' intercalation, as elsewhere demonstrated (Gorrasi, 2015; Biddeci et al., 2016; Hendessi et al., 2016). **Figure 2** reports

the weight (%) (TG) (A) and derivative weight (DTG) (B) analysis performed on the HNTs, carvacrol and the nano-hybrid HNTs-carvacrol. Data show that halloysite exhibits a degradation step at about 500°C, which can be attributed to the dehydroxylation of its matrix (Horvath et al., 2003). The thermal degradation of carvacrol occurs in one step centered at 170°C. A shift toward higher values for the carvacrol degradation temperature, centered at 195°C, is clearly evident for the nano-hybrid. The observed delay in the thermo-oxydative degradation of carvacrol molecules could be attributed to two different phenomena, namely: (i) a reduced oxygen permeability due to the barrier effect produced by fillers building a tortuous path (Monsiváis-Barrón et al., 2014), or (ii) the fact that large part of carvacrol was successfully entrapped into the nanotubes, and the degradation of the active molecule probably occurs at higher temperature, with respect to the free molecules only after a spillage from the tubes.

Figure 3 shows the XRD of composites' films and unfilled film based on TPs. Data reveal the presence of an amorphous structure in all of the sample, as evidenced by the presence of a broad halo centered at $2\theta \cong 21°$. The amorphous structure of the matrix is retained in all the composites obtained at different filler load. The inset of **Figure 3** shows the XRD spectrum of dehydrated HNTs, with the typical d-spacing at 7.3 Å, that

FIGURE 4 | (A) TGA and (B) DTG analysis evaluated on TPs100HNTs-carv0
(—), TPs97.5HNTs-carv2.5 (·····), TPs95HNTs-carv5 (- - -), TPs90HNTs-carv10
(- · -), TPs80HNTs-carv20 (— ·).

FIGURE 5 | Mechanical parameters for unfilled TPs film and composites.

represents the first order (001) basal reflection (Hillier et al., 2016). Such peak is not visible in the composites. It may be possible that during the milling process, in the reported experimental conditions, a part of the first order basal reflection of HNTs is partially de-structured, or such peak may be hidden under the main peak of the TPs' matrix.

Figure 4A shows the TGA and DTG (**Figure 4B**) analysis evaluated on composites films. Unfilled film made of tomato peels was analyzed for comparison. It is suggested that the pyrolysis of the investigated tomato processing residue is a rather complex process occurring in several stages as it is clearly reflected by the presence of several DTG peaks (**Figure 4B**), which are also reflected in less noticeable changes in the slope of the TG curves. The complicated thermal behavior exhibited by tomato peels is a likely consequence of its very complex chemical composition, which is characterized by the presence of several macro-components (i.e., cellulose, hemicelluloses, and lignin, see **Table 1**) and minor constituents (e.g., lipids, waxes,
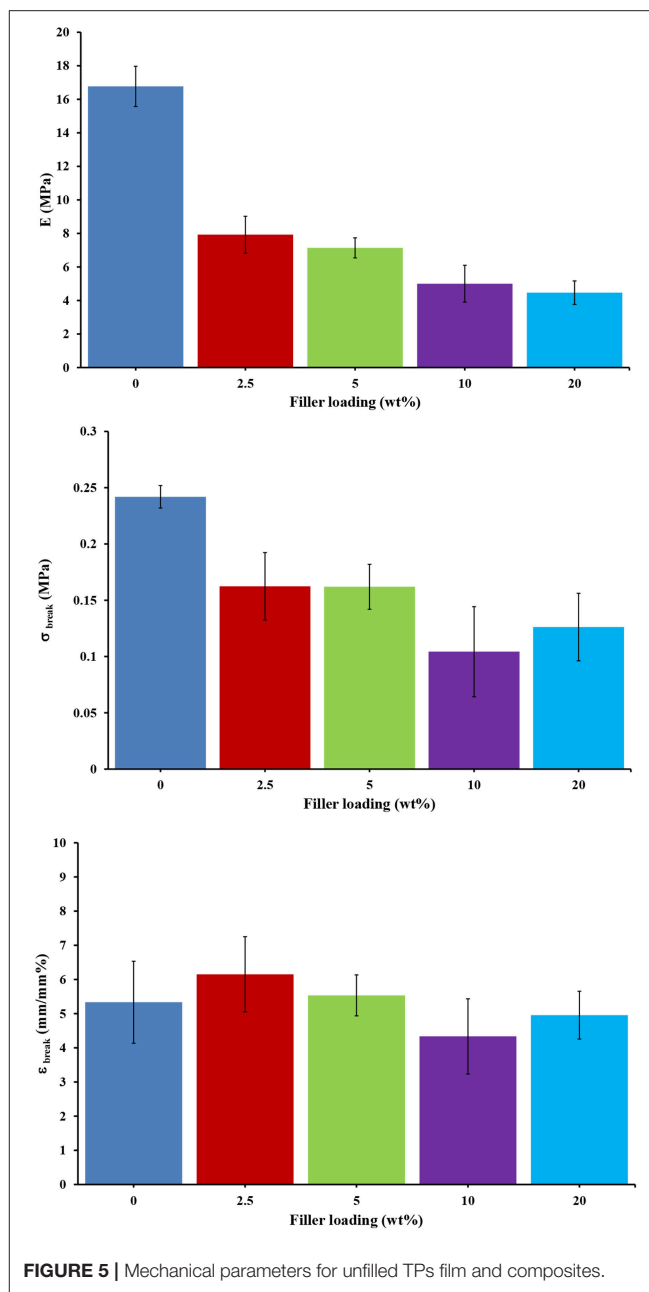
proteins, oil, etc.) in different percentages (Lazos and Kalathenos, 1988; Knoblich et al., 2005). The negligible weight loss (i.e., approximately 7 wt%) observed at a temperature lower than 200°C can be attributed to the removal of moisture and to the start of polysaccharides hydrolysis, whereas, the second and third decomposition stage can be most likely ascribed to the thermal degradation of hemicelluloses and cellulose. However, a clear attribution of all the decomposition events or peaks to a specific chemical species appeared to be hardly achieved when analyzing the DTG profiles only, because mass losses of several minor chemical components probably occurred during each step at the same time. It is evident that all degradation temperatures
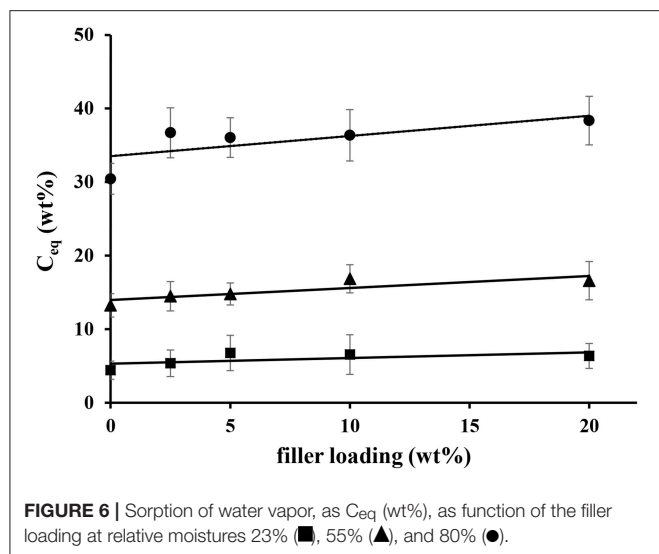
FIGURE 6 | Sorption of water vapor, as C_{eq} (wt%), as function of the filler loading at relative moistures 23% (■), 55% (▲), and 80% (●).

TABLE 3 | C_{eq} (wt%) of water vapor sorbed at different moisture for unfilled TPs film and composites.

Filler loading (wt%)	C_{eq} (wt%) at 23% of moisture	C_{eq} (wt%) at 55% of moisture	C_{eq} (wt%) at 80% of moisture
TPs100HNTs-carv0	4.41 ± 1.2	13.23 + 1.6	30.43 + 2.1
TPs97.5HNTs-carv2.5	5.35 + 1.8	14.47 + 2.1	36.70 + 3.4
TPs95HNTs-carv5	6.75 + 2.4	14.78 + 1.5	36.04 + 2.7
TPs90HNTs-carv10	6.55 + 2.6	16.84 + 1.9	36.36 + 3.5
TPs80HNTs-carv20	6.35 + 1.7	16.58 + 2.6	38.36 + 3.3

decrease with the filler loading. As already found in the case of pectins/HNTs-essential oil (Gorrasi, 2015), we hypothesize that the decomposition of volatile products due to oxidation phenomena, can have a synergistic effect in determining the thermal decomposition of the materials.

The stress-strain curves of tomato peels film and composites, which were not reported, allowed for evaluation of the mechanical parameters of the samples. In particular, the elastic modulus, E (MPa), the stress at break point, σ_{break} (MPa), and the elongation at break, ε_{break} (mm/mm%) were evaluated. The mechanical parameters are reported in **Figure 5**. The elastic modulus (MPa) tends to decrease with the filler content, and also the stress at break (MPa). HNTs filler, having an inorganic nature, is incompatible with the organic matrix. It is worth to note that they were dispersed into the organic matrix with no chemical treatment on the surface. The lowering of the mechanical properties is mainly due to this difference in nature of both components. A "disconnection" between the two phases is then evidenced from the mechanical response. Experimental results evidenced that the higher is the filler loading, the higher the degree of separation appears between the two phases.

The values of elongation at break point (mm/mm%) is not significantly modified with the filler loading, also at high
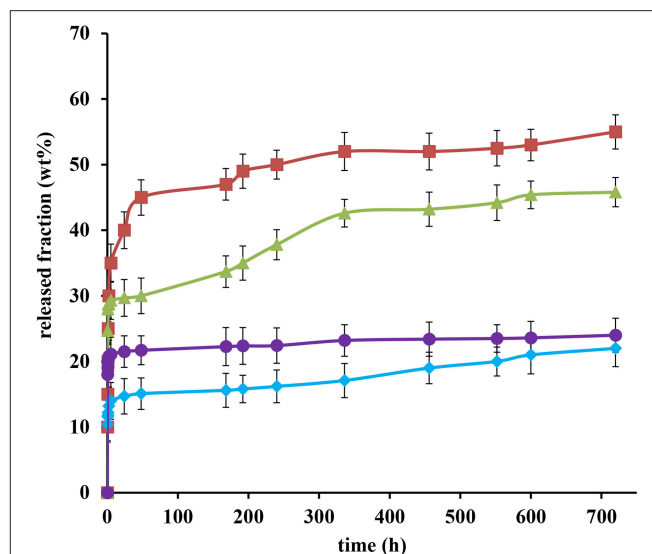

FIGURE 7 | Release fraction of carvacrol (wt%), as function of contact time (h) for TPs97.5HNTs-carv2.5 (■), TPs95HNTs-carv5 (▲), TPs90HNTs-carv10 (●), TPs80HNTs-carv20 (◆).

percentages (i.e., 10 and 20 wt%). This can be due to a plasticizing effect of the carvacrol oil with respect to the matrix, which helps to prevent the loss of mechanical consistence of the samples.

Figure 6 reports the sorption of water vapor, as C_{eq} (wt%), as a function of the filler loading for all the obtained composites and the unfilled sample at relative moistures 24, 55, and 80%. Data are reported in **Table 3**. As expected, the sorption of water increases with the moisture increasing. The presence of hydrophilic HNTs, even at a high percentage, does not dramatically increase the hydrophilicity of the materials, as found for other biodegradable materials filled with HNTs (Gorrasi, 2015; Bugatti et al., 2017). This may be due to the presence of hydrophobic carvacrol around the HNTs that can act as hydrophobic coating.

To study the ability of the considered composites to release carvacrol, measurements of controlled release in ethanol were conducted. In particular, **Figure 7** reports the release fraction of carvacrol (wt%), as function of contact time (h). It is evident that, in all cases, after 1 month no complete release occurred for any sample. A faster release occurs within the first hour, probably due to the release of carvacrol on the surface of the films, then the release rate decreases over time. The carvacrol release fraction (wt%) decreases with filler loading. This result can be interpreted in terms of lowered counter-diffusion of the carvacrol molecules from inside the matrix to the release medium. The dispersed HNTs increases to a large extent the tortuosity of the system, leading to a decrease in the rate of diffusion of carvacrol molecules. This result demonstrates that HNTs loaded carvacrol, embedded into the considered bio-based matrix, act as nano-containers that allow the sustained release of the active molecule. This could result in a longer-lasting antibacterial effect.

CONCLUDING REMARKS

This paper demonstrated how mechanical milling is a valuable technology to obtain green nanocomposites based on a largely available waste material, like tomato peels (TPs), and halloysite nanotubes (HNTs) filled with a natural antimicrobial, like carvacrol.

- XRD analysis on the composites showed that the TPs matrix presents an amorphous structure, which is retained in the composites at any filler loading. The basal peak of dehydrated HNTs tends to disappear and/or to be expanded after the intercalation of carvacrol, and the ball milling treatment with TPs in presence of water.
- TG-DTG analysis enabled us to hypothesize that the carvacrol molecules inside HNTs delay the thermo-oxydation, either for a barrier effect to oxygen inducted from the HNTs, or because some molecules were successfully loaded into the nanotubes. The degradation of the TPs matrix into the composites decreases with the filler loading. It was hypothesized that the decomposition of volatile products, due to oxidation phenomena, can have a synergistic effect in determining the thermal decomposition of the materials.
- Mechanical properties showed a decrease, or at least a maintenance, of all the mechanical parameters. It worth to note that natural HNTs were incorporated into the TPs matrix with no chemical treatment.
- The sorption of water vapor was evaluated at relative moistures 24, 55, and 80%. Data show that it increases with increasing the moisture. The presence of highly hydrophilic HNTs, even at high percentage, does not dramatically increase the hydrophilicity of the materials. This may be due to the presence of hydrophobic carvacrol around the HNTs that can act like an hydrophobic coating.
- The sustained release of carvacrol, *in vitro*, was studied as function of time. The carvacrol release fraction (wt%) decreases with filler loading and after 1 month no complete release is evident for any composite. The presence of the dispersed HNTs increasing the tortuosity of the system, led to a large decrease in the rate of counter-diffusion of carvacrol molecules from the TPs matrix. This result allows us to hypothesize the application of such materials in food packaging field, where it is needed longer-lasting antibacterial effect.

AUTHOR CONTRIBUTIONS

GG conceived the paper. GV, VB, and PB performed the experiments. GG, GV, VB, and PB interpreted the results. GG and PB wrote the paper.

FUNDING

ACKNOWLEDGMENTS

REFERENCES

Al Khraisat, A. A. A. (2015). Evaluation of metabolizable nutrient values of Tomato Pomace (TP) in Nile tilapia (*Oreochromis niloticus*). *Int. J. Fisc. Aquat. Sci.* 2, 164–167. Available online at: http://www.fisheriesjournal.com/vol2issue4/Pdf/2-4-7.1.pdf

Bellur, S. R., Coronella, C. J., and Vàsquez, V. R. (2009). Analysis of biosolids equilibrium moisture and drying. *Environ. Prog. Sustain. Energy* 28, 291–298. doi: 10.1002/ep.10353

Biddeci, G., Cavallaro, G., Di Blasi, F., Lazzara, G., Massaro, M., Milioto, S., et al. (2016). Halloysite nanotubes loaded with peppermint essential oil as filler forfunctional biopolymer film. *Carbohydr. Polym.* 152, 548–557. doi: 10.1016/j.carbpol.2016.07.041

Brachi, P., Chirone, R., Miccio, F., Miccio, M., Picarelli, A., and Ruoppolo, G. (2014). Fluidized bed co-gasification of biomass and polymeric wastes for a flexible end-use of the syngas: focus on bio-methanol. *Fuel* 128, 88–98. doi: 10.1016/j.fuel.2014.02.070

Brachi, P., Miccio, F., Miccio, M., and Ruoppolo, G. (2016a). Pseudo-component thermal decomposition kinetics of tomato peels via isoconversional methods. *Fuel Process. Technol.* 154, 243–250. doi: 10.1016/j.fuproc.2016.09.001

Brachi, P., Miccio, F., Miccio, M., and Ruoppolo, G. (2016b). Torrefaction of tomato peel residues in a fluidized bed of inert particles and a fixed-bed reactor. *Energy Fuel* 30, 4858–4868. doi: 10.1021/acs.energyfuels.6b00328

Bugatti, V., Sorrentino, A., and Gorrasi, G. (2017). Encapsulation of Lysozyme into halloysite nanotubes and dispersion in PLA: structural and physical properties and controlled release analysis. *Europ Polymer J.* 93, 495–506. doi: 10.1016/j.eurpolymj.2017.06.024

Cavallaro, G., Donato, D. I., Lazzara, G., and Milioto, S. (2011). Films of halloysite nanotubes sandwiched between two layers of biopolymer: from themorphology to the dielectric, thermal, transparency, and wettability properties. *J. Phys. Chem. C* 115, 20491–20498. doi: 10.1021/jp207261r

Cavallaro, G., Lazzara, G., and Milioto, S. (2013). Sustainable nanocomposites based on halloysite nanotubes and pectin/polyethylene glycol blend. *Polymer Degrad. Stab.* 98, 2529–2536. doi: 10.1016/j.polymdegradstab.2013.09.012

Delogu, F., Gorrasi, G., and Sorrentino, A. (2017). Fabrication of polymer nanocomposites via ball milling: present status and future perspectives. *Prog. Mater. Sci.* 86, 75–126. doi: 10.1016/j.pmatsci.2017.01.003

Eghbal, N., and Choudhary, R. (2018). Complex coacervation: encapsulation and controlled release of active agents in food systems. *LWT-Food Sci. Tech.* 90, 254–264. doi: 10.1016/j.lwt.2017.12.036

Fakhrullina, G. I., Akhatova, F. S., Lvov, Y. M., and Fakhrullin, R. F. (2015). Toxicity of halloysiteclay nanotubes *in vivo*: a Caenorhabditis elegans study. *Environ. Sci. Nano* 2, 54–59. doi: 10.1039/C4EN00135D

Giosafatto, C. V., Di Pierro, P., Gunning, A. P., Mackie, A., Porta, R., and Mariniello, L. (2014b). Trehalose-containing hydrocolloid edible films prepared in the presence of transglutaminase. *Biopolymer* 101, 931–937. doi: 10.1002/bip.22477

Giosafatto, C. V., Di Pierro, P., Gunning, P., Mackie, A., Porta, R., and Mariniello, L. (2014a). Characterization of citrus pectin edible films containing transglutaminase-modified phaseolin. *Carbohydrate Polym.* 106, 200–208. doi: 10.1016/j.carbpol.2014.02.015

Gorrasi, G. (2015). Dispersion of halloysite loaded with natural antimicrobials intopectins: characterization and controlled release analysis. *Carbohydrate Polym.* 127, 47–53. doi: 10.1016/j.carbpol.2015.03.050

Gorrasi, G., Attanasio, G., Izzo, L., and Sorrentino, A. (2017). Controlled release mechanisms of sodium benzoate from a biodegradable polymer and halloysite nanotube composite. *Polymer Intern.* 66, 690–698. doi: 10.1002/pi.5309

Gorrasi, G., and Bugatti, V. (2016). Edible bio-nano-hybrid coatings for food protection based on pectins and LDH-salicylate: preparation and analysis of physical properties. *LWT-Food Sci. Technol.* 69, 139–145. doi: 10.1016/j.lwt.2016.01.038

Gorrasi, G., Bugatti, V., and Vittoria, V. (2012). Pectins filled with LDH-antimicrobial molecules: preparation, characterization and physical properties. *Carbohydrate Polym.* 89, 132–137. doi: 10.1016/j.carbpol.2012.02.061

Gorrasi, G., Romeo, V., Sannino, D., Sarno, M., Ciambelli, P., Vittoria, V., et al. (2007). Carbon nanotube induced structural and physical property transitions of syndiotactic polypropylene. *Nanotechnology* 18:275703. doi: 10.1088/0957-4484/18/27/275703

Gorrasi, G., and Sorrentino, A. (2015). Mechanical milling as a technology to produce structural and functional bio-nanocomposites. *Green Chem.* 17, 2610–2625. doi: 10.1039/C5GC00029G

Gorrasi, G., and Vertuccio, L. (2016). Evaluation of zein/halloysite nano-containers as reservoirs of active molecules for packaging applications: preparation and analysis of physical properties. *J. Cereal Sci.* 70, 66–71. doi: 10.1016/j.jcs.2016.05.008

Hendessi, S., Sevinis, E. B., Unal, S., Cebecia, F. C., Menceloglu, Y. Z., and Unal, H. (2016). Antibacterial sustained-release coatings from halloysite nanotubes/waterborne polyurethanes. *Pro. Org. Coat.* 101, 253–261. doi: 10.1016/j.porgcoat.2016.09.005

Hillier, S., Brydson, R., Delbos, E., Fraser, T., Gray, N., Pendlowski, H., et al. (2016). Correlations among the mineralogical and physical properties of halloysite nanotubes (HNTs). *Clay Minerals* 51, 325–350. doi: 10.1180/claymin.2016.051.3.11

Horvath, E., Frost, R. L., Mako, E., Kristof, J., and Cseh, T. (2003). Thermal treatment of mechano-chemically activated kaolinite. *Thermochim. Acta* 404, 227–235. doi: 10.1016/S0040-6031(03)00184-9

Kam, W. Y. J., Mirhosseini, H., Abas, F., Hussain, N., Hedayatnia, S., and Chong, H. L. F. (2018). Antioxidant activity enhancement of biodegradable film as active packaging utilizing crude extract from durian leaf waste. *Food Control* 90, 66–72. doi: 10.1016/j.foodcont.2018.02.036

Kirwan, M. J., and Strawbridge, J. W. (2003). "Plastics in food packaging," in *Food Packaging Technology*, eds R. Coles, D. McDowell, and M. J. Kirwan (Oxford: Blackwell Publishing, CRC Press), 158–160.

Knoblich, M., Anderson, B., and Latshaw, D. (2005). Analyses of tomato peel and seed byproducts and their use and a source of carotenoids. *J. Sci. Food Agric.* 85, 1166–1177. doi: 10.1002/jsfa.2091

Lazos, E. S., and Kalathenos, P. (1988). Technical note: composition of tomato processing wastes. *Int. J. Food Sci. Technol.* 23, 649–665. doi: 10.1111/j.1365-2621.1988.tb01052.x

Lvov, Y., Wang, W., Zhang, L., and Fakhrullin, R. (2016). Halloysite clay nanotubes for loading and sustained release of functional compounds. *Adv. Mater.* 28, 1227–1250. doi: 10.1002/adma.201502341

Lvov, Y. M., Shchukin, D. G., Möhwald, H., and Price, R. R. (2008). Halloysite clay nanotubesfor controlled release of protective agents. *ACS Nano* 2, 814–820. doi: 10.1021/nn800259q

Mangut, V., Sabio, E., Gañán, J., González, J. F., Ramiro, A., González, C. M., et al. (2016). Thermogravimetric study of the pyrolysis of biomass residues from tomato processing industry. *Fuel Process. Technol.* 87, 109–115. doi: 10.1016/j.fuproc.2005.08.006

Massaro, M., Lazzara, G., Milioto, S., Noto, R., and Riela, S. (2017). Covalently modified halloysite clay nanotubes: synthesis, properties, biological and medical applications. *J. Mater. Chem. B* 5, 2867–2882. doi: 10.1039/C7TB00316A

Monsiváis-Barrón, A. J., Bonilla, J., and Sánchez-Fernández, A. (2014). Property relationship in organosilanes and nanotubes filled hybrid composites. *Materials* 7, 7073–7092. doi: 10.3390/ma7107073

Rossini, G., Toscano, G., Duca, D., Corinaldesi, F., Foppa Pedretti, E., and Riva, G. (2013). Analysis of the characteristics of the tomato manufacturing residues finalized to the energy recovery. *Biomass Bioenergy* 51, 177–182. doi: 10.1016/j.biombioe.2013.01.018

Saha, N. R., Sarkar, G., Roy, I., Rana, D., Bhattacharyya, A., Adhikari, A., et al. (2016). Studies on methylcellulose/pectin/montmorillonite nanocomposite films and their application possibilities. *Carbohydrate Polym.* 136, 1218–1227. doi: 10.1016/j.carbpol.2015.10.046

Scarfato, P., Avallone, E., Incarnato, L., and Di Maio, L. (2016). Development and evaluation of halloysite nanotube-based carrier for biocide activity in construction materials protection. *Appl. Clay Sci.* 132–133, 336–342. doi: 10.1016/j.clay.2016.06.027

Silva, Â., Duarte, A., Sousa, S., Ramos, A., and Domingues, F. C. (2016). Characterization and antimicrobial activity of cellulose derivatives films incorporated with a resveratrol inclusion complex. *LWT-Food Sci. Technol.* 73, 481–489. doi: 10.1016/j.lwt.2016.06.043

Templeton, D. W., Wolfrum, E. J., Yen, J. H., and Sharpless, K. E. (2014). Compositional analysis of biomass reference materials: results from an interlaboratory study. *Bioenergy Res.* 9, 303–314. doi: 10.1007/s12155-015-9675-1

Tomato News (2014). *Tomato Processing Industry*. Available online at: http://www.tomatonews.com/resources.html (Accessed June 26, 2015).

Toscano, G., Pizzi, A., Foppa Pedretti, E., Rossini, G., Ciceri, G., Martignon, G., et al. (2015). Torrefaction of tomato industry residues. *Fuel* 143, 89–97. doi: 10.1016/j.fuel.2014.11.039

Trends, N., Rhim, J. W., Park, H. M., and Ha, C. S. (2013). Bio-nanocomposites for food packaging applications. *Prog. Polymer Sci.* 38, 1629–1652. doi: 10.1016/j.progpolymsci.2013.05.008

Vasquez, V. R., and Coronella, C. J. (2009). A simple model for vapor-moisture equilibrium in biomass substrates. *AIChE J.* 55, 1595–1603. doi: 10.1002/aic.11762

Vergaro, V., Abdullayev, E., Lvov, Y. M., Zeitoun, A., Cingolani, R., Rinaldi, R., et al. (2010). Cytocompatibility uptake of halloysite clay nanotubes. *Biomacromolecules* 11, 820–826. doi: 10.1021/bm9014446

Zhiguo, L., Kun, L., Wang, Y., Zhao, B., and Yang, Z. (2015). Multi-scale engineering properties of tomato fruits related to harvesting, simulation and textural evaluation. *LWT-Food Sci. Tech.* 61, 444–451. doi: 10.1016/j.lwt.2014.12.018

Biodegradable and Water Resistant Poly(vinyl) Alcohol (PVA)/Starch (ST)/Glycerol (GL)/Halloysite Nanotube (HNT) Nanocomposite Films for Sustainable Food Packaging

Zainab Waheed Abdullah[1,2] and Yu Dong[1]

[1] School of Civil and Mechanical Engineering, Curtin University, Perth, WA, Australia, [2] Technical Engineering College-Baghdad, Middle Technical University, Baghdad, Iraq

As a novel biodegradable material, poly (vinyl) alcohol (PVA)/starch (ST)/ glycerol (GL)/ halloysite nanotube (HNT) nanocomposite films were prepared by solution casting at the HNT contents of 0.25, 0.5, 1, 3, and 5 wt%. Water absorption capacity and water solubility of nanocomposite films were decreased remarkably by 44.24 and 48.05%, respectively, with increasing the HNT content from 0 to 5 wt% when compared with those of biopolymer matrices. Moreover, the water contact angle of nanocomposite films increased by 21.36° with the incorporation of HNTs. The presence of HNTs appeared to reduce the overall migration rates for PVA/ST/GL/HNT nanocomposite films when interacting with either hydrophilic or lipophilic food simulants. However, the migration rates of HNTs alone were enhanced with increasing the HNT content in hydrophilic, lipophilic, and acidic food simulants. On the other hand, the biodegradation rate and light transmittance of nanocomposite films were reduced linearly by 18.56 and 26.90% with increasing the HNT content from 0 to 5 wt%. Overall, novel PVA/ST/GL/HNT nanocomposite films in this study offer highly competitive materials with excellent water resistance, good biodegradability, and acceptable transparency to be potentially used for sustainable food packaging particularly targeting lipophilic and acidic foodstuffs.

Keywords: polymer blends, nanocomposites, water resistance, migration rate, biodegradability

INTRODUCTION

Petro-based polymers generally possess good mechanical, thermal and barrier properties with easy processability and relatively low cost, which makes them widely used in different industrial sectors such as construction and building, appliances, and material packaging (Siracusa et al., 2008; Sam et al., 2016; Abdullah et al., 2017). Nevertheless, it is evident that plastic wastes in ~6,300 million metric tons were generated worldwide in 2015, and if this production rate continues without effective control it will be increased up to 12,000 million metric tons of plastic wastes by 2050 (Geyer et al., 2017). Non-degradable plastic wastes can be eliminated by recycling, landfilling, and incineration resulting in high processing cost and increasing global warming (Ray and Bousmina, 2005; Shah et al., 2008). Consequently, the

replacement of petro-based polymers with biopolymers becomes a suitable solution to tackle more severe environmental issues. Unfortunately, biopolymers have typical material demerits including high water/gas permeability, brittleness, and poor stability during processing as well as low heat resistance, so blending with other polymers and/or reinforcing with nanofillers can overcome these limitations (Sorrentino et al., 2007; Aslam et al., 2018).

Polyvinyl alcohol (PVA) is a synthetic water-soluble biopolymer, which possesses good mechanical and thermal properties as well as good transparency and resistance to oxygen permeation. Nonetheless, it has low degradation rates in some environments such as in soil along with relatively high cost and poor water resistance owing to the presence of hydroxyl groups in repeating units of PVA (Gupta et al., 2013; Gaaz et al., 2015; Lim et al., 2015; Aslam et al., 2018). Blending PVA with starch (ST) gives rise to the high improvement of biodegradability and cost reduction (Abdullah et al., 2017). ST is a completely biodegradable polymer in soil and compost, which is abundant as a spare storage in plants with non-toxic and relatively low-cost features. However, it is hard to process due to the high brittleness and limited flexibility (Avella et al., 2005; Tang et al., 2008; Jolanta et al., 2018). It is a semicrystalline polymer consisting of amylose and amylopectin at different ratios depending on plant sources. Amylose is a linear polymer in which glucopyranosyl repeating units are linked by α(1-4) linkages while the amylopectin is the branched counterpart with α(1-4) linked backbone and α(1-6) linked branches (Avella et al., 2005, Sam et al., 2016). Plasticized PVA/ST blends have been well-utilized since 1980s (Liu et al., 1999; Tang and Alavi, 2011). Such blends belong to a widespread material system used in numerous applications such as biomedical engineering and material packaging (Tang and Alavi, 2011; Luo et al., 2012; Tanase et al., 2015; Wang et al., 2015; Zanela et al., 2015). Glycerol (GL) is one of the most popular plasticisers mixed with PVA/ST blends due to their close solubility parameters, which are 22.50, 23.40, and 21.10 MPa$^{1/2}$ for PVA, ST, and GL, respectively (Rahman et al., 2010). Many hydroxyl groups in Plasticized PVA/ST blends yield weak water resistance. To overcome this drawback, it is essential to reinforce such blends with applicable nanofillers to improve not only mechanical and thermal properties but also their barrier properties (Mensitieri et al., 2011; Wang et al., 2015). For instance, Tian et al. (2017) found the water absorption capacity (W_a) of plasticized PVA/ST blend films was reduced by about 20% with the inclusion of 25 wt% montmorillonite (MMT) nanoclays. Similarly, Noshirvani et al. (2016) showed that the water solubility (W_s) and water vapor permeability (WVP) of plasticized PVA/ST/Cloisite-Na$^+$ MMT dropped by 50.81 and 16.46%, respectively, with increasing the nanofiller content from 0 to 7 wt% due to tortuous paths generated within nanocomposite films. Metal oxides can be employed to reinforce plasticized PVA/ST blends as well. For instance, nano-silicon dioxide (SiO_2) was used by Tang et al. (2008) to improve mechanical properties and water resistance of plasticized PVA/ST blend films. Moreover, Akhavan et al. (2017) reported that the W_a of plasticized PVA/ST blend films was reduced by 62% with the incorporation of 0.50 wt% nano-zinc oxide

(ZnO). In addition, cellulose nanocrystals (CNCs) were also used by Noshirvani et al. (2016) to reinforce plasticized PVA/ST blend films. Water resistance results demonstrated that the W_s and WVP of nanocomposites diminished by 25.19 and 4.85%, respectively, with increasing the CNC content from 0 to 7 wt%. Similarly, (Guimarães et al., 2015) found that the W_a and WVP of plasticized PVA/ST/bamboo nanofibril nanocomposite films were decreased by 30 and 20%, respectively, at the nanofiller content of 6.50 wt% when compared with those of plasticized PVA/ST blend films alone.

Halloysite nanotubes (HNTs) are a good nanofiller candidate to reinforce biopolymer blends because of their inherently good mechanical and thermal properties (Gaaz et al., 2017; Makaremi et al., 2017). To our best knowledge, HNTs as typical nanofillers have rarely been used to reinforce PVA/ST/GL blends despite their implementation in other bionanocomposite systems such as ST/HNT nanocomposites (Xie et al., 2011; He et al., 2012; Schmitt et al., 2015; Ren et al., 2018), PVA/HNT nanocomposites (Liu et al., 2007; Zhou et al., 2010; Qiu and Netravali, 2013; Fujii et al., 2014; Swapna et al., 2015), PVA/chitosan/HNT nanocomposites (Ali, 2016), soluble soybean polysaccharide (SSPS)/HNT nanocomposites (Alipoormazandarani et al., 2015), Pectin/HNT nanocomposites (Makaremi et al., 2017) and polylactic acid (PLA)/HNT nanocomposites (Dong et al., 2015; Castro-Aguirre et al., 2018; Chow et al., 2018). HNTs are naturally formed tubular nanoclays with a chemical formula $Al_2(OH)_4Si_2O_5 \cdot nH_2O$. Such a hollow tubular structure for HNTs is derived from warping octahedral and tetrahedral sheets in 1:1-layer clays (also called 1:1 phyllosilicate) with a lower number of hydroxyl groups on their outer surfaces to improve the HNT dispersion within polymer matrices (Gaaz et al., 2015). As compared with other tubular morphological structures of nanofillers like carbon nanotubes (CNTs), HNTs are cheap, widely available, and easily dispersed (Tully et al., 2015; Zhang et al., 2016). Moreover, it is considered as a non-toxic material mainly used for drug delivery in medical applications (Khoo et al., 2011; Rawtani and Agrewal, 2012; Salam et al., 2015; Yuan et al., 2015), and further for food packaging applications (Biddecia et al., 2016; Makaremi et al., 2017; Lee et al., 2018). Consequently, HNTs were used in this study as natural reinforcements for sustainable PVA/ST/GL/HNT nanocomposite films to improve their water resistance such as W_a, W_s and water contact angle as their mechanical and thermal properties were improved previously (Abdullah and Dong, 2017) when compared with those of PVA/ST/GL blend matrices.

When using nanocomposite materials for food packaging applications, the migration rate of nanocomposite constituents like nanofillers to foodstuffs should be seriously considered due to the food safety issue (Simon et al., 2008; Gressler et al., 2018). The overall migration rate and migration rate of nanofillers are studied widely for packaging materials based on petro-based nanocomposites such as low density polyethylene (LDPE) nanocomposites with different types of nanofillers like nanosilver (Hannon et al., 2016), nanocarbon black (Bott et al., 2014b), nanoclays (Echegoyen et al., 2016), and nanotitanium nitride (Bott et al., 2014a). PLA nanocomposites are also of a

particular concern in migration studies of bionanocomposite systems reinforced with different nanofillers such as sliver-based modified MMT nanoclays (Busolo et al., 2010), Cloisite nanoclays (Schmidt et al., 2009), CNCs (Fortunati et al., 2012), multi-walled CNTs (Velichkova et al., 2017). But very limited migration studies have been investigated based on other biopolymers like PVA and ST for potential material packaging applications. Avella et al. (2005) evaluated the migration rate of MMT nanoclays from ST/ 4 wt% MMT nanocomposite films in contact with lettuce and spinach. In a similar manner, Mauricio-Iglesias et al. (2010) found different quantities of aluminum ions (Al^+) and silicon ions (Si^+) in food simulants owing to the migration of MMT nanoclays from wheat-gluten/MMT nanocomposite films. Whereas, Cano et al. (2015b) concluded that the overall migration rate of PVA/ST/CNC nanocomposite films was increased by 26.08% with increasing the CNC content from 0 to 5 wt% in 10% ethanol simulant. Nonetheless, the overall migration rate was decreased by 66.67% in the isooctane simulant with increasing the CNC content from 0 to 5 wt%.

According to the Sustainable Packaging Coalition (2011) and Magnier and Crié (2015), the sustainable packaging should meet the following criteria: (i) useful, safe and healthy for individuals and communities throughout its life cycle, (ii) gathering market requirements for performance and cost, (iii) using renewable energy for manufacturing, transporting, and recycling, (iv) using renewable or recycled source materials, (v) using clean production technologies, (vi) made from materials healthy throughout their life cycle, (vii) designed to improve materials and energy, and (viii) effectively recovered and utilized in industrial/biological closed loop cycles. In this study, PVA, ST, and HNTs were selected as renewable materials for manufacturing nanocomposite films using solution casting as a clean production technology to meet the stringent criteria for sustainable packaging. Moreover, PVA/ST/GL/HNT nanocomposite films were characterized to investigate the effect of HNT contents on water resistance, transparency and biodegradability to study their material performance. The overall migration rates and HNT migration rates were explicitly investigated as well for PVA/ST/GL/HNT nanocomposite films with different food simulants mimicking hydrophilic, lipophilic, and acidic foodstuff conditions to evaluate their impact on critical food safety.

EXPERIMENTAL WORK

Materials

PVA (molecular weight: 89,000–98,000 g/mol and hydrolysis degree: 99%), soluble ST from potatoes (100% concentration), GL solution (molecular weight: 92.09 g/mol and 60–100% concentration), and nitric acid with 70% concentration were purchased from Sigma-Aldrich Pty. Ltd, Australia. Furthermore, HNTs were donated by Imerys Tableware Asia Ltd, New Zealand in form of as-received ultrafine particles with a relative density of 2.53 g/cm³. Glacial acetic acid with 96% concentration was supplied by Merck Pty. Ltd, Australia. Ethanol with 100% concentration was provided by Rowe Scientific Pty. Ltd, Australia. Aluminum standard solution with the concentration

of 1,000 mg/L in nitric acid was provided by ThermoFisher Scientific Pty. Ltd, Australia. Silicon standard solution also with the same concentration in nitric acid was purchased from High-Purity Standards, Inc. All materials were used as received without further modifications.

Fabrication of Films

Solution casting method was employed to fabricate neat PVA, PVA blends (i.e., PVA/GL, PVA/ST, PVA/ST/GL), and PVA/ST/GL/HNT nanocomposite films. An aqueous solution of 5 wt%/v PVA was obtained by dissolving 10 g PVA powders in 190 ml deionised water at 35°C to prepare neat PVA films. The solution was gradually heated up to 85°C with continuous stirring via an IKA®- RCT basic magnetic stirrer at 500 rpm for 3 h. Equal amounts of clear PVA solutions were poured into petri dishes (dish diameter: 15 cm) to produce thin films with uniform thickness of 0.110–0.125 mm. Then these films were subsequently dried at 50°C for 24 h. PVA/GL blends were also fabricated using the same procedure with the addition of 30 wt% GL as a plasticizer during the last 30 min in the fabrication process. PVA/ST aqueous solution at the blend ratio of 80/20 was prepared by mixing 8 g PVA and 2 g ST at room temperature in powder form, which was followed by dissolving them in 190 ml deionised water according to the same procedure mentioned earlier. PVA/ST blends were also plasticized with 30 wt% GL to fabricate PVA/ST/GL blends as final biopolymer matrices for corresponding nanocomposites. HNTs at different nanofiller contents of 0.25, 0.50, 1, 3, and 5 wt% were mechanically mixed using an IKA®- RW20 stirrer with 100 ml deionised water at 50°C and 500 rpm for 2 h to prepare the HNT aqueous suspension. Subsequently, the HNT suspension was sonicated using an ultrasonicating bath ELMA Ti-H-5 model at 50°C for 1 h with the frequency of 25 kHz and power intensity of 90%. The HNTs suspension was added in a dropwise manner to 100 ml PVA/ST/GL blend solution at 50°C and 500 rpm with the aid of mechanical stirring for 30 min. Finally, the prepared mixture solution was further homogenized via a magnetic stirrer at 50°C and 350 rpm for 30 min. The sonication process continued for extra 30 min in the same conditions to remove any entrapped air bubbles. Neat PVA, PVA blends, and PVA/ST/GL/HNT nanocomposite films were stored in a desiccator to dry all materials for at least 1 week prior to the following experimental characterization.

CHARACTERIZATION METHODS

Water Absorption Capacity (W_a)

Water absorption capacity (or water uptake) tests were carried out according to ASTM standard D570-98 with the customized modification in term of sample size and water amount. Square samples of all materials in size of 2 × 2 cm² were pre-dried in a vacuum oven at 50°C for 24 h, and then cooled to room temperature in a desiccator prior to weighing them as initial dry weight (W_o). These samples were immersed in 100 ml distilled water at room temperature until they reached an equilibrium condition after 24 h. Further they were removed from water and their surfaces were gently dried with paper tissues. Afterwards,

such samples were weighed again to measure their wet weight after the immersion (W_t). Three samples for each batch have been tested along with reported average data and associated standard deviations. Water absorption capacity (W_a) could be calculated according to the following equation:

$$W_a\ (\%) = \frac{W_t - W_o}{W_o} \times 100\% \qquad (1)$$

Water Solubility (W_s)

All swollen samples from water absorption tests were used to calculate the water solubility of materials according to ASTM standard D570-98. Samples were dried again in a vacuum oven at 60°C for 24 h, then they were cooled down to room temperature in a desiccator for about 30 min. The samples were weighed to acquire the dry weight after immersion (W_d). The water solubility (W_s) was then determined by using the formula below:

$$W_s\ (\%) = \frac{W_o - W_d}{W_o} \times 100\% \qquad (2)$$

Water Contact Angle

Water contact angles of neat PVA, PVA blends and PVA/ST/GL/HNT nanocomposite films were determined by using a Tensiometer KSV-CAM 101 (KSV Instruments Ltd., Finland). The surface hydrophilicity of films was evaluated by dropping 2 μL deionised water on their flat surfaces using a Sessile Drop Half-Angle™ Tangent line method (Sadegh-Hassani and Nafchi, 2014; Alipoormazandarani et al., 2015). At least five droplets at random places of different samples for each material batch were reported for test reliability.

Uv-Vis Spectra

The light transmittance of all materials was measured in a range of 200–800 nm on an ultraviolet-visible (UV-vis) spectrometer (Jasco-V670) with a blank glass plate being used as a reference. Light transmittance ($T\%$) of film samples, three samples per material batch, was determined with a scan rate of 200 nm/min.

Migration Tests

The migration rates of nanocomposite films were investigated according to (European Union Commission Regulation (EU) No. 10, 2011). In this study, three different food simulants, namely 10% (v/v) ethanol solution (simulant A), 50% (v/v) ethanol solution (simulant D1), and 3% (w/v) acetic solution (simulant B) were employed to mimic hydrophilic, lipophilic and acidic foodstuff conditions, respectively. Approximately 1 dm^2 PVA/ST/GL blend films and their corresponding nanocomposite films with different HNT contents were immersed in individual glass bottles filled with 100 ml food simulant solutions, as recommended by The European Standard EN. (2002). Glass bottles were tightened and then kept in the oven at 40°C for 10 days. Six samples were selected for each food simulant, in which initial three samples were used to calculate overall migration rates and the other three samples were particularly employed for migration rates of nanofillers. After 10 days, the bottles were removed from the oven, and then cooled down to room temperature before opening to reduce the evaporation of food

simulants. All samples were removed from food simulants gently. The food simulants of initial three samples were evaporated, and the residues were dried overnight at 105°C, which were then weighed after cooling down to room temperature with an analytical balance (±0.0001 g precision) to calculate the overall migration rates in mg/kg. Associated results were well compared with overall migration limit (OML) of 60 mg/kg (European Union Commission Regulation (EU) No 10/2011).

Inductivity coupled plasma-optical emission spectroscopy (ICP-OES) (PerkinElmer-Optima 8300) was implemented to evaluate the migration rates of Al$^+$ and Si$^+$ as a clear indication for the HNT migration from nanocomposite films. As a result, the residues for the other three samples were digested after being dried by using 15 ml HNO$_3$ (solution concentration: 3%) at 95°C for 2.5 h. The digestion process was used to convert the residues of elements to an ionic state, and meanwhile to diminish the effect of matrices and reduce the contamination of equipment with dust. The operation parameters of ICP-OES were listed in **Table 1**. For ICP-OES calibration, two blank solutions (i.e., distilled water and 3% nitric acid) and three standard solutions were used. Each standard solution contained an equal concentration of both Al$^+$ and Si$^+$. They were prepared by a serial dilution of stock standard solutions with the same concentration of 1,000 mg/L for both Al$^+$ and Si$^+$, which were further diluted to 1, 5, and 10 mg/L for Al$^+$ and Si$^+$.

Soil Burial Degradation

The biodegradability of neat PVA, PVA blends, and PVA/ST/GL/HNT nanocomposites with different HNT contents was evaluated by a soil burial method according to the studies carried out by Thakore et al. (2001). Plastic containers with the 2 L capacity were filled with sieved agricultural soil obtained from local plant nursery. The square samples (3 × 3 cm^2) were weighed first to record their initial weight (W_o), and then were buried at the under-surface depth of 5 cm. Such degradation tests were conducted at room temperature with 40–50% relative humidity (RH). In order to keep the identical conditions, the humidity level was controlled with a humidity meter and plastic containers were sprinkled with water to maintain the humidity at a constant level throughout the tests. The total testing period was monitored for 6 months (i.e., 24 weeks), in which these samples were removed from soil on a weekly basis in the initial 3 months, and then extended to every 3 weeks for the rest of months. Distilled water was utilized to wash samples and remove any soil from their surfaces. After these samples were dried in a vacuum

TABLE 1 | ICP-OES operating parameters for nanofiller migration tests.

Parameter	Value
Plasma viewing mode	Radial and Axial
Plasma gas flow rate	15 L/min
Auxiliary gas flow rate	0.50 L/min
Nebuliser gas flow rate	0.60 L/min
Pump flow rate	1.50 mL/min
Radiofrequency	1,400 Watts

oven at 70°C for 24 h, they were weighed to record a dried weight (W_d). As a result, biodegradation rate was calculated from the weight difference based on the given equation below:

$$Biodegredation\ rate\ (\%) = \frac{W_o - W_d}{W_o} \times 100\% \qquad (3)$$

Three samples for each batch were used for test reproducibility.

Scanning Electron Microscopy (SEM)

The surface morphology of neat PVA, PVA blends and PVA/ST/GL/HNT nanocomposite films were examined before, during, and after soil burial degradation tests by using a NEON-40EsB field emission scanning electron microscope (FE-SEM) at an accelerating voltage of 2 kV. All samples were fixed on aluminum stubs and coated with platinum layer (layer thickness: 3 nm) to improve the contrast of material constituents.

RESULTS AND DISCUSSION

Water Absorption Capacity

Since most biopolymers have the high sensitivity to water, the study of W_a parameter is essential particularly in relation to food packaging applications (Sadegh-Hassani and Nafchi, 2014; Aloui et al., 2016). The addition of 30 wt% GL tended to moderately decrease the W_a from 127.61% for PVA alone to 114.58% for PVA/GL blends, which could be associated with the strong interaction between PVA and GL resulting in the consumption of free hydroxyl groups of PVA in good agreement with Follain et al. (2005). On the other hand, as illustrated in **Figure 1**, one could see that PVA/ST blends had the highest W_a, which was ascribed to partial constituent miscibility with many free sites being occupied by water molecules. As expected, high hydrophilicity of starch with good water absorption inevitably yielded the increase in W_a for PVA/ST blends (Ali, 2016), which was believed to be associated with typical hygroscopic nature of starch (Azahari et al., 2011; Ismail and Zaaba, 2011; Salleh et al., 2017). It was implied that the equilibrium with the environment could be reached by water gain and loss. Nonetheless, the GL plasticization effect in PVA/ST/GL blends gave rise to much lower W_a, which may benefit from its improvement of phase miscibility and constituent interactions, as evidenced by Zou et al. (2008) to conclude that the presence of GL improved the compatibility between PVA and ST and reduced the W_a.

The incorporation of HNTs in PVA/ST/GL/HNT nanocomposites further reduced the W_a when compared with that of PVA/ST/GL blends, which could be explained by a typical reduction for water diffusion in the presence of HNTs within their morphological structures (Sadegh-Hassani and Nafchi, 2014). A drastic decrease in W_a from 128.23 to 74.23% was attributed to the fact that embedded HNTs generated tortuous paths to hinder the water diffusion when the HNT content was increased from 0 to 1 wt%. Similar effect of HNTs was reported on chitosan/HNT nanocomposites and chitosan/clove essential oil (CEO)/HNT nanocomposites by Lee et al. (2018). Their results showed that the W_a of chitosan/HNT nanocomposites and chitosan/CEO/HNT nanocomposites was reduced by 42.17 and 43.31%, respectively, at the HNT content
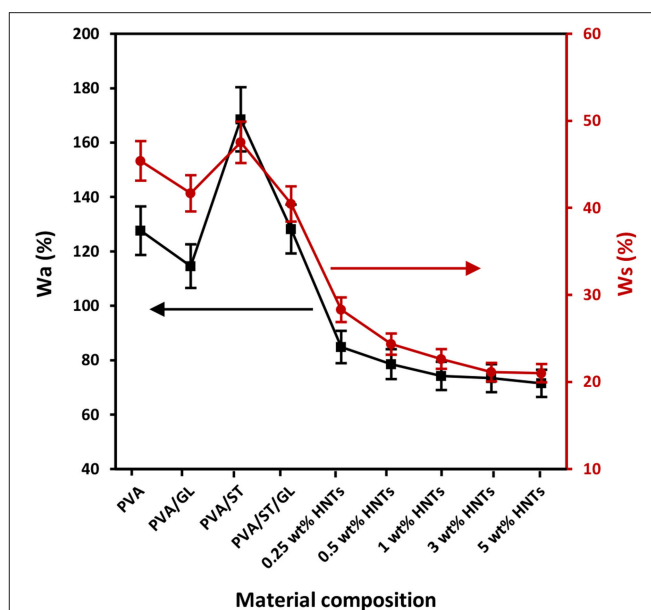

FIGURE 1 | Water absorption capacity (W_a) and water solubility (W_s) of neat PVA, PVA blends, and PVA/ST/GL/HNT nanocomposites at different HNT contents.

of 30 wt% as opposed to those of corresponding matrices due to the incorporation of nanofillers to affect the water absorption of matrices. Moreover, Abbasi (2012) stated that the W_a of plasticized PVA/ST blend films significantly diminished by 50% with increasing the nano-SiO_2 content from 1 to 5 wt% owing to highly active physical interaction between nanofillers and blend matrices to lower the number of hydroxyl groups in nanocomposite films. However, as illustrated in **Figure 1**, the W_a appeared to show a minor reduction up to 3.69% beyond 1 wt% HNTs. This phenomenon arose from the HNT agglomeration mentioned in our previous work (Abdullah and Dong, 2017). The above-mentioned findings obtained in this study were also consistent with relevant results in plasticized PVA/ST/MMT nanocomposite films (Taghizdeh et al., 2012; Tian et al., 2017) as well as plasticized PVA/ST/nano-SiO_2 nanocomposite films (Tang et al., 2008). Overall, the reduction of W_a in nanocomposite films could be determined based upon nanofiller content and nanofiller dispersion within polymer matrices.

Water Solubility

The W_s values of neat PVA, PVA blends and PVA/ST/GL/HNT nanocomposites were also demonstrated in **Figure 1**. In general, when material films have high W_a, they tend to easily dissolve in water as well because water molecules are absorbed onto hydroxyl groups particularly with hydrogen bonding to make the films easier to dissolve (Azahari et al., 2011). As such, W_a and W_s of all film materials possessed a very similar overall trend despite different magnitudes of parameters, as observed in **Figure 1**. The high values of W_s were accepted because all the constituents had hydrophilic nature including PVA, ST, and GL, which was consistent with other studies (Cano et al., 2015a;

Zanela et al., 2015). The W_s of neat PVA was decreased by 8.21% when blended with GL to decrease the number of free hydroxyl groups interacting with water molecules. PVA/ST blends yielded the highest W_s among all film materials resulting from the high water affinity of constituents according to the studies carried out by Negim et al. (2014). On the other hand, the W_s of PVA/ST/GL blends was found to be reduced by 14.89% due to the presence of GL as a plasticizer to increase the miscibility between PVA and ST with better interfacial bonding (Zanela et al., 2015; Cano et al., 2015a).

The incorporation of HNTs to PVA/ST/GL blend films appeared to reduce the W_s in a monotonically decreasing manner from 40.45 to 21.10% with increasing the HNT content from 0 to 5 wt% accordingly. This finding may be associated with the hydrophobic nature of HNTs resulting from a low number of hydroxyl groups on HNT surfaces (Liu et al., 2014). Moreover, SiO_2 groups in HNTs had the ability to form strong hydrogen bonds by consuming free hydroxyl groups of polymer matrices and reduce the number of interaction sites with water molecules (Sadegh-Hassani and Nafchi, 2014). The W_s reduction was more pronounced when the HNT content was in range of 0.25–1 wt% as shown in **Figure 1**, because of good HNT dispersion within blend matrices in nanocomposite films. Whereas, such a decrease tendency became insignificant in range from 22.64 to 21.10% when increasing the HNT content from 1 to 5 wt% owing to the same HNT agglomeration issue mentioned in previous W_a results. Our finding was in good accordance with those in plasticized PVA/ST/nano-SiO_2 nanocomposites (Tang et al., 2008) and plasticized PVA/ST/$CaCO_3$ nanocomposites (Kisku et al., 2014).

Water Contact Angle

Water contact angle of neat PVA, PVA blends, and PVA/ST/GL/HNT nanocomposites were measured in order to evaluate the hydrophilic nature of all material surfaces. It is well-known that low water contact angles <90° is referred to as the high material wettability whilst high contact angles >90° correspond to low wettability instead (Yuan and Lee, 2013). In other words, low water contact angles could signify higher hydrophilic nature of material surfaces and vice versa (Sadegh-Hassani and Nafchi, 2014, Alipoormazandarani et al., 2015). Apparently, neat PVA, which is considered as a popular water-soluble polymer, had a very low water contact angle of 28.35° in good agreement with the previous result (Lim et al., 2015). The addition of GL to PVA only slightly increased the water contact angle for PVA/GL blend films by 0.33°C, which could be interpreted by their insignificant reductions in W_a and W_s. Moreover, with the incorporation of ST, the hydrophilic level of PVA/ST blend films was further improved, as evidenced by a decrease in water contact angle by 9.70° compared with that of neat PVA counterpart, as illustrated in **Figure 2**. Moreover, an angle reduction of 2.78°C was reported for PVA/ST/GL blend films as opposed to that of neat PVA counterpart. The remarkable hydrophilic improvement for PVA blends, when compared with that of neat PVA, could be associated with more hydroxyl groups existing in PVA blends with the addition of ST.
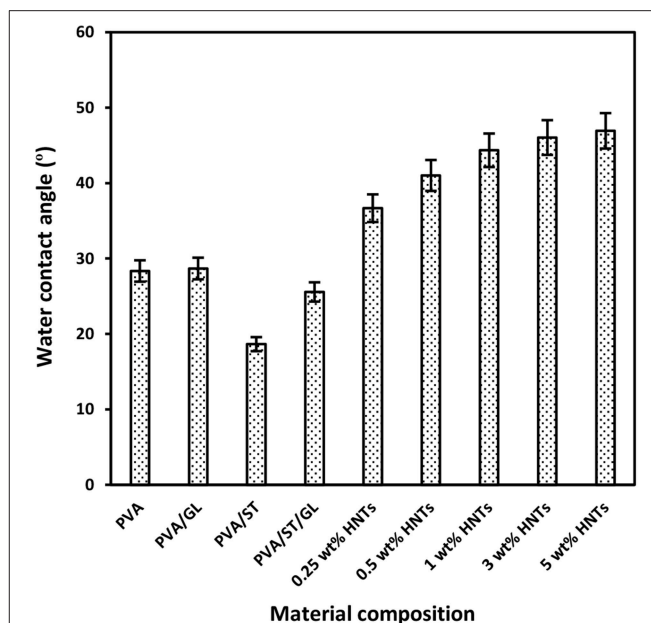

FIGURE 2 | Water contact angles of neat PVA, PVA blends, and PVA/ST/GL/HNT nanocomposite films at different HNT contents.

Such a finding further coincided with the increases in W_a and W_s of PVA blend films as compared to those of neat PVA.

On the other hand, a significant increase in water contact angles of nanocomposite films was pronounced from 25.57 to 46.93°C with increasing the HNT content from 0 to 5 wt%. This was attributed to relatively hydrophobic nature of HNTs with a low number of hydroxyl groups leading to a decrease in water absorption capacity so that nanocomposite surfaces tended to be less hydrophilic (Liu et al., 2014, Sadegh-Hassani and Nafchi, 2014, Alipoormazandarani et al., 2015). Moreover, well-dispersed HNTs within blend matrices could use some free hydroxyl groups to build hydrogen bonding between them. It is well-known that the presence of nanofillers can lead to increasing the surface roughness of polymer matrices in nanocomposites (Grunlan et al., 2003).Therefore, the surface roughness of nanocomposite films was enhanced in the presence of HNTs resulting in the further increase in water contact angle based on Wenzel's theory (Wenzel, 1949). According to this theory, the surface hydrophobicity would be improved with increasing the surface roughness as follows (Kubiak et al., 2011):

$$\cos \theta_m = r \cos\theta \tag{4}$$

Where θ_m and θ are the measured and ideal contact angles, respectively, which can be calculated from perfect smooth surface like mirror, and r is the roughness ratio where $r = 1$ for smooth surfaces and $r>1$ for rough surfaces (Kubiak et al., 2011). Similarly, Biddecia et al. (2016) found the water contact angle of pectin/modified HNT nanocomposite film surfaces was increased by 6°C as compared with that of neat pectin matrices due to increasing the surface roughness of nanocomposite films with the addition of HNTs.

PVA/ST/GL/HNT nanocomposite films were still within the hydrophilic-material range though their water contact angle was increased up to 21.57°C compared with that of PVA/ST/GL blends. The increased water contact angles for nanocomposite films were correlated well with corresponding reductions in their W_a and W_s, with increasing the HNT contents.

UV-Vis Spectra

One of important features in food packaging for consideration is the film transparency in terms of light transmittance (T%). Typical light transmittance curves for neat PVA, PVA blends and PVA/ST/GL/HNT nanocomposites as well as respective digital images of Curtin University logo observed through each of film batches were displayed in **Figures 3A,B**, respectively.

Neat PVA in possession of high crystallinity led to relatively high T% in range of 99–100.0%, which was close to previously determined results elsewhere (Gupta et al., 2013). Depending on the phase miscibility, PVA/ST/GL had a slightly reduced T% of 95.76–98.72%, which was believed to be induced by the incident light loss from the light transmission, scattering, absorption, reflection and refraction when striking an interface while such a loss was increased especially at interfacial areas (Cai et al., 2016). Regardless of different wavelengths used, nanocomposite films yielded a significant decrease in T% when the HNT content was increased from 0 to 5 wt%, which was mostly pronounced at
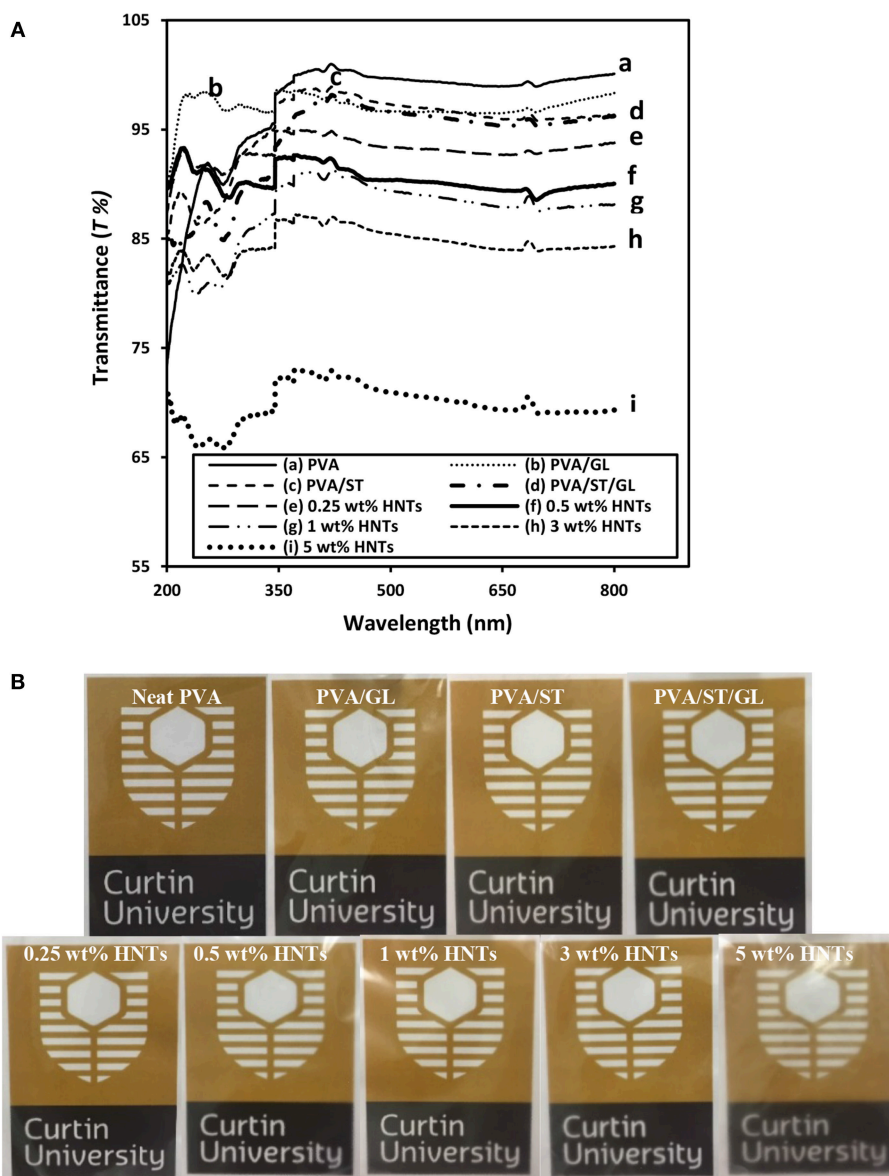

FIGURE 3 | (A) UV-vis spectra curves, and **(B)** digital images for the film transparency of neat PVA, PVA blends, and PVA/ST/GL/HNT nanocomposites at different HNT contents.

the higher content level of 5 wt%. Apparently, nanocomposite films with higher HNT contents inevitably led to higher surface roughness due to the inclusion of highly agglomerated nanofillers resulting in increased light scattering sites (Grunlan et al., 2003), as also confirmed by other studies in plasticized PVA/ST nanocomposite films (Tang et al., 2008, Akhavan et al., 2017). On the other hand, Lee et al. (2018) considered this reduction of $T\%$ as an advantage for food packaging applications since the UV-barrier properties of chitosan/CEO/HNT nanocomposite films could be improved leading to better protection of foodstuffs against nutrient loss, decolonization and lipid oxidation.
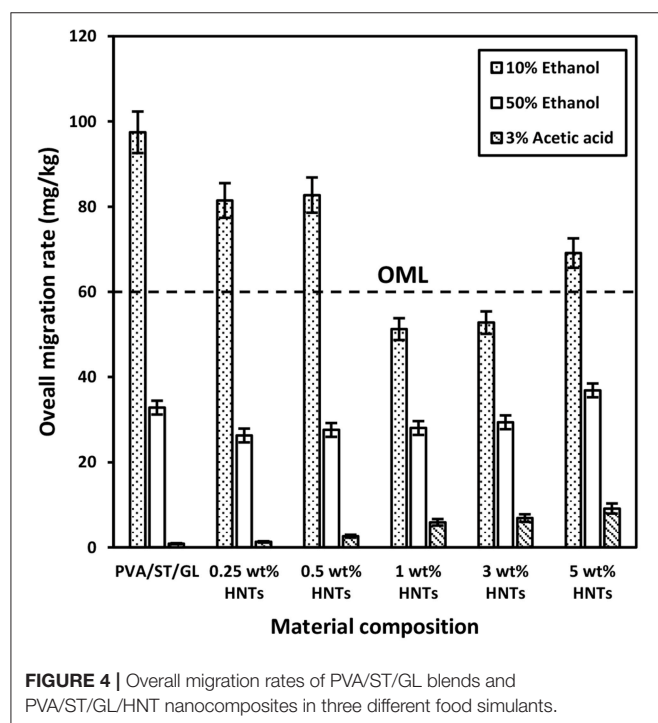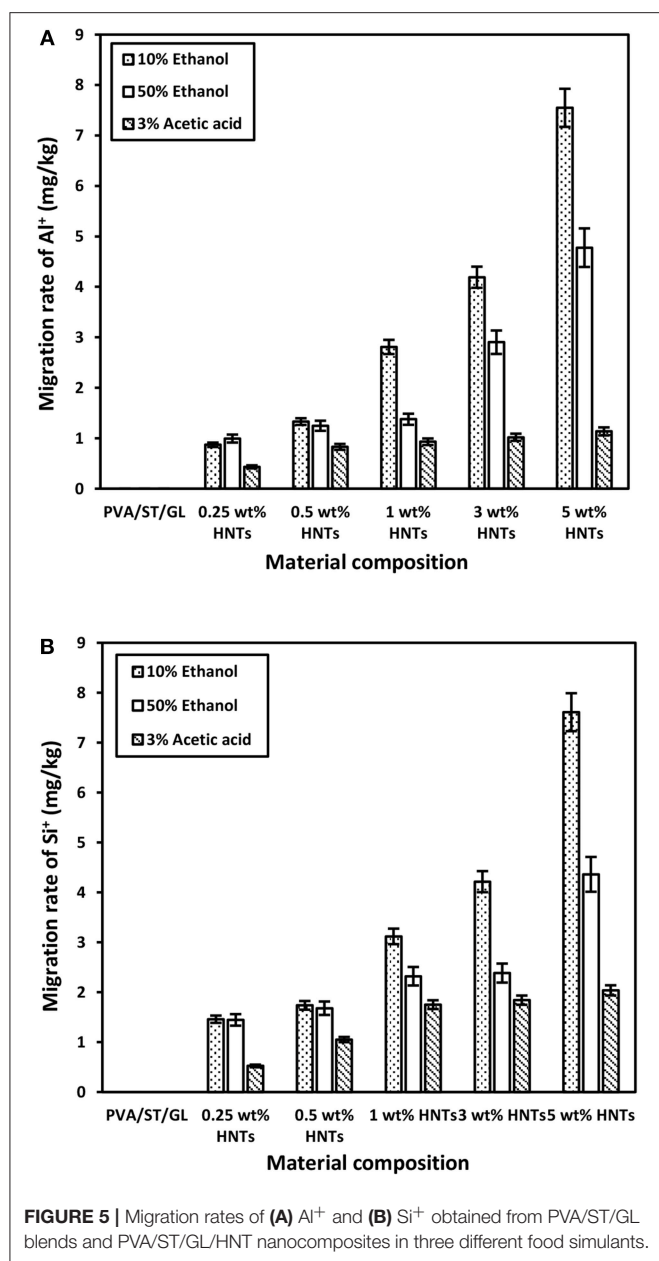
Overall Migration Rate

The overall migration rates in three different food simulants, namely 10% ethanol (simulant A), 50% ethanol (simulant D1), and 3% acetic acid (simulant B) were presented in **Figure 4**, which represented typical hydrophilic, lipophilic and acidic foodstuffs. It was evident that overall migration rates seemed to be much higher in PVA/ST/GL blends especially when contacting with simulant A as opposed to those of nanocomposite films, which stemmed from water soluble characteristic of PVA, ST and GL constituents in their blends (Mauricio-Iglesias et al., 2010). The overall migration rate of PVA/ST/GL blend and their nanocomposite films exceeded the OML of 60 mg/kg in food simulant A except those nanocomposites at HNT contents of 1 and 3 wt%, which could be applicable to safe food packaging. The hydrophilic nature of PVA/ST/GL blends and their nanocomposite films could improve their solubility in any hydrophilic solution like food simulant A. It was easily understood that with the addition of HNTs as hydrophobic nanofillers, the solubility of PVA/ST/GL blend matrices could

diminish as earlier mentioned. On the other hand, strong interfacial bonding between HNTs and blend matrices was another plausible reason to reduce the mass transfer while in contact with food simulants. Therefore, it was clearly indicated that optimal HNT contents of 1 and 3 wt% had significant impact on the remarkable reductions of overall migration rates by 47.41 and 45.85% in food simulant A, respectively, as opposed to that of PVA/ST/GL blends. Notwithstanding that the overall migration rate of nanocomposite films with the inclusion of 5 wt% HNTs was increased again by 30.97% possibly due to the HNT agglomeration, it was still lower than those of PVA/ST/GL blends and nanocomposites at the HNT contents of 0.25 and 0.50 wt%. Such a finding was further proven by Cano et al. (2015b), when dealing with PVA/ST/CNC nanocomposite films. With respect to simulant D1, overall migration rates of both PVA/ST/GL blends and nanocomposites were unanimously well below the OML of 60 mg/kg. The overall migration rates of nanocomposites were decreased at HNT contents of 0.25–3 wt% relative to that of PVA/ST/GL matrices and the maximum reduction by 19.93% was recorded at the lowest HNT content of 0.25 wt%. Finally, the lowest overall migration rates were recorded in food simulant B to mimic acidic foodstuffs at the pH level below 4.50. There was a clear modestly increasing trend for overall migration rates of nanocomposites from 1.29 to 9.13 mg/kg when increasing the HNT content from 0 to 5 wt%. The overall migration rates of PVA/ST/GL/HNT nanocomposites were highly influenced by the selection of food simulants in which they possessed a higher sensitivity to hydrophilic foodstuffs, followed by lipophilic foodstuffs and then acidic foodstuffs with the least impact. In view of safe food packaging, all polymer blend and nanocomposite films were satisfied with the OML criterion to be used for lipophilic and acidic foodstuff packaging while only nanocomposite films at the HNT contents of 1–3 wt% were suitable for hydrophilic foodstuffs.

Migration of HNTs

The HNT migration was evaluated by detecting the presence of Al^+ and Si^+ in migrated materials. There were no traces of Al^+ and Si^+ detected in migrated materials from PVA/ST/GL blend films. In other words, the overall migration rate of such polymer blend films clearly reflected the quantities of migrated polymeric molecules to different food simulants. On the other hand, different quantities of Al^+ and Si^+ were found in all migrated materials based on nanocomposite films, as shown in **Figures 5A,B**, respectively. The migration rates of both Al^+ and Si^+ were in good agreement with the overall migration rates in different food simulants. That means higher quantities of Al^+ and Si^+ were detected in food simulant A, which was followed by food simulant D1 along with their lowest quantities in food simulant B. Such a finding could be due to the hydrophilic nature of food simulant A, which worked as solvent-like water on nanocomposite films resulting in increasing the chain mobility of polymeric molecules and improving the release of nanofillers from nanocomposite films. Lee et al. (2018) discussed similar results based on the migration of CEO in chitosan/CEO films and chitosan/CEO/HNT nanocomposite films by migrating simulant molecules from external surfaces

FIGURE 4 | Overall migration rates of PVA/ST/GL blends and PVA/ST/GL/HNT nanocomposites in three different food simulants.

FIGURE 5 | Migration rates of **(A)** Al^+ and **(B)** Si^+ obtained from PVA/ST/GL blends and PVA/ST/GL/HNT nanocomposites in three different food simulants.

rate results mentioned earlier. Such phenomenal results may be interpreted by two different mechanisms of *diffusion* for the penetration of food simulants in nanocomposite films, and *embedding* to represent intermolecular forces between penetrated molecules and film materials according to the dual sorption theory (Huang et al., 2011; Farhoodi et al., 2014). Since the diffusion process could be much faster than embedding counterpart, the diffusion of hydrophilic molecules in PVA/ST/GL/HNT nanocomposite films further enlarged interconnecting spaces between polymeric chains to better facilitate the HNT release from nanocomposite films. As such, fast diffusion in film materials played a leading role in controlling migration rates, which tended to be much higher in hydrophilic foodstuffs as opposed to those in lipophilic and acidic counterparts.

According to European Union Commission Regulation (EU) No. 10 (2011), there was no specific migration limits for Al^+ and Si^+ that could be followed for comparison. However, HNTs were classified as a natural, biocompatible, non-toxic and EPA 4A listed material (Kamble et al., 2012; Kryuchkova et al., 2016; Lvov et al., 2016). Consequently, HNTs were widely used for medical applications such as drug delivery particularly for non-injectable drug formula, bone cement, dentist resin, tissue scaffolds, cosmetics, and antiseptic treatment of hospitals (Kamble et al., 2012; Lvov et al., 2016; Fizir et al., 2018). Numerous studies were carried out on the toxicity of HNTs by the *in-vitro* and *in-vivo* experiments. Their results showed that HNTs did not possess the toxicity up to a concentration of 75 μg/mL and about 90% of tested cells were still viable (Vergaro et al., 2010; Fizir et al., 2018; Santos et al., 2018). Whereas, other studies further extended such a concentration to 100 μg/mL (Lvov et al., 2016), and 200 μg/mL (Guo et al., 2012). As such, the migrated amounts of HNTs from PVA/ST/GL/HNT nanocomposite films were well within the safe limits (based on the part per million (ppm) as a scale for comparison) without any toxic effect on the nanoparticle intake by human bodies. Overall, no great difference was shown between the quantities of Al^+ and Si^+ migrated in each food simulant as a result of similar element contents of Al (20.90%) and Si (21.76%) detected in the HNT composition (Abdullah et al., 2017). It was expected that increasing the HNT content from 0.25 to 5 wt% inevitably enhanced the quantities of Al^+ and Si^+ despite various increasing levels depending on the use of three different food simulants. The consistently highest quantities of migrated Al^+ and Si^+ with the inclusion of 5 wt% HNTs in nanocomposite films might also be described by the detrimental effect of nanofiller agglomeration at high HNT content levels to induce their poor interfacial bonding with blend matrices (Abdullah and Dong, 2017) when compared with well-dispersed HNTs at the low contents, as shown in **Figure 6**. Consequently, the release of highly agglomerated HNTs to food simulants appeared to be much easier than those well-dispersed HNTs embedded in matrices in nanocomposite films.

Soil Burial Degradation

The biodegradability of most biopolymers was highly related to the W_a and W_s since their degradation was initiated with the water absorption on their surfaces, and then followed
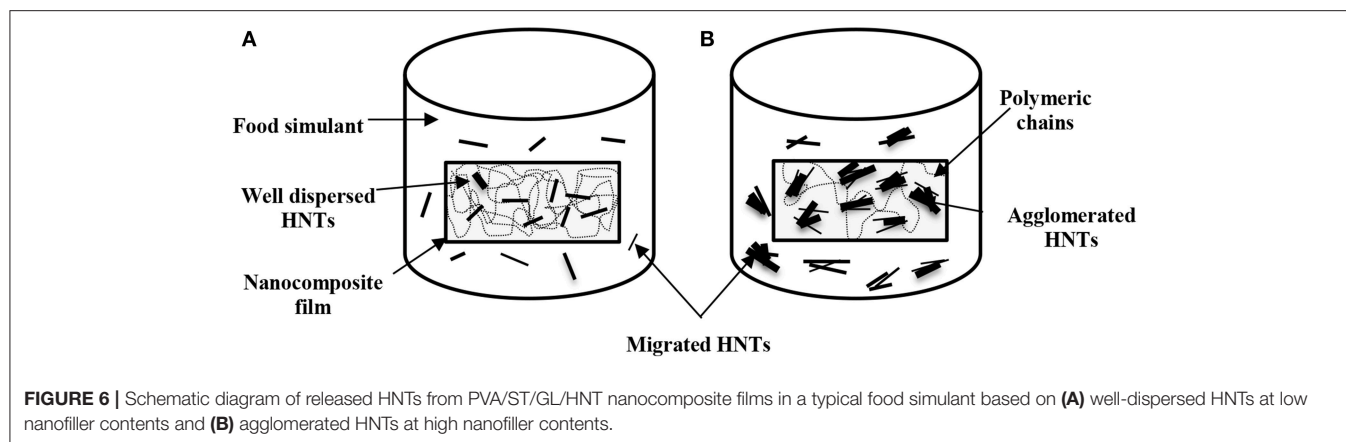
of the films to internal film structures, which resulted in weak and lost bonding networks between film constituents. As such, active agents trapped by continuous polymer matrices could be easily released, particularly when polymeric molecules were soluble in simulants. The amounts of migrated Al^+ and Si^+ in food simulant A were increased by 766.67 and 424.82% with increasing the HNT content from 0.25 to 5 wt%, respectively, which was followed by 381.82 and 202.87% in simulant D1 as well as 162.79 and 290.38% in simulant B accordingly. Once again, food simulant B had the weakest interaction with nanocomposite films especially for migrated Al^+ related to the inert nature of Al element to acidic foodstuffs, and this finding was consistent with the overall migration

FIGURE 6 | Schematic diagram of released HNTs from PVA/ST/GL/HNT nanocomposite films in a typical food simulant based on **(A)** well-dispersed HNTs at low nanofiller contents and **(B)** agglomerated HNTs at high nanofiller contents.

by the growth of microorganism like bacteria and fungi. On the other hand, high material solubility also accelerated the biodegradability, which was particularly the case in soil (Guohua et al., 2006; Zanela et al., 2015). The digital images of films before and after 24-week biodegradation tests clearly indicated that PVA/ST, PVA/ST/GL blends and PVA/ST/GL/HNT nanocomposite films diminished in size and intended to become more fragile and wrinkling films, as depicted in **Figure 7A**. Neat PVA and PVA/GL blend films possessed relatively good transparency after biodegradation tests. Whereas, PVA/ST, PVA/ST/GL blends and PVA/ST/GL/HNT nanocomposite films tended to undergo a great color change and become more yellowish after biodegradation tests. This phenomenon could be associated with the presence of potato-based soluble ST prone to the strong attack by microorganism when compared with the former PVA and PVA/GL blends (Hejri et al., 2013).

Biodegradation rates of neat PVA, PVA blends and PVA/ST/GL/HNT nanocomposites were evaluated as a function of time over 24-week periods, as shown in **Figure 7B**, which could be clearly divided into an "active-state period" in the initial 3 weeks where most materials degraded in very rapid pace as well as "steady-state period" for the rest of time at a relatively slow rate until the end of tests, as confirmed by other studies (Guohua et al., 2006; Hejri et al., 2013; Singha and Kapoor, 2014). Azahari et al. (2011) stated that such a phenomenon could take place in soil and compost degradation due to the composting process including active composting and curing stages. In the active stage, a strong microbial activity happened due to rising temperatures resulting from oxygen availability. In comparison, as the temperature decreased in the curing stage, the degradation process continued with a relatively slow rate. Neat PVA films possessed the lowest biodegradation rate of 5.87% among all materials after 24 weeks in this study, which suggested that PVA had high resistance to biodegradation in soil, and this slight weight loss was associated with its typical characteristic of hydrolysability (Imam et al., 2005; Guohua et al., 2006; Kopcilova et al., 2013). Normally, carbon backbone polymers like PVA are not susceptive to

biodegradation (Kale et al., 2007). However, polymeric chains of PVA were cleaved, decreased in molecular weight and finally consumed by microorganisms due to the enzymatic oxidation of hydroxyl and carbonyl groups, which was then followed by the hydrolysis of these groups (Kale et al., 2007). Nonetheless, blending GL with PVA in film materials was found to increase their biodegradation rate up to 23.33% because it increased the chain mobility of PVA molecules with the further improvement of water diffusion through their morphological structures. Moreover, the addition of ST, when considered as a fully biodegradable polymer (Guohua et al., 2006; Azahari et al., 2011), inevitably further increased the biodegradation rate up to 39.54%, which was attributed to easier microorganism attack to ST material structures than those of neat PVA (Hejri et al., 2013, Kale et al., 2007). It was well reported that increasing the ST content could improve the biodegradation rate of PVA/ST blends in a linear manner (Jayasekara et al., 2003; Azahari et al., 2011; Tanase et al., 2015). With respect to the biodegradability of nanocomposite films, it was manifested that their biodegradation rate dropped linearly from 56.94 to 41.28% with increasing the HNT content from 0 to 1 wt%, which directly benefited from the formation of hydrogen bonds between well-dispersed HNTs and blend matrices so that water diffusion, mass transfer and infiltration speed of microorganisms were restricted (Tang et al., 2008). At the HNT contents of 3 and 5 wt%, the biodegradation rates were modestly increased to 45 and 45.80%, respectively, due to the agglomeration of HNTs, which were still more significant when compared with that of neat PVA, in good agreement with other results (Imam et al., 2005; Tang et al., 2008; Heidarian et al., 2017).

SEM Analysis

Neat PVA, PVA blends and PVA/ST/GL/HNT nanocomposites were also examined via SEM analysis to understand structural damage due to soil burial degradation over different time periods, namely at initial week (0 W), during the active-state periods after 1 week (1 W) and 3 weeks (3 W) as well as at the end of the degradation tests (i.e., after 24 W), as shown in **Figures 8**, **9**. Only morphological structures of nanocomposite
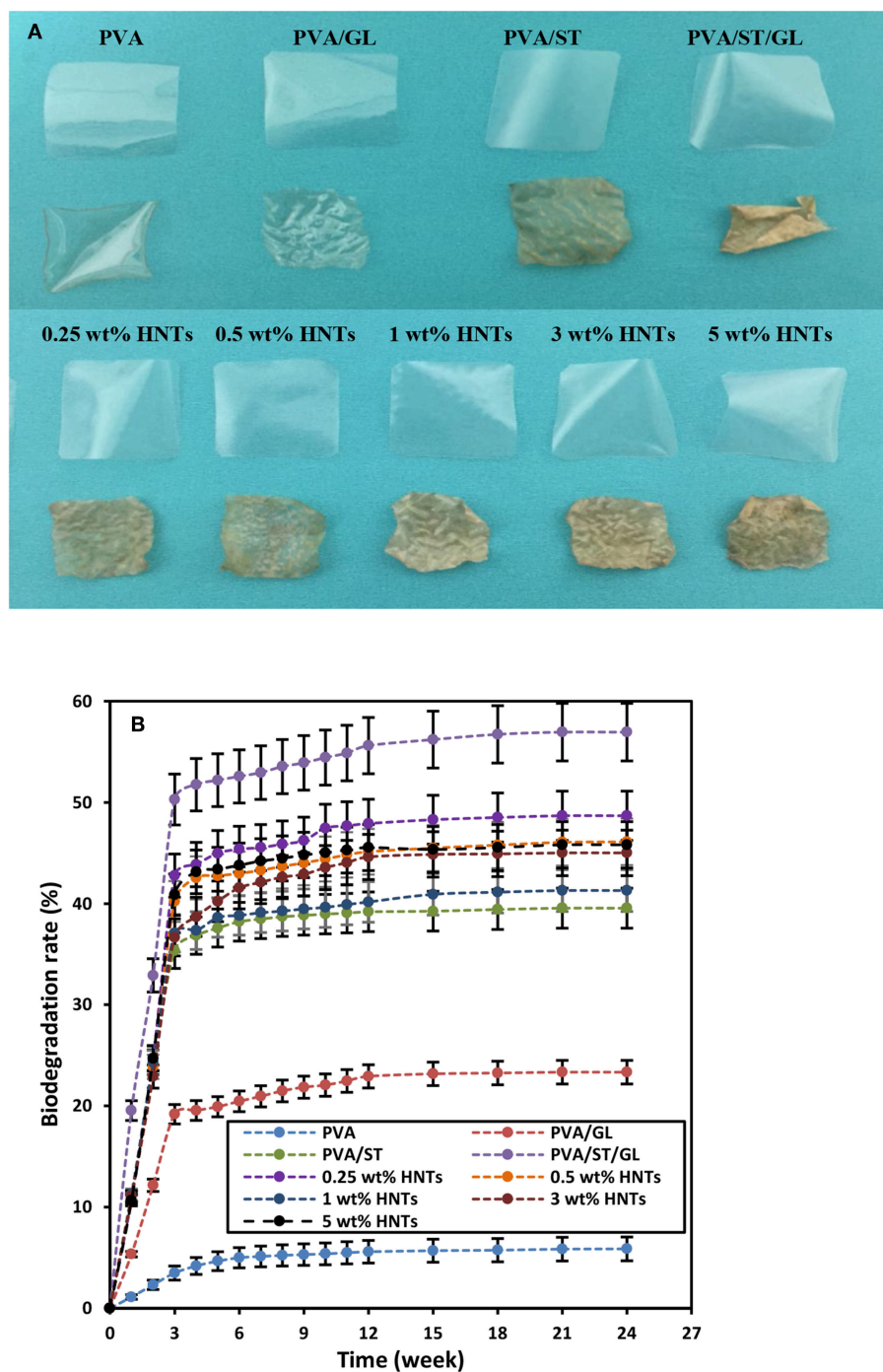
FIGURE 7 | (A) Digital images before and after biodegradation tests, and **(B)** biodegradation rates of neat PVA, PVA blend and PVA/ST/GL/HNT nanocomposite films.

films reinforced with 0.25 and 5 wt% were demonstrated as two typical cases for low and high HNT contents. As seen in **Figure 8**, neat PVA and PVA/GL blend films revealed similar smooth surface morphology as reported elsewhere (Cano et al., 2015b,c), which was completely different from a multitude of globular structures with much higher surface roughness

for PVA/ST blends. The latter observation was related to the incompatibility between PVA and ST as two separate constituents in blend films with the absence of plasticizers such as GL, which was in good agreement with Cano et al. (2015c). Such partial phase miscibility effect in PVA/ST blends in this study was believed to cause their higher W_a and W_s. It was
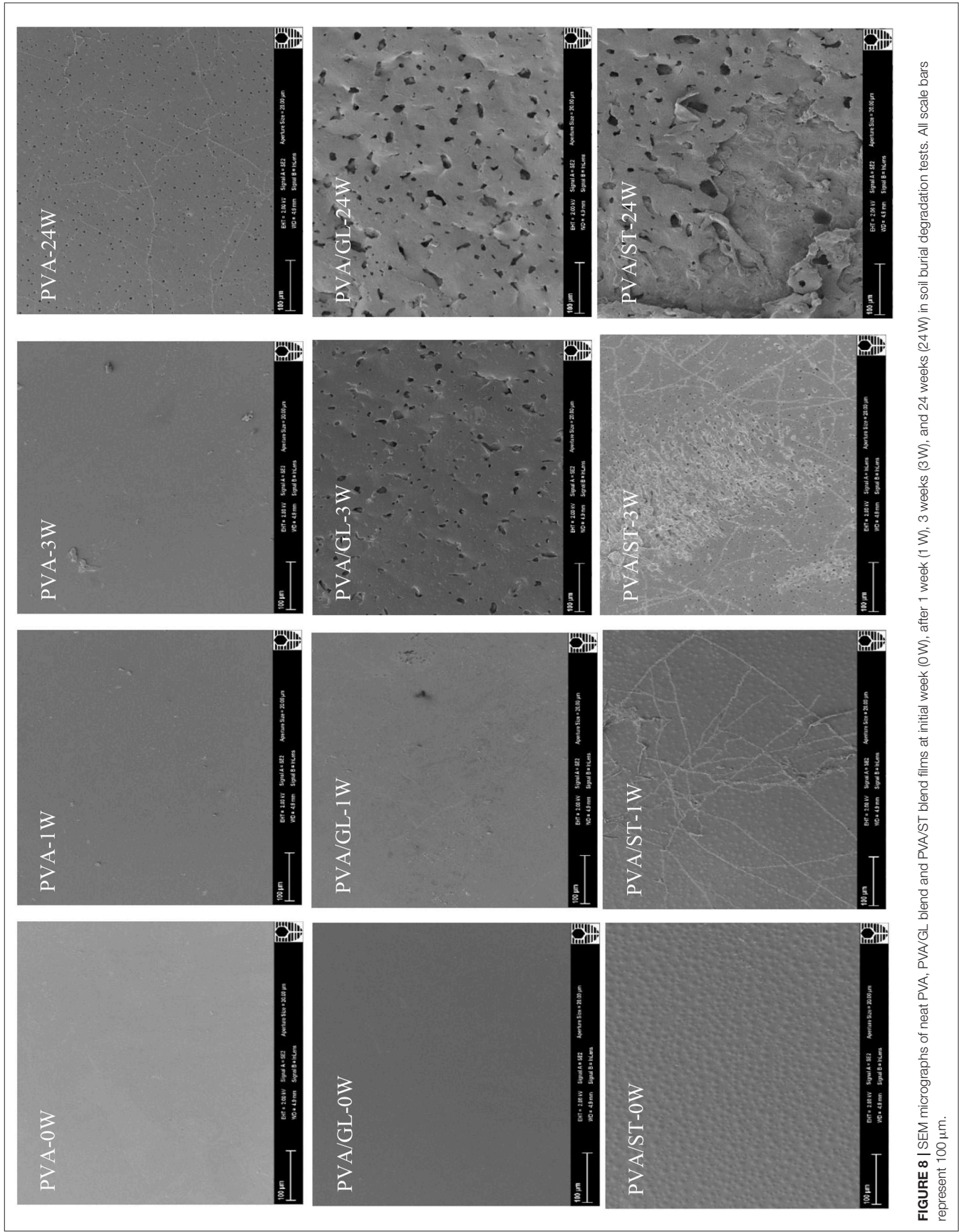
FIGURE 8 | SEM micrographs of neat PVA, PVA/GL blend and PVA/ST blend films at initial week (0W), after 1 week (1 W), 3 weeks (3W), and 24 weeks (24W) in soil burial degradation tests. All scale bars represent 100 μm.

FIGURE 9 | SEM micrographs of PVA/ST/GL blend and PVA/ST/GL/HNT nanocomposite films at the HNT contents of 0.25 and 5 wt% at initial week (0 W), after 1week (1 W), 3 weeks (3 W), and 24 weeks (24 W) in soil burial degradation tests. All scale bars represent 100 μm.
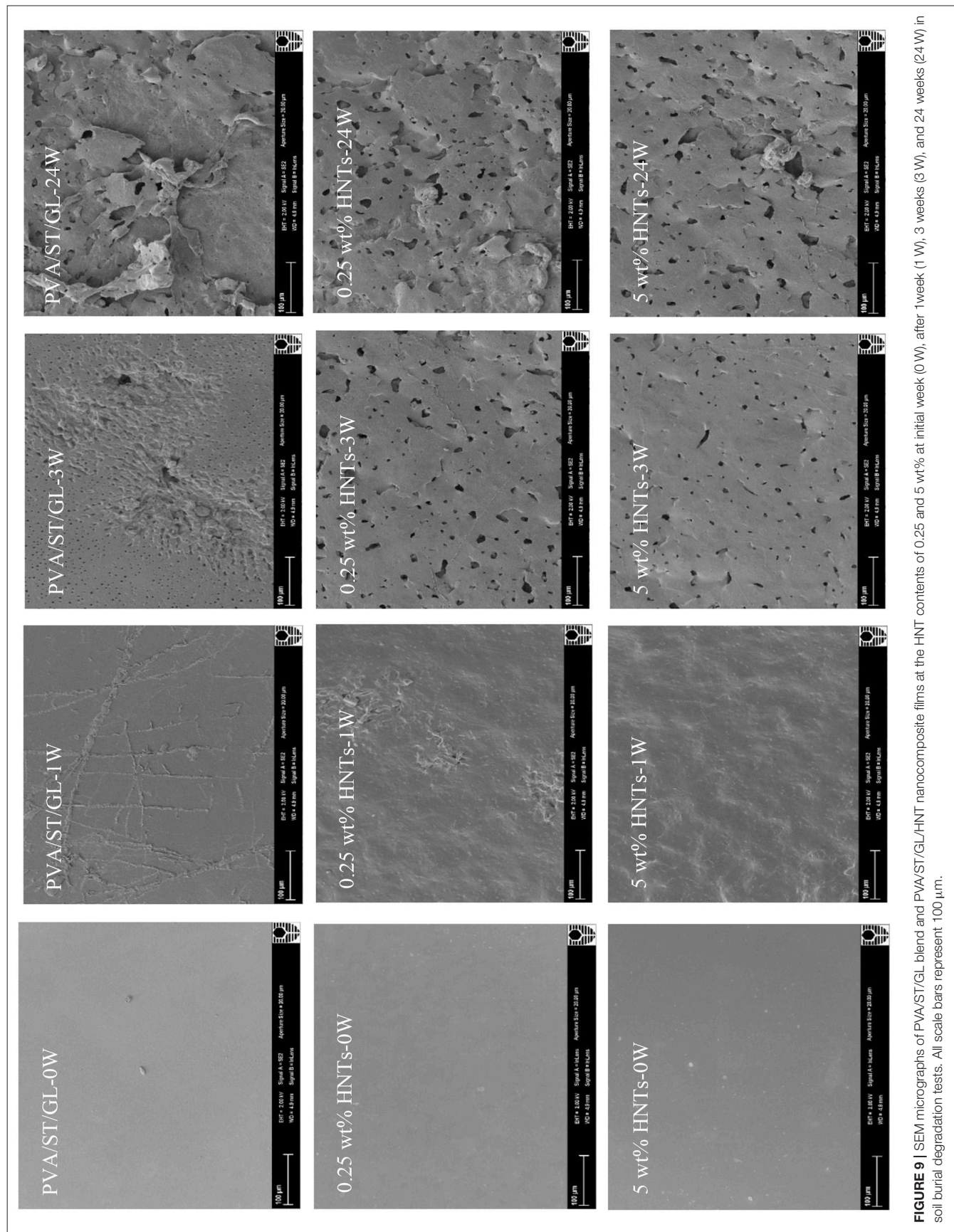
also interesting to note that smooth surface morphology took place in PVA/ST/GL blend films instead mainly because better compatibility between PVA and ST could be obtained in the presence of GL with their resulting slight reductions of W_a and W_s when compared with those of PVA/ST blend films. The addition of HNTs also increased the surface roughness of nanocomposite films particularly with the inclusion of 5 wt% HNTs in comparison with that of PVA/ST/GL blend films, as depicted in **Figure 9**.

In particular, neat PVA films did not show clear surface changes during the testing periods, as confirmed with the film appearance in **Figure 8**. "Branched traces" could be found slightly on the surfaces of PVA/GL blend films, but more clearly observed on the surfaces of PVA/ST blend films and PVA/ST/GL blend films, which are known as "fungal hyphae." According to Qiu and Netravali (2015) these fungal hyphae could be commonly generated during the biodegradation process at a suitable temperature level. The number and extension of these fungal hyphae increased with time by crossing each other to form grooves, as indicated elsewhere (Sang et al., 2002). The presence of fungal hyphae could be associated with high degradation rates during the first weeks of active-state periods. Nanocomposite films had rough surfaces after 1 week, but the HNTs prevented the formation of these fungal hyphae because the presence of nanofillers reduced the infiltration speed of microorganisms in good accordance with Tang et al. (2008).

Neat PVA films possessed much rougher surfaces after 3 weeks while PVA/GL blend films demonstrated considerable changes such as the formation of pores with average pore diameters in range of 0.12–1.64 μm. The presence of GL assisted in the chain-mobility improvement of polymeric molecules (Talja et al., 2007; Ismail and Zaaba, 2011), further increased the infiltration speed of microorganisms within blend films, and in turn enhanced the biodegradation rate when compared with that of neat PVA counterparts. The degradation process induced by fungal hyphae was much faster in PVA/ST blend films and PVA/ST/GL blend films than that in neat PVA films along with the existence of many small open pores in some surface areas (Negim et al., 2014). Nanocomposite films revealed a relatively small number of pores as compared with PVA/ST/GL blend films despite their bigger average pore diameters in range of 0.21–3.05 μm. After 24 weeks, fine porous structures were manifested for the surface morphology of neat PVA films with average pore diameters in range of 0.06–0.72 μm, which were more or less uniformly distributed around PVA film surfaces with low degradation rates. Nonetheless, surface morphological structures of PVA/ST and PVA/ST/GL blends as well as PVA/ST/GL/HNT nanocomposites were observed to deteriorate progressively from film external surfaces to their internal layers. Finally, the presence of ST had remarkable effect on morphological structures of PVA/ST, PVA/ST/GL, and nanocomposite films as opposed to those of neat PVA films.

CONCLUSIONS

Biopolymers were widely used to reduce plastic wastes for environmental sustainability. PVA has been considered as one of attractive synthetic biopolymers over a few decades. PVA was blended with ST and GL to improve its biodegradability and compatibility whilst reduce material cost. PVA/ST/GL blend films had poor water resistance because all the components belonged to hydrophilic materials.

The incorporation of HNTs improved the water resistance of PVA/ST/GL/HNT nanocomposite films by reducing the W_a and W_s by 44.24 and 48.05%, respectively, with increasing HNT contents from 0 to 5 wt%. The relatively hydrophobic nature of HNTs in addition to the generation of hydrogen bonds between polymeric matrices and nanofillers could restrict the diffusion of water molecules through polymer matrices. These findings were evidenced by decreasing the hydrophilic nature of nanocomposite films with the incorporation of HNTs, which was reflected by increasing the water contact angle of nanocomposite films by 21.36°C when compared with that of PVA/ST/GL blend films. Small HNT contents between 0.25 and 1 wt% had higher influence on the improvement of water resistance due to good HNT dispersion compared with typical HNT agglomeration at high nanofiller content levels beyond 1 wt%, thus resulting in the reduction of tortuous effect for water diffusivity. The use of PVA/ST/GL/HNT nanocomposite films still demonstrated the good transparency at an acceptable level despite its reduction from 96.23 to 70.48% when the HNT content was increased from 0 to 5 wt% at the wavelength of 550 nm. The similar trend was also observed with respect to the biodegradation rate of such nanocomposite films decreasing from 56.94 to 41.28% with increasing the HNT contents from 0 to 1 wt% where HNTs were well-dispersed. This result is in contrast with a further increase up to 45.80% with the inclusion of 5 wt% highly agglomerated HNTs despite being still higher than that of PVA/ST blend films. HNTs had significant effect on decreasing the overall migration rates of nanocomposite films in 10% ethanol food simulant as opposed to PVA/ST/GL blend films. Furthermore, the overall migration rates of nanocomposite films in 50% ethanol and 3% acidic food simulants were lower than the OML to meet stringent food safety requirements along with very low risk of nanoparticle migration of HNTs. Consequently, PVA/ST/GL/HNT nanocomposite films could be potentially used as versatile thin-film materials with high water resistance, good biodegradability, acceptable transparency and overall migration rates to target sustainable food packaging particularly for lipophilic and acidic foodstuffs.

AUTHOR CONTRIBUTIONS

ZA did the experimental work and preparation, characterization, and property measurements of material samples. ZA and YD analyzed the data and jointly prepared the research manuscript.

ACKNOWLEDGMENTS

REFERENCES

Abbasi, Z. (2012). Water resistance, weight loss and enzymatic degradation of blends starch/polyvinyl alcohol containing SiO_2 nanoparticle. *J. Taiwan. Inst. Chem. Eng.* 43, 264–268. doi: 10.1016/j.jtice.2011.10.007

Abdullah, Z. W., and Dong, Y. (2017). Preparation and characterisation of poly(vinyl) alcohol (PVA)/starch (ST)/halloysite nanotube (HNT) nanocomposite films as renewable materials. *J. Mater. Sci.* 53, 3455–3469. doi: 10.1007/s10853-017-1812-0

Abdullah, Z. W., Dong, Y., Davies, I. J., and Barbhuiya. S. (2017). PVA, PVA blends, and their nanocomposites for biodegradable packaging application. *Polym. Plast. Technol. Eng.* 56:1307–1344. doi: 10.1080/03602559.2016.1275684

Akhavan, A., Khoylou, F., and Ataeivarjovi, E. (2017). Preparation and characterization of gamma irradiated Starch/PVA/ZnO nanocomposite films. *Radiat. Phys. Chem.* 138, 49–53. doi: 10.1016/j.radphyschem.2017.02.057

Ali, M. (2016). Synthesis and study the effect of HNTs on PVA/chitosan composite material. *Int. J. Chem. Molecul. Nucl. Mater. Metall. Eng.* 10, 234–240. doi: 10.5281/zenodo.1111917

Alipoormazandarani, N., Ghazihoseini, S., and Nafchi, A. M. (2015). Preparation and characterization of novel bionanocomposite based onsoluble soybean polysaccharide and halloysite nanoclay. *Carbohyd. Polym.* 134, 745–751. doi: 10.1016/j.carbpol.2015.08.059

Aloui, H., Khwaldia, K., Hamdi, M., Fortunati, E., Kenny, J. M., Buonocore, G. G., et al. (2016). Synergistic effect of halloysite and cellulose nanocrystals on the functional properties of PVA based nanocomposites. *ACS Sust. Chem. Eng.* 4, 794–800. doi: 10.1021/acssuschemeng.5b00806

Aslam, M., Kalyar, M. A., and Raza, Z. A. (2018). Polyvinyl alcohol: a review of research status and use of polyvinyl alcohol based nanocomposites. *Polym. Engin. Sci.* 58, 2119–2132. doi: 10.1002/pen.24855

Avella, M., De, V. , Jan, J., Errico, M. E., Fischer, S., Vacca, P., and Volpe, M. G. (2005). Biodegradable starch/clay nanocomposite films for food packaging applications. *Food. Chem.* 93, 467–474. doi: 10.1016/j.foodchem.2004.10.024

Azahari, N. A., Othman, N. N., and Ismail, H. (2011). Biodegradation studies of polyvinyl alcohol/corn starch blend films in solid and solution media. *J. Phys. Sci.* 22, 15–31.

Biddecia, G., Cavallaro, G., Di Blasi, F., Lazzara, G., Massaro, M., Milioto, S., et al. (2016). Halloysite nanotubes loaded with peppermint essential oil as filler forfunctional biopolymer film. *Carbohyd. Polym.* 152, 548–557. doi: 10.1016/j.carbpol.2016.07.041

Bott, J., Störmer, A., and Franz, R. (2014a). A model study into the migration potential of nanoparticles from plastics nanocomposites for food contact. *Food. Packag. Shelf. Life.* 2, 73–80. doi: 10.1016/j.fpsl.2014.08.001

Bott, J., Störmer, A., and Franz, R. (2014b). Migration of nanoparticles from plastic packaging materials containing carbon black into foodstuffs. *Food Addit. Contam. Part A Chem. Anal. Control Expo. Risk Assess.* 31, 1769–1782. doi: 10.1080/19440049.2014.952786

Busolo, M. A., Fernandez, P., Ocio, M. J., and Lagaron, J. M. (2010). Novel silver-based nanoclay as an antimicrobial in polylactic acid food packaging coatings. *Food Addit. Contam. Part A Chem. Anal. Control Expo. Risk Assess.* 27, 1617–1626. doi: 10.1080/19440049.2010.506601

Cai, J., Chen, J., Zhang, Q., Lei, M., He, J., Xiao, A., et al. (2016). Well-aligned cellulose nanofiber-reinforced polyvinyl alcoholcomposite film: mechanical and optical properties. *Carbohyd. Polym.* 140, 238–245. doi: 10.1016/j.carbpol.2015.12.039

Cano, A., Fortunati, E., Chafer, M., Gonzalez-Martinez, C., Chiralt, A., and Kenny., J. M. (2015b). Effect of cellulose nanocrystals on the properties of pea starch-poly(vinyl alcohol) blend films. *J. Mater. Sci.* 50, 6979–6992. doi: 10.1007/s10853-015-9249-9

Cano, A., Fortunati, E., Chafer, M., Kenny, J. M., Chiralt, A., and Gonzalez-Martínez, C. (2015c). Properties and ageing behaviour of pea starch films as affected by blend with poly(vinyl alcohol). *Food Hydrocoll.* 48, 84–93. doi: 10.1016/j.foodhyd.2015.01.008

Cano, A. I., Cháfer, M., Chiralt, A., and González-Martínez, C. A. (2015a). Physical and microstructural properties of biodegradable films based on pea starch and PVA. *J. Food Eng.* 167, 59–64. doi: 10.1016/j.jfoodeng.2015.06.003

Castro-Aguirre, E., Auras, R., Selke, S., Rubino, M., and Marsh, T. (2018). Impact of nanoclays on the biodegradation of poly(lactic acid) nanocomposites. *Polymers* 10:202. doi: 10.3390/polym10020202

Chow, W. S., Tham, W. L., Poh, B. T., and Mohd Ishak, Z. A. (2018). Mechanical and thermal oxidation behavior of poly(lactic acid)/halloysite nanotube nanocomposites containing N,N′-ethylenebis(Stearamide) and SEBS-g-MA. *J. Polym. Environ.* 26, 2973–2982. doi: 10.1007/s10924-018-1186-7

Dong, Y., Marshall, J., Haroosh, H. J., Mohammadzadehmoghadam, S., Liu, D., Qi, X., et al. (2015). Polylactic acid (PLA)/halloysite nanotube (HNT) composite mats: influence of HNT content and modification. *Compos. Part A Appl. Sci. Manuf.* 76, 28–36. doi: 10.1016/j.compositesa.2015.05.011

Echegoyen, Y., Rodriguez, S., and Nerin, C. (2016). Nanoclay migration from food packaging materials. *Food Addit. Contam. Part A Chem. Anal. Control Expo. Risk Assess.* 33, 530–539. doi: 10.1080/19440049.2015.1136844

European Union Commission Regulation (EU) No. 10 (2011). Commission regulation on plastic materials and articles intended to come into contact with food. *Offic. J. Eur. Un. L* 12, 1–89.

Farhoodi, M., Mousavi, S. M., Sotudeh-Gharebagh, R., Emam-Djomeh, Z., and Oromiehie, A. (2014). Migration of aluminum and silicon from pet/clay nanocomposite bottles into acidic food simulant. *Packag. Technol. Sci.* 27, 161–168. doi: 10.1002/pts.2017

Fizir, M., Dramou, P., Dahiru, N. S., Ruya, W., Huang, T., and He, H. (2018). Halloysite nanotubes in analytical sciences and in drug delivery: a review. *Mikrochim. Acta* 185:389. doi: 10.1007/s00604-018-2908-1

Follain, N., Joly, C., Dole, P., and Bliard, C. (2005). Properties of starch based blends. Part 2. Influence of poly vinyl alcohol addition and photocrosslinking on starch based materials mechanical properties. *Carbohyd. Polym.* 60, 185–192. doi: 10.1016/j.carbpol.2004.12.003

Fortunati, E., Peltzer, M., Armentano, I., Torre, L., Jimenez, A., and Kenny, J. M. (2012). Effects of modified cellulose nanocrystals on the barrier and migration properties of PLA nano-biocomposites. *Carbohyd. Polym.* 90, 948–956. doi: 10.1016/j.carbpol.2012.06.025

Fujii, K., Nakagaito, A. N., Takagi, H., and Yonekura, D. (2014). Sulfuric acid treatment of halloysite nanoclay to improve the mechanical properties of PVA/halloysite transparent composite films. *Compos. Interf.* 21, 319–327. doi: 10.1080/15685543.2014.876307

Gaaz, T. S., Sulong, A. B., Akhtar, M. N., Kadhum, A. A., Mohamad, A. B., and Al-Amiery, A. A. (2015). Properties and applications of polyvinyl alcohol, halloysite nanotubes and their nanocomposites. *Molecules* 20, 22833–22847. doi: 10.3390/molecules201219884

Gaaz, T. S., Sulong, A. B., Kadhum, A. A. H., Al-Amiery, A. A., Nassir, M. H., and Jaaz, A. H. (2017). The impact of halloysite on the thermo-mechanical properties of polymer composites. *Molecules.* 22:E838. doi: 10.3390/molecules22050838

Geyer, R., Jambeck, J. R., and Law, K. L. (2017). Production, use, and fate of all plastics ever made. *Sci. Adv.* 3:e1700782. doi: 10.1126/sciadv.1700782

Gressler, S., Part, F., Gazsó, A., and Huber-Humer, M. (2018). Nanotechnological applications for food contact materials. *Nano. Trust. Dosseirs. Nr.* 49, 1–6. doi: 10.1553/ita-nt-049en

Grunlan, J. C., Grigorian, A., Hamilton, C. B., and Mehrabi, A. R. (2003). Effect of clay concentration on the oxygen permeability and optical properties of a modified poly(vinyl alcohol). *J. Appl. Polym. Sci.* 93, 1102–1109. doi: 10.1002/app.20564

Guimarães, M. Jr., Botaro, V. R., Novack, K. M., Teixeira, F. G., and Tonoli, G. H. D., (2015). Starch/PVA-based nanocomposites reinforced with bamboo nanofibrils. *Ind. Crop. Prod.* 70, 72–83. doi: 10.1016/j.indcrop.2015.03.014

Guo, M., Wang, A., Muhammad, F., Qi, W., Ren, H., and Zhu Guo, G. (2012). Halloysite nanotubes, a multifunctional nanovehicle for anticancer drug delivery. *Chinese J. Chem.* 30, 2115–2120. doi: 10.1002/cjoc.201200657

Guohua, Z., Ya, L., Cuilan, F., Min, Z., Caiqiong, Z., and Zongdao, C. (2006). Water resistance, mechanical properties and biodegradability of methylated-cornstarch/poly(vinyl alcohol) blend film. *Polym. Degrad. Stab.* 91, 703–711. doi: 10.1016/j.polymdegradstab.2005.06.008

Gupta, B., Agarwal, R., and Alam, M. S. (2013). Preparation and characterization of polyvinyl alcohol-polyethylene oxide-carboxymethyl cellulose blend membranes. *J. Appl. Polym. Sci.* 127, 1301–1308. doi: 10.1002/app.37665

Hannon, J. C., Kerry, J. P., Cruz-Romero, M., Azlin-Hasim, S., Morris, M., and Cummins, E. (2016). Assessment of the migration potential of nanosilver from nanoparticle-coated low-density polyethylene food packaging into food simulants. *Food Addit. Contam. Part A Chem. Anal. Control Expo. Risk Assess.* 33, 167–178. doi: 10.1080/19440049.2015.1114184

He, Y., Kong, W., Wang, W., Liu, T., Liu, Y., Gong, Q., et al. (2012). Modified natural halloysite/potato starch composite films. *Carbohyd. Polym.* 87, 2706–2711. doi: 10.1016/j.carbpol.2011.11.057

Heidarian, P., Behzad, T., and Sadeghi, M. (2017). Investigation of cross-linked PVA/starch biocomposites reinforced by cellulose nanofibrils isolated from aspen wood sawdust. *Cellulose.* 24, 3323–3339. doi: 10.1007/s10570-017-1336-4

Hejri, Z., Seifkordi, A. A., Ahmadpour, A., Zebarjad, S. M., and Maskooki, A. (2013). Biodegradable starch/poly (vinyl alcohol) film reinforced with titanium dioxide nanoparticles. *Int. J. Miner. Metall. Mater.* 20, 1001–1011. doi: 10.1007/s12613-013-0827-z

Huang, Y., Chen, S., Bing, X., Gao, C., Wang, T., and Yuan, B. (2011). Nanosilver migrated into food-simulating solutions from commercially available food fresh containers. *Packag. Technol. Sci.* 24, 291–297. doi: 10.1002/pts.938

Imam, S. H., Cinelli, P., Gordon, S. H., and Chiellini, E. (2005). Characterization of biodegradable composite films prepared from blends of poly(vinyl alcohol), cornstarch, and lignocellulosic fiber. *J. Polym. Environ.* 13, 47–55. doi: 10.1007/s10924-004-1215-6

Ismail, H., and Zaaba, N. F. (2011). Effect of additives on properties of polyvinyl alcohol (PVA)/Tapioca starch biodegradable films. *Polym. Plast. Technol. Eng.* 50, 1214–1219. doi: 10.1080/03602559.2011.566241

Jayasekara, R., Harding, I., Bowater, I., ,Christie, G. B. Y., and Lonergan, G. T. (2003). Biodegradation by composting of surface modified starch and PVA blended films. *J. Polym. Environ.* 11, 49–56. doi: 10.1023/A:1024219821633

Jolanta, W. K., Rydzkowski, T., Borowski, G., Szczypinski, M., Klepka, T., and Thakur, V. K. (2018). Recent progress in biodegradable polymers and nanocomposite-based packaging materials for sustainable environment. *Int. J. Polym. Anal. Charact.* 23, 383–395. doi: 10.1080/1023666X.2018.1455382

Kale, G., Kijchavengkul, T., Auras, R., Rubino, M., Selke, S. E., and Singh, S. P. (2007). Compostability of bioplastic packaging materials: an overview. *Macromol. Biosci.* 7, 255–277. doi: 10.1002/mabi.200600168

Kamble, R., Ghag, M., Gaikawad, S., and Panda, B. K. (2012). Halloysite nanotubes and applications: a review. *J. Adv. Sci. Res.* 3, 25–29.

Khoo, W. S., Ismail, H., and Ariffin, A. (2011). *Tensile and Swelling Properties of Polyvinyl alcohol/Chitosan/Halloysite Nanotubes Nanocomposite.* Kuala Lumpur: 2011 National Postgraduate Conference. doi: 10.1109/natpc.2011.6136541

Kisku, S. K., Sarkar, N., Dash, S., and Swain, S. K. (2014). Preparation of starch/PVA/CaCO$_3$ nanobiocomposite films: study of fire retardant, thermal resistant, gas barrier and biodegradable properties. *Polym. Plast. Technol. Eng.* 53, 1664–1670. doi: 10.1080/03602559.2014.919650

Kopcilova, M., Hubackova, J., Ruzicka, J., Dvorackova, M., Julinova, M., Koutny, M., et al. (2013). Biodegradability and mechanical properties of poly(vinyl alcohol)-based blend plastics prepared through extrusion method. *J. Polym. Environ.* 21, 88–94. doi: 10.1007/s10924-012-0520-8

Kryuchkova, M., Danilushkina, A., Lvov, Y., and Fakhrullin, R. (2016). Evaluation of toxicity of nanoclays and graphene oxide *in vivo*: a

Paramecium caudatum study. *Environ. Sci. Nano.* 3, 442–452. doi: 10.1039/c5en00201j

Kubiak, K. J., Wilson, M. C. T., Mathia, T. G., and Carval, P. (2011). Wettability versus roughness of engineering surfaces. *Wear.* 271, 523–528. doi: 10.1016/j.wear.2010.03.029

Lee, M. H., Kim, S. Y., and Park, H. J. (2018). Effect of halloysite nanoclay on the physical, mechanical, and antioxidant properties of chitosan films incorporated with clove essential oil. *Food Hydrocolloid.* 84, 58–67. doi: 10.1016/j.foodhyd.2018.05.048

Lim, M., Kwon, H., Kim, D., Seo, J., Han, H., and Khan, S. B. (2015). Highly-enhanced water resistant and oxygen barrier propertiesof cross-linked poly(vinyl alcohol) hybrid filmsfor packaging applications. *Prog. Org. Coat.* 85, 68–75. doi: 10.1016/j.porgcoat.2015.03.005

Liu, M., Guo, B., Du, M., and Jia, D. (2007). Drying induced aggregation of halloysite nanotubes in polyvinyl alcohol/halloysite nanotubes solution and its effect on properties of composite film. *Appl. Phys. A.* 88, 391–395. doi: 10.1007/s00339-007-3995-8

Liu, M., Jia, Z., Jia, D., and Zhou, C. (2014). Recent advance in research on halloysite nanotubes-polymernanocomposite. *Prog. Polym. Sci.* 93, 1498–1525. doi: 10.1016/j.progpolymsci.2014.04.004

Liu, Z., Feng, Y., and Yi, X. (1999). Thermoplastic starch/PVAl compounds: preparation, processing, and properties. *J. Appl. Polym. Sci.* 74, 2667–2673. doi: 10.1002/(SICI)1097-4628(19991209)74:11<2667::AID-APP14>3.0.CO;2-D

Luo, X., Li, J., and Lin, X. (2012). Effect of gelatinization and additives on morphology and thermal behavior of corn starch/PVA blend films. *Carbohyd. Polym.* 90, 1595–1600. doi: 10.1016/j.carbpol.2012.07.036

Lvov, Y. M., DeVilliers, M. M., and Fakhrullin, R. F. (2016). The application of halloysite tubule nanoclay in drug delivery. *Expert Opin. Drug Deliv.* 13, 977–986. doi: 10.1517/17425247.2016.1169271

Magnier, L., and Crié, D. (2015). Communicating packaging eco-friendliness. *J. Ret. Distribut. Manag.* 43, 350–366. doi: 10.1108/ijrdm-04-2014-0048

Makaremi, M., Pasbakhsh, P., Cavallaro, G., Giuseppe Lazzara, G., Aw, Y. K., Lee, S. M., et al. (2017). Effect of morphology and size of halloysite nanotubes on functional pectin bionanocomposites for food packaging applications. *ACS Appl. Mater. Interfaces* 9, 17476–17488. doi: 10.1021/acsami.7b04297

Mauricio-Iglesias, M., Peyron, S., Guillard, V., and Gontard, N. (2010). Wheat gluten nanocomposite films as food-contact materials: migration tests and impact of a novel food stabilization technology (high pressure). *J. Appl. Polym. Sci.* 116, 2526–2535. doi: 10.1002/app.31647

Mensitieri, G., Di Maio, E., Buonocore, G. G., Nedi, I., Oliviero, M., Sansone, L., et al. (2011). Processing and shelf life issues of selected food packaging materials and structures from renewable resources. *Trends. Food. Sci. Technol.* 22, 72–80. doi: 10.1016/j.tifs.2010.10.001

Negim, E. S. M., Rakhmetullayeva, R. K., Yeligbayeva, G. Z., Urkimbaeva, P. I., Primzharova, S. T., Kaldybekov, D. B., et al. (2014). Improving biodegradability of polyvinyl alcohol/starch blend films for packaging applications. *Int. J. Basic. Appl. Sci.* 3, 263–273. doi: 10.14419/ijbas.v3i3.2842

Noshirvani, N., Ghanbarzadeh, B., Fasihi, H., and Almasi, H. (2016). Starch–PVA nanocomposite film incorporated with cellulose nanocrystals and mmt: a comparative study. *Int. J. Food. Eng.* 12, 37–48. doi: 10.1515/ijfe-2015-0145

Qiu, K., and Netravali, A. N. (2013). Halloysite nanotube reinforced biodegradable nanocomposites using noncrosslinked and malonic acid crosslinked polyvinyl alcohol. *Polym. Compos.* 34, 799–809. doi: 10.1002/pc.22482

Qiu, K., and Netravali, A. N. (2015). "Polyvinyl alcohol based biodegradable polymer nanocomposites," in *Biodegradable Polymers,* eds C. C. Chu (New York, NY: Nova Science Publishers, Inc), 326–379.

Rahman, W. A. W. A., Sin, L. T., Rahmat, A. R., and Samad, A. A. (2010). Thermal behaviour and interactions of cassava starch filled with glycerol plasticized polyvinyl alcohol blends. *Carbohyd. Polym.* 81, 805–810. doi: 10.1016/j.carbpol.2010.03.052

Rawtani, D., and Agrewal, Y. K. (2012). Multifarious applications of halloysite nanotubes: a review. *Rev. Adv. Mater. Sci.* 30, 282–295.

Ray, S. S., and Bousmina, M. (2005). Biodegradable polymers and their layered silicate nanocomposites: In greening the 21st century materials world. *Prog. Mater. Sci.* 50, 962–1079. doi: 10.1016/j.pmatsci.2005.05.002

Ren, J., Dang, K., Pollet, E., and Avérous, L. (2018). Preparation and Characterization of thermoplastic potato starch/halloysite

nano-biocomposites: effect of plasticizer nature and nanoclay content. *Polymers* 10:808. doi: 10.3390/polym10080808

Sadegh-Hassani, F., and Nafchi, A. M. (2014). Preparation and characterization of bionanocomposite films based onpotato starch/halloysite nanoclay. *Int. J. Biol. Macromol.* 67, 458–462. doi: 10.1016/j.ijbiomac.2014.04.009

Salam, H., Dong, Y., and Davies, I. (2015). "Development of biobased polymer/clay nanocomposites," in *Fillers and Reinforcements for Advanced Nanocomposites*, eds Y. Dong, R. Umer, and A. Lau (Cambridge: Elsevier), 101–132.

Salleh, M. S. N., Mohamed Nor, N. N., Mohd, N., and Syed Draman, S. F. (2017). Water resistance and thermal properties of polyvinyl alcohol-starch fiber blend film. *AIP Conf. Proc.* 1809:020045. doi: 10.1063/1.4975460

Sam, S. T., Nuradibah, M. A., Chin, K. M., and Hani, N. (2016). "Current application and challenges on packaging industry based on natural polymer blending," in *Natural Polymers-Industry Technques and Applications*, ed O. Olatunji (London: Springer), 163–184.

Sang, K., Hori, Y., Tanji, H., and Unno, B. I. (2002). Fungal contribution to *in situ* biodegradation of poly(3-hydroxybutyrate- co—3-hydroxyvalerate) film in soil. *Appl. Microbiol. Biotechnol.* 58, 241–247. doi: 10.1007/s00253-001-0884-5

Santos, A. C., Ferreira, C., Veiga, F., Ribeiro, A. J., Panchal, A., Lvov, Y., et al. (2018). Halloysite clay nanotubes for life sciences applications: from drug encapsulation to bioscaffold. *Adv. Colloid Interface Sci.* 257, 58–70. doi: 10.1016/j.cis.2018.05.007

Schmidt, B., Petersen, J. H., Bender Koch, C., Plackett, D., Johansen, N. R., Katiyar, V., et al. (2009). Combining asymmetrical flow field-flow fractionation with light-scattering and inductively coupled plasma mass spectrometric detection for characterization of nanoclay used in biopolymer nanocomposites. *Food Addit. Contam. Part A Chem. Anal. Control Expo. Risk Assess.* 26, 1619–1627. doi: 10.1080/02652030903225740

Schmitt, H., Creton, N., Prashantha, K., Soulestin, J., Lacrampe, M. F., and Krawczak, P. (2015). Preparation and characterization of plasticized starch/halloysite porous nanocomposites possibly suitable for biomedical applications. *J. Appl. Polym. Sci.* 132:41341. doi: 10.1002/app.41341

Shah, A. A., Hasan, F., Hameed, A., and Ahmed, S. (2008). Biological degradation of plastics: a comprehensive review. *Biotechnol. Adv.* 26, 246–265. doi: 10.1016/j.biotechadv.2007.12.005

Simon, P., Chaudhry, Q., and Bakos, D. (2008). Migration of engineered nanoparticles from polymer packaging to food – a physicochemical view. *J. Food. Nutr. Res.* 47, 105–113.

Singha, A. S., and Kapoor, H. (2014). Effects of plasticizer/cross-linker on the mechanical and thermal properties of starch/PVA blends. *Iran. Polym. J.* 23, 655–662. doi: 10.1007/s13726-014-0260-9

Siracusa, V., Rocculi, P., Romani, S.a., and Rosa, M. D. (2008). Biodegradable polymers for food packaging: a review. *Trends. Food. Sci. Technol.* 19, 634–643. doi: 10.1016/j.tifs.2008.07.003

Sorrentino, A., Gorrasi, G., and Vittoria V. (2007). Potential perspectives of bio-nanocomposites for food packaging applications. *Trends. Food. Sci. Technol.* 18, 84–95. doi: 10.1016/j.tifs.2006.09.004

Sustainable Packaging Coalition. (2011). *Definition-of-Sustainable-Packaging*. Available online at: https://sustainablepackaging.org/wp-content/uploads/2017/09/Definition-of-Sustainable-Packaging.pdf (Accessed 1 October, 2011).

Swapna, V. P., Thomas, P. S., Suresh, K. I., Saranya, V., Rahana, M. P., and Stephen, R. (2015). Thermal properties of poly (vinyl alcohol)(PVA)/halloysite nanotubes reinforced nanocomposites. *Int. J. Plast. Technol.* 19, 124–136. doi: 10.1007/s12588-015-9106-3

Taghizdeh, M. T., Abbasi, Z., and Nasrollahzade, Z. (2012). Study of enzymatic degradation and water absorption of nanocomposites starch/polyvinyl alcohol and sodium montmorillonite clay. *J. Taiwan. Inst. Chem. Eng.* 43, 120–124. doi: 10.1016/j.jtice.2011.07.006

Talja, R. A., Helen, H., Roos, Y. H., and Jouppila, K. (2007). Effect of various polyols and polyol contents on physical and mechanical properties of potato starch-based films. *Carbohyd. Polym.* 67, 288–295. doi: 10.1016/j.carbpol.2006.05.019

Tanase, E. E., Popa, M. E., Rapa, M., and Popa, O. (2015). Preparation and characterization of biopolymer blends based on polyvinyl alcohol and starch. *Roman. Biotechnol. Lett.* 20, 10306–10315.

Tang, S., Zou, P., Xiong, H., and Tang, H. (2008). Effect of nano-SiO$_2$ on the performance of starch/polyvinyl alcohol blend films. *Carbohyd. Polym.* 72, 521–526. doi: 10.1016/j.carbpol.2007.09.019

Tang, X., and Alavi, S. (2011). Recent advances in starch, polyvinyl alcohol based polymer blends, nanocomposites and their biodegradability. *Carbohyd. Polym.* 85, 7–16. doi: 10.1016/j.carbpol.2011.01.030

Thakore, I. M., Desai, S., Sarawade, B. D., and Devi, S. (2001). Studies on biodegradability, morphology and thermomechanical properties of LDPE/modfied starch blends. *Eur. Polym. J.* 37, 151–160. doi: 10.1016/S0014-3057(00)00086-0

The European Standard EN. (2002). Materials and articles in contact with foodstuffs -plastics-part 1: guide to the selection of conditions and test methods for overall migration. *Eur. Committ. Stand.*1-52

Tian, H., Wang, K., Liu, D., Yan, J., Xiang, A., and Varada Rajulu, A. (2017). Enhanced mechanical and thermal properties of poly (vinylalcohol)/corn starch blends by nanoclay intercalation. *Int. J. Biol. Macromol.* 101, 314–320. doi: 10.1016/j.ijbiomac.2017.03.111

Tully, J., Fakhrullin, R., and Lvov, Y. (2015). "Halloysite clay nanotube composites with sustained release of chemicals," in *Nanomaterials and Nanoarchitectures,* eds M. Bardosova and T. Wagner (Dordrecht: Springer), 87–118.

Velichkova, H., Petrova, I., Kotsilkov, S., Ivanov, E., Vitanov, N. K., and Kotsilkova, R. (2017). Influence of polymer swelling and dissolution into food simulants on the release of graphene nanoplates and carbon nanotubes from poly(lactic) acid and polypropylene composite films. *J. Appl. Polym. Sci.* 134:45469. doi: 10.1002/app.45469

Vergaro, V., Abdullayev, E., Lvov, Y. M., Zeitoun, A. R., Cingolani, R., and Leporatti, S. (2010). Cytocompatibility and uptake of halloysite clay nanotubes. *Biomacromolecules* 11, 820–826. doi: 10.1021/bm9014446

Wang, W., Zhang, H., Dai, Y., Hou, H., and Dong, H. (2015). Effects of low poly(vinyl alcohol) content on properties of biodegradable blowing films based on two modified starches. *J. Thermoplast. Compos. Mater.* 30, 1017–1030. doi: 10.1177/0892705715614080

Wenzel, R. N. (1949).Surface roughness and contact angle. *J. Phys. Chem.* 53, 1466–1467. doi: 10.1021/j150474a015

Xie, Y., Chang, P. R., Wang, S., Yu, J., and Ma, X. (2011). Preparation and properties of halloysite nanotubes/plasticized dioscorea opposita thunb. Starch composites. *Carbohyd. Polym.* 83, 186–191. doi: 10.1016/j.carbpol.2010.07.039

Yuan, P., Tan, D., and Faïza, A. B. (2015). Properties and applications of halloysite nanotubes: recent research advances and future prospects. *Appl. Clay Sci.* 112–113, 75–93. doi: 10.1016/j.clay.2015.05.001

Yuan, Y., and Lee, T. R. (2013). "Contact angle and wetting properties," in *Surface Science Techniques*, eds G. Bracco and B. Holst (Berlin: Verlag Berlin Heidelberg; Springer), 3–34.

Zanela, J., Olivato, J. B., Dias, A. P., Grossmann, M. V. E., and Yamashita, F. (2015). Mixture design applied for the development of films based on starch, polyvinyl alcohol, and glycerol. *J. Appl. Polym. Sci.* 132:42697. doi: 10.1002/app.42697

Zhang, Y., Tang, A., Yung, H., and Ouyang, J. (2016). Applications and interfaces of halloysite nanocomposites. *Appl. Clay Sci.* 119, 8–17. doi: 10.1016/j.clay.2015.06.034

Zhou, W. Y., Guo, B., Liu, M., Liao, R., Rabie, A. B., and Jia, D. (2010). Poly(vinyl alcohol)/halloysite nanotubes bionanocomposite films: properties and *in vitro* osteoblasts and fibroblasts response. *J. Biomed. Mater. Res. A.* 93, 1574–1587. doi: 10.1002/jbm.a.32656

Zou, G. X., Ping-Qu, J., and Liang-Zou, X. (2008). Extruded starch/PVA composites: water resistance, thermal properties, and morphology. *J. Elastom. Plast.* 40, 303–316. doi: 10.1177/0095244307085787

Conflict of Interest Statement: The authors declare that the research was conducted in the absence of any commercial or financial relationships that could be construed as a potential conflict of interest.

Thermoplastic Starch Composites Filled With Isometric and Elongated TiO$_2$-Based Nanoparticles

Aleksandra Ujcic*, Martina Nevoralova, Jiri Dybal, Alexander Zhigunov, Jana Kredatusova, Sabina Krejcikova, Ivan Fortelny and Miroslav Slouf

Department of Polymer Morphology, Institute of Macromolecular Chemistry, Academy of Sciences of the Czech Republic, Prague, Czechia

Biodegradable thermoplastic starch (TPS) composites with isometric titanium dioxide nanoparticles (TiO$_2$; diameter ∼100 nm) and elongated titanate nanotubes (TiNT; diameter ∼20 nm and aspect ratio >50) were prepared from wheat and tapioca starch. The preparation was based on our recently developed two-step procedure consisting of the solution casting (SC) followed by the melt mixing (MM), which had been shown to yield highly homogeneous TPS in our previous study. In this work we demonstrated that the type of the TPS matrix and the type of the filler had significant impact on the morphology and the properties of the final composites. Multiple microscopic techniques (LM, SEM, and TEM) evidenced that the TPS/TiO$_2$ composites exhibited a very homogeneous dispersion of the filler, while the TPS/TiNT composites contained micrometer-size agglomerates of TiNT. Moreover, all composites with the wheat starch matrix [TPS(w)] showed a higher filler agglomeration than the corresponding composites with the tapioca starch matrix [TPS(t)]. Rheological experiments showed that the TiO$_2$ and TiNT fillers had quite small impact on the viscosity of the TPS(w) matrix, probably due to slightly higher agglomeration, poorer dispersion, and weaker matrix-particle interactions. On the other hand, the TPS(t) matrix was influenced by both fillers significantly: the TiO$_2$ nanoparticles with almost ideal dispersion formed a physical network in the TPS(t) matrix, which significantly increased the viscosity of the composite, whereas the TiNT nanotubes seemed to destruct the TPS(t) matrix partially, resulting in decreased viscosity of the composite. DMTA results confirmed the rheological measurements: Storage moduli (*G'*) showed that TPS(t) and its composites with TiO$_2$ were stiffer than the corresponding TPS(w) samples, while the TPS(t)/TiNT composites were less stiff than TPS(w)/TiNT. Also loss moduli (*G"*) confirmed the difference between tapioca starch and wheat starch composites, which differed by their glass transition temperatures [T_g of TPS(w) < T_g of TPS(t)]. The rheological and DMTA results were supplemented and supported by IR, XRD, and TGA measurements.

Keywords: wheat thermoplastic starch, tapioca thermoplastic starch, TiO$_2$, TiNT, morphology, thermomechanical properties, rheological properties

INTRODUCTION

Starch is one of the cheapest and the most abundant natural polymers. On this account, starch-based materials are employed in many applications, for example, in household, agriculture, textile, pharmacy, or medicine (Bertolini, 2010; Sarka et al., 2011, 2012; Saiah et al., 2012; Xie et al., 2013; Ghavimi et al., 2015; Campos-Requena et al., 2017; Javanbakht and Namazi, 2017; Kuswandi, 2017; Liu et al., 2017a,b). However, the biggest drawback of native granular starch is processing. The semicrystalline granular starch itself decomposes before melting when processed in classic devices (Biliaderis, 2009). In most applications, the semicrystalline granular starch is transformed into an almost amorphous thermoplastic starch (TPS) matrix by addition of low molecular weight compounds such as water, glycerol, citric acid etc. (Biliaderis, 2009; Bertolini, 2010; Visakh et al., 2012). The starch plasticization is influenced by many factors, mostly: the starch source (wheat, tapioca, corn etc.; Ao and Jane, 2007; Biliaderis, 2009; Bertolini, 2010; Liu et al., 2010), the plasticizer type and amount (Dai et al., 2008; Pushpadass et al., 2008), and the plasticization method and conditions (Altskar et al., 2008; Liu et al., 2013; Xie et al., 2013).

The botanic origin of starch determines the size and shape of starch granules as well as the range of the amylose/amylopectin content (Ao and Jane, 2007; Jane, 2009; Perez et al., 2009; Bertolini, 2010; Liu et al., 2010). In this work we selected two widely used types of starch: wheat starch from the grains of *triticum aestivum* (common wheat) and tapioca starch from the roots of *manihot esculenta* (aka cassava, manioc). Wheat starch has two types of the granules with the sizes ranging from 1 to 45 μm: A-granules (a lenticular shape, large: mean diameter 15 μm) and B-granules (a spherical shape, small: mean diameter 4 μm), and it is normally composed of 75% of amylopectin and 25% of amylose (Maningat et al., 2009). It tends to form an opaque and non-cohesive paste, with a medium resistance to shear and a high retrogradation (Biliaderis, 2009; Bertolini, 2010). Tapioca starch has the granules from 4 to 35 μm which are smooth and irregular spheres, and it is composed of amylopectin containing 17–20% amylose with a higher molecular weight than other types of starch (Breuninger et al., 2009). It forms a transparent and cohesive gel, with a low resistance to shear and a lower retrogradation (Biliaderis, 2009; Bertolini, 2010; Zhu, 2015). As just described, the wheat and tapioca starches vary not only in the size and the shape of their granules, but also in the chemical composition (the amylose/amylopectin ratio; the molecular weight of amylose), which results in the different behavior and properties of final thermoplastic starches.

Many researchers recently studied the properties of wheat thermoplastic starch (Sarka et al., 2011; Kelnar et al., 2013; Mahieu et al., 2015; Schmitt et al., 2015; Song et al., 2018) as well as tapioca thermoplastic starch (Chang et al., 2006; Garcia et al., 2009; Teixeira et al., 2009, 2012; Ajiya et al., 2017; Bergel et al., 2017; Campos et al., 2017, 2018; Gonzalez-Seligra et al., 2017; Guz et al., 2017; Kargarzadeh et al., 2017; Lopez-Cordoba et al., 2017; Genovese et al., 2018; Liu et al., 2018; Valencia-Sullca et al., 2018). It is worth noting that the greatest amount of the thermoplastic starches has been prepared exclusively by a melt mixing (Teixeira

et al., 2009, 2012; Sarka et al., 2011; Mahieu et al., 2015; Schmitt et al., 2015; Gonzalez-Seligra et al., 2017; Campos et al., 2018; Genovese et al., 2018; Liu et al., 2018; Song et al., 2018) or exclusively by a solution casting (Chang et al., 2006; Garcia et al., 2009; Kelnar et al., 2013; Ajiya et al., 2017; Bergel et al., 2017; Campos et al., 2017; Guz et al., 2017; Kargarzadeh et al., 2017; Lopez-Cordoba et al., 2017; Valencia-Sullca et al., 2018). Even though the TPS materials prepared by the mentioned single-method procedures were homogeneous at macroscopic level, they still contained non-fully plasticized starch granules and/or inhomogeneities at microscopic level. For example, Teixeira et al. (2012) found some partially destroyed starch granules in cassava TPS prepared by extrusion and Schmitt et al. (2015) found starch granules in continuous phase of wheat TPS prepared by extrusion as well. Gonzalez-Seligra et al. (2017) found that some of cassava TPS's prepared by an extrusion (processed at three different screw speeds) contained broken starch granules. They obtained one TPS with a homogenous surface and two TPS's with the presence of starch granules. Therefore, in our previous paper (Ostafinska et al., 2017) we developed a two-step method of the starch plasticization, consisting of a solution casting (SC), which was followed by a melt-mixing (MM). The two-step SC + MM procedure was shown to be reliable and reproducible method for preparation of homogeneous wheat TPS matrix with well-dispersed TiO$_2$. Surprisingly, there are not so many studies dealing with TPS/TiO$_2$ composites. Oleyaei et al. (2016a,b) and Razali et al. (2016) studied similar TPS/TiO$_2$ systems, but with different types of starches and different plasticization procedures. Moreover, just a few of the publications compared the properties of thermoplastic obtained from different starch sources. For example, Omotoso et al. (2015) studied cassava, corn, potato, and yam TPS prepared by solution casting. Bergel et al. (2017) prepared TPS foams from potato, cassava, and corn starches by solution casting followed by compression molding. Genovese et al. (2018) prepared TPS from wheat, potato, and corn starches by melt-mixing. Song et al. (2018) and Zuo et al. (2017) studied TPS prepared by the solution casting of wheat and corn starch mixture. To the best of authors' knowledge, there are no papers concerning wheat and tapioca thermoplastic starches prepared in the same way, which would compare the properties of both types of TPS that seems to differ significantly.

Due to the above, we focused our attention on the comparison of the systems prepared by our two-step procedure (SC + MM), using two types of starches (wheat and tapioca) and two types of TiO$_2$-based particles (isometric TiO$_2$ nanoparticles and high aspect ratio TiNT nanotubes). Titanium-based particles were chosen for our research because they were expected to modify the properties of TPS, while maintaining or even increasing the biocompatibility of the final composites. The TiX-particles were shown to be compatible with both soft tissues and bone cells (Webster et al., 2000; Sengottuvelan et al., 2017). The TPS/TiX composites with tunable properties could be suitable for broader range of medical applications. The morphology, structure, rheology, and thermomechanical properties of wheat and tapioca TPS/TiX composites were studied in order to: (i) verify if SC + MM is the universal method of TPS starch preparation, which yields homogeneous dispersion of filler

regardless of source starch type; (ii) to find possible differences among TPS composites prepared by SC + MM method from different starch types; and (iii) to assess if SC + MM method yields homogeneous dispersion of the filler also at increased concentrations (up to 6 wt.%).

MATERIALS AND METHODS

Materials

Wheat (w; A-granules) and tapioca (t) starches were supplied by Škrobárny Pelhrimov, a.s., Czech Republic. Glycerol anhydrous (G; min. 99%) and sodium bromide (reagent grade) were obtained from Lachner, Czech Republic. Commercial titanium dioxide (TiO₂; anatase, particle size 50–200 nm) was delivered by Sigma-Aldrich, USA. Titanate nanotubes (TiNT) with the low diameter (∼20 nm) and the high aspect ratio (AR = length of the nanotube/diameter of the nanotube >50) were prepared by the hydrothermal synthesis from TiO₂ as described in our previous work (Kralova et al., 2010).

Preparation of TPS/TiX Composites

All samples (**Table 1**) were prepared by our recently developed two-step method: the solution casting (SC) followed by the melt mixing (MM), according to the recipe described in our previous paper (Ostafinska et al., 2017). Briefly, we used SC with a ratio of starch/glycerol = 70/30 (wt.%) and a ratio of starch/water = 1/6 (wt.%) for all samples. In the first step, the TiX particles (TiX = either TiO₂ particles or TiNT nanotubes described above in Section Materials) were dispersed in water using ultrasonic bath for 1 min and then glycerol was added and sonicated for 2 min. The pre-mixed water suspension (starch/glycerol/TiX: 30 min, room temperature) was mixed at the elevated temperature until the viscosity significantly increased (at least 10 min at temperature above 65°C) and then until the mixture became visually homogenous (when temperature increased to 60–70°C for at least 10 min, the starch gelatinized, which resulted in the disruption of the insoluble granules, loss of the molecular organization and an increase in its viscosity Bertolini, 2010). The solution was casted onto thin foils and dried at ambient temperature for 2–3 days, followed by 4 days in a desiccator with saturated solution of sodium bromide (relative humidity = RH = 57%). The dried SC samples were processed by MM as follows: they were melt-mixed (8 min, 110°C, 100 rpm) in micro-extruder (μ-processing DSM; Netherlands) and then compression molded (SC + MM samples) at 120°C (4 min, 50 kN + 2 min, 150 kN) by hydraulic press (Fontijne Grotnes, Netherlands). As the properties of TPS samples are very sensitive to the humidity, all samples were stored in a desiccator with saturated solution of sodium bromide (RH = 57%); the samples were closed in the desiccator immediately after the preparation and kept there in between all experiments.

Characterization of TPS /TiX Composites
Light Microscopy

The overall homogeneity of the filler dispersion at lower magnifications was checked with a light microscope Nikon Eclipse 80i (Nikon, Japan) equipped with a digital camera

TABLE 1 | List of prepared TPS-based composites.

Sample	S [wt.%]	G [wt.%]	TiO₂ [wt.%]	TiNT [wt.%]
TPS(w)	70.0	30.0	–	–
TPS (w)/TiO₂ (3%)	68.0	29.0	3	–
TPS(w)/TiO₂ (6%)	65.8	28.2	6	–
TPS(w)/TiNT (3%)	68.0	29.0	–	3
TPS(t)	70.0	30.0	–	–
TPS(t)/TiO₂ (3%)	68.0	29.0	3	–
TPS(t)/TiO₂ (6%)	65.8	28.2	6	–
TPS(t)/TiNT (3%)	68.0	29.0	–	3

(w), wheat starch; (t), tapioca starch.
All samples contained residual water after processing by solution casting and melt mixing (ca 5%).

ProgRes CT3 (Jenoptik, Germany). Thin sections (∼40 μm) were cut with a rotary microtome RM 2155 (Leica, Germany), put in oil between the support and cover glasses and observed with transmitted light using the bright field imaging.

Scanning Electron Microscopy

The morphology of the TPS matrix and the TPS/TiX composites at higher magnifications was visualized with a high resolution field-emission gun scanning electron microscope (SEM; microscope MAIA3, Tescan, Czech Republic) using a secondary electron imaging (SEM/SE) and a backscattered electron imaging (SEM/BSE) at 10 kV. The homogeneity of the TPS matrix was visualized as follows: the samples were broken in liquid nitrogen (below the glass transition temperature of TPS), the specimens were fixed on a metallic support using silver paste (Leitsilber G302, Christine Groepl, Austria), the fracture surfaces were covered with a thin Pt layer (∼8 nm; vacuum sputter coater, SCD 050, Balzers, Liechtenstein) and observed with a SE detector, which yielded mostly topographic contrast. The dispersion of TiX fillers in composites was observed using BSE detector that yielded mostly material contrast. The samples for BSE imaging were covered just by thin carbon layer (∼5 nm; vacuum evaporation device JEE-4C; JEOL, Japan) in order to maintain high compositional contrast between the TiX filler and the TPS matrix.

Transmission Electron Microscopy

The dispersion of the individual TiO₂ nanoparticles in the TPS matrix at the highest magnifications was visualized with a transmission electron microscope (TEM; microscope Tecnai G2 Spirit, FEI, Czech Republic). The ultrathin sections were prepared by a dry cryo-ultramicrotomy (ultramicrotome Ultracut EM UC7; Leica, Austria; cutting conditions: knife temperature = −50°C, sample temperature = −80°C, and dry cutting = sections collected directly from the knife face, without using water trough, onto a standard carbon-coated TEM grids).

The dried samples were observed in the TEM microscope at 120 kV using bright field imaging.

Wide-Angle X-Ray Diffraction (WAXD)

Diffraction patterns were obtained using a high resolution diffractometer Explorer (GNR Analytical Instruments, Italy). The instrument is equipped with a one-dimensional silicon strip detector Mythen 1K (Dectris, Switzerland). Samples were measured in a reflection mode. The radiation CuKα (wavelength $\lambda = 1.54$ Å) monochromatized with Ni foil (β filter) was used for diffraction. The measurement was done in range $2\Theta = 10$–$40°$ with step $0.1°$. The exposure time at each step was 10 s. The peak deconvolution procedure was made using Fityk software (Wojdyr, 2010).

Attenuated Total Reflectance Infrared Spectroscopy

The infrared spectra of TPS and TPS/TiX composites were acquired using a Golden Gate single reflection attenuated total reflectance cell (ATR; Specac, Ltd., Orpington, Kent, UK) using a Fourier-transform infrared spectrometer (FTIR) Thermo Nicolet Nexus 870 (Thermo Fisher Scientific Inc., Waltham, Massachusetts, USA) purged with dry air. The spectrometer was equipped with a liquid nitrogen cooled MCT (mercury cadmium telluride) detector, and the ATR cell employed a diamond internal reflection element. ATR FTIR spectra were recorded with a resolution of 4 cm⁻¹; 256 scans were averaged per spectrum. After the subtraction of the spectrum of the ambient atmosphere, the baselines were corrected (linear base-line correction) and an advanced ATR correction was applied (the correction is defined and recommended within the control FTIR software OMNIC).

Rheometry

The rheological properties of the TPS matrices and the TPS/TiX composites were studied in oscillatory shear flow using a Physica MCR 501 rheometer (Anton Paar GmbH, Austria). A special anti-slipping parallel-plate geometry of 25 mm diameter plates was used. The sample thickness was around 1 mm. The experiments were performed at 120°C in the linear viscoelastic range (LVE range), confirmed from a strain sweep tests at the frequency of 1 Hz. Dynamic frequency sweeps test were carried out over the frequency range of 10^{-1}-10^2 rad/s at a strain of 0.02%.

Dynamic Mechanical Analysis

The mechanical properties of the TPS/TiX composites were tested by a dynamic-mechanical analysis (DMA). The linear viscoelastic characteristics—the absolute value of complex modulus $|G^*|$, storage modulus G', loss modulus G'', and loss factor $\tan(\delta)$—were measured in the rectangular torsion using a Physica MCR 501 rheometer (Anton Paar GmbH, Austria). The strain amplitude sweep tests (at $-90°C$ and $+120°C$) were conducted at the frequency 1 Hz in order to determine the linear viscoelastic range of all TPS/TiX composites. The temperature sweep measurements were carried out in the temperature range $-90°C$ to $120°C$ (with heating rate $3°C$/min), at a strain of 0.05% (in the linear viscoelastic range), and frequency 1 Hz.

Thermal Gravimetric Analysis

The thermal gravimetric analysis (TGA) of TPS/TiX samples (4–7 mg) was performed on a Perkin Elmer Pyris 1 TGA in the temperature range from 30 to 600°C at a rate of 10°C/min. The nitrogen purge gas flow rate was fixed at 25 ml/min of nitrogen.

RESULTS AND DISCUSSION

Morphology of TPS Composites

All TPS/TiO₂ and TPS/TiNT composites (**Table 1**) after the solution casting (SC) and its combination with the melt mixing (SC + MM) were visualized by LM (**Figure 1**). Lower magnification LM micrographs evidenced that the agglomerates of TiO₂ particles formed after SC (**Figures 1A–F**) were destroyed after SC + MM (**Figures 1G–L**). The LM micrographs also proved that the TPS(t)/TiX composites (**Figures 1D–F**, **J–L**) had a better TiX particles dispersion than the TPS(w)/TiX composites (**Figures 1A–C,G–I**), both after SC and after SC + MM. Both wheat and tapioca TPS/TiNT composites contained large agglomerates of TiNT after SC and also after SC+MM, but TPS(t)/TiNT composites exhibited less coarse morphology with slightly smaller agglomerates. The large agglomerates of TiNT dominated the morphology of all TPS/TiNT composites, being clearly visible even at low-magnification LM micrographs. Therefore, a morphological study of TPS/TiNT composites at higher magnifications was not necessary. In contrast, the fine morphology of TPS/TiO₂ composites was studied in more detail using SEM and TEM. Higher magnification SEM (**Figure 2**) micrographs showed that the TiO₂ particles tended to envelope plasticized, but not-fully-merged starch granules after SC (**Figures 2A,C**), while the following MM step resulted in complete merging of starch granules and very homogeneous distribution of TiO₂ nanoparticles (**Figures 2B,D**). The highest magnification TEM micrographs confirmed that tapioca TPS/TiO₂ composites had better dispersion of the fillers in nanoscale (**Figure 3**), which was not evident from SEM micrographs due to their limited resolution (higher magnification in SEM was impossible due to electron beam damage of the specimens). All three microscopic methods indicated that: (i) the two-step preparation (SC + MM) was necessary to get fully plasticized starch with homogeneous filler dispersion, which was in agreement with our previous study (Ostafinska et al., 2017) and that (ii) the two-step SC + MM method was quite universal, applicable not only to one particular wheat starch matrix, but also to different starch types.

XRD and IR Characterization

The structural changes of native wheat starch during its plasticization by our two-step preparation method (SC + MM) were studied in detail in our previous paper (Ostafinska et al., 2017). The paper dealt with wheat starch composites with low filler concentrations (up to 3%). In this paper we added characterization of the composites with different TPS matrices (tapioca starch and wheat starch from a different supplier) and the higher concentration of the fillers (up to 6 wt.%).

The XRD patterns of the samples containing wheat starch are present on **Figure 4A** and the tapioca-based samples are shown
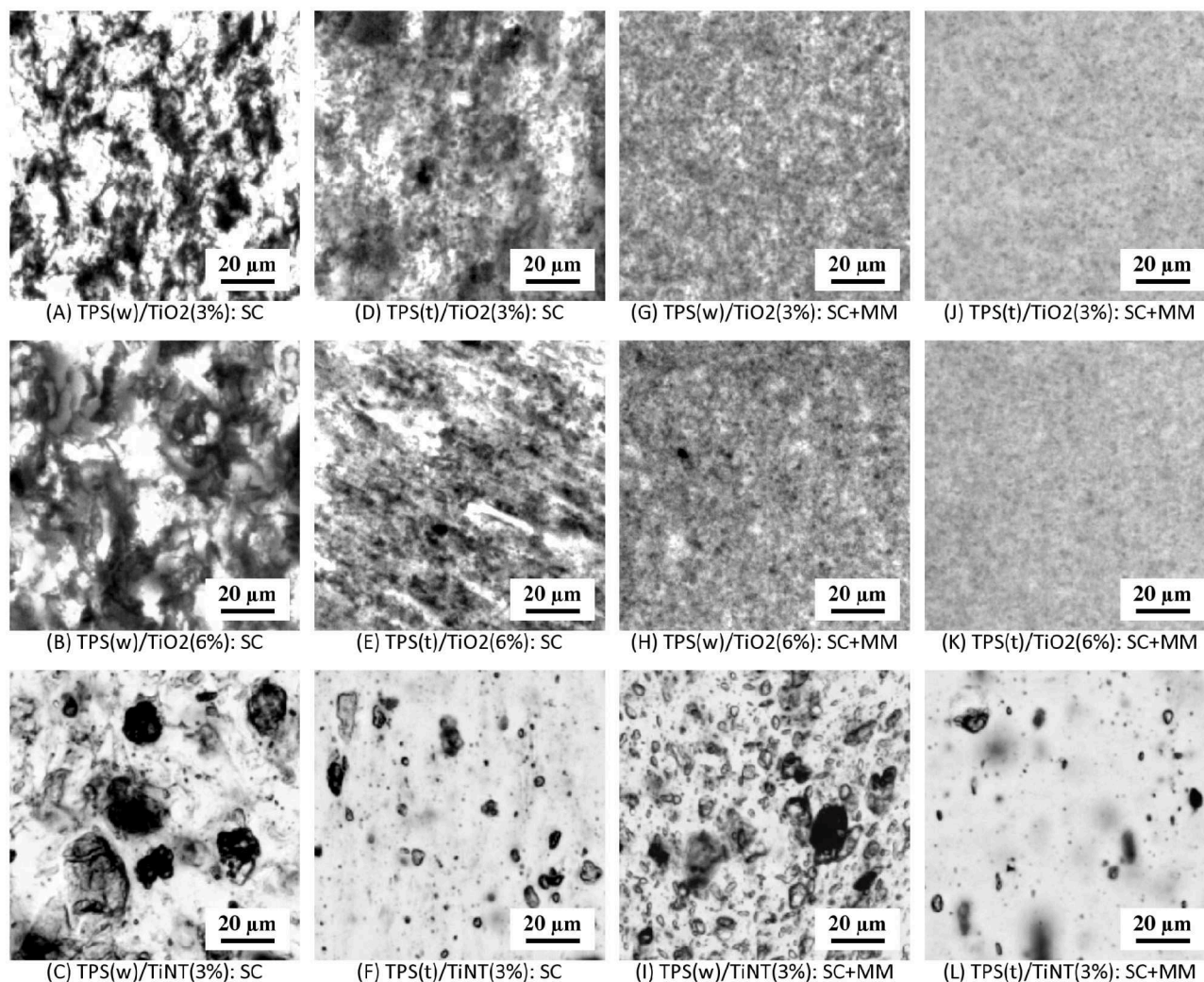
FIGURE 1 | LM micrographs showing the dispersion of filler in TPS/TiX composites: **(A–C)** wheat starch composites after solution casting, **(D–F)** tapioca starch composites after solution casting, **(G–I)** wheat starch composites after solution casting and melt-mixing, and **(J–L)** tapioca starch composites after solution casting and melt mixing.

on **Figure 4B**. Almost identical diffraction peaks were observed in native wheat and native tapioca starches. Those characteristic diffraction peaks of native starches (Zeng et al., 2011) disappeared in the plasticized samples, which proved the destruction of the original crystalline structure. Evidently, a retrogradation was taking place similarly to what was shown by Ostafinska et al. (2017). Two strong peaks at $2\Theta = 12.9°$ and $19.8°$ were visible in the case of wheat starch [TPS(w)], indicating molecule rearrangement into V_H crystal lattice (van Soest et al., 1996). For the plasticized tapioca starch [TPS(t)] both peaks were present as well, but their intensity was lower. We have not observed presence of the other two known processing-induced crystal structures of TPS (V_A and E_H), which were described elsewhere (van Soest et al., 1996). For the samples with TiO₂, intense sharp peak at $2\Theta = 25.3°$ corresponded to (101) diffraction of the TiO₂ anatase phase. The peak height was proportional to the

content of TiO₂. For the samples with TiNT, no specific peaks corresponding to titanate nanotubes were detected, probably due to their low intensity; this was in agreement with analogous systems studied in our previous work (Ostafinska et al., 2017). Nevertheless, both composites with titanate nanotubes exhibited low-intensity broad residual crystallinity shoulder at 17.6°.

The ATR FTIR spectra of pure plasticized wheat starch [TPS(w)] and tapioca starch [TPS(t)] were not significantly different. Similarly, the spectra of the composites with TiX did not show significant changes compared to the original pure starch. The only region indicating some structural changes of TPS matrix is shown in **Figure 5**. In order to emphasize the subtle changes in the spectra of the composites, we subtracted the spectrum of pure plasticized starch from the spectrum of the composite with such a subtraction factor that no counter-peaks appeared in the resulting difference spectrum
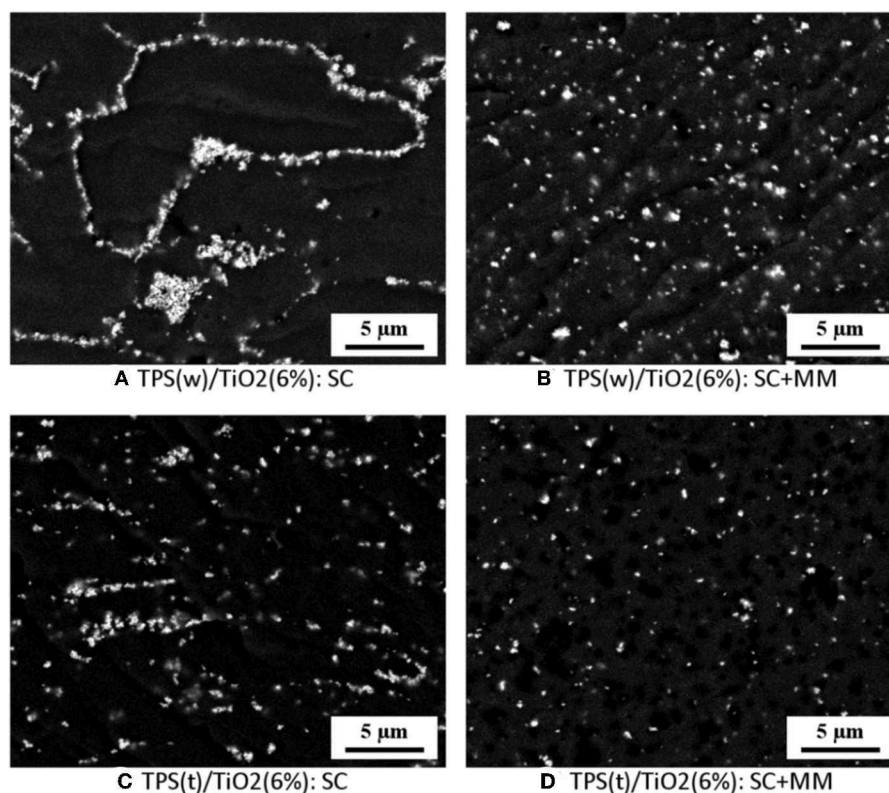
FIGURE 2 | SEM/BSE micrographs showing TPS/TiO$_2$(6%) composites: **(A,B)** wheat starch composite TPS(w)/TiO$_2$ (6%) and **(C,D)** tapioca starch composite TPS(t)/TiO$_2$ (6%); left column **(A,C)** shows composites after solution casting and right column **(B,D)** shows composites after solution casting and melt mixing.
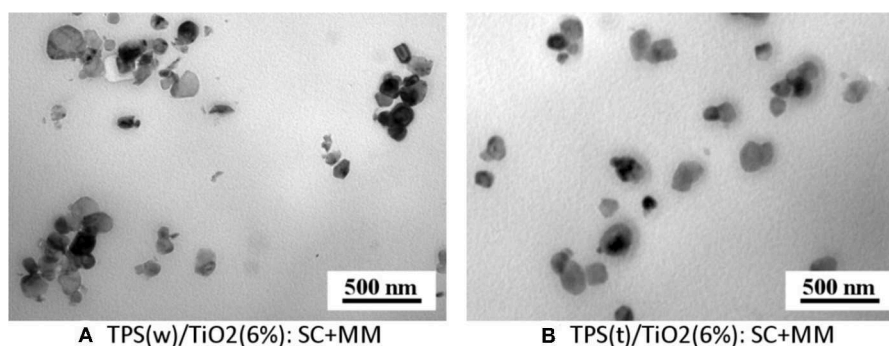

FIGURE 3 | TEM micrographs showing selected TPS/TiO$_2$ (6%) composites after solution casting and melt mixing: **(A)** wheat starch composite TPS(w)/TiO$_2$ (6%) and **(B)** tapioca starch composite TPS(t)/TiO$_2$ (6%).

(**Figure 5**). Relevant changes were detected in the region 1,100–950 cm^{-1} with bands corresponding to C-O, C-C stretching, and C-O-H bending vibrations. The bands at 1,045 and 1,000 cm^{-1} are assigned to crystalline and the band at 1,025 cm^{-1} to amorphous phase of starch. In the spectra of tapioca [TPS(t)/TiO$_2$] composites, the decrease in band intensity at 1,045 cm^{-1} indicated a decrease in crystallinity and a shift of the amorphous band from 1,025 cm^{-1} to higher wavenumbers suggested a strong interaction of the TiO$_2$ particles with the

amorphous part of TPS(t) matrix. It can be seen in the spectra that the addition of TiNT resulted in a much stronger interaction and matrix destruction which is supported by a new band at 1,057 cm^{-1} and a decrease of the band around 1,080 cm^{-1} (C-O-H bending). On the other hand, in wheat composites [TPS(w)/TiX], the interactions between TiX fillers and the matrix were negligible. The addition of TiO$_2$ seemed to increase the crystallinity of the composites, while TiNT had no clear effect on the composites.
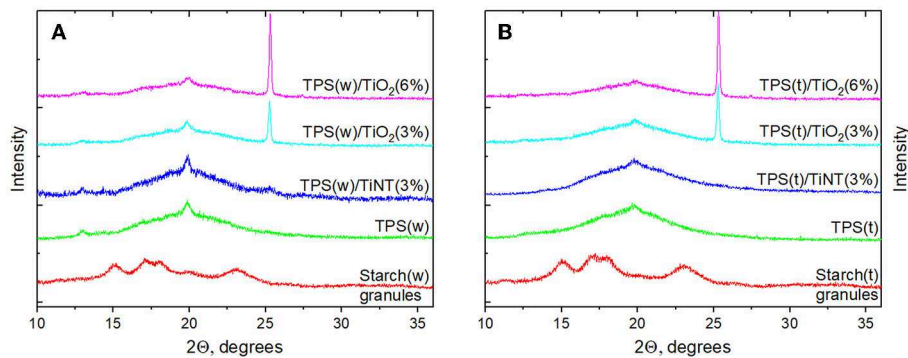
FIGURE 4 | X-ray diffraction patterns of wheat **(A)** and tapioca **(B)** TPS/TiX composites.
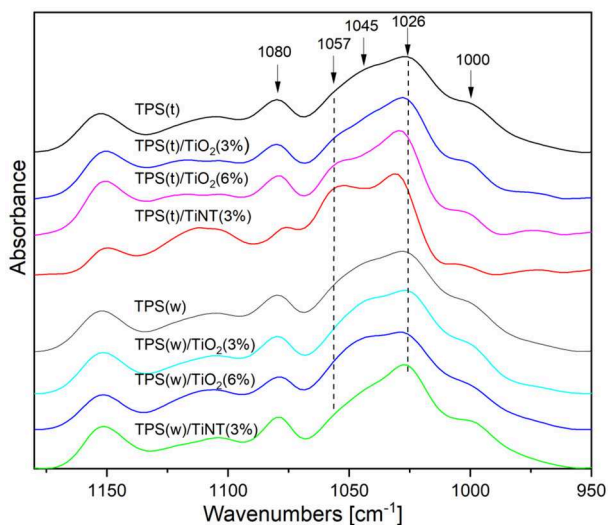

FIGURE 5 | IR spectra of plasticized tapioca and wheat starch and difference spectra of the TPS/TiX composites. From the spectra of all TPS/TiX composites, the spectra of the corresponding pure plasticized starches [TPS(t) or TPS(w)] were partially subtracted in order to emphasize difference peaks, as described in section XRD and IR characterization.

Rheological Properties

The rheological properties of the TPS/TiX composites in the oscillatory shear at 120°C are shown in **Figures 6**, **7**. The logarithmic dependence of the complex viscosity ($|\eta^*|$) on angular frequency (ω) for the wheat composites [TPS(w)/TiX] showed a linear decrease almost in the whole range 0.1–100 rad/s, whereas for the tapioca composites [TPS(t)/TiX] it showed significant curvature down for the lowest ω (region $\omega = 0.1$–0.4 rad/s; **Figure 6**). The values of the complex viscosity ($|\eta^*|$) of the TPS(t)/TiO$_2$ composites were higher in the whole range of frequencies than that of all TPS(w)/TiX composites. Influence of 3 wt.% TiX particles on the complex viscosity of wheat TPS was low, which accorded with our previous work (Ostafinska et al., 2017). The TPS(t)/TiX composites showed different rheological

behavior. Firstly, the addition of TiO$_2$ to the TPS(t) matrix increased the complex viscosity with a slight further increase for the composites with 3 and 6 wt.% of TiO$_2$ particles. Secondly, the addition of TiNT to the TPS(t) matrix decreased the complex viscosity. This was in agreement with the LM, SEM, TEM, and IR results described above: (i) all microscopic methods confirmed the finer dispersion of the TiO$_2$ particles in TPS(t) composites in comparison with the TPS(w) composites (**Figures 1–3**) and (ii) the IR spectroscopy results suggested the stronger interactions of the TiO$_2$ particles with the TPS(t) matrix in comparison with the TPS(w) matrix (**Figure 5** and its discussion in the previous section). Therefore, the very homogeneously dispersed TiO$_2$ particles, which strongly interacted with the TPS(t) matrix, formed a relatively strong physical network and *increased* the $|\eta^*|$ values of the TPS(t)/TiO$_2$ composites. Moreover, the IR spectra suggested that TiNT partially destroyed the internal structure of the TPS(t) matrix, which *decreased* the $|\eta^*|$ values of TPS(t)/TiNT composites. Finally, the IR spectra of TPS(w) composites indicated negligible interactions of all TiX fillers with the TPS(w) matrix, which resulted in just a small increase in the viscosity of TPS(w)/TiX composites, corresponding to the fact that we added a small amount of the hard inorganic filler into the soft polymer matrix.

The storage modulus (G') was larger than the loss modulus (G'') in the whole range of angular frequencies for both wheat and tapioca TPS/TiX composites (**Figure 7**), which is typical of crosslinked and high-molecular weight polymers. In the case of TPS(w) and TPS(w)/TiX composites, G' increased almost linearly for $\omega > 0.4$ rad/s in logarithmic plot. In the case of the TPS(t) and TPS(t)/TiX composites, the almost-linear growth of G' started at higher frequencies [for TPS(t) at $\omega > 30$ rad/s, for TPS(t)/TiNT at $\omega > 40$ rad/s, and for TPS(t)/TiO$_2$ at $\omega > 15$ rad/s]. The curving down of the G' value with the decreasing ω is typical of non-crosslinked polymers (Mezger, 2014). Surprisingly enough, this effect was observed for the higher-viscosity TPS(t) composites and not for the lower-viscosity TPS(w) composites. The higher values of G', G'', and $|G^*|$ for TPS(t)/TiO$_2$ composites in comparison with the TPS(t) matrix (**Figures 7**, **8**) confirmed our assumption that the TiO$_2$ nanoparticles in TPS(t) matrix formed a physical network due to their almost ideal dispersion.
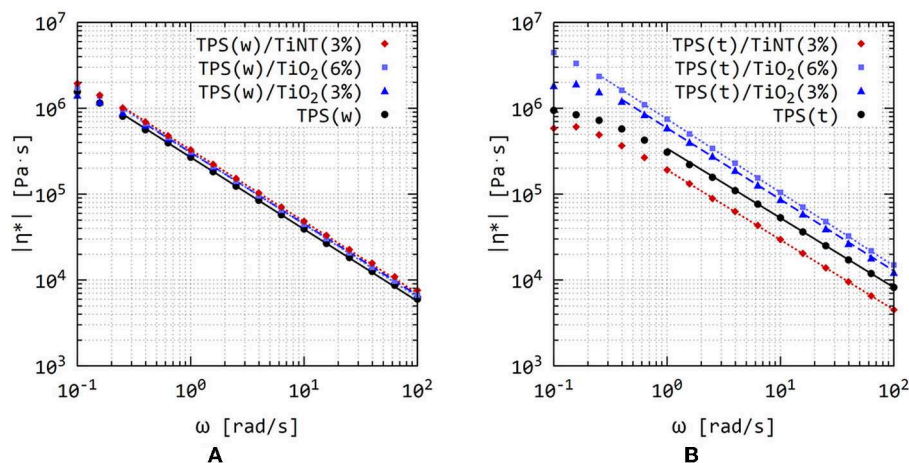
FIGURE 6 | The absolute values of complex viscosities of wheat **(A)** and tapioca **(B)** TPS/TiX composites at 120°C and strain 0.02%: the comparison of the frequency sweeps and their fitting with power-law model (dotted lines; description of the model in Ostafinska et al. (2017).
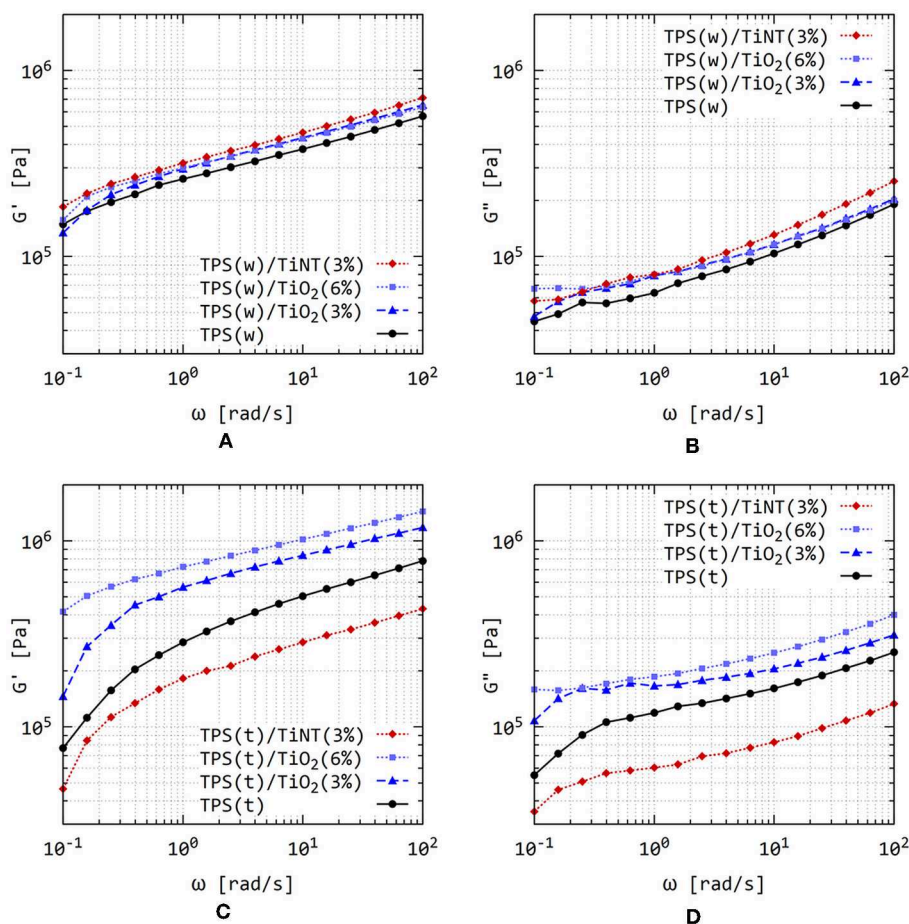

FIGURE 7 | The values of storage modulus (*G′*) **(A,C)** and loss modulus (*G″*) **(B,D)** of wheat **(A,B)** and tapioca **(C,D)** TPS/TiX composites at 120°C and strain 0.02%.
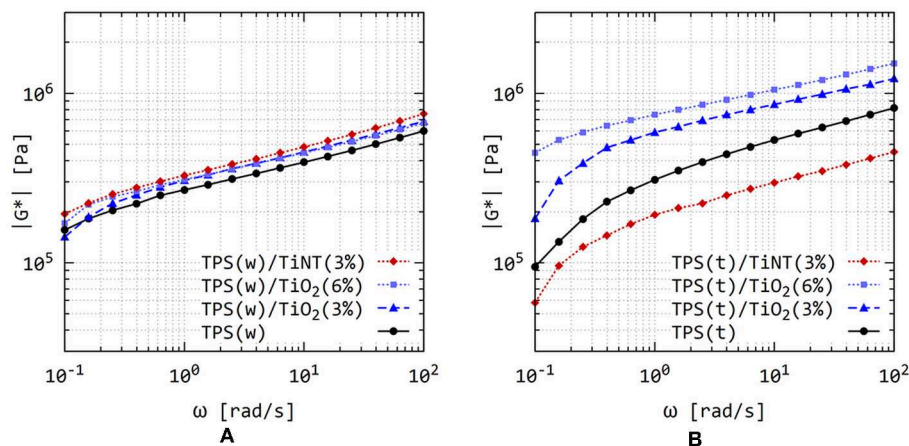
FIGURE 8 | The absolute values of complex modulus (|G*|) of wheat **(A)** and tapioca **(B)** TPS/TiX composites at 120°C and strain 0.02%.
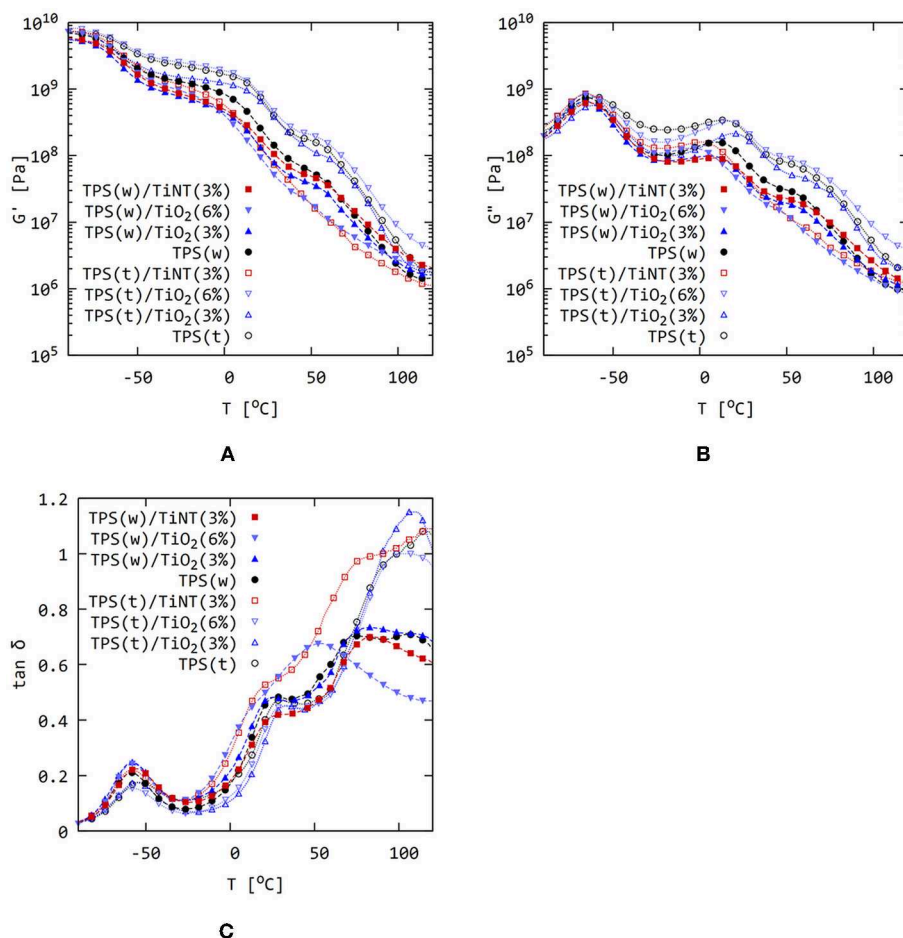

FIGURE 9 | Dynamic mechanical thermal analysis of wheat (w) and tapioca (t) TPS/TiX composites at angular frequency 1 Hz and strain 0.05%: **(A)** storage modulus (G'), **(B)** loss modulus (G''), and **(C)** damping factor [tan (δ)].

The lower values G', G'', and $|G^*|$ for TPS(t)/TiNT composites in comparison with neat TPS(t) can be explained as follows: Basic features of TPS in flow are typical of thermoplastic materials but the structure of TPS is more complex in comparison with simple polymer melts. We even detected two glass transition temperatures (see section Thermomechanical Properties below) related to the two-phase structure of TPS. Moreover, all phases of TPS have their own complex supramolecular structures due to multiple hydrogen bond-based interactions. The supramolecular structures obviously affect rheological properties (rheological response of ordered structures is similar to temporary crosslinks). The assumption that TiNT partially destroyed the original structure of TPS(t) matrix is the most probable explanation of observed decrease in viscosity and modulus. Further changes of supramolecular structure could occur due to possible TiNT-induced scissions of amylose and amylopectin chains. For all prepared composites, the G' and G'' were more-or-less parallel lines and the absolute value of complex moduli $|G^*|$ (**Figure 8**) were almost as high as G', which was in agreement with solid-like, crosslinked structure of TPS-based materials (Mezger, 2014). It should be mentioned that the solid-like behavior of TPS and its composites is not a consequence of chemical networks but of long-living entanglements between extremely long starch chains and/or aggregates kept by non-covalent interactions. Similar behavior of TPS matrix was observed in our previous study dealing with TPS(w)/TiX composites with lower concentration of fillers (Ostafinska et al., 2017). Complex rheological behavior of TPS matrices, including two glass transition temperatures, was observed by other research groups (Viguie et al., 2007; Sessini et al., 2017, 2018); this is discussed also in the following section dealing with DMTA results. Strong hydrogen bond interactions between TPS matrix and TiO$_2$ nanoparticles were observed also in the recent study of (Xiong et al., 2019).

Thermomechanical Properties

The dynamic mechanical thermal analysis (DMTA) of wheat and tapioca TPS/TiX composites was carried out in order to characterize the difference between the two starch types and the influence of the TiX particles on the phase changes of the TPS-based composites (**Figure 9**). The TPS(t) matrix and TPS(t)/TiO$_2$ composites were stiffer than the corresponding TPS(w) samples [G' of TPS(t) samples > G' of TPS(w) samples]. As expected, the G'-curves of all systems decreased with the increasing temperature (**Figure 9A**). G' was higher than G'' for most studied systems in the whole range of temperatures, which confirmed the gel-like structure and the physical stability of all systems (Ross-Murphy, 1995). In the case of TPS(t)/TiO$_2$ composites, the G' became equal to G'' at 90°C and then G'' became slightly higher than G'. This indicated a dominating viscous behavior of TPS(t) composites at elevated temperatures. The TPS(t)/TiNT composite showed low G' in the whole range of temperatures. Moreover, the TPS(t)/TiNT composites exhibited $G' = G''$ at 73°C. These facts supported our assumption from IR and rheological measurements (sections **XRD and IR Characterization** and Rheological Properties) that the original structure TPS(t) was partially destroyed due to the addition of TiNT. The loss modulus (G'') and the damping
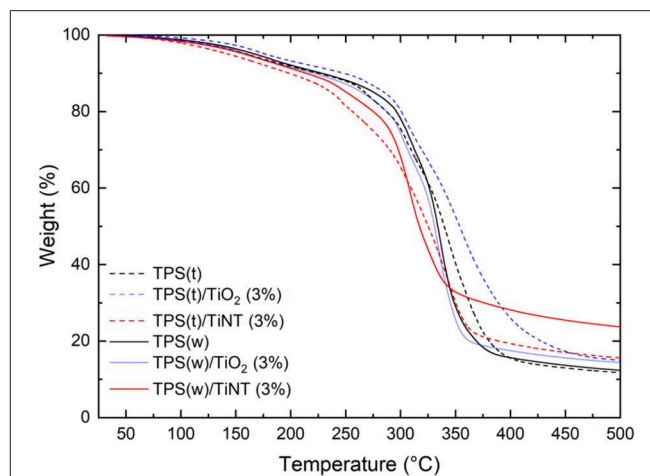

FIGURE 10 | TGA curves of TPS/TiX composites.

TABLE 2 | TGA Results: Weight losses and weight residue (wt.%) of starch samples during thermal degradation under nitrogen atmosphere and heating rate 10°C/min.

	Weight loss between 30 and 120°C (%)	Weight loss between 120 and 400°C (%)	Weight residue at 500°C (%)
TPS (t)	2.5	83	12
TPS (t)/TiO$_2$ (3%)	2.0	73	15
TPS (t)/TiNT (3%)	3.0	78	16
TPS (w)	2.5	83	12
TPS (w)/TiO$_2$ (3%)	2.5	81	14
TPS (w)/TiNT (3%)	2.5	70	24

(w), wheat starch; (t), tapioca starch.

factor [tan(δ)] curves (**Figures 9B,C**) showed two local maxima which corresponded to the two glass transition temperatures (T_g) of TPS matrices: "glycerol-rich phase" (below 0°C) and "amylopectin-rich phase" (above 0°C) as described elsewhere (Viguie et al., 2007; Sessini et al., 2017, 2018). **Figures 9B,C** show that the T_g value of the "glycerol-rich phase" was the same for both tapioca and wheat TPS and their composites, whereas the T_g values of "amylopectin-rich phase" differed [T_g of TPS(w) < T_g of TPS(t)]. This was attributed to different chain domains of the high-molecular weight branched amylopectin molecules in particular starches. Namely, this indicated a decreased mobility of "starch-rich phase" in TPS(t) systems in comparison to TPS(w) (Viguie et al., 2007; Sessini et al., 2018).

Thermal Stability

Figure 10 shows the thermal stability of the TPS(t) and TPS(w) composites. **Table 2** summarizes selected TGA parameters. The first step of thermal degradation between 30 and 120°C was connected with the release of absorbed water. The TGA curves suggested that all systems contained similar amount of water and that they were quite stable until ~250°C. The important exception was the TPS(t)/TiNT composite, which started to

degrade around 200°C. Also the TPS(w)/TiNT composite exhibited slightly lower thermal stability in comparison with the other samples. The second stage of thermal degradation was pyrolysis of starch and glycerol. The lower thermal stability of the TPS(t)/TiNT and TPS(w)/TiNT composites during the second stage of thermal degradation might indicate partial destruction of the TPS matrix structure. At temperatures above 400°C under nitrogen atmosphere, carbon black started to form. This was the reason of quite high weight residue at 500°C, which was approximately the same for all samples.

CONCLUSIONS

This paper was focused on the comparison of wheat and tapioca thermoplastic starches (TPS) and their composites with TiO₂-based nanoparticles (isometric TiO₂ nanoparticles and high aspect ratio TiNT nanotubes). The TPS composites were prepared by our recently developed two-step method that combines a solution casting and melt-mixing (SC + MM).

Main conclusions of our study can be summarized as follows: (i) The SC + MM procedure can be considered as the universal method for preparation of TPS composites with very homogeneous dispersion of the filler, regardless of the starch source and type. (ii) The type of TPS matrix (wheat or tapioca) has a significant impact on the properties of the final composite. (iii) The isometric TiO₂ nanoparticles exhibited very good filler dispersion in both TPS(w) and TPS(t) matrices, while TiNT nanotubes tended to form micrometer-sized agglomerates.

For all studied systems, the tapioca TPS [TPS(t)] composites showed somewhat better dispersion of the filler (as proved by three independent microscopic techniques—LM, SEM, and TEM), stronger interactions of the filler with the matrix (as indicated by IR) and, consequently, a higher impact of the filler on the final properties (as documented by the rheological and thermomechanical measurements). In the TPS(t)/TiO₂ composites, the dominating effect was the formation of the physical network of the well-dispersed filler particles,

resulting in a significant increase in the final value of the complex viscosity, $|\eta^*|$. In the TPS(t)/TiNT composites, the dominating effect was the partial destruction of the TPS matrix, resulting in a decrease in $|\eta^*|$. In wheat TPS [TPS(w)] composites, all matrix-filler interactions were weak and so all TPS(w)/TiO₂ and TPS(w)/TiNT composites exhibited just a slight increase in $|\eta^*|$ due to the fact that we added a stiff inorganic filler into a soft polymer matrix. The above-described complex viscosity changes correlated with other rheological and thermomechanical properties.

DATA AVAILABILITY STATEMENT

The datasets generated for this study are available on request to the corresponding author.

AUTHOR CONTRIBUTIONS

MS, IF, and AU designed the study. AU with the help of SK prepared the TPS and TPS composites by solution casting and melt mixing, and characterized the samples by light and electron microscopy. MN with AU performed and evaluated rheology and DMTA measurements. JD and AZ measured and processed IR and XRD data, respectively. JK carried out TGA measurements and helped with their interpretation. MS with IF made the final data interpretation, with an important contribution of JD. AU prepared draft of the manuscript, which was finalized by MS.

FUNDING

REFERENCES

Ajiya, D. A., Jikan, S. S., Talip, B. H. A., Badarulzaman, N. A., Matias-Peralta, H. M., Derawi, D., et al. (2017). The influence of glycerol on mechanical, thermal and morphological properties of thermoplastic tapioca starch film. *J. Sci. Technol.* 9, 24–29. Retrieved from: https://publisher.uthm.edu.my/ojs/index.php/JST/article/view/2054

Altskar, A., Andersson, R., Boldizar, A., Koch, K., Stading, M., Rigdahl, M., et al. (2008). Some effects of processing on the molecular structure and morphology of thermoplastic starch. *Carbohyd. Polym.* 71, 591–597. doi: 10.1016/j.carbpol.2007.07.003

Ao, Z., and Jane, J. (2007). Characterization and modeling of the A- and B-granule starches of wheat, triticale, and barley. *Carbohyd. Polym.* 67, 46–55. doi: 10.1016/j.carbpol.2006.04.013

Bergel, B. F., Machado da Luz, L., and Santana, R. M. C. (2017). Comparative study of the influence of chitosan as coating of thermoplastic starch foam from potato, cassava and corn starch. *Prog. Org. Coatings* 106, 27–32. doi: 10.1016/j.porgcoat.2017.02.010

Bertolini, A. (2010). *Starches: Characterization, Properties, and Applications*. Boca Raton, FL: CRC Press; Taylor & Francis Group.

Biliaderis, C. G. (2009). "Structural transitions and related physical properties of starch," in *Starch. Chemistry and Technology. A Volume in Food Science and Technology, 3rd Edn.*, ed J. BeMiller, and R. Whistler (Burlington; London; San Diego, CA; New York, NY: Academic Press), 293–372.

Breuninger, W. F., Piyachomkwan, K., and Sriroth, K. (2009). "Tapioca/cassava starch: production and use," in *Starch. Chemistry and Technology. A Volume in Food Science and Technology, 3rd Edn.,* ed J. BeMiller, and R. Whistler (Burlington; London; San Diego, CA; New York, NY: Academic Press), 541–568.

Campos, A., Sena Neto, A. R., Rodrigues, V. B., Luchesi, B. R., Mattoso, L. H. C., and Marconcini, J. M. (2018). Effect of raw and chemically treated oil palm mesocarp fibers on thermoplastic cassava starch properties. *Ind. Crops Prod.* 124, 149–154. doi: 10.1016/j.indcrop.2018.07.075

Campos, A., Senta Neto, A. R., Rodrigues, V. B., Luchesi, B. R., Moreira, F. K. V., Correa, A. C., et al. (2017). Bionanocomposites produced from cassava starch and oil palm mesocarp cellulose nanowhiskers. *Carbohyd. Polym.* 175, 330–336. doi: 10.1016/j.carbpol.2017.07.080

Campos-Requena, V. H., Rivas, B. L., Perez, M. A., Figueroa, C. R., Figueroa, N. E., and Sanfuentes, E. A. (2017). Thermoplastic starch/clay nanocomposites loaded with essential oil consituents as packaging for strawberries – *in vivo*

entimicrobial synergy over *Botrytis cinerea*. *Postharvest Biol. Technol.* 129, 29–36. doi: 10.1016/j.postharvbio.2017.03.005

Chang, Y. P., Karim, A. A., and Seow, C. C. (2006). Interactive plasticizing–antiplasticizing effects of water and glycerol on the tensile properties of tapioca starch films. *Food Hydrocolloids* 20, 1–8. doi: 10.1016/j.foodhyd.2005.02.004

Dai, H., Chang, P., Yu, J., and Ma, X. (2008). N,N-Bis(2-hydroxyethyl)formamide as a new plasticizer for thermoplastic starch. *Starch/Starke* 60, 676–684. doi: 10.1002/star.200800017

Garcia, N. L., Ribba, L., Dufresne, A., Aranguren, M. I., and Goyanes, S. (2009). Physico-mechanical properties of biodegradable starch nanocomposites. *Macromol. Mater. Eng.* 294, 169–177. doi: 10.1002/mame.200800271

Genovese, L., Dominici, F., Gigli, M., Armentano, I., Lotti, N., Fortunati, E., et al. (2018). Processing, thermo-mechanical characterization and gas permeability of thermoplastic starch/poly(butylene trans-1,4-cyclohexanedicarboxylate) blends. *Polym. Degrad. Stability* 157, 100–107. doi: 10.1016/j.polymdegradstab.2018.10.004

Ghavimi, S. A. A., Ebrahimzadeh, M. H., Shokrgozar, M. A., Solati-Hashjin, M., and Osman, N. A. A. (2015). Effect of starch content on the biodegradation of polycaprolactone/starch composite for fabricating in situ pore-forming scaffolds. *Polym. Test.* 43, 94–102. doi: 10.1016/j.polymertesting.2015.02.012

Gonzalez-Seligra, P., Guz, L., Ochoa-Yepes, O., Goyanes, S., and Fama, L. (2017). Influence of extrusion process conditions on starch film morphology. *LWT Food Sci. Technol.* 84, 520–528. doi: 10.1016/j.lwt.2017.06.027

Guz, L., Candal, R., and Goyanes, S. (2017). Size effect of ZnO nanorods on physicochemical properties ofplasticized starch composites. *Carbohyd. Polym.* 157, 1611–1619. doi: 10.1016/j.carbpol.2016.11.041

Jane, J.-L. (2009). "Structural features in starch granules II," in *Starch. Chemistry and Technology. A Volume in Food Science and Technology, 3rd Edn.*, eds J. BeMiller, and R. Whistler (Burlington; London; San Diego, CA; New York, NY: Academic Press), 193–236.

Javanbakht, S., and Namazi, H. (2017). Solid state photoluminescence thermoplastic starch film containing graphene quantum dots. *Carbohyd. Polym.* 176, 220–226. doi: 10.1016/j.carbpol.2017.08.080

Kargarzadeh, H., Johar, N., and Ahmad, I. (2017). Starch biocomposite film reinforced by multiscale rice husk fiber. *Composit. Sci. Technol.* 151, 147–155. doi: 10.1016/j.compscitech.2017.08.018

Kelnar, I., Kapralkova, L., Brozova, L., Hromadkova, J., and Kotek, J. (2013). Effect of chitosan on the behaviour of the wheat B-starch nanocomposite. *Ind. Crops Prod.* 46, 186–190. doi: 10.1016/j.indcrop.2013.01.030

Kralova, D., Slouf, M., Klementova, M., Kuzel, R., and Kelnar, I. (2010). Preparation of gramquantities of high-quality titanate nanotubes and their composites withpolyamide 6. *Mater. Chem. Phys.* 124, 652–657. doi: 10.1016/j.matchemphys.2010.07.029

Kuswandi, B. (2017). Environmental friendly food nano-packaging. *Environ. Chem. Lett.* 15, 205–221. doi: 10.1007/s10311-017-0613-7

Liu, G., Gu, Z., Hong, Y., Cheng, L., and Li, C. (2017b). Electrospun starch nanofibres: recent advances, challenges, and strategies for potential pharmaceutical applications. *J. Contr. Release* 252, 95–107. doi: 10.1016/j.jconrel.2017.03.016

Liu, P., Yu, L., Wang, Z., Li, D., Chen, L., and Li, X. (2010). Glass transition temperature of starches with different amylose/amylopectin ratios. *J. Cereal Sci.* 51, 388–391. doi: 10.1016/j.jcs.2010.02.007

Liu, S., Li, X., Chen, L., Li, L., Li, B., and Zhu, J. (2017a). Understanding physicochemical properties changes from multi-scale structures of starch/CNT nanocomposite films. *Int. J. Biol. Macromol.* 104, 1330–1337. doi: 10.1016/j.ijbiomac.2017.05.174

Liu, X., Wang, Y., Yu, L., Tong, Z., Chen, L., Liu, H., et al. (2013). Thermal degradation and stability of starch under different processing conditions. *Starch/Starke* 65, 48–60. doi: 10.1002/star.201200198

Liu, Y. X., Fan, L. L., Mo, X. Z., Yang, F., and Pang, J. Y. (2018). Effects of nanosilica on retrogradation properties and structures of thermoplastic cassava starch. *J. Appl. Polym. Sci.* 135:45687. doi: 10.1002/app.45687

Lopez-Cordoba, A., Medina-Jaramillo, C., Pineros-Hernandez, D., and Goyanes, S. (2017). Cassava starch films containing rosemary nanoparticles produced by solvent displacement method. *Food Hydrocolloids* 71, 26–34. doi: 10.1016/j.foodhyd.2017.04.028

Mahieu, A., Terrie, C., and Youssef, B. (2015). Thermoplastic starch films and thermoplastic starch/polycaprolactone blends with oxygen-scavenging

properties: Influence of water content. *Ind. Crops Prod.* 72, 192–199. doi: 10.1016/j.indcrop.2014.11.037

Maningat, C. C., Seib, P. A., Bassi, S. D., Woo, K. S., and Lasater, G. D. (2009). "Wheat starch: production, properties, modification and uses," in *Starch. Chemistry and Technology. A Volume in Food Science and Technology, 3rd Edn.*, eds J. BeMiller, and R. Whistler, 441–510.

Mezger, T. G. (2014). *The Rheology Handbook, 4th Edn.* Hannover: Vincentz Network GmbH.

Oleyaei, S. A., Almasi, H., Ghanbarzadeh, B., and Moayedi, A. A. (2016a). Synergistic reinforcing effect of TiO₂ and montmorillonite on potato starch nanocomposite films: thermal, mechanical and barrier properties. *Carbohyd. Polym.* 152, 253–262. doi: 10.1016/j.carbpol.2016.07.040

Oleyaei, S. A., Zahedi, Y., Ghanbarzadeh, B., and Moayedi, A.A. (2016b). Modification of physicochemical and thermal properties of starch films by incorporation of TiO₂ nanoparticles. *Int. J. Biol. Macromol.* 89, 256–264. doi: 10.1016/j.ijbiomac.2016.04.078

Omotoso, M. A., Adeyefa, O.S., Animashaun, E. A., and Osibanjo, O. O. (2015). Biogradable starch film from cassava, corn, potato and yam. *Chem. Mater. Res.* 7, 15–24.

Ostafinska, A., Mikesova, J., Krejcikova, S., Nevoralova, M., Sturcova, A., Zhigunov, A., et al. (2017). Thermoplastic starch composites with TiO₂ particles: preparation, morphology, rheology and mechanical properties. *Int. J. Biol. Macromol.* 101, 273–282. doi: 10.1016/j.ijbiomac.2017.03.104

Perez, S., Baldwin, P. M., and Gallant, D. J. (2009). "Structural features of starch granules I," in *Starch. Chemistry and Technology. A Volume in Food Science and Technology, 3rd Edn.*, eds J. BeMiller, and R. Whistler, 149–192.

Pushpadass, H., Marx, D. B., and Hanna, M. A. (2008). Effects of extrusion temperature and plasticizers on the physical and functional properties of starch films. *Starch/Starke* 60, 527–538. doi: 10.1002/star.200800713

Razali, S. M., Yusoff, M., Ramle, S. F. M., Bhat, I. U. H., Iman, A. H. M., and Razali, A. M. H. (2016). The potential of donax grandis hypodermal fiber as a reinforcement in starch-based composite. *J. Polym. Mater.* 33, 677–684.

Ross-Murphy, S. B. (1995). Structure-property relationships in food biopolymer gels and solutions. *J. Rheol.* 39, 1451–1463. doi: 10.1122/1.550610

Saiah, R., Gatin, R., and Sreekumar, P. A. (2012). "Properties and biodegradation nature of thermoplastic starch," in *Thermoplastic Elastomers*, ed A. El-Sonbati (Rijeka: InTech), 57–78. Available online at: http://www.intechopen.com/books/thermoplastic-elastomers/properties-andbiodegradation-nature-of-thermoplastic-starch

Sarka, E., Krulis, Z., Kotek, J., Ruzek Korbarova, A., Bubnik, Z., and Ruzkova, M. (2011). Application of wheat B-starch in biodegradable plastic materials. *Czech J. Food Sci.* 29, 232–242. doi: 10.17221/292/2010-CJFS

Sarka, E., Krulis, Z., Kotek, J., Ruzek, L., Vorisek, K., Kolacek, J., et al. (2012). Composites containing acetylated wheat B-starch for agriculture applications. *Plant Soil Environ.* 58, 354–359. doi: 10.17221/287/2012-PSE

Schmitt, H., Guidez, A., Prashantha, K., Soulestin, J., Lacrampe, M. F., and Krawczak, P. (2015). Studies on the effect of storage time and plasticizers on the structuralvariations in thermoplastic starch. *Carbohyd. Polym.* 115, 364–372. doi: 10.1016/j.carbpol.2014.09.004

Sengottuvelan, A., Balasubramanian, P., Will, J., and Boccaccini, A. R. (2017). Bioactivation of titanium dioxide scaffolds by ALP-functionalization. *Bioact. Mater.* 2, 108–115. doi: 10.1016/j.bioactmat.2017.02.004

Sessini, V., Arriera, M. P., Fernandez-Torres, A., and Peponi, L. (2018). Humidity-activated shape memory effect on plasticized starch-based biomaterials. *Carbohyd. Polym.* 179, 93–99. doi: 10.1016/j.carbpol.2017.09.070

Sessini, V., Raques, J.-M., Lourdin, D., Maigret, J.-D., Kenny, J. M., Dubois, P., et al. (2017). Humidity-activated shape memory effects on thermoplastic starch/EVA blends and their compatibilized nanocomposites. *Macromol. Chem. Phys.* 218:1700388. doi: 10.1002/macp.201700388

Song, X., Zuo, G., and Chen, F. (2018). Effect of essential oil and surfactant on the physical and antimicrobialproperties of corn and wheat starch films. *Int. J. Biol. Macromol.* 107, 1302–1309. doi: 10.1016/j.ijbiomac.2017.09.114

Teixeira, E. M., Curvelo, A. A. S., Correa, A. C., Marconcini, J. M., Glenn, G. M., and Mattoso, L. H. C. (2012). Review. Properties of thermoplastic starch from cassava bagasse and cassava starch and their blends with poly (lactic acid). *Ind. Crops Prod.* 37, 61–68. doi: 10.1016/j.indcrop.2011.11.036

Teixeira, E. M., Pasquini, D., Curvelo, A. A. S., Corradini, E., Belgacem, M. N., and Dufresne, A. (2009). Cassava bagasse cellulose nanofibrils reinforced thermoplastic cassava starch. *Carbohyd. Polym.* 78, 422–431. doi: 10.1016/j.carbpol.2009.04.034

Valencia-Sullca, C., Vargas, M., Atares, L., and Chiralt, A. (2018). Thermoplastic cassava starch-chitosan bilayer films containing essential oils. *Food Hydrocolloids* 75, 107–115. doi: 10.1016/j.foodhyd.2017.09.008

van Soest, J. J. G., Hulleman, S. H. D., de Wit, D., and Vliegenthart, J. F. G. (1996). Crystallinity in starch bioplastics. *Ind. Crops Prod.* 5, 11–12. doi: 10.1016/0926-6690(95)00048-8

Viguie, J., Molina-Boisseau, S., and Dufresne, A. (2007). Processing and characterization of waxy maize starch films plasticized by sorbitol and reinforced with starch nanocrystals. *Macromol. Biosci.* 7, 1206–1216. doi: 10.1002/mabi.200700136

Visakh, P. M., Mathew, P. A., Oksman, K., and Thomas, S. (2012). "Starch-basedbionanocomposites: processing and properties," in *Polysaccharide Building Blocks: A Sustainable Approach to the Development of Renewable Biomaterials*, eds Y. Habibi, and L. A. Lucia (Hoboken, NJ: John Wiley & Sons, Inc.), 287–306.

Webster, J., Ergun, C., Doremus, R. H., Siegel, R. W., and Bizios, R. (2000). Enhanced functions of osteoblasts on nanophase ceramics. *Biomaterials* 21, 1803–1810. doi: 10.1016/S0142-9612(00)00075-2

Wojdyr, M. (2010). Fityk: a general-purpose peak fitting program. *J. Appl. Cryst.* 43, 1126–1128. doi: 10.1107/S0021889810030499

Xie, F., Pollet, E., Halley, P. J., and Averous, L. (2013). Starch-based nano-biocomposites. *Prog. Polym. Sci.* 38, 1590–1628. doi: 10.1016/j.progpolymsci.2013.05.002

Xiong, J. Y., Scheng, C. H., Wang, Q., and Guo, W. H. (2019). Toughened and water-resistant starch/TiO$_2$ bio-nanocomposites as an environment-friendly food packaging material. *Mater. Res. Exp.* 6:055045. doi: 10.1088/2053-1591/ab058b

Zeng, J., Li, G., Gao, H., and Ru, Z. (2011). Comparison of A and B starch granules from three wheat varieties. *Molecules* 16, 10570–10591. doi: 10.3390/molecules161210570

Zhu, F. (2015). Review. Composition, structure, physicochemical properties, and modifications of cassava starch. *Carbohyd. Polym.* 122, 456–480. doi: 10.1016/j.carbpol.2014.10.063

Zuo, G., Song, X., Chen, F., and Shen, Z. (2017). Physical and structural characterization of edible bilayer films made with zein and corn-wheat starch. *J. Saudi Soc. Agric. Sci.* 18, 324–331. doi: 10.1016/j.jssas.2017.09.005

Cellulose Nanowhisker (CNW)/Graphene Nanoplatelet (GN) Composite Films With Simultaneously Enhanced Thermal, Electrical and Mechanical Properties

Dongyan Liu[1], Yu Dong[2], Yueyue Liu[1], Na Ma[1] and Guoxin Sui[1]*

[1] Institute of Metal Research (IMR), Chinese Academy of Sciences, Shenyang, China, [2] School of Civil and Mechanical Engineering, Curtin University, Perth, WA, Australia

Transparent cellulose nanowhisker (CNW)/graphene nanoplatelet (GN) composite films were produced via sonication mixing and solution casting methods. Such composite films exhibited improved thermal, electrical and mechanical properties. The material morphologies and microstructures were examined using scanning electronic microscopy (SEM), X-ray diffraction (XRD) analysis and Raman spectroscopy. Strong interaction was detected when CNWs were randomly attached onto graphene sheets, as evidenced by SEM images obtained in this study. In particular, the addition of GNs into CNWs had significant effect on the thermal behavior of composite films. The melting temperature (T_m) and initial thermal decomposition temperature (T_{id}) of CNW films were both increased by 23.2, 29.3, 26.3°C, and 70.2, 88.4, 87.8°C with the inclusions of 0.1, 0.25, and 0.5 wt% GNs, respectively. The electrical conductivity of composite films was enhanced in a monotonically increasing manner with the maximum level of 4.0×10^{-5} S/m detected at the GN content of 0.5 wt%. Their tensile strength was also improved by maximum 33.7% when increasing the GN content up to 0.25 wt% as opposed to that of CNW films. Such CNW/GN composite films can be potentially used in green anti-static and electronic packaging applications.

Keywords: cellulose nanowhiskers (CNWs), graphene nanoplatelets (GNs), electrical conductivity, thermal stability, mechanical strength

INTRODUCTION

Cellulose is one of the most widely used polymers in nature with the annual production of approximately 5×10^{11} tons on earth (Yuan et al., 2015). Cellulose nanowhiskers (CNWs) are generally extracted from natural cellulose-based materials including plants, bacteria, and sea creatures by using hydrolysis methods. It is sized by several nanometers to a few tens of nanometers in diameter and several 100 nm in length. CNWs possess high elastic modulus, large aspect ratios and surface areas, and are generally deemed as ideal reinforcing fillers in polymer composites. Being a natural nanosized polymer, CNWs can be manufactured into different multifunctional composite materials. In view of the wide applications of CNWs, it has been demonstrated that CNWs are

considered as one of the most important material components in waste water treatment (Carpenter et al., 2015; Karim et al., 2016), drug delivery (Jackson et al., 2011), electronic devices (Li and Lee, 2017), energy storage (Xing et al., 2019), food packaging (Li F. et al., 2015), etc. Jiang et al. (2015) reported that the UV-blocking ratios of nanocellulose/6wt% ZnO transparent composite films reached 97.8% and 99.1% at the wavelengths of 300 and 225 nm, respectively. Zhan et al. (2018) successfully prepared UV-induced and self-cleanable nanocellulose/TiO_2 composite membranes in possession of effective separation for various surfactant-stabilized emulsions with high oil rejection over 99.5%. Sadasivuni et al. (2016) demonstrated ultra-flexibility and high-level NO_2 sensitivity of iron oxide @ cellulose nanocrystal (CNC) composites. On the other hand, Meulendijks et al. (2017) and Drogat et al. (2011) proved that CNW/Ag composites had good electrical conductivity and antibacterial feature. As far as green materials and environmental sustainability are concerned, CNWs are gradually gaining more popularity in the development of functional nanomaterials.

Cellulose films are well known as a potential substrate/matrix for conductive materials due to its renewability, biodegradability and flexibility (Du et al., 2017; Agate et al., 2018). Because CNWs have excellent film formability and affinity with conductive polymers, they are widely used as CNW-based conductive ink (Latonen et al., 2017), sensors (Mahadeva et al., 2011; Esmaeili et al., 2015) and capacitors (Liew et al., 2013; Jose et al., 2019) when incorporated into conductive polymers (He et al., 2019). Carbon-based nanomaterials are functional nanofillers such as carbon nanotubes (CNTs) and graphene, which can be used for cellulosic materials when considering their extraordinary material properties including but not limited to electrical conductivity, mechanical strength and modulus, electromagnetic-shielding effectiveness and capacity. Yamakawa et al. (2017) reported a high electrical conductivity of 1.05 S/m, good mechanical properties such as high Young's modulus of 10.1 GPa and tensile strength of 173.4 MPa, as well as a low coefficient of thermal expansion (CTE) at 7 ppm/K. Pang et al. (2015) fabricated multifunctional cellulose/CNT composite papers using a filtration method. At the CNT contents of 10–71 wt% in the frequency range of 175–1,600 MHz, it was detected that such papers yielded an electrical conductivity of 9.9–216.3 S/m along with good electromagnetic interference (EMI) shielding effectiveness (SE) at 15–45 dB. In addition, these composite papers with the inclusion of 50 wt% CNTs possessed the capacitance of 46 F/g at a scan rate of 5 mV/s, reversible discharge capacity of 474.0 mAh/g when they were taken as an anode current collector for lithium ion battery (Pang et al., 2015). Dichiara et al. (2017) indicated that the addition of hydroxyl-functionalized CNTs with pre-absorbed alkali lignin gave rise to the improvement of dry and wet strengths of cellulose fibers along with good sensitivity of humidity. On the other hand, Ko et al. (2019) utilized a solution casting method to fabricate methyl cellulose/50 wt% CNT composite papers with a much higher electrical conductivity of 15.9 S/cm and better bending durability as opposed to those of graphene and indium tin oxide (ITO). Gnanaseelan et al. (2018) suggested cellulose/single-walled CNT (SWCNT) composite films should be considered as a promising thermoelectric material owing to their relatively high power factors when compared with those of other insulating polymer/CNT composites. In comparison with fiber-like CNTs, 2D graphene sheets could be a better nanofiller alternative, as evidenced by greatly improved tensile strength by 93% and significantly enhanced electrical conductivity by 10 folds in bacterial cellulose/graphene composite papers (Luo et al., 2019). More recently, Zhan et al. (2019) produced highly conductive cellulose nanofibrils/20 wt% exfoliated graphene composite films with a remarkable electrical conductivity of 568 S/m along with excellent mechanical properties including tensile strength of 389 MPa, elastic modulus of 8.0 GPa and elongation at break of approximately 20%. The associated multifunctional properties of cellulose composites are summarized in **Table 1** accordingly.

Nanocellulose/graphene composites are deemed as ideal electrode materials for flexible supercapacitors (Xing et al., 2019). The potential use of cellulose-based nanomaterials sheds light on widespread applications in material conductivity, energy storage and electronic devices, etc. The excellent material properties of cellulose and CNTs or graphene rely on their linkages by non-covalent interactions with well-maintained intrinsic properties of both nanomaterials. CNWs have been proven to be an effective aqueous-based dispersant for 2D nanosheet materials due to their unique characteristics of nanoscale size, surface charge and molecular chain structures (Li F. et al., 2015; Ma et al., 2017). Polyurethane sponges with superhydrophobicity and superamphiphilicity were produced by a simple dip-coating method, which was derived from the close interaction between CNWs and graphene (Zhang et al., 2017, 2018). Such an interaction can be confirmed not only from material morphologies, structural changes, but also from the characteristic peaks on thermal analysis. The thermal behavior can indicate the interaction between polymeric molecular chains and reinforcing fillers. In general, glass transition temperature (T_g), melting temperature (T_m), initial decomposition temperature (T_{id}) can be altered significantly with their strong interaction.

Nanocellulose/GN composites have been extensively studied for their mechanical and electrical properties. Nonetheless, thermal properties of CNW films and their composites may not be well investigated. Our initial work (Ma et al., 2017; Zhang et al., 2017, 2018) focused on the interaction between CNWs and GNs, and found that a small addition of GNs could greatly increase melting temperature and decomposition temperature of CNW films, which was ascribed to morphological absorption and enhanced physical parameters upon heating. The research objective and novelty of this study lie in the successful development and holistic evaluation of CNW/GN composite films in relation to the GN role as rigid fillers as well as filler-matrix interactions to simultaneously enhance their thermal, electrical and mechanical properties, which may be hard to achieve in conventional nanocomposite materials so that CNW/GN composite films are expected to be potentially effective multifunctional materials for electronic packaging applications.

EXPERIMENTAL WORK

Materials

Industrial flax linens as raw materials were purchased from Xuyi Textile Material Co. Ltd (Ningbo, China) for CNW extraction.

TABLE 1 | Multifunctional properties of cellulose composites.

Filler/Content	Method	Properties	References
6 wt% ZnO	Pressure extrusion Vacuum-oven drying	UV blocking ratios of 97.79% and 99.13% for wavelengths of 300 and 225 nm	Jiang et al., 2015
TiO_2	Filtration Vacuum-oven drying	Self-cleanable, high oil rejection over 99.5%	Zhan et al., 2018
Fe_2O_3	*In situ* synthesis	NO_2 sensitivity: ppm level	Sadasivuni et al., 2016
Ag	*In situ* synthesis	Minimum inhibitory concentration: *E. coli* strain:2.7 µg/mL; *S. Aureus* strain: 5.4 µg/mL	Drogat et al., 2011
5 wt% multi-walled CNTs (MWCNTs)	Filtration	Electrical conductivity: 1.05 S/cm Young's modulus: 10.1 GPa Tensile strength: 173.4 MPa CTE: 7 ppm/K	Yamakawa et al., 2017
10–71 wt% CNTs	Filtration	Electrical conductivity: 9.9–216.3 S/m EMI SE: 15–45 dB Capacitance: 46 F/g @ 50 wt% CNTs	Pang et al., 2015
20 wt% GNs	Oven drying	Electrical conductivity: 568 S/cm	Zhan et al., 2019

Graphene nanoplatelets (GNs) were supplied in powder form by Sichuan Jinlu Group Co., Ltd, Deyang, China. GNs consist of 5–8 layers based on single graphene sheet. Their lateral size is around 10–20 µm, and the atomic ratio between C and O elements is 80–100. All other used chemicals including uranyl acetate, sodium hydroxide, concentrated sulfuric acid, glacial acetic acid, toluene, ethanol and hydrogen peroxide were obtained from Shenyang Dongbao Company (Shenyang, China) without modification.

Preparation of CNWs

CNWs were isolated from bleached flax yarns by using a sulfuric acid method, as previously reported (Liu et al., 2010). The yarns were heated in 60 wt% sulfuric acid for 1 h at 55°C, which was followed by consecutive dilution and washing processes repeatedly in a centrifuge tube until the supernatant is neutral. The aqueous suspension of CNWs was stored in a fridge for the further experimental use.

Preparation of CNW/GN Composite Films

GNs were added in suspension of 0.5 wt% CNWs at the GN contents of 0.1, 0.25, and 0.5 wt%. The homogeneous aqueous dispersion of GN/CNW mixture was obtained by ultrasonicating (KH-1600TDE, Kunshan, China) graphene powders and CNWs in deionized water at a frequency of 80 kHz and an electrical power of 1,600 W until the uniform dispersion was obtained. The GN aggregates were broken up into GN sheets and became stabilized in CNW suspensions. CNW/GN composite films were successfully prepared by casting the mixture onto a plastic petri dish, which was followed by water evaporation at ambient temperature. Final composite films were peeled off from the petri dish after being dried under the ambient condition, which were denoted as "CNWs/0.1 GNs," "CNWs/0.25GNs," and "CNWs/0.5GNs" at the GN contents of 0.1, 0.25, and 0.5 wt%, respectively in the following result section.

Characterization Methods

The morphology of CNWs was characterized using a transmission electron microscope (TEM, Philips CM 12,

Holland) with an acceleration voltage of 100 kV. The aqueous CNW suspension was diluted to be 0.1g/L. A droplet of such suspension was dropped onto a copper grid covered with a carbon film. The samples were then stained with 2.0 wt% solution of uranyl acetate for 1 min prior to TEM observation.

The morphologies of CNW/GN composite films were observed on a field emission scanning electron microscope (JSM-6301F) at the accelerating voltage of 10 kV. The samples were sputter coated with gold about 10–20 nm in thickness prior to SEM observation. On the other hand, the photographs of CNW/GN composite films were recorded with a digital camera.

The electrical conductivity was measured by using a Keithley electrometer model 2000 (USA). Two round copper disks were used as the electrodes and their surfaces were polished and spread with silver paste in order to warrant good contact with the testing films. Volume resistance (R) was measured and the resistivity ρ was calculated as follows:

$$\rho = RS/t \tag{1}$$
$$\sigma = 1/\rho \tag{2}$$

where t is the film thickness in cm, S is the circular area of the film in cm^2, and subsequently corresponding electrical conductivity σ in S/m was calculated according to Equation (2).

Thermal behavior of films was studied using thermogravimetric analysis (TGA Q500, TA instruments, USA) and TA differential scanning calorimetry (DSC Q20, TA instruments, USA). Each sample weighing approximately 5 mg was heated from 50 to 800°C at a heating rate of 20°C/min for TGA while heated from 50 to 400°C at a heating rate of 10°C/min for DSC. Both thermal analyses were conducted under nitrogen atmosphere to prevent any thermoxidative degradation.

Wide-angle X-ray diffraction measurements were performed using a Rigaku D/max 2500PC diffractometer equipped with Cu Kα radiation (wave length λ = 1.54 Å) at 50 kV and 300 mA in the 2θ range of 5–50° with a step interval of 0.02° to study the influence of GNs on the crystalline structures of CNWs.

Raman spectroscopic measurement (JY Labram HR 800 spectrometer) was carried out to characterize the characteristic peaks of GNs at the wavelength of 632.8 nm under a laser power of 2.5 mW with 6 accumulations.

RESULTS AND DISCUSSION

Morphological Structures
Morphology of CNWs

CNWs used in this study were hydrolyzed with sulfuric acid. **Figure 1** demonstrates the TEM image of CNWs along with their aqueous suspensions at the CNW concentrations of 0.2 g/L (left) and 2 g/L (right). It is clearly seen that CNWs can be categorized as a nanosized polymer in rod shape with their diameter and length of approximately 30 and 500 nm, respectively. At the low CNW concentration about 0.2 g/L, their

aqueous suspensions appear to be transparent similar to water. Whereas, with increasing the CNW concentration, milky colored suspensions gradually become evident. CNW dispersion in water is very stable because of their hydrophilicity and negatively charged surfaces with sulfate groups. As such, CNWs can be potentially used as the dispersant for other nanomaterials. The surface charges can be evaluated by Zeta potential, which means that the higher the potential, the more stable the dispersion is. It is one of the most vital factors for dispersing graphene aggregates (Ma et al., 2017). The CNW films display high transparency, as evidenced by letters to form "CNWs film" underneath such films to be clearly seen in **Figure 1**. In fact, Yamakawa et al. (2017) confirmed that transparent CNW films could be regarded as the green matrix for electrodes.

Morphology of CNW /GN Composites

The cross sectional images of CNW/GN composites after surface fracture were observed under a scanning electron microscope, as depicted in **Figure 2**. Such composite films are densely packed in the film thickness direction, and there are no obvious gaps detected on fracture surfaces despite no applied pressure in the preparation process of films. Apparently, all composite films
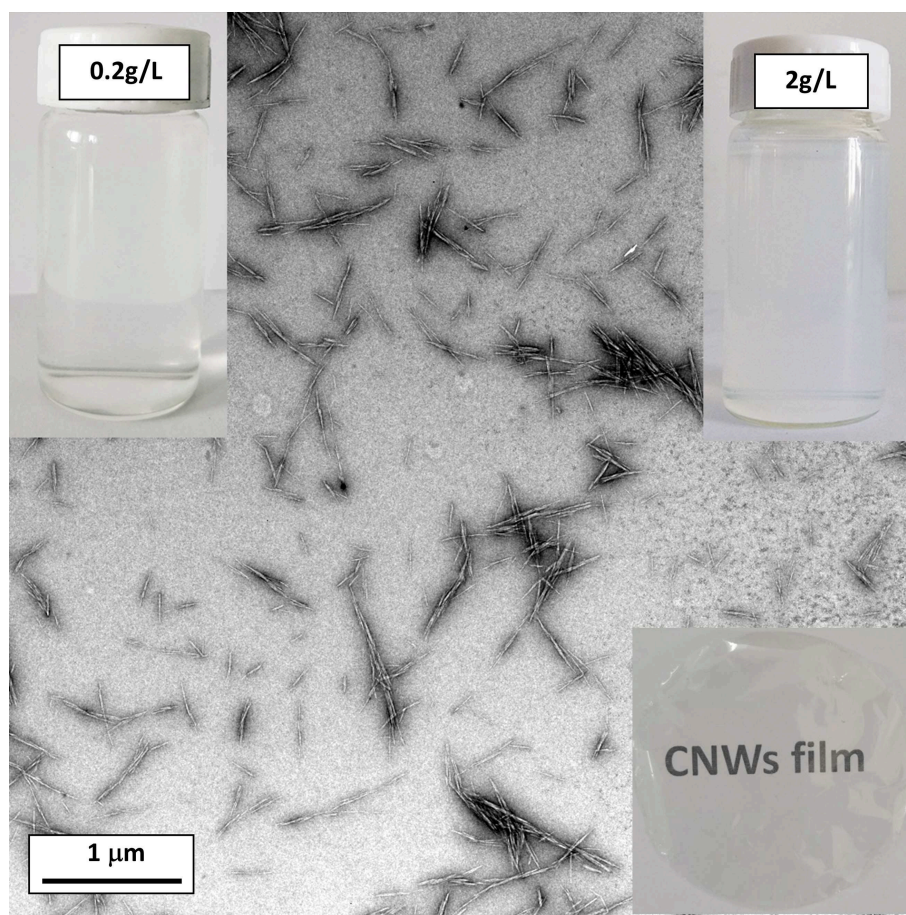

FIGURE 1 | TEM images of dispersed CNWs at the concentration of 0.2 g/L (inset: aqueous CNW suspensions at the CNW concentrations of 0.2 and 2 g/L on the top left and right, respectively, and transparent film on the bottom right).
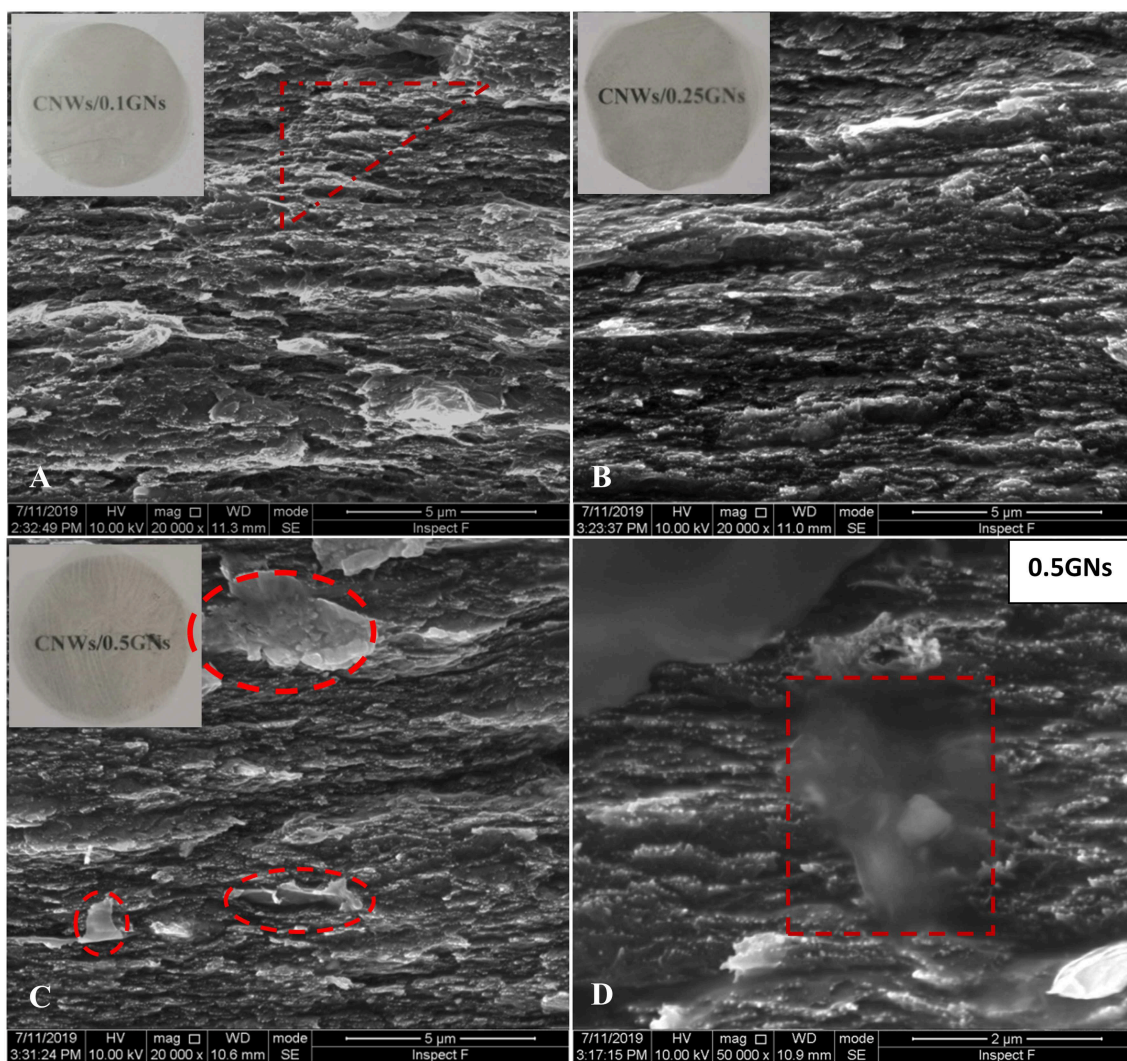
FIGURE 2 | Cross sectional SEM images of CNW/GN composite films at different GN contents: **(A)** 0.1 wt%, **(B)** 0.25 wt%, **(C)** 0.5 wt%, and **(D)** 0.5 wt% (indicating the thin GN sheets attached onto cross sectional surfaces).

appear to mainly comprise randomly oriented CNWs that are closely packed together due to the hydrogen bonding to generate typical layered structures. Many bright dots on SEM images are visible, and can be considered as the tips of individual CNWs. Meanwhile, some shell sheet-like structures become quite evident, indicating good bonding taking place among CNWs alone.

It is not easy to identify GNs particularly in CNW/GN composites at the GN contents of 0.1 and 0.25 wt% shown in **Figures 2A,B**, respectively, which may be ascribed to very uniform GN dispersion in CNW matrices with good interfacial adhesion. When the GN content increases up to 0.5 wt%, GN aggregates in CNW/GN composites appear to be more visible, as marked by red dash frames in **Figures 2C,D**. The lateral size of dispersed GNs is estimated to be 2–5 μm, which is relatively small when compared to that of as-received GN

powders, possibly arising from the disintegration effect during the ultrasonication treatment in material preparation. It is worth noting that thin graphene sheets that are marked with read dashed triangular and rectangular frames in **Figure 2D** may fall off on the cross sectional surfaces of composites during the surface fracture process.

The transparent feature of neat CNW films shown in **Figure 1** can be associated with smaller sizes of nanowhiskers than visible wavelength. With increasing the GN content, the color of composite films becomes much darker as expected despite still having good transparency even for composite films reinforced with 0.5 wt% GNs. The transparency of GNs depends primarily on their layered structures. According to Zhu et al. (2014), monolayer graphene grown by chemical vapor deposition (CVD) can achieve very high light transmittance of 97.4% at the normal incidence when the light wavelength of 550 nm

is used. Furthermore, the more number of layers, the lower transmittance is obtained (Zhu et al., 2014). This work clearly proves that the addition of small amounts of GNs can improve the material properties of CNWs without undermining their film transparency.

Thermal Properties

CNWs are well known as a semi-crystalline polymer with a degree of crystallinity in range of 54–88% (Moon et al., 2011). DSC curves in relation to CNW films and CNW/GN composite films are demonstrated in **Figure 3A**. The melting region of CNWs is quite narrow and sharp, which infers their perfect crystalline structures and a narrow range of molecular weight. The T_m of CNWs has been determined to be 209.6°C, which appears to be much lower than that of microcrystalline cellulose (MCC) at 358°C elsewhere (Trache et al., 2014). Such a far lower melting point of CNWs is attributed to their small size and the reduction in molecular weight resulting from the hydrolysis process. As illustrated in **Figure 3A**, when increasing the GN content from 0.1 to 0.25 wt%, the T_m values of composite films are enhanced from 232.8 to 238.9°C despite a slight decline to 235.9°C at the further increasing GN content of 0.5 wt%, which is still higher than that of neat CNW films at 209.6°C.

The significant increase in T_m by more than 20°C has been rarely reported in other polymer/graphene composites with only a minor increase in T_m (O'Neil et al., 2014). Such a greatly enhanced T_m level may benefit directly from strong interaction between CNWs and well dispersed rigid GNs that can restrict the molecular chain mobility of CNWs.

In addition to the remarkable increase in T_m, typical degradation temperature of CNWs can also be enhanced with the addition of GNs when characterized by the thermal stability generally applied to assorted polymers in practical applications. Extracted CNWs using sulfuric acid generally exhibit low initial decomposition temperature (T_{id}) when incorporated with sulfate groups (Roman and Winter, 2004). As seen in **Figures 3B,C**, CNWs possesses the T_{id} of only 148.3°C, which is much lower than that of mechanically disintegrated cellulose nanofibers in range of 270–295°C (Okahisa et al., 2018). In comparison, with increasing the GN contents from 0.1, 0.25 to 0.5 wt%, the T_{id} values of CNW/GN composites are increased substantially by 66.4, 78.6, and 87.4°C, respectively. This phenomenon results from the typical retardant effect of GNs on the cleavage of glycosidic linkages of cellulose. It also confirms the existing strong interactions between CNWs and GNs, which has not yet
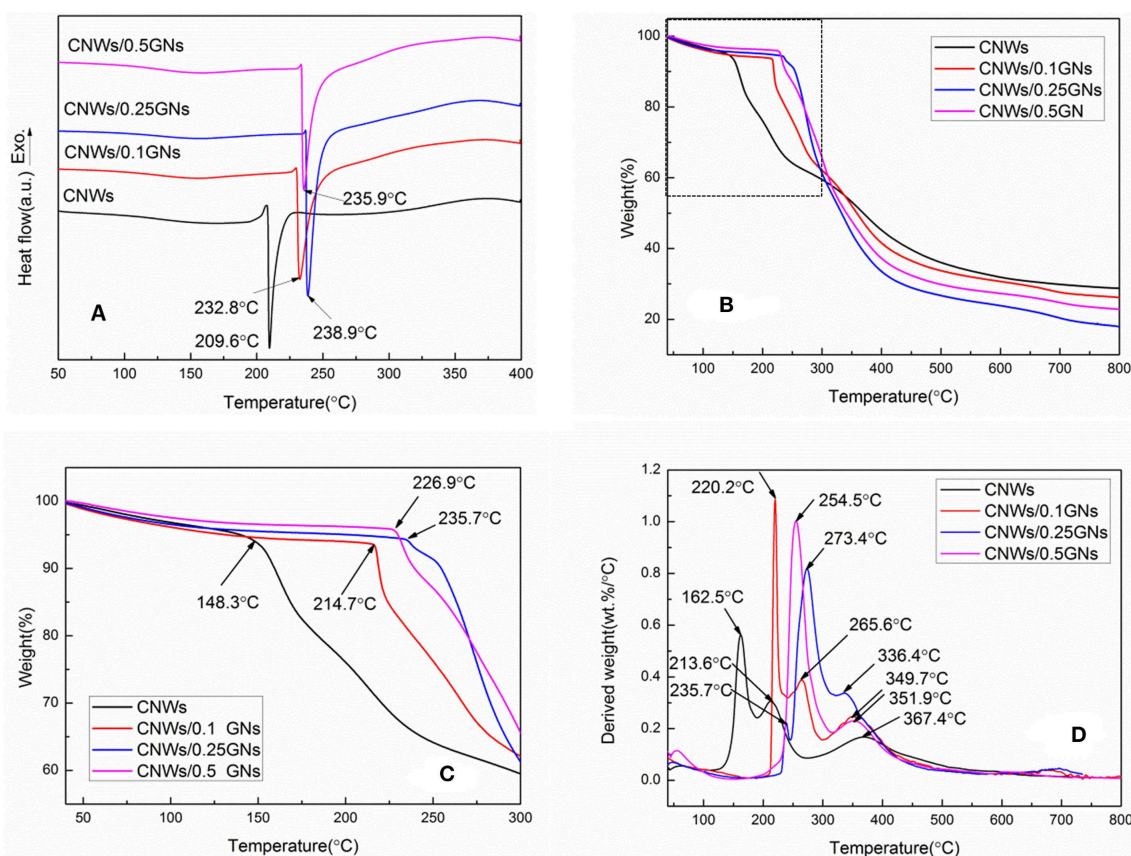

FIGURE 3 | Thermograms of CNW films and CNW/GN composite films: **(A)** DSC curves, **(B)** TGA curves, **(C)** enlarged TGA curve portion within the dash-line block in **(B)**, and **(D)** DTG curves.

been identified in other polymer/graphene composites. More surprisingly, the residual weight of CNWs exceeds those of all CNW/GN composites at 800°C, which can be ascribed to a large number of free end chains during the acid-hydrolysis process (Sofla et al., 2016). Such end chains have been proven to decompose at a lower temperature (Staggs, 2006) leading to an increase in the char yield of CNCs (Piskorz et al., 1989). Moreover, sulfate groups on CNW surfaces in the acid-hydrolysis process may work as flame retardants (Roman and Winter, 2004). Furthermore, Shimizu et al. (2019) also reported the thermal decomposition temperature of 2,2,6,6-tetramethylpiperidine-1-oxyl radical (TEMPO)-mediated oxidized cellulose nanofiber films decreased from 220°C to 182–202°C with increasing the alkyl chain length of quaternary alkyl ammonium (QAs).

Maximum weight loss rate W_{rmax} as a function of temperature can be determined in differential thermogravimetry (DTG) curves of CNW/GN composite films, (**Figure 3D**). There are three typical characteristic DTG peaks detected in composite films. Apparently, the temperature for maximum weight loss rate T_r shifts to higher temperature levels from 162.5 to 273.4°C when increasing the GN contents from 0 to 0.5 wt%. The other two T_r of composite films can be positioned in temperature ranges of 220–270°C and 330–370°C, which presents a similar temperature-increasing tendency with increasing the GN content. Nonetheless, W_{rmax} values of composite films are in range of 0.8–1.0%/°C, which exceed that of neat CNW films at 0.56%/°C, thus leading to lower weight residues at the finish temperature of 800°C.

The relatively low W_{rmax} identified in neat CNW films is associated with their higher char yield in this case (Piskorz et al., 1989). Such results have good agreement with the TGA measurements accordingly. Overall, typical thermal parameters determined in this study are listed in **Table 2**. The existence of sulfate on side chains seems to greatly affect thermal behaviors of CNWs, as evidenced by Ma et al. (2017) suggesting that CNWs under sulfation treatment had T_m and T_{id} values increased by more than 46 and 48°C, respectively.

There is a significant increase in thermal parameters of CNW/GN composites at very low GN contents of 0.1, 0.25, and 0.5 wt%, arising from strong interactions between GN fillers and CNW matrices, which is supported by other studies on 2D materials such as boron nitride (BN) and graphene nanosheets (Li Y. et al., 2015). Under the SEM observation displayed in **Figure 4**, one can clearly see the absorption of CNWs on GN sheets in CNW/GN composites at the GN content of 0.5 wt%. Since cellulose is an amphiphilic polymer, the presence of polar group –OH enables to induce the hydrophilicity while the exposure of –CH moieties gives rise to its hydrophobicity instead. As such, CNWs may interact closely with GNs with dual hydrophobic-hydrophobic effect (Li F. et al., 2015). It has also been suggested that the bonding between CNTs and carboxymethyl cellulose could be due to the π-π interactions (Son and Park, 2018).

TABLE 2 | Thermal parameters, tensile strain at break (ε), tensile strength (σₜ), and electrical conductivity (σ) of CNW films and CNW/GN composite films.

GN (wt%)	T_m (°C)	T_{id} (°C)	ε (%)	σ_t (MPa)	σ (S/m)
0	209.6	143.3	1.4	96.8	–
0.1	232.8	213.5	1.1	105.1	2.5×10^{-8}
0.25	238.9	231.7	1.0	129.4	1.7×10^{-7}
0.5	235.9	231.1	0.8	98.2	4.0×10^{-5}

Electrical Conductivity and Tensile Properties

Transparent and flexible CNW films show low thermal expansion coefficient, which makes them potentially used as packaging films or as substrates for flexible electronics (Yamakawa et al., 2017). The addition of GNs into CNW films increases the electrical conductivity and tensile strength, as shown in **Figure 5**. Neat CNW films as insulating materials undergoes measurement difficulty in electrical conductivity using our equipment, thus its value has not been reported in this study. The electrical conductivity of TEMPO-oxidized cellulose nanofibril (TOCN) reported by Zhan et al. (2019) was 4.8×10^{-12} S/m, indicating typical insulating nature of cellulose films. However, electrical conductivity has been found to increase in range from 2.5×10^{-8} to 4.0×10^{-5} S/m with increasing the GN content from 0.1 to 0.5 wt% shown in **Figure 5A**, which is satisfied with the requirement of anti-static property (Steinert and Dean, 2009). Anti-static property is generally characterized by conductive material surfaces to reduce the static charge induced by internal insulating structures of materials. Our results are close to that of bacterial cellulose (BC)/reduced graphene oxide (RGO) composites at the electrical conductivity level of approximately 1.1×10^{-4} S/m when the RGO content reaches 1.0 wt%, which is two-order higher than that of cellulose nanofiber/1.0 wt% MWCNT composite membranes at 10^{-6} S/m (Feng et al., 2012; Zhang et al., 2019). Luong et al. (2011) reported an even higher conductivity value of 4.8×10^{-4} S/m for amine-modified nanofibrillated cellulose/0.3 wt% RGO nanocomposite papers. All these results reveal the effective improvement in electrical conductivities of cellulose nanocomposites.

Tensile strengths of composite films are enhanced up to 105.1 and 129.4 MPa at the low GN contents of 0.1 and 0.25 wt%, respectively when compared with 96.8 MPa for neat CNW films, as depicted in **Figure 5B**. Conversely, tensile strength of composites declines to 98.2 MPa when incorporated with 0.5 wt% GNs as a result of the inhomogeneity of GN dispersion and typical GN aggregation at relatively high filler content levels. The tensile strain at break for CNW films was determined to be very low at 1.4. With increasing the GN content up to 0.5 wt%, the corresponding strains for their composites could be reduced modestly to 0.8% in a monotonic manner due to their more brittle nature with the inclusion of GNs as rigid fillers. The relevant data with respect to tensile strength, tensile strain at break and electrical conductivity of composite films are also summarized in **Table 2**. The reinforcing effect of GO and RGO can be more manifested owing to their abundant functional groups (Phiri et al., 2018). Very high tensile strength
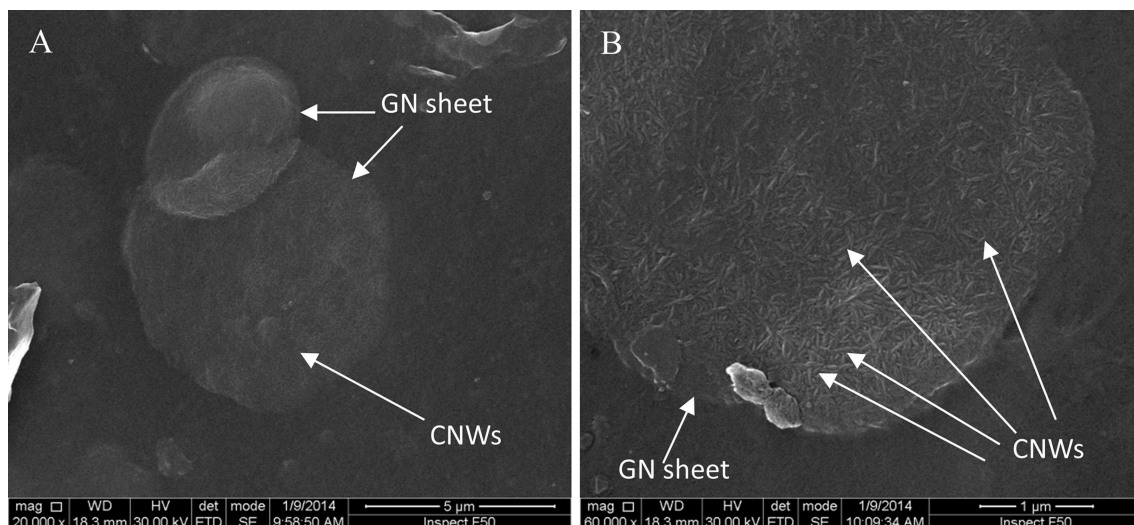
FIGURE 4 | SEM images of CNW adsorption on GN sheets in CNW/GN composite films at the GN content of 0.5 wt%: **(A)** at low magnification of 20,000× and **(B)** at high magnification of 60,000×.

FIGURE 5 | Effect of GN content on **(A)** electrical conductivity and **(B)** tensile strength and tensile strain at break of CNW/GN composite films.

FIGURE 6 | Structural analysis of CNW films and CNW/GN composite films: **(A)** XRD patterns and **(B)** Raman spectra.

of nanofibrillated cellulose (NFC)/1.25 wt% graphene composites was obtained at 351 MPa by means of *in-situ* exfoliation of graphite into graphene sheets in the NFC solutions via the filtration methods (Malho et al., 2012).
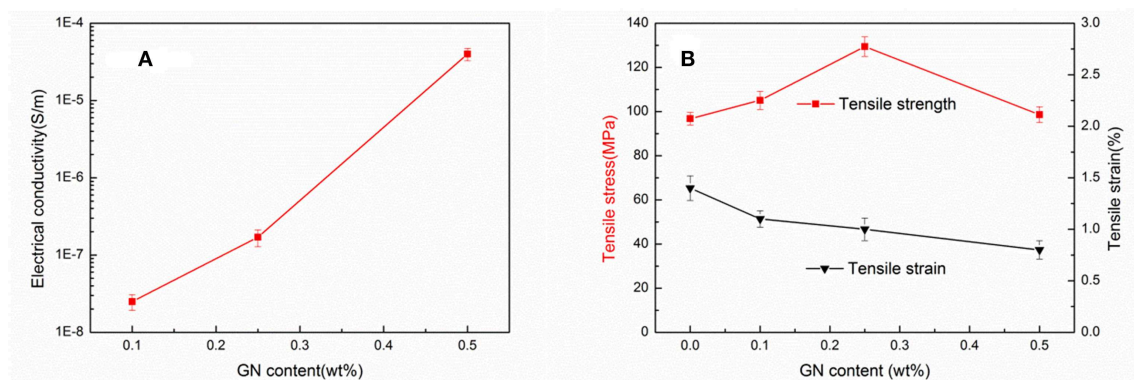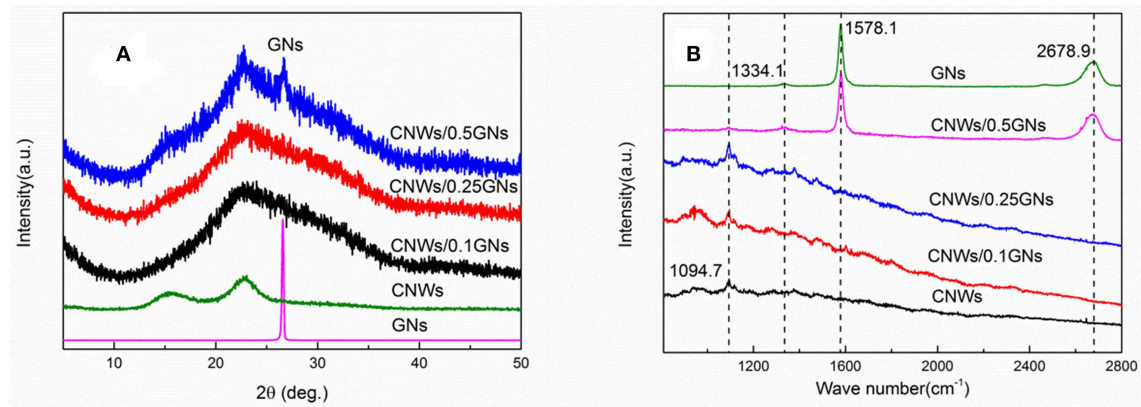
Structural Analysis

The crystalline structures of CNW films and CNW/GN composite films are characterized by XRD and Raman spectroscopy, as illustrated in **Figure 6**. High crystalline characteristic of CNWs is evident since their amorphous components are broken down by concentration acid during the hydrolysis process. The characteristic diffraction peaks of composite films positioned at approximately 22.6° corresponding to the reflection of crystal plane (200), are quite broad due to smaller crystalline sizes of CNWs. There is no obvious diffraction of graphene seen in **Figure 6A** in CNW/GN composite films at GN contents of 0.1 and 0.25 wt%, which is believed to be associated with a small amount of uniformly dispersed GNs embedded in CNW matrices (Son and Park, 2018). A tiny peak positioned at 26.8° can be observed on the XRD pattern of CNW/GN composites at the GN content of 0.5 wt%, corresponding to an interlayer distance of 0.34 nm in relation to crystal plane (002). This shows a clear sign of GN aggregation in CNW matrices in good accordance with morphological structures observed earlier. With respect to Raman spectra, the characteristic peak of cellulose is located at 1,095 cm^{-1}, which is consistent with Bulota et al. (2012). The characteristic peaks of GNs can be easily detected in Raman spectra with mainly three bands, namely G band at 1,578 cm^{-1}, D band at 1,334 cm^{-1} and 2D band at 2,679 cm^{-1}, as shown in **Figure 6B**. The vibration of sp^2 carbon atoms yields the appearance of G band as the primary characteristic band of graphene. The disordered vibrational peak of graphene is generally considered as the existence of D band, which is used for characterizing structural defects in graphene samples with rather low intensity in the spectra of GNs. It is clearly indicated that GNs are less defective in this study. Similar to the XRD results, typical GN peak is also not visible until the GN content reaches 0.5 wt% again due to the inclusion of very small amounts of GNs between 0.1 and 0.25 wt%.

CONCLUSIONS

CNW/GN composite films at the small GN contents of 0.1, 0.25, and 0.5 wt% were successfully prepared using solution casting, resulting in their high transparency, enhanced thermal, electrical and mechanical properties. Uniform GN dispersion in CNW matrices in composite films has been found at lower GN contents of 0.1 and 0.25 wt% as opposed to typical GN aggregation at the higher content level of 0.5 wt% along with the resulting decreased tensile strength of composites. The former case leads to the enhancement of tensile strengths of composite films from 96.8 to 129.4 MPa when increasing the GN content from 0 to 0.25 wt% owing to uniform GN dispersion mentioned earlier. GNs as rigid fillers can strongly restrict the molecular chain mobility of CNWs, thus improving the thermal properties of CNW/GN composite films, as evidenced by significantly enhanced T_m and T_{id}. More remarkably, electrical conductivities of composite films are increased by three orders with increasing the GN content from 0.1 to 0.5 wt%. In particular, at the GN content of 0.5 wt%, their electrical conductivity reaches 4.0×10^{-5} S/m with unique anti-static property. Such CNW/GN composite films with good transparency, high mechanical strength and flexibility, excellent thermal and electrical properties can be promising multifunctional materials when particularly targeting electronic applications.

DATA AVAILABILITY STATEMENT

All datasets generated for this study are included in the manuscript/supplementary files.

AUTHOR CONTRIBUTIONS

DL designed the experiments and prepared the manuscript. YL prepared the material samples and conducted XRD and Raman analyses. NM performed thermal analyses (i.e., DSC and TGA) and mechanical tests. DL did structural analysis and electrical conductivity measurements. YD and GS contributed to result discussion and manuscript revision.

REFERENCES

Agate, S., Joyce, M., Lucia, L., and Pal, L. (2018). Cellulose and nanocellulose-based flexible-hybrid printed electronics and conductive composites – a review. *Carbohydr. Polym.* 198, 249–260. doi: 10.1016/j.carbpol.2018.06.045

Bulota, M., Kreitsmann, K., Hughes, M., and Paltakari, J. (2012). Acetylated microfibrillated cellulose as a toughening agent in poly(lactic acid). *J. Appl. Polym. Sci.* 126, E449–E458. doi: 10.1002/app.36787

Carpenter, A. W., de Lannoy, C. F., and Wiesner, M. R. (2015). Cellulose nanomaterials in water treatment technologies. *Environ. Sci. Technol.* 49, 5277–5287. doi: 10.1021/es506351r

Dichiara, A. B., Song, A., Goodman, S. M., He, D., and Bai, J. (2017). Smart papers comprising carbon nanotubes and cellulose microfibers for multifunctional sensing applications. *J. Mater. Chem. A* 5, 20161–20169. doi: 10.1039/C7TA04329E

Drogat, N., Granet, R., Sol, V., Memmi, A., Saad, N., Koerkamp, C. K., et al. (2011). Antimicrobial silver nanoparticles generated on cellulose nanocrystals. *J. Nanopart. Res.* 13, 1557–1562. doi: 10.1007/s11051-010-9995-1

Du, X., Zhang, Z., Liu, W., and Deng, Y. (2017). Nanocellulose-based conductive materials and their emerging applications in energy devices - a review. *Nano Energy* 35, 299–320. doi: 10.1016/j.nanoen.2017.04.001

Esmaeili, C., Abdi, M. M., Mathew, A. P., Jonoobi, M., Oksman, K., and Rezayi, M. (2015). Synergy effect of nanocrystalline cellulose for the biosensing detection of glucose. *Sensors* 15, 24681–24697. doi: 10.3390/s151024681

Feng, Y., Zhang, X., Shen, Y., Yoshino, K., and Feng, W. (2012). A mechanically strong, flexible and conductive film based on bacterial cellulose/graphene nanocomposite. *Carbohydr. Polym.* 87, 644–649. doi: 10.1016/j.carbpol.2011.08.039

Gnanaseelan, M., Chen, Y., Luo, J., Krause, B., Pionteck, J., Pötschke, P., et al. (2018). Cellulose-carbon nanotube composite aerogels as novel thermoelectric materials. *Compos. Sci. Technol.* 163, 133–140. doi: 10.1016/j.compscitech.2018.04.026

He, J., Li, N., Bian, K., and Piao, G. (2019). Optically active polyaniline film based on cellulose nanocrystals. *Carbohydr. Polym.* 208, 398–403. doi: 10.1016/j.carbpol.2018.12.091

Jackson, J. K., Letchford, K., Wasserman, B. Z., Ye, L., Hamad, W. Y, and Burt, H. M. (2011). The use of nanocrystalline cellulose for the binding and controlled release of drugs. *Int. J. Nanomed.* 6, 321–330. doi: 10.2147/IJN.S16749

Jiang, Y., Song, Y., Miao, M., Cao, S., Xin, F. X., Fang, J. H., et al. (2015). Transparent nanocellulose hybrid films functionalized with ZnO nanostructures for UV-blocking. *J. Mater. Chem. C* 3, 6717–6724. doi: 10.1039/C5TC00812C

Jose, J., Thomas, V., Vinod, V., Abraham, R., and Abraham, S. (2019). Nanocellulose based functional materials for supercapacitor applications. *J. Sci. Adv. Mater. Dev.* doi: 10.1016/j.jsamd.2019.06.003. [Epub ahead of print].

Karim, Z., Claudpierre, S., Grahn, M., Oksman, K., and Mathew, A. P. (2016). Nanocellulose based functional membranes for water cleaning: tailoring of mechanical properties, porosity and metal ion capture. *J. Membr. Sci.* 514,418–428. doi: 10.1016/j.memsci.2016.05.018

Ko, J. O., Kima, S. K., Lim, Y. R., Han, J. K., Yoon, Y., Ji, S., et al. (2019). Foldable and water-resist electrodes based on carbon nanotubes/methyl cellulose hybrid conducting papers. *Compos. Part B Eng.* 160, 512–518. doi: 10.1016/j.compositesb.2018.12.060

Latonen, R. M., Määttänen, A., Ihalainen, P., Xu, W., Pesonen, M., Nurmie, M., et al. (2017). Conducting ink based on cellulose nanocrystals and polyaniline for flexographical printing. *J. Mater. Chem. C* 5, 12172–12181. doi: 10.1039/C7TC03729E

Li, F., Mascheroni, E., and Piergiovanni, L. (2015). The potential of nanocellulose in the packaging field: a review. *Packaging Technol. Sci.* 28, 475–508. doi: 10.1002/pts.2121

Li, S., and Lee, P. S. (2017). Development and applications of transparent conductive nanocellulose paper. *Sci. Technol. Adv. Mater.* 18, 620–633. doi: 10.1080/14686996.2017.1364976

Li, Y., Zhu, H., Shen, F., Wan, J., and Hu, L. (2015). Nanocellulose as green dispersant for two-dimensional energy materials. *Nano Energy* 13, 346–354. doi: 10.1016/j.nanoen.2015.02.015

Liew, S. Y., Walsh, D. A., and Thielemans, W. (2013). High total-electrode and mass-specific capacitance cellulose nanocrystal-polypyrrole nanocomposites for supercapacitors. *RSC Adv.* 3, 9158–9162. doi: 10.1039/c3ra41168k

Liu, D. Y., Yuan, X. W., Bhattacharyya, D., and Easteal, A. J. (2010). Characterisation of solution cast cellulose nanofibre – reinforced poly(lactic acid). *eXPRESS. Polym. Lett.* 4, 26–31. doi: 10.3144/expresspolymlett.2010.5

Luo, H., Xie, J., Xiong, L., Zhu, Y., Yang, Z., and Wan, Y. (2019). Fabrication of flexible, ultra-strong, and highly conductive bacterial cellulose-based paper by engineering dispersion of graphene nanosheets. *Compos. Part B Eng.* 162, 484–490. doi: 10.1016/j.compositesb.2019.01.027

Luong, N. D., Pahimanolis, N., Hippa, U., Korhonen, J. T., Ruokolainen, J., Johansson, L. S., et al. (2011). Graphene/cellulose nanocomposite paper with high electrical and mechanical performances. *J. Mater. Chem.* 21, 13991–13998. doi: 10.1039/c1jm12134k

Ma, Y. L., Liu, D. Y., Zhang, X. T., and Sui, G. X. (2017). De-sulfation of cellulose nanowhiskers and its effects on the dispersion behavior of graphene. *J. Dispersion Sci. Technol.* 38, 1798–1803. doi: 10.1080/01932691.2017.1283512

Mahadeva, S. K., Yun, S., and Kim, J. (2011). Flexible humidity and temperature sensor based on cellulose–polypyrrole nanocomposite. *Sens. Actuat. A Phys.* 165, 194–199. doi: 10.1016/j.sna.2010.10.018

Malho, J. M., Laaksonen, P., Walther, A., Ikkala, O., and Linder, M. B. (2012). Facile method for stiff, tough, and strong nanocomposites by direct exfoliation of multilayered graphene into native nanocellulose matrix. *Biomacromolecules* 13, 1093–1099. doi: 10.1021/bm2018189

Meulendijks, N., Burghoorn, M., van Ee, R., Mourad, M., Mann, D., Keul, H., et al. (2017). Electrically conductive coatings consisting of Ag-decorated cellulose nanocrystals. *Cellulose* 24, 2191–2204. doi: 10.1007/s10570-017-1240-y

Moon, R. J., Martini, A., and Simonsen, J., Youngblood J. (2011). Cellulose nanomaterials review: structure, properties and nanocomposites. *Chem. Soc. Rev.* 40, 3941–3994. doi: 10.1039/c0cs00108b

Okahisa, Y., Fukuwawa, Y., Ishimoto, K., Narita, C., Intharapichai, K., and Ohara, H. (2018). Comparison of cellulose nanofiber properties produced from different parts of the oil palm tree. *Carbohydr. Polym.* 198, 313–319. doi: 10.1016/j.carbpol.2018.06.089

O'Neil, A., Bakirtzis, D., and Dixon, D. (2014). Polyamide 6/graphene composites: the effect of *in situ* polymerisation on the structure and properties of graphene oxide and reduced graphene oxide. *Eur. Polym. J.* 59, 353–362. doi: 10.1016/j.eurpolymj.2014.07.038

Pang, Z., Sun, X., Wu, X., Nie, Y., Liu, Z., and Yue, L. (2015). Fabrication and application of carbon nanotubes/cellulose composite paper. *Vacuum* 122, 135–142. doi: 10.1016/j.vacuum.2015.09.020

Phiri, J., Johansson, L. S., Gane, P., and Malone, T. (2018). A comparative study of mechanical, thermal and electrical properties of graphene-, graphene oxide- and reduced graphene oxide-doped microfibrillated cellulose nanocomposites. *Compos. Part B Eng.* 147, 104–113. doi: 10.1016/j.compositesb.2018.04.018

Piskorz, J., Radlein, D. S. A., Scott, D. S., and Czernik, S. (1989). Pretreatment of wood and cellulose for production of sugars by fast pyrolysis. *J. Anal. Appl. Pyrol.* 16, 127–142. doi: 10.1016/0165-2370(89)85012-0

Roman, M., and Winter, W. T. (2004). Effect of sulfate groups from sulfuric acid hydrolysis on the thermal degradation behavior of bacterial cellulose. *Biomacromolecules* 5, 1671–1677. doi: 10.1021/bm034519+

Sadasivuni, K. K., Ponnamma, D., Ko, H. U., Kim, H. C., Zhai, L., and Kim, J. (2016). Flexible NO_2 sensors from renewable cellulose nanocrystals/iron oxide composites. *Sens. Actuat. B Chem.* 233, 633–638. doi: 10.1016/j.snb.2016.04.134

Shimizu, M., Kusumi, R., Saito, T., and Isogai, A. (2019). Thermal and electrical properties of nanocellulose films with different interfibrillar structures of alkyl ammonium carboxylates. *Cellulose* 26, 1657–1665. doi: 10.1007/s10570-018-2155-y

Sofla, M. R. K., Brown, R. J., Tsuzuki, T., and Rainey, T J. (2016). A comparison of cellulose nanocrystals and cellulose nanofibres extracted from bagasse using acid and ball milling methods. *Adv. Nat. Sci. Nanosci. Nanotechnol.* 7:035004. doi: 10.1088/2043-6262/7/3/035004

Son, Y. R., and Park, S. J. (2018). Green preparation and characterization of graphene oxide/carbon nanotubes-loaded carboxymethyl cellulose nanocomposites. *Sci. Rep.* 8:17601. doi: 10.1038/s41598-018-35984-2

Staggs, J. E. J. (2006). Discrete bond-weighted random scission of linear polymers. *Polymer* 47, 897–906. doi: 10.1016/j.polymer.2005.11.085

Steinert, B. W., and Dean, D. R. (2009). Magnetic field alignment and electrical properties of solution cast PET–carbon nanotube composite films. *Polymer* 50, 898–904. doi: 10.1016/j.polymer.2008.11.053

Trache, D., Donnt, A., Khimeche, K., Benelmir, R., and Brosee, N. (2014). Physico-chemical properties and thermal stability of microcrystalline cellulose isolated from Alfa fibres. *Carbohydr. Polym.* 104, 223–230. doi: 10.1016/j.carbpol.2014.01.058

Xing, J., Tao, P., Wu, Z., Xing, C., Liao, X., and Nie, S. (2019). Nanocellulose-graphene composites: a promising nanomaterial for flexible supercapacitors. *Carbohydr. Polym.* 207, 447–459. doi: 10.1016/j.carbpol.2018.12.010

Yamakawa, A., Suzuki, S., Oku, T., Enomoto, K., Ikeda, M., Rodrigue, J., et al. (2017). Nanostructure and physical properties of cellulose nanofiber-carbon nanotube composite films. *Carbohydr. Polym.* 171, 129–135. doi: 10.1016/j.carbpol.2017.05.012

Yuan, Z., Zhang, J., Jiang, A., Lv, W., Wang, Y., Geng, H., et al. (2015). Fabrication of cellulose self-assemblies and high-strength ordered cellulose films. *Carbohydr. Polym.* 117, 414–421. doi: 10.1016/j.carbpol.2014.10.003

Zhan, H., Peng, N., Lei, X., Huang, Y., Li, D., Tao, R. (2018). UV-induced self-cleanable TiO_2/nanocellulose membrane for selective separation of oil/water emulsion. *Carbohydr. Polym.* 201, 464–470. doi: 10.1016/j.carbpol.2018.08.093

Zhan, Y., Xiong, C., Yang, J., Shi, Z., and Yang, Q. (2019). Flexible cellulose nanofibril/pristine graphene nanocomposite films with high electrical conductivity. *Compos. Part A Appl. Sci. Manuf.* 119, 119–126. doi: 10.1016/j.compositesa.2019.01.029

Zhang, H., Sun, X., Hubbe, M. A., Pal, L. (2019). Highly conductive carbon nanotubes and flexible cellulose nanofibers composite membranes with semi-interpenetrating networks structure. *Carbohydr. Polym.* 222:115013. doi: 10.1016/j.carbpol.2019.115013

Zhang, X. T., Liu, D. Y., Ma, Y. L., Nie, J., and Sui, G. X. (2017). Super-hydrophobic graphene coated polyurethane (GN@PU) sponge with great oil-water separation performance. *Appl. Surf. Sci.* 422, 116–124. doi: 10.1016/j.apsusc.2017.06.009

Zhang, X. T., Liu, D. Y., and Sui, G. X. (2018). Superamphiphilic polyurethane foams synergized from cellulose ers and graphene nanoplatelets. *Adv. Mater. Interf.* 5:1701094. doi: 10.1002/admi.2017 01094

Zhu, S. E., Yuan, S., and Janssen, G. C. A. M. (2014). Optical transmittance of multilayer graphene. *Europhys. Lett.* 108:17007. doi: 10.1209/0295-5075/108/17007

Insight Into the Current Directions in Functionalized Nanocomposite Hydrogels

Rasoul Esmaeely Neisiany [1*], Mohammad Saeid Enayati [2*], Paweł Sajkiewicz [2], Zari Pahlevanneshan [3] and Seeram Ramakrishna [4]

[1] Department of Materials and Polymer Engineering, Faculty of Engineering, Hakim Sabzevari University, Sabzevar, Iran, [2] Institute of Fundamental Technological Research, Polish Academy of Sciences, Warsaw, Poland, [3] Department of Biomaterials and Tissue Engineering, School of Advanced Technology in Medicine, Isfahan University of Medical Sciences, Isfahan, Iran, [4] Centre for Nanofibers and Nanotechnology, Department of Mechanical Engineering, National University of Singapore, Singapore, Singapore

Since the introduction of tissue engineering as an encouraging method for the repair and regeneration of injured tissue, there have been many attempts by researchers to construct bio-mimetic scaffolds which mimic the native extracellular matrix, with the aim of promoting cell growth, cell proliferation, and restoration of the tissue's native functionality. Among the different materials and methods of scaffold fabrication, one particularly promising class of materials, hydrogels, has been extensively studied, with the inclusion of nano-scaled materials into hydrogels leading to the creation of an exciting new generation of nanocomposites, known as nanocomposite hydrogels. To closely mimic the native tissue behavior, scientists have recently focused on the functionalization of incorporated nanomaterials via chiral biomolecules, with reported results showing great potential. The current article aims to introduce a perspective of nano-scaled cellulose as a promising nanomaterial which can be multi-functionalized for the fabrication of nanocomposite hydrogels with applications in tissue engineering and drug delivery systems. This article also briefly reviews the recently reported literature on nanocomposite hydrogels incorporated with chiral functionalized nanomaterials. Such knowledge paves the path for the development of tailored hydrogels toward practical applications.

Keywords: scaffold, nanocomposite hydrogels, biodegradable hydrogels, chiral biomolecules, self-healing

INTRODUCTION

Tissue engineering using polymeric biomaterials has emerged as a promising and novel medical alternative to current transplantation therapies in the treatment of various diseases (Nezhad-Mokhtari et al., 2019). Transplantation poses several shortcomings such as the risk of immune rejection, infection, stress shielding, limitation in availability of proper tissues, long-lasting, and high-cost surgeries, disease-transmitting possibility, contaminations by bacteria, and incompatibility. The aforementioned limitations can potentially be overcome with tissue engineering techniques, with recent advances showing its great potential for repairing and regeneration of injured tissues (Xu et al., 2015).

At its core, tissue engineering is an approach involving the design of tissue constructs with the capability of mimicking native tissue *in vitro*. These constructs are subsequently implanted *in vivo*

to regenerate damaged tissue functionality and to help millions of people who suffer from diseases, or impaired organs (Kock et al., 2012). This method combines scaffolds, cells, and growth factors in which the cells are cultured on the scaffold and grown. Subsequently, this tissue construct is implanted at the site of injury without the need for multiple surgeries, thereby reducing the costs, risks, and recovery time associated with conventional treatments (Mohammadzadehmoghadam and Dong, 2019). In general, extracellular matrix (ECM) as a hierarchical hybrid nanostructure, plays a pivotal role in cellular activities such as cell promotion and regulating the conditions under which cells can grow, migrate, proliferate, differentiate, and communicate with each other (Zagris, 2001). The adhesion of cells to the ECM is controlled by specific sites on glycoproteins including fibronectin, laminin, and collagen (Gullberg and Ekblom, 1995). Nanocomposite (NC) hydrogels incorporating functionalized nanomaterials (NMs) are therefore of tremendous research interest precisely because they can mimic and simulate the organization and characteristics of native ECM, such as having a nanoporous morphology and functionality for cellular activities (Schexnailder and Schmidt, 2009).

TAILORED HYDROGELS FOR TISSUE ENGINEERING

Understanding tissue organization from the molecular to the macroscopic level helps in the process of designing scaffolds (Zhang et al., 2005). Among the diverse techniques for producing tissue engineering scaffolds, the design and fabrication of hydrogels have shown attractive features and gained popularity among researchers. Hydrogels, with a three-dimensional (3D) structure, present the capability to absorb and retain large amounts of water molecules (Bakaic et al., 2015). Hydrogels can also be injected directly into the site of injury, circumventing the need for complex surgeries. There is also a further benefit of seamlessly integrating the engineered implant into the existing tissue, thereby preventing stress shielding and damaging the healthy surrounding tissue (Hu et al., 2019).
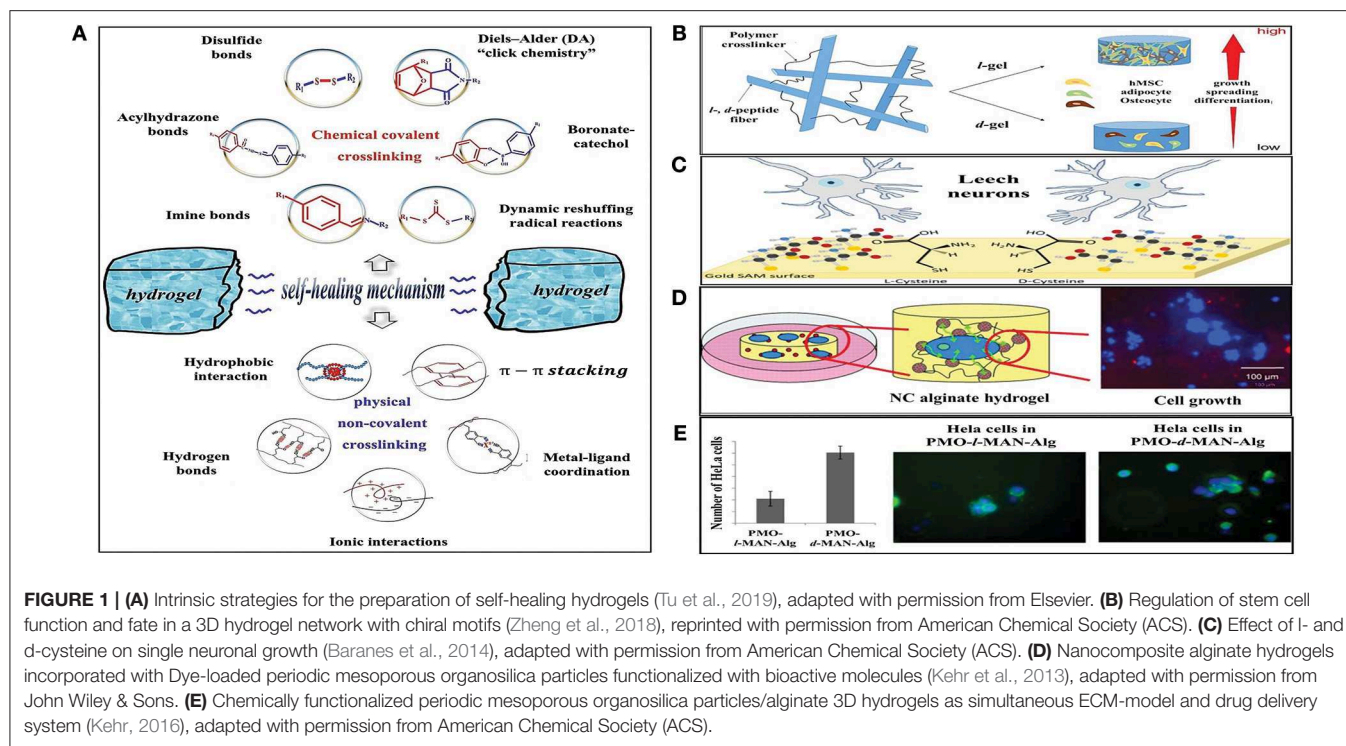
The essential requirements for tissue engineering scaffolds are biocompatibility, biodegradability, having an interconnected porous structure, adequate mechanical properties, and appropriate surface chemistry. Since hydrogels have the potential to maintain a large water content, they are highly biocompatible (Thürmer et al., 2014). In addition, due to the hydrogel's inherent flexible and soft structure, they cause minimal harm when exposed to body tissue. Furthermore, their highly permeable nature makes hydrogels an ideal scaffold to provide the required nutrient permeability to sustain cell growth. Such features make hydrogels an exceptional choice for bio-therapeutic applications.

The hydrogel degradation within the body can proceed via hydrolytical or enzymatical mechanisms in which the erosion of the scaffold occurs in bulk or at the surface of the hydrogel (Curvello et al., 2019). Bulk erosion is the predominant mechanism of hydrogel biodegradation which is attributable to the permeability and large water content present

in hydrogels. The erosion type and degradation rate depend on the *in vivo* hydrogel characteristics and can be tuned for different applications. In general, the best *in vivo* performance of hydrogels can be achieved through optimizing the degradation rate via control over the polymer characteristics such as surface properties and degree of cross-linking (Tan and Marra, 2010; Bae et al., 2013; Tanan et al., 2019).

Although the biodegradability of the employed hydrogel for tissue engineering is a significant parameter, the scaffold's mechanical durability is considered the critical characteristic of scaffold materials with the target of long-term applications. The integrity of the implanted hydrogels may deteriorate when they are subjected to constant load due to wearing effects from repetitive body movements, leading to a reduction in their performance and a higher risk of infection. The created cavities or cracks provide locations for the intrusion of the bacteria and microorganisms, leading to acceleration in the scaffold failure It should be noted that a wide range of mechanical properties could be tailored through the changes in the concentration of the constituents, composition, and cross-linking density of the 3D network; however, manipulation of these could compromise the particular composition or chemistry of the hydrogels and reduce its targeted therapeutic effect. It follows then that these approaches have also shown some pitfalls, especially considering the difficulty in manipulating the mechanical properties *in vivo*, which also does not guarantee stable mechanical properties during the implant's lifetime. The missing link that could allow NC hydrogels approach to reach functional integrity could, therefore, lie in the preparation of the hydrogels with self-healing ability (Wang et al., 2018). Similar to other self-healing polymers, the self-healing hydrogels were developed based on two strategies—intrinsic and extrinsic, where the former has garnered more attention. The extrinsic strategy is applied by incorporation of the modified nanoparticles (Rao et al., 2019) and nanocellulose (Bai et al., 2019) or via the release of healing agents from ruptured micro/nanoscale capsules and fibers (Fang et al., 2013). The intrinsic self-healing ability of hydrogels is mostly induced through the physical non-covalent interactions and reversible chemical covalent bonds. The physical non-covalent interactions could include hydrogen bonding, metal-ligand coordination, hydrophobic interaction, and π-π stacking. This is in contrast with reversible chemical covalent bonds which provide hydrogels with the self-healing properties via Diel-Alder (DA) "click chemistry," imine bonds, boronate-catechol complexation, and other dynamic reshuffling radical reactions (Hao et al., 2019; Jing et al., 2019; Tu et al., 2019). **Figure 1A** schematically illustrates the strategies for the preparation of self-healing hydrogels using intrinsic approaches (Tu et al., 2019).

Some advantageous features such as 3D porous structure, biocompatibility, and hydrophilicity, make hydrogels a suitable analog of natural tissue. However, due to their mechanical weakness upon dehydration, they possess only limited potential in bioapplications (Billiet et al., 2012). This shortcoming has been successfully addressed by developing NC hydrogels (Sanka et al., 2019) where certain organic/inorganic NMs are used to physically/chemically cross-link a water-soluble polymer and serve to enhance the mechanical strength of the

FIGURE 1 | (A) Intrinsic strategies for the preparation of self-healing hydrogels (Tu et al., 2019), adapted with permission from Elsevier. **(B)** Regulation of stem cell function and fate in a 3D hydrogel network with chiral motifs (Zheng et al., 2018), reprinted with permission from American Chemical Society (ACS). **(C)** Effect of l- and d-cysteine on single neuronal growth (Baranes et al., 2014), adapted with permission from American Chemical Society (ACS). **(D)** Nanocomposite alginate hydrogels incorporated with Dye-loaded periodic mesoporous organosilica particles functionalized with bioactive molecules (Kehr et al., 2013), adapted with permission from John Wiley & Sons. **(E)** Chemically functionalized periodic mesoporous organosilica particles/alginate 3D hydrogels as simultaneous ECM-model and drug delivery system (Kehr, 2016), adapted with permission from American Chemical Society (ACS).

polymeric matrix. In addition, inorganic NMs can boost the optical, magnetic, or biological properties of the 3D hybrid hydrogel (Gaharwar et al., 2014). The right selection, proper functionalization, and careful design of polymer/nanomaterial play crucial roles in developing a novel and advanced NC hydrogel for tissue engineering applications. From another perspective, due to the large surface area, NMs can effectively increase biological functionality, hence NC hydrogels have been shown to more closely mimic native tissues compared with free-NM hydrogels (Kehr et al., 2015). In the case of some specific applications, e.g., regeneration of the central nervous system, the addition of nanofibers to a hydrogel matrix can be morphologically beneficial because the elongated shape of the scaffold is favored by neural cells (Niemczyk et al., 2018).

NC HYDROGELS

NC hydrogels have been categorized based on their stimulus-sensitivity which includes thermo-responsive, light-responsive, electro-responsive, and magnetic-responsive hydrogels. In addition, they have been classified based on their applications, such as in sensors, catalysts, drug delivery systems, wound dressings, and tissue engineering (Song et al., 2015; Vashist et al., 2018). They are also classified according to the type of incorporated nanomaterials, which is the more common type of classification (Sharma et al., 2018; Vashist et al., 2018; Rafieian et al., 2019). Frequently reported nanofillers in NC hydrogels are silica such as nano-clay (Jin et al., 2018) and fumed silica (Kehr et al., 2013), carbon in the form of carbon nanotubes,

graphene (Servant et al., 2014) and graphene oxide (GO) (Rasoulzadeh and Namazi, 2017; Tarashi et al., 2019), metal and metal oxide nanoparticles (Tan et al., 2019) such as gold, silver, iron oxide, titanium oxide (TiO_2), nanohydroxyapatite, alumina and zirconia, and polymeric nanoparticles such as nano-scaled cellulose (NSC) (Dutta et al., 2019), including cellulose nanofibers, nanocrystals, and nanowhiskers. In general, depending on the surface chemistry of the nanomaterials, they can act as physical or chemical crosslinkers in NC hydrogels. Nanoparticles such as carbon, silica, and NSC, owing to the presence of hydroxyl groups on their surfaces, possess active surfaces for physical crosslinking such as hydrogen bonding. They could also serve as chemical crosslinkers in polymeric hydrogels containing reactive functional groups on their backbone, which would either require reaction initiators or coupling agents such as silanes. Some NMs without active surface chemistry, such as metals and metal oxides, need surface treatment or modification to act as a crosslinker within the NC hydrogel. In the following section, some recent advances on NC hydrogels are reviewed.

As a bone tissue engineering platform, injectable NC hydrogels from methacrylated glycol chitosan-montmorillonite were studied by Cui et al. (2019). In this work, the direct stem cell differentiation in a 3D micro-porous structure was addressed. The photocrosslinked chitosan/silicates NC hydrogels showed a six-fold Young's modulus increase. In addition, *in vitro* mesenchymal stem cell studies proved the NC hydrogel's efficacy in cell proliferation, promotion, and differentiation induction (Cui et al., 2019). In one contribution, Rasoulzadeh and Namazi developed bio-NC hydrogels based on carboxymethyl

cellulose and GO with anticancer drug delivery potential (Rasoulzadeh and Namazi, 2017). The physically crosslinked (with $FeCl_3.6H_2O$) NC hydrogels were loaded with Doxorubicin as the anticancer drug to be delivered. In comparison with the neat carboxymethyl cellulose hydrogel, the incorporation of GO led to NC hydrogels with enhanced loading capacity and a lasting release of the loaded therapeutic drug. Most recently, the stimuli-responsive load-bearing double network NC hydrogels, based on κ-carrageenan (κ-Car)/polyacrylamide (PAm) crosslinked and reinforced with GO nanosheets, were fabricated (Tarashi et al., 2019). Compared to the non-loaded GO hydrogel, at 3 wt. % of GO nanosheets, optimum mechanical properties i.e., 21.7 MPa compression strength, 0.64 MPa ultimate tensile strength, 2,398% elongation at break, and 5.7 MJ/m^3 fracture energy were obtained. These improvements, as well as the self-healing performance of NC hydrogels, were attributed to the synergistic influence of the reversible interactions due to bonding of the GO nanosheets between the κ-Car and PAm networks. In a novel and interesting piece of research, Toledo et al. explored the additional effect of low contents (<1.0 wt.%) of both non-functionalized, and functionalized TiO_2 nanoparticles into poly (2-hydroxyethylmethacrylate) based physical NC hydrogels (Toledo et al., 2018). While pristine TiO_2 resulted in higher swelling capacity and greater solvent diffusion coefficient, functionalized TiO_2-filled NC hydrogels behaved contrarily. In addition, functionalized NC hydrogels exhibited improved ability in retaining aggregates of skeletal muscle cells (C2C12). Hydroxyapatite nanorods were also employed in the fabrication of chitosan NC hydrogels as potential scaffolds in cartilage regeneration (Kumar et al., 2019). In this contribution, Kumar et al. reported essential improvement in the mechanical properties of developed NC hydrogels at the optimum level (1.5 wt.%) of nanohydroxyapatite. Antimicrobial tests against three different microbes (*Escherichia coli*, *Staphylococcus aureus* bacteria, and *Candida albicans* fungi) demonstrated significant enhancement in the antimicrobial activity of the NC hydrogel. L929 fibroblast cell cultures (after 72 h) also confirmed 90% cell viability. In another novel work, Lee et al. (2018) investigated the application of functionalized gold nanoparticles (GNPs) in developing NC hydrogels for bone tissue engineering. The GNPs were modified with N-acetyl cysteine (G-NAC) and then incorporated into tryamine-gelatin (Gel-Ty) hydrogel. The fabricated NC hydrogel (Gel-Ty/G-NAC) supported human adipose-derived stem cell growth. Moreover, G-NAC had a crucial role in promoting osteo-differentiation and stimulating bone regeneration. This group suggested Gel-Ty/G-NAC hydrogels as a biodegradable platform in bone-related applications such as bone treatment, drug delivery, and cell delivery. In another effort, methoxy (polyethylene glycol)-polyalanine (mPA), as a di-block copolymer based thermo-responsive hydrogel, was incorporated by superparamagnetic Fe_3O_4 (osteoinductive) and hydroxyapatite (osteoconductive) nanoparticles in various contents (Huang and Chu, 2019). Modulation of bone differentiation bio-markers, as well as bone mineralization enhancement, was the result of the inclusion of such nanoparticle combinations into the polypeptide hydrogel. Recently, a fully physically crosslinked

NC hydrogel based on polyacrylamide/cellulose nanofibers (PAM/CNF) was introduced (Niu et al., 2018). Initially, NC hydrogels were produced via radical polymerization and then further strengthened by ferric ions (from $FeCl_3$) via ionic interactions between the ferric ions and carboxyl groups on CNF. Hydrogen bonding and ionic interactions induced dual physical crosslinks in NC hydrogels, which in turn led to structures with enhanced stiffness and toughness, rapid recovery, and self-healing abilities.

CHIRALITY FUNCTIONALIZED NC HYDROGELS

In recent years, the fabrication of NC hydrogels, including functionalized NMs has been a hot button research topic (Kehr, 2016; Zhao et al., 2017; Motealleh et al., 2018; Zheng et al., 2018). The aim of NM functionalization can be, for example, the improvement of cell-scaffold interactions, the creation of crosslinking between organic polymer and NM, drug delivery, or the development of the self-healing ability. Meanwhile, using chiral biomolecules to functionalize NMs has gained significant attention due to the various impacts on cell behaviors. **Table 1** summarizes the research activities carried out on chirality functionalized systems i.e., NC hydrogels, hydrogels, and nanoparticles. In biological systems, the majority of the biologically significant molecules are chiral. For instance, natural proteins composed of laevorotatory (l-) amino acids. It is not yet known the reason why naturally-occurring proteins prefer only one of the chiral positions and under what criteria hemochorial molecules prefer selective interactions (Zheng et al., 2018).

In an attempt by Wang et al. to explore chiral effects on cell behavior, three chiral species including, l(d)-alanine, l(d)-valine, and l(d)-leucine were grafted onto silicon substrates (Wang et al., 2012). Fabricated chiral polymer brush films proved that chirality is effective for triggering cell differentiation and regulating multifold cell behaviors. In addition, l-films exhibited higher cytocompatibility. Zheng et al. reported the impact of chirality on function and fate of stem cells in fibrous hydrogels including self-assembled l-and d-form Fmoc-Phe-Phe-Cys networks which were photocrosslinked with poly (ethylene glycol) (l- and d-gel), respectively. Encapsulating human bone marrow-derived mesenchymal stem cells in hydrogels, it was found that cells tended to spread and grow in the l-gel (**Figure 1B**; Zheng et al., 2018). Using simultaneous opposite enantiomers in so-called Janus NC hydrogels was explored by Motealleh et al. (2018) to observe the reaction of healthy and cancer cells to a single biomaterial under the same condition. They used enantiomers of biodegradable poly-d (l)-lysine (PDL and PLL) to the functionalized external surface of zeolites and periodic mesoporous organosilicas (PMOs). Their findings showed higher affinity and migration of cells to the portion of the Janus NC hydrogel including the biopolymer enantiomer that the cells opt. In another contribution, Shefi et al. coated chiral d (l)-cysteine onto gold self-assembled monolayers and explored chirality influence on neuronal structure and adhesion (**Figure 1C**) (Baranes et al., 2014). Kehr et al. (2013)

System	Bioactive molecule	The objective of the research	References
Chiral brush polymer films (three amino acids with different hydrophobic side groups grafted into silicon substrate)	l(d)-alanine, l(d)-valine, and l(d)-leucine	Interaction of chiral units with cells and other biological entities	Wang et al., 2012
The ultra-short peptide, photocrosslinked by poly(ethylene glycol) dimethacrylate	cystatin-ended Fmoc-FF (l- and d-Fmoc-FFC)	Effect of chirality on function and fate of stem cells	Zheng et al., 2018
Surface functionalized Zeolites and Periodic mesoporous organosilicas in Janus NC hydrogel	poly-d (l)-lysine	The reaction of healthy and cancer cells to a single biomaterial	Motealleh et al., 2018
Gold self-assembled monolayers	d (l)-cysteine	Chirality effect on the neuronal morphology and adhesion	Baranes et al., 2014
Periodic mesoporous organosilica particles (PMO)/Alginate	tripeptide Arg-Gly-Asp (RGD)	Developing NC hydrogels with enhanced mechanical and biological properties	Kehr et al., 2013
Alginate/periodic mesoporous organosilica (PMO)	aminoacid d(l)-penicillamine/carbohydrate mannose derivative d(l)-	ECM-model (for cell adhesion and cell enrichment) and drug delivery system	Kehr, 2016
Plasmonic chiral Au nanoparticle	l(d)- penicillamine (PEN)	Facilitating the cell culture in biomedical application	Zhao et al., 2017
Zeolite l nanocrystals	Fluorescent dye molecules	Controlling the movement of pathogenic bacteria/Removing the bacteria from a solution	Kehr et al., 2014
Alginate	d(l)-penicillamine (PEN)	Developing novel 3D scaffolds for cell adhesion investigations	Benson et al., 2014

prepared PMOs/ biodegradable alginate-based NC hydrogels in which POMs were functionalized with cell adhesive bioactive tripeptide Arg-Gly-Asp (RGD) molecules (Kehr et al., 2013). The incorporation of PMOs only improved the mechanical properties of the alginate-based NC hydrogel marginally, however, the inclusion of biomolecule functionalized PMOs significantly increased the quantity of live cells which adhered to the NC hydrogel scaffold (**Figure 1D**). In another study, Kehr reported the development of multifunctional 3D NC hydrogels composed of enantiomerically functionalized PMOs [with amino acid d(l)-penicillamine (PEN) and carbohydrate mannose derivative d(l)-MAN)] and biodegradable alginate as ECM-model (for cell adhesion and cell enrichment) and drug delivery system (**Figure 1E**; Kehr, 2016). In another contribution, Au l(d)-penicillamine (Pen) was employed to modify plasmonic chiral nanoparticle films (PEN-NP films) by Zhao et al. (2017). It was found that l-PEN-NP films accelerated cell proliferation, while d-PEN-NP films behaved in the opposite manner. The preparation of functionalized zeolites and its effect on cell adhesion was also studied by Kehr et al. (2014).

NANO-SCALED CELLULOSE: A ROBUST NANOMATERIAL

Till date, a variety of NMs based on silica, carbon, gold, iron oxide, calcium phosphate, cellulose nanocrystals, and chitin whiskers have been used to develop mechanically strong biodegradable NC hydrogels with enhanced cell activities, and/or for drug release applications (Motealleh and Kehr, 2017). Among the various NMs, NSC has attracted great attention within recent years (Enayati et al., 2019). Since 2000 to the present, publications show significant growth in developing cellulose-based hydrogels for tissue engineering (Trache et al.,

2017; Dutta et al., 2019). Besides the good biocompatibility and biodegradability, NSCs, derived from abundant and renewable resources, have high elastic moduli (110–220 GPa) and tensile strength (7.5–7.7 GPa), low density, high aspect ratio and surface area. These characteristics dramatically enhance their possible applications in the biomedical and tissue engineering fields. Usov et al. (2015) also studied structurally the rod-like cellulose nanoparticles and proved their right-handed chirality. Furthermore, due to the high concentration of hydroxyl groups on cellulose chains, the NSC's surface can be modified in myriad ways, i.e., oxidation, esterification, etherification, silylation, or polymer grafting—consequently, it can play multifunctional roles such as bioactive molecule container, reinforcing agent, and cross-linker. From another point of view, chemical isolation via sulfuric acid hydrolysis inserts negatively charged sulfate ester groups on the NSC's surface. This is a positive characteristic for NSC-functionalized NC hydrogels as they resemble native ECM sulfated glycosaminoglycans which stimulate and tune microscale cell functionalities (Domingues et al., 2015). In recent years, some notable research has been carried out on cellulose-based composite hydrogels. In the following paragraph, the most recent literature on research conducted on NSC-based NC hydrogels is highlighted.

Pereira et al. (2018) studied gellan-gum hydrogels reinforced by nanocellulose for the regeneration of annulus fibrous (AF) tissue. Upon nanocellulose incorporation, the compressive modulus of NC hydrogels approximated natural AF tissue. *In vitro* cell studies also demonstrated cell viability promotion. In another contribution, Phogat and Bandyopadhyay-Ghosh developed injectable bio-NC hydrogels of ultrafine fluorcanasite glass-ceramic particles incorporated into nanocellulose with enhanced stiffness, injectability, swelling behavior, and structural integrity (Phogat and Bandyopadhyay-Ghosh, 2018). Recently,

Cheng et al. exploited chitosan-cellulose nanofiber self-healing hydrogels for neural regeneration. Improved neural differentiation and oxygen metabolism were observed upon embedding neural stem cells (Cheng et al., 2019). In other study by Li et al. (2018) polyacrylamide grafted cellulose nanocrystals (CNC-g-PAM), as physical crosslinkers and interfacial compatible nanofillers, were incorporated into poly(acrylic acid) to develop NC hydrogels. NC hydrogels showed significant improvement in tensile properties and self-recovery ability compared to the pure poly(acrylic acid) hydrogel. In a new effort to develop self-healing cellulose NC hydrogels, Xiao et al. (2019) exploited acylhydrazine-terminated polyethylene glycol to crosslink dialdehyde cellulose nanocrystals. Apart from an increase in the tensile and compressive strength of the hydrogel, self-healing efficiency, and biocompatibility of the hydrogel improved by 90 and 100%, respectively. Three-dimensional bioprinted constructs composed of either alginate/cellulose nanocrystals or alginate/cellulose nanocrystals containing fibroblast and hepatoma cells, namely bioinks, were introduced by Wu et al. as liver-mimetic platforms (Wu et al., 2018). The bioprinted constructs were crosslinked by CaCl$_2$. It was reported that prepared hydrogels had shear storage moduli of 8–300 Pa and cell viability higher than 67%. The NC hydrogels of polyurethane/cellulose nanofibers were also fabricated by Chen et al., through the bioprinting process (Chen et al., 2019). The 3D-printed NC hydrogels exhibited a compression storage modulus of ~1.57 MPa and demonstrated excellent mouse and human fibroblast cell proliferation. In addition, taking into account the noteworthy features of NSCs, recently, self-healing hydrogels have been developed by the incorporation of cellulose nanocrystals within the poly(acrylic acid) mediated hydrogels. It was shown that incorporation of surface-modified CNC resulted in self-healing properties with up to ~90% self-healing efficiency (Bai et al., 2019).

CONCLUSION AND PERSPECTIVES

This article reviews the progress in the development of biodegradable nanocomposite (NC) hydrogels with an emphasis on the chiral functionalized nanomaterials to provide a perspective for future research in the field. Due to the outstanding features of nano-scaled cellulose (NSC), one promising future direction of chiral functionalized NC hydrogels can be the application of this renewable, cheap, biocompatible, and biodegradable nanomaterial in developing the next generation of biotherapeutic materials. There is also much potential in the development of multi-functionalized NSC. On the one hand, it can function as a physical and chemical crosslinker in the fabrication of NC hydrogels and act as a reinforcing agent due to its significant mechanical strength. On the other hand, its surface modification with chiral biomolecules will allow the fabrication of novel biodegradable NC hydrogels as an advanced model implant for both tissue engineering and drug delivery systems. Furthermore, with some chemical modifications on the NSC, it would be possible to induce self-healing ability in the prepared hydrogels for autonomous self-healing and minimum invasive implantation.

AUTHOR CONTRIBUTIONS

RE, ME, and ZP summarized literature and wrote a major part of the manuscript. PS and SR conducted deep review, editing, guidance, and supervision. All authors have read and approved the article for publication.

ACKNOWLEDGMENTS

REFERENCES

Bae, K. H., Wang, L.-S., and Kurisawa, M. (2013). Injectable biodegradable hydrogels: progress and challenges. *J. Mater. Chem.* 1, 5371–5388. doi: 10.1039/c3tb20940g

Bai, L., Jiang, X., Sun, Z., Pei, Z., Ma, A., Wang, W., et al. (2019). Self-healing nanocomposite hydrogels based on modified cellulose nanocrystals by surface-initiated photoinduced electron transfer ATRP. *Cellulose* 26, 5305–5319. doi: 10.1007/s10570-019-02449-2

Bakaic, E., Smeets, N. M. B., and Hoare, T. (2015). Injectable hydrogels based on poly(ethylene glycol) and derivatives as functional biomaterials. *RSC Adv.* 5, 35469–35486. doi: 10.1039/C4RA13581D

Baranes, K., Moshe, H., Alon, N., Schwartz, S., and Shefi, O. (2014). Neuronal growth on l- and d-cysteine self-assembled monolayers reveals neuronal chiral sensitivity. *ACS Chem. Neurosci.* 5, 370–376. doi: 10.1021/cn500015s

Benson, K., Galla, H. J., and Kehr, N. S. (2014). Cell adhesion behavior in 3D hydrogel scaffolds functionalized with D-or L-aminoacids. *Macromol. Biosci.* 14, 793–798. doi: 10.1002/mabi.201300485

Billiet, T., Vandenhaute, M., Schelfhout, J., Van Vlierberghe, S., and Dubruel, P. (2012). A review of trends and limitations in hydrogel-rapid prototyping for tissue engineering. *Biomaterials* 33, 6020–6041. doi: 10.1016/j.biomaterials.2012.04.050

Chen, R.-D., Huang, C.-F., and Hsu, S.-H. (2019). Composites of waterborne polyurethane and cellulose nanofibers for 3D printing and bioapplications. *Carbohydr. Polym.* 212, 75–88. doi: 10.1016/j.carbpol.2019.02.025

Cheng, K.-C., Huang, C.-F., Wei, Y., and Hsu, S.-H. (2019). Novel chitosan–cellulose nanofiber self-healing hydrogels to correlate self-healing properties of hydrogels with neural regeneration effects. *NPG Asia Mater.* 11:25. doi: 10.1038/s41427-019-0124-z

Cui, Z.-K., Kim, S., Baljon, J. J., Wu, B. M., Aghaloo, T., and Lee, M. (2019). Microporous methacrylated glycol chitosan-montmorillonite nanocomposite hydrogel for bone tissue engineering. *Nat. Commun.* 10:3523. doi: 10.1038/s41467-019-11511-3

Curvello, R., Raghuwanshi, V. S., and Garnier, G. (2019). Engineering nanocellulose hydrogels for biomedical applications. *Adv. Colloid Interface Sci.* 267, 47–61. doi: 10.1016/j.cis.2019.03.002

Domingues, R. M., Silva, M., Gershovich, P., Betta, S., Babo, P., Caridade, S. G., et al. (2015). Development of injectable hyaluronic acid/cellulose nanocrystals bionanocomposite hydrogels for tissue engineering applications. *Bioconjug. Chem.* 26, 1571–1581. doi: 10.1021/acs.bioconjchem.5b00209

Dutta, S. D., Patel, D. K., and Lim, K.-T. (2019). Functional cellulose-based hydrogels as extracellular matrices for tissue engineering. *J. Biol. Eng.* 13:55. doi: 10.1186/s13036-019-0177-0

Enayati, M. S., Neisiany, R. E., Sajkiewicz, P., Behzad, T., Denis, P., and Pierini, F. (2019). Effect of nanofiller incorporation on thermomechanical and toughness of poly (vinyl alcohol)-based electrospun nanofibrous bionanocomposites. *Theor. Appl. Fract. Mech.* 99, 44–50. doi: 10.1016/j.tafmec.2018.11.006

Fang, Y., Wang, C.-F., Zhang, Z.-H., Shao, H., and Chen, S. (2013). Robust self-healing hydrogels assisted by cross-linked nanofiber networks. *Sci. Rep.* 3:2811. doi: 10.1038/srep02811

Gaharwar, A. K., Peppas, N. A., and Khademhosseini, A. (2014). Nanocomposite hydrogels for biomedical applications. *Biotechnol. Bioeng.* 111, 441–453. doi: 10.1002/bit.25160

Gullberg, D., and Ekblom, P. (1995). Extracellular matrix and its receptors during development. *Int. J. Dev. Biol.* 39, 845–854.

Hao, Y., Zhou, X., Shao, J., and Zhu, Y. (2019). The influence of multiple fillers on friction and wear behavior of epoxy composite coatings. *Surf. Coat. Tech.* 362, 213–219. doi: 10.1016/j.surfcoat.2019.01.110

Hu, X., Gao, Z., Tan, H., Wang, H., Mao, X., and Pang, J. (2019). An injectable hyaluronic acid-based composite hydrogel by DA click chemistry with pH sensitive nanoparticle for biomedical application. *Front. Chem.* 7:477. doi: 10.3389/fchem.2019.00477

Huang, W.-S., and Chu, I.-M. (2019). Injectable polypeptide hydrogel/inorganic nanoparticle composites for bone tissue engineering. *PLoS ONE* 14:e0210285. doi: 10.1371/journal.pone.0210285

Jin, Y., Shen, Y., Yin, J., Qian, J., and Huang, Y. (2018). Nanoclay-based self-supporting responsive nanocomposite hydrogels for printing applications. *ACS Appl. Mater. Interfaces* 10, 10461–10470. doi: 10.1021/acsami.8b00806

Jing, Z., Xu, A., Liang, Y.-Q., Zhang, Z., Yu, C., Hong, P., et al. (2019). Biodegradable Poly(acrylic acid-co-acrylamide)/Poly(vinyl alcohol) double network hydrogels with tunable mechanics and high self-healing performance. *Polymers* 11:952. doi: 10.3390/polym11060952

Kehr, N. S. (2016). Enantiomorphous periodic mesoporous organosilica-based nanocomposite hydrogel scaffolds for cell adhesion and cell enrichment. *Biomacromolecules* 17, 1117–1122. doi: 10.1021/acs.biomac.5b01739

Kehr, N. S., Atay, S., and Ergün, B. (2015). Self-assembled monolayers and nanocomposite hydrogels of functional nanomaterials for tissue engineering applications. *Macromol. Biosci.* 15, 445–463. doi: 10.1002/mabi.201400363

Kehr, N. S., Ergün, B., Lülf, H., and De Cola, L. (2014). Spatially controlled channel entrances functionalization of zeolites L. *Adv. Mater.* 26, 3248–3252. doi: 10.1002/adma.201305745

Kehr, N. S., Prasetyanto, E. A., Benson, K., Ergün, B., Galstyan, A., and Galla, H. J. (2013). Periodic mesoporous organosilica-based nanocomposite hydrogels as three-dimensional scaffolds. *Angew. Chem. Int. Ed.* 52, 1156–1160. doi: 10.1002/anie.201206951

Kock, L., Van Donkelaar, C. C., and Ito, K. (2012). Tissue engineering of functional articular cartilage: the current status. *Cell Tissue Res.* 347, 613–627. doi: 10.1007/s00441-011-1243-1

Kumar, B. Y. S., Isloor, A. M., Kumar, G. C. M., Inamuddin, and Asiri, A. M. (2019). Nanohydroxyapatite reinforced chitosan composite hydrogel with tunable mechanical and biological properties for cartilage regeneration. *Sci. Rep.* 9:15957. doi: 10.1038/s41598-019-52042-7

Lee, D., Heo, D. N., Nah, H. R., Lee, S. J., Ko, W.-K., Lee, J. S., et al. (2018). Injectable hydrogel composite containing modified gold nanoparticles: implication in bone tissue regeneration. *Int. J. Nanomed.* 13:7019–7031. doi: 10.2147/IJN.S185715

Li, B., Zhang, Y., Wu, C., Guo, B., and Luo, Z. (2018). Fabrication of mechanically tough and self-recoverable nanocomposite hydrogels from polyacrylamide grafted cellulose nanocrystal and poly(acrylic acid). *Carbohydr. Polym.* 198, 1–8. doi: 10.1016/j.carbpol.2018.06.047

Mohammadzadehmoghadam, S., and Dong, Y. (2019). Fabrication and characterization of electrospun silk fibroin/Gelatin Scaffolds crosslinked with glutaraldehyde vapor. *Front. Mater.* 6:91. doi: 10.3389/fmats.2019.00091

Motealleh, A., Hermes, H., Jose, J., and Kehr, N. S. (2018). Chirality-dependent cell adhesion and enrichment in Janus nanocomposite hydrogels. *Nanomedicine* 14, 247–256. doi: 10.1016/j.nano.2017.10.014

Motealleh, A., and Kehr, N. S. (2017). Nanocomposite hydrogels and their applications in tissue engineering. *Adv. Healthc. Mater.* 6:1600938. doi: 10.1002/adhm.201600938

Nezhad-Mokhtari, P., Ghorbani, M., Roshangar, L., and Soleimani Rad, J. (2019). A review on the construction of hydrogel scaffolds by various chemically techniques for tissue engineering. *Eur. Polym. J.* 117, 64–76. doi: 10.1016/j.eurpolymj.2019.05.004

Niemczyk, B., Sajkiewicz, P., and Kolbuk, D. (2018). Injectable hydrogels as novel materials for central nervous system regeneration. *J. Neural Eng.* 15:051002. doi: 10.1088/1741-2552/aacbab

Niu, J., Wang, J., Dai, X., Shao, Z., and Huang, X. (2018). Dual physically crosslinked healable polyacrylamide/cellulose nanofibers nanocomposite hydrogels with excellent mechanical properties. *Carbohydr. Polym.* 193, 73–81. doi: 10.1016/j.carbpol.2018.03.086

Pereira, D. R., Silva-Correia, J., Oliveira, J. M., Reis, R. L., Pandit, A., and Biggs, M. J. (2018). Nanocellulose reinforced gellan-gum hydrogels as potential biological substitutes for annulus fibrosus tissue regeneration. *Nanomedicine* 14, 897–908. doi: 10.1016/j.nano.2017.11.011

Phogat, K., and Bandyopadhyay-Ghosh, S. (2018). Nanocellulose mediated injectable bio-nanocomposite hydrogel scaffold-microstructure and rheological properties. *Cellulose* 25, 5821–5830. doi: 10.1007/s10570-018-2001-2

Rafieian, S., Mirzadeh, H., Mahdavi, H., and Masoumi, M. E. (2019). A review on nanocomposite hydrogels and their biomedical applications. *Sci. Eng. Compos. Mater.* 26, 154–174. doi: 10.1515/secm-2017-0161

Rao, Z., Liu, S., Wu, R., Wang, G., Sun, Z., Bai, L., et al. (2019). Fabrication of dual network self-healing alginate/guar gum hydrogels based on polydopamine-type microcapsules from mesoporous silica nanoparticles. *Int. J. Biol. Macromol.* 129, 916–926. doi: 10.1016/j.ijbiomac.2019.02.089

Rasoulzadeh, M., and Namazi, H. (2017). Carboxymethyl cellulose/graphene oxide bio-nanocomposite hydrogel beads as anticancer drug carrier agent. *Carbohydr. Polym.* 168, 320–326. doi: 10.1016/j.carbpol.2017.03.014

Sanka, R. V. S. P., Krishnakumar, B., Leterrier, Y., Pandey, S., Rana, S., and Michaud, V. (2019). Soft self-healing nanocomposites. *Front. Mater.* 6:137. doi: 10.3389/fmats.2019.00137

Schexnailder, P., and Schmidt, G. (2009). Nanocomposite polymer hydrogels. *Colloid Polym. Sci.* 287, 1–11. doi: 10.1007/s00396-008-1949-0

Servant, A., Leon, V., Jasim, D., Methven, L., Limousin, P., Fernandez-Pacheco, E. V., et al. (2014). Graphene-based electroresponsive scaffolds as polymeric implants for on-demand drug delivery. *Adv. Healthc. Mater.* 3, 1334–1343. doi: 10.1002/adhm.201400016

Sharma, G., Thakur, B., Naushad, M., Kumar, A., Stadler, F. J., Alfadul, S. M., et al. (2018). Applications of nanocomposite hydrogels for biomedical engineering and environmental protection. *Environ. Chem. Lett.* 16, 113–146. doi: 10.1007/s10311-017-0671-x

Song, F., Li, X., Wang, Q., Liao, L., and Zhang, C. (2015). Nanocomposite hydrogels and their applications in drug delivery and tissue engineering. *J. Biomed. Nanotechnol.* 11, 40–52. doi: 10.1166/jbn.2015.1962

Tan, H., and Marra, K. G. (2010). Injectable, biodegradable hydrogels for tissue engineering applications. *Materials* 3, 1746–1767. doi: 10.3390/ma3031746

Tan, H.-L., Teow, S.-Y., and Pushpamalar, J. (2019). Application of metal nanoparticle-hydrogel ydrogel composites in tissue regeneration. *Bioengineering* 6:E17. doi: 10.3390/bioengineering6010017

Tanan, W., Panichpakdee, J., and Saengsuwan, S. (2019). Novel biodegradable hydrogel based on natural polymers: Synthesis, characterization, swelling/reswelling and biodegradability. *Eur. Polym. J.* 112, 678–687. doi: 10.1016/j.eurpolymj.2018.10.033

Tarashi, S., Nazockdast, H., and Sodeifian, G. (2019). Reinforcing effect of graphene oxide on mechanical properties, self-healing performance and recoverability of double network hydrogel based on κ-carrageenan and polyacrylamide. *Polymer* 183:121837. doi: 10.1016/j.polymer.2019.121837

Thürmer, M. B., Diehl, C. E., Brum, F. J. B., and Santos, L. A. D. (2014). Preparation and characterization of hydrogels with potential for use as biomaterials. *Mater. Res.* 17, 109–113. doi: 10.1590/1516-1439.223613

Toledo, L., Racine, L., Pérez, V., Henríquez, J. P., Auzely-Velty, R., and Urbano, B. F. (2018). Physical nanocomposite hydrogels filled with low concentrations of TiO2 nanoparticles: swelling, networks parameters and cell retention studies. *Mater. Sci. Eng. C Mater. Biol. Appl.* 92, 769–778. doi: 10.1016/j.msec.2018.07.024

Trache, D., Hussin, M. H., Haafiz, M. M., and Thakur, V. K. (2017). Recent progress in cellulose nanocrystals: sources and production. *Nanoscale* 9, 1763–1786. doi: 10.1039/C6NR09494E

Tu, Y., Chen, N., Li, C., Liu, H., Zhu, R., Chen, S., et al. (2019). Advances in injectable self-healing biomedical hydrogels. *Acta Biomater.* 90, 1–20. doi: 10.1016/j.actbio.2019.03.057

Usov, I., Nyström, G., Adamcik, J., Handschin, S., Schütz, C., Fall, A., et al. (2015). Understanding nanocellulose chirality and structure–properties relationship at the single fibril level. *Nat. Commun.* 6:7564. doi: 10.1038/ncomms8564

Vashist, A., Kaushik, A., Ghosal, A., Bala, J., Nikkhah-Moshaie, R., A Wani, W., et al. (2018). Nanocomposite hydrogels: advances in nanofillers used for nanomedicine. *Gels* 4:E75. doi: 10.3390/gels4030075

Wang, S., Zhang, Z., Chen, B., Shao, J., and Guo, Z. (2018). Self-healing hydrogel of poly(vinyl alcohol)/graphite oxide with pH-sensitive and enhanced thermal properties. *J. Appl. Polym. Sci.* 135:46143. doi: 10.1002/app.46143

Wang, X., Gan, H., Zhang, M., and Sun, T. (2012). Modulating cell behaviors on chiral polymer brush films with different hydrophobic side groups. *Langmuir* 28, 2791–2798. doi: 10.1021/la204143g

Wu, Y., Lin, Z. Y., Wenger, A. C., Tam, K. C., and Tang, X. (2018). 3D bioprinting of liver-mimetic construct with alginate/cellulose nanocrystal hybrid bioink. *Bioprinting* 9, 1–6. doi: 10.1016/j.bprint.2017.12.001

Xiao, G., Wang, Y., Zhang, H., Chen, L., and Fu, S. (2019). Facile strategy to construct a self-healing and biocompatible cellulose nanocomposite hydrogel via reversible acylhydrazone. *Carbohydr. Polym.* 218, 68–77. doi: 10.1016/j.carbpol.2019.04.080

Xu, T., Miszuk, J. M., Zhao, Y., Sun, H., and Fong, H. (2015). Electrospun polycaprolactone 3D nanofibrous scaffold with interconnected and hierarchically structured pores for bone tissue engineering. *Adv. Healthc. Mater.* 4, 2238–2246. doi: 10.1002/adhm.201500345

Zagris, N. (2001). Extracellular matrix in development of the early embryo. *Micron* 32, 427–438. doi: 10.1016/S0968-4328(00)00011-1

Zhang, Y., Venugopal, J., Huang, Z.-M., Lim, C., and Ramakrishna, S. (2005). Characterization of the surface biocompatibility of the electrospun PCL-collagen nanofibers using fibroblasts. *Biomacromolecules* 6, 2583–2589. doi: 10.1021/bm050314k

Zhao, X., Xu, L., Sun, M., Ma, W., Wu, X., Xu, C., et al. (2017). Tuning the interactions between chiral plasmonic films and living cells. *Nat. Commun.* 8:2007. doi: 10.1038/s41467-017-02268-8

Zheng, H., Yoshitomi, T., and Yoshimoto, K. (2018). Analysis of chirality effects on stem cell fate using three-dimensional fibrous peptide hydrogels. *ACS Appl. Bio Mater.* 1, 538–543. doi: 10.1021/acsabm.8b00123

Conflict of Interest: The authors declare that the research was conducted in the absence of any commercial or financial relationships that could be construed as a potential conflict of interest.

Advantages of publishing in Frontiers

OPEN ACCESS
Articles are free to read for greatest visibility and readership

FAST PUBLICATION
Around 90 days from submission to decision

HIGH QUALITY PEER-REVIEW
Rigorous, collaborative, and constructive peer-review

TRANSPARENT PEER-REVIEW
Editors and reviewers acknowledged by name on published articles

REPRODUCIBILITY OF RESEARCH
Support open data and methods to enhance research reproducibility

DIGITAL PUBLISHING
Articles designed for optimal readership across devices

FOLLOW US
@frontiersin

IMPACT METRICS
Advanced article metrics track visibility across digital media

EXTENSIVE PROMOTION
Marketing and promotion of impactful research

LOOP RESEARCH NETWORK
Our network increases your article's readership